ASME
SETTING THE STANDARD

Journal of Engineering for Gas Turbines and Power

Published Bimonthly by ASME

VOLUME 130 • NUMBER 3 • MAY 2008

Transactions of the ASME, Journal of Engineering for Gas Turbines and Power (ISSN 0742-4795) is published bimonthly (Jan., Mar., May, July, Sep, Nov.) by The American Society of Mechanical Engineers, Three Park Avenue, New York, NY 10016. Periodicals postage paid at New York, NY and additional mailing offices. POSTMASTER: Send address changes to Transactions of the ASME, Journal of Engineering for Gas Turbines and Power, c/o THE AMERICAN SOCIETY OF MECHANICAL ENGINEERS, 22 Law Drive, Box 2300, Fairfield, NJ 07007-2300.
CHANGES OF ADDRESS must be received at Society headquarters seven weeks before they are to be effective. Please send old label and new address.
STATEMENT from By-Laws. The Society shall not be responsible for statements or opinions advanced in papers or ... printed in its publications (B7.1, par. 3).

RESEARCH PAPERS

(Contents continued on inside back cover)

This journal is printed on acid-free paper, which exceeds the ANSI Z39.48-1992 specification for permanence of paper and library materials. ♾™
♻ 85% recycled content, including 10% post-consumer fibers.

(Contents continued)

Journal of Engineering for Gas Turbines and Power MAY 2008

Volume 130, Number 3

(Contents continued on facing page)

Journal of Engineering for Gas Turbines and Power MAY 2008

Volume 130, Number 3

The ASME Journal of Engineering for Gas Turbines and Power is abstracted and indexed in the following:

AESIS (Australia's Geoscience, Minerals, & Petroleum Database), Applied Science & Technology Index, Aquatic Sciences and Fisheries Abstracts, Civil Engineering Abstracts, Compendex (The electronic equivalent of Engineering Index), Computer & Information Systems Abstracts, Corrosion Abstracts, Current Contents, Engineered Materials Abstracts, Engineering Index, Enviroline (The electronic equivalent of Environment Abstracts), Environment Abstracts, Environmental Science and Pollution Management, Fluidex, INSPEC, Mechanical & Transportation Engineering Abstracts, Mechanical Engineering Abstracts, METADEX (The electronic equivalent of Metals Abstracts and Alloys Index), Pollution Abstracts, Referativnyi Zhurnal, Science Citation Index, SciSearch (The electronic equivalent of Science Citation Index), Shock and Vibration Digest

Interlaminar Crack Growth Resistances of Various Ceramic Matrix Composites in Mode I and Mode II Loading

Sung R. Choi[1]
e-mail: sung.choi1@navy.mil

Robert W. Kowalik

Naval Air Systems Command,
Patuxent River, MD 20670

Interlaminar crack growth resistances were evaluated for five different SiC fiber-reinforced ceramic matrix composites (CMCs) including three gas-turbine grade melt-infiltrated SiC/SiC composites. Modes I and II crack growth resistances, G_I and G_{II}, were determined at ambient temperature using double cantilever beam and end notched flexure methods, respectively. The CMCs exhibited $G_I = 200–500\ J/m^2$ and $G_{II} = 200–900\ J/m^2$. All the composites (except for one SiC/CAS composite) showed a rising R-curve behavior either in mode I or in mode II, presumably attributed to fiber bridging (in modes I and II) and frictional constraint (mode II) in the wake region of a propagating crack. A glass fiber-reinforced epoxy polymer matrix composite showed typically two to three times greater G_I and eight times greater G_{II}, compared to the CMCs. An experimental error analysis regarding the effect of the off-the-center of a crack plane on G_I and G_{II} was also made. [DOI: 10.1115/1.2800349]

Introduction

The successful development and design of continuous fiber-reinforced ceramic matrix composites (CMCs) are dependent on the understanding of their basic mechanical properties such as deformation, strength, fracture resistance, and delayed failure (fatigue, slow crack growth, or stress rupture) behavior. Although fiber-reinforced CMCs have shown improved resistance to fracture and increased damage tolerance compared with the monolithic ceramics, inherent material/processing defects or cracks in the matrix-rich interlaminar and/or interface regions can still cause delamination under interlaminar normal or shear stress, resulting in loss of stiffness or, in some cases, structural failure [1–4]. CMCs also have shown life limiting susceptibility even in interlaminar shear, particularly at elevated temperatures, resulting in time-dependent strength degradation or shortening of component life [5,6].

In a previous study [7], both interlaminar tensile and shear strengths were determined for six different SiC fiber-reinforced CMCs at ambient temperature. The CMCs, 2D woven or cross plied, exhibited poor interlaminar properties with interlaminar shear strength of 30–50 MPa and interlaminar tensile strength of 10–20 MPa. The interlaminar shear strength was two to three times greater than the interlaminar (or transthickness) tensile strength [7–10], implying a difference in crack growth resistance between modes I and II loading. Little work has been done for CMCs to determine systematically and simultaneously both modes I and II interlaminar crack growth resistances. Only limited data on mode II are found for CMCs from the literature [11]. This contrasts with polymer matrix composites (PMCs), where extensive data as well as analytical work on crack growth resistance have been found and accumulated for several decades [12–18].

The purpose of this work was to determine systematically both modes I and II crack growth resistances (G_I and G_{II}) at ambient temperature for four different SiC fiber-reinforced SiC/SiC CMCs and one SiC fiber-reinforced SiC/CAS (calcium aluminosilicate), including three gas-turbine grade melt-infiltrated (MI) SiC/SiC composites. Crack growth resistances G_I and G_{II} were evaluated with the compliance approach using double cantilever beam (DCB) and end notched flexure (ENF) methods, respectively. A 2D woven glass fiber-reinforced epoxy matrix composite was also used for comparison. The microstructural aspects of the composites were characterized to better understand mechanisms related to crack propagation under different modes of loading. Experimental error analysis regarding the effect of the off-the-center of a crack plane on crack growth resistance was also made.

Experimental Procedures

Materials. Five different SiC fiber-reinforced CMCs, four SiC/SiCs and one SiC/glass ceramic, were used in this study. These include 2D woven MI Hi-Nicalon™ fiber-reinforced SiC (designated as Hi-Nic SiC/SiC), 2D woven MI Sylramic™ fiber-reinforced SiC (designated as S-SiC/SiC), 2D woven MI Nicalon™ fiber-reinforced SiC (designated as U-SiC/SiC), 2D plain-woven Nicalon™ fiber-reinforced SiC (designated as SiC/SiC ('90)), and 1D Nicalon™ fiber-reinforced calcium aluminosilicate (designated SiC/CAS). Note that Hi-Nic SiC/SiC, S-SiC/SiC, and U-SiC/SiC were for gas-turbine grade CMCs with upper temperature limits of 1200–1300°C [19,20]. Some information regarding preform descriptions and resulting laminates of the CMCs is summarized in Table 1. For comparison, a 2D woven glass-fiber-reinforced epoxy PMC was also used.

Briefly, the fiber cloth preforms in the MI SiC/SiC composites were stacked and chemically vapor infiltrated with a thin BN-based interface coating followed by SiC matrix overcoating. The remaining matrix porosity was filled with SiC particulates and then with molten silicon at 1400°C, a process termed slurry casting (SC) and melt infiltration [19]. Details regarding the processing of these CMCs can be found elsewhere [19]. The silicon carbide matrix in the SiC/SiC ('90) composite was processed through chemical vapor infiltration (CVI) into the fiber preforms. The SiC/CAS composite was fabricated through hot pressing followed by ceraming of the composite by a thermal process [22]. Some of the CMCs used in this work have been employed previously for determinations of time-dependent in-plane tensile and

[1]Corresponding author.

Contributed by the International Gas Turbine Institute of ASME for publication in the JOURNAL OF ENGINEERING FOR GAS TURBINES AND POWER. Manuscript received May 23, 2007; final manuscript received May 25, 2007; published online April 2, 2008. Review conducted by Dilip R. Ballal. Paper presented at the ASME Turbo Expo 2007: Land, Sea and Air (GT2007), Montreal, Quebec, Canada, May 14–17, 2007.

Table 1 Continuous SiC fiber-reinforced CMCs used in this work. (Fiber manufacturers: Nippon Carbon (Japan) for Materials 1,3–5; Dow Corning (Midland, MI) for Material 2. Composite manufacturers: General Electric Power System Composites (Newark, DL) for Materials 1–3; Du Pont (Newark, DL) for Material 4; Corning Inc. (Corning, NY) for Material 5.)

	Materials	Fiber volume fraction	Process and Laminates[a]	Elastic modulus E (GPa)[b]
1	Hi-Nic SiC/SiC ('02)	0.40	*i*BN;SC/MI;5HS;8 ply; t=2.1 mm;20 epi	183
2	S–SiC/SiC ('01)	0.39	*i*BN;SC/MI;5HS;8 ply, t=2.5 mm;20 epi	222
3	U–SiC/SiC ('02)	0.39	*i*BN;SC/MI;5HS;8 ply, t=2.1 mm;20 epi	195
4	SiC/SiC ('90)	0.39	CVI; plain woven;12 ply; t=3.4 mm	215
5	SiC/CAS ('90)	0.39	HP;18 ply;t=3.4 mm	137
6	Glass/epoxy PMC	0.30	30 ply;t=6.3 mm	23

[a]*i*BN: in situ boron nitride; SC: slurry casting; MI: melt infiltration; HS: harness satin; CVI: chemical vapor infiltration; HP: hot pressed; epi: ends per inch; t(=2 h): as-fabricated thickness.
[b]Elastic modulus E (in-plane) was determined by the impulse excitation of vibration technique, ASTM C 1259 [21].

interlaminar shear strength behaviors at elevated temperatures [6,7,23], foreign object damage (FOD) behavior [24], interlaminar shear and tensile properties at ambient temperature [7], etc.

Interlaminar Double Cantilever Beam (Mode I) and End Notched Flexure (Mode II) Tests. Modes I and II crack growth resistances (or called "energy release rates") were determined at ambient temperature in air by using DCB and ENF methods, respectively. The ENF method has been widely and commonly used for PMCs. It gives a significant simplicity in test and allows the use of the same test specimens as prepared for the DCB method. The nominal dimensions of both modes I and II test specimens were typically L=50 mm in length, b=10–13 mm in width, and t=2h=2.1–3.4 mm inthickness (see Fig. 1). The thickness of test specimens was the same as the as-fabricated, nominal thickness of each CMC panel (see Table 1).

A precrack was generated at one end of each test specimen along its interlaminar midplane using a specially designed precrack fixture together with a razor blade. A typical precrack length used was $a \geqslant 10$ mm either in DCB test specimens or in ENF test specimens. Each DCB test specimen precracked was loaded by a test frame at 0.25 mm/min in displacement control via pin-loaded grips. Crack propagation and crack mouth opening displacement (COD) were monitored using a traveling telescope and an extensometer, respectively. Force, crack length, and COD of each test specimen were in situ recorded during testing through a data acquisition system. For ENF testing, each specimen was loaded in a symmetric three-point flexure with a span length of 2S=40 mm (see Fig. 1) at 0.25 mm/min via the test frame that was used in DCB testing. Deflection of each test specimen at the load point was determined using a linear variable capacitance transducer (LVCT), and crack length was determined using the traveling telescope as well. Crack length measurements in DCB or ENF testing were greatly enhanced by using a thin coat of white correction fluid[2] applied to both sides of each test specimen. Typically, for a given material, a total of three to five test specimens were used for each test method. The DCB and ENF methods have been widely used to determine G_{I} and G_{II} of many unidirectional fiber-reinforced PMCs, although their recommended "precracking" procedure [25] is different from that used in this work for CMCs.

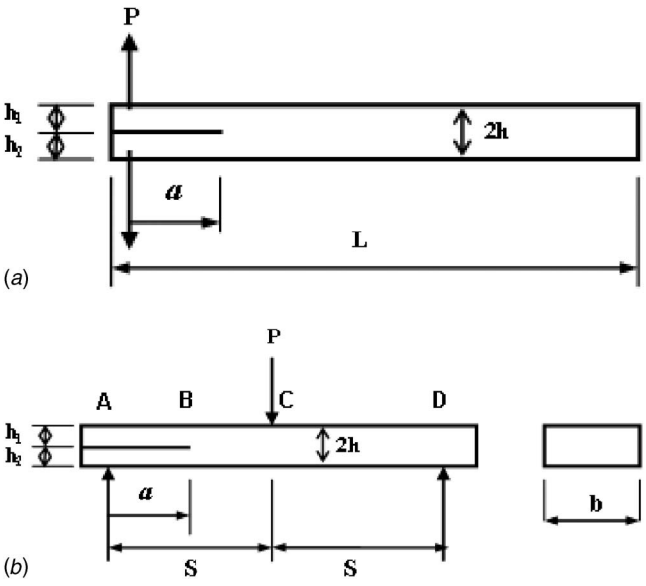

Fig. 1 Schematics of test specimen/loading configurations used in (*a*) DCB test for mode I and (*b*) ENF test for mode II

Results and Discussion

Modes I and II Interlaminar Crack Growth Resistances. In the compliance method, crack growth resistance (or energy release rate) in either mode I or mode II can be expressed as follows [26]:

$$G_{\mathrm{I}}, G_{\mathrm{II}} = \frac{P^2}{2b}\frac{\partial C}{\partial a} \tag{1}$$

where G_{I} and G_{II} are the energy release rate in mode I and II, respectively. P is the applied force, b is the test specimen's width (see Fig. 1), C is the compliance of a test specimen, and a is the crack length. This compliance method has been used to evaluate interlaminar crack growth resistance or interlaminar fracture toughness of PMCs [12–16,18,25]. Equation (1) can be further simplified using appropriate compliance relations based on the simple beam theory, pertinent to each of the specimen/loading configurations given in Fig. 1, as follows:

$$G_{\mathrm{I}} = \frac{3P^2C^{2/3}}{4A_1bh} \tag{2}$$

[2]It is not certain as to whether the use of correction fluid might induce stress corrosion cracking due to the presence of this material on the crack surfaces. However, the depth of penetration by this material was observed to be negligible as compared to the width (b) of test specimens so that the influence was believed to be insignificant. A study of stress corrosion behavior of the correction fluid using a stress-corrosion susceptible material such as glass would be of great interest.

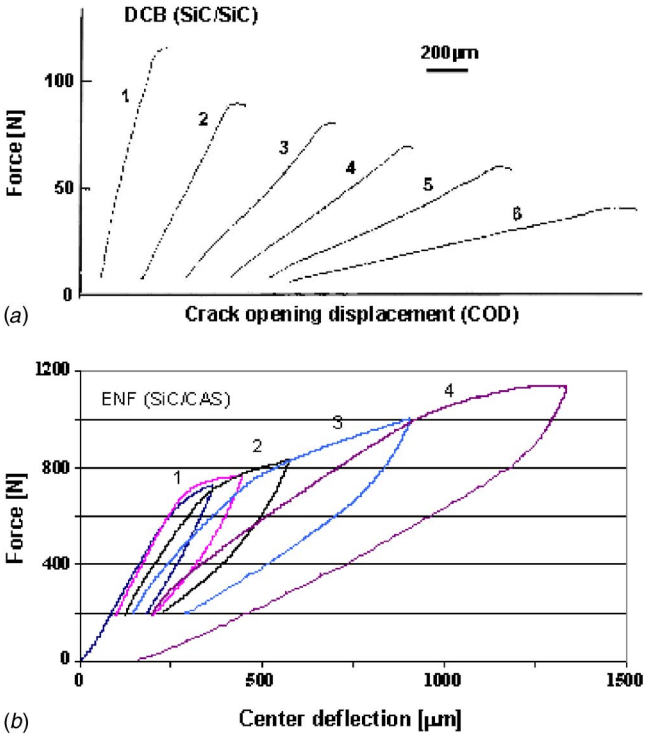

Fig. 2 Typical force versus displacement curves determined in (*a*) DCB (mode I) test for SiC/SiC ('90) and (*b*) ENF (mode II) test for SiC/CAS. Each curve numbered represents one loading(/unloading) sequence for a given crack length.

$$G_{II} = \frac{9a^2P^2C}{2b(2S^3 + 3a^3)} \tag{3}$$

which is the case for $h_1 = h_2 = h$. In either expression, the compliance C can be determined from force-versus-COD curves in mode I (DCB) and force-versus-deflection curves in mode II (ENF). The constant A_1 is a slope in the relation of normalized crack length $(a/2h)$ versus compliance $(C^{1/3})$, determined by a linear regression analysis. Equation (2) is one formula recommended in Ref. [25]. There are several different expressions of G_I or G_{II} in the literature, but they are essentially the same, but only in different forms. Equations (2) and (3) are based on the assumptions that two cantilever beams are rigidly fixed at their ends in DCB test specimens and that no shear deformation occurs in ENF test specimens. These assumptions are more relevant to CMC test specimens for their thin configurations and much higher elastic modulus, as compared to PMCs (see elastic modulus in Table 1).

Typical examples of force-versus-COD curves in mode I and force-versus-center deflection curves in mode II are depicted in Fig. 2. Linearity existed between force and COD or center deflection for a given crack length. Crack growth occurred after reaching the peak force in the linear region, followed by an increase in compliance with subsequent loading. Typical results of $a/2h$ versus $C^{1/3}$ in mode I and C versus $(a/S)^3$ in mode II for the S-SiC/SiC composite are shown in Fig. 3, where a linear relationship between the two related parameters holds with the coefficients of correlation of curve fit all greater than $r_{coef} > 0.99$. This linearity validates the use of Eqs. (2) and (3). However, some scatter, as seen in the figure, was inevitable among test specimens, implying the existence of a certain degree of material inhomogeneity.

It should be noted that ENF specimens, particularly for S-SiC/SiC and SiC/SiC ('90), were more difficult to test than DCB specimens when precrack lengths were less than 10 mm since undesirable flexure failure occurred frequently before the

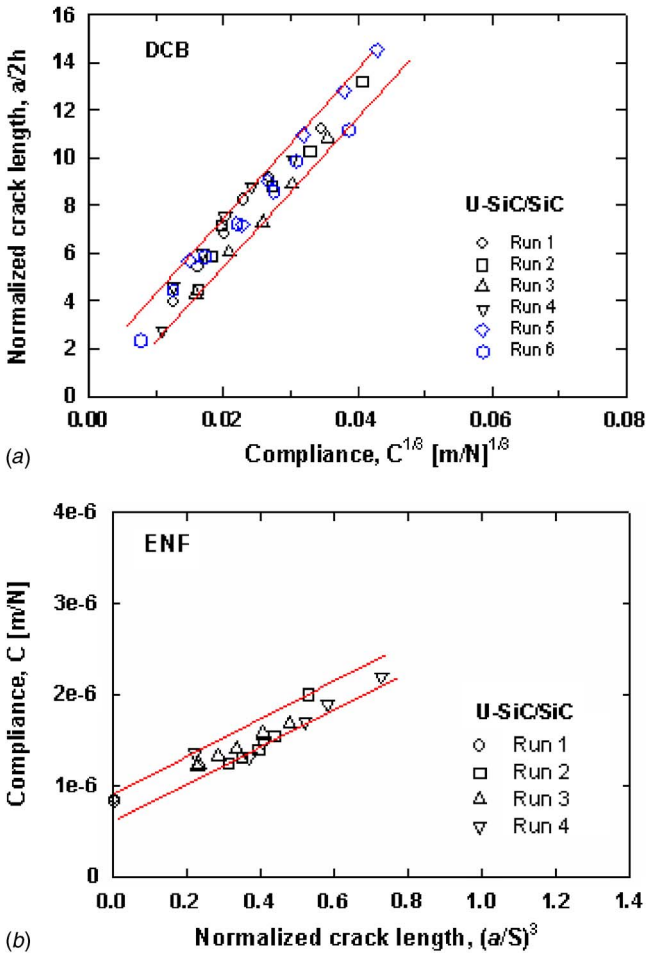

Fig. 3 Typical results of compliance-crack length relations determined for *U*-SiC/SiC composite: (*a*) normalized crack length (*a*/*t*) versus (compliance)$^{1/3}$ in DCB (mode I) and (*b*) compliance versus normalized crack length (*a*/*S*)^3 in ENF (mode II)

precrack propagated. It was also observed that for some CMCs a propagating crack, when approaching the load point $(a/S \approx 1)$, tended to deviate from the midplane toward the outside surface of an ENF specimen. Flexure failure was able to be mitigated by using a precrack length of $a/S \geq 0.5$, where mode II crack driving force (G_{II}) would be greater than mode I flexure-failure driving counterpart. As a result, the ENF test method was found to be effective in a range of $0.5 \leq a/S < 1.0$ for the CMCs used in this work.

A summary of energy release rates of G_I and G_{II} is shown in Figs. 4 and 5, where G_I was plotted as a function of crack length (a) while G_{II} was plotted as a function of normalized crack length (a/S). Except for the SiC/CAS composite, mode I interlaminar energy release rate (G_I) increased with increasing crack length, termed *R*-curve behavior, ranging from 200 J/m^2 to 500 J/m^2. G_I was greatest for the Hi-Nic SiC/SiC composite and appeared to be similar for the other three SiC/SiC composites. The SiC/CAS composite exhibited a flat *R* curve with a value of $G_I \approx 150$ J/m^2 and showed a much less scatter in data as compared with other CMCs. The glass/epoxy composite showed significant G_I ranging from 400 J/m^2 to 1200 J/m^2 with a rising *R* curve. G_I of the glass/epoxy composite was two to three times greater than that of the SiC/SiC composites.

Mode II interlaminar energy release rate (G_{II}) was similar in behavior to G_I, as seen in Fig. 5. All the composites exhibited a rising *R*-curve behavior, resulting in an overall G_{II}

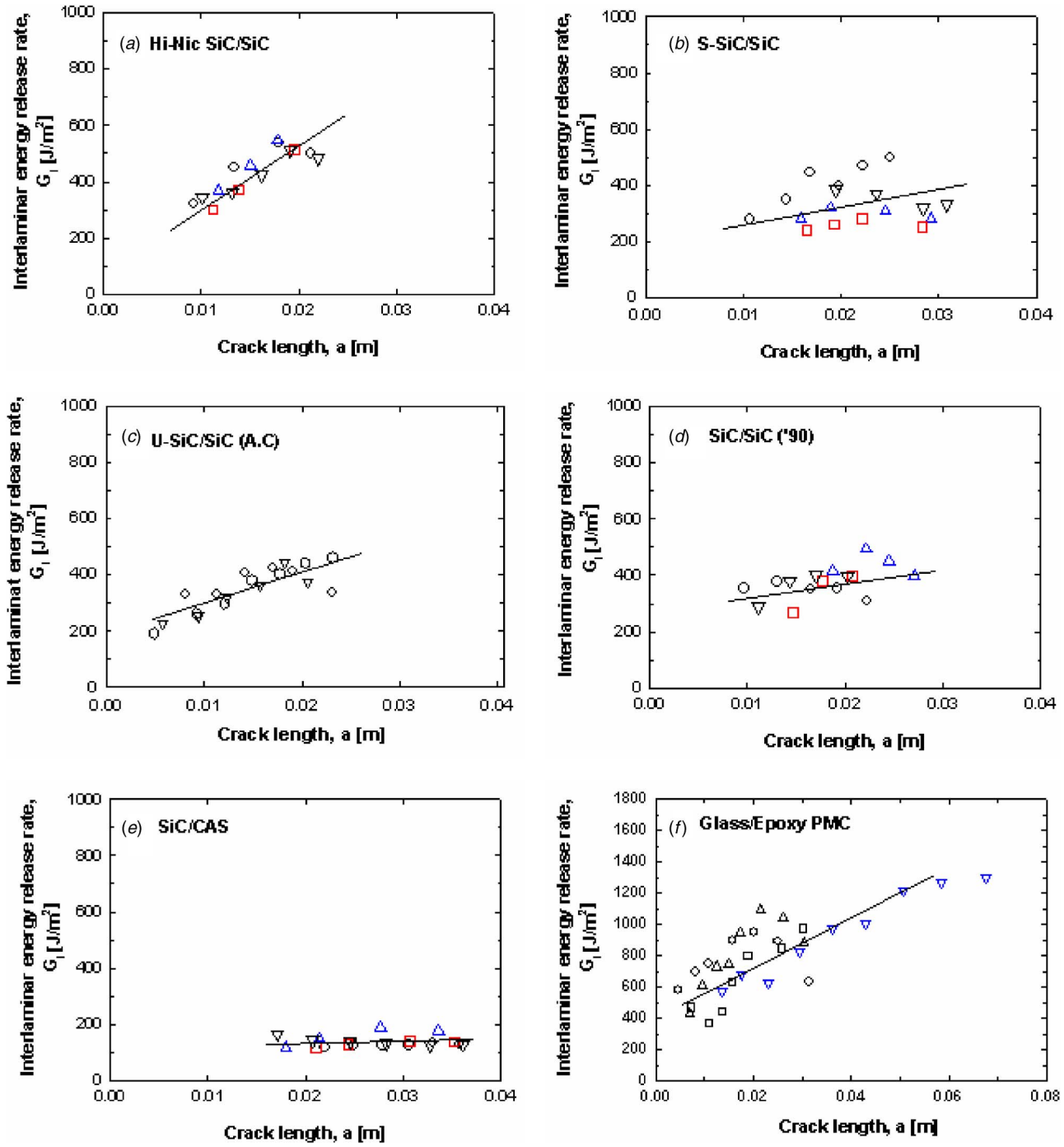

Fig. 4 Mode I interlaminar energy release rate (G_I) as a function of crack length determined for five different SiC continuous fiber-reinforced CMCs by the DCB method. Glass/epoxy PMC was included for comparison. Different symbols for a given plot represent different test specimens.

$=200-900\ \mathrm{J/m^2}$. Both *U*-SiC/SiC and SiC/CAS seemed to yield greater G_{II} than other CMCs. The glass/epoxy composite exhibited significantly greater $G_{II}(=1000-4000\ \mathrm{J/m^2})$ than the CMCs, which was almost eight times greater than that of the CMCs, estimated around $a/S=0.8$. As compared with the PMC, the CMCs were typified of considerably lower G_I or G_{II}, which needs to be improved to be comparable to the PMC.

The rising *R*-curve behavior shown in both G_I and G_{II} would be primarily attributed to fiber bridging occurring in the wake region of a propagating crack. A repeated process of fiber bridging and subsequent fiber breakage as a propagated crack was clearly observed during mode I testing (see Fig. 6 for an example). This process is believed to be operative even in shear mode occurring in the interlaminar midplane of an ENF specimen through which a shear crack propagated. Furthermore, friction between two crack planes in the wake region of ENF specimen would take place as applied force monotonically increased and as a sliding motion occurred between the two mating crack planes because of their opposite modes of deformation. This would contribute as an added resistance to crack propagation so that more energy would be required for a crack to propagate. This phenomenon of frictional constraint was evident from fracture surfaces of ENF speci-

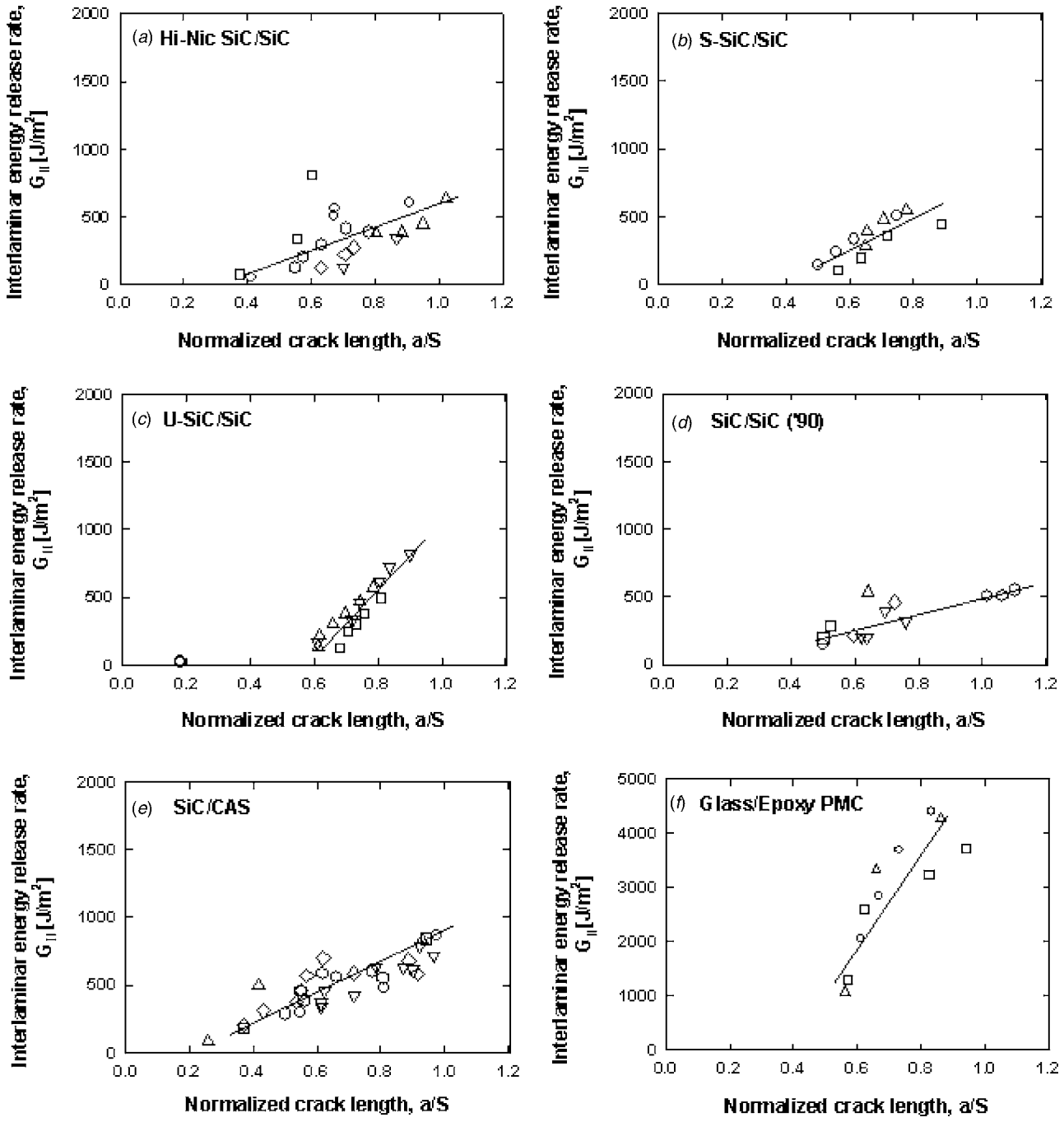

Fig. 5 Mode II interlaminar energy release rate (G_{II}) as a function of normalized crack length (a/S) determined for five different SiC continuous fiber-reinforced CMCs by the ENF method. Glass/epoxy PMC was included for comparison. Different symbols for a given plot represent different test specimens.

mens where many broken fibers/debris were observed, as shown in Fig. 7(*b*). This friction-associated feature was not seen in mode I testing in which much cleaner fracture surfaces were characterized (see Fig. 7(*a*)). Therefore, the main reason for greater G_{II} than G_I observed in this work would be primarily due to significant frictional constraint occurring in the very *rough* wake region of a propagating crack. Some coarse-grained monolithic ceramics also exhibited such a frictional constraint, resulting in greater mode II fracture toughness than the mode I counterpart [27].

Although not detailed here, additional mode I and mode II testing was conducted using polymethyl methacrylate (PMMA) [28]. Two as-processed, very smooth beams of PMMA were superglued together to form DCB and ENF test specimens. The dimensions/

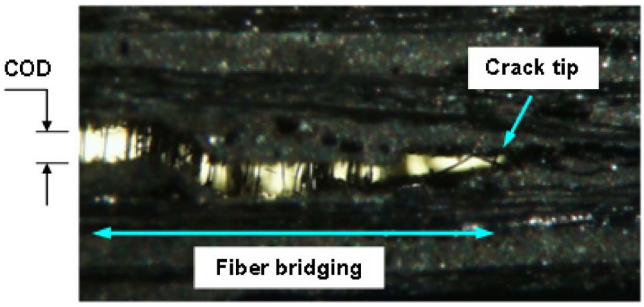

Fig. 6 Typical example showing fiber bridging in the wake region of a propagating crack during DCB (mode I) testing for *S*-SiC/SiC composite

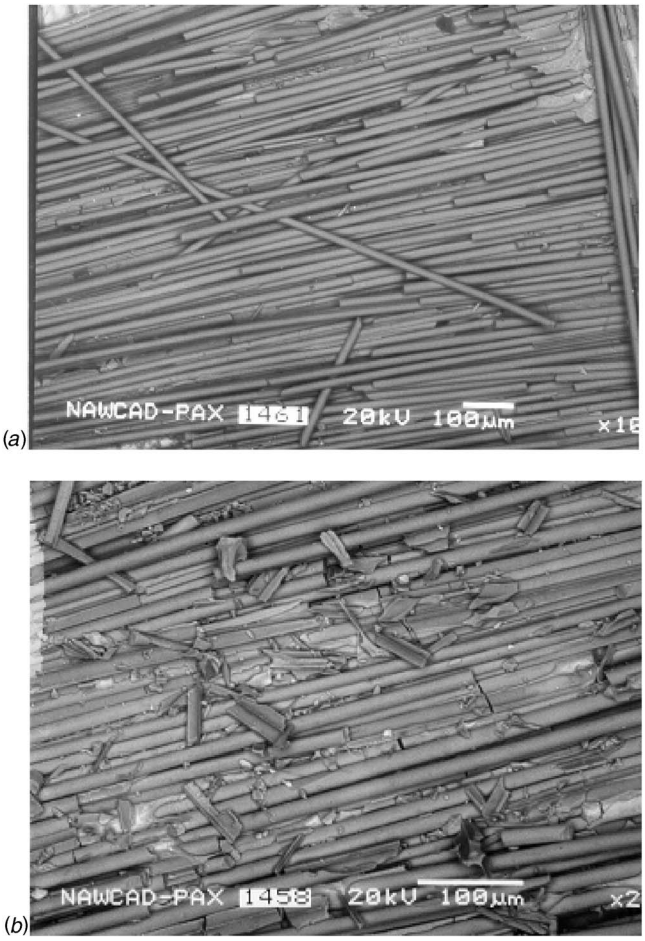

Fig. 7 Fracture surfaces of Hi-Nic SiC/SiC composite specimens in (*a*) DCB test in mode I and (*b*) ENF test in mode II. Note the existence of broken fibers/debris in (*b*) due to the frictional sliding motion of two mating crack planes in an ENF specimen.

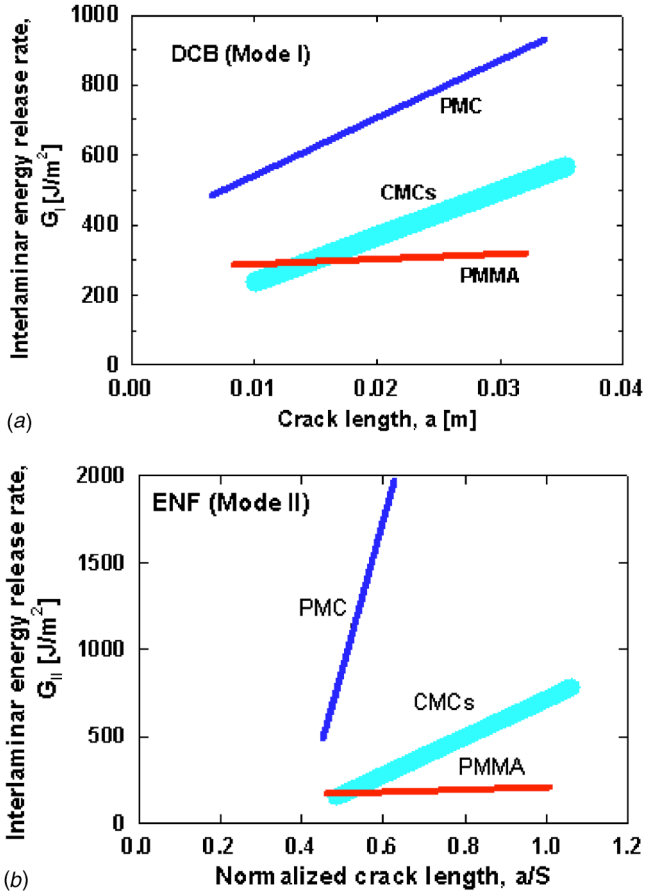

Fig. 8 Simplified summary of interlaminar energy release rates (crack growth resistances) of CMCs, PMC, and PMMA: (*a*) G_I by the DCB method in mode I and (*b*) G_{II} by the ENF method in mode II. G_I and G_{II} of PMMA were determined by DCB and ENF, respectively, with two as-fabricated glossy test beams superglued together [28].

configuration of test specimen and test fixture were $2h=6.5$ mm, $b=13$ mm, $2S=40$ mm, and $L\sim75$ mm for mode I. Despite some scatter, particularly in G_{II}, PMMA exhibited virtually no rising R curve in either mode I or II and showed no appreciable difference in G_I and G_{II} with $G_I, G_{II}=250-300$ J/m^2. This clearly indicates that smooth surfaces would generate no rising R curve or $G_{II}>G_I$. Based on these additional test results for PMMA, the aforementioned reasoning of fiber bridging and frictional constraint as a rising R curve and $G_{II}>G_I$ for the CMCs and PMC would be justified. Figure 8 is a summary of illustrations of G_I and G_{II} compared among CMCs, PMC, and PMMA.

Finally, it was observed from this work that, overall, neither melt infiltration nor BN coating did have any significant (beneficial) effect on G_I or G_{II}.

Effect of Off-the-Center of a Crack Plane on G_I and G_{II}. The scatter of data on G_I and G_{II} observed in this work may have two major plausible sources: the materials' microscopic inhomogeneity and the experimental errors. The former is inherent and beyond the scope of this work to explore. The latter, the experimental errors, may come from several factors such as force and crack length measurements and test specimen dimensional inaccuracy. Two main sources of the experimental errors are believed to be associated with the crack length measurements and the preparation of a crack at the midplane of a test specimen. It was experienced that to produce a precrack at the midplane, that is, $h_1=h_2=h$, was a more daunting task than the crack length measurements, mainly due to rough as-fabricated surfaces of test specimens (surface machining, if applied, may cause possible damage to fiber/matrix architecture). Moreover, in some cases, a crack propagated along the midplane but then deviated from the midplane. Therefore, it is worthy to estimate quantitatively the effect of $h_1\neq h_2$ on G_I and G_{II}.

The total energy release rate G_{Id} of a DCB test specimen with $h_1\neq h_2$ (see Fig. 1) is a summation of G_{I1} and G_{I2} [29]

$$G_{Id}=G_{I1}+G_{I2}=\frac{a^2P^2}{2Eb}\left[\frac{1}{I_1}+\frac{1}{I_2}\right]=\frac{6a^2P^2}{Eb^2h_2^3}\left[\frac{1+\gamma^3}{\gamma^3}\right] \tag{4}$$

where

$$\gamma=\frac{h_1}{h_2} \tag{5}$$

and I_1 and I_2 are the second moment of inertia of each cantilever arm about its neutral axis. The above equation can be easily derived from the simple beam theory together with Eq. (1). This equation is fundamentally the same as Eq. (2), but in a different form. The term outside the bracket in Eq. (4) represents G_I for the case of $h_1=h_2=h$. Therefore, the ratio of G_{Id} to G_I, noting $h_1+h_2=2h$, is simply

$$\frac{G_{Id}}{G_I}=\frac{1}{16}(\gamma+1)^3\left[\frac{1+\gamma^3}{\gamma^3}\right] \tag{6}$$

Note that when $h_1=h_2$, Eq. (6) reduces to $G_{Id}/G_I=1$.

In the same way, the ratio of G_{IId}/G_{II} in mode II can be derived

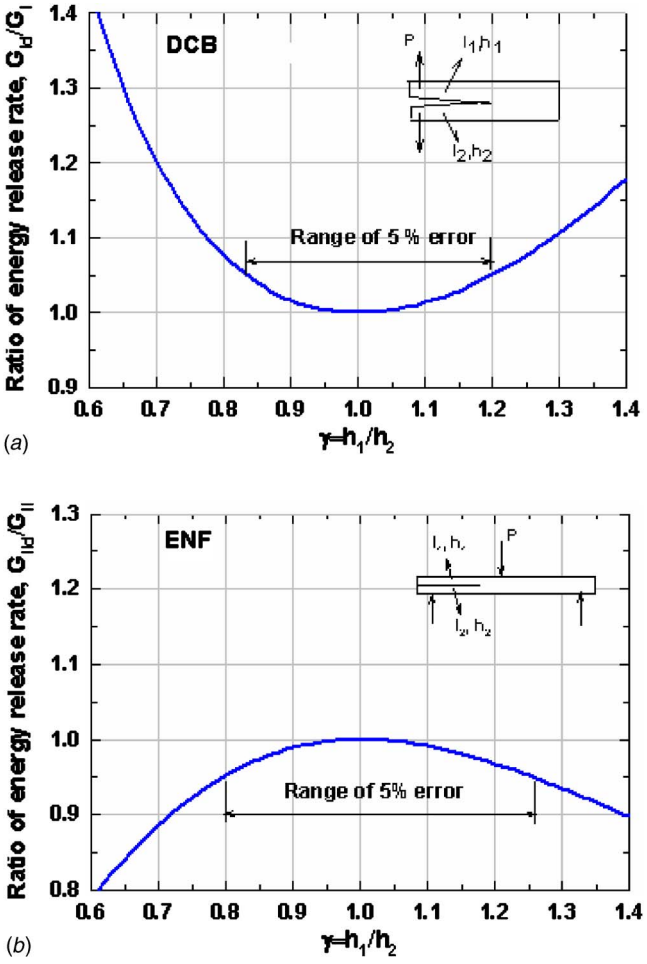

Fig. 9 Ratio of energy release rate (G_d/G) as a function of h_1/h_2: (*a*) mode I DCB test and (*b*) mode II ENF test, showing an error due to the off-the-center of a midcrack plane

based on the simple beam theory. Beam deflections are considered in three different sections of AB, BC, and CD (see Fig. 1(*b*)) with a condition of $h_1 \neq h_2$. The total deflection at the load point of the beam is a summation of deflections associated with sections AB, BC, and CD. Following the procedure done by Carlsson et al. [14], neglecting the shear deformation, and some mathematical manipulations in compliances of the three different sections together with Eq. (1) yield a solution of total energy release rate G_{IId} of the beam for $h_1 \neq h_2$ as follows:

$$G_{IId} = -\frac{3a^2P^2}{16Eb^2h^3} + \frac{3a^2P^2}{2Eb^2h_2^3}\left[\frac{1}{1+\gamma^3}\right] \tag{7}$$

When $h_1 = h_2 = h$, Eq. (7) can be reduced to G_{II} as

$$G_{II} = \frac{9a^2P^2}{16Eb^2h^3} \tag{8}$$

which is identical to Eq. (3) after a substitution of $C = (2S^3 + 3a^3)/8Ebh^3$ in Eq. (3) [13,14]. Therefore, the ratio of G_{IId}/G_{II}, noting $h_1 + h_2 = 2h$, becomes

$$\frac{G_{IId}}{G_{II}} = -\frac{1}{3} + \frac{1}{3}(\gamma+1)^3\left(\frac{1}{1+\gamma^3}\right) \tag{9}$$

When $h_1 = h_2$, Eq. (9) reduces to $G_{IId}/G_{II} = 1$.

The effect of h_1/h_2 on G_I or G_{II} can now be estimated using Eq. (6) or (9). Equations (6) and (9) are illustrated in Fig. 9. In order to have a 5% error in G_I and G_{II}, for example, the variation of h_1 with respect to h_2 (and vice versa) should be within 17–20% for G_I, whereas the variation should be within 20–25% for G_{II}. This indicates that to have a negligible error ($\leqslant 5\%$) in G_I or G_{II}, h_1 and h_2 should remain within about 20% in tolerance to each other. In fact, this would be a relatively large allowance since the variation in h_1 or h_2 was observed much less than 20% from the experiments. Therefore, it is believed that the effect of h_1/h_2 on G_I or G_{II} appears to be minimal and that the major variation, discrepancy, or data scatter would have been associated with the materials' inherent microscopic inhomogeneity. This also implies that the number of plies of the composites would have an insignificant effect on the values of G_I or G_{II}.

Conclusions

Interlaminar crack growth resistances were in the range of $G_I = 200-500\ \mathrm{J/m^2}$ and $G_{II} = 200-900\ \mathrm{J/m^2}$ for all the CMCs tested. G_I was greatest for the Hi-Nic SiC/SiC composites and appeared to be similar to that for the other SiC/SiC composites. Both *U*-SiC/SiC and SiC/CAS composites seemed to yield greater G_{II} than the other composites. Neither MI nor BN coating had a significant effect on G_I or G_{II}. The CMCs (except SiC/CAS in mode I) exhibited a rising *R* curve behavior in both G_I and G_{II}, attributed to fiber bridging in modes I and II and to frictional constraint in mode II. The frictional constraint occurring in the very rough wake region of ENF test specimens might have yielded greater G_{II} than G_I. The variation in crack midplane showed only a minor effect on G_I or G_{II}: 20% variation in h_1 or h_2 resulted in only 5% error in G_I or G_{II}. The glass/epoxy PMC exhibited significantly greater G_I (two to three times) and G_{II} (eight times) than the CMCs.

Acknowledgment

This work was supported by the Office of Naval Research (ONR). Mechanical testing was conducted at NASA Glenn, Cleveland, OH through the Ultra-Efficient Engine Technology (UEET) Project. The authors are grateful to R. Pawlik of NASA for experimental work during the course of this work.

References

[1] Brondsted, P., Heredia, F. E., and Evans, A. G., 1994, "In-Plane Shear Properties of 2-D Ceramic Composites," J. Am. Ceram. Soc., **77**(10), pp. 2569–2574.
[2] Lara-Curzio, E., and Ferber, M. K., 1997, "Shear Strength of Continuous Fiber Ceramic Composites," American Society for Testing and Material, ASTM Report No. STP 1309, p. 31.
[3] Fang, N. J. J., and Chou, T. W., 1993, "Characterization of Interlaminar Shear Strength of Ceramic Matrix Composites," J. Am. Ceram. Soc., **76**(10), pp. 2539–2548.
[4] Ünal, Ö., and Bansal, N. P., 2002, "In-Plane and Interlaminar Shear Strength of a Unidirectional Hi-Nicalon Fiber-Reinforced Celsian Matrix Composite," Ceram. Int., **28**, pp. 527–540.
[5] Choi, S. R., and Bansal, N. P., 2004, "Shear Strength as a Function of Test Rate for SiC_f/BSAS Ceramic Matrix Composite at Elevated Temperature," J. Am. Ceram. Soc., **87**(10), pp. 1912–1918.
[6] Choi, S. R., Bansal, N. P., Calomino, A. M., and Verrilli, M. J., 2005, "Shear Strength Behavior of Ceramic Matrix Composites at Elevated Temperatures," *Advances in Ceramic Matrix Composites X*, J. P. Singh, N. P. Bansal, and W. M. Kriven, eds., The American Ceramic Society, Westerville, Ohio; 2005, Ceram. Trans., **165**, pp. 131–145.
[7] Choi, S. R., and Bansal, N. P., 2006, "Interlaminar Tension/Shear Properties and Stress Rupture in Shear of Various Continuous Fiber-Reinforced Ceramic Matrix Composites," *Advances in Ceramic Matrix Composites XI*, N. P. Bansal, J. P. Singh, and W. M. Kriven, eds, The American Ceramic Society, Westerville, Ohio; 2006, Ceram. Trans., **175**, pp. 119–134.
[8] Yun, H. M., and DiCarlo, J. A., 2004, "Through-Thickness Properties of 2D Woven SiC/SiC Panels With Various Microstructures," Ceram. Eng. Sci. Proc., **25**(4), pp. 71–78.
[9] Zawada, L. P., 1998, "Longitudinal and Transthickness Tensile Behavior of Several Oxide/Oxide Composites," Ceram. Eng. Sci. Proc., **19**(3), pp. 327–339.
[10] Lara-Curzio, E., Bowers, D., and Ferber, M. K., 1996, "The Interlaminar Tensile and Shear Behavior of a Unidirectional C-C Composite," J. Nucl. Mater., **230**, pp. 226–232.
[11] Mall, S., Vozzola, R. P., and Zawada, L., 1989, "Characterization of Fracture in Fiber-Reinforced Ceramic Composites Under Shear Loading," J. Am. Ce-

ram. Soc., **72**(7), pp. 1175–1178.
[12] Martin, R. H., 1977, "Delamination Characterization of Woven Glass/Polyester Composites," J. Compos. Technol. Res., **19**(1), pp. 20–28.
[13] Sela, N., and Ishai, O., 1989, "Interlaminar Fracture Toughness and Toughening of Laminated Composite Materials: Review," Composites, **20**(5), pp. 423–435.
[14] Carlsson, L. A., Gillespie, J. W., and Pipes, R. B., 1986, "On the Analysis and Design of the End Notched Flexure (ENF) Specimen for Mode II Testing," J. Compos. Mater., **20**, pp. 594–604.
[15] O'Brien, T. K., and Martin, R. H., 1993, "Round Robin Testing for Mode I Interlaminar Fracture Toughness of Composite Materials," J. Compos. Technol. Res., **15**(4), pp. 269–281.
[16] Williams, J. G., 1989, "The Fracture Mechanics of Delamination Tests," J. Strain Anal. Eng. Des., **24**(4), pp. 207–214.
[17] Kumar, D. V. T. G. P., and Prasad, B. K. R., 2003, "Higher-Order Beam Theories for Mode II Fracture of Unidirectional Composites," Trans. ASME, J. Appl. Mech., **70**, pp. 840–852.
[18] Smiley, A. J., and Pipes, R. B., 1987, "Rate Effects on Mode I Interlaminar Fracture Toughness in Composite Materials," J. Compos. Mater., **21**, pp. 670–687.
[19] Brewer, D., 1999, "HSR/EPM Combustor Materials Development Program," Mater. Sci. Eng., A, **261**, pp. 284–291.
[20] Calomino, A. M., 2002, "Mechanical Behavior and Characterization/1316°C In-Situ BN Coated MI/SiC/SiC," *Technology Forum*, UEET, Glenn Research Center, National Aeronautics and Space Administration, Cleveland, Ohio, October.
[21] ASTM C 1259, 2006, "Test Method for Dynamic Young's Modulus, Shear Modulus, and Poisson's for Advanced Ceramics by Impulse Excitation of Vibration," *Annual Book of ASTM Standards*, American Society for Testing and Materials, West Conshohocken, PA, Vol. 15.01.
[22] Worthem, D. W., 1995, "Thermomechanical Fatigue Behavior of Three CFCCs," National Aeronautics and Space Administration, Glenn Research Center, NASA Report No. CR-195441.
[23] Choi, S. R., and Gyekenyesi, J. P., 2005, "Load-Rate Dependency of Ultimate Tensile Strength in Ceramic Matrix Composites at Elevated Temperatures," Int. J. Fatigue, **27**, pp. 503–510.
[24] Choi, S. R., Bhatt, R. T., Pereira, J. M., and Gyekenyesi, J. P., 2004, "Foreign Object Damage Behavior of a SiC/SiC Composite at Ambient and Elevated Temperatures," ASME Paper No. GT2004-53910.
[25] ASTM D 5528, 2005, "Test Method for Mode I Interlaminar Fracture Toughness of Unidirectional Fiber-Reinforced Polymer Matrix Composites," *Annual Book of ASTM Standards*, American Society for Testing and Materials, West Conshohocken, PA.
[26] See any text, e.g., Broek, D., 1983, *Elementary Engineering Fracture Mechanics*, Martinus Nijhoff, Boston.
[27] Singh, D., and Shetty, D. K., 1989, "Fracture Toughness of Polycrystalline Ceramics in Combined Mode I and Mode II Loading," J. Am. Ceram. Soc., **72**(1), pp. 78–84.
[28] Choi, S. R., Kowalik, R. W., and Alexander, D. J., 2007, "Mode I and Mode II Interlaminar Crack Growth Resistances of Ceramic Matrix Composites at Ambient Temperature," Naval Air Systems Command, Report No. NAWCADPAX/TR-2007/4.
[29] Tada, H., Paris, P. C., and Irwin, G. R., 2000, *The Stress Analysis of Cracks Handbook*, ASME, New York, p. 418.

Carbon-Free Hydrogen and Electricity From Coal: Options for Syngas Cooling in Systems Using a Hydrogen Separation Membrane Reactor

Luca De Lorenzo

Thomas G. Kreutz

Princeton Environmental Institute,
Princeton University,
Princeton, NJ 08544

Paolo Chiesa
Dipartimento di Energetica,
Politecnico di Milano,
Piazza Leonardo da Vinci,
32-20133 Milan, Italy

Robert H. Williams
Princeton Environmental Institute,
Princeton University,
Princeton, NJ 08544

Conversion of coal to carbon-free energy carriers, H_2 *and electricity, with* CO_2 *capture and storage may have the potential to satisfy at a comparatively low cost much of the energy requirements in a carbon-constrained world. In a set of recent studies, we have assessed the thermodynamic and economic performance of numerous coal-to-*H_2 *plants that employ* O_2*-blown, entrained-flow gasification and sour water-gas shift (WGS) reactors, examining the effects of system pressure, syngas cooling via quench versus heat exchangers, "conventional"* H_2 *separation via pressure swing adsorption versus novel membrane-based approaches, and various gas turbine technologies for generating coproduct electricity. This study focuses on the synergy between* H_2 *separation membrane reactors (HSMRs) and syngas cooling with radiant and convective heat exchangers; such "syngas coolers" invariably boost system efficiency over that obtained with quench-cooled gasification. Conventional* H_2 *separation requires a relatively high steam-to-carbon ratio (S/C) to achieve a high level of* H_2 *production, and thus is well matched to relatively inefficient quench cooling. In contrast, HSMRs shift the WGS equilibrium by continuously extracting reaction product* H_2*, thereby allowing a much lower S/C ratio and consequently a higher degree of heat recovery and (potentially) system efficiency. We first present a parametric analysis illuminating the interaction between the syngas coolers, high temperature WGS reactor, and HSMR. We then compare the performance and cost of six different plant configurations, highlighting (1) the relative merits of the two syngas cooling methods in membrane-based systems, and (2) the comparative performance of conventional versus HSMR-based* H_2 *separation in plants with syngas coolers.* [DOI: 10.1115/1.2795763]

1 Introduction

Concern about global climate change has prompted significant new research on low carbon energy systems. One approach, which acknowledges the likely dominance of fossil fuels as primary energy source in the coming decades, is the conversion of fossil fuels into carbon-free energy carriers, H_2 and electricity, with CO_2 capture and storage (CCS). Coal is a feedstock of particular interest because of its great abundance (~200 years of reserves), widespread geographical distribution, and low, stable cost. The high carbon content of coal makes this fuel a particularly attractive candidate for CCS.

In a series of previous studies (see Table 1), we and others have investigated the thermodynamics and economics of converting coal to H_2 and electricity with CO_2 capture, exploring numerous plant designs, operating parameters, and choices of technology (Chiesa et al. [1], Chiesa et al. [2], Kreutz et al. [3], Kreutz et al. [5], Gray and Tomlinson [6], and Badin [7]). Examples include various gasifier pressures, syngas cooling via quench versus heat exchangers, pure CO_2 capture versus cocapture of CO_2+H_2S, CO_2/H_2 separation via "conventional" methods (a combination of physical absorption and pressure swing adsorption (PSA)) versus more "novel" means (a H_2 separation membrane reactor (HSMR)), and various gas turbine technologies. Despite the fact that syngas cooling via heat exchangers (or "syngas coolers") yields higher system efficiencies than quench cooling, our work thus far has focused on the latter for two reasons. First, the quench adds enough water to the syngas—yielding a steam-to-carbon ratio (S/C, given on a mole basis throughout the paper) of ~2.3—to sufficiently promote the water-gas shift (WGS) reaction $H_2O+CO \rightarrow H_2+CO_2$, which is necessary for high levels of CO_2 capture and H_2 production. Second, despite their higher efficiency, we have found that syngas coolers are not the most economical option, i.e., quench cooling leads to lower costs for electricity and H_2 in plants that employ conventional gas separation technology (Kreutz et al. [3]).

However, it was brought to our attention (Tomlinson [8]) that H_2 plants with WGS membrane reactors are particularly attractive candidates for syngas heat recovery with syngas coolers. The reasoning is thus by removing H_2 continuously from the WGS reaction, the HSMR "shifts" the WGS equilibrium to the right, allowing a high degree of H_2 production and CO_2 separation with a relatively dry syngas (or relatively low S/C ratio). This allows the use of syngas coolers, with the potential for higher system efficiency. This hypothesis is the motivation for the present study, which fits in with our previous work, as shown schematically in Table 1. The paper first presents a parametric analysis of the synergies between syngas cooling and membrane reactor, and then focuses on specific and optimized plants to be compared with the previous works.

Contributed by the International Gas Turbine Institute (IGTI) of ASME for publication in the JOURNAL OF ENGINEERING FOR GAS TURBINES AND POWER. Manuscript received May 10, 2006; final manuscript received May 31, 2007; published online March 28, 2008. Review conducted by Umberto Desideri. Paper presented at the ASME Turbo Expo 2005: Land, Sea and Air (GT2005), Reno, NV, June 6–9, 2005, Paper No. GT2005-68572.

Table 1 Schematic view of our work on coal-to-H_2 plants

	PSA	HSMR
Quench	Previous work (Chiesa et al. [1] and Kreutz et al. [3])	Previous work (Chiesa et al. [1] and Kreutz et al. [5])
Syngas cooling	Previous work (Chiesa et al. [1] and Kreutz et al. [3])	Current paper

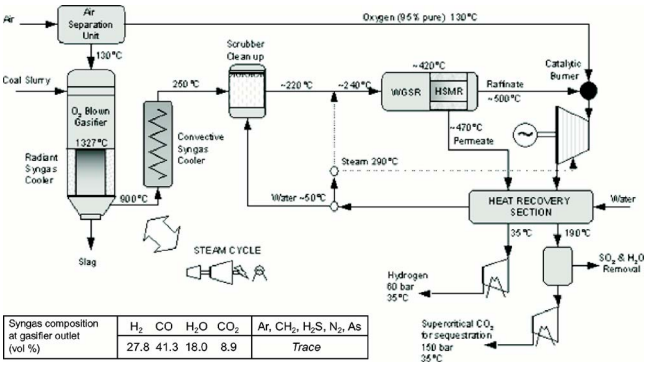

Fig. 1 Schematic layout of a membrane-based plant. The table shows the composition if the syngas is exiting the gasifier.

Brief Plant Overview. The plants studied in this paper are shown schematically in Fig. 1. A coal-water slurry is gasified in a pressurized (70 bar), oxygen-blown, entrained-flow, slagging gasifier based on Texaco (now GE energy) technology. The resulting high temperature (~1327°C) raw syngas is cooled in radiant and convective heat exchangers to a temperature of 250°C. The heat recovered raises steam that is used to (1) generate power via a steam cycle, and/or (2) further humidify the syngas, and/or (3) cool the exhaust of the uncooled raffinate turbine combustor, and/or (4) cool the first few sets of blades in the cooled raffinate turbine. The cooled syngas (S/C~0.36) is cleaned and humidified (to S/C~0.43) in a scrubber, and then further heated and humidified by injecting a variable amount of steam (70 bars, 290°C) to provide the desired S/C ratio. The syngas then enters an adiabatic water-gas shift reactor (WGSR), where CO is converted to H_2 and CO_2; the mildly exothermic (41.2 kJ/mole) WGS reaction raises the temperature of the syngas to 400–430°C, depending on the S/C ratio. The shifted syngas enters the H_2 separation membrane reactor (HSMR), which further promotes the WGS reaction and separates H_2 from the syngas (via H_2 permeation through an inorganic membrane, driven by the drop in H_2 partial pressure across it). The HSMR divides the syngas into two streams: (1) a low-pressure (~2 bar) H_2 permeate, which is cooled (to 35°C) and compressed to 60 bars (a typical value for pipeline transport), and (2) a high-pressure (~67 bars), high temperature (475–530°C) raffinate stream.[1] The heating value of the raffinate is recovered by catalytic combustion in oxygen and expansion in a raffinate turbine, whose blades are either cooled or uncooled to generate electric power. The membrane can therefore be interpreted as a device that splits the chemical enthalpy (carried by H_2) from the carbon (carried by CO_2) and the electrical output. The turbine exhaust is cooled to just above its acidic dew point (190°C), generating steam for use upstream; condensed water is separated, treated, and recycled. The raffinate turbine exhaust is sent to a wet limestone, flue gas desulfurization (FGD) unit to remove the SO_2 as gypsum. To achieve the conditions for storage (supercritical 150 bars and ~20–25 ppmv of water content), the flow is compressed via a series of four intercooled compressors and dried in a traditional glycol unit. The final composition of the gas is primarily CO_2 (~97%, with traces of Ar, N_2, O_2, and SO_2) ready for pipeline transport and geologic storage.

[1]Composition depends on the actual operating conditions of the HSMR, but it primarily consists of H_2O and CO_2, with some traces of unconverted CO, CH_4, H_2S, and unpermeated H_2.

Table 2 Assumptions adopted for performance calculations

Gasifier:
Operating conditions: 70 bars, 1327°C. Slurry water/raw coal weight ratio: 2.3. Cold gas efficiency: 87.3% HHV. Heat loss: 0.005 of the coal LHV thermal input. Carbon conversion: 99.2%

Syngas coolers:
Heat losses: 0.007 times heat released by the hot stream. Pressure loss: 2%. Ash discharge temperature: 350°C. Outlet temperature: 250°C.

Air separation unit (ASU):
Power consumption: 0.261 kW h_{el}/kg_{pure} O_2.
Oxygen composition: 95% O_2, 1.4% N_2, 3.6% Ar

O_2 and H_2 compressors:
O_2 outlet pressure: 84 bars (1.2 times the gasification pressure), H_2 outlet pressure: 60 bars. Number of intercoolers set so that stage output temperature <200°C. Isentropic efficiency: 0.85. Organic/electric efficiency: 0.94. Temperature at the cooler exit: 35°C. Pressure drop in the intercoolers: 0.01.

CO_2 compressor:
Four intercooled stages. Compression ratio/stage: 3.5. Isentropic efficiency: 0.82. Final pump efficiency: 0.75. Temperature at intercooler exits: 35°C. Pressure drop in each intercooler: 0.01. Pressure drop drying intermediate dehydration process: 0.01.

High temperature WGS reactor:
Pressure drop, $\Delta p/p$: 2%. Inlet S/C ratio 0.7–3. Heat loss: 2% of the WGS heat release.

Hydrogen membrane separation reactor (HMSR):
Pressure drop, $\Delta p/p$: 2%. Heat loss: 0.02 of heat released in the shift reaction. H_2 backpressure: 2 bars.

Heat exchangers:
Heat losses: 0.007 times heat released by the hot stream. Pinch point for heat recovery steam generators: 8°C. Subcooling at economizer outlet: 5°C. Minimum ΔT for gas-liquid heat exchangers: 10°C. Pressure loss: 2%.

Pumps:
Hydraulic efficiency: 0.75. Organic/electric efficiency: 0.94. For cooling media pumps, electric power consumption is 0.01× heat power released.

Raffinate combustor:
O_2 flow rate: 1.05× stoichiometric. Pressure loss: 0.03.

Heat loss: 0.005× the raffinate LHV.
Raffinate turbine:
Uncooled TIT: 850°C, cooled TIT: 1250°C. Organic/electric efficiency: 0.975. Efficiency calculated by the model for uncooled turbine from ~70 bars is equivalent to 0.88 polytropic (or 0.919 isentropic).

FGD:
Inlet gas temperature: 190°C. Maximum temperature of recoverable heat: 50°C. SO_2 removal efficiency: 0.90. FGD also produces CO_2 at mass rate 0.6875 times the SO_2 removed (mole rate=1× the SO_2 removed).

2 Detailed System Description

The primary assumptions used in plant performance modeling are detailed in Table 2. A more detailed description of each section of the plant and its main components follows.

Table 3 Input coal characteristics

Characteristics of raw and moisture free (MAF) Illinois No. 6 coal. Composition in wt %; heating values MJ/kg		
	Raw	MAF
C	61.27	77.26
H	4.69	5.91
O	8.83	11.13
N	1.10	1.39
S	3.41	4.30
H_2O	12.00	—
Ash	8.70	—
LHV	24.83	32.97
HHV	26.14	31.31

Gasification process. Illinois No. 6 coal (Table 3) is wet ground in an open rod mill with treated water and slag fines recycled from the gasifier. The resulting coal slurry (67 wt % solids) is fed to the gasifier together with 95% pure oxygen produced by a stand-alone air separation unit (ASU) at a pressure of 84 bars (1.2 the operating pressure of the gasifier). The ASU is not explicitly modeled here; rather, we adopt the composition and specific work (261 kW h_e/ton of pure O_2 for production) given by Simbeck [9]. The mass ratio of pure O_2 to moisture and ash free coal is 0.895, sufficient to raise the temperature of the raw syngas exiting the gasifier to 1327°C. A small amount of additional oxygen is produced for use in the catalytic combustor of the raffinate turbine.

Coal gasification occurs at 70 bars in an entrained-flow gasifier that emulates the commercial technology currently licensed by GE Energy. Oxygen and slurry are injected into the reaction chamber where they react to produce raw syngas (at 1327°C, above the ash melting point) and molten slag. The relatively high operating temperature (controlled by varying the oxygen-slurry ratio) enables the gasifier to be modeled with reasonable accuracy using chemical equilibrium calculations.

The raw syngas (composition: 28% H_2, 41% CO, 18% H_2O vapor, 9% CO_2, and traces of Ar, CH_4, H_2S, N_2) and the molten slag exit the gasifier and flow through a high temperature radiant heat exchanger, in which they are cooled to ~900°C. At this temperature, the slag solidifies and is discharged through a lock-hopper system to a shaker screen, which separates the slag into a coarse fraction and a fine fraction; the former is disposed, while the latter is recycled to the gasifier. The overall carbon conversion of the gasifier is assumed to be 99.2%. The raw syngas is further cooled (to 250°C) in a convective heat exchanger, and sent to a scrubber to remove water-soluble species and any remaining particulates. The scrubber is conceptually analogous to a total water quench, but its lower operating temperature (200–250°C) introduces less water into the syngas, yielding a S/C ratio of 0.43. The S/C ratio of the syngas can be increased at this point (prior to entering the WGS reactor) by injecting steam into the clean syngas; this option provides a plant design variable (i.e., S/C ratio) that will be explored extensively in this study.

H_2 production and separation. The clean, humidified syngas passes through an adiabatic WGSR containing a sulfur-tolerant cobalt-molybdate catalyst, which promotes the slightly exothermic WGS reaction $CO+H_2O \rightarrow CO_2+H_2+41.15$ kJ/mole. This component has been inserted upstream of the HSMR because, without it, most of the WGS reaction (and consequent heat release and temperature rise) occurs within the first ~20% of the HSMR. Effectively replacing that portion of the HSMR with a simple upstream adiabatic WGSR serves to shield the relatively delicate and expensive membrane reactor from (1) unnecessary thermal stress, (2) mechanical damage during regular catalyst replacement, and (3) contamination from trace chemicals and particulate matter. The percentage of CO converted and the consequent temperature raise in the WGSR both depend on the chosen S/C ratio (discussed below). Although the catalyst is designed to operate between ~300°C and 475°C, a few extreme parametric cases studied here extend that range to ~225–530°C with the explicit understanding that the catalyst may lose activity via either reduced reactivity (at low temperature) or sintering (at high temperature).[2]

After exiting the WGSR, the syngas enters the "raffinate" side of the HSMR where the WGS reaction continues, aided by the same shift catalyst; at the same time, pure H_2 is extracted from the raffinate via permeation through the H_2-selective membrane to the low-pressure "permeate" side of the HSMR. By continuously removing the reaction product H_2 from the raffinate stream, the WGS chemical equilibrium is "pulled" toward higher values of CO conversion.

The membrane modeled in this study is an inorganic composite membrane, made up of a dense metal film of Pd–40Cu alloy (i.e., 60 wt % Pd in Cu) supported by a porous metallic substrate. The operating temperature range for such membranes is ~300–600°C, and their permeance has been modeled using experimental data available; at 500°C with 1000 ppmv H_2S poisoning, 1 bar backpressure, 50 μm thickness, Edlund and Henry [10] measured a H_2 permeance of 0.0228 moles/(m^2 s $bar^{0.5}$). To minimize the membrane cost and increase its performance, we assume a thickness[3] of 20 μm, increasing the permeation flux by a factor of 2.5 according to Sievert's law. Furthermore, we assume that this performance can be achieved at higher H_2S concentrations that result when using high sulfur Illinois No. 6 coal as feedstock, thus enabling a comparison between these results and those in previous papers (Chiesa et al. [1] and Kreutz et al. [3]), which investigate similar plants employing conventional gas separation technologies.

The driving force for H_2 permeation is the drop in H_2 partial pressure across the membrane. Given the large difference in total pressure ($\Delta p \sim 65$ bars) across the membrane, we assume a standard shell-tube configuration, in which the raffinate stream flows inside an array of porous tubes that contain the WGS catalyst and support the thin film membrane, while the H_2 permeates radially outward through the tubes and is collected at low pressure in the outer vessel. This low-pressure permeate stream operates at "H_2 backpressure" of ~2 bars. The backpressure affects the H_2 flux through the membrane, and thus the surface area (and hence HSMR cost) required to achieve the design hydrogen recovery factor (HRF). In addition, it affects the size, cost, and power requirements of the H_2 compressor. As described in Ref. [5], the backpressure is optimized for each plant in order to minimize the cost of producing H_2. The pure H_2 stream exiting the HSMR is cooled (its heat is recovered) and compressed to its final delivery pressure of 60 bars in a multistage, intercooled, reciprocating H_2 compressor (seven parallel trains with a spare).[4]

The performance of the HSMR is simulated using a one-dimensional, steady-state model that assumes ideal gas behavior, infinite H_2 selectivity, and instantaneous chemical equilibrium along the length of the reactor. Spatially resolved heat transfer is not explicitly calculated here; rather, the H_2 outlet temperature is given as the average of the inlet syngas and outlet raffinate temperatures. The overall HSMR heat balance is verified considering the WGS exothermicity and overall adiabatic conditions.

Power island. The plants studied here produce electric power at two primary locations: (1) the steam cycle, which uses the recov-

[2]The low temperature limit could be overcome through a regenerator to increase the temperature before the reactor. This expensive solution was not investigated in this study.

[3]Recent research by Way et al. indicates that such values are in the reach of technological progress.

[4]This H_2 compressor design (number of trains and costs) is derived from our database on commercially available reciprocating compressors. Were large H_2 production facilities such as these to become commonplace, it is likely that large scale centrifugal compressors would become commercially available, lowering compression costs significantly by reducing the number of parallel trains.

ered heat from the syngas coolers, and (2) the raffinate turbine, which recovers the exergy of the hot, high-pressure raffinate stream that exits the HSMR. The configuration of the steam cycle—565°C and 166 bars, with one reheat—puts it at the front line of commercial technology of the heat recovery steam cycles. The size of the turbine (~30–150 MW) varies according to the amount of heat recovered in the syngas coolers; this depends on the S/C ratio and the type of raffinate turbine (i.e., cooled or uncooled, described below).

The raffinate turbine converts the raffinate stream to electricity by first combusting it, catalytically if necessary in oxygen and then expanding it to 1.05 bars (to avoid leakage from ambient into the CO_2 stream). This paper investigates the use of two different types of raffinate turbines: (1) uncooled (turbine inlet temperature (TIT) 850°C) and (2) cooled (TIT 1250°C), where heat transfer to the initial rows of turbine blades is moderated via open-circuit steam cooling. The plant operating conditions vary considerably between the two turbine types, as explained in the next section.

The uncooled raffinate turbine used here has a high expansion ratio ($\beta \sim 65$, justified by the relative simplicity of its design) and a TIT of 850°C. When the temperature of the gas exiting the turbine combustor exceeds this value, the temperature of the flow is moderated (to 850°C) by steam injection or insertion of a heat exchanger prior to expansion in the turbine. In contrast, the cooled raffinate turbine has a pressure ratio that is limited to $\beta \sim 45$ (because of the relative complexity of its cooled blades), corresponding to the current maximum value found in commercial aeroderivative turbomachines. In plants that use the cooled turbine, a syngas expander is inserted upstream to reduce the pressure (from ~65 bars to 45 bars) of the raffinate flow exiting the HSMR, and to generate extra power. Since this turbine already employs open-circuit steam cooling, we do not inject into combustor exhaust gases prior to the turbine inlet; the temperature of this stream is already well matched to the 1250°C TIT over the HRF range of interest (80–90%).

It is worth noting that when conducting the parametric analysis by varying S/C ratios and HRF, significant changes are observed in the sizes of both the raffinate turbine and the steam cycle. Both for simplicity and to keep a consistent framework for comparison, we scale the raffinate turbine to the gasification process (instead of vice versa), without attempting to achieve particular turbomachinery power outputs that would match currently available commercial gas turbines.

CO_2 capture and storage. Prior to pipeline transport, the CO_2 stream is dehydrated to 50 ppmv (~3°C dew point) by flowing through a circulating triethylene glycol (TEG) desiccant, a relatively low cost technique that is widely employed for drying both natural gas and CO_2. Before dehydrating, the gas is typically compressed to 40–55 bars in order to reduce the water load and the size of the absorber. In our system, based on the SACROC CO_2 pipeline, dehydration takes place at 43 bars after three stages of intercooled (to 30°C, 3% pressure drop) compression using a centrifugal compressor that has a single stage pressure ratio of 3.5 and an isentropic efficiency of 82%. Selected components of both the compressor (e.g., intercooler coils) and dehydrator (e.g., contactor trays) are made of stainless steel to reduce the rate of corrosion from the acidic condensate. The dehydrated gas stream exiting the absorber at 38°C is compressed in a fourth compressor stage, with the same pressure ratio and efficiency as the previous stages, to the final pressure of 150 bars, a typical value for supercritical CO_2 pipelines. The composition of the final stream is, with FGD sulfur removal, 95.9% CO_2, 2.0% Ar, 1.3% N_2, 0.7% O_2, 300 ppmv SO_2, and 50 ppmv H_2O. Relative to a pure stream of CO_2 near its critical point, the presence of noncondensable impurities serves to increase the critical pressure of the mixture and significantly decrease the saturated water content of the CO_2-rich fluid. Considerations such as these motivate the somewhat conservative design specifications adopted for the final pressure and water content of the gas.

3 Plant Design and Dynamics

Before analyzing the dynamics of the various plant designs studied in this work, it is useful to understand the limits on the key design parameters, particularly the S/C ratio and the HRF. As discussed above, the use of syngas coolers for heat recovery introduces a degree of freedom in plant design; we are free to choose the S/C ratio that yields the most favorable system performance. As will be seen, we strive to obtain the highest overall system efficiency and also minimize the size (and therefore cost) of the HSMR. The HRF quantifies the extent of H_2 production/extraction from the syngas, and is defined as

$$\mathrm{HRF} \equiv \frac{(H_2)_{out}}{(H_2 + CO)_{in}}$$

where $(H_2)_{out}$ is the moles of permeate H_2 out of the HSMR, and $(H_2+CO)_{in}$ represents the "potential" (or maximum possible) number of moles of H_2 in the syngas entering the WGSR. In general, we design H_2 plants to have HRF exceeding 85%, both to achieve a high "effective" efficiency (see footnote b in Table 4) and so that the cost of H_2 production is not unduly affected by the value of the electricity coproduct, whose price is an exogenous variable. In this work, we consider HRF values of 85% and 89%.

The boundaries on plant design, i.e., limits on S/C and HRF, are fixed by four curves shown in Fig. 2, each representing a specific physical limit; also included are the locations (in design parameter space) of specific plants examined in this paper. The top curve, labeled "WGSR," results from the stoichiometry of the WGS reaction. In order for the reaction to go to completion, there must be at least as many moles of H_2O as CO in the entering syngas. In Fig. 2, it can be seen that below the limiting value of $S/C \sim 0.825$, total H_2 recovery (i.e., HRF=100%) is no longer possible. As the S/C ratio becomes smaller, so too does the maximum possible value of HRF.

While curve WGSR has pedagogical value, it suffers from two implicit, unphysical assumptions: (1) no reverse WGS reaction and (2) complete H_2 separation. Mirroring the shape of curve WGSR in Fig. 2 is a second curve labeled "HSMR," which represents the actual performance of the WGSR+HSMR H_2 separation system. Its more stringent limits on HRF reflect the fact that H_2 permeation is driven by the difference in (the square root of the) H_2 partial pressure across the membrane, and therefore not all of the H_2 produced in the WGS reaction can be recovered when the H_2 backpressure (or permeate pressure) is finite. Typically, the H_2 backpressure is ~2 bars. Only the area below curve HSMR is physically achievable. (The curve represents HRF_{max}, the maximum HRF value that can be achieved at any given S/C ratio. As we increase HRF, so does the membrane surface area required to achieve that level of membrane reactor performance. As HRF approaches HRF_{max}, the required membrane surface area becomes infinite (Kreutz et al. [5]).)

Notice that the HSMR curve presents a maximum around $S/C=1.5$; for low values of S/C, it is bent by the requirements of the WGR; for high values of S/C, the decrease is less evident and is due to the decrease of H_2 partial pressure because of water dilution.

The remaining two curves in Fig. 2 arise from the use of a turbine expander for generating electric power from the raffinate stream, and specifically to achieving a desired TIT, which is equal to the adiabatic flame temperature of the raffinate stream when burned in oxygen within the turbine combustor. In order to maximize the turbine efficiency, we seek to achieve the highest TIT that is technologically feasible: 850°C for the "uncooled" turbine (i.e., no blade cooling) and 1250°C for the "cooled" turbine (which uses open-circuit steam cooling of the first few rows of blades). The two curves depict the locus of points in the HRF-S/C parameter space where, in the absence of extra steam added to reduce the TIT (as described below), the TIT is either 850°C or 1250°C. The negative slope has a clear physical interpretation: As

Table 4 Performance of membrane-based H_2 plants. "Conventional" technology plant, SCC-PSA, is included for comparison in the right hand column. (Labels in parentheses refer to SCC-PSA.) Coal input is 1796 MW_{th} LHV in all plants.

Separation system	HSMR				HSMR	PSA
Syngas cooling	Quench	Syngas coolers			Syngas coolers	
Turbine type		Uncooled		Cooled	Cooled	
Plant identifier[a]	QU	SCU	SCU-HX	SCC	SCC-set	SCC-PSA
Component power (MW_e):						
O_2 production	−64.7	−65.0	−65.0	−64.8	−68.1	−51.5
O_2 compression	−41.3	−39.9	−39.9	−39.2	−41.1	−32.9
H_2 (or PSA purge) compression	−53.8	−53.6	−53.6	−53.7	−48.8	−12.5
CO_2 compression	−67.9	−69.7	−69.7	−69.7	−69.7	−41.3
Syngas expander	0	0	0	7.7	8.9	0
Raffinate (or gas) turbine	249.1	212.2	129.6	164.6	191.2	81.0
Steam turbine	0.0	46.5	148.8	122.7	116.6	168.4
Auxiliaries	−25.1	−27.0	−26.4	−26.5	−26.7	−37.4
Net electric power output (MW_e)	−3.8	3.4	23.7	40.9	62.2	73.8
H_2 stream heat recovery (MW_{th})	70.1	71.9	71.9	73.2	68.7	—
Turbine exhaust heat rec. (MW_{th})	37.3	46.4	109.0	97.0	107.4	—
Total steam generated (MW_{th})	37.5	365.2	385.0	364.1	394.4	—
Hydrogen product (MW_{th}, LHV)	1089	1085	1085	1088	1037	1032
Effective efficiency[b] (% LHV)	60.3	60.7	62.8	64.6	63.8	64.7
Power/H_2 (MW_e/MW_{th},% LHV)	−0.3	0.3	2.2	3.8	6.0	7.2
Steam-to-carbon ratio	2.39	1.00	1.00	0.73	0.89	1.48
H_2 recovery factor, HRF (%)	89.0	89.0	89.0	89.4	85.0	85.0
Membrane H_2 backpressure (bar)	1.9	1.9	1.9	1.9	2.2	—
Avg. membrane flux (kW/m^2)	23.5	23.5	23.5	23.2	24.5	—
CO_2 disposal (kg/GJ H_2 LHV)	147.9	151.4	151.4	151.0	158.4	142
CO_2 emissions (kg/GJ H_2 LHV)	0	0	0	0	0	13.8

[a]The first letters identify the type of cooling adopted: Q=quench; SC=syngas coolers. The second identify the type of raffinate turbine adopted: U=uncooled; C=cooled. In the last two columns: the suffix "set" indicates that the plant has been set at a different HRF for a better comparison; PSA indicates the different separation system used (PSA).
[b]Effective efficiency=(H_2 product)/(coal input—coal used for coproduced electricity); assuming a coal-to-electricity LHV efficiency of 36.8% for IGCC with pure CO_2 capture, plant 70EPQ (Chiesa et al. [1] and Kreutz et al. [3]).

S/C increases, so does the water content and thermal inertia of the raffinate; unless the HRF is also lowered, the required TIT will not be met. To the left of the line, the adiabatic flame temperature exceeds the desired TIT, leading to premature turbine failure; to the right of the line, the TIT falls below the desired value, leading to suboptimal plant efficiency.

The characteristics of three plants that employ a cooled raffinate turbine are indicated as points along the line labeled "TIT 1250°C" in Fig. 2.[5] The first, labeled QC, is a plant with quench cooling that was investigated in a previous study (Kreutz et al. [5]); its high S/C ratio—a result of quench cooling—and high TIT require that almost 40% of the potential H_2 remain in the raffinate, leading to a rather low HRF (~60%). The adoption of syngas coolers in this work allows plant operation at much lower S/C ratios, which can be envisioned in Fig. 2 as traveling along the TIT 1250°C line—leftward and upward to lower S/C and higher HRF. We focus, in particular, on two plants with HRF values of 85% or higher, labeled SCC (S/C=0.73) and SCC-set (S/C=0.89). (The latter is a minor variant of the former, designed only for comparison with plant SC-PSA, described below.)

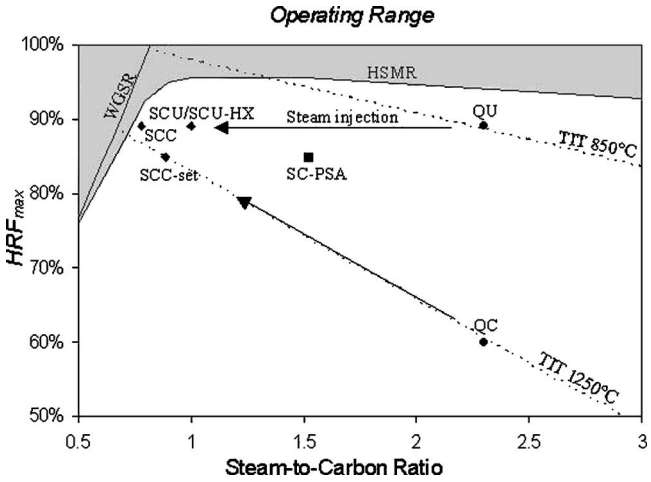

Fig. 2 Allowed operating range (light region) and principal limits. The different plant configurations analyzed have been located on this HRF-S/C framework.

Three plants using uncooled turbines are also shown in Fig. 2. The first, labeled QU, is a quench cooled plant studied previously (Kreutz et al. [5]), lying close to the line labeled "TIT 850°C." Because of the low TIT of the uncooled turbine, our target HRF of ~85% is met at the high S/C provided by the quench. As in the cooled turbine cases, we now switch to syngas coolers and decrease S/C. However, if we were to follow the line labeled TIT 850°C in Fig. 2, we would achieve HRF values significantly higher than those considered in the other plants, making a fair comparison difficult, and we would eventually reach the nonfeasible region. In the previous work, we have seen that plant efficiency is quite sensitive to the HRF (rising monotonically with increasing HRF); for that reason, we take pains to closely match HRF values when comparing the performance of any two plants.

[5]Neither plant QC nor plant QU lies *exactly* on the lines labeled "TIT 1250 C" and "TIT 850 C" for reasons having to do with minor parameter variations between the plants in this study and those of the previous one (Kreutz et al. [3])

Thus, when lowering S/C in the uncooled turbine cases, we leave the TIT 850°C line and follow instead the path of constant HRF, labeled "steam injection." Traveling leftward along this path from point QU would normally yield TIT values exceeding 850°C; to prevent this outcome, we either (i) inject steam (the amount varies with (S/C)) into the raffinate turbine combustor in order to lower the TIT to 850°C for all values of S/C (this trajectory ends at S/C=1, plant "SCU") or (ii) insert a heat exchanger between the combustor and the turbine, plant "SCU-HX".[6] This allows to jump directly to a low S/C ratio and increase the production of steam available for the steam cycle. Both plants are compared with plant QU at the same value of HRF=89%.

The final plant shown in Fig. 2, labeled SC-PSA, denotes a previously studied H_2 plant that employs conventional gas separation technology, i.e., removal of CO_2 from the syngas via physical absorption into a solvent (Selexol) followed by PSA for H_2 purification (Kreutz et al. [3]). This plant is compared with plant SCC-set, which shares its HRF of 85%.

4 Results: Syngas Cooling and H_2 Production/Separation (Water-Gas Reactor and Hydrogen Separation Membrane Reactor)

Having defined the limits on HRF and S/C, and discussed the region of that design space to be studied, we next describe the physical effects of movement within that space, concentrating primarily on variations in the S/C ratio. The water content of the syngas plays a key role in the performance of both the upstream WGSR and the downstream HSMR, affecting the syngas composition and temperature, and the CO conversion factor. We describe some of the primary interactions below.

CO conversion. Since water is one of two reactants in the WGS reaction, lowering the S/C ratio inhibits the chemical conversion of CO to H_2, quantified here by the "CO conversion factor" (CF) for each reactor:

$$\mathrm{CF} \equiv \frac{\mathrm{CO_{conv}}}{\mathrm{CO_{in}}}$$

where CO_{in} represents the moles of CO entering the WGSR, and CO_{conv} denotes the moles of CO converted to H_2. (Note that CO_{in} is not defined as the moles of CO entering the specific reactor in question but rather the moles of CO in the scrubbed syngas, ahead of both the reactors; thus, the total CF is simply the sum of the CF values for the two WGS reactors.) Figure 3 shows how WGS reactivity is split between the two reactors. At S/C=3, the WGSR is responsible for virtually all CO conversion. As S/C falls, however, so does the CF of the WGSR, passing on some of the burden of CO conversion to the HSMR, whose CF increases monotonically with decreasing S/C. Despite the ability of the HSMR to augment WGS reactivity by equilibrium shifting (via H_2 extraction from the reacting syngas), this effect is unable to compensate for lower humidity; the total CF falls from 98% to 83% as S/C is lowered from 3 to 0.7.

Water gas shift reactor temperature. The temperature of the WGS reactors plays a critical role in both their kinetic and equilibrium performance. Both reactors are assumed to be adiabatic and in thermal equilibrium with the syngas flowing through them. In designing a plant, care must be taken to ensure that the temperatures lie within the operating range of the sulfur-tolerant CoMo WGS catalyst, roughly 200–500°C; lower temperatures cause exceedingly low reactivity, while excess temperatures lead to sintering of the catalyst support and consequent catalyst deactivation. The syngas temperature is affected by (1) the heat released in the exothermic WSG reaction and (2) the thermal inertia of the stream. As the S/C ratio is lowered, the thermal inertia of the syngas falls, making it susceptible to high temperature excursions. However, lowering S/C also reduces WGS reactivity (discussed above) and heat release, thereby moderating temperature jumps. These opposing trends largely balance each other, with the fortunate result that, using the basic plant flow sheet in Fig. 1, S/C can be varied from 0.7 to 3.0 without encountering temperature constraints. Over this range of S/C, the WGSR operates between 240°C (inlet) and 420°C (outlet/HSMR inlet), and the HSMR raffinate outlet is ~500°C (increasing to a maximum of ~530°C at S/C~0.825).

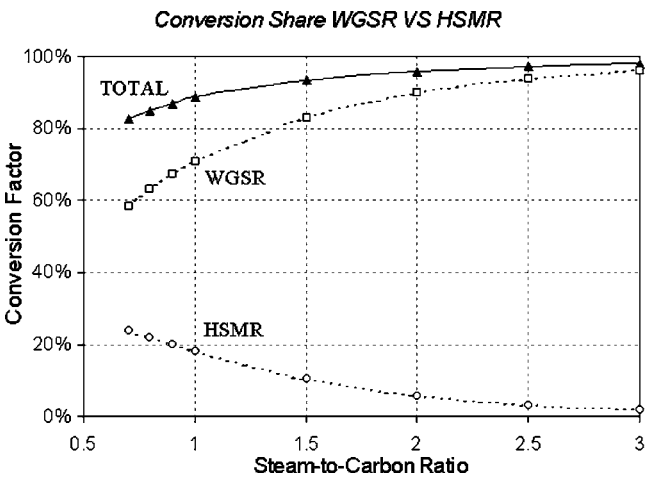

Fig. 3 CO conversion factors as a function of steam-to-carbon ratios, divided among the WGSR and HSMR

H_2 partial pressure and membrane flux. The H_2 separation process is driven by the difference in (the square root of) the H_2 partial pressure across the membrane. High H_2 concentration enhances the performance of the membrane reactor, raising the plant efficiency and lowering the cost of H_2 production. Varying the syngas S/C ratio affects the concentration of H_2 in two disparate ways. Reducing S/C (i.e., removing water) shifts the WGS equilibrium toward the reactant side (from H_2 to CO); e.g., the H_2/CO mole ratio drops by more than a factor of 8 as S/C drops from 3.0 to 0.7. At the same time, removing water (or any species) from the syngas increases the mole fraction of the remaining species. These competing effects yield the somewhat counterintuitive result shown in Fig. 4 where the mole fraction of H_2 in the syngas entering the HSMR is seen to increase monotonically as S/C is reduced from 3 to 0.7 (a result found for all WGSR temperatures between 250°C and 530°C). We also graph in Fig. 4 the membrane performance, quantified by the average flux of H_2 through

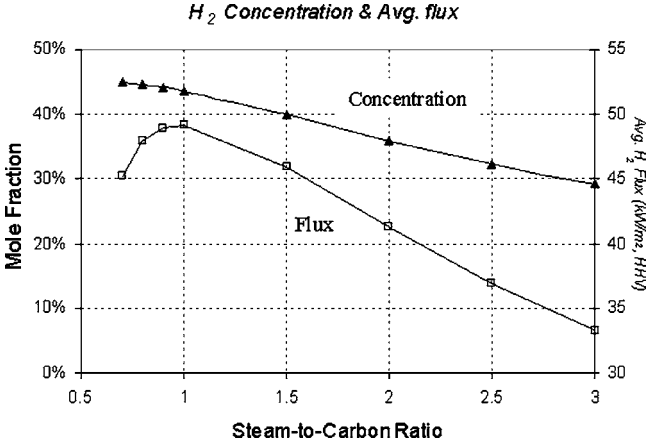

Fig. 4 Composition of the shifted syngas entering the HSMR and average H_2 flux across the membrane (HRF=85%)

[6]In Fig. 2, this plant lies perfectly on plant SCU since it is working at the same S/C-HRF conditions.

the membrane, which is seen to mirror the H_2 partial pressure, rising with decreasing S/C, until $S/C \sim 1$ where the average flux peaks and falls thereafter. The downturn in H_2 flux is caused by the proximity of the plant to limits on HRF and S/C shown in Fig. 2 (curve HSMR); at HRF=85%, the minimum value of S/C is 0.7 (or conversely, at $S/C=0.7$, $HRF_{max}=85.2\%$). In previous work, we have shown that because achieving HRF_{max} requires infinite membrane area, attempting to achieve HRF values exceeding $\sim 90\%$ of HRF_{max} typically leads to unacceptable performance and cost penalties. (This rule of thumb is confirmed in Figs. 2 and 4. In Fig. 4, the membrane performance at HRF=85% is seen to peak at $S/C \sim 1$; note that HRF=85% is $\sim 90\%$ of HRF_{max} =95% at $S/C=1$ in Fig. 2.) It is worth noting that the membrane performance is found to peak at $S/C \sim 1$ over a wide range of variations in both H_2 backpressure and HRF. Since the average H_2 flux at $S/C=1$ is $\sim 25\%$ higher than at $S/C=2.39$ (in the quench plant), adopting of syngas coolers yields performance and cost advantages that were originally unanticipated.

5 Plant Configurations

The plant configurations studied in this section derive from the general considerations discussed previously. Table 4 summarizes the performances of the different plants. Starting from the plants with quench cooling studied in previous papers (plants labeled QU and QC in Fig. 2), we explore in this work the high HRF-low S/C region shown in Fig. 2, a region of plant design space that can be accessed by adopting syngas coolers. This "target zone" is reached by means of two primary approaches (both of which involve lowering the S/C ratio): (1) use an uncooled turbine, keeping the TIT at 850°C either by injecting steam into the combustor (in Fig. 2, horizontal motion left along the line labeled steam injection) or by inserting a heat exchanger upstream the turbine, and (2) use a cooled turbine without any steam injection, keeping the TIT at 1250°C by varying HRF (in Fig. 2, a diagonal climb from lower right to upper left along the line labeled TIT =1250°C). The new plants that result from these different paths through HRF-S/C design space are tuned for optimal thermodynamic performance, and compared below in detail.

Uncooled raffinate turbine. Three plants with syngas coolers and uncooled raffinate turbine were designed. The first lies as close possible in HRF-S/C space to the original quench plant QU ($S/C=2$ and HRF=89%); we do not report the details of this plant because its performance is very close to that of QU. Rather, it provides a starting point for our parametric investigation. The second and third plants, SCU and SCU-HX, are optimized for a much lower S/C ratio in order to exploit potential gains from lowering the S/C ratio. As will be seen, the gains for SCU are negligible, while SCU-HX shows increased performances.

Comparing the performance of these new plants with QU is straightforward because the H_2 output is kept constant (i.e., constant HRF); only the electrical output differs.

Let us first focus on the SCU plant. Only a slight increase in power generation is observed, and thus the gain in overall plant efficiency is negligible. In hindsight, this behavior is readily explained. First, recall that we lower the S/C ratio in order to reduce the amount of steam injected into the syngas prior to the WGSR, and thus boost system efficiency. As the S/C ratio falls at constant HRF, the heating value of the raffinate stream increases and higher adiabatic flame temperatures are achieved in the combustor. In order for the TIT not to exceed 850°C, more steam must be injected prior to expansion in the turbine as S/C falls. It turns out that this steam requirement closely matches the steam that was made available by lowering the S/C ratio. In other words, the overall steam injected in the system is almost constant as S/C varies; only its location of injection changes. The S/C ratio at the turbine inlet is almost a constant value, ~ 2.3. The location of the steam injection does not influence the power generation but rather the WGSR and the membrane reactor as shown before. It is not surprising, therefore, that all the plant configurations lying on this "horizontal path" do not present significant efficiency variations. Note that, from an economic perspective, this influence might be significant. In particular, it has been observed that lower S/C implies less membrane surface requirement and therefore lower costs.

This still leaves the question of why there is such a small increment in performance when introducing syngas coolers unsolved. The reason in this case is found in the relatively small fraction of the total plant output on which we exert an efficiency improvement. Having set HRF to 89%, the power generation represents only $\sim 40\%$ of the total plant output, and of this only 15.4% is produced by the steam cycle. The efficiency increase due to a more elegant heat exchange between syngas and water steam (instead of a quench) and a more performing steam turbine (instead of a gas turbine) acts only on a small fraction of the plant output ($\sim 6\%$) and does not influence much the overall performance of the system, which is dominated by hydrogen production. The effective efficiency increases just by 0.4 points.

The SCU-HX plant overcomes most of the issues encountered in the SCU plant. In SCU-HX instead of injecting steam to lower the TIT to 850°C, we insert a heat exchanger prior the raffinate turbine. Rather than "injecting" steam we "produce" steam. The consequences are quite clear: Up to the combustor, the functioning of the two plants is exactly the same (i.e., the WGRS and membrane behavior is the same) while the power generation undergoes a radical change. Even when working at the same S/C-HRF conditions as SCU, in the SCU-HX case, the fraction of power produced in the raffinate turbine decreases significantly (−82.6 MW), in favor of the more efficient steam turbine (+102.3 MW). The difference reflects the higher-pressure ratio and thus higher efficiency of the *condensing* steam turbine relative to the raffinate turbine, which expands to only 1.05 bars. The ~ 20 MW_e increase in net power translates into an effective efficiency increase of 2.1 points.

Cooled raffinate turbine. The high temperatures obtained in the combustor ($\sim 1200-1300$°C) over the HRF range of interest (80–90%) motivate the use of a cooled raffinate turbine. Previous work showed that using a cooled turbine in a quench system, with its high S/C ratio, yields a low HRF of $\sim 60\%$ (Kreutz et al. [5]). When syngas coolers are employed, however, it becomes possible to reduce the S/C ratio and return to the high HRF values investigated with uncooled turbine systems. This "path" is represented in Fig. 2 by a diagonal movement in which both HRF and S/C vary simultaneously. The thermodynamic behavior of the plant along the path is not simple, but some aspects—as detailed in Table 4—can be described (with the overall effect on efficiency given in parentheses) as follows:

1. The total conversion of CO within both WGSR and HSMR diminishes, although the latter becomes more important on a percentage basis (overall negative effect on efficiency).
2. The production of H_2 increases (and power production falls) due to the fact that HRF is raised to meet the TIT requirements (overall positive effect on efficiency).
3. Power production shifts from the raffinate turbine to the more efficient steam cycle (overall positive effect on efficiency).

The overall outcome is an increase in performance as S/C becomes lower. Higher H_2 output offsets lower power production. This is consistent with the fact that the reference plant for electricity production is an IGCC with carbon capture ($\eta \sim 37\%$); the raffinate turbine is not as efficient as the power plant it displaces, and therefore the less electrical power it produces the better.

Plant performance comparison. The thermodynamic performance of each plant is summarized in Table 4. Plants were designed at an almost constant HRF to avoid the issue of the relative values, both economic and thermodynamic, of H_2 and electricity. The first set of comparisons is conducted between the quench

Table 5 Economic assumptions employed in this study

Coal price[a]	1.35 $/GJ HHV
Capacity factor	80%
Capital charge rate	15% per year
Interest during construction[b]	12.3% of overnight capital
O&M costs	4% of overnight capital
CO_2 transport+storage costs	5.5 $/tonne CO_2
Coproduct electricity price	7.14 ¢/kW h
Carbon tax	96.2 $/tonne C
U.S. dollars valued in year	2006

[a]Average cost[7] to U.S. electric generators in 2005 (EIA [4]).
[b]Based on a four-year construction schedule with equal, annual payments, and a discount rate of 10%/yr.

cooling base case QU and three comparable syngas cooler plants: SCU, with an uncooled raffinate turbine and steam injection, SCU-HX, with uncooled raffinate turbine and heat exchanger cooling, and SCC, with a cooled turbine. As anticipated, SCC is the most attractive of the four plants; at the same H_2 output (~1088 MW_{th} LHV), its power production is ~37 MW higher than QU, changing the plant from electricity consumer to electricity producer. Changing from a simple steam injection to a more complex heat exchange solution in the case of uncooled turbine yields a larger steam cycle and a first step increase in effective efficiency from 60.7% (SCU) to 62.8% (SCU-HX). Completely changing the turbine type from uncooled to cooled yields a more efficient raffinate turbine and a second step increase in effective efficiency from 62.8% (SCU-HX) to 64.6% (SCC).

In order to make the fairest comparison between plant SCC and its conventional technology analog, SCC-PSA, we first create a variant of SCC (labeled SCC-set) with a slightly lower HRF of 85%, exactly matching that of SCC-PSA. (Note that this implies operating the membrane-based plant slightly off its optimized point.) The effective efficiency of the conventional plant SCC-PSA is seen to be higher than SCC-set by ~1.2%; while their H_2 production is almost the same (<0.5% difference), SCC-PSA produces 14 MW (~23%) more power. The reason for the higher net power production in SCC-PSA is found in a substantial lower consumption of the plant compressors. SCC-PSA uses less oxygen (it does not employ O_2 combustion like SCC), and its compression requirements for high-pressure products CO_2 and H_2 are significantly less than in SCC. The lower power consumption in SCC-PSA for oxygen (and to a lesser extent compressed CO_2) is caused by the plant's lower CO_2 capture efficiency (90.5% instead of 100%). In SCC-PSA, the purge gas is combusted in air instead of oxygen, resulting in lower oxygen requirements; at the same time, the CO_2 generated by this combustion is vented, resulting in a lower power required for CO_2 compression.

6 Plant Economics

In this section, we provide the economic parameters used to estimate the cost of producing H_2 and electricity (Table 5), the model for estimating component capital costs (Table 6), and the resulting plant economics (Table 7). This methodology is derived from that used in previous studies (Kreutz et al. [1] and Kreutz et al. [7]); it is intentionally simple and transparent to facilitate revision by readers wishing to use different economic assumptions. To save space, many of the explanations underlying our economic and capital cost assumptions are not reproduced here; please refer to these papers for more detail.

Some assumptions warrant brief comment. Our choice of $5.5/tonne.[7] CO_2 for pipeline transport and aquifer storage costs is a gross estimate based on engineering cost estimates for coal-fired plants of this scale and "average" aquifer characteristics (Odgen); additional costs associated with leakage monitoring, liability, insurance, regulatory fees, etc., are not included. Byproduct gasifier slag and FGD gypsum are assumed to have no disposal cost or market value. Coproduct electric power is valued using the least costly coal IGCC+CCS power, 7.14 ¢/kW h[7]; we assume a carbon tax of 96.2 $/tonne C, the value[7] at which CCS becomes economically viable for coal IGCC (Kreutz et al. [3]).

Capital cost estimation. Capital cost estimates for each system component are adopted from studies of coal-fired IGCC plants. Following Holt, for components within the gasification island (GI), our balance of plant (BOP) costs are 23% of GI installed capital costs, engineering fees (EFs) are 15% of GI+BOP, and process and project contingency are 15% of GI+BOP+EF. Cost

[7]Recalculated in 2006 U.S. dollars using implicit price deflators for the US gross domestic product. We did not take into account the recent escalation in project costs associated with engineering, labor, and materials

Table 6 Parameters used for estimating overnight capital costs (including installation, BOP, general facilities, engineering, overhead and contingencies) in 2006 US dollars. The overnight cost C of a component having size S is related to the cost, C_0, of a single train of a reference component of size, S_0, by the relationship $C=nC_0[S/(nS_0)]^f$, where n is the number of equally sized trains operating at a capacity of 100%/n and f is the scale factor.

Plant component	Scaling parameter	C_0 (M$)	S_0	Specific cost	f	n
Air separation unit	Pure O_2 input	37.8	1839 tonne/day	32 $/kg/day	0.5	2
O_2 compression	Compression power	59.4	10 MW_e	816 $/$kW_e$	0.67	2
Coal storage, prep, handling	Raw coal feed	8.2	2367 tonne/day	16 $/kg/day	0.67	2
Gasifier+quench cooling/scrub	Coal input (LHV)	80.3	680 MW_{th}	118 $/$kW_{th}$	0.67	2
Gasifier+syngas coolers/scrub	Coal input (LHV)	187.3	697 MW_{th}	267 $/$kW_{th}$	0.67	2
HT-WGS reactor	Coal input (LHV)	0.2	437 MW_{th}	0.46 $/$kW_{th}$	0.67	2
Membrane reactor	Membrane area	28.5	10,000 m^2	2850 $/$m^2$	1	2
H_2 compressor	Compression power	—	—	~3600 $/$kW_e$	—	8×14%
Raffinate turbine	Expander power	4.1	355 MW_e	111 $/$kW_e$	0.8	1
Flue gas desulfurization	Pure CO_2 flow	39.4	267 tonne/h	91 $/kg/h	0.67	1
CO_2 drying and compression	Compression power	24.4	13 MW_e	1455 $/$kW_e$	0.67	1
Syngas expander	Expander power	19.2	10 MW_e	408 $/$kW_e$	0.67	1
Steam boilers and heat exch.	Heat transferred	116.8	100 MW_{th}	117 $/$kW_{th}$	1	1
Steam cycle (turbine+condenser)	ST gross power	76.8	136 MW_e	565 $/$kW_e$	0.67	1

Table 7 Costs for membrane-based H_2 production. Costs for "commercially ready" technology H_2 plant, SCC-PSA, are included for comparison in right hand column.

Plant identifier	QU	SCU	SCU-HX	SCC	SCC-set	SCC-PSA
	Plant component cost[a] (M$):					
Coal storage, prep, handling	78.2	78.2	78.2	78.2	78.2	78.2
Air separation unit	129.7	129.9	129.9	129.8	133.0	102.1
Extra O_2 compressor	0.0	0.0	0.0	0.0	0.0	19.5
Gasifier, syngas cooling and scrub	166.1	394.3	394.3	394.3	394.3	380.8
HT-WGS reactor	0.6	0.6	0.6	0.6	0.6	66.6
Membrane reactor	132.0	131.6	131.6	133.9	120.5	85.4
H_2 compressor	200.2	199.8	199.8	200.1	191.9	10.2
Syngas expander	0	0	0	3.7	4.1	0
Raffinate turbine expander	25.4	22.4	15.1	18.2	20.6	34.1
Flue gas desulfurization	35	36	36	36	36	145.3
CO_2 drying and compression	49.4	50.3	50.3	50.3	50.3	44.5
H_2 HRSG	7.0	7.2	7.2	7.3	6.9	—
Raffinate turbine exhaust HRSG	3.7	4.7	10.9	9.7	10.8	32.8
Steam cycle (turbine+condenser)	0.0	32.1	70.0	61.5	59.5	76.1
Total overnight cost (M$)	827.5	1086.6	1123.5	1123.3	1106.1	1075.7
Construction interest (16% of OC)	101.8	133.7	138.2	138.2	136.1	133.4
Total plant investment (M$)	929.3	1220.3	1261.7	1261.5	1242.2	1217.8
Overnight cost ($/kW$_{th}$ H_2, LHV)	760	1001	1035	1032	1067	1051
	H_2 Cost Components ($/kg H_2):					
Capital (15% of TCR)	0.609	0.802	0.829	0.827	0.854	0.842
O&M (4% of OC per year)	0.145	0.190	0.197	0.196	0.203	0.200
Fuel (at 1.35 $/GJ, HHV)	0.282	0.283	0.283	0.282	0.296	0.304
Electricity sales (at 7.7 ¢/kW h)	0.008	–0.007	–0.052	–0.089	–0.143	–0.166
CO_2 disposal ($6.5/tonne CO_2)	0.098	0.100	0.100	0.100	0.105	0.094
CO_2 emissions ($93.3/tonne C)	0	0	0	0	0	0.135
Total ($/kg H_2)	1.14	1.37	1.36	1.32	1.32	1.41
Total ($/GJ H_2 LHV)	9.52	11.41	11.32	10.97	10.96	11.74
Total ($/GJ H_2 HHV)	8.05	9.65	9.57	9.28	9.28	9.94

[a]Installed capital costs include apportioned BOP and general facilities, engineering, and process/project contingencies.
[b]Includes both high and low temperature WGS reactors, and associated heat exchangers.
[c]Includes Selexol CO_2 absorption and flashing, and PSA.
[d]PSA purge gas compressor.
[e]Gas turbine.
[f]H_2S removal with Selexol.
[g]HRSG.
[h]Steam turbine.

estimates for power block components, ASU, and O_2 and N_2 compressors include BOP, engineering, and a 5% contingency. Our cost model (see Table 6) is based on year 2006[7] overnight capital investment costs, scale factors, and training information assumed for each component. These costs include installation, apportioned BOP and general facilities, engineering, and process/project contingencies; other costs such as owner's fees, royalties, start-up and preproduction costs, initial inventory, working capital, spare parts, and land are not included.

Membrane reactor cost. We assume a 20 μm thick, dense layer of a PdCu alloy (60% Pd) supported by a porous ceramic or metallic substrate. The overnight cost of the entire membrane reactor module is assumed to be a multiple of the membrane material cost (assumed to be dominated by the Pd cost). At a 2002–2006 average market price of ~$260 per troy ounce, the Pd cost is ~$1200/m^2, so we add $650/m^2 for the underlying module (i.e., support tubing, shell, and interconnections) and $1000/m^2 for fabrication. Thus, our working estimate for the overnight cost of the HSMR is $2850/m^2. The actual cost in dollars depends on the membrane area, which in turn depends on the system size (i.e., flow of syngas), HRF value, and H_2 backpressure (which is optimized in each plant to minimize the cost of produced H_2). Table 7 shows that the cost of the HSMR is ~10% of the total plant investment, and thus some uncertainty in the HSMR cost is not expected to significantly increase the uncertainty in the cost of product H_2.

Other costs (see Kreutz et al. [5]). The cost model for multistage intercooled reciprocating H_2 compressors is taken from an analysis by Cox. We employ eight H_2 four-stage compressor trains, each train sized at 14% capacity (i.e., one spare train). The average overnight capital cost of the H_2 compressors among all plants is ~$3800/kW$_e$. Our cost estimate for the raffinate turbine is based on the comparably sized GE Frame 7FA gas turbine. Note that the absence of a compressor enables the raffinate turbine to boast a specific cost of 95 $/kW$_e$, less than one-third that of the 7FA.

Cost of H_2 Production. The cost of membrane-based H_2 production is detailed in Table 7; we also compare these results with the cost of H_2 from "commercial ready" technology H_2 plant, SCC-PSA.

Quench versus syngas cooling. The most striking feature of Table 7 is that all plants, with the exception of the quench case QU, have roughly the same plant capital cost, regardless of whether the gas separation technology is novel (HSMR) or conventional (Selexol). The quench case is significantly less costly than the others because of the exceptionally high cost of the specialized radiant and convective heat exchangers that are employed in the syngas cooling plants. We have seen previously in plants that convert coal to H_2, electricity, and CO_2 that the increase in plant efficiency gained by using these syngas coolers is not justified by their high cost (Kreutz [3]), an observation that is consistent with systems that combine a low cost feedstock with a capital-intensive conversion facility. The plants studied here are

no exception to this rule. While some efficiency gains have been realized in moving from quench plant QU to syngas cooler plant SCC, the cost of H_2 is nevertheless 10% higher.

Steam injection versus heat exchanger. It is worth noting that the method of cooling the raffinate stream before entering the uncooled turbine does not affect the cost of hydrogen production. The efficiency gain in employing a more refined and complex heat exchanger is almost completely offset by the higher capital cost. Once again, economics go against pure thermodynamic reasoning and justify the more simple steam injection solution.

Comparison with commercially ready H_2 plant. The comparison between membrane-based and conventional plants is less straightforward because of (1) their different CO_2 capture efficiencies and (2) uncertainties about the novel HSMR technology. Given the uncertainties in our assumptions, the cost of H_2 from SCC-set is essentially equivalent to that from SCC-PSA. Note that the assumed carbon tax adds a significant cost to the H_2 from SCC-PSA. If plant SCC-PSA were redesigned more like the HSMR-based plants and use O_2 combustion to capture virtually all of the CO_2, the plant efficiency would drop (and the feedstock costs increase), but the emissions tax disappear; we expect that the overall cost of H_2 would not change very significantly. We found previously (Kreutz et al. [5]) that, in plants with quench cooling, the cost of H_2 using conventional and membrane-based gas separation technologies is comparable, which seems to be the case also in plants that use more efficient and costly syngas coolers. It is worth noting that this is not a foregone conclusion but rather depends on the membrane technology. If we imagine a membrane whose H_2 permeance is orders of magnitude higher, as exhibited by some current H_2 separation membranes in H_2S-free environments (Mundschau [11]), both the membrane and H_2 compression will be substantially less costly, substantially reducing the cost of H_2. These technologies bear watching, and plant designs that desulfurize the syngas upstream of the membrane merit further consideration.

7 Conclusions

We have investigated the potential benefits of using HSMRs in coal-to-H_2 plants with CO_2 capture based on gasifiers that use radiant and convective heat exchangers for syngas cooling. We have explored the complicated plant behavior as a function of both the S/C ratio and HRF. Based on the results, we note the following findings.

First, compared with quench cooling, the more costly syngas coolers provide a modest increase in plant efficiency, but do not appear to be economically justified.

Second, plants employing HSMRs appear to have efficiencies and economics that are comparable to those of analogous plants that employ more conventional gas separation technologies (Selexol absorption of CO_2 and H_2 purification with PSA). The expected gains due to a continuous removal of H_2 in a HSMR are present but do not significantly improve the economics of the plant. This situation may tilt in favor of HSMR-based systems that are built around advanced membranes with H_2 permeances that are dramatically higher than that used here.

Third, in plants that do employ HSMRs, the best power island technology is represented by the cooled raffinate turbine, which is well matched to the low S/C ratios and high HRF values explored in this paper.

Nomenclature

CCS = carbon capture and storage
CF = conversion factor
FGD = flue gas desulfurization
HRF = hydrogen recovery factor
HSMR = hydrogen separation membrane reactor
PSA = pressure swing adsorption
QU = quench uncooled turbine
RT = raffinate turbine
S/C = steam-to-carbon ratio
SCC = syngas cooler cooled turbine
SCC-PSA = syngas cooler cooled turbine-pressure swing adsorption gas separation
SCC-set = syngas cooler cooled turbine-HRF set to 85%
SCU = syngas cooler uncooled turbine-steam injection
SCU-HX = syngas cooler uncooled turbine-heat exchanger
WGS = water gas shift reaction
WGSR = water gas shift reactor

References

[1] Chiesa, P., Consonni, S., Kreutz, T. G., and Williams, R. H., 2005, "Co-Production of Hydrogen, Electricity and CO_2 From Coal With Commercially Ready Technology. Part A: Performance and Emissions," Int. J. Hydrogen Energy, **30**, pp. 747–767.

[2] Chiesa, P., Kreutz, T. G., and Lozza, G., 2007, "CO_2 Sequestration From IGCC Power Plants by Means of Metallic Membranes," ASME J. Eng. Gas Turbines Power, **129**, pp. 123–134.

[3] Kreutz, T. G., Williams, R. H., Consonni, S., and Chiesa, P., 2005, "Co-Production of Hydrogen, Electricity and CO_2 From Coal With Commercially Ready Technology. Part B: Economic Analysis," Int. J. Hydrogen Energy, **30**, pp. 769–784.

[4] EIA, 2005, "2005 Annual Coal Report," Energy Information Administration, U.S. Department of Energy Report No. DOE/EIA-0584, Oct. 2006 (http://www.eia.doe.gov/cneaf/coal/acr/acr.pdf).

[5] Kreutz, T. G., Chiesa, P., and Williams, R. H., 2007, "Techno-Economic Analysis of Hydrogen and Electricity Production From Coal With Near Zero Pollutant and CO_2 Emissions Using an Inorganic Hydrogen Separation Membrane Reactor: System Optimization and Comparative Analysis," Int. J. Hydrogen Energy, submitted.

[6] Gray, D., and Tomlinson, G., 2001, "Coproduction of Ultra Clean Transportation Fuels, Hydrogen, and Electric Power From Coal," Mitretek Report No. MTR 2001–43 to U.S. DOE (NETL) Contract No. DE-AM26–99FT40465, Project No. 0601CTC2-C2, Jul. 2001.

[7] Badin, J. S., DeLallo, M. R., Klett, M. G., Rutkowski, M. D., and Temchin, J. R., 1999, "Decarbonized Fuel Production Facility—A Technical Strategy for Coal in the Next Century," *Proceedings of the 1999 Gasification Technologies Conference*, San Francisco, CA, Oct. 17–20.

[8] Thomlinson, G., and Kreutz, Tom, 2002, private communication.

[9] Simbeck, D. R., Korens, N., Biasca, F. E., Vejtasa, S., and Dickenson, R. L., 1993, "Coal Gasification Guidebook: Status, Applications, and Technologies," Electric Power Research Institute Final Report No. TR-102034, Palo Alto, CA, Dec.

[10] Edlund, D. L., and Henry, M. H., 1995, "A Catalytic Membrane Reactor for Facilitating the Water-Gas-Shift Reaction at High Temperatures," Phase II Final Report to the U.S. DOE Contract No. DE-FG03–91-ER81229, Nov. 30.

[11] Mundschau, M., 2004, "Simultaneous Hydrocarbon Reforming, Carbon Dioxide Sequestration and Hydrogen Separation Using Dense Inorganic Membranes," *Proceedings of the Third Annual Conference on Carbon Capture and Sequestration*, Arlington, VA, May 3–6.

Ahsan R. Choudhuri
e-mail: ahsan@utep.edu

Mahesh Subramanya
e-mail: msubrama@bechtel.com

Combustion and Propulsion Research Laboratory,
University of Texas at El Paso,
El Paso, TX 79968-0521

Subramanyam R. Gollahalli
Combustion and Flame Dynamics Laboratory,
University of Oklahoma,
Norman, OK 73019-1052
e-mail: gollahal@ou.edu

Flame Extinction Limits of H_2-CO Fuel Blends

The flame extinction limits of syngas (H_2-CO) *flames were measured using a twin-flame counterflow burner. Plots of extinction limits (%f: volumetric percent of fuel in air) versus global stretch rates were generated at different fuel blend compositions and were extrapolated to determine the flame extinction limit corresponding to an experimentally unattainable zero-stretch condition. The zero-stretch extinction limit of* H_2-CO *mixtures decreases with the increase in* H_2 *concentration in the mixture. The average difference between the measured flame extinction limit and the Le Chatelier's calculation is around 7% of the mean value. The measured OH chemiluminescence data indicates that regardless of blend composition the OH radical concentration reduces to a critical value prior to the flame extinction. The measured laminar flame velocity close to the extinction indicates that regardless of fuel composition, the premixed flame of hydrogen fuel blends extinguishes when the mixture laminar flame velocity falls below a critical value.*
[DOI: 10.1115/1.2835059]

1 Introduction

With an emerging need to address gas turbine combustor issues such as fuel variability and fuel flexibility, and fundamental information and data regarding the combustion characteristics of commercial and alternative fuels are essential [1,2]. Future generation gas turbine combustors are expected to tolerate fuel compositions ranging from that of natural gas to a broad range of syngases without sacrificing their low pollutant emission characteristics [3]. Hydrogen-containing fuel blends such as various coal synthesized gases (syngases) have unique flame dynamics and chemical kinetics [4–6]. Even a small amount of hydrogen in a fuel blend can trigger the onset of flashback by altering the kinetics and transport properties of the fuel mixture. The presence of hydrogen in the fuel blend significantly changes the flame response to stretch, preferential diffusion, and instabilities. Despite this immense practical importance, quantitative information on combustion of hydrogen containing synthetic fuels is limited. Although one may expect that the combustion characteristics of fuel blends fall intermediate to those of the primary fuels, some recent investigations have clearly demonstrated that blended fuels can have significantly different characteristics from those of the original fuels [4–6], and interpolation is not direct.

One of the characteristics, i.e., the flame extinction limit of a fuel blend, is important to understand the basic combustion mechanisms and flame stability in practical systems. The term flame extinction limit has a different implication compared to flammability limit. Generally, the flammability limit is an experimentally determined limiting concentration of fuel in an oxidizer beyond which flame does not propagate in a standard apparatus and at a set of standard test conditions, and hence its value is dependent on apparatus and test protocol. In contrast, the flame extinction limit is a limiting concentration of fuel in a mixture of fuel and oxidizer at which chemical reaction is not self-sustaining [7–9], which is a more fundamental thermochemical characteristic than the flammability limit. Factors such as fuel type, and thermochemical and transport properties affect its value. Flame extinction occurs when the energy loss rate due to mechanisms, such as chain-terminating reactions, radiative heat loss, and nonequidiffusion, exceeds the energy release rate.

In recent years, there has been a renewed interest in chemical kinetics of hydrogen blends with other fuels (especially H_2-CO mixtures) due to their importance in the application of syngases in terrestrial gas turbine power generation [1,2]. Flame extinction measurements are also useful for verifications of computational schemes. Maruta et al. [9] and Guo et al. [10] have compared computed and measured flame extinction limits of CH_4-air flame at normal and microgravity conditions. However, flame extinction data for most of the hydrogen fuel blends are lacking. This paper provides flame extinction data for H_2-CO mixtures. The range of mixture conditions used in the present investigation represents typical mixture conditions of syngas (Table 1).

A widely accepted technique for determining the flame extinction limit utilizes a twin-flame counterflow arrangement proposed by Ishizuka and Law [7] (see Table 2). This technique uses a planar, twin-flame-counterflow nozzle system to determine the stretch rate at which flames are extinguished. By repeating the experiment at diminishing fuel/air ratios, it is possible to extrapolate the results to identify the equivalence ratio corresponding to an experimentally unattainable zero-stretch condition. Unlike the flammability limit measurement, this technique entirely avoids issues associated with the ignition system.

Also, a twin-flame counterflow configuration allows quantification of the effects of hydrodynamic strain on flames. This is essential to understand how turbulence induced strain affects flame behavior (such as extinction and flashback) in practical combustors. In this configuration, unburned reactants are issued from two identical burners placed in opposed flow configurations and twin flames are formed on both side of the stagnation flame. It can be shown[1] that the global flame stretch factor K is the magnitude of the axial velocity gradient U/z [12].

Currently, there is no theoretical or empirical relation available to estimate the extinction limit of fuel blends. Le Chatelier's rule is commonly used to evaluate the flammability limit of fuel blends. This rule uses an additive formula to calculate the flammability limit of the fuel blend from the limiting mole fractions X_i of each ingredient i. The lower flammability limit of a gas fuel mixture is thus

Manuscript received February 22, 2007; final manuscript received September 26, 2007; published online March 28, 2008. Review conducted by Nader Rizk.

[1]"The axial flow velocity U is given by $\pm 2cz$, where c is constant and z is the axial distance from the stagnation plane, which is independent of the radial coordinate r. The radial velocity V is given by cr and is independent of z. The stretch acting on the flame is the sum of the extensional strains in the two directions orthogonal to the z axis, that is, $\partial V/\partial x + \partial V/\partial y = 2c = -\partial U/\partial z$. Thus, the flame stretch Σ is simply the magnitude of the axial velocity gradient" [12].

Table 1 Compositions of low calorific value gases (source: Ref. [11])

Gasification	Type of coal	CO (%)	H_2 (%)	CH_4 (%)	N_2 (%)	CO_2 (%)	Calorific value (MJ/m^3)
	Brown coal	16	25	5	40	14	6.28
Coal	Bituminous	17.2	24.8	4.1	42.7	I1	6.13
	Lignite	22	12	I	55	10	4.13
	Coke	29	15	3	50	3	6.08
Wood		2.1	21	1.83	43	12	7.07

$$\mathrm{LFL} = \frac{100}{\frac{M_1}{\mathrm{LFL}_1} + \frac{M_2}{\mathrm{LFL}_2} + \frac{M_3}{\mathrm{LFL}_3} + \cdots}$$

where LFL is the lower flammability limit of the fuel M_1, M_2, $M_3,\ldots$ are the volumetric percentage of each fuel in the fuel gas mixture ($M_1+M_2+M_3+\cdots=100$), and $\mathrm{LFL}_1+\mathrm{LFL}_2+\mathrm{LFL}_3+\cdots$ are the lower flammability limits of individual fuels [13].

It seems logical to extend the Le Chatelier's rule to predict the extinction limits of fuel blends. However, the applicability and accuracy of this rule to estimate the flame extinction limit of a fuel blend have not been experimentally verified. The extinction behavior of a fuel depends largely on complex interactions of burning velocity, energy release, and external loss mechanisms, which depend nonlinearly on X_i. Previous investigations have shown that in a fuel blend, the fuel with the lower burning velocity generally dominates as a reaction inhibitor [14]. Additionally, the fuel blends have different physicochemical characteristics, which depend nonlinearly on X_i. Thus, the prediction accuracy of Le Chatelier's relation for determining the flame extinction limit of fuel blends needs examination [13,14].

The primary objectives of this investigation are (i) to generate flame extinction data of H_2-CO mixtures (syngas), and (ii) to establish the precision of using Le Chatelier's rule for estimating flame extinction data of fuel mixtures. The paper compares experimentally measured extinction values of fuel blends with those estimated using Le Chatelier's relation. Laminar flame velocity (S_L), flame temperature, and chemiluminescent emission measurements of OH^* and CH^* were also used to gain an insight into the extinction behavior of hydrogen blends with other fuels (CO and CH_4). The flame extinction limit is expressed as a volumetric percent of fuel ($\%f$) in a fuel-air mixture instead of equivalence ratio (ϕ) to avoid ambiguity as the latter masks the effects of the components in the blend.

2 Experimental Techniques

2.1 Twin-Flame Counterflow Burner System. The counterflow twin-flame burner assembly is engineered to control combustion conditions and to achieve flame extinction over a wide range of flame-stretch values. The top burner is mounted on a computer-controlled high-precision traverse mechanism to change the distance between top and bottom burner exits. This mechanism allows the generation of twin flames for a wide range of flow conditions and fuel compositions. The two identical burner assemblies (Fig. 1) consist of five distinctive parts: (i) acoustic housing, (ii) manifold, (iii) stem, (iv) connector, and (v) burner nozzles. The smooth inside surface of the burner nozzle was machined to fit a fifth-order polynomial curve to provide a top-hat exit flow velocity profile [15]. The burner nozzle also includes a coannular passage to introduce nitrogen to shield the flame from the ambient surroundings. The acoustic source housing is designed to create an external excitation and was not used for the present study.

The air and fuel blend is fed to the top and bottom burner assemblies through four symmetric inlets. The fuel air supply lines, each with a digital mass flow-meter, precision metering shut-off plug valves, are used to control and quantify air and fuel flow rates.

To avoid fuel stratification effects, homogeneous mixing of air and fuels is ensured by blending the streams far upstream of the burner. The flow rate to bottom burner assembly is adjusted by an additional metering valve, to compensate for the differences in pressure drop in the flow lines. The air-fuel streams are passed through several layers of honeycomb matrices that function as a flow-straightener. Figure 2 shows the axial velocity profile at the burner exit measured with a thermal anemometer. The measured velocity shows a top-hat velocity profile with minimum wall effects and turbulent fluctuations.

Preheating of air-fuel mixtures can significantly lower the lean flammability limits of fuels. Therefore, the burner assemblies are wound with copper coils through which cold water was circulated to insure that the air-fuel mixtures enter combustion zone at room temperature. As discussed earlier, the nitrogen co-flow also reduces preheating of the burner significantly.

A high resolution CCD camera is used to capture magnified, real-time images of the extinction process. A computer controlled triple grating monochromator is used to measure chemiluminescent emissions from OH and CH radicals. A pair of plano-convex lenses is used to focus the flame emission on the input slit of the monochromator. A 500 μm diameter pinhole mounted on the input slit is used to define the probe volume. The light intensity at the desired wavelength was monitored by a high sensitivity photomultiplier tube (PMT). The photomultiplier output is amplified

Table 2 Extinction limits for pure methane (source: Ref. [7])

Author	Method	Flame extinction limit, % methane
Zabetakis	Propagating flame (tube)	5.00
Andrews and Bradley	Propagating flame (vessel)	4.50
Egerton and Thabet	Flat flame	5.10
Sorenson, Savage, and Strehlow	Tent flame	4.00
Yamaoka and Tsuji	Double flame	4.70
Ishizuka and Law	Binary flame	4.80
Womeldorf and Grosshandler [16]	Twin flame	4.90
Present Investigation	Twin flame	4.66

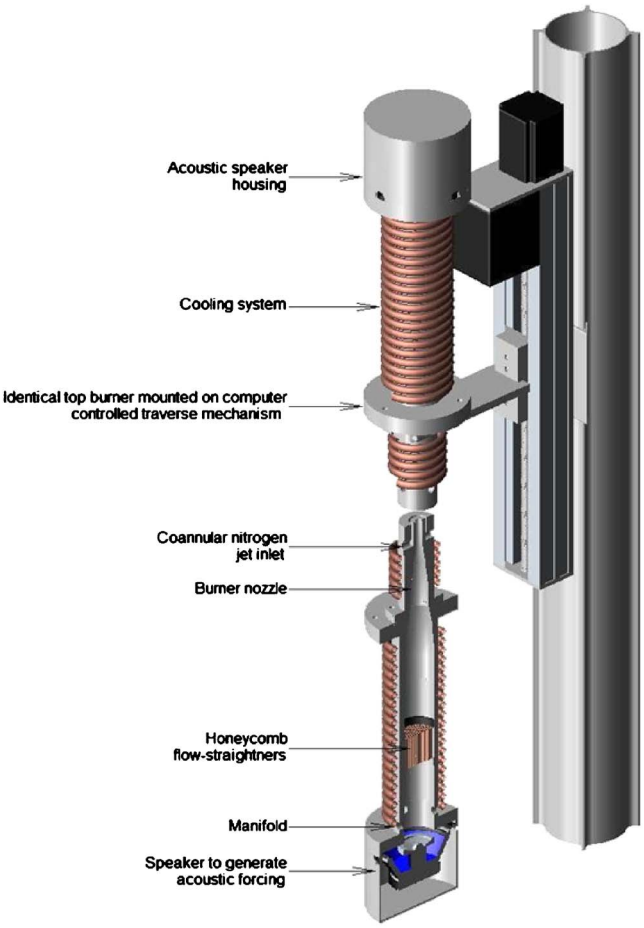

Fig. 1 Counterflow twin-flame burner assembly

and acquired through a data acquisition system (Lab-View, National Instruments Inc.). The output of the PMT at a particular wavelength was sampled at 1 kHz rate and averaged online over 5 s.

Fuel blends with predetermined fuel flow rates and composition are fed through the burner system and the homogeneous fuel mixture at the burner exit is ignited with a pilot flame. Nitrogen is introduced through the concentric annulus of the burner exit, and a metered flow rate of air is gradually added to the fuel mixture. As the air flow rate is increased in the fuel-air mixture, an increase in flame stretch follows, which eventually leads to flame extinction (Fig. 3) and the volumetric percent of fuel blend in the air-fuel mixture at this flame-extinction condition is noted. For methane-air flame, this value was 6.2. The process is repeated by varying the fuel flow rates while maintaining the mixture composition, thereby providing different extinction flame-stretch rates. The equivalence ratio ranged from 0.9 to the leanest experimentally attainable condition.

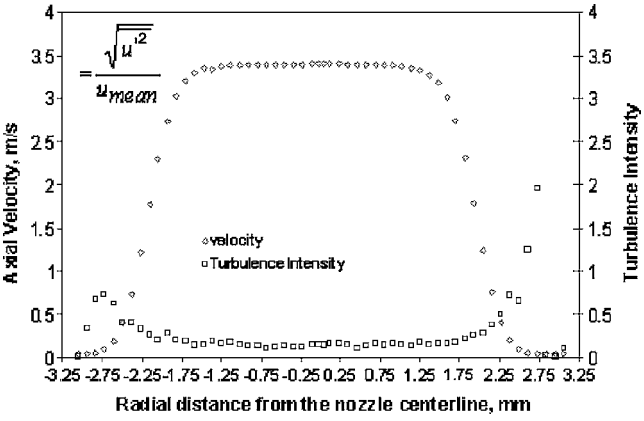

Fig. 2 Hotwire anemometry data on the burner exit profile analyzed without the effect of acoustic oscillations

2.2 Flat-Flame Burner System. Figure 4 shows the flat-flame burner apparatus consisting of a 6 cm diameter sintered stainless steel porous disk. Nitrogen flowing through a concentric 0.5 cm wide porous metal strip shields the flame from the surroundings. The water cooling system extends throughout the porous disk system to vary the heat loss rate from the burner. The flames are ignited at fuel-rich conditions and subsequently the air/fuel flow rates are adjusted to the desired settings with precision needle valves. Once a stable flame front is established, the nitrogen flow rate was adjusted to truncate the flame edges. To measure the laminar burning velocity at near extinction conditions, the equivalence ratio is reduced while maintaining the fuel composition until the flame extinction occurs. The process is repeated for several heat loss rates from the burner and the results are extrapolated to zero heat-flux conditions to obtain the near extinction laminar burning velocity data at the adiabatic condition. Temperature measurements were obtained with the use of an R-type thermocouple, mounted on a precision traverse mechanism, and placed at a set distance above the burner surface. OH radical concentration was imaged with the planar laser induced fluorescence technique. For fluorescence imaging of OH, the excitation of (1,0) band of $A^2\Sigma^+ \leftarrow X^2\Pi$ system combined with detection of the strong (1,1) band has been used. A Nd:YAG pumped optical parametric oscillator was used to generate the 285.2 nm ($P_1[8]$ line) laser plane for excitation and an ICCD based camera system was used for fluorescence imaging. The fluorescence signal was filtered through a 2 mm UG5 and WG305 Schott glass filter to keep the spectral detection window at 315 ± 8 nm.

3 Results and Discussion

3.1 Extinction Limits. First, the flame extinction limits of pure CH_4 (99.97%) were measured for the qualification and validation of the present twin-flame counterflow burner system. Figure 5 shows the extinction values ($\%f$) of CH_4 at different stretch conditions. The equation $\%f = 0.003\ K + 4.66(\pm 0.12)$ represents the linear fit of the measured data with a R^2 value of 0.98, and estimated at 95% confidence interval with Student's-t distribution, where K is the global flame stretch rate (U/y). The intercept value of 4.66 is the extinction value of CH_4 at the zero stretch condition.

Table 1 shows the comparison of the present measurements with various extinction limit values reported in the literature for CH_4. The present value is within 3% of the value reported by Ishizuka and Law [7] using a similar burner system. Two assumptions were made to calculate the zero-stretch extinction limit of the CH_4 flames: (i) the global stretch rate is proportional to the local stretch rate, and (ii) the variation of extinction limit with the stretch rate is linear toward the zero-stretch limit. Previous investigations have shown the validity of the first assumption [16,17]. Additionally, extinction data of pure CH_4 flames presented in Ref. [16] showed a linear variation of extinction equivalence ratio with the stretch for a low K range of 30 s^{-1} to 80 s^{-1}. If the present measurements are included with the data from Ref. [16], the extinction limit shows a linear behavior for a wide range of stretch conditions [50 s^{-1} to 500 s^{-1}]. Thus, the linearity of the variation of extinction limit with K is a reasonable assumption.

Figure 6 shows the extinction data of H_2-CO flame at different fuel-blend compositions and stretch conditions. For a given stretch rate, flame extinguishes at a leaner condition when the H_2 concentration in the mixture is increased. This is attributed to the

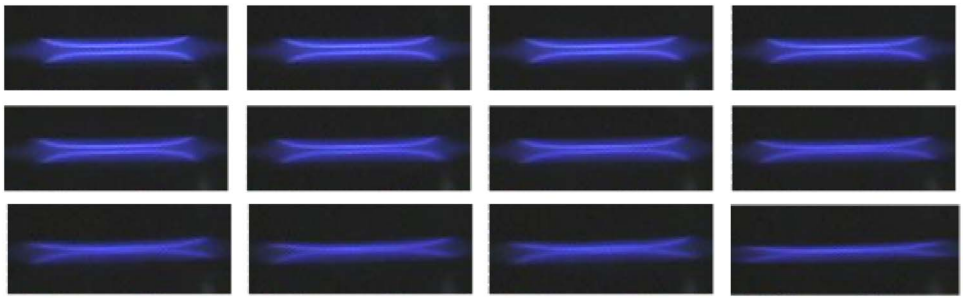

Fig. 3 Twin-flame images of pure CH_4-air flame at different stretch conditions leading to extinction ($K_{ext} \sim 500\ s^{-1}$, $\%f = 6.2$)

increase in CO oxidation rate [$CO+OH \rightarrow CO_2+H$] and branching reaction [$O+H_2 \rightarrow OH+H$; $OH+H_2 \rightarrow H_2O+H$; $H+O_2 \rightarrow OH+O$] due to the enhancement of radical pool. For a given blend composition, the flame extinguishes at a richer condition with the increase in flame stretch rate. It is noteworthy that initially a large change in the extinction fuel concentration occurs with a small addition of H_2 ($<10\%$). However, with further addition of H_2 the extinction limit of fuel concentration follows the law of diminishing returns. This is consistent with the sensitivity analysis of H_2-CO kinetics reported by Vagelopoulos and Egolfopoulos [18]. Initially, a small amount of H_2 in the fuel blend significantly accelerates the mass burning rate due to the domination of reaction $CO+OH \rightarrow CO_2+H$. With the further addition of H_2 the hydrogen kinetics dominate instead of CO reaction. Figure 7 shows the normalized sensitivity analysis data reproduced from Ref. [18] with nomenclature consistent with this paper. The analysis shows the reduction in sensitivity to CO oxidation with the increase in H_2 concentration in the blend.

Figure 8 shows the extinction values ($\%f$) of 5%–95% H_2-CO extrapolated to the zero-stretch condition. The equation $\%f = 0.023\ K + 12.32(\pm 0.32)$ represents the linear fit of the measured data with an R^2 value of 0.96. The intercept value of 12.32 represents the zero stretch extinction limit ($\%f$) for the 5%–95% H_2-CO fuel blend. Zero-stretch limits of different of H_2-CO are also determined and shown in Fig. 9.

Figure 9 shows the variation of the fuel concentration limit at zero stretch extinction of H_2-CO blend decreases with increase in hydrogen content. The maximum overall uncertainty of the measurement is less than $\pm 2.5\%$ of the mean value. The solid line in Fig. 9 shows the same result derived by applying the Le Chatelier's rule. The average difference between the measured data

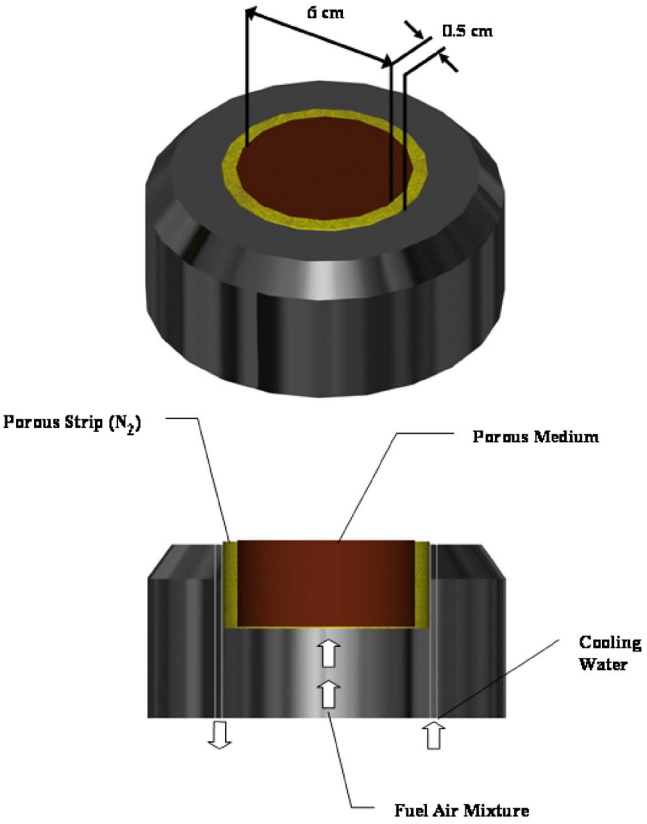

Fig. 4 Flat-flame burner system

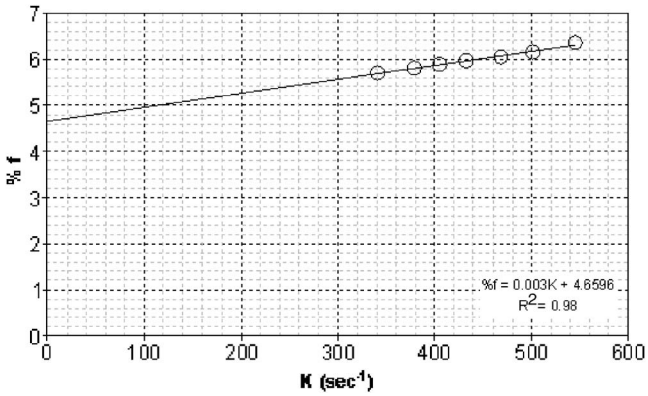

Fig. 5 Flame extinction limit for pure-methane fuel at different stretch conditions

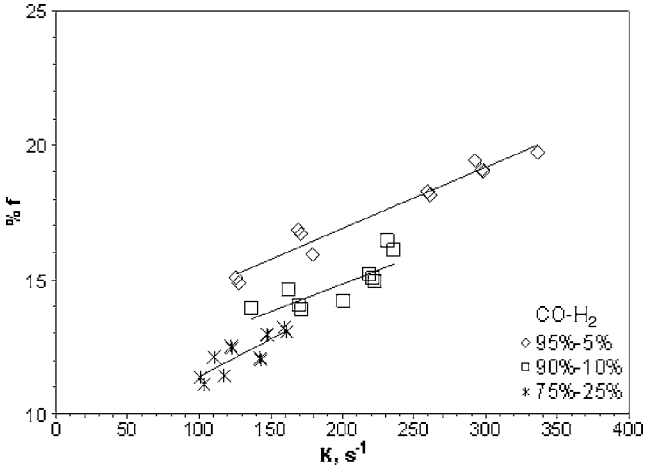

Fig. 6 Flame extinction limits of H_2-CO fuel blend composition at different stretch conditions

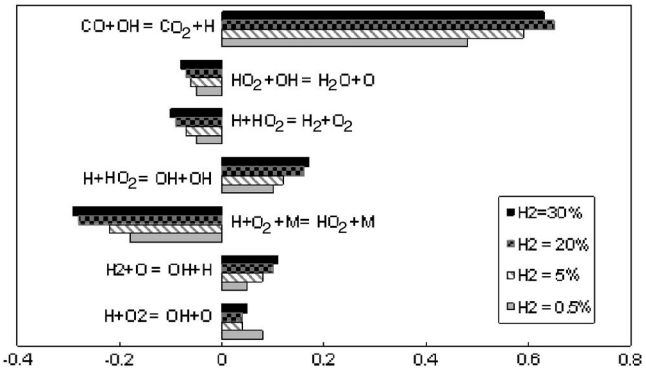

Fig. 7 Normalized sensitivity analysis data (Ref. [8])

and the Le Chatelier's calculation is around 7%.

In order to understand the effects of H_2 addition to a hydrocarbon fuel, extinction measurements were extended to H_2-CH_4 blends. Figure 9 also includes the measured zero-stretch extinction limits of H_2-CH_4 blend flames at different H_2 concentrations along with the values calculated by Le Chatelier's rule. The estimated maximum uncertainty of the measurement is same as that with the H_2-CO measurements ($< \pm 2.5\%$ of the mean value). In this case also, the zero-stretch extinction occurs at leaner conditions with the increase in H_2 concentration. The average difference between the measured and the calculated values are 3.5% which is close to the measurement uncertainties. Figure 10 shows the same H_2-CH_4 zero-stretch extinction value in an expanded scale for better visualization of the data.

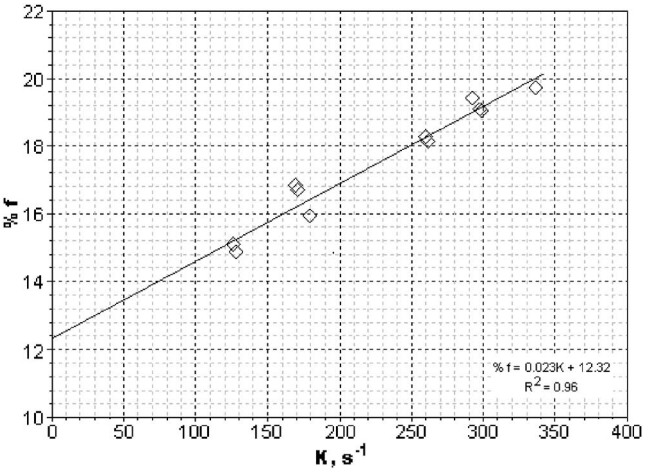

Fig. 8 Extrapolation of 5%–95% H_2-CO extinctions to zero-stretch condition

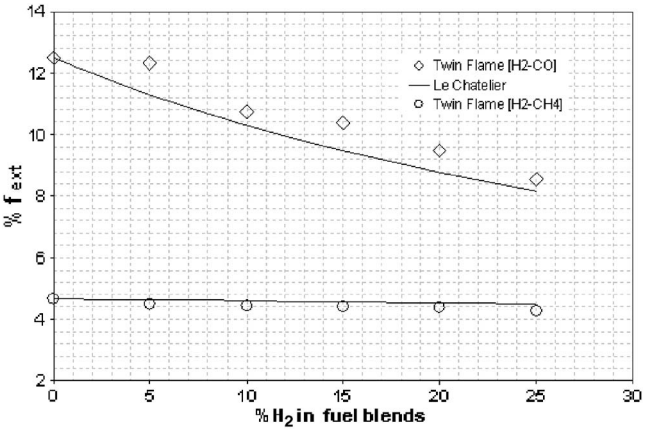

Fig. 9 Zero-stretch flame extinction limits of H_2-CO and H_2-CH_4 fuel blends at different H_2 concentration in the fuel mixture

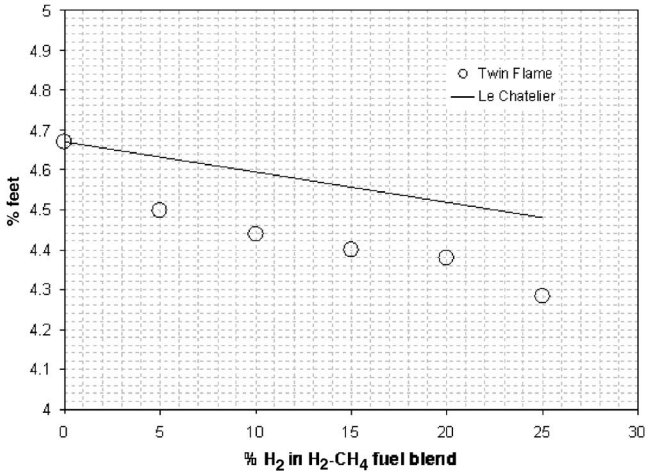

Fig. 10 Plot of zero-stretch flame extinction limits of H_2-CH_4 fuel blends in an expanded scale

The flame extinction values calculated using Le Chatelier's rule compare better with the experimental measurements (0%–30% of H_2) for H_2-CH_4 than H_2-CO mixture. The extinction values of H_2 and CO used for the calculation are 4% and 12.5% respectively. In binary or ternary fuel mixtures, the fuel with lower flame speed generally acts as an inhibitor. For H_2-CO mixtures, CO acts as a flame inhibitor due to its lower flame speed ($CO+O_2$ reaction requires large activation energy) and thus causes the discrepancies between measured and calculated values. On the other hand, the relatively higher reactivity of CH_4 with multiple reaction pathways leads to a lower inhibition effect in H_2-CH_4 mixture flames, and hence the calculated extinction limits agree fairly well with the measured values. Recently, the authors [19] have also reported that the discrepancies between measured and calculated values are especially significant (as high as 19%) for hydrocarbon fuel blends where both components have comparable burning velocities and fuel properties. The inhibition effects of additives are especially pronounced for their blends with hydrocarbons having comparable laminar burning velocities. It is apparent that the prediction accuracy of the Le Chatelier rule is higher for fuel blends with less inhibition effects.

3.2 Near Extinction Flame Temperature. Figure 11 shows the measured maximum flame temperature of H_2-CO mixtures as the flame approaches the extinction limit. It appears that regardless of the mixture composition, the temperature hovers around 740°C for the H_2-CO mixtures prior to extinction. As energy loss mechanisms overtake the energy release mechanisms at this temperature, the measured extinction flame temperature can be used to validate heat loss models used in computational schemes.

3.3 Radical Concentration at Extinction. Figures 12 and 13 show the chemiluminescence emission signals (in arbitrary unit) of OH and CH measured at the maximum temperature location from H_2-CO flames prior to extinction. The chemiluminescence of OH^* and CH^* radicals are useful for tracking the changes in flame characteristics [20] near the extinction condition. Additionally, the radicals are prime indicators of heat release rate. First, for a given blend composition a leanest experimentally achievable flame condition was established. The $\%f$ of this condition was such that a slight increase in stretch rate causes the flame to become extinct. The flame stretch rate was then increased slowly

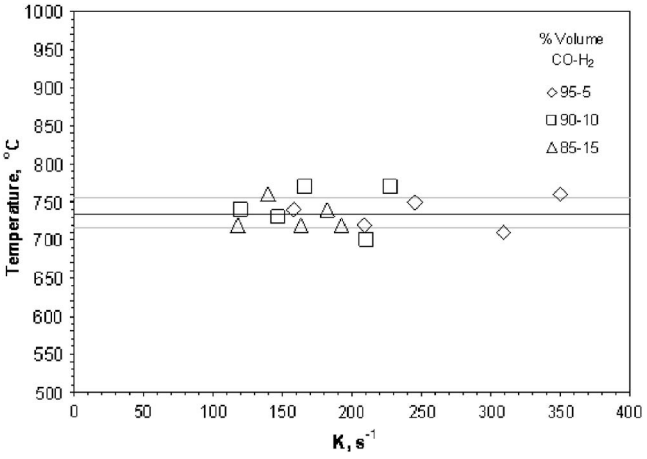

Fig. 11 Maximum flame temperature of CO-H_2 mixtures as flames approach to extinction

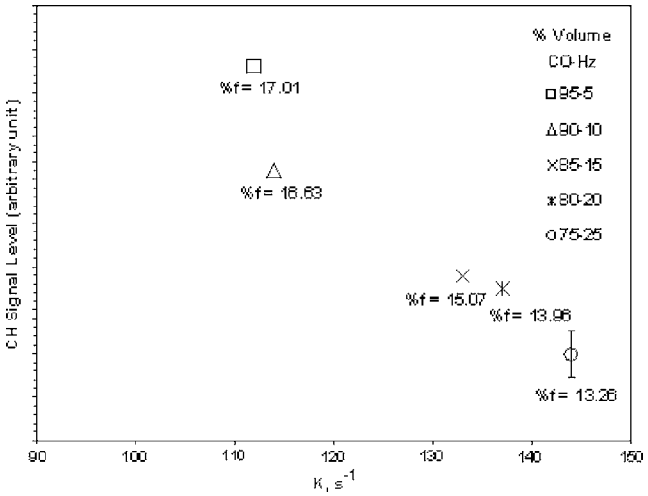

Fig. 13 Chemiluminescent emissions of CH^* radicals measured from H_2-CO fuel blends as flames approach extinction

(keeping the $\%f$ constant) until extinction occurred. The OH and CH signals recorded continuously through out the sequence. To keep the monochromator focused on the predetermined maximum temperature point, the vertical position of the monochromator assembly was continuously adjusted using a laser target and a computer controlled traverse mechanism. For each flame, the process was repeated several times to estimate the uncertainty level of OH signal at extinction conditions. The dashed line in Fig. 12 represents the mean OH signal at the extinction condition for different fuel blends. The data points indicate the OH signal acquired at the inception of the leanest flame.

The chemiluminescent data indicate that the OH radical concentration reduces (within the experimental uncertainties) to an almost the same minimum value prior to the flame extinction regardless of mixture compositions. As the flames approach the extinction condition, production of OH decreases due to the termination of the branching reactions. Although most of the computational studies [21,22] showed that there was no kinetically driven limit criterion for flame extinction; in reality, extinction occurs when the decrease of OH production causes a lower limit in laminar burning velocity beyond which the loss processes suppress the energy release.

It is interesting to note that compared to other fuel blends the

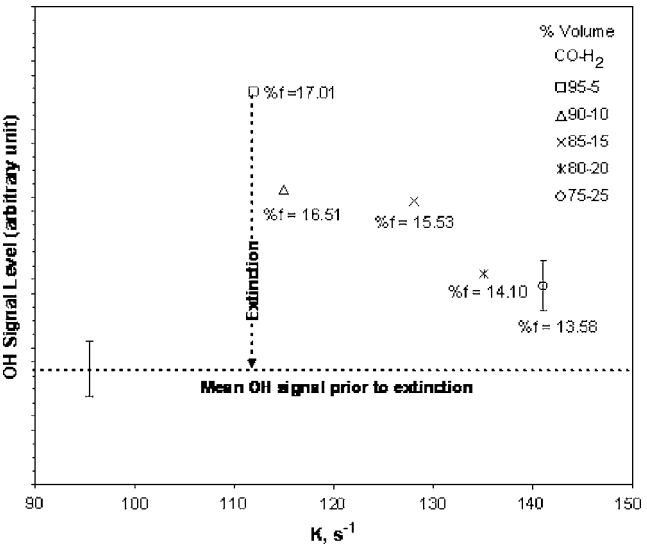

Fig. 12 Chemiluminescent emissions of OH^* radicals measured from H_2-CO fuel blends as flames approach extinction

OH^* concentration is significantly higher for the experimentally achievable leanest stable flame ($\%f=17.01$) for 5%–95% H_2-CO blends. Figure 12 clearly indicates that flames of fuel blends with low H_2 concentration require high OH concentration (at lean conditions) to propagate. This is due to the relative importance of CO oxidation [$CO+OH \rightarrow CO_2+H$] and branching reactions [$O+H_2 \rightarrow OH+H$; $OH+H_2 \rightarrow H_2O+H$; $H+O_2 \rightarrow OH+O$] varies at different H_2 concentration in fuel blends. At low H_2 concentration, the CO oxidation reaction dominates the mass burning rate and the flame propagation depends primarily on the OH concentration. However, with the increase in H_2 concentration in fuel blends the effect of branching reactions becomes significant and H/O radicals dictates the mass burning rate. However, as stated earlier, very close to extinction the OH level attains a limiting value regardless of mixture compositions. Although the CH chemiluminescent emission data (Fig. 13) show a similar trend for lean flames, they do not show any definitive monotonic trend prior to extinction. The CH signals just prior to extinction vary randomly and do not confirm to any mean value. This is most likely due to the fact that the laminar burning velocity of a fuel mixture is determined primary by the radicals and atoms such as OH, O, and H [23–26].

3.4 Laminar Burning Velocity. The laminar flame velocities at extinction of H_2-CO flames at different concentrations of H_2 in the mixtures were measured using a flat-flame burner method. The measurements are performed to confirm the argument that close to the extinction equivalence ratio the laminar burning velocity attains a nonzero asymptotic value. The flat-flame burner is chosen due to the fact that it yields very accurate burning velocity measurements for lean flames.

The flame velocity data (Fig. 14) clearly indicate that regardless of fuel type and compositions, the flame ceases to propagate when the laminar flame velocity reduces to a critical value. This supports the fact that although there exists no extinction flame speed based on the theoretical calculation, the one-dimensional premixed flame extinguishes when the mixture laminar flame speed falls below a certain threshold. This limiting flame speed is tied with the loss mechanisms and is only weakly affected by the rate parameters. The average laminar flame velocity at extinction for H_2-CO measured in the present flat-flame burner configuration is $3.77(\pm 0.38)$ cm/s.

As indicated earlier, several classical theories [27] have described a direct correlation between the laminar flame velocity and the concentration of intermediate radicals and atoms such as OH, H, and O. These theories postulate that the rate of diffusion

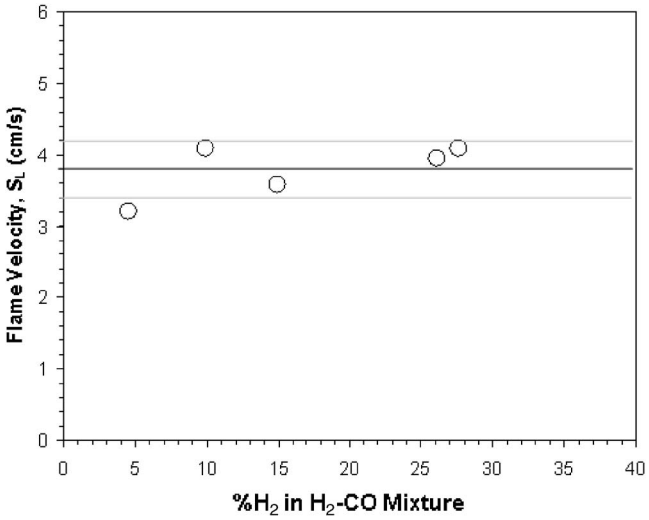

Fig. 14 Average laminar flame velocity of 3.77 (±0.38) cm/s measured close to extinction for H_2-CO flames, measurements obtained using flat-flame burner

of active radicals into the unburned gas region determine the flame speed of particular fuel mixtures. These theories are particularly helpful to compute the laminar flame speed of fuel mixtures since simple additive formulas are not adequate to predict the laminar flame speed of fuel blends [23–26]. In the present study qualitative planar laser induced fluorescence images of OH radical concentration in a one-dimensional flame were captured for different compositions of H_2-CO mixture. Figure 15 shows the OH radical concentration in a 24%–76% H_2-CO flame as it approaches the extinction point. The OH radical concentration decreases significantly as the flame approaches the extinction value.

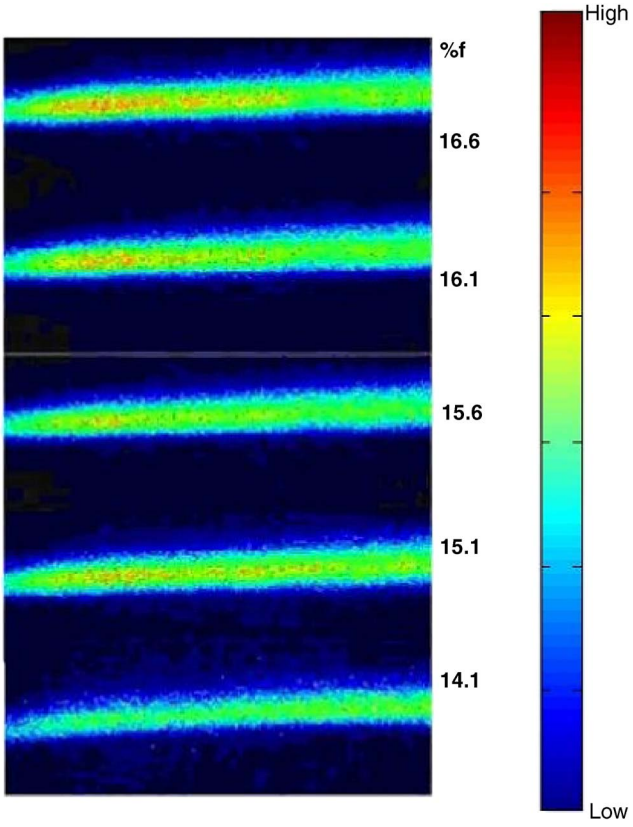

Fig. 15 OH radical concentrations measured close to extinction in 24% H_2-76% CO fuel blend compositions for various %*f*, as measured using flat-flame burner

4 Concluding Remarks

Despite their practical importance, the fundamental flame data of hydrogen fuel blends are scarce. These data such as flame extinction limits or laminar burning velocity are necessary not only to aid the development efforts of fuel flexible combustors but also to provide data for the verification and validation of computational schemes. The report presents new data on flame extinction measurements of H_2-CO premixed flames at different mixture compositions. The study concludes that:

1. The flame extinction limit of H_2-CO fuel blends decreases with the increase in H_2 concentration in the mixture.
2. The average difference between the measured zero-stretch extinction limits of H_2-CO blends and those estimated applying the Le Chatelier's calculation is around only 7% of the mean value.
3. Regardless of the mixture composition the extinction flame temperature of H_2-CO blends approaches the limit value prior to the extinction $[740 \pm 10\,^{\circ}\mathrm{C}]$.
4. The inflame concentration level of OH radical decreases to a limiting value as the premixed flame of a given fuel blends approaches the extinction equivalence ratio.

Acknowledgment

This research was done with the support of the U.S. Department of Energy, under awards DE-FG26-03NT41917 (Project Manager Ben Hsieh) and DE-FG26-05NT42495 (Project Manager Rondle Harp). However, any opinions, findings, conclusions, or recommendations expressed herein are those of the authors and do not necessarily reflect the views of the Department of Energy. The authors like to acknowledge the help of Rogelio Franco, Deepthi Davu, Chendhil Periasamy, and Norman Love during experiments.

Nomenclature

K = global stretch-rate U/y
M = volume percentage of individual fuels in a fuel mixture
U = exit velocity of air-fuel mixture
y = distance between stagnation plane and nozzle exit
$\%f$ = volumetric percent of fuel in air-fuel mixture
$\%f_{\mathrm{ext}}$ = volumetric percent of fuel in air-fuel mixture at extinction
LFL = lower flammability limit of fuel

References

[1] Advanced Gas Turbine Systems Research, 1998, "Request for Proposals," No. AGTSR 98-01, South Carolina Energy Research and Development Center, Clemson, SC.
[2] Support of Advanced Fossil Resource Conversion and Utilization Research by Historically Black Colleges and Universities and Other Minority Institutions, 2005, "Announcement of Funding Opportunity," DE-PS26-05NT42317, National Energy Technology Laboratory, Department of Energy, Pittsburgh, PA.
[3] Narula, R. G., 1998, "Alternative Fuels for Gas Turbine Plants—An Engineering Procurement, and Construction Contractor's Perspective," ASME Paper No. 98-GT-122.
[4] Yu, G., Law, C. K., and Wu, C. K., 1986, "Laminar Flame Speeds of Hydrocarbon+Air Mixtures with Hydrogen Addition," Combust., Explos. Shock Waves, **63**, pp. 339–347.
[5] Choudhuri, A. R., and Gollahalli, S. R., 2000, "Combustion Characteristics of Hydrogen-Hydrocarbon Hybrid Fuel," Int. J. Hydrogen Energy, **25**, pp. 451–462.
[6] Sher, E., and Ozdor, N., 1992, "Laminar Burning Velocities of n-Butane/Air Mixture Enriched With Hydrogen," Combust., Explos. Shock Waves, **89**, pp. 214–220.
[7] Ishizuka, S., and Law, C. K., 1982, "An Experimental Study on Extinction and Stability of Stretch Premixed Flames," *Nineteenth Symposium (International)*

on Combustion, The Combustion Institute, Pittsburgh, PA, pp. 327–335.
[8] Law, C. K., and Egolfopoulos, F. N., 1990, "Experimental and Numerical Determination of Laminar Flame Speeds: Mixtures of C2—Hydrocarbons with Oxygen and Nitrogen," *Twenty-Third Symposium (International) on Combustion*, The Combustion Institute, Pittsburgh, PA, Vol. 109, pp. 413–420.
[9] Maruta, K., Yoshida, M., Guo, H., Ju, Y., and Niioka, T., 1996, "Experimental Study of Methane-Air Premixed Flame Extinction at Small Stretch Rates in Microgravity," Combust., Explos. Shock Waves, **112**, pp. 181–187.
[10] Guo, H., Ju, Y., Maruta, K., Niioka, T., and Liu, F., 1997, "Radiation Extinction Limit of Counterflow Premixed Lean Methane-Air Flames," Combust., Explos. Shock Waves, **109**, pp. 639–646.
[11] Chomiak, J., Longwell, J. P., and Sarofim, A. F., 1989, "Combustion of Low Calorific Value Gases: Problems and Prospects," Prog. Energy Combust. Sci., **15**, pp. 109–129.
[12] Ronney, P. D., 2001, "Premixed-Gas Flame," *Microgravity Combustion. Fire in Free Fall*, H. D. Ross, ed., Academic Press, New York, pp. 35–82.
[13] Burgess, D. S., Furno, A. L., Kuchta, J. M., and Mura, K. E., "Flammability of Mixed Gases," Report of Investigations 8709, Bureau of Mines, U.S. Department of the Interior.
[14] Bui-Pham, M. N., Lutz, A. E., Miller, J. A., Desjardin, M., O'Shaughnessaey, D. M., and Zondlak, R. J., 1995, "Rich Flammability Limits in CH3OH/CO/Diluent Mixtures," Combust. Sci. Technol., **109**, pp. 71–91.
[15] Vargas, A., 2002, "A Numerical Investigation on Elliptic Coaxial Jets," MS thesis, University of Texas at El Paso, Texas.
[16] Womeldorf, C. A., and Grosshandler, W. L., 1999, "Flame Extinction Limits in CH_2F_2/Air Mixtures," Combust., Explos. Shock Waves, **118**(1–2), pp. 25–36.
[17] Kobayashi, H., and Kitano, M., 1991, "Flow Fields and Extinction of Stretched Cylindrical Premixed Flames," Combust. Sci. Technol., **75**, pp. 227–239.
[18] Vagelopoulos, C. M., and Egolfopoulos, F. N., 1994, "Laminar Flame Speed and Extinction Strain Rates of Mixtures of Carbon Monoxide With Hydrogen, Methane, and Air," *Twenty-Fifth Symposium (International) on Combustion*, The Combustion Institute, Pittsburgh, PA, pp. 1317–1323.
[19] Subramanya, M., Davu, D., and Choudhuri, A., 2005, "Experimental Investigation on the Flame Extinction Limit of Fuel Blends," AIAA Paper No. 2005-374.
[20] Farhat, S. A. Ng. W. B., and Zhang, Y., 2005, "Chemiluminescent Emission Measurement of A Diffusion Flame Jet in a Loudspeaker Induced Standing Wave," Fuel, **84**, pp. 1760–1767.
[21] Lakshmisha, K. N., Paul, P. J., and Mukunda, H. S., 1990, "On the Flammability Limit and Heat Loss in Flames With Detailed Chemistry," Sym. (Int.) Combust., [Proc.], **23**, pp. 37–41.
[22] Giovangigli, V., and Smooke, M., 1992, "Application of Continuation Methods to Plane Premixed Laminar Flames," Combust. Sci. Technol., **87**, pp. 241–256.
[23] Yumlu, V. S., 1968, "The Effects of Additives on the Burning Velocities of Flames and Their Possible Prediction by a Mixing Rule," Combust., Explos. Shock Waves, **12**(1), pp. 14–18.
[24] Yumlu, V. S., 1967, "Prediction of Burning Velocities of Saturated Carbon Monoxide-Air Flames by Application of Mixing Rules," Combust., Explos. Shock Waves, **11**(5), pp. 389–396.
[25] Yumlu, V. S., 1967, "Prediction of Burning Velocities of Carbon Monoxide-Hydrogen-Air Flames," Combust., Explos. Shock Waves, **11**(3), pp. 190–194.
[26] Law, C. K., and Kwon, O. C., 2004, "Effects of Hydrocarbon Substitution on Atmospheric Hydrogen-Air Flame Propagation," Int. J. Hydrogen Energy, **29**, pp. 867–879.
[27] Kuo, K. K., 1986, *Principles of Combustion*, Wiley-Interscience, New York.

Fuel Injection Scheme for a Compact Afterburner Without Flameholders

Shai Birmaher
Philipp W. Zeller
Petter Wirfalt
Yedidia Neumeier
Ben T. Zinn

School of Aerospace Engineering,
Georgia Institute of Technology,
Atlanta, GA 30332

State-of-the-art afterburners employ spray bars and flameholders to burn the fuel. Such afterburner designs significantly increase the length (and thus weight), pressure losses, and observability of the engine. This paper presents a feasibility study of a compact "prime and trigger" afterburner that eliminates the flameholders and, thus, eliminates the above-mentioned problems. In this concept, afterburner fuel is injected just upstream or in between the turbine stages. As the fuel travels through the turbine stages, it evaporates and mixes with the bulk flow without any significant heat release from combustion, a process referred to as "priming." Downstream of the turbine stages, combustion is initiated either through autoignition or by using a low power plasma radical generator to "trigger" the combustion process. The prime and trigger injection and ignition scheme has been investigated using an experimental setup that simulates the operating conditions in a typical gas turbine engine. In this study, a trigger was not used and combustion of the fuel was initiated by autoignition. In a parallel effort, a physics-based theoretical model of the priming stage was developed in order to predict the location of fuel autoignition. The theoretical predictions and the experimental measurements of temperature and CH^* *chemiluminescence confirm the feasibility of the proposed prime and trigger concept by demonstrating the controlled autoignition of the afterburner fuel.*
[DOI: 10.1115/1.2836478]

1 Introduction

Current afterburners consist of a long duct with radial fuel spray bars for fuel injection and a bluff body flameholder to anchor the combustion zone. The increased thrust provided by the afterburner comes at the cost of significantly increased engine length and weight, increased losses due to drag from the spray bars and flameholder, and increased observability caused by the flameholder thermal signature. In addition, difficulties in maintaining stable afterburner combustion are becoming more pronounced as improvements in combustors and turbines lead to higher afterburner inlet temperatures and velocities [1]. Consequently, there exists a need for new afterburner designs that would overcome these problems.

This paper introduces a new "prime and trigger" (PAT) approach for burning the fuel in the afterburner that eliminates the flameholders altogether. In the "prime" stage of this concept, the afterburner fuel is injected into the engine just upstream or within the turbine stages in such a manner that the fuel evaporates, mixes with the flow, and exits the turbine stage without significant heat release. This is achieved by adjusting the fuel injection location and the initial fuel droplet size so that the travel time of the fuel through the turbine stages is less than the combined evaporation time and chemical ignition delay of a significant fraction of the fuel. Combustion of the fuel downstream of the turbine stages occurs through autoignition or is "triggered" by a low power plasma radical generator being developed in a parallel investigation. Successful implementation of the PAT concept will eliminate the penalties associated with flameholders and may lead to more compact afterburners due to the shift upstream of the fuel injection site and the potentially shorter combustion zone.

The results of the investigation of the PAT concept may also help in the development of the interstage turbine burner (ITB). The ITB burns fuel between the high and low pressure turbine stages or between the stator and rotor and offers such potential advantages as higher engine efficiency, higher specific thrust, and reduced NO_x emissions [2,3]. The required length for autoignition and the use of a trigger in the PAT concept could be used to determine the required length and a possible method of ignition for the ITB.

This paper describes an experimental investigation of the PAT concept that demonstrates the feasibility of priming and autoignition of fuel under flow conditions that are representative of realistic gas turbine engines. The trigger techniques will be addressed in subsequent investigations. The paper proceeds as follows: First, the experimental setup is discussed, next, a phenomenological model is introduced for use in the interpretation of the experimental measurements, and finally, the results from various test conditions are discussed.

2 Experimental Setup

The experimental facility developed for this study was designed to simulate the velocity, temperature, and oxygen content of the flow through the primary combustor, turbine, and afterburner of a turbine engine. Turbine engine operating pressures were not simulated in this study due to the added cost and complexity of constructing a high pressure facility (see Ref. [4] for a discussion of the effects of high pressure on the PAT concept). Figures 1 and 2 show schematics of the side and top views of the facility, respectively, and include designations for the different sections of the facility and for the ports that are used for measurements and fuel injection. In this facility, air first enters the primary combustor where it reacts with methane to generate a vitiated air stream of desired properties. Next, the vitiated air passes through a plenum, where the cross-sectional area changes from circular to rectangular, and then through a converging section where the flow accelerates to high subsonic Mach numbers. Liquid Jet A for afterburner combustion is injected in the plenum or the converging section with the coaxial airblast atomizer shown in Fig. 3. The flow then passes through a turbine simulator (TS), which is discussed below. Finally, the flow passes through a diverging section, which is equipped with a quartz window for optical access, fol-

Manuscript received April 26, 2007; final manuscript received October 1, 2007; published online March 28, 2008. Review conducted by Dilip R. Ballal.

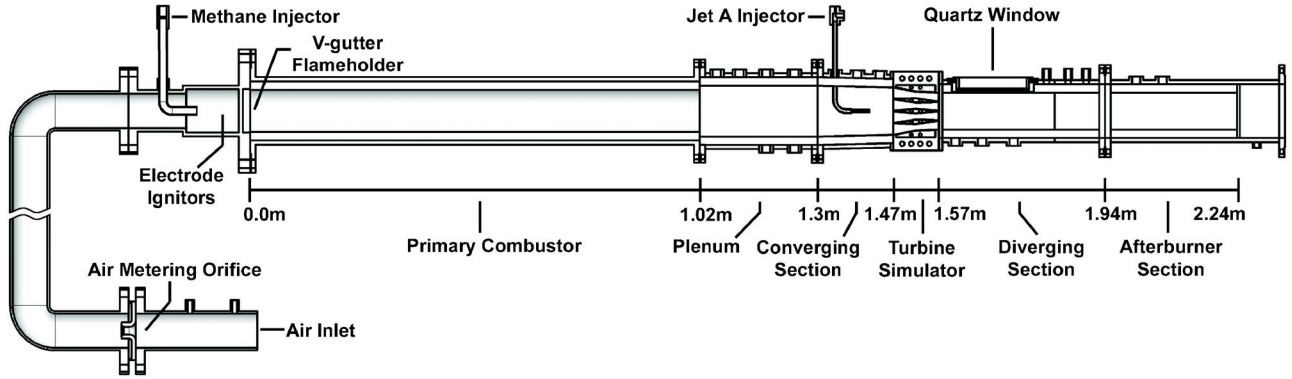

Fig. 1 Schematic of the developed facility

lowed by a straight duct, termed the afterburner section. Autoignition of the afterburner fuel is intended to occur either in the diverging section or the afterburner section, depending on the injection location and operating conditions.

Figure 4 shows a cross section of the TS as well as a schematic of an actual turbine stage for comparison. The TS was designed to simulate the temperature drop and velocity change through a turbine stage. In the turbine stage of an aircraft engine, the flow accelerates through the stator and decelerates through the rotor with a net increase in velocity. There are also sharp pressure and temperature drops due to gas expansion and work extraction by the rotor. In the TS, the stator and rotor are simulated by a row of water-cooled, diamond-shaped blades. Between the blades, the flow passages converge and diverge with a net decrease in cross-sectional area in order to simulate the change in velocity across the stator and rotor. Since work extraction is not possible in the TS, a temperature drop is achieved by heat transfer from the hot flow to the water cooled blades and also by a small amount of water injection into the bulk flow from holes on the leading edges of the blades. Other than lowering the bulk flow temperature, the presence of the additional water in the vitiated air stream is assumed to have little effect on the chemical kinetics of the afterburner fuel, as suggested by Yang and Kee [5].

With the exception of the TS, the inner walls of the facility are lined with insulation that consists of 5/8 in. thick alumina ceramic and 1/8 in. thick quartz. This was done to minimize heat losses and to protect the walls from the hot flow without the need for an extensive set of regenerative, air-cooled liners such as those employed in real engines. The alumina ceramic provides the majority of the insulation, and the quartz is used to prevent erosion of the ceramics.

The developed facility has capabilities for measuring temperature, pressure, fuel and air flow rates, and chemiluminescence. These measurements were used during operation to bring the facility to turbine operating conditions and to detect the combustion of the afterburner fuel. The temperature of the bulk flow was measured using *B*-type thermocouples, which measure temperatures up to 1700°C. The methane and air flow rates were determined from pressures and temperatures measured upstream of choked metering orifices. Jet A flow rates were measured using a rotameter and a flow meter with a range of 1–1250 ml/min. CH^* chemiluminescence was measured by a charge coupled device (CCD) video camera equipped with a filter (430 ± 5 nm) that was positioned over the quartz window in the diverging section.

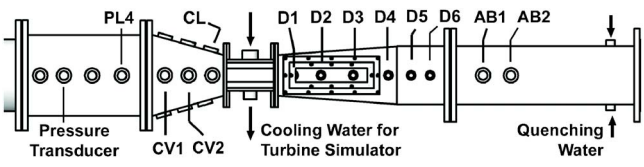

Fig. 2 Top view of sections downstream of the primary combustor. Ports are labeled according to section and downstream order. The section labels are plenum, PL; converging section, CV; diverging section, D; and afterburner section, AB. "CL" is the port on the left side of the converging section.

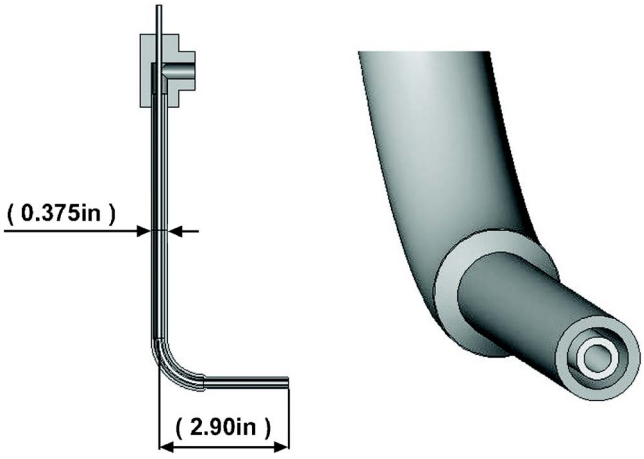

Fig. 3 Coaxial airblast atomizer for Jet A injection. Jet A flows from the inner tube and air flows through the annulus. The i.d. and o.d. of fuel tube are 0.08 in. and 0.125 in., respectively. At the discharge, the i.d. of the air tube is 0.18 in.

3 Developed Model

A reduced-order, physics-based model was developed to predict the autoignition location of the afterburner fuel and to interpret the measured data. The autoignition of the afterburner fuel was assumed to be governed by three processes: evaporation, mixing,

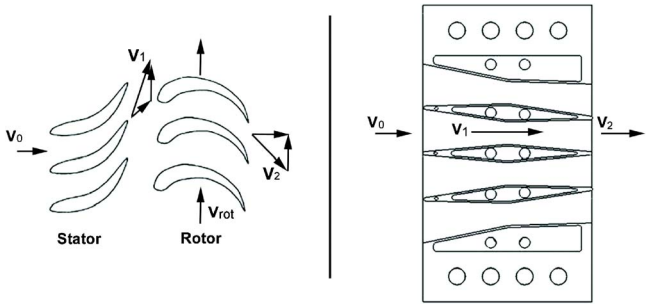

Fig. 4 Vector diagram and schematic showing the relation between the velocity vectors across a turbine stage and across the turbine simulator

and chemical reactions. The developed model follows a group of Jet A droplets, which was produced by the airblast atomizer shown in Fig. 3, as it is carried through the facility by the bulk flow. The vaporization rate of the droplets is computed in increments of time and space, and the quantity of fuel that evaporates from the group of droplets in each increment is referred to as a "fuel element." As the group of droplets moves down the facility, it "releases" fuel elements of varying mass depending on the vaporization rate. Each fuel element is then tracked independently. It is assumed that a fuel element "acquires" the velocity of the local bulk flow as soon as it forms. As it travels along the facility, the fuel element approaches the temperature of the local bulk flow through a mixing process that is modeled using a characteristic mixing time. Concurrent with this mixing process, each fuel element undergoes chemical reactions that ultimately result in its autoignition. The autoignition process is modeled using a simple expression for ignition delay time that takes into account transient bulk flow temperature and pressure. By computing the ignition delay time (and, thus, the autoignition location) of all the fuel elements, the model determines the percent of fuel that has ignited at each position along the facility.

It should be noted that the evaluation of the above processes requires prior knowledge of the axial profiles of bulk flow temperature, pressure, and velocity. These are estimated by assuming one-dimensional flow and solving the corresponding conservation equations of mass, momentum, and energy. The boundary conditions for the conservation equations are given by measurements of temperature, pressure, and mass flow rate. This is discussed further in Sec. 4.

The following sections provide descriptions of the submodels for evaporation, mixing, and chemistry.

3.1 Evaluation of Droplet Evaporation. The vaporization submodel uses a procedure developed by Abramzon and Sirignano [6] to calculate the vaporization rate, velocity, and temperature of a group of Jet A droplets. In this application of the vaporization model given in Ref. [6], the droplet density is held constant at 815 kg/m^3, the initial fuel temperature is set to 300 K, and all droplets are assumed to have the same diameter and velocity. The initial diameter of the droplets is assumed to be the Sauter mean diameter (SMD) of the spray produced by the afterburner fuel injector, which is estimated using the following empirical expression developed by Jasuja [7] for coaxial airblast atomizers:

$$\mathrm{SMD} = 0.19\left(\frac{\sigma_f}{\rho_f}\right)^{0.35}(u_{\mathrm{air,inj}}\rho_{\mathrm{air,inj}}^{0.35})^{-1}\left(1+\frac{\dot{m}_{\mathrm{fuel}}}{\dot{m}_{\mathrm{air,inj}}}\right)^{0.25} + 0.127\mu_f\left(\frac{D}{\rho_f\sigma_f}\right)^{0.5}\left(1+\frac{\dot{m}_{\mathrm{fuel}}}{\dot{m}_{\mathrm{air,inj}}}\right) \tag{3.1}$$

where $\dot{m}_{\mathrm{fuel}}$, σ_f, μ_f, and ρ_f are the fuel mass flow rate, surface tension, dynamic viscosity, and density, respectively; D is the inner diameter of the fuel tube, see Fig. 3; and $\dot{m}_{\mathrm{air,inj}}$, $\rho_{\mathrm{air,inj}}$, and $u_{\mathrm{air,inj}}$ are the injector air flow rate, density, and velocity, respectively. Jet A fuel properties were obtained from Refs. [8–10], although some decane properties were used when values for Jet A were not available.

The vaporization of the group of fuel droplets was calculated in constant increments of time, $\Delta t = 10\ \mu$s, starting from $t=0$ at the injector. In the ith increment of time, from $t=t_i$ to t_{i+1}, the ith fuel element vaporizes from the group of droplets. The mass of this fuel element, denoted as Δm_i, is given by

$$\Delta m_i = N_{\mathrm{drops}}\dot{m}_{\mathrm{drop},i}\Delta t \tag{3.2}$$

where $\dot{m}_{\mathrm{drop},i}$ and N_{drops} are the vaporization rate of a fuel droplet in the ith increment of time and the number of droplets in the group, respectively. N_{drops} is constant throughout the vaporization process. However, the vaporization rate depends on the local bulk flow pressure, temperature, velocity, and composition, as well as the diameter and temperature of the droplets, as described below.

Following the model developed in Ref. [6], the vaporization rate of a droplet is given by

$$\dot{m}_{\mathrm{drop}} = \pi d_{\mathrm{drop}}\bar{\rho}\bar{D}_M\mathrm{Sh}^*\ln(1+B_M) \tag{3.3}$$

where d_{drop}, $\bar{\rho}$, $\bar{D}_M$, Sh^*, and B_M are the droplet diameter, average gas density, average molecular diffusivity, modified Sherwood number, and Spalding mass transfer coefficient, respectively. Note that for simplicity, the subscript i denoting the time increment has been omitted. Unless stated otherwise, all the terms in the equations correspond to values at time t_i or, equivalently, to the values at the position of the droplets along the facility at t_i. Average properties such as $\bar{\rho}$ were calculated using the film temperature and film fuel mole fraction given by

$$\bar{T} = T_{\mathrm{drop}} + \tfrac{1}{3}(T_{\mathrm{bulk}} - T_{\mathrm{drop}}) \tag{3.4}$$

$$\bar{\chi}_F = \chi_{F,s} + \tfrac{1}{3}(\chi_{F,\mathrm{bulk}} - \chi_{F,s}) \tag{3.5}$$

where T_{drop}, T_{bulk}, $\chi_{F,s}$ and $\chi_{F,\mathrm{bulk}}$ are the droplet temperature, bulk flow temperature, fuel mole fraction at the surface of the droplet, and bulk flow fuel mole fraction, respectively. $\chi_{F,s}$ was calculated using the ratio of decane fuel vapor pressure given in Ref. [10] to the local ambient pressure. $\chi_{F,\mathrm{bulk}}$ was calculated by assuming that all fuel previously vaporized has fully mixed with the bulk flow. The utilized Spalding mass transfer coefficient is given by

$$B_M = \frac{Y_{F,s} - Y_{F,\mathrm{bulk}}}{1 - Y_{F,s}} \tag{3.6}$$

where $Y_{F,s}$ and $Y_{F,\mathrm{bulk}}$ are the fuel mass fraction at the droplet surface and in the bulk flow, respectively. The modified Sherwood number is given by

$$\mathrm{Sh}^* = 2 + \frac{\mathrm{Sh} - 2}{F_M} \tag{3.7}$$

where F_M is a correction factor used to account for the Stefan flow and Sh is the Sherwood number. F_M is given by

$$F_M = (1+B_M)^{0.7}\frac{\ln(1+B_M)}{B_M} \tag{3.8}$$

and Sh is given by

$$\mathrm{Sh} = 2(1 + \mathrm{F\ddot{o}}\ \mathrm{Re}_{\mathrm{drag}}^{1/2}\ \mathrm{Sc}_{\mathrm{film}}^{1/3}) \tag{3.9}$$

where Fö is the Frössling coefficient, which has a value of 0.276 [11], and $\mathrm{Sc}_{\mathrm{film}}$ is the Schmidt number, which was evaluated using the film temperature, film composition, and the bulk flow pressure. The Reynolds number, $\mathrm{Re}_{\mathrm{drag}}$, is given by

$$\mathrm{Re}_{\mathrm{drag}} = \frac{\rho_{\mathrm{bulk}}|u_{\mathrm{drop}} - u_{\mathrm{bulk}}|d_{\mathrm{drop}}}{\bar{\mu}} \tag{3.10}$$

where ρ_{bulk}, u_{bulk}, u_{drop}, and $\bar{\mu}$ are the local bulk flow density, bulk flow velocity, droplet velocity, and average dynamic viscosity, respectively. The droplet velocity after each time increment is computed using the following equation:

$$u_{\mathrm{drop},i+1} = u_{\mathrm{drop},i} + \frac{3C_{\mathrm{drag}}}{d_{\mathrm{drop}}}\frac{\rho_{\mathrm{bulk}}}{\rho_f}|u_{\mathrm{bulk}} - u_{\mathrm{drop},i}|(u_{\mathrm{bulk}} - u_{\mathrm{drop},i})\Delta t \tag{3.11}$$

where C_{drag} is a drag coefficient given by

$$C_{\mathrm{drag}} = \frac{24}{\mathrm{Re}_{\mathrm{drag}}}\left(1 + \frac{1}{6}\mathrm{Re}_{\mathrm{drag}}^{2/3}\right) \tag{3.12}$$

The initial droplet velocity is approximated as the fuel flow rate divided by the fuel density and the injector fuel discharge area. u_{drop} is also used to track the position of the group of droplets in

time. Having computed $\dot{m}_{\text{drop}}$ using Eqs. (3.3)–(3.12), the droplet diameter is then given by

$$d_{\text{drop},i+1} = d_{\text{drop},i} - \frac{2\dot{m}_{\text{drop}}}{\pi\rho_f d_{\text{drop},i}^2}\Delta t \tag{3.13}$$

As indicated by Eq. (3.4), the vaporization model also requires knowledge of droplet temperature. The droplet temperature after each time increment is given by

$$T_{\text{drop},i+1} = T_{\text{drop},i} + \frac{\dot{Q}_{l,i}}{\rho_f V_f c_l}\Delta t \tag{3.14}$$

where V_f, c_l, and $\dot{Q}_{l,i}$ are the droplet volume, liquid fuel specific heat, and heat transfer rate into the liquid phase during the ith time step, respectively. $\dot{Q}_l$ is given by

$$\dot{Q}_l = \dot{m}_{\text{drop}}\left(\frac{\bar{c}_{p,F}(T_{\text{bulk}} - T_{\text{drop}})}{B_T} - h_{fg}\right) \tag{3.15}$$

where $\bar{c}_{p,F}$, h_{fg}, and B_T are the average fuel vapor specific heat, the fuel heat of vaporization given in Ref. [10], and the Spalding heat transfer coefficient, respectively. B_T is determined by simultaneously solving the following set of equations:

$$\dot{m}_{\text{drop}} = \pi d_{\text{drop}}\frac{\bar{k}}{\bar{c}_{p,F}}\text{Nu}^* \ln(1 + B_T) \tag{3.16}$$

$$\text{Nu}^* = 2 + \frac{\text{Nu} - 2}{F_T} \tag{3.17}$$

$$\text{Nu} = 2(1 + \text{FöRe}_{\text{drag}}^{1/2}\text{Pr}_{\text{film}}^{1/3}) \tag{3.18}$$

$$F_T = (1 + B_T)^{0.7}\frac{\ln(1 + B_T)}{B_T} \tag{3.19}$$

where $\bar{k}$, Nu, Nu*, and F_T are the average gas thermal conductivity, Nusselt and modified Nusselt numbers, and correction factor, respectively. The Prandtl number, Pr_{film}, is evaluated using the film temperature and film composition. The value for $\dot{m}_{\text{drop}}$ in Eq. (3.16) is provided by the solution of Eq. (3.3).

3.2 Evaluation of Mixing. The temperature of the fuel element is initially equal to the temperature of the droplet and increases as the fuel element mixes with the bulk flow. Denoting the temperature of the ith fuel element as $T_{\Delta m_i}$, this mixing process is modeled by the following first order rate equation:

$$\frac{dT_{\Delta m_i}}{dt} = \frac{1}{\tau_{\text{mix}}}(T_{\text{bulk}} - T_{\Delta m_i}) \tag{3.20}$$

where τ_{mix} is a characteristic mixing time. To estimate the characteristic mixing time, the bulk flow turbulence is assumed to be the dominant mechanism for mixing. Upstream of the diverging section, τ_{mix} is defined as the time it takes for a turbulent eddy to bring a fluid element from the bulk flow to the center of the Jet A fuel jet, which is estimated as follows:

$$\tau_{\text{mix}} = \frac{R}{u'} \tag{3.21}$$

where R is the radius of the injector tube that carries the liquid fuel, equal to 1/16 in., and u' is the rms turbulent velocity fluctuation of the bulk flow, which is assumed to be 5% of the local bulk flow velocity. It should be noted that the contribution to the mixing process of the air used by the atomizer is neglected because it is a relatively small quantity. Downstream of the TS, it is assumed that there is intense turbulent mixing due to strong flow separation and turbulent wakes associated with the TS blades. Therefore, τ_{mix} is set to zero in this region, which corresponds to infinitely fast mixing. As a result, the temperature of a fuel element is discontinuously set to the temperature of the local bulk flow if it is downstream of the TS.

3.3 Evaluation of Chemistry. Concurrent with the mixing process, each fuel element undergoes chemical reactions with the bulk flow that ultimately result in its autoignition. The ignition delay of a fuel element is estimated using empirical correlations that are adapted for use in an environment with transient temperature and pressure.

Typically, experimentally measured ignition delay times are correlated with an inverse Arrhenius-type expression of the form

$$\tau_{\text{ign}} = A[\text{O}_2]^n P^b \exp\left(\frac{E_a}{RT}\right) \tag{3.22}$$

where τ_{ign} is the ignition delay; A, E_a, n, and b are empirical coefficients; and $[\text{O}_2]$ is the initial oxygen concentration [12–18]. However, Eq. (3.22) is only valid when the bulk flow temperature and pressure are constant during the ignition delay. In this application, the fuel elements experience varying temperature and pressure as they heat up and travel down the facility. Under these conditions, the ignition delay of a fuel element can be estimated using the following "ignition integral," which was derived in Ref. [19] and used more recently in Refs. [20,21]:

$$I = \int_0^{t'} \frac{1}{\tau_{\text{ign}}(P_{\text{bulk}}, T_{\Delta m_i})}dt' \tag{3.23}$$

where t' is the time elapsed from the creation of the fuel element under consideration, τ_{ign} is again the empirical correlation for the ignition delay of Jet A at constant ambient temperature and pressure, and I is a progress variable, termed the ignition integral value. In this model, the ignition location of a fuel element is determined by simultaneously solving Eqs. (3.20) and (3.23) as the fuel element travels along the facility. When $I=1$, the fuel element is predicted to autoignite and the time in the upper limit of the ignition integral is the predicted ignition delay time of that fuel element.

The expression for τ_{ign} used in this investigation is based on the results of the experimental investigation of Jet A autoignition by Freeman and Lefebvre [13], which was performed at atmospheric pressure. The data and figures from Ref. [13] are used to give

$$\tau_{\text{ign}} = 1.06 \times 10^{-10}[\text{O}_2]^{-0.65}\exp\left(\frac{20{,}582}{T_{\Delta m_i}}\right) \tag{3.24}$$

The initial bulk flow oxygen concentration $[\text{O}_2]$ can be expressed in terms of mole fraction and atmospheric pressure to obtain

$$\tau_{\text{ign}} = 1.06 \times 10^{-10}\left(\frac{\chi_{\text{O}_2}101{,}325}{RT_{\Delta m_i}}\right)^{-0.65}\exp\left(\frac{20{,}582}{T_{\Delta m_i}}\right) \tag{3.25}$$

where χ_{O_2} is the oxygen mole fraction of the bulk flow before afterburner fuel injection and R is the universal gas constant. To accommodate changes in bulk flow pressure, the above equation is modified by including the inverse pressure term suggested in Ref. [16,18], giving

$$\tau_{\text{ign}} = 1.06 \times 10^{-10}\left(\frac{\chi_{\text{O}_2}101{,}325}{RT_{\Delta m_i}}\right)^{-0.65}\exp\left(\frac{20{,}582}{T_{\Delta m_i}}\right)\left(\frac{101{,}325}{P_{\text{bulk}}}\right) \tag{3.26}$$

4 Application of the Model

In this section, the theoretical model is demonstrated using a typical operating point of the facility. The purpose of this demonstration is to show how the submodels of mixing, evaporation, and

chemistry work together to predict the autoignition of the fuel and to identify the theoretical results that can be compared with the experimental results.

An operating point of the facility is described by the following set of parameters:

$$[P_{PL}(\text{psi (absolute)}), T_{tot}(\text{K}), \Delta T_{TS}(\text{K}), \dot{m}_{air}(\text{kg/s}), \ldots,$$
$$\phi_{vit}, \dot{m}_{Jet\ A}(\text{g/s}), \text{Port}, \text{SMD } (\mu\text{m})]$$

which are the plenum static pressure, total temperature upstream of the TS, total temperature drop across the TS, bulk air flow rate, primary combustor equivalence ratio, Jet A flow rate, Jet A injector port (see Fig. 2), and predicted spray SMD, respectively. All of the values in the above operating point are measured experimentally, with the exception of the spray SMD, which is estimated using Eq. (3.1).

The following operating point, denoted as Case A, will be used to demonstrate the model:

$$[P_{PL}, T_{tot}, \Delta T_{TS}, \dot{m}_{air}, \phi_{vit}, \dot{m}_{Jet\ A}, \text{Port}, \text{SMD}]$$
$$= \text{Case A:}[30 \text{ psi (absolute)}, 1500 \text{ K}, 150 \text{ K}, 0.22 \text{ kg/s},$$
$$0.42, 2.03 \text{ g/s}, \text{CV1}, 35\ \mu\text{m}]$$

where injection through port CV1 corresponds to an injector discharge at 1.41 m, see Fig. 1. The values in the above operating point are used to estimate the axial profiles of temperature, pressure, and velocity from the plenum to the end of the facility. These profiles are estimated by solving one-dimensional conservation equations of mass, momentum, and energy with terms for friction and heat transfer. First, the composition of the primary combustor exhaust is computed using ϕ_{vit}, assuming complete combustion with no dissociation. Then, with gas composition, P_{PL}, T_{tot}, and $\dot{m}_{air}$ as plenum inlet conditions, the flow profiles are computed by stepping through the facility and evaluating the effects of area change, friction, and heat loss. Some constraints are imposed on the flow analysis through the TS. According to experimental observations, the static pressure at the TS throat is set to 1 atm. In addition, the total temperature profile across the TS is assumed to be linear and is computed using the measured value of ΔT_{TS}. With these constraints, the flow analysis is performed along the TS to find the remaining flow properties. The resulting flow profiles, the injector port, and the SMD are then input into the submodels of vaporization, mixing, and chemistry in order to evaluate the autoignition of the afterburner fuel.

Figures 5(*a*) and 5(*b*) show the estimated pressure and temperature profiles along the facility for Case A, respectively. The total pressure profile in Fig. 5(*a*) indicates that there is negligible total pressure loss outside of the TS. The large total pressure drop across the TS occurs mostly because of the strong flow separation downstream of the TS blades. The total temperature profile in Fig. 5(*b*) shows that the predicted total temperature loss from the plenum to the end of the setup excluding the TS is only about 45 K. This low temperature loss is possible because of the insulation along the interior of the facility. The inner wall temperatures are predicted to be within 100 K of the bulk flow temperature, except for the TS, which is water cooled.

Figure 6 shows the predicted profiles of bulk flow and droplet velocity for Case A. The bulk velocity at the TS throat is 580 m/s, which corresponds to a Mach number of 0.82. The velocity through the diverging and afterburner sections ranges from 340 m/s to 140 m/s, which correspond to Mach numbers of about 0.5–0.2, respectively. These represent the typical velocities and Mach numbers achieved in this facility. The initial droplet velocity is 1.6 m/s and immediately increases due to the drag force exerted by the bulk flow. There is a lag in the droplet velocity with respect to the bulk flow due to the relatively large inertia of the droplets. Figure 6 shows that in the TS, the droplet velocity lag can reach values upward of 100 m/s, which leads to large vaporization rates as a consequence of Eq. (3.10).

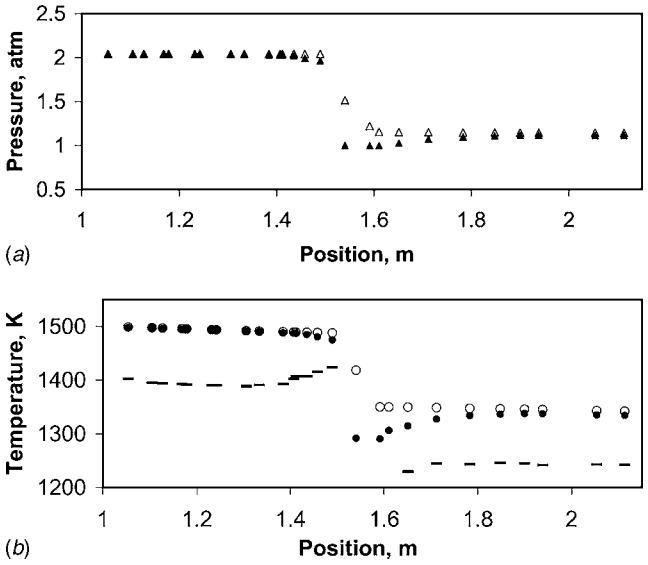

Fig. 5 Flow analysis results for Case A: (*a*) total pressure (open) and static pressure (closed) and (*b*) total temperature (open), static temperature (closed), and wall temperature (dash)

Figure 7 shows the results of the analysis of vaporization, mixing, and chemistry for Case A. The dash-dot line is the axial profile of the normalized droplet diameter. It shows that the predicted location of complete droplet evaporation for Case A is about 1.76 m. The variations in the slope of the droplet diameter line reflect the effect of axial variations of bulk flow velocity and temperature on the droplet vaporization rate. The set of dotted lines are the profiles of the ignition integral value I for every fifth fuel element (to reduce clutter). Recall that a fuel element is predicted to autoignite at the location where the corresponding ignition integral line reaches a value of 1. Upstream of the TS outlet (1.57 m), the ignition integral lines begin with nearly zero slopes due to the low initial temperature of those fuel elements. As discussed previously, at the TS outlet, τ_{mix} is discontinuously set to zero so that the temperature of each fuel element is set to the bulk flow temperature. Thus, the ignition integral lines of fuel elements originating just upstream of the TS outlet will increase sharply from zero at approximately the same time, which causes them to

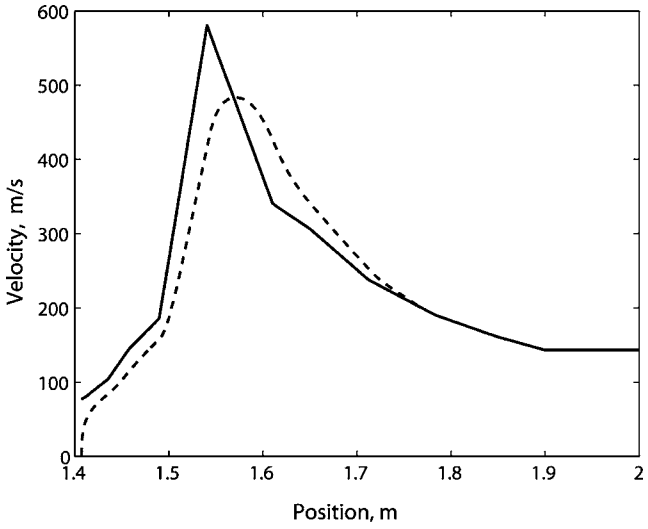

Fig. 6 Predicted bulk velocity (solid) and predicted droplet velocity (dashed) for Case A. Injection location is 1.41 m.

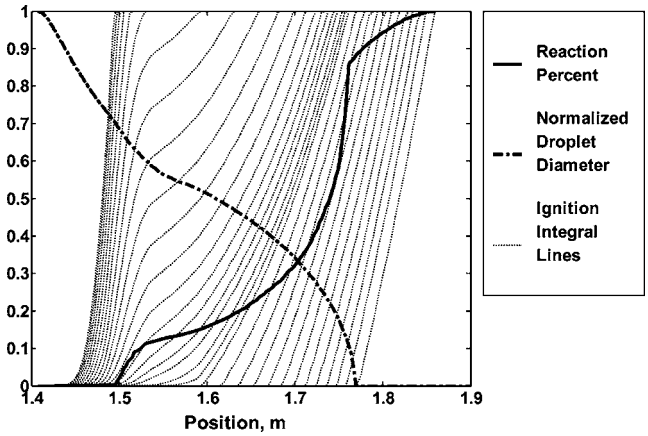

Fig. 7 Case A priming process indicators: reaction percent line, normalized droplet diameter, ignition integral lines for each element. Fuel injection location is 1.41 m.

appear to group together near $I=1$. The solid line is the "reaction percent line," which is a profile of the percent by mass of fuel that has reached autoignition at a given location along the facility. This is computed by summing the masses of all the fuel elements that have already autoignited by a given location and dividing by the total mass of fuel originally in the group of droplets. The reaction percent line begins to increase at about 1.5 m. This indicates that for Case A, some of the fuel elements are predicted to autoignite within the TS, which is between 1.47 m and 1.57 m. The reaction percent line continues to increase rapidly to a value of about 0.15 and then it levels off until about 1.7 m. This decrease in slope is caused by the drop in temperature and increase in velocity across the TS. Between 1.7 m and 1.76 m, the reaction percent line increases sharply to about 0.9, which indicates that most of the fuel is predicted to autoignite by 1.76 m. The discontinuous change in the slope of the reaction percent line at about 1.76 m occurs because of the discontinuous change in τ_{mix} at the TS outlet.

The reaction percent line can be used to compare the autoignition of fuel at varying injection locations. This is demonstrated in Fig. 8 for Case A operating conditions. From left to right, each reaction percent line corresponds to a downstream shift of the injection location starting from the plenum and ending at the end of the diverging section. Figure 8 clearly shows that the behavior

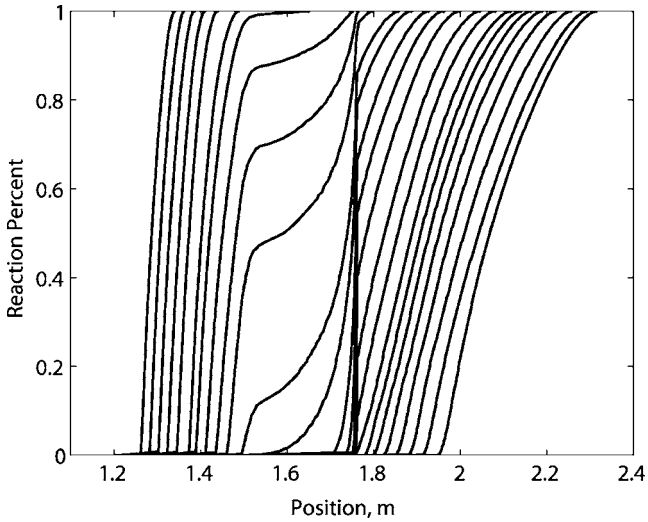

Fig. 8 Reaction percent lines for Case A with varying injection locations

of the reaction percent line depends on the injection location. This varied behavior can also be illustrated by plotting the position of 0.05, 0.25, and 0.95 on each reaction percent line versus the corresponding injection location, yielding an "injection/ignition" map.

Figure 9 shows the injection/ignition map for Case A. The reaction percent lines from Fig. 8 have been mapped into points on the 5% (circle), 25% (plus), and 95% (x-mark) reaction lines. Also shown on the map are pairs of vertical and horizontal lines, which delineate the location of the TS, and a "zero delay" line, which represents the instant ignition of all the fuel upon injection. To aid in the interpretation of the map, the injection locations have been divided into four regions. The first is Region I, where fuel injection and fuel autoignition both occur completely upstream of the TS. Here, the 5%, 25%, and 95% lines are parallel because of the nearly constant bulk temperature, pressure, and velocity experienced by the fuel. Next is Region II, which contains the injection locations for which some of the fuel elements ignite before or within the TS and some after. The shape of the reaction percent line in Fig. 7 is typical for this range of injection locations. The significant increase in the slopes of the 5%, 25%, and 95% lines in Region II is caused by the decrease in the bulk flow temperature and pressure, which increases the ignition delay time, and by the increase in velocity, which increases the distance traveled by the fuel before autoignition. Next is Region III, which encompasses the injection locations upstream of the TS that result in autoignition only downstream of the TS. In the transition from Region II to Region III, the 5% line jumps to a distance of about 0.15 m downstream of the TS, and then the 5% and 25% lines become nearly horizontal and close together, which is explained below. This indicates that injection anywhere within Region III will result in autoignition at a compact and safe distance downstream of the TS that is relatively insensitive to small changes in injection location. Therefore, injection within Region III is ideal for the PAT concept. In other words, the model predicts that the region just upstream of a turbine stage is, in fact, the best injection location for achieving autoignition in the afterburner. The last range of injection locations is denoted as Region IV. Here, fuel injection occurs within or downstream of the TS. As in Region I, the fuel experiences nearly constant pressure, temperature, and velocity. However, the 5%, 25%, and 95% lines are farther apart because the velocity is higher and the temperature and pressure are lower.

Figure 10 shows the dependence of evaporation time on injection location. It clearly indicates that in Region III, the evaporation time is shortest and is least sensitive to changes in injection location. This is due to the proximity of Region III to the TS, where the large velocity lag between the droplets and the bulk flow leads to locally high vaporization rates, see Fig. 6. As a consequence, for injection locations within Region III, the fuel elements originating in the TS contain a large percent by mass of the fuel from the group of droplets. These "neighboring" fuel elements have nearly overlapping axial temperature profiles due to the mixing delay imposed by Eq. (3.20), and therefore autoignite at approximately the same location. As a result, the 5% and 25% lines in Region III of the injection/ignition map are close together and nearly horizontal.

5 Results and Discussion

In this section, the temperature and chemiluminescence measurements are presented and compared with the predictions from the theoretical model.

5.1 Temperature Measurements. For the temperature measurements, the opening for the quartz window was blocked with ceramic in order to reduce radiative losses and thus maintain the nearly adiabatic conditions afforded by the insulation. The first set of temperature measurements was obtained for the following operating point, which is referred to as Case 1 and is described using the notation introduced in the previous section:

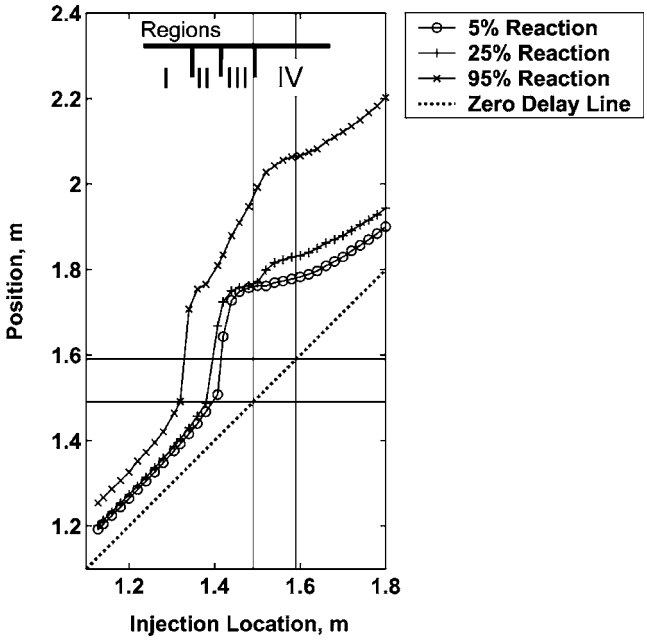

Fig. 9 Injection/ignition map for Case A. The pairs of vertical and horizontal lines delineate the location of the TS. Four regions of injection locations are identified that characterize different ignition behaviors.

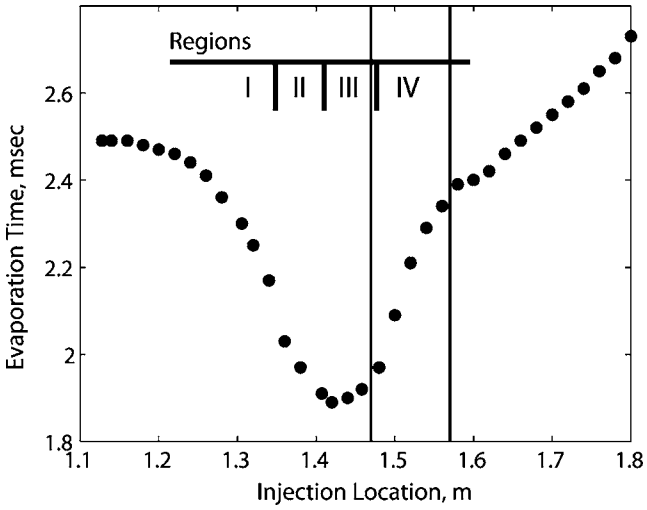

Fig. 10 Droplet evaporation time for Case A operating conditions with varying injection locations. Vertical lines delineate location of the TS.

$$[P_{PL}, T_{tot}, \Delta T_{TS}, \dot{m}_{air}, \phi_{vit}, \dot{m}_{Jet\ A}, \text{Port}, \text{SMD}]$$
$$= \text{Case 1: } [25 \text{ psi (absolute)}, 1400 \text{ K}, 175 \text{ K}, 0.194 \text{ kg/s}, 0.44, 2.26 \text{ g/s}, \text{CV2}, 32\ \mu\text{m}]$$

where the CV2 port corresponds to an injection location of 1.46 m, see Fig. 1. Figure 11 shows the time history of the thermocouple and plenum pressure measurements for Case 1. The traces in Fig. 11 exhibit low frequency oscillations, which were caused by pressure variations in the methane supply system. Injection of the afterburner fuel took place at approximately 1270 s. Prior to this time, there was an approximately 175 K temperature difference between the CL thermocouple and the thermocouples downstream of the TS. This temperature drop was achieved by the water cooling and water injection in the TS. Subsequent to the afterburner fuel injection, the thermocouple measurements downstream of the TS increased monotonically due to autoignition of the fuel until the system reached thermal equilibrium. Figure 11 shows that the CL thermocouple and the plenum pressure did not respond to the fuel injection, indicating that little or no heat release took place upstream of the TS throat. Downstream of the TS, the first thermocouple, D3, reached an average temperature of 1263 K and the last thermocouple, AB2, reached an average temperature of 1468 K. The thermocouples between D3 and AB2 measured successively increasing temperatures. The data in Fig. 11 demonstrated that the combustion of the fuel occurred spontaneously without the need for a flameholder or even a trigger. Moreover, the ignition delay time of the fuel was observed to be sufficient so that injection upstream of the TS resulted in autoignition only downstream of the TS, which is an essential part of the PAT concept.

To correlate the temperature measurements with the predictions from the model, the measured temperature increase was normalized by the expected temperature increase due to complete combustion of the fuel. In the discussed case, complete combustion would result in a temperature increase of 354 K. The results of this normalization are shown in Fig. 12. The last thermocouple, AB2, measured 72% of the expected temperature rise. It is not known if more heat addition occurred downstream of AB2. The normalized temperature can be compared to the reaction percent line predicted by the model, which is also shown in Fig. 12. Although by definition the reaction percent line does not correspond to the normalized temperature increase due to the autoignition of the fuel, it was assumed to give a good approximation, especially at the onset of combustion. The comparison of the reaction percent line with the normalized temperature measurements shows that the predicted autoignition location lies within the region of measured temperature increase. However, the model predicts that most of the autoignition occurs sharply at about 2 m, while the thermocouple measurements show a gradual temperature increase that begins at approximately 1.75 m. Figure 12 also shows a scale of the predicted bulk flow travel time from the injector discharge. According to this scale, the locations of the first and last downstream thermocouples, D3 and AB2, correspond to convection times of about 1.3 ms and 3.9 ms, respectively. Taking D3 as the location of autoignition, the model over-predicts the ignition delay time by about 1.5 ms.

Figure 13 shows the predicted injection/ignition map for the operating conditions of Case 1 with varying injection locations. In addition to the reaction percent lines discussed in the previous section, the map in Fig. 13 also includes a line marking the predicted location of complete droplet evaporation (solid, diamond). The actual injection location for Case 1 is represented by the bold vertical line. Figure 13 indicates that the injection location for Case 1 lies within the injection range that yields a relatively compact ignition zone downstream of the TS. This range of injection locations corresponds to Region III in Fig. 9, which was identified as the optimal region for the PAT concept. The map also shows that the injector could have been moved upstream to a location of about 1.4 m and still kept the afterburner fuel combustion downstream of the TS. The line representing the droplet lifetime shows that the predicted location of complete droplet evaporation for Case 1 occurs at about 1.81 m, which is just slightly downstream of the D3 thermocouple. Referring to Fig. 12, this indicates that the predicted location of complete droplet evaporation occurs upstream of both the predicted and the measured position of significant heat release.

Next, another operating point is analyzed in which the primary combustor operated slightly richer and the afterburner fuel was injected farther upstream. This operating point, referred to as Case 2, is given by the following parameters:

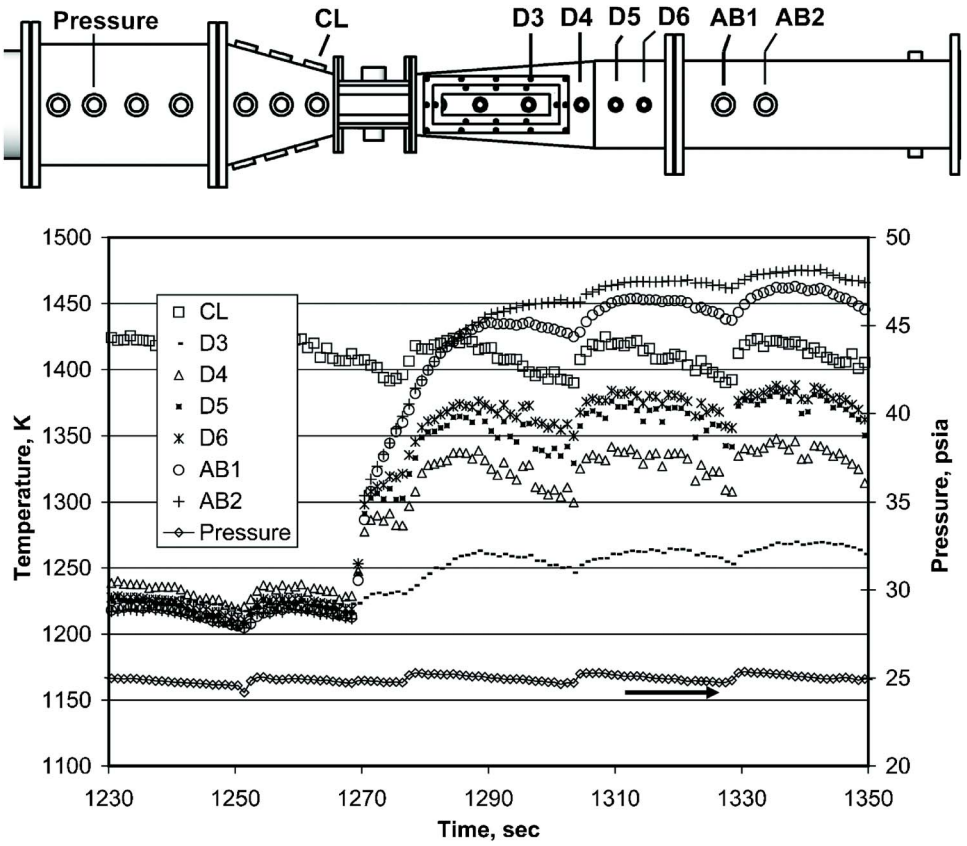

Fig. 11 Thermocouple and pressure transducer data for Case 1

$$[P_{PL}, T_{tot}, \Delta T_{TS}, \dot{m}_{air}, \phi_{vit}, \dot{m}_{Jet\ A}, \text{Port}, \text{SMD}]$$

$$= \text{Case 2: } [28 \text{ psi (absolute)}, 1425 \text{ K}, 200 \text{ K}, 0.197 \text{ kg/s}, 0.475, 2.26 \text{ g/s}, \text{PL4}, 38\ \mu\text{m}]$$

where the PL4 port corresponds to injection at 1.3 m, see Fig. 1. Figure 14 shows the time history of the thermocouple measurements for Case 2. During this test, thermocouples D2 and AB2 developed a bias that is evident prior to 440 s by the shift with respect to the other downstream thermocouples. The data from the D2 and AB2 thermocouples were used after subtracting this bias. Injection of the afterburner fuel occurred at approximately 440 s. In marked contrast with Case 1, after autoignition of the fuel, there was an increase in both the CL thermocouple temperature and the plenum pressure. This indicates that significant heat re-

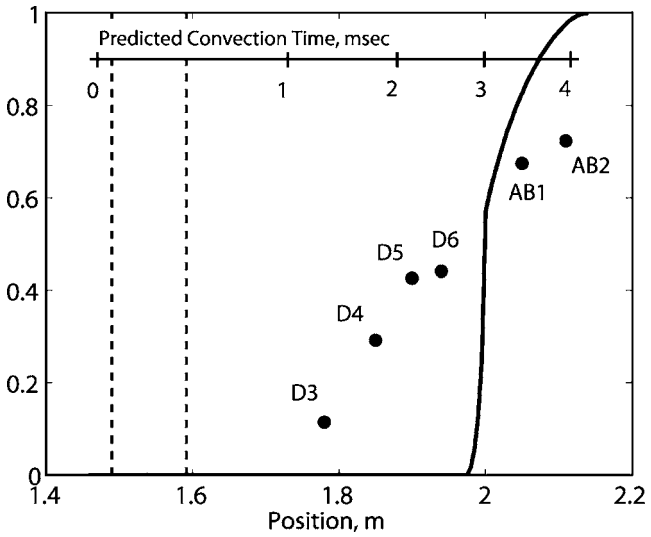

Fig. 12 Case 1 normalized temperature increase (circles) and theoretical reaction percent (solid line). Dashed vertical lines delineate the TS.

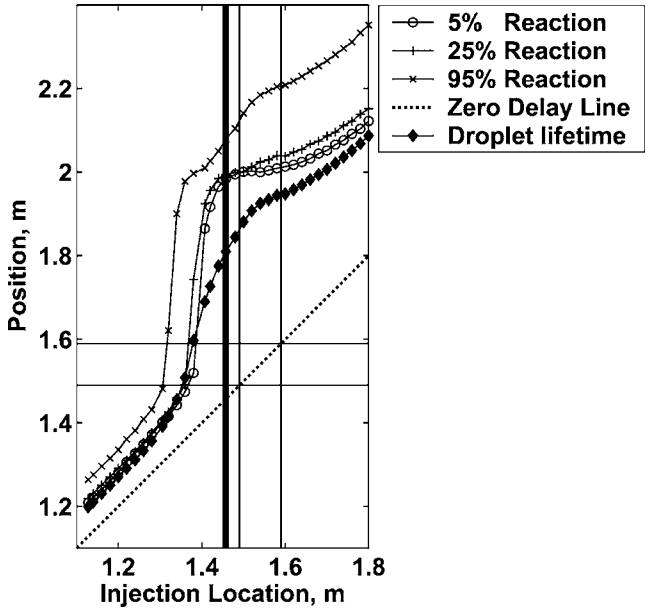

Fig. 13 Injection/ignition map for Case 1. Thick vertical line extends from the fuel injection location at 1.46 m.

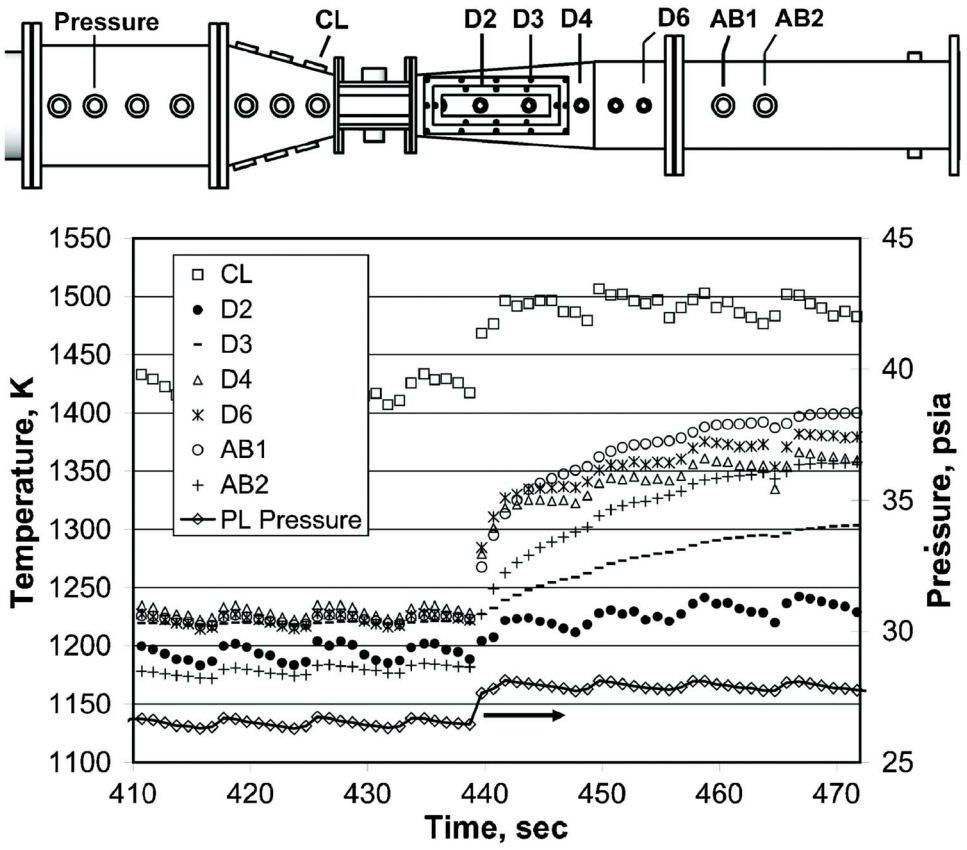

Fig. 14 Thermocouple and pressure transducer measurements for Case 2

lease from fuel autoignition occurred upstream of the TS throat. Downstream of the TS, the temperature measured by subsequent thermocouples continued to increase, reaching approximately 1400 K at AB1. The data in Fig. 14 demonstrate a case of upstream injection that is undesirable for the PAT concept, since there should not be significant heat release until after the TS. Thus, for Case 2 operating conditions, the injection location was too far upstream.

Figure 15 shows the normalized temperature increase for Case 2 together with the predicted reaction percent line and convection time. Also shown is the reaction percent line for an injection location of 1.38 m, which is slightly downstream of the nominal injection location. As expected, the PL3 thermocouple, which is upstream of the injection location, did not measure a temperature

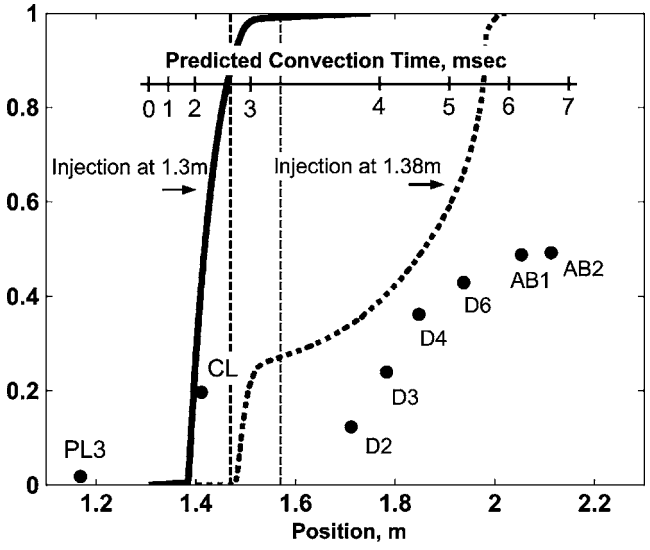

Fig. 15 Case 2 normalized temperature increase (circles), reaction percent line for injection at 1.3 m (bold, solid line), and reaction percent line for injection at 1.38 m (bold, dashed line). Dashed vertical lines delineate the TS.

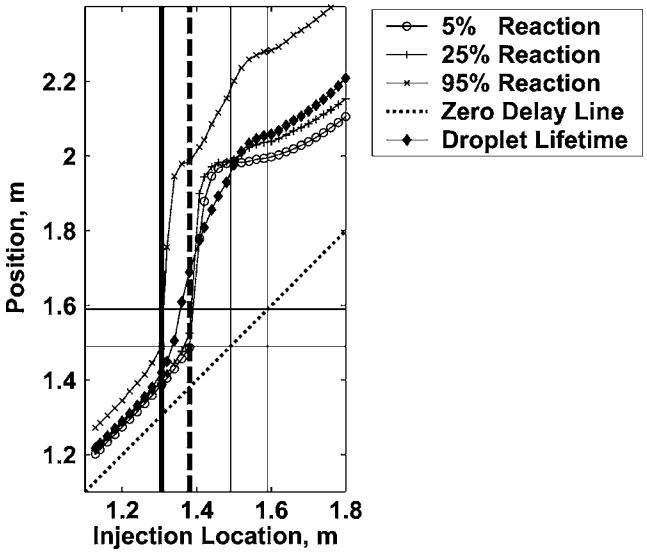

Fig. 16 Injection/ignition map for Case 2. Thick vertical lines extend from injection locations at 1.3 m (solid) and 1.38 m (dashed).

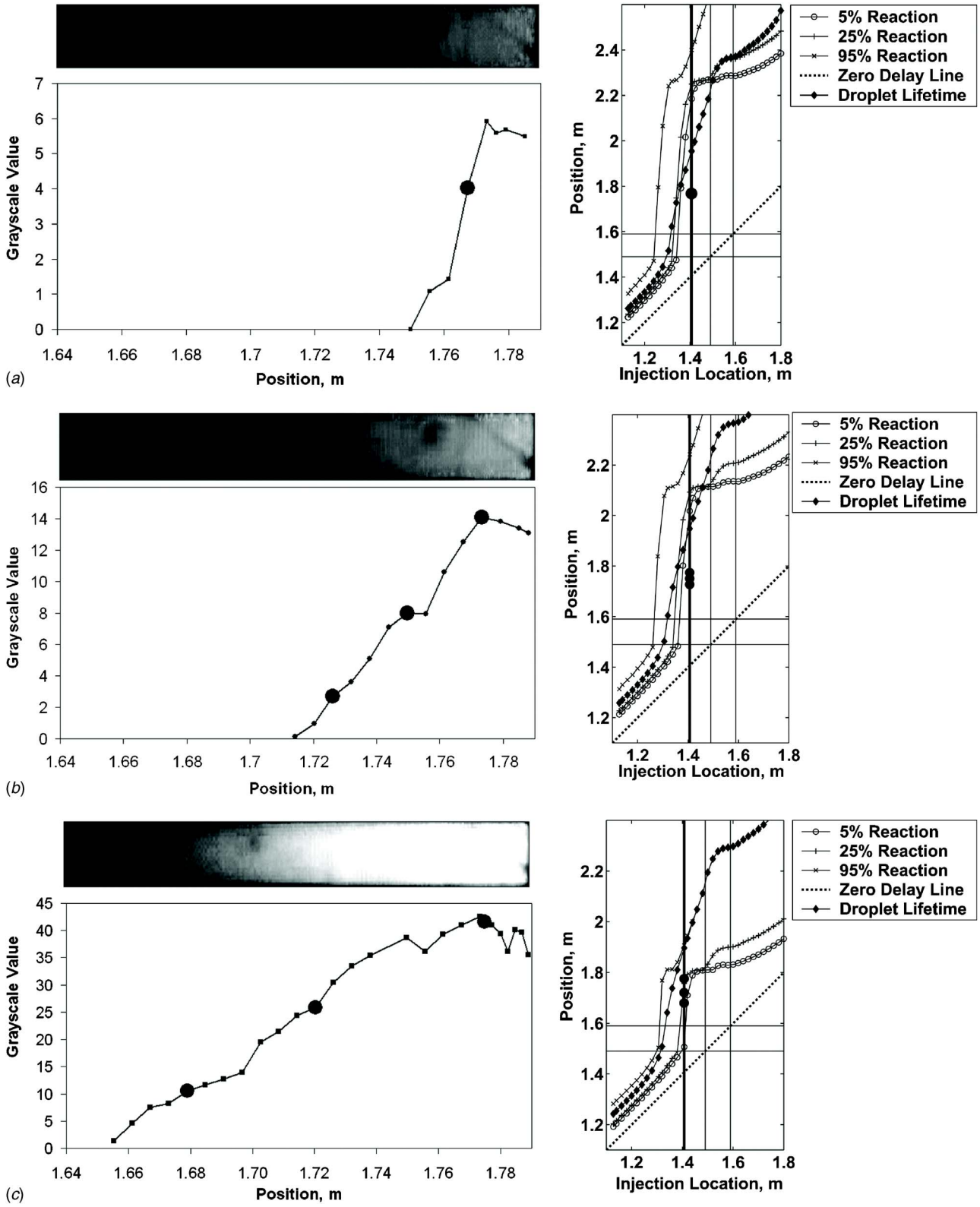

Fig. 17 Chemiluminescence images, intensity plots, and predicted injection/ignition maps for (*a*) Case 3, (*b*) Case 4, and (*c*) Case 5

increase. In contrast, the CL thermocouple, which is upstream of the TS but downstream of the injection location, measured a 20% normalized temperature increase. This heat addition between the injector and the CL thermocouple was responsible for the pressure increase measured in the plenum. The normalized temperature increase approximately leveled off between the CL and D3 thermocouples and then continued to increase up to 49% at the AB2 thermocouple. This trend is not predicted by the model for the nominal injection location at 1.3 m, as indicated by the corresponding reaction percent line. Although the model predicts that

combustion will begin in the converging section, as indeed occurred, the model also predicts that autoignition occurs completely before the TS outlet, which is obviously not the case. This discrepancy may be resolved by examining the injection/ignition map for Case 2 operating conditions, given in Fig. 16. The map shows that the vertical bold line for the nominal injection location is in close vicinity to the steep portion of the reaction percent lines where autoignition occurs both upstream and downstream of the TS. The model predictions in this range of injection locations are more similar to the thermocouple measurements. To illustrate this, the reaction percent line for an injection location of 1.38 m, indicated by the vertical dashed line, was plotted in Fig. 15. Referring back to Fig. 15, it is observed that the 1.38 m profile does exhibit the trends of the thermocouple measurements including the leveling off between the CL and D3 thermocouples. Thus, for Case 2, small changes in the operating point parameters can result in a reaction percent line that is in much closer agreement with the measurements.

5.2 Chemiluminescence Measurements. Chemiluminescence images were recorded through the quartz window in the diverging section, which had been blocked during the temperature measurements. The following three cases, listed in order of increasing primary combustor equivalence ratio, were evaluated:

$$[P_{\mathrm{PL}}, T_{\mathrm{tot}}, \Delta T_{\mathrm{TS}}, \dot{m}_{\mathrm{air}}, \phi_{\mathrm{vit}}, \dot{m}_{\mathrm{Jet\ A}}, \mathrm{Port}, \mathrm{SMD}] = \begin{cases} \text{Case 3: } [37.5 \text{ psi (absolute)}, 1315 \text{ K}, 115 \text{ K}, 0.275 \text{ kg/s}, 0.40, 2.03 \text{ g/s}, \mathrm{CV1}, 45\ \mu\mathrm{m}] \\ \text{Case 4: } [38.3 \text{ psi (absolute)}, 1350 \text{ K}, 130 \text{ K}, 0.273 \text{ kg/s}, 0.43, 2.03 \text{ g/s}, \mathrm{CV1}, 45\ \mu\mathrm{m}] \\ \text{Case 5: } [38.5 \text{ psi (absolute)}, 1475 \text{ K}, 155 \text{ K}, 0.260 \text{ kg/s}, 0.51, 2.03 \text{ g/s}, \mathrm{CV1}, 44\ \mu\mathrm{m}] \end{cases}$$

where again the CV1 port corresponds to injection at 1.41 m, see Fig. 1. These tests had higher flow rates than the previously discussed cases, resulting in higher plenum pressures and choked flow at the throat between the TS blades.

Figure 17 shows the recorded chemiluminescence images, intensity plots, and predicted injection/ignition maps for Cases 3–5. The chemiluminescence images recorded by the CCD camera have been converted to grayscale and further processed to enhance their quality. Intensity plots are shown below each chemiluminescence image. The intensity plots were obtained from the CCD images by using Adobe Photoshop to measure a grayscale value from 0 (black) to 255 (white) within selections of the image. This grayscale value was chosen to represent intensity.

The chemiluminescence images in Fig. 17 clearly indicate that the autoignition of the fuel shifts upstream from Case 3 to Case 5. More specifically, the intensity plots show that chemiluminescence started at approximately 1.750 m, 1.715 m, and 1.655 m for Cases 3, 4, and 5, respectively. This is expected in view of the increasing bulk flow temperature between these cases. The intensity profiles level off or decrease toward the end of the window. If this is a real effect, it would imply that the reactions began to weaken toward the end of the window. However, it is more likely that this is an artifact of the image processing.

Figure 17 also includes the predicted injection/ignition maps for Cases 3–5. On each map, the thick vertical line represents the 1.41 m injection location, and the large circles are reference points, which correspond to the large circles on the intensity profiles. In Fig. 17(*a*), the reference point on the injection/ignition map is well below the 5% reaction line. This indicates that the model over-predicts the autoignition location for Case 3, because the corresponding point on the intensity profile is at a location where the measured chemiluminescence intensity was greater than zero. Following the same procedure with Fig. 17(*b*), it is observed that the model also overpredicts the ignition location for Case 4, although to a lesser extent. In contrast, Fig. 17(*c*) shows that for Case 5, there is good agreement between the model and the measurements. This comparison between the injection/ignition maps and the chemiluminescence measurements reaffirms that the model is able to predict the shift in the autoignition location due to changing operating conditions and suggests that the accuracy of the current model increases as the actual ignition delay decreases.

6 Conclusion

An experimental and theoretical investigation of the feasibility of a "prime and trigger" concept for aircraft afterburners was performed. The experimental setup provided realistic turbine velocities, temperatures, and oxygen contents, but not realistic turbine pressures. A temperature drop of 100–200 K across the turbine simulator was achieved using water cooling inside the blades and some water injection. The experimental results demonstrated the autoignition of Jet A for afterburner combustion. It was shown that injection of Jet A upstream of the turbine simulator can result in autoignition only downstream of the turbine simulator provided that injection occurs within a limited range that is a function of the operating conditions. This is a significant result as it establishes the feasibility of the proposed concept, at least at low pressure. Moreover, the experimental results suggest that low power triggering at the afterburner inlet for control of the combustion zone should be readily achievable, since the mixture in this vicinity is already close to autoignition.

A theoretical model was developed to predict the autoignition location of the fuel. Despite the simplicity of the model, it accurately predicted the trends of the experimental measurements and provided reasonable estimates of the autoignition location. Importantly, the results from the model suggested that the ideal fuel injection location for autoignition in the afterburner is indeed just upstream of a turbine stage. The results from the model also indicated that evaporation and chemistry are significantly coupled, and thus the system is neither evaporation nor chemistry controlled.

Future investigation of the PAT concept will include detailed measurements of the combustion zone characteristics such as length, stability, and combustion efficiency. An investigation of trigger mechanisms will follow to determine if a low power trigger can be used to decrease the length of the combustion zone, increase stability, increase combustion efficiency, and decrease sensitivity to changing operating conditions.

References

[1] Lovett, J. A., Brogan, T. P., and Philippona, D. S., 2004, "Development Needs for Advanced Afterburner Designs," *Proceedings of 40th Joint Propulsion Conference and Exhibit*, Fort Lauderdale, FL, Paper No. AIAA-2004-4192.

[2] Liew, K. H., Urip, E., and Yang, S. L., 2005, "Parametric Cycle Analysis of a Turbofan Engine With an Interstage Turbine Burner," J. Propul. Power, **2**(3), pp. 546–551.

[3] Sirignano, W. A., and Liu, F., 1999, "Performance Increases for Gas-Turbine Engines Through Combustion Inside the Turbine," J. Propul. Power, **15**(1), pp. 111–118.

[4] Birmaher, S., Neumeier, Y., and Zinn, B., 2007, "Development of a 'Prime and Trigger' Concept for Compact Afterburner Combustion," *Proceedings of 45th AIAA Aerospace Sciences Meeting and Exhibit*, Reno, NV, Paper No. AIAA 2007-562.

[5] Yang, W., and Kee, R., 2002, "The Effect of Monodispersed Water Mists on the Structure, Burning Velocity, and Extinction Behavior of Freely Propagat-

ing, Stoichiometric, Premixed, Methane-Air Flames," Combust. Flame, **130**(4), pp. 322–335.
[6] Abramzon, B., and Sirignano, W. A., 1989, "Droplet Vaporization Model for Spray Combustion Calculations," Int. J. Heat Mass Transfer, **32**(9), pp. 1605–1618.
[7] Jasuja, A. K., 1979, "Atomization of Crude and Residual Fuel Oils," ASME J. Eng. Power, **101**, pp. 250–258.
[8] Cargaftik, N., Vinogradov, Y., and Yargin, V., 1996, *Handbook of Physical Properties of Liquids and Gases*, 3rd ed., Begell House, New York.
[9] Turns, S. R, 1996, *An Introduction to Combustion*, 2nd ed., McGraw-Hill, Boston.
[10] Reid, R. C., Prausnitz, J. M., and Poling, B. E., 1987, *The Properties of Gases and Liquids*, 4th ed., McGraw-Hill, New York.
[11] Gokalp, I., Chauveau, C., Simon, O., and Chesneau, X., 1992, "Mass Transfer From Liquid Fuel Droplets in Turbulent Flow," Combust. Flame, **89**(3–4), pp. 286–298.
[12] Ducourneau, F., 1969, "Inflammation Spontanée de Mélanges Riches Air-Kérosène," Entropie, **59**, pp. 11–18.
[13] Freeman, G., and Lefebvre, A. H., 1984, "Spontaneous Ignition Characteristics of Gaseous Hydrocarbon-Air Mixtures," Combust. Flame, **58**, pp. 153–162.
[14] Lefebvre, A., Freeman, W., and Cowell, L., 1986, "Spontaneous Ignition Characteristics of Hydrocarbon Fuel/Air Mixtures," NASA Technical Report No. 175064.
[15] Mullins, B. P., 1947, "Studies on the Spontaneous Ignition of Fuels Injected Into a Hot Air Stream," J. Inst. Pet., **33**, pp. 211–253; **33**, pp. 327–342.
[16] Mullins, B. P., 1949, "Combustion in Vitiated Atmospheres—Parts I, II, III, and IV," Fuel, **28**, pp. 181–188, 200–207, 225–228.
[17] Mullins, B. P., 1953, "Studies on the Spontaneous Ignition of Fuels Injected Into a Hot Air Stream V—Ignition Delay Measurements on Hydrocarbons," Fuel, **32**, pp. 363–379.
[18] Spadaccini, L. J., and Tevelde, J. A., 1980, "Autoignition Characteristics of Aircraft Type Fuels," NASA Technical Report No. 159886.
[19] Livengood, C. J., and Wu, C. P., 1955, "Correlation of Autoignition Phenomena in Internal Combustion Engines and Rapid Compression Machines," *Fifth International Symposium on Combustion*, University of Pittsburgh, Pittsburgh, PA, pp. 347–356.
[20] Assanis, D. N., Filipi, Z. S., Fiveland, S. B., and Syrimis, M., 2003, "A Predictive Ignition Delay Correlation Under Steady-State and Transient Operation of a Direct Injection Diesel Engine," ASME J. Eng. Gas Turbines Power, **125**, pp. 450–457.
[21] Colin, O., Pires da Cruz, A., and Jay, S., 2005, "Detailed Chemistry-Based Auto-Ignition Model Including Low Temperature Phenomena Applied to 3-D Engine Calculations," Proc. Combust. Inst., **30**, pp. 2649–2656.

Laboratory Study of Premixed H_2-Air and H_2-N_2-Air Flames in a Low-Swirl Injector for Ultralow Emissions Gas Turbines

R. K. Cheng

D. Littlejohn

Environmental Energy Technologies Division,
Lawrence Berkeley National Laboratory,
Berkeley, CA 94720

The objective of this study is to conduct laboratory experiments on low-swirl injectors (LSIs) to obtain the basic information for adapting LSI to burn H_2 and diluted H_2 fuels that will be utilized in the gas turbines of the integrated gasification combined cycle coal power plants. The LSI is a novel ultralow emission dry-low NO_x combustion method that has been developed for gas turbines operating on natural gas. It is being developed for fuel-flexible turbines burning a variety of hydrocarbon fuels, biomass gases, and refinery gases. The adaptation of the LSI to accept H_2 flames is guided by an analytical expression derived from the flow field characteristics and the turbulent flame speed correlation. The evaluation of the operating regimes of nine LSI configurations for H_2 shows an optimum swirl number of 0.51, which is slightly lower than the swirl number of 0.54 for the hydrocarbon LSI. Using particle image velocimetry (PIV), the flow fields of 32 premixed H_2-air and H_2-N_2-air flames were measured. The turbulent flame speeds deduced from PIV show a linear correlation with turbulence intensity. The correlation constant for H_2 is 3.1 and is higher than the 2.14 value for hydrocarbons. The analysis of velocity profiles confirms that the near field flow features of the H_2 flames are self-similar. These results demonstrate that the basic LSI mechanism is not affected by the differences in the properties of H_2 and hydrocarbon flames and support the feasibility of the LSI concept for hydrogen fueled gas turbines. [DOI: 10.1115/1.2836480]

Introduction

The motivation of our research is to develop a robust ultralow emission combustor for the gas turbines in FutureGen power plants that burn syngases derived from the gasification of coal. The objective is to adapt a novel low-swirl combustion (LSC) method to these utility size gas turbines that operate on fuels with very high H_2 constituency. LSC is a dry-low-NO_x (DLN) lean premixed combustion method conceived at the Lawrence Berkeley National Laboratory. This technology has been commercialized for industrial heaters by Maxon Corporation of Muncie, IN and is being developed for natural gas and fuel-flexible industrial turbines (5–7 MW) in partnership with Solar Turbines of San Diego, CA. It is also being adapted to 100 kW microturbines in partnership with Elliott Energy Systems of Stuart, FL for integration into a large boiler for combined heat and power generation.

FutureGen power plants utilize the integrated gasification combined cycle (IGCC) approach to produce hydrogen, which is separated from a concentrated CO_2 stream that is then captured for subsequent sequestration. One of its key components is a cost-competitive all-hydrogen fueled turbine with ultralow NO_x emission and high efficiency. To lower NO_x to the FutureGen near zero emission goal of 2 ppm (at 15% O_2), the current approach is to operate the H_2 turbine at lower firing temperatures in combination with selective catalytic reduction. This approach sacrifices efficiency and impacts costs of electricity (via capital cost, efficiency, and capacity output). Therefore, a cost-effective combustion technology that meets the FurtureGen emissions and efficiency targets is critical to achieving its ultimate goal of no more than a 10% increase in the cost of electricity for mature FutureGen-type plants that include CO_2 capture and sequestration.

The purpose of this paper is to conduct laboratory studies of low-swirl injectors (LSIs) burning pure hydrogen and nitrogen-diluted hydrogen fuels to characterize the overall flame behavior, stabilization limits, turbulent flame speeds, and flow field characteristics. The analysis of these data and comparison with those obtained previously for hydrocarbon flames is a necessary first step toward building the scientific and technical foundation for the adaptation of LSI to accept pure and diluted H_2 fuels.

Background

LSC combustion was originally conceived as a research burner for fundamental premixed turbulent flame experiments (e.g., Refs. [1–3]). Through laboratory studies and analyses, its basic operating principle is relatively well understood. LSC supports premixed turbulent flames under a very broad range of operating conditions. Its capability to support robust and stable flames at very fuel lean conditions can be exploited as an ultralow emission combustion technology. LSC operates on the principle of flame propagation. It is therefore not applicable to nonpremixed combustion because the diffusion flames do not propagate.

LSC is an aerodynamic flame stabilization method that utilizes a divergent flow to sustain a freely propagating premixed turbulent flame. The divergent flow is formed only when the swirl intensities are well below the critical vortex breakdown threshold. The linear axial velocity decay region within the divergent flow allows the flame to settle where the local velocity is equal and opposite to the turbulent flame speed. Matching the flow field velocities to the turbulent flame speed is the critical design process. The main advantage of the LSC concept is its very large turndown capacity (demonstrated as 90:1 in laboratory) and its capability to support very lean premixed turbulent flames in a turbulent flow field that allows the flame to withstand swings in operational and mixture conditions without high risk of flame instability, flashback, or blowoff. The flame propagation principle of LSC is fundamentally different from the flame attachment concept

Manuscript received May 9, 2007; final manuscript received September 17, 2007; published online April 2, 2008. Review conducted by Dilip R. Ballal.

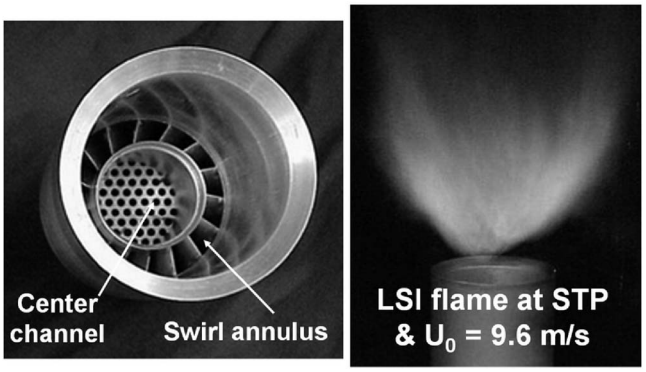

Fig. 1 The first prototype LSI for Taurus 70 engine

of the high-swirl concept utilized in current gas turbine DLN combustors (e.g., GE, Siemens, and Solar) where toroidal vortices with strong recirculation and intense shear turbulence are generated to hold and continuously ignite the turbulent premixed flames.

The key component for a practical implementation of LSC is a patented swirler. This swirler is simpler and easier to operate and control than the first embodiment of LSC using air jets to impart swirl [2,4–6]. Figure 1 shows the first prototype LSI configured for Solar Turbine's 7 MW Taurus 70 (T70) engine [7]. The flow of the premixed reactants through this LSI, as well as all other LSC devices, is separated into two passages: An outer annular with swirl vanes and an open center channel that allows a portion of the reactants to remain unswirled. The unswirled reactants flowing through the center channel is a critical requirement of LSC whose presence retards the recirculation and promotes the formation of flow divergence. The flame is detached from the LSI. Its liftoff position is controlled by the divergence rate that is adjustable by the flow split between the swirled and the unswirled flows. The most convenient means to vary this flow split is by changing the blockage ratio of the perforated screen covering the center channel.

The LSI prototype utilizes a swirler engineered for the T70 SoLoNO$_x$ engines. To configure this swirler into a LSI, the center body was removed and replaced by a perforated plate selected according to the engineering rules developed for industrial low-swirl burners (LSBs). The rules are specified in terms of acceptable ranges of swirl number ($0.4<S<0.55$) and swirler recess ($2<L_i/R_i<3$). The swirl number is defined as

$$S=\frac{2}{3}\tan\alpha\frac{1-R^3}{1-R^2+[m^2(1/R^2-1)^2]R^2} \tag{1}$$

where α is the vane angle, $R=R_c/R_i$, and $m=m_c/m_s$ (where m_c and m_s are, respectively, the mass fluxes of the unswirled and the swirled flows). The SoLoNO$_x$ swirler has an internal radius of 3.175 cm with 16 curved vanes with a discharge angle α =40 deg. The ratio of the center channel to injector radii R is 0.63. To meet the design criteria, a 58% blockage perforated plate with circular holes in a hexagonal arrangement was chosen. This LSI has a swirl number S=0.54 and generates a flame that has an optimum liftoff height, x_f, of approximately $0.5R_i$ from the nozzle exit. Another key parameter is the swirler recess distance L_i. It controls the residence time for the interaction between the swirled and unswirled flows and has a direct effect on the LSI performance. As in the industrial burners, L_i was set at L_i/R_i=3.

Rig tests of the first LSI at elevated temperatures and pressures [7] showed that the LSI flame remained stable and oscillation free throughout the test matrix covering full load (800°F,15 atm) and partial load (450°F,6 atm) conditions. The NO$_x$ emissions are 60% lower than those of the SoLoNO$_x$ high-swirl injector. The results demonstrated that the LSI can attain ultralow emissions at conditions farther away from the lean-blowoff (LBO) limit to avoid inciting combustion oscillations. The lowest levels of NO$_x$ (<2 ppm) and CO (<10 ppm) at a firing temperature of 2670°F are comparable with those from much more costly and less durable catalytic options. The LSI achieves the performance targets with only a few design iterations because the knowledge gained from the laboratory experiments is directly useful to guide the turbine hardware design. As the bulk of the optimization can be accomplished in the laboratory, this brings about significant cost savings in the development process.

A fully functional engine-ready LSI prototype has also been developed. It employs a simple fuel spoke injection scheme similar to the one for the current SoLoNO$_x$ injector. For load following, a pilot is imbedded into the center plate. Again, laboratory experiments played a key role in optimizing the fuel injector placement position and the size of the pilot. Single injector tests at simulated gas turbine conditions and multiinjector tests at atmospheric conditions in the T70 annulus combustor liner show that the performance of the engine-ready LSI prototype is similar to the first prototype [8]. A set of the engine-ready LSI prototypes was fabricated and tested successfully in a T70 in June 2006.

The scientific foundation obtained for LSC plays a critical role for its adaptation to gas turbines. In a continuing effort to expand the knowledge base, a recent study focused on gaining better understanding of how the LSI flow field structures and flame properties evolve with Reynolds numbers [9]. These experiments were performed in open flames to circumvent the difficulties and uncertainties associated with laser studies of flames within a quartz enclosure. The conveniences offered by open flame studies facilitate the collection of a large amount of data to examine the overall flame behaviors and flow field evolution that is of significant value to gas turbine development. Moreover, previous studies (e.g., Ref. [10]) showed that the enclosure effects are minimal when the enclosure radius is about three times larger than the injector (or burner) radius. The 3:1 enclosure ratio has been adopted as the guideline for sizing the enclosures for industrial burners and for optimizing the LSI radius for the T70 combustor. Field experiences and rig-test results confirmed that the knowledge gained open flames are directly relevant to the enclosed flames in gas turbines.

Analyses of the velocity measurements obtained from particle image velocimetry (PIV) of these open CH_4 flames show that the flow field generated by the LSI exhibits a self-similarity behavior. Two parameters derived from the centerline velocity profiles of the LSI flow fields are invoked to characterize self-similarity. They are the virtual origin of the divergent flow x_0 and the nondimensional axial aerodynamic stretch rate a_x. To characterize the flame, the turbulent flame speeds S_T and the position of the leading edge of the flame brush, x_f, are used. These parameters can be deduced by using the velocity profiles obtained along the centerline (see Fig. 9 of Ref. [9]).

The analysis of S_T shows a linear dependency on turbulence intensity u'. An analytical equation (Eq. (2)) for the velocity balance at x_f shows that a coupling of the self-similar flow field and linear turbulent flame speed correlations with u' is the reason why the LSI flame remains stationary through a wide range of velocities and fuel air equivalence ratios ϕ.

$$1-\frac{dU}{dx}\frac{(x_f-x_0)}{U_0}=\frac{S_T}{U_0}=\frac{S_L}{U_0}+\frac{Ku'}{U_0} \tag{2}$$

The two terms on the far right hand side simply state that S_T for hydrocarbon flames increases linearly with u' above the base line value of the laminar flame speed S_L at a slope of K. This slope is an empirical correlation constant derived from the experimental measurements[1] and is 2.16 for hydrocarbon flames. The first term

[1]The linear dependency of S_T on u' is not universal as S_T in other burners tends to be nonlinear and shows "bending."

on the right hand side tends to a small value at large bulk flow velocity U_0 because the laminar flame speeds of typical hydrocarbon fuels are on the order of 0.2–0.7 m/s. The second term on the right hand side is a constant because turbulence in the central region of the LSI is controlled by the perforated plate and scales with U_0. On the left hand side, self-similar means that $a_x = dU/dx/U_0$ in the second term is constant. The main consequence is that the flame position x_f-x_0 has an asymptotic value at large U_0. Therefore, when S_L is held constant at a given ϕ, flame shift, i.e., changes in x_f, occurs only at low velocities where U_0 is in the same order as S_L. When $U_0 \gg S_L$, changing stoichiometry and/or U_0 do not result in a significant flame shift. These flame behaviors have been confirmed by laboratory experiments and testing of industrial burners and gas turbine injectors.

Equation (2) provides an analytical expression that describes the relationship between the LSI flow field and the turbulent flame properties. Because the aerodynamic stretch rate is proportional to the swirl number, this expression gives a first order estimate on how the LSI can be adjusted to accept different fuels. For example, it shows that a significant adjustment may not be necessary for burning different hydrocarbon fuels. This is due to the fact that the S_L and heat release rates are close to those of natural gas. As long as the turbulent flame speeds have a linear correlation with u' at a rate of increase close to that of natural gas flames, the axial aerodynamic stretch rate, i.e., swirler design, does not need to be adjusted to accommodate these other hydrocarbon fuels. Recent laboratory studies of CH_4, C_3H_8, C_2H_4, and CH_4/H_2 flames [9,11] have produced the data to support this conjecture.

To develop the LSI for H_2 fuels, the key question concerns the correlation of the turbulent flame speeds for these flames with significantly higher S_L and preferential diffusion than those of hydrocarbons. Determining the correlation of the S_T for H_2 flames with u' is therefore the critical information needed to adapt LSI for burning H_2. Additionally, characterizing the effects of the H_2 flames on the flow field, particularly how they alter the axial aerodynamic stretch rate in the near field region, is important in gaining insight on predicting the H_2 flame behavior at higher velocities, temperatures, and pressures. The purpose of this investigation is to obtain the experimental data on H_2 flames to begin building a body of knowledge needed for guiding the development of LSI for FutureGen turbines.

Approach

The LSI configuration for the T70 engine is a logical starting point for the evaluation of LSC operation with H_2. Following the same approach for natural gas development, the first step is to explore the operating regime and characterize the performance through laboratory open H_2 flame experiments. The operating regime is defined by the flame stability and LBO limits as a function of U_0. The performance criteria are flame uniformity, flame position, and any other flame behaviors that may affect the operation of the LSI. The discussion on Eq. (2) shows that the LSI can be adapted to accommodate differences in flame properties by adjusting the axial aerodynamic stretch rate. The most convenient way is by changing the blockage ratio of the center-channel plate to vary its swirl number S (i.e., varying m in Eq. (1)). The optimum LSI configuration for H_2 fuels can be then determined by comparing the operating regimes and the performance criteria for a range of S.

Next, the flow field and flame properties of these LSIs are characterized by PIV measurements. The velocity results can be analyzed the same way as those from the hydrocarbon flames to obtain a set of empirical constants for H_2 fuels. In addition, the swirl number effects and the flow field responses to H_2 flames can also be examined.

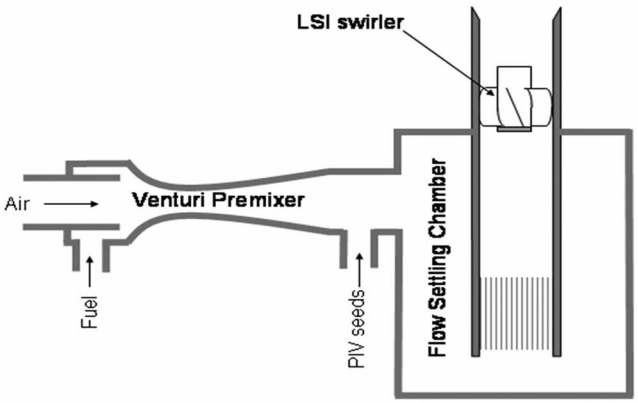

Fig. 2 Schematics of the LSI setup

Experimental Apparatus and Diagnostics

The physical dimensions of the LSI are given above. For the LBO and PIV investigations, the LSIs were mounted vertically on top of a cylindrical settling chamber (Fig. 2). Air supplied by a fan blower enters at the side of a 25.4 cm diameter chamber and flows into the LSI via a centrally placed 30 cm long straight tube. To produce a uniform flow into the LSI, a perforated screen is placed 5 cm upstream. Air flow from a blower is adjusted by a PC controlled valve and monitored by a turbine meter. Fuel is injected in a commercial venturi premixer to ensure a homogeneous mixture for the injector. Both the fuel and the PIV seeder flows are controlled by electronic mass flow controllers and set according to a predetermined value of mixture compositions and ϕ. The fuel and air supply system for this study has a larger capacity than the one used previously [7,9,11] to enable experiments up to $U_0 = 22$ m/s (65 g/s air). Increasing the bulk flow velocity is necessary for the H_2-air flame studies as these flames flash back at a high U_0 than their hydrocarbon counterparts [9]. The experiments utilize research grade H_2 with and without N_2 dilution. Because premixed H_2 flames are invisible to the naked eye, a webcam is used as a safety monitor and to examine the overall flame features. To detect the near-infrared emissions from the H_2 flame, the IR filter of the webcam was removed. The PIV experimental conditions are summarized in Table 1 with the combustion properties calculated using an algorithm by Zhang et al. [12]. Due to the very low adiabatic temperatures of all these H_2 flames, their NO_x emissions are expected to be well below detectable limits and therefore not sampled.

Flow field information for the nonreacting flows and flames was obtained using PIV. To facilitate data collection, the flows and the flames were nonenclosed. The PIV system consists of a New Wave Solo PIV laser with double 120 mJ pulses at 532 nm and a Kodak/Red Lake ES 4.0 digital camera with a 2048×2048 pixel resolution. The optics were configured to capture a field of view of approximately 13×13 cm^2 covering the near field as well as the far field of the flames with a 0.065 mm/pixel resolution. A

Table 1 Mixtures for PIV measurements

Fuel	ϕ	T_{ad} (K)	S_L (m/s)
H_2	0.3	1189	0.12
H_2	0.35	1312	0.18
H_2	0.38	1383	0.22
0.75 H_2/0.25 N_2	0.31	1182	0.09
0.75 H_2/0.25 N_2	0.37	1317	0.14

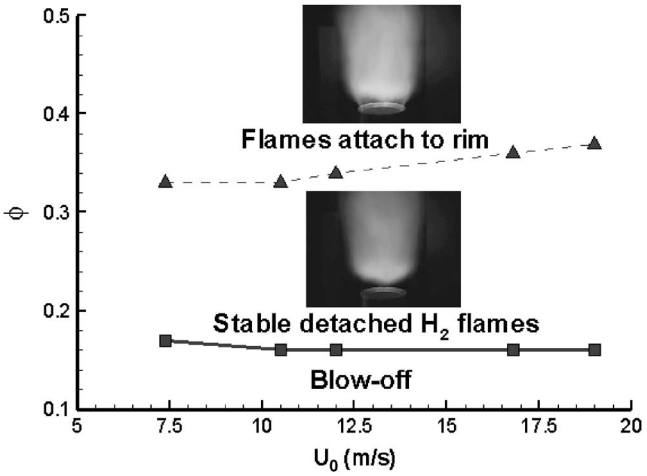

Fig. 3 Operating regime of LSI-R for H_2

cyclone-type particle seeder seeds the air flow with 0.6–0.8 μm Al_2O_3 particles, which should track velocity fluctuations up to 10 kHz [13].

Data acquisition and analysis were performed using a software developed by Wernet [14]. Because of the complex and 3D nature of the swirling flow field, care had to be taken to optimize interframe timing, camera aperture setting, light-sheet thickness, and seed density to ensure high data fidelity. Using a portion of the light sheet with approximately 1.1 mm thickness (away from the 0.3 mm waist produced by the 450 mm spherical lens) and a short interframe time (30 μs) helped to freeze the out-of-plane motion of seed particles. Sets of 224 image pairs were recorded for each experiment corresponding to a minimum criterion required to produce stable mean and rms velocities. The PIV data were processed using 64×64 pixel cross-correlation interrogation regions with 50% overlap. This rendered a spatial resolution of approximately 2 mm. The velocity statistics were checked to ensure that a significant spatial bias or "peak locking" was not taking place.

Results

The first experiments involved the use of the LSI from previous studies [7,9,11] to obtain base line information on H_2 operation. This LSI has a swirl number $S=0.54$ and is referred to here as LSI-R. Shown in Fig. 3 is the operating regime of LSI-R for $10<U_0<22$ m/s. Here, the LBO limit is nearly constant at $\phi\approx0.17$ and is consistent with the result reported previously for $U_0<10$ m/s [11]. This shows again that the LBO of LSI is relatively insensitive to the Reynolds number.

The LSI-R H_2 flames propagate closer to the exit than the hydrocarbon flames. In addition, there is an upper limit shown by the broken line at $\phi\approx0.32$. Above this boundary, the trailing edges of the flames curl back upstream and attach to the burner rim. This phenomenon indicates burning within the mixing layer formed between the reactants and the ambient air. It is a consequence of the high diffusivity and flammability of H_2.

Higher H_2 concentrations in these richer mixtures promote H_2 diffusion into the outer region of the mixing layer. The outer low velocity region becomes flammable, allowing the trailing edge of the flame to burn back upstream toward the rim. Flame attachment also occurs in CH_4/H_2 flames when the concentration of H_2 is high (>50) but does not occur in pure hydrocarbon flames. The slight upward trend of the flame attachment limit, as shown in Fig. 3, suggests that the phenomenon may not occur at high velocities.

When the flame attaches to the burner rim, it forms an envelope over the reactants. Consequently, the flow field and the flame/flow dynamics will be different from those of lifted flames. The close proximity of the H_2 flames in LSI-R to the exit also restricts laser access to the near field regions where information is needed to characterize the flame and flow properties. Therefore, LSI-R is not ideally suited for the current study and the swirl number needs to be lowered to relax the axial aerodynamic stretch rate so that the H_2 flames lift off farther from the exit.

Table 2 Perforated plates to vary the swirl number of LSI

	Hole diameter (mm)	S
LSI-R	3.05	0.54
LSI-UH1	3.18	0.53
LSI-UH2	3.45	0.50
LSI-UH3	3.66	0.47
LSI-UH4	3.86	0.41

To lower the swirl number, a series of perforated plates with decreasing blockage ratios was fitted to the center channel of the LSI swirler. These plates were made by enlarging the holes of the perforated plate for LSI-R. LSI-R uses a standard perforated plate with holes in a hexagonal arrangement. The hole diameter is 3.05 mm with a center-to-center spacing of 4.8 mm to give a blockage ratio of 40%. Table 2 shows the different plates used to produce a set of LSIs (designated as UH for uniform holes) with $0.53<S<0.41$.

Tests performed on the four LSI-UHs with H_2 air mixtures confirm that the flame liftoff distance increases with decreasing S as indicated by Eq. (2). Figure 4 compares their operating maps with that of LSI-R. The results show that a reduction of S from 0.54 to 0.50 has little effect on the LBO limits. Further reduction in S (<0.5) shifts LBO to higher ϕ and degrades the performance. The corresponding flame attachment limits show some changes but do not suggest a consistent upward trend with decreasing S. As indicated by the lengths of the vertical lines marking the extent of the effective operating regimes, decreasing S using these perforated plates tends to reduce the range of lifted H_2 flame operations.

In an effort to mitigate the H_2 flame attachment phenomenon, we applied a flame shaping method to elongate the H_2 flames so that their trailing edges are slightly swept back to reduce its propensity to ignite the mixing layer. This is accomplished by progressively increasing the size of holes on the center-channel perforated plate from small in the middle to large at the edge. These plates generate a slightly nonuniform axial velocity profile that is faster at the edges of the center channel, thus producing a slightly curved flame front at the center instead of a relatively flat flame when a UH plate is used.

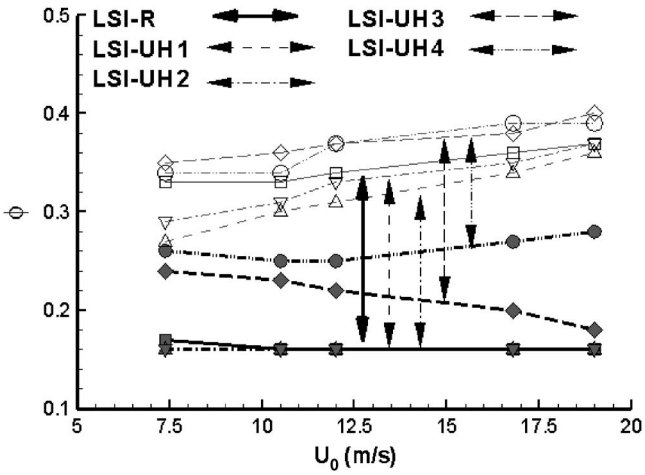

Fig. 4 Operating maps of LSIs with UH center plates

Table 3 Hexagonal perforated plates with variable hole sizes to vary the swirl number of LSI

	Hole diameter (mm)			
	Center	Second and third	Fourth and fifth	S
LSI-VH1	3.05	3.26	3.45	0.51
LSI-VH2	3.26	3.45	3.57	0.50
LSI-VH3	3.05	3.45	3.66	0.48
LSI-VH4	3.05	3.7	3.8	0.43

Table 3 shows the four LSIs configured by varying hole (VH) diameter plates. These plates were made from the reference plate of LSI-R. The holes on these plates have three different diameters: one for the center hole, one for the second and third rings of holes from the center, and one for the fourth and fifth rings. The range of center-channel hole sizes for the LSI-VH is the same as that for LSI-UHs. Their swirl numbers $0.51 < S < 0.43$ are also similar.

Figure 5 shows the operating regimes of the LSI-VHs compared to that for LSI-R. It can be seen that the VH perforated

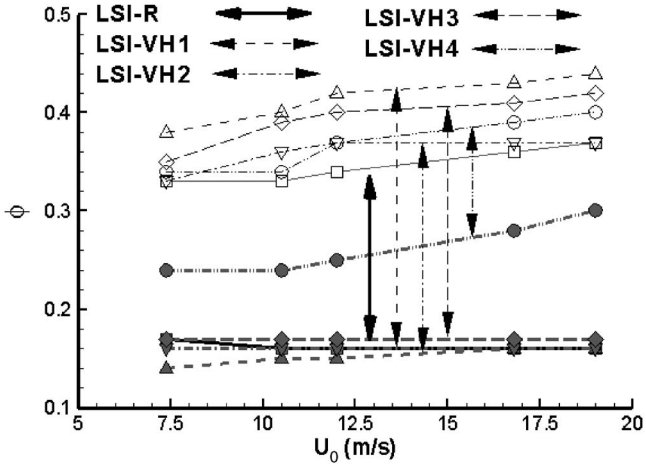

Fig. 5 Operating maps of LSIs with UH center plates

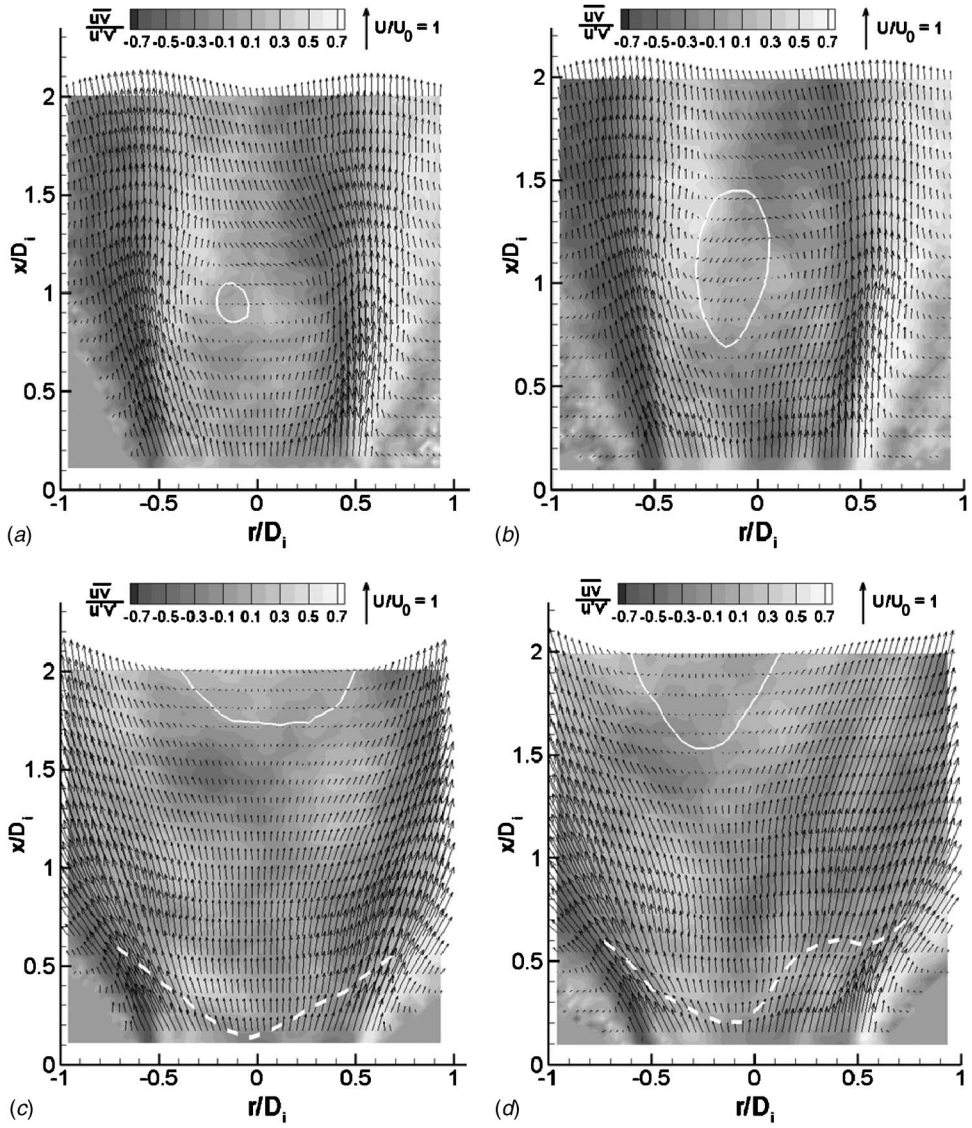

Fig. 6 Normalized 2D velocity vectors and normalized shear stresses measured in nonreacting flows of U_0=18 m/s in (*a*) LSI-R and (*b*) LSI-VH1 and in H_2/air flames of ϕ=0.35 and U_0 =18 m/s in (*c*) LSI-R and (*d*) LSI-VH. Dashed lines mark the leading edges of the flame brushes.

plates improve the ranges of operation. Except for LSI-VH4, all the LBO limits are the same as LSI-R. More significantly, the flame attachment limits of some of the LSI-VHs are higher than that of the LSI-R. Therefore, flame shaping enables the study of lifted H_2 flame at higher stoichiometries. Consequently, the PIV measurements were made in the LSI-VHs and compared with those made in LSI-R.

The PIV measurements consist of 32 flames with $10 < U_0 < 20$ m/s using the mixtures of Table 1. Figure 6 compares the flow fields of LSI-R and LSI-VH1. From Fig. 5, LSI-VH1 with $S=0.51$ offers the largest range of operation among the LSI evaluated in this study and is considered the optimum configuration. The normalized 2D velocity vectors obtained in the nonreacting flows produced by LSI-R and LSIVH1 at $U_0=18$ m/s are shown, respectively, in Figs. 6(*a*) and 6(*b*). In the near field region of LSI-VH1 ($0.3 < x/D_i$), a slight retardation in the flow velocities near the centerline is a direct consequence of the VH size plate. As outlined by the white line showing the zero velocity contour, both LSI-R and LSI-VH1 generate very weak recirculation zones in the far field. However, the one produced by LSI-VH1 is larger and elongated. Otherwise, there are no significant differences between the overall features of the nonreacting flow fields of the two LSIs.

The flow fields of H_2 flames at $\phi=0.35$ m/s and 18 m/s in LSI-R and LSI-VH1 are shown, respectively, in Figs. 6(*c*) and 6(*d*). At this stoichiometry, the leading edge of the flame brush of LSI-R is very close to the LSI exit at $x/D_i=0.2$. Therefore, the velocity data in Fig. 6(*c*) cannot show the details of the near field reactant region. However, in the far field, flow features such as combustion induced flow acceleration and an enlarged recirculation zone are similar to the features found in hydrocarbon flames. Hence, the overall changes in the flow fields induced by H_2 and hydrocarbon flames are not significantly different. The reacting flow field of LSI-VH1 is shown in Fig. 6(*d*). This flame has a larger liftoff ($x/D_i=0.3$) but is asymmetric. The velocity vectors below the flame show noticeable nonuniform distributions because of the varying perforated plate hole sizes. Though the flow field is slightly off center, all other features of the velocity vectors, i.e., combustion heat release, flow discharge angle, and far field recirculation zone, are not significantly different from those shown in Fig. 6(*c*) for LSI-R.

According to Eq. (2), the flow fields of the LSI can be characterized by the parameters S_T, a_x, and x_0 deducible from the centerline velocity profiles. The correlation of the turbulent flame speed S_T is of particular importance because it quantifies the governing process of the LSI method. Turbulent flame speed data for H_2 are very rare and those reported in the literature show a nonlinear correlation with turbulence intensity u' commonly known as the bending effect. This so-called bending is also reported for S_T of hydrocarbon flames [15,16]. In contrast, S_T for hydrocarbon flames deduced from LSBs and LSI show a clear linear increasing trend with u' [11]. According to Eq. (2), the linear correlation is the significant flame property that enables the LSI to operate within a very wide range of flame and flow conditions. If the S_T correlation is nonlinear or bends, it implies that the flame drifts downstream with increasing U_0 and blows off.

Figure 7 compares the S_T data deduced from the 32 H_2 and H_2/N_2 flames with those reported previously for CH_4, C_3H_8, C_2H_4, and CH_4/H_2 [11]. The H_2 flame results show that their turbulent flame speeds are higher than those of the hydrocarbon flames. They are also more scattered, especially at the high u'/S_L conditions. The increase in scatter may be due to the uncertainties in the values of the laminar flame speed S_L for lean H_2 mixtures. Nevertheless, the H_2 turbulent flame speed data indicate a linear trend with increasing u'. The linear correlation constant K is 3.15 and is higher than the 2.1 value for hydrocarbon flames. The significant implication of the linear H_2 flame speed correlation is that the LSI concept should also be valid for hydrogen.

In addition to the linear flame speed correlation, the self-

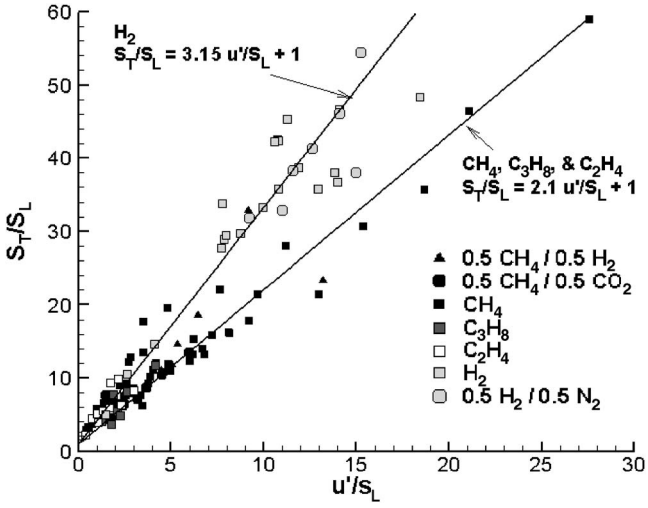

Fig. 7 Comparison of the turbulent flame speed S_T of H_2 and hydrocarbon flames

similarity of the near field region is the other important feature for the LSI operation. The two parameters in Eq. (2) that characterize the near field are the nondimensionalized axial aerodynamic stretch rate a_x and the virtual origin of the linear divergent region, x_0. The values of a_x deduced from the nonreacting and reacting flow fields are shown in Fig. 8 as functions of the flow Reynolds number, Re. The profiles in Fig. 8(*a*) show that the values of a_x

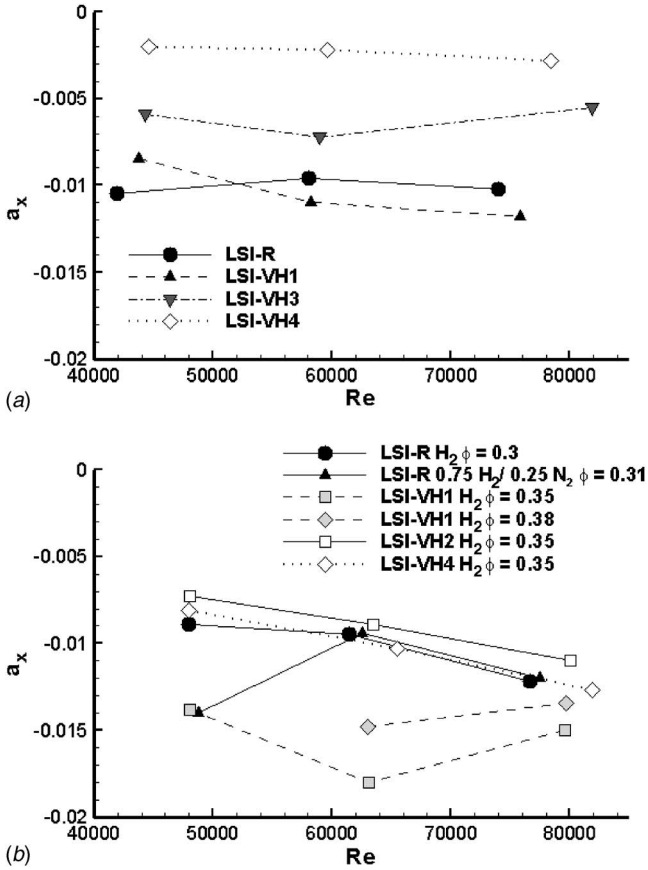

Fig. 8 Nondimensionalized axial aerodynamic stretch rate a_x measured in the nonreacting (*a*) and reacting (*b*) flow fields of the LSIs

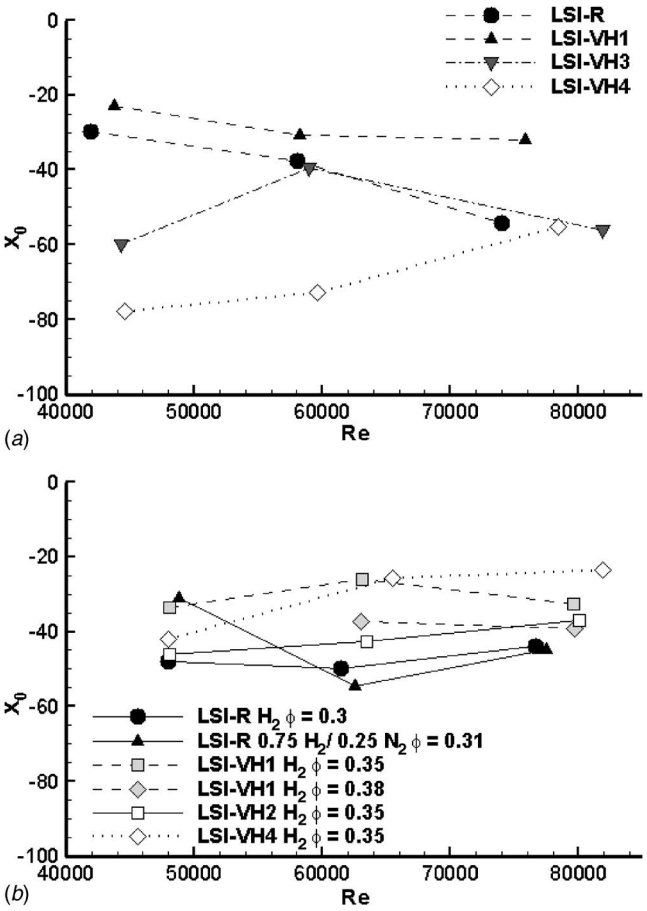

Fig. 9 Virtual origin x_0 deduced for the nonreacting (*a*) and reacting (*b*) flow fields of the LSIs

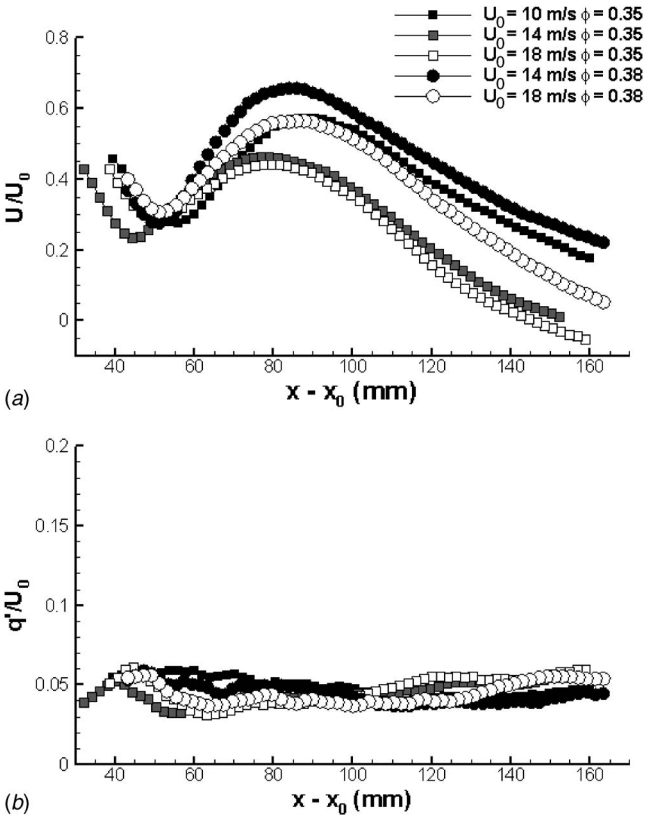

Fig. 10 Centerline velocity profiles of H_2 flames by LSI-VH1

for each LSI remain relatively constant within the range of Re investigated. This seems to indicate that the basic flow structures of these nonreacting flows are fully developed at Re > 40,000. There is also a dependency of the divergence rate (represented by the absolute value of a_x) on the increasing swirl number. The trend does not seem to be linear because a change from $S=0.43$ (LSI-VH4) to $S=0.51$ (LSI-VH1) reduces a_x from -0.003 l/mm to -0.01 l/mm. The corresponding a_x measured in H_2 flames are shown in Fig. 8(*b*). These values are generally lower than those of the nonreacting flows and indicate a systematic increase in the aerodynamic stretch rate induced by combustion heat release. This notion is supported by the fact that the more significant changes are found in flames with higher T_{ad} (e.g., $\phi \geq 0.35$).

The behaviors of the nonreacting and reacting a_x are generally consistent with those observed in the hydrocarbon flames. In addition, the data in Fig. 8(*b*) show a convergence to $a_x \approx -0.015$ l/mm at high Re. This is the same level as those measured in CH_4 and other hydrocarbon flames [11]. The convergence trend seems to suggest that the flow structures in the near field regions of the reacting flows are still evolving but may become more similar at higher flow velocities.

The values of the virtual origins x_0 for the nonreacting and reacting flows are compared in Fig. 9. The nonreacting flow data of Fig. 9(*a*) show some scatter at Re < 50,000, with x_0 decreasing with S. At the higher Re range, the x_0 profiles tend to converge to about -60 mm. Together with the a_x data of Fig. 8(*a*), these results imply a systematic shift of the position of the divergent flow structure with increasing Re without a significant change in the divergence rate.

The results in Fig. 9(*b*) for the reacting flows show that the effects of H_2 flames on the LSI near fields are not very different from the effects of hydrocarbon flames. At Re > 70,000, the values of x_0 for all H_2 flames fall within a $-30 < x_0 < -50$ mm. These values are consistent with those reported in previous studies. Collectively, the present and previous data imply that with increasing U_0, the flow structures and the divergence rates of the near field produced by a LSI tend toward a self-similar structure that is independent of the flame property.

The self-similar behavior of the H_2 flame flow field is illustrated by the centerline velocity profiles (Fig. 10) and the transverse velocity profiles at $x=12$ mm (Fig. 11) of LSI-VH1. In Fig. 10(*a*), the features of the U/U_0 profiles are similar to those reported for hydrocarbon flames. All show linear velocity decays near the LSI exit whose slopes correspond to a_x. The positions where the profiles deviate from the linear decays correspond to the leading edges of the flame brushes. Further downstream, the increases in U/U_0 indicate combustion induced flow acceleration. A subsequent drop in U/U_0 in the far field is associated with the formation of the weak recirculation zone. In comparison, flow acceleration through the flame is not very pronounced on the velocity data obtained for a very lean flame ($\phi < 0.3$) burning a fuel mixture consisting of 50% CO_2 and 50% H_2 [11]. This shows that the effects of combustion heat release are manifested mainly in the far field.

The corresponding centerline profiles of the normalized turbulent kinetic energy q' show that they all show relatively flat distributions throughout the near field and the far field. The lack of increases in the far field near where the recirculations are formed is the only significant difference between the flow fields of the H_2 and the hydrocarbon flames.

The radial profiles at $x=12$ mm are shown in Fig. 11. This axial position is below the leading edge of the turbulent flame brushes, and the profiles are characteristic of the reactants entering the flame brushes. Within the central region, $-20 < r < 20$ mm, a

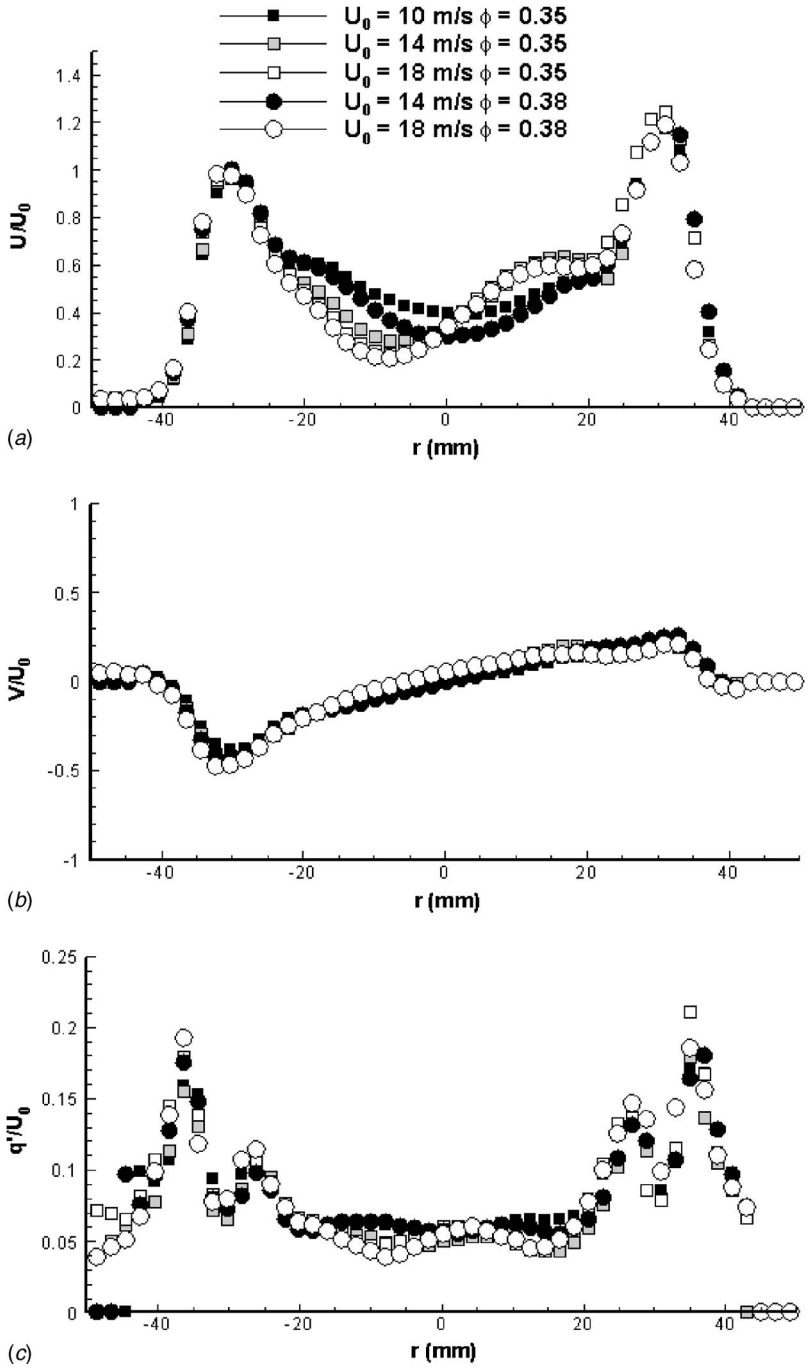

Fig. 11 Radial profiles at $x=12$ mm of H_2 flames by LSI-VH1

slight velocity deficit is clearly shown. This is a feature of the flow generated by these LSIs with VH plates. The slight asymmetries of the flow fields of three flames are also noticeable, but the differences in the U/U_0 levels within the central region are not any higher than those reported for hydrocarbon flames. In Fig. 11(*b*), all of the V/U_0 profiles collapse into a consistent distribution. The corresponding profiles of the turbulent kinetic energy q'/U_0 in Fig. 11(*c*) shows some scatter within the central region. However, all other features remain the same as those observed in hydrocarbon flames. The axial and radial velocity profiles of Figs. 10 and 11 show the self-similar nature of the near field regions of the H_2 flame flow fields.

It is very encouraging that the H_2 flames have near fields that are self-similar and turbulent flame speeds that correlate linearly with u'. These results show that the LSI concept will be amenable to burning of H_2 fuels. However, due to the complication caused by flame attachment, our investigation is limited to relatively lean H_2 mixtures of $\phi \leqslant 0.38$. A more extensive investigation at higher stoichiometries and bulk flow velocities is necessary to obtain additional data to support the development of the analytical model for guiding the design of a LSI prototype suitable for evaluation at high temperature and pressure with H_2.

Conclusions

Laboratory experiments have been conducted to obtain the basic information needed to guide the adaptation of the LSI to burn pure H_2 and N_2 diluted H_2 fuels that will be utilized in the gas

turbines of the IGCC coal power plants. Starting with the LSI-R ($S=0.54$) developed for natural gas as a reference, the LBO limits for H_2 and H_2 diluted with N_2 were determined. The results show that LSI-R supports very lean flames ($\phi \approx 0.17$) and the blowoff limits are independent of velocity within the range investigated ($10 < U_0 < 20$ m/s). However, the LSI-R is less than optimum for the open H_2 flame experiments because of flame reattachment to the LSI-R rim at $\phi > 0.3$. The attached flame phenomenon is an impediment for the investigation of near field flow features of lifted flames. This problem was addressed by a flame shaping method that involved the use of center channel plates with VH sizes. Four LSI configurations with the VH plates of $0.41 < S < 0.51$ were evaluated. The best performance was provided by LSI-VH1 with $S=0.51$ that produced a lifted H_2 flame at $\phi=0.4$.

Extensive PIV measurements were made in 32 H_2 flames generated by LSI-R and four LSI-VHs. The experimental conditions consist of U_0 from 10 m/s to 20 m/s and ϕ from 0.3 to 0.38. The adiabatic flame temperatures of these H_2 flames are below 1400 K, and the NO_x formation is expected to be below the detectable limit. Consequently, emission measurements were not made in these flames.

The PIV results showed that the overall flow field features of the H_2 flames are not significantly different from those of the hydrocarbon flames. The turbulent flame speeds of the H_2 flames deduced from the centerline velocity profiles show a linear correlation with turbulence intensity u'. The value of the correlation constant of 3.1 is 50% higher than the value determined for hydrocarbon flames. A comparison of the near field features below the lifted H_2 flames was based on examining the changes in the normalized axial aerodynamic stretch rate a_x and the virtual origin x_0 with flow Reynolds numbers. The results show that the near field of the H_2 flames is self-similar. The values of a_x and x_0 for H_2 flames are similar to those found in hydrocarbon flames. Therefore, the basic LSI mechanism is not affected by the differences in the basic flame properties of hydrocarbons and H_2. The results of our laboratory studies show that the LSI concept is amenable to burning of H_2 fuels.

Acknowledgment

This work was supported by the U.S. Department of Energy, Office of Fossil Energy under Contract No. DE-AC02-05CH11231.

Nomenclature

a_x = normalized axial aerodynamic stretch rate (l/mm)
D_i = injector diameter (mm)
L_i = swirler recess distance
$m = m_c/m_s$ = mass flux ratio
m_c = mass flux through the center channel
m_s = mass flux through the swirl annulus
q' = 2D turbulent kinetic energy $= 1/2(u'^2+v'^2)^{1/2}$
Re = Reynolds number $2R_iU_0/\nu$
$R = R_c/R_i$ = ratio of the center-channel radius R_c to the injector radius R_i
r = radial distance
S = swirl number
S_L = laminar flame speed
S_T = turbulent flame speed
T_{ad} = adiabatic flame temperature
U_0 = bulk flow velocity
U = axial velocity
u' = axial rms velocity
v' = radial rms velocity
uv = shear stress
x = axial distance from the injector exit
x_f = leading edge position of the flame brush
x_0 = virtual origin of the divergent flow

References

[1] Bell, J. B., Cheng, R. K., Day, M. S., and Shepherd, I. G., 2006, "Numerical Simulation of Lewis Number Effects on Lean Premixed Turbulent Flames," Proc. Combust. Inst., **31**, pp. 1309–1317.
[2] Cheng, R. K., Shepherd, I. G., Bedat, B., and Talbot, L., 2002, "Premixed Turbulent Flame Structures in Moderate and Intense Isotropic Turbulence," Combust. Sci. Technol., **174**(1), pp. 29–59.
[3] Shepherd, I. G., Cheng, R. K., Plessing, T., Kortschik, C., and Peters, N., 2002, "Premixed Flame Front Structure in Intense Turbulence," Proc. Combust. Inst., **29**, pp. 1833–1840.
[4] Chan, C. K., Lau, K. S., Chin, W. K., and Cheng, R. K., 1992, "Freely Propagating Open Premixed Turbulent Flames Stabilized by Swirl," Proc. Combust. Inst., **24**, pp. 511–518 (1992).
[5] Cheng, R. K., 1995, "Velocity and Scalar Characteristics of Premixed Turbulent Flames Stabilized By Weak Swirl," Combust. Flame, **101**(1–2), pp. 1–14 (1995).
[6] Shepherd, I. G., and Cheng, R. K., 2001, "The Burning Rate of Premixed Flames in Moderate and Intense Turbulence," Combust. Flame, **127**(3), pp. 2066–2075.
[7] Johnson, M. R., Littlejohn, D., Nazeer, W. A., Smith, K. O., and Cheng, R. K., 2005, "A Comparison of the Flowfields and Emissions of High-Swirl Injectors and Low-Swirl Injectors for Lean Premixed Gas Turbines," Proc. Combust. Inst., **30**, pp. 2867–2874.
[8] Nazeer, W. A., Smith, K. O., Sheppard, P., Cheng, R. K., and Littlejohn, D. 2006, "Full Scale Testing of a Low Swirl Fuel Injector Concept for Ultra-Low NO_x Gas Turbine Combustion Systems," ASME Turbo Expo 2006: Power for Land, Sea and Air, Barcelona, Spain.
[9] Cheng, R. K., Littlejohn, D., Nazeer, W. A., and Smith, K. O. 2006, "Laboratory Studies of the FLowfield Characteristics of Low-Swirl Injectors for Adaptation to Fuel-Flexible Turbines," ASME Turbo Expo 2006: Power for Land, Sea and Air, Barcelona, Spain.
[10] Yegian, D. T., and Cheng, R. K., 1998, "Development of a Lean Premixed Low-Swirl Burner for Low NO_x Practical Applications," Combust. Sci. Technol., **139**(1–6), pp. 207–227.
[11] Littlejohn, D., and Cheng, R. K., 2006, "Fuel Effects on a Low-Swirl Injector for Lean Premixed Gas Turbines," Proc. Combust. Inst., **31**(2), pp. 3155–3162.
[12] Zhang, Q., Noble, D. R., Meyers, A., Xu, K., and Lieuwen, T., 2005, "Characterization of Fuel Composition Effects in $H_2/CO/CH_4$ Mixtures Upon Lean Blowout," ASME Turbo Expo 2005: Power for Land, Sea and Air, Reno, NV.
[13] Mellings, A., 1997, "Tracer Particles and Seeding for Particle Image Velocimetry," Meas. Sci. Technol., **8**, pp. 1406–1416.
[14] Wernet, M. P. 1999, "Fuzzy Logic Enhanced Digital PIV Processing Software," 18th International Congress on Instrumentation for Aerospace Simulation Facilities, Toulouse, France.
[15] Lipatnikov, A. N., and Chomiak, J., 2002, "Turbulent Flame Speed and Thickness: Phenomenology, Evaluation, and Application in Multi-Dimensional Simulations," Prog. Energy Combust. Sci., **28**(1),: pp. 1–74.
[16] Kido, H., Nakahara, M., Hashimoto, J., and Barat, D., 2002, "Turbulent Burning Velocities of Two-component Fuel, Mixtures of Methane, Propane and Hydrogen," JSME Int. J., Ser. B, **45**(2), pp. 355–362.

Off-Design Performance Investigation of a Low Calorific Value Gas Fired Generic-Type Single-Shaft Gas Turbine

Raik C. Orbay
Department of Energy Sciences,
Lund University,
Lund 22100, Sweden
e-mail: raik.orbay@vok.lth.se

Magnus Genrup
Siemens Industrial Turbomachinery AB,
Finspong, Sweden

Pontus Eriksson

Jens Klingmann

Department of Energy Sciences,
Lund University,
Lund 22100, Sweden

When low calorific value gases are fired, the performance and stability of gas turbines may deteriorate due to a large amount of inertballast and changes in working fluid properties. Since it is rather rare to have custom-built gas turbines for low lower heating value (LHV) operation, the engine will be forced to operate outside its design envelope. This, in turn, poses limitations to usable fuel choices. Typical restraints are decrease in Wobbe index and surge and flutter margins for turbomachinery. In this study, an advanced performance deck has been used to quantify the impact of firing low-LHV gases in a generic-type recuperated as well as unrecuperated gas turbine. A single-shaft gas turbine characterized by a compressor and an expander map is considered. Emphasis has been put on predicting the off-design behavior. The combustor is discussed and related to previous experiments that include investigation of flammability limits, Wobbe index, flame position, etc. The computations show that at constant turbine inlet temperature, the shaft power and the pressure ratio will increase; however, the surge margin will decrease. Possible design changes in the component level are also discussed. Aerodynamic issues (and necessary modifications) that can pose severe limitations on the gas turbine compressor and turbine sections are discussed. Typical methods for axial turbine capacity adjustment are presented and discussed. [DOI: 10.1115/1.2836482]

Introduction

Current gas turbine systems are mostly designed for single fuel usage, and modifications may be needed for them to operate on new fuels [1].

Due to geopolitical circumstances, the cost of firing fossil based fuels for power production has increased drastically through the past years. Therefore, biofuels, despite their low calorific value, are becoming increasingly attractive alternatives for the power industry. In the longer perspective, concerns about global warming and the need for sustainable energy systems already motivate a switch to biofuels.

Biogas is a gaseous fuel that is produced from biodegradable organic materials [2]. It differs from fossil fuels being renewable in a reasonable time scale.

Sources of biogas include natural production in swamps, wastes from agriculture or food industry, effluents from livestock farming, municipal wastes, and sludge from purification stations. The chemical decomposition of various waste materials also produces biogas by-products such as the pyrolysis gas. Samples of different biogases are shown in Table 1. For a comparison, a typical fossil-based natural gas is also given.

As an example, landfill gas produces approximately less than half of the heating value from typical natural gas in the market. Thus, an in-service high grade fuel design which will be shifted to landfill gas firing may be in need for modification for more fuel mass flow for a given combustor outlet temperature (COT), as well as other special considerations [3].

Possible complications arise due to increase in turbine mass flow, starting problems, purge/cooling system insufficiencies, impurity concentrations, and environmental impact from emissions.

For a start, a high heating value gas may be needed. Hence, dual fuel nozzles are designed with dual inner circuits and modified fuel manifolds for usage of high and low lower heating value (LHV) fuels. In some cases, swirler diameters should be increased to accept the modified fuel nozzle. There may be hot gas ingestion due to relatively larger injection orifice diameters so an air purge system may be needed [4].

The high operating temperatures as well as high mechanical and thermal stresses in turbine sections dictate the working fluid to be free from corrosive constituents. For landfill gas, the amount of impurities such as siloxanes, chlorinated hydrocarbons (that dissociate into acids which cause wear), and particulates may be a restraint for the turbomachinery. Due to presence of these compounds inherent to landfill gas, maintenance intervals need to be substantially reduced to prevent damage to critical components and reduced service life.

Additional considerations may be related to environmental impact. Biogas firing may lead to harmful emissions and especially to NO_X [4,5].

Materials and Methods

Implications of Low Calorific Value Fuels. Operation with fuels other than the design will affect the engine performance to a varying extent, depending on how different the fuel is from that specified for the design. An engine is typically designed for a certain cycle, i.e., efficiency and power output with a certain fuel in mind (normally high calorific natural gas). The cycle requirements will set the engine firing temperature, pressure ratio, and air flow. The fuel composition will directly affect the combustion section and fuel delivery system (namely, manifolds and control valves). If a low-LHV fuel is used, more fuel has to be added to the combustion system typically leading to complications such as how to admit fuel into the burner, velocities, mixing, flame anchoring, etc.

The mass flow implication is typically quantified by the Wobbe index, which can be thought as a gauge of the available energy flux through a certain area, ultimately at the critical velocity.

Manuscript received May 10, 2007; final manuscript received September 24, 2007; published online April 2, 2008. Review conducted by Dilip R. Ballal.

Table 1 Representative natural gas and biogas compositions

	Representative constituents (% vol)				
	Natural gas	Landfill gas	Digestion gas	Biomass gasification gas	Pyrolysis gas
CH_4	87.2	51	66	3	15.6
O_2	0	0.4	0	0	0
CO	0	0	0	20	44.4
CO_2	1.4	35.4	30	15	12.2
N_2	0.3	12.7	2	47	0
H_2	0	0.5	2	15	22
LHV MJ/N m^3	40	17	23	5	18
Wobbe index MJ/N m^3	55	18	25	5	20

Other issues are normally related to the individual burner and combustion chamber designs, and it is therefore hard to generalize [6]. If, on the other hand, hydrogen-rich fuels are used, the nature of the problem is quite different, and typical encountered issues are flashback and increased heat transfer from the flame. The remainder of the discussion is aimed on low-LHV fuels. Since a low-LHV fuel carries large quantities of inert ballast, the mass flow in the turbine section will increase. An increased mass flow, at a certain temperature and properties, can only be forced into the turbomachinery at the expense of increased pressure (π increases). This is easily realized by inspection of the expression for turbine swallowing capacity or flow number,

$$\mathrm{FN} = \frac{\dot{m}_{40}\sqrt{\mathrm{COT}}}{P_{40}}\sqrt{\left(\frac{\gamma_{\mathrm{ref}}R}{\gamma R_{\mathrm{ref}}}\right)} \tag{1}$$

The expression can be derived from the Buckingham Π theorem or directly from the velocity triangles and is in full analogy with the flow through a nozzle. Hence, it can be thought of as a gauge of the turbine size. This relation has a strong influence of the engine pressure ratio, and the relative effects of the components for a single-shaft engine can be shown, following a logarithmic differentiation, to yield

$$\underbrace{\frac{\Delta\pi}{\pi}}_{(A)} \cong \underbrace{\frac{\Delta\dot{m}_{40}}{\dot{m}_{40}}}_{(B)} + \underbrace{\frac{1}{2}\frac{\Delta\mathrm{COT}}{\mathrm{COT}}}_{(C)} - \underbrace{\frac{\Delta\mathrm{FN}}{\mathrm{FN}}}_{(D)} + \underbrace{\frac{1}{2}\frac{\Delta R}{R} - \frac{1}{2}\frac{\Delta\gamma}{\gamma}}_{(E)} \tag{2}$$

It should be noted that the equation is only valid at first order since the terms are not totally independent of each other. This can be realized if a compressor map is studied, where a decreased normalized flow results in a higher pressure ratio (or vice versa). The previous statement is, however, only valid for an unchoked compressor. If an engine is operated with a low-LHV fuel, the mass flow (B) through the turbine section will be increased, and if no other term on the right-hand side is reduced, then the pressure ratio (A) of the engine has to be increased. If the pressure ratio becomes too high, there is a risk of encountering compressor instability (e.g., surge) or high-cycle fatigue due to flutter. The designer then has the option to either redesign the compressor (B), reduce the firing temperature (C), or increase the turbine capacity (D). The second option (C) is less desirable since it will reduce the engine power density and, to some extent, the thermal efficiency. The next section will describe a performance deck, which is a standard type of tool to calculate gas turbine performance at off-design conditions. Such a program, when properly programed, can predict a gas turbine's (single or multishaft) performance at varying ambient conditions, loads, speed levels, fuels, and water/steam injection situations.

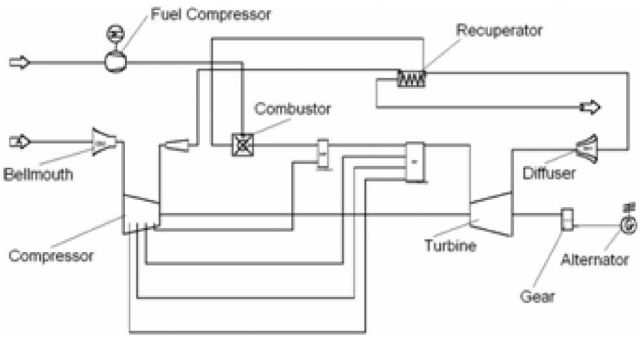

Fig. 1 Off-design deck schematics

In this investigation, two typical natural gas fired gas turbines with typical component performance levels have been modeled (nonexistent, but realistic),

- recuperated 200 kW, $\pi=5.5$, COT=800°C
- simple cycle 800 kW, $\pi=8$, COT=1000°C

The recuperated 200 kW and the simple cycle (both single-shaft) units will serve as vehicles for the analysis. The choice of small-size engines will not influence the general applicability for larger-size single-shaft engines. Both engines, due to their size, are assumed to have radial compressors and can thus be modeled with the same relative compressor map.

The investigated fuels are as follows:

- CH_4/CO_2 mixtures with LHV in the range of 5–50 MJ/kg
- CH_4/N_2-mixtures with LHV in the range of 5–50 MJ/kg
- the biomass gasification gas from Table 1

Performance Modeling. Gas turbine off-design performance is typically modeled with a performance deck or engine matching program. The matching calculation is highly recursive and hence not suited for hand calculation. The calculation procedure is based on, to a first order, matching the compressor, combustion section, and turbine into a system that operates as a unit. The performance deck is developed in-house and based on the commercially available heat and mass balance program suite IPSEPRO™. The layout of the designed recuperated cycle is shown in Fig. 1.

The off-design modeling package consists of the following building blocks:

- inlet and bellmouth, including a model for bellmouth condensation
- compressor and compressor diffuser
- combustor and fuel compressor
- turbine and turbine diffuser
- recuperator and exhaust system

The components are described in great detail by Lorenz [7], and only a brief explanation is given here. The bellmouth accounts for the inlet total pressure drop upstream the compressor. Due to acceleration of the flow, the static temperature will drop. Pressure drops in adiabatic ducts (scales on dynamic head) are calculated with the relation

$$\frac{\Delta p_{0,\mathrm{cc}}}{p_{0,\mathrm{in}}} \propto \left(\frac{\dot{m}\sqrt{T_{0,\mathrm{in}}}}{p_{0,\mathrm{in}}}\right)^2 \tag{3}$$

The combustor section pressure drop, due to its complex nature, cannot be evaluated with the previous expression. Therefore, the combustor is modeled with empirical models. The pressure drop is represented with the following equation, which includes two components representing hot and cold penalties [8].

$$\frac{\Delta p_{0,\mathrm{cc}}}{p_{0,\mathrm{in}}} = \left(\frac{\dot{m}\sqrt{T_{0,\mathrm{in}}}}{A_{\mathrm{cc}} p_{0,\mathrm{in}}}\right)^2 \left(K_c + K_H\left(\frac{T_{0,\mathrm{out}}}{T_{0,\mathrm{in}}} - 1\right)\right) \quad (4)$$

To simplify heat losses from the engine, they are lumped into a single sink term, which is a constant fraction of the total heat release. In this way, the efficiency descriptions for other components are also simplified since they can be thought of as adiabatic. For this study, $K_C = 7500$ and $K_H = 0.2K_C$ lead to an overall relative total pressure drop of 4.0% at the design point.

Following design point considerations of the model, off-design modules for components are designed for part load. Off-design engine performance modeling determines each component's operating point as it is matched to the others [9]. This requires successive guesses of the operating point on component maps. Essentially, the unity values of the map correspond to design values for pressure ratio, efficiency, aerodynamic speed, and normalized flow. The off-design modules constitute several tunable coefficients to take into account variable geometries of the compressor.

The centrifugal compressor is modeled using a nondimensional compressor map as an input to the system study program. A published industrial compressor map is modified for this purpose. Here, we assumed that the engine is operating at fixed physical speed, although for smaller engines this is not necessarily the case. Smaller-size units have very high speed levels, and this makes the use of a frequency converter attractive.

A recuperator is fitted to the 200 kW machine to alleviate the performance penalty due to low component efficiencies. The recuperator model constitutes empirical coefficients from open literature. The design efficiency of the recuperator is 0.9.

For the turbine, a typical turbine map according to Ref. [9] is implemented. The part-load behavior depending on the speed, mass flow, pressure ratio, and isentropic efficiency is simulated. All cooling and packing flows are mixed before the turbine for simplicity reasons. This approach is acceptable for this level of calculation, and the losses due to mixing of lower-momentum air and coolant pump work air are accounted for in the turbine efficiency definition.

The exhaust diffuser pressure drop is modeled according to a recent model by Japikse [10]. For electricity production, losses at the gear and load-dependent alternator behavior are also modeled. Finally, the efficiencies and net outputs are computed including a single stage fuel compressor.

Results

Gas turbine performance is modeled for different turbine outlet temperatures and LHV.

The additional ballast in the combustion chamber decreases the resulting heating value of the fuel. Due to this fact, more fuel mass must be compressed, leading to losses. In Fig. 2, the decrease in Wobbe index and heating value are shown.

Compressor Off-Design Behavior. In this work, biogas fuel is mimicked using a mixture of CH_4 and CO_2. Two different gas turbine models (200 kW and 600 kW outputs) are introduced. The effect of different fuel compositions on gas turbine behavior is modeled as the diluent concentration in fuel is altered through the calculations. To illuminate the consequences of the changes in fuel composition, similar calculations are run using CH_4 and N_2. A 200 kW gas turbine fired on biomass gasification gas from Table 1 is also calculated for a unique fixed exhaust gas temperature (EGT) value. This rather simple control strategy is typical for engines in this size range. The reason for the implementation of this rather simple control function instead of a more advanced one is that the engine has to be furnished with more operational instruments (e.g., compressor discharge pressure and temperature). Generally, except the slight difference at the calculation point of the lowest calorific value, calculations proved to be relatively unaffected from the constituents of the fuel.

Figures 3 and 4 show that the surge margin is adversely affected by dilution. The following plots will use the same legend as this figure. The presence of inert CO_2 in the fuel causes the turbine to swallow more mass and, thus, causes compressor pressure ratio to increase, as the calculations in Fig. 5 show. Therefore, the surge margin will decrease. The increase in turbine outlet temperature decreases the surge margin.

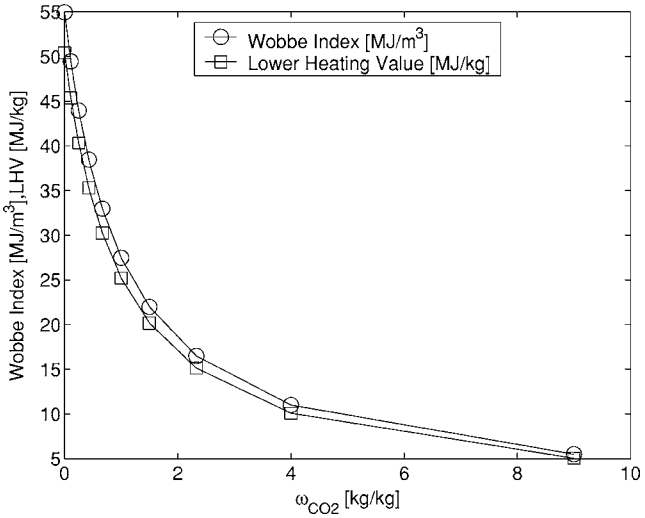

Fig. 2 Heating value and Wobbe index versus ω_{CO_2}

Combustion Chamber Off-Design Behavior. At constant EGT, the COT was found to be almost constant at increased CO_2 or N_2 concentration in fuel. This means that the overall equivalence ratio must increase in order to raise the temperature of the increasing mass flow. Assuming constant air split (fraction of combustor air going to primary zone), the primary zone equivalence ratio will increase, but not sufficiently enough to retain primary zone temperature. This indicates that lean blowoff (LBO) may become a problem.

As a combustor gets close to blowoff, emissions of both CO and HC increase, and often the combustor becomes unstable. In a previous investigation of premixed combustion of CO_2-diluted natural gas [11], this onset of CO emissions was used as a marker for LBO. The equivalence ratio where CO emissions start to increase due to incomplete combustion is shown in Fig. 6. Also shown are the primary zone equivalence ratios from the perfor-

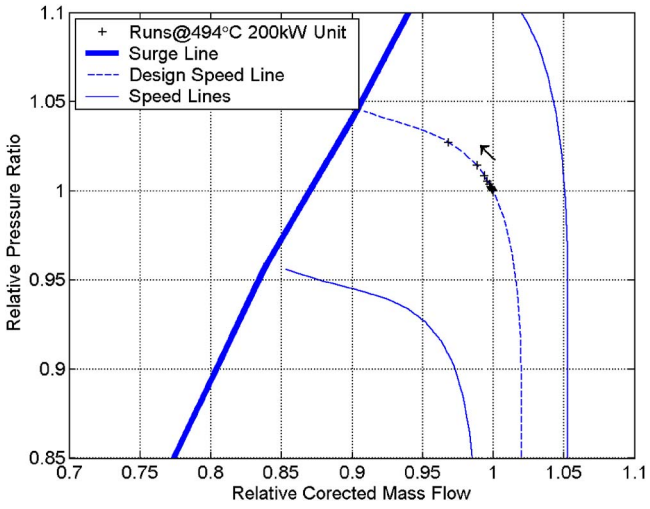

Fig. 3 Centrifugal compressor map for $\pi \cong 5.5$

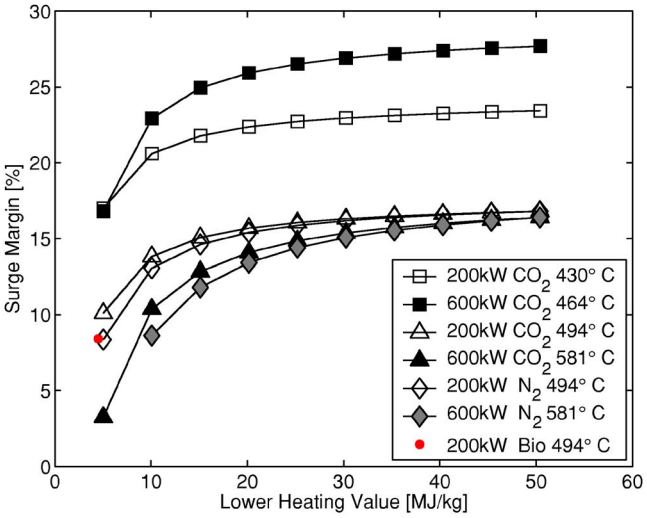

Fig. 4 Surge margin versus LHV for different EGTs

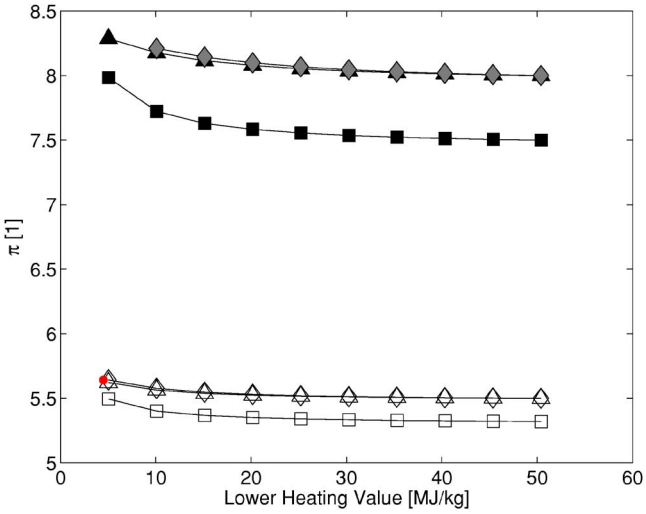

Fig. 5 Pressure ratio versus LHV for different EGTs. Legend as in Fig. 4.

mance deck computations for the recuperated 200 kW machine.

These values were computed using a fixed air split of 27%. This air split will give a primary zone adiabatic temperature of around 1490 °C for pure methane. It can be seen that the machine will not be able to run premixed at diluted conditions.[1]

Changing the air split by increasing the dilution hole area is a relatively small modification. Increasing primary zone temperatures is generally associated with increasing thermal NO_X production. This is, however, mitigated by the decreasing O_2 and N_2 concentrations.

The generic combustion chamber for the experimental campaign is fired under atmospheric pressure. Laminar flame speed decreases with pressure; however, various experiments have indicated the opposite behavior of turbulent flame speeds and burning velocities [12]. Nevertheless, in practically important range of pressures from 10 kPa to 5 MPa, the weak flammability limit is not strongly pressure dependent [13,17].

As more fuel mass is admitted into the combustor in order to reach the fixed EGT, a slight decrease in combustor loading is observed. Although the mass flow through the combustor increases, the raised pressure will dominate when more inerts are introduced. This effect is more pronounced for nitrogen dilution due to its higher specific heat ratio. The combustor loading versus LHV is shown in Fig. 7. The loading formulation is taken from Ref. [9] and modified to include fuel mass flow.

Turbine Off-Design Behavior. In Fig. 8, an almost constant value of the turbine inlet temperature (TIT) through the calculations can be seen, except for the CO_2-diluted gases at very low heating values and high temperatures. Every time the turbine outlet temperature is locked at a value for a new calculation, the inlet temperature also takes another value that does not change as the amount of CO_2 dilution increases.

Net Efficiency. The overall efficiency of the unit is decreasing slightly after dilution; this is shown in Fig. 9. The efficiency decreases abruptly when the turbine outlet temperature is decreased. This introduces a limit for quick-fix remedies for low calorific value firing.

Due to the increased mass through the turbine, the power production for the alternator increases. The increase in net output, however, will be abated by the increased fuel compressor power consumption. The combined effect is shown (as net power) in Fig. 10.

Modification of Turbomachinery. When an engine is fired with a fuel that deviates from the intended design range, it typically has to be modified to accept an imbalance in mass flow that passes through the cold and hot section. This section will discuss aerodynamic issues, typical necessary modifications for capacity adjustment and limitations.

The discussion has so far been related to low specific flow turbomachinery, where radial flow components are mostly used. There is no firm value for when a design is better off with axial flow components, and the design organization may rely on previous experience. Typically, one can expect to find centrifugal compressors below 5 kg/s and axial compressors predominately above 15 kg/s. In the midrange (5–15 kg/s), both types exist, and it is hard to distinguish which technology is superior to the other. For the turbine, the situation is quite different since the inlet state varies with cycle data, and it is therefore more appropriate to reason in terms of swallowing capacity, $\dot{m}\sqrt{T}/p$ [kg/s$\sqrt{\text{K}}$/bar].

The previous relation gives, in full analogy with a normal convergent nozzle, a gauge of the turbine size. It is typical to use a

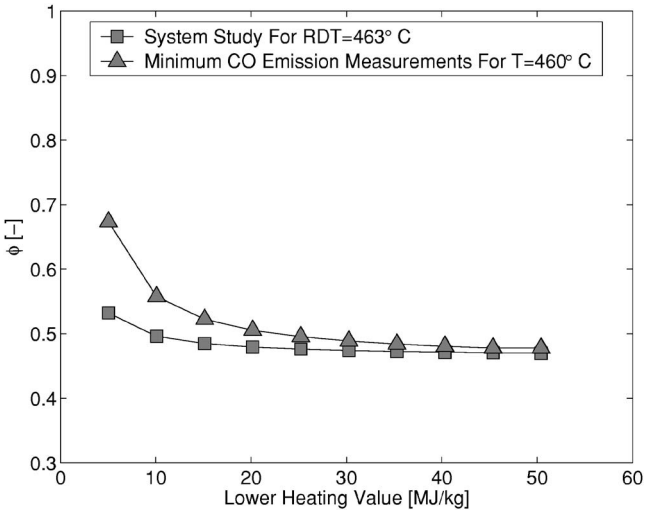

Fig. 6 LBO limits for the CO_2/CH_4 mixture

[1]At the lowest heating values, the increased mass flow through the swirlers will change the air split toward less air and thus higher equivalence ratio in the primary zone. This is not taken into account here.

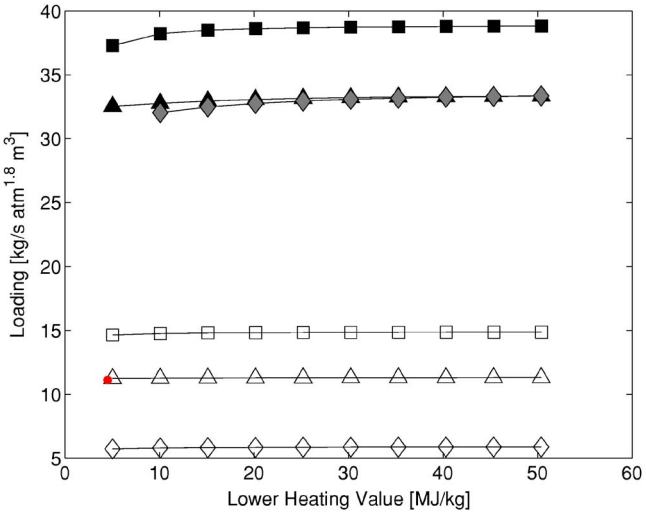

Fig. 7 Combustor loading versus LHV for different EGTs. Legend as in Fig. 4.

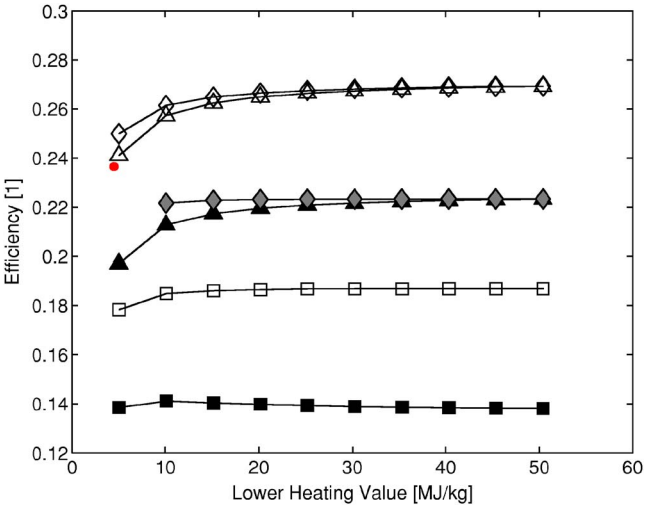

Fig. 9 Net efficiency versus LHV for different EGTs. Legend as in Fig. 4.

radial inflow (IFR) turbine when the capacity requirement is below 15 and the axial is approximately above 50. Both types exist in the 15–50 range, and the choice is driven by the application and engine cost. The choice is not solely driven by the size as the work duty is also a parameter. An IFR turbine can typically have twice the pressure ratio than a single axial turbine stage (due to the U terms in the Euler turbomachinery equation), and it may be more appropriate to use the specific speed as a parameter when designing the gas turbine. The specific speed can be seen as a dimensionless number, which is characteristic of the shape of the stage and is defined as

$$N_S = \frac{\omega\sqrt{\dot{m}/\rho_{\text{outlet}}}}{(\Delta h_{0,\text{ideal}})^{3/4}}$$

Again, it is possible to distinguish between the type of turbines, and radial technology is used predominately below 0.776 [14].

When dealing with low-LHV applications, surge margin and choke/stall flutter are the most significant parameters. A radial flow compressor, by virtue of the working principle, often has a better surge margin compared to an axial ditto. This is, however, dependent on the individual designs, and one cannot draw firm conclusions. The mechanisms for instability and, ultimately, stall, are outside the scope of this paper and will only be discussed briefly: A centrifugal compressor typically has its limitation in the diffuser section. The flow breaks down due to boundary layer separation when the swirl angle gets too big, i.e., too much diffusion between the impeller exit and the throat in the diffuser. This can be improved by using either a low solidity or vaneless diffuser at the expense of peak efficiency and maximum pressure ratio. The situation is somewhat different in a multistage axial machine, where typically the rear stages run into positive stall, hence ultimately causing flow breakdown. The impact of having a large amount of inert ballast on the engine matching is shown in an earlier section (Eq. (2)), and it is clear that there are only three viable engine matching options at hand if the surge margin is to be kept. The first is to reduce the compressor pumping capacity, i.e., a smaller compressor. The second is to reduce the firing temperature. The third is to increase the turbine capacity. The common misperception that throttling the compressor inlet will restore the surge margin is, however, incorrect since the engine will maintain the pressure ratio regardless of the pressure upstream the compressor. The second option results in a lower engine power density and is normally not a preferred option. The third option is prob-

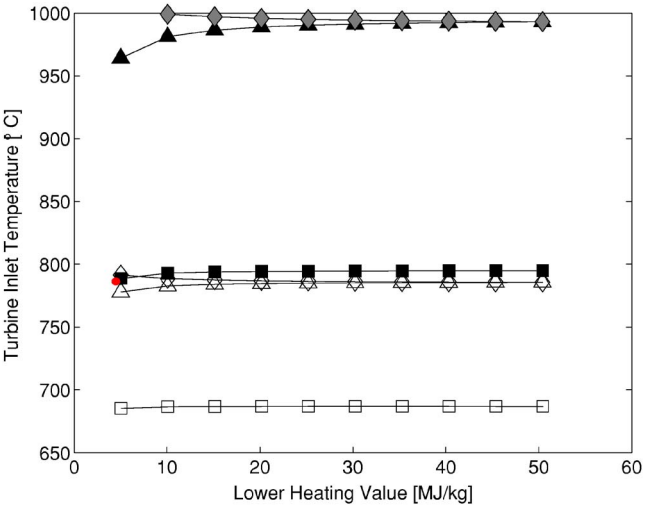

Fig. 8 TIT versus turbine outlet temperature. Legend as in Fig. 4.

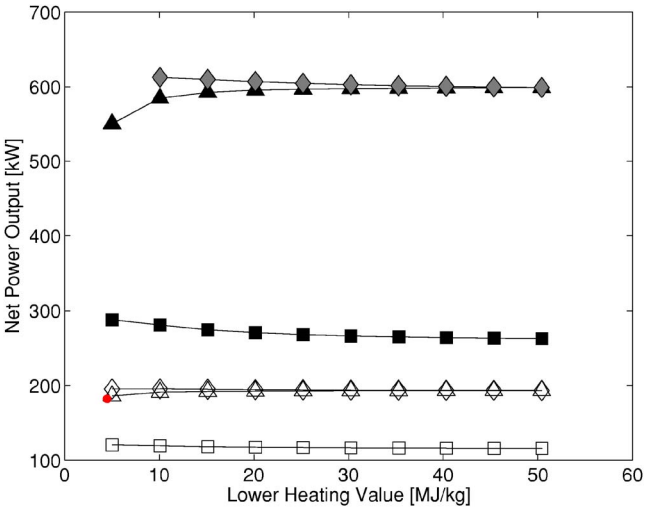

Fig. 10 Net power versus LHV for different EGTs. Legend as in Fig. 4.

Table 2 Turbine design data

	Stage 1	Stage 2
Swallowing capacity	15.70	N/A
Stage loading ($\Delta h_0/u^2$)	1.50	1.30
Flow function (c_m/u)	0.47	0.53

Table 3 Restaggered option (5% increased cycle pressure)

	Stage 1	Stage 2
Swallowing capacity	17.90	N/A
Stage loading ($\Delta h_0/u^2$)	1.20	1.40
Flow function (c_m/u)	0.45	0.65

ably the most efficient but results in a redesigned turbine section. Another option is to use a compressor discharge bleed to lower the matching point at the expense of performance. The penalty is normally too severe and should only be considered if no other options are available. The situation can, however, be somewhat relived if there is a need for high pressure and temperature elsewhere, e.g., fuel preparation process.

Capacity adjustment is common for IFR turbines in automotive turbocharger applications since the charger has to be matched for a certain engine operation point and, therefore, cannot be optimum over the whole load range. Capacity adjustment is very well described in many excellent textbooks, and the reader is referred to, e.g., the texts by Baines [15] and Moustapha et al. [16] for an exhaustive treatment. An interesting point, however, is that the IFR turbine has its peak efficiency at some 20–30 deg negative incidence due to the impeller potential field and strong Coriolis acceleration within the impeller. This typically indicates that an IFR turbine has less incidence sensitivity than an axial stage [16].

The remainder of this section will discuss capacity adjustment for an axial turbine. The vehicle for the analysis will be again an assumed 600 kW single-shaft, fixed speed, industrial gas turbine. The chosen 600 kW engine does not limit the general applicability for different single-shaft engine designs. The turbine stage count is mainly driven by the cycle pressure ratio, and for simplicity and clarity reasons, a two stage design is chosen for this study. The engine has a pressure ratio of 8, and the COT is set to 1000°C. The engine spins at 34,000 rpm and the subsonic turbine section is comprised of two stages. The design stage loadings are shown in Table 2, corresponding to a work split of 51:49, respectively. This can be considered as conventional since it is typical to have a less loaded, more or less, zero-swirling final stage. The total to static isentropic efficiency, including diffuser with a recovery of 0.6, is 83.6% and the total-total efficiency is 86.6%. The final stage annulus is determined by an AN^2 level of 43×10^6, which can be considered to be on the high side in this size range. The level can be justified by having an unshrouded blade and by the fact that the rim speed is below 400 m/s. The actual level is not important for the discussion, but it sets the datum annulus that cannot be changed without affecting both the low cycle fatigue (LCF) lifing as well as the creep lifing. The analysis has been performed with a validated in-house reduced-order throughflow tool in MATLAB™ [10].

The design case has an assumed flow of 3.32 kg/s and a fuel air ratio (FAR) (with pure CH_4) of 0.016, and the airflow is assumed to be independent of the compressor pressure ratio. The low-LHV case is assumed to be a case with CO_2-diluted methane with the volumetric proportions of 76.6:23.4. The resulting LHV is 5 MJ/kg (compared to approximately 50 for pure CH_4), and the same fired temperature requires a FAR value of 0.2120 (i.e., 13 times higher). This means that the turbine capacity has to be increased to 18.72 if the same engine pressure ratio is to be maintained. The required increase in swallowing capacity is on the order of 19.5%, and three typical options discussed here are

(i) restagger of the first vane
(ii) trailing edge cutting
(iii) complete new blading within the unchanged meridional flow path.

The first option (i) is the simplest, but it will distort the loading distribution in the turbine, potentially yielding a too highly loaded and swirling last stage. Typically, 4–6% capacity is gained per degree of restaggering (opening). In this work, the maximum change in stagger angle is set to 4 deg, which translates to 15% higher turbine capacity. The reason for not having the full potential is due to the fact that the capacity is not solely controlled by the first throat for a sub- or transonic design. The turbine therefore cannot swallow the increased mass flow without an increase in pressure ratio. The increase in pressure ratio will, however, be limited to approximately 5% (Table 3). This order of magnitude is normally possible for a "normal" design since the surge margin should be at least twice that number. All rows downstream of the first vane will operate with varying incidence levels (rotor 1 on the order of 40 deg), hence causing additional loss and blockage. Reference [14] discusses "quick fixes" where restaggering is described as well as leading edge cutback, in which the profile nose is simply shortened to match the incoming flow angle. Restaggering of rotors is more complicated since the platform fit and root stagger may be of concern. The turbine leaving loss due to the fixed annulus will be higher than the design case since the exhaust Mach number has increased by 0.15. The increased velocity level also reduces the turbine total pressure ratio since the exhaust diffuser total pressure drop is increased, assuming a constant diffuser recovery factor of 0.6.

The second option (ii) is, from a practical point of view, identical to the former. It may, however, be justified if the blade cannot be restaggered due to, e.g., cooling issues. This approach may introduce suction side diffusion (velocity distribution) issues and should be checked before a redesign.

The third option (iii) is the best possible since the turbine can be optimized for the increased flow within the original meridional flow path. The turbine total pressure ratio is, however, again reduced ($7.13\rightarrow6.93$) as the exhaust Mach number has increased by 0.1. The total to static efficiency has dropped by 2.5 points, compared to the design case (Table 4).

All the mentioned modifications are, however, to be considered as "nonoptimal" compromises since, among others, the exhaust loss will increase. This means that the engine efficiency will be significantly lower than its feasible potential. In all low-LHV cases, the power increased by some 200 kW, which is less than the full potential. The best solution would have been to increase the flow path annulus, but this would have a negative influence on the lifing (LCF and creep) of the last stage since the AN^2 would have been increased. In this case, the increase in power would have been on the order of 250 kW, and the total to static efficiency more or less the same as the original design. The AN^2 would have been increased from 43×10^6 to 51×10^6, which is indeed considered as a high number. Another possibility is to lower the speed level, but it has consequences; for instance, the compressor has to be redesigned. For a radial compressor, this would probably result in a larger diameter or less back-sweep,

Table 4 Redesigned option

	Stage 1	Stage 2
Swallowing capacity	18.72	N/A
Stage loading ($\Delta h_0/u^2$)	1.30	1.20
Flow function (c_m/u)	0.52	0.64

while an axial probably would have needed an additional stage. In this latter case, by adding a stage to compensate for a lower speed level, a complete redesign of the whole flow path is necessary.

A twin-shaft engine is probably a much better candidate due to its speed flexibility. The compressor and its driving turbine spin with a speed that is suitable for the inlet side of the compressor and the compressor stage count. The power turbine is typically at a lower speed level and is normally geared. This means that it is a more or less straightforward matter to redesign for an optimum flow path since the designer has some freedom to choose speed. The swallowing capacity of the power turbine can be altered to control the work distribution between the turbines, hence alleviating some of the gas generator related issues.

Conclusions

In this work, off-design behavior of a generic-type simple gas turbine cycle is modeled. The fuel is chosen as methane diluted with CO_2 or N_2 to be representative for a generic biogas. Through the calculations with the system study performance deck, the following results are obtained.

- The calculations are performed by locking the turbine outlet temperature. The TIT was found to be fairly constant, except for CO_2-diluted gases at very low heating values.
- The compressor pressure ratio is increased, and surge margin is decreased as dilution increases. The latter is more pronounced for the N_2-diluted gas. The changes are fairly small at heating values above 20 MJ/kg.
- Higher equivalence ratios are required in order to avoid LBO when inerts are added.
- Decreasing firing temperatures will reduce pressure ratios and increase surge margin but will also increase the risk for LBO besides obviously reducing efficiency.
- Combustion intensity and combustor loading change relatively little as dilution is increased.
- The overall efficiency decreases as the amount of dilution increases. As for the pressure ratio and the TIT, the changes are relatively small at heating values above 20 MJ/kg.

Acknowledgment

The financial support from E.ON. Sweden is gratefully acknowledged. Ito is also acknowledged for his input.

Nomenclature

A = area (m^2)

$\dot{m}$ = mass flow (kg/s)

$\omega_{CO_2} = \dot{m}_{CO_2}/\dot{m}_{CH_4}$ = CO_2 dilution (kg/kg)

$\eta_{th} = \dot{W}_{generator}/(\dot{m}_f \mathrm{LHV})$ = thermal efficiency (1)

π = pressure ratio (1)

$\eta = (\dot{W}_{generator} - \dot{W}_{fuel\_compressor})/(\dot{m}_f \mathrm{LHV})$ = overall efficiency (1)

N = rotational speed (1/min)

$(\dot{m}_{air} + \dot{m}_{fuel})/P_{31}^{1.8} V 10^{0.00145(T_{31}-400)}$ = combustor loading (kg/s $atm^{1.8}$ m^3)

$\dot{m}_{fuel}\eta_{cc}\mathrm{LHV}/P_{31}V$ = combustion intensity (kW/atm m^3)

$\mathrm{SM} = 100 - [100[\dot{m}_{working\_line}(\pi_{surge}-1)/\dot{m}_{surge}(\pi_{working\_line}-1)]]$ = surge margin (%)

$\mathrm{FN} = \dot{m}\sqrt{T_{0,in}}/P_{0,in}\sqrt{(\gamma R_{ref}/\gamma_{ref}R)}$ = flow number (1)

u = speed in general coordinates (m/s)

c = speed in engine coordinates (m/s)

$N/\sqrt{T_{0,in}}\sqrt{(\gamma_{ref}R_{ref}/\gamma R)}$ = speed parameter (1)

$R = C_p - C_v$ = gas constant (kJ/(kg K))

$\gamma = C_p/C_v$ = isentropic exponent (1)

$u/\sqrt{\gamma RT}$ = Mach number (1)

$\mathrm{HHV}/\sqrt{\rho_{rel}}$ = Wobbe index (MJ/kg)

K = constant for pressure drop (1)

Subscripts

0 = stagnation property
air = air property
C = cold
CC = combustion chamber
in = inlet
out = outlet
H = hot
fuel = fuel property
surge = surge line value
31 = combustor inlet property
40 = combustor outlet property
ref = relative to design value
m = meridional
ideal = reversible and adiabatic

Abbreviations

COT = combustor outlet temperature (°C)
EGT = exhaust gas temperature (°C)
FAR = fuel air ratio (1)
HHV = higher heating value (MJ/kg)
LHV = lower heating value (MJ/kg)
RDT = recuperator discharge temperature (°C)
TIT = turbine inlet temperature (°C)

References

[1] Neilson, C., 1998, "LM2500 Gas Turbine Modifications for Biomass Fuel Operation," Biomass Bioenergy, **15**(3), pp. 269–273.
[2] Klass, L. D., 2004, "Biomass for Renewable Energy and Fuels," *Encyclopedia of Energy*, Elsevier, New York.
[3] Goossens, M. A., 1996, "Landfill Gas Power Plants," *World Renewable Energy Congress* (WREC).
[4] Eriksson, P., Walch, S., Gabrielsson, R., Waldheim, L., and Hermann, F., 2002, "Design and Evaluation of an LCV Combustor for the Volvo VT4400 Industrial Gas Turbine," ASME Paper No. GT-2002–30088.
[5] Adouane, B., Hoppesteyn, P., de Jong, W., van der Wel, M., Hein, K. R. G., and Spliethoff, H., 2002, "Gas Turbine Combustor for Biomass Derived LCV Gas: A First Approach Towards Fuel-NOx Modelling and Experimental Validation," Appl. Therm. Eng., **22**, 959–970.
[6] Brooks, F. J., 2000, "GE Gas Turbine Performance Characteristics," GE Power Systems, Repoet No. GER-3567H.
[7] Lorenz, M., 2004, "Modeling and Off Design Simulation of the Evaporative Gas Turbine," MS thesis, Department of Heat and Power Engineering, Lund Institute of Technology.
[8] Cohen, H., Rogers, G. F. C., and Saravanamuttoo, H. I. H., 1998, *Gas Turbine Theory*, Addison-Wesley, Reading, MA.
[9] Walsh, P. P., and Fletcher, P., 1998, *Gas Turbine Performance*, Blackwell Science, Oxford.
[10] Genrup, M., Karlsson, I., Engdar, U., and Assadi, M., 2005, "A Reduced-Order Through-Flow Program for Choked and Cooled Axial Turbines," ASME Paper No. GT2005–68716.
[11] Hermann, F., Orbay, R. C., Herrero, A., and Klingmann, J., 2005, "Emission Measurements in an Atmospheric Preheated Premixed Combustor With CO_2 Dilution," *Proceedings of the European Combustion Meeting*.
[12] Lipatnikov, A. N., and Chomiak, J., 2002, "Turbulent Flame Speed and Thickness: Phenomenology, Evaluation, and Application in Multi-Dimensional Simulations," Prog. Energy Combust. Sci., **28**, pp. 1–74.
[13] Lefebvre, A. H., 1999, *Gas Turbine Combustion*, Taylor & Francis, Philadelphia.
[14] Baskharone, E. A., 2006, *Principles of Turbomachinery in Air-Breathing Engines*, Cambridge University Press, Cambridge, England.
[15] Baines, N. C., 2005, *Fundamentals of Turbocharging*, Concepts NREC, White River Junction, VT.
[16] Moustapha, H., Zelesky, M. F., Baines, N. C., and Japikse, D., 2003, *Axial and Radial Turbines*, Concepts NREC, White River Junction, VT.
[17] 1980, "Physical Properties of Natural Gases," N. V. Nederlandse Gasunie.

Flame Structure and Stabilization Mechanisms in a Stagnation-Point Reverse-Flow Combustor

Mohan K. Bobba
Priya Gopalakrishnan
Karthik Periagaram
Jerry M. Seitzman

School of Aerospace Engineering,
Georgia Institute of Technology,
Atlanta, GA 30332-0150

A novel combustor design, referred to as a stagnation-point reverse-flow (SPRF) combustor, was recently developed to overcome the stability issues encountered with most lean premixed combustion systems. The SPRF combustor is able to operate stably at very lean fuel-air mixtures with low NO_x emissions. The reverse flow configuration causes the flow to stagnate and hot products to reverse and leave the combustor. The highly turbulent stagnation zone and internal recirculation of hot product gases facilitates robust flame stabilization in the SPRF combustor at very lean conditions over a range of loadings. Various optical diagnostic techniques are employed to investigate the flame characteristics of a SPRF combustor operating with premixed natural gas and air at atmospheric pressure. These include simultaneous planar laser-induced fluorescence imaging of OH radicals and chemiluminescence imaging, and spontaneous Raman scattering. The results indicate that the combustor has two stabilization regions, with the primary region downstream of the injector where there are low average velocities and high turbulence levels where most of the heat release occurs. High turbulence levels in the shear layer lead to increased product recirculation levels, elevating the reaction rates and thereby enhancing the combustor stability. The effect of product entrainment on the chemical time scales and the flame structure is quantified using simple reactor models. Turbulent flame structure analysis indicates that the flame is primarily in the thin reaction zone regime throughout the combustor. The flame tends to become more flameletlike, however, for increasing distance from the injector. [DOI: 10.1115/1.2836614]

Introduction

Lean premixed combustion systems are advantageous because of their potentially low pollutant emissions. For example, NO_x emissions, which are highly temperature sensitive, are low since lean premixed combustion limits the maximum flame temperatures compared to more stoichiometric combustion conditions, which can occur in nonpremixed combustion. A critical issue, however, in these combustors is stability, as the weaker combustion process is more vulnerable to small perturbations in combustor operating conditions.

Flame stability in such systems can be enhanced in various ways, including reactant preheating and exhaust gas recirculation. Preheating the combustion air with the exhaust gases from a combustor provides many benefits, such as enhanced efficiency and flame stability. Gupta [1,2] reported that flames with highly preheated combustion air were much more stable and homogeneous (both temporally and spatially) as compared to room-temperature combustion air and hence could operate at much leaner equivalence ratios. In most premixed combustors employed in land-based gas turbines, stabilization is partially achieved by swirl-induced internal recirculation of products and reactants [3]. Very high levels of internal recirculation in combustors, combined with other restrictions such as significant combustor heat loss, can lead to "flameless oxidation," where no visually distinct flame is observed [4,5].

A new, compact combustor design that incorporates some aspects of these other approaches has recently been demonstrated [6]. In its simplest configuration, a nearly adiabatic combustor consists of a tube with one end open and the other closed. Unlike most combustors, the reactants and products enter and leave this combustor at the same end. The reactants are injected (without swirl) along the combustor centerline, moving toward the closed end. The reactants burn as they reach the end wall and hot product gas reverse to exit the combustor. This opposing reactant and product gas stream configuration facilitates entrainment of a portion of the hot product gases back into the flame zone. This stagnation-point reverse-flow (SPRF) combustor has been shown to produce low NO_x emissions for both gaseous and liquid fuels, and in premixed and nonpremixed operating modes [6]. In addition, the combustor operates stably without external preheating, even at very low fuel-air ratios and high loadings.

To better understand the combustion and stability mechanisms of the SPRF combustor, the flow field of a typical SPRF combustor operating at atmospheric pressure is characterized with various optical diagnostic techniques. Planar laser-induced fluorescence (PLIF) [7] of OH radicals and chemiluminescence imaging is used to visualize hot product gases and the combustion (reaction) zone. Lastly, spontaneous Raman scattering (SRS) [8] is employed to quantify recirculation of products by measuring instantaneous mole fractions of all major species to quantify product entrainment.

Experimental Setup

The SPRF combustor used here consists of a central injector located at the open end of a 70 mm diameter and 304.8 mm long quartz tube (Fig. 1(*a*)). The 12.5 mm diameter (D) injector is formed by two concentric tubes, with premixed natural gas and air flowing through the annulus. For nonpremixed operation (not employed for this work), the central tube is used for fuel injection. Fuel and air flow rates are monitored with calibrated rotameters, and the two flows are mixed well upstream of the injector.

A quartz base plate forms the closed end of the tube and allows introduction of a laser sheet for the OH PLIF measurements. The combustor is also insulated with a hollow alumina cylinder with an inner diameter that is slightly larger than the outer diameter of the quartz tube. The insulation is cut into four segments; one of these has a ~150 deg section removed to form a window for

Manuscript received June 6, 2007; final manuscript received July 3, 2007; published online April 2, 2008. Review conducted by Dilip R. Ballal.

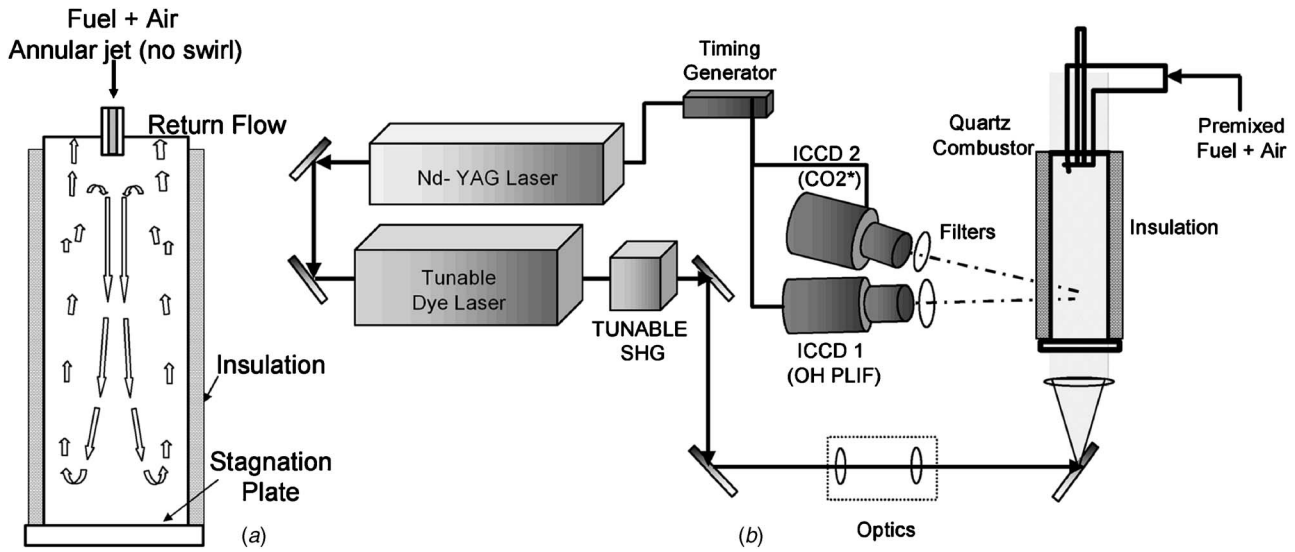

Fig. 1 Schematic of (*a*) SPRF combustor and (*b*) layout of the OH PLIF and PIV setups

optical access. Thus, only one-quarter of the length of the combustor can be imaged with the insulation installed; the complete combustor is mapped by moving the window segment to a different axial location.

The product gases exiting the combustor flow over the injector, increasing the temperature of the incoming reactants. To monitor this internal preheating, an unshielded thermocouple (K type) can be placed in the injector annulus, roughly 4 mm upstream of the injector exit plane. The thermocouple is not present during the optical diagnostic measurements.

As presented in detail in an earlier work [9], a particle image velocimetry (PIV) system was used to characterize the velocity field in the SPRF combustor. For these measurements, the combustion air was seeded with $1-2$ μm aluminum oxide particles before being mixed with the fuel. The two PIV laser pulses are provided by the second harmonic outputs of a dual-head, neodymium-doped yttrium aluminum garnet (Nd:YAG) laser (Continuum Surelite I-10). The output beams are converted into a sheet (68×0.6 mm^2) using three cylindrical lenses. The particle scattering images produced by a pair of laser pulses are recorded with a 12 bit interline charge coupled device (CCD) camera (MicroMAX, 1300×1030) equipped with a 50 mm Nikkor ($f/1.8$) lens and synchronized to the lasers. Fast Fourier transform (FFT) based cross-correlation software (INSIGHT 6, TSI) is employed to find the average particle displacement in a 64×64 pixel region with a 50% overlap in the interrogation areas. Each vector represents the average velocity in an interrogation volume $2.19\times2.19\times0.4$ mm^3.

OH Planar Laser-Induced Fluorescence and Chemiluminescence Imaging. The laser system for the OH PLIF measurements consists of a dye laser (Lambda Physik Scanmate 2) pumped by the second harmonic of a Nd:YAG, as shown in Fig. 1(*b*). The dye laser output is frequency doubled (Inrad Autotracker, BBO crystal) and formed into a thin sheet ($\sim65\times0.3$ mm^2) with three fused-silica lenses. The laser sheet enters through the closed end of the combustor and cuts through the central axis. The laser is tuned to the $Q_1(6)$ line of the $A\,^2\Sigma^+(\nu'=1)\leftarrow X\,^2\Pi(\nu''=0)$ band of OH with a sheet energy of 10–12 mJ/pulse. The emitted fluorescence is detected at right angles to the sheet with a 25 mm, intensified camera (PI-MAX, 1024×256 pixels) equipped with a UV-Nikkor lens (105 mm, $f/4.5$). The detected fluorescence is limited to 300–370 nm with WG305 and UG11 Schott glass filters placed in front of the camera lens. The field of view is set such that it covers the whole width of the combustor, resulting in a pixel resolution of approximately 300 μm.

The natural chemiluminescence from the combustor is also collected at right angles to the sheet with a second intensified camera (Princeton Instruments ICCD-576-S/RB-E, 18 mm intensifier, 384×576) equipped with a narrow-band interference filter (430 ± 5 nm), which passes CH^* and CO_2^* chemiluminescence. This camera is synchronized such that the exposure (250 μs) begins 100 ns after the OH laser pulse, which allows for complete decay of the OH fluorescence. Thus, the cameras record nearly simultaneous features of the combustor. In addition, the camera views the full width of the combustor (matching the OH field of view), which results in a pixel resolution of ~250 μm.

Raman Diagnostics. As shown in the schematic for Raman measurements (Fig. 2), a second harmonic (532 nm) of an injection seeded, Q-switched Nd:YAG laser (Quanta-Ray Pro-250, Spectra Physics) is used. The pulse energy is restricted to 250 mJ at a 10 Hz repetition rate to prevent laser-induced spark/plasma formation at the probe volume, which can occur due to breakdown of the gas under the intense electric field generated by tightly focusing a Q-switched laser, and to avoid damage to the combustor quartz walls. The laser beam is focused into a flattened 2×0.3 mm^2 probe volume using a spherical (50 mm diameter, f

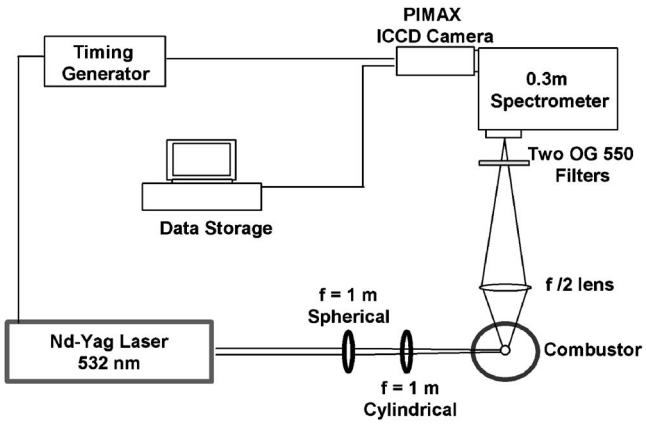

Fig. 2 Optical layout of SRS setup

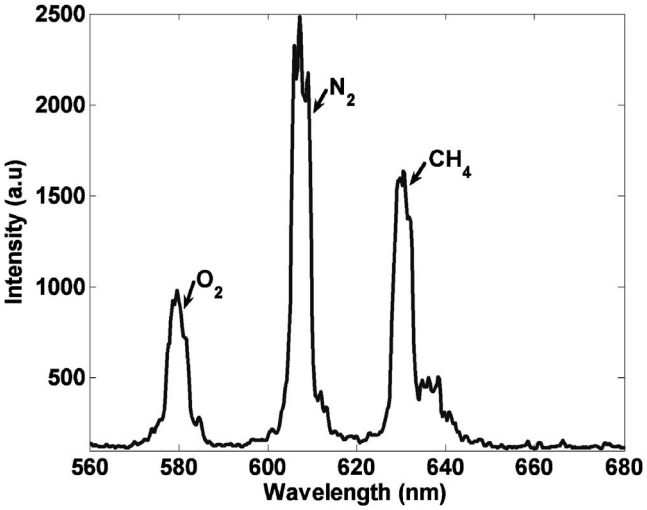

Fig. 3 Typical single shot Raman spectra recorded close to injector in the SPRF combustor at ϕ=0.58

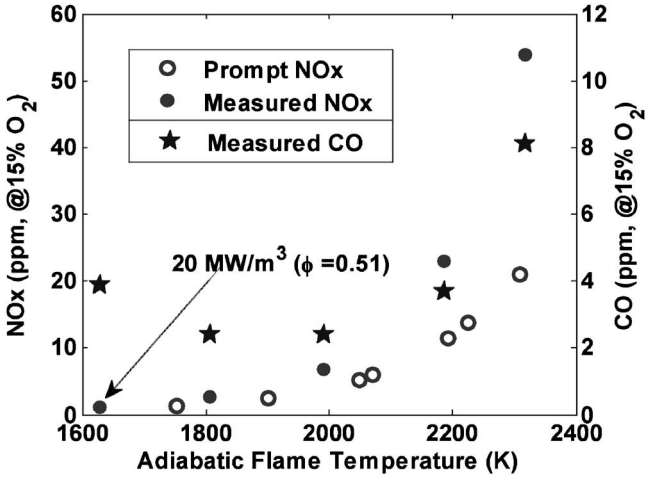

Fig. 4 Variation of NO_x and CO emissions with adiabatic flame temperature for a total loading of 8.1 g/s in comparison to a laminar flame model for NO_x

=1000 mm) and cylindrical (25×50 mm^2, f=1000 mm) lens combination. Such a probe volume is chosen to keep the laser fluence under the breakdown threshold and still provide good spectral resolution by aligning the 300 μm projection with the spectrometer slit. The laser beam enters the combustor through the transparent quartz base plate at the bottom of the combustor, similar to the PLIF setup, but in this case is not spread out into a sheet.

The Raman scattering signal was collected at a 90 deg angle relative to the beam propagation direction using an 80 mm diameter and 160 mm focal length spherical lens. The collected light is focused onto the 300 μm slit of a 0.3 m spectrometer (f/4, SpectraPro-300i, Acton Research Corporation) at f/5.3 and a magnification of 0.5. A combination of two OG 550 Schott glass filters is used to attenuate Rayleigh and Mie scattered light (from dust particles) entering the spectrometer. The spectrometer dispersed the incident light using a 300 grooves/mm grating, which is then recorded on a PI Acton ICCD camera (512×512 pixels). This arrangement allowed us to capture a spectral range of 555–685 nm with a resolution of 0.256 nm/pixel. The camera is equipped with an 18 mm (Gen III, HB filmless) intensifier tube with 30% quantum efficiency in the visible range. The intensifier is gated on for a 100 ns window synchronized with the laser pulse. This short gate timing helps reject background emissions from the flame and blackbody radiation from the combustor walls. The collected spectra were binned on chip over 170 pixels in the spatial direction to increase the signal-to-noise ratio of the measurements, resulting in a spatial resolution of 2 mm along the laser beam. The combustor and injector assembly are mounted on a vertical traverse, while the optics setup remains fixed. This configuration allowed us to make instantaneous single point Raman measurements from the injector to 170 mm into the combustor along the centerline.

Raman signals are obtained from the background subtracted spectra by integrating under the respective peaks for each species. Figure 3 shows a typical single shot spectrum recorded close to the injector in SPRF combustor operating on premixed CH_4 and air.

The Raman signal (S_i) is proportional to the number density of the scattering species and can be expressed in terms of species mole fractions (X_i) and temperature (T), i.e.,

$$S_i = \frac{C_i X_i}{T}$$

Assuming that CO_2, O_2, N_2, CH_4, and H_2O are the only major species present, then including the additional constraint

$$\sum X_i = 1$$

provides a complete set of equations. Equilibrium calculations indicate that neglecting CO and other minor species yields an error less than 0.5% in mole fractions at the operating equivalence ratio of 0.58. The calibration constants C_i for CO_2, O_2, N_2, and CH_4 are determined from measurements obtained at the exit of a preheated laminar jet (300–800 K) with a known concentration gas mixture. The calibration constants are found to be constant to within 5% in the reactant temperature range of interest. The Raman signal for H_2O is calibrated with measurements at the exit of the SPRF combustor (at ϕ=0.58), where the equilibrium water concentration is known to be twice the CO_2 concentration. A matrix formulation [8] is used to solve the above complete set of equations to find mole fractions of CO_2, O_2, N_2, CH_4, H_2O, and local temperature. The error in major species concentrations calculated as above, neglecting CO and other minor species, is estimated from equilibrium calculations and found to be within 2% of the actual value.

Signal interpretation can be complicated by fluorescence interactions from polycyclic aromatic hydrocarbons (PAHs) and soot or due to overlap of Raman rotation and vibration bands from different species [8]. The fluorescence interactions are expected to be negligible in the current work due to lean operation of the combustor. Overlap in Raman spectra is most prominent between CO_2, O_2, and CH_4. These interferences are corrected based on calibration spectra obtained at 300 K as outlined by Miles [10].

Results and Discussion

As might be expected in lean premixed operation, the SPRF combustor has low NO_x emissions. For example, Fig. 4 shows the NO_x emissions at the exit of the SPRF combustor for various equivalence ratios (ϕ) plotted as a function of the adiabatic flame temperature. The NO_x ($NO+NO_2$) emissions are measured with a sampling probe and a Horiba (PG-250) gas analyzer [6]. The uncertainty in the NO_x concentration measurements with this system was 1 ppm, which translates to an uncertainty of 0.7 ppm corrected to 15% excess oxygen at ϕ=0.5 ppm and 2 ppm corrected at ϕ=1. The measurements at the exit of the SPRF combustor indicate NO_x emissions of around 1 ppm for the leanest operating condition ($\phi\sim0.51$), and they are also seen to be nearly invariant of loading (mass flow rate) for a given operating temperature. The adiabatic flame temperatures shown are calculated based on the equivalence ratio and the reactant temperature determined from

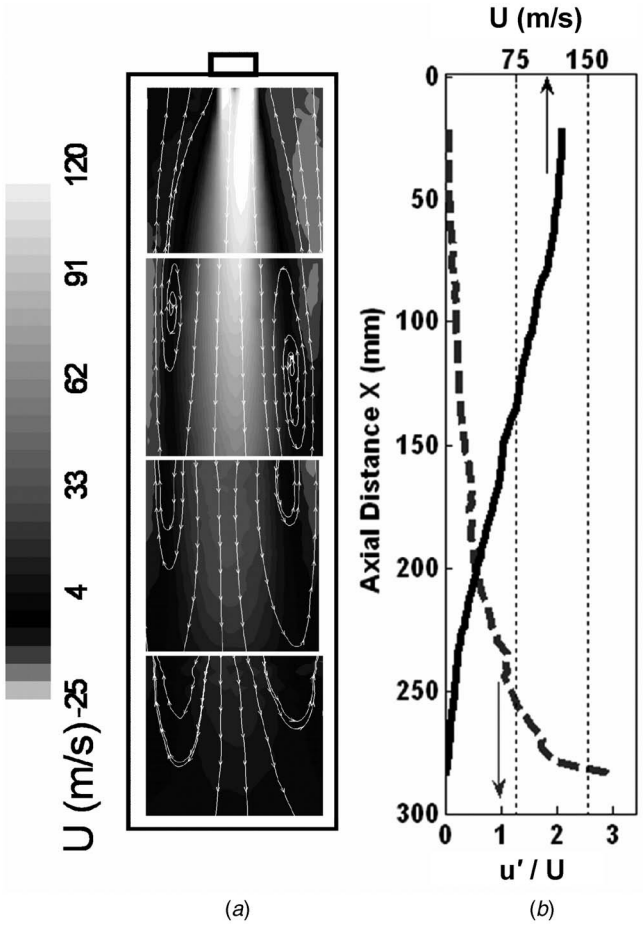

Fig. 5 Velocity fields for a flow rate of 8.1 g/s: (*a*) mean axial velocity contours and (*b*) mean centerline velocity and turbulence intensity profiles

the injector thermocouple. For comparison, the figure also shows NO_x levels from a laminar, one-dimensional, premixed flame, based on a CHEMKIN simulation and the GRIMECH 3.0 mechanism [11] over a range of equivalence ratios and reactant temperatures.

The model results represent the prompt NO_x produced in the flame front, i.e., up to the point where the heat release has dropped to 1% of its peak value, as opposed to thermal NO_x produced in the product gases. In this sense, the model results represent a minimum expected emission level for a premixed flame. The measured emissions from the combustor are reasonably close to the minimum levels, until the flame temperatures exceed ~1800–2000 K, where thermal NO_x formation in the postflame region is expected to become dominant [12].

One advantage of the SPRF combustor over other premixed combustors is its ability to produce a compact, stable flame even under very lean (low NO_x) conditions, without external preheating or swirl. For example, the leftmost point in Fig. 4 was acquired with the combustor operating at $\phi=0.51$ and with a combustor power density of 20 MW/m^3 (at atmospheric pressure). At these conditions, the combustor is still stable. This is very close to the lean flammability limit of $\phi=0.46$ for methane at room temperature [13]. Thus, we devote the remainder of this paper in examining the features of the combustor that contribute to its stability.

We begin by examining the velocity field in the combustor. As presented by Bobba et al. [14], the time-averaged flow field in the combustor is shown in Fig. 5(*a*) as a combination of axial velocity contours and interpolated streamlines. These results were obtained by averaging 300 instantaneous PIV images for a total mass flow rate of 8.1 g/s and at an equivalence ratio of 0.58, where the SPRF combustor was found to produce NO_x emissions of around 1 ppm. The reactant temperature in the injector, after heating by the exiting products, was nearly 500 K. Thus, the velocity right at the injector exit, based on the measured flow rate and temperature, should be 130 m/s. Velocity data obtained using PIV start from an axial location (x) of 22 mm ($x/D=1.8$) from the injector exit plane. The average velocity measured at this location was 120 m/s closely matching the air injection velocity estimate. In some ways, the flow field resembles that of a confined jet, but the presence of the closed end causes the axial velocity to decay rapidly. As seen in Fig. 5(*b*), the average axial velocity (U) drops to half its initial value by $x=150$ mm ($x/D=12$). At the same time, the rms fluctuations (u') and turbulence intensity rapidly increase, with the centerline u'/U increasing from 0.23 to 0.5 over a small distance ($x/D=10-12.5$). Thus, the geometry of the SPRF combustor ensures the existence of a region of both "low" average velocity (though still tens of m/s) and high fluctuating velocity, which exists over a wide range of combustor loadings. The rapid decay in velocity results from the high shear between the incoming forward flow and the reverse flow of the exiting gases. This can also lead to entrainment of exiting high temperature products and flame radicals into the incoming reactants, which can significantly enhance chemical reaction rates [15]. The temperature increase due to mixing with hot product gases along with the presence of radicals tends to increase the mixture reactivity, while the dilution of this reactant mixture with inert product gases tends to reduce it. As shown later, the net effect is an increase in reactivity with increasing product recirculation at the levels found in the SPRF combustor.

The influence of these flow field features on flame stabilization mechanisms was investigated by imaging the OH field in the SPRF combustor over a range of combustor loadings. These images were acquired at stoichiometric conditions so that we can explore all the possible stabilization mechanisms in the combustor, some of which are not evident in fuel lean conditions. In these instantaneous images (Fig. 6), the reaction zone is usually indicated by the sharp gradients in the OH PLIF signal adjacent to the reactant gases. For the lowest loading (0.14 g/s), the velocities in the combustor are laminar, and the combustor flow is essentially an annular, Bunsen-like jet flame. Since the inner tube of the annular injector is closed off upstream in premixed operation, the flame can stabilize on both the outer rim of the injector and the inner, bluffbodylike recirculation zone. For this low velocity condition, the flame sits just above the injector, and what is primarily seen in Fig. 6(*a*) is the decrease in OH concentration as the products cool (since OH equilibrium concentrations are extremely temperature sensitive). For increasing injection velocity (Figs. 6(*b*) and 6(*c*)), the increased strain causes the flame to progressively lift at the outer rim, while it remains anchored on the inner tube. For these low velocity conditions, the shear between the inflow and exhaust is low. In addition, the lack of OH PLIF signal in the exhaust gases indicates that the combustion products are relatively cool, due to heat losses to the combustor walls.

Only at higher loadings (beyond ~1.8 g/s) does the entrainment of high temperature products appear to return the flame closer to the highly strained outer lip region (as indicated by the OH signal in the reverse flow of Figs. 6(*d*) and 6(*e*)). At 1.8 g/s, there is still a small flame in the inner recirculation zone, but it does not stabilize the rest of the combustor. Beyond this loading, the inner region disappears and the flame appears stabilized on the outer shear layer (Fig. 6(*e*)). The highest OH concentrations are seen toward the bottom of these images, which suggests that the highest temperatures (or most of the heat release) occur in that region ($x=80-140$ mm). This roughly coincides with the low average velocity region observed in the PIV results for the insulated combustor operating lean and at high loadings. This suggests a second possible stabilization mechanism; high u' in the midregion of the combustor creates a highly corrugated flame that can propa-

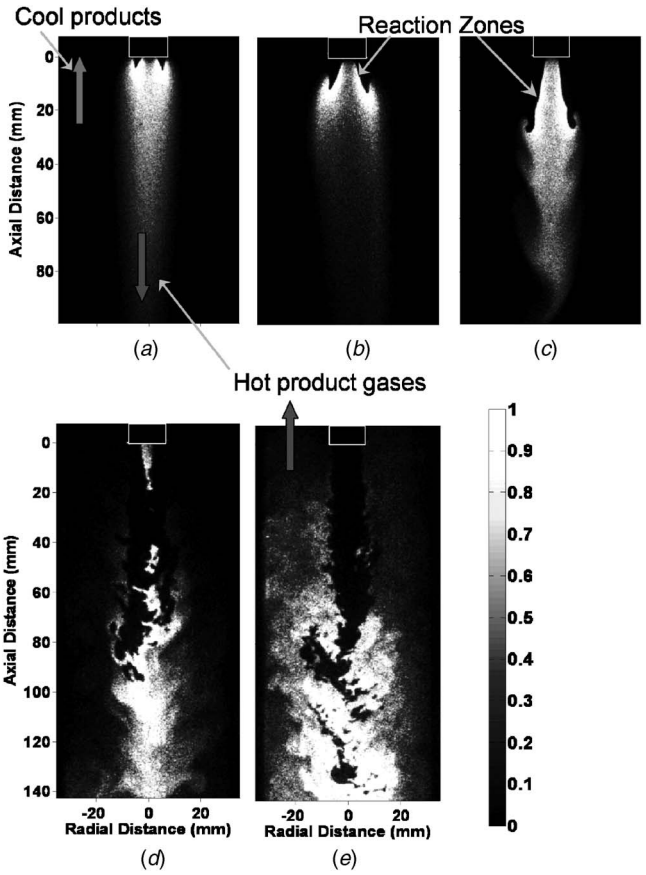

Fig. 6 Instantaneous OH images of the near injector region of the noninsulated SPRF combustor for ϕ=1 with increasing mass flow rates; (*a*) 0.14, (*b*) 0.2, (*c*) 0.43, (*d*) 1.8, and (*e*) 5.7 g/s

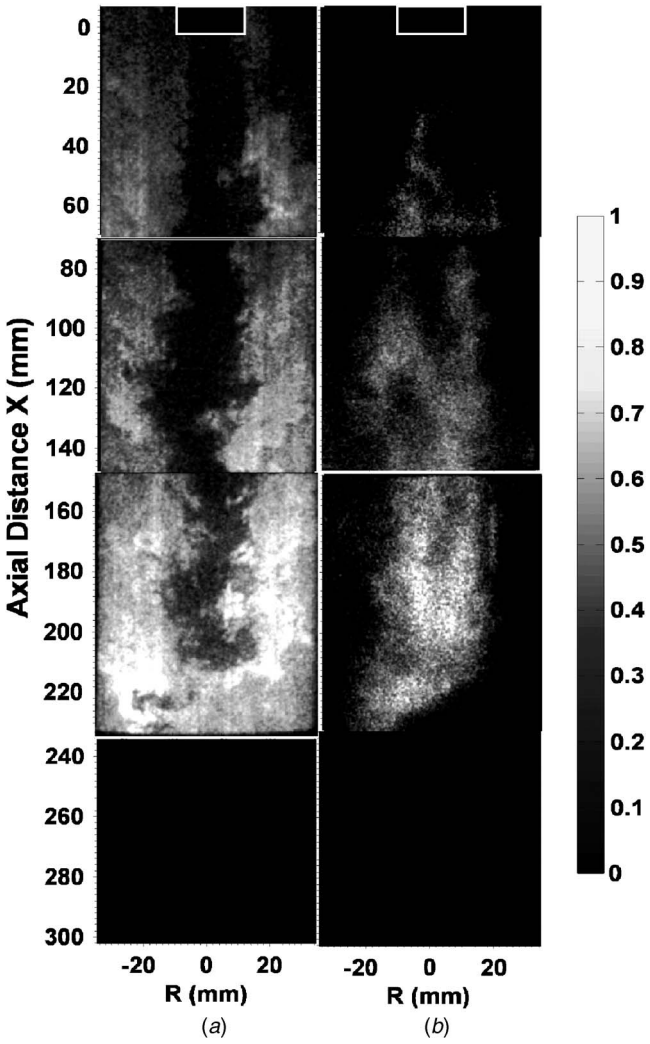

Fig. 7 (*a*) Instantaneous OH and (*b*) simultaneous chemiluminescence images at ϕ=0.58 and a loading of 8.1 g/s in the premixed SPRF combustor acquired in different widows

gate against the local mean flow (which is still 20–50 m/s). Like the flame seen in the shear layer between entering and exiting gases, any entrainment of hot products into the reactants before reaching the low velocity region will also act to increase the flame speed.

These observations were verified by obtaining simultaneous OH PLIF and chemiluminescence fields in the insulated combustor under the same lean (ϕ=0.58) flow conditions as the PIV data. The dark central regions in Fig. 7(*a*) represent unburned reactants (possibly mixed with some products). These regions of reactants seen in the OH PLIF image seem to match with the bright signal region in the simultaneously acquired chemiluminescence field (Fig. 7(*b*)) representing heat release zones. The heat release zones surrounding reactant packets suggest a flamelike burning in this combustor. It should also be noted that most of the heat release occurs downstream of the cold reactant core, as opposed to the upstream edges of the jet, and that the main heat release zone coincides with the low U, high u' region. Unlike a standard confined jet, where vortices are initiated at the initial shear region and propagate downstream, the SPRF geometry allows vortices carried by the return flow to propagate back toward the injector, resulting in higher turbulence levels. If the flame is lifted or the reaction zone is broken, as seen in Fig. 7, this can allow entrainment of products into the reactant stream. The hot products entrained and mixed into the reactants will tend to increase reaction rates (and flame speeds), enhancing flame stabilization in the downstream regions.

The possibility of hot product entrainment is further explored by making concentration measurements of all the major species in the combustor using SRS at the same loading of 8.1 g/s and equivalence ratio of 0.58. Figures 8(*a*) and 8(*b*) show the axial variation of mean mole fractions (averaged over 500 acquisitions) along the centerline of the combustor. The data were acquired starting from close to the injector to halfway into the combustor (x/D=0.4–14). Results show the presence of product gases (CO_2 and H_2O) as early as x/D=5 along the centerline. The chemiluminescence images shown above rule out the possibility that significant reactant burning occurs in this region. Thus, the appearance of the products is primarily due to product entrainment, which starts very close to the injector plane. The Raman temperature measurements acquired along the centerline (Fig. 8(*c*)) indicate an inlet temperature of 450 K, which matches the inlet temperature measured with the thermocouple at the injector to within 30 K. Beyond x/D=5, the temperature is found to increase linearly, approaching the adiabatic flame temperature of 1750 K in this case. The spike in temperature at x/D=12 is attributed to a decrease in laser power while acquiring data at this point.

The decrease in average concentration of fuel and the appearance of product gases along the combustor centerline could either be due to mixing of hot product gases with the reactants or it could be the result of intermittent appearance of pure product packets. To isolate the first effect from the second, the data points are conditionally averaged eliminating points in pure product gases. Pure product gases were defined to be points when the CH_4 concentration is less than a threshold value chosen to be 10% of

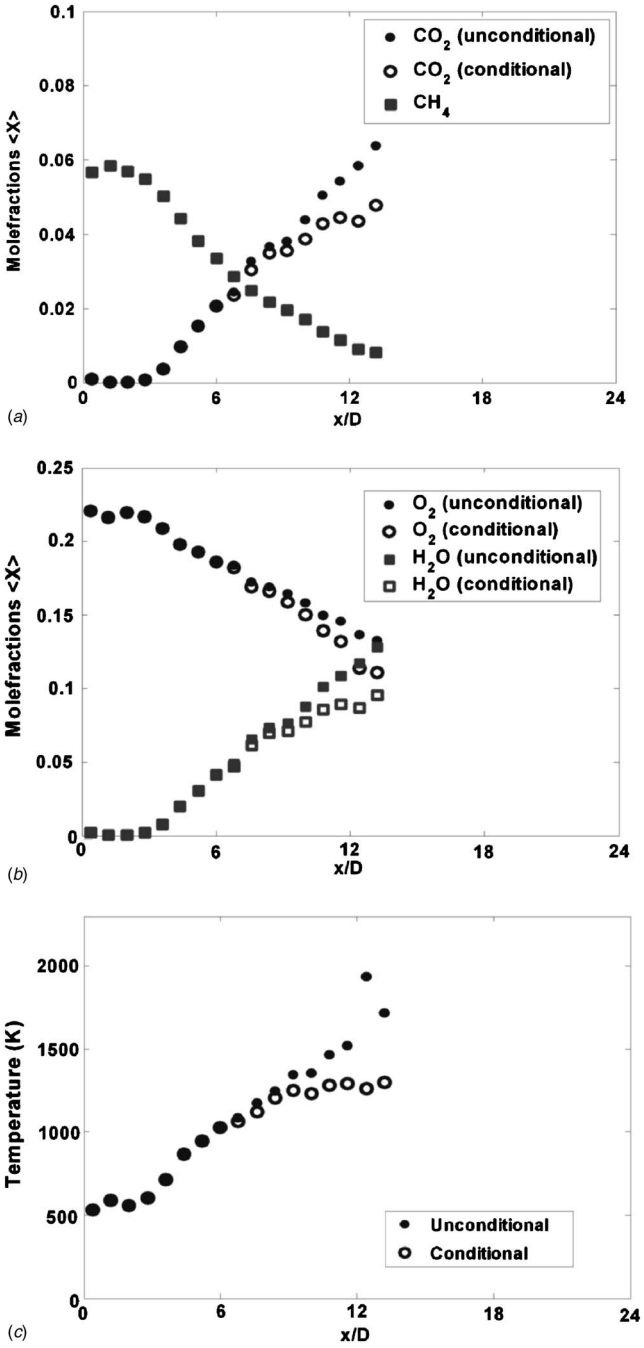

Fig. 8 Axial variation of mean species mole fractions: (*a*) CO_2 and CH_4, (*b*) O_2 and H_2O, and (*c*) temperature along the combustor centerline. Conditionally averaged values of these quantities over data points only in reactants are also plotted.

the injected global fuel fraction, which is at least twice the noise in the CH_4 mole fraction measurement. The mean axial variation of species mole fractions conditionally averaged in this fashion is also shown in Figs. 8(*a*) and 8(*b*). The results are nearly the same as the unconditioned averages up to $x/D \cong 9$. The mixing of product gases into the reactants, as represented by the rising amount of CO_2 and H_2O, starts at x/D of 5 and reaches significant levels before reaching the flame zone in the second half of the combustor, where most of the heat release occurs. The oxygen and the fuel concentrations are also found to decrease due to dilution with the product gases. A reduction in oxygen concentration as seen here has been identified as possible source of reduced NO_x emissions by Christo and Dally [16]. The distribution of the reactant temperature (with entrained products) in Fig. 8(*c*) is quite similar to the unconditional average close to the injector, but it saturates at ~1300 K before reaching the heat release zone. The lower temperature values found after conditional averaging are due to exclusion of data points with pure hot products.

In systems with recirculation of product gases, the amount of product entrainment is typically quantified by a single variable such as the product fraction (f_P), which denotes the ratio of mass of products to that of the reactants at a given point. Based on this definition, f_P of 0 corresponds to pure reactants while pure products have a f_P of ∞. Histograms of product fractions at six different axial locations along the combustor centerline are shown in Fig. 9. The product fraction not only increases (on average) with axial distance but also is characterized by a wider distribution. By x/D of 12, the product fraction reaches values as high as 2, which correspond to 67% of the incoming mixture being hot products by mass.

Combustors with large recirculation ratios and large residence times can have reactant mixtures that can reach the ignition temperature and thereby burn in what is called a flameless or mild combustion mode [4]. To explore such a possibility, the current combustion process has been modeled with a plug flow reactor model (CHEMKIN) [11] and the time required for various reactant mixtures to autoignite is determined. The effect of hot product gas entrainment was simulated by adding a fraction of hot, adiabatic products (produced from a pure reactant mixture) into the inlet reactant stream. The initial reactant temperature (before addition of products) was set to the reactant temperature determined from the injector thermocouple. The reactor inlet temperature further increases as hot product gases are added, simulating the entrainment of products before reaching the flame zone in the SPRF combustor. The ignition delay as a function of product fraction level in the reactant mixture is shown in Fig. 10 for a range of equivalence ratios. With increasing recirculation ratio, the reactant temperature increases, reducing the ignition delays in the combustor. Also shown are three dotted lines at time delays that correspond to the average centerline flow time (calculated from the mean velocity fields) needed to reach a given centerline axial location in the combustor starting from $x/D=5$, where the product gases first appear according to the Raman data. Even with the worst case assumption that the reactants reach the near maximum product fraction level of 2 instantly at $x/D=5$, the simulations suggest that the flow times needed to reach the measured heat release region at $x/D>12$ are too short for the mixtures to autoignite at the operating equivalence ratio ($\phi=0.58$).

Since the SPRF does not appear to operate in a flameless, or mild combustion, mode, we examine the turbulent flame structure of the SPRF combustor using the approach developed by Borghi [17] and modified by Peters [18]. This requires determining the total rms velocity (u'), laminar flame speed (S_L), integral length scale (L_T), and flame thickness (δ_L) in the SPRF combustor. The rms velocities were obtained from 400 instantaneous PIV images. Since only two velocity components were measured, the total rms velocity was estimated by assuming that the out-of-plane velocity component was comparable to the in-plane, lateral component [19]. Further, the integral length scale is found by integrating the turbulent velocity correlation function computed from the instantaneous velocities. The flow parameters and turbulence characteristics estimated at different locations are listed in Table 1.

The flame speed and thickness, S_L and δ_L, were estimated with premixed, laminar flame simulations (CHEMKIN PREMIX and GRIMECH 3.0) [11] for conditions close to the measured entrainment levels, as listed in Table 2. The effect of hot product gas entrainment was simulated as in the plug flow case. The flame speed was defined to be the simulated approach velocity, while the flame thickness was assumed to be the difference between the burned and unburned gas temperatures divided by the peak temperature gradient in the preheat zone.

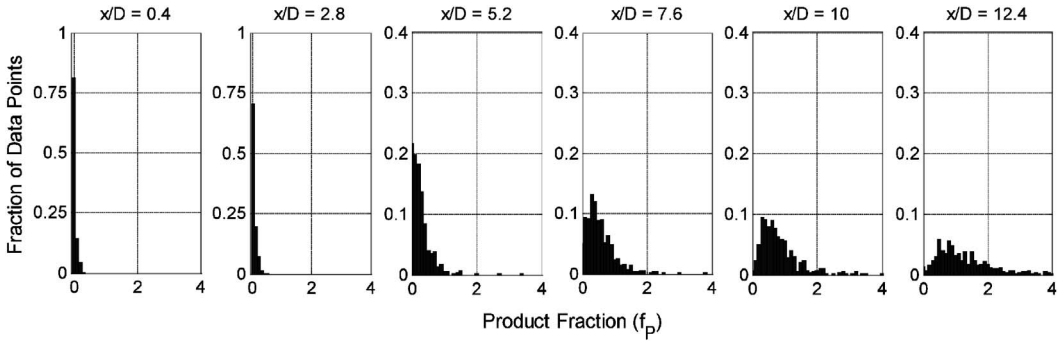

Fig. 9 Histogram of product fraction (f_P) over 500 data points measured at various axial locations along the combustor centerline

The flame structure analysis was performed for five entrainment levels and three spatial locations in the combustor. The first two locations chosen are in the shear layer at $x/D=3$ and 9. These regions are highly strained due to high incoming reactant velocities and reverse flow, product gas velocities. The third spatial location is $x/D=15$ on the centerline, where the OH and chemiluminescence images indicate that most of the heat release occurs. It can be seen from Fig. 11 that the conditions at all these locations (except with zero product entrainment) fall in the thin reaction zone regime suggested by Peters [18]. In this region, one expects a distinct reaction zone unaffected by turbulence. For comparison, typical flames in stationary gas turbines are also characterized by thin reaction zones, but with extremely high turbulent Reynolds numbers ($Re_T > 10^4$), $Da \sim 1$ and $Ka > 10$ (see Fig. 11) [19].

The likely turbulent flame structure is seen to evolve through the combustor. Close to the injector, u'/S_L is high since there has been little chance for product entrainment, and L_T/δ_L is low because the shear layer is thin and the vortices are smaller. As the flow moves farther from the injector, L_T/δ_L increases and u'/S_L decreases because the characteristic eddy size increases and because the amount of product entrainment is expected to increase (producing faster S_L and thinner δ_L). Hence, we expect the combustion structure to evolve as indicated by the diagonal arrow in Fig. 11, making the combustion more flameletlike farther from the injector. As mentioned before, the reactant temperature increase and the presence of radicals due to product entrainment boost the mixture reactivity more than the reduction in reactivity due to dilution. This is evident from the flame speeds calculated including all these effects shown in Table 2. Increasing product recircu-

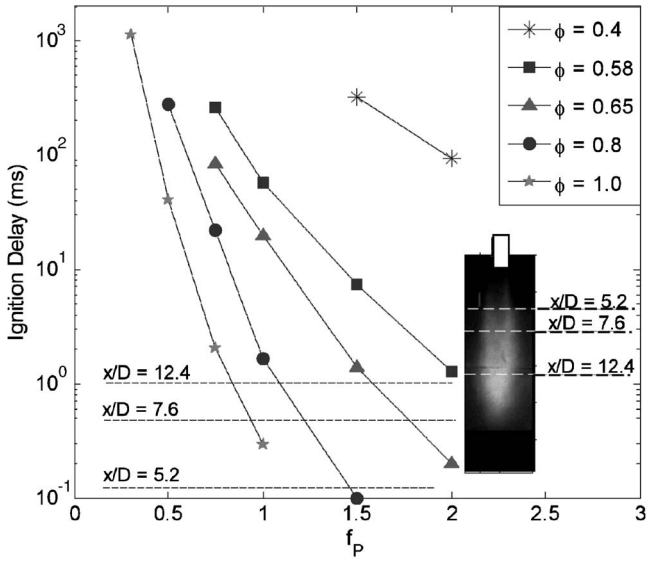

Fig. 10 Variation of ignition delays in milliseconds with increasing product entrainment levels (f_P) over a range of equivalence ratios. Flow times to reach various axial locations estimated from the mean velocity field are also shown for reference.

Table 1 Flow conditions and spatial locations used for regime analysis

Equivalence ratio ϕ				0.58
Mass loading				8.1 g/s
Reactant injection temperature T_{react}				450 K
Location	x/D	r/D	u'	L_T (mm)
1	3	1.1	14.4	2.7
2	9	1.8	13.3	5.6
3	15	0	15.9	10.4

Table 2 Flame properties obtained from CHEMKIN (GRIMECH 3.0)

f_P	Flame thickness δ_L (mm)	Laminar flame speed S_L (m/s)
0	0.73	0.27
0.5	0.60	0.90
1.0	0.57	1.6
1.5	0.565	2.3
2.0	0.58	3.0

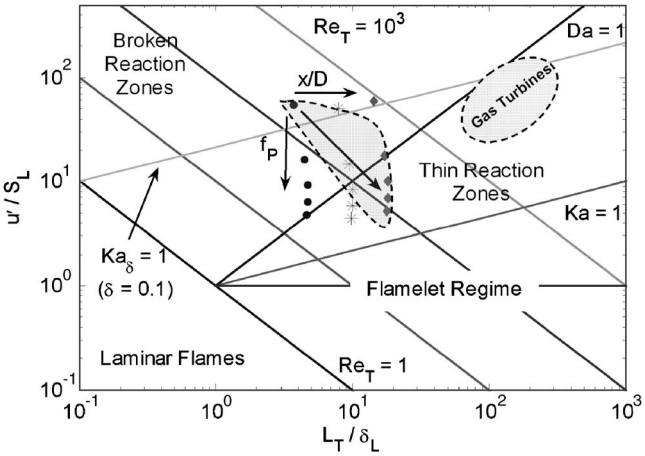

Fig. 11 Estimate of turbulent combustion regimes for the SPRF combustor: points shown for same axial locations, product fractions, and flow conditions in Tables 1 and 2

lation level from zero to 2 causes the reactant temperature to go up to 1300 K. This translates to an order of magnitude increase in flame speed despite the reactants being diluted with twice their mass in products. It should be noted that the flame calculations assume recirculation/entrainment of equilibrium products. In practice, the concentrations of flame radicals in the entrained products may be higher, which would increase S_L further and push the combustion structure even closer to the flamelet regime.

These results are consistent with the previous observations. In most of these regions, we see high OH gradients, consistent with thin reaction zone. Very close to the injector, the flame is lifted due to the high values of U/S_L. While the flame can exist further from the injector, in the shear layer between the forward flowing reactants and the reverse flow products, high intensity, small vortices may be able to extinguish the flame. This would permit products to be entrained into the unburned reactants. Further downstream, there would then exist reactant-product mixtures with high turbulent flame speeds, due to high S_L and u' (but $u'/S_L < 10$). As the mean velocities drop in this region, the flame can be stabilized, even at very lean conditions where the NO_x emissions from the combustor are minimal.

Conclusions

The flow field and combustion characteristics of a premixed SPRF combustor with central injection have been studied. The SPRF combustor has been shown to operate stably over a range of equivalence ratios and loadings without the need of external preheating or swirl. Further, emission measurements performed on this combustor indicate that NO_x levels around 1 ppm or less (corrected to 15% O_2) can be achieved due to its ability to operate very lean. Comparison of the measured emission levels with laminar flame calculations indicates that the NO_x levels are close to the minimum levels that would be expected just due to NO_x produced in the heat release regions.

Measurements of the premixed velocity field show a low average velocity zone with high levels of turbulence in the bottom half of the combustor. Based on the geometry of the combustor, this zone is expected to exist over a range of flow conditions (for very low loadings, the flow is laminar and combustion occurs before the "stagnation zone" is reached). Chemiluminescence and OH PLIF fields indicate that the flame is indeed anchored in this region of high turbulence intensity and that this is where most of the heat release occurs. This results in stable operation of the combustor even at high loadings and very lean equivalence ratios. Raman concentration measurements show entrainment of hot products from about five injector diameters into the combustor reaching an average reactant temperature of $\sim$1300 K just before the flame zone. This tends to increase chemical reactivity, especially of lean mixtures. Closer to the injector, a weaker flame exists in the shear and mixing layer between the forward flowing reactants and the reverse flow of products. Although the reaction rates are elevated due to product entrainment, the reactant mixture does not autoignite as in mild combustion due to relatively small flow times in the combustor.

An analysis of the turbulent combustion structure in the premixed SPRF combustor indicates that the flame is primarily in the thin reaction zone regime throughout most of the combustor. However, the flame tends to become more flameletlike farther from the injector, due to increases in the turbulent length scales and increases in the chemical rates due to entrainment of heated products and radicals into the reactants.

In summary, the geometry of the SPRF combustor creates a combination of a low velocity, high turbulence region, "the stagnation point," and internal product recirculation due to the "the reverse flow" that creates a stable combustion process under a large range of combustor operating conditions. In addition, most of the heat release occurs at conditions close to the thin reaction zone regime.

Acknowledgment

The authors would like to thank Mr. John Crane for performing the NO_x measurements in the SPRF combustor. This research was supported by NASA through the University Research, Engineering, and Technology Institute for Aeropropulsion and Power under Grant/Cooperative Agreement No. NCC3-982.

References

[1] Gupta, A. K., Bolz, S., and Hasegawa, T., 1999, "Effect of Air Preheat and Oxygen Concentration on Flame Structure and Emission," ASME J. Energy Resour. Technol., **121**, pp. 209–216.
[2] Gupta, A. K., 2000, "Flame Characteristics with High Temperature Air Combustion," Paper No. AIAA-2000–0593.
[3] Lefebvre, A., 1983, *Gas Turbine Combustion*, McGraw-Hill, New York.
[4] Wunning, J. G., 2000, "Flameless Combustion in Thermal Process Technology," Second International Seminar on High Temperature Combustion, Stockholm, Sweden.
[5] Plessing, T., Peters, N., and Wünning, J. G., 1998, "Laser Optical Investigation of Highly Preheated Combustion With Strong Exhaust Gas Recirculation," *27th Symposium (International) on Combustion*, The Combustion Institute, pp. 3197–3204.
[6] Neumeier, Y., Weksler, Y., Zinn, B. T., Seitzman, J. M., Jagoda, J., and Kenny, J., 2005, "Ultra Low Emissions Combustor With Non-Premixed Reactants Injection," Paper No. AIAA 2005–3775.
[7] Seitzman, J. M., and Hanson, R. K., 1993, "Planar Fluorescence Imaging in Gases," *Instrumentation for Flows With Combustion*, A. M. K. P. Taylor, ed., Academic, London.
[8] Nooren, P. A., Versluis, M., van der Meer, T. H., Barlow, R. S., and Frank, J. H., 2000, "Raman-Rayleigh-LIF Measurements of Temperature and Species Concentrations in the Delft Piloted Turbulent Jet Diffusion Flame," Appl. Phys. B: Lasers Opt., **71**, pp. 95–111.
[9] Gopalakrishnan, P., Bobba, M. K., and Seitzman, J., 2007, "Controlling Mechanisms for Low NOx Emissions in a Non-Premixed Stagnation Point Reverse Flow Combustor," Proc. Combust. Inst., **31**, pp. 3401–3408.
[10] Miles, P. C., 1999, "Raman Line-Imaging for Spatially and Temporally Resolved Mole Fraction Measurements in Internal Combustion Engines," Appl. Opt., **38**, pp. 1714–1732
[11] Smith, G. P., Golden, D. M., Frenklach, M., Moriarty, N. W., Eiteneer, B., Goldenberg, M., Bowman, C. T., Hanson, R. K., Song, S., Gardiner, Jr. W. C., Lissianski, V., and Qin, Z., 1999, GRI-Mech Homepage, Gas Research Institute, Chicago, www.me.berkeley.edu/gri_mech/.
[12] Miller, J. A., and Bowman, C. T., 1989, "Mechanisms and Modeling of Nitrogen Chemistry in Combustion," Prog. Energy Combust. Sci., **15**, pp. 287–338.
[13] Barnett, H. C., and Hibbard, R. R., 1957, "Basic Considerations in the Combustion of Hydrocarbon Fuels With Air," NACA Report No. 1300.
[14] Bobba, M. K., Gopalakrishnan, P., Seitzman, J. M., and Zinn, B. T., 2006, "Characteristics of Combustion Processes in a Stagnation Point Reverse Flow Combustor," ASME Paper No. GT2006–91217.
[15] Kalb, J. R., and Sattelmayer, T., 2004, "Lean Blowout Limit and NOx-Production of a Premixed Sub-PPM NOx Burner With Periodic Flue Gas Recirculation," ASME Paper No. GT 2004–53410.
[16] Christo, F. C., and Dally, B. B., 2005, "Modeling Turbulent Reacting Jets Issuing Into a Hot and Diluted Coflow," Combust. Flame, **142** pp. 117–129.
[17] Borghi, R., 1985, *Recent Advances in Aerospace Science*, C. Bruno and S. Casci, eds. Plenum, New York, p. 117.
[18] Peters, N., 1999, "The Turbulent Burning Velocity for Large-Scale and Small-Scale Turbulence," J. Fluid Mech., **384**, pp. 107–132.
[19] Griebel, P., Scharen, R., Siewert, P., Bombach, R., Inauen, A., and Kreutner, W., 2003, "Flow Field And Structure Of Turbulent High-Pressure Premixed Methane/Air Flames," ASME Paper No. GT2003–38398.

On the Use of Thermoacoustic Analysis for Robust Burner Design

Valter Bellucci[1]
Dariusz Nowak
Weiqun Geng
Christian Steinbach

ALSTOM,
CH-5401 Baden,
Switzerland

Advanced thermoacoustic analysis is now routinely used in gas turbine combustor development. A thermoacoustic approach based on a combination of numerical analysis (CFD and three-dimensional acoustics), acoustic network models, and dedicated measurements of acoustic flame response is well accepted across the industry. However, its application to specific combustor upgrade or development programs in "prediction mode" as opposed to "analysis mode" remains a challenge. This is mainly due to the large sensitivity of the complex methodology to key inputs, such as flame transfer functions, that can be only predicted in the burner design phase. This paper discusses an example where we made an effort to apply the thermoacoustic approach in predictive mode. The example refers to the upgrade of a first generation diffusion burner with a partially premix burner to achieve low emissions. Thermoacoustic instabilities were predicted as a limiting factor for combustor operation and thus a design parameter was identified to perform the thermoacoustic combustor tuning at engine level. A particular challenge of this development program was that no test rig was available. Therefore, the new premix burner was directly installed into a field engine where it was successfully tested.
[DOI: 10.1115/1.2800348]

Introduction

In heavy-duty gas turbines operating with lean premix flames, the suppression of acoustic pulsations is an important task related to the quality of the combustion process and to the structural integrity of engines. Pressure pulsations may occur when acoustic resonance frequencies are excited by heat release fluctuations independent of the acoustic field (combustion noise). Heat release fluctuations can also be generated by acoustic fluctuations in the premix stream. The feedback mechanism inherent in such process may lead to combustion instabilities, the amplitude of pulsations being limited only by nonlinear effects (combustion instability). To predict the acoustic field generated in gas turbine combustors, several methodologies have been proposed based on the thermoacoustic network approach [1–6]. In the network approach, the combustion system is lumped into several elements that are independently modeled. Hoods and combustors may be represented in the frequency domain by means of approximate analytical solutions [1,3] or by acoustic finite element methods (FEMs) [2,5,6]. Both approaches solve the Helmholtz equation and lead to a transfer matrix linking acoustic pressures and acoustic velocities at burner locations. Moreover, to predict combustion instabilities, a model for the thermoacoustic response of the flame must be derived. When the geometrical length of the flame is small compared to acoustic wavelengths, only plane wave propagation may be considered. Compact flames are treated as two-port elements, where acoustic pressure and acoustic velocity upstream and downstream the element are coupled linearly via a four-element transfer matrix. For existing burners, the flame transfer matrix may be measured using loudspeakers for the acoustic forcing and reconstructing the acoustic field by means of the multimicrophone method [7]. The combustion dynamics of lean premix flames depends, in general, on one or more of the physical mechanisms affecting the heat release process (e.g., fuel injection, mixing, convective and diffusive transport, flame stabilization, and chemical kinetics). Thus, measured flame transfer matrices also give more physical insight to the interactions occurring in the flame and may be used to identify the mechanisms responsible for the thermoacoustic feedback. In particular, the sensitivity of heat release fluctuations to equivalence ratio oscillations usually results in a strong feedback mechanism [1,3–6]. In this case, heat release fluctuations are induced by fuel concentration oscillations caused by acoustic fluctuations at the fuel injector location. The time lag occurring between heat release and fuel concentration oscillations is the convective time that fuel concentration fluctuations need to travel from the injector to the flame. Once the flame transfer matrix has been determined, pressure pulsations may be predicted by introducing nonlinearities to limit the growth of pressure amplitude [5,6,8].

This work describes the application of our thermoacoustic approach during the design phase of a partially premix burner, which was developed to upgrade an existing diffusion burner with the purpose of reducing NO_x emissions in a specific engine application. The design of the new burner was entirely performed by means of computational fluid dynamics (CFD) and thermoacoustic simulations, without the support of test rig experiments. In particular, the flame transfer matrix of the new burner was predicted by using CFD results. The comparison between thermoacoustic predictions and engine tests performed with the new burner is also reported in the present work.

LEV Single Burner Design

In the ALSTOM single diffusion burner (SDB) shown in Fig. 1, reactions start in a zone of stoichiometric air-fuel mixture thus ensuring good flame stability. The mixing achieved by injecting dilution air after the reaction zone reduces the temperature to the turbine inlet limit. However, the high temperatures in the reaction zone give NO_x dry emissions close to 200 vppm (vapor parts per million) in gas operation (reduced to 25–42 vppm with H_2O injection). In order to reduce burner emissions, a single burner retrofit project was launched in ALSTOM. The approach was to

[1]Present address: Combustion Research Laboratory, Paul Scherrer Institut (PSI), CH-5232 Villigen, Switzerland.

Contributed by the International Gas Turbine Institute of ASME for publication in the JOURNAL OF ENGINEERING FOR GAS TURBINES AND POWER. Manuscript received May 23, 2007; final manuscript received June 13, 2007; published online April 3, 2008. Review conducted by Dilip R. Ballal. Paper presented at the ASME Turbo Expo 2007: Land, Sea and Air (GT2007), Montreal, Quebec, Canada, May 14–17, 2007.

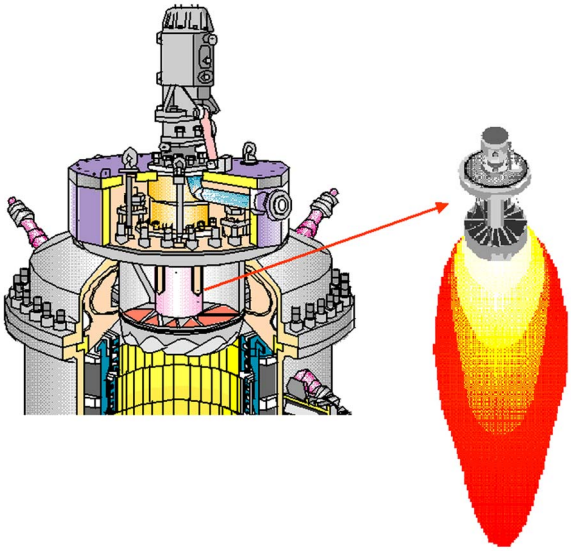

Fig. 1 SDB

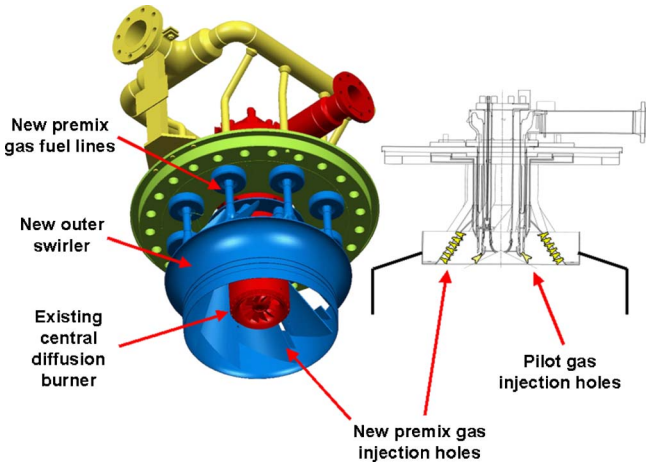

Fig. 3 LEV single burner

transfer the EV burner concept [9] into a single burner configuration with moderate changes of combustor hardware.

As illustrated in Fig. 2, the EV burner consists of two half cone shells that are displaced parallel to the axis, generating two tangential slots. The swirl strength of the flow entering through the tangential slots increases in the axial direction and is adjusted such that a vortex breakdown of the core flow occurs close to the burner exit. In the EV premix burner, no specific flame stabilizer hardware exists that is exposed upstream to the ignitable mixture and downstream to the flame stabilization zone. As a result, the EV burner has an inherent safety against autoignition and flame flashback events. The gaseous fuel is injected through a row of holes in a cross flow direction into the air entering the tangential burner slots. Each gas injection jet has to penetrate only a small portion of the air and has to be mixed only with "its own" small portion of the incoming air. Since the air, which enters the burner slots, is equally distributed along the length of the slot, the gas jets have to mix with the same portion of the air. This means that the mixing boundary conditions are equal and therefore the gas to air mixing performance is equally distributed in the whole flow field of the burner. The gas injection concept in the air slot stands for an inherent, equal distribution of the fuel into the incoming air, and is therefore the precondition for the high mixing effectiveness, which leads to a homogeneous air to fuel mixture in spite of the extremely compact mixing section of the EV burner. The relatively small volume in the cone is sufficient to generate a very homogeneous air-fuel mixture, which is a precondition to achieve premix combustion with NO_x dry emissions lower than 25 vppm in gas operation. Note that no or little dilution air is needed when using EV burners.

Therefore, the goal of the single burner retrofit project was to develop a premix flame diffusion stabilized burner (LEV single burner), able to achieve NO_x dry emissions lower than 80 vppm (25–42 vppm with reduced H_2O injection with respect to SDB). Neither water tunnel nor combustion rig experiments were performed because of the large burner size. On the contrary, CFD tools were extensively used to optimize the burner flow, combustor flow, and gas hole pattern (including backflow margin of premix gas). The CFD simulations have been performed with FLUENT using finite rate and eddy dissipation model with parameters optimized by means of genetic algorithms [10]. The resulting LEV burner is illustrated in Fig. 3. An EV-like conical swirl generator replaced the original outer swirler. The gas fuel was premixed with the combustion air along eight air inlet slots. The SDB gas injection lance was kept to generate a pilot diffusion flame used to stabilize the premix flame (see Fig. 4). Concerning the

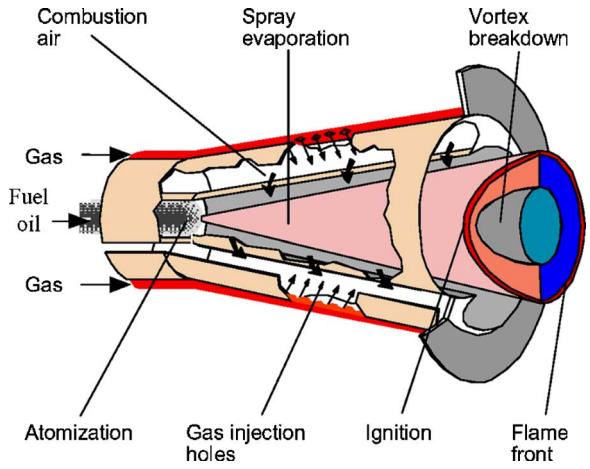

Fig. 2 EV burner principle

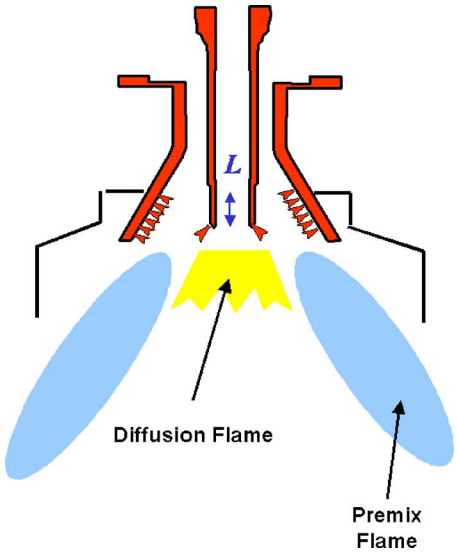

Fig. 4 LEV burner concept

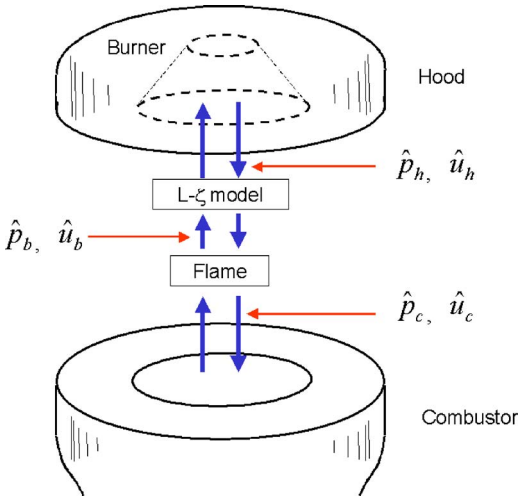

Fig. 5 Thermoacoustic network

fuel distribution system, the existing gas pipe single branch was replaced by two split pipe branches (pilot and premix) equipped with control valves.

LEV Thermoacoustic Model

In parallel with the CFD study, the thermoacoustic analysis of a real silo combustion chamber type of engine in the field equipped with LEV burner was performed using the thermoacoustic three dimensional (TA3) network [6,11]. In TA3, acoustic wavelengths are supposed to be much larger than burner dimensions (low-frequency assumption). Hence, the acoustic pressure $\hat{p}$ and normal acoustic velocity $\hat{u}$ are assumed uniform on the burner exit area A. The acoustic unknowns $\hat{p}$ and $\hat{u}$ are expressed by making use of Green functions and modal expansion [12]. It reads as

$$\hat{p}_j = i\omega\bar{\rho}\bar{c}^2 \sum_{n=0}^{N} \frac{\psi_n^2(\boldsymbol{x}_j)A}{V_j\Lambda_n(\omega^2 - 2i\omega\alpha - \omega_n^2)}\hat{u}_j \tag{1}$$

where $j=h$ and $j=c$ refer to the hood and combustor, respectively (see Fig. 5). Moreover, $\Lambda_n=\int_V \psi_n^2(\boldsymbol{x})dV$ and in our notation, the acoustic velocity is defined as positive when its direction points outside the volume. In Eq. (1), mean flow effects have been neglected (small flow Mach number hypothesis) and the acoustic damping has been directly introduced by means of the modal damping coefficient α. The eigenfunctions $\psi_n(\boldsymbol{x})$ and eigenfrequencies ω_n are the solutions of the problem

$$\bar{c}^2\nabla^2\psi + \omega^2\psi = 0 \tag{2}$$

$$\nabla\psi\cdot\boldsymbol{n} = 0 \quad \text{on } V \text{ boundary} \tag{3}$$

Boundary condition (3) corresponds to acoustically closed boundaries for hood and combustor. This assumption is motivated by the large area jump between air supply channels and the hood and by the large flow Mach number at the combustor exit. As a solution of a real problem, both eigenfunctions and eigenfrequencies are real functions. Equations (2) and (3) are numerically solved by applying acoustic FEM to the hood (with burners inside) and combustor geometry [13]. The SDB and LEV hood models used for the FEM modal analysis are presented in Fig. 6. In Eq. (2), the three-dimensional speed of sound distribution obtained from CFD is used. Equation (1) yields the exact solution for $N=\infty$. However, a limited number of modes (depending on the frequency range of interest) is generally sufficient to model hood and combustor.

To account for mean flow effects and acoustic losses inside the burner, the L-ζ model is applied at the burner exit (see Fig. 5). The L-ζ model is expressed as [6]

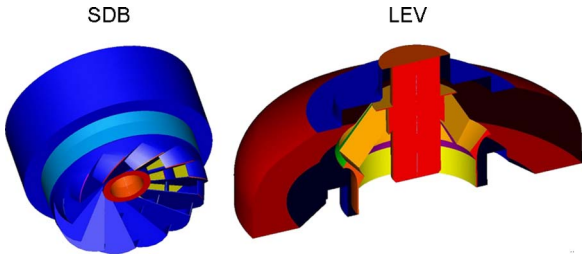

Fig. 6 FEM models of engine hood with SDB and LEV burner

$$\hat{p}_b = \hat{p}_h + (i\bar{\rho}\omega\ell + \bar{\rho}\zeta\bar{u}_b)\hat{u}_h \tag{4}$$

$$\hat{u}_b = \hat{u}_h \tag{5}$$

The pressure loss term ζ is obtained from steady CFD simulations. The end correction ℓ is in general a function of the area change between burner and combustor [14]. To obtain the end correction for the engine geometry, FEM and TA3 simulations of the combustion system model including hood, burner, and combustor are performed. Then, the burner end correction of the TA3 model is tuned to obtain the same eigenfrequencies of the FEM model. Two modes obtained from the FEM models of SDB and LEV combustors are shown in Fig. 7. In Fig. 7, the modal frequencies are normalized with the reference frequency corresponding to the LEV pulsation peak (see next section).

Finally, the thermoacoustic response of the flame must be prescribed in TA3. A theoretical expression for a premix flame transfer matrix is obtained starting from the acoustic jump relations written for planar flames in low-Mach number flows. They read as [15]

$$\hat{p}_c = \hat{p}_b + S_p(\omega) \tag{6}$$

$$\hat{u}_c = \hat{u}_b + \bar{u}_b\left(\frac{\bar{T}_c}{\bar{T}_b} - 1\right)\frac{\hat{Q}}{\bar{Q}} + S_u(\omega) \tag{7}$$

where the states b and c refer to upstream and downstream of the flame, respectively (see Fig. 5). The frequency dependent source terms S_p and S_u represent combustion noise, i.e., the acoustic excitation due to the flame acting as a sound source independent of the acoustic field. The term $\hat{Q}/\bar{Q}$ is in general a function of the acoustic variables $\hat{p}_b$ and $\hat{u}_b$. EV flame transfer matrix measurements have been successfully approximated by Eqs. (6) and (7) where a "time-lag" model was used to describe heat release fluctuations related to fluctuations of fuel mass fraction Y_F. To derive

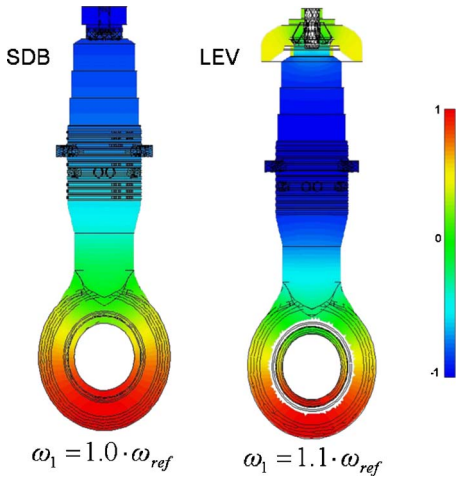

Fig. 7 Acoustic modes of SDB and LEV combustor

the time-lag model, we first consider the transport equation for fuel concentrations upstream of the flame. For an inviscid flow, it is written as

$$\frac{\partial Y_F}{\partial t} + \boldsymbol{u} \cdot \nabla Y_F = 0 \tag{8}$$

By neglecting the gradients of $\bar{Y}_F$ upstream of the flame, the acoustic perturbation of Eq. (8) reads as

$$\frac{\partial Y'_F}{\partial t} + \bar{\boldsymbol{u}} \cdot \nabla Y'_F = 0 \tag{9}$$

whose solution at the flame location is given by

$$Y'_F(\bar{\boldsymbol{x}}_b, t) = Y'_F(\bar{\boldsymbol{x}}_i, t - \tau) \tag{10}$$

where $\bar{\boldsymbol{x}}_i$ and $\bar{\boldsymbol{x}}_b$ are the average locations of fuel injection point and flame front, respectively. Moreover,

$$\tau = \int_{\bar{x}_i}^{\bar{x}_f} \frac{d\xi}{|\bar{\boldsymbol{u}}|} \tag{11}$$

is the time lag that the mean flow fluid element needs to travel from the injector to the flame front along the trajectory ξ. In the frequency domain, Eq. (10) reads as

$$\hat{Y}_F(\bar{\boldsymbol{x}}_b, \omega) = e^{-i\omega\tau} \hat{Y}_F(\bar{\boldsymbol{x}}_i, \omega) \tag{12}$$

When turbulent diffusion, spacial distribution of injectors, and flame front shape are taken into consideration instead of a single-value time-lag, one has to consider a probability distribution of delays. According to Eq. (10), the time-domain impulse response $Y'_{F\delta}$ is

$$Y'_{F\delta}(\bar{\boldsymbol{x}}_b, t) = \delta(t - \tau) \tag{13}$$

In the case of particles diffusing in stationary and homogeneous turbulent fields, the probability distribution of delays has a Gaussian form [16]. In this case, Eq. (13) may be replaced by the expression

$$Y'_{F\delta}(\bar{\boldsymbol{x}}_b, t) = \frac{1}{\sqrt{2\pi}\sigma} e^{-(t-\tau)^2/2\sigma^2} \tag{14}$$

where σ is the variance of the time-lag distribution. Finally, the Laplace transform of Eq. (14) is used to express Eq. (12) as

$$\hat{Y}_F(\bar{\boldsymbol{x}}_b, \omega) = e^{-i\omega\tau} e^{-1/2\omega^2\sigma^2} \hat{Y}_F(\bar{\boldsymbol{x}}_i, \omega) \tag{15}$$

To close the model, the fuel concentration fluctuations $\hat{Y}_{F,i} = \hat{Y}_F(\bar{\boldsymbol{x}}_i, \omega)$ must be computed. One can write

$$\frac{Y'_{F,i}}{\bar{Y}_{F,i}} = \frac{[m_F/(m_O + m_F)]'}{\bar{m}_F/(\bar{m}_O + \bar{m}_F)} = \frac{m'_F/\bar{m}_F - m'_O/\bar{m}_O}{1 + \bar{m}_f/\bar{m}_O} \approx \frac{m'_F}{\bar{m}_F} - \frac{m'_O}{\bar{m}_O} \tag{16}$$

where m_O is the mass flow rate of air (oxidant), m_F the mass flow rate of fuel, and the lean combustion condition $\bar{m}_O \gg \bar{m}_F$ has been used. The air mass flow rate fluctuations in Eq. (16) may be expressed as

$$\frac{m'_O}{\bar{m}_O} \approx \frac{u'_b}{\bar{u}_b} \tag{17}$$

where density fluctuations have been neglected. Under the incompressibility hypothesis, the fuel mass flow rate through the injector is given by

$$m_F = \sqrt{\frac{2\rho_F \Delta p_i}{\zeta_i}} A_i \tag{18}$$

where ρ_F is the fuel density, Δp_i the injector pressure drop, A_i the injector cross-sectional area, and ζ_i the injector pressure loss coefficient. The acoustic perturbation of Eq. (18) reads as

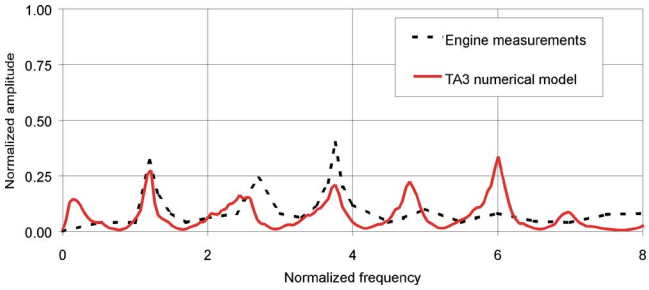

Fig. 8 Pressure pulsations in SDB combustor: engine measurements versus TA3 network simulations

$$\frac{m'_F}{\bar{m}_F} = \frac{1}{2} \frac{\Delta p'_i}{\overline{\Delta p_i}} \tag{19}$$

In the following, we assume $\overline{\Delta p_i} \gg |\Delta p'_i|$, i.e., according to Eq. (19) fuel mass flow rate fluctuations may be neglected in Eq. (16). Finally, heat release fluctuations due to fuel concentration oscillations are expressed as

$$\frac{\hat{Q}}{\bar{Q}} = \frac{\hat{Y}_{F,b}}{\bar{Y}_{F,b}} = -e^{-i\omega\tau} e^{-1/2\omega^2\sigma^2} \frac{\hat{u}_b}{\bar{u}_b} \tag{20}$$

The time-lag term in Eq. (20) may lead to the mathematical instability of the thermoacoustic model, a situation that corresponds physically to the generation of a combustion instability in the combustion system. In linear unstable systems, the pulsation amplitude growth is unbounded in time. The amplitude growth may be bounded by introducing nonlinear saturation to the model [5,6,8]. Thus, Eq. (16) is rewritten as $Y'_{F,i}/\bar{Y}_{F,i} = -\mathcal{H}(u'_b)/\bar{u}_b$ where the function $\mathcal{H}(u'_b)$ is expressed as

$$\mathcal{H}(u'_b) = \begin{cases} u'_b & \text{if } |u'_b(t)| < u'_{lim} \\ \text{sign}(u'_b) \cdot u'_{lim} & \text{if } |u'_b(t)| > u'_{lim} \end{cases} \tag{21}$$

being $u'_{lim} > 0$ the saturation velocity. When the flame transfer matrix and the combustion noise sources are known, the combustion system elements are assembled together in the TA3 network, written in the MATLAB environment [17]. The problem is expressed in the time domain by a *state-space* formulation and pulsation spectra are finally computed by postprocessing the time-domain solution.

Results

In order to validate the thermoacoustic model, TA3 simulations of an existing engine equipped with SDB burner were performed. The analysis of the SDB pulsation data showed a resonance behavior, i.e., pulsation peaks mainly excited by combustion noise. Therefore, in the thermoacoustic analysis of the SDB combustor, no flame transfer matrix was applied (i.e., $\hat{Q}/Q = 0$). The combustion noise source terms in Eq. (20) were approximated with the sources measured in the EV burner under conditions close to the SDB operating point. Figure 8 shows the capability of the model to predict the resonance peaks of the engine in the low-frequency region of interest. Note that the TA3 spectra were computed immediately downstream the flame front, whereas the engine pulsation probe was located in the middle of the combustion chamber. For higher frequencies, this may be a cause of disagreement between computed and measured pulsation amplitudes, because acoustic modes become less uniform in space with increasing frequency.

On the contrary, in the thermoacoustic LEV model the flame transfer matrix (20) was used. In particular, in Eq. (20) heat release fluctuations were obtained by calculating the time-lag average value τ and its variance σ from steady CFD results [18].

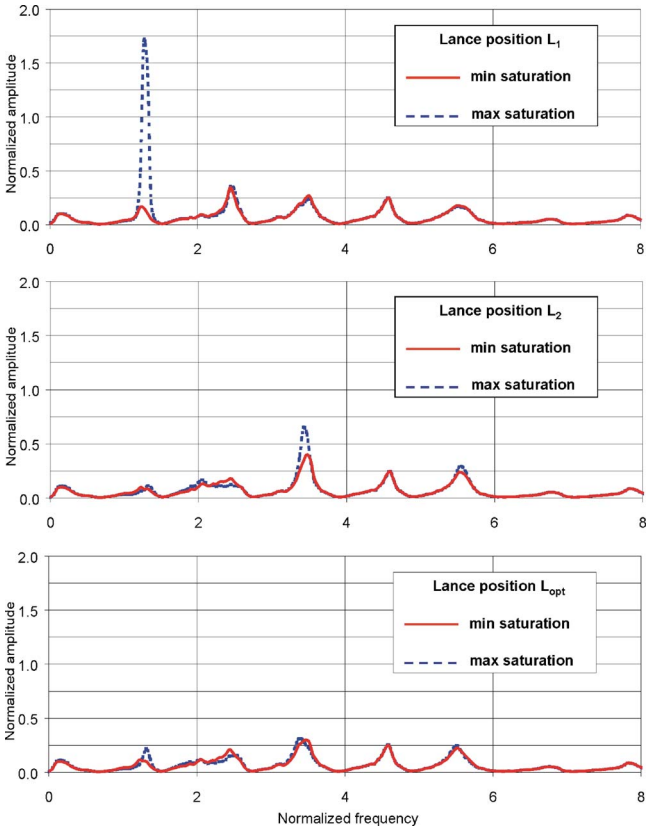

Fig. 9 Pressure pulsations in LEV combustor: TA3 network simulations with minimum and maximum heat release saturations for the three axial lance positions L_1, L_2 and L_{opt} ($L_1 < L_{opt} < L_2$)

Pulsation spectra were computed by varying the fuel saturation parameter u'_{lim} of Eq. (21) between a minimum and a maximum value. The choice of the minimum and maximum values of u'_{lim} was made according the experience acquired from thermoacoustic simulations of EV burners installed on different ALSTOM heavy-duty engines [6]. Figure 9 presents pulsation spectra predicted in the LEV combustor using both the minimum and maximum saturation values. In the first LEV analysis, the pilot lance axial position L (see Fig. 4) was kept equal to the fuel lance position L_1 of the SDB. For the case $L=L_1$, Fig. 9 shows that the pulsation peak is largely affected by the saturation value (lower pulsation amplitudes are obtained when further limiting the magnitude of heat release fluctuations using a smaller saturation). This indicates that such a pulsation peak is generated by a combustion instability that was then identified as a limiting factor for combustor operation.

In order to suppress pulsation amplitudes, the thermoacoustic effect related to a different axial position of the fuel lance was investigated. In fact, an axial shift of the lance modifies the burner flow and then the position of the vortex breakdown, the flame front location, and finally the time lag. Therefore, a CFD steady analysis was performed using a lance position $L_2 > L_1$. The analysis gave a lower time-lag, in agreement with a more flat flame front (this effect being stronger than the time-lag increase related to the downstream displacement of the vortex breakdown bubble). The thermoacoustic simulation corresponding to the axial lance position L_2 is also reported in Fig. 9, showing the suppression of the pulsation peak of the case L_1 and the excitation of a pulsation peak at a larger frequency. Thus, simulations were performed for lance positions between L_1 and L_2 by interpolating linearly both time-lag average and variance. An optimum lance position L_{opt} was found corresponding to minimum pressure amplitudes. The

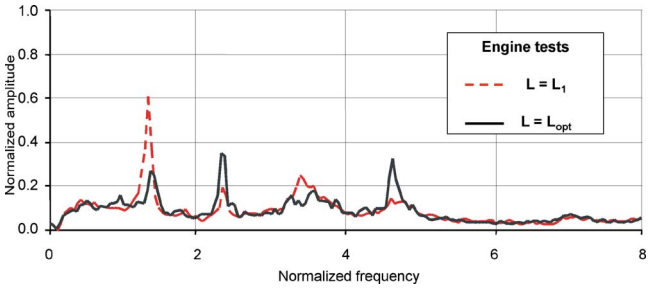

Fig. 10 Pressure pulsations in LEV combustor: engine tests for axial lance positions L_1 and L_{opt}

spectrum for the case L_{opt} is also reported in Fig. 9 (note that for this lance position the saturation value does not affect the amplitude, i.e., the system is stable). Hence, based on the input from the thermoacoustic analysis, the first LEV burner was designed with the capability of shifting the lance position between L_1 and L_{opt}. Moreover, a pulsation probe in the LEV combustor was located close to flame front, where the thermoacoustic analysis predicted a maximum of the acoustic modes excited in the pulsation spectra. Figure 10 shows two spectra, measured in a silo combustion chamber of a field engine equipped with a LEV burner. First, tests with the L_1 lance position were performed. These tests confirmed the pulsation problem predicted by TA3 for the case L_1. However, as predicted by our thermoacoustic analysis, when the lance was shifted to the L_{opt} position, thermoacoustic pulsations were no longer a limiting factor for combustor operation. For the two cases $L=L_1$ and $L=L_{opt}$, emissions at baseload without water injection were very similar and fulfilled the project target (see Fig. 11).

Finally, the engine spectrum for the case L_1 of Fig. 10 was used to calibrate the value of the heat release saturation. The TA3 results obtained with the calibrated saturation value for the cases L_1 and L_{opt} are reported in Fig. 12. Figure 12 shows that the prediction of the low-frequency peak is very accurate, whereas the simulated amplitude of the second peak is overestimated for the L_1 case and underestimated for the L_{opt} case. However, simulations show that the first peak is unstable (the amplitude being mainly determined by the flame transfer function) whereas the second peak is stable, i.e., its amplitude is mainly related to the combustion noise term that generates resonance at that frequency. Therefore, the use of the same EV combustion noise source term for all the LEV simulations is probably responsible for the inaccurate pulsation trend of the second peak.

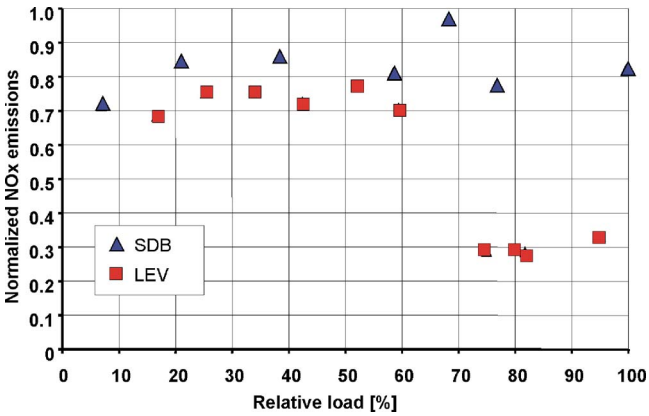

Fig. 11 NO_x emissions from engine tests (no water injection): SDB versus LEV with axial lance position L_{opt}

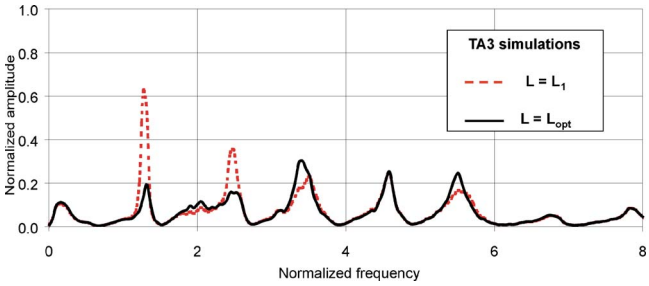

Fig. 12 Pressure pulsations in LEV combustor: TA3 network simulations for axial lance positions L_1 and L_{opt}

Conclusions

In this work, a thermoacoustic approach has been applied in "predictive mode" for the development of a partially premix burner to be used as retrofit upgrade for a specific engine application. Since burner tests were not available, the thermoacoustic analysis was performed by modeling the acoustic flame response by means of pulsation data of engines equipped with the existing diffusion burner, CFD (flame transfer matrix time lag), and data from thermoacoustic modeling of other engines (heat release saturation). The analysis predicted a combustion instability representing a limiting factor for combustor operation and indicated the potential of thermoacoustic combustor tuning by varying the axial position of the pilot fuel lance. This burner design engineering methodology was validated in the field engine and we found good coincidence between predictions and actual field behavior. In particular, engine tests fully confirmed the validity of the suggested pulsation mitigation strategy.

Nomenclature

$\overline{(\cdot)}$ = mean flow quantities
$(\cdot)'$ = acoustic perturbations
$\hat{(\cdot)}$ = Laplace transform of acoustic perturbations
A = cross-sectional area of burner exit
c = speed of sound
ℓ = end correction
L = axial position of pilot fuel lance
$\boldsymbol{n}$ = outward normal vector
m = mass flow rate
N = number of acoustic modes
p = pressure
Q = heat release per unit area and time
S_p, S_u = combustion noise source terms
t = time
T = temperature
u = flow velocity magnitude
$\boldsymbol{u}$ = flow velocity vector
V = volume of the hood or combustor
$\boldsymbol{x}$ = space coordinate
Y_F = fuel mass fraction
α = acoustic damping coefficient
ζ = pressure loss coefficient
Λ_n = mode normalization factor
ρ = density
σ = standard deviation of τ distribution
τ = time delay
ψ_n = acoustic mode
ω = circular frequency$=2\pi\cdot$frequency
ω_n = acoustic eigenfrequency

Subscripts

b = location between L-ζ element and flame
c = burner exit location on combustor volume
h = burner exit location on hood volume
i = fuel injection point

References

[1] Paschereit, C. O., Flohr, P., and Schuermans, B., 2001, "Prediction of Combustion Oscillations in Gas Turbine Combustors," AIAA Paper No. 2001-0484.
[2] Evesque, S., and Polifke, W., 2002, "Low-Order Acoustic Modelling for Annular Combustors: Validation and Inclusion of Modal Coupling," ASME Paper No. GT-2002-30064.
[3] Akamatsu, S., and Dowling, A. P., 2001, "Three-Dimensional Thermoacoustic Oscillations in a Premix Combustor," ASME Paper No. 2001-GT-0034.
[4] Dowling, A. P., and Stow, S. R., 2003, "Modal Analysis of Gas Turbine Combustor Acoustics," J. Propul. Power, **19**(5), pp. 751–764.
[5] Pankiewitz, C., and Sattelmayer, T., 2002, "Time Domain Simulation of Combustion Instabilities in Annular Combustors," ASME Paper No. GT-2002–30063.
[6] Bellucci, V., Schuermans, B., Nowak, D., Flohr, P., and Paschereit, C. O., 2005, "Thermoacoustic Modeling of a Gas Turbine Combustor Equipped With Acoustic Dampers," J. Turbomach., **127**(2), pp. 372–379.
[7] Schuermans, B., Polifke, W., and Paschereit, C. O., 1999, "Modeling Transfer Matrices of Premixed Flames and Comparison With Experimental Results," ASME Paper No. 1999-GT-0132.
[8] Dowling, A. P., 1997, "Non-Linear Self-Excited Oscillations of a Ducted Flame," J. Fluid Mech., **346**, pp. 271–290.
[9] Döbbeling, K., Hellat, J., and Koch, H., 2005, "25 Years of BBC/ABB/ALSTOM Lean Premix Combustion Technologies," ASME Paper No. GT-2005-68269.
[10] Polifke, W., Geng, W., and Döbbeling, K., 1998, "Optimization of Rate Coefficients for Simplified Reaction Mechanisms With Genetic Algorithms," Combust. Flame, **113**, pp. 119–134.
[11] Schuermans, B., Bellucci, V., and Paschereit, C. O., 2003, "Thermoacoustic Modeling and Control of Multi-Burner Combustion Systems," ASME Paper No. GT-2003-38688.
[12] Morse, P. M., and Ingard, K., 1968, *Theoretical Acoustics*, McGraw-Hill, New York.
[13] 1999, *SYSNOISE 5.4 Documentation*, LMS International, Brussels, Belgium.
[14] Bellucci, V., Paschereit, C. O., and Flohr, P., 2002, "Impedance of Perforated Screens With Bias Flow," AIAA Paper No. 2002–2437.
[15] Chu, B. T., 1953, "On the Generation of Pressure Waves at a Plane Flame Front," *Fourth Symposium (International) on Combustion*, Massachusetts Institute of Technology, pp. 603–612.
[16] Scarinci, T., and Freeman, C., 2000, "The Propagation of a Fuel-Air Ratio Disturbance in a Simple Premixer and Its Influence on Pressure Wave Amplification," ASME Paper No. 2000-GT-0106.
[17] 1999, *Using MATLAB Version, 6*, MathWorks, Natick, MA.
[18] Flohr, P., Paschereit, C. O., and Bellucci, V., 2003, "Steady CFD Analysis for Gas Turbine Burner Transfer Functions," AIAA Paper No. 2003-1346.

A Way to Deal With Model-Plant Mismatch for a Reliable Diagnosis in Transient Operation

S. Borguet
e-mail: s.borguet@ulg.ac.be

P. Dewallef
e-mail: p.dewallef@gmail.com

O. Léonard
e-mail: o.leonard@ulg.ac.be

Turbomachinery Group,
University of Liège,
Chemin des Chevreuils 1,
4000 Liège, Belgium

Least-squares health parameter identification techniques, such as the Kalman filter, have been extensively used to solve diagnosis problems. Indeed, such methods give a good estimate provided that the discrepancies between the model prediction and the measurements are zero-mean, white, Gaussian random variables. In a turbine engine diagnosis, however, this assumption does not always hold due to the presence of biases in the model. This is especially true for a transient operation. As a result, the estimated parameters tend to diverge from their actual values, which strongly degrades the diagnosis. The purpose of this contribution is to present a Kalman filter diagnosis tool where the model biases are treated as an additional random measurement error. The new methodology is tested on simulated transient data representative of a current turbofan engine configuration. While relatively simple to implement, the newly developed diagnosis tool exhibits a much better accuracy than the original Kalman filter in the presence of model biases. [DOI: 10.1115/1.2833491]

Keywords: engine health monitoring, Kalman filter, model-plant mismatch

Introduction

The diagnosis tool considered herein is basically a gas path analysis method whose purpose is to assess the deviations of some health parameters on the basis of measurements collected within the gas path of the engine [1]. The health parameters are coefficients affecting the efficiency and the flow capacity of the components (fan, low pressure compressor (lpc), high pressure compressor (hpc), high pressure turbine (hpt), low pressure turbine (lpt), and nozzle), while the measurements are intercomponent temperatures, pressures, as well as rotational speeds. The health assessment leads to a diagnosis of the engine condition, which allows suitable maintenance actions to be undertaken.

The health parameter estimation is achieved by a Kalman filter, which is a minimum mean square error (variance) estimator within a recursive framework [2]. This means that the estimated health parameters minimize the distance (in the least-squares sense) between a model prediction and the observed measurements. Moreover, the recursive structure of the Kalman filter updates the values of the identified health parameters as new data are available, which is a useful property in real-world applications such as on-board performance monitoring [3].

Since the first research efforts of Urban [4], most of the gas path analysis methods were restricted to measurements observed under *steady-state operation* of the engine, mainly for computational load reasons. For a few years, the ability to extract the engine condition from *transient data* has been investigated using various techniques such as least-squares estimation [5,6], artificial neural networks [7] for a batch treatment of the data, and Kalman filters [8–11] in a recursive framework.

More specifically, it has been shown in Ref. [10] that the use of measurements representative of transient behavior significantly improves both the diagnosis accuracy and the isolation capability under negative redundancy (i.e., more health parameters than sensors), provided that a faithful dynamic model is available. Indeed, a transient operation allows a much greater number of operating points to be considered, thereby increasing the analytical redundancy.

Although the existence of a perfectly faithful model is generally assumed, this hypothesis is rarely met in practice. In fact, complex phenomena, such as heat transfer, volume dynamics, clearances, and secondary airflow and power off-takes, are poorly modeled or unmodeled in current state-of-the-art aerothermodynamic engine models [12,13]. Consequently, the performance predictions generated by the dynamic model are biased with respect to measurements taken on the engine. As reported in Ref. [11], those biases strongly reduce the efficiency of the diagnosis tool.

The present contribution proposes a solution to the model biases by considering them as an additional measurement error. Indeed, from the point of view of an external observer, it is not possible to distinguish a model bias from a sensor error. However, unlike sensor errors, which are basically unpredictable beforehand, the model biases of interest have a more predictable nature that can be studied by comparing the model outputs and the measurements observed on a healthy engine during a learning phase previous to the health parameter assessment.

Description of the Method

The scope of this section is to provide a short description of our diagnosis tool and to present the methodology we have developed to cope with model-plant mismatch and its integration within the diagnosis algorithm.

Diagnosis Tool. Our diagnosis tool belongs to the family of model-based approaches, meaning that a simulation model of the turbine engine must be available. In the framework of gas path analysis, these are basically nonlinear aerothermodynamic models based on mass, energy, and momentum conservation laws applied to the engine.[1]

As mentioned in the Introduction, the framework in which this contribution takes place is the development of a diagnosis tool processing transient data and reliance on the Kalman filter estimation algorithm. Since the system model is nonlinear, the unscented Kalman filter [14] is used instead of the generic linear Kalman filter. A few adjustments and assumptions govern the applicability

Manuscript received June 20, 2006; final manuscript received October 29, 2007; published online March 26, 2008. Review conducted by Jeffrey W. Bird.

[1]Linearized models are often used to lower the computational burden.

of the unscented Kalman filter. The first one consists in formulating the simulation model of the engine in terms of a state-space model, namely,

$$\mathbf{x}_k = \mathcal{F}(\mathbf{u}_k, \mathbf{v}_k, \mathbf{w}_k, \mathbf{x}_{k-1}) + \boldsymbol{\nu}_k \tag{1}$$

$$\mathbf{y}_k = \mathcal{G}(\mathbf{u}_k, \mathbf{v}_k, \mathbf{w}_k, \mathbf{x}_k) + \boldsymbol{\epsilon}_k \tag{2}$$

where k is a discrete time index, $\mathbf{u}_k$ are the command parameters (e.g., fuel flow), $\mathbf{v}_k$ are measurable exogenous inputs (e.g., Mach number and altitude), $\mathbf{w}_k$ are the aforementioned health parameters, and $\mathbf{x}_k$ are the state variables. The state variables are intended to handle the transient effects taking place in the gas path of the engine. Generally speaking, these transient effects belong to three categories, namely, the heat transfers between the gas path and the components of the engine, the shaft inertia, and the fluid transport delays.

Equation (2) is called the measurement equation and joins the deterministic simulation model $\mathcal{G}(\cdot)$ and a random variable $\boldsymbol{\epsilon}_k$ intended to represent the stochastic influence of the measurement uncertainties. Similarly, Eq. (1) is named the state prediction equation and links the deterministic integration routine $\mathcal{F}(\cdot)$ of the simulation model and a random variable $\boldsymbol{\nu}_k$, which represents an error term. In addition to these two equations, a third one, named the health parameter transition equation, is often included which states that the health parameters may vary in time by following a first-order Markov process (see Ref. [3] for further details).

The second assumption is that both $\boldsymbol{\nu}_k$ and $\boldsymbol{\epsilon}_k$ are zero-mean, white, and Gaussian random variables[2] which is denoted by

$$\boldsymbol{\epsilon}_k = \mathcal{N}(\mathbf{0}, \mathbf{R}_\mathbf{y}) \quad \text{and} \quad \boldsymbol{\nu}_k = \mathcal{N}(\mathbf{0}, \mathbf{R}_\mathbf{x}) \tag{3}$$

Since the state variables are unknown (not all of them are measurable), they must be estimated together with the health parameters from the same sequence of measurements $\mathbf{y}_k$. This problem, known as the dual estimation problem, is solved herein by a so-called dual estimation Kalman filter (DEKF). This dual Kalman filter relies on two unscented Kalman filters running concurrently, one for the health parameters and the other for the state variables. The interested reader may consult Ref. [15] for a detailed description of the algorithm. Basically, once the former filter has updated the health parameters, the current value is used by the latter to update the corresponding state variables.

Provided that a prior value for the health parameters and the state variables is available, the basic step consists of observing the discrepancies between the model outputs, denoted by $\hat{\mathbf{y}}_k$, and the observed measurements $\mathbf{y}_k$. These discrepancies, also called residuals and denoted by $\mathbf{r}_k$, are processed by the DEKF, which recursively updates the health parameters and the state variables so that the average value of $\mathbf{r}_k$ is driven to zero. In other words, the identified health parameters provide a means of observing the actual health condition of the engine. Figure 1 summarizes this recursive, closed-loop process. The engine performance model, actually embedded in the DEKF, has been represented outside of it in order to underline its important role in the estimation process.

Dealing With Model Biases. The physical meaning of the identified health parameters is only valid provided that the model is faithful. Otherwise, as reported by Volponi in Ref. [11], the health parameters become "tuners," which are adjusted by the identification process to fit the behavior of the real engine, losing sense for diagnosis reports. Indeed, as formulated in the preceding section, the Kalman filter assumes that the discrepancies between the model and the measurements are zero on average.

Unfortunately, model biases do not have a pure stochastic nature, but should rather be seen as systematic errors whose mean values are different from zero. The assumption on the noise characteristics is therefore violated, which perturbs the health parameter identification. In practice, it has been observed that model biases as small as the measurement noise standard deviation can dangerously reduce the reliability of the diagnosis. Therefore, the biases have to be modeled in some way so that the residuals will reflect only the degradation of the engine. In reality, the model-plant mismatch depicts the approximations made in both the state transition equation (Eq. (1)) and the measurement equation (Eq. (2)). A possible mathematical translation of this fact is to consider that neither $\boldsymbol{\epsilon}_k$ nor $\boldsymbol{\nu}_k$ are zero-mean, Gaussian random variables.

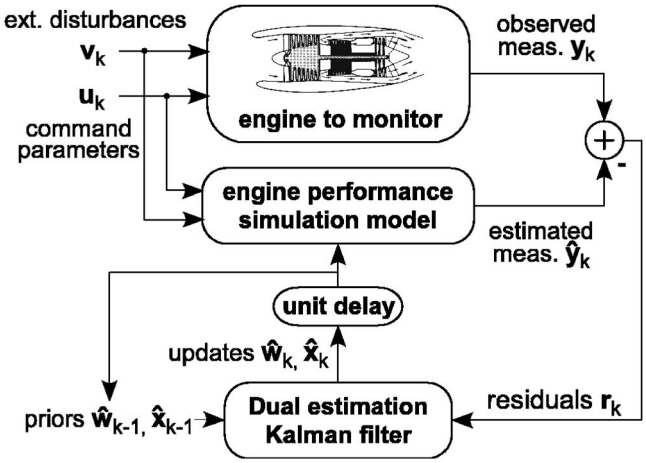

Fig. 1 Health parameter and state variable update mechanism using a DEKF

In this contribution, it is proposed to gather all the effects caused by modeling errors in the single measurement equation (Eq. (2)). The measurement noise $\boldsymbol{\epsilon}_k$ is now seen as a *hybrid* bias-noise term gathering the measurement noise and the model-plant mismatch. Mathematically speaking, $\boldsymbol{\epsilon}_k$ is considered as a Gaussian random variable of variable properties (i.e., mean and covariance). Two reasons favored this choice: First, the Kalman filter deals with this type of random variables. Second, a Gaussian random variable is totally defined by its mean and its covariance, which is simple to handle in practice,

$$\boldsymbol{\epsilon}_k = \mathcal{N}(\mathbf{b}_k, \mathbf{R}_{\mathbf{b},\mathbf{k}}) \tag{4}$$

Provided that $\mathbf{b}_k$ and $\mathbf{R}_{\mathbf{b},\mathbf{k}}$ are known, the mechanism of the unscented Kalman filter can be applied by making the following substitutions:

$$\mathbf{r}_k = \mathbf{y}_k - \hat{\mathbf{y}}_k \rightarrow \mathbf{r}_k = \mathbf{y}_k - \hat{\mathbf{y}}_k - \mathbf{b}_k \tag{5}$$

$$\mathbf{R}_\mathbf{y} \rightarrow \mathbf{R}_{\mathbf{b},\mathbf{k}} \tag{6}$$

Determination of $\mathbf{b}_k$ and $\boldsymbol{R}_{\mathbf{b},\mathbf{k}}$. As already mentioned above, the model biases are not, strictly speaking, random variables. Consequently, they can be studied beforehand, for example, during the acceptance tests that every engine undergoes before it is brought into service. The purpose of this offline learning is to build a model that predicts $\mathbf{b}_k$ and $\mathbf{R}_{\mathbf{b},\mathbf{k}}$ as precisely as possible. This approach is very close to the eStorm philosophy [11], with the difference that in our study both the mean bias and its uncertainty are modeled.

During this learning phase, model outputs are compared to the observed measurements without estimating the health parameters, which are assumed to be at their healthy nominal values. As the engine transient model is not perfect, the observed residuals $\mathbf{r}_k$ correspond to the model biases. The next step of the learning phase consists of characterizing the mean $\mathbf{b}_k$ and the covariance matrix $\mathbf{R}_{\mathbf{b},\mathbf{k}}$ of the observed biases.

[2]In addition, $\boldsymbol{\nu}_k$ and $\boldsymbol{\epsilon}_k$ are assumed uncorrelated.

Modeling the mean bias $\mathbf{b}_k$ is typically a function approximation problem. In the following, some general considerations about this problem are recalled. Numerous textbooks address this problem in a more exhaustive way (see, for instance, Ref. [16]).

The cloud of data of the learning set has to be fitted with a function $\mathcal{H}$, which may depend on the controls, the ambient variables, the state variables, and, possibly, past values of them and which also contains fitting parameters $\mathbf{p}$, as stated in

$$\mathbf{b}_k = \mathcal{H}(\mathbf{u}_k, \mathbf{v}_k, \mathbf{x}_k, \ldots, \mathbf{p}) \tag{7}$$

The first step is to decide on which input variables the function $\mathcal{H}$ depends, with the aim of reducing the dimensionality of the input space by performing a so-called feature extraction. A feature can be seen as an intelligent transformation of the original input variables. Then, the structure (e.g., polynomial fit or neural networks) and the complexity (e.g., order of the polynomial or number of hidden nodes) have to be selected. As a result, the number of fitting parameters $\mathbf{p}$ is obtained. For example, in the case of a scalar, second-order polynomial fit, the fitting parameters $\mathbf{p}$ are the three coefficients of the parabola.

The choice of the flexibility of the fitting function must be done in a very careful way. Indeed, the goal is to obtain the best representation of the underlying properties of the data in the learning set and hence to obtain the best generalization performance. In other words, over-fitting of the data must be avoided. So, the number of samples in the learning set should be large enough with respect to the flexibility of the approximation function. On the other hand, a general result of learning theory states that for a given number of fitting parameters, the larger the database, the more meaningful the values of these parameters from a statistical point of view (see Ref. [16]).

The fitting parameters $\mathbf{p}$ are generally computed through the minimization of an error function (e.g., sum of squares error). The determination of the covariance matrix $\mathbf{R}_{\mathbf{b},\mathbf{k}}$ is to be explained later.

Considering the present application, a rather basic, but physically meaningful, model is chosen. First, fixed ambient conditions (e.g., sea-level static) are selected when collecting the learning set. Then, three assumptions are made in order to simplify the determination of $\mathbf{b}_k$ and $\mathbf{R}_{\mathbf{b},\mathbf{k}}$.

1. The engine steady-state model is highly accurate. To this end, model-matching techniques such as those described in Refs. [17] or [18] can be applied.
2. The engine undergoes *moderate* transient maneuvers. This constraint can be expressed in terms of an upper limit on the engine acceleration. This bound is application dependent and was set here for the sake of simplicity to a value of ± 200 rpm/s on the fan rotor acceletation.[3]
3. During the *learning phase*, the engine is in healthy nominal condition, hence the values of the health parameters are known and set to their nominal values.

The problem of modeling the mean $\mathbf{b}_k$ is first investigated. We can reasonably suppose that the more rapid and complex the transient is, the greater the model-plant mismatch is. Therefore, it is desirable to link the mean bias $\mathbf{b}_k$ to a scalar quantity, which is representative of the "intensity" of the transient and which is easy to compute. To this end, the following transient index (TI) is defined:

$$\mathrm{TI}_k = \frac{1}{n_x} \sum_{i=1}^{n_x} \frac{\dot{\hat{\mathbf{x}}}_k(i)}{\mathbf{x}^{\mathrm{ref}}(i)} \tag{8}$$

where n_x is the number of state variables of the on-board model, $\dot{\hat{\mathbf{x}}}_k(i)$ is the derivative of state variable i at time index k, and $\mathbf{x}^{\mathrm{ref}}(i)$ is the reference value of state variable i (e.g., at take-off rating). The unit of TI is s^{-1}. The normalization by a reference state value is required given the different orders of magnitude of the state variables. The TI is zero in a steady-state operation, positive when the engine is accelerating, and negative otherwise.

[3]Note that another indicator of engine acceleration could be chosen, e.g., core acceleration.

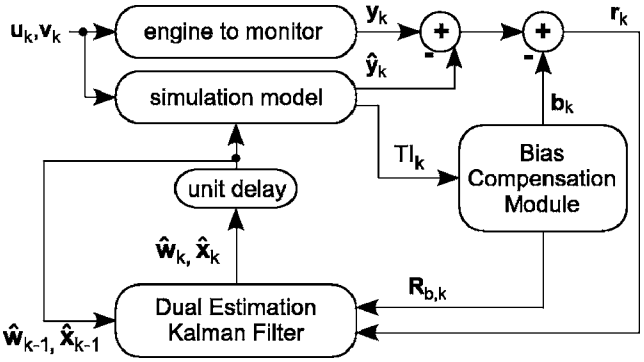

Fig. 2 Integration of the BCM

The TI is computed based on state derivatives provided by the engine model rather than on actual measurements. Two reasons dictate this choice: First, the engine model produces noise-free signals and outputs directly the state derivatives; second, not all state variables are normally measurable on the real engine (e.g., the metal temperatures involved in the heat transfers) but are available in the engine model.

So, modeling the mean value of the bias amounts to determining the mapping $\mathbf{b}_k = f(\mathrm{TI}_k)$ from the database of biases. This problem is solved through a least-squares polynomial fit. The selection of the polynomial order and a possible partitioning of the TI axis is a question of engineering judgment. Additional indications are provided in the application detailed later in the paper.

The model of the mean value of the bias available, the covariance matrix of the bias, $\mathbf{R}_{\mathbf{b},\mathbf{k}}$, can now be computed. The procedure is given in Algorithm 1. Depending on the partitioning adopted for the mean bias, one covariance matrix is computed per TI segment. As a first step, the gap between each data point and the mean bias is computed for all data points belonging to a particular segment (lines 2–5, note that each vector $\mathbf{e}_i$ is a $ny \times 1$ vector). Finally, each element of the symmetric covariance matrix is obtained using the well-known definition of the covariance of random variables (line 6).

Algorithm 1. Covariance matrix computation.

1. Set $N=0$
2. for all k such that $\mathrm{TI}^{\min} < \mathrm{TI}_k \leq \mathrm{TI}^{\max}$ do
3. $N=N+1$
4. $\mathbf{e}_N = \hat{\mathbf{r}}_k - \mathbf{b}(\mathrm{TI}_k)$
5. end for
6. $\mathbf{R}_{\mathbf{b}} = \frac{1}{N-1} \Sigma_{i=1}^{N} \{\mathbf{e}_i \mathbf{e}_i^T\}$

The covariance matrix takes into account both the measurement noise (sensor inaccuracies) and the possible variability of the mean bias. Also, it should not be surprising that some off-diagonal terms of that matrix are nonzero. This simply indicates that the sensor biases are interdependent as the modeling errors introduce some relationships between the measurements: for instance, the bias on the exhaust gas temperature (EGT) sensor measurement is linked to that of the low pressure spool speed since temperature recovery factor for thermocouples will vary with mass flow.

This concludes the offline modeling of the bias model, which can now be integrated within the diagnosis algorithm in order to make it more robust to model-plant mismatches.

Modification of the Diagnosis Algorithm. The block diagram of the modified diagnosis algorithm is shown in Fig. 2. A short

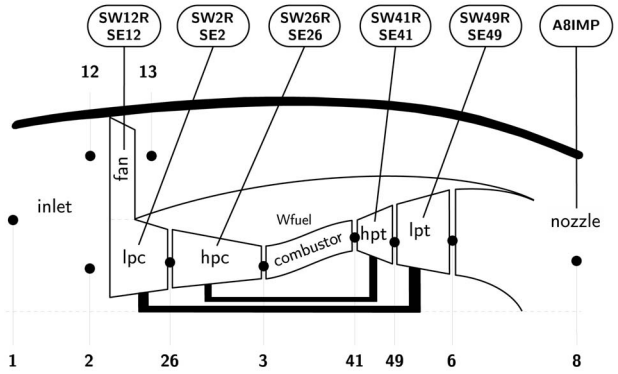

Fig. 3 Turbofan layout with station numbering and health parameter location

description of the procedure is given in this section. Similar to the original procedure detailed in Fig. 1, the previous estimates of the state variables $\hat{\mathbf{x}}_{k-1}$ and health parameters $\hat{\mathbf{w}}_{k-1}$ are used together with the current inputs $\mathbf{u}_k$ and $\mathbf{v}_k$ by the engine performance model to generate an estimation of the measurements. Additionally, the TI_k is computed using relation (8). From this TI, the mean bias $\mathbf{b}_k$ and its covariance matrix $\mathbf{R}_{\mathbf{b},\mathbf{k}}$ are obtained according to the bias model previously set up. The bias $\mathbf{b}_k$ is taken into account in the residual $\mathbf{r}_k$, which is fed into the original DEKF, with the only difference that the measurement noise covariance matrix $\mathbf{R}_\mathbf{y}$ is replaced by $\mathbf{R}_{\mathbf{b},\mathbf{k}}$. Loosely speaking, the mean bias $\mathbf{b}_k$ and its covariance matrix $\mathbf{R}_{\mathbf{b},\mathbf{k}}$ are now extra inputs to the original DEKF. The integration of the bias compensation module (BCM) within the diagnosis algorithm has a very limited impact on the computational load. Indeed, only a polynomial evaluation is used to return $\mathbf{b}_k$ and $\mathbf{R}_{\mathbf{b},\mathbf{k}}$.

Application of the Method

Engine Configuration. The application used as a test case is a high bypass ratio mixed-flow turbofan. The engine layout is described in Fig. 3 where the health parameter location and the station numbering are also indicated. One command variable, which is the fuel flow rate fed in the combustor, is considered in the following.

The engine performance model has been developed and validated as part of the OBIDICOTE [4] project. A detailed description of the model can be found in Ref. [19].

As real data were not available, we worked with simulated data only. To introduce modeling errors, we considered two different configurations of the OBIDICOTE model with regard to transient operation. Our hypothesis concerning the perfect fidelity of the steady-state model to the data used is hence implicitly satisfied.

The sensor configuration adopted in the test cases is representative of typical instrumentation available on modern turbofan engines and is detailed in Table 1. The stated uncertainties have been selected according to the OBIDICOTE documentation and account for the magnitude of random errors only.

"Real" Engine and On-Board Model. The OBIDICOTE model plays the role of the "real" engine. The shaft dynamics and the heat transfers in the hpc, burner, and hpt are thus supposed to be perfectly modeled. The seven state variables involved in this first model are listed in Table 2.

Gaussian noise, whose magnitude is specified in Table 1, is added to the clean measurements generated by the real engine model to make them closer to typical test data. The sampling rate is set to 50 Hz, which is a typical value to capture the transient effects described above.

A second model is embedded in the diagnosis algorithm and plays the role of the imperfect on-board model. It suffers from model-plant mismatch since the heat transfer processes are poorly modeled with respect to the real engine. As shown in Table 3, only three state variables are involved in this second model. They are related to the spool inertia and to a bulk heat transfer in the hpt.

Heat transfer processes are the slowest dynamics in a turbine engine and they quite strongly influence the transient response of the engine (see Ref. [13]). Considering the present application, the heat transfer is placed on the hpt since it is the hottest part of the engine; therefore, the thermal effects are expected to be more important than in other components. Moreover, the observability of the hpt thermal state is satisfactory with the selected sensor suite (see Ref. [10]).

Modeling the Bias. The methodology for bias modeling described in a previous section is applied to the turbofan layout. The task of bias modeling is obviously application dependent. Reported here are the main issues of the process for the real engine and on-board model setup.

The first step is to build a database of residuals for the healthy engine, which will serve as a learning set for determining the bias model. Figure 4 depicts the fuel flow trajectory input to the real engine and the on-board model. In this contribution, the engine model is run in open loop; therefore, the set point is specified in terms of fuel flow rather than fan speed or engine pressure ratio. For reference, the lowest fuel flow value (slightly less than 0.2 kg/s) corresponds to the ground idle rating, and the greatest one (slightly higher than 1.2 kg/s) gives the take-off power rating. The sequence is 1900 s long so that the database contains 95,000 samples (per sensor). Other scenarios could be added to the database.

Table 1 Sensor configuration and assumed uncertainty

Label	Uncertainty
T_{13}	±2 K
P_{13}	±100 Pa
T_3	±2 K
P_3	±5000 Pa
N_{lp}	±6 rpm
N_{hp}	±12 rpm
T_6	±2 K

Table 2 State variables for the real engine

Label	Description
N_{lp}	Low pressure spool rotational speed
N_{hp}	High pressure spool rotational speed
T_{m3b}	hpc blade temperature
T_{m3c}	hpc casing temperature
T_{m4b}	Combustion chamber casing temperature
T_{m42b}	hpt blade temperature
T_{m42c}	hpt casing temperature

Table 3 State variables for the on-board model

Label	Description
N_{lp}	Low pressure spool rotational speed
N_{hp}	High pressure spool rotational speed
T_{m42}	hpt metal temperature

[4] A Brite/Euram project for on-board identification, diagnosis, and control of turbofan engine.

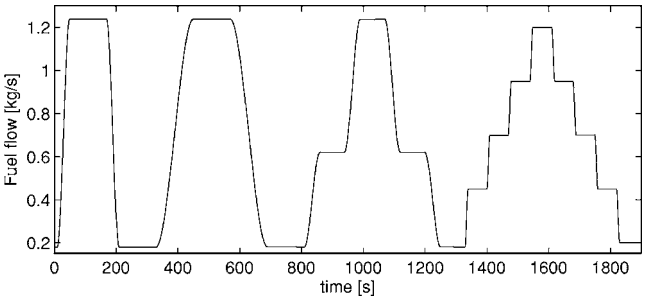

Fig. 4 Fuel flow profile for learning set generation

The mismatch between the real engine and the on-board model appears in Fig. 5, where the normalized root mean square error (NRMSE) is plotted for each sensor. The NRMSE for the ith sensor is defined according to

$$\mathrm{NRMSE}(i) = \sqrt{\frac{1}{n-1}\sum_{k=1}^{n}\frac{(\mathbf{y}_k(i)-\hat{\mathbf{y}}_k(i))^2}{\mathbf{R}_\mathbf{y}(i,i)}} \tag{9}$$

As can be seen in Fig. 5, the NRMSE should be equal to 1 if the on-board model were perfect (white bars). Indeed, in that case, the only source of variation in the response of the real engine and the on-board model is the sensor noise. For the incomplete on-board model considered in this application (gray bars), it can be seen that the prediction for T_{13} is quite faithful; modeling errors, however, have a significant effect on the other measurements and particularly on T_3. Note that the T_3 prediction error could be reduced by introducing heat transfer on the hpc.

Now, the job consists in defining a model for the residuals from the real and BCM-off data. Plotted in Fig. 6 is the cloud of T_3 residuals (black circles) with respect to TI for the operation of the engine under the inputs of Fig. 4.

After examining the residual cloud of each measurement, it was decided to split the TI axis into three distinct regions and to apply a quadratic least-squares fit on the data to determine the mean bias

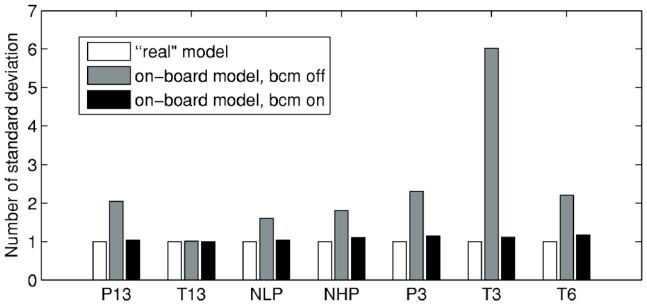

Fig. 5 Model-plant mismatch

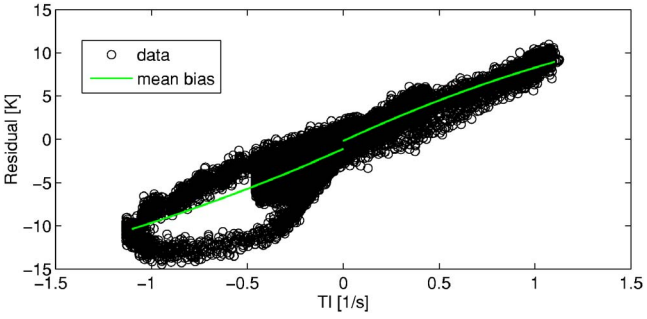

Fig. 6 Mean bias extraction for T_3

Table 4 Summary of the bias model

Region	Mean bias	Covariance matrix
$TI_k > \mathrm{TI}^\star$	$\mathbf{b}_k = \mathbf{p1}\mathrm{TI}_k^2 + \mathbf{p2}\mathrm{TI} + \mathbf{p3}$	$\mathbf{R}_{\mathbf{b},\mathbf{k}}$ per Algorithm 1
$\mathrm{TI}_\mathbf{k} < -\mathrm{TI}^\star$	$\mathbf{b}_k = \mathbf{p4}\mathrm{TI}_k^2 + \mathbf{p5}\mathrm{TI} + \mathbf{p6}$	$\mathbf{R}_{\mathbf{b},k}$ per Algorithm 1
$\lvert TI_k \rvert < \mathrm{TI}^\star$	$\mathbf{b}_k = \mathbf{0}$	$\mathbf{R}_{\mathbf{b},\mathbf{k}} = \mathbf{R}_\mathbf{y}$

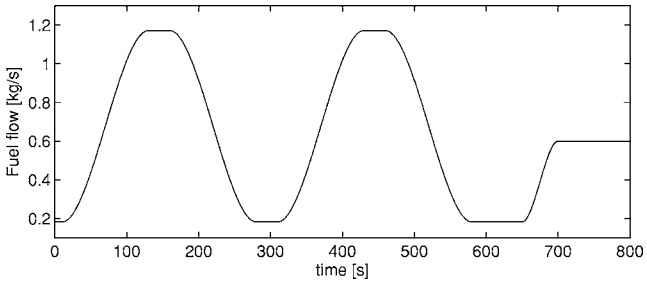

Fig. 7 Fuel flow profile, test bench conditions

(green lines in Fig. 6). The covariance matrices were then computed using Algorithm 1. Higher-order polynomials were rejected since the aim is to extract the global trend in the bias.

The resulting bias model is summarized in Table 4. $\mathrm{TI}^\star$ is a threshold value (set to 10^{-3} in this application) that makes operating points with small absolute values of TI considered as steady-state ones. For these operating points, the mean bias is set to zero and the covariance matrix $\mathbf{R}_{\mathbf{b},\mathbf{k}}$ reduces to the original measurement noise covariance matrix $\mathbf{R}_\mathbf{y}$ given the assumption of a perfect steady-state model. The vectors **p1**, **p2**, **p3** and **p4**, **p5**, **p6** are the coefficients of the quadratic least-squares fit for the $\mathrm{TI} > \mathrm{TI}^\star$ and $\mathrm{TI} < -\mathrm{TI}^\star$ regions, respectively.

The effect of the BCM on the prediction error can be seen in Fig. 5. The black bars represent the NRMSE for each sensor when the BCM is turned on. Obviously, the simple model defined above enhances the accuracy of the prediction provided by the on-board model as all NRMSEs are closer to unity than when the BCM is disabled (gray bars).

Test-Case A: Diagnosis at Test Bench. To assess the improvements brought by the BCM, the following test case has been developed: It is representative of a maintenance session on a test bench for which sea-level static (SLS), standard day conditions are assumed. The evolution of the fuel flow with respect to time is sketched in Fig. 7. It is an 800 s sequence made of two successive power sweeps between idle and max-continuous regimes, followed by an acceleration between idle and part-power regimes.[5]

Engine deterioration is simulated from the component fault case proposed in Ref. [20]. It consists of a deviation of nearly all health parameters at $t=0$ s with the following magnitude: −1.5% on SW12R, −1.2% on SE12, −1.0% on SW2R, −1.0% on SE2, −2.3% on SW26R, −1.4% on SE26, +0.88% on SW41R, −1.6% on SE41, and −1.3% on SE49.

The evolution of the health parameters identified with the original DEKF (i.e., with the BCM disabled) is plotted in Fig. 8. The health parameters exhibit an erratic behavior. Clearly, little valuable information about the health condition of the engine can be derived from the graphs. The health parameters are used by the DEKF as tuners to drive the residuals to zero (on average). The health parameters of the hpc and both turbines seem to be particularly sensitive to the model-plant mismatch.

When the BCM is enabled, the identification of the health parameters is depicted in Fig. 9. The improvement with respect to the disabled-BCM case is obvious. The health parameters do not

[5]Recall that the engine is open loop, fuel flow piloted.

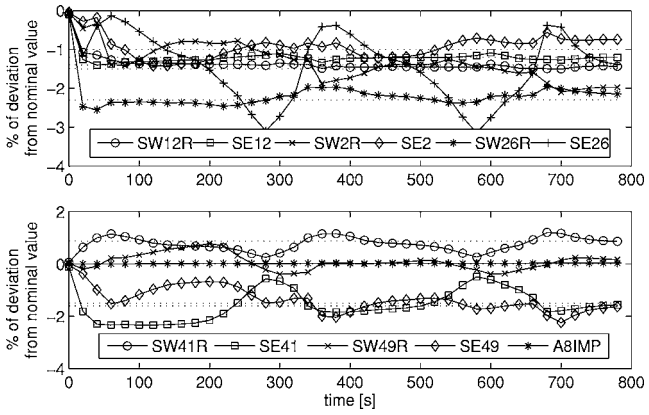

Fig. 8 Diagnosis with BCM disabled

wander according to the transient but converge to their actual value, and the actual condition of the engine can be stated. About 300 s is required to converge to the actual engine health as can be noted on the lower graph reporting the health parameters of the hot section. The small variations in SW26R, SE26, and SW41R are due to the remaining modeling error on T_3 (see Fig. 5).

To underline the originality of our approach that models the mean bias level, and also the uncertainty associated with this bias (through the covariance matrix $\mathbf{R}_{\mathbf{b},\mathbf{k}}$), Fig. 10 depicts the identification of the hpt degradation when using a hybrid BCM setting. The mean bias is computed based on the model presented in Table 4, but the covariance matrix of the measurement is set to $\mathbf{R}_{\mathbf{b},\mathbf{k}} = \mathbf{R}_{\mathbf{y}}$, whatever the TI value is. In doing so, no information about the accuracy of the bias $\mathbf{b}_k$ is transmitted to the DEKF. This corresponds to the assumption that $\mathbf{b}_k$ perfectly matches the model bias.

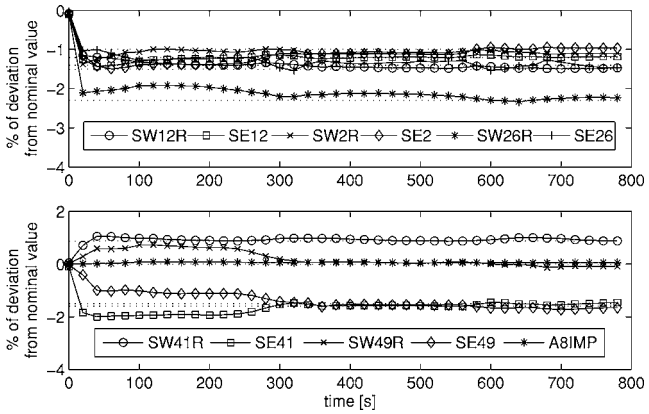

Fig. 9 Diagnosis with BCM enabled

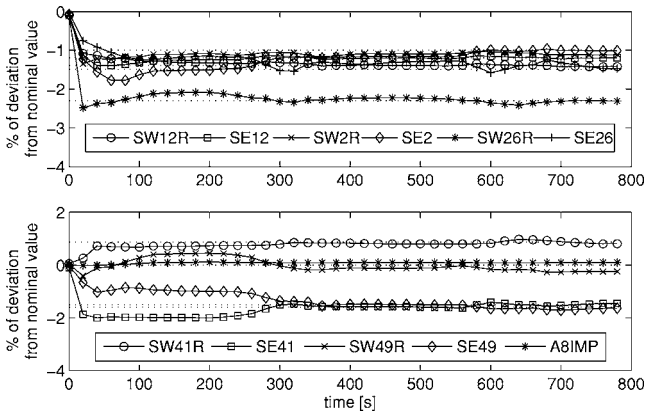

Fig. 10 Diagnosis with hybrid BCM

These results are much better than those presented in Fig. 8 where the BCM was totally disabled. This hints at the fact that the mean bias has indeed the most disruptive effect on the diagnosis algorithm. Yet, some instabilities are still present in Fig. 10, which disappear when the covariance matrix $\mathbf{R}_{\mathbf{b},\mathbf{k}}$ is used (i.e., in Fig. 9). This can readily be seen by comparing the smoothness of the curves between Figs. 10 and 9.

From this last result, it can be concluded that even if the modeling of the bias is quite simple and not always very accurate, taking the uncertainty in the bias into account can improve the quality of diagnostics. Hence, the role of the covariance matrix $\mathbf{R}_{\mathbf{b},\mathbf{k}}$ in the Kalman filter algorithm is to deemphasize the influence of the residuals on the health parameter update when a model bias is likely to be expected or when our knowledge about the bias is not very accurate.

Adapting the Bias Compensation Module to Non-Sea-Level Static Conditions. In the previous subsection, the positive effect of the BCM on the diagnosis algorithm has been demonstrated. The diagnosis was performed in the same atmospheric conditions as for the extraction of the bias model (i.e., SLS conditions). Practically, it is indeed difficult to collect biases outside of a pass-off test. Hence, it would be highly valuable to use the predefined BCM for any other operating conditions.

The extension of the BCM to the whole flight envelope of the engine is nearly immediate by having recourse to the concept of corrected parameters, which relies on similarity laws and first-order approximation of the gas turbine aerothermodynamic processes. The basic idea behind similarity laws is to define dimensionless groups of parameters that are associated with the flow field in the engine. Those corrected parameters allow a comparison, generally on a Mach number basis, of the performance of the engine operating under different atmospheric conditions. As a reminder, the general expression for the corrected parameter X is given by

$$X^{co} = \frac{X}{\theta^a \delta^b} \tag{10}$$

where $\theta = T_2/T_{\text{ref}}$, $\delta = P_2/P_{\text{ref}}$, $T_{\text{ref}} = 288.15$ K, and $P_{\text{ref}} = 101{,}325$ Pa.

Parameter correction is a common practice in the gas turbine community, and the theoretical values of the exponents a and b for the steady-state and transient variables of interest can be found in many references (See, for instance, Refs. [21,22].) Yet, additional physical phenomena, such as the modification of the thermophysical properties of the working fluid, Reynolds number effects, and geometrical effects (e.g., clearance and blade untwist), make the engine behavior deviate from the assumptions of the Mach number similarity. Hence, a fine tuning of the a and b exponents for each parameter involved in the BCM should be carried out as explained in Ref. [23] for improved accuracy.

The following operations allow the adaptation of the original BCM to any ambient conditions.

1. Get current state derivatives from the on-board model.
2. Compute corrected state derivatives.
3. Build corrected TI from corrected state derivatives according to Eq. (8).
4. Call the BCM with corrected TI on input; get $\mathbf{b}_\mathbf{k}$ and $\mathbf{R}_{\mathbf{b},\mathbf{k}}$ on output.
5. "Decorrect" $\mathbf{b}_\mathbf{k}$ to current ambient conditions.

As can be noted in item 5, the mean bias $\mathbf{b}_\mathbf{k}$ is decorrected, but not its associated covariance matrix. Hence, we implicitly assume that the uncertainty in the mean bias is constant for different ambient conditions. It means that the highest contribution to the measure-

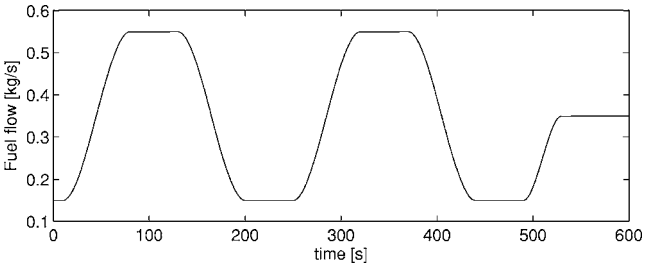

Fig. 11 Fuel flow profile, cruise conditions

ment covariance is the measurement noise (the magnitude of which is independent of the operating conditions) rather than the uncertainty in the mean bias. It is worth mentioning that these adaptations are applied outside of the core of the BCM, which is thereby not affected at all.

Test-Case B: Validation for Non-Sea-Level Static Conditions. To validate the correction procedure applied to the BCM, a second test case has been designed. Cruise flight conditions (altitude=10,800 m, flight Mach number=0.82) are assumed. The simulated fault is the same engine deterioration as previously described. The open-loop scheduled fuel flow is plotted in Fig. 11 and is similar in shape to the one of test-case A. The reader will certainly notice the simplified nature of this test case, which is intended here for validation purposes only.

Figure 12 sketches the evolution of the identified health parameters when using the corrected BCM. It can be seen that the engine deterioration is accurately assessed (localization and magnitude). As for the identification under SLS conditions, one can notice slight oscillations in SW26R, SE26, and SW41R due to the remaining prediction error in T_3.

For the considered application, it can thus be stated that first-order corrections brought by corrected parameters appear to be sufficient to use the original BCM, determined from SLS data, for monitoring the condition of the engine under other ambient conditions. It can be explained by the fact that the shortcomings of the model are intrinsic and hence do not depend on the atmospheric conditions. The proposed methodology for bias compensation is therefore very appealing, given that it is much easier to collect biases on the test bench than in flight.

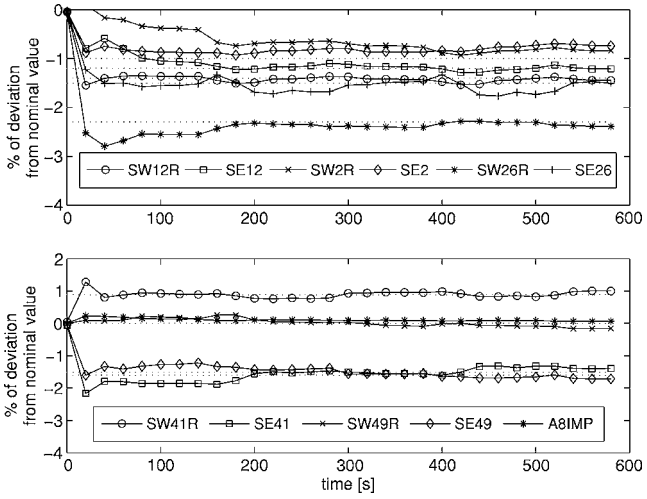

Fig. 12 Diagnosis with the corrected BCM, cruise conditions

Discussion

The enhancement of the diagnosis capabilities possible with the BCM in the presence of model-plant mismatch has been discussed in the previous section. However, some more issues have to be discussed to complete the analysis of the results.

The first question is related to the continuity of the bias model with respect to the TI. In this paper, three different TI patterns have been defined, and both the mean bias **b** and the covariance $\mathbf{R_b}$ are discontinuous between adjacent patterns. No instabilities of the DEKF have been noticed so far. It is supposed that the DEKF is unaware of those discontinuities because it is not sensitive to the derivative of the bias model. TI segments might be developed to match the specific acceleration and deceleration features of a particular control system (fuel control and actuators).

Another open question is linked to the complexity of the bias model. A very simple piecewise quadratic bias model has been considered in this application, and it has been shown to be sufficient for providing a rather accurate diagnosis. However, more complex models, such as neural networks, could be tested. Another research direction concerning the complexity of the bias model is the definition itself of that model. Throughout the paper, it has been assumed that the bias model only depends on the TI. A formulation with two input arguments such as TI and its time derivative, or TI and a state index, should be investigated. Data mining techniques could be used to this end.

An essential work is to further investigate the applicability of the BCM, defined from SLS mismatch data, throughout the flight envelope. This approach has been proven successful for the particular application considered in the present study, somewhat simplified with respect to real-world situations. Indeed, new-generation engines are more complex, from the standpoint of architecture as well as control systems. The structure of the model-plant mismatch might then depend on the ambient and operating conditions, too. In that case, collection of mismatch data in an altitude test facility and/or on a flying test bed would become mandatory for a complete determination of the BCM.

Finally, some more studies still need to be undertaken concerning robustness issues. Those are twofold: First, the capability of the algorithm to cope with sensor malfunctions is still under development. Second, the applicability of the methodology presented herein has to be verified for other modeling errors such as sensor/actuator dynamics, fluid dynamics effects, bleed air and power take-offs, and especially biased steady-state engine modeling.

Conclusion

The ability to perform a reliable diagnosis in transient operation with an imperfect model of a gas turbine has been investigated. A methodology has been developed to compensate for the bias induced by model-plant mismatch by treating it as a pseudo-Gaussian variable. The improvements to the quality of the diagnosis with the new algorithm have been demonstrated on simple, but realistic test cases.

More specifically, it has been pointed out that taking into account both the mean bias and its related uncertainty improves the identification procedure in terms of stability and accuracy even with a rather simple structure of the bias model. The BCM, built from data gathered on a test bench, has also shown interesting generalization properties in order to carry out health monitoring for other ambient conditions. A simple approach relying on corrected parameters addresses this issue for the simulated test data available.

Acknowledgment

The authors wish to thank the reviewers and the Associate Editor for their valuable comments during the review process.

Nomenclature

$\hat{\mathbf{a}}$ = estimation of an unknown variable $\mathbf{a}$
A8IMP = nozzle exit area (nominal value: 1.4147 m^2)
$\mathbf{b}_k$ = mean of the model bias
EGT = exhaust gas temperature
k = discrete time index
P_i = total pressure at station i
$\mathbf{R}_{\mathbf{b},\mathbf{k}}$ = covariance matrix of the model bias
SEi = efficiency scaler of the component whose entry is located at section i (nominal value: 1.0)
SWiR = flow capacity scaler of the component whose entry is located at section i (nominal value: 1.0)
T_i = total temperature at station i
$\mathbf{u}_k$ = actual command parameters
$\mathbf{v}_k$ = actual external disturbances
$\mathbf{w}_k$ = actual but unknown health parameters
$\mathbf{x}_k$ = actual but unknown state variables
$\mathbf{y}_k$ = observed measurements
$\boldsymbol{\epsilon}_k$ = measurement noise vector
$\boldsymbol{\nu}_k$ = process noise vector
$\mathcal{N}(\mathbf{m},\mathbf{R})$ = a Gaussian probability density function with mean $\mathbf{m}$ and covariance matrix $\mathbf{R}$

References

[1] Volponi, A. J., 2003, *Foundation of Gas Path Analysis (Part I and II)*, Gas Turbine Condition Monitoring and Fault Diagnosis, Lecture Series No. 2003-01, von Karman Institute for Fluid Dynamics, Brussels, Belgium.
[2] Kalman, R. E., and Bucy, R. S., 1961, "New Results in Linear Filtering and Prediction Theory," ASME J. Basic Eng., **83**, pp. 95–107.
[3] Dewallef, P., 2005, "Application of the Kalman Filter to Health Monitoring of Gas Turbine Engines: A Sequential Approach to Robust Diagnosis," Ph.D. thesis, University of Liège.
[4] Urban, L. A., 1972, "Gas Path Analysis Applied to Turbine Engine Condition Monitoring," Eighth Joint Propulsion Specialist Conference, Paper No. 72-1082.
[5] Duponchel, J.-P., Loisy, J., and Carillo, R., 1992, "Steady and Transient Performance Calculation Method for Prediction, Analysis and Identification," Paper No. AGARD LS-183.
[6] Grönstedt, T., 2005, "Least Squares Based Transient Nonlinear Gas Path Analysis," ASME Paper No. GT2005-68717.
[7] Ogaji, S., Li, Y., Sampath, S., and Singh, R., 2003, "Gas Path Fault Diagnosis of a Turbofan Engine from Transient Data Using Artificial Neural Networks," ASME Paper No. GT2003-38423.
[8] Simon, D., and Simon, D. L., 2003, "Aircraft Turbofan Engine Health Estimation Using Constrained Kalman Filtering," ASME Paper No. GT2003-38584.
[9] Dewallef, P., and Léonard, O., 2003, "On-Line Performance Monitoring and Engine Diagnostic Using Robust Kalman Filtering Techniques," ASME Paper No. GT2003-38379.
[10] Borguet, S., Dewallef, P., and Léonard, O., 2005, "On-Line Transient Engine Diagnostics in a Kalman Filtering Framework," ASME Paper No. GT2005-68013.
[11] Volponi, A. J., 2005, "Use of Hybrid Engine Modeling for On-Board Module Performance Tracking," ASME Paper No. GT2005-68169.
[12] RTO, 2002, "Performance Prediction and Simulation of Gas Turbine Engine Operation," Research and Technology Organisation, Technical Report No. 44.
[13] Nielsen, A. E., Moll, C. W., and Staudacher, S., 2005, "Modeling and Validation of the Thermal Effects on Gas Turbine Transients," ASME J. Eng. Gas Turbines Power, **127**, pp. 564–572.
[14] Wan, E., and van der Merwe, R., 2001, "The Unscented Kalman Filter," *Kalman Filtering and Neural Networks*, Wiley Series on Adaptive and Learning Systems for Signal Processing, Communications and Control, Wiley, New York.
[15] Nelson, A. T., 2000, "Nonlinear Estimation and Modeling of Noisy Time Series by Dual Kalman Filtering Methods," Ph.D. thesis, Oregon Graduate Institute of Technology.
[16] Bishop, C. M., 1995, *Neural Networks for Pattern Recognition*, Clarendon, Oxford.
[17] Roth, B. A., Doel, D. L., and Cissell, J. J., 2005, "Probabilistic Matching of Turbofan Engine Performance Models to Test Data," ASME Paper No. GT2005-68201.
[18] Cerri, G., Borghetti, S., and Salvini, C., 2005, "Inverse Methodologies for Actual Status Recognition of Gas Turbine Components," ASME Paper No. PWR2005-50033.
[19] Stamatis, A., Mathioudakis, K., Ruiz, J., and Curnock, B., 2001, "Real-Time Engine Model Implementation for Adaptive Control and Performance Monitoring of Large Civil Turbofans," ASME Paper No. 2001-GT-0362.
[20] Curnock, B., 2000, "Obidicote Project -WP4: Steady-State Test Cases," Rolls-Royce plc, Technical Report No. DNS62433.
[21] Walsh, P. P., and Fletcher, P., 1998, *Gas Turbine Performance*, Blackwell Science, London.
[22] Volponi, A. J., 1999, "Gas Turbine Parameter Corrections," ASME J. Eng. Gas Turbines Power, **121**, pp. 613–621.
[23] Kurzke, J., 2003, "Model Based Gas Turbine Parameter Corrections," ASME Paper No. GT2003-38234.

Development of Elemental Technologies for Advanced Humid Air Turbine System

Hidetoshi Kuroki
Shigeo Hatamiya
Takanori Shibata
Tomomi Koganezawa
Nobuaki Kizuka
Shinya Marushima

Hitachi Ltd. Power & Industrial Systems
R&D Laboratory,
7-2-1 Omika-cho,
Hitachi-shi 319-1221 Japan

The advanced humid air turbine (AHAT) system improves the thermal efficiency of gas turbine power generation by using a humidifier, a water atomization cooling (WAC) system, and a heat recovery system, thus eliminating the need for an extremely high firing temperature and pressure ratio. The following elemental technologies have been developed to realize the AHAT system: (1) a broad working range and high-efficiency compressor that utilizes the WAC system to reduce compression work, (2) turbine blade cooling techniques that can withstand high heat flux due to high-humidity working gas, and (3) a combustor that achieves both low NO_x *emissions and a stable flame condition with high-humidity air. A gas turbine equipped with a two-stage radial compressor (with a pressure ratio of 8), two-stage axial turbine, and a reverse-flow type of single-can combustor has been developed based on the elemental technologies described above. A pilot plant that consists of a gas turbine generator, recuperator, humidification tower, water recovery system, WAC system, economizer, and other components is planned to be constructed, with testing slated to begin in October 2006 to validate the performance and reliability of the AHAT system. The expected performance is as follows: thermal efficiency of 43% (LHV), output of* 3.6 MW*, and* NO_x *emissions of less than* 10 ppm *at 15% O2. This paper introduces the elemental technologies and the pilot plant to be built for the AHAT system.* [DOI: 10.1115/1.2833490]

Introduction

Gas turbines play a major role in the generation of power and are necessary to both improve thermal efficiency and reduce environmental impact. Presently, a combined cycle system is the most efficient form of power generation, for which thermal efficiency has been improved by increasing the turbine inlet temperature. However, a higher turbine inlet temperature poses the problems of increased NO_x emissions and a shorter service life for hot section parts.

This situation has lead to studies conducted on ways to improve the heat cycle for enhancing thermal efficiency without increasing turbine inlet temperature. Recently, various novel cycles using humid air, such as the humid air turbine (HAT), cascaded humidified advanced turbine (CHAT), REVAP, and TOPHAT have been proposed to improve gas turbine efficiency [1–5].

The AHAT cycle is a system that uses humid air and a heat recovery system, and which offers the advantage of achieving high thermal efficiency without an extremely high combustion temperature, pressure ratio, or an intercooler [6,7]. The AHAT system has been studied as follows: (1) as an experiment with a combustor that burns high-humidity air [8], (2) as an analysis of turbine blade cooling with humid air [9], (3) as a design study on a humidification tower for the AHAT system [10], and (4) as an evaluation of a water recovery system for the AHAT system [11,12]. Based on these studies, a pilot plant and a prototype gas turbine adapted to the AHAT system have been developed. This research is supported by the Agency for Natural Resources and Energy of Japan's Ministry of Economy, Trade and Industry.

Advanced Humid Air Turbine System

Figure 1 shows a concept of the AHAT cycle. The water atomization cooling (WAC) system is set in the compressor's inlet duct from which fine droplets of water are sprayed (see Fig. 2). Some water droplets evaporate at the compressor entrance and cool the inlet air. The remaining droplets evaporate while being compressed in the compressor, thus causing a decrease in the rise in air temperature. The compressed air comes into direct contact with hot water in the humidification tower, thus forming air of high humidity. As a result, the flow rate and specific heat of the working fluid increase, thus increasing turbine generation power. High-humidity air flows into the combustion chamber after being preheated by the turbine exhaust gas with the recuperation heat exchanger. The high-temperature combustion gas discharged after driving the turbine allows the recuperator and economizer to collect exhaust heat. The exhaust gas that exits the economizer contacts directly with the cold-water recovery system to be cooled and the moisture condenses. The exhaust gas that exited the water recovery system is then discharged into the atmosphere from a stack after being heated by the exhaust gas heater.

The cost of AHAT plant installation is less than that of a combined cycle plant because AHAT requires no steam turbine or such related equipment as a condenser.

3 MW-Advanced Humid Air Turbine Pilot Plant

The 3 MW AHAT pilot plant is expected to demonstrate AHAT system performance. Table 1 lists the planned specifications of this pilot plant. Figure 3 shows the development schedule of the pilot plant. The detailed design of the pilot plant began in October 2004. Testing is planned to begin after manufacturing, assembly, procurement, and construction are completed by September 2006. Figure 4 shows the arrangement of the pilot plant. The plant consists of a gas turbine generator, WAC system, recuperator, humidification tower, economizer, and water recovery system. The plant area has been enlarged in consideration of easier accessibility to and maintenance for the pilot plant.

Gas Turbine

A prototype gas turbine adapted to the AHAT system has been developed. The gas turbine, which is fully designed and manufactured by Hitachi, consists of a two-stage radial compressor, two-

Manuscript received June 20, 2006; final manuscript received October 13, 2007; published online March 26, 2008. Review conducted by Dilip R. Ballal.

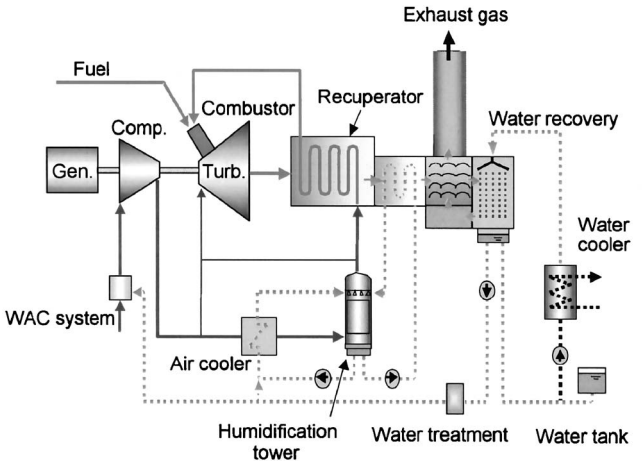

Fig. 1 Schematic of AHAT system

stage axial turbine, and reverse-flow type of single-can combustor. The rotor is supported at both ends by two tilting pad-type bearings, and has one thrust bearing on the compressor side. The ring casing is mounted on a steel frame basement by using two supports.

Special attention has been given to the gas turbine used in the AHAT system as follows: (1) materials should be resistant to dew-point corrosion and steam oxidation, (2) the compressor must achieve both a broader working range and high efficiency due to the large amount of water added by the WAC system and humidification tower, (3) the turbine blades must tolerate large heat flux from the humid main flow gas, and (4) the combustor must deal with both flame stability and the reduction of NO_x emissions.

Materials

Special attention is paid to the resistance of gas turbine materials to dew-point corrosion and steam oxidation caused by humid air in the AHAT system.

The first-stage and second-stage compressor impellers are made of AISI S17400. The first-stage and second-stage turbine wheels are made of Inconel718. Both AISI S17400 and Inconel718 feature superior resistance to corrosion and oxidation, coupled with high tensile strength.

The turbine blades are made of a nickel-based superalloy that is characterized by superior resistance to corrosion at high temperature, high tensile strength, and high creep strength.

The casing material adopts AISI304 to prevent dew-point corrosion during a long-term suspension in operation.

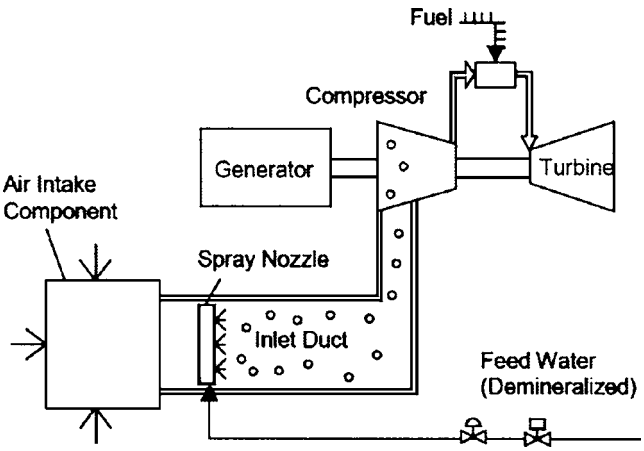

Fig. 2 WAC system

Table 1 Pilot plant specifications

Item	Unit	Value
Output (ISO condition)	kW	3600
Thermal efficiency	%LHV	43
Gas turbine speed	rpm	17,800
Generator speed	rpm	1500
Inlet airflow	kg/s	10
Turbine inlet temperature	°C	1180
Gas turbine exhaust temperature	°C	655
NO_x emissions	ppm	<10

Bore scope inspection and disassembly inspection will be conducted to investigate the status of materials after operation is started.

Compressor

In the AHAT gas turbine, the WAC system and humidifier add a large amount of water to the working air, thus changing the matching point between a compressor and a turbine for dry air. Therefore, the compressor must have a broader working range in addition to high efficiency.

Table 2 lists the specifications of the compressor. The WAC system is set in the inlet duct and supplies 1.0 wt % water into the inlet air. The WAC spray nozzles jointly developed by Hitachi and Kyoritu Gokin provide fine droplets of water (with a Sauter mean diameter of 20 μm or less).

The spray nozzles are set at a distance of about 3 m from the compressor entrance. The distance from the spray nozzle to the compressor entrance and the residence time of water droplets in a small gas turbine are less than those for a large gas turbine, because the installation area is restricted in a practical small gas turbine. Moreover, it is difficult to develop a spray nozzle providing much smaller droplets. Therefore, it is more difficult to evaporate water droplets in a small gas turbine than in a large gas turbine. The cooling efficiency of the WAC system is calculated to evaluate the effects of this system. Figure 5 shows the calculation results of the relationship between the cooling efficiency and the residence time of water droplets. The calculation results indicate that a cooling efficiency above 90% can be achieved by oversaturation spraying. Moreover, such inlet conditions as ambient temperature and humidity have little influence on cooling efficiency. The 1.0 wt % WAC achieves a 9% increase in output and 2% increase in thermal efficiency at 15°C in the 3 MW AHAT system.

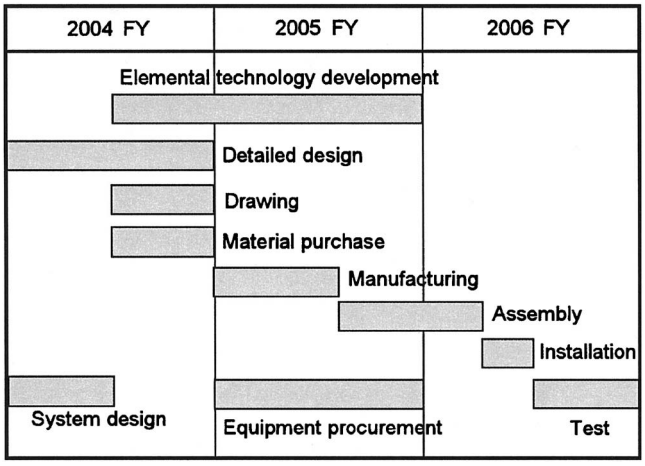

Fig. 3 Development schedule of AHAT pilot plant

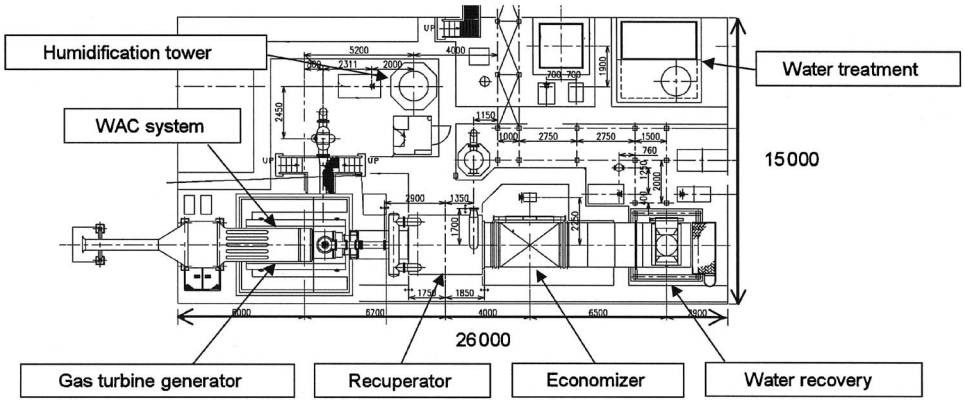

Fig. 4 3 MW AHAT pilot plant arrangement

WAC shifts the matching point between a compressor and a turbine. Therefore, the velocity triangle of the compressor is designed in consideration of the WAC effect, thus achieving both high efficiency and enough surging margin.

In the AHAT cycle, the compressor-discharged air retains the humidity and heat expelled by the humidifier and recuperator. Therefore, a relatively larger turbine (i.e., larger than the compressor) is needed. In this way, it is possible to make the outer diameter of the compressor diffuser larger than that of the impeller, thus reducing the velocity at the first-stage and second-stage exits, and to reduce flow loss. The ratio of the diffuser's outer diameter to that of the impeller is 2.0 (at the first stage) and 2.2 (at the second stage) in this compressor, while previous compressors using dry air had respective ratios from 1.7 to 1.9.

In the first stage, the volume flow is so large that the relative velocity at the entrance is transonic. Therefore, the first-stage impeller adopts splitter blades and small camber angle blades in order to reduce the Mach number at the impeller entrance and suppress the acceleration of flow, thus reducing shockwave loss at the entrance (see Fig. 6). In the second stage, full blades are adopted in the impeller due to the subsonic relative velocity.

A low-solidity diffuser without a throat area is adopted. As a result, there is no choke flow that widens the working range. In the second stage, a tandem diffuser is adopted in addition to the low-solidity diffuser to obtain a broad working range. Figure 7 shows the compressor characteristics of the tandem diffuser and previous channel diffuser (see Fig. 8). The tandem diffuser can be effectively used, especially at startup. The channel diffuser has a narrow working range of about 6% at 50% speed, but the tandem diffuser can improve the working range up to 25%. Moreover, the tandem diffuser increases compressor efficiency by 0.5% at normal operating speed.

Table 2 Compressor specifications

Item	Unit	Value
Compressor type	—	two-stage radial
Inlet airflow	kg/s	10.1
Pressure ratio	—	8.0
Adiabatic efficiency	%	83
Discharge temperature	°C	260
WAC	wt %	1.0

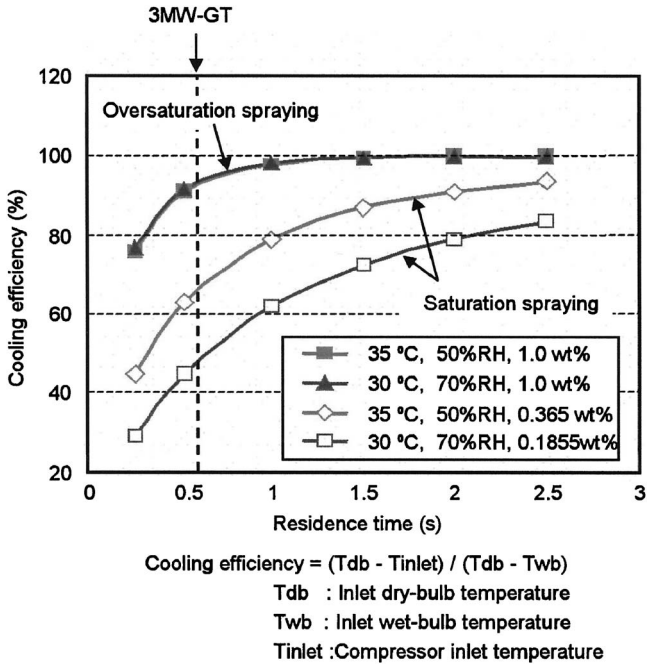

Fig. 5 Relationship between cooling efficiency of WAC and residence time

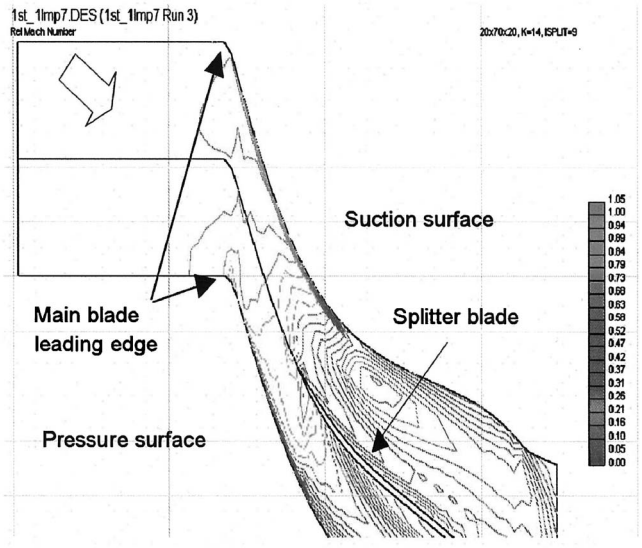

Fig. 6 Relative Mach number distribution of first-stage impeller

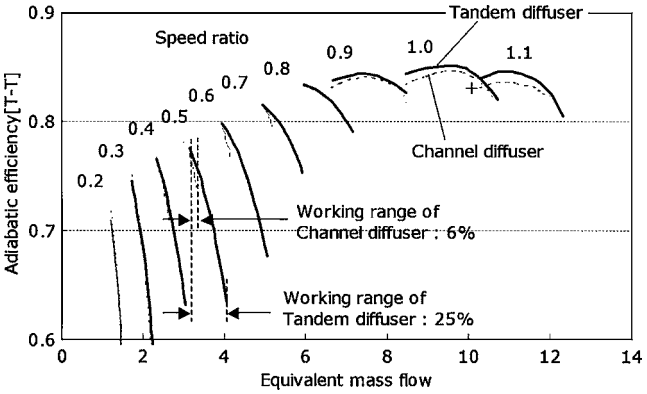

Fig. 7 Comparison of compressor characteristics between tandem and channel diffusers

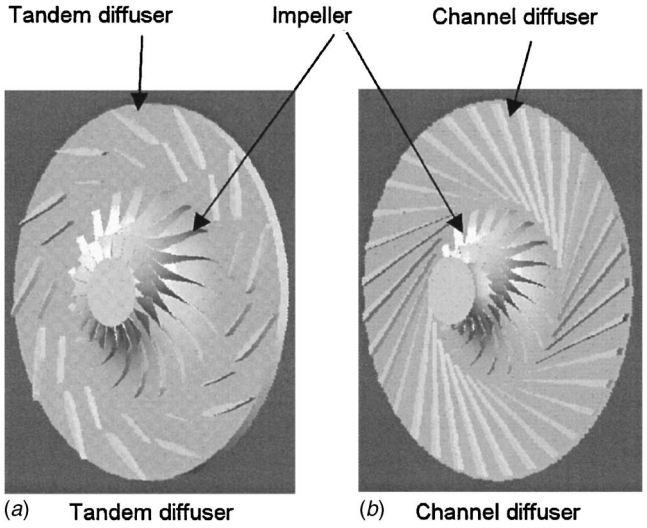

Fig. 8 Second-stage diffuser

Turbine

In the AHAT cycle, the turbine blades have about 20% larger heat flux than that of the cycle using dry air due to such humid air properties as specific heat, gas constant, and thermal conductivity. Consequently, the required cooling flow rate in the AHAT cycle increases, while the thermal efficiency of the gas turbine decreases. There are two ways of solving this problem: (1) using humid air as the coolant or (2) improving the cooling structure.

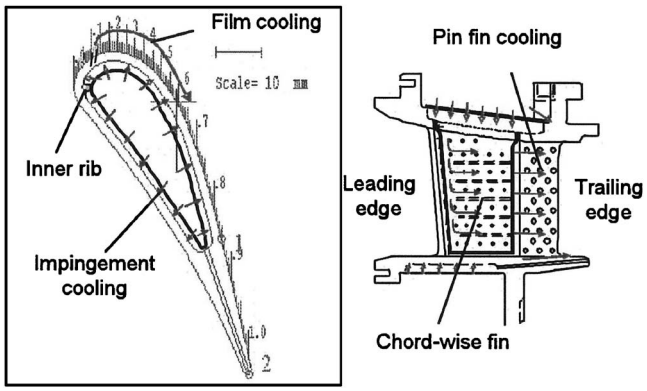

Fig. 9 Schematic of first-stage stator blade

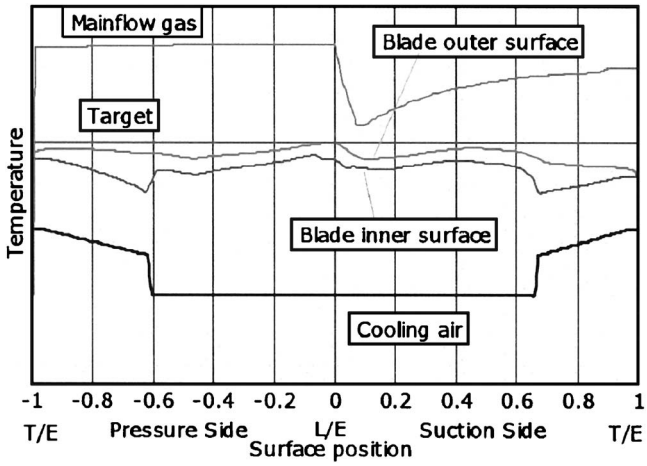

Fig. 10 Calculation result of mean section temperature in first-stage stator blade

Though it is effective to use humid air as a coolant, such use necessitates a more complicated structure for supplying cooling air to the blades. Therefore, this 3 MW class gas turbine does not use humid air for cooling, but adopts cooling reinforcement through an improved cooling structure.

Figure 9 shows the cooling schematic diagram of the first-stage stator blade. The blade is cooled by both impingement cooling and film cooling. The inner rib on the leading edge and the chordwise fin on the inner surface are set to reinforce impingement cooling. At the trailing edge, pin fin cooling is adopted in consideration of both cooling capability and casting. Figure 10 shows the calculation result (using in-house calculation code) of the mean section in the first-stage stator blade. "L/E" and "T/E" stand for "leading edge" and "trailing edge." The blade temperature almost satisfied the target temperature.

Figure 11 shows the cooling schematic diagram of the first-stage rotor blade. The blade employs a serpentine cooling passage equipped with V-shaped staggered turbulence promoter ribs. At the trailing edge, pin fin cooling is used for the first-stage stator blade. The calculation result shown in Fig. 12 indicates that the blade temperature is below the target temperature.

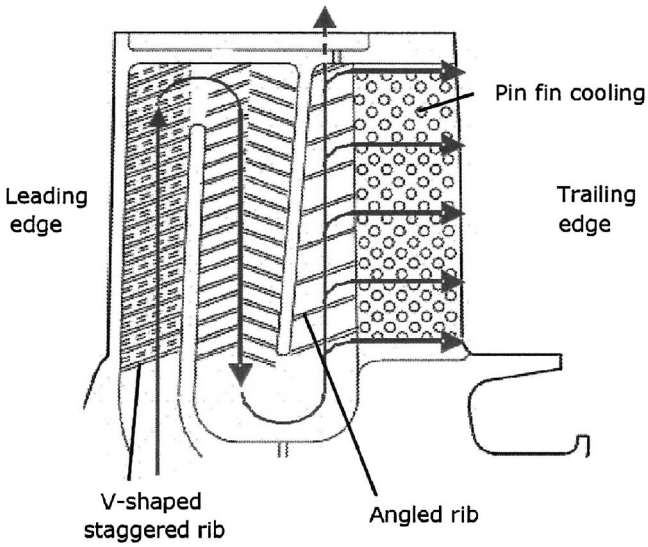

Fig. 11 Schematic of first-stage rotor blade

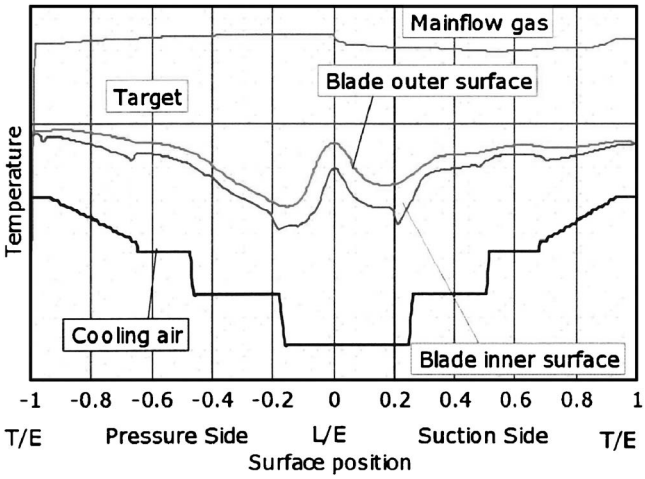

Fig. 12 Calculation result of mean section temperature in first rotor blade

The second-stage stator blade uses both impingement cooling and conventional cooling. The second-stage rotor blade is not cooled. The blade metal temperature during operation will be measured during verification testing.

Combustor

Table 3 lists the operating conditions of the combustor under a base load in the AHAT cycle. The conditions in the AHAT cycle are characterized by both high temperature (629°C) and high humidity (17.6 wt %, 22.1 vol %) air. The important problem to be addressed is coping with both the low NO_x emissions and flame stability under the AHAT cycle conditions.

Figure 13 shows the combustor burner. The so-called cluster burner consists of about 230 fuel nozzles, an air holes plate, and a fuel header. Fuel is discharged from the fuel nozzles into the center of the air holes so that coaxial jets of fuel are encircled by air. The cluster burner can mix air and fuel effectively within a short length and (see Fig. 14). Moreover, there is no possibility of flashback phenomena occurring since fuel in the premixture is separated from the air. This burner has been developed based on the one used for the dimethyl ether (DME) gas turbine [13].

The combustion fuel supply system operates in one of four modes: (1) supplying fuel to the center nozzles (F1 section shown in Fig. 13 from startup until reaching full speed), (2) fueling (F1+F2) sections to a 25% load, (3) fueling (F1+F2+F3) sections to about a 70% load (with humidification by the saturator starting from a 50% load), or (4) supplying fuel to all nozzles (the (F1+F2+F3+F4) sections) at about a 70% load or higher. The full-size combustor test has been conducted under the conditions listed in Table 3 to determine the characteristics of combustion. Figure 15 shows the experimental results of (F1+F2+F3) mode combustion under dry and humid conditions and (F1+F2+F3 +F4) mode combustion under humid condition. The fuel/air ratio

Table 3 Combustor conditions

Item	Unit	AHAT conditions	Test conditions
Airflow	kg/s	10.4	7
Air pressure	MPa	0.78	0.5
Air temperature	°C	629	629
Firing temperature	°C	1180	1180
Air humidity	wt %	17.6	max 15.4
	vol %	22.1	max 19.3
Fuel/air ratio	—	0.0170	parameter
Fuel	—	LNG	LNG

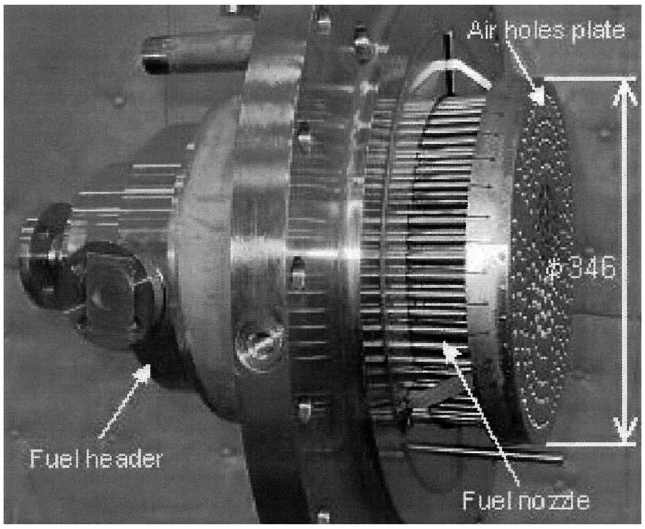

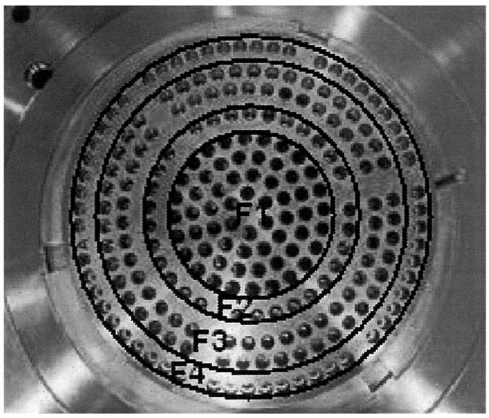

Fig. 13 Cluster burner

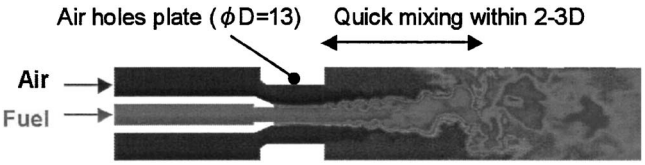

Fig. 14 Mixture analysis result of coaxial jet cluster nozzle burner

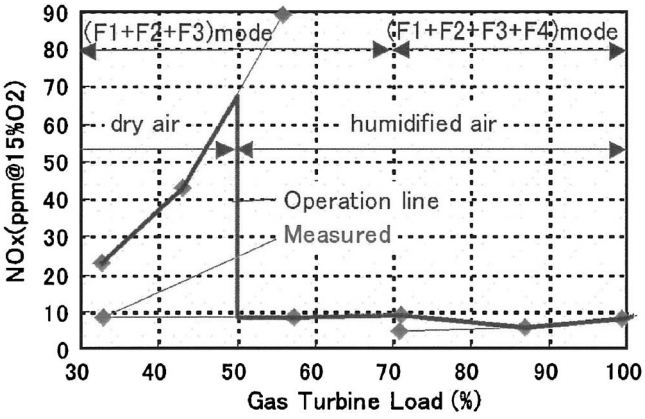

Fig. 15 NO_x emission as function of gas turbine load

used as parameter is converted to the gas turbine load shown in Fig. 15. The blue line indicates the operation line of the gas turbine. The NO_x emissions are below 10 ppm under a load above 50% due to the start of humidification. Moreover, the combustor has good characteristics in terms of a stable flame condition from startup to reaching the base load. According to this test, this combustor can be used for the AHAT system meeting the set targets.

Conclusions

The elemental technologies for the AHAT system were developed as follows:

(1) A compressor using the WAC system with a broad working range and high efficiency. A cooling efficiency above 90% was calculated for WAC employing oversaturation spraying. The 1.0 wt % WAC increases output by 9% and thermal efficiency by 2% at 15°C in the 3 MW AHAT system.
(2) The first-stage impeller adopts splitter blades and small camber angle blades to reduce shockwave loss at the entrance. A low-solidity diffuser and tandem diffuser were adopted to widen the working range and increase compressor efficiency.
(3) The turbine blades were designed to withstand high heat flux from the high-humidity gas. The blade temperature calculated satisfies the target temperature.
(4) The combustor test results indicated that NO_x emissions were below 10 ppm when under a load above 50% and without the possibility of an unstable flame condition occurring.

A 3 MW AHAT pilot plant using the elemental technologies above has been developed and will be tested beginning in October 2006.

Acknowledgment

This research was made possible with the assistance of the Agency for Natural Resources and Energy of Japan's Ministry of Economy, Trade and Industry. The authors wish to express their deep gratitude to those concerned.

References

[1] Mori, Y., and Nakamura, H., 1983, "A Highly Efficient Regenerative Gas Turbine System by New Method of Heat Recovery With Water Injection," IGTC, Tokyo.
[2] Rao, A. D., 1991, "A Comparison of Humid Air Turbine (HAT) Cycle and Combined-Cycle Power Plants," EPRI IE-7300.
[3] Nakhamkin, M., 1995, "The Cascaded Humidified Advanced Turbine (CHAT)," ASME Cogen-Turbo.
[4] De Ruyck, J., et al., 1997, "REVAP CYCLE: A New Evaporative Cycle Without Saturation Tower," Trans. of the ASME, **119**, pp. 893–897.
[5] van Liere, J., 1998, "The TOPHAT Cycle," IERE Workshop, Kobe, Japan.
[6] Hatamiya, S., 2002, "Gas Turbine Power Generation Technology Utilizing High Humidity Air," The Thermal and Nuclear Power, **53**(9), pp. 1031–1038.
[7] Nakamura, H., and Yamamoto, K., 1992, "HAT (Humid Air Cycle) Cycle," The Thermal and Nuclear Power, **43**(12), pp. 1587–1592.
[8] Koganezawa, T., Inoue, H., and Kobayashi, N., 2002, "Experimental Study on Diffusion Flame Combustor for Advanced Humid Air Turbine," *JSME Annual Meeting*, Vol. 4, pp. 187–188.
[9] Higuchi, S., Hatamiya, S., Seiki, N., and Marushima, S., 2003, "A Study of Performance on Advanced Humid Air Turbine Systems," IGTC-03 TS-090.
[10] Araki, H., Higuchi, S., Marushima, S., and Hatamiya, S., 2005, "Design Study of a Humidification Tower for the Advanced Humid Air Turbine System," ASME GT2005–68671.
[11] Numata, S., Yokota, O., and Hatamiya, S., 2002, "Analysis Condensation Heat Transfer to Water Spray for Water Recovery System," *JSME 39th National Heat and Mass Transfer Symposium*, pp. 661–662.
[12] Hatamiya, S., Araki, H., and Higuchi, S., 2004, "An Evaluation of Advanced Humid Air Turbine System With Water Recovery," ASME GT2004-54031.
[13] Saitou, T., Miura, K., Inoue, H., and Kobayashi, N., 2005, "Performance Demonstration of the Full Size Multi Cluster Combustor for DME under Real Engine Condition," ASME GT2005-68647.

Qualitative and Quantitative Comparison of Two Promising Oxy-Fuel Power Cycles for CO_2 Capture

Wolfgang Sanz
e-mail: wolfgang.sanz@tugraz.at

Herbert Jericha

Bernhard Bauer

Emil Göttlich

Institute for Thermal Turbomachinery and Machine Dynamics,
Graz University of Technology,
Graz 8010, Austria

Since the Kyoto conference, there is a broad consensus that the human emission of greenhouse gases, mainly CO_2, has to be reduced. In the power generation sector, there are three main alternatives that are currently studied worldwide. Among them oxy-fuel cycles with internal combustion with pure oxygen are a very promising technology. Within the European project ENCAP (enhanced CO_2 capture) the benchmarking of a number of novel power cycles with CO_2 capture was carried out. Within the category oxy-fuel cycles, the Graz Cycle and the semiclosed oxy-fuel combustion combined cycle (SCOC-CC) both achieved a net efficiency of nearly 50%. In a second step, a qualitative comparison of the critical components was performed according to their technical maturity. In contrast to the Graz Cycle, the study authors claimed that no major technical barriers would exist for the SCOC-CC. In this work, the ENCAP study is repeated for the SCOC-CC and for a modified Graz Cycle variant as presented at the ASME IGTI Conference 2006. Both oxy-fuel cycles are thermodynamically investigated based on common assumptions agreed upon with the industry in previous work. The calculations showed that the high-temperature turbine of the SCOC-CC plant needs a much higher cooling flow supply due to the less favorable properties of the working fluid. A layout of the main components of both cycles is further presented, which shows that both cycles rely on the new designs of the high-temperature turbine and the compressors. The SCOC-CC compressor needs more stages due to a lower rotational speed but has a more favorable operating temperature. In general, all turbomachines of both cycles show similar technical challenges and are regarded as feasible. [DOI: 10.1115/1.2800350]

Introduction

In the last two years, global warming, environmental change, and destruction of natural resources—such as water and forest reserves—have reached exasperating speed. Very little doubt remains regarding the effect and the extent of anthropologic contribution. Countermeasures should be put into effect quickly and in all realms of human activity.

The main reason—the worldwide ever rising emission of greenhouse gases to the atmosphere—has been recognized since 1988 by the 700 scientists who formulated the Call of Action of the Toronto Conference. Other events have followed, and today the Kyoto Goal of reducing the global greenhouse gas emissions by a substantial amount compared to the 1990 emissions is acknowledged by the majority of governments around the world. The combustion generated gas CO_2 and the very active biologically emitted methane (melting permafrost) are the most important contributors to atmospheric change and global warming.

Within the European Union (EU), there is a strong pressure on utilities and the industry to reduce the CO_2 emissions from power generation. So, several EU projects were funded within Frame Program 6, which copes with carbon capture and storage (CCS). In September 2006, the first general assembly of the European Technology Platform for zero emission fossil fuel power plants (ETP ZEP) [1] was held, whose goal is the creation of highly efficient power plants with near-zero emissions by 2020 within the current Frame Program 7.

CCS is considered as an urgently needed short-term and midterm solution to curb the emissions from fossil fuel combustion before new and regenerative energy resources can take over. Technology leaders discuss three possibilities of CO_2 capture on a grand scale.

- Oxy-fuel systems with combustion of fossil fuels by pure oxygen, leading to a working fluid of mainly CO_2 and water. After separation of the water by proper condensation, the combustion generated CO_2 can be retained, stored, or used for other technical applications.
- Postcombustion capture of CO_2 from exhaust gases by chemical means or membranes, which appears up to now to be costly, to be ineffective in use of solvents, and to remarkably lower air-breathing gas turbine efficiency.
- Precombustion transformation of hydrocarbons, especially natural gas or syngas from coal gasification, into a mixture of CO_2 and H_2 from which the heat engine or gas turbine fuel H_2 can be derived. CO_2 is retained in the transformation process; separation is intended to be effected by solvents or by membranes.

Up to now, it is not clear which technology has the best chances of dominating future power generation, but it is expected that they will all have their own application area. Within the project ENCAP (enhanced CO_2 capture) [2], a EU funded research project with more than 20 partners from the industry, government institutions, and universities, several technologies for power generation that would meet the target of at least 90% CO_2 capture rate and

Contributed by the International Gas Turbine Institute of ASME for publication in the JOURNAL OF ENGINEERING FOR GAS TURBINES AND POWER. Manuscript received May 24, 2007; final manuscript received May 25, 2007; published online April 2, 2008. Review conducted by Dilip R. Ballal. Paper presented at the ASME Turbo Expo 2007: Land, Sea and Air (GT2007), May 14–17, 2007, Montreal, Canada, Paper No. GT2007–27375.

50% CO_2 capture cost reduction are investigated. A benchmarking of a number of pre-combustion and oxy-fuel types of cycles was carried out to identify the most promising candidates.

Among the oxy-fuel cycles investigated, the highest efficiencies were reported for the S-Graz Cycle (48.9%) and the semiclosed oxy-fuel combustion combined cycle (SCOC-CC) [3], (47.7%). Although the S-Graz Cycle turned out to achieve the highest efficiency, the value given by the ENCAP study is remarkably lower (by 3.6% points) than the one reported by Sanz et al. [4], probably due to different assumptions on losses and component efficiencies. Furthermore, a feasibility study of the key components was performed, and they were classified according to their technology readiness and expected costs. In this analysis, the SCOC-CC plant was evaluated to be technically favorable, whereas three components of the S-Graz Cycle plant were ranked as critical. This statement arises partly because not the latest version of the Graz Cycle as presented at the ASME 2006 [5] was investigated in the ENCAP study.

Because of the differences in efficiency between ENCAP and Ref. [4] and because of the new scheme of the Graz Cycle not considered in the study, the comparison between both plants is repeated in this work to give a correct picture. Both oxy-fuel cycles are thermodynamically investigated based on assumptions agreed upon with the industry in previous work [4]. It is succeeded by a layout and discussion of the main components for a 400 MW power plant.

In this work, the nomination "Graz Cycle" means the "S-Graz Cycle," as presented in Ref. [5].

Thermodynamic Evaluation

All thermodynamic simulations were performed using the commercial software IPSEPRO by SIMTECH Simulation Technology [6]. This software allows to implement user-defined fluid properties to simulate the real gas properties of the cycle medium. The physical properties of water and steam are calculated using the IAPWS_IF97 formulations [7]; CO_2 is also modeled as a real gas based on the correlation of Ref. [8]. Furthermore, a simulation module was developed for the calculation of cooled turbines, as described below.

The oxy-fuel system is suited for all kinds of fossil fuels, e.g., methane or syngas from coal or biomass gasification (for the Graz Cycle, see Refs. [9,10]). In this work, thermodynamic data are presented for a cycle fired with methane with a lower heating value of 50,015 kJ/kg.

The component efficiencies and losses were agreed upon with the Norwegian oil and gas company Statoil ASA in the course of a thermodynamic evaluation of the Graz Cycle and can be found in Ref. [4]. Some important assumptions are listed: (1) The isentropic efficiency of the cooled gas turbines is 90.3% and includes the flow losses due to cooling. It corresponds to a polytropic efficiency of 85.5%. The demand of cooling flow is calculated as described below. (2) Oxygen production is considered with an effort of 900 kJ/kg (0.25 kWh/kg); the compression needs 325 kJ/kg. (3) The compression of combustion generated CO_2 to 100 bars is considered in the power balance with a value of 310 kJ/kg CO_2 for the Graz Cycle and with 350 kJ/kg for the SCOC-CC plant since in the Graz Cycle compression starts at 1.7 bars compared to 1 bar for the SCOC-CC.

Simulation of a Cooled Gas Turbine. The outcome of this thermodynamic study largely depends on the different demands of gas turbine cooling flow for both cycles, so that the simulation model of the cooled gas turbine is explained in detail. A simple stage-by-stage approach similar to the first model in Ref. [11] is applied, which allows us to calculate the amount of cooling steam.

In a gas turbine, the decrease in temperature stems from the expansion process, from the convective cooling of the main flow at the "cold" blade surfaces, and from the mixing of the cooling flow with the main flow. The convective heat transfer to the cold blade surfaces in a stage is

$$Q_{st} = fA_{ax}\alpha(T - T_m) \tag{1}$$

By relating to the stage temperature decrease due to polytropic expansion ΔT_1, the differential convective heat transfer can be calculated (Eq. (2)). It leads to a differential temperature decrease of the main gas flow dT_2,

$$dQ/dT_1 = Q_{st}/dT_1 \tag{2}$$

$$dQ = \dot{m}c_{p,g}dT_2 = \rho w \sin\beta A_{ax}c_{p,g}dT_2 \tag{3}$$

Thus, the following relationship between the differential temperature decrease due to convective heat transfer and due to expansion can be derived:

$$dT_2 = \frac{T - T_m}{\Delta T_1} f \,\mathrm{St} \frac{1}{\sin\beta} dT_1 \tag{4}$$

with $\mathrm{St} = \alpha/\rho c_{p,g} w$ as the Stanton number.

The heat transferred to the blades is absorbed by the internal cooling mass flow, which is heated to a temperature ΔT_d below the metal temperature T_m,

$$dQ = d\dot{m}_c c_{p,c}(T_m - \Delta T_d - T_c) \tag{5}$$

This allows us to determine the differential demand of cooling mass flow depending on the differential temperature drop due to polytropic expansion,

$$d\dot{m}_c = \dot{m}\frac{c_{p,g}}{c_{p,c}} \frac{T - T_m}{T_m - \Delta T_d - T_c} f \,\mathrm{St} \frac{1}{\sin\beta} \frac{dT_1}{\Delta T_1} \tag{6}$$

Within the thermodynamic simulation with IPSEPRO, the integration of Eq. (6) is done for partial turbines using mean values denoted by an overbar:

$$\dot{m}_c = \dot{m}\frac{c_{p,g}}{c_{p,c}} \frac{\bar{T} - T_m}{T_m - \Delta T_d - T_c} (\bar{f} n_{st}) \overline{\mathrm{St}} \frac{1}{\sin\bar{\beta}} \tag{7}$$

Since both cycles use very different working and cooling fluids (steam versus CO_2), their properties have to be considered in the determination of the cooling mass flow demand. The heat capacities are calculated from the physical fluid properties, so that for similar turbomachinery design parameters (see below), only the differences in Stanton number have to be considered. Louis [12] suggested the following correlation to calculate the Stanton number for the convective heat transfer on the hot side of a gas turbine blade:

$$\mathrm{St} = 0.5\,\mathrm{Re}^{-0.37}\,\mathrm{Pr}^{-2/3} \tag{8}$$

Equation (8) is evaluated for the working fluids of both cycles in the temperature range of 600–1000 °C (where the Prandtl number and viscosity data were available), and it was found that the Stanton number for the high-temperature turbine (HTT) of the Graz Cycle is 7% higher than that for the SCOC-CC for a speed of 3000 rpm. However, for the fast-running first two stages of the Graz Cycle HTT (see below), the Stanton number is 15% lower. Because of the large uncertainty in the evaluation of the Stanton number, for the thermodynamic simulation the same Stanton number of 0.0041 (found by an analysis of air-breathing gas turbines) was used for all cooled gas turbines in both cycles. However, considering the estimates for the Stanton number according to Eq. (8) would result in a lower cooling flow demand for the Graz Cycle than calculated.

A comparative calculation of one high-temperature stage using the same parameters showed that the favorable heat capacities of the Graz Cycle working and cooling fluid lead to a 20% lower demand of cooling mass flow.

The contribution of the cooling mass flow to the total expansion

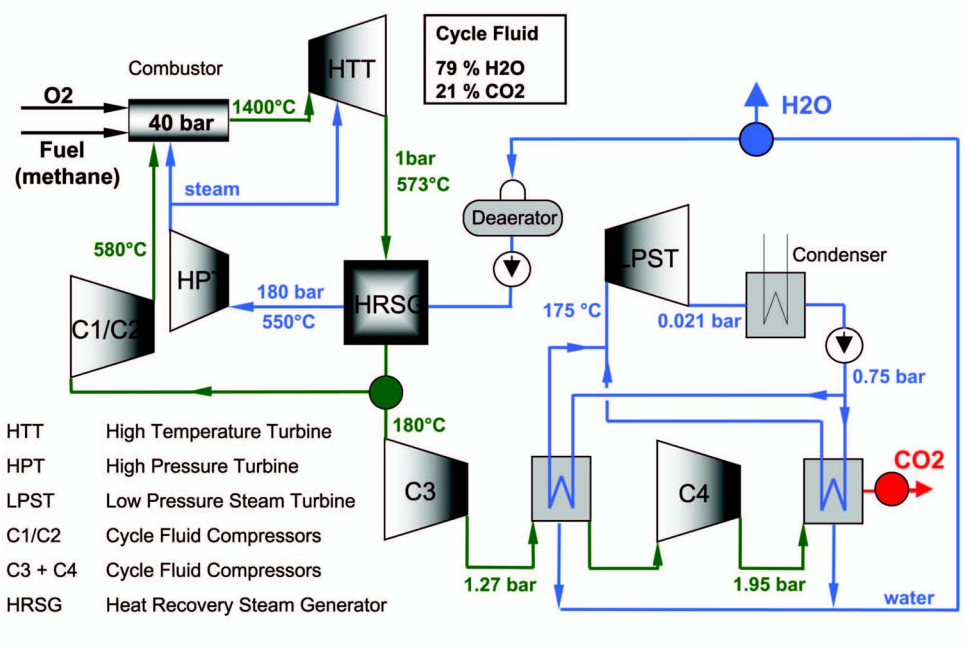

Fig. 1 Principle flow scheme of the modified Graz Cycle power plant with condensation/evaporation in 1 bar range [5]

work is considered on a stage-by-stage basis. Half of the stage cooling mass flow contributes to the stage expansion work; the rest is added at the stage exit.

Graz Cycle Scheme. The basic principle of the so-called Graz Cycle has been developed by Jericha in 1985 [13] for solar generated oxygen-hydrogen fuel, and changed to fossil fuels in 1995 [14,15]. This was a first proposal for this type of oxy-fuel power cycle with CO_2 capture. Improvements and further developments since then were presented at several conferences [9,10,16–19]. Any fossil fuel gas is proposed to be combusted with oxygen so that neglecting small impurities, only the two combustion products CO_2 and H_2O are generated. The cycle medium of CO_2 and H_2O allows an easy and cost-effective CO_2 separation by condensation. Furthermore, the oxygen combustion enables a power cycle with a thermal efficiency higher than that for state-of-the-art combined cycle plants, thus largely compensating the additional efforts for oxygen production.

The Graz Cycle plant, as presented in Ref. [4] and investigated in the ENCAP study, suffers from the disadvantages of the working fluid expansion into vacuum (very large and expensive condenser, corrosion risk for low pressure turbine (LPT) with exit below dew point temperature). Therefore, at the ASME IGTI Conference 2006 in Barcelona [5], it was suggested according to the Austrian patent of the Graz Cycle [20] to condense the working fluid at atmospheric pressure, separate the combustion generated CO_2, and use the condensation heat for evaporation in a bottoming steam cycle. Figure 1 shows the principle flow of this Graz Cycle variant with the main cycle data.

Basically, the Graz Cycle consists of a high-temperature cycle (compressors C1 and C2, combustion chamber, HTT, heat recovery steam generator (HRSG), and high pressure turbine (HPT)) and a low-temperature cycle (low pressure steam turbine (LPST), condenser and compressors C3 and C4). The fuel, together with the nearly stoichiometric mass flow of oxygen, is fed to the combustion chamber, which is operated at a pressure of 40 bars. Steam drives the burner vortex core, bringing together the reaction components. The high flame temperature is further reduced by the inflow of the working gas (CO_2/H_2O) around the burners and into the combustion chamber liner.

A mixture of about 75.5% steam, 24% CO_2, 0.4% O_2, and 0.1% N_2 (mass fractions) leaves the combustion chamber at a mean temperature of 1400°C, a value exceeded by G and H class turbines nowadays. The fluid is expanded to a pressure of 1.06 bar and 580°C in the HTT. Cooling is performed with steam coming from the HPT at about 330°C (13.7% of the HTT inlet mass flow), increasing the steam content to 78.4% at the HTT exit. The hot exhaust gas is cooled in the following HRSG to vaporize and superheat steam for the HPT: the pinch point of the HRSG is 5°C (an aggressive value used for both cycles) and the approach point at the superheater exit is 25°C. After the HRSG, about 55% of the cycle mass flow is recompressed using the main cycle compressors C1 and C2 with an intercooler and is fed to the combustion chamber with a maximum temperature of 580°C.

The remaining mass flow, which contains the combustion generated CO_2, is fed to a condensation process in the 1 bar range in order to avoid the problems described above. The heat content in the flow is still quite high, so reevaporation and expansion in a bottoming cycle is mandatory. For proper reevaporation, two sections of working fluid condensation are provided, each following a compressor stage with a reasonable increase of flow pressure, resulting in a higher partial condensation pressure of the water content. The two compressor stages can be regarded as prerunners of the CO_2 delivery compressor and will be helpful in cleaning the turbomachinery, piping, and HRSG interior from air in preparation of a cold start. The heat exchangers are well developed modern boiler elements providing steam just below atmosphere (0.75 bar) for the condensing LPST.

At the first pressure level of 1.27 bars, about 63% of the water content can be segregated, so that the power demand of the second compression stage is considerably reduced. It compresses up to 1.95 bars, which allows the segregation of further 25% of the contained water. Further cooling of the working fluid, also for water preheating, leads to the separation of additional 11%, so that the water content of the CO_2 stream, which is supplied after pressure losses at 1.7 bars for further compression, is below 1%. More details of the condensation/evaporation process can be found in Ref. [5]. After the segregation of the water stemming from the combustion process, the water flow is degassed in the deaerator,

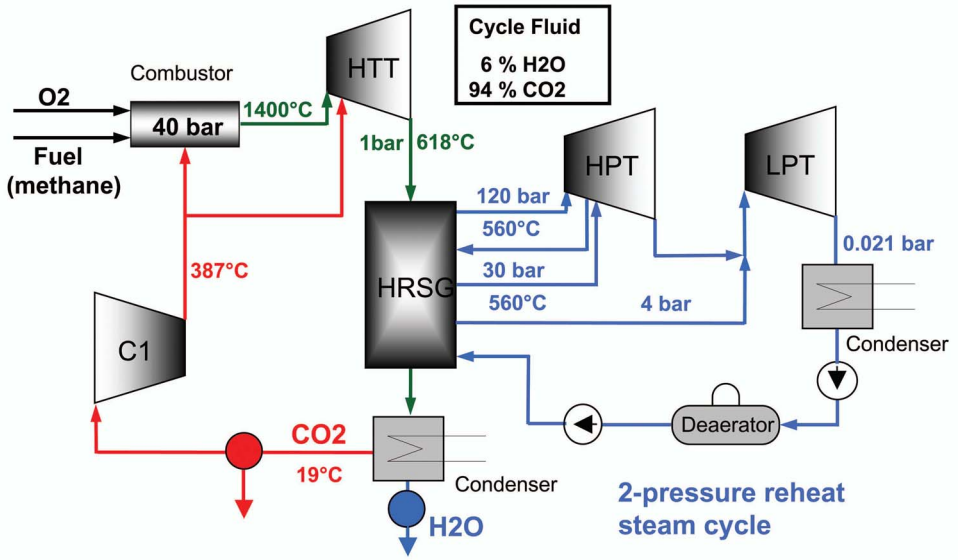

Fig. 2 Principle flow scheme of SCOC-CC

with steam extracted after the HPT and fed to the HRSG for vaporization and superheating. The steam is then delivered to the HPT at 180 bars and 550°C. After the expansion, it is used to cool the burners and the HTT stages. For transonic stages, the authors suggested the use of a special cooling system by transonic steam layers [21].

The two-step condensation/evaporation counteracts the effect of sinking H_2O partial pressure due to condensed water extraction from working fluid and thus allows reasonable steam inlet conditions of 0.75 bar and 175°C at the LPST inlet. Expanding the steam to a condensation pressure of 0.021 bar for a cooling water temperature of 8°C (Northern Europe) provides about 72 MW power output. A three-stage four-flow design is necessary to handle the high LPST volume flow for a 400 MW Graz Cycle plant.

The detailed flow sheet used for the thermodynamic simulation can be found in Ref. [5] and gives mass flow, pressure, temperature, and enthalpy of all streams.

Semiclosed Oxy-Fuel Combustion Combined Cycle Scheme. In the ENCAP investigation, the SCOC-CC plant turned out to be very promising because of its technical simplicity and relatively high efficiency [3]. Figure 2 shows the principle flow scheme of the SCOC-CC.

Basically, the SCOC-CC consists of a high-temperature Brayton cycle (HTT, combustion chamber, compressor C1, and HRSG) with an unusual working fluid consisting mainly of CO_2 and a conventional bottoming steam cycle (HPT, LPT, condenser, and feed pumps). The fuel, together with the nearly stoichiometric mass flow of oxygen, is fed to the combustion chamber, which is also operated at 40 bars. In SCOC-CC, recycled CO_2 is supplied to cool the burners and the liner.

This leads to a quite different working fluid leaving the combustion chamber at the same mean temperature of 1400°C. It consists of about 92.5% CO_2, 7.1% steam, 0.3% O_2, and 0.1% N_2 (mass fractions). The fluid is expanded to a pressure of 1.06 bar at 618°C in the HTT. Turbine cooling is performed with CO_2 fed from the compressor C1 at 387°C. However, the necessary cooling mass flow is 30.5% of the HTT inlet mass flow and thus remarkably higher than the 13.7% needed for the Graz Cycle HTT. The reasons are a less favorable ratio of heat capacities of working and cooling fluid consisting mainly of CO_2, a higher cooling flow inlet temperature, and a larger number of stages needed in the hot section, as described in the section on turbomachinery design. The higher cooling mass flow decreases the cycle efficiency by 1.8% points compared to a cycle with only 13.7% cooling mass flow demand. The cooling flow increases the CO_2 content of the working fluid to 94% in the HTT.

In the following HRSG, the hot exhaust gas is cooled to 65°C vaporizing and superheating steam for the bottoming steam cycle. In the atmospheric condenser, the working fluid is cooled to 18°C, so that most of the combustion generated H_2O can be extracted in the liquid state. The CO_2 stream then has a purity of 98.8%. After separation of the combustion generated CO_2, it is fed to compressor C1, where it is compressed to combustion pressure under continuous fluid extraction for cooling of the HTT.

The steam cycle is arranged as a double pressure reheat process for good efficiency. The live steam and reheat temperature is 560°C. The pressure levels are set to 120/30/4 bars similar to the ENCAP layout [3], which gives optimum efficiency for a minimum allowed humidity of 89% at the LPT exit (compared to 94% for the Graz Cycle). This low humidity is obtained for the same condenser pressure of 0.021 bar for a cooling water temperature of 8°C.

The detailed flow sheet used for the thermodynamic simulation can be found in Ref. [22] and gives the mass flow, pressure, temperature, and enthalpy of all streams.

Thermodynamic Balance. Table 1 gives a comparison of the power balance of the Graz Cycle plant and of the SCOC-CC for a 400 MW net power output. The C1/C2 compressors of the Graz Cycle are compared with the CO_2 compressor C1 of the SCOC-CC since they both have the same task of working fluid compression. C3 and C4 compressors are only needed in the Graz Cycle. They help in the startup and can be regarded as prerunners of CO_2 recompression to 100 bars.

The Graz Cycle HTT has a lower mass flow, but a higher power output because of the higher heat capacity of steam. On the other side, in the SCOC-CC a higher portion of the total turbine power is provided by the steam cycle. The compression power is very similar for both cycles, with a slightly higher power demand of the CO_2 compressor, which has to compress all the cycle fluid. The net mechanical and electrical power is slightly higher for the SCOC-CC, but at the expense of a remarkably higher heat input. This results in a lower thermal efficiency and net electrical efficiency of about 3% points. Due to the higher fuel input needed, the efforts for oxygen supply and CO_2 compression are higher for the SCOC-CC plant. Additionally, the higher CO_2 segregation

Table 1 Graz Cycle and SCOC-CC power balance

	Graz cycle	SCOC-CC
HTT power (MW)	623.6	557
HPT power (MW)	47	95
LPST/LPT power (MW)	72	95
Total turbine power P_T (MW)	743	747
C1/C2 power (MW)	220.2	235
C3/C4 power (MW)	16.7	
Pump power (MW)	4.3	3.5
Total compression power P_C (MW)	241.2	238.5
Net shaft power (MW) without mechanical losses	501.4	508.5
Total heat input Q_{zu} (MW)	753.4	804.6
Thermal cycle efficiency (%)	**66.55**	**63.20**
Electrical power output (MW) including mechanical, electrical, and auxiliary losses	487.4	494.5
Net electrical cycle efficiency (%)	**64.70**	**61.45**
O_2 generation and compression P_{O_2} (MW)	74.3	78.6
Efficiency considering O_2 supply (%)	**54.84**	**51.68**
CO_2 compression to 100 bar P_{CO_2} (MW)	13.1	15.5
Net power output (MW)	**400.0**	**400.0**
Net efficiency η_{net} (%)	**53.09**	**49.75**

pressure of 1.7 bars in the Graz Cycle reduces the specific compression power from 350 kJ/kg to 310 kJ/kg CO_2. This results in a higher net efficiency of the Graz Cycle of 53.09% compared to 49.75% for the SCOC-CC plant.

In the ENCAP study, the corresponding efficiencies were evaluated to 48.9% and 47.7% and thus differ remarkably from the values in this investigation. The reasons for the general higher efficiencies are mainly the following:

- higher inlet temperature of oxygen and fuel of 150°C, because it is expected that heat released from the air compression for the cryogenic air separation unit (ASU) can be used for fuel and oxygen prewarming
- oxygen provided with 99% purity at an energy requirement of 0.25 kWh/kg compared to 95% purity at 0.30 kW h/kg in the ENCAP study. Even lower energy requirements are published in Ref. [23]
- probably different assumptions of component efficiencies and losses, which are not published for the ENCAP project

Whereas the ENCAP study shows an advantage of the Graz Cycle of 1.2% points, in this work the difference is 3.35% points. A difference of 1.8% points can be attributed to the higher cooling flow demand of the SCOC-CC HTT turbine because of the lower heat capacity of the cooling gas and the need for more cooled stages (see below). It is not clear if this effect is considered in the ENCAP study. A further difference stems from the higher efficiency of the modified Graz Cycle scheme as compared to the one used in the ENCAP study.

Turbomachinery Design and Comparison

In the evaluation of different oxy-fuel concepts within the ENCAP project [3], the Graz Cycle variant investigated [4] showed three critical components.

- Working fluid condenser working at very low pressure bears the risk of corrosion and very low heat transfer, thus leading to high costs.
- The LPT turbine working with a steam/CO_2 mixture expands below the dew point, thus leading to corrosion risks.
- The HTT needs a completely new design due to the working fluid.

The Graz Cycle presented in Ref. [5] avoids the first two problems since condensation takes place at atmospheric pressure and the LPT is replaced by a LPST. The HTT is the key component of the Graz Cycle as well as of the SCOC-CC plant, but the working fluid is very different. Whereas the Graz Cycle works mainly with steam, the SCOC-CC working fluid is also unusual consisting mainly of CO_2. Despite the fact that a new design is required for both turbines, in the ENCAP study the technical and economic barriers of the Graz Cycle HTT were seen to be larger, probably due to the high content of steam as a condensable fluid in the working and cooling media.

In order to clarify the differences between the components of both cycles, in this work the design concept for a Graz Cycle power plant of 400 MW electrical net output as described in Ref. [24] is compared with the turbomachinery layout of a SCOC-CC plant of a similar net power. The turbomachines are compared with respect to the number of stages, stage dimensions, and feasibility. For the layout of turbomachinery, each manufacturer employs its own design philosophy regarding the optimum nondimensional parameters for the operating points. In this study, the following common rules are applied for the turbomachinery layout of both cycles: (1) maximum relative inlet tip Mach number of 1.35 for compressors, (2) compressor work coefficient ($2^*\Delta H/u^2$) of 0.814 [25], (3) constant inner diameter and constant axial velocity throughout the compressors, (4) reaction-type turbine blades with 50% degree of reaction at the midsection, and (5) turbine work coefficient of close to 2 for optimum efficiency.

Graz Cycle Turbomachinery

For the Graz Cycle plant, the layout of turbomachinery has already been presented at the ASME IGTI Conference 2006 [5] and slightly modified in Ref. [24]. Figure 3 shows the arrangement of the main turbomachinery; its main parameters and dimen-

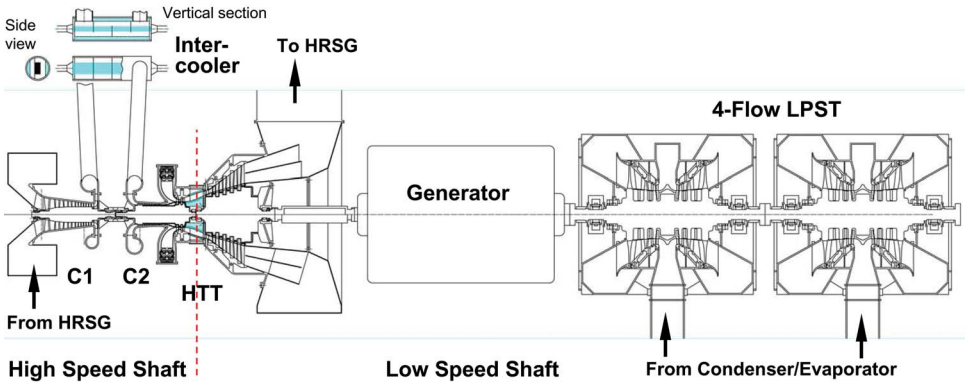

Fig. 3 Arrangement of the main turbomachinery for a 400 MW Graz Cycle plant

Table 2 Main turbomachinery dimensions for a 400 MW Graz Cycle plant

		HTTC	HTTP	C1[a]	C2
Inlet mass flow	(kg/s)	367	401	221	221
Inlet volume flow	(m^3/s)	61	156	309	43
Outlet mass flow	(kg/s)	401	417	221	221
Outlet volume flow	(m^3/s)	157	1263	46	18
Inlet mean diameter D	(m)	1.065	1.77	1.037	0.95
Inlet inner diameter	(m)	0.965	1.506	0.67	0.77
Inlet blade length l	(m)	0.1	0.251	0.367	0.09
Inlet D/l	(—)	10.6	6.5		
Inlet D_{in}/D_{out}	(—)			0.48	081
Outlet mean diameter D	(m)	1.14	3.107	0.882	0.85
Outlet inner diameter	(m)	0.965	2.46	0.77	0.77
Outlet blade length l	(m)	0.177	0.647	0.112	0.04
Outlet D/l	(—)	6.46	4.8		
Outlet D_{in}/D_{out}	(—)			0.77	0.9
Enthalpy drop	(kJ/kg)	582	978	590	379
Work coefficient	(—)	2.2	2.5	0.814	0.814
Stage number	(—)	2	5	$6+R$	7
Speed	(rpm)	8500	3000	8500	8500

[a]For C1, outlet dimensions are given for the last axial stage.

sions are given in Table 2. A maximum tip Mach number of 1.35 at the inlet allows a rotational speed of 8500 rpm for the C1 compressor. Therefore, a two-shaft design for the HTT was chosen with a free-running compressor turbine HTTC driving the C1 and C2 compressors at 8500 rpm. This relatively high speed is selected for reasons of obtaining sufficient blade length at the outlet of C2 and of reducing the number of stages in both compressors as well as in the HTT. The second part of the HTT, the power turbine HTTP, delivers the main output to the generator at 3000 rpm. In a detailed study by a major gas turbine manufacturer ordered by Statoil ASA, the feasibility of the two-shaft design was confirmed [4].

A further elongation of the shaft is done by coupling the four-flow LPST at the opposite side of the generator. The HPT can be coupled to the far end of the LPST or can drive a separate generator. A high-speed gear-drive steam turbine is proposed. The two shafts are based on the same spring supported foundation. The intercooler between C1 and C2 is located on the solid foundation.

C1/C2 Compressor Design With Intercooler. The rotational speed of 8500 rpm of the C1 compressor leads to a high inlet tip Mach number, so that with the help of a slight positive inlet swirl, an inlet Mach number of 1.33 is designed. The low hub to tip ratio at the inlet of 0.48 together with a blade length of 367 mm leads to high centrifugal loads. Therefore, a titanium blisk is suggested for the first rotor, as shown in Fig. 4. Its radial elongation due to the centrifugal forces is carried by elastic axial rings, which center the blisk and keep it on right angles to the shaft. The final radial wheel has to be milled separately from nickel alloy and is mounted to the main drum also by the same elastic ring design. The blading is a splitter vane design with axial inflow and radial outflow with a 45 deg backswept outlet. The wide vaneless diffuser and scroll improve the flow transfer to the intercooler. The drum rotor is made of ferritic steel and reaches only 390°C. This design leads to only six axial and one radial stages for C1.

For the rotor dynamics layout [24], the C1 drum rotor can be seen as a symmetric shaft. The rotor passes at 0.622×8500 rpm its first critical speed under consideration of all masses and stiffnesses of the drum and of the bearing oil films. The second eigenfrequency is 16,790 rpm and is thus well above the operational speed. The arrangement of two bearings between C1 and C2 in a double-wedge design serves to allow safe passage of critical speed in both rotors. The operating speed distinctly above critical speed leads to self-centering of both rotors and allows very narrow tip gaps on the blading.

The inlet temperature to C2 is somewhat lowered by the intercooler but still reaches 380°C. During the course of compression, the working fluid reaches an outlet temperature of 580°C, so that from the second stage onward cooling has to be applied on the rotor surface of the bladed annular flow channel. Seven axial stages with a stepwise decrease of blade length from 90 mm to 40 mm are supported on a drum rotor by an axial fir-tree root. The same design as used for the five center stages of C1 is also applied to the seven axial stages of C2. Figure 5 shows the C2 rotor, with the counterflow of cooling steam close to the drum surface. It is guided by means of openings under the blade roots and is sealed by strips carried on the guide vane diaphragms. By a proper selection of the feed pressure, this flow can be optimized at a small penalty in dilution of the main flow.

Excellent flow properties of this compressor can be expected due to its blade mounting on a drum rotor, with optimized rotor dynamics enabling small radial tip clearances. The outlet hub to tip ratio is 0.9.

High Temperature Turbine HTT. The same drum rotor carries not only the C2 but also the compressor turbine HTTC. The flow design of the HTTC will be a two-stage reaction turbine with 50% reaction at the mean section of both blade rows. The high rotor speed of 8500 rpm, as mentioned before, provides for long blade lengths, i.e., a first stage blade of 100 mm and a second

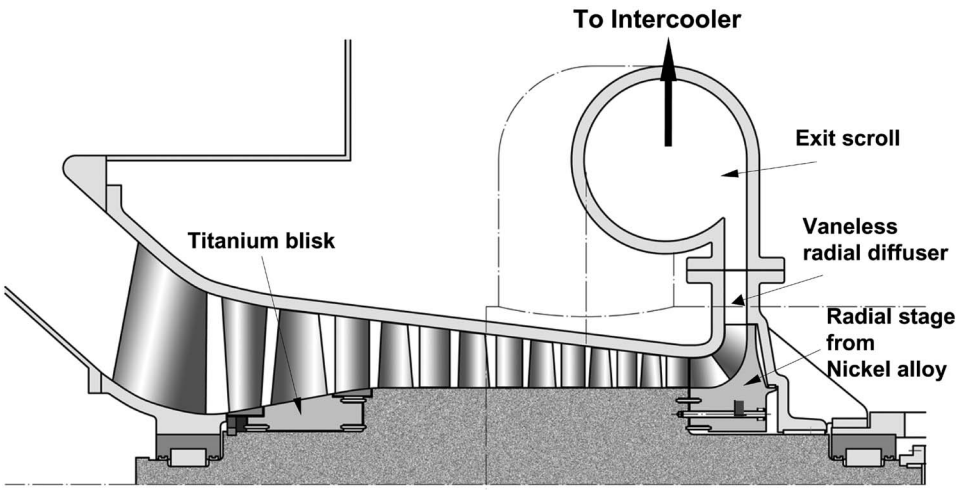

Fig. 4 C1 compressor with titanium blisk and radial last stage

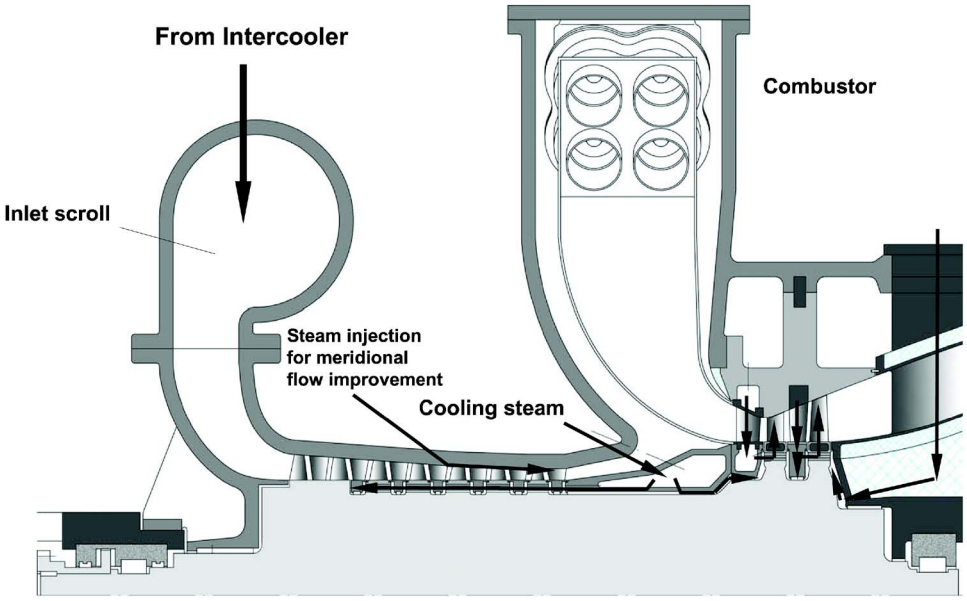

Fig. 5 Design of the C2 drum rotor with cooling steam flow arrangement, combustor, and HTTC

stage blade of 177 mm with an inner diameter of 965 mm (see Fig. 5).

The high speed and power of this turbine is made possible by ample steam cooling. Generally, the authors rely on cooling by clean steam in all parts of blading and accessible surfaces of the rotor drum. Nozzles and blades are cooled in a conventional serpentine passage design with holes as shown in the cooling arrangement of Fig. 5. Rotor cooling steam is supplied along the whole drum surface. It is fed into a labyrinth seal in the inner range of the combustion chamber, allowing the steam to flow to both sides. One flow is directed backward under the dump diffuser into the outer surface of the C2 providing cooling steam, as described above. The main amount of cooling steam flows along the rotor drum at the inner radius of the combustor casing toward the disk of the HTTC. More details of the cooling flow arrangement can be found in Ref. [5].

Alternatively, the HTTC expansion could also be done with one transonic stage, as shown in Refs. [5,24]. This can be achieved by a higher radius and stage loading at a somewhat reduced degree of reaction. Such a stage would sit on the same rotor as described before, and it would have a mean radius of 750 mm at a blade length of 120 mm. For the comparison with the SCOC-CC, the two-stage subsonic design is chosen because it is the conventional design for heavy-duty gas turbines.

The power turbine is proposed with a strong change of inner radius on a solid shaft. Five stages are necessary for the 50 Hz design of Fig. 6. The axial outlet speed should be kept at a medium value in order to reduce the exhaust loss, to reduce the axial diffuser exit length, and to facilitate the flow transfer to the HRSG inlet. The design proposed provides last blade lengths of 647 mm at 2460 mm inner diameter.

Detailed deliberations on the intermediate bearing casing in its hot environment and on thrust equalization using a steam operated balance piston are given in Ref. [5].

Steam Turbines. The LPST is fed with steam of 0.75 bar at 175°C. Expanding the steam to a condensation pressure of 0.021 bar leads to a high volume flow. At 50 Hz, a four-flow

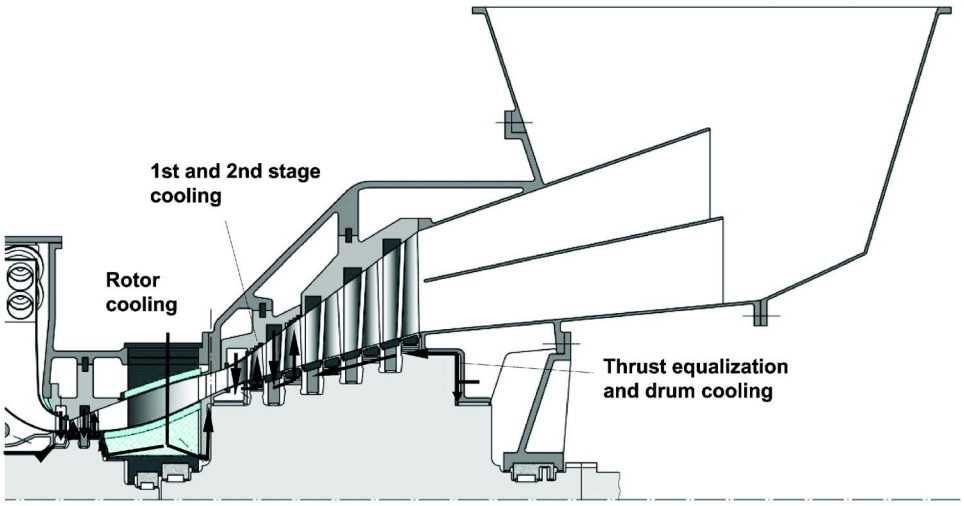

Fig. 6 Design of the two-stage HTTC and 50 Hz HTTP

Table 3 Turbomachinery dimensions for a 400 MW SCOC-CC plant

		HTTC[a]	HTTP[a]	C1
Inlet mass flow	(kg/s)	565	725	657
Inlet volume flow	(m^3/s)	50	180	363
Outlet mass flow	(kg/s)	725	737	645
Outlet volume flow	(m^3/s)	180	1270	19.5
Inlet mean diameter D	(m)	1.483	1.912	1.595
Inlet inner diameter	(m)	1.369	1.639	1.07
Inlet blade length l	(m)	0.114	0.273	0.525
Inlet D/l	(—)	13	7	
Inlet D_{in}/d_{out}	(—)			0.5
Outlet mean diameter D	(m)	1.881	2.853	1.11
Outlet inner diameter	(m)	1.612	2.283	1.07
Outlet blade length l	(m)	0.269	0.57	0.04
Outlet D/l	(—)	7	5	
Outlet D_{in}/D_{out}	(—)			0.93
Enthalpy drop	(kJ/kg)	391	439	361
Work coefficient	(—)	2.2	2	0.814
Stage number	(—)	5	3	19
Speed	(rpm)	3000	3000	3000

[a]HTT compressor turbine and power turbine are physically one turbine.

design with three stages, as shown in Fig. 3, is able to handle this steam flow with excellent efficiency. The last stage is transonic with a blade length of 970 mm.

The HPT is a standard high-speed backpressure steam turbine of 50 MW power output for which many designs are in the market. A geared type seems to be a superior solution since better flow efficiency and operability due to nozzle boxes and low number of stages with long blades and low leakage loss can be achieved. It can be coupled to the far end of the LPST or can be used to drive a separate smaller electric generator.

Both turbines can be considered as conventional and correspond to the HPT and LPT of a steam turbo set with an intermediate pressure turbine in between.

Compressors C3 and C4. The delivery compressors C3 and C4, which increase the pressure of the working fluid prior to condensation in order to obtain better evaporation conditions for the bottoming steam cycle, are also needed to vent the internal volume before startup. They are two one-stage compressors and are driven by two separate speed-controlled motors.

Semiclosed Oxy-Fuel Combustion Combined Cycle Turbomachinery

The thermodynamic calculations allow an estimate of turbomachinery power and dimensions for the SCOC-CC plant based on the same assumptions as for the Graz Cycle. The resulting main parameters and dimensions are given in Table 3. The working fluid contains largely CO_2, so that it has significantly lower values of gas constant (−43%) and heat capacity (−37%) compared to the steam rich working fluid of the Graz Cycle. This results in lower sonic velocities and lower enthalpy differences for a given pressure difference.

Compressor C1. Despite the much higher mass flow, the inlet and outlet flow volumes are similar to the C1/C2 conditions. However, due to the lower sonic velocity at the compressor inlet (−33%), the limit of a maximum tip Mach number of 1.35 leads to a rotational speed of 3000 rpm for this compressor. Therefore a one-shaft design is reasonable, with the HTT driving the C1 compressor as well as the generator. Based on the flow parameters stated above, a design with 19 stages is suggested, with an inner diameter of 1070 mm. The hub to tip ratio is 0.5 at the inlet and 0.93 at the exit, leading to relatively small blades of 40 mm for this large diameter. A slightly different design is presented in the ENCAP project [3]. For a 20% reduced mass flow, the C1 compressor needs 24 stages with a work coefficient of 0.5 for similar hub to tip ratios at the same speed of 3000 rpm. Both designs need high stage numbers, which bear the risk of deterioration of the meridional flow profile toward the last stages because of end wall boundary layer growth leading to reduced flow efficiency.

In contrast, the Graz Cycle compressors have a more favorable hub to tip ratio and a total number of only 13 axial and 1 radial stages. The intercooler between C1 and C2 interrupts the compression process and thus enables an undisturbed and compact flow profile at the inlet of the C2 compressor. On the other hand, additional pressure losses are caused by the C1 outlet and C2 inlet scroll.

Regarding the operating conditions, the exit flow temperature of the SCOC-CC compressor is below 400°C compared to 580°C for the C2 compressor, so that no rotor cooling is necessary. The centrifugal load is only a quart of the C1/C2 compressors, so that high stresses and expensive materials, such as titanium or nimonic, can be avoided. However, the long and slender rotor may result in rotor dynamics problems.

A further risk for the operation of the CO_2 compressor is the inlet working fluid, with its steam content at saturation. Flow acceleration there with its temperature decrease can lead to the formation of water droplets, which can cause blade erosion.

High Temperature Turbine. The maximum speed of 3000 rpm for the C1 compressor leads to a one-shaft design for the HTT (compressor turbine+power turbine) running at the same speed. Despite the higher mass flow, the volume flows at the inlet and exit are similar. The total enthalpy drop is 830 kJ/kg compared to 1560 kJ/kg for the Graz Cycle. However, in the hot section, the expansion of a pressure ratio similar to the one of the Graz Cycle HTTC needs five cooled stages compared to two because of the lower speed and thus stage enthalpy drop. Therefore, the cooled surface area and thus cooling mass flow demand of the HTT are remarkably higher than those for the Graz Cycle. A further reason for the increase of necessary cooling mass flow is that the cooling medium is largely CO_2, with a smaller heat capacity than steam (see Eq. (7)). As a third reason, the cooling flow of the hot section has an inlet temperature of 387°C compared to a cooling steam temperature of 330°C of the Graz Cycle. So, the total cooling flow demand is calculated to be 30.5% of the inlet mass flow to the HTT compared to 13.7% for the Graz Cycle. About one-fourth of this high increase can be attributed to the unfavorable fluid properties of CO_2, about one-third to a higher cooling flow temperature, and the rest to the increased stage number. This higher cooling demand is also the main reason for the high difference in cycle efficiency.

The rotational speed of 3000 rpm leads to a total stage number of 8 compared to 7 for the Graz Cycle, despite of only about half the total enthalpy drop. The inlet diameter is larger than that for the Graz Cycle turbine at a similar blade length, whereas the outlet inner diameter is slightly smaller at a smaller blade length due to smaller flow volume change. The work coefficient is 2.2 for the first five stages similar to the Graz Cycle HTTC and 2 for the last three stages as compared to 2.5 for the five stages of the Graz Cycle HTTP.

Cooling is done with nearly pure CO_2. The circulating inventory of CO_2 is continuously replaced by inflow from the burners and is held constant by separation at the low pressure end. So, attention has to be paid on the danger of accumulation of fine particles from soot and ash. There is high risk of deposition of particles on the surfaces of the internal cooling channels of the blades because of the high centrifugal forces, which can lead to clogging of the serpentine passages and the small laser-drilled film cooling holes [26]. On the other hand, the use of steam from an evaporation process in the Graz Cycle allows a high purity of the cooling flow medium.

Steam Turbines. The steam cycle data of the SCOC-CC plant

Table 4 Comparison of equipment size for a plant of 400 MW net power output

	Conventional CC plant (MW)	Graz cycle (MW)	SCOC-CC (MW)
Turbine of "gas turbine"/HTT	667	623	557
Compressor of "gas turbine"/C1+C2+C3+C4	400	241	235
Steam turbines/ HPT+LSPT	133	120	190
HRSG	380	360	461
Generator	400	487	495

is very conventional, and suitable turbines for this power range are in operation in combined cycle plants worldwide. The high steam volume flow at the exit of the LPT will also demand a four-flow design at 3000 rpm.

Startup. The startup procedure of the SCOC-CC is very similar to a conventional combined cycle plant. It is expected that before startup the gas turbine cycle is filled with CO_2 at 1 bar. During startup, additional CO_2 has to be sucked in from a storage tank, which has to keep a pressure of 1 bar.

For the Graz Cycle, a detailed startup procedure is given in Ref. [5]. An auxiliary steam boiler is needed to provide steam for the startup.

Economic Evaluation

In Ref. [5], an economic evaluation of the Graz Cycle was done, resulting in relatively low CO_2 mitigation costs of 21–28 \$/ton CO_2. The variation in costs stems from the uncertainty in the costs of oxygen supply. In this work, a similar rough evaluation is performed in order to compare the SCOC-CC plant with the Graz Cycle on an economic basis.

The evaluation is based on a comparison with a state-of-the-art combined cycle power plant of 58% efficiency. For the economic balance, the following assumptions are used: (1) The yearly operating hours is assumed at 8500 h/yr. (2) The capital charge rate is 12%/yr, which corresponds to an interest rate of 8% over a depreciation period of 15 years. (3) Methane fuel costs are 1.3 ¢/kWh_{th}. (4) In order to estimate the investment costs, the power of the main components is compared with the reference plant in Table 4. For the Graz Cycle, all components are of the same size or smaller (compressor), besides the generator. For the SCOC-CC plant, the power of the generator, HRSG, and steam turbines is higher, and the compression and gas turbine power are smaller. So, for this rough economic estimate, the same total plant costs are assumed for all three plants, i.e., the same specific costs related to the 400 MW net output instead of to generator power (see Table 5). Development efforts needed especially for HTT and combustor are not considered in the investment costs. (5) Additional investment costs are assumed for the cryogenic ASU, for additional equipment, and for CO_2 compression to 100 bars (see Table 5 with low-cost data according to Göttlicher [27]). 6) The costs of CO_2 transport and storage are not considered because they depend largely on the site of a power plant.

Table 5 Estimated specific investment costs

Component	Scale parameter		Specific costs
Reference plant			
Investment costs	Electric power	\$/kW_{el}	414
Oxy-fuel plants			
Plant investment costs	Electric power	\$/kW_{el}	414
ASU [27]	O_2 mass flow	\$/(kg O_2/s)	1,500,000
Other costs (Piping, CO_2 recirculation) [27]	CO_2 mass flow	\$/(kg CO_2/s)	100,000
CO_2 compression system [27]	CO_2 mass flow	\$/(kg CO_2/s)	450,000

Table 6 Economic comparison for a 400 MW plant

	Reference plant	Graz Cycle plant	SCOC-CC plant
Plant capital costs (\$/kW_{el})	414	414	414
Additional capital costs (\$/kW_{el})		288	300
CO_2 emitted (kg/kW h_{el})	0.342	0.0	0.0
Net plant efficiency (%)	58.0	53.09	49.75
COE f. plant amort. (¢/kW h_{el})	0.58	0.99	1.01
COE due to fuel (¢/kW h_{el})	2.24	2.45	2.61
COE due to O&M (¢/kW h_{el})	0.7	0.8	0.8
Total COE (¢/kW h_{el})	3.52	4.24	4.42
Comparison			
Differential COE (¢/kW h_{el})		0.72	0.90
Mitigation costs (\$/ton CO_2)		21.0	26.2

Table 6 shows the result of the economic evaluation. Compared to the reference plant, the capital costs are about 70% higher for the Graz Cycle and 73% for the SCOC-CC by considering the additional components for O_2 generation and CO_2 compression. So, they contribute mostly to the difference in costs of electricity (COE). The fuel costs have the major influence on the COE, and there is the largest difference between both CO_2 free cycles due to the difference in efficiency. The O&M costs are assumed to be 15% higher for both plants due to the operation of the additional equipment.

Based on these assumptions, the increased COE compared to the reference plant is 0.72 ¢/kWh_{el} for the Graz Cycle and 0.90 ¢/kWh_{el} for the SCOC-CC. This results in mitigation costs of 21.0 \$/ton and 26.2 \$/ton of CO_2 avoided if CO_2 liquefaction is considered. Both values are clearly below a threshold value of 30 \$/ton, showing the economic potential of both cycles, with some advantages for a Graz Cycle plant.

The results of the economic study depend mainly on the assumptions about investment costs, fuel costs, and capital charge rate. A cost sensitivity analysis performed in Ref. [4] showed that a variation of the capital costs has the main influence on the economics since they contribute most to the mitigation costs. Unfortunately, there is a large uncertainty of these costs (e.g., the cost estimates of the most expensive additional unit, the ASU, vary between 230 \$/kW_{el} and 400 \$/kW_{el}), and the values presented above can be regarded as a lower limit until a more cost-saving method of oxygen generation, e.g., by membranes, is developed.

Pathway to Commercial Demonstration

The feasibility of oxy-fuel power generation from natural gas was demonstrated by Clean Energy Systems (CESs) in their 5 MW Kimberlina test plant in Bakersfield, CA [28]. In Norway, their technology shall be used for a demonstration plant of 50–70 MW within the ZENG project [29]. However, in order to achieve good efficiency, the CES technology needs a HTT nearly identical to the one of the Graz Cycle. Although many design deliberations for the HTT were made by the authors, the final design and building can only be done by a large gas turbine manufacturer. Within a DOE program [30], Siemens Westinghouse investigates a HTT-type gas turbine, but a pilot turbine cannot be expected before 2015. In the meantime, it is planned to adopt expanders of standard gas turbines for noncooled low-temperature operation in the ZENG project.

The authors expect that the Graz Cycle will be a beneficiary of these activities. So, the ZENG project will demonstrate most of

the components needed and thus help to pave the way toward a Graz Cycle plant. There is also current interest of end-users, but they depend on a manufacturer ready to get in. So, under the current circumstances, work toward a demonstration plant will not start before 2010.

Conclusions

Within the European project ENCAP, several oxy-fuel power cycles were compared based on their thermodynamic efficiencies and technical maturity. The Graz Cycle and the SCOC-CC emerged as two very promising variants, the Graz Cycle due to its high efficiency and the SCOC due to its relatively low complexity at a slightly smaller efficiency.

In this work, the ENCAP study is repeated for the SCOC-CC and a modified Graz Cycle variant as presented at the ASME IGTI Conference 2006 [5]. Both oxy-fuel cycles were thermodynamically investigated, and a layout of the main components of both cycles was presented and discussed thoroughly. Contrary to the ENCAP study, the Graz Cycle achieves a remarkably higher efficiency, mainly because of the very high cooling demand of the SCOC-CC HTT. This is a result of the less favorable properties of the working fluid consisting mainly of CO_2.

The layout of the turbomachinery showed that both cycles need new designs for the HTT and the compressors because of their unusual working fluids. The low sonic velocity of CO_2 leads to a rotational speed of 3000 rpm for all SCOC-CC turbomachinery. So, more stages for the compressor and the HTT as compared to the Graz Cycle turbomachines are needed despite a much lower enthalpy drop. On the other hand, the SCOC-CC compressor has the advantage of a lower operating temperature. The cooling of the SCOC-CC HTT is done with working fluid in contrast to steam for the Graz Cycle HTT. Since the combustion process can lead to the accumulation of soot and ash in the working fluid, there is high risk of clogging of the internal cooling channels and film cooling holes. All turbomachinery of both cycles is regarded as feasible; no decisive advantage for the SCOC-CC components was seen contrary to the ENCAP study.

In a comparative economical analysis, the Graz Cycle power plant showed lower CO_2 mitigation costs of 5 \$/ton CO_2 mainly due to the higher efficiency of the Graz Cycle scheme.

So, the authors believe that their Graz Cycle is a very efficient and feasible solution for a future CCS scheme. Its possibility to use syngas from coal gasification makes it also attractive for an emission-free use of coal as a relatively cheap and long-term available fuel [31].

Nomenclature

A_{ax} = flow cross section
$c_{\rho,c}$ = heat capacity of cooling medium
$c_{p,g}$ = heat capacity of main fluid
dQ = differential convective heat transfer
dT_1 = differential temperature decrease due to polytropic expansion
dT_2 = differential temperature decrease due to convective cooling
$d\dot{m}_c$ = differential cooling mass flow
f = ratio of cooled surface to flow cross section
$\dot{m}$ = main mass flow
$\dot{m}_c$ = total cooling mass flow of a partial turbine
n_{st} = stage number of partial turbine
Pr = Prandtl number
Q_{st} = stage convective heat transfer
Re = Reynolds number
St = Stanton number
T = temperature of main gas flow
T_c = temperature of inlet cooling mass flow
T_m = allowable metal temperature
ΔT_1 = stage temperature decrease due to polytropic expansion
w = velocity at blade row exit
α = heat transfer coefficient
β = flow angle at blade row exit
ρ = density

References

[1] Haege, K., 2006, www.zero-emissionplatform.eu
[2] Brandels, L., 2006, www.encapco2.org
[3] Franco, F., Mina, T., Woolatt, G., Rost, M., and Bolland, O., 2006, "Characteristics of Cycle Components for CO_2 Capture," *Proceedings of the Eighth International Conference on Greenhouse Gas Control Technologies*, Trondheim, Norway.
[4] Sanz, W., Jericha, H., Luckel, F., and Heitmeir, F., 2005, "A Further Step Towards a Graz Cycle Power Plant for CO_2 Capture," *ASME Turbo Expo 2005*, Reno-Tahoe, USA, ASME Paper No. GT2005-68456.
[5] Jericha, H., Sanz, W., and Göttlich, E., 2006, "Design Concept for Large Output Graz Cycle Gas Turbines," *ASME Turbo Expo 2006*, Barcelona, Spain, ASME Paper No. GT2006-90032.
[6] SimTech Simulation Technology, 2003, "IPSEpro Overview," http://www.simtechnology.com/IPSEpro
[7] Wagner, W., and Kruse, A., 1998, "Properties of Water and Steam," Springer-Verlag Berlin.
[8] Span, R., and Wagner, W., 1996, "A New Equation of State for Carbon Dioxide Covering the Fluid Region From the Triple-Point Temperature to 1100 K at Pressures up to 800 MPa," J. Phys. Chem. Ref. Data, **25**(6), pp. 1509–1596.
[9] Jericha, H., Lukasser, A., and Gatterbauer, W., 2000, "Der 'Graz Cycle' für Industriekraftwerke gefeuert mit Brenngasen aus Kohle- und Schwerolvergasung," (in German), *VDI Conference*, Essen, Germany, VDI Berichte 1566.
[10] Sanz, W., Jericha, H., Moser, M., and Heitmeir, F., 2004, "Thermodynamic and Economic Investigation of an Improved Graz Cycle Power Plant for CO_2 Capture," *ASME Turbo Expo 2004*, Vienna, Austria, ASME Paper No. GT2004-53722 [2005, ASME J. Eng. Gas Turbines Power, **127**, pp. 765–772].
[11] Jordal, K., Bolland, O., and Klang, A., 2003, "Effects of Cooled Gas Turbine Modelling for the Semi-Closed O_2/CO_2 Cycle With CO_2 Capture," *ASME Turbo Expo 2003*, Atlanta, USA, ASME Paper No. 2003-GT-38067.
[12] Louis, J. F., 1977, "Systematic Studies of Heat Transfer and Film Cooling Effectiveness," AGARD Report No. CP 229.
[13] Jericha, H., 1985, "Efficient Steam Cycles With Internal Combustion of Hydrogen and Stoichiometric Oxygen for Turbines and Piston Engines," *CIMAC Conference Paper*, Oslo, Norway.
[14] Jericha, H., Sanz, W., Woisetschläger, J., and Fesharaki, M., 1995, "CO_2-Retention Capability of CH_4/O_2-Fired Graz Cycle," *CIMAC Conference Paper*, Interlaken, Switzerland.
[15] Jericha, H., and Fesharaki, M., 1995, "The Graz Cycle—1500°C Max Temperature Potential H_2-O_2 Fired CO_2 Capture With CH_4-O_2 Firing," *ASME Cogen-Turbo Power Conference*, Vienna, Austria, ASME Paper No. 95-CTP-79.
[16] Jericha, H., and Göttlich, E., 2002, "Conceptual Design for an Industrial Prototype Graz Cycle Power Plant," *ASME Turbo Expo 2002*, Amsterdam, The Netherlands, ASME Paper No. 2002-GT-30118.
[17] Jericha, H., Göttlich, E., Sanz, W., and Heitmeir, F., 2003, "Design Optimisation of the Graz Cycle Prototype Plant," *ASME Turbo Expo 2003*, Atlanta, USA, ASME Paper No. 2003-GT-38120 [2004, ASME J. Eng. Gas Turbines Power, **126**, pp. 733–740].
[18] Heitmeir, F., Sanz, W., Göttlich, E., and Jericha, H., 2003, "The Graz Cycle—A Zero Emission Power Plant of Highest Efficiency," *XXXV Kraftwerkstechnisches Kolloquium*, Dresden, Germany.
[19] Jericha, H., Sanz, W., Pleringer, P., Göttlich, E., and Errol, P., 2004, "Konstruktion der ersten Stufe der HTT-Gasturbine für den Graz Cycle" (in German), *VDI Tagung, Stationäre Gasturbinen: Fortschritte und Betriebserfahrungen*, Leverkusen, Germany, VDI Berichte 1857.
[20] Jericha, H., and Sanz, W., 2001, "Warmekraftanlagen mit Verbrennung von Kohlenwasserstoffen mit reinem Sauerstoff zur Stromerzeugung bei Rückhaltung von Kohlendioxyd" (in German), Austrian Patent No. AT 409 162 B.
[21] Göttlich, E., Innocenti, L., Vacca, A., Sanz, W., Woisetschläger, J., Facchini, B., Jericha, H., and Rossi, E., 2004, "Measurement and Simulation of a Transonic Innovative Cooling System (ICS) for High-Temperature Transonic Gas Turbine Stages," *ASME Turbo Expo 2004*, Vienna, ASME Paper No. GT2004-53712.
[22] Sanz, W., Jericha, H., Bauer, B., and Göttlich, E., 2007, "Qualitative and Quantitative Comparison of Two Promising Oxy-Fuel Power Cycles for CO_2 Capture," *ASME Turbo Expo 2007*, Montreal, Canada, ASME Paper No. GT2007-27375.
[23] IEA, 2004, "Prospects for CO_2 Capture and Storage," IEA/OECD, Paris, France.
[24] Jericha, H., Sanz, W., and Göttlich, E., 2006, "Gasturbine mit CO2-Rückhaltung—490 MW (System Graz Cycle)" (in German), *VDI Tagung,*

Stationäre Gasturbinen: Fortschritte und Betriebserfahrungen, Leverkusen, Germany.
[25] Hennecke, D. K., 1997, "Transsonik-Verdichter-Technologien für stationäre Gasturbinen und Flugtriebwerke" (in German), *Festschrift zum Jubiläum 100 Jahre Turbomaschinen TU-Darmstadt*, TU-Darmstadt, Darmstadt, Germany.
[26] König, P., and Rossmann, A., 1999, *Ratgeber für Gasturbinenbetreiber* (in German), Vulkan-Verlag, Essen.
[27] Göttlicher, G., 1999, "Energetik der Kohlendioxidrückhaltung in Kraftwerken" (in German), Fortschritt-Berichte VDI, Reihe 6, Energietechnik, Nr. 421.
[28] Anderson, R. E., and Bischoff, R. W., 2006, "Durability and Reliability Demonstration of a Near-Zero-Emission Gas-Fired Power Plant," PIER Final Project report (www.cleanenergystems.com).
[29] Hustad, C.-W., Tronstad, I., Anderson, R. E., Pronske, K. L., and Viteri, F., 2005, "Optimization of Thermodynamically Efficient Nominal 40 MW Pilot and Demonstration Power Plant in Norway," *ASME Turbo Expo 2005*, Reno-Tahoe, USA, ASME Paper No. GT2005-68640.
[30] U.S. Department of Energy, 2005, http://www.fossil.energy.gov/news/techlines/2005/tl_enabling_turbines_awards.html
[31] Simmons, H., 2005, "The Importance of Turbo Expo," Mech. Eng. (Am. Soc. Mech. Eng.), **127**(12), p. 18.

Zhao Qingjun
Institute of Engineering Thermophysics,
Chinese Academy of Sciences,
P.O. Box 2706,
Beijing 100080, China
e-mail: qingjunzhao@163.com

Tang Fei
Institute of Engineering Thermophysics,
Chinese Academy of Sciences,
P.O. Box 2706,
Beijing 100080, China;
Graduate School of the Chinese Academy of Sciences,
P.O. Box 2706,
Beijing 100080, China

Wang Huishe

Du Jianyi

Zhao Xiaolu

Xu Jianzhong

Institute of Engineering Thermophysics,
Chinese Academy of Sciences,
P.O. Box 2706,
Beijing 100080, China

Influence of Hot Streak Temperature Ratio on Low Pressure Stage of a Vaneless Counter-Rotating Turbine

In order to explore the influence of hot streak temperature ratio on the low pressure stage of a vaneless counter-rotating turbine, three-dimensional multiblade row unsteady Navier–Stokes simulations have been performed. The predicted results show that hot streaks are not mixed out by the time they reach the exit of the high pressure turbine rotor. The separation of colder and hotter fluids is observed at the inlet of the low pressure turbine rotor. After making interactions with the inner-extending and outer-extending shock waves in the high pressure turbine rotor, the hotter fluid migrates toward the pressure surface of the low pressure turbine rotor, and most of the colder fluid migrates to the suction surface of the low pressure turbine rotor. The migrating characteristics of the hot streaks are dominated by the secondary flow in the low pressure turbine rotor. The results also indicate that the secondary flow intensifies in the low pressure turbine rotor when the hot streak temperature ratio is increased. The effects of the hot streak temperature ratio on the relative flow angle at the inlet of the low pressure turbine rotor are very remarkable. The isentropic efficiency of the vaneless counter-rotating turbine decreases as the hot streak temperature ratio is increased. [DOI: 10.1115/1.2836615]

Introduction

A vaneless counter-rotating turbine (VCRT) is composed of a highly loaded single stage high pressure turbine (HPT) and a single stage vaneless counter-rotating low pressure turbine/rotor (LPT/LPR). Compared with the conventional two stage turbine, the VCRT can offer significant benefits due to the part elimination and size reduction. These benefits include elevating thrust-to-weight ratio, reducing cooling flow and cost, and so on (Keith et al., 2000 [1]; Haldeman et al., 2000 [2]). From the 1950s, counter-rotating turbines have been carefully investigated (Wintucky, et al., 1958 [3]; Louis, 1985 [4]; Zhao, et al., 2006 [5,6]).

The research on the secondary flow of rotating system, which was performed by Lakshminarayana and Horlock (1973 [7]), indicated that inlet temperature nonuniformities led to secondary flow in the rotating blade rows. By means of the large-scale rotating rig (LSRR), Butler et al. (1989 [8]) also found that the temperature gradients have significant impact on the flow of the rotor blade rows when the inlet total pressure was uniform. Their conclusions had been verified by some other experimental and numerical investigations (Rai and Dring 1990 [9]; Roback and Dring, 1992 [10]; Dorney, 1996 [11]). The experimental and numerical investigations, which were carried out by Butler et al. (1989 [8]), Sharma et al. (1990 [12]), Roback and Dring (1992 [10]), showed that hot streaks caused hotter gas to accumulate on the rotor blade pressure surface (PS) and colder gas to accumulate on the suction surface (SS). However, the numerical investigation of Gundy-Burlet and Dorney (1996 [13]) indicated that the migrating patterns of the hot streak were directly related to the position of the hot streak in relation to the first-stage stator. They found that the hotter gas mixed with the first-stage stator wake and migrated to the first-stage rotor SS as the hot streak directly impinged on the leading edge (LE) of the first-stage stator. On the contrary, the hotter gas migrated to the first-stage rotor PS when the hot streak was located in the midpassage of two adjacent first-stage stator vanes. The results also showed that the heat loadings of the first-stage rotor and second-stage stator were all alleviated when the hot streak impacted on the LE of the first-stage stator. In addition to the effects of the secondary flow and circumferentially relative locations, Shang (1995 [14]) showed that the migrating action of the hot streak in the rotor blade rows was also affected by the buoyancy, which tended to drive the hot streak toward the hub.

The experimental facilities most often used in hot streak investigations include the LSRR (Butler et al., 1989 [8]; Roback and Dring, 1992 [10]), NASA Warm Core Turbine Test Rig (WCTTR) (Schwab et al., 1983 [15]; Stabe et al., 1984 [16]), and MIT Blowdown Turbine Test Rig (BTTR) (Shang, 1995 [14]; Guenette, 1985 [17]). In the LSRR, only low speed experiments can be performed. Although the WCTTR experiments may be performed at high speed, the blade surface temperature cannot be measured. Compared with the LSRR and WCTTR, BTTR not only may be operated at high speed, but also the blade surface temperature can be acquired in the experiments. By means of the BTTR, Shang (1995 [14]) obtained the effects of hot streak migration on blade surface temperature at high speed.

Some numerical investigations were performed focusing on the effects of the hot streak temperature ratio on the temperature distribution in the LSRR turbines. An investigation, which was performed by Dorney et al. (1991 [18]), qualitatively predicted the temperature redistribution patterns within the turbine rotor at a hot

Manuscript received June 13, 2007; final manuscript received October 28, 2007; published online April 2, 2008. Review conducted by Je-Chin Han.

streak temperature ratio of 1.2. However, the quantitative levels of surface temperature distributions were not satisfied compared with the experimental data. Krouthen and Giles (1988 [19]) performed a two-dimensional numerical simulation at a hot streak temperature ratio of 2.0. The predicted results were closer to the experimental data than the results obtained at a hot streak temperature ratio of 1.2. Takahashi and Ni (1990 [20]; 1991 [21]) performed two- and three-dimensional numerical investigations about the hot streak migration using hot streak temperature ratios of 1.5 and 2.0. Their results showed that the hot streak temperature ratio played an important role in the accurate prediction of turbine blade temperature distribution. Dorney (1996 [11]) carried out two-dimensional unsteady hot streak simulations at hot streak temperature ratios of 1.5, 2.0, and 2.5. An interesting phenomenon that a thin layer of cooler air separated the rotor PS from the hotter fluid was found under certain flow condition. The source of cooler fluid layer was traced to intermittent flow separation, which became more frequent as the inlet hot streak temperature ratio was increased.

Some researchers also performed hot streak simulations using other turbine geometries at different hot streak temperature ratios (Schwab et al., 1983 [15]; Weigand and Harasgama, 1994 [22]; Shang, 1995 [14]; Dorney et al., 1999 [23]). Their investigations are a benefit in exploring the effects of hot streak temperature ratio on the turbine heat transfer.

To the best of our knowledge, there are no results in the open literature about the effects of the hot streak temperature ratio on a VCRT. The VCRT has some unique characteristics, which are different from the conventional two stage turbine. These characteristics include the following:

- The HPT rotor and LPT/LPR are counter-rotating.
- The LPT is vaneless.
- There are high relative Mach number ($\sim$1.5) and relative flow angle ($\sim$70 deg) at the outlet of the HPT.

All of these characteristics cause more remarkable unsteady effects in the VCRT. Maybe, there are some new phenomena about the hot streak migration in the HPT rotor and LPR. The hot streak temperature ratio maybe also plays an important role in the hot streak migration. So, it is very necessary to perform an investigation about the effects of the hot streak temperature ratio on the VCRT heat transfer.

In this paper, the effects of the hot streak temperature ratio on the LPT/LPR airfoil surface temperature distributions will be explored first.

Numerical Algorithm

NUMECA software systems are employed to study this problem. The numerical method is described in detail in the user manual [24]. Here, only a brief description about the main features is reported.

The governing equations in NUMECA are the time dependent, three-dimensional Reynolds-averaged Navier–Stokes equations. The solver of NUMECA is FINE/TURBO and it is based on a cell centered finite volume approach, associated with a central space discretization scheme together with an explicit four-stage Runge–Kutta time integration method.

Residual smoothing, local time stepping, and multigridding are employed to speed up convergence to the steady state solution. The dual time stepping method (Jameson, 1991 [25]) and domain scaling method (Rai, 1989 [26]) are used to perform time accurate calculations.

Various turbulence models have been included in the solver for the closure of governing equations. The widely used approach based on one transport equation (Spalart and Allmaras, 1992 [27]) has been selected in this paper. The Spalart–Allmaras model has become quite popular in the last years because of its robustness and its ability to treat complex flows. The main advantage of Spalart–Allmaras model when compared to the one of Baldwin–Lomax is that the turbulent eddy viscosity field is always continuous. Its advantage over the k-ε model is mainly its robustness and the lower additional CPU and memory usage.

The time step limitations arising from the turbulent source terms are accounted for in the model so that computations can be performed with the maximum allowable CFL number without penalizing numerical efficiency.

Table 1 The flow conditions in the VCRT

Inlet total temperature (K)	500
Inlet total pressure (kPa)	300
Mass flow (kg/s)	17.7
Rotational speed of HPT rotor (rpm)	6970
Rotational speed of LPR (rpm)	−6970
Step-down pressure ratio of HPT	2.93
Step-down pressure ratio of LPT	2.07
SWR	1.77

Boundary Conditions

The theory of characteristics is used to determine the boundary conditions at the inlet and exit of computational domain. At the inlet, total pressure, total temperature, and circumferential and radial flow angles are specified as many constants in the simulation without inlet hot streak. In those simulations with inlet hot streaks, the inlet total temperature is specified as a function of the spatial coordinates. The total pressure and the circumferential and radial flow angles are still given as many constants at the inlet. Due to selecting the Spalart–Allmaras turbulence model, the kinematic turbulent viscosity should be specified in the inlet boundary conditions. In this paper, it is 0.0001 m^2/s.

In these simulations with inlet hot streaks, the flow variables in the hot streak must be modified. In the hot streak, the inlet flow variables used to define the specified boundary conditions can be written as

$$u_{\mathrm{hs}} = u_\infty \sqrt{t_{\mathrm{hs}}/t_\infty} \quad v_{\mathrm{hs}} = v_\infty \sqrt{t_{\mathrm{hs}}/t_\infty}$$

$$w_{\mathrm{hs}} = w_\infty \sqrt{t_{\mathrm{hs}}/t_\infty} \quad p_{\mathrm{hs}} = p_\infty \tag{1}$$

$$a_{\mathrm{hs}} = a_\infty \sqrt{t_{\mathrm{hs}}/t_\infty} \quad \rho_{\mathrm{hs}} = \rho_\infty/(t_{\mathrm{hs}}/t_\infty)$$

At the exit, the circumferential and radial velocity components, entropy, and the downstream running Riemann invariant are extrapolated from the interior of the computational domain. The static pressure p_6 is specified at the hub of the exit and the static pressure values at all other radial locations are obtained by integrating the equation for radial equilibrium. Periodicity is enforced along the outer boundaries of H–O–H grids in the circumferential direction.

No-slip boundary conditions should be enforced at solid wall surfaces for viscous simulations. In this paper, absolute no-slip boundary conditions are enforced at the hub and tip end walls of the HPT stator regions, along the surface of the HPT vane, and along the casing walls of the HPT rotor and LPR regions. Relative no-slip boundary conditions are imposed at the hub end walls of the HPT rotor and LPR regions, and the surfaces of the HPT rotor and LPR blades. It is assumed that the normal derivative of pressure is zero at the solid wall surfaces, and that the walls are adiabatic.

Vaneless Counter-Rotating Turbine

The VCRT studied in this paper is composed of a highly loaded single stage HPT coupled with a vaneless counter-rotating LPT/LPR. It has high step-down pressure ratios and operates in transonic regimes. The design conditions of the VCRT are shown in Table 1.

Table 2 Grid dimensions (*i*-azimuthal direction, *j*-spanwise direction, *k*-streamwise direction)

Row	$i \times j \times k$	Nodes	Blocks
HPT inlet	$33 \times 49 \times 25$	40,425	1
HPT stator	$25 \times 49 \times 185$	226,625	1
HPT rotor	$17 \times 49 \times 241$	200,753	1
LPT/LPR	$17 \times 49 \times 193$	160,769	1
LPT outlet	$41 \times 49 \times 25$	50,225	1

Table 3 Flow conditions in the NASA test turbine

Inlet total temperature (K)	672.2
Inlet total pressure (Pa)	3.103×10^5
Mass flow (kg/s)	6.13
Specific work (J/kg)	1.299×10^5
Rotational speed (rpm)	11373
Total pressure ratio	2.36
Load factor	1.675
Flow coefficient	0.449

The airfoil counts in the steady and unsteady model are reduced from the actual count 36/36/36 for the HPT stator, HPT rotor, and LPR, respectively, to 1/1/1 for computational efficiency. No tip clearance of the rotor is modeled. The typical y^+ values of less than 15 are used at the boundaries. All of these results in a CFD model with about 0.68×10^6 grid points employing a sheared "H–O–H" mesh generated by NUMECA AUTOGRID (see Table 2 and Fig. 1). It will take about one week to compute an unsteady case using a 3.0 GHz one-Intel-CPU computer. According to the past experiences, which were obtained in the steady three-dimensional viscous analyses about the VCRT (Zhao et al., 2006 [6]), the grid size in Table 2 is adequate to the investigation in this paper. Although the effects of the airfoil counts and tip clearance on the hot streak migration have not been considered in this paper, the general characteristics about the hot streak migration in the VCRT can still be obtained using the above-mentioned geometry. The general effects of the hot streak temperature ratio on the VCRT heat transfer can also be attained through the investigation.

Validating of Numerical Code

In order to validate the predicted accuracy of the numerical code, a three-dimensional multistage unsteady Navier–Stokes simulation with inlet radial hot streak has been performed in a test turbine. Then the time-averaged numerical data are compared with the available experimental data. The test turbine is a 0.767 scale rig modeling the first stage of a two-stage core turbine designed for a modern high bypass ratio engine. The vane has a constant section, and was designed for a constant exit flow angle of 75 deg from axial. The rotor inlet was designed to accept the vane exit flow with either zero or slight negative incidence. The rotor outlet is a free-vortex design. Both vane and blade axial chords are constant radially. The experimental turbine has 26 vane airfoils and 48 rotor airfoils. It was tested in the NASA Lewis Research Center's WCTTR (Stabe et al. 1984 [16]; Dorney et al. 1999 [23]). The test conditions for the turbine are shown in Table 3.

The inlet radial temperature profile in the experiment was produced using the combustor exit radial temperature simulator (CERTS) inlet, which injected cool air through circumferential slots in the hub and tip end walls upstream of the vane. Figure 2 shows the inlet radial temperature distribution. The ratio of the maximum total temperature to the average total temperature is approximately 1.05, and the ratio of maximum to minimum total temperature is approximately 1.20 at the turbine inlet.

For reducing the cost of the calculation, the number of vanes in the first row is decreased to 24 and the size of the vane is increased by a factor of 26/24 to maintain the same blockage. So, a 1-vane/2-rotor airfoil count ratio is used in the unsteady numerical simulation.

Figures 3–5 show comparisons between the predicted and experimental time-averaged critical velocity ratio distributions at the hub, midspan, and tip of the vane. The predicted data are very close to the experimental data, except for near the trailing edge (TE) region of the vane and the SS at the tip of the vane.

Figure 6 illustrates the predicted and experimental total pressure distributions at the outlet of the turbine. There is a good agreement between the predicted and experimental results.

Figure 7 shows the predicted and experimental total temperature distributions at the outlet of the turbine. The predicted values show close agreement with the experimental values from hub to 70% span. The discrepancies near the tip region are due to the differences in the experimental (1.2%) and numerical (0%) tip clearances.

The above-mentioned results indicate that the predicted accuracy of the numerical code is acceptable in this investigation.

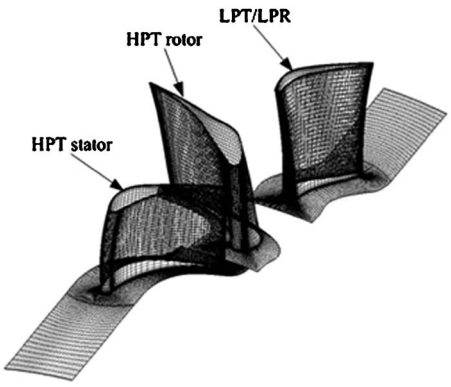

Fig. 1 Three-dimensional grid topology of the VCRT

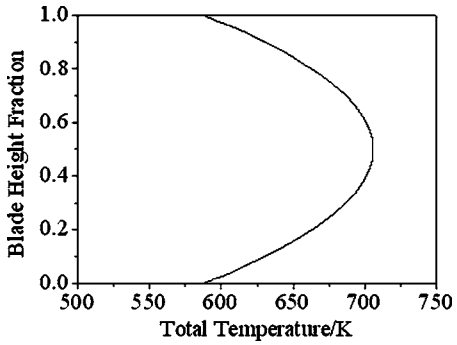

Fig. 2 Turbine inlet radial temperature profile

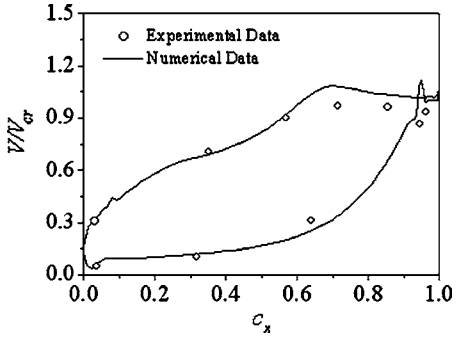

Fig. 3 Critical velocity ratio at the hub of the vane

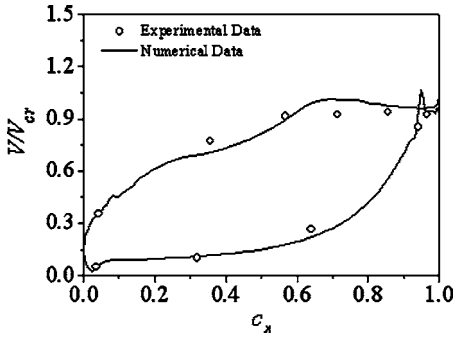

Fig. 4 Critical velocity ratio at the midspan of the vane

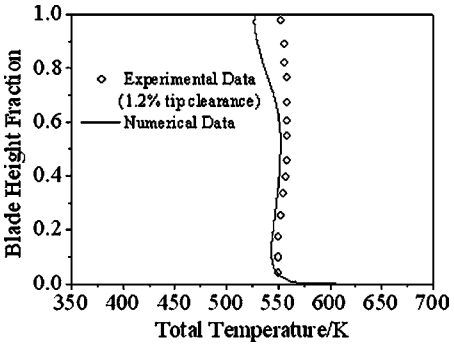

Fig. 7 Total temperature distribution at the outlet of the turbine

Inlet Hot Streak Profiles

In this paper, five hot streak temperature ratios, including 1.0 (uniform inlet temperature distribution), 1.2, 1.6, 2.0, and 2.4, are selected. The hot streak is circular in shape with a diameter equal to 25% of the HPT vane span. The circular hot streak can be used to simulate the radial and circumferential inlet temperature distortions. The results in Ref. [28] have indicated that it is of benefit to the cooling design of the VCRT when the hot streak directly impacts on the LE of the HPT vane compared with other locations. So, the hot streak location directly impinged on the LE of the HPT vane is adopted in the investigation. The hot streak center is located at 50% of the span for eliminating the effects of the hub and tip end walls. Figure 8 shows the inlet hot streak profiles.

Numerical Results

A series of numerical experiments simulating hot streak migration through the VCRT has been performed by means of a three-dimensional unsteady Navier–Stokes procedure called FINE/TURBO. The hot streak temperature ratios of between 1.0 and 2.4, including 1.0, 1.2, 1.6, 2.0, and 2.4, are used in these numerical simulations.

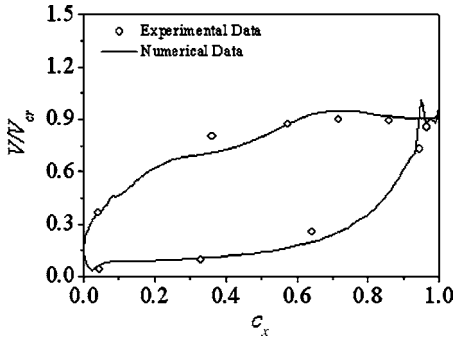

Fig. 5 Critical velocity ratio at the tip of the vane

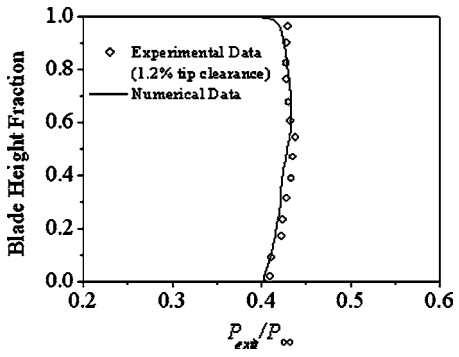

Fig. 6 Total pressure distribution at the outlet of the turbine

Figure 9 shows the static temperature contours on the midspan of the HPT rotor and LPR at one instant in time for all the cases. In the case without inlet hot streak (i.e., $T_{hs}/T_{\infty}=1.0$), the temperature distribution is almost uniform at the inlet of the HPT rotor. However, there is a separating phenomenon of colder fluid (the outer-extending shock wave of the HPT rotor) and hotter fluid (the wake of the HPT rotor) at the inlet of the LPR. The wake of the HPT rotor is cut by the LPR and convects to the PS of the LPR after making an interaction with the outer-extending shock wave (OESW) of the HPT rotor. The OESW cut by the LPR migrates toward the SS of the LPR. In addition to the wake and the OESW, other fluids, which still maintain lower temperature at the inlet of LPR, convect toward the PS after being cut by the LPR. That causes a lower heat loading on the PS. Surely, the heat loading on the PS is still higher than that on the SS except for the TE region. At the TE region, the heat loading on the SS is higher than that on the PS due to the effect of a shock wave on about 70% axial chord of the SS.

The migrating paths of the hot streaks in the HPT rotor and LPR are also exhibited by means of the static temperature contours in Fig. 9 for those cases with inlet hot streak. According to the report in Ref. [29], the secondary flow induced temperature redistribution does not occur in the HPT stator as the hot streak directly impinges on the LE of the HPT stator. However, secondary flow and buoyancy cause the temperature redistribution in the HPT rotor when the hot streak mixes with the HPT vane wake and flows into the HPT rotor. The hotter fluid convects toward the PS of the HPT rotor. Most of the colder fluid migrates to the SS of the HPT rotor. These phenomena are also indicated in Fig. 9. The hotter fluid, which has migrated to the PS of the HPT rotor, goes through the HPT rotor along the PS. It penetrates through the inner-extending shock wave (IESW) at the TE of the HPT rotor and encounters the OESW at the interface between the HPT rotor and the LPR. Then it mixes with the wake of the HPT rotor. The OESW also has an effect on the mixed fluid. Finally, the mixed fluid is cut by the LPR and convects toward the PS of the LPR. On the other hand, most of the colder fluid, which has migrated to the SS of the HPT rotor, goes through the HPT rotor along the SS. It penetrates through the IESW at about 60% axial chord of the HPT rotor and pierces the OESW at the TE of the HPT rotor. After making an interaction with the OESW, it is cut by the LPR and migrates to the SS of the LPR. Figure 9 also illustrates that the hotter fluid, which has mixed with the wake of the HPT stator, more easily migrates to the PS of the HPT rotor as the hot streak temperature ratio is increased. The result indicates that the secondary flow in the HPT rotor becomes more intensive with the increase of the hot streak temperature ratio. These conclusions have been drawn in Ref. [29]. The similar conclusions can also been drawn in the LPR.

Generally, the temperature dissipated degree of the fluid in tur-

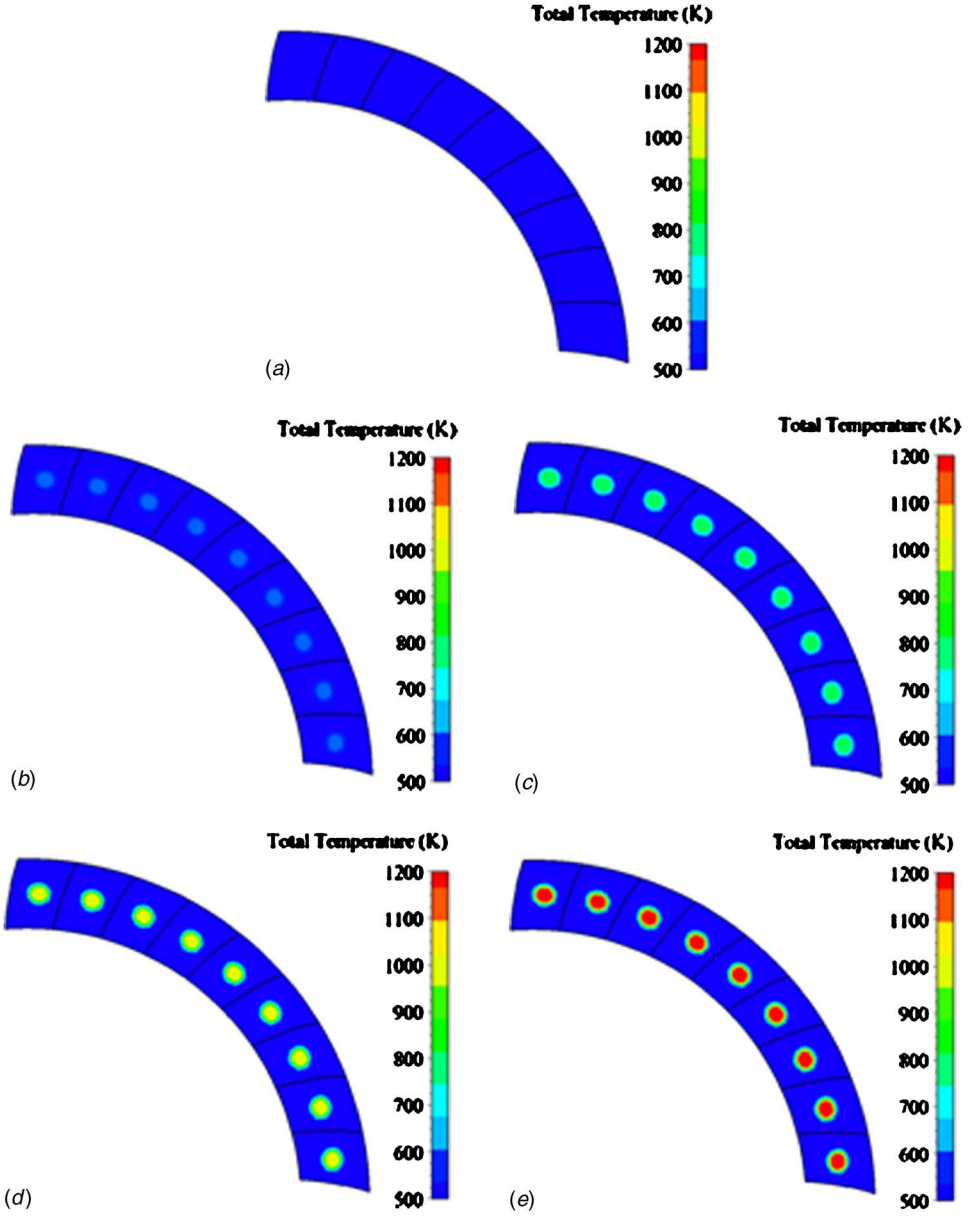

Fig. 8 Inlet hot streak profiles

bines is affected by the secondary flow, shock wave, wake, and so on. In the LPR, the dissipated degree of the static temperature is defined as follows:

$$D_t = \left(\frac{t_5 - t_6}{t_5} \right) \times 100\% \tag{2}$$

Figure 10 shows the span distributions of the static temperature dissipated degree in the LPR for different hot streak temperature ratios. The results indicate that the hot streak temperature ratio has almost no effect on the static temperature dissipated degree at the region from 75% span to the tip. At the region from 45% span to 75% span, the increase of the hot streak temperature ratio trends to increase the dissipated degree. On the contrary, the dissipated degree decreases as the inlet hot streak temperature ratio is increased at the region from the hub to 45% span.

Figure 11 illustrates the time averaged static temperature contours on the LPR for different hot streak temperature ratios. The results indicate that the static temperature distribution on the PS of the LPR is relatively uniform for the case without inlet hot streak. However, a nonuniform temperature distribution is observed on the SS of LPR for the case. There are two regions that elevated adiabatic wall temperature on the SS. The larger high-temperature region originates from the hub at about 15% axial chord, and extends radially toward the TE at about 40% span. The second high-temperature region emanates from the tip at the LE, and extends inverse radially to the 50% axial chord at about 90% span. The similar high-temperature regions are also observed in the cases with inlet hot streak. The result indicates that the existence of these two high-temperature regions on the SS is not directly associated with the inlet hot streak. Figure 12 illustrates the limiting streamlines superimposed onto instantaneous static temperature contours on the SS of the LPR in the case with a hot streak temperature ratio of 2.0. The results indicate that these two high-temperature regions are directly associated with the secondary flow in the LPR. In addition to the influence of secondary flow, the shock wave in the LPR also makes an effect on the high-temperature region, which emanates from the hub. So, the high-temperature region originating from the hub is directly associated with the interaction between the secondary flow and the shock wave. The results in Fig. 11 also indicate that the size and tem-

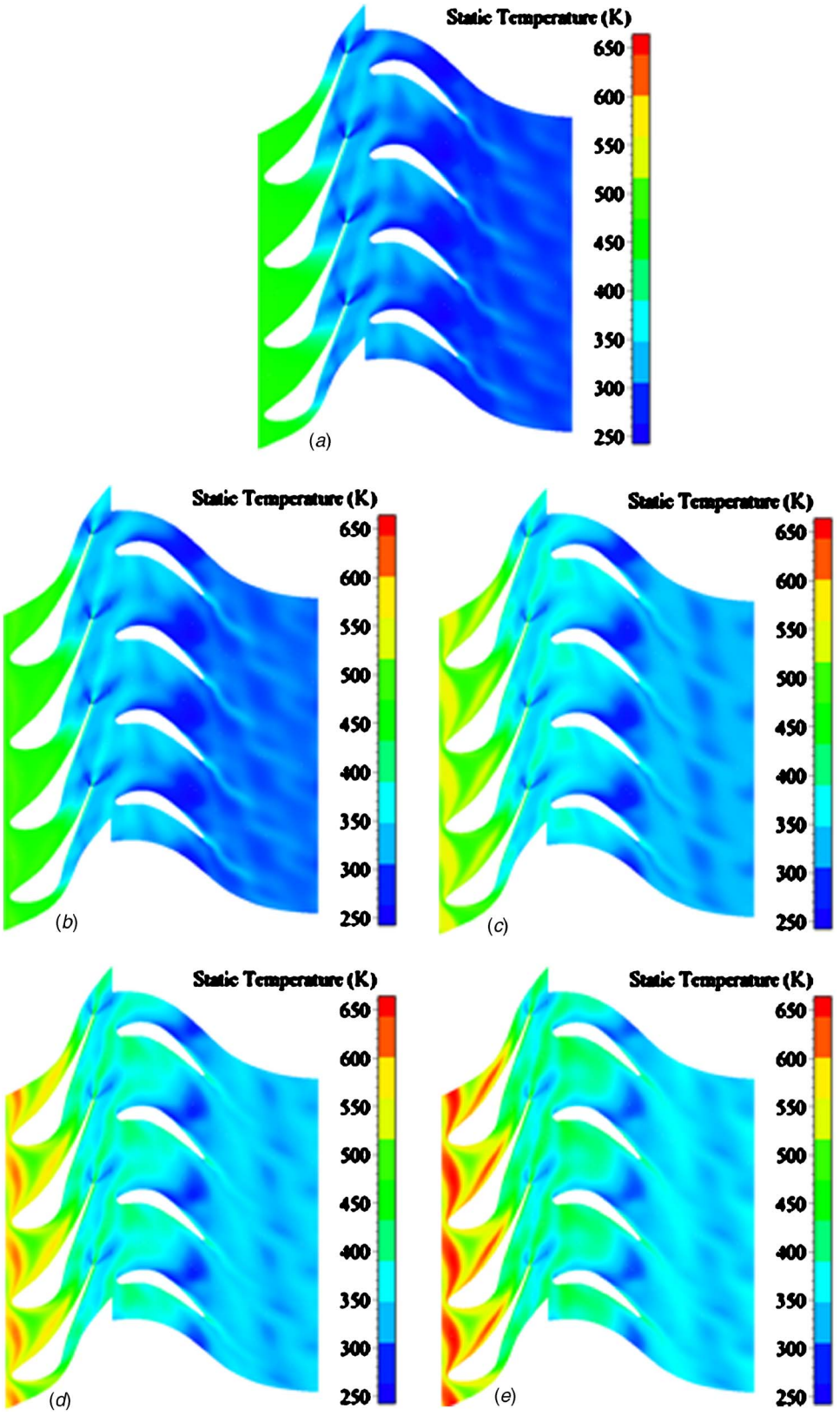

Fig. 9 Instantaneous temperature contours on the midspan of the HPT rotor and LPR

perature of these two high-temperature regions increase as the hot streak temperature ratio is increased. It indicates that the secondary flow is intensified in the LPR with the increase of the hot streak temperature ratio. In those cases with inlet hot streak, there is still a larger high-temperature region on the SS of the LPR besides the above-mentioned two high-temperature regions. The region emanates from the LE, and extends axially toward the TE. The radial extent of this region decreases, approaching the TE due

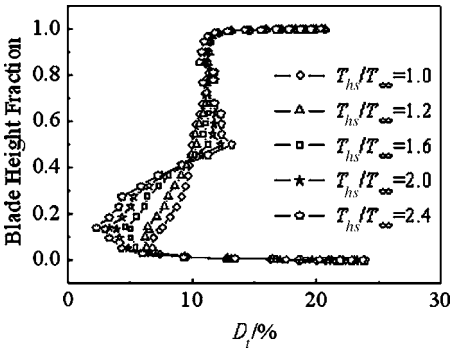

Fig. 10 Span distributions of static temperature dissipated degree in the LPR

to the effect of the strong secondary flow. On the other hand, Fig. 11 also indicates that there is a larger high-temperature region on the PS of the LPR for these cases with inlet hot streak. The region originates from the LE, and extends axially towards the TE. The radial extent of this region increases approaching the TE due to the influence of the strong secondary flow. The results in Fig. 11 show that the higher hot streak temperature ratio induces stronger secondary flow. The secondary flow drives the hotter fluid toward the hub and tip on the PS and towards the midspan on the SS. According to the report in Ref. [29], the migrating characteristics of the hot streak in the HPT rotor are predominated by the combined effects of the secondary flow and buoyancy. So, the effect of the buoyancy on the hotter fluid in the LPR should also be investigated. In the HPT rotor, the buoyancy induces the hotter fluid near the rotor blade surface to migrate towards the hub (Zhao et al., 2007 [29]). However, this phenomenon has not been observed in the LPR. The result indicates that the effect of the buoyancy on the high-temperature fluid near the LPR blade surface is very weak. The effect of the buoyancy on the hotter fluid can be explained by using the simple radial equilibrium theory. According to the simple radial equilibrium theory, the formula (3) (see the Ref. [29]) can be deduced.

$$\frac{d^2\delta}{dx^2} = \frac{1}{r}\frac{U^2}{W_x^2}\left(\frac{t_{\mathrm{hs}}}{t_\infty} - 1\right) = \frac{1}{r}\left(\frac{t_{\mathrm{hs}}}{t_\infty} - 1\right)\frac{1}{\phi^2} \tag{3}$$

The formula (3) offers an evaluation criterion on the buoyancy effect from physical mechanism. The buoyancy effect is propor-

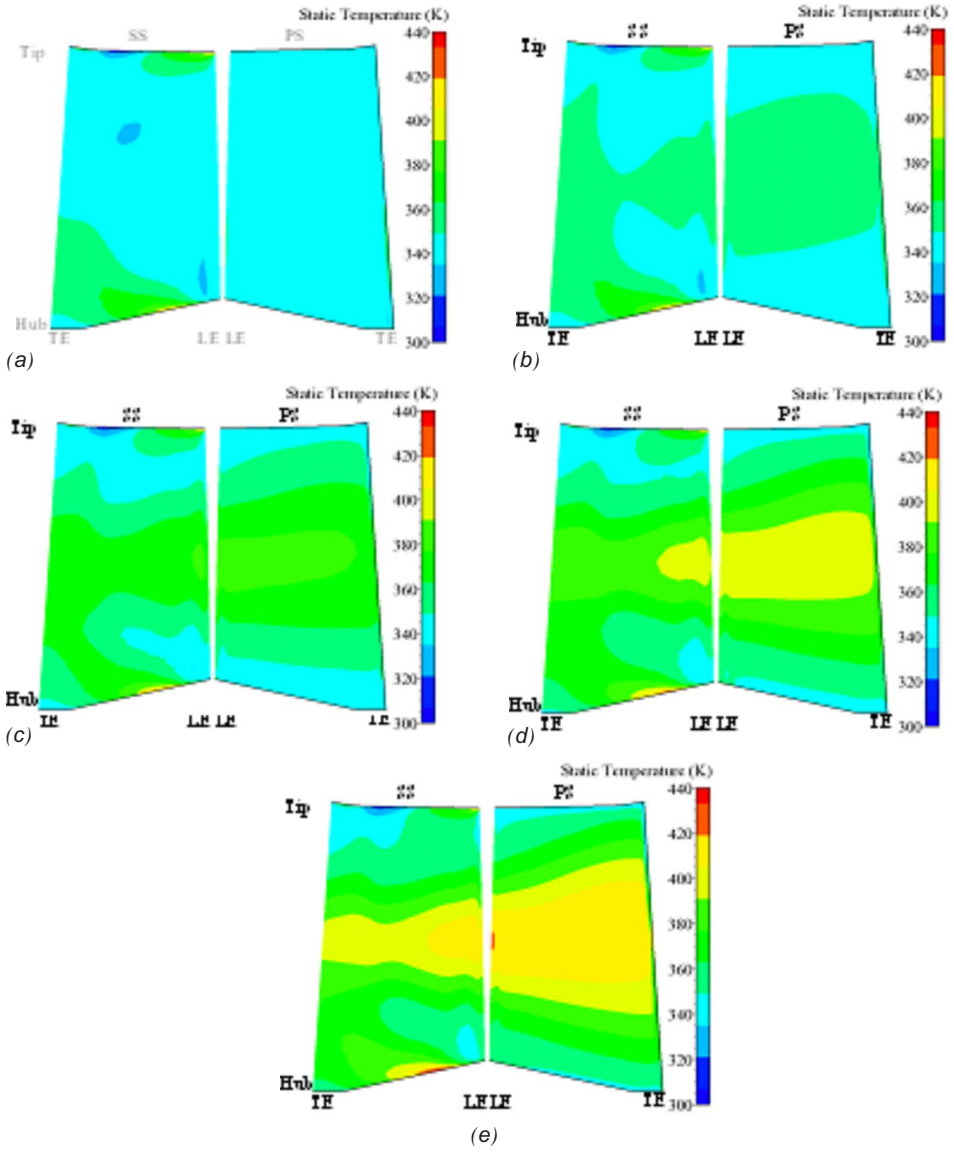

Fig. 11 Time-averaged static temperature contours on the LPR

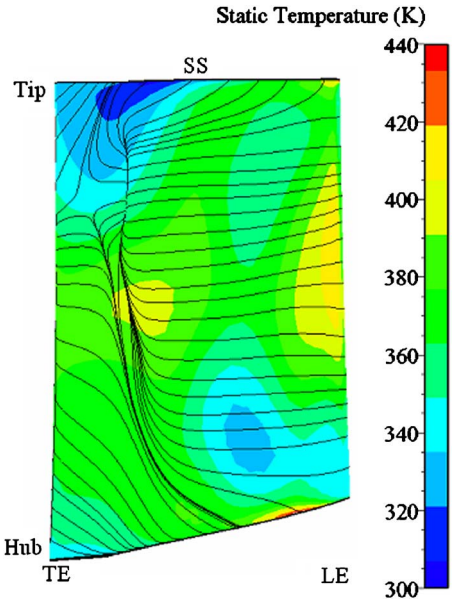

Fig. 12 Instantaneous static temperature and limiting streamlines on the SS of the LPR in the case with a hot streak temperature ratio of 2.0

tional to the ratio of static temperature of the hot streak to that of the free stream, and depends on the square of the flow coefficient with inverse proportion.

Figures 13 and 14 show the span distributions of the time and pitch averaged static temperature and relative axial velocity at the inlet of the LPR for all the cases. The results in Fig. 13 indicate that the static temperature ratio between the hot streak and the freestream is very small for all the cases. The maximum value is

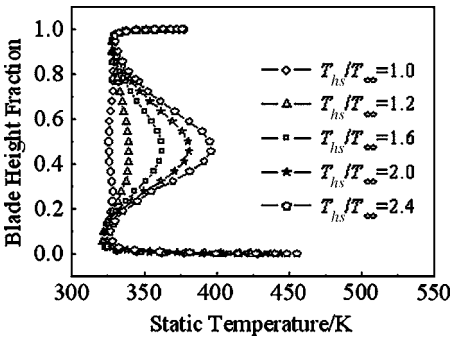

Fig. 13 Span distributions of time and pitch averaged static temperature at the inlet of the LPR

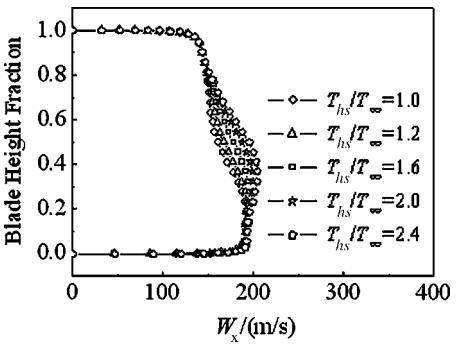

Fig. 14 Span distributions of time and pitch averaged relative axial velocity at the inlet of the LPR

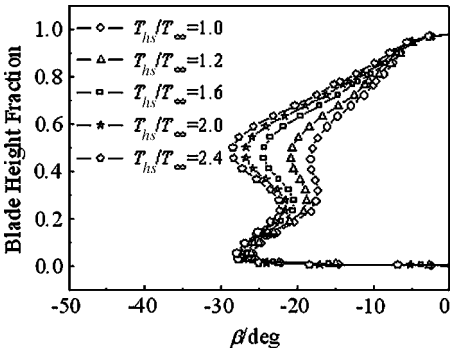

Fig. 15 Span distributions of time and pitch averaged relative flow angle at the inlet of the LPR

only near 1.2. The results in Fig. 14 show that the relative axial velocity is about 200 m/s at 50% span of the LPR inlet. It results in the square of the flow coefficient that is close to 1.0 at the midspan of the LPR inlet. So, according to the formula (3), this conclusion that the effect of the buoyancy on the hotter fluid near the LPR blade surface is very weak can be drawn for all the cases. It illustrates that the migrating characteristics of the hot streak are dominated by the secondary flow in the LPR.

Figures 15 and 16 show the span distributions of the time and pitch averaged relative flow angle at the inlet and outlet of the LPR, respectively. The results in Fig. 15 indicate that the relative flow angle increases as the hot streak temperature ratio is increased at the inlet of the LPR. The results in Fig. 16 show that the relative flow angle decreases as the hot streak temperature ratio is increased at the region from about 30% span to 70% span of the LPR outlet. In other regions of the LPR outlet, the relative flow angle increases when the inlet hot streak temperature ratio is increased. The results in Figs. 15 and 16 also indicate that the effect of the hot streak temperature ratio on the LPR outlet relative flow angle is weaker than that on the LPR inlet relative flow angle.

Figure 17 illustrates the effect of the hot streak temperature ratio on the total-total efficiency of the VCRT. The result indicates that the total-total efficiency of the VCRT decreases with the increase of the hot streak temperature ratio.

Conclusions

The objective of this paper is to study the effect of the hot streak temperature ratio on the LPT of a VCRT. The major conclusions can be summarized as follows:

(1) A separating phenomenon of colder and hotter fluids is observed at the LPR inlet for all the cases. The hotter fluid migrates toward the PS of the LPR, and most of the colder fluid migrates to the SS of the LPR.

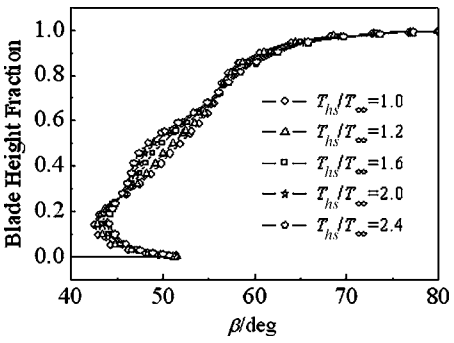

Fig. 16 Span distributions of time and pitch averaged relative flow angle at the outlet of the LPR

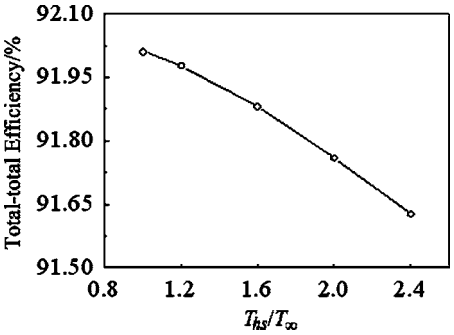

Fig. 17 The influence of the hot streak temperature ratio on the total-total efficiency of the VCRT

(2) The static temperature dissipated degree decreases as the hot streak temperature ratio is increased at the region from the hub to 45% span. At the region from 45% span to 75% span, the increase of the hot streak temperature ratio trends to increase the dissipated degree. At the region from 75% span to the tip, the dissipated degree is not basically influenced by the hot streak temperature ratio.
(3) The secondary flow induces a high-temperature temperature region on the SS of the LPR, which emanates from the LE at the tip. The interaction between the shock wave and the secondary flow induces another high-temperature region on the SS of the LPR, which originates from the hub. The size and temperature of these two high-temperature regions increase as the hot streak temperature ratio is increased.
(4) The migrating characteristics of the hot streak are dominated by the secondary flow in the LPR. On the PS of the LPR, the secondary flow drives the hotter fluid toward the hub and tip. On the SS of the LPR, the secondary flow makes the hotter fluid migrate toward the midspan. The secondary flow is intensified in the LPR with the increase of the hot streak temperature ratio.
(5) The LPR inlet relative flow angle increases as the hot streak temperature ratio is increased. The relative flow angle decreases as the hot streak temperature ratio increases at the region from about 30% span to 70% span of the LPR outlet. In other regions of the LPR outlet, the relative flow angle increases when the hot streak temperature ratio is increased.
(6) The isentropic efficiency of the VCRT decreases as the hot streak temperature ratio is increased.

Acknowledgment

This work has been partly funded by Chinese National 973 programs (G1999022305), fiscal year 2004.

Nomenclature

a = velocity of sound
c = nondimensional chord
D = dissipated degree
p = static pressure
P = total pressure
r = radius
SWR = ratio of specific work of the high pressure turbine to that of the low pressure turbine
t = static temperature
T = total temperature
u, v, w = x, y, z components of velocity
U = rotor wheel speed
V = absolute velocity
W = relative velocity
x = axial displacement
ρ = density
δ = radial displacement
ϕ = flow coefficient

Subscripts

5 = LPR inlet quantity
6 = LPR outlet quantity
cr = critical value
hs = hot streak
t = static temperature
x = axial direction
∞ = freestream quantity

References

[1] Keith, B. D., Basu, D. K., and Stevens, C., 2000, "Aerodynamic Test Results of Controlled Pressure Ratio Engine (COPE) Dual Spool Air Turbine Rotating Rig," ASME Paper No. 2000-GT-0632.
[2] Haldeman, C. W., Dunn, M. G., Abhari, R. S., Johnson, P. D., and Montesdeoca, X. A., 2000, "Experimental and Computational Investigation of the Time-Averaged and Time-Resolved Pressure Loading on a Vaneless Counter-Rotating Turbine," ASME Paper No. 2000-GT-0445.
[3] Wintucky, W. T., and Stewart, W. L., 1958, "Analysis of Two-Stage Counter-Rotating Turbine Efficiencies in Terms of Work and Speed Requirements," NACA RM E57L05.
[4] Louis, J. F., 1985, "Axial Flow Contra-Rotating Turbines," ASME Paper No. 85-GT-218.
[5] Zhao, Q. J., Wang, H. S., Zhao, X. L., and Xu, J. Z., 2006, "Numerical Analysis of 3-D Unsteady Flow in a Vaneless Counter-Rotating Turbine," J. Eng. Thermophys., **27**(1), pp. 35–38.
[6] Zhao, Q. J., Wang, H. S., Zhao, X. L., and Xu, J. Z., 2006, "Three-Dimensional Numerical Investigation of Vaneless Counter-Rotating Turbine," J. Propul. Technol., **27**(2), pp. 114–118.
[7] Lakshminarayana, B., and Horlock, J. H., 1973, "Generalized Expressions for Secondary Vorticity Using Intrinsic Coordinates," J. Fluid Mech., **59**, pp. 97–115.
[8] Butler, T. L., Sharma, O. P., Joslyn, H. D., and Dring, R. P., 1989, "Redistribution of an Inlet Temperature Distortion in an Axial Flow Turbine Stage," J. Propul. Power, **5**(1), pp. 64–71.
[9] Rai, M. M., and Dring, R. P., 1990, "Navier–Stokes Analyses of the Redistribution of Inlet Temperature Distortions in a Turbine," J. Propul. Power **6**(3), pp. 276–282.
[10] Roback, R. J., and Dring, R. P., 1992, "Hot Streaks and Phantom Cooling in a Turbine Rotor Passage: Part 1—Separate Effects," ASME Paper No. 92-GT-75.
[11] Dorney, D. J., 1996, "Numerical Investigation of Hot Streak Temperature Ratio Scaling Effects," AIAA Paper No. 96-0619.
[12] Sharma, O. P., Pichett, G. F., and Ni, R. H., 1990, "Assessment of Unsteady Flows in Turbines," ASME Paper No. 90-GT-150.
[13] Gundy-Burlet, K. L., and Dorney, D. J., 1996, "Three-Dimensional Simulations of Hot Streak Clocking in a 1-1/2 Stage Turbine," AIAA Paper No. 96-2791.
[14] Shang, T., 1995, "Influence of Inlet Temperature Distortion on Turbine Heat Transfer," Philosophy Doctor's thesis, MIT.
[15] Schwab, J. R., Stabe, R. G., and Whitney, W. J., 1983, "Analytical and Experimental Study of Flow Through an Axial Turbine Stage With a Nonuniform Inlet Radial Temperature Profile," NASA-TM-83431.
[16] Stabe, R. G., Whitney, W. J., and Moffitt, T. P., 1994, "Performance af a High-Work Low-Aspect Ratio Turbine Tested With a Realistic Inlet Radial Temperature Profile," AIAA Paper No. 84-1161.
[17] Guenette, G. R., 1985, "A Fully Scaled Short Duration Turbine Experiment," Sc.D. thesis, MIT.
[18] Dorney, D. J., Davis, R. L., and Sharma, O. P., 1991, "Two-Dimensional Inlet Temperature Profile Attenuation in a Turbine Stage," ASME Paper No. 91-GT-406.
[19] Krouthen, B., and Giles, M. B., 1988, "Numerical Investigation of Hot Streaks in Turbines," AIAA Paper No. 88-3015.
[20] Takahashi, R., and Ni, R. H., 1990, "Unsteady Euler Analysis of the Redistribution of an Inlet Temperature Distortion in a Turbine," AIAA Paper No. 90-2262.
[21] Takahashi, R., and Ni, R. H., 1991, "Unsteady Hot Streak Simulation Through a 1-1/2 Stage Turbine," AIAA Paper No. 91-3382.
[22] Weigand, B., and Harasgama, S. P., 1994, "Computations of a Film Cooled Turbine Rotor Blade With Non-Uniform Inlet Temperature Distribution Using a Three-Dimensional Viscous Procedure," ASME Paper No. 94-GT-15.
[23] Dorney, D. J., Sondak, D. L., and Cizmas, P. G. A., 1999, "Effects of Hot Streak/Airfoil Ratio in a High-Subsonic Single-Stage Turbine," AIAA Paper No. 99-2384.
[24] 2005, FINE TURBO User Manual 6-2-9, NUMECA International.
[25] Jameson, A., 1991, "Time Dependent Calculations Using Multigrid With Applications to Unsteady Flows Past Airfoils and Wings," AIAA Paper No. 91-1596.

[26] Rai, M. M., 1989, "Three-Dimension Navier–Stokes Simulations of Turbine Rotor-Stator Interaction, Part I—Methodology," J. Propul. Power, **5**(3), pp. 305–311.
[27] Spalart, P., and Allmaras, S., 1992, "A One-Equation Turbulence Model for Aerodynamic Flows," AIAA Paper No. 92-0439.
[28] Zhao, Q. J., Wang, H. S., Zhao, X. L., and Xu, J. Z., 2005, "Numerical Investigation of 3-D Unsteady Hot Streak Migration in a Vaneless Counter-Rotating Turbine," CSET-2005-052003.
[29] Zhao, Q. J., Wang, H. S., Zhao, X. L., and Xu, J. Z., 2007, "Numerical Investigation on the Influence of Hot Streak Temperature Ratio in a High-Pressure Stage of Vaneless Counter-Rotating Turbine," Int. J. Rotating Mach., **2007**, pp. 1–14.

R. C. Payne
e-mail: rcp27@cam.ac.uk

A. J. White

Hopkinson Laboratory,
Cambridge University,
Engineering Department,
Trumpington Street,
Cambridge CB2 1PZ, UK

Three-Dimensional Calculations of Evaporative Flow in Compressor Blade Rows

The present paper describes a three-dimensional computational method developed to solve the flow of a two-phase air-water mixture, including the effects of evaporation for a monodispersion of liquid droplets. The calculations employ a fully Eulerian method for the conservation of droplet number and liquid mass and are applicable to multiple blade rows, both stationary and rotating. The method is first tested to ensure that it computes the correct droplet evaporation rate and the correct physical behavior for evaporation within a 1D duct. Results are then presented for flow within a single compressor stage, i.e., a rotor-stator combination. [DOI: 10.1115/1.2836742]

1 Introduction

The evaporation of water to cool air as a means of reducing compressor work is a well established technique for improving the performance of industrial gas turbines. The most mature technology based on this principle is inlet fog boost (IFB), where water is evaporated in the inlet duct before compression. IFB with overspray, where enough water is injected that some is carried over into the compressor, is a natural extension of this method. Cycles based on greater quantities of water evaporating within the compressor have been proposed such as MAT [1] and the TopHAT cycle [2]. Such cycles, at least in principle, offer significant increases in work output and cycle efficiency compared to simple gas turbine cycles [1].

Figure 1 compares the results of cycle calculations for recuperated and unrecuperated gas turbines, with and without evaporative cooling in the compressor. These calculations are based on simple thermodynamic analysis, in order to give some insight into the relative performance of wet and dry cycles for equivalent gas turbines. It should be noted that, while the values for cycle parameters have been chosen to be conservative, and consistent across the different cycles compared, no particular gas turbine was used as a prototype. The values used may be found in Appendix A, and are not typical of the current state of the art machines (particularly, turbine inlet temperature).

While wet compression leads to a significant improvement of net work output, in a simple cycle the improvement in efficiency is small (a result described by, for example, Refs. [1–3]). One effect of significant water evaporation in the compressor is to significantly reduce the compressor delivery temperature, which allows any recuperator fitted to recover much more heat from the exhaust stream than an equivalent dry cycle. As the calculations for these results are simple thermodynamic models rather than detailed aerodynamic flows, these calculations require the assumption to be made that sufficiently small droplets can be produced such that evaporation proceeds at near-saturated conditions, and that the design value of compression efficiency can be maintained while water is injected. As has been shown by a number of studies (e.g., Refs. [4–6]), evaporative cooling will normally lead to the compressor operating substantially off design, thereby compromising the potential thermodynamic benefits and limiting the amount of water that can be injected.

The majority of investigations into wet compression that have so far appeared in the literature (e.g., Refs. [5,6]) are based on essentially one-dimensional mean-line calculations. While attempts have been made to allow for velocity slip effects in some of the methods, many of the phenomena are inherently three dimensional in nature. The situation in a real compressor is likely to be extremely complex, involving the cetrifuging of large droplets toward the outer casing, the formation and migration of films and rivulets, and the subsequent reentrainment of droplets into the main flow [7,8]. The current work does not attempt to model all these phenomena, but a preliminary assessment is made of some of the ways in which the evaporation processes impinge upon the detailed flow behavior. The governing equations are presented in a form appropriate for flows with velocity slip, but the calculations presented here have been undertaken for very small droplets, which move with the gas-phase velocity.

2 Conservation Equations for Flow With Slip

The flow of both the gas phase and the disperse droplet phase is solved using an Eulerian method on a single grid. The gas phase is treated as a semiperfect gas, with its properties being a function of temperature and composition (i.e., specific humidity, ω). For simplicity, the droplets are assumed monodispersed and it is, therefore, sufficient to supplement the usual conservation equations (applied to the two-phase mixture as a whole) with equations representing conservation of droplet number, mass of dry air, droplet mass, and droplet momenta. (An additional energy equation is not required as droplets are assumed at the wet-bulb temperature.) The complete set of equations is presented below (see Ref. [9], for derivations and discussion).

The mixture conservation equations are,

$$\frac{\partial}{\partial t}\begin{pmatrix}\rho\\ \rho w_i\\ \rho E\end{pmatrix}+\frac{\partial}{\partial x_j}\begin{pmatrix}\rho w_j\\ \rho\{(1-f)u_iu_j+fv_iv_j\}+p\delta_{ij}\\ \rho\{(1-f)u_jH_g+fv_jH_\ell\}\end{pmatrix}=\begin{pmatrix}0\\ F_i^v\\ S_e\end{pmatrix} \quad (1)$$

where $w_i=(1-f)u_i+fv_i$ (the mass-averaged mixture velocity), and E, H_g, and H_l are stagnation quantities. (The reader is referred to Ref. [9] for details of how these should be evaluated.) The mixture density in these equations is given by

$$\frac{1}{\rho}=\frac{1-f}{\rho_g}+\frac{f}{\rho_\ell} \quad (2)$$

The dry air mass conservation equation is,

$$\frac{\partial}{\partial t}(\rho a)+\frac{\partial}{\partial x_j}(\rho a u_j)=0 \quad (3)$$

where a is the mass fraction of dry air, which is related to the specific humidity and liquid mass fraction through

Manuscript received May 7, 2007; final manuscript received January 2, 2008; published online April 2, 2008. Review conducted by Dilip R. Ballal.

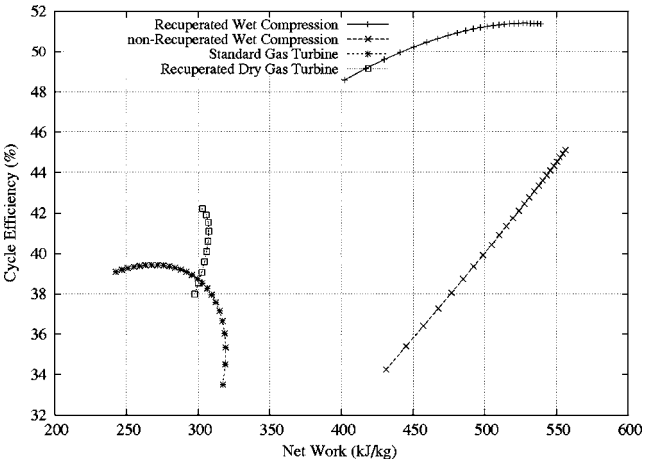

Fig. 1 Comparison of the thermodynamic performance of wet and dry cycles. All turbomachinery is 90% efficient, heat exchangers have 75% effectiveness, combustion chambers and heat exchangers 5% pressure drop.

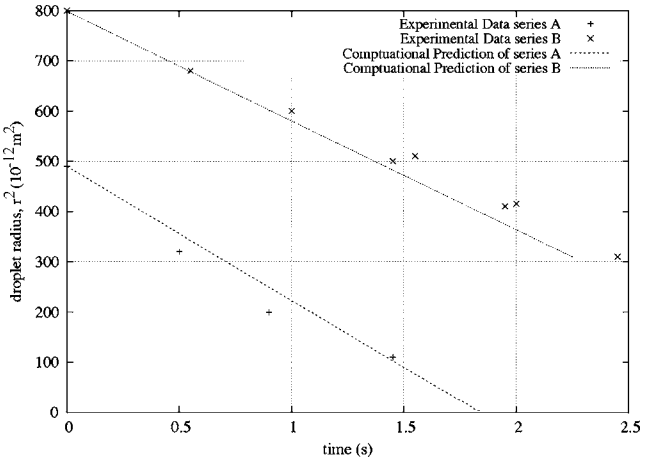

Fig. 2 Comparison between the computed evaporation rates and the experimentally measured rates from [15]

$$a(1+\omega)+f=1 \tag{4}$$

The droplet conservation equations are,

$$\frac{\partial}{\partial t}\begin{pmatrix}\rho n\\ \rho f\\ \rho f v_i\end{pmatrix}+\frac{\partial}{\partial x_j}\begin{pmatrix}\rho n v_j\\ \rho f v_j\\ \rho f v_i v_j\end{pmatrix}=\begin{pmatrix}0\\ -\rho n\dot{m}_e\\ \rho n(F_i^d-\dot{m}_e v_i)\end{pmatrix} \tag{5}$$

where $\dot{m}_e$ is the droplet evaporation rate and F_i^d is the droplet drag force (defined on the basis that mass transferred to the gas phase carries the droplet velocity).

The equations have been given here in Cartesian tensor form for clarity of presentation. In practice, they are solved in cylindrical polar coordinates using an extended version of the finite volume scheme due to Denton [10,11]. In this method, viscous and heat transfer effects are included via a distributed body force and source term (F_i^v and S_e, respectively, in Eq. (1)). Various loss model options are possible, ranging from specification of a polytropic efficiency distribution to solution of the Reynolds-averaged Navier–Stokes equations. That used here (described in Ref. [11]) computes F_i^v from surface shear stress, distributed over the flow assuming a mixing length model of viscosity. More details on this method can be found in Appendix B.

2.1 Evaporation and Droplet Slip. Closure of the conservation equations requires expressions for the droplet evaporation rate $\dot{m}_e$ and droplet drag force F_i^d. Droplet evaporation is computed from an extended version of the method originally due to Spalding [12], and described in detail in Ref. [5]. It has been observed in 1D tests that for the time scales of flow involved in compressor flows, the variation of the droplet temperature from the wet bulb temperature is insignificant. For the sake of computational efficiency, the droplet temperature is, therefore, fixed to the wet bulb temperature. The effects of velocity slip on evaporation rate can be included via correlations for the droplet Sherwood and Nusselt numbers, as discussed in Ref. [13], but these have not yet been implemented in the current calculations, which, therefore, underestimate evaporation rates for large droplets exhibiting substantial slip.

The droplet drag force is computed from the following empirical relationship for the drag coefficient [14]:

$$C_D=\frac{24}{\mathrm{Re}_d}(1+0.197\,\mathrm{Re}_d^{0.63}+0.00026\,\mathrm{Re}_d^{1.38}) \tag{6}$$

where Re_d is the Reynolds number based on droplet diameter and slip velocity. Slip Reynolds numbers are unlikely to exceed 500, whereas the above expression is valid up to $\mathrm{Re}_d=5\times10^4$.

3 Preliminary Validation of the Method

Thorough validation of the complete scheme is hampered by the lack of appropriate experimental data. However, a number of checks have been made to ensure that the evaporation rate is correctly computed, and that realistic physical behavior is reproduced for simple geometries. Two cases are presented here.

3.1 Evaporation of Stationary Droplets. Experimental investigations of evaporation rate that are of relevance to nonslip wet compression involve the evaporation of stationary droplets of water in air. By computing droplet-laden flow down a duct (with a low droplet number concentration), it is possible to chart the evaporation of a single droplet group over time, and thus make comparisons with stationary droplet evaporation measurements. Figure 2 shows the typical level of agreement obtained in such a comparison, confirming (at least for the no-slip case) that the evaporation rate is reasonably well predicted.

3.2 Condensation at High Mach Numbers. Exchanges of heat, mass, and momentum between evaporating or condensing droplets and the gas phase have a particularly pronounced effect on the flow at near-sonic conditions. Due to the high latent heat of H_2O, the main impact of phase change at such conditions may be considered equivalent to sources or sinks of heat distributed throughout the flow. Thus, for inviscid flow in a parallel duct, behavior similar to Rayleigh line flow is to be expected. Figure 3 shows the high Mach number droplet-laden flow in such a duct computed with a 75% saturated inlet stagnation state. The static conditions at high speed are thus supersaturated (in this case with a saturation ratio at inlet of about 3:1) such that the droplets grow. (This requires no modification to the evaporation model, which is equally valid for condensation.) The consequent release of heat into the flow causes acceleration toward sonic conditions, in accord with Rayleigh line behavior. It is a well-known feature of this type of flow that the addition of heat causes a reduction of temperature for Mach numbers in the range $1/\sqrt{\gamma}<M<1$, and this is indeed demonstrated by the calculations. ($1/\sqrt{\gamma}=0.845$ in this case, close to the maximum observed in the plot.) The figure also shows comparison with a 1D duct calculation, based on Lagrangian style evaporation/condensation computations (as described in Ref. [5]) coupled with the steady flow conservation equations. The minor differences between the two curves are due to the inclusion of droplet temperature relaxation effects in the Lagrangian calculations. These results indicate that coupling between the phases is correctly modeled in the current method, at least for this restricted 1D no-slip case.

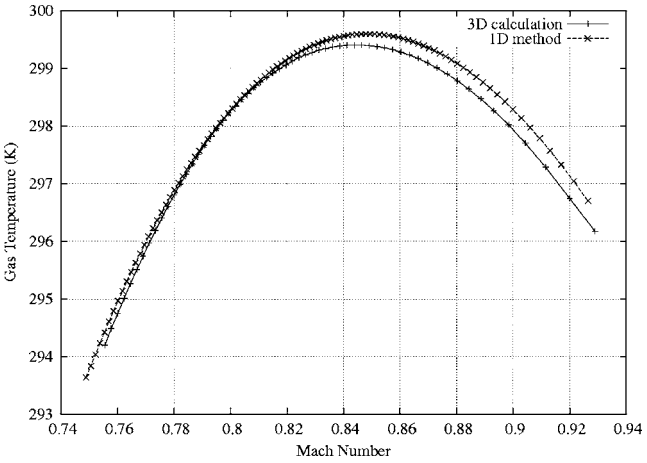

Fig. 3 Condensing flow at high Mach number. Inlet stagnation conditions are 325.5 K, 1 bar, and 75% relative humidity with 5% by mass of 5 μm diameter droplets.

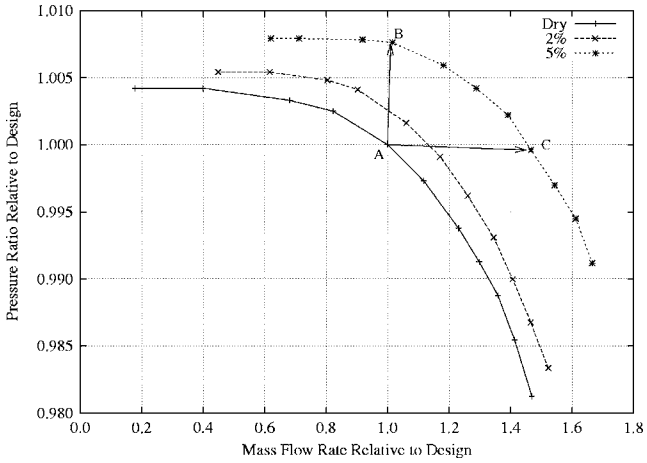

Fig. 5 Compressor map for a single stage compressor with 4 μm droplets at 2% and 5% liquid mass fractions

4 Compressor Stage Calculations

For the purpose of examining the effect of evaporation on blade aerodynamics, the flow through a single low-turning compressor stage has been computed. Essential aspects of the geometry are given in Appendix C. The calculations have been undertaken with small droplets of 4 μm diameter, and with an elevated inlet temperature of 350 K, in order to enhance the evaporation rate and thereby emphasize the impact on the flowfield. Such small droplets exhibit very little slip, so that $u_i=v_i=w_i$ in Eq. (1), and Eqs. (2) and (5) are, therefore, not solved. The flow is circumferentially averaged between the rotor and stator in a manner similar to that described in Ref. [11].

Figure 4 shows the computed streamwise distributions of liquid mass fraction and relative humidity (at midspan and pitch), indicating that substantial evaporation occurs and that close to saturated exit conditions are attained for the 5% injection case. The discontinuities observed at $x \simeq 0.2$ are a result of the mixing calculations at the interface between the stationary and rotating grids.

The primary objective here is to investigate the effect of evaporation on blade pressure distributions and flow angles. However, in so doing it is important to recognize that one of the major effects of water injection is to change the operating point of the compressor. Figure 5 shows the stage stagnation pressure ratio characteristic computed with the current method for dry flow and for 2% and 5% water injection rates. With increasing water injection, the characteristic is seen to shift to higher pressure ratios and higher mass flow rates, in accord with the trends predicted by mean-line calculations for complete compressors [5].

Figure 6 shows the computed blade surface pressure distributions at midspan with dry flow and 5% injection. The comparisons are made at the same (total) mass flow rate (Curve B) and the same stagnation pressure ratio (Curve C) as the nominal design point, as indicated by the points in Fig. 5. For Curve C, the pressure distributions in both rotor and stator are radically altered, but most of the change may be attributed to the induced increase in mass flow rate. This increase in mass flow rate is principally due to the increase in density resulting from the evaporative cooling, and is discussed in some detail (in light of mean-line predictive methods) by Ref. [5]. For Curve B, the shape of the pressure distribution around the rotor is similar to that for the dry case, but there are appreciable changes for the stator. As evaporation proceeds, the density of the flow increases relative to the dry flow case. Mass continuity thus dictates that the axial velocity will be lower than for dry flow and by consideration of the velocity triangle (Fig. 7), it is then seen that the flow angle onto the stator is increased. The change in flow angle across the blade pitch is shown in Fig. 8, which compares wet and dry calculations with the same inlet velocity (not mass flow rate). It is essentially this change in blade incidence angles that brings about the observed modifications in surface pressure distributions. Given that the evaporation rates here are likely to be significantly above those which can be achieved in practice, it is reasonable to suppose that the effect of phase change is a gradual one, operating on a stage by stage basis. This is in contrast to condensation effects in steam turbines, where the impact may be very localized [16].

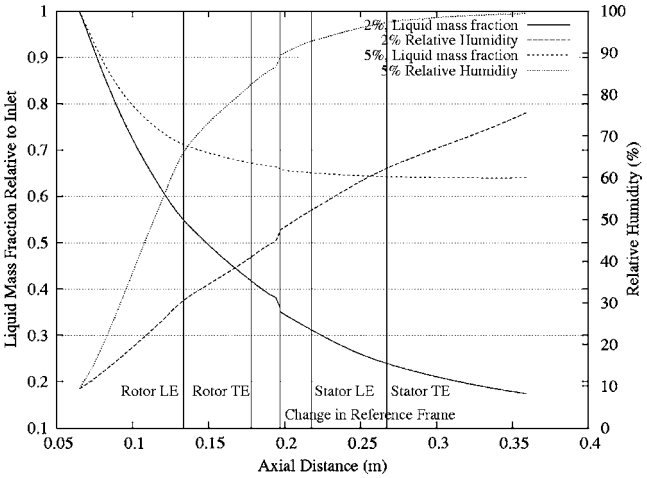

Fig. 4 Streamwise variations of liquid mass fraction and relative humidity. 4 μm droplets at 2% and 5% liquid mass fractions. $T_{01}=350$ K, $p_{01}=1$ bar, and $\phi=10\%$.

4.1 Note on Slip Effects. Once slip between phases occurs (as it will for droplet sizes typical of IFB), a host of phenomena arises, which may have significant impact on the flow detail. Chief amongst these are likely to be evaporation from films, spanwise and pitchwise nonuniformities in droplet concentrations, and the splashing and rebounding of droplets from surfaces. The wherewithal to treat some of these phenomena has not yet been implemented in the computer program, and so presentation of slip results here would be premature. However, it should be noted that evaporation from films, in particular, may be significant: from simple geometric considerations, it may be shown that the ratio between the internal compressor casing surface area and droplet surface area (for uniformly distributed droplets) is

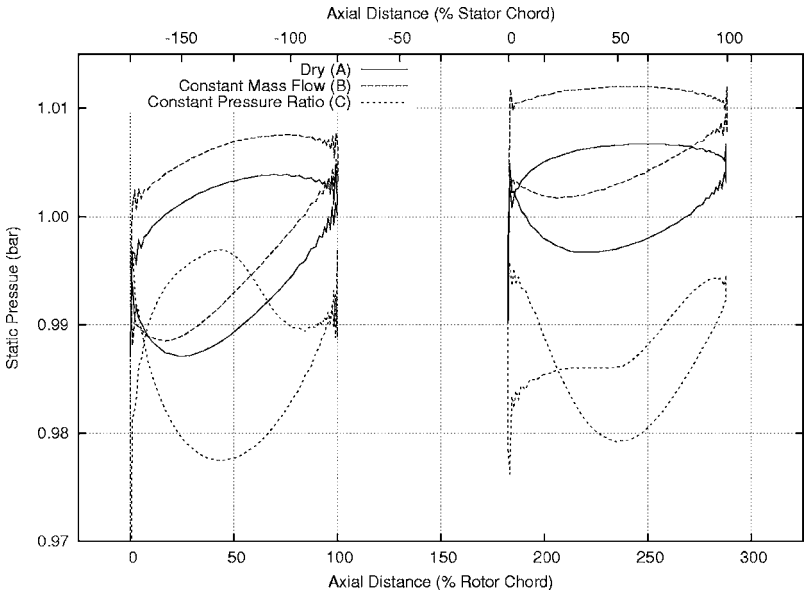

Fig. 6 Blade surface pressure distributions at midspan for Cases A, B, and C

$$\frac{A_c}{A_d} = \frac{2\rho_\ell r}{3f\rho R_c(1-\lambda^2)} \tag{7}$$

where R_c is the casing radius and λ is the hub-casing ratio. For the geometry used in this section, and for a droplet mass fraction of 2%, the two areas are equal for droplet diameters of just 13 μm. Since the casing and other surfaces are likely to be wetted, it is clear that film areas cannot be neglected in comparison with that of the droplets. Against this, these surfaces are not uniformly distributed throughout the volume (in the manner that droplet surfaces are) and will tend to lead to the concentration of water vapor in near-saturated boundary layers. The coupling of film evaporation models with 1D calculations, as is done in Ref. [6], for example, may, therefore, be misleading.

5 Conclusions

A computational method has been presented for calculating the evaporation of water droplets within compressor flows. The method has been applied to compute the flow within a single compressor stage with the injection of small droplets that are assumed to follow the gas-phase flow. The main change in the flow resulting from evaporation is a progressive reduction in axial velocity, relative to dry flow, which affects the flow incidence onto successive blade rows. Blade pressure distributions are changed as a consequence, but the effects are global rather than local. Further work is required to include all the effects of velocity slip relevant to the larger doplets associated with IFB and similar technologies.

Nomenclature

a = mass of dry air per unit mass of mixture
A = surface area (m^2)
C_D = drag coefficient
e = specific internal energy (J/kg)
f = mass of liquid per unit mass of mixture
F^d = droplet drag force (N)
F^v = viscous body force (N/m^3)
H = stagnation specific enthalpy (J/kg)
p = pressure (N/m^2)
r = droplet radius (m)
Re = Reynolds number
T = temperature (K)

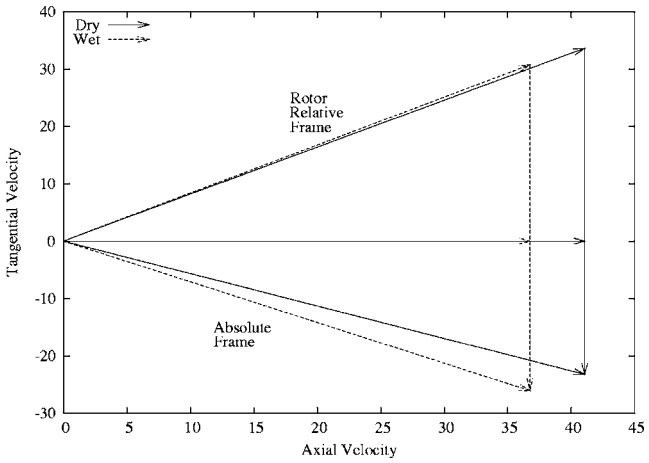

Fig. 7 Velocity triangle at rotor exit for dry and 5% evaporative flows at midspan. Axial velocity at inlet is the same in each case.

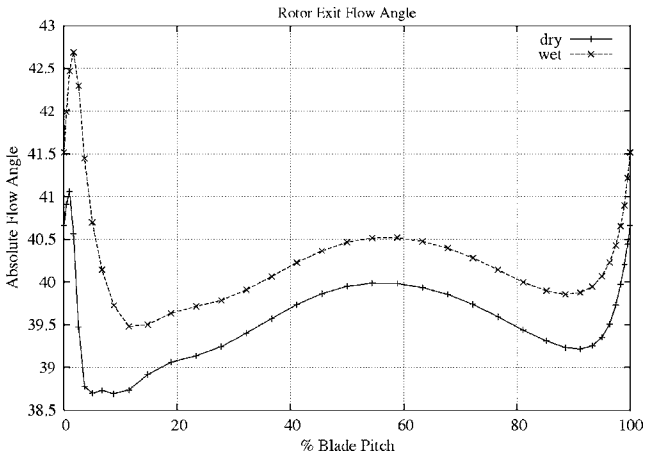

Fig. 8 Absolute flow angle downstream of the rotor for dry and 5% evaporative flows at midspan. Axial velocity at inlet is the same in each case.

u = gas-phase velocity (m/s)
v = droplet absolute velocity (m/s)
λ = hub-casing ratio
ρ = mixture density (kg/m^3)
ϕ = relative humidity
ω = specific humidity

Subscripts

a = dry air
d = droplet
i, j = Cartesian coordinate indices
ℓ = liquid water
v = water vapor

Unsubscripted quantities refer to the mixture, where relevant.

Appendix A: Standard Cycle Assumptions

Gas turbine cycle standard parameters

Fuel type	Methane
Ambient pressure	1.013 bars
Ambient temperature	15°C
Ambient relative humidity	0%
Overal cycle pressure ratio	30
Water injection pressure	150 bars
Water pump isentropic efficiency	75%
Wet compressor relative humidity	100%
Compressor polytropic efficiency	85%
Combustor exit temperature	1100°C
Combustor pressure loss	5%
Turbine polytropic efficiency	90%
Maximum heat exchanger effectiveness	75%

Appendix B: Conservation Equations and Computational Method

The numerical method and geometry input are described in some detail by Ref. 10. The geometry is built as a sheared grid where the hub and casing are taken to be solids of revolution, with all meridional planes being identical (an "H mesh"). Any blade row can rotate on its axis. Flow properties are stored at cell vertices, with conditions for each face taken to be the average of the four nodal values defining that face. Two levels of "multigrid" are employed to speed convergence.

In the general case, the conservation equations solved are of the general form,

$$\frac{\partial X}{\partial t} + \nabla \cdot (X\mathbf{u}) = S \tag{B1}$$

where X is the property of interest and S is the sum of the volume source terms (such as evaporative mass transfer) per unit volume and the surface source terms per unit area (such as pressure and viscous forces). These equations are solved for a grid of finite volume cells in 3D, with finite time steps. In order to evaluate the $\nabla \cdot (X\mathbf{u})$ term, the average value of X for the surface is found:

$$\bar{X} = \frac{1}{4}\sum_{i=1}^{4} X_i \tag{B2}$$

Using this average property, the flux across the relevant face Q_F is set:

$$Q_f = (\mathbf{u} \cdot \mathbf{a}_f)\bar{X} \tag{B3}$$

where $\mathbf{a}_f$ is the vector area of the face. For volume flux terms, the average for the whole cell must be found:

$$Q_v = V\frac{1}{8}\sum_{i=1}^{8} S_i \tag{B4}$$

where V is the volume of the cell. The sum of these terms for the whole cell is found, which determines the value of $\partial X/\partial t$. This term is integrated in time by stepping forward Δt. This change is then divided evenly across the eight vertices, to find updated values of X.

The values of properties are updated for each cell according to the "SCREE" scheme, where

$$\Delta u' = 2\Delta u^n - \Delta u^{n-1} \tag{B5}$$

The values of u' are then spatially smoothed, according to a balanced second and fourth order methods, and the change for each cell is distributed equally to the eight cell vertices (special provision is made at cells on the edge of the geometry).

Appendix C: Compressor Geometry Data

The compressor stage geometry used in Sec. 3 is fictitious in the sense that it does not represent any real machine. The main parameters are as follows:

Rotor	
Inner radius	0.0887 m
Outer radius	0.2515 m
Hub-tip ratio	0.353
Rotational speed	3000 rpm
Midspan blade angle (LE)	55 deg
Midspan blade angle (TE)	34 deg

Stator	
Inner radius	0.1334 m
Outer radius	0.2704 m
Hub-tip ratio	0.493
Midspan blade angle (LE)	−36 deg
Midspan blade angle (TE)	9 deg

References

[1] Utamura, M., Takehara, I., and Karasawa, H., 1998, "MAT, A Novel, Open Cycle Gas Turbine for Power Augmentation," Energy Convers. Manage., **39**, pp. 1631–1642.
[2] van Liere, J., 2001, "The TopHAT Cycle," Mod. Power Syst., April, pp. 35–37.
[3] Bhargava, R., and Mehr-Homji, C. B., 2005, "Parametric Analysis of Existing Gas Turbines With Inlet Evaporative and Overspray Fogging," Trans. ASME: J. Eng. Gas Turbines Power, **127**, pp. 145–158.
[4] Sexton, M., and Urbach, H., 1998, "Evaporative Compressor Cooling for NO_x, Supression and Enhanced Engine Performance for Naval Gas Turbine Propulsion Plants," *ASME International Gas Turbine & Aeroengine Congress and Exhibition*, Paper No. 98-GT332.
[5] White, A. J., and Meacock, A. J., 2004, "An Evaluation of the Effects of Water Injection on Compressor Performance," Trans. ASME: J. Eng. Gas Turbines Power, **126**, pp. 748–754.
[6] Zhluktov, S., Bram, S., and De Ruyck, J., 2001, "Injection of Water Droplets in an Axial Compressor," *Proceedings of the Fifth World Conference on Experimental Heat Transfer, Fluid Mechanics, and Thermodynamics, Thessaloniki*, Greece, pp. 1415–1420.
[7] Day, I., Williams, J., and Freeman, C. 2005, "Rain Ingestion in Axial Flow Compressors at Part Speed," *Proceedings of ASME Turbo Expo*, Reno.
[8] Williams, J. C., and Young, J. C., 2006, "Movement of Deposited Water Droplets on Turbomachinery Rotor Blade Surfaces," *Proceedings ASME Turbo Expo*.
[9] Young, J., 1995, "The Fundamental Equations of Gas-Droplet Multiphase Flow," Int. J. Multiphase Flow, **21**, pp. 175–191.
[10] Denton, J. D., 1985, "Calculation of Three Dimesnional Flow Through Any Type of Turbomachine," AGARD Lecture Series, Vol. 140.

[11] Denton, J. D., 1992, "Calculation of 3d Viscous Flow Through Multistage Turbomachines," ASME J. Turbomach., **114**, pp. 18–26.
[12] Spalding, D. B., 1979, *Combustion and Mass Transfer*, Pergamon, Chaps. 2–5.
[13] Abramzon, B., and Sirignano, W., 1989, "Droplet Vaporization Model for Spray Combustion Calculations," Int. J. Heat Mass Transfer, **32**, pp. 1605–1618.
[14] Young, J. B., and Yau, K. K., 1988, "The Inertial Deposition of Fog Droplets on Steam Turbine Blades," ASME J. Turbomach., **110**, pp. 155–162.
[15] Taflin, D., Zhang, S., Allen, T., and Davis, E., 1988. "Measurement of Droplet Interfacial Phenomena by Light-Scattering Techniques," Am. Inst. Chem. Eng. J., **34**, pp. 1310–1320.
[16] Bakhtar, F., White, A., and Mashmoushy, H., 2005, "Theoretical Treatments of Two-Dimensional Two-Phase Flows of Steam and Comparison With Cascade Measurements," Proc. Inst. Mech. Eng., Part C: J. Mech. Eng. Sci., **219**, pp. 1335–1355.

Stephen Schoonbaert

Xiao Huang
e-mail: xhuang@mae.carleton.ca

1125 Colonel By Drive,
Department of Mechanical and Aerospace Engineering,
Carleton University,
Ottawa, Canada, K1S 5B6

Scott Yandt

Peter Au

Institute for Aerospace Research,
Structures and Materials Performance Laboratory,
National Research Council,
1200 Montreal Road,
Ottawa, Canada K1A 0R6

Brazing and Wide Gap Repair of X-40 Using Ni-Base Alloys

Co-base superalloys are commonly used for vanes and parts of the combustion chamber in gas turbine engines. The Co-base superalloys are primarily solid solution strengthened and have good resistance to hot corrosion, creep, and thermal fatigue. In particular, Co-base alloy X-40 was used to fabricate the first stage NGV airfoils of T56 series engines; inspections after service have revealed that X-40 airfoils suffered from severe thermal fatigue damages. In this study, a new braze repair scheme is proposed; in which Ni-base alloys are used to repair the X-40 substrate in both narrow and wide gap configurations. Metallographic examination, X-ray mapping, and energy dispersive spectroscopy semiquantitative compositional analyses were carried out to study the microstructures in the braze joint in the as-brazed condition and after thermal exposure at 950°C. *The results obtained so far suggest the formation of Cr-rich borides, eutectic phases, and various carbides in the joint. No TCP phases were found in the brazed joint and base metals adjacent to the joint. The high carbon content in the alloy X-40 may have played an important role in preventing the formation of TCP phases during brazing and subsequent thermal exposure.* [DOI: 10.1115/1.2836743]

Keywords: braze repair, wide gap brazing, Co-base superalloy X40, microstructure

Introduction

Repair and overhaul of service stressed gas turbine engine components are an economic necessity for life-cycle cost reduction of engines [1]. There is an increasing demand for the development of repair schemes, which both restore component integrity and further enhance component performance through the use of advanced repair materials and surface coatings. Successful repair of gas turbine components is dependent on the stress field in the area of the repair, the criticality of the component, and the properties of the repaired region. Current repair practices include TIG welding, PTA welding, laser welding, and brazing. Traditional brazing is not a viable solution for hot section component repair due to the low melting temperature of the braze alloy used. Narrow gap diffusion brazing, however, has been successfully used to repair small cracks ($\sim$50 μm) on mechanically low stress regions, such as stationary turbine guide vanes and turbine blade tips. Narrow gap diffusion brazing makes use of highly diffusible melting point depressant, such as boron and sufficient diffusion to achieve the required strength at high temperatures [2,3]. Due to the diffusion of the filler material into the substrate, it is possible to achieve a joint that is nearly indistinguishable from the base material.

Transient liquid phase (TLP) bonding, developed in the 1970s at P&W [4], is similar to diffusion brazing and utilizes a liquid forming alloy at a temperature below the solidus temperature of the substrate. It was based on the concept of isothermal solidification under equilibrium conditions in order to prevent the formation of brittle intermetallic phases. TLP bonding incorporates a thin interlayer composed of similar composition as the base material with small additions of high diffusivity melting point depressant(s). In the TLP process, upon heating to bonding temperature, the faying surfaces are wetted and the alloying elements within the interlayer quickly diffuse into the base material. This results in a compositional change within the region, raising the solidus and achieving an isothermal solidification in the bond region. This technique has also been used to repair wide gap defects on turbine blades when additional filler metal is included in the joint [5].

Manuscript received June 20, 2007; final manuscript received June 22, 2007; published online April 2, 2008. Review conducted by Dilip R. Ballal.

In wide gap repair where the gap size is greater than 1 mm (0.040 in.), the typical microstructure in the gap consists of base metal (filler) particles, surrounded by the braze alloy with boride-rich chains and clusters [6]. The addition of filler functions as a diffusion sink for the boron and enhances the bridgeability of the filler alloy. Due to the incorporation of filler alloy, the overall amount of melting temperature depressant(s) can be reduced to prevent the formation of excessive brittle borides. Wide gap superalloy brazing using powder based materials was pioneered by P&W (TLP) and GE (activated diffusion healing (ADH)) [7,8]; other successful variations of the wide gap braze repair methods include LPM™ developed by Liburdi Engineering Ltd. [9] and M-Fill™ by Avco Lycoming [10].

Co-base alloy X-40 was used to fabricate the first stage NGV airfoils of T56 series engines. The purpose of the stationary NGV is to focus the hot gases exiting the combustor onto the rotating turbine blades. NGVs are prone to cracking and the primary cause is thermal fatigue, which arises from alternating compressive and tensile stresses experienced within the component during engine operation [1]. The weldability of X-40 is quite reasonable but the brazing technique has the advantage to repair multiple cracks using single braze operation without incurring distortion; it also provides opportunities for further improvement to the joint properties utilizing new materials. A repair scheme using Co-base alloys was able to achieve about 60% of the original component life [11]. An LPM™ process incorporating IN 738 in the wide gap repair of NGVs has resulted in improvement to the stress rupture properties of the joint [9]. Since the thermal fatigue life of X-40 was about 50% of Ni-base superalloy IN 738 [11], it is perceived that the utilization of IN 738 in the wide gap repair of NGV airfoils would provide opportunities to further extend the life of the repair component. However, the microstructure of this complex alloy system containing X-40, IN 738, and boron (B) bearing braze alloy was not well understood and the mechanical properties, particularly the thermal fatigue life after long term thermal exposure, has not been characterized so far. As such, in the first phase of this study, the microstructure and joint mechanical properties of both narrow gap (with BNi-9) and wide gap (BNi-9+X-40 and BNi-9+IN 738) braze joints will be evaluated. The selection of braze alloy BNi-9 is based on its compositional simplicity (Ni–B–Cr) and the unavailability of Si-free Co-base braze alloys.

Table 1 Base alloy and filler metal nominal compositions

Alloy	Condition	Al	C	Cr	Co	Fe	Mo	Nb	Ta	Ti	W	Zr	Ni
X-40	As cast	—	0.5	25	Bal.	1.5	—	—	—	—	7.5	—	10
IN738	Cast	3.4	0.17	16	8.5	—	1.75	0.9	1.75	3.4	2.6	0.1	Bal.

Another objective of this study is to investigate the TCP formation, if any, and its impact on the mechanical properties of this complex alloy system containing three alloys. The occurrence of complex TCP phases, σ, μ, P, Laves phases, and the like, and their detrimental effects on both ductility and creep rupture strength have been well documented [12]. Both σ and μ phases can manifest as plates (or acicular in 2D) nucleating from carbides. Their compositions are assumed to be $(Cr,Mo/W)_x(Ni,Co)_y$ where x and y range from 1 to 7 [12]. The μ phase tends to contain more Mo+W and Co and prefers elements with greater differences in atomic size. The Laves phase in Co-base alloys can take the form of $Co_2M(Ta)$ and the presence of Si promotes the formation of Laves. Additionally, the presence of a τ phase based on Cr–Co–W was also reported in the brazement of Co alloys [9]. Since the compositions of superalloys are always optimized to prevent the formation of TCP phases, the interactions between X-40, IN 738, and BNi-9 could have the potential to introduce TCP phases to the joint and adjacent areas. Identification of the TCP phase in this study will be primarily based on the morphology of the phases and the use of standardless energy dispersive spectroscopy (EDS) technique to identify phase composition in a semiquantitative manner.

Materials and Experimental Procedure

Materials. The base alloys used in this study were cast polycrystallic IN 738 and X-40 bars with compositions shown in Table 1. Braze alloy BNi-9 (also known as Ni-276 and Amdry 775) was used in both narrow gap and wide gap braze repairs. The specification for braze alloy BNi-9 is given in Table 2. Two filler metal powders made of IN 738 and X-40 were used in the wide gap braze repair.

Sample Preparation. Narrow gap specimens were prepared specifically for microstructural analysis in the as-brazed condition and after isothermal exposure. They were fabricated by welding 6.35 mm (0.250 in.) thick sections of cast IN 738 and X-40 bars with a 50 μm (0.002 in.) space between them to simulate a narrow gap crack for brazing. The gap width of 50 μm between the specimens was achieved by tack welding the pieces together with 50 μm stainless steel shim-stock acting as a spacer, as shown in Fig. 1. All samples were ultrasonically cleaned before welding, and swabbed with acetone to remove any contaminants left after welding. The braze gap was blown with compressed air and left overnight to dry completely. The BNi-9 braze alloy was mixed with a braze binder and then applied as a consistent bead around the simulated narrow gap using a syringe. The specimens were then dried fully before the braze cycle. Wide gap repair specimens were machined from cast X-40 bar stock to create the gap. A diagram of the wide gap repair specimens can be seen in Fig. 2. The X-40 substrate was ultrasonically cleaned and thoroughly dried before the filler metal powder and braze alloy were added. The specimens were filled with filler metal and braze alloy powders in a 7:4 weight ratio. After the alloy powders were weighed and placed in the simulated void, drops of braze cement were added to ensure no material will be lost during the braze cycle. The specimens were then left to dry before the braze cycle.

Table 2 Properties of braze powder BNi-9

Product name	Composition	Solidus	Liquidus	Brazing range
BNi-9	Ni–15Cr–3.5B	1020	1050	1066–1149

Braze Cycle and Isothermal Heat Treatment. All samples were vacuum brazed between 10^{-5} Torr and 10^{-6} Torr in an Oxy-Gon vacuum furnace using a predetermined braze cycle, as shown in Fig. 3. The samples were placed in ceramic containers at the center of the furnace to ensure uniform heating. The furnace was

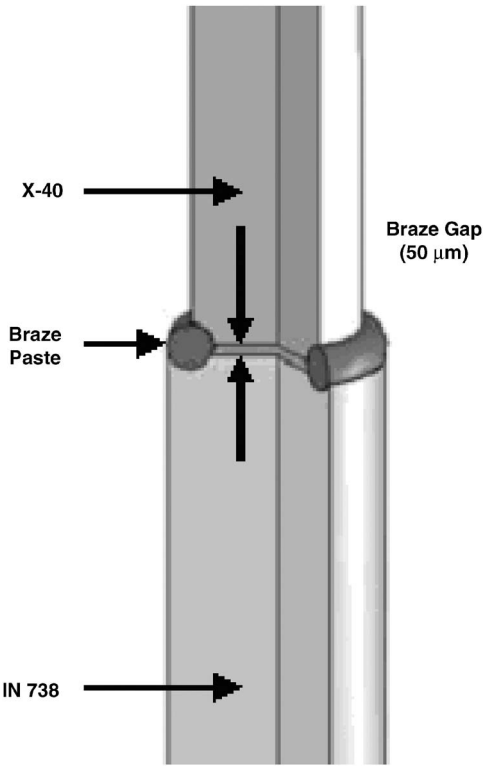

Fig. 1 Narrow gap joint with controlled gap using tack weld

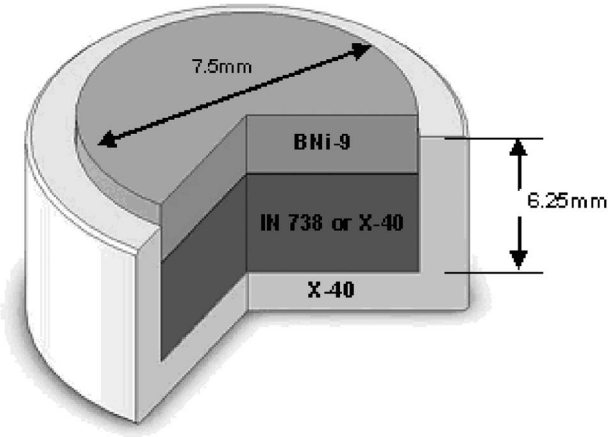

Fig. 2 Specimen cutaway showing the 7:4 ratio of filler metal powder (IN 738 or X-40) to braze powder (BNi-9)

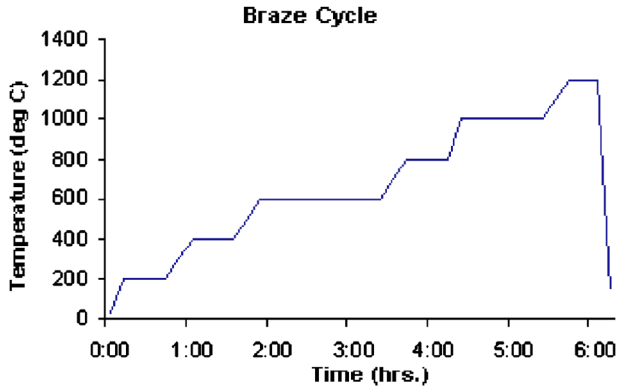

Fig. 3 Braze cycle

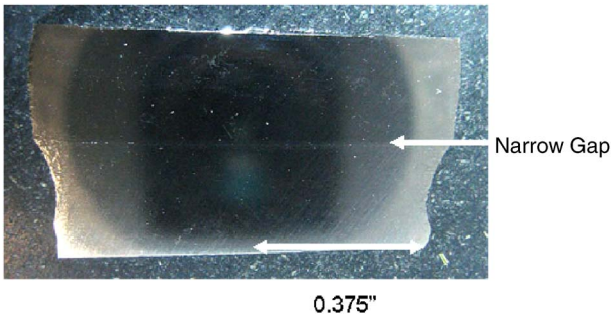

Fig. 5 Optical image of narrow gap repair area

purged with argon gas three times prior to the start of each cycle to minimize contamination. Once the brazing cycle was completed, the specimens were left to cool to room temperature under vacuum.

Isothermal exposure of the as-brazed samples took place in air using a radiation furnace. A constant temperature of 950°C was ensured during thermal exposure, which was varied from 240 h to 1000 h. The results after 840 h of exposure will be presented in this study.

Microstructure Examination. After brazing and isothermal heat treatment, the samples were sectioned using a high-speed liquid-cooled abrasive cutting wheel. The samples were prepared by lightly removing the cross section surface with 400 grit sandpaper, then mounting in Bakelite, and polishing using standard metallographic procedures. After each polishing step, the samples were cleaned ultrasonically and swabbed to remove contaminates. Kalling's reagent was used as etchant to reveal the phases in the braze and adjacent regions. Specimens were masked during etching to allow for step etching of different regions. Microstructural examination was carried out using the backscatter electron (BSE) and secondary electron (SE) techniques in a scanning electron microscope (Philips XL30S-FEG). The standardless EDS technique was used to semiquantitatively analyze the compositions of various phases observed in the braze joint and adjacent area. Only metallic elements are reported for the EDS results since the B and C contents of the examined phases could not be accurately determined using the standardless EDS technique. Additionally, as seen from Fig. 4, elemental mapping was carried out using EDS. However, boron (B) and carbon (C) could not be resolved by the equipment used in this study. Therefore, the presence of B or C in various phases will be based on the examination of the EDS spectrum.

Results and Discussion

Microstructure of Narrow Gap Brazed Joints. X-40 and IN 738 disks were brazed together with a Ni-base braze alloy BNi-9 to simulate the narrow gap (50 μm) brazing process. Microstructure evaluation was conducted on samples in the as-brazed and isothermally exposed conditions using BSE and SE images, elemental maps, and semiquantitative EDS spot analysis.

As-Brazed Condition. The narrow brazed joint was examined visually. As seen from Fig. 5, there is no visible macrodefect found along the joint, i.e., the narrow gap was completed filled by braze alloy via capillary action during brazing. The joint can be better distinguished in Fig. 6(*a*) in which borides and other phases formed in the braze and interface regions are discernable. Also, microstructural changes in the X-40 substrate near the braze were evident, and were likely due to the higher Cr and W contents in the interdendritic region, promoting more borides or carbon borides in the substrate. It can be observed that as a result of base metal erosion during brazing, the braze region was extended from the initial gap of 50 μm to approximately 100 μm. The presence of various phases in the braze and interface regions was further analyzed at higher magnification and using EDS spot analysis. As shown in Fig. 6(*b*), there are three typical phases throughout the brazed region and along the interfaces, including a refractory element-rich phase (RP), Cr-rich boride (CB), and an acicular-shaped phase (AP).

The refractory element-rich phase was observed as bright particles and mostly found as large blocky and small cubic phases directly along the X-40/braze and IN 738/braze interfaces and within the braze region (Fig. 6(*c*)). The compositions of this phase are given in Table 3. Since it contains large amount of carbide formers, Nb, Ta/Ti, and W, and the carbon peak in the EDS spectrum is quite high, it is believed that this phase may be a refractory-rich carbide. As EDS does not give accurate values for both B and C, the possibility of being a carbon boride cannot be

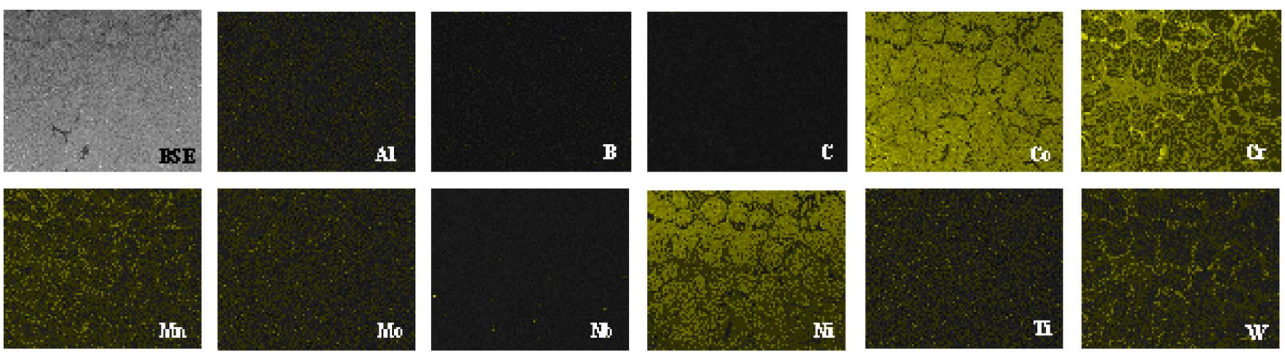

Fig. 4 Example of elemental mapping of all selected elements (wide gap braze with X-40 and BNi-9)

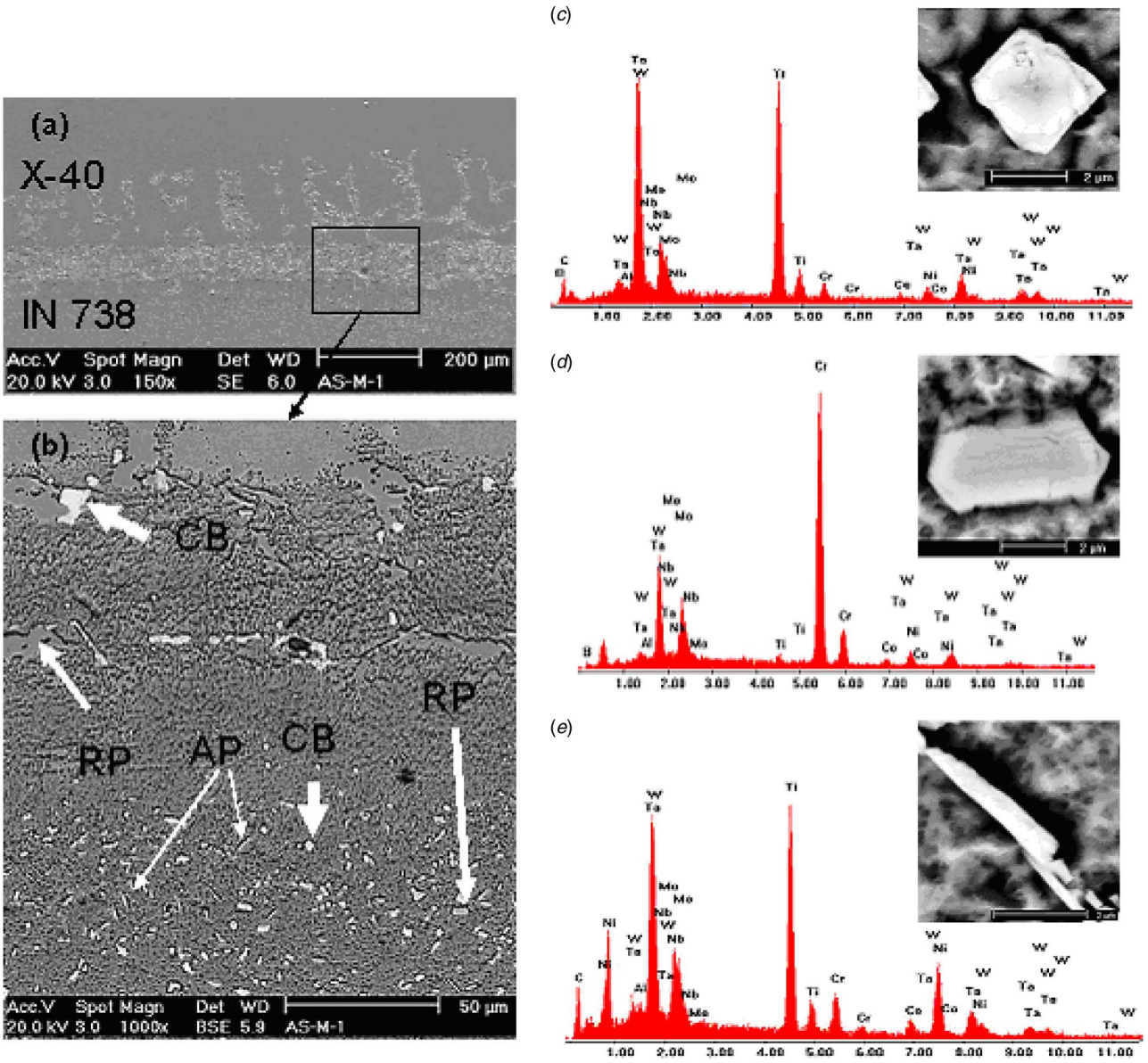

Fig. 6 (*a*) **Narrow gap braze region between IN 738 and X-40.** (*b*) **Microstructure in braze gap region. Phases observed: refractory RP, CB, and APs in the IN 738 matrix.** (*c*) **RP phase observed along the IN 738/braze and X-40/braze interface.** (*d*) **Hexagonal CB in the IN 738 matrix.** (*e*) **Acicular carbon-rich phase found near the IN 738/braze interface.**

excluded.

Figure 6(*d*) shows that Cr-rich phase with irregular and hexagonal morphologies is present at the X-40/braze and IN-738/braze interfaces as well as in the braze region. Also, a similar Cr-rich phase was seen in the same regions as small cubic particles with a size between 1 μm to 4 μm. These Cr-rich phases had a small amount of W as indicated in Table 3, and contained B and C based on the EDS spectrum. From the observations reported [13] in the literature and our previous study in brazing of IN 738, this phase is believed to be Cr-rich boride or Cr-rich carbon boride.

Additionally, acicular-shaped phase was observed in the region adjacent to the IN 738/braze interface, as indicated in Fig. 6(*e*). This acicular-shaped phase ranged between 1 μm and 10 μm in length, and was scattered in random orientations throughout the region. Quantitative EDS analysis revealed the presence of Ti, Cr, Ta, Mo, and Nb. At the same time, strong C peak was resolvable in the EDS spectrum in Fig. 6(*e*). Based on the metallic content of this phase, the presence of C, and its orientation, this phase can be

Table 3 EDS semiquantitative analyses of three phases observed in the joint and interface regions (wt %)

Phase	Al	Nb	Mo	Ti	Cr	Co	Ni	Ta	W
Cr-rich borides (CBs)	0.18	0.47	4.83	0.6	60.66	9.01	3.88	0.31	20.06
Refractory rich (RP)	0.96	16.04	2.23	27.13	2.56	2.01	2.72	28.52	17.83
Acicular (AP)	0.00	9.70	3.54	26.94	6.90	3.81	22.40	23.63	3.08

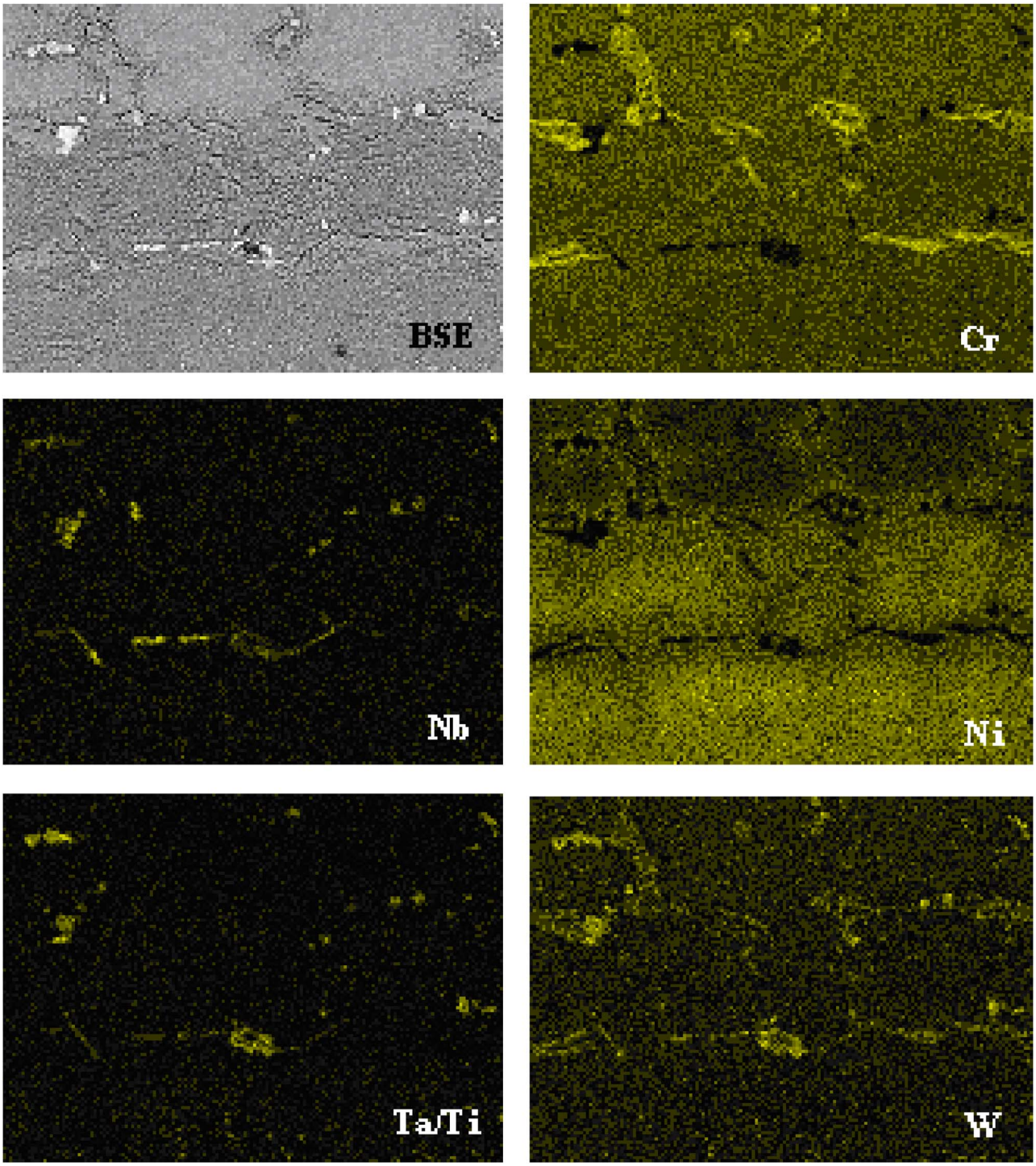

Fig. 7 Elemental maps of selected elements for the narrow gap joint in the as-brazed condition

identified as either *M*C or $M_{23}C_6$ type carbide. Further, transmission electron microscopy (TEM) study is required to distinguish this phase. Despite the elevated refractory and transition metal contents, no TCP was found in the interface region. This is perhaps due to the diffusion of C from X-40 into the IN 738/braze interface region. It has been reported that carbon addition in a superalloy can inhibit the precipitation of TCP phases by absorbing TCP phase formers into naturally occurring carbides [14]. Furthermore, there is no eutectic phase formed in the braze region (Fig. 6(*b*)), indicating the occurrence of a TLP brazing process. The braze alloy was in a liquid state when the peak brazing temperature was reached; subsequently, the diffusion of B resulted in isothermal solidification of the braze alloy. As such, upon cooling from brazing temperature, only solid state precipitation took place.

Elemental mapping was conducted to study the general distribution of various alloying elements in the braze joint. As seen in Fig. 7, the braze and interface regions showed strong segregation of Cr, Nb, Ni, Ta/Ti, and W. This indicates the presence of various phases and the preferential element partitioning in these phases. For example, Cr and W are heavily segregated to the borides and carbides and Ni is depleted in both Cr-rich borides

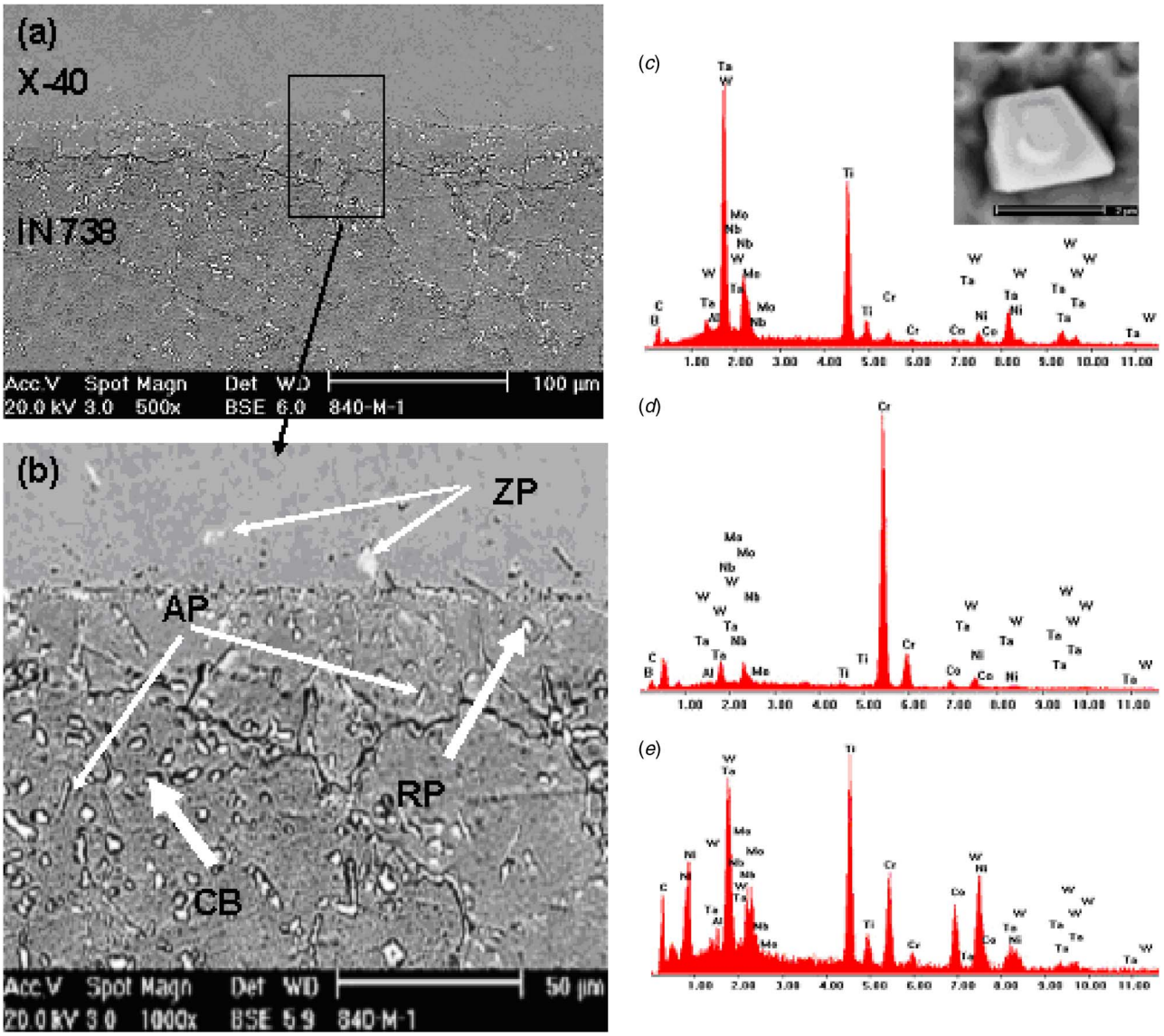

Fig. 8 (*a*) **Narrow gap braze between IN 738 and X-40 after 840 h thermal exposure at 950°C.** (*b*) **Phases observed in the braze and interface regions:** (*c*) **refractory RP,** (*d*) **CB,** (*e*) **acicular carbon-rich phase (AP), and Zr-rich phase (ZP).**

and refractory element-rich carbides. Other elements such as Ta, Ti, and Nb show a similar partition trend. The presence of B or C cannot be mapped reliably in this study.

After Isothermal Exposure. The narrow gap brazed IN 738 and X-40 joint was subsequently exposed to 950°C for 840 h in order to further study the microstructural changes during service. As shown in Figs. 8(*a*) and 8(*b*), the joint and interface regions became more homogeneous after exposure and particularly very little secondary phases were observed in the area adjacent to the X-40/braze interface. In contrast, the IN 738 substrate exhibited the presence of various secondary phases. Four different types of phases were found, namely, Cr-rich boride, refractory carbide, acicular carbide phase, and Zr-rich phase. However, the size of various phases was significantly reduced due to thermal exposure, as compared to that in the as-brazed sample. In particular, more refractory element-rich carbide (Fig. 8(*c*)), with reduced particle size, was found in both the braze joint and in the IN 738 substrate adjacent to the braze joint. The Cr-rich boride particle (Fig. 8(*d*)) was much smaller than that observed in the as-brazed sample. However, the occurrence of acicular intermetallic phase has increased substantially after thermal exposure, as illustrated in Fig. 8(*e*). A new angular-shaped Zr-rich phase, Fig. 8(*b*) (marked as (*f*)), was observed in the X-40 substrate adjacent to the braze region after thermal exposure. The nature of this phase is not clear. Since the occurrence is space, it may not have a significant influence on the integrity of the braze joint. The results from the EDS quantitative analyses are summarized in Table 4 and similar to that measured in the as-brazed sample.

Similarly, elemental mapping of selected metallic elements was conducted on samples after thermal exposure. As presented in Fig. 9, the Cr is concentrated in the Cr-rich borides in both substrates. While no Cr-rich borides were revealed in the BSE and SE images of the X-40 substrate, the Cr map clearly indicated the presence of Cr segregation in the X-40 substrate. The presence of Cr in the IN 738 region is evidently associated with borides when compared to that shown in Fig. 8(*b*). The presence of refractory element-rich carbides or carbon boride phases in the IN 738 region is also clearly seen in the elemental maps of W, Ta/Ti, and Nb. The acicular phase was too fine to be resolved from the maps.

Microstructure of Wide Gap Brazed X-40 With X40+BNi-9. Simulated wide gap brazed X-40 samples were analyzed in the

Table 4 EDS quantitative analyses of various phases in the brazed joint (wt %)

Phase	Al	Si	Zr	Nb	Mo	Ti	Cr	Co	Ni	Ta	W
Refractory rich	0.78	1.39	2.60	15.78	3.71	23.55	4.57	2.42	4.48	35.04	5.45
Cr-rich borides	0.29	0.42	0.62	0.48	6.54	0.66	74.82	3.55	7.33	0.56	4.74
Acicular phase	1.16	5.68	0.89	9.51	4.50	25.52	9.44	9.82	19.08	11.05	3.19
Zr-rich phase	0.19	1.70	60.42	10.26	0.00	1.54	4.11	4.76	3.25	4.08	9.46

as-brazed condition and after isothermal exposure. These samples were "repaired" using a mixture of X-40 filler metal and NIi-276 braze alloy. As seen in Fig. 10, the cross section of the repair region does not show any macrovoids and the interface between X-40 substrate and the braze region is completely bonded. There is a noticeable recession in the braze region due to the consolidation of the powder materials. Subsequently, the samples were studied using scanning electron microscopy (SEM) SE and BSE imaging as well elemental mapping techniques. Discrete particles in the braze region were analyzed semiquantitatively using EDS. Detailed results are given in the following sections.

As-Brazed Condition. The microstructure after brazing in both the braze and the interface regions are shown in Fig. 11. The braze region can be distinguished by the presence of eutectic phases and other blocky and angular phases, while the interface region is characterized by the lack of the above. The interface region is different from the X-40 matrix where large amount of carbides are present. Detailed spot analysis using EDS was subsequently conducted, as summarized in Table 5, to study the nature of these phases. As shown in Fig. 11, there are three distinct phases in the braze region, namely dark blocky phase (Fig. 11(*c*)), angular Cr-rich borides or carbon borides (Fig. 11(*d*)), and eutectic phases (Fig. 11(*b*) marked as 11(*e*)). The dark blocky phase is rich in Cr and observed throughout the braze region, but in very limited quantities along the braze interface. Additionally, this phase is generally found surrounding the X-40 filler particles. From the semiquantitative EDS analysis, it is determined that this phase exhibits a strong C peak; therefore, it could be a carbide containing two metallic elements Cr and W.

In addition to the presence of blocky Cr-rich carbides, another angular phase was also observed (Fig. 11(*d*)); it has a composition similar to the Cr-rich carbides but contains more W. This phase was found in the braze region in a limited quantity but much larger in size. From the EDS quantitative analysis results, it is speculated that this phase may be a (Cr, W)-rich boride or carbon boride.

Eutectic phase was also found in the braze region, as shown in Fig. 11(*b*) (marked as 11(*e*)), and it is likely to have formed from residual liquid at the end of solidification during brazing. This eutectic phase was observed to surround the X-40 filler particles and was mainly present in the braze region. The compositions for both components of the eutectic phase were analyzed and the presence of B was detected in one of the component. In a typical Ni–Cr–B ternary alloy, eutectic FCC-γ +Ni_3B+CrB were observed to form at 997°C [15], which was well below the brazing temperature used in this study.

Due to the higher content of Co in the matrix phase and the phase analysis shown in Table 5, the eutectic phase observed is believed to be γ-(Ni,Co,Cr)–$(Cr,W)_xB$ eutectic. The formation of eutectic constituent in the joint is deleterious to the properties of the joint. The low melting temperature of these boride-rich eutectic phases could also lower the service temperature of the braze repair parts. Increasing the percentage of X-40 in the braze mixture will help to reduce or remove the eutectic phase.

The microstructure in the interface region was also studied. In this region, the presences of both (Cr,W)-rich borides (Fig. 12(*b*)) and blocky Cr-rich carbides (Fig. 12(*c*)) were observed. The compositions of these two phases are similar to those given in Table 5.

After Isothermal Exposure. The microstructure of the wide gap brazed sample with BNi-9 and X-40, after exposure at 950°C for 840 h, is shown in Fig. 13. In the braze region, the eutectic phase is very similar in composition and morphology as that in the as-brazed sample. The angular Cr-rich carbon boride remains to be the same in particle size and morphology; however, the dark blocky phase has changed its contrast and degenerated into two

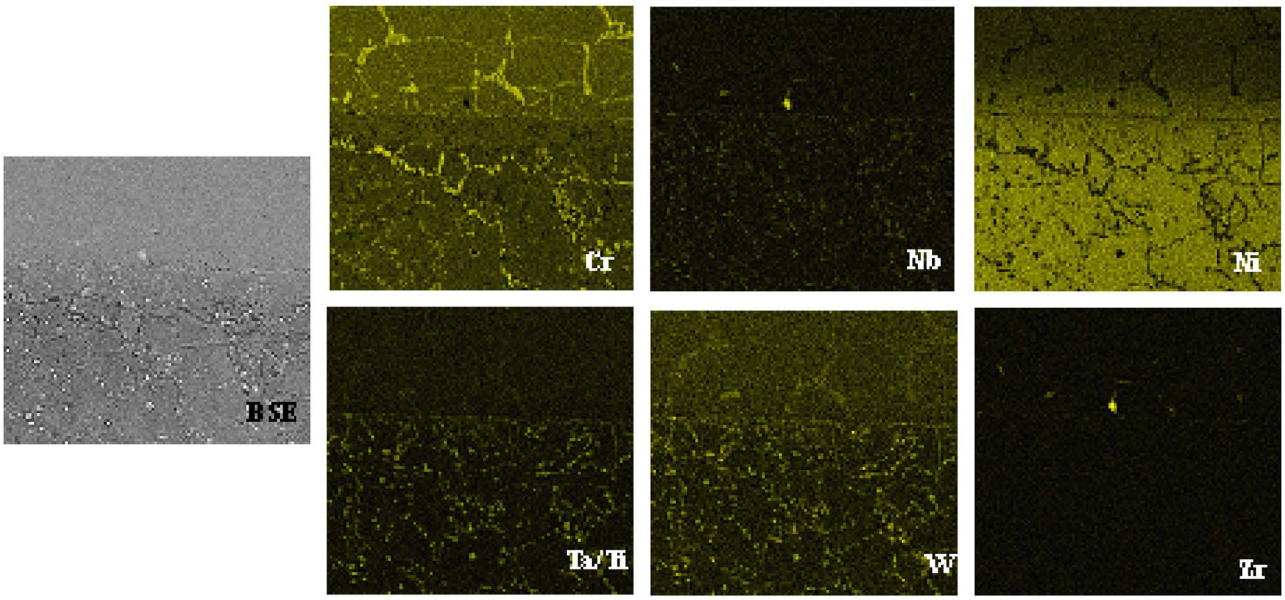

Fig. 9 Elemental maps of the narrow gap joint after thermal exposure

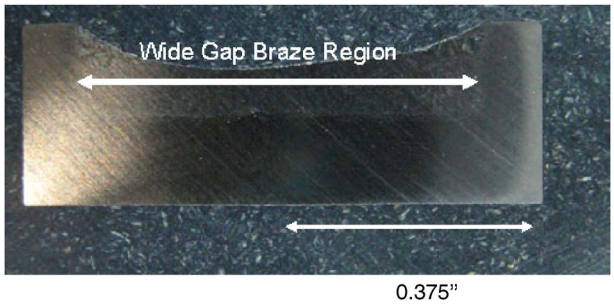

Fig. 10 Optical image of repair of a wide gap repaired X-40 sample

phases, a (Cr, W)-rich phase and another phase containing Cr-CoNi in equal at. % as shown in Fig. 13 (marked as 13(*c*)). The occurrence of W-rich phase in the interface region and X-40 substrate has become more prominent, as illustrated by the bright particles in the interface region in Fig. 13 (marked as 13(*d*)). It is speculated that the formation of this W-rich phase after thermal exposure may have occurred as a result of B diffusion from the braze joint into the X-40/braze interface region.

Wide Gap Braze of X-40 With IN 738+BNi-9. The evaluation of the wide gap brazed X-40 samples with BNi-9 and IN 738 is currently under investigation. The preliminary results suggest that the braze region contains typical Ni-base wide gap braze

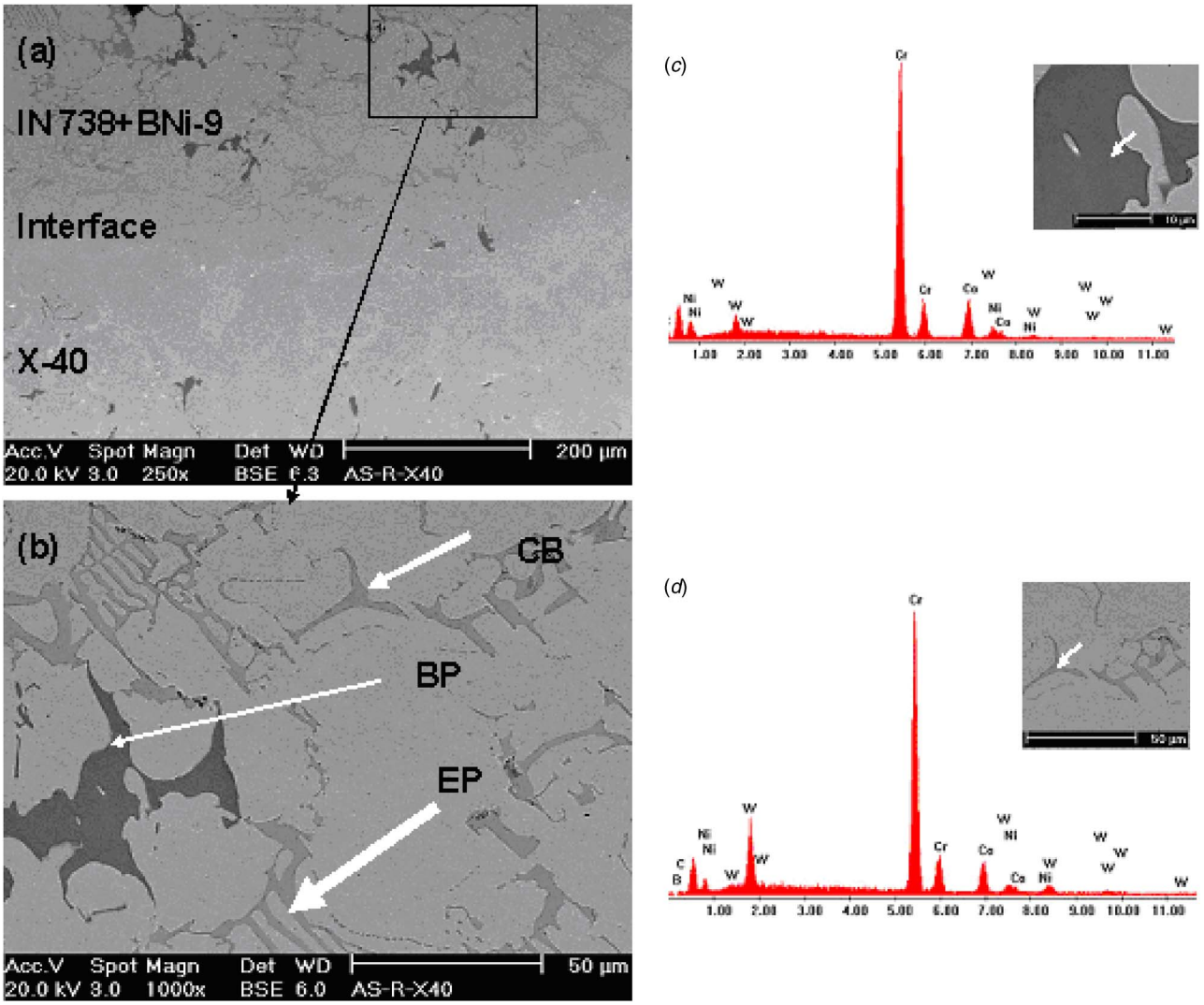

Fig. 11 (*a*) Wide gap braze and interface regions. (*b*) Microstructure constituents in the region: (*c*) dark blocky phases (BPs), (*d*) angular CB, and (*e*) eutectic phases (EPs)

Table 5 EDS Quantitative analyses of various phases observed in the braze region of wide gap braze region with X-40+BNi-9 (wt %)

Phase	Cr	Co	Ni	W
Dark blocky phase (BP)	70.99	18.8	3.57	6.64
Angular Cr-rich boride (CB)	67.29	13.23	3.06	16.43
Eutectic phase (EP)—precipitate	61.09	14.36	5.69	18.86
Eutectic matrix (EP)—matrix	17.37	39.75	37.67	5.22

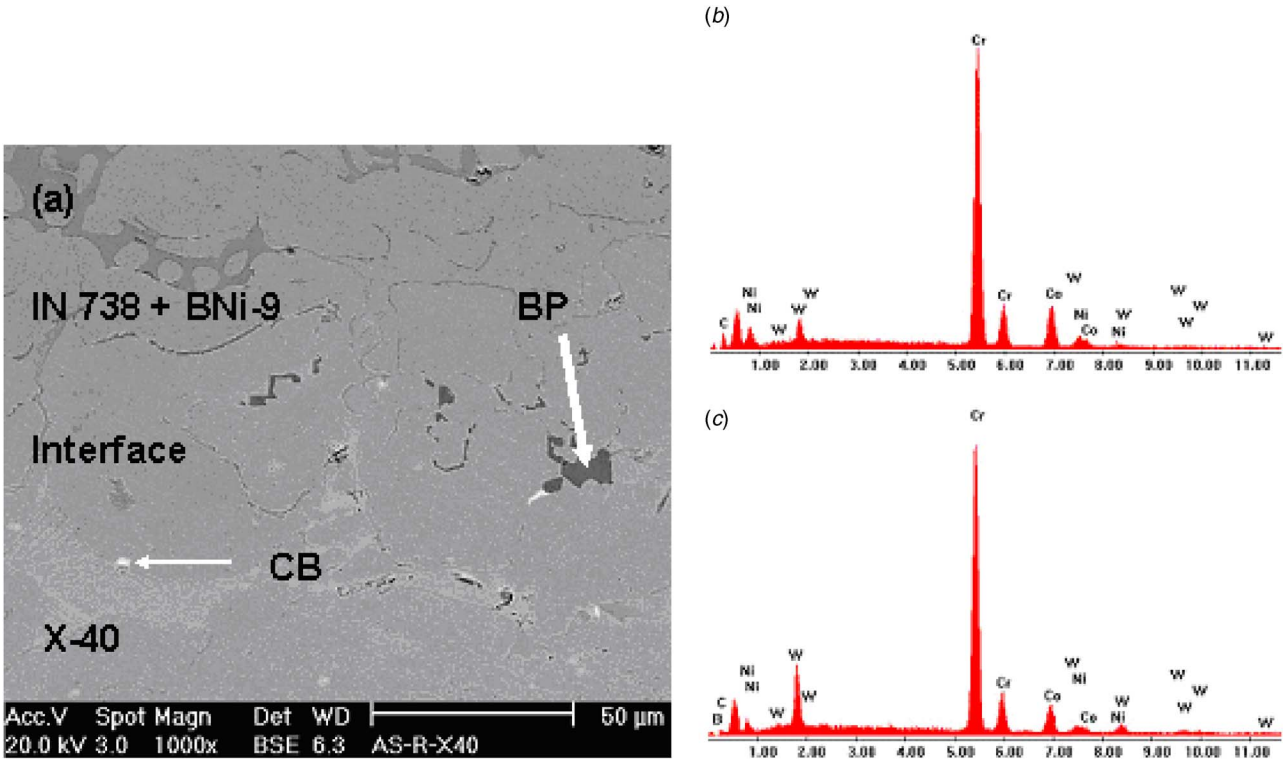

Fig. 12 (*a*) **Microstructure of the interface in the wide gap braze with X-40+BNi-9.** (*b*) **Dark blocky carbide phase (BP).** (*c*) **Cr-rich carbon boride phase (CB).**

structure, including original IN 738 filler particles, eutectic γ-boride phase, and Cr-rich borides. More detailed results will be reported in the future.

Conclusion

Braze repair techniques that have been developed over the last several decades will continue to make significant contributions to the gas turbine after market industry. As suggested in this study, both narrow and wide gap brazings can be particularly effective for repairing nozzle guide vanes. The possibility of using an IN 738 filler alloy in wide gap repair of X-40 was attempted and it was able to produce defect free wide gap joints. From the results obtained so far, it is concluded that the Ni-base braze alloy BNi-9 can be used in the wide gap repair of Co-base X-40 superalloy without the formation of detrimental phases in the braze and interface regions. It is also found that when BNi-9 is used to join X-40 and IN 738 and to repair X-40 with X-40 or IN 738 filler, the likelihood of TCP phase formation can be prevented due to the elevated carbon content in the X-40. While no TCP phase was found, it is necessary to conduct more detailed microstructural and thermal mechanical property studies as dissociation of carbides may induce the formation of TCP phase during prolong high temperature exposure. Additionally, since long term thermal exposure increased the formation of acicular-shaped carbides, it is important that mechanical tests to be conducted on samples containing these particles.

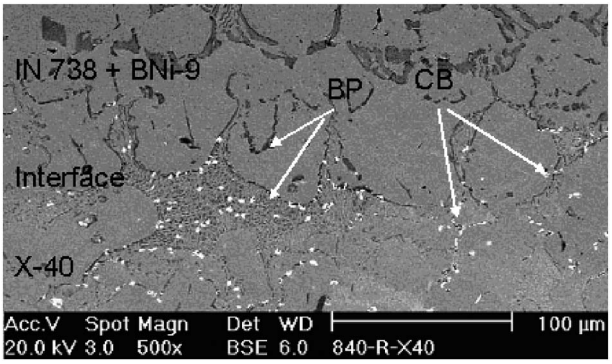

Fig. 13 Microstructure of wide gap brazed joint after 840 hours thermal exposure at 950°C

Acknowledgment

The authors would like to thank Mr. Ryan McNeil in conducting vacuum furnace brazing. They greatly thank Mr. Douglas Nagy from Liburdi Engineering for providing research expertise and materials for this research.

References

[1] O'Neil, W. M., and Kennedy, A., 2000, "Braze Reparing GT Component: Retrospective, Perspective and Prospective," *20th ASM Heat Treating Conference Proceedings*, Oct. 9–12, pp. 1040–1045.
[2] Fritsche, B., and Satir-Kolorz, A., 2000, "Repair Brazing of Nickel-Base Turbine Blades," Weld. World, **44**(5), pp. 10–14.
[3] Gandy, D., Frederick, G., Stover, J., and Viswanathan, R., 2003, "Overview of Hot Section Component Repair Methods," www.my.epri.com.
[4] Duval, D. S., Owczarki, W. A., and Paulonic, D. F., 1974, "TLP Bonding—A New Method for Joining Heat Resistant Alloy," Weld. J. (Miami, FL, U.S.), **53**, pp. 203–215.
[5] McComas, C. C., and Stewart, D. C., 1987, "Repair of Surface Defects in Superalloy Articles," U.S. Patent No. 4,705,203.
[6] Juergon, W., and Malik, M. P., 1985, "Wide Gap Brazing in Maintenance of Turbine Guide Vanes," DVS-Ber., **98**, pp. 78–82.
[7] Demo, W. D., and Ferrigno, S. J., 1992, "Brazing Method Helps Repair Aircraft Gas-Turbine Nozzles," Advanced Materials and Processes, **141**, pp. 43–45.
[8] Heikinheimo, L., 2001 "Repair Brazing of Gas Turbine Hot Parts—Method and Joint Characterization," VTT (Valtion Teknillinen Tutkimuskeskus), **211**, pp. 149–162.

[9] Liburidi, J., and Ellision, K. A., 1993, "Novel Approach to the Repair of Vane Segment," *International Gas Turbine and Aero Engine Congress*, OH, May, pp. 24–27.
[10] McMurray, J. H., and Miller, J. A., 1983, U.S. Patent No. 4,394,347.
[11] Au, P., Dainty, R. V., and Patnaik, P., 1989, "Isothermal Low Cycle Fatigue Properties of Diffusion Aluminide Coated Nickel and Cobalt Based Superalloys," *Surface Modification Technology III*, T. S. Sundarshan and D. G. Bhat, eds. Switzerland, Aug. 28–Sept. 1.
[12] Sims, C. T., Stoloff, N. S., and Hagel, W. C., 1987, *Superalloy II*, Wiley, Chap. 8.
[13] Leon, H., 2007, M.A.Sc. thesis, Carleton University.
[14] Tin., S., and Pollock, T. M., 2003, "Phase Instability in Single-Crystal Nickel-Base Superalloys," Mater. Sci. Eng., A, **348**, pp. 111–121.
[15] Ohsasa, K., Shinmura, T., and Narita, T., 1999, "Numerical Modeling of Transient Liquid Phase Bonding Process of Ni Using Ni–B–Cr Ternary Filler Metal," J. Phase Equilib., **20**, pp. 199–206.

Multi-Objective Optimization of a Microturbine Compact Recuperator

Diego Micheli

Valentino Pediroda

Dipartimento di Ingegneria Meccanica,
Università degli Studi di Trieste,
Trieste 34100, Italy

Stefano Pieri

Dipartimento di Ingegneria Navale,
del Mare e per l'Ambiente,
Università degli Studi di Trieste,
Trieste 34100, Italy

An automatic approach for the multi-objective shape optimization of microgas turbine heat exchangers is presented. According to the concept of multidisciplinary optimization, the methodology integrates a CAD parametric model of the heat transfer surfaces, a three-dimensional meshing tool, and a CFD solver, all managed by a design optimization platform. The repetitive pattern of the surface geometry has been exploited to reduce the computational domain size, and the constant flux boundary conditions have been imposed to better suit the real operative conditions. A new approach that couples cold and warm fluids in a periodic unitary cell is introduced. The effectiveness of the numerical procedure was verified comparing the numerical results with available literature data. The optimization objectives are maximizing the heat transfer rate and minimizing both friction factor and heat transfer surface. The paper presents the results of the optimization of a 50 kW MGT recuperator. The design procedure can be effectively extended and applied to any industrial heat exchanger application. [DOI: 10.1115/1.2836479]

Introduction

The achievement of high performances in small gas turbines depends significantly on the availability of recuperators having advanced characteristics from the viewpoint of thermofluid-dynamics effectiveness, mechanical strength and corrosion resistance at high temperatures, materials, and manufacturing costs.

As far as the thermofluid-dynamics aspects are taken into account, recuperators must have effectiveness values equal to at least 85%. Values of 90% and higher are usually considered today, because an effectiveness increase of 1% gives a gas turbine efficiency improvement of about 0.35 points [1]. Unfortunately, starting from so high values, every further increase involves a dramatic growth of the heat transfer surface with the recuperator core dimensions that can easily double. So, it is evident that the requested cycle efficiency and recuperator effectiveness improvements can be practically obtained only looking for innovative design solutions, capable to maximize the heat transfer coefficient as well as the compactness and lightness of the device.

Pressure loss must also be minimized due to its strong influence on gas turbine efficiency. The fluid dynamics of the flow channels and of the air and exhaust gas ducts must be carefully studied to maintain the total pressure losses under the value of 4–5%. A loss reduction of 1% brings an improvement in gas turbine efficiency of about 0.33% [1].

From a mechanical point of view, materials must be chosen suitable to withstand the more and more high thermal stresses, which result from the expected increase, in the small turbine field also, of the combustor mean temperature. Temperature of the gas at the recuperator inlet could increase from actual 650°C and reach 850°C [2]. At so high temperatures, alloys must be utilized, which are less subject to creep distortion and more corrosion resistant than the usual austenitic stainless steel [3]. The material choice process must also take into account the requirement of assuring to the device an in service life that should be of about 80.000 h, that is two times the turbine one, so allowing the recuperator to be reused [4]. Such a goal is difficult to be obtained also because recuperators are manufactured with metal sheets, which thickness could be lesser than 100 μm. Moreover, creep can cause the dilatation of the compressed air channels and then the narrowing of the exhaust gas ones provoking a counterpressure increase. As a whole, the distortions can cause not negligible in service variations to the heat transfer surface geometry [5].

The above considerations are linked to economical aspects. The recuperator cost should not exceed the 25–30% of the whole microturbine price [6], but if its effectiveness rises from 85% to 90%, the cost increases of about 50% [7]. Moreover, the core cost, which represents 50–75% of the whole recuperator one, can be valued in 1.5 times the material cost [8], and highly corrosion and creep resistant alloys as Type 625 and HR120 cost 3.5–4 times the 347 stainless steel [9].

With reference to the briefly described context, several criteria for the optimum selection and design of micro gas-turbine recuperator have been presented in the recent technical literature. In Ref. [10], performances of four different kinds of heat transfer surfaces are compared on the basis of the so-called volume goodness factor and flow area goodness factor, and a simple design criterion is presented. In Ref. [8], an approach is suggested for the optimum design of recuperators, which is based on literature correlation for the heat exchange coefficient evaluation, and a particular care is turned on the integration among technical and economical issues. In Ref. [11], design optimization is carried out by means of a classic mono-objective genetic algorithm. It maximizes a fitness function based on the recuperator weight, or a suitably defined compactness coefficient, while total pressure drop must be lower than 3%, but it is not considered as an objective. The recuperator simulation model is a zero-dimensional one, based on literature correlations relative to cross-wavy and cross-corrugated primary surfaces, found in Refs. [8,10], and other references from the authors. The chosen geometrical variables define mainly channels and overall package dimensions, while channel shape is kept almost unchanged.

Aim of the present research is to define a general strategy for the automatic, multi-objective shape optimization of recuperator modules, based on a three-dimensional CFD numerical model. The motivations of the work are, with reference to the optimization strategy, that the considered design problem is a truly multi-objective one, since it is desired to both maximize the heat transfer rate, in order to reduce the volume of the equipment, and to minimize the friction losses. These two goals are clearly conflicting, so that the so-called Pareto dominance criterion is used to obtain an optimum design set, rather than the single optimum design given by the less sophisticated mono-objective procedures.

Manuscript received May 25, 2007; final manuscript received May 29, 2007; published online April 2, 2008. Review conducted by Dilip R. Ballal.

As far as the numerical model is concerned, a fully three-dimensional model has been preferred, in spite of its complexity and high computational time, because such an approach has the advantage of being more accurate and, most important, not limited by the zero-dimensional correlation validity field, so that also not conventional but very efficient geometries can be eventually obtained. All the phases throughout the design process, i.e., the different mechanical, thermal, and fluid dynamical aspects, are correlated according to the concept of multidisciplinary optimization (MDO). The basic idea of the proposed technique is the automatic integration of the different industrial design tools, i.e., CAD, mesher, and CFD solver, managed by means of the mentioned optimization platform.

In the first phase of the research, geometrical configuration and prameterization of the primary surface have been defined, and the definition and validation of the thermofluid-dynamical numerical model have been carried out [12]. Cross-corrugated (CC) surfaces have been chosen because both CC and cross-wavy surfaces have globally shown good performance [10], but cross-corrugated ones are better documented in the open literature [13–15] and are also probably easier to manufacture than cross-wavy ones, due to the reduced passage dimensions required for small gas turbine applications [10]. So we believed that CC surfaces could both allow real applications to be considered and permit the computational model to be fully validated by comparison with literature data. Moreover, for this kind of surface, due to the absence of welding or brazing processes, the quantity of material in the recuperator, which in turn means also its weight, is the main parameter that affects the final cost. The weight can be directly evaluated for every considered geometry by the proposed CAD procedure, while the corresponding cost can be obtained if a reference case is available. Nevertheless, it must be pointed out that additional parts, such as packaging, ducting, and mounting accessories, are strongly dependent on engine size and configuration, so it is hard to include them in a general cost model. The numerical model presents a new approach for the solution of heat transfer periodic problems: by solving both cold and hot domains, no boundary condition must be applied at the interface wall, avoiding applying no physical or unnecessary simplified conditions. In this way, the limitations of the uniform flux or temperature boundary conditions usually employed are overcome.

The present paper reports on the second phase of the research. The results obtained with the multi-objective approach, by using an advanced optimization algorithms, are presented. The remarkable efficiency of the adopted algorithms allows the computational time consuming CFD model to be really used in design problems involving, at this step of the planned activities, up to six geometrical variables and three objectives.

The last step of the research will be the development of a suitable robust design approach. In fact, recuperators could operate in off-design situations and different boundary conditions. The first ones occur at partial loads, with constant or variable turbine speed. The second ones change with atmospheric conditions, site position, fouling, or fuel properties. Moreover, the heat transfer surfaces shape can withstand folding process dimensional variability [16] and, as it has been previously observed, variations could also happen during service life. The design process should then take into account also the uncertain variable influence, according to the Robust Design concept.

The final objective of the whole research is to find optimum configurations for high effectiveness, high compactness and high reliability recuperators.

Multi-Objective Optimization

Many practical engineering designs involve simultaneous optimizations of multiple objectives, which is remarkably different by the single-objective optimization. The goal of the single-objective optimization is to find the best solution, which corresponds to the maximum value of one objective function. On the contrary, in the multi-objective case, the goal is to find the best compromise solutions among different conflicting criterions.

The mathematical formulation of the multi-objective optimization problem is find

$$\mathbf{X} = \begin{Bmatrix} x_1 \\ x_2 \\ \vdots \\ x_n \end{Bmatrix} \tag{1}$$

which maximizes

$$f_1(\mathbf{X}), f_2(\mathbf{X}), \ldots, f_k(\mathbf{X})$$

subject to

$$g_j(\mathbf{X}) \leq 0 \quad j = 1, \ldots, m$$

where k denotes the number of objective functions to be maximized.

To solve this problem, many different numerical methodologies have been proposed [17]. The classical method is the so-called weighted sum formulation, where multiple objective functions are combined into one overall objective function F as follows:

$$\text{Min } F = \sum_{i=1}^{K} w_i f_i(\mathbf{X}) \tag{2}$$

where w_i is the weight of the ith objective function.

This formulation, which is valid for simple cases, has considerable disadvantages (as well explained in Ref. [18]): one problem is the numerical definition of weights, which leads to different final optimization results; another drawback is that the methodology cannot be used in the case of nonconvex optimization problems (high nonlinearity among the different objective functions).

When a multicriterion optimization problem is performed, there is more than one objective function. Each of them have a different individual optimal solution, and in general one objective is in conflict with each other; so the multi-objective optimization gives a set of optimal solutions, instead of one optimal final design. For these reasons, new methodologies have been developed, and among these, the theory of Pareto dominance has the major interest. The definition of dominance is

Design A dominates Design B if and only if

$$(\forall i \, f_i(A) \geq f_i(B)) \cap (\exists j : f_j(A) > f_j(B))$$

where f_i is the ith objective function. For simplicity, it is assumed that we are considering the maximization of all objectives.

It is clear that according to this definition, the final solution is not unique, but a set of optimal design is selected: the not-dominated solutions or Pareto frontier. One solution belonging to Pareto frontier is the best compromises between the different objective functions; this means that it is impossible to find a better solution for one objective without decreasing the others.

This behavior matches well the design in engineering cases. As long as there are many, possibly conflicting, objectives to be optimized simultaneously, there is no longer a single optimal solution, but rather a whole set of possible solutions of equivalent quality. This can be the case of heat exchangers where the objectives are in conflict.

To find the solutions belonging to Pareto frontier, an optimization algorithm is needed. Optimization algorithms can be divided into classical and evolutionary algorithms. The majority of the classical techniques are based on the gradient evaluation of objective function; instead, the evolutionary algorithms are based just on the calculation of the function value. The main numerical difference between the two optimization algorithm classes concern to the risk that the optimization algorithm reaches a local minimum.

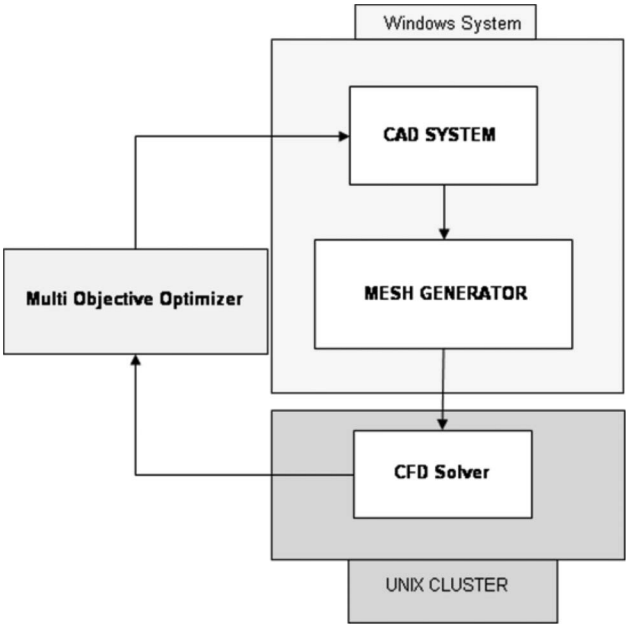

Fig. 1 Design loop for the microturbine compact recuperator with the use of a process integration environment

It is well known that this risk is higher for the classical gradient-based algorithms, especially with the increasing design variable number. Another fact is that, especially for the present CAD-CFD-based optimization, it is impossible to guarantee the absence of failed design due to the possible inconsistency of CAD geometry definition, to the mesh generation, or to the lack of numerical convergence. This is an essential problem in the gradient calculation and in the application of the gradient-based optimization method. The final point for the optimization technique choice is the impossibility of the gradient method to obtain efficiently the Pareto frontier. Regarding all these considerations, in this work we used the multi-objective genetic algorithm (MOGA) [19], which mimics the evolution of living organism in nature.

This algorithm is an evolution of the classical genetic algorithm, with improvements in the basic operators: local selection, multi-objective directional crossover, and elitism.

MDO, Multidisciplinary Design Optimization

The current interest for rapid prototyping techniques leads to the requirement of a fast passage between design ideas and final solutions. For this purpose, different industrial software tools have to be linked in order to build the industrial design chain from the design variables to the final optimized design. The use of an informatics platform for building the automatic procedure in the design process is now highly recommended, in order to integrate the different tools in a design chain: industrial CAD, mesher software, CAE software (CFD, thermal, and structural), postprocessing tools, integration with databases, etc. All these different and complex engineering tools have to be managed in flexible automatic manner by numerical design tools, such as multi-objective algorithms, design of experimental methodologies, and response surface method. Another key point for the use of an integrate platform in the engineering design is the possibility of managing at the same time the different operating systems (WINDOWS, UNIX clusters).

To perform the optimization task, the process integration environment MODEFRONTIER [20] has been chosen. The optimization process follows these tasks inside the design platform: automatic generations of the initial candidate geometries by means of Design of Experiments (in numerical terms definition of the initial design variables), generation of the solid model with industrial CAD software (CATIA V5), once the geometry is defined and deemed feasible, generation of the mesh (ICEM CFD), then preprocessing stage for the boundary condition definition and finally model CFD simulation, and postprocessing to evaluate the objective function (ANSYS CFX 10.0) (Fig. 1). It is interesting to note how the different softwares run onto different operating systems: the CAD system and the mesh generator in a server WINDOWS, while the CFD solver in a parallel cluster with 16 processors.

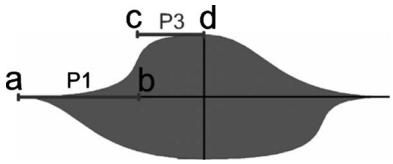

Fig. 3 Bezier prameterization of the inlet surface

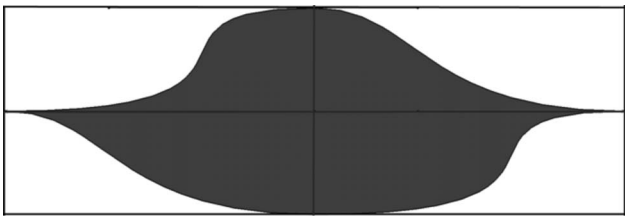

Fig. 4 A possible cross section obtained by setting the parameters

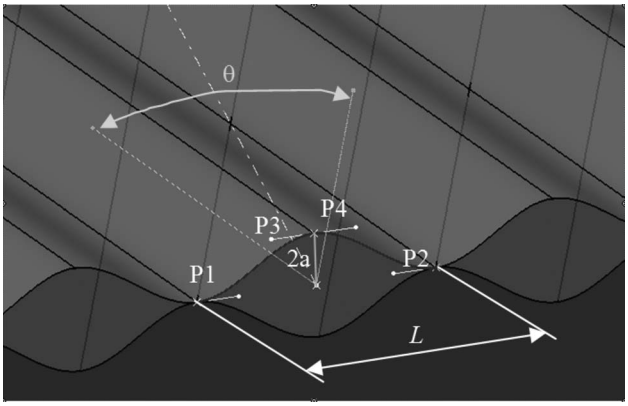

Fig. 2 Geometric modeling and parameterization in Catia

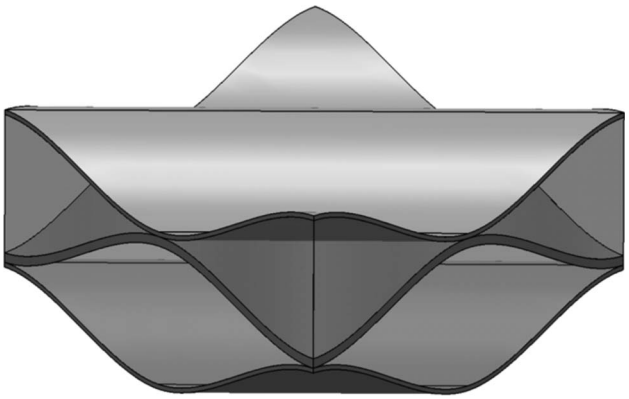

Fig. 5 Final CAD model for the recuperator (90 deg case)

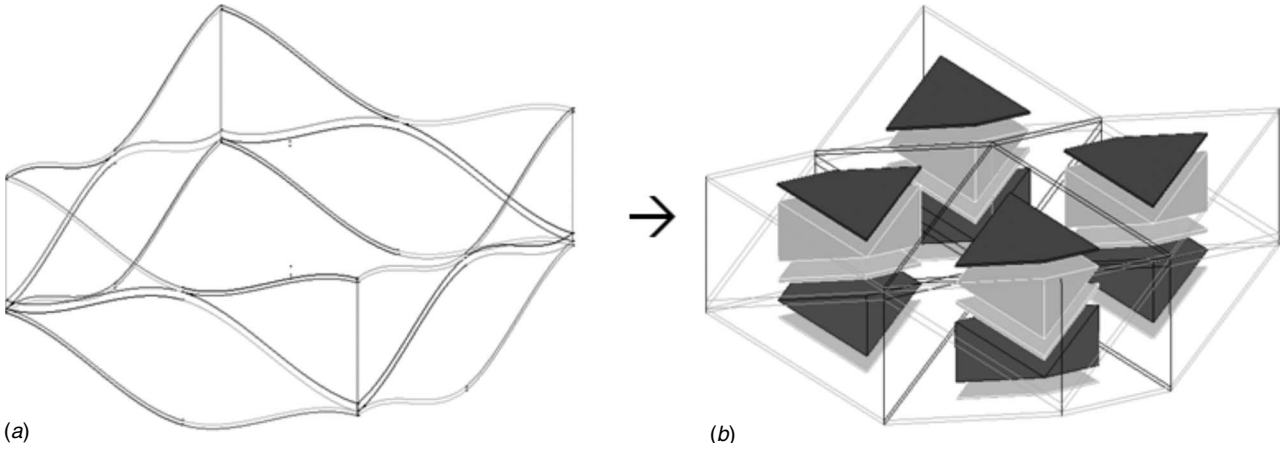

Fig. 6 Passage from CAD model to meshing model (blocks)

Numerical Loop

To perform the numerical loop for the microturbine compact recuperator, now we need to define the three main phases in the design: prameterization, numerical analysis of the model and post-processing.

The prameterization is the passage from the numerical definition of the variables to the solid model (in our case, the geometry of the recuperator). Changing the variable value, the geometry is modified; the numerical analysis of the model gives the possibility to calculate (by means of the post processing phase) the objective values, which have to be optimized.

Prameterization

The CAD package CATIA has been used to develop the heat transfer surface geometry, thanks to its key feature of allowing the generation of parametric drawings. In Fig. 2, the parameters required to describe the geometry of a cross-corrugated surface are presented. Points P1, P2, P3, and P4 define the Bezier curves, which give the shape of both the extruded virtual profiles forming the flow channel.

A Bezier curve is a smooth curve defined by the x_k and y_k coordinates of its control points as indicated in the formula:

$$\begin{cases} x(t) = \sum_{k=0}^{n} \dfrac{n!}{k!(n-k)!} t^k (1-t)^{n-k} x^k \\ y(t) = \sum_{k=0}^{n} \dfrac{n!}{k!(n-k)!} t^k (1-t)^{n-k} y^k \end{cases} \tag{3}$$

where n is the degree of the curve ($n+1$ represents the number of the control points).

One property of the Bezier curve is that the tangents to edges are given by the first and last two points. In this case, each sinusoidal curve of the heat exchange surface is formed by two separated Bezier curves, each one generated by four points. In Fig. 3, a and d are fixed, b and d are placed on the same horizontal axis of a and c, respectively, because in that way we force the curve to have a horizontal tangent in the origin point and in the end point. Therefore, $P1$ represents the distance between points a and b, and in an analogous way $P3$ is the distance between c and d.

The half height of the channel is given by parameter a, while its width is defined by parameter L. The extrusion inclination of the upper and lower plates is controlled by the parameter θ. Changing the parameter values, different geometries can be easily produced: for example, Fig. 4 presents a possible configuration of the cross section.

In particular, it is possible to run CATIA in batch mode, so that the CAD software reads the original geometry (in the present study, the classic sinusoidal profile has been considered for both the plates), reads the new parameters by means of an external file, and produces a model file describing the new geometry.

This file can be read by the meshing tool, which is the intermediate step before the evaluation of fluid-dynamic behavior or thermal phenomena of the new geometry and thus its fitness, so this methodology can be directly integrated in the main optimization loop. In this way, it is possible to modify and control the geometry in real time with the creation of the CAD model.

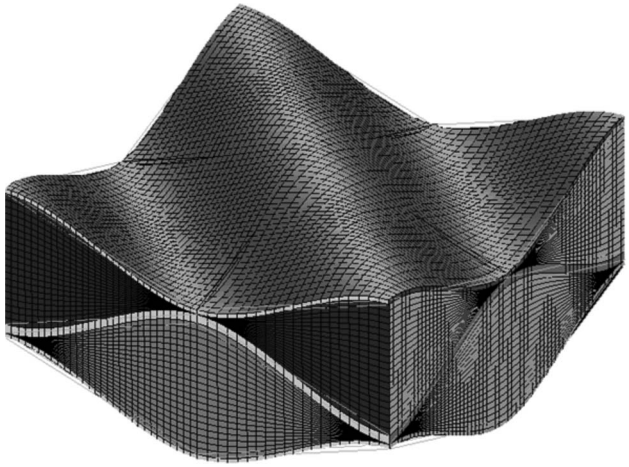

Fig. 7 Final mesh (case 90 deg)

Table 1 Initial variables range

Variable name	Min value	Max value
P1	0.8	1.2
P2	0.8	1.2
P3	0.8	1.2
P4	0.8	1.2
L_{tot}	110 mm	130 mm
θ	58 deg	62 deg

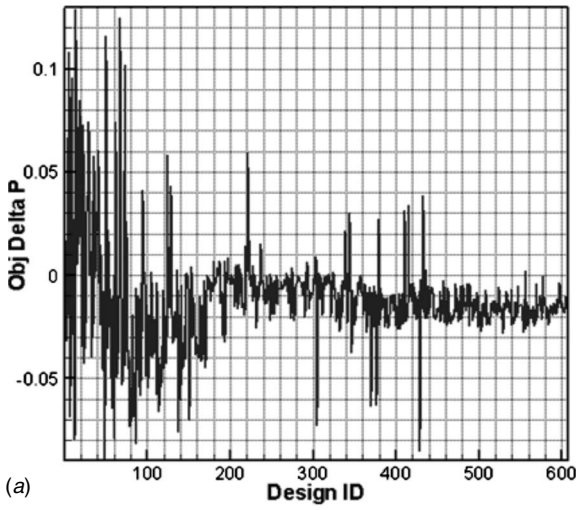

(*a*)

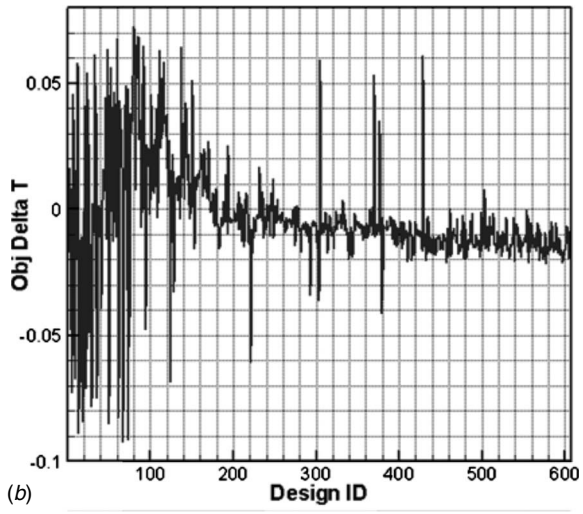

(*b*)

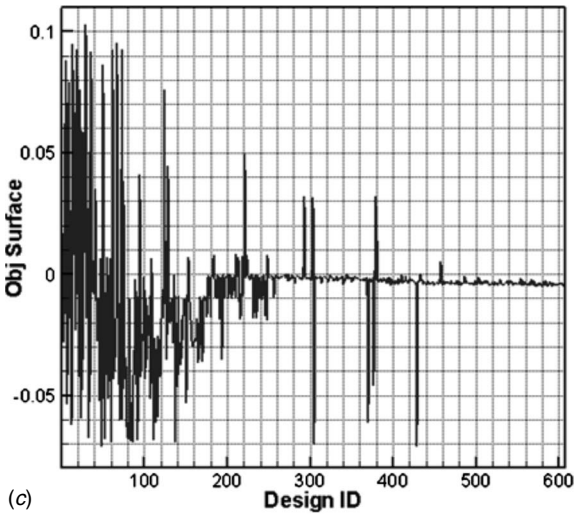

(*c*)

Fig. 8 Convergence profiles for the three objectives; it is possible to note how the multi-objective algorithm finds the compromises between the objective functions

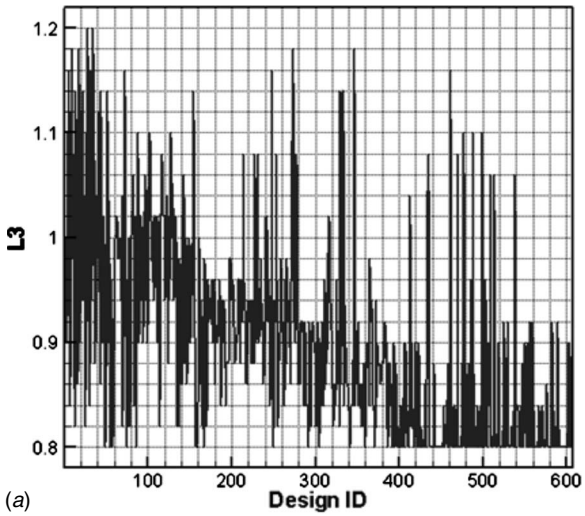

(*a*)

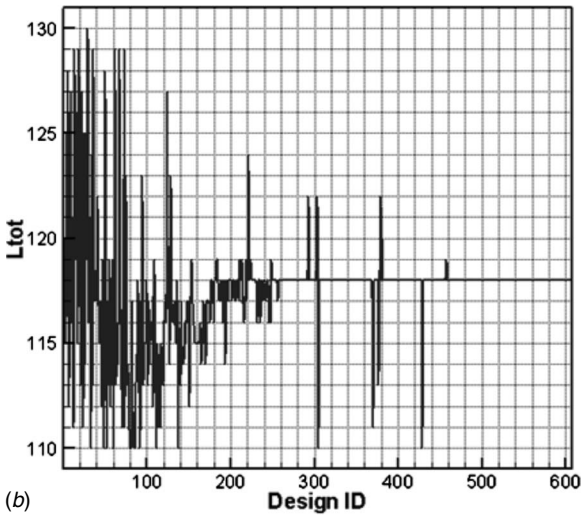

(*b*)

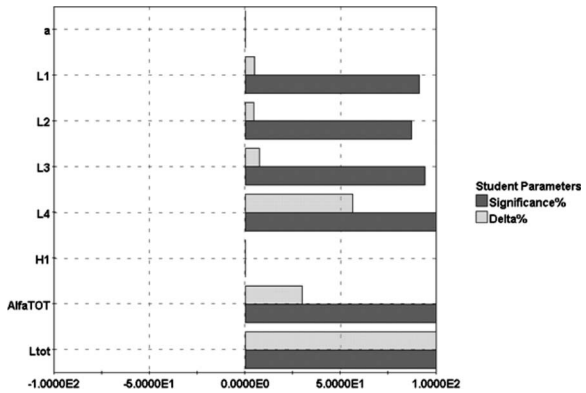

(*c*)

Fig. 9 Convergence profiles for the design variables and t-student chart

As it will be discussed later, the complete geometry must be cut (to reduce the computational time) and only a periodic module, which comprises both cold and hot fluid channels and thin solid layers can be considered. The final geometry obtained with a 90 deg cross angle, shown in Fig. 5, is then saved using CATIA's native $*.model$ extension, and subsequently natively loaded by the software ICEM-CFD where the grid is generated. In this work, only structured grids have been used, but alternative possibilities exist for more complicated geometries.

Computational Fluid Dynamics

To generate a structured mesh with ICEM-CFD, the user has to start importing the model file, with points, curves, and surfaces defined in it, because these entities will be the base lines on which the mesh should lie down (Fig. 6).

The next step is to subdivide the main block in different subblocks, as shown in Fig. 6, and assign the correlation between the edges of the blocks and the curves of the geometry by means the "*projection*" function. The main challenge is to cut the domain in the minimum number of subblocks needed to maintain the integrity of the calculation grid and avoid the mesh to collapse.

One of the most difficult goals is to conform the meshing process; in fact, the more the parameters are different from the original geometry, the higher is the probability that the generation would not succeed. In an optimization process, in fact, a high number of evaluations are performed, so a great robustness is needed to give stability to the optimization algorithm.

The grid visible in Fig. 7 is then imported into the preprocessor *cfx5pre* where fluid characteristics and boundary conditions are automatically defined. In this step, important parameters for the numerical solution, such as convergence criteria and maximum number of iterations, are also set.

Then the case file exported by the cfx5pre module is processed by the *cfx5solve* one that solves fluid and thermal equations. Finally, the results are postprocessed by the *cfx5post* code to obtain the not-dimensional synthetic data for performance evaluation. The structured grid is composed by 154,800 hexahedral cells, and has been selected as a trade-off between accuracy and computational costs. Computations with refined grids up to 591,300 hexahedral elements have been carried out to obtain the mesh independence.

The numerical simulation of the fluid flow and heat transfer capabilities of the cross-corrugated channels in a recuperator is a critical passage for a successful deployment of an automatic design methodology. In this framework, the numerical simulation has to satisfy some important constraints, for instance, the results have to be accurate but they must be obtained using reasonable computational resources too, so the simulation of the whole recuperator is clearly unfeasible.

To reduce the size of the computational domain, the symmetries and the repetitive pattern of the geometry can be exploited. Actually, after a short entrance region, which can involve up to five modules, the flow and thermal fields become fully developed and repeat themselves from module to module in an identical or similar way. Therefore, it is possible to reduce the numerical analysis to the single periodic element using suitable periodic boundary conditions [15]. Such an approach is acceptable also in the present case of short heat exchanger if, as can be deduced from the data given in Ref. [10], the length of the device is equal to almost 15 or 20 modules. Details of the implementation of the periodic boundary condition setup are reported in Ref. [12].

The results of the simulations of this 90 deg cross angle geometry have been successfully validated by comparison with literature data, so that it can be assumed that also the other various geometrical shapes, which will be generated during the automatic design procedure, could be reliably analyzed and compared. [12]

Objectives

Once the whole automatic process has been completed and tested, the choice of the objective of the optimization needs to be made. Traditionally, the objective of all heat transfer techniques is to enhance the thermal performance by increasing the surface heat transfer coefficient. Unfortunately, it is well known that an increase of the thermal contact will cause an increase in the mechanical power dissipated in heat exchange device. A parallel goal is to reduce the size and the cost of the recuperator itself, so the optimization needs to be multi-objective. Several authors [21–23] have proposed Performance Evaluation Criteria (PEC) which define the benefits correlation of a heat exchanger subjected to various design constraints. There are three basic objectives:

1. reduce the heat transfer surface maintaining constant the pressure losses and the heat rate;
2. increase UA (i.e., reduce the overall thermal resistance $R_t = 1/UA$) with fixed total length of the recuperator and pressure losses;
3. reduce the pressure losses for equal heat rate and length of the exchanger.

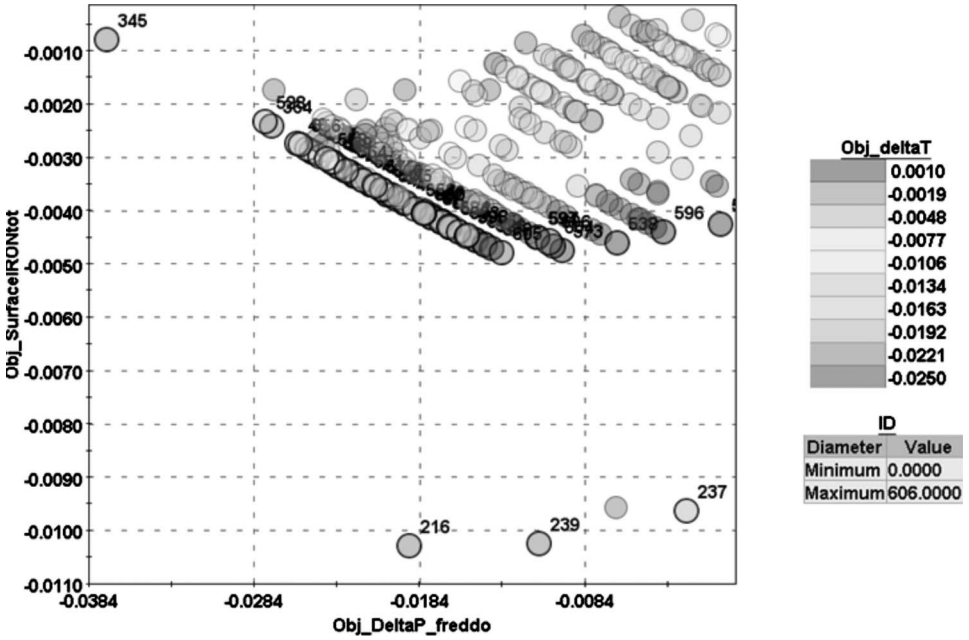

Fig. 10 Pareto frontier graph; encircled in black the solutions belonging to the Pareto frontier

To increase *UA*, two ways are allowed: to obtain a higher heat rate for fixed entering fluid temperatures or to reduce logarithmic mean temperature (LMTD) for fixed heat rate.

In the present study, the frontal area and the mass flow have been considered constant, and the same for the average inlet temperature of the hot and cold domains.

Considering those observations, three entities as objectives have been considered, which are the synchronous minimization of pressure losses, primary surfaces area, and difference between the hot and cold bulk temperatures.

Optimization Phases

When a complex engineering design is performed, it is not possible to define a unique optimization phase; normally, during the development of the project, there is the necessity to insert some changing: fix some design variables, add some others, change the value of the constraint or, in multi-objective case, change the number of the criterions to optimize. Therefore, there is the necessity to use a process integration environment to help the designers in the optimization phases by means of statistical tools. As explained in Ref. [24], the statistical analysis for reducing the number of design variables is an important tool for decreasing the total number of simulations needed to get the best final design.

We also have used two series of optimization in the design process of the recuperator: the first has been useful to understand better the problem (which variables are the most influent, and which objectives are really interesting) and the second one has got the final optimal design for the microturbine compact recuperator.

First Optimization

In the first design phase, we have used all six variables (P1, P2, P3, P4, L_{tot}, θ) to optimize the three main objectives: to minimize the difference of pressure between inlet and outlet (correlated to the pumping power), to minimize the difference of pressure (correlated to the heat transfer rate per unit volume), and to minimize the total surface of the recuperator (correlated with the total cost). The ranges of the variables are in Table 1.

With the objectives, we defined three different constraints: the aim of these constraints is that the final design must have better performances than the original one; so we constrained the total cost, the pressure drop, and the temperature difference with the values calculated with the original geometry, which is characterized by a corrugation angle $\theta=60$ deg, following Stasiek et al. [13], as a good compromise in terms of heat transfer rate and friction factor. Moreover, the hydraulic diameter has been kept constant equal to 1.54 mm for all different geometries as in Ref. [10].

For the optimization, we used an initial Design of Experiment (DOE) obtained by the Sobol method [25] with 40 different designs added by the original one (to help the convergence). The multi-objective optimization by MOGA has been terminated after 15 generations, with a total number of calculated designs of 600. In Fig. 8, it is possible to observe the convergence profiles for the three objectives.

From the observation of the convergence profiles, it is possible to note how the optimization algorithm works in two different phases; in the first (from the design id 1 to around 250), the algorithm finds the geometries feasible, which satisfy the imposed constraints; this phase is characterized by a high instability, index that the algorithm explores different region in the variable space definition. In the second phase (from design 250 to the end, design 600), the algorithm finds the variable region with the best compromise between the objectives and increases the objective function values.

An interesting and useful aspect is to analyze the influence of the design variables in the design performances. The two important points of this work phase are as follows: to understand which are the most important variables and if there are some useless, and to understand if the variable boundaries (range) are fixed in the right values.

To explain these two points, we have used together the convergence profile of the variables and the t-student parameter [26]. The t-student parameter is a statistical tool to explain if two data distributions are really different, and it could be used to understand the influence of the variables.

Table 2 New variables range

Variable name	Min value	Max value
P1	0.2	0.8
P2	0.2	0.8
P3	0.2	0.8
P4	0.2	0.8
L_{tot}	118 mm	118 mm
θ	40 deg	60 deg

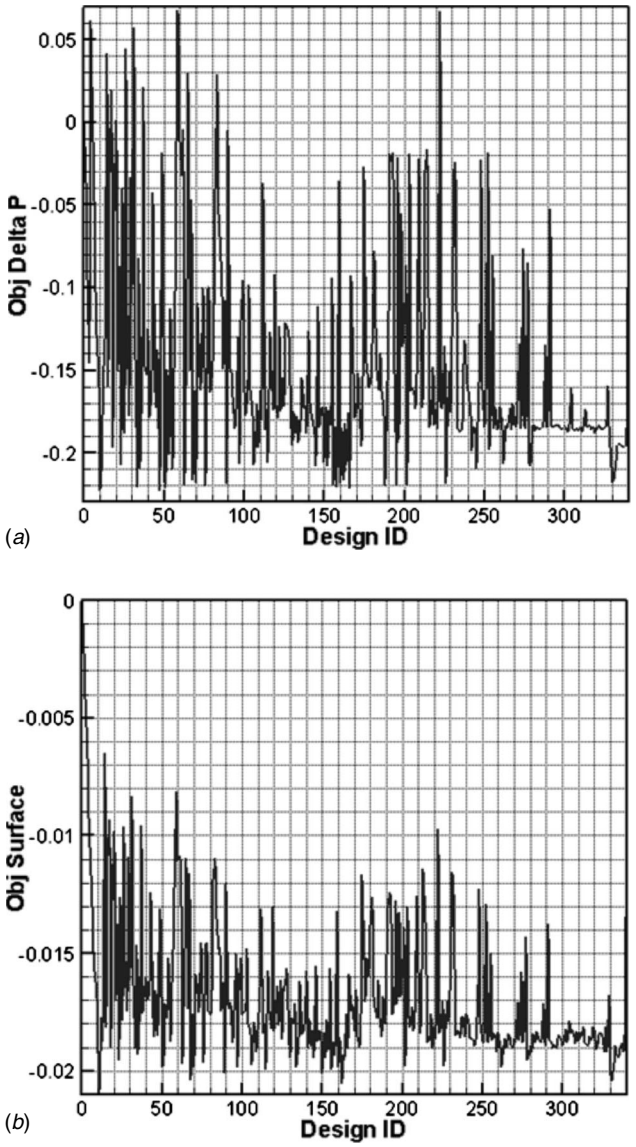

Fig. 11 Objective function convergence profiles for the second optimization

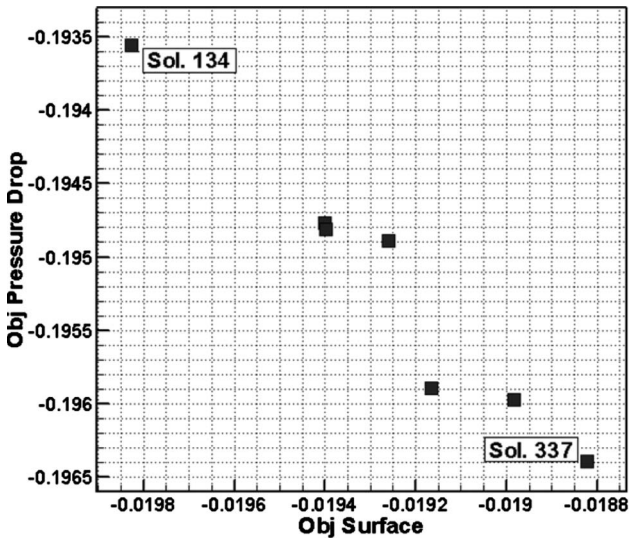

Fig. 12 Pareto frontier of the final optimization. Design 134 has been chosen as best configuration of the entire project.

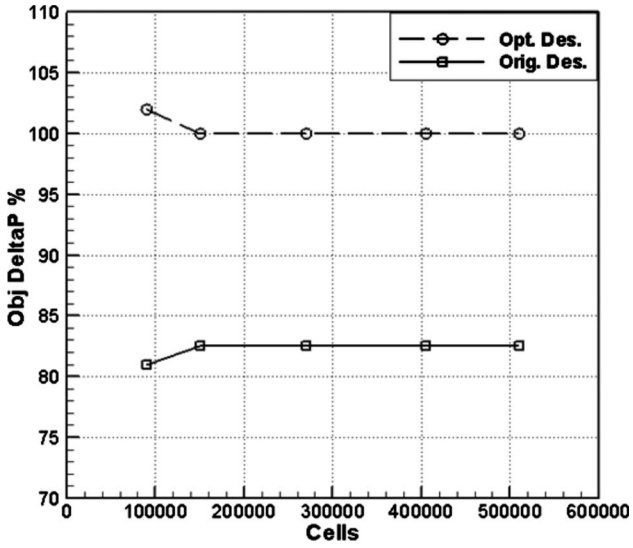

Fig. 13 Grid independence comparison

From the observation of the Fig. 9, it is possible to argue some interesting remarks: first, it is easy to observe how the range of the variables has not been set with right values. Moreover, during the optimization, the algorithm has found many designs with the lower variable level, this means that with high probability relaxing the variables range would be possible to find better solutions in terms of objective function values. This behavior happens for the variables: P1, P2, P3, P4, and θ.

The relations between the objective functions and the variable L_{tot} are different; from the variable convergence profile, we note how the algorithm gets the value of 118 mm after six generations. This trend is due to the total length of the recuperator (defined by the parameter L_{tot}), which is the most important variables in this design phase; this is well visible from the t-student chart. So the algorithm fixes the value as the original one, allowing to not violate the constraints.

How reported, the final result of a multi-objective optimization is the Pareto frontier, the set of optimal solutions. The visualization of the Pareto frontier is shown in Fig. 10, where an innovative method is used: the bubble chart.

In this graph, the two axes represent two objectives (pressure drop and surface), while the bubble color (gray scale) the heat transfer objective. An interesting behavior is the discontinuous linear distribution of the objectives that depends on the angle variable definition, which is not continuous but with a step of 0.02 deg (for manufacturing reasons).

In the Pareto frontier, we found 80 different designs, the best compromises among the objectives considering the set variable range.

Second Optimization

From the clear considerations derived from the first optimization phase, a second one has been performed. The changes are new range from the variables (Table 2, fixing the variable L_{tot} to the original value), and only two objective functions, minimum pressure drop and minimum total surface. We did not use the objective heat transfer to help the optimization algorithm in the convergence. However we do not lose in performances because we have fixed a constraint for the heat transfer to the value reached in the first optimization (better than the original design).

As initial design of experiments for the multi-objective genetic algorithm, we have chosen 20 different solutions inside the Pareto frontier of the previous optimization. We ran the optimization for 17 generations, with 340 total configurations calculated. The objective function convergence profiles are shown in Fig. 10.

From Fig. 11, we can note how the optimization algorithm works well, minimizing both objectives. It is also possible to observe the two behaviors as in the first optimization phase; at the beginning, algorithm reaches the best region as compromise between the objectives, while in the second one, there is a refinement in order to get the best designs.

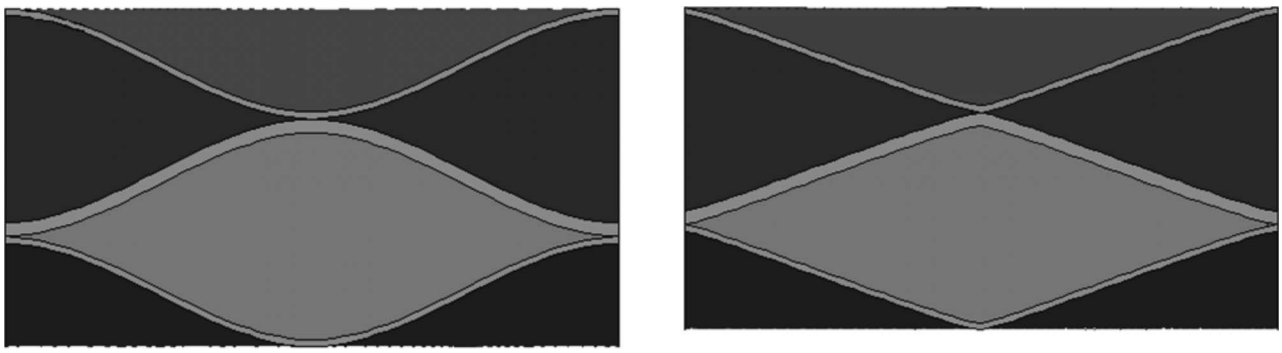

(*a*) (*b*)

Fig. 14 Initial geometry final optimized geometry (Design 134)

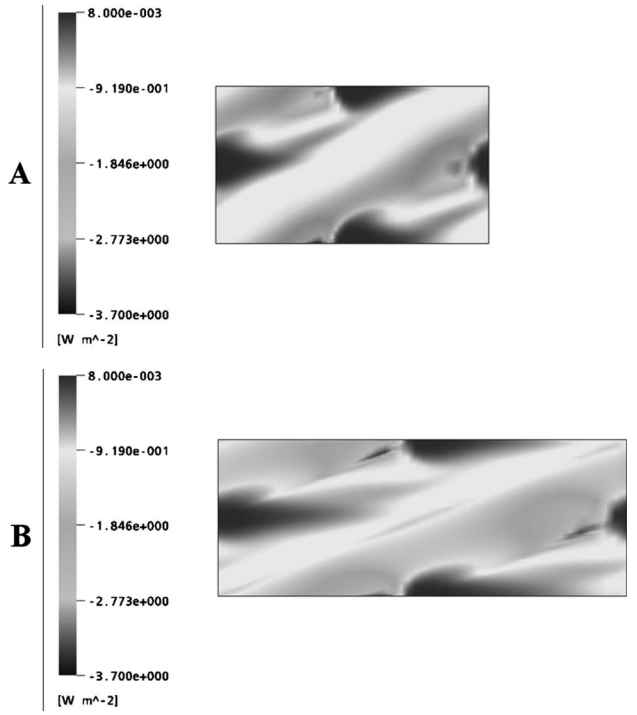

Fig. 15 Wall heat flux for the initial geometry (*a*) and the final optimized geometry (design 134) (*b*)

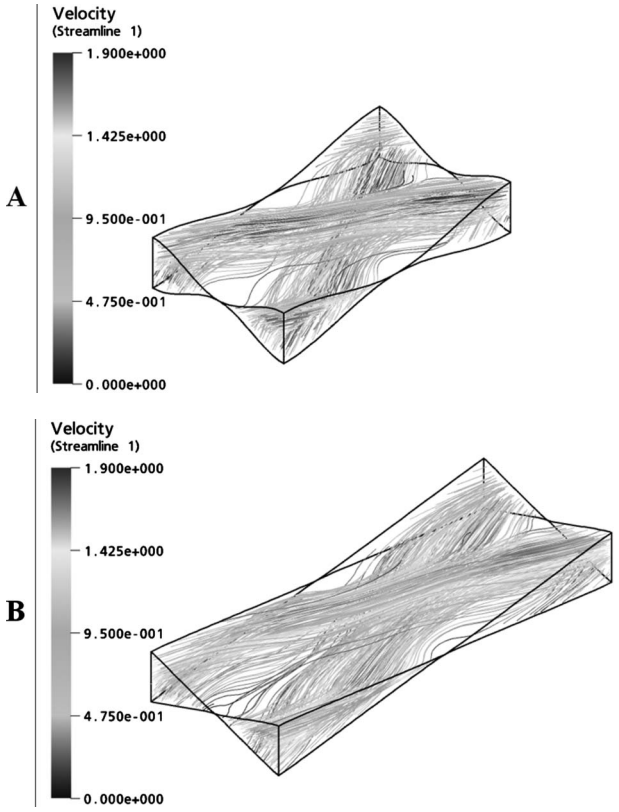

Fig. 16 Streamlines for both the geometries

The final result of the optimization (the Pareto frontier) is visible in Fig. 12. The set is composed by seven different designs, everyone is the best compromise between the two objectives: cost and pressure drop. For the choice of the final design inside the Pareto frontier, there is the possibility to use different methods such as the multicriteria decision making algorithms [26].

In this case, as there are only two criteria, we have used an engineering approach, that is, the designer directly chooses the best design, according to his preferences.

Among the seven designs that belong to the Pareto front, design 134 has been chosen as the best design; in fact it has a surface area reduced of 1.98% and pressure gradient reduced of 19.36%, compared to the original one, maintaining a lower ΔT.

The other designs have better fluid-dynamics performance with lower pressure drops, e.g., design 337 has the lowest value of ΔP equal to 19.64% less than the original, but just 1.44% less than design 134. So, in terms of goodness increment, it is not significant because design 337 has a surface area of 1.88% lower than the original, but 5% higher than design 134. For these reasons, design 134 should be the best choice between the objectives.

These results have been duly verified by running grid independence tests at five grid resolutions, from 82,500 up to 5×10^5 cells for each design belonging to the Pareto set.

In Fig. 13, the comparison of the objective ΔP between the original and the optimized geometries is shown. Assuming the value of the objective for the original design with the finest mesh equal to 100%, it can be noticed that the difference between the values is maintained during the mesh refinement process. This is the reason why a coarser mesh (highlighted in Fig. 7) could be used to lower the total computational time throughout the optimization phase.

The new optimized geometry has a sharper shape of the primary surfaces and a lower value of the corrugation angle, i.e., $\theta = 42$, which means a minor number of unit cells across the length of the recuperator due to the major length of the repeating module. The sharp corners could lead to premature failures, so a structural analysis tool should be included in the design phase. The comparison between the original and optimized geometries is given in Fig. 14, while in Fig. 15 the heat flux contours on the wall for the hot domain are shown. It is possible to notice that the heat flux peaks at the points where the flow first impinges on the wall and then deviates to follow the channel are almost the same. In fact, the thermal behavior is maintained constant due to the constraints setup in the optimization process (the hot flow goes from the right to the left).

In Table 3 all the details of the original and the Pareto front geometries are given.

From a purely fluid-dynamics point of view, in Fig. 16, the two streams that tend to mix causing a vortex effect can be evidenced, which enhances the heat transfer of the cross-corrugated channel. Thanks to the sharpness of the surfaces, the optimized geometry

Table 3 Variables design and performance comparison between the original geometry and the entire Pareto frontier

	P1	P2	P3	P4	θ (deg)	ΔP (%)	Surf (%)	ΔT (%)
Des.0	1	1	1	1	60	0	0	0
Des.134	0.3	0.2	0.3	0.2	42	−19.36	−1.98	−0.28
Des.337	0.6	0.3	0.25	0.2	42	−19.64	−1.88	−0.08

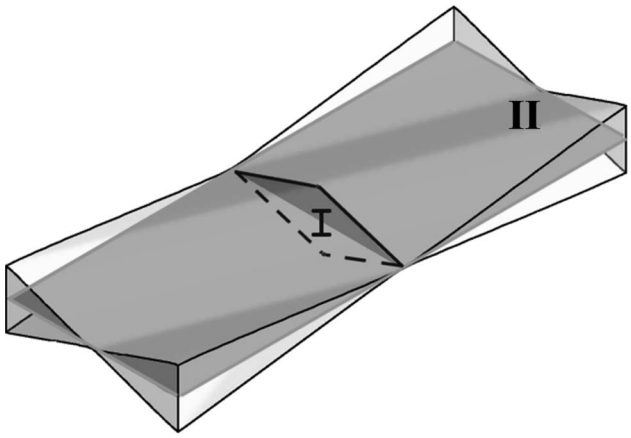

Fig. 17 Cross sections for plot visualization

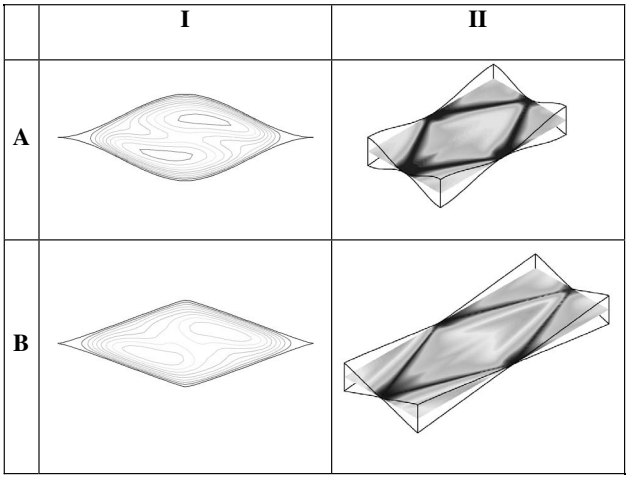

Fig. 18 Velocity contours at perpendicular cross sections for both geometries

induces a greater separation and so a recirculation downstream the edges (Fig. 17). Moreover, in Fig. 18, it can be noticed by the velocity contours plotted on the cross section I (Fig. 17) that the best design has a more uniform distribution with lower peak values. The opposite behavior happens at section II; in fact, higher values of velocity occur where the flow meets the wall.

Conclusions

In this paper, a new approach for a small gas turbine recuperator design is described. It refers to the carrying on of a previous work, where the numerical model for a cross-corrugate surface recuperator was developed. The methodology consists in a design chain based on an automatic iterative process. In this context, a process integration environment is used to link in efficient way different industrial softwares. A multicriterion optimization approach is applied, in order to not limit the designer choice. To solve the optimization problem, the Pareto concept is adopted. In particular, a MOGA is used. An advantage of the proposed methodology is the possibility of splitting the design in different phases, in order to improve the efficiency of the entire project. In our case, thanks to statistical tools, the number of design variables and objectives was decreased, and the variables boundaries have been rearranged.

A final optimal primary surface shape has been obtained, which differs remarkably from the usual geometries found in literature. It improves all the objectives, in particular, pressure drop and, more slightly, cost, without loss in wall heat flux. It must be noted that such results have been obtained with constant hydraulic diameter and, consequently, constant mean flow velocity, and Reynolds number. The values of these parameters were chosen according to best practice design rules.

The numerical results have been validated managing a comparative grid independence with respect to the results of the original geometry. The difference between the values is maintained during the mesh refinement process, so an effective errorless improvement of the performances has been reached.

In the next phase of the research, a new approach will be implemented taking into account the variability of the design point. A probabilistic definition of the boundary conditions will be adopted, and the design problem will be solved by means of a Multi-Objective Robust Design methodology.

Acknowledgment

Research supported by the MIUR-COFIN 2004 funding protocol 2004097349. The integration platform used was MODEFRONTIER 3.2 provided by ES.TE C.O srl[1] to the authors. Special thanks to Professor Manzan for his suggestions and useful advices.

Nomenclature

a = plate corrugation amplitude (m)
A = module heat exchange area (m^2)
b = channel height (m)
c_p = specific heat (J/(kg K))
f = friction factor $f=\alpha 2b/(2\rho u^2)$
h = local heat transfer coefficient ($W/(m^2\ K)$)
H = module length in streamwise direction (m)
L = wavelength of the corrugation (m)
$\dot{m}$ = mass flow rate (kg/s)
$\mathbf{n}$ = unit vector normal to a surface
Nu = Nusselt number, $Nu=h\ 2\ b/\lambda$
p = pressure (Pa)
Pr = Prandtl number, $Pr=c_p\mu/\lambda$
Re = Reynolds number, $Re=(\rho\bar{u}2b)/\mu$
T = temperature (K)
u = velocity in flow direction (m/s)
U = global heat transfer coefficient ($W/(m^2\ K)$)
$\mathbf{W}$ = velocity vector (m/s)
x,y,z = Cartesian coordinates (m)
α = overall pressure gradient in the flow direction (Pa/m)
β = temperature gradient in the flow direction (K/m)
ϕ = heat flux (W/m^2)
λ = thermal conductivity (W/(m K))
μ = dynamic viscosity (kg/(m s))
ρ = density (kg/m^3)
θ = included angle between corrugations (degs)

Sub-/Superscripts

b = bulk
c = cold
h = hot
i = inlet
o = outlet
w = wall
$\sim$ = periodic component
$-$ = mean value

References

[1] Lagerstrom, G., and Xie, M., 2002, "High Performance & Cost Effective Re-

[1] www.esteco.com.

cuperator for Micro-Gas Turbines," *Proceedings of ASME TurboExpo 2002*, Jun. 3–6, Amsterdam, The Netherlands.
[2] Curzio, E. L., Trejo, R., More, K. L., Maziasz, P. A., and Pint, B. A., 2004, "Screening and Evaluation of Materials for Microturbine Recuperators," *Proceedings of ASME TurboExpo 2004*, Jun. 14–17, Vienna, Austria.
[3] Maziasz, P. J., and Swindeman, R. W., 2001, "Selecting and Developing Advanced Alloys for Creep-Resistance for Microturbine Recuperator Applications," *Proceedings of ASME TurboExpo 2001*, Jun. 4–7, New Orleans, LA.
[4] Matthews, W. J., 2006, "Additional Engine Testing of an Advanced Alloy for Microturbine Primary Surface Recuperators," *Proceedings of ASME TurboExpo 2006*, May 8–11, Barcelona, Spain.
[5] Rakowski, J. M., Stinner, C. P., Lipschutz, M., and Montagne, J. P., 2004, "The Use and Performance of Oxidation and Creep Resistant Stainless Steels in Exhaust Gas Primary Surface Recuperator Application," *Proceedings of ASME TurboExpo 2004*, Jun. 14–17, Vienna, Austria.
[6] McDonald, C. F., 2000, "Low Cost Recuperator Concept for Microturbine Applications," *Proceedings of ASME TurboExpo 2000*, May 8–11, Munich, Germany.
[7] Kesseli, S., Wolf, T., Nash, J., and Freedman, S., 2003, "Micro, Industrial and Advanced Gas Turbines Employing Recuperators," *Proceedings of ASME TurboExpo 2003*, Jun. 16–19, Atlanta.
[8] Traverso, A., Zanzarsi, F., and Massardo, A., 2004, "CHEOPE: A Tool for the Optimal Design of Compact Recuperators," *Proceedings of ASME TurboExpo 2004*, Jun. 14–17, Vienna, Austria.
[9] Maziasz, P. J., Pint, B. A., Shingledecker, J. P., More, K. L., Evans, N. D., and Curzio, E. L., 2004, "Austenitic Stainless Steels and Alloys With Improved High-Temperature Performance for Advanced Microturbine Recuperators," *Proceedings of ASME TurboExpo 2004*, Jun. 14–17, Vienna, Austria.
[10] Utriainen, E., and Sundèn, B., 2001, "A Comparison of Some Heat Transfer Surfaces for Small Gas Turbine Recuperators," *Proceedings of ASME TurboExpo 2001*, Jun. 4–7, New Orleans, LA.
[11] Liang, H. X., Xie, G. N., Zeng, M., Wang, Q. W., Luo, L. Q., and Feng, Z. P., 2006, "Genetic Algorithm Optimization for Primary Surfaces Recuperator of Microturbine," *Proceedings of ASME TurboExpo 2006*, May 8–11, Barcelona, Spain.
[12] Manzan, M., Micheli, D., and Pieri, S., 2006, "Automatic Integration in the Design of a Microturbine Compact Recuperator," *Proceedings of ASME TurboExpo 2006*, May 8–11, Barcelona, Spain.
[13] Stasiek, J., Collins, M. W., and Ciofalo, M., 1996, "Investigation of Flow and Heat Transfer in Corrugated Passages—I. Experimental Results," Int. J. Heat Mass Transfer, **39**(1), pp. 149–164.
[14] Ciofalo, M., Stasiek, J., and Collins, M. W., 1996, "Investigation of Flow and Heat Transfer in Corrugated Passages—II. Numerical Simulations," Int. J. Heat Mass Transfer, **39**(1), pp. 165–192.
[15] Croce, G., and D'Agaro, P., 2002, "Numerical Analysis of Forced Convection in Plate and Frame Heat Exchangers," Int. J. Numer. Methods Heat Fluid Flow, **12**(6), pp. 756–771.
[16] Escola, G., Bucey, C. W., Montague, P., and Telfer, M. J., 2006, "Improvement of Microturbine Recuperators Using Taguchi Methodology," *Proceedings of ASME TurboExpo 2006*, May 8–11, Barcelona, Spain.
[17] Rao, S., 1996, *Engineering Optimization*, Wiley, New York.
[18] Deb, K., 1999, "Evolutionary Algorithms for Multi-Criterion Optimization Engineering Design," *Evolutionary Algorithms in Engineering and Computer Science*, Wiley, New York.
[19] Poloni, C., and Pediroda, V., 1996, "GA Coupled With Computationally Expensive Simulations: Tools to Improve Efficiency," *Genetic Algorithms and Evolution Strategy in Engineering and Computer Science*, Wiley, New York, Chap. 13, pp. 267–288.
[20] MODEFRONTIER, version 3.2 Documentation, http://www.esteco.it.
[21] Webb, R. L., 1981, "Performance Evaluation Criteria for Use of Enhanced Heat Transfer Surfaces in Heat Exchanger Design," Int. J. Heat Mass Transfer, **24**, pp. 715–726.
[22] Webb, R. L., and Eckert, E. R. G., 1972, "Application of Rough Surfaces to Heat Exchanger Design," Int. J. Heat Mass Transfer, **21**, pp. 1647–1658.
[23] Bergles, A. E., Bunn, R. L., and Junkhan, G. H., 1974, "Extended Performance Evaluation Criteria for Enhanced Heat Transfer Surfaces," Lett. Heat Mass Transfer, **1**, pp. 113–120.
[24] Valentino, P., Clarich, A., Mosetti, Giovanni, and Poloni, C., 2005, "Application of Evolutionary Algorithms and Statistical Analysis in the Numerical Optimization of an Axial Compressor," Int. J. Rotating Mach., **2**, pp. 143–151.
[25] Press, W. H., 1990, *Numerical Recipes*, Cambridge University Press, Cambridge.
[26] Clarich, A., Pediroda, V., and Poloni, C., 2006, "Multi Attribute Design Of Airfoil Under Uncertainties By Combining Game Theory And MCDM Methods," *MCDM 2006 The 18th International Conference on Multiple Criteria Decision Making*, Chania, Greece, Jun. 19–23.

A Fracture-Mechanics-Based Methodology for Fatigue Life Prediction of Single Crystal Nickel-Based Superalloys

Srikant Ranjan
e-mail: srikant@ufl.edu

Nagaraj K. Arakere[1]
e-mail: nagaraj@ufl.edu

Mechanical and Aerospace Engineering Department,
University of Florida,
Gainesville, FL 32611-6300

A comprehensive fracture-mechanics-based life prediction methodology is presented for fcc single crystal components based on the computation of stress intensity factors (SIFs), and the modeling of the crystallographic fatigue crack growth (FCG) process under mixed-mode loading conditions. The 3D finite element numerical procedure presented for computing SIFs for anisotropic materials under mixed-mode loading is very general and not just specific to fcc single crystals. SIFs for a Brazilian disk specimen are presented for the crack on the {111}) plane in the ⟨101⟩ and ⟨121⟩ directions, which represent the primary and secondary slip directions. Variation of SIFs as a function of thickness is also presented. Modeling of the crystallographic FCG behavior is performed by using the resolved shear stress intensity coefficient, K_{rss}. This parameter is sensitive to the grain orientation and is based on the resolved shear stresses on the slip planes at the crack tip, which is useful in identifying the active crack plane as well as in predicting the crack growth direction. A multiaxial fatigue crack driving force parameter, ΔK_{rss}, was quantified, which can be used to predict the FCG rate and, hence, life in single crystal components subject to mixed-mode fatigue loading. [DOI: 10.1115/1.2838990]

Introduction

Turbine blades in high performance aircraft and rocket engines are increasingly being made of single crystal nickel-based superalloys. Turbine blades and vanes, used in aircraft and rocket engines, are typically the most demanding structural applications for high temperature materials due to the combination of high operating temperature, corrosive environment, high monotonic and cyclic stresses, and long expected component lifetimes, and the enormous consequence of structural failure. Failures of blade components account for 40% of all turbine engine component failures attributable to high cycle fatigue (HCF) [1]. Estimation of blade fatigue life, therefore, represents a very important aspect of durability assessment.

Nickel-based single crystal superalloy materials have a fcc crystal structure, and differ from polycrystalline alloys in that they have orthotropic properties making the position of the crystal lattice relative to the part geometry a significant factor in the overall analysis [2]. The modified Goodman approach currently used for component design does not address important factors that affect HCF, such as crystallographic crack initiation and propagation, magnitude of resolved shear stress amplitudes on slip planes, fretting damage, and interaction with low cycle fatigue (LCF). Rocket engine service presents a different set of requirements that shifts the emphasis to low temperature fatigue and fracture capability, with particular attention given to thermal, cryogenic, and high pressure hydrogen gas exposure [3]. Toward addressing HCF induced component failures, a large body of fatigue test has been collected by the gas turbine and space propulsion industries. However, there currently exists no systematic method for applying this knowledge toward the design of more robust single crystal gas turbine engine components. There is a need to establish a mechanistically based life prediction methodology for fcc single crystal components.

Fatigue failure in PWA1480/1493, a single crystal nickel-based turbine blade superalloy, was investigated by Swanson and Arakere [4] using a combination of experimental LCF fatigue data and 3D finite element (FE) modeling of HPFTP/AT space shuttle main engine (SSME) turbine blades. The maximum shear stress amplitude ($\Delta\tau_{max}$) on the primary slip systems was found to be an effective multiaxial fatigue failure parameter based on the curve fit between $\Delta\tau_{max}$ and cycles to failure. This failure parameter reduces LCF fatigue data obtained with specimens in different crystallographic orientations to an effective *S-N* diagram, with $\Delta\tau_{max}$ as the stress amplitude. This approach is equivalent to a stress-life method used for fatigue design. This procedure was used to evaluate the fatigue life of a SSME turbopump turbine blade using 3D FE analysis (FEA) incorporating elastic anisotropy. Results revealed that a secondary crystallographic orientation had a pronounced effect on fatigue life, leading to the conclusion that control of a secondary orientation has the potential to significantly increase a component's resistance to fatigue crack growth (FCG).

The objectives of this paper are to extend the stress-life approach to the life prediction of single crystal components using the fatigue damage parameter ($\Delta\tau_{max}$), presented by Swanson and Arakere [4], by implementing a fracture mechanics approach to life prediction. This will require computation of stress intensity factors (SIFs) for cracks in fcc single crystals, as a function of crystallographic orientation, under mixed-mode loading conditions, and also modeling of the FCG process. The orientation dependence of material properties for single crystals results in shear coupling and interdependence of (x,y,z) crack tip displacements, leading to mixed-mode loading conditions even when the loading appears to be purely Mode I. Hence, SIF for fcc single crystal materials depends on remote loading, crack size, structural geometry, and crystallographic orientation. In fact, the crystallographic orientation dependence of crack tip displacements, leading to the coupling of KI, KII, and KIII, highlights the difficulty in obtaining generalized SIF solutions for anisotropic and orthotropic materials, and perhaps also explains the dearth of such solutions for practical specimen geometries in published literature. We present

[1]Corresponding author.

Manuscript received October 16, 2006; final manuscript received October 17, 2006; published online March 26, 2008. Review conducted by Dilip R. Ballal.

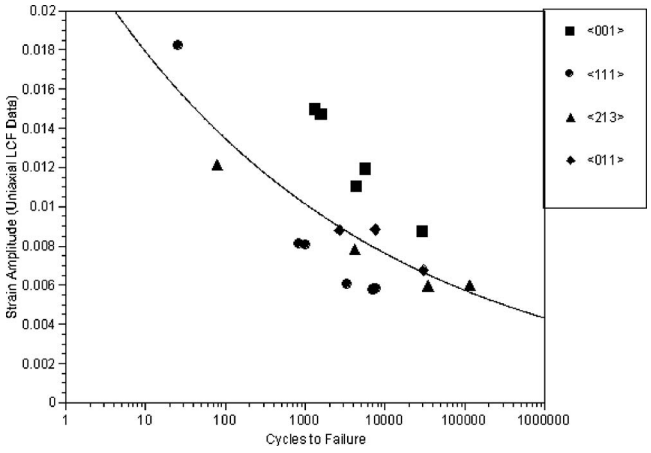

Fig. 1 Strain range versus cycles to failure (N_f) for LCF test data (PWA1493 AT 1200F) [4]

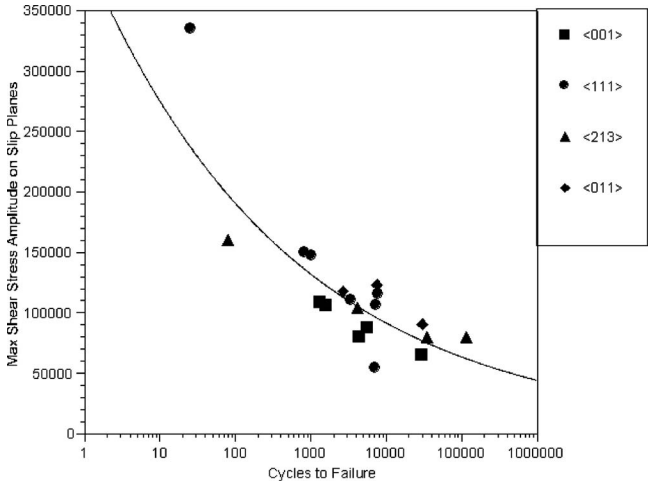

Fig. 2 Shear stress amplitude [$\Delta\tau_{max}$] versus cycles to failure (N_f) [4]

a general numerical procedure for computing SIFs for cracks in fcc single crystals, subject to mixed-mode loading. This represents the first detailed compilation of SIFs for Brazilian disk (BD) specimen as a function of crystallographic orientation. Results are presented for a center-cracked BD specimen, with two specific crystallographic orientations: a (111) crack plane with crack directions $\langle 10\bar{1}\rangle$ and $\langle 12\bar{1}\rangle$. These two crack directions typically represent the fastest and slowest crystallographic crack growth rates, respectively, on the (111) family of octahedral planes of a fcc single crystal and hence, have important implications on estimating FCG life for single crystal components [3]. Even if cracks nucleate on other planes because of local influence from intrinsic defects, such as micropores, carbide particles, and undissolved eutectics, they tend to migrate to the octahedral planes, in the primary slip directions ($\langle 10\bar{1}\rangle$ family of directions), since they represent the paths of least resistance for crack propagation [5]. Results presented show that SIF values are consistently higher for the $\langle 10\bar{1}\rangle$ crack direction, compared to the $\langle 12\bar{1}\rangle$ direction, for identical crack angles and loads [6].

We also present FCG modeling results using a crack driving force parameter based on resolved shear stresses on primary slip planes (ΔK_{rss}). This crack driving force parameter was first highlighted by the experimental work from Telesman and Ghosn [7], which we have adapted in a numerical framework. The ability to compute mixed-mode SIFs and model the FCG process provides tools necessary for establishing a mechanistically based life prediction system. The proposed methodology can be used for computing crystallographic FCG life in single crystal components.

Fatigue Damage Parameter in fcc Single Crystals: Stress-Life Approach for Life

We present a brief description of the fatigue damage parameter, $\Delta\tau_{max}$, developed by Swanson and Arakere [4], for the sake of completeness and also to highlight the differences between the stress-life approach to life prediction and the fracture-mechanics-based life prediction system presented later.

Strain controlled LCF tests conducted at 1200°F in air for PWA1480/1493 uniaxial smooth specimens, for four different orientations are shown in Fig. 1. A wide scatter is observed in the data with poor correlation (R^2=0.469) for a power law fit. The maximum resolved shear stress amplitude ($\Delta\tau_{max}$) on the primary octahedral slip systems for each data point, based on minimum and maximum test strain values and specimen orientation, was calculated based on linear elastic anisotropic assumptions. Figure 2 shows a plot of $\Delta\tau_{max}$ versus cycles to failure. A good correlation (R^2=0.674) is seen for a power law curve fit (Eq. (1)). The plane on which the resolved shear stress reaches a maximum value is also the plane where the critical resolved shear stress (CRSS) is exceeded first, thus making it the dominant slip system to initiate slip or plasticity,

$$\Delta\tau_{max} = 397{,}758N^{-0.1598} \tag{1}$$

We have conducted further experimental and numerical investigations on the evolution of slip in triaxial states of stress and concluded that once slip is initiated on the dominant slip system, if tends to stay on this plane [8]. This sheds further light on why the $\Delta\tau_{max}$ multiaxial fatigue damage parameter collapses the fatigue test data very effectively. The failure planes on the LCF specimens were investigated by Naik et al. [9] and it was found that those planes were indeed the planes where the resolved shear stresses were maximum. The correlation for ($\Delta\tau_{max}$) versus N would be better if some of the high stress data points are corrected for inelastic effects.

Computation of Stress Intensity Factors for fcc Single Crystals Under Mixed-Mode Loading

SIF about a crack tip plays a significant role in the propagation of the crack. The SIF is a measure of intensity near the crack tip under linear elastic conditions. The knowledge of SIF is necessary to predict the growth of a fatigue crack or to determine the residual strength of a cracked structure.

Many methods have been proposed to calculate SIFs for cracks subjected to mixed-mode loading conditions in isotropic elastic solids. Some commonly used methods are J integral [10,11], virtual crack extension [12,13], modified crack closure integral, displacement extrapolation methods [14], etc. None of these proposed methods are able to provide the complete solution for all the three modes (Mode I, II, and III) of SIF for an anisotropic material.

Although a substantial body of literature describes the computation of SIF [11,13,15–29], a generalized numerical solution to calculate SIF for a 3D anisotropic material under a mixed-mode loading condition is unavailable.

It can be shown that mixed-mode SIFs for an anisotropic material can be computed by [6]

$$\begin{Bmatrix} K_{\mathrm{I}} \\ K_{\mathrm{II}} \\ K_{\mathrm{III}} \end{Bmatrix} = [B]^{-1}\{A\}\sqrt{\frac{\pi}{2L_1}} \tag{2}$$

where L_1 is the element length along the crack face (AC=GF) and $\{A\}$ is given as

$$\begin{aligned}\{A\} = {} & 2u_B - u_C + 2u_E - u_F + u_D + \frac{1}{2}\eta(-4u_B + u_C \cdots 4u_E - u_F) \\ & + \frac{1}{2}\eta^2(u_F + u_C - 2u_D)2v_B - v_C + 2v_E - v_F + v_D \\ & + \frac{1}{2}\eta(-4v_B + v_C + \ \ldots \ + 4v_E - v_F) \\ & + \frac{1}{2}\eta^2(v_F + v_C - 2v_D)2w_B - w_C + 2w_E - w_F + w_D \\ & + \frac{1}{2}\eta(-4w_B + w_C + \ \ldots \ + 4w_E - w_F) \\ & + \frac{1}{2}\eta^2(w_F + w_C - 2w_D)\end{aligned} \tag{3}$$

Here u, v, and w are the nodal displacements of nodes B, C, D, E, and F at the crack tip relative to B′, C′, D′, E′, and F′, as shown in Fig. 3.

η is the natural coordinate system value defined as

$$\eta = -\left(\frac{2z}{L_2} + 1\right) \tag{4}$$

L_2 is the length of the element along the crack front (AG=CF) and $[B]^{-1}$ is defined as

$$[B]^{-1} = \begin{bmatrix} \mathrm{Re}\left[\frac{i}{\mu_1 - \mu_2}(q_2 - q_1)\right]\frac{1}{D} & \mathrm{Re}\left[\frac{-i}{\mu_1 - \mu_2}(p_2 - p_1)\right]\frac{1}{D} & 0 \\ \mathrm{Re}\left[\frac{-i}{\mu_1 - \mu_2}(\mu_1 q_2 - \mu_2 q_1)\right]\frac{1}{D} & \mathrm{Re}\left[\frac{i}{\mu_1 - \mu_2}(\mu_1 p_2 - \mu_2 p_1)\right]\frac{1}{D} & 0 \\ 0 & 0 & \frac{1}{\sqrt{c_{44}c_{55} - c_{45}^2}} \end{bmatrix} \tag{5}$$

As is apparent from the $[B]^{-1}$ matrix, the K_{I} and K_{II} are the only coupled SIFs (functions of u and v) and the K_{III} is a function of w only.

D is the determinant of the equation

$$D = \begin{vmatrix} \mathrm{Re}\left[\frac{i}{\mu_1 - \mu_2}(\mu_1 p_2 - \mu_2 p_1)\right] & \mathrm{Re}\left[\frac{i}{\mu_1 - \mu_2}(p_2 - p_1)\right] \\ \mathrm{Re}\left[\frac{i}{\mu_1 - \mu_2}(\mu_1 q_2 - \mu_2 q_1)\right] & \mathrm{Re}\left[\frac{i}{\mu_1 - \mu_2}(q_2 - q_1)\right] \end{vmatrix} \tag{6}$$

μ_1 and μ_2 are the roots of the fourth order characteristic equation

$$a_{11}\mu^4 - 2a_{16}\mu^3 + (2a_{12} + a_{66})\mu^2 - 2a_{26}\mu + a_{22} = 0 \tag{7}$$

and are given by

$$\mu_j = \alpha_j + i\beta_j \text{ and } \beta_j > 0$$

(as μ_j can only be a complex number [30] (for the details, refer to Ranjan [6]),

$$p_j = a_{11}\mu_j^2 + a_{12} - a_{16}\mu_j$$

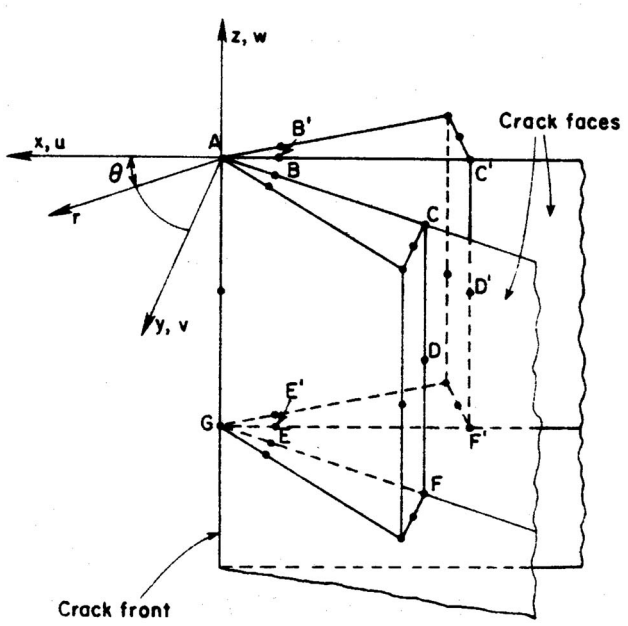

Fig. 3 Arrangement of quarter-point wedge elements along segment of crack front with nodal lettering convention [31]

$$q_j = a_{12}\mu_j + \frac{a_{22}}{\mu_j} - a_{26} \tag{8}$$

For plane stress,

$$a_{11} = \frac{1}{E_{11}}, \quad a_{22} = \frac{1}{E_{22}}, \quad a_{21} = a_{12} = -\frac{\nu_{12}}{E_{11}}, \quad a_{66} = \frac{1}{G_{12}} \tag{9}$$

For plane strain,

$$a_{ij} = a_{ij} - \frac{a_{i3}a_{j3}}{a_{33}} \tag{10}$$

Equation (2) is used to calculate the SIF at the crack tip by the displacement method, which is one of the most commonly used methods to get the value accurately. The FE method was used to calculate the displacements at the crack tip. The commercial software ANSYS was used for FEA modeling. The crack tip nodal displacements were then extracted from the FEA model and fed to the analytical equations explained above to calculate all the three modes of SIFs.

Single Crystal Specimen Geometries Used for Mixed-Mode Loading

The specimen modeled was a circular BD specimen, loaded in compression. Details of the BD specimen analyzed are given in Table 1. This specimen with center crack has a mode mixity at the crack tip, which varies as function of the crack angle ϕ, shown in Fig. 4. The crack lies on the {111} plane, and the crack directions used are the ⟨101⟩ and ⟨121⟩ families of directions. These specimen and crack orientations have been checked very carefully based on experimentally observed FCG rates (FCGRs) [32].

Table 1 Geometrical and material properties of the BD specimen analyzed

E	106.2 GPa	G	108.2 GPa	ν	0.4009
W	2.794 cm	$2a/W$	0.2–0.8	t	0.254 cm
F	4.448 kN				

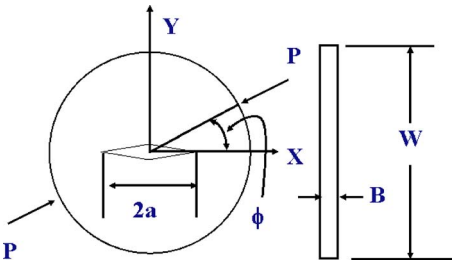

Fig. 4 BD specimen with center crack lying in the (111) plane and oriented along the $[10\bar{1}]$ direction

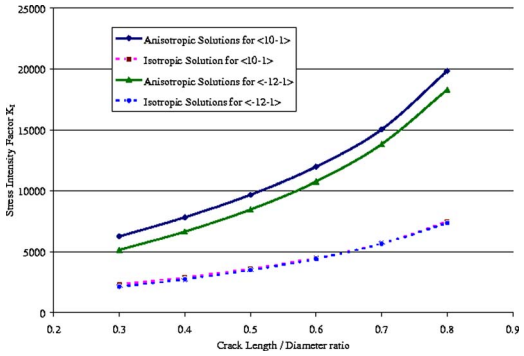

Fig. 6 K_I versus $2a/W$ ratio for $[10\bar{1}]$ and $[\bar{1}2\bar{1}]$ orientations of BD specimen at $\phi=0$ deg

Figure 5 shows that the crack plane lies on the (111) plane and is directed along the $\langle\bar{1}2\bar{1}\rangle$ direction. This slip system has been explained with the help of octahedral slip planes (Fig. 5, right side).

SIF Results. From the BD specimen results (Figs. 6–11), it can be seen that the magnitude of SIF for the $[10\bar{1}]$ orientation is always greater than the corresponding values of the $[\bar{1}2\bar{1}]$ orientation, thus enabling a crack to propagate faster on the $[10\bar{1}]$ plane than on the $[\bar{1}2\bar{1}]$ plane under identical fatigue loading. For the $[10\bar{1}]$ orientation, the crack closure angle is ~18 deg, whereas it is ~30 deg for the $[\bar{1}2\bar{1}]$ orientation (Fig. 9).

Following the work of Saouma and Sikiotis [31], the calculated values for K_{III} were found to be negligible. The discrepancies were found in the formulation of Eq. (5), and we believe that the form of Eq. (5), shown in this paper is appropriate to use in fcc single crystals, as it correctly gives rise to all the three modes of SIFs. As a result of the coupling of displacements at the crack tip due to anisotropy, non-negligible values of K_{III} were found, and they varied with respect to the applied force, crack length, and crack angle.

The BD specimen SIFs were further analyzed along the thickness for the $[10\bar{1}]$ and $[\bar{1}2\bar{1}]$ crack orientations due to change in crack length and crack angle. They were calculated at five different points along the thickness at the crack front, as shown in Fig. 12. A plane stress assumption was made at the surface of the BD specimen (Planes 1 and 5), and a plane strain assumption was made at all the interior points (Planes 2–4).

In order to check the difference in SIF of isotropic BD specimen and orthotropic BD specimen with change in load angle and with crack, under similar loading condition and specimen geometry, two models were analyzed. Due to the limitation of space, this analysis could not be presented here, but can be found in Ranjan [6].

From Figs. 13 and 15, it can be seen that the crack closure angle (where K_I is almost zero) was reached at ~18 deg for the $[10\bar{1}]$ orientation, whereas it was ~30 deg for the $[\bar{1}2\bar{1}]$ orientation, as was observed in Fig. 9. K_I can be seen as symmetric for the $[\bar{1}2\bar{1}]$ orientation across the thickness, whereas it is not for the $[10\bar{1}]$ orientation. In general, K_I inside the surface (Planes 2, 3, and 4, Fig. 12) than those at the crack edges (Planes 1 and 5, Fig. 12).

The absolute value of K_{II} becomes maximum at an angle of ~24 deg for the $[10\bar{1}]$ orientation, whereas for the $[\bar{1}2\bar{1}]$ orientation, it is ~36 deg (Figs. 14 and 16), as also illustrated in Fig. 10. It is interesting to observe that SIFs (Figs. 15–18) (K_I, K_{II}, and K_{III}) are symmetric about the midplane for the $[\bar{1}2\bar{1}]$ orientation. This is due to the symmetry observed more only for the crack lying along the $\langle 121\rangle$ direction than for that lying along the $\langle 101\rangle$ direction on the {111} plane, as shown in Fig. 19.

K_{III} is maximum at an angle of ~48 deg for the $[\bar{1}2\bar{1}]$ orientated BD specimen, as can be clearly seen in Fig. 11. The values of K_{III} (Fig. 17) for the $[10\bar{1}]$ orientation at one of the faces (Plane 1, thickness=0) are always greater than those at the other face (Plane 5, thickness=1), and reach maximum at an angle of 30–36 deg. The maximum value of K_{III} shown in Fig. 11 is at ~25 deg because the values were calculated at an offset to the midplane, which can be verified from the offset value taken from Fig. 17.

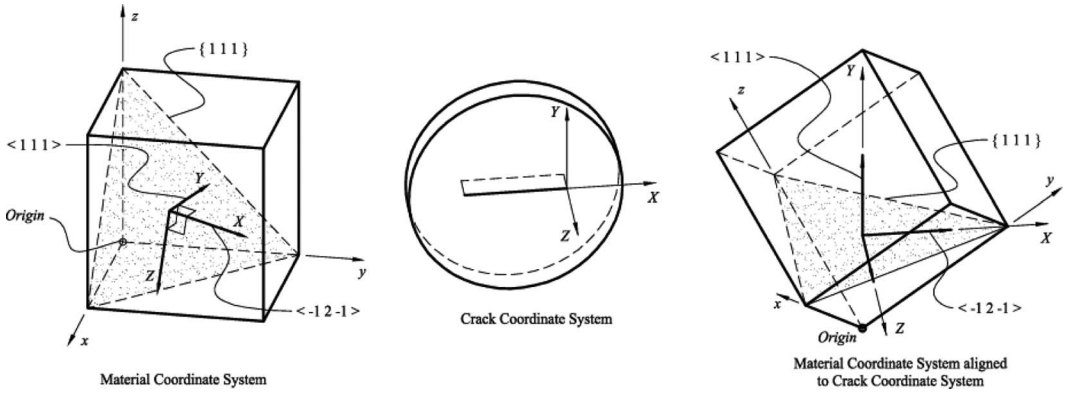

Fig. 5 BD specimen having center crack lying in the {111} slip plane and aligned along the $[\bar{1}2\bar{1}]$ direction

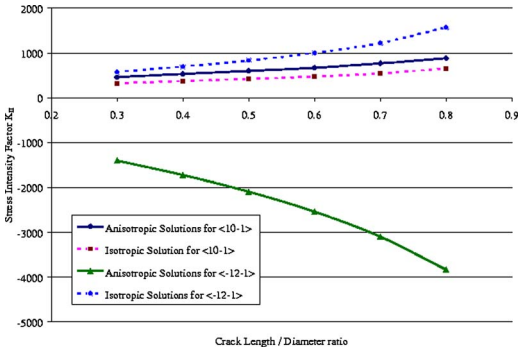

Fig. 7 K_{II} versus $2a/W$ ratio for $[10\bar{1}]$ and $[\bar{1}2\bar{1}]$ orientations of BD specimen at $\phi=0$ deg

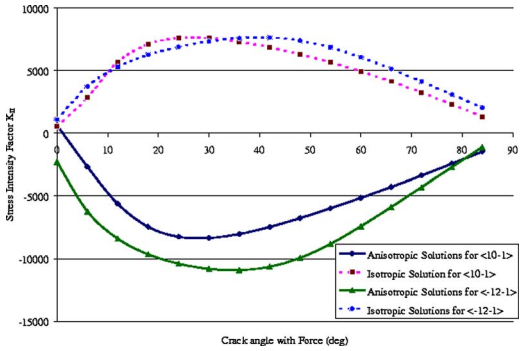

Fig. 10 K_{II} versus crack angle with force for $[10\bar{1}]$ and $[\bar{1}2\bar{1}]$ orientations of BD specimen at $2a/W=0.55$

For the $[\bar{1}2\bar{1}]$ orientation (Figs. 15–18), it can be seen that K_I, K_{II}, and K_{III} are always symmetric across the thickness (because of the symmetry about the midplane, as shown in Fig. 19). At the midplane, K_{III} is always zero, which means that there is no out of plane displacement at the midplane.

Using the above analysis, we can find the profile of the crack growth inside a specimen, which can be crucial for the life assessment of an anisotropic material.

Crystallographic Fatigue Crack Growth

Several studies have been conducted on FCG of Ni-based single crystals [33–37], and all of these studies have shown that FCG is highly sensitive to the orientation of the crystal and that the crack plane is crystallographic and follows a single slip plane or a combination of slip planes. Since shear decohesion on a slip plane is caused by dislocation motion, many researchers have suggested that the resolved shear stress acting on the active slip plane ahead of a crack tip must be responsible for the propagation of the fatigue crack [35,38,39]. The dislocation motion is controlled by the forces at the crack tip, which is directly related to the resolved shear stress on the slip plane. Therefore, the rate of shear decohesion must be related to the "resolved shear stress intensity" (RSSI) at the crack tip. The active shear decohesion plane or planes must be the slip plane(s) with a high RSSI. If the RSSI on a plane is much higher than all the other slip planes, then the plane must be the primary plane for shear decohesion and the slip plane becomes the crack plane. However, if the resolved shear stresses on two or more of the slip systems are comparable, then the shear decohesion will take place on all of those slip planes and the macrocrack

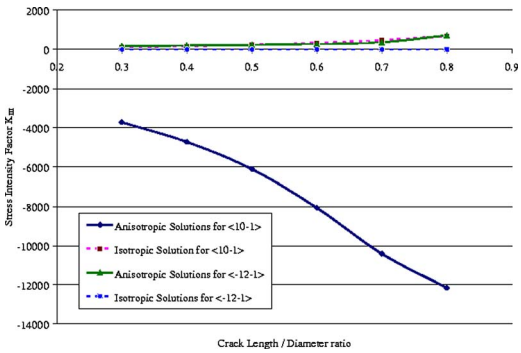

Fig. 8 K_{III} versus $2a/W$ ratio for $[10\bar{1}]$ and $[\bar{1}2\bar{1}]$ orientations of BD specimen at $\phi=0$ deg

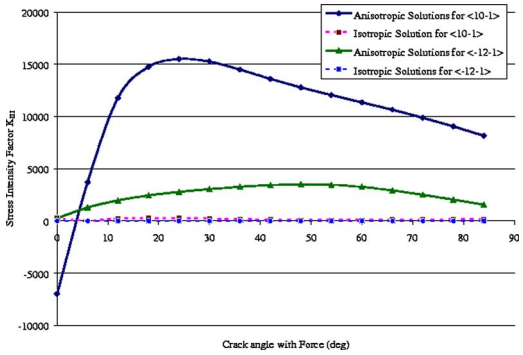

Fig. 11 K_{III} versus crack angle with force for $[10\bar{1}]$ and $[\bar{1}2\bar{1}]$ orientations of BD specimen at $2a/W=0.55$

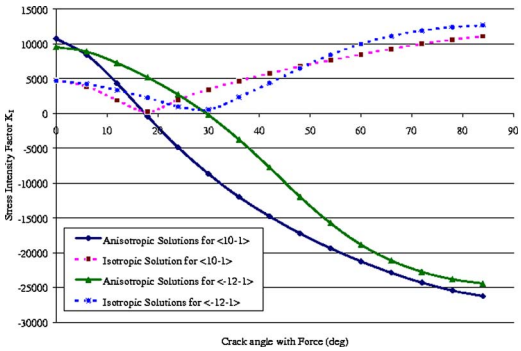

Fig. 9 K_I versus crack angle with force for $[10\bar{1}]$ and $[\bar{1}2\bar{1}]$ orientations of BD specimen at $2a/W=0.55$

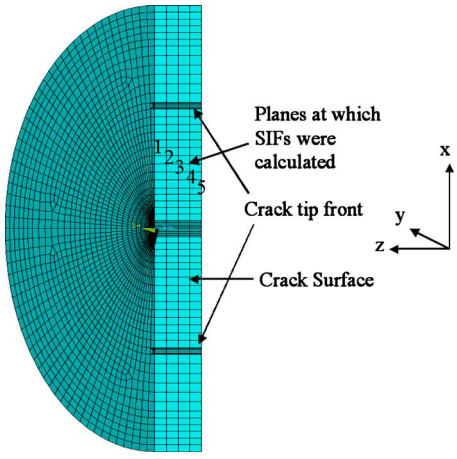

Fig. 12 Half meshed model of BD specimen and the crack coordinate system

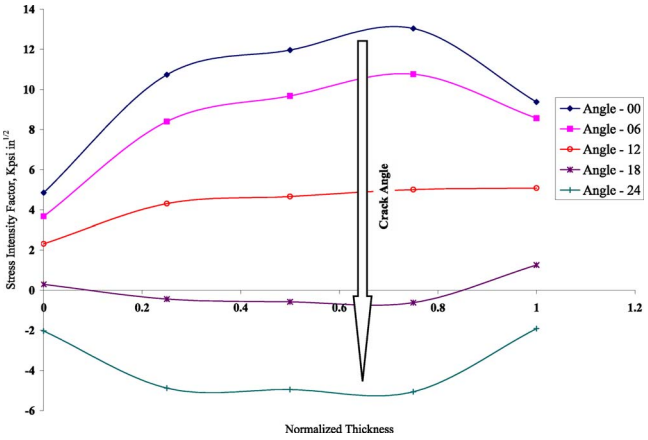

Fig. 13 Variation of SIF K_I along BD specimen thickness at different crack angle for the $[10\bar{1}]$ orientation

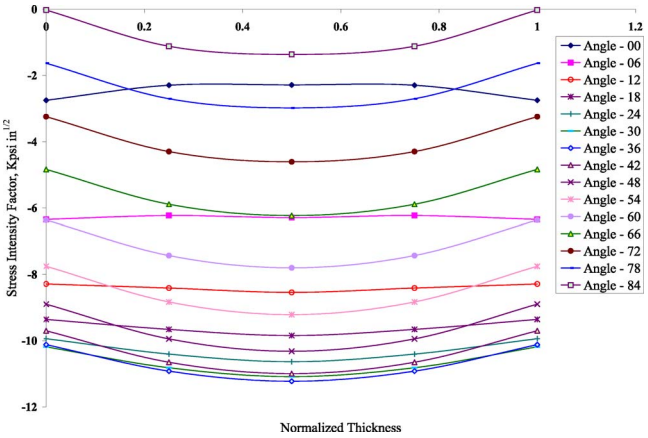

Fig. 16 Variation of SIF K_{II} along BD specimen thickness at different crack angle for the $[\bar{1}2\bar{1}]$ orientation

plane will not follow a single slip plane; this was shown by Telesman and Ghosn [7]. Even though macroscopic crack was observed along the (001) plane inclined 7 deg to the starter notch, the microscopic slip was observed on the (111) slip planes, inclined 52 deg and −38 deg to the starter notch.

If a crack surface is a slip plane, it is logical that the crack growth rate on that slip plane will correlate with its RSSI.

Chen and Liu [40] proposed a crack driving force parameter for correlating FCG data, which is based on the resolved shear stresses on the active slip plane(s). This parameter may be better than ΔK for the correlation of FCG data since it takes into consideration the deformation mechanisms, grain orientation, and actual crack path.

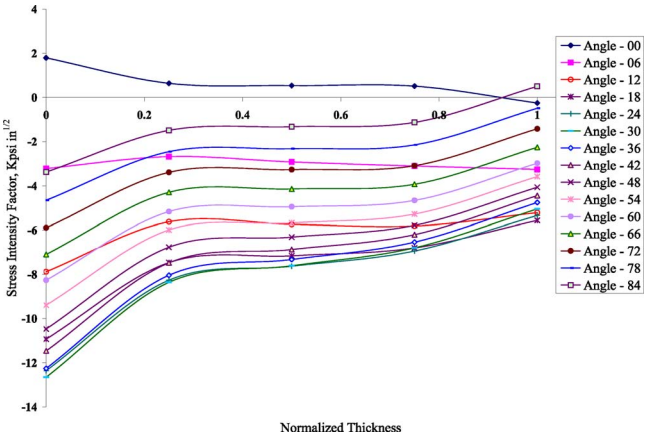

Fig. 14 Variation of SIF K_{II} along BD specimen thickness at different crack angle for the $[10\bar{1}]$ orientation

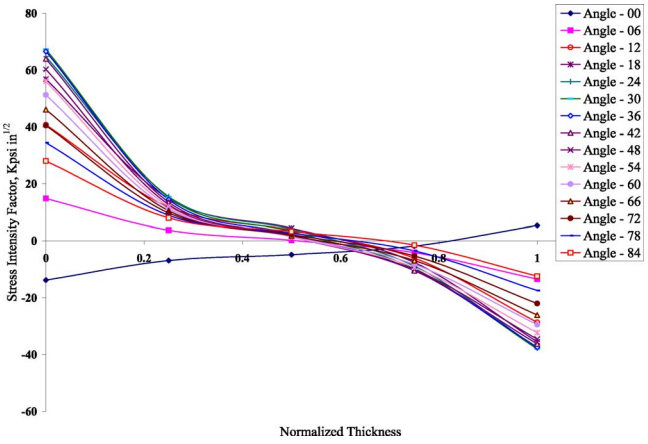

Fig. 17 Variation of SIF K_{III} along BD specimen thickness at different crack angle for the $[10\bar{1}]$ orientation

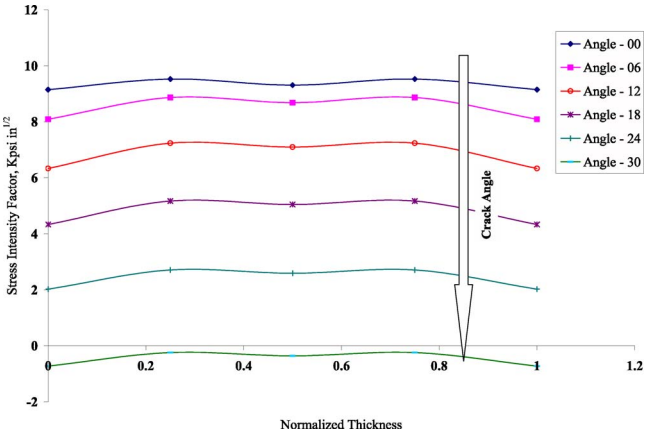

Fig. 15 Variation of SIF K_I along BD specimen thickness at different crack angle for the $[\bar{1}2\bar{1}]$ orientation

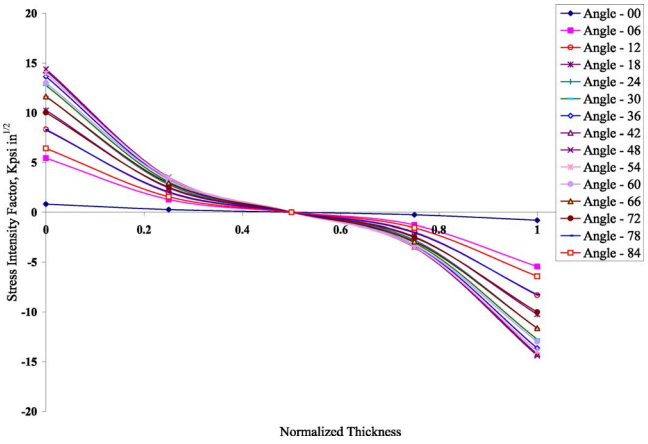

Fig. 18 Variation of SIF K_{III} along BD specimen thickness at different crack angle for the $[\bar{1}2\bar{1}]$ orientation

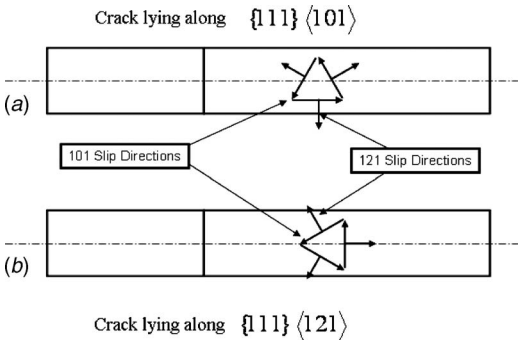

Fig. 19 (*a*) Unsymmetry about midplane for crack oriented along {111} ⟨101⟩; (*b*) symmetry for crack lying along {111} ⟨121⟩

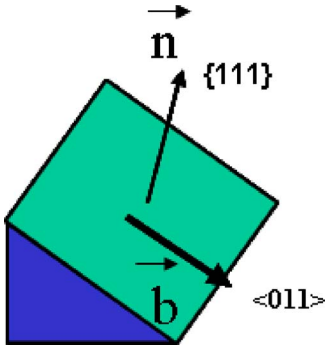

Fig. 21 Burgers vector b is along slip direction ⟨011⟩ and slip plane direction is normal vector n along ⟨111⟩

The resolved shear stress field of a slip system is defined by its intensity coefficient, which can be calculated once Modes I, II, and III crack tip fields are obtained.

The resolved shear stress is given by [41]

$$\tau_{\text{rss}} = \frac{1}{b} b_i \sigma_{ij} n_j \tag{11}$$

where b_i and b are the Burgers vector and its magnitude, n_j is the unit normal vector of the slip plane, and σ_{ij} is the crack tip stress tensor field given by [40]

$$[\sigma_{ij}] = \frac{1}{\sqrt{2\pi r}}[K_{\text{I}} f_{ij}^{\text{I}}(\theta) + K_{\text{II}} f_{ij}^{\text{II}}(\theta) + K_{\text{III}} f_{ij}^{\text{III}}(\theta)] \tag{12}$$

where r and θ are the local polar coordinates at the crack tip, as shown in Fig. 20; $f_{ij}(\theta)$ are the angular component of the stress field. Substituting Eq. (12) into Eq. (11), the resolved shear stress is

$$\tau_{\text{rss}} = \frac{1}{\sqrt{2\pi r}}[b_i^n][K_{\text{I}} f_{ij}^{\text{I}}(\theta) + K_{\text{II}} f_{ij}^{\text{II}}(\theta) + K_{\text{III}} f_{ij}^{\text{III}}(\theta)][n_j] \tag{13}$$

where b_i^n and n_j are the unit Burgers vectors and unit normal vectors of the slip planes, respectively.

The above equation indicates that τ_{rss} preserves the $1/\sqrt{r}$ singularity, and the intensity of τ_{rss} is dependent on the crystal orientation relative to the crack surface. For a given crystal orientation and crack geometry, the angle θ is equal to the angle between the trace of a particular slip plane on the plane normal to the slip plane and the horizontal axis. The intensity of τ_{rss} is linearly proportional to the quantity RSSI coefficient K_{rss}, which for a given slip system can be defined as the limiting value of the resolved shear stress τ_{rss} multiplied by $\sqrt{2\pi r}$ as r approaches zero [7,40]

$$K_{\text{rss}} = \lim_{r \to 0} \tau_{\text{rss}} \sqrt{2\pi r} \tag{14}$$

where r is the distance of the crack tip and τ_{rss} is defined as the projection of the stress tensor $[\sigma]$ on a plane whose outward normal is **n** in the direction of slip **b** (Fig. 21). The two distinct advantages in using K_{rss} are as follows: (1) The dependency of τ_{rss} on r is eliminated; (2) the angle θ has a definite physical meaning, which is directly related to the orientation of the slip system.

The state of stress on a slip plane, under mixed-mode loading, whose trace on a plane normal to crack plane makes an angle θ with the horizontal axis (Figs. 20 and 22), can be defined as [6]

$$\begin{Bmatrix} \sigma_x \\ \sigma_y \\ \sigma_z \\ \tau_{yz} \\ \tau_{zx} \\ \tau_{xy} \end{Bmatrix} = \frac{1}{\sqrt{2\pi r}} \begin{bmatrix} d_{11} & d_{12} & 0 \\ d_{21} & d_{22} & 0 \\ d_{31} & d_{32} & d_{33} \\ 0 & 0 & d_{43} \\ 0 & 0 & d_{53} \\ d_{61} & d_{62} & 0 \end{bmatrix} \cdot \begin{Bmatrix} K_{\text{I}} \\ K_{\text{II}} \\ K_{\text{III}} \end{Bmatrix} \tag{15}$$

where

$$d_{11} = \text{Re}\left[\frac{\mu_1\mu_2}{\mu_1 - \mu_2}\left(\frac{\mu_2}{b_2} - \frac{\mu_1}{b_1}\right)\right], \quad d_{12} = \text{Re}\left[\frac{1}{\mu_1 - \mu_2}\left(\frac{\mu_2^2}{b_2} - \frac{\mu_1^2}{b_1}\right)\right]$$

$$d_{21} = \text{Re}\left[\frac{1}{\mu_1 - \mu_2}\left(\frac{\mu_1}{b_2} - \frac{\mu_2}{b_1}\right)\right], \quad d_{22} = \text{Re}\left[\frac{1}{\mu_1 - \mu_2}\left(\frac{1}{b_2} - \frac{1}{b_1}\right)\right]$$

$$d_{3j} = \begin{cases} 0 & \text{plane stress} \\ -\dfrac{d_{1j}a_{13} + d_{2j}a_{23} + d_{6j}a_{36}}{a_{33}} & \text{plane strain} \end{cases} \qquad j = 1,2$$

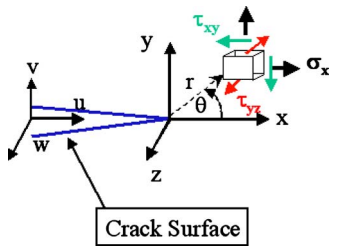

Fig. 20 Details of crack tip displacements and stresses at a distance r and θ from the crack tip in the crack coordinate system

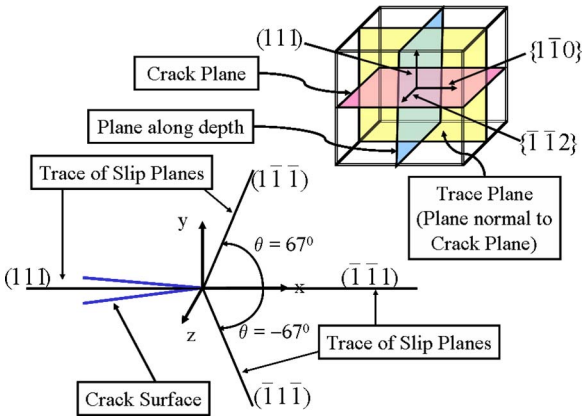

Fig. 22 Trace of primary slip planes on the plane normal to the crack plane

Table 2 The geometry and loading condition of the three BD specimens tested [43].

Specimen	orientation	Test temperature (°C)	Test frequency (Hz)	Load ratio R
A	(111) ⟨110⟩	23	40	0.1
B	(111) ⟨110⟩	23	10	0.1
C	(111) ⟨110⟩	23	10	0.1

Specimen	Diameter W (mm)	Thickness t (mm)	Initial crack length a (mm)	Crack angle with load θ (deg)
A	28.00	2.12	4.16	27.27
B	27.97	2.23	4.16	16
C	28.03	2.20	2.27	16

$$d_{33} = \begin{cases} 0 & \text{plane stress} \\ -\dfrac{d_{43}a_{34} + d_{53}a_{35}}{a_{33}} & \text{plane strain} \end{cases}$$

$$d_{43} = \mathrm{Re}\left[\frac{1}{b_3}\right], \quad d_{61} = \mathrm{Re}\left[\frac{\mu_1\mu_2}{\mu_1 - \mu_2}\left(\frac{1}{b_1} - \frac{1}{b_2}\right)\right]$$

$$d_{53} = -\mathrm{Re}\left[\frac{\mu_3}{b_3}\right], \quad d_{62} = \mathrm{Re}\left[\frac{1}{\mu_1 - \mu_2}\left(\frac{\mu_1}{b1} - \frac{\mu_2}{b2}\right)\right]$$

$$b_i = \sqrt{\cos(\theta) + \mu_i \sin(\theta)}, \quad i = 1,2,3$$

μ_1 and μ_2 are the two roots with positive imaginary parts as defined by the equation

$$a_{11}\mu^4 - 2a_{16}\mu^3 + (2a_{12} + a_{66})\mu^2 - 2a_{26}\mu + a_{22} = 0 \qquad (16)$$

and μ_3 is the root of the characteristic equation [42]

$$a_{55}\mu^2 - 2a_{45}\mu + a_{44} = 0 \qquad (17)$$

It should be noted that the compliance constants ($a_{i,3}(i = 1,2,\ldots,6)$) used for the expression ($d_{3,j}(j = 1,2,3)$) are the ones as given by Eq. (9).

The above equations, when used in conjunction with Eqs. (11) and (14), give K_{rss} on all the 12 slip systems for a fcc single crystal superalloy,

$$K_{rss} = [b_i^n][n_j]\begin{bmatrix} d_{11} & d_{12} & 0 \\ d_{21} & d_{22} & 0 \\ d_{31} & d_{32} & d_{33} \\ 0 & 0 & d_{43} \\ 0 & 0 & d_{53} \\ d_{61} & d_{62} & 0 \end{bmatrix} \cdot \begin{Bmatrix} K_I \\ K_{II} \\ K_{III} \end{Bmatrix} \qquad (18)$$

Three BD specimen of a PWA1422 single crystal material were tested (Table 2) to correlate the FCG data with the calculated ΔK_{rss}.

The mixed-mode SIFs were calculated for all the three specimens on the midplane of the BD specimens, based on plane strain assumption. K_{rss} was calculated using Eq. (14), where the state of stress obtained from Eq. (15) was multiplied by Schmid's factor for fcc single crystal (refer to Ranjan [6]) to get the RSS on all the 12 primary slip systems. The traces of the two slip planes $(\bar{1}1\bar{1})$ and $(1\bar{1}\bar{1})$ were found to make equal angles with the (111) plane (67.78 deg), while the trace of the plane $(\bar{1}\bar{1}1)$ was found to make 0 deg with the crack plane (111), as shown in Fig. 22.

The load ratio R (minimum load/maximum load) was 0.1 (Table 2), as the load on the BD specimen was always tensile. As SIFs are linearly proportional to the load applied, K_{rss} was multiplied with R to get the ΔK_{rss}.

The maximum K_{rss} was found to be on the (111) slip plane for all the three specimens (first row of Tables 3–5), as observed in the experiment test results (Fig. 23). The calculated ΔK_{rss} was plotted against da/dN on a log-log scale to check the validity of the model (Fig. 24). After ΔK_{rss} reaches 10 MPa $\sqrt{\mathrm{m}}$, a linear plot can be seen, which might correspond to Region II (Paris region) where the crack growth rate is directly proportional to the applied ΔK on a log-log basis. However, not enough data are available to support the theory. However, below a ΔK_{rss} of 8 MPa $\sqrt{\mathrm{m}}$, an accelerated crack growth can be seen between 5 MPa $\sqrt{\mathrm{m}}$ and 7 MPa $\sqrt{\mathrm{m}}$, in the threshold region, region or Stage I. The lines drawn through those points yield ΔK_{th} on the ΔK_{rss} axis, which is called fatigue threshold SIF. The average ΔK_{th} of the three speci-

Table 3 K_{rss} for 12 primary slip systems with increasing crack length for specimen *A*

Slip plane	Slip direction	K_{rss} in MPa $\sqrt{m}$ for Specimen A with increasing crack length a in mm: 5.25	5.36	5.66	5.82	6.09	6.10	6.12
(111)	$[10\bar{1}]$	−6.45	−6.59	−6.59	−7.18	−7.58	−7.61	−7.64
(111)	$[0\bar{1}1]$	1.91	1.97	2.13	2.22	2.40	2.42	2.43
(111)	$[1\bar{1}0]$	−4.54	−4.63	−4.83	−4.96	−5.18	−5.19	−5.21
$(\bar{1}1\bar{1})$	$[10\bar{1}]$	−1.17	−1.18	−1.21	−1.23	−1.27	−1.27	−1.27
$(\bar{1}1\bar{1})$	[110]	1.00	0.99	0.95	0.92	0.85	0.85	0.85
$(\bar{1}1\bar{1})$	[011]	2.17	2.17	2.16	2.16	2.12	2.12	2.12
$(1\bar{1}\bar{1})$	[110]	0.83	0.87	0.98	1.05	1.18	1.18	1.19
$(1\bar{1}\bar{1})$	$[0\bar{1}1]$	3.07	3.09	3.10	3.12	3.11	3.11	3.11
$(1\bar{1}\bar{1})$	[101]	3.90	3.96	4.08	4.16	4.28	4.29	4.30
$(\bar{1}\bar{1}1)$	[011]	1.91	1.97	2.13	2.22	2.40	2.42	2.43
$(\bar{1}\bar{1}1)$	[101]	−2.99	−3.02	−3.08	−3.11	−3.15	−3.15	−3.16
$(\bar{1}\bar{1}1)$	$[1\bar{1}0]$	−4.91	−4.99	−5.20	−5.33	−5.55	−5.57	−5.59

Table 4 K_{rss} for 12 primary slip systems with increasing crack length for specimen *B*

Slip plane	Slip direction	K_{rss} in MPa $\sqrt{m}$ for Specimen *B* with increasing crack length *a* in mm						
		8.06	8.38	8.67	9.09	9.46	9.87	10.13
(111)	$[10\bar{1}]$	−6.11	−5.95	−6.20	−6.39	−6.56	−6.75	−6.91
(111)	$[0\bar{1}1]$	1.03	1.12	1.29	1.51	1.71	1.93	2.10
(111)	$[1\bar{1}0]$	−5.08	−4.83	−4.91	−4.88	−4.85	−4.81	−4.81
$(\bar{1}1\bar{1})$	$[10\bar{1}]$	−1.61	−1.48	−1.46	−1.39	−1.33	−1.25	−1.21
$(\bar{1}1\bar{1})$	[110]	2.59	2.29	2.14	1.84	1.56	1.23	1.02
$(\bar{1}1\bar{1})$	[011]	4.20	3.77	3.60	3.23	2.89	2.49	2.22
$(1\bar{1}\bar{1})$	[110]	−0.17	−0.02	0.13	0.36	0.56	0.79	0.96
$(1\bar{1}\bar{1})$	$[0\bar{1}1]$	5.42	4.90	4.73	4.31	3.92	3.47	3.17
$(1\bar{1}\bar{1})$	[101]	5.25	4.89	4.86	4.67	4.48	4.26	4.13
$(\bar{1}\bar{1}1)$	[011]	1.03	1.12	1.29	1.51	1.71	1.93	2.10
$(\bar{1}\bar{1}1)$	[101]	−4.66	−4.25	−4.15	−3.86	−3.60	−3.29	−3.10
$(\bar{1}\bar{1}1)$	$[1\bar{1}0]$	−5.68	−5.37	−5.44	−5.37	−5.30	−5.22	−5.19

mens has been taken (~4.3 MPa $\sqrt{m}$) at a given load ratio R(=0.1). Below this value ($\Delta K_{rss} < \Delta K_{th}$) either crack growth does not occur by cyclic loading, i.e., $da/dN=0$ and the specimen can have infinite life, or it grows at undetectable rates. The value of ΔK_{th} can be affected by alterations in the material microstructure, load ratio, environment, and crack size [44]. However, the cyclic SIF (ΔK_{rss}) is not the only load parameter to control the FCG rate because da/dN, at a given ΔK_{rss}, can increase with the increase in load ratio R as

$$K_{max} = \frac{\Delta K_{rss}}{(1-R)}$$

The advantage of ΔK_{rss} lies in the ability to predict the actual microscopic fatigue fracture mechanisms, and it also takes into consideration the orientation of the grain. The ΔK_{rss} is also a multiaxial fatigue stress parameter, incorporating resolved shear stress on primary slip systems.

Conclusions

The results obtained can be summarized as follows:

1. An analytical method was developed for the calculation of all three modes of SIFs as a function of crystallographic orientation for an orthotropic material, which can be applied to any anisotropic material if all the material constants are known.
2. Mode *I* (K_I) was always found to be greater for $[10\bar{1}]$ than for the $[\bar{1}2\bar{1}]$ orientation. For an orthotropic material, K_I was

Table 5 K_{rss} for 12 primary slip systems with increasing crack length for specimen *C*

Slip plane	Slip direction	K_{rss} in MPa $\sqrt{m}$ for Specimen *C* with increasing crack length *a* in mm						
		7.74	8.31	8.78	9.02	9.79	10.93	11.55
(111)	$[10\bar{1}]$	−12.42	−14.40	−16.41	−17.54	−21.82	−30.65	−37.37
(111)	$[0\bar{1}1]$	1.82	2.62	3.50	4.02	6.10	10.75	14.46
(111)	$[1\bar{1}0]$	−10.60	−11.78	−12.91	−13.52	−15.72	−19.91	−22.91
$(\bar{1}1\bar{1})$	$[10\bar{1}]$	−3.45	−3.65	−3.82	−3.90	−4.14	−4.41	−4.48
$(\bar{1}1\bar{1})$	[110]	5.80	5.74	5.50	5.32	4.34	1.53	−0.86
$(\bar{1}1\bar{1})$	[011]	9.24	9.39	9.32	9.22	8.48	5.94	3.62
$(1\bar{1}\bar{1})$	[110]	−0.68	−0.16	−0.46	−0.83	−2.38	6.02	9.01
$(1\bar{1}\bar{1})$	$[0\bar{1}1]$	11.85	12.18	12.27	12.24	11.73	9.48	7.33
$(1\bar{1}\bar{1})$	[101]	11.17	12.02	12.72	13.07	14.11	15.50	16.33
$(\bar{1}\bar{1}1)$	[011]	1.82	2.62	3.50	4.02	6.10	10.75	14.46
$(\bar{1}\bar{1}1)$	[101]	−10.09	−10.52	−10.78	−10.88	−10.99	−10.37	−9.50
$(\bar{1}\bar{1}1)$	$[1\bar{1}0]$	−11.91	−13.14	−14.29	−14.90	−17.09	−21.12	−23.96

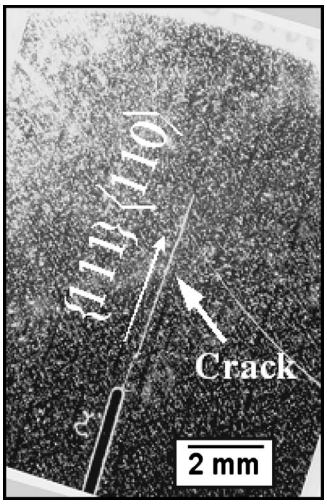

Fig. 23 Crack growth on the {111} slip plane can be observed for BD specimen *B* [43]

found to be nonzero at the crack closure due to the coupling of the nodal displacements, whereas for an isotropic material, it was zero.

3. The magnitude of K_{II} for $[\bar{1}2\bar{1}]$ was always found to be greater than that for the $[10\bar{1}]$ orientation, but the difference was not much.
4. Mode III SIF (K_{III}) existed because of the coupling of displacements at the crack tip due to anisotropy. K_{III} for $[10\bar{1}]$ was found to be much bigger than that for the $[\bar{1}2\bar{1}]$ orientation for the BD specimen. This plays an important role in the calculation of effective K to predict the life of an anisotropic material.
5. SIFs calculated for the $[\bar{1}2\bar{1}]$ crack orientation was found to be symmetric, which was due to the symmetry of $\langle 121\rangle$ about the midplane, as shown in Fig. 19, whereas due to the unsymmetrical nature of the $\langle 101\rangle$ orientation, the calculated SIFs varied along the thickness for the $[10\bar{1}]$ crack orientation. This variation can very well be used to predict the crack growth profile across the thickness.
6. The crack closure for the $[10\bar{1}]$ orientation was found to be 18 deg, whereas it was 30 deg for the $[\bar{1}2\bar{1}]$ orientation for the BD specimen, which shows the importance of knowledge of secondary orientation.
7. As shear decohesion is caused by dislocation motion, it was expected that the orientation of the crack plane must be related to the active slip plane(s). The fatigue damage parameter K_{rss} was calculated for all the 12 primary slip systems and for all the three BD specimens. The $K_{rss,max}$ was found on the {111} plane, which also happened to be the crack growth plane for all the three BD specimens. Therefore, for a single active slip plane, the maximum resolved shear stress provides the primary driving force for dislocation motion, the shear decohesion process leading to the crack growth process.
8. The parameter K_{rss} is well suited in identifying the active crack plane, as well as in predicting the microscopic crack growth direction. It is also an effective multiaxial crack driving force parameter.
9. The method developed is not related to any specific geometry. Therefore, it can be used for any kind of geometry and for any general anisotropic material to calculate mixed-mode SIFs at the crack tip. Therefore, crack growth rate and, hence, life of any material can be predicted.

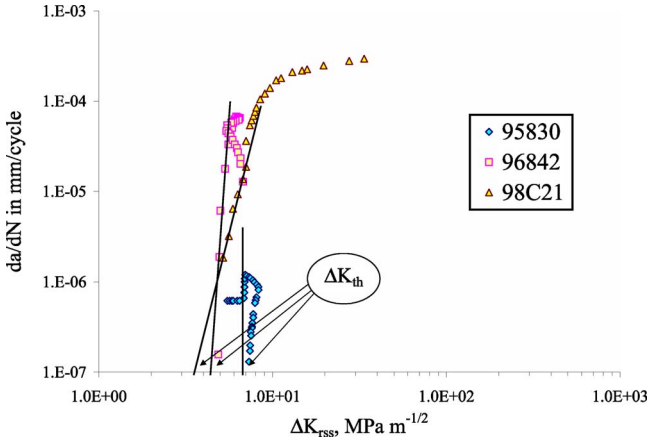

Fig. 24 FCG rate of three specimens *A*, *B*, and *C* as a function of ΔK_{rss}

However, additional experimental data are required to study FCG on the {111} family of planes for the $\langle 101\rangle$ family of crack directions. More experimental data are needed in Region II to get the accurate result to predict lifing. Also, experimental data for crack plane orientations other than slip planes, e.g., $\langle 100\rangle$, can be used to check the validity of the model.

Acknowledgment

This work was partially supported by the NASA Marshall Space Flight Center, Huntsville, AL. The authors would like to thank Dr. Gregory R. Swanson at NASA MSFC for his extended help and support. The authors would also like to thank Dan Deluca, a fellow at Pratt & Whitney, East Hartford, CT, for his precious advice and active participation in the discussion.

References

[1] Cowles, B. A., 1996, "High Cycle Fatigue Failure in Aircraft Gas Turbines: An Industry Perspective," Int. J. Fract., **80**, pp. 147–163.
[2] Moroso, J., 1999, "Effect of Secondary Crystal Orientation on Fatigue Crack Growth in Single Crystal Nickel Turbine Blade Superalloys," MS thesis, University of Florida, Gainesville, FL.
[3] Deluca, D. P., and Annis, C., 1995, "Fatigue in Single Crystal Nickel Superalloys," Office of Naval Research, Department of the Navy, Technical Report No. FR23800.
[4] Swanson, G. R., and Arakere, N. K., 2000, "Effect of Crystal Orientation on Analysis of Single-Crystal, Nickel-Based Turbine Blade Superalloys," NASA, Marshall Space Flight Center, Technical Publication No. NASA/TP-2000-210074.
[5] Telesman, J., Fisher, D. N., and Holka, D., 1986, "Variables Controlling Fatigue Crack Growth of Short Crack," *Proceedings of the International Conference on Fatigue Corrosion Cracking Fracture Mechanics and Failure Analysis*, pp. 53–69.
[6] Ranjan, S., 2005, "Development of a Numerical Procedure for Mixed Mode K-Solutions and Fatigue Crack Growth in FCC Single Crystal Superalloys," Ph.D. thesis, University of Florida.
[7] Telesman, J., and Ghosn, L., 1989, "The Unusual Near-Threshold FCG Behavior of a Single Crystal Superalloy and the Resolved Shear Stress as the Crack Driving Force," Eng. Fract. Mech., **34**(5/6), pp. 1183–1196.
[8] Siddiqui, S., 2003, "Finite Element Analysis of Slip Systems in Single Crystal Superalloy Notched Specimens," MS thesis, University of Florida.
[9] Naik, R. A., Deluca, D. P., and Shah, D. M., 2004, "Critical Plane Fatigue Modeling and Characterization of Single Crystal Nickel Superalloys," Trans. ASME: J. Eng. Gas Turbines Power, **126**, pp. 391–400.
[10] Rice, J. R., 1968, "A Path Independent Integral and the Approximate Analysis of Strain Concentration by Notches and Cracks," ASME J. Appl. Mech., **35**, pp. 379–386.
[11] Sosa, H. A., and Eischen, J. W., 1986, "Computation of Stress Intensity Factors for Plate Bending Via a Path-Independent Integral," Eng. Fract. Mech., **25**(4), pp. 451–462.
[12] Parks, D. M., 1974, "A Stiffness Derivative Finite Element Technique for the Determination of Crack Tip Stress Intensity Factors," Int. J. Fract., **10**(4), pp. 487–502.
[13] Ishikava, H., 1980, "A Finite Element Analysis of Stress Intensity Factors for

Combined Tensile and Shear Loading by Only a Virtual Crack Extension," Int. J. Fract., **16**, pp. 243–246.
[14] Raju, I. S., 1987, "Calculation of Strain-Energy Release Rates With Higher Order and Singular Finite Elements," Eng. Fract. Mech., **28**(3), pp. 251–274.
[15] Atkinson, C., Smelser, R. E., and Sanchez, J., 1982, "Combined Mode Fracture Via the Cracked Brazilian Disk Test," Int. J. Fract., **18**(4), pp. 279–291.
[16] Shih, C. F., DeLorenzi, H. G., and German, M. D., 1976, "Crack Extension Modeling With Singular Quadratic Isoparametric Elements," Int. J. Fract., **12**(3), pp. 647–650.
[17] Awaji, H., and Sato, S., 1978, "Combined Mode Fracture Toughness Measurement by the Disk Test," ASME J. Eng. Mater. Technol., **100**, pp. 175–182.
[18] Su, R. K. L., and Sun, H. Y., 2003, "Numerical Solutions of Two-Dimensional Anisotropic Crack Problems," Int. J. Solids Struct., **40**, p. 4615–4635.
[19] Hwu, C., and Liang, Y., 2000, "Evaluation of Stress Concentration Factors and Stress Intensity Factors From Remote Boundary Data," Int. J. Solids Struct., **37**, pp. 5957–5972.
[20] Heppler, G., and Hansen, J. S., 1981, "Mixed Mode Fracture Analysis of Rectilinear Anisotropic Plates by High Order Finite Elements," Int. J. Numer. Methods Eng., **17**, pp. 445–464.
[21] Denda, M., and Marante, M. E., 2004, "Mixed Mode BEM Analysis of Multiple Curvilinear Cracks in the General Anisotropic Solids by the Crack Tip Singular Element," Int. J. Solids Struct., **41**, pp. 1473–1489.
[22] Mews, H., and Kuhn, G., 1988, "An Effective Numerical Stress Intensity Factor Calculation With No Crack Discretization," Int. J. Fract., **38**, pp. 61–76.
[23] Huang, H., and Kardomateas, G. A., 2001, "Stress Intensity Factors for a Mixed Mode Center Crack in an Anisotropic Strip," Int. J. Fract., **108**, pp. 367–381.
[24] Sun, Y.-Z., Yang, S.-S., and Wang, Y.-B., 2003, "A New Formulation of Boundary Element Method for Cracked Anisotropic Bodies Under Anti-Plane Shear," Comput. Methods Appl. Mech. Eng., **192**, pp. 2633–2648.
[25] Tweed, J., Melrose, G., and Kerr, G., 2000, "Stress Intensification Due to an Edge Crack in an Anisotropic Elastic Solid," Int. J. Fract., **106**, pp. 47–56.
[26] Pan, E., and Yuan, F. G., 2000, "Boundary Element Analysis of Three-Dimensional Cracks in Anisotropic Solids," Int. J. Numer. Methods Eng., **48**, pp. 211–237.
[27] Denda, M., 2001, "Mixed Mode I, II and III Analysis of Multiple Cracks in Plane Anisotropic Solids by the BEM: A Dislocation and Point Force Approach," Eng. Anal. Boundary Elem., **25**, pp. 267–278.
[28] Sih, G. C., Paris, P. C., and Irwin, G. R., 1965, "On Cracks in Rectilinearly Anisotropic Bodies," Int. J. Fract. Mech., **1**, pp. 189–203.
[29] Ingraffea, A., and Manu, C., 1980, "Stress-Intensity Factor Computation in Three Dimensions With Quarter-Point Elements," Int. J. Numer. Methods Eng., **15**, pp. 1427–1445.
[30] Lekhnitskii, S. G., 1963, *Theory of Elasticity of an Anisotropic Elastic Body*, Holden-Day, San Francisco.
[31] Saouma, V. E., and Sikiotis, E. S., 1986, "Stress Intensity Factors in Anisotropic Bodies Using Singular Isoparametric Elements," Eng. Fract. Mech., **25**(1), pp. 115–121.
[32] Deluca, D. P., private communication.
[33] Gell, M., and Liverant, G. R., 1968, "The Characteristics of Stage I Fatigue Fracture in a High Strength Nickel Alloy," Acta Metall., **16**(4), pp. 553–561.
[34] Gell, M., and Liverant, G. R., 1968, "The Fatigue of the Nickel-Base Superalloy, MAR-M200, in Single Crystal and Columnar-Grained Forms at Room Temperature," Trans. Metall. Soc. AIME, **242**, pp. 1869–1879.
[35] Duquette, D. J., Gell, M., and Piteo, J. W., 1970, "A Fractographic Study of Stage I Fatigue Cracking in a Nickel-Base Superalloy Single Crystal," Metall. Trans., **1**, pp. 3107–3115.
[36] Chen, O. Y., 1985, "Crystallographic Fatigue Crack Propagation in Single Crystal Nickel-Base Superalloy," Ph.D. thesis, University of Connecticut.
[37] Chan, K. S., Hack, J. E., and Liverant, G. R., 1987, "Fatigue Crack Growth in MAR-M200 Single Crystals," Metall. Trans. A, **18A**, pp. 581–591.
[38] Nageswararao, M., and Gerold, V., 1976, "Fatigue Crack Propagation in Stage I in an Aluminum-Zinc-Magnesium Alloy: General Characteristics," Metall. Trans. A, **7A**, pp. 1847–1855.
[39] McEvily, A. J., and Boettner, R. G., 1963, "On Fatigue Crack Propagation in F.C.C. Metals," Acta Metall., **11**(7), pp. 725–743.
[40] Chen, Q., and Liu, H. W., 1988, "Resolved Shear Stress Intensity Coefficient and Fatigue Crack Growth in Large Crystals," NASA, Syracuse University, Contractor Report No. CR-182137.
[41] Peach, M., and Koehler, J. S., 1950, "The Forces Exerted on Dislocations and the Stress Fields Produced by Them," Phys. Rev., **80**(3), pp. 436–439.
[42] Tada, H., Paris, P. C., and Irwin, G. R., 1985, *The Stress Analysis of Cracks Handbook*, Paris Productions, St. Louis.
[43] John, R., Deluca, D. P., Nicholas, T., and Porter, J., 1999, "Near Threshold Crack Growth Behavior of a Single Crystal Ni-Base Superalloy Subjected to Mixed Mode Loading," *Mixed-Mode Crack Behavior*, American Society for Testing Materials, Philadelphia, pp. 312–328.
[44] Suresh, S., 1998, *Fatigue of Materials*, 2nd ed., Cambridge University Press, Cambridge, England.

Thermohydrodynamic Analysis of Compliant Flexure Pivot Tilting Pad Gas Bearings

Kyuho Sim

Daejong Kim
e-mail: djkim@tamu.edu

Mechanical Engineering,
Texas A&M University,
College Station, TX 77843-3123

A new thermohydrodynamic (THD) analysis for compliant flexure pivot tilting pad gas bearings is presented. Unlike many previous THD analyses on oil-lubricated bearings and gas bearings, the new THD analysis solves the rotor and bearing pad temperatures as well as the gas film temperature simultaneously upon adequate thermal boundary conditions on the bearing shell and rotor ends are given. All the previous studies assume that the rotor and bearing temperatures are given as thermal boundary conditions to solve 2D or 3D energy equation in the bearing film. The developed computational method is unique because these boundary conditions are found internally through global energy balance around the bearing. A numerical procedure involves solving the generalized Reynolds equation, 3D energy equation, and heat flux equations around the bearings simultaneously through iterative process. Furthermore, rotor thermal and centrifugal expansions are also considered during the iteration. Parametric studies were performed for the various temperature fields, i.e., rotor temperature, gas film temperature, and pad temperature as a function of nominal clearance, external load, and various thermal boundary conditions. Nominal clearance showed the most significant influence on overall THD behavior. The analyses also show that the rotor-bearing system can go to thermal runaway if adequate cooling mechanism does not exist. Linear perturbation analysis was also performed to investigate the thermal effects on the rotordynamic performance. Rotor thermal growth and increased viscosity increased direct stiffness and damping coefficients compared to the isothermal case. [DOI: 10.1115/1.2836616]

Keywords: tilting pad gas bearing, microturbomachinery, THD analyses, thermal stability

1 Introduction

Microturbomachinery with power ranges less than 200 kW (from definition of Gas Turbine Institute) and journal (bearing) diameter of 25–50 mm have broad applications in power generations [1], fuel cells [2,3], propulsions [4], and gas processes. Representative applications in fuel cell are air blowers and micro-gas-turbines (MGTs) as auxiliary systems. The MGT is harnessed to high temperature solid oxide fuel cells (SOFCs) and molten carbonate fuel cell (MCFC) to provide pressurized air to the fuel cell to decrease parasitic irreversible loss within the fuel cell stack, while producing additional electricity using exhaust gas from the fuel cell by driving the turbine. The combined thermal efficiency of SOFC-MGT hybrid fuel cell is claimed about 60% [2,3]. Those microturbomachineries for fuel cell applications require clean operation to avoid oil contamination on the process gas and to avoid degradation of the fuel cell performance.

Many applications in gas process areas have used oil-lubricated sleeve-type bearings, and recently, magnetic bearings began to replace the oil-lubricated bearings for oil-free operation [5]. The magnetic bearings require mechanical catcher bearings to avoid catastrophic disaster from breakdown of electrical system. Current mechanical catcher bearings are ball bearings in most applications and they pose significant technical problems (wear, reverse whirling, instability, etc).

In propulsion and stationary power generation areas, the bearing lubrication at hot section (turbine side) requires very complicated oil-lubrication circuits and oil-cooling devices for extended life of the ball bearings. The maximum operating temperatures of various synthetic oils are about 250°C [6,7], and the temperature limit is one of the factors that prevent design of high efficiency turbines.

Gas-lubricated bearings are the most promising to the microturbomachinery applications mentioned above because they are compact, near frictionless, and maintenance free, while having enough load capacity. In fuel cell areas, low friction and contamination-free gas (air) bearings allow high-speed operation with high efficiency. In gas process industry, replacing the ball catcher bearings by gas-lubricated bearings eliminates the wear, reverse whirl, and instability issues, while providing additional bearing action to the magnetic bearings to aid the control of the magnetic bearings. Replacing the radial ball bearings at hot section of the gas turbines with air-lubricated bearings can eliminate the complicated oil lubrications while enabling design of environment-friendly high efficiency turbines.

Due to the well-recognized benefits of the gas lubrications, significant research on gas-lubricated bearings has been performed in the past decades [8–26]. However, most research activities (except for a few experimental investigations [17,18,21]) on the gas bearings have assumed isothermal operation neglecting the heat generation within the gas film. Many different types of gas bearings were studied at these periods. Even if much research has been done on understanding the hydrodynamic behavior of the gas bearings, understanding thermal behavior is quite lacking. Externally pressurized hydrostatic air bearings, which are very popular in precision machine tools [27] and precision motion guides [28] for semiconductor processing and inspections, do not suffer any thermal issue in general. The thermal issues may arise when one attempts to adopt the gas bearings in hydrodynamic mode under very high speeds where load-bearing pressure is generated by pure hydrodynamic action between the moving (rotor) and stationary parts.

Manuscript received June 11, 2007; final manuscript received October 29, 2007; published online April 2, 2008. Review conducted by Jaroslaw Szwedowicz.

Fig. 1 Photo of CFTPB

When one adopts the hydrodynamic gas bearings to the microturbomachinery where journal surface speeds exceed 150 m/s, significant heat can be generated within the gas film. The associated thermal instability (or maybe called thermal runaway [18,21]) with the high-speed operation compromises the bearing performance and damages the system. Industry professionals working on the gas bearings for turbomachinery applications rely on trial-and-error-based approach to find appropriate bearing design and cooling strategy to avoid the thermal instability.

Among many gas-lubricated bearings, tilting pad gas bearing is very attractive due to its inherent rotordynamic stability. However, tolerance accumulation and wear issue associated with multiple assembly components in the pivot area is one of the technical barriers to the wide usage of the tilting pad gas bearings. One approach to avoid these issues is a flexure pivot arrangement [19,20,23] adopted from oil-lubricated tilting pad journal bearings introduced in Refs. [29–31]. However, the small bearing clearance in tilting pad gas bearings is still a technical challenge to overcome for their wide applications.

Due to the tight bearing clearance of the tilting pad gas bearings, small change of rotor diameter can cause large change of bearing performance. Possible sources of change of the rotor diameter within the operating envelope are the rotor centrifugal growth and thermal growth. Estimation of the rotor centrifugal growth may be relatively easy from elasticity theory. However, estimation of the thermal growth requires complete understanding of the heat generation source and heat paths.

Along with the rotor growth issue, the pads should be compliant along the radial direction to absorb the rotor growth effectively. One approach to avoid the accumulation of manufacturing tolerances and to provide the radial compliance is a flexure pivot tilting pad bearing with pad radial compliance (denoted as CFTPB in this paper) investigated in Ref. [23]. The researchers in Ref. [23] performed analytical parametric design studies on the CFTPBs using orbit simulations. An example of the CFTPBs is shown in Fig. 1, where each pad has a straight beam structure behind the pad to provide the compliance in the radial direction.

In this paper, a new thermohydrodynamic (THD) analysis for the CFTPB is presented. The simulation studies in this work are on a specific flexure pivot tilting pad gas bearing but can be easily extended to other tilting pad gas bearings with different pivot geometry once the heat transfer mechanism through the pivot is known. The developed computational method is applicable to any rotor-bearing subsystem with various global thermal boundary conditions at the bearing housing and rotor ends away from the bearing. The thermal model of the rotor-bearing subsystem is composed of the rotor (inside and outside the bearing), bearing (pad and bearing shell), and air film in the bearing clearance. A numerical procedure involves solving the generalized Reynolds equation, 3D energy equation, and heat flux equations around the bearings simultaneously.

The associated thermal boundary conditions for the air film (inlet flow temperatures at the pad leading edges, rotor surface temperature inside the bearing, and pad temperatures) are internally calculated through the iterative evaluations of heat balances at these boundaries. Furthermore, rotor thermal and centrifugal expansions are also considered during the iteration. Parametric studies were performed with different bearing nominal clearances and cooling conditions on the rotor. Based on the calculated temperature fields from the THD analyses, the perturbation analysis was also performed to calculate stiffness and damping coefficients of the bearing considering air film temperature and rotor growth (thermal and centrifugal).

1.1 Literature Review on Thermodynamic Analyses on Oil and Gas Lubricated Bearings. Numerous studies on THD analyses have been carried out for fluid film bearings. Cope [32] proposed a simplified energy equation neglecting temperature variations across the fluid film. Numerical studies in Refs. [33,34] presented simultaneous solutions for the Reynolds equation and the energy equation including temperature variations across the film, and showed that the inclusion of the temperature variation may have a significant influence on the pressure and temperature distributions in the film. Dowson et al. [35] introduced the generalized Reynolds equation and the energy equation, taking into account the viscosity and density variations across the film.

Knight and Barrett [36] established a 2D THD model for oil-lubricated tilting pad bearings, where the bulk temperature was calculated only in the circumferential direction. Temperature profile across the film was approximated by a second order polynomial using the journal and pad surface temperatures as wall boundary conditions, and temperature gradients at the journal and pad surfaces were obtained from the second order polynomials. Heat conduction in the pads was assumed to be purely radial with a uniform temperature on the back side of each pad. Journal surface temperature was assumed to be constant along the circumference and was calculated by averaging the film temperature around the circumference. Inlet flow temperature at the leading edge of the pad was obtained by mass and heat balance of the exit flow from the preceding pad, supply oil, and inlet flow to the pad in the mixing chamber between the pads, while neglecting heat transfer through the solid walls. Results of sample calculations indicated that the two bottom pads were slightly warmer than the two top pads, and temperature distribution of the lubricant within the pad region was slightly increased at the trailing edge. Knight and Barrett [36] present a simple method to calculate the bulk temperature considering the rotor and pad temperatures as wall boundary conditions.

Taniguchi et al. [37] performed 3D THD analyses with the upwind finite difference scheme in both laminar and turbulent flow regimes for oil-lubricated tilting pad bearings. Film temperature of the exit and side flows at the pad edges was obtained by parabolic extrapolation of the near edge temperatures. Experimental studies were also conducted with a 482.6 mm test bearing. The numerical simulations showed a good agreement in film pressure, pad surface temperature, and film thickness with the experimental results. Kim et al. [38] introduced a thermoelastohydrodynamic (TEHD) model incorporating heat transfer in the lubricant and elastic deformation of pads into the calculation of dynamic force coefficients. A 2D energy equation was formulated with an assumption of negligible temperature variation in the axial direction. Thermal shaft expansion was taken into account in calculating the film thickness. As a result, the simulated temperature distribution of the shaft and the loaded pads had a good agreement with the

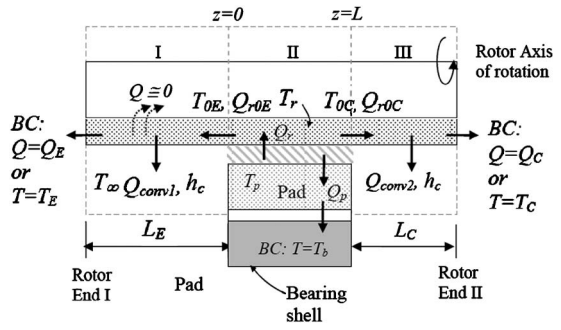

Fig. 2 Schematics of thermal subsystem of typical rotor-bearing configuration

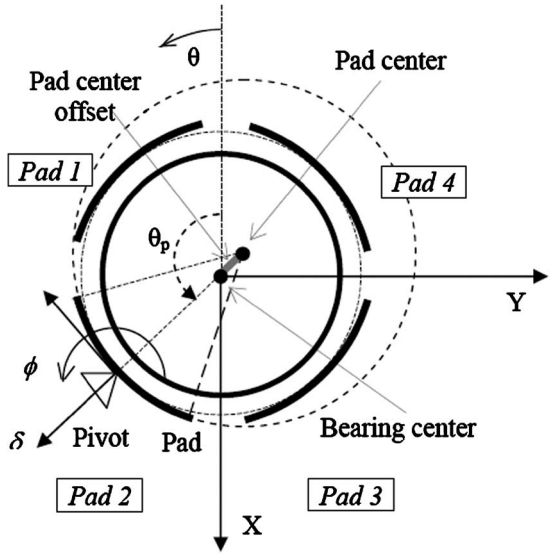

Fig. 3 Reference coordinates and variables describing the rotor and pad motions

experimental results given in Ref. [39]. The two papers above, Refs. [38,39], commonly made use of a 2D heat conduction model in the radial and circumferential directions for pad temperature solution, and employed the mass and heat balance in the mixing chamber for the calculation of inlet flow temperature to the next pad. Journal surface temperature was assumed to be constant along the circumference, and they assumed that net heat flux from the pads to the shaft is zero as adopted in Ref. [40].

Salehi et al. [17] conducted analytical and experimental investigations on the thermal characteristics of air-lubricated compliant foil bearing. In their analysis, a linear viscosity-temperature relation, which agrees well with measurements in the range of 0–550°C, was employed. They adopt Couette flow approximation [41] to simplify the energy equation to 1D problem, where heat flows induced by pressure gradients are negligible compared to those by the Couette flow. As a result, the simplified analyses uncouple the energy equation (temperature) from the Reynolds equation (pressure), leading to only a temperature variation along the circumferential direction. Even though the uncoupling of the temperature field in the film from pressure fields yields at least 20% overestimation of the film temperature, their work elucidates overall thermal characteristics of compliant air foil bearings.

The most advanced THD analysis so far on the air foil bearing was performed by Peng and Khonsari [22]. They developed a 3D THD model accounting for the compressibility and viscosity-temperature characteristic of air and the compliance of the bearing surface. In their analysis, the heat conduction across the air film was assumed to be dominant over heat conductions along the film plane as adopted in Ref. [17], and only the velocity gradients across the film were considered. The linear viscosity-temperature relationship adopted in Ref. [17] was used. However, their model assumed that the top foil could take subambient pressure at the trailing edge of the top foil and generate suction flow into the foil bearing, which cannot be realistic for actual foil bearings. Inlet flow temperature at the leading edge of the top foil was calculated by averaging temperatures of the suction and recirculation flows. Shaft temperature was estimated by the mean temperature of the side flow without calculating the rotor temperature directly. Heat transfer to the rotor was not considered, and only the radial heat conduction through the top foil (and convection by cooling air through the space between the top foil and bearing sleeve) was taken into account.

2 Theory

Figure 2 shows the thermal subsystem including the rotor, rotor ends, bearing pad, and bearing shell, and overall heat paths. Within the subsystem, the heat generated by viscous dissipation in the air film is transported to the bearing pads and rotor. The heat to the rotor is conducted through the rotor shell and convected to the ambient air through the exposed rotor surfaces. The heat flux to the bearing pad (modeled as lumped heat capacity) is transported to the bearing shell through the pivot web by heat conduction. At the interfaces of the subsystem (rotor ends and bearing shell), either temperature or heat flux boundary conditions can be given. Axial heat flux within the rotor shell and heat convection to the ambient is modeled using the 1D fin theory [42]. Multiple iteration loops are located within the program to satisfy the heat flux continuities at multiple interfaces. Note that the arrows shown are for sign convention purpose and the model can be further extended to other circumstances such as opposite direction of heat flow at the rotor ends. Detailed approach on the solution procedures will follow.

Reference coordinates and variables describing the rotor and pad motions are presented in Fig. 3. Each pad has finite tilting and radial stiffnesses. For the arbitrary pad and rotor positions, local film thickness is described by

$$h(\theta) = C - (r_{gc} + r_{gt}) + e_X \cos\theta + e_Y \sin\theta - R\phi \sin(\theta - \theta_p) - C(r_p - \delta)\cos(\theta - \theta_p) \quad (1)$$

where e_X and e_Y are respective eccentricities of the journal center along the X and Y directions, ϕ is the pad tilting angle, δ is the pad radial displacement, r_{gc} is the rotor centrifugal growth, r_{gt} is the rotor thermal growth averaged along the rotor axis, and r_p is the preload (pad center offset divided by nominal clearance C). The nominal clearance is defined as the clearance at $\pm 90°$ from the pivot, and physically, it is the set bore clearance (clearance at pivot) plus the pad center offset. θ_p is the angle of the pivot and defines the pivot offset, which is the ratio of the angle of the pivot from the pad leading edge to the total pad angle.

The rotor centrifugal growth for the hollow rotor is estimated from cylindrical plane stress model [43]. The equation shows good agreement with finite element analysis results [23] and is given by

$$r_{gc} = \frac{\rho_r R \Omega^2}{4E}[R^2(1-\nu) + R_i^2(3+\nu)] \quad (2)$$

where ρ_r, E, and ν are density, Young's modulus, and Poisson's ratio of the rotor material, respectively, and R and R_i are the outer and inner radii of the rotor. Thermal rotor growths are estimated by the following equation:

$$r_{gt} = \alpha R(T_{r\_av} - T_\infty) \quad (3)$$

where α is the linear thermal expansion coefficient of the rotor ($12 \times 10^{-6} \circ \mathrm{C}^{-1}$ for stainless steel) and T_{r_av} and T_∞ are the rotor temperature averaged along the rotor axis and the ambient tem-

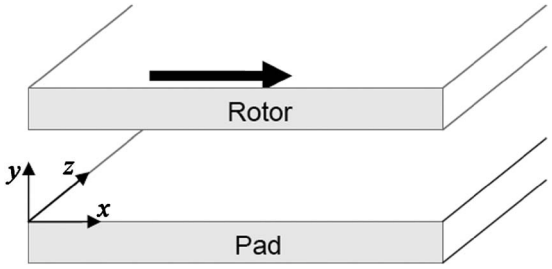

Fig. 4 Coordinate systems for the energy equation and the generalized Reynolds equation in the air film

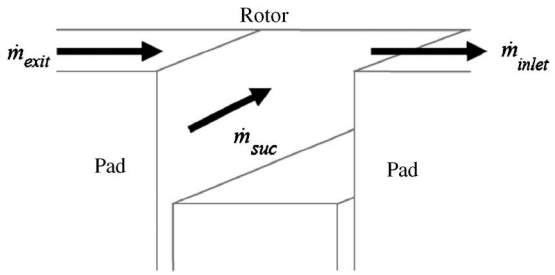

Fig. 5 Mass flow around the mixing chamber between pads

perature, respectively. The total rotor growth is a summation of the centrifugal and thermal growths. However, thermal distortion of the pad was not considered in this paper.

2.1 Thermodynamics Model for Air Film

2.1.1 Governing Equations. The generalized Reynolds equation and the energy equation are employed to calculate temperature fields in the air film. For most operating conditions, air flow in the film is laminar due to very small Reynolds number much less than 1000. Temperature evaluation in the air film at steady state operations requires simultaneous calculation of the generalized Reynolds equation and the energy equation given by

$$\frac{\partial}{\partial x}\left(\frac{\rho h^3}{\mu}\frac{\partial p}{\partial x}\right)+\frac{\partial}{\partial z}\left(\frac{\rho h^3}{\mu}\frac{\partial p}{\partial z}\right)=6U\frac{\partial}{\partial x}(\rho h) \tag{4}$$

$$\rho c_p\left(u\frac{dT}{dx}+w\frac{dT}{dz}\right)=k\left(\frac{\partial^2 T}{\partial x^2}+\frac{\partial^2 T}{\partial y^2}+\frac{\partial^2 T}{\partial z^2}\right)+\left(u\frac{dP}{dx}+w\frac{dP}{dz}\right)+\Phi \tag{5}$$

with

$$\Phi=\mu\left[\left(\frac{\partial u}{\partial y}\right)^2+\left(\frac{\partial w}{\partial y}\right)^2\right] \tag{6}$$

where c_p is the air specific heat capacity under constant pressure, $\mathbf{V}$ is the air velocity vector, k is the air heat conductivity, and Φ is the heat dissipation function. In Eq. (6), all the velocity gradients except for $\partial u/\partial y$ and $\partial w/\partial y$ were neglected. The coordinate system for the governing equations in the air film is given in Fig. 4, where x, y, and z denote the circumferential, cross-film, and axial directions, respectively. The two equations are coupled by temperature and pressure dependences of the air viscosity and density. The ideal gas equation and the linear viscosity-temperature relation [17] lead the governing equations to be coupled only by temperature and pressure fields.

The Reynolds equation is solved to find the pressure field with a given temperature field, and then with the calculated pressure, the energy equation is solved to calculate the temperature field. The iteration continues until convergence of the temperature fields is achieved. Mismatch of the 2D pressure field from the Reynolds equation with the 3D temperature field is resolved by the assumption of constant pressure across the film from the order of magnitude analysis of the momentum equation. Discretization of the energy equation follows the power-law scheme [44] to ensure all the coefficients to be positive for convective terms with large Peclet numbers. The number of grid points within one pad was increased gradually until both pressure and temperature do not change within 0.3%. Final grid scheme for the THD studies was $30\times20\times8$ for x, z, and y directions, respectively.

2.1.2 Boundary Conditions. Appropriate thermal boundary conditions at the pad edges, as well as on the rotor and pad surfaces, should be determined for the solution to the governing equations. In the air film on a pad, there are one incoming flow from the leading edge, two side flows from the side edges, and one exit flow through the trailing edge. The thermal boundary condition for the inlet flow is determined in a different way from those for the outgoing (side and exit) flows. The thermal boundary conditions on the rotor and bearing pad will be discussed later.

Inlet flow temperature has large influence on the air film temperature [45]. Mixing between the exit flow from the previous pad and the ambient air sucked into the chamber between pads (Fig. 5) is assumed to occur intensively accompanying severe turbulence because the dimension of the chamber is much higher than the film thickness and the exit flow is very fast. The inlet flow temperature (T_{inlet}) is defined as a weighted value of the suction flow temperature (T_{suc}) and the exit flow temperature (T_2) from the previous pad, i.e., $T_{\text{inlet}}=T_{\text{suc}}C_1+T_{\text{exit}}C_2$ [46]. The coefficients of C_1 and C_2 can be determined by experiments considering heat transfer through the wall [45]. However, a reasonable inlet flow temperature can be found without resorting to empiricism by utilizing the mass and energy balance in the chamber among the exit flow from the previous pad ($\dot{m}_{\text{exit}}$), the suction flow ($\dot{m}_{\text{suc}}$), and the inlet flow ($\dot{m}_{\text{inlet}}$), assuming full mixing of the exit flow with the suction flow and negligible heat transfer to the surrounding solid walls. This method is very simple and widely used in Refs. [22,37,38], and thus adopted in this THD analysis.

In a chamber between pads, the suction flow $\dot{m}_{\text{suc}}$ is determined by the mass balance

$$\dot{m}_{\text{exit}}+\dot{m}_{\text{suc}}=\dot{m}_{\text{inlet}} \tag{7}$$

Applying energy balance to the air flows in the chamber and assuming constant heat capacity of the air flows within temperature ranges of interest, the inlet flow temperature is determined by

$$\dot{m}_{\text{exit}}T_{\text{exit}}+\dot{m}_{\text{suc}}T_{\text{suc}}=\dot{m}_{\text{inlet}}T_{\text{inlet}} \tag{8}$$

where T_{exit}, T_{inlet}, and T_{suc} are the temperatures of $\dot{m}_{\text{exit}}$, $\dot{m}_{\text{inlet}}$, and $\dot{m}_{\text{suc}}$, respectively. The calculated inlet flow temperature becomes the boundary condition at the leading edge of the corresponding pad.

Thermal boundary conditions for the exit and side flows at the pad edges are simple compared to the inlet boundary condition. All the pads have a positive pressure field due to self-adjusting motion of tilting pads and have strong negative pressure gradients toward the trailing and side edges, which generate fast outgoing flows. From hydrodynamic analyses, the side flows as well as the exit flow have large Peclet numbers much higher than 10, which results from the high flow velocity and small air conductivity. In the power-law scheme [44], temperature boundary conditions at the flow exits are not defined when Peclet number is larger than 10, which makes corresponding nodal coefficients zero in finite difference methods.

2.2 Heat Transfer Model to Pads. Rotor and pad surface temperatures become wall boundary conditions for the THD model in the film. While rotor temperature is assumed uniform in the circumferential direction, each pad has a different temperature because of the rotor eccentricity.

CFTPBs have narrow pivot web and beam structures. If the heat conduction within the pad occurs only in the radial direction,

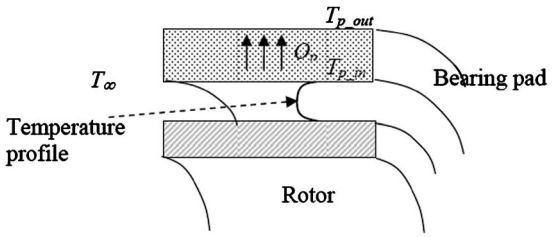

Fig. 6 Heat flux model for bearing pads

the heat conduction through the pad is equal to the outgoing heat flux from the back side surface of pad to the surrounding air (Fig. 6), i.e.,

$$Q_p = k_p \frac{T_{P\_\text{in}} - T_{P\_\text{out}}}{t_p} = h_n (T_{P\_\text{out}} - T_\infty) \tag{9}$$

where k_p is the heat conduction coefficient of pad, T_{P_in} and T_{P_out} are the pad temperatures on the surfaces to the air film and to the ambient, respectively, and t_p is the pad thickness. For stainless steel, $k_p = 50.2$ W/m K, and typical natural convection coefficients on flat surfaces (h_n) are approximately 5 W/m^2 K. The pad thickness is in the range of 3–5 mm in most cases. Rearranging the above equation leads to $T_{P\_\text{in}} = \text{Bi}(T_{P\_\text{out}} - T_\infty) + T_{P\_\text{out}}$, where Biot number $\text{Bi} = h_n t_p / k_p$. Substitution of the thermal properties and typical pad geometries yields $\text{Bi} \approx 10^{-4}$. Another heat transfer mechanism is the heat conduction through the pivot web. Numerical simulations were conducted with the 2D heat conduction model using commercial software. Figure 7 shows a temperature field at one pad with the pad inner surface and bearing shell outer surface at 30°C and 15°C, respectively, and other surfaces are assumed adiabatic. Overall, the pad temperature is approximately uniform with the given temperature of 30°C and bearing shell temperature is also almost uniform as the room temperature. Maximum temperature variation in both the pad and bearing shell is about 1.5°C. Large temperature variation is observed only at pivot. From the simulations, a linear relation of heat conduction through the pivot web can be found as

$$Q_p = C_w (T_p - T_b) \tag{10}$$

where T_p and T_b denote the pad and bearing shell temperatures, respectively. C_w is a proportionality constant, which may be evaluated for given flexure pivot or any tilting pad configuration through numerical simulation or experimental measurement. For given bearing geometry, C_w was estimated as 0.195 J/°C from numerical simulations using commercial finite element software. The bearing shell temperature T_b is a boundary condition (given as 15°C in the simulations) because the bearing shell temperature can be measured in most cases.

Remarkably, the ratio of heat convection to the back side of the pad (assuming natural convection to ambient air) to the heat conduction through the pivot web is in the order of $O(10^{-2})$. Consequently, the pad temperature is estimated using the lumped heat capacity model accounting for only heat conduction through the pivot by Eq. (10).

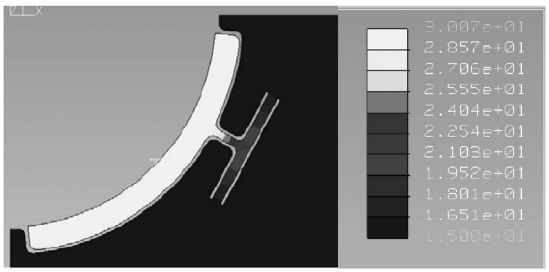

Fig. 7 Temperature field at pad and bearing shell; the numbers in scale bar are in °C

2.3 Heat Transfer Model to Rotor. In many microturbomachinery applications, hollow rotors are used to reduce the rotor mass and increase bending critical speed. Therefore, the model developed in this paper assumes that the rotor is a hollow shaft. The heat transferred to the rotor from the air film travels through the rotor shell by conduction, and then is convected from the rotor surface to the ambient air.

At any axial position, temperature of the rotor shell (T_r) is assumed to be constant in the radial direction due to high thermal rotor conductivity and small rotor shell thickness. It is further assumed that the rotor temperature is constant along the circumferential direction due to high thermal conductivity of the rotor and high speeds. Therefore, the heat conduction within the rotor shell is modeled as a 1D heat conduction problem along the axial direction.

The developed THD model can handle general boundary conditions of the thermal subsystem such as temperature or heat flux at the rotor ends. Conceptually, the total thermal subsystem is composed of three domains as presented in Fig. 2, and the subdomains are interconnected by the rotor. The interfaces of Domain I are the cross section of the rotor at the bearing edge ($z=0$) and the rotor end surface on the left. The rotor end surface can be defined as a heat source (Q_E) or fixed temperature (T_E). Domain II encloses the bearing and the rotor inside the bearing: The boundaries in the rotor have heat fluxes Q_{r0E} and Q_{r0C} to Domains I and III, respectively, and the bearing outer surface is defined with a given temperature ($T_b = T_\infty$ in this paper). Domain III includes the exposed rotor from the right bearing edge ($z=L$) to the other rotor end with heat flux Q_{r0C} at the boundary with Domain II and thermal boundary condition Q_C or T_C at the other rotor end. Domains I and III include the heat convection to the ambient air (Q_{conv1}, Q_{conv2}) within the domain, respectively. The three domains should meet the heat balances within the domain, and also total global heat balance should be satisfied.

2.3.1 Heat Convection on the Exposed Rotor Outer Surface. The heat convection from the exposed rotor surface to the ambient air is calculated using the heat convection theory for a rotating cylinder. Given a rotor geometry and a rotating speed, the heat convection coefficient on the exposed rotor surface is a function of rotor diameter (D) and rotation speed (Ω) defined as function of Reynolds number Re and Prandtl number Pr as [47]

$$h_c = 0.133\, \text{Re}^{2/3}\, \text{Pr}^{1/3} (k_a / D) \tag{11}$$

where $\text{Re} = \Omega D^2 / \nu_a$ and $\text{Nu} = 0.133 \text{Re}^{2/3} \text{Pr}^{1/3}$ for $\text{Re} < 4.3 \times 10^5$ and $0.7 < \text{Pr} < 670$. At 300 K of air, kinetic viscosity $\nu_a = 15.66 \times 10^{-6}$ m^2/s, and heat conductivity of air $k_a = 0.0267$ W/(m K). In the simulations, Prandtl number was assumed constant as 0.713.

2.3.2 Heat Convection on the Rotor Inner Surface. Heat convection from the rotor shell to the rotor inner surface follows the same heat convection coefficient as Eq. (11). However, in many applications, both ends of the hollow rotor are sealed by impellers or other components. Due to the very small thermal capacity of the air, heat transfer to the air inside the hollow rotor is much less than heat conduction within the rotor shell. Therefore, in this THD model, the heat convection from the rotor inner surface was neglected.

2.3.3 Axial Heat Flux Within the Rotor at the Bearing Edge. Heat flux at the bearing edge serves as a boundary condition to find the temperature profile of the rotor inside the bearing. The heat fluxes at the left and right bearing edges are

$$Q_{r0E} = Q_{\text{conv1}} + Q_E \tag{12a}$$

$$Q_{r0C} = Q_{\text{conv2}} + Q_C \tag{12b}$$

where Q_{conv1} and Q_{conv2} are the axial heat fluxes in the rotor at the left and right bearing edges, respectively, caused by the heat convections on the corresponding rotor outer surfaces when $Q_E = Q_C = 0$. The heat convections Q_{conv1} and Q_{conv2} are calculated by the fin theory [20] using the heat convection coefficient, Eq. (11). Evaluation of Q_{conv1} and Q_{conv2} assumes adiabatic conditions at the rotor end surfaces. From the fin theory, the heat convections on the rotor outer surface can be given by

$$Q_{\text{conv1}} = k_r A[m(T_{0E} - T_\infty)\tanh mL_E] \tag{13a}$$

$$Q_{\text{conv2}} = k_r A[m(T_{0C} - T_\infty)\tanh mL_C] \tag{13b}$$

where $m^2 = h_c P / k_r A$, R and R_i are outer and inner radii of the rotor, respectively, $P = 2\pi R$ is a circumferential length of the rotor, $A = \pi(R^2 - R_i^2)$ is the cross-sectional area of the rotor, h_c is the heat convection coefficient on the exposed rotor surface given by Eq. (11), and k_r is the heat conduction coefficient of the rotor.

When temperature boundary conditions are given at the rotor end surfaces instead of heat flux, equivalent conductive heat fluxes through the rotor shell [48] are evaluated as

$$Q_{E\_C} = k_r \frac{2\pi L_E}{\ln(R/R_i)}(T_{0E} - T_E) \tag{14a}$$

$$Q_{C\_C} = k_r \frac{2\pi L_C}{\ln(R/R_i)}(T_{0C} - T_C) \tag{14b}$$

which replace Q_E and Q_C, respectively, in Eqs. (12*a*) and (12*b*).

2.4 Numerical Solution Procedure. The flowchart for numerical solution procedures is given in Fig. 8. At a given rotor speed and external load (rotor weight), an initial equilibrium position of the rotor center and pads, and isothermal air film pressure field are obtained using orbit simulation method [23] by solving the isothermal Reynolds equation. Starting from the initial equilibrium pressure and film thickness, the pressure-temperature iterations are performed. In the air film, the generalized Reynolds equation, Eq. (4), and the energy equation, Eq. (5), are solved simultaneously implementing the ideal gas equation and the viscosity-temperature relation. While pressure and temperature of the air film are iterated, the rotor temperature is determined by solving a 1D heat conduction problem in the axial direction and the pad temperature is solved using lumped heat capacity model. At the same time, inlet flow temperature to each pad is found from the mass and energy balance in the chamber between the pads. The calculated rotor, pad, and inlet flow temperatures act as boundary conditions for the calculation of air film temperature. Iterations between the film temperature and the boundary conditions are required. Once all the temperature fields are calculated for the initial equilibrium point, a new equilibrium position is searched accounting for thermal rotor growth, which is determined from the calculated rotor temperature. The iterations for the pressure temperature and equilibrium position continue until global convergence of all the temperatures, pressure, and static equilibrium point is reached. The rotor centrifugal growth is taken into account in all the iteration loops.

3 Results and Discussion

The developed THD analysis method was applied to the designed rotor-bearing system consisted of a rotor, two CFTPBs, and drive turbines at both ends. Assuming that the rotor-bearing configuration is symmetric, thermal boundary condition at the right end of the rotor renders $Q_C = 0$. Furthermore, the left end of the rotor is modeled as a heat sink (such as air turbine). Initial study assumes $Q_E = 5Q_{\text{conv1}}$ i.e., the heat loss at the left rotor end is five times the heat convection loss on the left hand side of the exposed rotor surface. Table 1 provides the parameters used in the simulations. Both rotor centrifugal and thermal growths were considered in all the simulations.

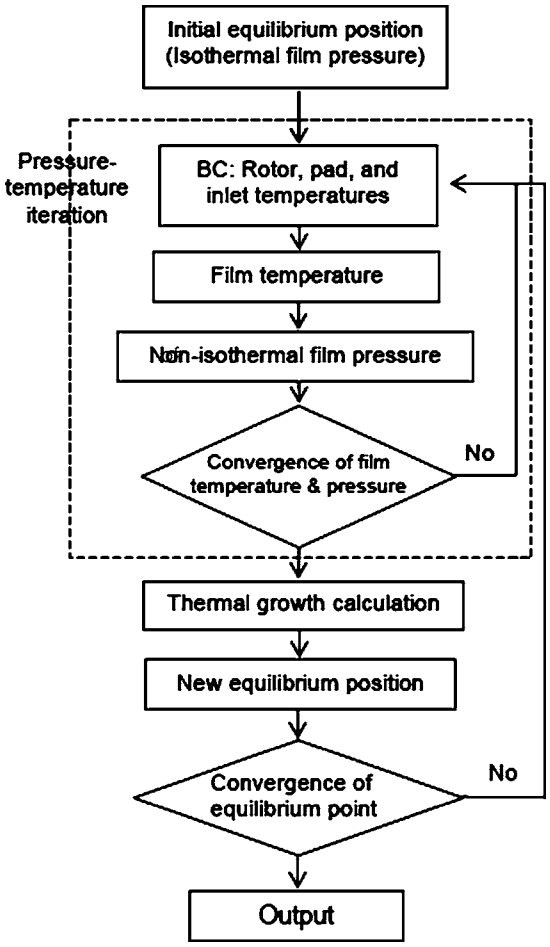

Fig. 8 Flowchart for the THD analysis

The load corresponds to the rotor weight from the virtual design, which is under construction for the experimental verification of the model. The THD numerical simulations can provide more accurate understandings of thermal behaviors of gas bearing systems and allow identifying important design parameters for thermal stability.

Table 1 Parameters for THD analysis

CFTPB parameters	Value
Number of pads	4
Pad mass	16 g
Pad mass moment of inertia	1.0×10^3 g mm^2
Pad start angle	5 deg
Pad arclength	80 deg
Pad thickness (t_p)	0.003 m
Pivot offset	0.7
Preload (r_p)	0.5
Pad tilting stiffness (k_ϕ)	20 N m/rad
Pad radial stiffness (k_δ)	1×10^7 N/m
Bearing length (L)	0.033 m
Nominal clearance (C)	35 μm
Load to bearing	4.06 N
Rotor outer diameter ($2R$)	0.0286 m
Rotor inner diameter ($2R_i$)	0.0226 m
Exposed rotor lengths (L_E,L_C)	0.017, 0.010 m

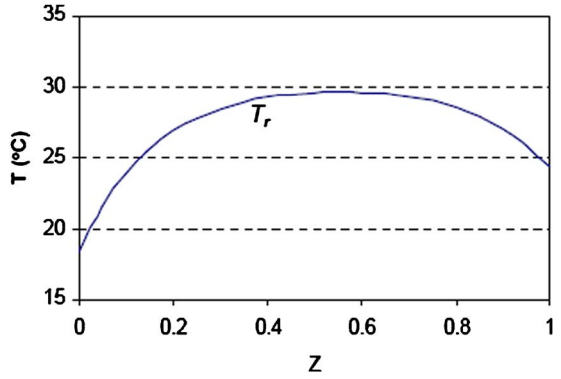

Fig. 9 Rotor temperature along the rotor axis, 60 krpm, C =35 μm

Figure 9 shows the rotor temperature along the nondimensional rotor axis ($Z=z/L$) within the bearing at 60 krpm. As described in Sec. 2.3, heat transfer within the rotor is modeled as 1D heat conduction along the rotor axis with constant temperature in the circumferential direction. Outgoing heat fluxes at the bearing edges through the rotor shell cause rotor temperature profile inside bearing to appear paraboliclike. Rotor temperature at the left bearing edge (where Q_E is imposed) is smaller than that at the right bearing edge (adiabatic, $Q_C=0$).

Figure 10 shows the pad temperatures and inlet flow temperatures to the corresponding pads. The lower pads (Pads 2 and 3) have slightly higher temperatures than the upper pads (Pads 1 and 4) due to rotor eccentricity toward the lower pads. However, the nondimensional eccentricity under the applied load is very small (about 0.02) and the temperature difference between the upper and lower pads is relatively small, less than 0.2°C. Inlet flow temperatures to each pad have also small differences less than 0.5°C. The variations of the pad temperature are also very small (<0.5°C). The inlet flow temperature to Pad 1 is slightly higher than those to other pads due to higher exit temperature from Pad 4, where the temperature drop at the exit is small due to smaller pressure gradient (Pad 4 has smaller negative pressure gradient at the exit than Pads 2 and 3). Therefore, exit temperatures from Pads 2 and 3 are slightly lower than that from Pad 4, which causes relatively lower inlet flow temperatures to Pads 3 and 4.

Figure 11 presents air film temperature field in the xy plane (see Fig. 4) at the bearing axial center of Pad 3 at 60 krpm. The film temperature in the middle is higher, which indicates cross-film heat transfer to the rotor and pad. Overall, temperature gradient in the cross-film direction near the pad surface is higher because the pad temperature (27.7°C, Fig. 10) is lower than the rotor temperature (30°C, Fig. 9) at the axial center. The lower temperature of the pad than the rotor indicates more heat transfer to the pad than

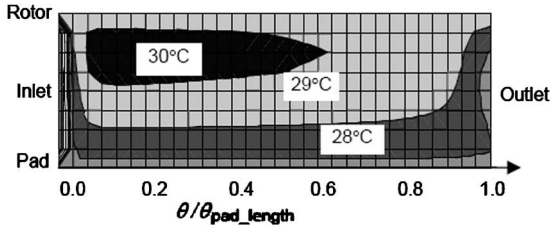

Fig. 11 2D cross-film temperature field in the xy plane at the axial center of Pad 3, 60 krpm, C=35 μm

the rotor. The prompt temperature rise of the inlet flow from around 22°C to around 28°C is observed at the inlet area due to heat conductions from both the rotor and pad. Note that the rotor and pads are thermal reservoirs once they are heated by continuous heat transport from the gas film. However, the inlet flow temperatures are lower than those of the rotor and pads because of the mixing with suction air at the chamber between the pads.

Figure 12(a) presents the bulk film temperature (averaged over the film thickness) at Pad 3, where $\theta_{\text{pad\_length}}$ is the pad arclength along the circumferential direction. The axial film temperature profile follows the parabolic pattern similar to that of the rotor shown in Fig. 9. Figure 12(b) presents bulk film temperature in the circumferential direction at the axial center of each pad. The insert shows slightly higher air film temperatures in the lower pads (Pads 2 and 3). As shown in Fig. 11, the inlet flow gains the temperature right after entering the bearing land area due to the heat conductions from the pad and rotor. Figure 13 presents nondimensional film pressure in the circumferential direction at the axial center of each pad. Pressure increases until 80% of the pad arclength causing large amount of side flows. The slight drop of the film temperature toward the pivot and large temperature drop near the exit in Fig. 12 are related to the pressure profile. The slight drop of the temperature toward the pivot is due to the large side leakage flow and the large drop near the exit is due to the pressure-related work with strong negative pressure gradients, the third term in Eq. (5).

Figure 14 presents averaged rotor, pad, and bulk film temperatures over rotor speeds of 10–80 krpm. The averaged bulk film temperature is higher than the averaged pad and rotor temperatures by small differences less than 1.5°C. However, all the temperatures are approximately parabolic function with rotor speeds, and reach up to about 45°C at 80 krpm (temperature rise of about 30°C). Rotor thermal growth due to the parabolic temperature rise is expected to affect overall bearing performance significantly at high speeds.

3.1 Effect of Different Nominal Clearances and External Loads. THD analyses were performed with various nominal clearances from 30 μm to 40 μm at a rotor speed of 60 krpm. Figure

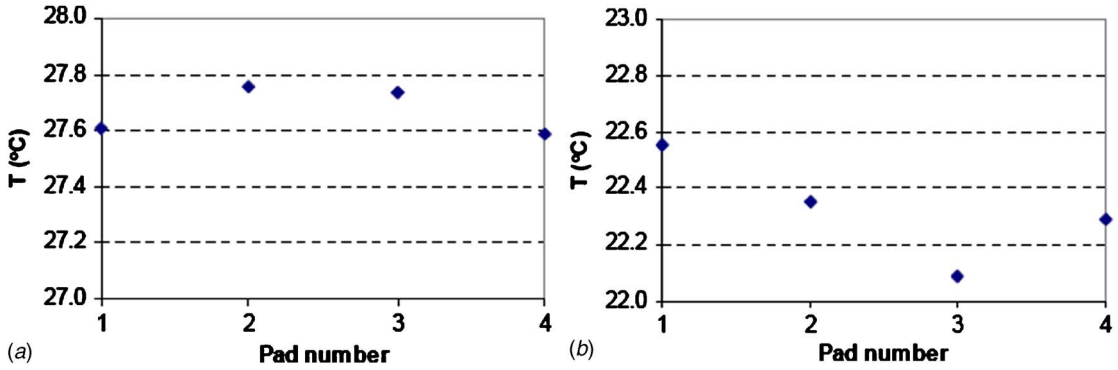

Fig. 10 Pad temperatures and inlet flow temperatures to pads, 60 krpm, C=35 μm

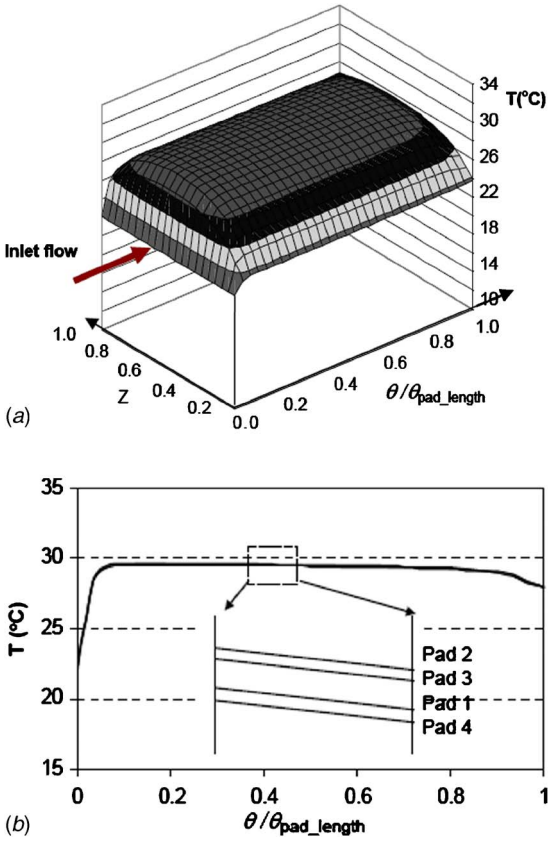

Fig. 12 Bulk film temperatures, 60 krpm, C=35 μm

15 presents three rotor temperature profiles plotted along the rotor axis for nominal clearances of 30 μm, 35 μm, and 40 μm. A similar tendency of temperature rise with decreasing nominal clearance is also observed in the pad and bulk film temperatures, as shown in Figs. 16 and 17. On the other hand, increase of the inlet flow temperature is less than those of the rotor and pad temperatures due to mixing with the ambient air. All the temperature plots for the rotor, pad, inlet flow, and bulk film show nonlinear behaviors with respect to the nominal clearance. For example, the temperature rise due to clearance change from 35 μm to 30 μm is higher than that due to the clearance change from 40 μm to 35 μm (Fig. 18).

Effects of external loads on the THD behavior were investigated by increasing the external loads to 16.23 N (3×rotor weight) and 28.4 N (5×rotor weight) at 60 krpm, causing nondimensional rotor eccentricities ($\varepsilon_{X,Y}=e_{X,Y}/C$) to increase to 0.11

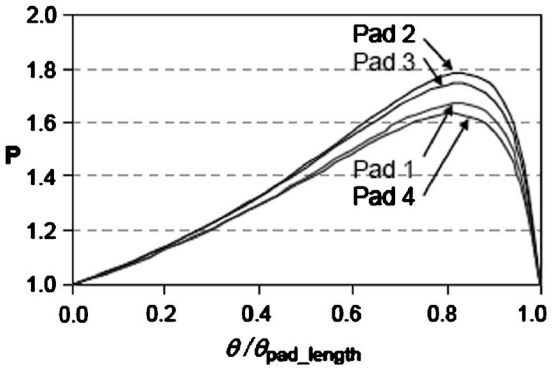

Fig. 13 Nondimensional film pressures in the circumferential direction at the axial center of each pad, 60 krpm, C=35 μm

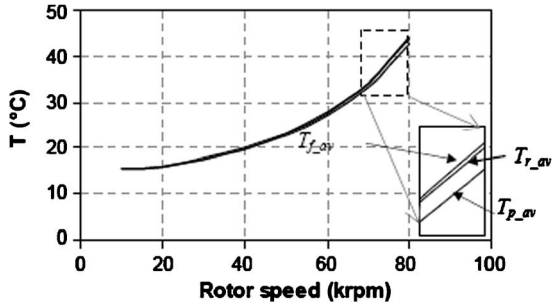

Fig. 14 Averaged temperatures of rotor, pad, and bulk film versus rotor speed

and 0.19, respectively (Fig. 19). Figures 20–22 present the temperatures of the rotor, pads, and inlet flow to the pads, respectively. In Fig. 20, the rotor temperature is not very sensitive to the increased external load, and only loaded pads experience the temperature rise as in Fig. 21. As load increases, the inlet flow temperature to Pad 1 is the highest due to the highest exit temperature from Pad 4. Note that the exit temperature difference from Pad 4 is within 1°C for different loads but inlet temperature difference to Pad 1 is about 2°C due to different mixing behaviors and exit flows with loads (pad tilting angles and pressure gradients). The larger external load renders larger rotor eccentricity, resulting in higher pad tilting angles and increased side leakage in the loaded pads (Pads 2 and 3). For example, the increased side flow in Pad 2 allows larger suction flow at the next mixing chamber, lowering the inlet flow temperature to Pad 3. However, as shown in Fig. 23, the loaded pads have higher overall bulk film temperature. Bulk film temperatures also show uneven temperature rises with loads

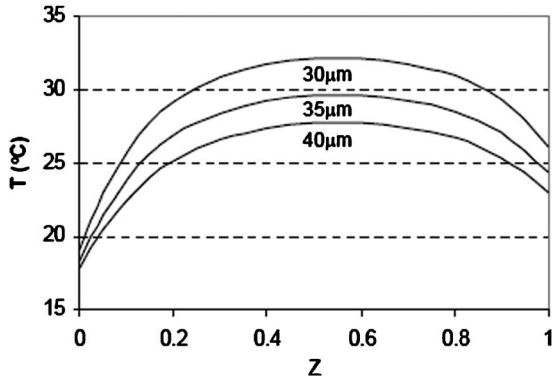

Fig. 15 Rotor temperatures along the rotor axis with different clearances, C=30–40 μm, 60 krpm

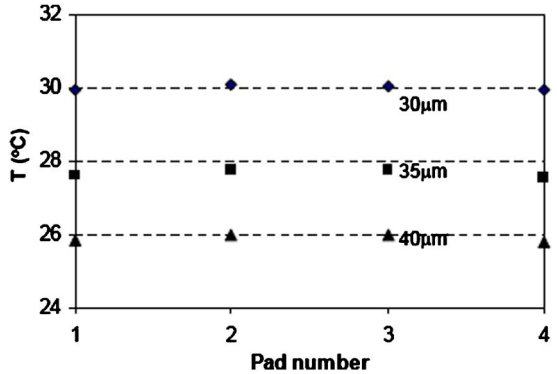

Fig. 16 Pad temperatures with different clearances, C =30–40 μm, 60 krpm

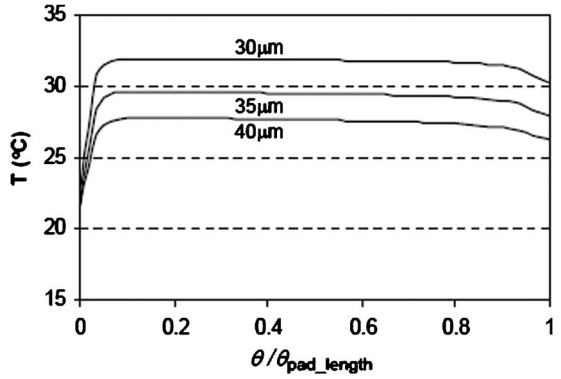

Fig. 17 Bulk film temperatures along the circumferential direction at the axial center of Pad 3, C=30–40 μm, 60 krpm

among pads (Fig. 24); the loaded pads experience higher film temperature rise than the unloaded pads. In conclusion, the external load has less effect (within the investigated range of external loads) on the temperature rise than the nominal clearance.

3.2 Effect of Thermal Boundary Conditions at the Rotor End. Thermal analyses were performed for different boundary conditions at the rotor end. Case 1 is the same as the base line simulations presented earlier (Q_E=5Q_{conv1}). Case 2 simulates the

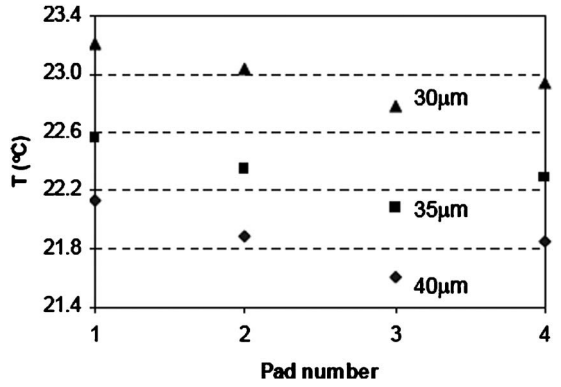

Fig. 18 Inlet flow temperatures to pads with different clearances, C=30–40 μm, 60 krpm

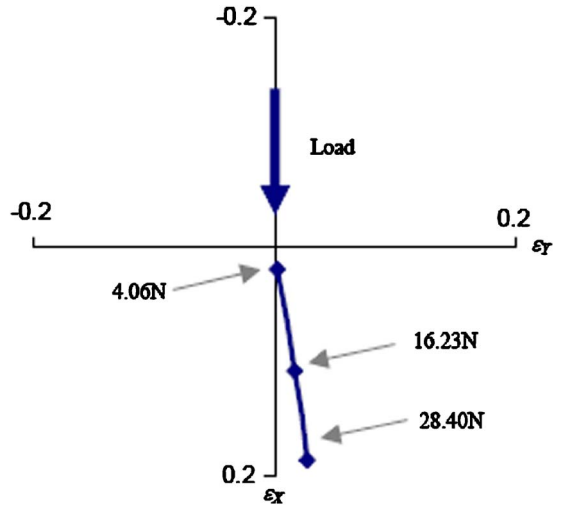

Fig. 19 Equilibrium positions of rotor for different external loads, 60 krpm, C=35 μm

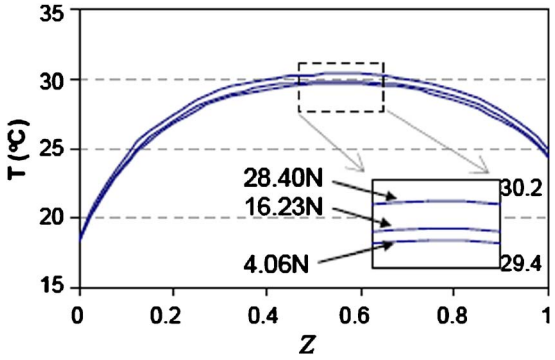

Fig. 20 Rotor temperatures along the rotor axis for different external loads, 60 krpm, C=35 μm

case when heat loss is only due to heat convection on the rotor surface and the rotor end is adiabatic (Q_E=0). Case 3 is a limiting case of Case 1; the rotor end temperature is specified as the ambient temperature, T_E=15°C.

Figure 25 presents centrifugal and thermal growths for Case 1, coplotted with total rotor growth. In general, rotor growth is equivalent to reduction of average clearance, which leads to increase of system natural frequency. Figure 26 presents rotor temperature for different cases over rotor speed ranges of 10–80 krpm. Thermal boundary condition of Q_E=5Q_{conv1} yields very similar but slightly higher rotor temperature compared to Case 3, where the rotor end temperature is specified as room temperature. However, Case 2 (Q_E=0) reaches up to 60°C at 80 krpm with temperature difference of more than 15°C from Cases 1 and 3. Not shown is the rotor thermal growth for Case 2,

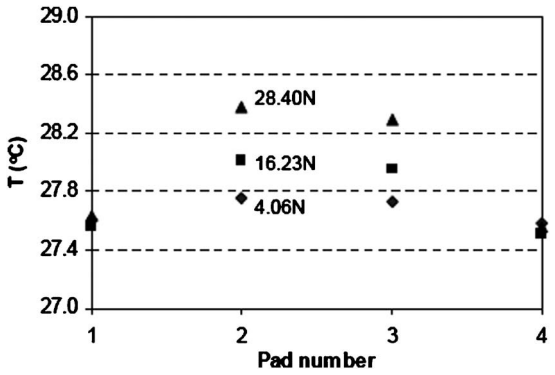

Fig. 21 Pad temperatures for different external loads, 60 krpm, C=35 μm

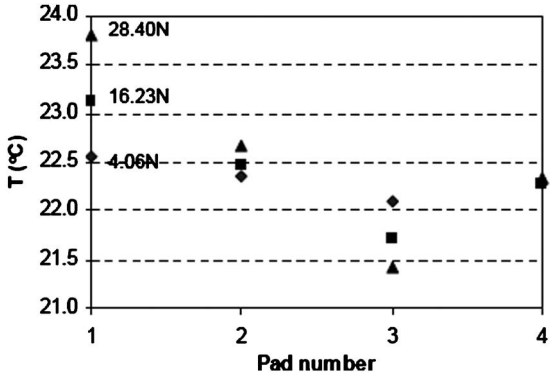

Fig. 22 Inlet flow temperatures to pads for different external loads, 60 krpm, C=35 μm

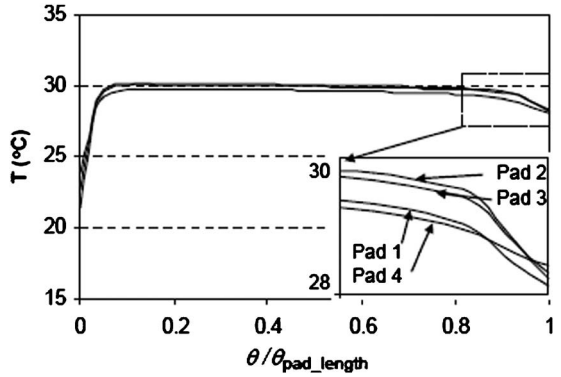

Fig. 23 Bulk film temperatures along the circumferential direction at the axial center of each pad for external load of 28.40 N, 60 krpm, C=35 μm

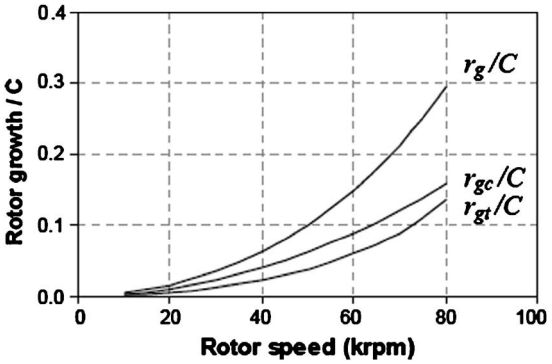

Fig. 25 Rotor radial growths for Case 1 (Q_E=5Q_{conv1}) over rotor speeds of 10–80 krpm

which is quite significant rendering total rotor growth (including centrifugal growth) approaching set bore clearance at 80 krpm. Consequently, bearing operations without an adequate cooling mechanism can cause thermal runaway at high speeds.

Figure 27 presents rotor temperatures within the bearing at 60 krpm for different levels of heat flux boundary conditions at the rotor end. As heat loss at the rotor end approaches infinite, the rotor temperature at the bearing edge approaches Case 3. On the other hand, the temperature variation at the right end where the adiabatic boundary condition is applied is much smaller than at the left end. As Figs. 26 and 27 suggest, imposing heat flux boundary condition beyond five times, the heat convection on the rotor surface yields similar rotor temperature profile regardless of the level of the heat loss at the rotor end. The simulation also suggests minimum necessary amount of cooling for near-isothermal operation of the given rotor-bearing configuration.

3.3 Bearing Stiffness and Damping Coefficients. To better understand the effect of thermal aspect on the rotor dynamic performance, linear perturbation analyses were performed to calculate the stiffness and damping coefficients of the bearing. In the linear perturbation analysis, a steady state operating point (zeroth order solution) is found using THD analysis for the given external load. Viscosity and temperature variations across the bearing surface are considered in the zeroth order solution. From the zeroth order solution, infinitely small perturbation motions of the rotor and pads are imposed. The resulting pressure gradient (first order solution) from the perturbation motions yields stiffness and damping coefficients of the bearing. If pad perturbed motions are synchronous to the rotor perturbed motion, the perturbed pressures by pad motions can be found using a linear superposition principle

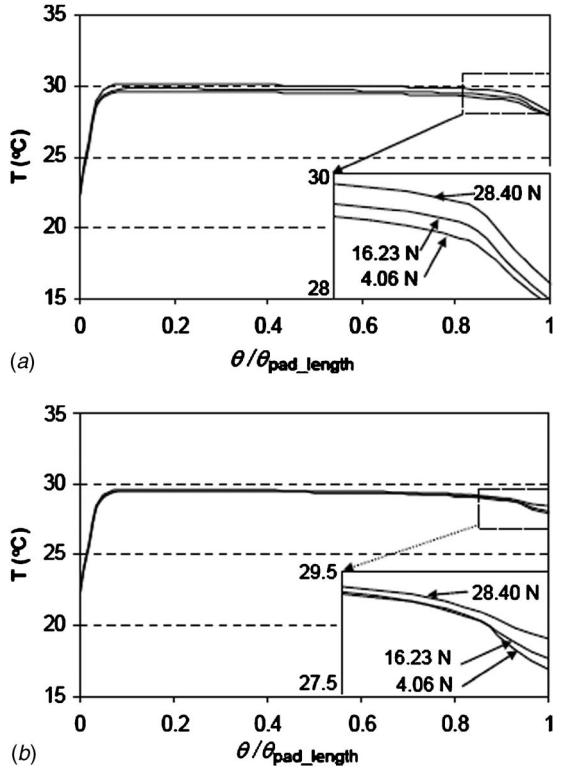

Fig. 24 Bulk film temperatures along the circumferential direction at the axial center for different external loads, 60 krpm, C =35 μm

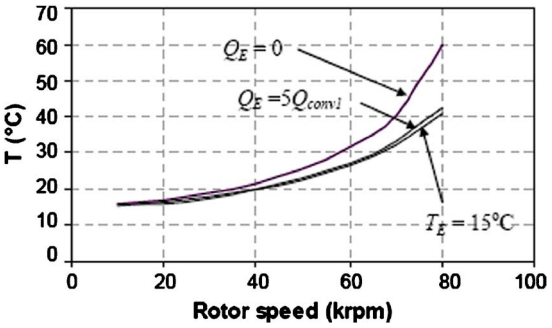

Fig. 26 Rotor temperatures with speeds for different thermal boundary conditions at the rotor end

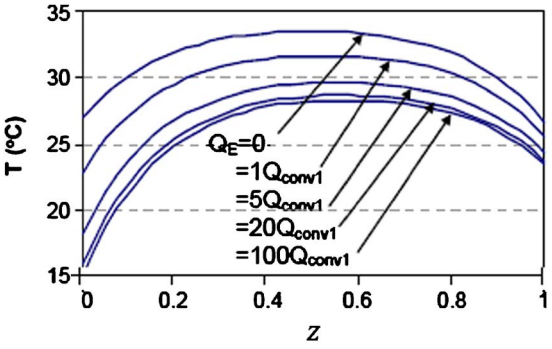

Fig. 27 Rotor temperatures along the rotor axis for different heat fluxes at the rotor end, 60 krpm, C=35 μm

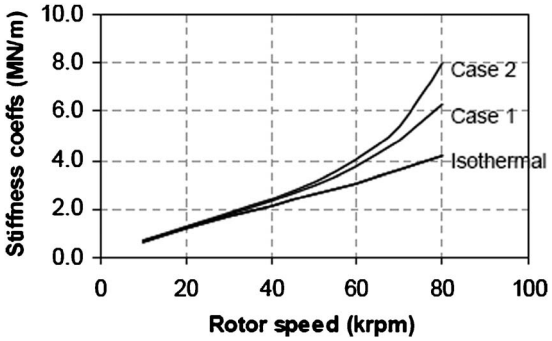

Fig. 28 Synchronous direct stiffness coefficients

from perturbed pressure by rotor motion only. Overall procedure followed the mathematical scheme for isothermal tilting pad gas bearings proposed in Ref. [49].

Synchronous direct stiffness and damping coefficients were calculated for isothermal bearing as a reference and the results were compared in Figs. 28 and 29 with other two cases, i.e., Cases 1 and 2. Case 3 yields very similar results to Case 1. The large increase of direct stiffness at high speeds for Case 2 is attributed to the increased preload via the decreased nominal clearance by the rotor thermal expansion and higher air viscosity at elevated temperature. A large difference of bearing coefficients is observed between the isothermal and nonisothermal cases. The bearing coefficients calculated using the THD analysis are expected to predict more accurate rotor-bearing performance.

4 Conclusions

A new THD model for tilting pad gas bearings that can predict the temperature of rotor and pads as well as air film was developed. The new THD model solves generalized Reynolds equation, 3D energy equation, and energy balance equations for surrounding subdomains including bearing shell and exposed rotor surfaces. Boundary conditions such as inlet flow temperatures, rotor temperature, and pad temperatures are also calculated simultaneously from iterative procedure to meet global thermal balance.

The developed THD model can handle general boundary conditions (temperature or heat flux) of the thermal subsystem for various system configurations and operating conditions. Once the bearing shell temperature and the thermal boundary conditions at the rotor ends away from the bearing edges are known or measured, the developed THD model can predict temperature profiles of the rotor, pads, and gas film. It is expected that the thermal submodule can be used to analyze and design various tilting pad gas bearings for wide range of operation conditions.

Parametric studies on nominal clearance and external load were conducted to provide useful design guide. Nominal clearance showed the most significant influence on the temperature fields, and external load had uneven thermal effects among pads. Case studies with different heat fluxes and temperature boundary conditions were also performed to provide physical insight on the thermal behavior of the tilting pad gas bearings. Adiabatic conditions on the rotor ends lead to much higher rotor temperature at high-speeds than cooled rotor simulated using either heat flux or temperature boundary conditions, demonstrating the necessity of an adequate cooling system for high-speed operations.

Linear perturbation analyses were also performed to investigate thermal effects on the bearing stiffness and damping coefficients. The rotor thermal growth with increased viscosity increased direct stiffness and damping coefficients.

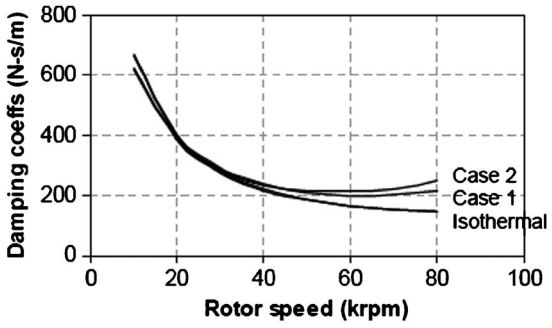

Fig. 29 Synchronous direct damping coefficients

Nomenclature

C = nominal bearing clearance (μm)
c_p = air specific heat capacity under constant pressure (J/(kg K))
$e_{X,Y}$ = journal movements in X and Y directions (μm)
E = elastic modulus of rotor (N/m^2)
h = film thickness (μm)
h_c = heat convection coefficient ($W/(m^2\,K)$)
k = heat conductivity of air (W/(m K))
k_r = heat conductivity of rotor (W/(m K))
k_ϕ = tilting stiffness of pivot (N m/rad)
k_δ = radial stiffness of pivot (N/m)
L = axial length of bearing (m)
L_E, L_C = exposed rotor lengths (m)
$\dot{m}_{\text{exit}}$ = exit flow (kg/s)
$\dot{m}_{\text{suc}}$ = suction air flow (kg/s)
$\dot{m}_{\text{inlet}}$ = inlet flow (kg/s)
P = nondimensional pressure ($=p/p_a$)
p = pressure in gas film (Pa)
p_a = atmospheric pressure (Pa)
$Q_{\text{conv1,2}}$ = convection on the exposed rotor surfaces (W)
Q_E, Q_C = heat flux boundary condition at rotor end (W)
T_E, T_C = temperature boundary condition at rotor end (°C)
r_p = preload
r_g = total rotor growth (μm)
r_{gc} = rotor centrifugal growth (μm)
r_{gt} = rotor thermal growth (μm)
R = rotor outer radius (m)
R_i = rotor inner radius (m)
T_b = bearing shell temperature (°C)
T_{exit} = exit flow temperature (°C)
T_{inlet} = inlet flow temperature (°C)
T_{suc} = suction air temperature (°C)
T_{r_av} = averaged rotor temperature along the rotor axis (°C)
T_{f_av} = averaged air film temperature for all pads (°C)
T_{p_av} = averaged pad temperature for all pads (°C)
T_r = local rotor temperature along rotor axis (°C)
T_p = pad temperature (°C)
T_∞ = ambient temperature (°C)
U = circumferential linear velocity of rotor surface (m/s)
u, v, w = air velocity component in the x, y, and z directions (m/s)
x, y, z = Cartesian coordinates for air film (see Fig. 4)
X, Y = Cartesian coordinates for rotor motion (see Fig. 3)
Z = nondimensional axial coordinate for the bearing ($=z/L$)

Greek

α = linear thermal coefficient of rotor ($°C^{-1}$)
ϕ = tilting angle of each pad (rad)
δ = radial motion of each pad (m)

$\varepsilon_{X,Y}$ = journal eccentricities in X and Y directions ($=e_{X,Y}/C$)
θ = circumferential coordinate (rad) ($=x/R$)
θ_p = angular location of pivot web (rad)
ρ = density of air (kg/m^3)
ρ_r = density of rotor (kg/m^3)
Ω = rotor spin speed (rad/s)
ν = Poisson's ratio of rotor
μ = viscosity of air (Pa s)
Φ = heat dissipation function

References

[1] Online source: www.microturbine.com
[2] Veyo, S. E., Shockling, L. A., Dederer, J. T., Gillet, J. E., and Lundberg, W. L., 2002, "Tubular Solid Oxide Fuel Cell/Gas Turbine Hybrid Cycle Power Systems: Status," ASME J. Eng. Gas Turbines Power, **124**, pp. 845–849.
[3] Costamagna, P., Magistri, L., and Massardo, A. F., 2001, "Design and Part-Load Performance of a Hybrid System Based on a Solid Oxide Fuel Cell Reactor and a Micro Gas Turbine," J. Power Sources, **96**, pp. 352–368.
[4] Online source: www.jetcatusa.com
[5] Online source: www.manturbo.com
[6] Trivedi, H. K., Klenke, C. J., and Saba, C. S., 2004, "Effect of Formulation and Temperature on Boundary Lubrication Performance of Polyphenylethers (5P4E)," Tribol. Lett., **17**(1), pp. 1–10.
[7] Trivedi, H. K., Saba, C. S., and Givan, G. D., 2002, "Thermal Stability of a Linear Perfluoropolyalkylether in a Rolling Contact Fatigue Tester," Tribol. Lett., **12**(3), pp. 171–182.
[8] Lund, J., 1964, "Spring and Damping Coefficients for the Tilting Pad Journal Bearing," ASLE Trans., **7**, pp. 342–352.
[9] Pan, C. H. T., 1965, "Spectral Analysis of Gas Bearing Systems for Stability Studies," Developments in Mechanics, *Proceedings of the Ninth Midwestern Mechanics Conference*, T. C. Huang and M. W. Johnson, Jr., eds., Wiley, New York, Vol. 3, Pt. 2, pp. 431–448.
[10] Lund, J. W., 1968, "Calculation of Stiffness and Damping Properties of Gas Bearings," ASME J. Lubr. Technol., **90**(4), pp. 793–803.
[11] Heshmat, H., Shapiro, W., and Gray, S., 1982, "Development of Foil Journal Bearings for High Load Capacity and High Speed Whirl Stability," ASME J. Lubr. Technol., **104**, pp. 149–156.
[12] Heshmat, H., 1994, "Advancements in the Performance of Aerodynamic Foil Journal Bearings: High Speed and Load Capacity," ASME J. Tribol., **116**, pp. 287–295.
[13] Agrawal, G. L., 1997, "Foil Air/Gas Bearing Technology—An Overview," ASME Paper No. 97-GT-347.
[14] DellaCorte, C., and Valco, M. J., 2000, "Load Capacity Estimation of Foil Air Journal Bearings for Oil-Free Turbo-Machinery Applications," STLE Tribol. Trans., **43**(4), pp. 795–801.
[15] Carpino, M., and Talmage, G., 2003, "A Fully Coupled Finite Element Formulation for Elastically Supported Foil Journal Bearings," STLE Tribol. Trans., **46**, pp. 560–565.
[16] Peng, J. P., and Carpino, M., 1993, "Calculation of Stiffness and Damping Coefficients for Elastically Supported Gas Foil Bearings," ASME J. Tribol., **115**(1), pp. 20–27.
[17] Saleui, M., Swanson, E., and Heshmat, H., 2001, "Thermal Features of Compliant Foil Bearings—Theory and Experiments," ASME J. Tribol., **123**, pp. 566–571.
[18] Dykas, B., and Howard, S. A., 2004, "Journal Design Considerations for Turbomachine Shafts Supported on Foil Air Bearings," STLE Tribol. Trans., **47**, pp. 508–516.
[19] Zhu, X., and San Andrés, L., 2004, "Rotordynamic Performance of Flexural Pivot Hydrostatic Gas Bearings for Oil-Free Turbomachinery," ASME Paper No. GT2004-53621.
[20] San Andrés, L., 2006, "Hybrid Flexure Pivot-Tilting Pad Gas Bearings: Analysis and Experimental Validation," ASME J. Tribol., **128**, pp. 551–558.
[21] Radil, K., and Zeszotek, M., 2004, "An Experimental Investigation Into the Temperature Profile of a Compliant Foil Air Bearing," *Proceedings of the STLE 59th Annual Meeting*, Toronto, pp. 470–479.
[22] Peng, Z.-C., and Khonsari, M. M., 2006, "A Thermohydrodynamic Analysis of Foil Journal Bearings," ASME J. Tribol., **128**, pp. 534–541.
[23] Sim, K. H., and Kim, D., 2007, "Design of Flexure Pivot Tilting Pad Gas Bearings for High Speed Oil-Free Micro Turbomachinery," ASME J. Tribol., **129**(1), pp. 112–119.
[24] Kim, D., 2007, "Parametric Studies on Static and Dynamic Performance of Air Foil Bearings With Different Top Foil Geometries and Bump Stiffness Distributions," ASME J. Tribol., **129**(2), pp. 354–364.
[25] Pan, C. T., and Kim, D., 2007, "Stability Characteristics of a Rigid Rotor Supported by a Gas Lubricated Spiral-Groove Conical Bearing," ASME J. Tribol., **129**(2), pp. 375–383.
[26] Song, J.-H., and Kim, D., 2007, "Foil Gas Bearing With Compression Springs: Analyses and Experiments," ASME J. Tribol., **129**(3), pp. 628–639.
[27] Online source: http://westwind-airbearings.com/airBearing/index. html
[28] Online source: http://www.rockwellautomation.com/anorad/products/airbearingsystems/index.html
[29] Online source: http://www.kmcbearings.com/images/kmc_images/fp_journal.jpg
[30] Zeidan, F., and Paquette, D. J., 1994, "Application of High-Speed and High Performance Fluid Film Bearings in Rotating Machinery," *Proceedings of the 23th Turbomachinery Symposium*, Dallas, TX, pp. 209–234.
[31] Chen, W. J., Zeidan, F. Y., and Jain, D., 1994, "Design, Analysis and Testing of High Performance Bearing in a High-Speed Integrally Geared Compressor," *Proceedings of the 23rd Turbomachinery Symposium*, Dallas, TX.
[32] Cope, W. F., 1949, "Hydrodynamic Theory of Film Lubrication," Proc. R. Soc. London, Ser. A, **197**, pp. 201–216.
[33] Zienkiewicz, O., 1958, "Temperature Distribution Within Lubrication Film between Parallel Bearing Surfaces and Its Effect on the Pressures Developed," *Proceedings of the Conference on Lubrication and Wear*, Institution of Mechanical Engineers, London, Vol. 28, pp. 135–141.
[34] Hunter, W., and Zienkiewicz, O., 1960, "Effect of Temperature Variation Across the Lubrication Film in the Theory of Hydrodynamic Lubrication," J. Mech. Eng. Sci., **2**(1), pp. 52–58.
[35] Dowson, D., Hudson, J., Hunter, B., and March, C., 1966, "An Experimental Investigation of the Thermal Equilibrium of Steadily Loaded Journal Bearings," Proc. Inst. Mech. Eng., **101**(3B), pp. 70–80.
[36] Knight, J. D., and Barrett, L. E., 1988, "Analysis of Tilting Pad Journal Bearings With Heat Transfer Effects," ASME J. Tribol., **110**, pp. 128–133.
[37] Taniguchi, S., Makino, T., Takeshita, K., and Ichimura, T., 1990, "A Thermohydrodynamic Analysis of Large Tilting Pad Journal Bearing in Laminar and Turbulent Flow Regimes With Mixing," ASME J. Tribol., **112**, pp. 542–549.
[38] Kim, J., Palazzolo, A., and Gadangi, R., 1994, "TEHD Analysis for Tilting-Pad Journal Bearings Using Upwind Finite Element Method," STLE Tribol. Trans., **37**, pp. 771–783.
[39] Fillon, M., Bligoud, J.-C., and Frene, J., 1992, "Experimental Study of Tilting-Pad Journal Bearings—Comparison With Theoretical Thermoelastohydrodynamic Results," ASME J. Tribol., **114**, pp. 579–567.
[40] Khonsari, M. M., and Beaman, J. J., 1986, "Thermohydrodynamic Analysis of Laminar Incompressible Journal Bearings," ASLE Trans., **29**, pp. 141–150.
[41] Pinkus, O., and Bupara, S. S., 1979, "Adiabatic Solution for Finite Journal Bearings," ASME J. Lubr. Technol., **101**, pp. 578–587.
[42] Holman, J. P., 1997, *Heat Transfer*, 8th ed., McGraw-Hill, New York, pp. 44–47.
[43] Timoshenko, S. P., and Goodier, J. N., 1970, *Theory of Elasticity*, McGraw-Hill, New York.
[44] Patankar, S. V., 1980, *Numerical Heat Transfer and Fluid Flow*, McGraw-Hill, New York, Chap. 5.
[45] Heshmat, H., and Pinkus, O., 1986, "Mixing Inlet Temperatures in Hydrodynamic Bearings," ASME J. Tribol., **108**, pp. 231–248.
[46] Ettles, C., 1980, "The Analysis and Performance of Pivoted Pad Journal Bearings Considering Thermal and Elastic Effects," ASME J. Lubr. Technol., **102**, pp. 182–192.
[47] Mills, A. F., 1999, *Heat Transfer*, 2nd ed., Prentice-Hall, Upper Saddle River, NJ, pp. 362–365.
[48] Mills, A. F., 1999, *Heat Transfer*, 2nd ed., Prentice-Hall, Upper Saddle River, NJ, pp. 162–164.
[49] Delgado, A., Justak, J. F., and San Andrés, L., 2004, "Analysis of Performance and Rotordynamic Force Coefficients of Brush Seals With Reverse Rotation Ability," ASME Paper No. GT-2004-53614.

Nonlinear Dynamic Characterization of Oil-Free Wire Mesh Dampers

Bugra H. Ertas
Rotating Equipment Group,
Vibrations and Dynamics Laboratory,
GE Global Research Center,
Niskayuna, NY 12309
e-mail: ertas@research.ge.com

Huageng Luo
Noise and Vibration Group,
Vibrations and Dynamics Laboratory,
GE Global Research Center,
Niskayuna, NY 12309
e-mail: luoh@crd.ge.com

The present work focuses on the dynamic characterization of oil-free wire mesh dampers. The research was aimed at determining nonlinear stiffness and damping coefficients while varying the excitation amplitude, excitation frequency, and static eccentricity. Force coefficients were extracted using a forced response method and also a transient vibration method. Due to the nonlinearity of the dampers, controlled amplitude single frequency excitation tests were required for the forced excitation method, whereas the transient response was analyzed using a Hilbert transform procedure. The experimental results showed that eccentricity has minimal influence on force coefficients, whereas increasing excitation amplitude and frequency yields decreasing stiffness and damping trends. In addition to the parameter identification tests, a rotating test was performed demonstrating high-speed damping capability of the oil-free wire mesh dampers to 40,000 rpm, which was also simulated using a nonlinear rotordynamic response to imbalance analysis. [DOI: 10.1115/1.2836744]

1 Introduction

Traditional rotor-bearing systems use oil based bearing support dampers to mitigate imbalance response and rotordynamic stability [1,2]. With a careful design, squeeze film dampers (SFDs) can provide large amounts of direct damping at bearing support locations, thus alleviating undesired rotor vibrations. Although oil based SFD systems are used effectively to reduce machine vibrations, application is restricted into oil-free turbomachinery. One possible method for introducing damping into oil-free rotor-bearing systems is using wire mesh bearing support dampers. The use of these oil-free dampers has been mainly investigated for application in cryogenic fuel turbopumps. Childs [3] reported bench tests performed on metal mesh dampers in efforts to solve rotordynamic stability problems in the space shuttle main engine fuel turbopump. Metal mesh dampers were also used to solve subsynchronous instability problems and high synchronous vibrations for the LE-7 liquid hydrogen turbopump by Okayasu et al. [4]. Further cryogenic testing of different wire mesh damper materials for stiffness and damping was conducted by Ertas et al. [5].

Another application that has been investigated for wire mesh dampers is in turbo-prop gas turbine rotor-bearing systems. Past experiments by Zarzour and Vance [6] and Al-Khateeb and Vance [7,8] conducted rotating tests on a 15 kg rotor to 7000 rpm and 10,000 rpm, respectively, showing well-damped operation through the first critical speed. These experiments used the wire mesh dampers in series with oil-lubricated ball bearings and had limited success in application to oil-lubricated rotor systems, due to the already existing SFD design paradigm. However, recent interests in developing oil-free operation of high-performance gas turbine aircraft engines [9] encourage further work into wire mesh dampers at higher speeds and testing of a wider variation of test parameters.

The present study focuses on the influence of several dynamic parameters on wire mesh stiffness and damping. The effect of vibration amplitude and excitation frequency was investigated using a forced response method (FRM). Another parameter varied during testing was the static eccentricity of the damper, which has not been investigated in the past work. To complement the FRM, a time domain Hilbert transform analysis was used to identify the nonlinear characteristics at higher frequency ranges. The last portion of the paper demonstrates well-damped high-speed rotating tests to 40,000 rpm and presents a nonlinear rotordynamic simulation of the imbalance response.

1.1 Wire Mesh Dampers. A wire mesh damper is a weave of metal wires usually compressed into a toroidal shape at a particular percent mesh density. Figure 1 shows examples of copper wire mesh dampers and Table 1 lists the damper parameters used for this study.

2 Forced Excitation Testing

Forced excitation tests are widely used for characterizing the stiffness and damping of structures and mechanical components. Several past researchers [10–12] have used more sophisticated versions of the frequency domain based method presented here. For linear systems, tests using forced response can be performed with an impulse, a periodic chirp, or even a random noise excitation. However, when considering systems that exhibit strong nonlinear behaviors, test parameters require more careful control.

2.1 Forced Response Experimental Setup. The experimental test rig is shown in Fig. 2. Originally developed for testing high-speed oil-free bearings [13], the rotating test rig in Fig. 2 was used to support a soft mounted rotor system using wire mesh dampers. There are two sets of duplex mounted ceramic angular contact ball bearings supporting the rotor. Each bearing set is mounted in series with double-fold beam style squirrel cage, which is in parallel with the wire mesh damper donuts. Damping or energy dissipation is generated when there exists a relative motion between the inner and outer squirrel cage rims. Each copper damper was designed to have a 25% density mesh, a 4.8 in. (122 mm) outside diameter (o.d.), a 2.75 in. (70 mm) inside diameter (i.d.), and a 1.2 in. (30 mm) width.

The test setup for forced excitation tests required using an electrohydraulic exciter to statically position and dynamically modulate the rotor. Test parameters were excitation amplitude, excitation frequency, and static eccentricity. The static position and dynamic motion were monitored using two noncontact eddy current proximity probes. Dynamic forces were measured from a force transducer, while the system acceleration was measured from the loading shoe. Determining stiffness and damping was based on a linear single-degree-of-freedom system model, de-

Manuscript received June 20, 2007; final manuscript received October 7, 2007; published online April 3, 2008. Review conducted by Jaroslaw Szwedowicz.

Fig. 1 Wire mesh dampers

scribed by Eq. (2.1). Although this model represents a linear system, it can be applied to nonlinear parameter identification for small perturbations about the equilibrium position in combination with the precisely controlled test parameters. Assuming harmonic functions for the system motion and force (Eq. (2.2)), the time dependent equation (2.1) can be transformed to a frequency domain equation of motion (Eq. (2.3)). By performing fast Fourier transform (FFT) analysis on the time domain signals, the complex variables X, F, and A are measured, where X is the displacement, F is the excitation force, and A is the system acceleration.

$$\ddot{x}(t) \cdot m + \dot{x}(t) \cdot c + x(t) \cdot k = f(t) \tag{2.1}$$

$$x(t) = X \cdot e^{i\omega t} \quad f(t) = F \cdot e^{i\omega t} \tag{2.2}$$

$$m \cdot A + i\omega X \cdot c + X \cdot k = F \tag{2.3}$$

Using the excitation force signal (F) to which the acceleration and motion responses are phased from, the system inertia force is subtracted from the excitation force, which results in the effective force of the system (Eq. (2.4)). Next, the bearing support impedance (Eq. (2.5)) can be resolved by dividing both sides of Eq. (2.4) by the response X. The real part of the impedance (modified dynamic stiffness) represents the direct stiffness and the imaginary part divided by the excitation frequency yields the direct damping (Eq. (2.6)).

$$F_{\text{eff}} = F - mA = k \cdot X + i\omega X \cdot c \tag{2.4}$$

Table 1 Wire mesh damper parameters

Properties	Value (unit)
Outside diameter	122 (mm)
Inside diameter	70 (mm)
Width	22.61 (mm)
Material	Cu 25% density mesh
Wire gage	0.32 (mm)

$$H(\omega) = \frac{F_{\text{eff}}}{X} = k + ic\omega \tag{2.5}$$

$$H_{(\text{Re})} = k \quad H_{(\text{Im})} = c\omega \tag{2.6}$$

An example forced excitation test is shown in Fig. 3. The motions from Probes 1 and 3 were averaged from the time domain followed by a FFT calculation for all signals. The example shown in Fig. 3 was for the peak excitation amplitude of 1.5 mil (0.0381 mm) at 56 Hz. Each test point is an average of ten different sets of data and the coherence between the excitation signal and response signals was 0.95 or better. The squirrel cages were designed for a radial stiffness of 40,000 lb/in. (7 MN/m) each. To identify the wire mesh damper coefficients, the stiffness and damping of the squirrel cages need to be subtracted from the overall coefficients. This was achieved by performing forced response impact hammer base line tests on the individual squirrel cages without the dampers being installed.

2.2 Stiffness and Damping Results Forced Response Method. The direct stiffness and damping results for two dampers are shown in Fig. 4. The top two plots represent testing where the excitation amplitudes varied from 0.5 mil (0.0127 mm) peak-peak to 3 mil (0.0762 mm) peak-peak, while the static eccentricity was held constant. The damping was shown to decrease with increasing excitation frequency and agrees with past experiments in Ref. [8]. The damping also decreases with increasing excitation amplitude. The results of the damping trend suggest compatibility with soft mounted rotor-bearing systems due to the maximum damping values residing at lower frequencies. This is advantageous as soft mounted rotor-bearing systems used in aircraft engines possess rigid body modes for the first two critical speeds and also exhibit lower imbalance forces due to the lower critical speed locations. In addition, the decrease in damping at high frequencies contributes to lower dynamic bearing loads. However, a decreasing damping trend with increasing frequency is not advantageous for machines operating above the third critical speed and would require an additional damping source, such as a damper seal [4]. The stiffness is highly sensitive to the excitation amplitude, whereas the frequency has minimal influence on the stiffness. As the excitation amplitude increases, the stiffness decreases, which portrays the behavior of a softening spring.

The plots in Fig. 4 represent tests where the static eccentricity of the damper was varied from 1 mil (0.0254 mm) to 5 mil (0.127 mm) for a fixed peak excitation amplitude. The results indicate that static eccentricity or the static equilibrium position of the damper has no influence on the damping or stiffness. This result is unique among nonlinear mechanical elements, because most nonlinear mechanical elements have stiffness and damping coefficients that are dependent on both the static equilibrium position and excitation amplitude. One explanation of the stiffness

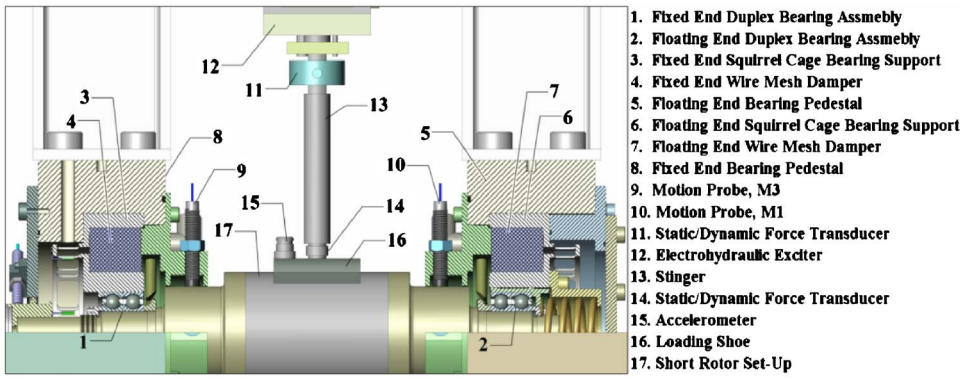

Fig. 2 Nonrotating forced excitation test setup

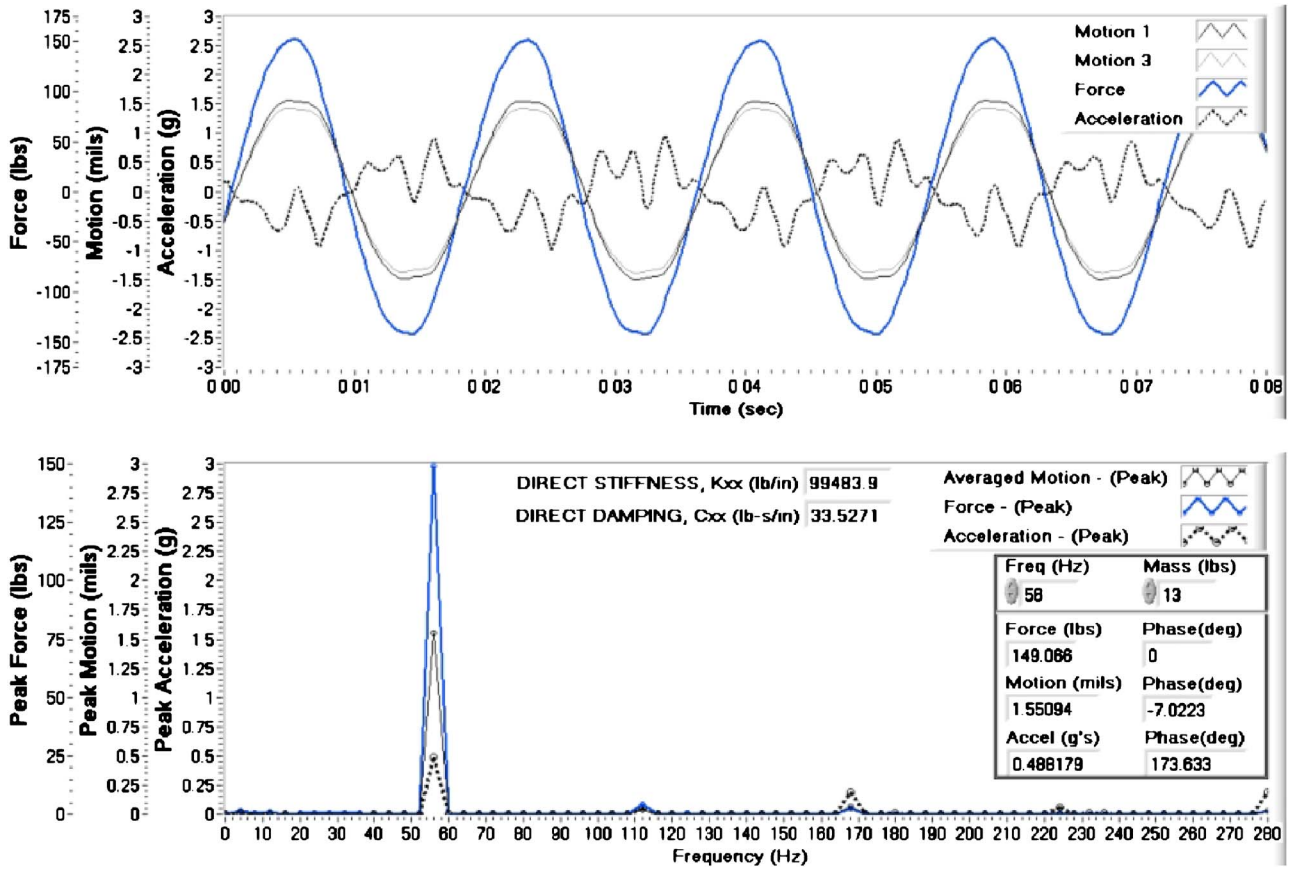

Fig. 3 Example forced excitation impedance test: bearing support parameters

and damping behavior is a stick-slip model presented by Al-Khateeb [8] (Fig. 5). The stick-slip model arranges the wires in series connected by hysteretic dampers (h) and linear springs. As the applied force (f) increases for a given frequency, more of the stick-slip joints between wires are freed through overcoming the friction force (fd) and result in a greater number of spring-damper systems in series. The increased spring-damper layers in Al-Khateeb's stick-slip model result in lower values of equivalent stiffness and damping. Note that this reduction in force coefficients for an increasing force was shown to only hold true in the dynamic case; there was no effect due to static preload force or static eccentricity. This suggests that the individual wires in the mesh individually behave as linear spring-damper systems, whereas the nonlinear dynamic behavior with excitation amplitude is derived from the stick-slip behavior at the wire junctions.

3 Hilbert Transform

In this section, the basic formulation of the Hilbert transform and empirical modal decomposition used in the present research is discussed. Let $x(t)$ be a real-valued signal. The Hilbert transform, $x(t)$, is given as [14]

$$\bar{x}(t) = H[x(t)] = \frac{-1}{\pi} P \int_{-\infty}^{\infty} \frac{x(\tau)}{\tau - t} d\tau \tag{3.1}$$

$$x(t) = H^{-1}[\bar{x}(t)] = \frac{1}{\pi} P \int_{-\infty}^{\infty} \frac{\bar{x}(\tau)}{\tau - t} d\tau \tag{3.2}$$

These integrals are improper integrals in the sense of the Cauchy principal value denoted by P. Equation (3.2) yields

$$x(t) = \lim_{\varepsilon \to 0; A \to \infty} \frac{1}{\pi} \left\{ \int_{-A}^{t-\varepsilon} (\cdot) d\tau + \int_{t+\varepsilon}^{A} (\cdot) d\tau \right\} \tag{3.3}$$

The Hilbert transform described by Eqs. (3.1) and (3.2) is frequently written in terms of convolution notation

$$\bar{x}(t) = \frac{1}{\pi t} x(t) \tag{3.4}$$

$$x(t) = -\frac{1}{\pi t} \bar{x}(t) \tag{3.5}$$

The functions $x(t)$ and $\bar{x}(t)$ are called a pair of Hilbert transforms and denoted by

$$x(t) \overset{H}{\Leftrightarrow} \bar{x}(t) \tag{3.6}$$

The complex signal whose imaginary part is the Hilbert transform of the real part is called the analytic signal, i.e., an analytic signal, $X(t)$, is formulated as

$$X(t) = x(t) + j \cdot \bar{x}(t) = A(t) e^{j\theta} \tag{3.7}$$

in which

$$A(t) = \sqrt{x^2(t) + \bar{x}^2(t)}$$
$$\theta(t) = tg^{-1}\left(\frac{\bar{x}(t)}{x(t)} \right) \tag{3.8}$$

The instantaneous frequency of the signal is defined as

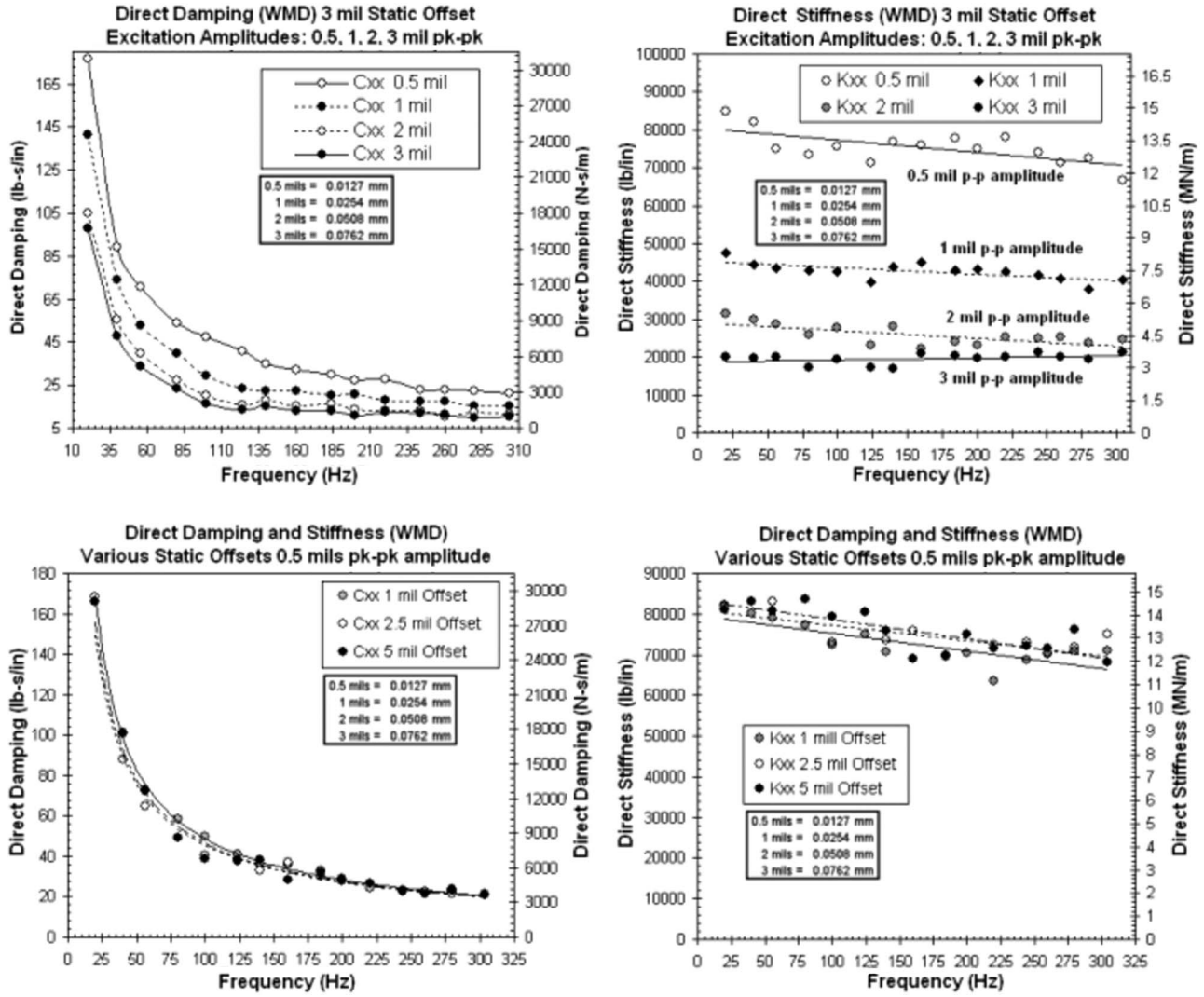

Fig. 4 Direct stiffness and damping results for two wire mesh dampers: forced excitation tests

$$\omega(t) = 2\pi f(t) = \frac{d\theta(t)}{dt} \tag{3.9}$$

or

$$\omega(t) = \frac{d}{dt}\left(tg^{-1}\frac{\bar{x}(t)}{x(t)}\right) = \frac{x(t)\dot{\bar{x}}(t) - \dot{x}(t)\bar{x}(t)}{x^2(t) + \bar{x}^2(t)} \tag{3.10}$$

The aforementioned Hilbert analysis provides a basis for determining the instantaneous power and frequency of a signal. However, determining an instantaneous frequency directly from Eq. (3.10) for an arbitrary function is intriguing, because for an arbitrary function, Eq. (3.10) may lead to a negative or even an undetermined value. For the instantaneous frequency to make sense, the signal has to be "monocomponent" or "narrow banded." Detailed discussions can be found in Ref. [15]. Huang et al. [16] introduced a so-called empirical mode decomposition (EMD) method to extend the notion of the analytic signal to multicomponent signals. The decomposition is based on the simple assumption that each datum consists of different simple intrinsic modes of oscillations. Each intrinsic mode, linear or nonlinear, represents a simple oscillation, which will have the same number of extrema and zero crossings. Furthermore, the oscillation will also be symmetric with respect to the "local mean." At any given time, the data may have many different coexisting modes of oscillation, one superimposing on the other. The result is the original data. Each mode is represented by an intrinsic mode function (IMF) with the following definition:

(i) In the whole dataset, the number of extrema and the number of zero crossings must either equal or differ at most by 1,
(ii) At any point, the mean value of the envelope defined by the local maxima and the envelope defined by the local minima is zero.

As detailed in Ref. [16], an IMF can be extracted from an arbitrary vibratory signal, $x(t)$, through the following steps:

(1) identify all the local maxima, connect all the local maxima by a cubic spline line to form the upper envelope
(2) identify all the local minima, connect all the local minima by a cubic spline line to form the lower envelope
(3) obtain the mean, $m_{10}(t)$, of the upper and lower envelopes
(4) remove the mean to get the first mode: $h_{10}(t)=x(t)-m_{10}(t)$
(5) repeat Steps (1)–(4) on $h_{1(i-1)}(t)$ to get $m_{1i}(t)$ and $h_{1i}(t)=h_{1(i-1)}(t)-m_{1i}(t)$, until the predetermined criteria are met
(6) define the first mode $c_1(t)=h_{1i}(t)$
(7) define the residual $r_1(t)=x(t)-h_1(t)$

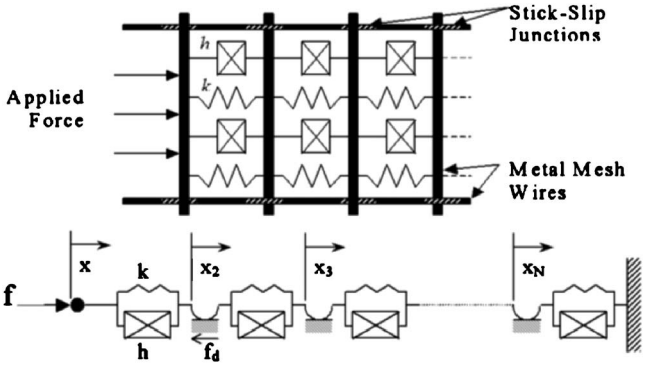

Fig. 5 Al-Khateeb's stick-slip model [8]

(8) repeat Steps (1)–(6) on $r_k(t)$ to get $(k+1)$th mode $c_{k+1}(t) = h_{(k+1)i}(t)$
(9) define the residual $r_{k+1}(t) = x(t) - \Sigma_{j=1}^{k} h_j(t)$
(10) repeat Steps (8) and (9) until required number of modes is extracted. Thus, the total signal can be expressed as a combination of the IMFs as

$$x(t) = \sum_{k=1}^{n} c_k(t) + r(t) \tag{3.11}$$

where $r(t)$ is the final residual. Having obtained the IMFs, we can apply the Hilbert transform to each IMF and compute the instantaneous frequency according to Eqs. (3.8)–(3.10).

3.1 Nonlinear Parameter Identification. By using the Hilbert transform, the linear damping parameter from an impulse response function is identified. It has been demonstrated that this technique possesses some advantages, especially when the frequency domain resolution is limited [17]. Feldman [18] proposed a Hilbert transform based method to identify the nonlinear parameters in a quasilinear system by using the system impulse response time history. Numerical simulations in the paper indicate good identification results.

For a general single-degree-of-freedom (SDOF) system, its free vibration response, with viscous damping, is governed by

$$m(t)\ddot{x}(t) + c(t)\dot{x}(t) + k(t)x(t) = 0 \tag{3.12}$$

On the condition that m is time invariant, Eq. (3.12) can be written as

$$\ddot{x}(t) + 2h_0(t)\dot{x}(t) + \omega_0^2(t)x(t) = 0 \tag{3.13}$$

where $h_0(t) = c(t)/2m$ is the viscous damping ratio multiplied by undamped natural frequency, and $\omega_0(t) = \sqrt{k(t)/m}$ is the undamped natural frequency. Assuming that the analytical signal, $X(t)$, corresponding to the free vibration response, $x(t)$, is $X(t) = x(t) + j \cdot \bar{x}(t) = A(t)e^{j\theta}$, and further assuming that $h_0(t) = h_0(A)$ and $\omega_0(t) = \omega_0(A)$, we have the equation of free vibration response as

$$\ddot{x}(t) + 2h_0(A)\dot{x}(t) + \omega_0^2(A)x(t) = 0 \tag{3.14}$$

Applying the Hilbert transform to Eq. (3.14), we have

$$\ddot{X}(t) + 2h_0(A)\dot{X}(t) + \omega_0^2(A)X(t) = 0 \tag{3.15}$$

where h_0 and ω_0 are assumed to be varying at a rate much slower than the free vibration response x, i.e., the system is quasilinear such that the Bedrosian's theorem [19] can be applied during the Hilbert transform. From Eq. (3.7), we have

$$\dot{X}(t) = \frac{d}{dt}(A(t)e^{j\theta}) = X(t)\left[\frac{\dot{A}}{A} + j\omega\right] \tag{3.16}$$

and

$$\ddot{X}(t) = \frac{d^2}{dt^2}(A(t)e^{j\theta}) = X(t)\left[\frac{\ddot{A}}{A} - \omega^2 + 2j\frac{\dot{A}\omega}{A} + j\dot{\omega}\right] \tag{3.17}$$

Substituting Eqs. (3.16) and (3.17) into Eq. (3.15) yields

$$X(t)\left[\frac{\ddot{A}}{A} - \omega^2 + \omega_0^2 + 2h_0\frac{\dot{A}}{A} + j\left(\frac{2\dot{A}\omega}{A} + \dot{\omega} + 2h_0\omega\right)\right] = 0 \tag{3.18}$$

or

$$\begin{cases} \omega_0^2 = \omega^2 - \dfrac{\ddot{A}}{A} + \dfrac{2\dot{A}^2}{A^2} + \dfrac{\dot{A}\dot{\omega}}{A\omega} \\ h_0 = -\dfrac{\dot{A}}{A} - \dot{\omega}2\omega \end{cases} \tag{3.19}$$

For a system with structural damping, as pointed out in Ref. [18], the Hilbert transform of the free vibration equation is

$$\ddot{X}(t) + \omega_0^2(A)\left[1 + j\frac{\delta(A)}{\pi}\right]X(t) = 0 \tag{3.20}$$

where δ is the logarithmic decrement. The corresponding system parameters are

$$\begin{cases} \omega_0^2 = \omega^2 - \dfrac{\ddot{A}}{A} \\ \delta = -\dfrac{2\pi\dot{A}\omega}{A\omega_0^2} - \pi\dot{\omega}\omega_0^2 \end{cases} \tag{3.21}$$

A similar approach can be found in a paper by Allara et al. [20].

3.2 Transient Impact Hammer Tests. The cross section of the test setup for the transient impact hammer tests is shown in Fig. 6. The inner rim of the squirrel cage bearing support is constrained using a washer clamp and tie bolt. The vibration decay measurement was triggered from the instrumented impact hammer and the motion of the outer squirrel cage rim was reordered from a noncontact proximity probe. Seven different tests were con-

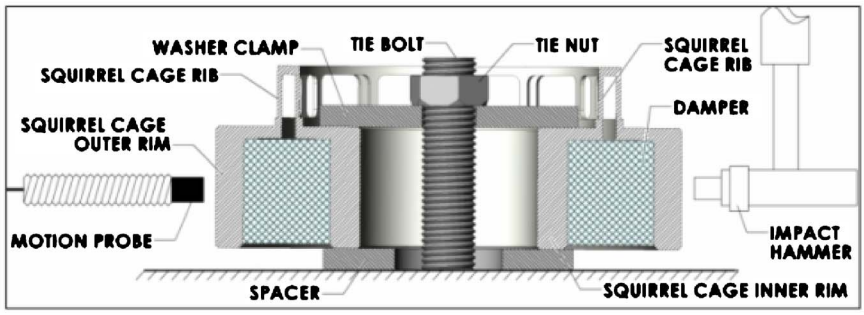

TEST	MAX PEAK AMPLITUDE			
1	0.20	mils,	0.0051	mm
2	0.27	mils,	0.0069	mm
3	0.43	mils,	0.0114	mm
4	0.65	mils,	0.0165	mm
5	0.92	mils,	0.0233	mm
6	1.20	mils,	0.0304	mm
7	1.70	mils,	0.0431	mm

Fig. 6 Transient impact hammer test setup and test matrix

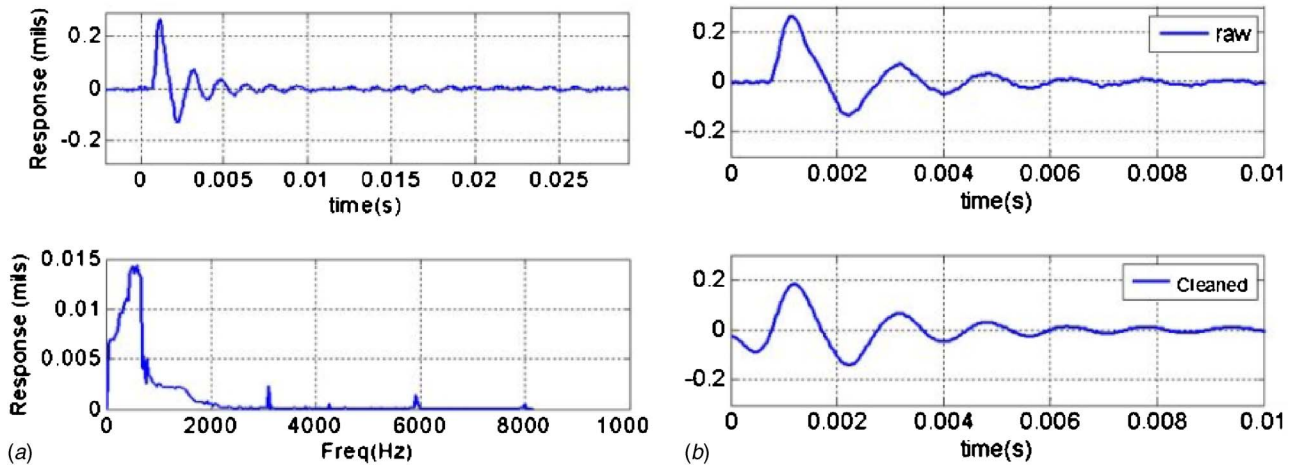

Fig. 7 (*a*) An impulse response and its Fourier spectrum and (*b*) raw impulse response and cleaned mode

ducted and were controlled based on the initial peak amplitude of the time transient response. The initial peak amplitude of excitation ranged between 0.20 mil (0.0051 mm) and 1.7 mil (0.0431 mm).

An impulse response is shown in Fig. 7(*a*). In the figure, the top portion is the damper displacement response time history excited by an impulse, while the bottom portion is the frequency spectrum. From the frequency spectrum, it is seen that the system is most likely nonlinear. From both time history and frequency spectrum, it is also seen that the impulse response contains some high frequency response as well as other nonmode related noise. The wavelet transform was then applied to the raw response signal to remove the high frequency noise without altering the phase information of the signal. In our study, the Daubechies wavelets were used. The comparison between the raw response and the cleaned version is shown in Fig. 7(*b*). The Hilbert transform based identification method was then applied to the cleaned modal response to identify the modal parameters, such as the damping and the frequency. The identification results are shown in Fig. 8. In the upper right portion of the figure, the cleaned modal response and the reconstructed response, based on the identified parameters, are overlaid. The fitting error is defined as the energy ratio between error and the modal response:

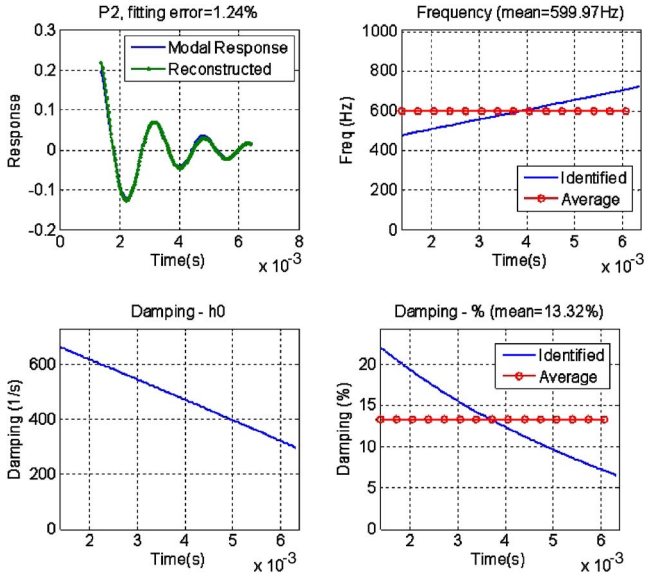

Fig. 8 Identification results

$$\text{error} = \frac{(X-\bar{X})^T(X-\bar{X})}{X^TX} \times 100\%$$

where X is the cleaned modal response and $\bar{X}$ is the reconstructed response from the identified parameters. With the current method, the fitting error can be easily below 5%. For the particular case discussed here, the fitting error is 1.24%.

The identified frequency versus time is shown in the upper left portion of Fig. 8, which indicates that the frequency slightly increases with time, or in other words, the frequency decreases with the increase of vibration amplitude in the range of this modal response. The identified damping versus time is shown in the bottom portion of Fig. 8. The bottom left is the viscous damping ratio and the bottom right is the equivalent critical damping ratio. For this particular case, the damping decreases with time, or decreases with the modal response amplitudes. To identify the amplitude dependency of the damping and frequency, different levels of impulse were applied to the damper and the responses were recorded. With the similar signal processes as stated above, the values of damping and frequency were identified for each excitation level. In the left portion of Fig. 9, the identified parameters from seven cases were overlaid. From these cases, the overall trends were extracted and displayed in the right portion of Fig. 9. From Fig. 9, it is seen that the dependency of the damping to the response amplitude is not monotonic: The damping increases with the magnitude of the response at low amplitude region. For the current damper setup, the damping reaches to maximum at around 0.1 mil. Then, with the amplitude of response further increasing, the damping decreases monotonically and asymptotically. On the other hand, the frequency monotonically decreases with the magnitude of response. It also asymptotically approaches a fixed value as the response magnitude increases. Also, superimposed in Fig. 9 are the FRM results for the average stiffness for each excitation amplitude and show good agreement at low amplitudes and moderate agreement at higher amplitudes. The differences in the methods can be attributed to the different mode shapes for the two experimental setups in Fig. 2 compared to Fig. 6. Since the damping is frequency dependent, a direct correlation for damping cannot be made between the two methods: however, interpolating the FRM results in very close agreement with the transient time domain method.

4 Rotating Tests

The rotating tests were conducted using a longer rotor than shown in Fig. 2. The rotor model of the long rotor is shown in Fig. 10. The imbalance was determined through a balance machine check and was used in the appropriate locations and phases. The

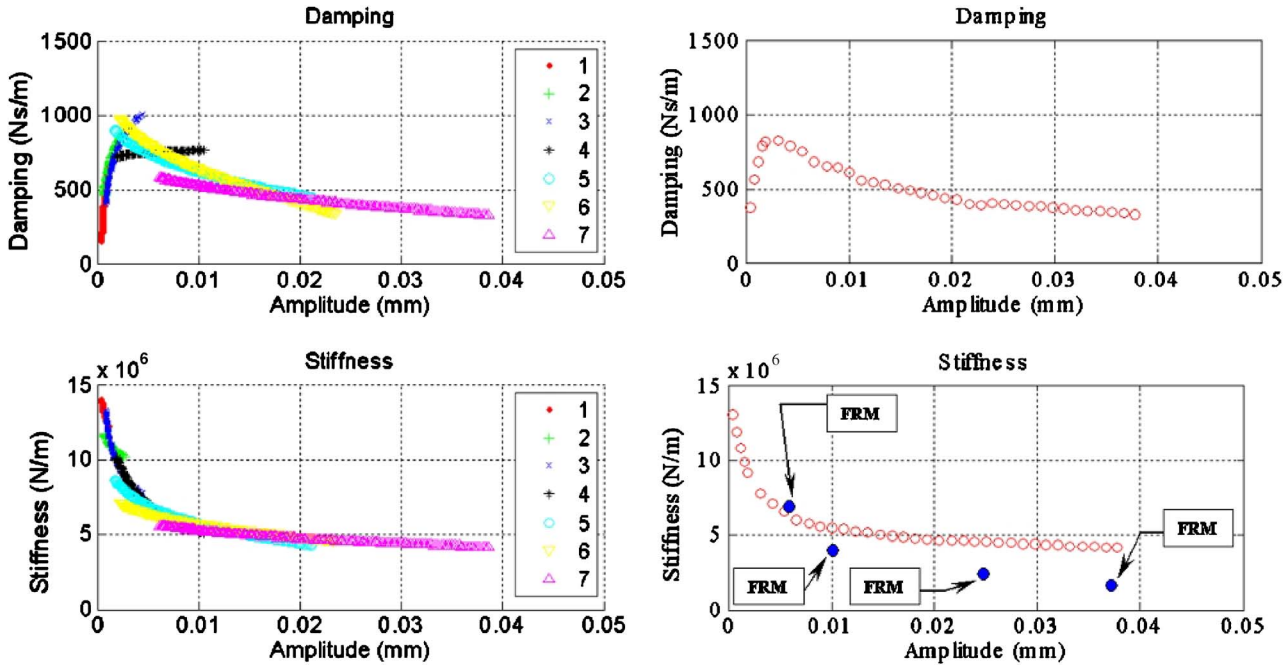

Fig. 9 Amplitude dependency of the damper characteristics

synchronous response to imbalance (Fig. 11) was calculated for Station 8 (motion Probe 3) using the damping and stiffness results from nonrotating testing and shows two well-damped critical speed locations at 11,000 rpm and 24,000 rpm. Since the stiffness and damping coefficients are functions of both frequency and amplitude, the synchronous response calculation required iteration between the vibration amplitude and force coefficient at each rotor speed. An example Bode plot (Fig. 12) for motion Probe 3 shows a rotating test of the long rotor to 40,000 rpm and also has good comparison with the predicted rotordynamics.

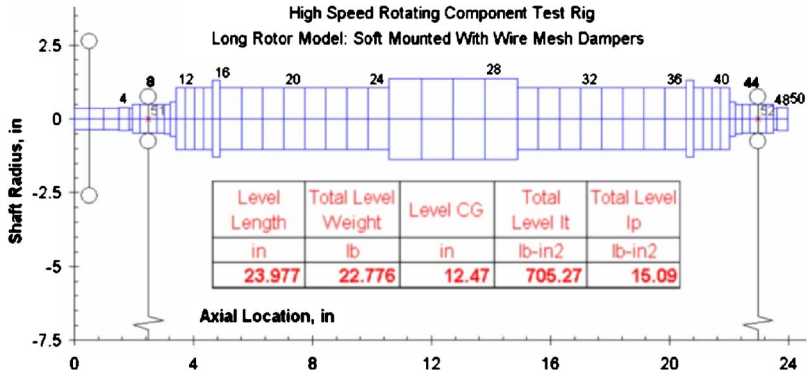

Fig. 10 Rotordynamic model: long rotor configuration

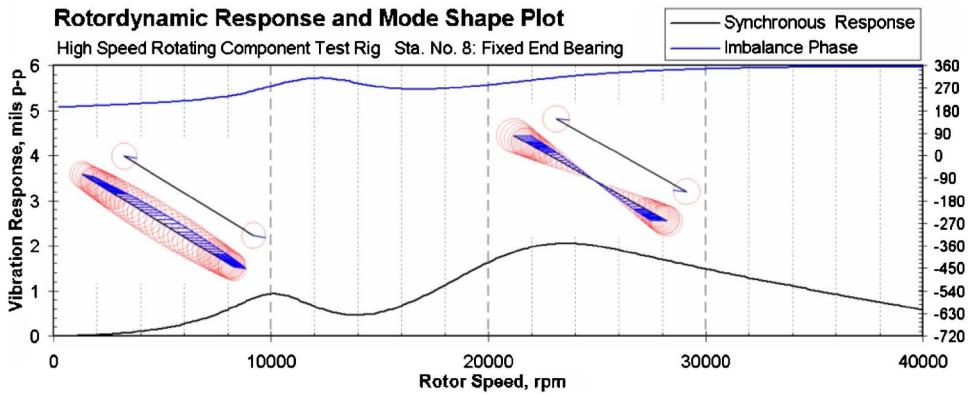

Fig. 11 Predicted rotordynamics: long rotor with integral wire mesh dampers

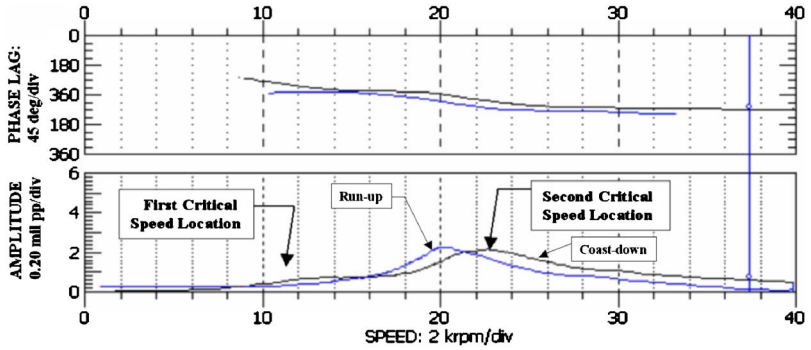

Fig. 12 Measured rotordynamics: fixed end synchronous response to imbalance

5 Concluding Remarks

The present work has been focused on characterizing the nonlinear stiffness and damping of wire mesh dampers, while varying the vibrating amplitude, excitation frequency, and static damper eccentricity. Both the FRM and transient time domain methods revealed similar behavior of the damper stiffness and damping and showed good comparison in coefficient values. It was shown that the static eccentricity had very little influence on the force coefficients, whereas increasing vibration amplitude contributed to decreasing the stiffness and damping. Maximum damping values were shown to exist at lower frequency ranges, making the wire mesh damper compatible with soft mounted rotor-bearing systems. Lastly, high-speed rotating tests were conducted indicating good damping and low vibration through the first two critical speeds. The experimentally measured imbalance response was closely matched to a nonlinear response to imbalance simulation.

References

[1] Della Pietra, L., and Adiletta, G., 2002, "The Squeeze Film Damper Over Four Decades of Investigations. Part I: Characteristics and Operating Features," Shock Vib. Dig., **34**(1), pp. 3–26.

[2] Adiletta, G., and Della Pietra, L., 2002, "The Squeeze Film Damper Over Four Decades of Investigations. Part II: Rotordynamic Analyses With Rigid and Flexible Rotors," Shock Vib. Dig., **34**(2), pp. 97–126.

[3] Childs, D. W., 1978, "Space Shuttle Main Engine High-Pressure Fuel Turbopump Rotordynamic Instability Problem," ASME J. Eng. Power, **100**, pp. 48–57.

[4] Okayasu, A., Ohta, T., Azuma, T., Fujita, T., and Aoki, H., 1990, "Vibration Problems in the LE-7 Liquid Hydrogen Turbopump," *Proceedings of the 26th AIAA/SAE/ASME/ASEE 26th Joint Propulsion Conference*, pp. 1–5.

[5] Ertas, B., Al-Khateeb, E. M., and Vance, J. M., 2004, "Rotordynamic Bearing Dampers for Cryogenic Rocket Engine Turbopumps," J. Propul. Power, **20**, pp. 674–682.

[6] Zarzour, M., and Vance, J., 2000, "Experimental Evaluation of a Metal Mesh Bearing Damper," ASME J. Eng. Gas Turbines Power, **121**, pp. 326–329.

[7] Al-Khateeb, E. M., and Vance, J. M., 2001, "Experimental Evaluation of a Metal Mesh Bearing Damper in Parallel With a Structural Support," ASME Paper No. 2001-GT-0247.

[8] Al-Khateeb, E. M., 2002, "Design, Modeling, and Experimental Investigation of Wire Mesh Vibration Dampers," Ph.D. thesis, Texas A&M University, College Station, TX.

[9] Spring, S. D., Kaminske, M., Leone, S., Drexel, M. V., Ertas, B. H., GE Research Center, Ames, E. C., Agarwal, G., Burr, D., and Brophy, M., 2006, "Application of Compliant Foil Air Bearings for Oil Free Operation of Advanced Turboshaft Engines," *American Helicopter Society 62nd Annual Forum*, May 8–11, Vol. III, pp. 2070–2075.

[10] Murphy, B., Scharrer, J., and Sutton, R., 1990, "The Rocketdyne Multifunction Tester Part I: Test Method," Workshop on Rotordynamic Instability Problems in High Performance Turbomachinery, Texas A&M University, College Station, TX.

[11] Childs, D. W., and Hale, K., 1994, "A Test Apparatus and Facility to Identify the Rotordynamic Coefficients of High Speed Hydrostatic Bearings," J. Am. Inst. Electr. Eng., **116**, pp. 337–334.

[12] Ertas, B., Gamal, A., and Vance, J., 2006, "Rotordynamic Force Coefficients of Pocket Damper Seals," ASME J. Turbomach., **128**(4), pp. 725–737.

[13] Ertas, B. H., Drexel, M., VanDam, J., and Hallman, D., 2008, "A General Purpose Test Facility for Evaluating Gas Lubricated Journal Bearings," Paper No. ISROMAC12–2008-20207.

[14] Bendat, J. S., and Piersol, A. G., 1986, *Random Data: Analysis and Measurement Procedures*, 2nd ed., Wiley, New York.

[15] Boashash, B., 1992, "Estimating and Interpreting the Instantaneous Frequency of a Signal—Part I. Fundamentals," Proc. IEEE, **80**(4), pp. 520–538.

[16] Huang, N. E., Shen, Z., Long, S. R., Wu, M. C., Shih, E. H., Zheng, Q., Tung, C. C., and Liu, H. H., 1998, "The Empirical Mode Decomposition and the Hilbert Spectrum for Nonlinear and Nonstationary Time Series Analysis," Proc. R. Soc. London, Ser. A **454**, pp. 903–995.

[17] Thrane, N., Wismer, J., Konstantin-Hansen, H., and Gade, S., "Practical Use of the Hilbert Transform," B&K Application Note No. bo0437-11.

[18] Feldman, M., 1994, "Nonlinear System Vibration Analysis Using Hilbert Transform—I. Free Vibration Analysis Method FREEVIB," Mech. Syst. Signal Process., **8**(2), pp. 119–127.

[19] Bedrosian, E., 1963, "A Product Theorem for Hilbert Transforms," Proc. IEEE, **51**(5), pp. 868–869.

[20] Allara, M., Filippi, S., and Gola, M., 2006, "An Experimental Method for the Measurement of Blade0root Damping," ASME Paper No. GT-2006-90774.

Scaling Concept for Axial Turbine Stages With Loosely Assembled Friction Bolts: The Linear Dynamic Assessment

J. Szwedowicz
e-mail: jaroslaw.szwedowicz@ch.abb.com

Th. Secall-Wimmel

Thermal Machinery Laboratory,
ABB Turbo Systems Ltd.,
CH-5401 Baden, Switzerland

P. Dünck-Kerst

A. Sonnenschein

Power Generation/Industrial Applications,
Siemens AG,
D-47053 Duisburg, Germany
e-mail: peter.duenck-kerst@siemens.com

D. Regnery
Power Generation/Service Steam Turbines,
Siemens AG,
D-45473 Muelheim/Ruhr, Germany
e-mail: david.regnery@siemens.com

M. Westfahl
Power Generation,
Siemens AG,
D-10553 Berlin, Germany
e-mail: martin.westfahl@siemens.com

In the early 1980s, Siemens developed a last stage fast rotating condensation blading (SK) blade with strongly twisted and tapered profiles for industrial condensing steam turbines, which operate with variable speed under high steam mass flow and excessive condensing pressures. To suppress alternating stresses of the lowest blade resonances, conical friction bolts are loosely mounted at the upper parts of adjacent airfoils. Also, these bolts couple the rotating blades, since steam excitation is lower than the friction threshold force on the bolt contacts. These coupling and damping capabilities were proven experimentally for the smallest SK blade at the test rig of the real turbine. By considering the similar mechanical and aerodynamic characteristics based on the tested smallest airfoil, the entire SK-blade family has been scaled up for reliable utilization in more than 500 industrial turbines operating for diverse ranges of power and speed. A recent trend to very large compression units, like gas to liquids, acid terephtalic, or methanol plants, imposes a need for further enlargement of the SK-blade family and its friction bolt, whose mechanical properties have been proven experimentally for the smallest airfoil. In this paper, the mechanical capabilities of the smallest and large SK blades coupled by the bolts are verified by using the finite element (FE) method. The static analyses with friction sliding on airfoil interfaces and the linear dynamic behavior of tuned disk assemblies are considered. The FE mesh quality and the proper boundary conditions at the radial fork root are accomplished by getting good agreements between the computed and measured resonance frequencies of the large freestanding blade at standstill. The validated mesh refinement and root boundary conditions are used further in all numerical FE analyses. For the large SK-disk assembly under spin-pit conditions, the obtained FE results are in very good agreement with the experimental Campbell diagrams, which are measured with the three gauges that also identify the stick-slip and stuck bolt's contact conditions. Concerning the gauge outputs and the FE steady-state blade resonances computed for the analytically determined air jet excitation, the experimental spin-pit results demonstrate that the bolts are mainly in stuck contact conditions. Only in very narrow frequency ranges around resonance peaks, microslips on the bolts occur due to the resonance amplification of blade vibrations. This is proven indirectly by comparison of the overall damping values evaluated from the blade resonances at standstill and in the spin pit. The described linear dynamic concept assesses properly static stresses and free vibrations of the scaled disk assembly with friction bolts. For the steam excitation, which generates dynamic contact reactions bigger than the friction threshold forces, the realistic blade responses need to be obtained from the blade simulation with friction (Szwedowicz, J., Secall-Wimmel, T., and Duenck-Kerst, P., 2007, "Damping Performance of Axial Turbine Stages With Loosely Assembled Friction Bolts; the Non-Linear Dynamic Assessment; Part II," Proceedings of ASME Turbo Expo 2007, Montreal, Canada, May 14–17, ASME Paper No. GT2007-27506). [DOI: 10.1115/1.2838995]

Introduction

In spite of contemporary computer aided design (CAD), computational fluid dynamics (CFD), and finite element (FE) computer systems accelerating engineering work, blade design remains still a time-consuming engineering process, which might involve many calculation loops for satisfying all required objectives of the new turbine stage. The confident turbine design, which has accumulated many hours of reliable operation, is frequently scaled to sizes of the turbine unit demanded by market. The comparable scaling design philosophies have been developed independently by different companies like for GE gas turbines [1] or for ALSTOM GT26 gas turbine [2], scaled up from the GT24 unit designed for 60 Hz market, so that their compressors are principally identical on a 1.2 scale basis. The evaluation of the newest Siemens W501ATS from the W501 gas turbine [3] is based on the scaling concept. Also, Mitsubishi Heavy Industries show good experiences with the upgraded M701G2 compressor, which is a scale design of M501H unit [4]. For many years, the Brown Boveri modular concept had been used for developing different industrial steam turbines [5]. Siemens HE- and KN-modular design concepts [6] are still applied for lower and upper power ranges of steam turbine product lines. These modular concepts provide significant flexibility in the design process and fulfill customers' demands for fast delivery periods and moderate prices with the proven performance and reliability. The scaling of unsteady pressures allows for rapid forced response computations of

Manuscript received July 3, 2007; final manuscript received November 9, 2007; published online April 3, 2008. Review conducted by Dilip R. Ballal.

the Rolls–Royce turbine blades for a wide operating range. Green and Fransson [7] find the error induced by pressure scaling of the order of 6%, which is acceptable for designers. But, too rapid scale-up/down of turbine components without sufficient numerical or experimental verification can lead to equipment failures and unexpected maintenance costs [8,9]. Reimann [10] presents a list of items and technical challenges, which have to be proven by scaling steam turbines. For the scaled-up low pressure last turbine stages, the bending pressure and excitation forces can be responsible for severe loading of the rotating airfoil, which should be validated in the design process.

For industrial condensing steam turbines operating at variable speed, Siemens has developed a last stage fast rotating condensation blading (SK)-blade family in the early 1980s. The principal goal was to design a robust blade profile for highest reliability and good performance, which allows the operation in resonances under high steam mass flow and excessive condensing pressures. To suppress resonance stresses through friction dissipation, loosely fitted conical bolts are applied to the upper part of adjacent airfoils. In the early 1980s, these capabilities were experimentally investigated and validated for the smallest SK blade at a setup of the real turbine unit. The tapered and twisted geometry of the smallest SK blade has been scaled under consideration of the similar mechanical and aerodynamic characteristics. The entire scaled-up SK-blade family has proven its reliability in more than 500 industrial turbine units arranged for different powers and speeds. In past years, there could be seen a trend of very large compression units, like gas to liquid (GTL), acid terephthalic (PTA), or methanol plants. Therefore, the SK-blade family has been extended to larger airfoils using the well established scale concept based on the smallest SK unit.

In this paper, the FE methodology, which is implemented in the ordinary design process of the scaled SK blades with friction bolts, is explained in detail. Due to nonlinear coupling effects between the bolt and airfoil, the design process has to be divided into the linear (presented in this paper) and the nonlinear part [11]. By using commercial FE program ABAQUS [12], the elaborated nonlinear computational process of the rotating bladed disk with loosely coupled conical bolts is novel in the literature and is developed straightforwardly for engineering requirements. For excitation generating dynamic reactions on the bolt contact smaller than the friction threshold forces, the major objective is to calculate the reliable FE static stresses and Campbell diagrams in the entire operation range of the SK blades. These blades and bolts must be represented with moderate FE mesh sizes, which are computable in acceptable time with typical computers used in industry.[1] The reliability of the numerical results is proven with the experimental data from different blade measurements at standstill and under spin-pit conditions. Because the mode shapes of the blades are very sensitive in terms of contact conditions at the bolts, the special arrangement of three strain gauges is used, besides measuring blade resonances of the three lowest eigenfamilies, additionally for identifying stuck-slips or stuck contact conditions on the bolts. This successful gauge instrumentation is confirmed by very good agreements of the computed Campbell diagrams with the measured ones. In the literature, strain gauge applications for shrouded disks (e.g., Ref. [13]) or for freestanding blades with the under-platform dampers (e.g., Ref. [14]) can be mainly found. For these blades, their mode shapes do not depend so strongly on the microcontact motions on the shroud or the under-platform damper, as it is for the SK blades with the friction bolts.

For good agreement of the numerical results obtained with the experimental data, all scaling design criteria of the SK blades are confirmed for static stresses, eigenfrequencies, and excitabilities given in Campbell diagrams. The real blade responses, which depend on the excitation amplitudes, need to be obtained from the nonlinear dynamic simulation with friction effects on the bolts [11].

[1]All computations were done on IBM computer with two CPUs (EM64) with 8 Gbyte RAM with LINUX SLES 9.0 system.

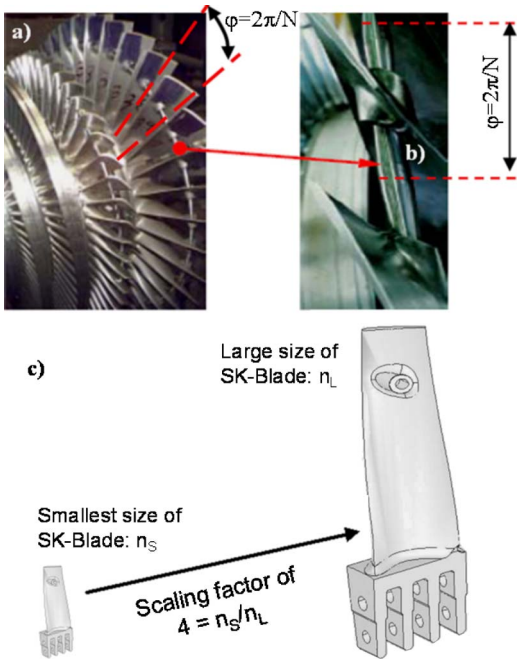

Fig. 1 (*a*) **The last LP stage of industrial Siemens steam SK turbine with** (*b*) **friction bolts, where the angle** $\varphi=2\pi/N$ **illustrates the geometrical periodicity of the disk sector for** *N* **number of blades in the row;** (*c*) **the considered scaled-up SK blades**

Design Concept of SK Blades

The last low pressure (LP) steam turbine SK stage, shown in Fig. 1, has strongly twisted and tapered airfoils. The blade is bolted to the rotor through four fingers of its radial fork root with two conical pins. In the upper airfoil part, friction bolts with conical ends are loosely fitted within the cylindrical holes of adjacent blades according to the given assembly tolerances.

By increasing the rotational speed, blades untwist themselves and are simultaneously coupled by the friction bolts. During operation, the blades are elastically coupled by these bolts, which become friction dampers, in case that the excitation exceeds the threshold friction forces on the bolt's interface. Then, the resonance stresses of the SK blades operating with variable rotational speed are effectively reduced to a level below the allowable stress. At the setup of the smallest turbine unit in the early 1980s, these damping capacities were developed experimentally to find the optimal mass of the bolt [15]. This design concept, based mainly on the constant speed at the airfoil tips, has been used to generate a family of geometrical similar SK blades. Here, the large and smallest turbine stages, which differ from each other by a scale factor of 4, are considered (Fig. 1(*c*)).

Theoretical Model of Blade Dynamics

For rotational speed Ω and given temperature distribution T, the well-known static matrix equation of the rotating turbine blade is expressed with the cyclic FE model by [16]

$$[\mathbf{K}(\Omega,T,q,\sigma,C_\mu)]\{q\}=\{F_A\}+\{F(\Omega)_c\}+\{P_0\} \tag{1}$$

where F_A, $F(\Omega)_c$, and P_0 denote the assembly forces at the root pins, the centrifugal load, and flow pressure acting on the blade, respectively. For the identical deformations on the circumferential sides of the rotor and bolts (Fig. 2), and by including centrifugal stiffening effects, the stiffness matrix $[\mathbf{K}]$ depends on temperature

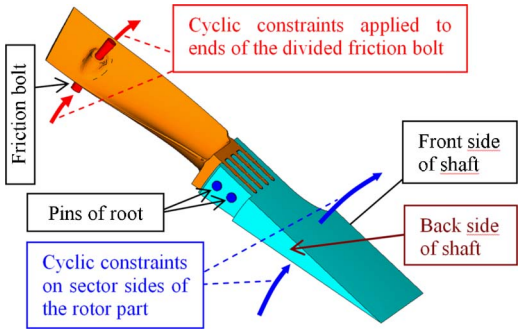

Fig. 2 Cyclic sector model representing one SK blade, the rotor part, and one bolt divided into two symmetrical halves

T, rotational speed Ω, deformation q, stress σ, and friction contact forces C_μ. These friction forces on bolt, pin, and rotor groove depend on the friction coefficient μ and reaction contact forces, which are generated by the centrifugal load $F(\Omega)_c$.

By increasing the rotational speed Ω from standstill up to the speed of interest, Eq. (1) has to be solved iteratively in terms of the deformations q, stresses σ spatial moving of the airfoil, and friction sliding on the bolt contacts. Therefore, the bolt contacts have to be represented with a fine FE mesh assuring the reliable numerical results. According to the previous measurement [15], the rotor part has a minor impact on frequencies of the smallest SK blades. Then, the disk coupling affects minor airfoil deformations. After solving Eq. (1), the FE contact area, which is expressed by the number of nodes in contact between the airfoil and bolt, determines the influence of the bolt coupling on vibrations of the rotating disk assembly. Similar considerations for the shrouded disk assemblies are given in Refs. [16,13,17].

In reality, the bladed disk is a system of N blades. Their geometries differ slightly from each other due to manufacturing tolerances, resulting in the mistuning effect. In the design process, the blade mistuning is not a deterministic quantity and therefore, the tuned system of the SK blades has to be taken into consideration for the numerical assessment of the static and dynamic behavior of the blade under design. Then, by using the cyclic theory [18] and neglecting viscous damping, forced vibrations of the SK-bladed disk excited by nonuniform pressure distribution $P(\alpha)$ along the circumferential direction α are represented for the nth nodal diameter by

$$[\mathbf{M}(e^{j2\pi n/N})]\begin{Bmatrix}\{\ddot{z}\}_n^{(\ell)}\\ \{\ddot{q}\}_n\end{Bmatrix}+[\mathbf{K}(C_\mu,e^{j2\pi n/N})]\begin{Bmatrix}\{z\}_n^{(\ell)}\\ \{q\}_n\end{Bmatrix}=\{P(\alpha)\}\quad j=\sqrt{-1} \tag{2}$$

In Eq. (2), the nodes in vector $\{z\}^{(\ell)}$, which are located on the (ℓ)th circumferential side of the cyclic FE model, represent the boundary deformations between the ℓth and $(\ell+1)$th disk sectors with the cyclic constraint equations as

$$z_{\text{bolt}}^{(\ell+1)}=z_{\text{bolt}}^{(\ell)}e^{j2\pi n/N},\quad z_{\text{rotor}}^{(\ell+1)}=z_{\text{rotor}}^{(\ell)}e^{j2\pi n/N} \tag{3}$$

where the nodal diameter number n equals $\{0,1,2,\ldots,(N-1)/2\}$ for the odd number N of the SK blades in the stage. For each nth nodal diameter, the global mass $[\mathbf{M}]$ and stiffness $[\mathbf{K}]$ matrices are arranged individually with respect to the generalized vector $\{\phi_n\}=\{\{z_n\},\{q_n\}\}^T$ of vibrations around the centrifugally deformed blade. For the considered steady-state dynamics, first the free vibrations need to be computed by neglecting the pressure $\{P(\alpha)\}$ and substituting harmonic responses $\{\phi_{i,n}\}\exp(j\omega_{i,n}t)$ in Eq. (2) from

$$([\mathbf{K}(\Omega,n,C_{\mu=\infty})]-\omega_{i,n}^2[\mathbf{M}(n)])\{\phi_{i,n}\}=0 \tag{4}$$

where each eigenform i of the nodal diameter n (besides $n=0$ and $n=N/2$) is determined with two identical eigenfrequencies $\omega_{i,n}$ with their two mode shapes $\{\phi_{i,n}\}_c$ and $\{\phi_{i,n}\}_s$ of the disk assembly, which are orthogonal to each other. For sticking contact conditions (see $C_{\mu=\infty}$ in Eq. (4)) imposed on those nodes that are in contact after the static calculation, Eq. (4) is solved linearly. In other words, this free vibration analysis corresponds to weak excitations, which induce dynamic reaction forces on the contact smaller than the friction threshold load.

The excitation spectrum is obtained from the circumferential pressure $\{P(\alpha)\}$, which is known either from flow measurements or from unsteady CFD computations (e.g., Ref. [19]). The pressure $\{P(\alpha)\}$ is decomposed harmonically by complex Fourier transformation for K equidistant points describing the circumferential pressure distribution from 0 deg up to 360 deg by

$$F_k=\sum_{r=0}^{K-1}P(\alpha_r)e^{-j(2\pi/K)rk}\quad k=0,1,\ldots,K \tag{5}$$

where $F_k=F_{k,c}+jF_{k,s}$ is the complex Fourier coefficient (excitation amplitude) of the kth engine order. At the particular circumferential angle α_δ of the excited node δ on the blade contour, the excitation amplitude is given by $F_{k,\alpha}=F_{k,c}\cos(k\alpha_\delta)+jF_{k,s}\sin(k\alpha_\delta)$, where $k=0,1,2,\ldots,\infty$.

For the excitation amplitudes $\{F_k\}$ and two FE eigenfrequencies $\omega_{i,n}$ with their mass-normalized eigenforms $\{\Phi^\circ\}_{i,n}=\{\overset{\circ}{\phi}_{i,n}\}_c+j\{\overset{\circ}{\phi}_{i,n}\}_s$, the forced response analysis of the coupled blade is performed in the modal domain for each nodal diameter n separately. Then, Eq. (2) is redefined with the modal steady-state response equation for resonance $\omega_{i,n}$ and the modal damping ratio $\xi_{i,n}$ by [20]

$$m_{i,n}\ddot{u}_{i,n}+2\omega_{i,n}\xi_{i,n}\dot{u}_{i,n}+k_{i,n}u_{i,n}=f_{i,n}e^{jk\Omega t} \tag{6}$$

where $u_{i,n}$ is the modal displacement and

$$f_{i,n}=\{\Phi^\circ\}_{i,n}^{*T}\{F_{k,\alpha}\}\quad\text{modal force} \tag{7}$$

$$m_{i,n}=\{\Phi^\circ\}_{i,n}^{*T}[M(n)]\{\Phi^\circ\}_{i,n}=1.0\quad\text{modal mass} \tag{8}$$

and

$$k_{i,n}=\{\Phi^\circ\}_{i,n}^{*T}[\mathbf{K}(\Omega,n,C_{\mu=\infty})]\{\Phi^\circ\}_{i,n}=\omega_{i,n}^2\quad\text{modal stiffness} \tag{9}$$

of the cyclic FE blade model and $\{\Phi^\circ\}_{i,n}^{*T}$ is the conjugate transposed vector. For the harmonic response $u_{i,n}\exp(jk\Omega t)$, the response η_δ at a particular degree of freedom of an arbitrary node δ of the blade vibrating with the nth nodal diameter is calculated in the Cartesian system from

$$\eta(t)_{\delta,n}=\left(\sum_{i=1}^{I}\frac{\Psi_{i,n,\eta_\delta}\overset{\circ}{f}_{i,n}[\Delta\omega_{i,n,k}+j\Delta\xi_{i,n,k}]}{\Delta\omega_{i,n,k}^2+\Delta\xi_{i,n,k}^2}e^{-j\gamma_{i,n}}\right)e^{jk\Omega t} \tag{10}$$

$$\gamma_{i,n}=\tan^{-1}\left(\frac{\Delta\xi_{i,n,k}}{\Delta\omega_{i,n,k}}\right)\quad\text{phase delay of response } u_{i,n} \tag{11}$$

$$\Delta\omega_{i,n,k}=\omega_{i,n}^2-(k\Omega)^2\quad\text{frequency participation} \tag{12}$$

and

$$\Delta\xi_{i,n,k}=2\xi_{i,n}\omega_{i,n}k\Omega\quad\text{dissipation participation} \tag{13}$$

In Eq. (10), $\overset{\circ}{\Psi}_{i,n,\eta\delta}$ is the mass-normalized mode shape of displacement $\Phi_{i,n}$, stress $\sigma_{i,n}$, or strain $\varepsilon_{i,n}$ of node δ for the degree of freedom of interest. Here, the strain mode shapes are taken into account for computing resonance responses at gauges of the measured large SK blades.

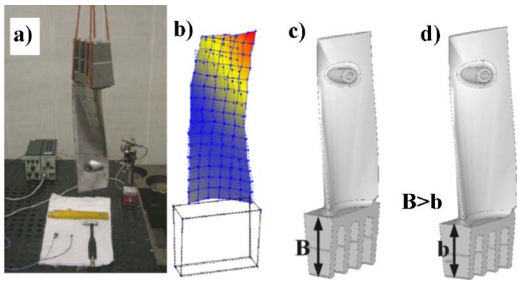

Fig. 3 (*a*) **Siemens' hammer setup with the airfoil measured at** (*b*) **100 points for the mode shape identification of the large SK blade with** (*c*) **"long" and** (*d*) **"short" roots**

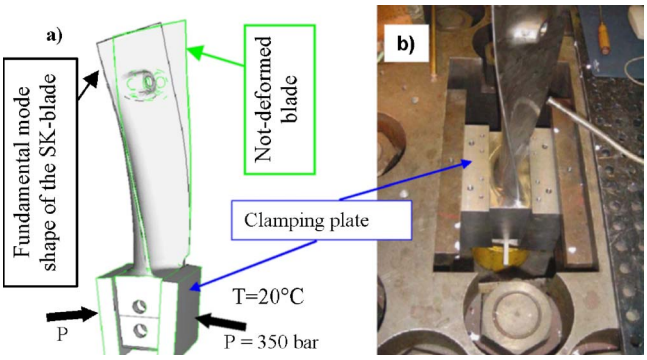

Fig. 4 (*a*) **FE model of** (*b*) **Siemens' setup for hydraulic clamping of the airfoil root on its circumferential sides**

Quality Assessment of Finite Element Airfoil Meshes

The accuracy of the FE results can be dealt with the accessible known refinement techniques (e.g., Ref. [21]) that lead usually toward very fine meshes at regions with high strain/stress gradients. In the case of SK blades, very fine meshes would be required on the contact interfaces of the bolt and root pins. For computers used in industry,[1] unacceptable long computational time in the design process would be demanded for the blade simulation with friction.

To find the most adequate mesh for the twisted and tapered SK airfoil, modal measurements [22] are first done for the large blade with unrestrained (free-free) boundary condition (Fig. 3(*a*)). For the evaluated 100 measuring points (Fig. 3(*b*)), oscillations primarily occur in the thinner upper part of the blade in the region for the bolt coupling. This measurement is simulated by the MECHANICA[2] code in 2005, which is based on the "P" FE technique. The P element automatically increases the order of its shape functions, since the numerically estimated elemental error is higher than the allowable value. For the eight lowest mode shapes of the large blade with "long" roots (Fig. 3(*c*)), the maximum relative error of the computed eigenfrequencies is below 1.4% with respect to the experimental frequencies measured up to 1.8 kHz. The acceptable value of these relative errors (Table 1) should be below 3.0% for the considered minimum mistuning ratio of the smallest freestanding SK airfoils measured at standstill [23].

As the large blade with "short" roots (Fig. 3(*d*)) is not measured, the P-FE solution is considered as the reference results for the ABAQUS outputs. For reducing the relative numerical error, the ABAQUS FE, based on the H-FE approach, requires the mesh refinement in regions of high strain/stress gradients. For the obtained maximum relative frequency error below 1.1% (Table 2), the most favorable H-FE grid is determined for meshing all SK blades for further numerical simulations.

Contact Boundary Conditions at Root

For right FE modeling of boundary conditions at the fork-shaped root, the large SK airfoil is clamped hydraulically on its circumferential root sides at the setup (Fig. 4). Up to 1.4 kHz, the lowest resonance frequencies are measured under an acting pressure of 350 bars. The experimental data and P-FE and H-FE results of the large blade with short root (Fig. 3(*d*)) are compared in Table 3. The maximum relative error of the H-FE solution is below 1.4% for the six lowest mode shapes. The P-FE frequencies differ from the measurement up to 4.3%, because the clamping plates are not considered, as it is simulated with small sliding contact conditions in the H-FE model (Fig. 4(*a*)). The rigidly clamped nodes on the circumferential root sides of the P-FE model overestimate the real boundary conditions in the test rig.

The proven FE refinement of the large blade is used for analogous FE representation of the smallest SK airfoil. Then, frequencies of the smallest airfoil are calculated for the same boundary conditions of the hydraulic test rig. The FE frequencies of both airfoils differ from each other between 4.05 and 4.08 (Table 4), which result in the relative errors between 1.2% and 2.1% in relation to a scaling factor of 4. These acceptable small dissimilarities are caused mainly by slight differences in geometry of both airfoils.

[2]The MECHANICA code cannot be applied for nonlinear problems with large frictional sliding on contacts like the analyzed SK blades.

Table 1 Relative errors $\delta f_i=(f_{exp,i}-f_{P\_FEM,i})/f_{exp,i}$ between the experimental and P-FE results of the unrestrained large blade with "long" root (Fig. 3).

Large SK blade with "long" root (Fig. 3(*b*))	δf_1 (%)	δf_2 (%)	δf_3 (%)	δf_4 (%)	δf_5 (%)	δf_6 (%)	δf_7 (%)	δf_8 (%)
Relative frequency error between the measurement and FE MECHANICA results	0.46	1.20	1.11	0.32	−0.81	1.39	−0.20	−0.07

Table 2 Relative errors $\delta f_i=(f_{P\_FEM,i}-f_{H\_FEM,i})/f_{P\_FEM,i}$ between the P-FE and H-FE solutions of the unrestrained large blade with "short" root (Fig. 3(*d*))

Large SK blade with "short" root (Fig. 3(*d*))	δf_1 (%)	δf_2 (%)	δf_3 (%)	δf_4 (%)	δf_5 (%)	δf_6 (%)	δf_7 (%)	δf_8 (%)
Relative frequency error between the P-FE Mechanica and H-FE ABAQUS results	1.03	0.63	0.27	0.56	0.14	−0.07	−0.06	0.31

Table 3 Differences of the P-FE and H-FE frequencies with the measured resonances for the large blade with "short" root clamped by a pressure of 350 bars (Figs. 3(*d*) and 4)

Large SK blade with "short" root (Fig. 3(*d*))	δf_1 (%)	δf_2 (%)	δf_3 (%)	δf_4 (%)	δf_5 (%)	δf_6 (%)
Relative frequency error between the P-FE MECHANICA and experimental (Fig. 4(*b*)) results	−1.31	2.52	0.00	4.27	0.79	2.88
Relative frequency error between the H-FE ABAQUS and experimental (Fig. 4(*b*)) results	−0.42	0.39	0.47	0.65	−0.06	1.36

To prove possible centrifugal boundary conditions at the fork-shaped root with four fingers, the large airfoil is assembled to the test rig by two tight conical pins. The blade frequencies are measured for a radial load S of 270 kN acting on each guide bolt, as illustrated in Fig. 5.

The load S induces the axial and radial deformations of the fork root, which comes into contact with the grooves of the setup through both pins and outer surfaces of root fingers. For the experimental friction coefficient of 0.15, static deformations of the FE blade model at the setup are computed first to find contact conditions on the fingers and pins. Then, the FE natural frequencies are calculated and compared with the eight lowest experimental resonances. The best agreement between the numerical and experimental results (Fig. 6) is obtained for the contact FE model, shown in Fig. 5(*b*), in which boundary conditions on the second and third root fingers are neglected in the nonlinear FE static computation for saving computational time. Possible contact on these fingers would have minor influence on the blade frequencies in relation to the coupling condition on the outer interfaces of the first and fourth fingers.

The three lowest FE frequencies of interest (Fig. 6) differ less than 2.7% from the experimental results. For the higher FE modes, the allowable error of 3% is exceeded due to bending deformations of root pins under acting loads S (Fig. 5(*b*)). These deformations relieve contacts at ends of both pins, which are not simulated exactly enough by the used mesh refinement at the pin ends. Also, the FE model represents the real geometry of the rotor part (Fig. 5(*b*)), which differs from the set-up geometry (Fig. 5(*a*)).

For the proven contact model of the fork-shaped root, the frequencies of the large SK-disk assembly are computed at standstill in the spin-pit bunker. The FE results are in very good agreement with the measured frequencies. For all considered eight lowest modes up to 2 kHz, the maximum relative frequency error is below 2.4%. For eight measured blades without friction bolts, the mistuning ratios equal 1.4%, 2.7%, and 1.3% for the three lowest frequencies (Fig. 7), respectively.

Static and Free Vibration Analysis

For the validated FE mesh and boundary contact conditions with friction, the centrifugal static analyses (see Eq. (1)) are performed for the smallest and large blades at their nominal speeds and ambient temperature. The computed stresses of both blades coupled by the friction bolts are identical to each other (Fig. 8). Only negligible differences can be noticed in the lower part of their rotors due to slight geometrical dissimilarities. The computed clearances at the bolt ends for the smallest and large blades are shown in Fig. 9. In the design process, this FE analysis confirms the allowable tolerances of the scaled bolts made of different alloys.

In Fig. 10(*a*), the FE normal contact stresses are shown for the bolt of the large blade at its nominal speed. For low speeds, this contact reduces to edge connections at ends of the bolt, as it is illustrated in Fig. 10(*b*) for 25% of the nominal speed. This variable blade coupling through bolts has an influence on the eigenfrequencies of the bladed disk, given in the Campbell diagram. The numerical Campbell diagram is determined from the nodal diameter curves (Fig. 11) obtained from the free vibration calculations (see Eq. (4)) at different rotational speeds.

The FE natural frequencies of the freestanding and coupled large blades are compared to each other in the Campbell diagram in Fig. 12, where a coupling effect of bolts on blade frequencies begins above 50% of the nominal speed. The bolt connection shifts frequencies of the freestanding blade from the third (see $k=3$ in Fig. 12) above the sixth harmonic excitation. Due to the geometry of the turbine outlet after the last stage of the SK blades, crucial excitations with the sixth engine order cannot be excluded entirely. Therefore, the bolt mass is optimized in this manner that bolts can operate as friction dampers, since tangential dynamic reactions on the bolt contact exceed the friction threshold forces, which depends on the centrifugal load and friction coefficient. For the smallest SK blades, this concept has been confirmed experimentally [15] as well as empirically by long experience with reliable operation of different scaled SK blades. The efficiency of the bolt coupling is also demonstrated in the computed nodal diameter curves at 50% and 100% of the nominal speed. In the excitation region indicated by dashed lines in Fig. 11, the frequencies of the first, second, and third blade eigenfamiles increase, due to the centrifugal effect and the bolt coupling, about $\Delta\omega_1=41\%$ (weak bending), $\Delta\omega_2=98\%$ (hard bending), and $\Delta\omega_3=37\%$ (torsion). By increasing speed from 50% to 100% of the nominal speed, the centrifugal effect increases the first, second, and third eigenfrequencies of the freestanding blade about 16%, 7%, and 2% (Fig. 12), respectively.

Table 4 Comparison of the lowest frequencies of the smallest and large blades clamped by a pressure of 350 bars (Fig. 4)

Both SK blades for boundary conditions at hydraulical setup for a pressure of 350 bars, $T=20°C$ (Fig. 4(*b*))	δf_1 (%)	δf_2 (%)	δf_3 (%)	δf_4 (%)	δf_5 (%)	δf_6 (%)
Relative frequency error between the large and smallest SK blades	−1.15	−1.98	−1.17	−2.07	−1.95	−1.78
Frequency relation of the smallest to large SK blade	4.05	4.08	4.05	4.08	4.08	4.07

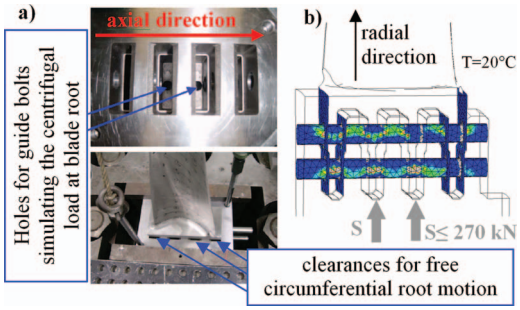

Fig. 5 (*a*) Siemens' setup for hydraulic pressing of two guide bolts to the second and third airfoil fingers of the radial root; (*b*) the FE normal contact stresses, where blue color refers to noncontact state

For eigenfamily i vibrating with nodal diameter n, the frequency scaling factor $\upsilon(\Omega\%)_{i,n}$ between both blades is expressed by

$$\vartheta(\Omega\,\%)_{i,n} = \frac{\omega_{i,n}^{/S/}}{\omega_{i,n}^{/L/}} \quad i=\{1,2,3\} \quad n=0,1,2,\ldots,\frac{N-1}{2} \tag{14}$$

and

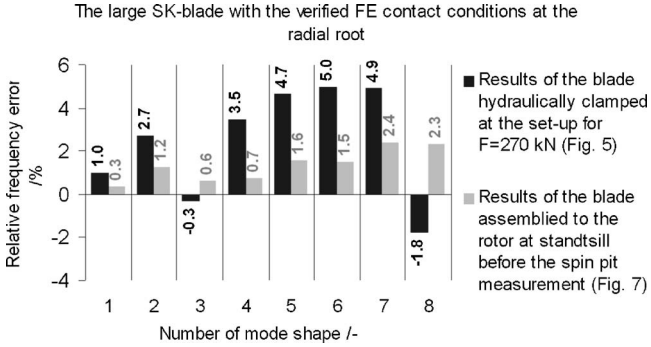

Fig. 6 Relative errors of the FE blade frequencies computed with the contact root model illustrated in Fig. 5(*b*) in relation to the measurements at the hydraulic setup (Fig. 5(*a*)) and at standstill (Fig. 7) before spin-pit tests

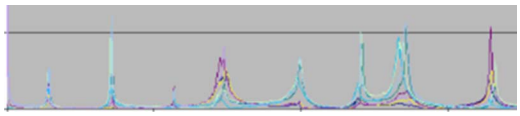

Fig. 7 The experimental resonance frequencies of eight large SK blades assembled to the rotor without bolts at standstill before the spin-pit test (T=20°C)

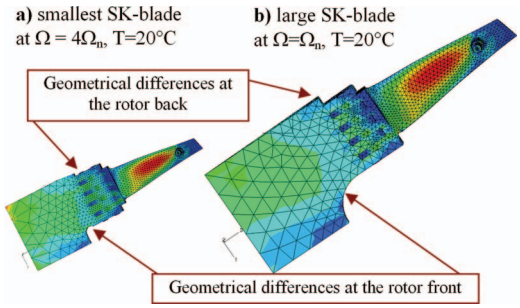

Fig. 8 Comparison of the centrifugal stresses between the smallest (*a*) and large (*b*) blades coupled by the friction bolts at their nominal speeds and T=20°C

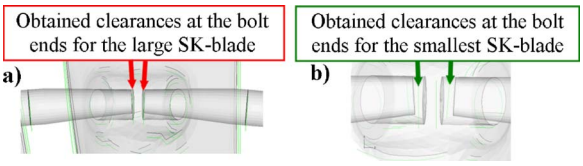

Fig. 9 Computed final clearances at the ends of the bolts for (*a*) their maximum and (*b*) nominal dimensions of the large and small blades at their nominal speeds

$$\Omega\,\% = \frac{100}{\Omega_{\text{nominal}}^{/S/}}\sqrt{\upsilon_0\Omega^{/L/}\Omega^{/S/}} \quad \text{if } \Omega^{/S/} \equiv \vartheta_0\Omega^{/L/} \tag{15}$$

where υ_0 is the design scaling factor, which equals 4. The $\Omega_{\text{nominal}}^{/S/}$ denotes the nominal speed of the smallest SK blade, whereby $\Omega^{/S/}$ and $\Omega^{/L/}$ are arbitrary turbine speeds of the smallest and large blades, respectively. Since $\Omega^{/S/}=\upsilon_0\Omega^{/L/}$, the frequency scaling factors $\upsilon(\Omega\%)_{i,n}$ are obtained with the FE frequencies $\omega_{i,n}^{/S/}$ and $\omega_{i,n}^{/L/}$ of the smallest and large blades computed at their rotational speeds $\Omega^{/S/}$ and $\Omega^{/L/}$, respectively. In the entire range of speed, all determined frequency scaling factors υ differ slightly from the design scaling factor υ_0 of 4, as it is shown in Fig. 13. From the designing point of view, these discrepancies are acceptable and they are caused by minor differences in the blade geometries, FE meshes (Table 4), and bolt dimensions (Fig. 10).

Results From the Spin-Pit Measurements

For the air jet excitation, which induces usually small blade response amplitudes, the spin-pit measurement of the large SK blades (Fig. 21(*a*)) is considered principally as the experimental proof of the coupling capabilities of the friction bolts. Regarding the real measuring condition with very fine oil moisture coming from bearings, a thin oil film might be spread on the bolts. Then,

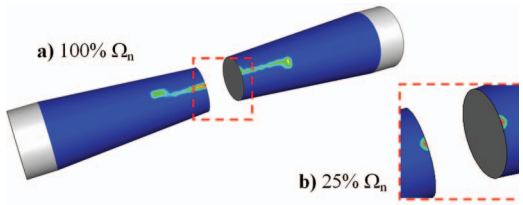

Fig. 10 FE normal contact stresses on the bolt of the large blade at (*a*) 100% and (*b*) 25% of its nominal speed Ω_n

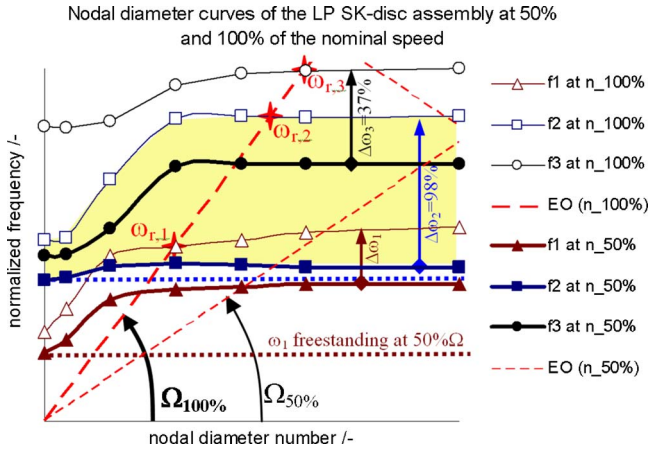

Fig. 11 Coupling bolt effect demonstrated by a frequency increase of the large SK disk assembly at 50% and 100% of the nominal speed $n\equiv\Omega_n$, where $\omega_{r,1}$, $\omega_{r,2}$, and $\omega_{r,3}$ are the resonances at $\Omega_{100\%}$

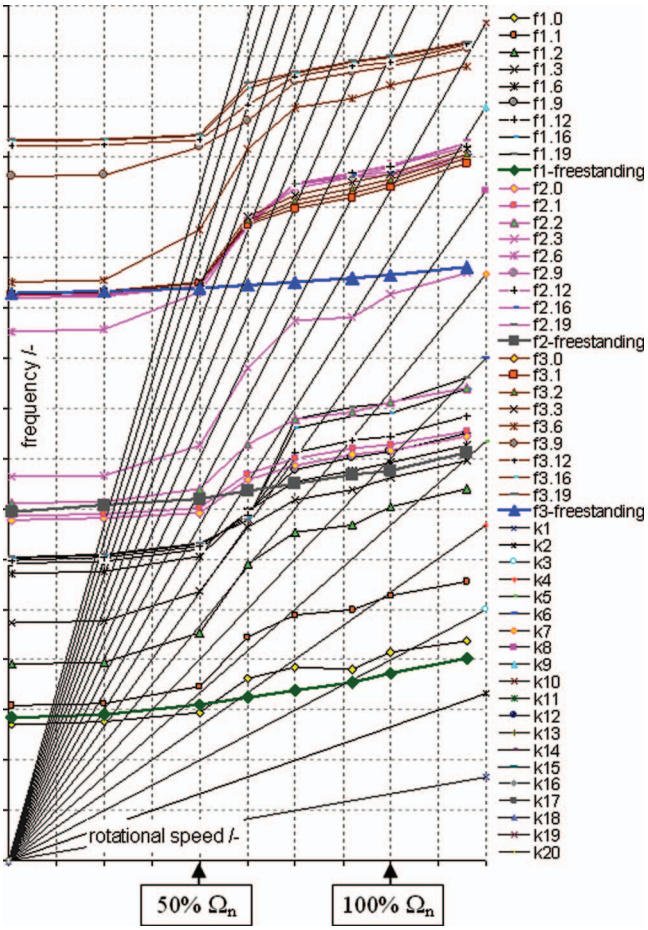

Fig. 12 The numerical Campbell diagrams of the freestanding (f_i is the ith eigenfamily) and coupled large SK blade in the spin pit, where $f_{i,n}$ means the eigenfamily i vibrating with the nodal diameter n, and $k=\{1,2,\ldots,\infty\}$ is engine order

even small excitation loads of the air jet acting at the airfoil tip (Fig. 21(*b*)) might cause microslips on the bolt contacts in very narrow frequency ranges of the excited blade resonances. Therefore, favorable positions of 12 strain gauges need to be determined not only for measuring blade resonances but also for identifications of possible sticking, stick-slip, or sliding contact conditions on the bolts.

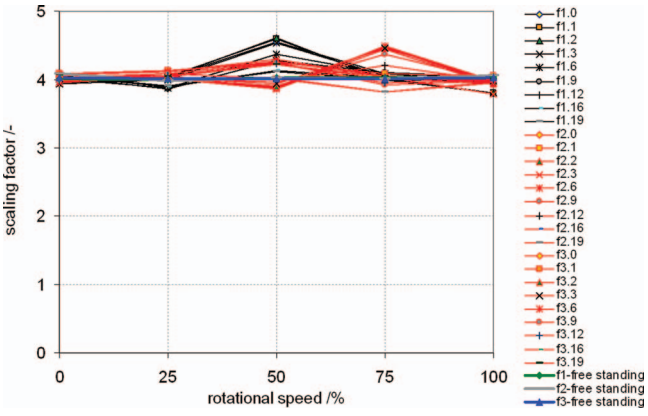

Fig. 13 Validation of the frequency scaling factors determined from the FE spin-pit Campbell diagrams of the smallest and large SK blades (Fig. 12), where the design scaling factor v_0 equals 4

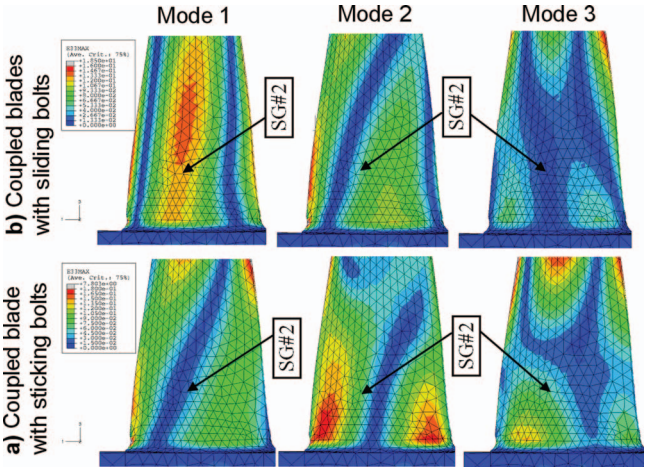

Fig. 14 Three lowest mode shapes of the blade coupled by (*a*) sticking and (*b*) slipping bolts, where SG#2 indicates the position of Gauge 2. Parameter E33MAX means the relative strain magnitude in the radial direction determined by $\{\varepsilon^\circ\}_{i,n}=[\{\varepsilon^\circ_{i,n}\}_c+f\{\varepsilon^\circ_{i,n}\}_s]^{1/2}$

With respect to the fully sticking and frictionless slipping contact conditions on the bolts, the sensitivity of the FE mode shapes of the three lowest resonances (see $\omega_{r,1}$, $\omega_{r,2}$, and $\omega_{r,3}$ in Fig. 11) is illustrated in Fig. 14. By increasing slip regions on the contact bolt area (Fig. 10(*a*)), the bolt coupling becomes weaker and the friction dissipation increases. Then, the resonance frequencies of the blade decrease slightly. Since the sticking regions on the contact area are larger than the slipping zones, then the resonance blade vibrations correspond mostly to the mode shapes presented in Fig. 14(*a*) and the resonance frequencies do not vary from that given in the nodal diameter curves (Fig. 11) or in the Campbell diagram (Fig. 12). If the slipping dominates on the contact area, then the eigenfrequencies diminish from the values for the fully sticking[3] contact conditions. Also their vibration forms change toward the mode shapes illustrated in Fig. 14(*b*), which are computed for frictionless slipping[4] conditions on the bolt contact area given in Fig. 10(*a*).

For the FE mode shapes shown in Fig. 14, the position and orientation of the gauges are determined with respect to Ref. [24]:

(I) sufficient strong signals of strain
(II) measuring of various mode shapes with a single gauge considering different contact conditions on the bolt
(III) a good location for the instrumentation of gauges and
(IV) a good relation of the measured strain magnitude to the maximum resonance von Mises stress

To measure the three lowest eigenfamilies of the blades with respect to either sticking or partly sliding-sticking bolt motions, three strain gauges need to be applied to one airfoil (Fig. 15). For measuring up to the 15th engine orders (Fig. 12), four adjacent blades are instrumented with three strain gauges and on the opposite side of the disk assembly, and four adjacent blades are instrumented with one strain gauge SG#1 (Fig. 15) for the proper identification of the measured nodal diameter vibration.

In spin-pit tests in vacuum, rotating blades are excited periodically by an air jet during every rotation with period $T=2\pi/\Omega$.

[3]Degrees of freedom of the nodes on the bolt and airfoil contact area (Fig. 10) are tied rigidly in the normal and in two tangential contact directions.

[4]Only in the normal direction of the contact, degrees of freedom of the nodes on the bolt and airfoil contact area (Fig. 10) are tied rigidly.

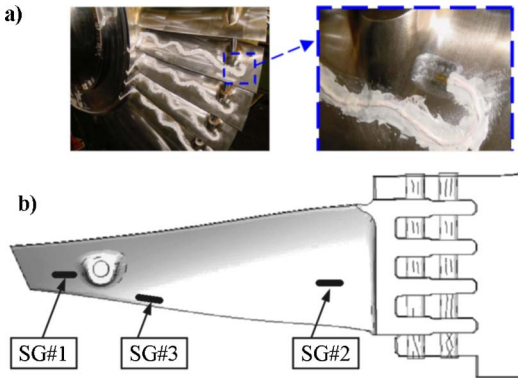

Fig. 15 (*a*) Position of Strain Gauge 1 (SG#1) instrumented on four adjacent blades for measuring the disk vibrations up to the 15th engine order (Fig. 12) and (*b*) Location of three gauges on four adjacent blades

After reaching 120% of the nominal speed, the rotational speed Ω decreases slowly in idle motion of the turbine train (Fig. 21(*a*)). The excitation frequency $\omega = k\Omega/(2\pi)$ depends on the rotation speed Ω and engine order $k = 1, 2, \ldots, \infty$. For 22 min of one measurement, while turbine speed reduces from 100% to 10% of the nominal speed, transient resonance effects are minimized. As it is shown in Fig. 16 (see $\omega_{C,i=1,\ldots}$, $\omega_{C,i=4}$), the four lowest eigenfamilies of the large SK blades are measured very well with the 12 gauges.

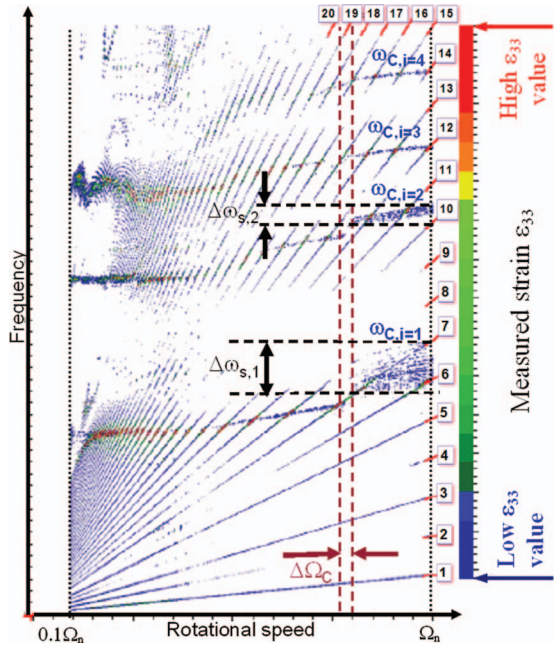

Fig. 16 The measured Campbell diagram of the four lowest eigenfamilies ($\omega_{C,i=1}, \ldots, \omega_{C,i=4}$) of the large SK blades excited by air jet in vacuum at 20°C, where $\Delta\Omega_C$ is the speed region while the bolts begin to couple the blades

The rotating blades are coupled effectively by the bolts in the speed range $\Delta\Omega_C$ (Fig. 16) between 70% and 80% of the nominal speed Ω_n. Up to $0.7\Omega_n$, resonance ranges of the blades are very narrow in comparison to the measured vibrations of the coupled system above $0.8\Omega_n$. In this range of speed, practically all nodal diameters of the first and second eigenfamilies of the mistuned coupled blades (see $\Delta\omega_{s,1}$ and $\Delta\omega_{s,2}$ in Fig. 16) are excited by the air jet. Therefore, double resonance peaks ω' and ω'' are given in the measured order tracking (Fig. 17). However, the major response amplitudes (red dots in Figs. 16 and 18–20) occur only for the harmonic resonance condition of the coupled blades, when the excitation frequency $k\Omega$ coincides with the eigenfrequency $\omega_{i,n}$ and also the engine order k is equal to the nodal diameter n for $n \leqslant N/2$ [11].

The FE eigenfrequencies $f_{i,n}$ correspond very well to the measured resonances (Fig. 18). Also, the experimentally proved coupling effect of the blades by bolts is identified numerically in the speed range $\Delta\Omega_C$. In addition, the FE results recognize possible presence of nonsynchronic vibrations of the lowest nodal diameters of the eigenfamily $i+1$ in harmonic resonances of the lower eigenfamily i (e.g., $f_{2.0}$, $f_{2.1}$, $f_{2.2}$ in resonance regions of $f_{1.6}$ and $f_{1.7}$ in Fig. 18).

With respect to the rotational speed Ω, the degree of the blade coupling is determined for each mode shape i,n from

$$\gamma(\Omega_{a,b})_{i,n} = \frac{\omega(\Omega_a)_{i,n} - \omega(\Omega_b)_{i,n}}{\Omega_a - \Omega_b} \tag{16}$$

where $\omega(\Omega_a)_{i,n}$ and $\omega(\Omega_b)_{i,n}$ are either the experimental or numerical frequencies at the rotational speeds Ω_a and Ω_b (where $\Omega_a > \Omega_b$), respectively. For the speed between $0.9\Omega_n$ and Ω_n, the experimental and numerical degrees γ of the blade coupling are compared to each other in Table 5. The numerical coupling degrees of these nodal diameter vibrations are lower than that determined from the experimental resonances (Figs. 19 and 20). These differences approve that the computed bolt area (Fig. 10(*a*)) might to be too narrow due to the used mesh refinement in relation to the real contact coupling. By applying a very fine contact mesh, the experimental coupling degree can be recalculated.

In the frequency region $\omega_{C,i=1}$, shown in Figs. 16 and 17, the number of the "dotted lines" representing the measured disk vibrations is larger than those which are calculated with the tuned FE model of the bladed disk. This is due to the mistuning effect, which generates always two different resonance peaks at frequencies ω' and ω'' (Fig. 17) instead of two identical resonances $\omega' = \omega''$ for the two FE orthogonal mode shapes $\{\phi^0_{i,n}\}_c$ and $\{\phi^0_{i,n}\}_s$. Then, the number of the possible FE disk resonances is equal to

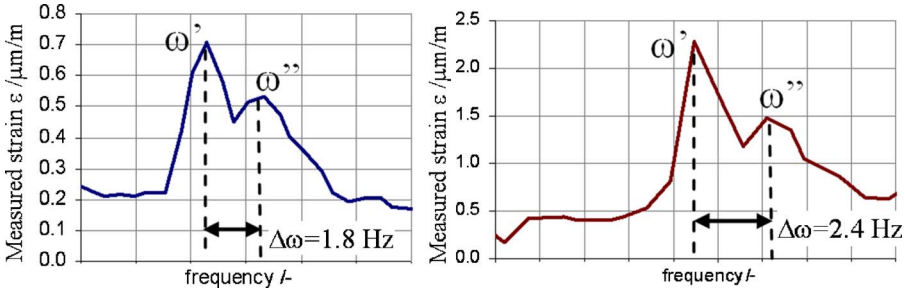

Fig. 17 Order tracking of harmonic excitations of (*a*) $k=7$ for resonance $i,n=1.7$, (*b*) $k=6$ for resonance $i,n=1.6$ (Fig. 19) with the measured double resonances ω' and ω'' due to mistuning effects, where $\Delta\omega = \omega'' - \omega'$

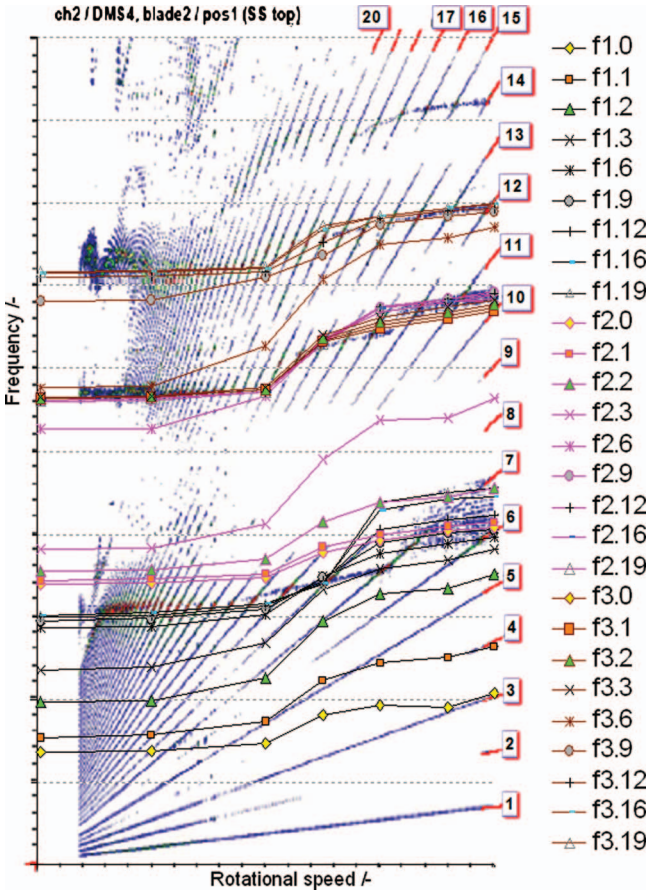

Fig. 18 The comparison of the computed and measured Campbell diagrams of the large SK blades, where the FE eigenfrequencies $f_{i,n}$ refer to eigenfamily number $i=\{1,2,3\}$ and nodal diameter numbers $n=\{0,1,2,3,6,9,12,16,19\}$

$1+(N-1)/2$ for each eigenfamily i, whereby the mistuned disk assembly has up to $1+(N-1)$ resonances. For higher frequency regions $\omega_{C,i=2}$, $\omega_{C,i=3}$, and $\omega_{C,i=4}$ (Fig. 16), this phenomenon is less perceptible, because the FE eigenfrequencies (see high nodal diameters in Fig. 11) focus toward a narrow frequency band. In contrary, the eigenfrequencies of the first eigenfamily vary strongly among themselves in the entire range of the nodal diameters from 0 up to $(N'-1)/2$ because of the bolt coupling. The bolt coupling affects mainly vibrations of the second and higher eigenfamilies with the lowest nodal diameters. These possible nonsynchronous vibrations are damped by the friction bolts.

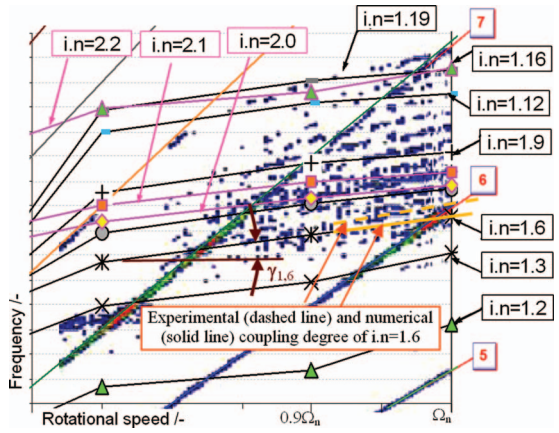

Fig. 19 The numerical and experimental Campbell diagrams for resonances of the first family excited by engine orders k of 6 and 7, where $\gamma_{1,6}$ is the degree of blade coupling for disk mode $i,n=1.6$

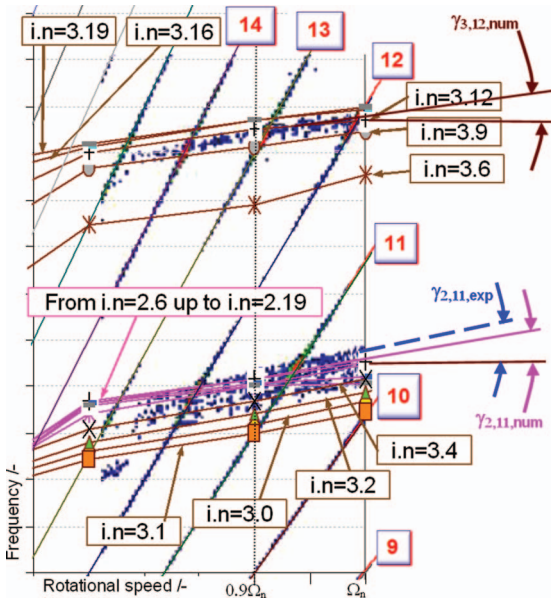

Fig. 20 The numerical and experimental Campbell diagrams for resonances of the second and third eigenfamilies, where $\gamma_{2,11}$ and $\gamma_{3,12}$ are coupling degrees of disk modes i,n of 2.11 and 3.12

Linear Dynamic Analysis of Spin-Pit Tests

According to the mode shapes shown in Fig. 22(*b*), a location of the air jet pipe above the bolts at the airfoil tip (Fig. 21) assures a good excitability. Another end of the jet pipe is set outside the test bunker. In tests, a gust air generates itself due to the pressure difference between the vacuum and atmospheric air condition.

Table 5 Degrees γ of the large SK-blade coupling determined from the numerical and experimental frequencies for the speed between $0.9\Omega_n$ and Ω_n in the spin-pit condition

Disk resonance for i,n	Coupling degree of blades γ (Hz/rps)	
	Experimental value	Numerical value
1.6	1.39	1.14
2.11	1.32	1.02
3.12	1.82	1.47

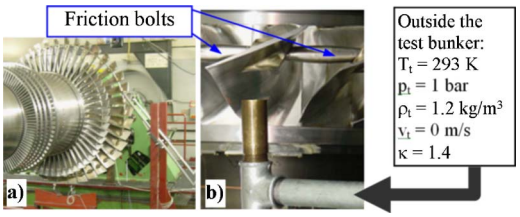

Fig. 21 (*a*) SK turbine train in the spin-pit chamber and (*b*) the pipe arrangement for the airfoil excitation, where κ is dimensionless polytropic constant and T_t, p_t, ρ_t, and v_t are the temperature, atmospheric pressure, air density, and flow velocity outside the bunker

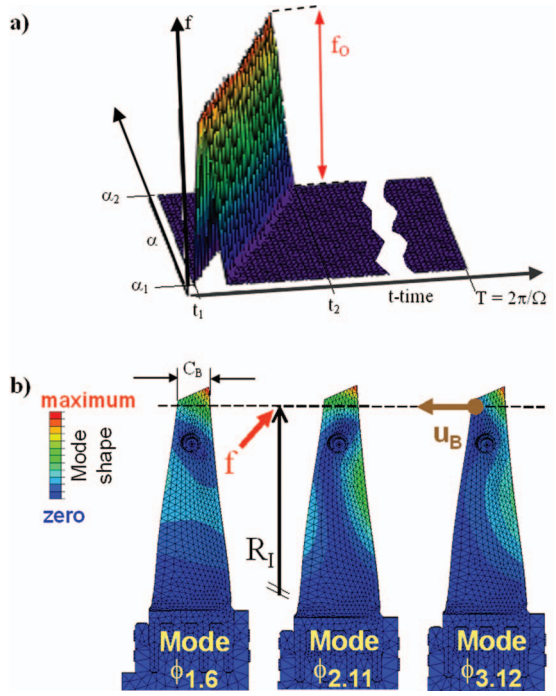

Fig. 22 (*a*) The air jet excitation force $f(\alpha)$ and (*b*) blade mode shapes $\phi_{1.6}$, $\phi_{2.11}$, $\phi_{3.12}$, where α_1 and α_2 are angles at the entry and exit of the blade contours by the air gust at time t_1 and t_2 during one period $T=2\pi/\Omega$ of the turbine rotation

For the assumed isentropic air flow, vacuum condition (inside pressure $p=0$), and the parameters shown in Fig. 21(*b*), the air velocity v of about 760 m/s at the end of the pipe in the spin-pit bunker is obtained analytically from

$$v = \sqrt{\frac{2\kappa}{\kappa-1}\frac{p_t}{\rho_t}\left(1-\frac{p}{p_t}\right)^{(\kappa-1)/\kappa}} \tag{17}$$

Then, an impulse force F_I of 29.96 N is determined by means of Newton's Law with

$$F_I = \dot{m}_{\text{air}} v \tag{18}$$

for the maximum mass flow of 0.0395 kg/s. This flow mass is calculated by

$$\dot{m}_{\max} = A\sqrt{2p_t\rho_t\frac{\kappa}{\kappa+1}}\left(\frac{2}{\kappa+1}\right)^{1/(\kappa+1)} \tag{19}$$

where A is the cross section of the end of the pipe in the bunker. It is assumed that the air jet meets the blade surface on a circle with two times the diameter of the pipe end.

A half-sinusoidal force distribution f is assumed to result from the air jet excitation acting on the rotating blade, which is defined in terms of the angular airfoil position α by

$$f(\alpha) = \begin{cases} 0 & \alpha < \alpha_1 \\ \dfrac{\pi F_I}{2(\alpha_2-\alpha_1)}\sin\left(\dfrac{\pi}{\alpha_2-\alpha_1}(\alpha-\alpha_2)\right) & \text{if } \alpha_2 \leq \alpha \leq \alpha_1 \\ 0 & \alpha > \alpha_2 \end{cases} \tag{20}$$

where α_1 and α_2 are the circumferential angles at the leading and trailing edges of the rotating blade by the air jet gust. For the known blade speed $u_B=(2\pi\Omega)/R_I$ and the length of the airfoil chord C_B at radius R_I opposite the air jet pipe (Fig. 22(*b*)), the excitation load is determined in the time domain t as it is illustrated in Fig. 22(*a*). According to Eq. (5), the excitation amplitudes are obtained from the complex Fourier transformation of the periodic load function $f(\alpha)$ and they are given in Fig. 23.

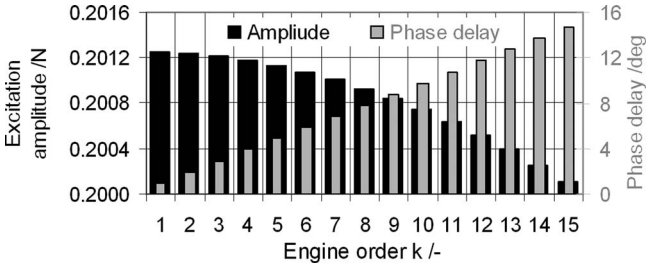

Fig. 23 Excitation amplitudes F_k and phase delays κ_k of engine orders k of the air jet excitation f

For simulating blade rotations, two rotating excitation waves $F_{c,k}=F_k\cos(\kappa_k)\cos(k\alpha_\delta)$ and $F_{s,k}=F_k\sin(\kappa_k)\sin(k\alpha_\delta)$ are determined for all nodes δ_e located on the blade contour (Fig. 22(*b*)) of the air gust reaction (where α_δ is the circumferential position of node $\delta=1,2,\ldots,\delta_e$). For engine orders k of 6, 11, and 12, the steady-state strain resonance responses of mode shapes of 1.6, 2.11, and 3.12 (Fig. 24) are calculated (see Eqs. (6)–(13) at a gauge of 1 (Fig. 15).

The computed resonance response amplitude depends strongly on the damping value. In vacuum condition, principally the friction dissipation can be expected due to microsliding on contacts of the blade root and bolts. According to the experimental investigations of Matveev et al. [25], the dissipation at the hinged radial roots does not differ from the damping ratio measured at standstill. These experimental damping values practically are equal to the material damping ratio, unless the bending load acts on the airfoil. Under a centrifugal load of 30 kN and a temperature of 350°C, the measured damping ratio ξ at the radial root, made of titanium alloy, increases linearly from 0.03% up to 0.7% by changing the bending load from 0 N up to 350 N. At ambient temperature and no acting pressure, the measured modal damping ratio varies between 0.01% and 0.03% under a centrifugal force of 30 kN [25]. These damping ratios correspond almost to the material damping of titanium alloy.

According to the experimental findings of Matveev et al., for the expected minor resonance stresses and sticking bolts, the steady-state computations are done for a material modal damping ratio ξ of 0.07% of X20Cr13 alloy [26] of the SK blade. The obtained results are much bigger than the experimental resonance strains measured in four different runs (see Runs 08, 14, 20, and 41 in Fig. 25). By increasing the modal damping ratio from 0.07% to 0.14%, the FE resonance strains at Gauge 1 are in good agreement with the measured values, as presented in Fig. 25.

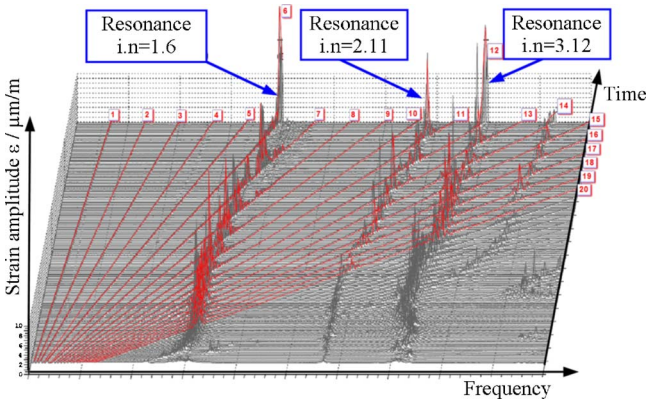

Fig. 24 A waterfall diagram of the spin-pit measurement of the large SK blade at strain gauge SG#1

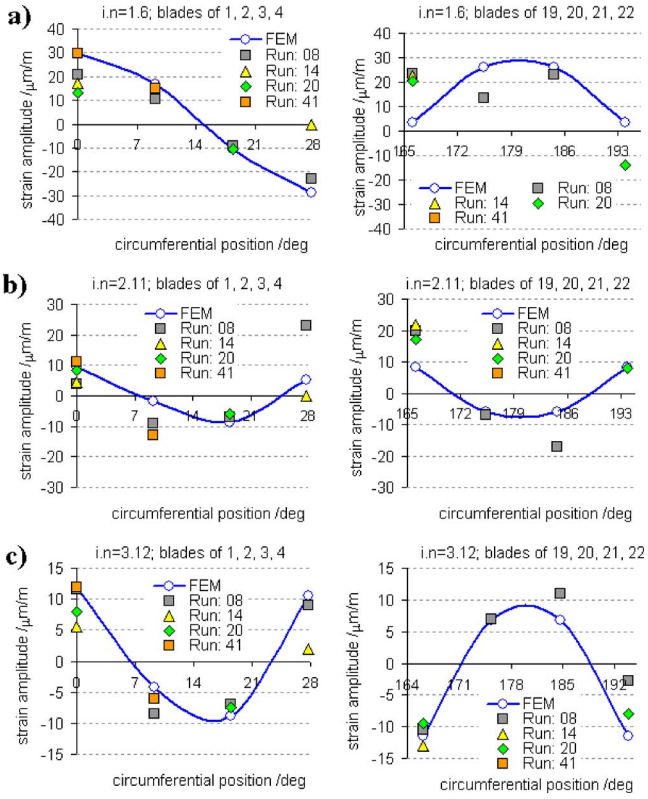

Fig. 25 The computed (the overall damping ξ=0.14%) and measured strain responses at SG#1 gauges on eight blades in the spin pin (Test Runs 08, 14, 20, and 41) for resonances (*a*) *i*, *n*=1.6 excited by *k*=6, (*b*) *i*, *n*=2.11 excited by *k*=11, and (*c*) *i*, *n*=3.12 excited by *k*=12

The obtained discrepancies between the experimental and numerical strains can be caused by the mistuning. For the SK blades coupled by bolts, the mistuning influence cannot be assessed by Whitehead's [27] criterion, which is adequate only for weakly coupled blades[5] In relation to freestanding airfoils attached to elastic disk, the SK-bladed disk is coupled strongly by bolts above 80% of the nominal speed. Then, mistuning would not induce the localization phenomena but rather the effect of double mistuned resonance peaks, as it can be seen in the measured order tracking in Fig. 17. The evaluation of damping values from these types of the measured frequency response functions cannot be done in a reliable manner by using the known half-band power method, which is adequate for the single symmetrical steady-state resonance response function. For the resonances shown in Fig. 17, an equivalent numerical model with few degrees of freedom is needed for the vibration's representation of the coupled blade. This model could be used for the computational tuning of the measured order tracking in terms of the unknown damping value. Even then, stick-slip bolt motions might not allow for reliable application of the linear method of the damping evaluation. Therefore, the nonlinear dynamic analysis is applied to assess the damping capacity of the scaled SK blades [11].

The statement by Matveev's et al. [25] is based on tests with symmetrical specimen and cannot be assigned entirely to the dissipation mechanism in the real radial root. The moment of the airfoil untwisting and centrifugal deformations of the pinned radial root causes weak surface contacts between the root fingers and rotor grooves that would generate friction dissipation. However, the small air jet excitation as well as insensitivity of the mode shapes in the root region (Fig. 22(*b*)) confirm indirectly the lack of friction damping in the blade root. Then, the numerically assessed damping ratio of 14% comes mainly from the friction dissipation at bolts. The micro-stick-slip effects take place on contours of the real elliptical contact area (Fig. 10(*a*)), on which normal contact stresses are significantly lower than those in the center of the contact. This microslip relative contact behavior can provide notable damping even for high friction coefficients, as investigated in Ref. [21].

[5]Because of spatial localization of the vibration energy, certain airfoils, which are disordered by manufacturing and assembling tolerances as well as by divergences in material properties, might experience substantially larger oscillations than the numerical response amplitudes of the tuned bladed disk.

Conclusions

The FE static and dynamic methodologies for the turbine blades coupled by loosely assembled friction bolts are presented for the first time in literature. The FE results confirm the correctness of the scaling design concept of the SK blades regarding their equal static stresses, scalable natural frequencies, and the same computed excitability proven in the Campbell diagrams. The utilization of this validated numerical process increases the reliability of the new scaled blades.

The elaborated analytical method for prediction of air jet excitation acting on the rotating blades in the spin-pit measurement is reported for the first time in the literature. By replacing this analytical process with the unsteady CFD results and applying the fluid structure interaction (FSI) technique, designers of blades might obtain reliable air jet excitation forces for more exact verification of the blade dynamics in spin tests. Up to now, spin-pit tests confirm only the blade excitability in the measured Campbell diagram.

Acknowledgment

The authors thank Siemens AG for support and permitting the publication of this paper.

References

[1] Brandt, D. E., and Wesorick, R. R., 1994, "GE Gas Turbine Design Philosophy," GE Power Generation Marketing No. GER-3434D.
[2] Eckardt, D., and Rufli, P., 2002, "Advanced Gas Turbine Technology: ABB/BCC Historical Firsts," ASME J. Eng. Gas Turbines Power, **124**, pp. 542–549.
[3] Diakunchak, I. S., Gaul, G. R., McQuiggan, G., and Southall, L. R., 2002, "Siemens Westinghouse Advanced Turbine Systems Program Final Summary," ASME Paper No. GT-2002-30654.
[4] Maekawa, A., Magoshi, R., and Iwasaki, Y., 2003, "Development and In-House Shop Load Test Results of M701G2 Gas Turbine," *Proceedings of the International Gas Turbine Congress*, Tokyo, Nov. 2–7, Paper No. IGTC2003, Tokyo-TS-100.
[5] Hohn, A., 1974, "Steam Turbines for Industrial and Medium Sized Power Plants," BBC No. CH-T 010122 D/E, Baden, Switzerland, pp. 39–56.
[6] Pollak, H., Pfitzinger, E.-W., Thamm, N., and Schwarz, M.-A., 2004, "Design and Materials for Modern Steam Turbines With Two Cylinder Design up to 700 MW," *Proceedings of Power-Gen 2004 (PG04) Conference*, Barcelona, Spain, May 25–27.
[7] Green, J. S., and Fransson, T. H., 2006, "Scaling of Turbine Blade Unsteady Pressures for Rapid Forced Response Assessment," ASME Paper No. GT2006-90613.
[8] Swanekamp, R., 2000, "Gas Turbines, Combined Cycles Harvest Record Orders," Power Magazine, Vol. 144, No. 2.
[9] Wan, E. S., Crimi, P., Scheibel, J., and Viswanathan, R., 2002, "Combustion Turbine F-Class Life Management of 1st Stage Turbine Blades," ASME Paper No. TE02.
[10] Reimann, P., 2000, "Stretching the Size of Geothermal Steam Turbines," *Proceedings of World Geothermal Congress 2000*, Kyushu-Tohoku, Japan, May 28–Jun. 10, pp. 3283–3288.
[11] Szwedowicz, J., Secall-Wimmel, T., and Duenck-Kerst, P., 2007, "Damping Performance of Axial Turbine Stages With Loosely Assembled Friction Bolts; the Non-Linear Dynamic Assessment; Part II," ASME Paper No. GT2007-27506.
[12] 2005, ABAQUS User's Manual, Version 6.5, ABAQUS Inc., Pawtucket, RI.
[13] Szwedowicz, J., Visser, R., Sextro, W., and Masserey, P. A., 2003, "On Forced Vibrations of Shrouded Turbine Blades," ASME Paper No. GT2003-38808.
[14] Panning, L., Popp, K., Sextro, W., Goetting, F., Kayser, A., and Wolter, I., 2004, "Asymmetrical Underplatform Dampers in Gas Turbine Bladings: Theory and Application," ASME Paper No. GT2004-53316.
[15] Wachter, J., Pfeiffer, R., and Jarosch, J., 1983, "Experimental Study to Gain

Insight in the Vibration Characteristics of a Steam Turbine LP-Wheel With Lashing Pins," *The Ninth Biennial Conference on Mechanical Vibration and Noise*, Dearborn, MI, Sept. 11–14, ASME Paper No. 83-72174, pp. 83–89.
[16] Szwedowicz, J., 1999, "Cyclic Finite Element Modeling of Shrouded Turbine Blades Including Frictional Contact," ASME Paper No. 99-GT-92.
[17] Szwedowicz, J., Slowik, S., Mahler, A., and Hulme, C. J., 2005, "Nonlinear Dynamic Analyses of a Gas Turbine Blade for Attainment of Reliable Shroud Coupling," ASME Paper No. GT2005-69062.
[18] Thomas, D. L., 1974, "Standing Waves in Rotationally Periodic Structures," J. Sound Vib., **37**, pp. 288–290.
[19] Dickmann, H.-P., Secall-Wimmel, T., Szwedowicz, J., Filsinger, D., and Roduner, C., 2006, "Unsteady Flow in a Turbocharger Centrifugal Compressor—3D-CFD-Simulation and Numerical Analysis of Impeller Blade Vibration," ASME J. Turbomach., **128**(3), pp. 455–465.
[20] Filsinger, D., Szwedowicz, J., and Schäfer, O., 2002, "Approach to Unidirectional Coupled CFD-FEM Analysis of Axial Turbocharger Turbine Blades," ASME J. Turbomach., **124**, pp. 125–131.
[21] Zeng, F. L., 1991, "On Adaptive Finite Element Procedures for Static and Dynamic Problems," Ph.D. thesis, Chalmers University of Technology, Goteborg, Sweden.
[22] Fischer, C., 2003, "Experimentelle Modalanalyse SK-Schaufeltyp (Einspannung frei/frei)," Siemens Intern Bericht S329/2003/008, Müllheim, Nov.
[23] Jarosch, J., 1983, "Beitrag zum Schwingungsverhalten gekoppelter Schaufelsystem," Ph.D. thesis, Universitat Stuttgart, Stuttgart.
[24] Szwedowicz, J., Senn, S. M., and Abhari, R. S., 2002, "Optimum Strain Gage Application to Bladed Assemblies," ASME J. Turbomach., **124**, pp. 606–613.
[25] Matveev, V. V., Chaikoskii, B. S., and Rzhavin, L. N., 1970, "Damping Capacity of the Hinged Locking Joint of Turbomachine Compressor Blades (in Russian)," Problemy Prochnosti, **12**, pp. 106–109.
[26] Pfeiffer, R., 1985, "Einfluss Unterschiedlicher Paketierungen auf Schwingungsverhalten und Verbundfaktoren von Dampfturbinen-Beschaufelungen (Influence of Different Arrangements of Steam Turbine Blades in Packet on Disc Coupling and Vibration Behavior)," Ph.D. thesis, University of Stuttgart, Stuttgart.
[27] Whitehead, D. S., 1988, "The Maximum Factor by Which Forced Vibration of Blades Can Increase Due to Mistuning," ASME J. Eng. Gas Turbines Power, **120**, pp. 115–119.

Damping Performance of Axial Turbine Stages With Loosely Assembled Friction Bolts: The Nonlinear Dynamic Assessment

J. Szwedowicz
e-mail: jaroslaw.szwedowicz@ch.abb.com

Th. Secall-Wimmel

ABB Turbo Systems Ltd.,
Thermal Machinery Laboratory,
CH-5401 Baden, Switzerland

P. Dünck-Kerst
Siemens AG,
Power Generation/Industrial Applications,
D-47053 Duisburg, Germany
e-mail: peter.duenck-kerst@siemens.com

An entire family of twisted and tapered low pressure steam turbine fast rotating condensation blading (SK) blades with pinned radial root and loosely assembled conical bolts is designed by scaling the aerodynamic and mechanical properties of the smallest airfoil. For SK blades operating with variable speed, the friction bolts, mounted in the upper airfoil part, provide either damping or coupling capabilities for the blades with respect to resonance conditions. The damping and coupling performance have been proven experimentally in the test rig of the real turbine. The measurements of the smallest SK-disk assembly under different operating conditions have allowed us to understand the dynamic and damping behavior of the bolts that are either friction dampers or coupling devices for the vibrating blades depending on the excitation level. In this paper, nonlinear dynamic analyses of the smallest and large SK-turbine stage are performed and compared with the experimental data. The modal blade dynamics is defined by 30 complex finite element (FE) mode shapes of the freestanding blades coupled by the disk whereby the bolt's motion is described by six rigid body modes. The sticking contact condition between the blades and bolts is represented by the normal and tangential contact stiffnesses. These values are firstly estimated analytically with Hertz's formulas for the FE reaction forces and contact areas. More realistic contact stiffness values are obtained from the iterative process, in which the resonance frequencies are calculated with the steady-state simulations and compared to the FE nodal diameter curves for sticking contact conditions that meet the experimental frequencies very well (Szwedowicz, J. et al., 2007, "Scaling Concept for Axial Turbine Stages With Loosely Assembled Friction Bolts: The Linear Dynamic Assessment Part 1," Proceedings of ASME Turbo Expo 2007, Montreal, Canada, May 14–17, ASME Paper No. GT2007-27502). In nonlinear simulations, in case of exceeding the sticking contact condition, the induced friction forces are linearized by the harmonic balance method. In this manner, the microslipping and sticking contact behavior at all contact points are calculated iteratively for the specified excitation amplitudes, friction coefficient, contact roughness, and aerodamping values that are known from the experiment. The computed results of the tuned smallest SK blades agree with the experimental resonance stresses of 12 measured blades. Differences between the computed and measured stresses are caused by mistuning, which was not quantified in the experiment. The nonlinear dynamic analyses provide evidence of good damping performance for the smallest and large SK blades with respect to a wide range of excitation forces, different friction coefficients, and various aerodynamic damping values. For the analyzed resonances of the eighth engine order, the scalability of damping performance is found for the SK blades of different sizes. [DOI: 10.1115/1.2838998]

Introduction

To prevent low pressure (LP) steam turbine blades from high cyclic fatigue (HCF) failures, caused either by harmonic or by nonengine excitation such as flutter or extreme part load condition known as windage [1], freestanding airfoils are coupled by different types of elements. Besides blades with integrally machined shrouds or winglets, not discussed here, lacing wires or zigzag pins, which are threaded through a hole in the airfoil, are used often for minimizing the resonance responses. The disk vibrations are characterized with the well-known interference (or nodal diameter) and Campbell diagrams [2] whereas, nonlinear blade vibrations are assessed by the performance diagram [3]. Different linear and nonlinear dynamic aspects of the tuned and mistuned disk assemblies are outlined in a good way in Ref. [4].

Manuscript received July 3, 2007; final manuscript received November 9, 2007; published online April 3, 2008. Review conducted by Dilip R. Ballal.

In the literature, contacts of a loosely assembled wire or pin at the airfoil are idealized frequently by a rigid coupling [5–7]. To determine more realistically their vibrations, a rigid coupling is replaced by torsional and flexural contact springs [8,9]. However, the computed blade vibration with the spring contact model has to be adjusted firstly with the existing spin pit measurement of this blade for getting reliable spring stiffness values. Recently, the finite element (FE) methodology, whose results predict correctly the measured Campbell diagrams of the LP turbine blades coupled by loose bolts, is worked out in Ref. [10].

The friction damping, based on micro sliding on the contact, can lead to fretting fatigue. The fretting wear and corrosion are avoided usually by using proper oxide coatings, which are proven by a series of fretting experiments [11]. In addition, from these measurements the friction coefficients are evaluated.

For many years, all damping or coupling design features of wires and pins have been developed by using the empirical knowledge, which was gathered from various measurements on special

Table 1 The experimental overall modal damping ratios [14,15] of the test-rig disk with two packets with seven airfoils and the real LP disk containing 48 airfoils

The experimental modal damping ratios ξ (%) for the fundamental blade frequency	Standstill	740 rpm	1000 rpm	2000 rpm	3000 rpm
Freestanding test-rig blades	0.77	0.57			
Test-rig blades with loose pins	0.91	0.80			
Test-rip blades with tight pins	1.44	1.32			
Test-rig blades with nominal pins	0.90	1.79			
Real LP blades with nominal pins	1.71		1.81	2.13	2.25
Real LP blades with tight pins	1.58		1.81	2.55	2.10
Mistuned LP blades with tight pins	1.21		1.45	1.90	2.39

test rigs, and also from the actual operating experience. However, a limited number of papers about these investigations and practical experiences can be found in the literature. In the experimental setup, Kellerer [12] measured the damping capabilities of zigzag pins in terms of the number of blades in a packet. At standstill, he investigated the rectangular beamlike blades coupled by zigzag pins. Regarding the centrifugal loading, each pin is pulled out by a force of 1030 N in the radial blade direction. These beams are attached to a disk of a thickness of 10 mm (considered as an "elastic" model), which is four times thinner than the reference disk with real 48 twisted LP blades. For the number of $N_P=[2,3,4,6,12]$ beamlike blades in a packet attached to the elastic disk, the evaluated modal damping ratios are nearly constant and are equal to about 0.5%. The damping ratio increases up to 0.6% for $N_P=16$. For the "rigid" disk of a thickness of 40 mm, the damping values of about 0.3% are found for up to 12 beamlike blades in a packet and 0.4% for $N_P=16$. For the real LP blades coupled by the zigzag pin and by the rigid disk, the measured modal damping ratio increases linearly from 0.11% up to 0.6% by increasing the number of blades in the packet from 2 up to 24, respectively. Kellerer's experiment shows that the damping capability increases linearly with a number of airfoils at the rigid disk and can be up to four to six times higher than a damping ratio of 0.1% of the freestanding blade. Borishanskii [13] measured a steam LP turbine stage in vacuum coupled by a welded bandage and, additionally, by a freely assembled wire. By applying the wire, a decrease in the resonance blade stresses was found by a factor of 2.3–3.5 times in comparison to the stress results of the blades coupled only by the welded shroud [13]. In Borishanskii's test model, effective blade vibrations at the wire coupling are limited by the shroud. Therefore, the damping capacity is smaller than that found for the blades coupled only by the zigzag pins [12].

The valuable outline about the damping capability of pins within LP steam turbine blades was given in Refs. [14,15]. In these work, two packets of seven blades were placed on diametrically opposite disk sectors. Each airfoil has a radial root, which contains two fingers for fastening to the rotor with two bolts. For different manners of the pin assembly, the vibration measurements were done in vacuum at standstill and a rotational speed of 740 rpm. The damping magnitudes, which were evaluated with the logarithmic decrement formula from the recorded transient signals, are presented in Table 1. The same experimental technique was used for the measurements of 47 real LP steam turbine blades, which were coupled either by tight pins or by pins with nominal clearances within the airfoil hollow. At standstill and speeds of 1000 rpm, 2000 rpm, and 3000 rpm, the evaluated modal damping ratios [15] of this bladed disk are compared to those of the test-rig measurement [14]. The high damping values above $\xi=2\%$ of the real LP wheel were found at speeds above 2000 rpm for all considered pin arrangements. A relative low damping magnitude of 0.8% was measured at $\Omega=740$ rpm for the test-rig blades with the loose pin coupling. This was probably due to a not optimized mass m_d of the pin or too small excitation, which generated dynamic tangential reaction forces lower than the induced friction load $F_\mu=\mu m_d r(2\pi\Omega)^2$, depending on the friction coefficient μ, the pin mass m_d, the radial pin position r, and the rotational speed Ω. This finding shows that numerical approaches are required in the design process of the turbine blades with friction bolts for a reliable prediction of their dissipation capabilities.

In this paper, the nonlinear dynamic analysis of the LP steam turbine blades with loosely assembled bolts is performed numerically to reproduce the experimental results from the test rig with the real turbine [16]. For the static and free vibration results of the cyclic FE system [10], the modal model of blade vibrations with friction is created. Nonlinear forced blade vibrations with frictional sliding on bolt connection are computed with the DATES code [17], which uses the harmonic balance method (HBM) for the linearization of friction forces with one complex Fourier coefficient. A more advanced HBM model with an arbitrary number of Fourier harmonics as well as with the exact analytical solution of the nonlinear equations is developed by Petrov [18]. With multiharmonic expansion of the periodic motion, Petrov's method predicts the major, super- and subharmonic blade resonances in terms of different design parameters, such as excitation amplitudes, normal contact forces or damper mass, surface roughness and clearance at the contact, friction coefficient, and contact stiffness. Varying friction forces and excitation amplitudes, his results are demonstrated for the test-rig disk assembly of 24 blades with underplatform dampers, but not related to the measurements.

Each technique using HBM needs the contact stiffness values, which are very essential parameters for a reliable solving of the blade dynamic equations with friction. In this paper, available methods given in the literature are discussed shortly and the most favorable formulation, based on the FE-modal adjustment technique, is used [19–21]. Moreover, the aerodynamic damping values of the measured freestanding and coupled SK blades are evaluated and compared to each other with respect to the nominal flow condition and partial arc admission of steam.

The here presented methodology for the numerical analysis of the blade dynamics with friction bolts is validated with the experimental Campbell results. This is a straightforward approach considering engineering needs in the design process of the blades with friction at shrouds, winglets, bolts, lacing wires, or underplatform dampers including the elastic disk coupling. The whole numerical process is done for the tuned disk assemblies. For the first time in the literature, this work demonstrates the reliable prediction of the friction dissipation on the bolts loosely assembled to the real LP twisted and tapered turbine blades. The described procedure can be applied to the blade analysis with the zigzag pin or wire coupling, too.

SK-Blade Investigation at the Test Rig

The last LP steam turbine fast rotating condensation blading (SK) stage has strongly twisted and tapered blades, as shown in Fig. 1. The airfoil is bolted to the rotor through four fingers of its radial root with two conical pins (Fig. 1(*a*)). In the upper airfoil

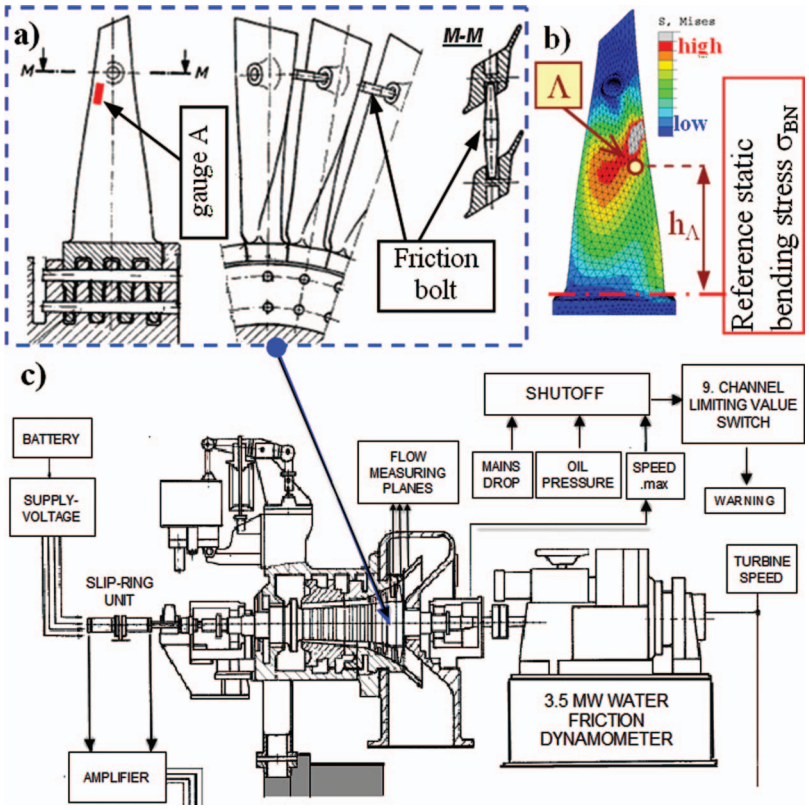

Fig. 1 (*a*) **The last LP steam turbine SK blades.** (*b*) **FE static bending stresses.** (*c*) **The test rig with the SK turbine [16], where Λ is the position of the excitation force at the radius h_Λ.**

part, bolts with conical ends are loosely fitted within the cylindrical hollows of adjacent blades. By increasing the rotational speed, N blades are coupled by these bolts. They can operate as friction dampers in the case that the excitation exceeds the threshold friction forces F_μ between the bolt and the airfoil. Then, resonance stresses of the SK blades operating with variable rotational speed are effectively reduced below the maximum allowable value. For the first frequency family, this damping capability of the smallest SK blades was experimentally developed and validated at the setup of the real turbine unit (Fig. 1(*c*)) at the Stuttgart's University in the early 1980's [2,13,22–25]. The experimental results of the dynamic and damping behavior of these blades are well summarized in Ref. [16]. Disk vibrations were measured with 12 gauges placed at position A of 12 adjacent airfoils (Fig. 1(*a*)). This gauge location was determined by Wolter [25] for the freestanding blade, and the influence of the sticking bolts on the change of the blade mode shapes was not proven [10]. Between 4500 rpm and 15,000 rpm, the blades with bolts were investigated for different mass flow and back-pressure indicated by tests A, B, C, and D, whose results for resonant stresses of the first eigenfamily are shown in Fig. 2. In all these tests, double resonances ω' and ω'' were measured, which relates to two standing vibration waves in the mistuned disk assembly. The same effect was measured for the large SK blades under spin pit conditions [10]. The alternating stress σ_A in Fig. 2 refers to the maximum resonance stress in the blade and is determined from [13]

$$\sigma_A = K_\varepsilon E_S \varepsilon_A \tag{1}$$

where E_S means Young's modulus of the airfoil, ε_A denotes the measured strain at position A (Fig. 1(*a*)) and K_ε is a transmission factor of 1.5 for the first blade mode [25].

Following Traupel's stimulus concept [26], the dynamic stress σ_A is related to the static bending stress σ_{BN} at the blade hub (Fig. 1(*b*)) induced by the static steam pressure acting on the freestanding airfoil and is given by

$$\sigma_A = \chi s f \sigma_{BN}/(2\xi) \tag{2}$$

where s is the stimulus factor, which can vary from 0.02 up to 0.1 [24] and ξ is the overall modal damping ratio caused by material,

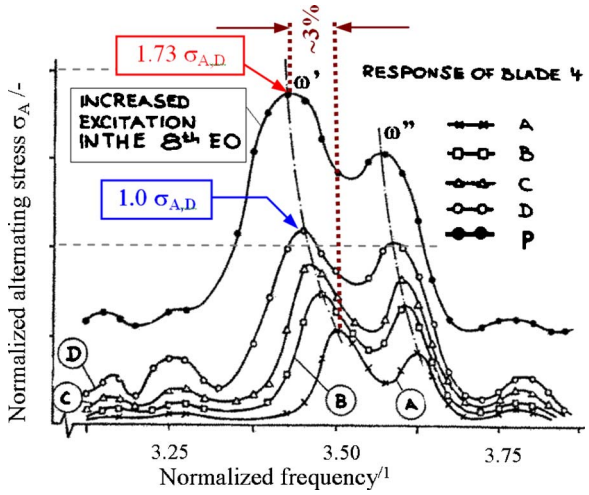

Fig. 2 Variation of the order tracking of the eighth engine order of the first resonance frequencies[5] at blade 4 for different service conditions A, B, C, D with full steam loading and P with partial arc admission, where ω' and ω'' are resonance amplitudes of the mistuned bladed disk

friction, and aerodynamic viscous dissipations. The parameter f denotes the excitability factor, which is as the modal excitation force $f_{i,n,k}$ [10] given by

$$f_{i,n,k} = \{\Phi^o\}_{i,n}^{*T}\{F_k\} \tag{3}$$

where index i,n means the disk mode shape of the ith eigenfamily vibrating with the nodal diameter n and $\{\Phi^o\}_{i,n}^{*T}$ is the conjugate transposed vector of the FE mass-normalized mode shape, $\{\Phi^o\}_{i,n}=\{\phi_{i,n}^o\}_c+j\{\phi_{i,n}^o\}_s$, of the blade represented by the cyclic FE model. The parameter F_k is the excitation amplitude of the engine order k. The parameter χ in Eq. (2) indicates the coupling factor, which can be determined for each disk mode shape i,n (where $i=\{1,2,3\}$ and $n=\{0,1,2,\ldots,(N-1)/2\}$) from the coupling degree γ of the blade [10] as

$$\chi = \cos^{-1}[\gamma(\Omega_{a,b})_{i,n}] = \cos^{-1}\left[\frac{\omega(\Omega_a)_{i,n} - \omega(\Omega_b)_{i,n}}{\Omega_a - \Omega_b}\right] \tag{4}$$

where $\omega(\Omega_a)_{i,n}$ and $\omega(\Omega_b)_{i,n}$ are either experimental or numerical frequencies at the rotational speeds Ω_a and Ω_b (where $\Omega_a > \Omega_b$), respectively.

According to the measured Campbell diagram of the SK blades operating with variable speed (Fig. 12), the amplification of the harmonic excitation for the eighth engine order was needed to prove experimentally friction damping capabilities of the bolts. By blocking off selected nozzles in the stator wheel of 40 vanes, the partial arc admission was arranged and the measured resonant stresses, indicated by P in Fig. 2, are related to the reference measurement D. For water brake loads of 800 N and 700 N, the resonance amplitudes ω' of the partial arc admission are 173% (see Fig. 2) and 193% larger than the resonance stress measured at test D, respectively.

Blade Dynamcis With Friction at Bolts

In the dynamics of SK blades, the friction dissipation at the radial root is neglected regarding the minor disk influence on blade vibrations and insignificant mode shape oscillations in its lower part of the blade [10]. For different mass flow conditions between tests A and P (see 3% difference between $\omega'_P - \omega'_A$ in Fig. 2 and dashed-pointed lines), the identified frequency shifting proves the presence of friction dissipation on the bolt contacts. Therefore, the dynamic reactions and friction forces $F(t)_\mu$ have to be included in the SK-blade vibrations.

At the rotational speed Ω temperature T, and friction coefficient μ, the static blade deformations and reaction forces at the bolt contact regions are obtained from the cyclic FE model [10]. The FE contact area and resulting forces R_{S3} and R_{P3} are illustrated in Fig. 3. The expected elliptical contact area $A=\pi a_0 b_0$ has to be approximated with the equivalent rectangular contact area $A=ab$ (Fig. 3) because of the limitation in the applied software.

Periodic blade vibrations with friction bolts are described with the cyclic symmetrical hypothesis and the component mode synthesis. For the computational accuracy, the frequency response functions (FRFs) of the bladed disk have to be represented at least with 15 FE mode shapes as it is proven for the shrouded blade in Ref. [27]. Because the natural frequencies of the unconstrained friction bolt are far away from the frequency range of interest (see the Appendix), the flexibility of the damper is not essential for reliable computations, and it can be modeled as a rigid body.

The cyclic FE dynamic equations of the tuned disk assembly, whose nth nodal diameter number is excited harmonically by engine order k, are expressed in the time domain t as

$$[\mathbf{M}(e^{jn\varphi})]\{\ddot{w}_n\} + [\mathbf{D}]\{\dot{w}_n\} + [\mathbf{K}(e^{jn\varphi})]\{w_n\} = \{F_k\}e^{jk\Omega t} + \{F(t)_C\} \tag{5}$$

where the Rayleigh damping matrix $[\mathbf{D}]$ is defined by a linear combination of the mass $[\mathbf{M}(e^{jn\varphi})]$ and stiffness $[\mathbf{K}(e^{jn\varphi})]$ matrices depending on the cyclic sector angle $\varphi=2\pi/N$ and nodal diameter $n=0,1,2,\ldots,(N-1)/2$ for the odd number N of SK blades. In the modal domain for the excitation orders of interest, the proportional damping matrix $[\mathbf{D}]$ is redefined with the modal damping ratios ξ, which are known from the experiment. The generalized complex vector $\{w\}=\{\{z\},\{q\}\}^T$ describes vibrations of the internal nodes $\{q\}$ and external nodes $\{z\}$ located on the cyclic boundaries of the FE model [10]. In terms of excitation magnitude, the generalized vector $\{F(t)_C\}$ contains either two tangential $R(t)_s$ and one normal $R(t)_n$ contact reaction forces for sticking contact condition or two friction forces $F(t)_\mu$ and one normal reaction force $R(t)_n$ for sliding contact condition at the bolt. For the high centrifugal load acting on the bolts, the contact separation $(F(t)_n<0)$ should not occur for the analyzed first blade eigenfamily. In simulations, the separation is proven by validation of the load equilibrium on the contact regarding a negative resulting normal force as undesired results from the design point of view. Then, the mass of the bolt needs to be increased for preventing it from possible impacting effects in the contact region, which can induce fretting fatigue [20].

For the harmonic excitation, the blade response is treated also as a harmonic vibration by representing the periodical nonlinear friction forces $F(t)_\mu$ with the complex Fourier series. This HBM linearization is applicable for weak nonlinearities, which depend on the frictional hysteresis determined by both velocity and displacement of the contact point. For simplicity, only the fundamental Fourier coefficient is taken into account, which assures a conservative assessment of the minimum friction dissipation on the contact. By application of more Fourier coefficients [18], the real shape of frictional hysteresis is determined more exactly, instead of the elliptical form obtained with one complex Fourier coefficient. Besides the main blade resonance $\omega_{i,n}=k\Omega$ as it is calculated for the fundamental Fourier harmonic, the utilization of

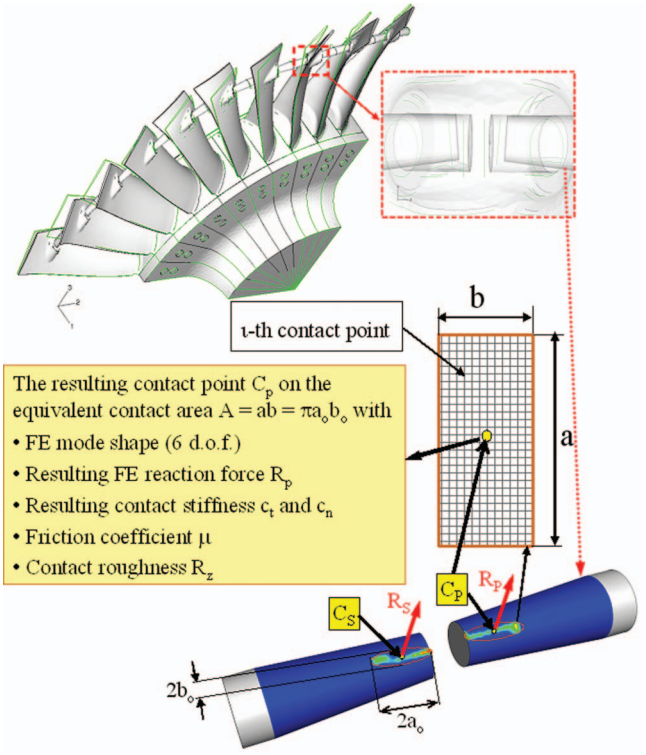

Fig. 3 Numerical representation of the bolt contact, where mode shapes at points C_S and C_P, contact areas, and static reaction forces R_{S3} and R_{P3} are obtained from the cyclic FE computation of the disk sector

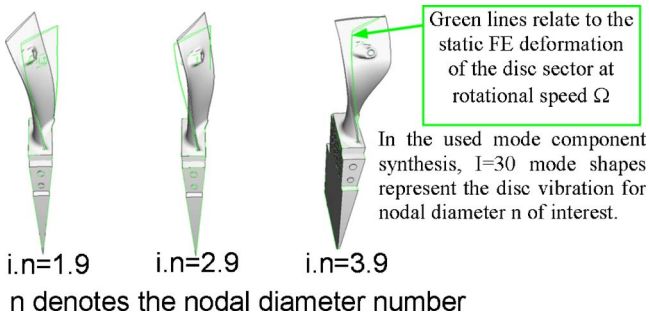

Fig. 4 Illustration of the three lowest mode shapes of the smallest SK blade without bolt coupling used for the modal transformation of the FE disk vibrations of the nodal diameter *n*=9 (see also Appendix)

higher numbers of the Fourier harmonics predicts also the sub- and superharmonic responses due to contact nonlinearity.

In the design process, the blade mistuning is not a deterministic quantity, and therefore, the tuned system of the SK blades is taken into account. Then, according to the orthogonal condition between the disk mode shape and excitation form, the blade resonances with the satisfied condition $k=n$ are considered only. By applying the modal transformation to Eq. (5), the blade dynamics with the linearized contact forces are reduced to modal equations of nth nodal diameter vibration [10,21] as

$$h_{i,n,k}u_{i,n} = f_{i,n,k}e^{jk\Omega t} + \{\Phi^o\}_{i,n}^{*T}\{f_c(\Delta u_{i,n})\}_{i,n}, \quad i = 1,2,\ldots,I \quad (6)$$

where $(\,)^{*T}$ denotes the conjugate transposed complex mode shape vector $\{\Phi^o\}_{i,n}$ and $f_{i,n,k}$ is the modal force (Eq. (3)) whereas the modal dynamic stiffness is given as

$$h_{i,n,k} = -(k\Omega)^2 + j2\omega_{i,n}\xi_{i,n}k\Omega + \omega_{i,n}^2 \quad (7)$$

The contact forces f_c, which depend on the relationship $\Delta u_{i,n}$ between the blade and the bolt modal displacements on the contact, is expressed by Ref. [28].

$$\{f_c(\Delta u_{i,n})\}_{i,n} = [C(\Delta u_{i,n})]\{\Phi^o\}_{i,n}\{u\}_{i,n} \quad (8)$$

The theory is explained in detail in Ref. [17]. Owing to the DATES limitations used for the nonlinear simulations, the FE elliptical contact area has to be defined by the equivalent rectangular shape ab (Fig. 3) for the contact discretization on each end of the bolt. Each contact area is represented with $100\eta\zeta$ contact points (where $\eta=10$, $\zeta=10$). At each contact point $\eta_\iota\zeta_\iota$, three contact conditions, such as slipping, sticking, and separation, can be determined. This discretization allows the prediction of local microslips, sticking, and separation in different regions of the contact.

For the applied multipoint constraints, the local contact stiffness and contact forces at each ιth contact point $\eta_\iota\zeta_\iota$ are obtained from the resulting normal c_n and tangential c_t contact stiffnesses and resulting FE reaction forces R. Using the kinematic constraints, the initial spatial motion of each contact point ι is determined from the oscillations of the resulting contact point C_S and C_P (Fig. 3) known from the FE free vibration calculation.

The FRFs of the fundamental eigenfamily of the SK blade coupled by friction bolts are of interest. For the used component mode synthesis, the blade dynamic property is represented by number I (where $i=1,2,\ldots,I$) of complex mode shapes $\{\Phi^o\}_{i,n} = \{\phi_{i,n}^o\}_c + j\{\phi_{i,n}^o\}_s$ of the disk vibrating with the nth nodal diameter of interest. The accurate modal transformation of the SK blade is assured for $I=30$ complex cyclic FE mode shapes of disk sector without the bolt coupling, as shown in Fig. 4. According to Treyde's investigation [27], at least 15 mode shapes must be used for accurate computations of FRFs of the fundamental natural frequency of the shrouded blade.

Because the fundamental natural frequency of the unconstrained bolt is 40 times higher than the first blade eigenfrequency (see the Appendix), the bolt is considered as a rigid body for the analysis of the first eigenfamily vibrating with nodal diameters between 6 and 13 according to the Campbell diagram (Fig. 12). Then, six rigid body motions of the bolt are used in the modal simulations.

The modal steady-state response analysis is performed with a sweep excitation for a chosen frequency step $\Delta\Omega$ varying from the start frequency $\Omega_{\text{lower\_band}}$ up to the end frequency $\Omega_{\text{upper\_band}}$, where $\Omega_{\text{lower\_band}} < k\Omega < \Omega_{\text{upper\_band}}$. For each excitation frequency $\Omega_e = \Omega_{\text{lower\_band}} + p\Delta\Omega$, where $p=0,1,2,\ldots$ $(\Omega_{\text{upper\_band}} - \Omega_{\text{lower\_band}})/\Delta\Omega$, the nonlinear modal dynamic Eq. (6) is solved by using the Newton–Raphson method. The blade dynamic stress σ_n, strain ε_n, or displacement w_n amplitudes are determined by the transformation of the calculated complex modal responses $u_{i,n}$ into the Cartesian system from

$$\{w(t)\}_n = \sum_{i=1}^{I} \{\phi^o\}_{i,n}u_{i,n}e^{-j\Omega_e t}, \quad j = \sqrt{-1} \quad (9)$$

The entire modal nonlinear dynamic analysis is very efficient in practical application. Using ordinary computers, any order tracking of the specified nth nodal diameter (e.g., see Fig. 2) is computed in a short time within the frequency range of interest for the known excitation force, friction coefficient, and resulting contact stiffnesses c_n and c_t.

Determination of Contact Properties

For the known alloys of the blade and bolt, the friction coefficients are measured with the experimental setup for fretting analyses [29] with respect to service temperature, normal load, and resonance frequencies of interest. In the test, the specimen slips harmonically on the standing sample, which is normally loaded. The specific uncertainty of the friction coefficients evaluated from these measurements is included in the performance diagram of the blade with the bolt (Fig. 14).

The resulting tangential contact stiffness c_t can also be evaluated from these fretting measurements [19]. The experimental way of contact stiffness assessment can result in high costs, and the evaluated results might contain unidentified uncertainties in measured relative displacements in the nearest contact regions of both specimens [30], especially in evaluated temperatures. In addition, in the case of geometrical redesign, the experimentally evaluated stiffness values become worthless. Therefore, the numerical prediction of the normal and tangential stiffness contact values is very essential from the design point of view.

Methods for Predictions of the Contact Stiffness Values. For the contact stiffness assessment, four approaches based on (i) the analytical solution, (ii) the nonlinear FE analysis, (iii), the residual stiffness analysis, and (iv) the FE-modal contact adjustment are known. The analytical manners are limited to the circular or elliptical contact areas, which are calculated with the Hertz [31] or the Catteano-Mindlin theory [32], respectively. The shape of the contact area is unlimited in the nonlinear FE methodology of the stiffness contact computation proposed and validated in Refs. [19,21]. In this method, by using fine FE meshes at the contact, the stiffness values are usually overestimated in relation to the experimental results of about 6–11% because of the neglected surface roughness. For the correct prediction of the static blade deformation in the modal domain by using I number of mode shapes, the residual stiffness is introduced in Ref. 17. The same pressure is imposed on the contact of the uncoupled blade in the FE and on the contact area of the modal blade model (Eq. (6)). Then, the quasistatic contact deformations are calculated with the nonlinear modal model for an excitation $\Omega_{\text{lower\_band}}$ of about 1 Hz. The same is done with the FE model. Finally, the residual stiffness

is calculated by relating both solutions to each other [28].

Here, the FE-modal stiffness adjustment is used in Refs. [2,21,29] and is based generally on the well-known 1D characteristic of disk vibrations. Firstly, the initial normal $c_{n,0}$ and tangential $c_{t,0}$ contact stiffness values between the bolt and airfoil are estimated with Hertz's formulas. For the neglected friction dissipation and the sticking contact condition, the modal nodal diameter curves are computed by solving Eq. (6) for the estimated contact stiffness $c_n = c_{n,0} \pm \Delta c_n$ and $c_t = c_{t,0} \pm \Delta c_t$. Then, the modal and FE nodal diameter curves are compared to each other. If the discrepancy between the FE and modal resonance frequencies is above the allowable relative error, the computation of the modal diameter curves is repeated again for new $\pm\Delta c_n$ and $\pm\Delta c_t$ values. This iterative process finally delivers the resulting contact normal and tangential stiffnesses $C_{n,S}$ and $C_{t,S}$ at the left and $C_{n,P}$ and $C_{t,P}$ at the right contact points C_S and C_P of the bolt (Fig. 3). According to the comparison of the experimental and numerical results for the shroud coupling as well as for the underplatform damper, the nonlinear FE and the FE-modal contact adjustment method predict contact stiffness values, whose applications in the nonlinear blade dynamics deliver a better agreement with the measured resonance frequencies and resonance amplitudes [28] than, e.g., the residual stiffness approach. For the SK blades with the conical bolts, the analytical approach cannot be used because the contact area on the bolt differs from the elliptical contact area for low speeds of the turbine [10]. Therefore, the FE-modal stiffness adjustment method needs to be applied to assure unlimited possibilities in the design process.

A constant surface roughness R_Z of 1 μm is applied as a reference value. This value corresponds to a polished contact ($R_z = 0.2-1$ μm). The influence of the surface roughness on the contact stiffness behavior is explained in Refs. [17,28].

Resulting Contact Stiffness Values for SK Blades. For the outer bolt radius r_D and inner radius r_S within the airfoil hollow, the bolt and blade Young's modules E_D and E_S, the bolt and blade Poisson's ratios υ_D and υ_S, as well as the FE reaction force $R \equiv F_n$ (Fig. 3), the normal contact stiffness $c_{n,0}$ is estimated firstly with the analytical Hertz's formula as

$$c_{n,0} = \frac{1}{2}\sqrt[3]{12e^2\left(\frac{r_D r_S}{r_S + r_D}\right)F_n} \tag{10}$$

where

$$e = \frac{8}{3}\frac{E_D E_S}{E_S(1-\upsilon_D^2) + E_D(1-\upsilon_S^2)} \tag{11}$$

Then, the tangential contact stiffness $c_{t,0}$ can be estimated roughly [19] from

$$c_{t,0} = \frac{2(1-\upsilon_D)}{(2-\upsilon_D)}c_{n,0} \tag{12}$$

After the determination of the initial contact values $c_{n,0}$ and $c_{t,0}$, the FE-modal stiffness adjustment method is applied for two different speeds of the smallest SK blade. According to the comparison of the FE and modal diameter curves in Fig. 5, within the nodal diameter range between 6 and 12, the maximum relative errors are below 7% and 4% for the first eigenfamily for 62.5% and 100% of the nominal speed Ω_n, respectively. These relative errors below 7% for the three lowest blade eigenfamilies at the different speeds are acceptable with respect to the relative errors of 13–22%, which are obtained from the comparison of the experimentally evaluated and the nonlinearly FE computed tangential contact stiffness of the solid underplatform damper in various temperature ranges between 20°C and 600°C [29].

In Tables 2 and 3, the analytically and numerically determined contact stiffness values are compared to each other. At the nominal speed, the analytical prediction (relative errors $\delta c_n = (c_{n,0}\text{-}c_n)/c_n$ are below 9%) of the normal contact stiffness is in

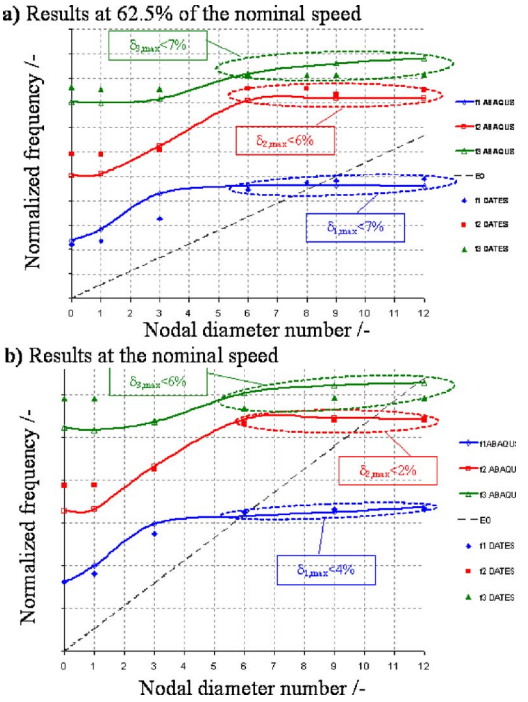

Fig. 5 Comparison of the FE and modal diameter curves of the smallest SK blade for the determination of the resulting normal c_n and tangential c_t contact stiffness at the bolt at (*a*) 0.625Ω_n and (*b*) at Ω_n nominal speed

tolerable agreement with the results from the FE-modal stiffness adjustment analysis. Because of the simplified formula (Eq. (12)), the analytical tangential stiffness differs up to 30% (Table 3) in relation to the obtained numerical values. For speed 0.625Ω_n in Tables 2 and 3, the analytical stiffness values differ too much with respect to the numerically predicted results. Relative errors of 33% and 183% are obtained for the normal and tangential contact stiffnesses, respectively. These high discrepancies of the analytical calculation are caused by the shape variation of the contact area from the elliptical contact area at Ω_n to the edge form at the ends of the bolt, as shown in Ref. [10]. This confirms the necessity for applying the numerical manner as the FE-modal contact adjustment method [21,29], which provides the best results in relation to the measurements as it was proven in Ref. [28].

For the nodal diameters between 1 and 5, which are never excited during SK-blade operation, the modal and FE nodal diameter curves differ from each other remarkably. A better adjustment was impossible because in the applied software, only the translation normal and tangential contact stiffnesses are available. For a better adjustment in the entire nodal diameter range, the resulting bending and torsion contact stiffnesses are needed in addition to the translation contact stiffness.

Excitation of Partial Arc Admission

Excitation amplitudes of the partial arc admission can be assessed with an unsteady computational fluid dynamics (CFD) simulation, for instance, with a 2D flow model at the midspan section of the full annulus. Using the turbulent k-ω model, the predicted spectrum includes mainly engine order excitation as well as possible pressure pulsations in the turbine inlet before the stator stage with blocked off nozzles and behind the rotating turbine stage in the turbine outlet [33]. These unsteady CFD calculations are time consuming simulations in the ordinary design process. Therefore, the excitation spectrum of the partial arc

Table 2 The analytical $c_{n,0}$ and numerical c_n resulting normal contact stiffnesses for stuck bolts at the smallest SK blade

	Resulting normal stiffness at the bolt contact					
	On the suction airfoil side			On the pressure airfoil side		
Rotational speed Ω_n	Analytical $c_{n,0}$ (MN/m)	Numerical c_n (MN/m)	Relative error δc_n (%)	Analytical $c_{n,0}$ (MN/m)	Numerical c_n (MN/m)	Relative error δc_n (%)
100.0%	53.70	58.98	−8.95	51.30	56.36	−8.98
62.5%	39.25	58.98	−33.45	37.50	56.36	−33.46

admission, used in the test rig (Fig. 1), is estimated for the assumed pressure distribution $P(\alpha)$, shown in Fig. 6, where α is the circumferential angle.

Applying the Fourier decomposition [10] to the idealized pressure distribution, the excitation spectrum is calculated and presented in Fig. 7. Between 6 and 12 engine orders of interest, the ninth harmonic also has a significant stimulus besides the highest excitation amplitude of the demanded eighth engine order. As the static pressure distribution was not measured, at least one engine order of the determined relative excitation spectrum needs to be adjusted to one measured blade resonance by using the stimulus concept [26] given in Eq. (2).

Evaluation of Aerodamping

In the stimulus concept (see Eq. (2)), the alternating stress σ_A among other things depends on the overall damping properties due to friction, aerodynamic viscosity, and hysteretic (material) dissipation. The material modal damping ratio ξ_m can be determined as [34]

$$\xi_m = \frac{\int J\sigma_A^{\eta} dV}{4\pi(E_{p,B} + E_{p,C})} \tag{13}$$

where J and η are material constants obtained from experiments,[1] V is the volume of the vibrating structure, $E_{p,B}$ and $E_{p,C}$ denote strain energies for the bending and centrifugal loadings of the blade, respectively. These energies can be obtained from the static FE blade calculation. In terms of the dynamic stress σ_A in Eq. (13), the material damping is remarkable for martensitic steel alloys with 12% chromium (Cr) and insignificant for most other steel alloys. For the X20Cr13 alloy of the SK blade, in ambient temperature the experimental material modal damping ratio ξ [24] changes linearly from 0.04% up to 0.27% by increasing the dynamic normal stress from 40 MPa up to 100 MPa. Below 40 MPa, which is expected for the blade operation conditions, the material damping is not measured and a value of 0.04% is used in further forced vibration computations.

[1]For X20Cr13 blade alloy, $J=2\times10^{-10}$ and $\eta=2.1$ at 500°C [34].

Table 3 The analytical $c_{t,o}$ and numerical c_t resulting tangential contact stiffnesses for stuck bolts at the smallest SK blade

	Resulting tangential stiffness at the bolt contact					
	On the suction airfoil side			On the pressure airfoil side		
Rotational speed Ω_n	Analytical $c_{t,0}$ (MN/m)	Numerical c_t (MN/m)	Relative error δc_t (%)	Analytical $c_{t,0}$ (MN/m)	Numerical c_t (MN/m)	Relative error δc_t (%)
100.0%	38.13	29.49	29.29	36.42	38.19	29.21
62.5%	27.87	9.83	183.49	26.63	9.40	183.24

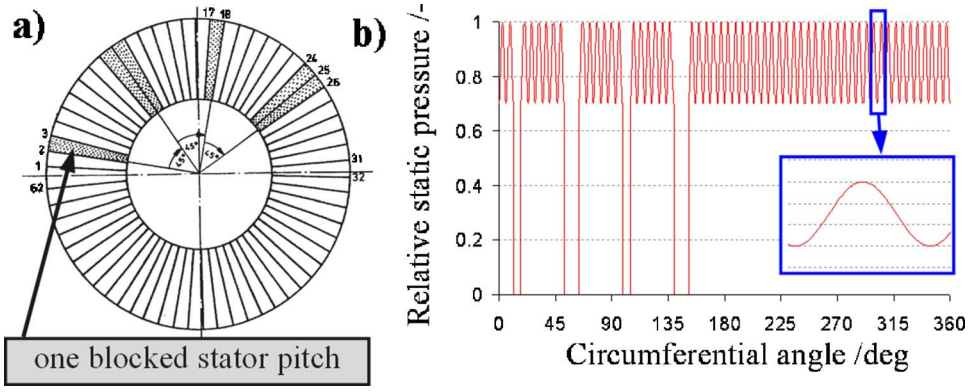

Fig. 6 (*a*) The partial arc admission arranged for the amplification of the eighth engine order within the stator of 40 vanes at the setup in Fig. 1 (*c*). (*b*) Its idealized pressure alteration from 0 up to 1 with nozzle effects (from 0.7 up to 1) from unblocked stator pitches modeled as sinus wave (see zoom).

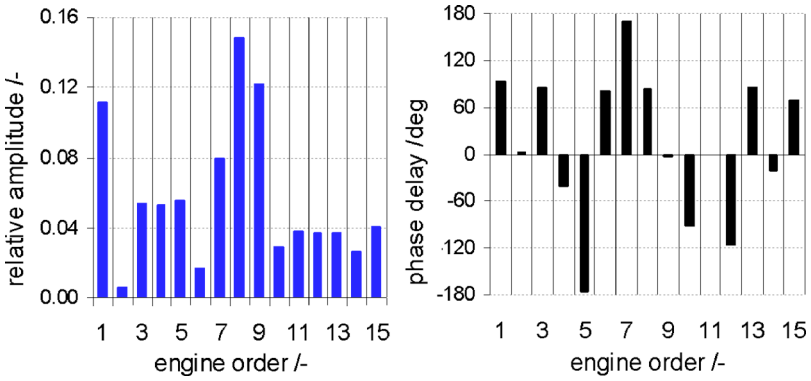

Fig. 7 The estimated relative excitation spectrum for the assumed pressure distribution of the partial arc admission shown in Fig. 6(*a*)

Besides the friction dissipation at the bolts, the essential damping comes from the aerodynamics of the SK blade measured under service conditions. The aerodamping can be determined either with the numerical flutter analysis [35] or from the measured resonance frequency responses [36]. For the partial arc admission, the 12 freestanding blades were measured by Wolter [25] at the same test rig. The measured resonance FRFs are presented in Fig. 8(*a*). Using the half-band method [36], the evaluated modal damping ratios varies between 0.21% and 0.40% for the partial arc admission excitation. For the nominal service condition, the damping ratios of these blades are slightly smaller and the damping ratio varies between 0.17% and 0.19% (Fig. 8(*b*)). This is probably due to the lower contribution of the material damping to the reduction of resonance stresses in the blades. Considering uncertainties in this evaluation as well as in the measurements, the damping magnitudes of the freestanding blades in service can alter between 0.2% and 0.3% mainly due to the aerodamping dissipation. In the comparable range between 0.23% and 0.35%, the experimental modal damping ratios ξ are found experimentally in [37] for the rotating axial blades.

From Beckbissinger's [13] experimental resonance response curves given in Fig. 8(*c*), the evaluated modal damping ratios of the smallest SK blades coupled by the bolts can vary between 1.6% and 1.8% for the excitation arranged by the partial arc admission. For the nominal service condition with the ordinary stator arrangement, their damping values become smaller and alter between 0.7% and 1.2%. For all operation conditions, the evaluated overall damping magnitudes of the blades coupled by bolts are at least three times higher than those for the freestanding blades. According to the evaluated damping magnitudes (Fig. 8), the modal damping ratio of 0.3% is assumed for further numerical simulations of the SK blades with the bolt coupling as the reference minimum overall aero- and material damping.

Besides the considered friction dissipation at the bolts, the friction damping can occur also in the blade root. For different centrifugal and bending loads, Matveev et al. [38] measured damping dissipation in the radial root with two fingers assembled by one pin to the rotor. For a centrifugal load of 30 kN and a temperature of 350°C, the measured damping ratio ξ at this root, made of titanium alloy, changes linearly from 0.03% up to 0.70% by increasing the bending airfoil load from zero to 350 N. The SK roots with four fingers assembled with two conical pins to the rotor (Fig. 1) are much more rigid than the specimens of Matveev et al. Therefore, the overall damping magnitudes of the freestanding SK blade are two times smaller (Fig. 8(*b*)) than the results of Matveev [38]. Then, friction dissipation in the SK root will not be considered for further simulations.

Comparison of the Experimental and Numerical Campbell Diagrams

According to the experimental results in Fig. 9, a brake load of 800 N in the water friction dynamometer (Fig. 1(*c*)) relates to a mass flow rate of 2.5 kg/s. For this mass flow, the resulting static axial F_{ax} of 2[2] and circumferential F_{ci} of 2.85[3] bending forces at point Λ (Fig. 1(*b*)) are obtained from the stationary flow calculation. For these forces, the average FE bending static von Mises stress σ_{BN} of 1[3] is found at the bottom of the freestanding SK blade (Fig. 1(*b*)) at a rotational speed of $0.625\Omega_n$. Then, by substituting Eq. (2) into Eq. (1), for the unknown stimulus s, the experimental dynamic strain ε_A at gauge A is given by

$$\varepsilon_A = \frac{\chi s f \sigma_{BN}}{2\xi K_\varepsilon E_S} \tag{14}$$

for the measured ε_A, and by substituting Eqs. (3) and (4) into Eq. (14), the unknown stimulus s can be obtained from

$$s = \frac{2\varepsilon_A \xi K_\varepsilon E_S}{\sigma_{BN} f \cos^{-1}(\gamma(\Omega_{62.5\%})_{i,n})} \tag{15}$$

where $\chi = \cos^{-1}(\gamma(\Omega_{62.5\%})_{i,n=1,s})$. The excitability factor (modal force) $f \equiv f_{\Lambda,i,n}$ at the driving node Λ (Fig. 1(*b*)) is expressed with

$$f_{\Lambda,i,n} = \begin{Bmatrix} \phi'^{0/}_{\Lambda,ax,i,n,c} - j\phi'^{o/}_{\Lambda,ax,i,n,s} \\ \phi'^{o/}_{\Lambda,ci,i,n,c} - j\phi'^{o/}_{\Lambda,ci,i,n,s} \end{Bmatrix}^T \begin{Bmatrix} F_{ax} \\ F_{ci} \end{Bmatrix} \tag{16}$$

where $\Phi'^{o/}_\Lambda = \text{col}\{\phi'^{o/}_{\Lambda,ax}, \phi'^{o/}_{\Lambda,ci}\}$ are the mass-normalized FE complex mode shapes of node Λ in axial and in circumferential direction, respectively.

If the Campbell diagram is not computed and the measurement is not done at the particular rotational speed of interest, the coupling order $\gamma_{i,n}$ between the resonances $\omega_{i,n}$ and $\omega_{i,m}$ is obtained from the FE nodal diameter curves for the specified rotational speed Ω_s of $0.625\Omega_n$ by

$$\gamma(\Omega_s)_{i,n} = \frac{\omega_{i,m} - \omega_{i,n}}{(m-n)\Omega_s} \tag{17}$$

where the nodal diameter number m and n fulfill the condition of $m > n$. For the freestanding blade rigidly coupled at the rotor, whose eigenfrequencies are identical for all nodal diameters ($\omega_{i,m} = \omega_{i,n}$), the coupling order $\gamma_{i,n}$ is equal to zero and the cou-

[2]All static loads are normalized with the same constant factor n_F.
[3]All bending stresses are normalized by the same factor n_σ.

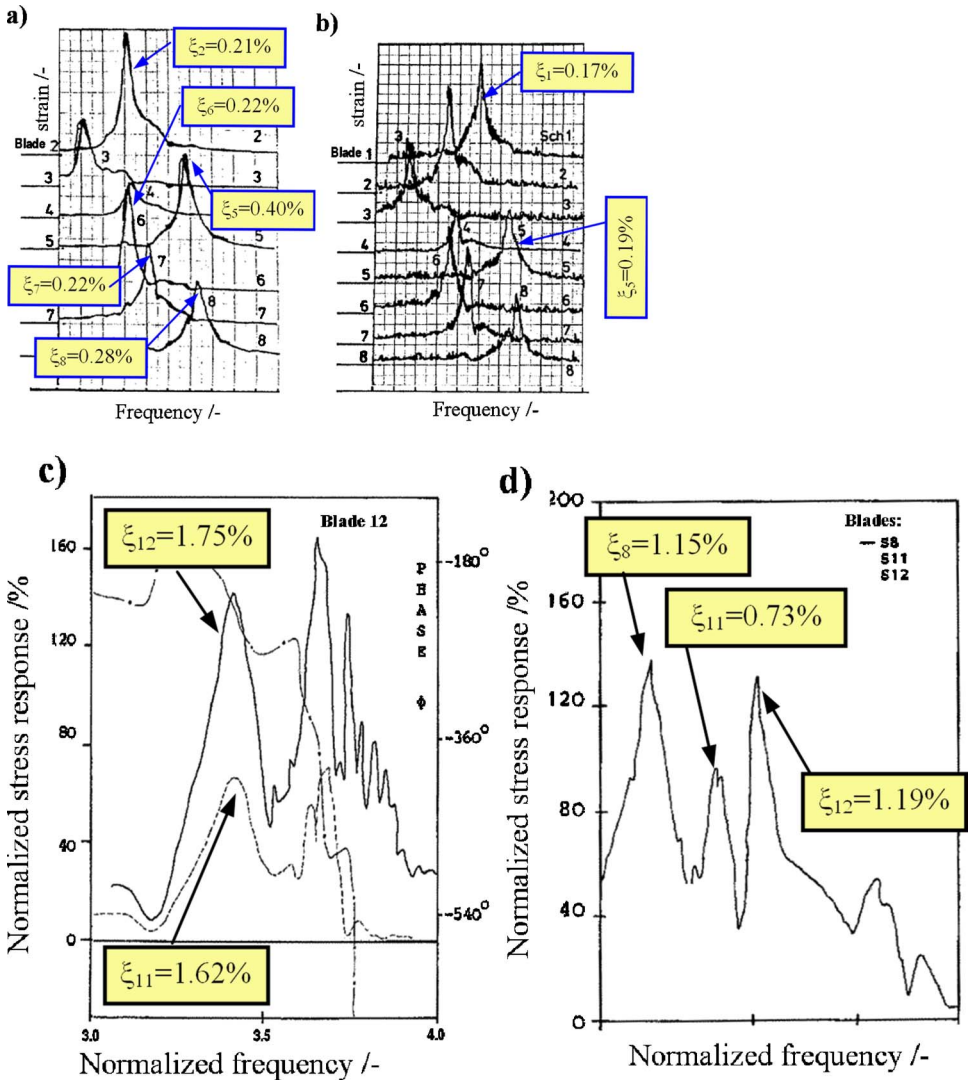

Fig. 8 The experimental overall modal damping ratios where ξ_m denotes the damping value for blade *m*. (*a*) Freestanding blades for the excitation of the partial arc admission. (*b*) Freestanding blades under the nominal service condition with the ordinary stator arrangement. (*c*) Blades with bolts for the excitation arranged by the partial arc admission. (*d*) Blades with bolts under the nominal service condition with the ordinary stator arrangement.

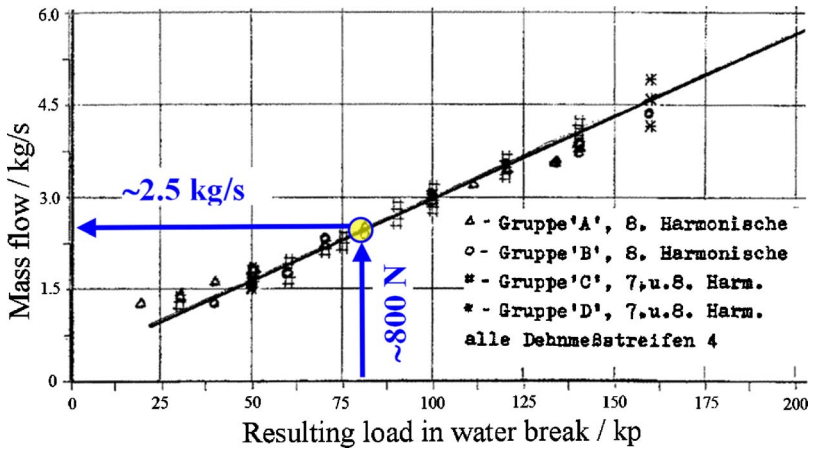

Fig. 9 The measured mass flow rate in the smallest SK turbine at the test rig with respect to the break load [39], where 80 *kp*≈800 N

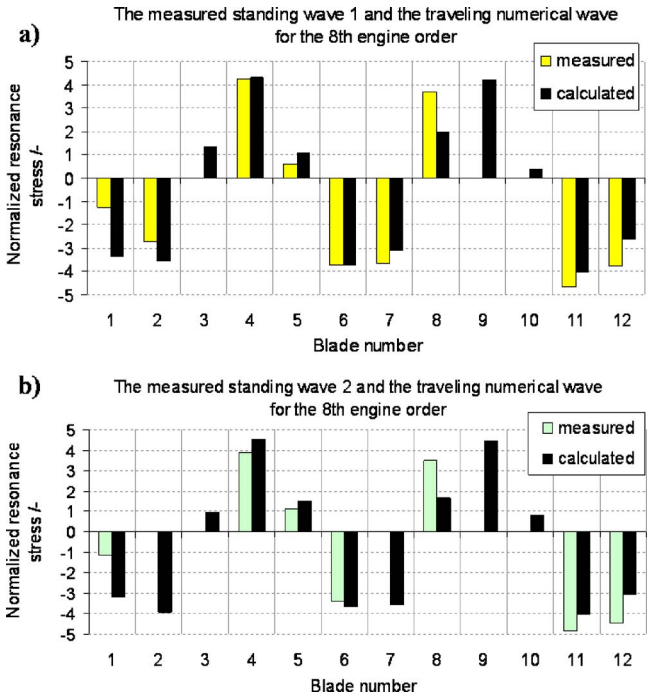

Fig. 10 The comparison of the numerical results of the tuned model with the measured stresses of the real mistuned smallest SK blades excited by the partial arc admission for the resonance frequency (*a*) ω' and (*b*) ω'' shown in Fig. 2

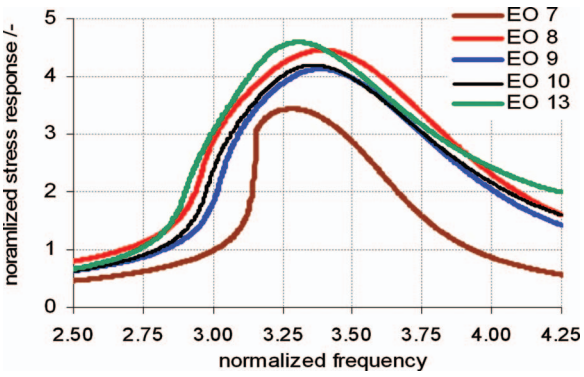

Fig. 11 The numerical resonance frequency responses of the smallest SK blade rotating with $\Omega_s=0.625\Omega_n$ in service at the setup with the arranged partial arc admission (aerodamping $\xi_0=0.3\%$, $\mu=0.15$)

pling factor $\chi_{i,n}=\cos^{-1}(\gamma_{i,n})$ equals 1, as suggested by Traupel [26].

For the arc partial admission and a break load of 700 N, Beckbissinger [13] carried out the measurements at the constant speed $\Omega_s=0.625\Omega_n$. For blade 4, he obtained the resonance stresses $\sigma_{A,P}$ of 4.32[4] and 4.40[4] at the resonance frequencies ω' and ω'' (Fig. 2), which correspond to two standing waves of the mistuned disk assembly. Then, for the measured strains $\varepsilon_A=\sigma_A/(K_\varepsilon E_S)$, the stimulus values s are estimated from Eq. (15) and are equal to 0.0368[4] and 0.0361[5] for the FE mode shapes regarding the sticking contact condition at the bolts. The FE mode shapes for frictionless slipping contact conditions at the bolts are not used because the FE eigenfrequency $\omega_{1,8}$ computed for the sticking bolts corresponds very well to the measured resonance frequency [10].

For the determined stimulus s, static bending forces F_{ax} and F_{ci}, an evaluated aerodamping value ξ_0 of 0.30%, a given friction coefficient μ of 0.15, determined contact stiffnesses c_n and c_t as well as the FE reactions R_{S3} and R_{P3} (Fig. 3) and the FE contact area represented with 100 contact points ($\iota=100$), the nonlinear forced vibration analyses of the smallest SK blade are performed for an engine order of 8 at turbine speed $\Omega_s=0.625\Omega_n$. By the adjustment of the numerical stress $\sigma_{A,num}$ with the measured one, the numerical stimulus s_{num} of about 0.0364[5] is obtained. The resonance stresses at 12 measured and computed blades are compared to each other in Fig. 10.

For a few blades, the measured signals had a bad quality and were not represented in Fig. 10. The traveling FE wave of the stresses is determined with respect to the circumferential angle α from

$$\sigma(\alpha)_{i,n}=\sigma_{0,i,n}\cos[2\pi n(B-1)N+\alpha_0] \tag{18}$$

where $n=8$ is the engine order, $B=1,2,\ldots,N$ denotes the blade number, and $\sigma_{0,i,n}$ is the numerical resonance stress amplitude. A circumferential angle α_0 of 140 deg is the required shifting angle to make the FE traveling wave coincident with the standing experimental wave at the measured maximum stresses at blade 4 for waves ω' and ω'' (Fig. 10). Then, the relative excitation spectrum in Fig. 7 is adjusted with respect to the proven numerical stimulus s_{num} of the eighth engine order. By updating the FE reaction forces and FE contact area, the nonlinear forced vibration responses ($\mu=0.15$, $\xi_0=0.3\%$) of the smallest SK blade with bolts are calculated for engine orders of 7, 9, 10, and 13. The calculated resonance frequency functions are given in Fig. 11. All these resonance response functions indicate the presence of friction dissipation regarding their asymmetrical forms, especially for an engine order of 7.

The numerical resonance amplitudes and resonance frequencies (Fig. 11) are compared with the experimental results in the measured Campbell diagram shown in Fig. 12. For the maximum relative error of 12% (Table 4), the computed resonance stresses are in good agreement with the experimental results of the real mistuned blades except for the ninth engine order. A stress difference of 43% (Table 4) for the ninth engine order is probably caused by too far idealization of the pressure distribution of the partial arc admission (Fig. 6(*b*)). For this hypothetical pressure, unexpected high excitation amplitude of the ninth engine order is determined in relation to that of the eighth harmonic. This seems to be confirmed by the experimental results in the Campbell diagram, where the response for the eighth engine order dominates significantly over the measured resonance stresses of engine orders of 7 and 9. Also, the numerical CFD results in Ref. [33] confirm irregular pressure distributions in the partial arc admission instead of the regular hypothetical shape.

In addition, for the seventh engine order, the significant difference is obtained between the numerical and experimental frequencies in the Campbell diagram (Fig. 12), which cannot be explained by the mistuning effect. Indeed, for all considered engine orders of 7, 8, 9, 10, and 13, the nonlinear dynamic analyses are performed with the same contact stiffness values and modal blade definition corresponding to 62.5% of the nominal speed. Only the FE reaction forces and contact area are changed always with respect to the rotational speed of the analyzed engine order. The normal contact stress c_n does not vary in terms of the speed (Tables 2 and 3), but magnitudes of the tangential contact stiffness c_t increase significantly from 9.8 MN/m up to 29.5 MN/m by increasing the speed from 62.5% to 100% of the nominal speed. Thus, for the resonance computation of the seventh engine order, the used tangential contact stiffness was too weak, and the computed resonance frequency was too low. By using a higher tangential contact stiffness at the speed of the excitation of the sev-

[4]Each stimulus is normalized with the same constant factor.
[5]All frequencies are scaled by the same constant factor n_0.

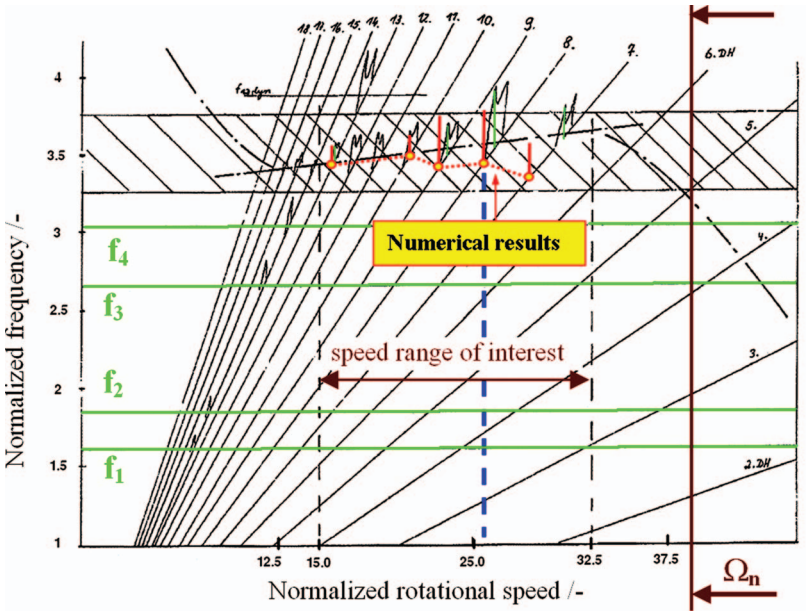

Fig. 12 Comparison of the numerical resonance stresses and frequencies with the experimental Campbell diagram of the first eigenfamily of the smallest SK blades with the bolt coupling excited by the partial arc admission, where f_1-f_4 show frequencies of the freestanding blade

enth engine order, the calculated resonance frequency will be found in the range of the measured results shown in the Campbell diagram.

The here described numerical process of the contact stiffness assessment based on the FE-modal adjustment is intensive work. Therefore, the contact properties were determined only at two different speeds to verify the sensitivity of the contact stiffness values in terms of the speed. In the future, the whole process of the stiffness prediction for different speeds and then the nonlinear dynamic simulations will be a self-acting numerical process.

Damping Performance of SK Blades

By comparing the resonance blade responses with the sticking bolt connection and with the friction bolt coupling, the damping effectiveness of the smallest SK blade is illustrated in Fig. 13. In relation to the blade vibration with fully sticking bolts, the frequency shift $\Delta\omega=(\omega_{\mu=\infty}-\omega_{\mu=0.15})/\omega_{\mu=\infty}$ of ~3.4% is found, which is comparable to an experimental value of ~3% (Fig. 2). The resonance stresses are reduced by factor $\Psi_\sigma=6$, which corresponds to an equivalent damping ratio $\xi_E=\Psi_\sigma\xi_0$ of 1.8% for the reference viscous damping value ξ_0 of 0.3%. The estimated equivalent damping value ξ_E is in the range of the overall damping ratio ξ evaluated from the measured resonance response functions shown in Fig. 8(*b*).

In the design process of the blades with dampers, bolts, or shrouds, the performance curve [13] is a valuable diagram that assesses the nonlinear blade responses in relation to the allowable resonance stress. This allowable resonance stress is obtained from the Haigh diagram, which is created with the linear FE results of the blade either with frictionless or with sticking bolt coupling. Then, from each nonlinear dynamic simulation of the smallest and large SK blades with friction dissipation at bolts, the computed resonance amplitude is entered as one result point into the performance diagram with respect to the excitation magnitude, as illustrated in Fig. 14 for an initial modal damping ratio ξ_0 of 0.5% corresponding to the overall material and aerodynamic damping. Considering uncertainty with friction coefficients depending on many physical aspects, which are not accomplished in the used Coulomb law, the nonlinear dynamic analyses of both smallest and large SK blades are performed for the expected minimum of

Table 4 The relative errors $\delta\sigma=(\sigma_{num}-\sigma_{expt})/\sigma_{expt}$ between the measured and computed ($\mu=0.15$, aerodamping $\xi_0=0.3\%$) resonance stresses, where the experimental stress for the eighth engine order was used to determine the stimulus (Fig. 10)

	Normalized resonance stress		
Engine order (EO)	Experimental σ_{expt}	Numerical σ_{num}	Relative error $\delta\sigma$ (%)
7	3.11	3.44	10.6
8	4.50	4.46	−0.9
9	2.86	4.08	42.5
10	2.07	1.82	−11.9
13	2.05	2.20	7.6

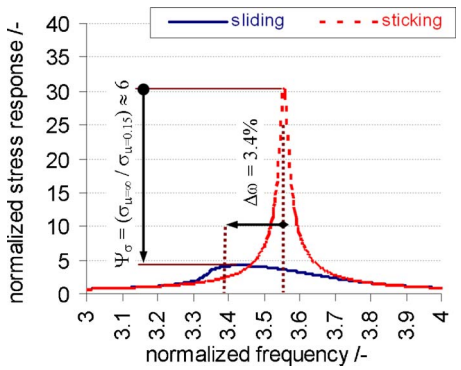

Fig. 13 Resonance responses of the smallest SK blade with the full sticking and with the sliding bolt coupling excited by the eighth engine order for a reference viscous aerodamping damping ξ_0 of 0.3% and a friction coefficient μ of 0.15

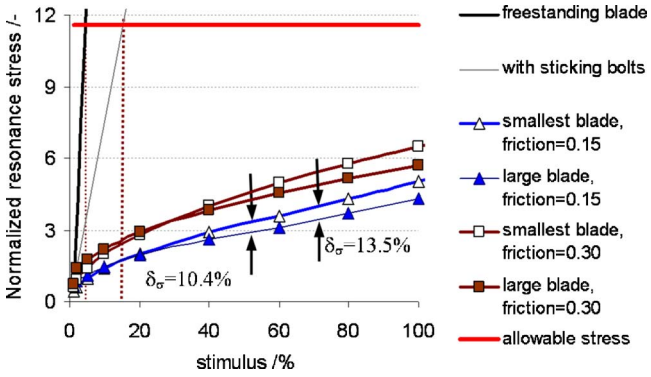

Fig. 14 Performance curves of the smallest and large SK blades excited by the eighth engine order at $\Omega_s=0.625\Omega_n$ under the service condition for the assumed aerodamping ξ_0 of 0.5%, where a stimulus of 100% is equal to the static steam bending load at speed $\Omega_s=0.625\Omega_n$

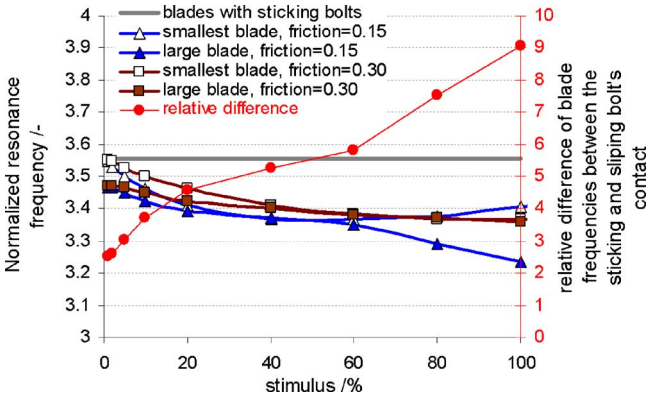

Fig. 16 Sensitivity curves of the resonance frequencies of the smallest and large SK blades excited by the eighth engine order at $\Omega_s=0.625\Omega_n$ under service conditions for the assumed aerodamping $\xi_0=0.5\%$

0.15 and maximum of 0.30 of friction coefficient, where the large airfoil is identical on a four scale-up of the smallest SK blade.

In the whole excitation range up to 100% stimulus, which refers to the steam static bending load at $\Omega_s=0.625\ \Omega_n$, the resonance vibrations of both blades with friction at bolts are significantly lower than those of the freestanding blade or with sticking bolts. Above 4% and 16% stimulus of the static steam bending load, the resonance stresses of the freestanding blade and blades coupled with sticking bolts, respectively, exceed the allowable stress. On the contrary, both blade resonances with friction effects at bolts are in the stress range of infinite life according to Haigh criteria.

Regarding the scaling criteria, the computed dynamic stresses of both smallest and large blades should be identical to each other. For friction coefficients of 0.15 and 0.30, the computed resonance stresses of both blades differ from each other between 3.5% and 14.3% (see δ_σ in Fig. 14). This is an acceptable result for the considered slight differences in the bolt dimensions applied for the smallest and large blades [10].

Both smallest and large SK blades are principally identical on a four scale-up basis v_O. For different stimuli, the scaling factors of their resonance frequencies obtained from the nonlinear dynamic simulations are determined and shown in Fig. 15. All determined scale factors $v_\omega=\omega_{small}/\omega_{large}$ vary between 3.98 and 4.2, and they are completely acceptable from the design point of view.

From the design point of view, the friction dissipation on the bolt should not change too much the blade frequency in relation to the sticking contact condition. In the whole considered stimulus range, the computed resonance frequencies of the smallest and large SK blades differ maximally about 9% with respect to their resonance frequencies for the contact with the stuck bolts, as shown in Fig. 16.

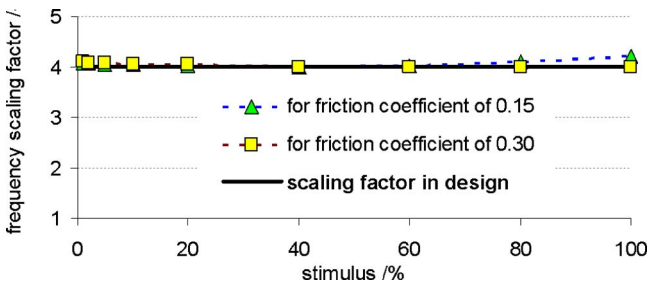

Fig. 15 Validation of the scaling factors of the resonance frequencies $v_\omega=\omega_{small}/\omega_{large}$ determined from the nonlinear dynamic simulations of the smallest and large SK blade scaled by the design factor v_O of 4

Conclusions

The experimentally developed bolt coupling system for the smallest blades has been applied to all SK units of different turbine sizes, and their effectiveness has been proven by actual operating experience. For the numerically determined tangential and normal contact stiffnesses and the considered friction sliding, the nonlinear dynamic analyses of the smallest SK blade with this bolt coupling are performed for the reference aerodamping values evaluated form the experimental resonance results of the freestanding blades in service. The computed Campbell diagram matches well the experimental results measured on the test rig of the real turbine in Stuttgart. The numerical results of the tuned disk assembly agree well with the experimental resonance stresses of 12 smallest mistuned SK blades measured with strain gauges.

The nonlinear dynamic analyses provide obvious evidence of frictional dissipation for both smallest and large SK disks in relation to the calculated resonance stresses with sticking bolts. The numerical results presented in the performance curves and sensitivity frequency diagrams confirm the scalability of the damping capabilities between the smallest and large SK blades for different stimuli, friction coefficients, and aerodamping ratios. The field experiences with the different SK blades, which operate with variable speed and in a variety of loading regimes, do not show any wear problems on the bolt and airfoil coatless contacts, as presented in Fig. 17.

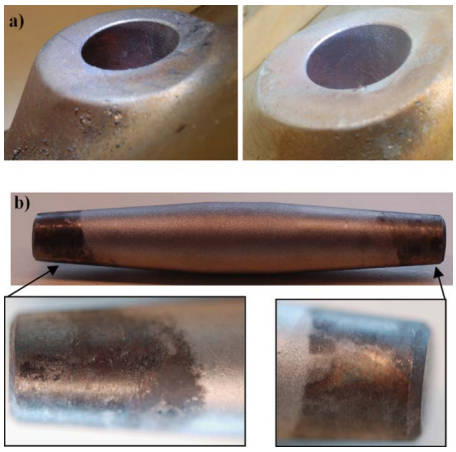

Fig. 17 Example of coatless contact conditions of SK blade (*a*) in airfoil holes and (*b*) on friction bolt after 20 years in service

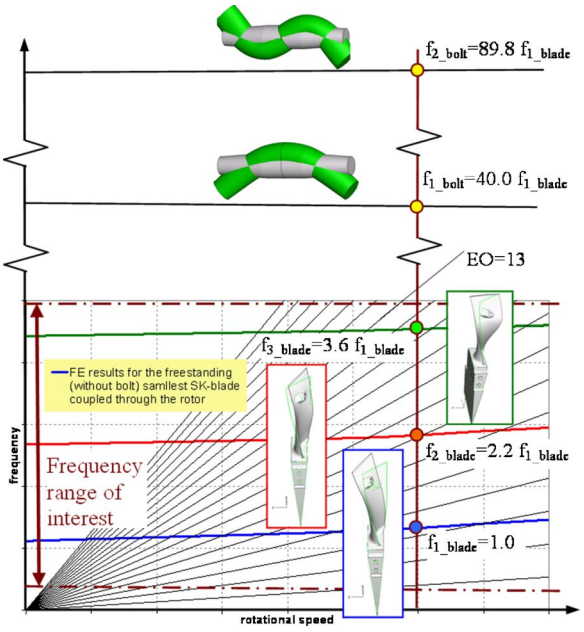

Fig. 18 The FE Campbell diagram of the freestanding smallest SK blade coupled by the rotor and the lowest natural frequencies of the friction bolt with unrestrained (free-free) boundary condition, where EO denotes the engine order and f_{1_blade} and f_{1_bolt} are the fundamental natural frequencies of the blade and bolt, respectively

The here proposed nonlinear and linear [10] numerical processes can be applied to different types of blade couplings, such as shrouds, winglets, lacing wires, zigzag pins, and underplatform dampers.

Acknowledgment

The authors thank Siemens AG for the support and for permitting the publication of this paper.

Appendix

The computed Campbell diagram (Fig. 18) illustrates the first three eigenfrequencies of the freestanding SK blade coupled by the disk, which are used in the mode synthesis for the nonlinear dynamic analysis. The fundamental natural frequency of the unconstrained friction bolt is 40 times higher than the lowest airfoil eigenfrequency of interest. Therefore, the friction bolt can be modeled as a rigid body in the nonlinear dynamic analysis of the SK blades with friction on contacts.

References

[1] Truckenmüller, F., 2003, "Untersuchungen Zur Aerodynamische Induzierten Schwingungsanregung Von Niederdruck-Laufschaufen Bei Extremer Teillast," Ph.D. thesis, Thermische Strömungsmaschinen, Universität Stuttgart.
[2] Ewins, D. J., 1973, "Vibration Characteristics of Bladed Disc Assemblies," J. Mech. Eng. Sci., **15**(3), pp. 165–186.
[3] Griffin, J. H., and Labelle, R. F., 1996, "A Rational Method for Optimizing Shrouded Damping," ASME Paper No. 96-GT-402.
[4] Srinivasan, A. V., 1997, "Flutter and Resonant Vibration Characteristics of Engine Blades," ASME Paper No. 97-GT-533.
[5] Huang, W.-H., 1981, "Free and Forced Vibration of Closely Coupled Turbomachinery Blades," AIAA J., **19**(7), pp. 918–924.
[6] Urlichs, K., 1991, "Schwingunssichere Auslegung Gebundener Turbinschaufeln," AIAA J., **71**(12), pp. 1108–1112.
[7] Filsinger, D., Szwedowicz, J., and Schäfer, O., 2002, "Approach to Unidirectional Coupled CFD-FEM Analysis of Axial Turbocharger Turbine Blades," ASME J. Turbomach., **124**, pp. 125–131.
[8] Borishanskii, K., 1974, "Characteristics of the Vibrations of Blades With Bandage Shelves," Problemy Prochnosti, **9**, pp. 97–102, in Russian.
[9] Namura, K., Siato, E., and Okabe, A., 1996, "A Method for Calculating the Natural Frequencies of Continuous Blade Structures With Three Different Types of Loose Coupling Means," *Proceedings of the Institution of Mechanical Engineers*, Paper No. C500/051IMechE.
[10] Szwedowicz, J., Secall-Wimmel, T., Dünck-Kerst, P., Sonnenschein, A., Regnery, D., and Westfahl, M., 2007, "Scaling Concept for Axial Turbine Stages With Loosely Assembled Friction Bolts: The Linear Dynamic Assessment. Part I," ASME Paper No. GT2007-27502.
[11] Swikert, M. A., and Johnson, R. L., 1968, "Friction and Wear Under Fretting Conditions of Materials for Use as Wire Friction Dampers of Compressor Blade Vibration," NASA Technical Note No. TN D-4630.
[12] Kellerer, R., 1994, "Beitrag Zum Schwingungs-Verhalten Gekoppelter Axiallaufschaufeln Unter Berück-Sichtigung Der Radscheibenelastizität," Ph.D. thesis, Institut für Thermische Strömungsmaschinen, Universität Stuttgart.
[13] Beckbissinger, L., 1982, "Schwingungsuntersuchungen vonGekoppelten Turbinenlaufschaufeln Bei Verschiedenen Betriebszuständen"," MS thesis D-54-82, Institut für Thermische Strömungsmaschinen, Universität Stuttgart.
[14] Jaiswal, B. L., Goyal, S. K., and Bhave, S. K., 1993, "Dynamic Analysis of Turbine Blade With Damping Pins," *Proceedings of the 11th International Modal Analysis Conference*, Kissimmee, FL, SPIE Vol. 1923, pp. 1544–1549.
[15] Jaiswal, B. L., and Bhave, S. K., 1994, "Experimental Evaluation of Damping in a Bladed Disc Model," J. Sound Vib., **177**(1), pp. 111–120.
[16] Wachter, J., Pfeiffer, R., and Jarosch, J., 1983, "Experimental Study to Gain Insight in the Vibration Characteristics of a Steam Turbine LP-Wheel With Lashing Pins," *ASME Proceedings on the Vibration of Bladed Disk Assemblies*, Dearborn, MI, Sept. 11–14, pp. 83–89.
[17] Sextro, W., 2002, "Dynamical Contact Problems With Friction: Models, Methods, Experiments and Applications," *Lecture Notes in Applied Mechanics*, Springer-Verlag, Berlin, Vol. 3.
[18] Petrov, E. P., 2006, "Direct Parametric Analysis of Resonance Regimes For Nonlinear Vibrations of Bladed Discs," ASME Paper No. GT2006-90147.
[19] Szwedowicz, J., Kissel, M., Ravindra, B., and Keller, R., 2001, "Estimation of Contact Stiffness and its Role in the Design of a Friction Damper," ASME Paper No. 2001-GT-0290.
[20] Szwedowicz, J., Slowik, S., Mahler, A., and Hulme, C. J., 2005, "Nonlinear Dynamic Analyses of a Gas Turbine Blade for Attainment of Reliable Shroud Coupling," ASME Paper No. GT2005-69062.
[21] Szwedowicz, J., Sextro, W., Visser, R., and Masserey, P. A., 2003, "On Forced Vibration of Shrouded Turbine Blades," ASME Paper GT-2003-38808.
[22] Figurski, H., 1981, "Schwingungsuntersuchung an Einem Realen Endstufenschaufelpaket Mit Eingelegten Dämpferelementen," Studienarbeit, Institut für Thermische Strömungsmaschinen, Universität Stuttgart.
[23] Jarosch, J., 1983, "Beitrag Zum Schwingungsverhalten Gekoppelter Schaufelsystem," Ph.D. thesis, Institut für Thermische Strömungsmaschinen, Universität Stuttgart.
[24] Pfeiffer, R., 1985, "Einfluss Unterschiedlicher Paketier-Ungen Auf Schwingungs-Verhalten Und Verbundfaktoren Von Dampfturbinen-Beschaufelungen," Ph.D. thesis, Institut für Thermische Strömungsmaschinen, Universität Stuttgart.
[25] Wolter, I., 1980, "Experimentelle Untersuchung Des Schwingungsverhaltens Von Turbinenlaufschaufeln Unter Realen Betriebsbedingungen Mit Und Ohne Kopplung Durch Einen Eingelegten Dämpferdraht," Ph.D thesis, Institut für Thermische Strömungsmaschinen, Universität Stuttgart.
[26] Traupel, W., 1982, *Termische Turbomaschinen*, 3rd ed., Springer-Verlag, New York.
[27] Treyde, T., 1994, "Koppeldaempfungen Und-Steifigkeiten Zwischen Den Kontakflaechen Der Deckplatten Von Laufschaufeln (Contact Damping and Stiffness Between the Interfaces of the Shrouds of Rotating Turbine Blades," FVV Report No. 525, BMWi/AIF Report No. 8803.
[28] Siewert, C., Panning, L., Schmidt-Fellner, A., and Kayser, A., 2006, "The Estimation of the Contact Stiffness for Directly and Indirectly Coupled Turbine Blading," ASME Paper No. GT2006-904-73.
[29] Szwedowicz, J., Gibert, C., Sommer, T. P., and Kellerer, R., 2006, "Numerical and Experimental Damping Assessment of Thin-Walled Friction Dampers in the Rotating Set-up With High Pressure Turbine Blades," ASME Paper No. GT2006–9-0951.
[30] Berutti, T., Filippi, S., Goglio, L., Gola, M. M., and Salvano, S., 2002, "A Test Rig for Frictionally Damped Bladed Segments," Trans. ASME: J. Eng. Gas Turbines Power, **124**, pp. 388–394.
[31] Koh, K.-H., and Griffin, J. H., 2006, "Dynamic Behaviour of Spherical Friction Dampers and its Implication to Damper Contact Stiffness," ASME Paper No. GT2006-90102.
[32] Balmer, B., 1993, "Erhöhung Der Dämpfung Von Turbinenschaufeln Durch Reibelemente," Fortschritts-Berichte VDI, Reihe 11, Nr. 197, VDI-Verlag, Düsseldorf.
[33] Lampert, P., Szymaniak, M., and Rzadkowski, R., 2004, "Unsteady Load of Partial Admission Control Stage Rotor of a Large Power Steam Turbine," ASME Paper No. GT2004-53886.
[34] Lazan, B. J., 1968, *Damping Materials and Members in Structural Mechanics*, Pregammon, New York.

[35] Li, H. D., and He, L., 2005, "Blade Aerodynamic Damping Variation With Rotor-Stator Gap: A Computational Study Using Single-Passage Approach," ASME J. Turbomach., **127**, pp. 573–579.
[36] Brown, W. G., 1981, "Determination of Damping Values for Turbine Blades," ASME Paper No. 81-DET-131.
[37] Kielb, J. J., and Abhari, R. S., 2003, "Experimental Study of Aerodynamic and Structural Damping in a Full-Scale Rotating Turbine," Trans. ASME: J. Eng. Gas Turbines Power, **125**, pp. 102–112.
[38] Matveev, V. V., Chaikoskii, B. S., and Rzhavin, L. N., 1970, "Damping Capacity of the Hinged Locking Joint of Turbomachine Compressor Blades (in Russian)," Problemy Prochnosti, **12**, pp. 106–109.
[39] Figurski, H., 1982, "Schwingungsuntersuchungen Von Gekoppelten Turbinenlauf-Schaufeln Bei Verschiedenen Betriebszuständen," MS thesis, Institut für Thermische Strömungsmaschinen, Unniversitä Stuttgart.

Cycle-Controlled Water Injection for Steady-State and Transient Emissions Reduction From a Heavy-Duty Diesel Engine

Rudolf H. Stanglmaier
Markisches Werk GmbH,
Haus Heide 21,
58553, Halver, Germany

Philip J. Dingle
Delphi Diesel Systems,
5725 Delphi Drive,
Troy, MI 48098

Daniel W. Stewart
Southwest Research Institute,
6220 Culebra Rd.,
San Antonio, TX 78228

A system for coinjecting mixtures of diesel fuel and water into a heavy-duty diesel engine has been developed and evaluated at the Southwest Research Institute. This system features prototype Lucas electronically controlled injectors, full electronic control, and can vary the percentage of water in the mixture on a cycle-resolved basis. Tests of this system were conducted on a production Volvo D-12 engine, and have produced reduced NO_x *and smoke emissions over steady-state and transient conditions. Water-diesel coinjection yielded a considerable improvement in* NO_x*-smoke and* NO_x*-BSFC trade-offs under steady-state engine operation. In addition, control of the water percentage on a cycle-resolved basis was shown to be an effective method for mitigating* NO_x *and smoke emissions over step-load transients. Results from this work show that a combination of aggressive EGR and* diesel+water *coinjection is very promising for producing very low levels of engine-out exhaust emissions, reducing the water storage requirements, and improving fuel efficiency. Further refinement of this injection technology is in progress.*
[DOI: 10.1115/1.2830856]

Introduction

It has been recognized for some time that water-in-fuel emulsions are effective for reducing NO_x and smoke emissions from diesel engines [1,2]. However, use of water-in-fuel emulsions can result in increased ignition delays and hydrocarbon (HC) emissions [3–6]. In-cylinder water injection systems through a separate injection nozzle are in production in the large engine industry, with no reported deterioration of engine components over 6000 h of operation [7]. Such systems are effective in reducing NO_x emissions but do not reduce smoke emissions as effectively as emulsions [2]. Recently, systems for coinjecting stratified mixtures of diesel fuel and water through a single nozzle have been shown to produce equal or superior NO_x and PM emissions benefits to emulsions [8,9]. These systems allow the percentage of water in the mixture to be varied according to the engine speed and load, and thus optimize the benefits under all operating conditions. Another important advantage of stratified diesel+water injection systems is that, by injecting a portion of fuel prior to any water, they eliminate increases in the ignition delay. Fuel+water coinjection in combination with exhaust gas recirculation (EGR) has been claimed to be the most efficient in-cylinder NO_x and PM reduction method available [9].

Diesel+Water Injection System

The injection system developed in this program features prototype Lucas 200 electronically controlled injectors (EUIs), to which water addition passages have been added. The water passage within the injectors connect a delivery line to the annulus volume of the injector through a spring-loaded check valve, as illustrated schematically in Fig. 1. Similar injector nozzle designs have been unveiled in recent years [8,9], but this is believed to be the first such application in a high-pressure unit injector. A single pressurized water manifold (4 bar water pressure) is used to supply all six cylinders, and solenoid-controlled valves (Clean Air Power, Inc. "Servojet" valves) are used to modulate the water flow into the EUI. After the desired water quantity has been introduced into the EUI, the water and diesel fuel are coinjected into the engine. In order to maintain a constant fuel delivery rate to the engine as the water quantity is varied, the injection angle of the EUI must be adjusted, as shown schematically on Fig. 2. That is, the period of time over which the injector must be actuated to inject an equal volume of fuel must be changed. This compensation is performed automatically by the electronic control system. A Southwest Research Institute Rapid Prototyping Electronic Control System (RPECS) is used to control all functions of the engine, including the water-metering valves and EUI. This controller incorporates all algorithms and calibrations necessary for operation of this engine. One notable disadvantage of this injection system design is that variability in the water-metering system directly affects the variability in the fuel metering system. For instance, a reduced amount of water delivered into the EUI on a given cycle will result in an excessive amount of fuel being injected into the cylinder on that same cycle. Prior to the test program, extensive calibration of the fuel+water injection system was performed over the engine's operating range using in-line Coriolis mass flow meters.

A production Volvo D-12 heavy-duty engine was used to evaluate the diesel+water injection system. This is a turbocharged, in-line six cylinder engine, with EUI. The original engine was a 1995 production model, rated at 400 hp. Installation of a slightly faster injection rate camshaft and modification to the valve cover to incorporate the water supply hardware were required. A cooled, low-pressure loop EGR system was used to explore the combined effects of water injection and EGR. De-ionized water was used in these trials, and a commercial additive to inhibit corrosion was added to the water supply (Octel DCI-4A, ~10 ppm).

Cylinder 1 of the engine was equipped with a cylinder pressure transducer, and the rocker arm on that same cylinder was instrumented to record injection pressures. A standard emission bench was used to measure steady-state gaseous emissions, and a Bosch smoke meter was used to correlate the steady-state PM emissions (to increase the sensitivity of this measurement, five consecutive "pulls" were performed onto each filter paper). A prototype NGK-Locke brand exhaust NO_x sensor was used to measure the tran-

Manuscript received June 2, 2005; final manuscript received September 25, 2007; published online March 26, 2008. Review conducted by Jim Cowart.

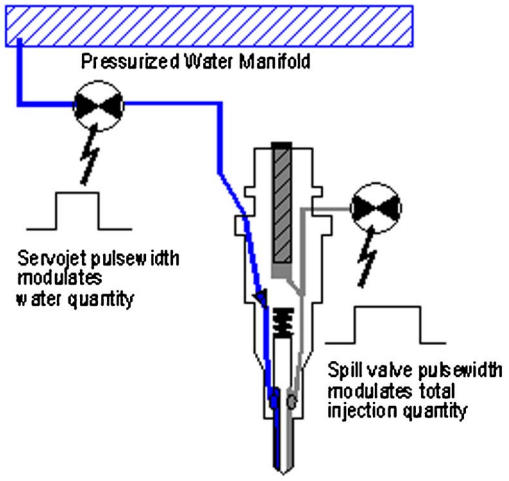

Fig. 1 Schematic of the fuel+water coinjection system

sient NO_x concentration in the exhaust stream, and an end-of-line PHS brand smoke opacity meter was used to quantify the engine's transient smoke emissions. EGR percentages are reported in percent by volume.

Effects of Water Addition on the Engine

Coinjection of diesel fuel and water significantly impacts the injection and combustion characteristics of the engine. These effects are discussed here and illustrated on Figs. 3–5. In order to accommodate the additional volume of water within the injection event, it is necessary to increase the injection duration or injection angle. This is illustrated in Fig. 3, which shows the normalized injector pressure for two cases under identical engine power (1450 rpm, 1300 N m torque) and injection timing. It can be seen that the injection event must be lengthened by about 5 CAD (crank angle degree) for the fuel+30% water (by volume) injection case, compared to the fuel-only base line, and that this results in a 12% increase in the peak injection pressure. These changes in the injection event have important repercussions on the heat release rate, as discussed in the following paragraphs.

Figure 4 shows the normalized heat release rate (HRR) for these same two engine tests (average of 100 cycles). This plot shows that the peak HRR is reduced for the fuel+30% water condition, but that the combustion duration is extended. Note that the premixed portion of the burn is nearly identical for both cases, and that the ignition delay is also nearly unchanged. Emulsified fuel/water mixtures are known to lengthen the ignition delay and increase the premixed portion of the heat release [1,3,4]. Fuel and water coinjection systems employing nozzles similar to those used for this work have been shown to generate stratified water-fuel mixtures [9], which eliminate changes to the ignition delay by injecting a fraction of the fuel prior to any of the water. Mixture stratification was not investigated directly in this study. However,

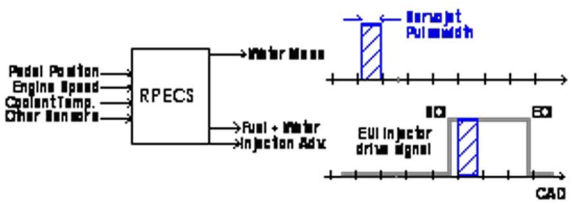

Fig. 2 Schematic of control system for fuel+water coinjection system

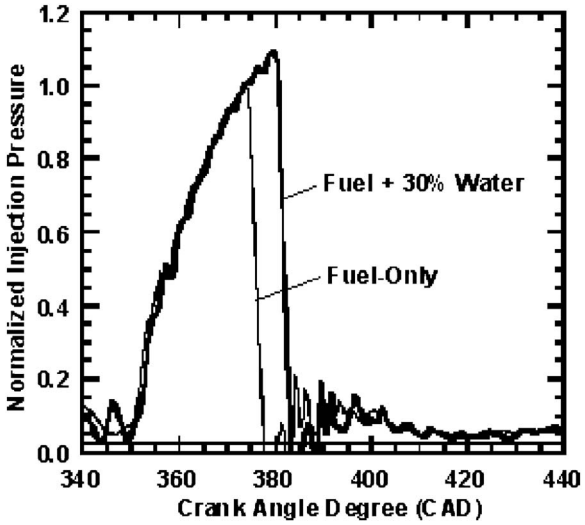

Fig. 3 Normalized injection pressure comparing fuel-only and fuel+30% water injection cases, under equal engine operating conditions (1450 rpm, 1300 N m)

it may be deduced by the absence of large changes to the ignition delay that stratification of the fuel and water most likely occurs with this particular injector design.

The normalized cylinder pressure history for the same two engine tests is shown in Fig. 5. This plot shows that the peak cylinder pressure for the fuel+30% water case is reduced by about 5% in comparison with the fuel-only base line. The effects of fuel +water coinjection on the engine's emissions and performance are discussed in the following sections.

Engine Emissions and Performance Tests

The performance of the fuel+water injection system was evaluated in a series of steady-state and step-load-transient engine tests. The focus of the steady-state tests was to evaluate the potential emissions and efficiency improvements attainable over a standardized engine test cycle. The step-load-transient tests, on the other hand, investigated the potential use of cycle-resolved water control for transient emission mitigation.

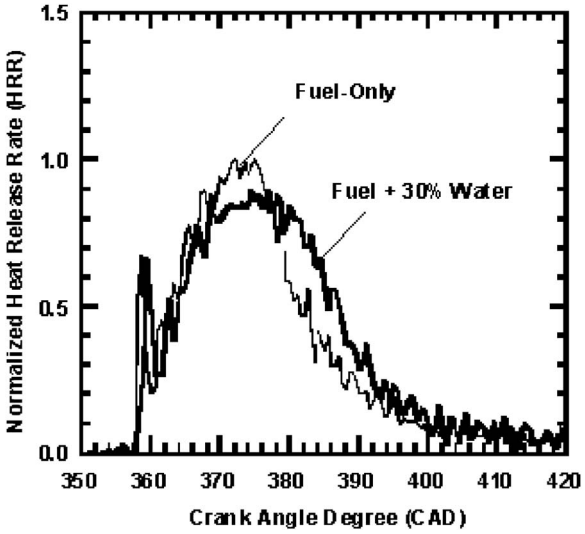

Fig. 4 HRR comparing fuel-only and fuel+30% water injection cases, under equal engine operating conditions (1450 rpm, 1300 N m)

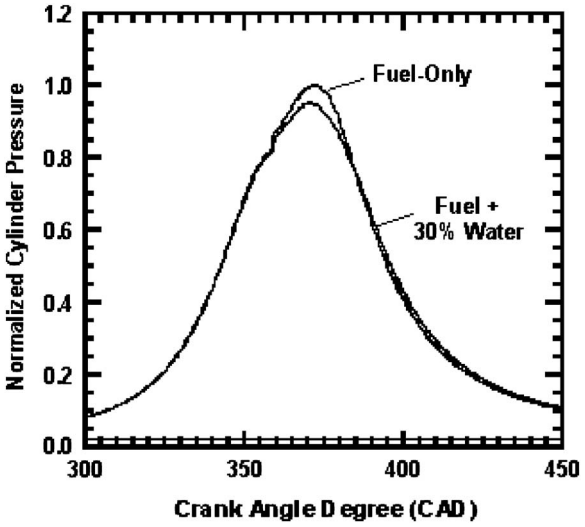

Fig. 5 Normalized cylinder pressure comparing fuel-only and fuel+30% water injection cases, under equal engine operating conditions (1450 rpm, 1300 N m)

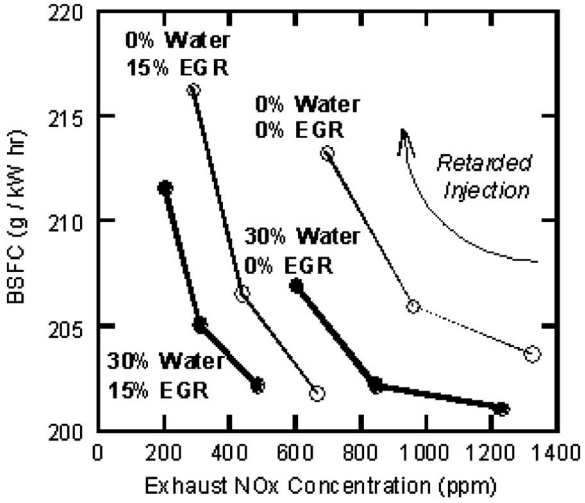

Fig. 7 BSFC versus NO_x for fuel only and fuel+30% water, as a function of injection timing. 1450 rpm, 875 N m with and without EGR

Steady-State Engine Tests. A series of steady-state engine tests was performed to assess the effect of fuel+water coinjection on the performance and emissions of the test engine with and without EGR. A selection of these results is shown in Figs. 6–9, which show results for an engine operation condition of 1450 rpm and 875 N m of torque. Figure 6 compares the five pull Bosch smoke number (Bosch smoke test in which five samples of gas are drawn through the same filter to increase the test's sensitivity) versus exhaust NO_x concentration, for fuel-only and fuel+30% water injection, with and without EGR. The EGR in this work is presented as a percent by volume in the intake charge. This plot shows that, in addition to the expected NO_x reduction, water injection results in a very large reduction in smoke emissions. Figure 7 shows that water injection at this percentage also has a beneficial effect on brake specific fuel consumption (BSFC). An even larger BSFC benefit is possible at equivalent NO_x emissions than the fuel-only base line if the injection timing is advanced (note that injection timings on Figs. 6 and 7 correspond to those in Figs. 8 and 9). Figures 8 and 9 show the effect of water injection on the carbon monoxide (CO) and total HC concentrations, respectively. A reduction in engine-out CO and HC was observed at this and all other steady-state test conditions examined. However, no points below 50% load were possible with this prototype water injection system. Note that increases in HC and/or CO emissions are commonly reported with water-in-fuel emulsions and other water introduction methods [1,3–6,10].

The NO_x reduction obtained with emulsified or stratified water injection is proportional to the water percentage in the mixture. It is possible to coinject large amounts of water with the fuel to obtain correspondingly large NO_x reductions [8]. However, from a practical standpoint, it is desired to minimize the water percentage that is used, particularly for road-going engine applications.

In this project, it was determined that a combination of EGR and water injection was most effective for achieving simultaneous reductions in NO_x and smoke emissions. Water injection and EGR have an additive effect on NO_x reduction, and fuel+water coinjection overcomes the smoke increase due to EGR. This potential benefit of this approach was evaluated over the European steady-

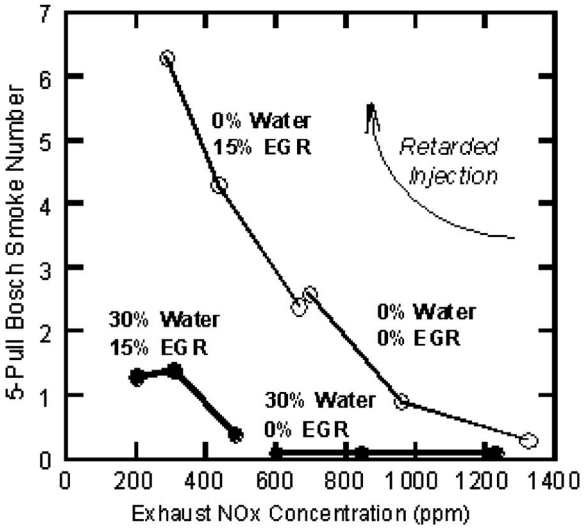

Fig. 6 Smoke versus NO_x for fuel only and fuel+30% water, as a function of injection timing. 1450 rpm, 875 N m with and without EGR

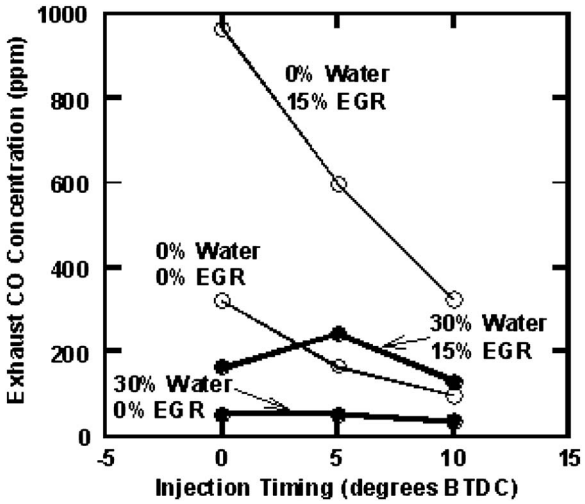

Fig. 8 Exhaust CO concentration for fuel only and fuel+30% water, as a function of injection timing. 1450 rpm, 875 N m with and without EGR.

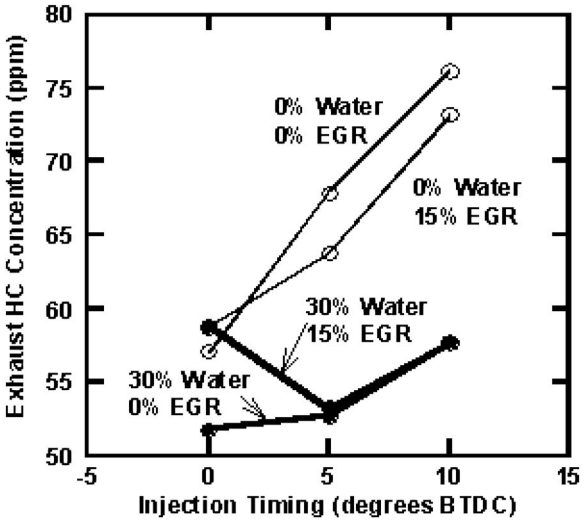

Fig. 9 Exhaust HC concentration for fuel only and fuel+30% water, as a function of injection timing. 1450 rpm, 875 N m with and without EGR

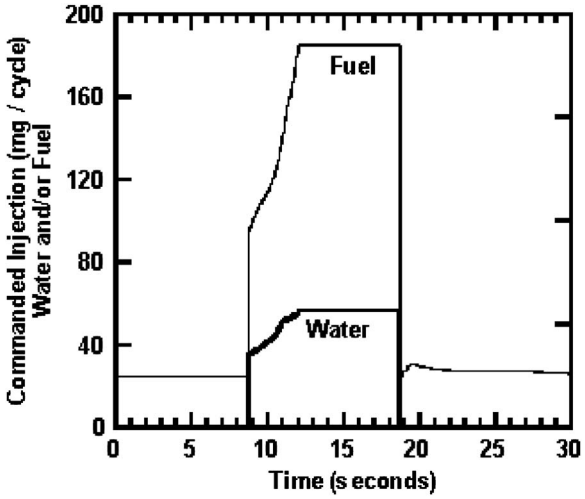

Fig. 10 Commanded water and/or fuel injection rate during step-load transient

state cycle (ESC) test.

A simulated ESC (also known as the OICA) 13-mode test was performed using the fuel+water coinjection system and aggressive levels of EGR. The ESC test and corresponding test conditions are described in Appendix. This prototype injection system was not able to meter small volumes of water accurately, so that engine test points using the fuel+water system were limited to 50% load and higher. In order to examine the effect of water at lower engine loads, an emulsified fuel containing 13% water (by mass) was used at the 25% load and idle test points. Particulate emissions were not measured directly but were estimated by adding 27% of the BSHC to the estimated soot emissions. A correlation proposed by Homan [11] was used to estimate soot emissions from the Bosch smoke measurements. The cycle-averaged results of this test are shown on Table 1 and compared to the proposed Euro V standards for heavy-duty engines. These test results suggest that the combination of EGR and fuel+water coinjection may potentially achieve the proposed standards, with the exception of PM. However, a current-technology particulate trap could probably be used in combination with this technology to achieve the Euro V standard.

Step-Load-Transient Engine Tests. Fuel+water coinjection was shown to produce attractive reductions in NO_x and smoke emissions during steady-state engine operation. However, the most interesting feature of this system is probably its ability to mitigate emission during engine transients. One of the main distinguishing features of this injection system, compared to other water injection systems in the past, is the ability to modulate the water percentage in the injected mixture on a cycle-resolved basis, which enables the possibility for using water injection to control transient engine emissions. Step-load transient were used to investigate the transient emission reduction potential of this technology. This approach is exemplified in Figs. 10–14.

Two identical step-load-transient tests were performed to compare the engine's behavior when running exclusively on diesel fuel (fuel only), and on diesel and water coinjection (fuel +water). Figure 10 shows the commanded water and/or fuel injection schedule during one step-load transient (y-axis scale refers to fuel amount and is intended to illustrate timing). This transient goes from a 10% torque condition to peak torque and back to 10% torque, at near-constant engine speed. This test cycle is made to represent part of the European load response (ELR) test cycle, but with a slightly more aggressive step-load transient (10–100% load used here, but 15–100% load in the ELR). The injection timing was held constant throughout the test, and equal manifold air pressure (MAP)-based smoke-limiting algorithms were used for both cases.

Figure 11 shows that the fuel-only and fuel+water cases produced nearly identical torque rise rates, and Fig. 12 shows that comparable air-to-fuel ratios were achieved during the up tran-

Table 1 ESC (OICA) cycle averaged results using fuel+water coinjection and EGR.[a]

ESC (OICA) 13-mode test	Units	Fuel+water coinjection and EGR	EURO V standard (2008)
$BSNO_x$	g/kW h	1.71	2.0
BSPM	g/kW h	NA[a]	0.02
BSCO	g/kW h	0.71	1.5
BSHC	g/kW h	0.14	0.46
BSFC	g/kW h	215	—
BSWC	g/kW h	75	—

[a]An estimated BSPM value of 0.08 g/kW h was calculated using the procedure proposed by Homan [11].

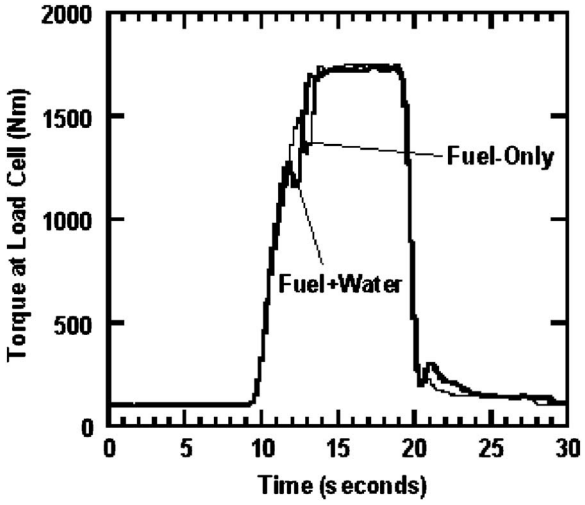

Fig. 11 Torque rise rate during step-load transient

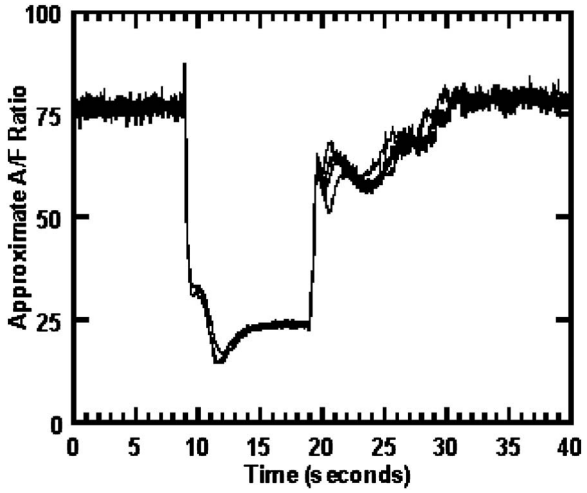

Fig. 12 Approximate air to fuel ratio during the step-load transient

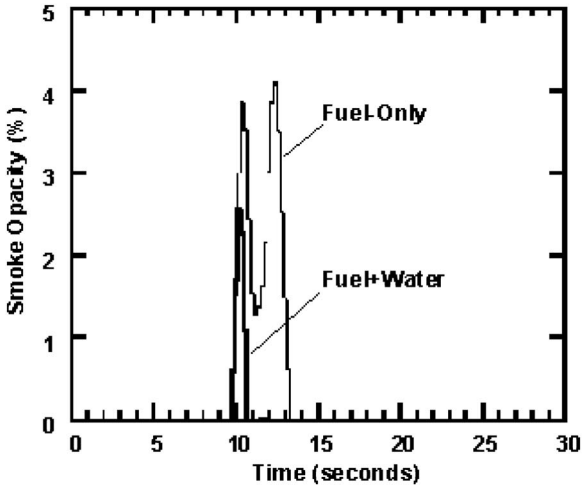

Fig. 14 Smoke opacity during the step-load transient

sient in both cases. Hence, the effect of cycle-controlled water injection was evaluated versus the fuel-only base line under nearly identical test conditions. The exhaust NO_x concentration was measured postturbocharger with the prototype NGK-Locke brand exhaust NO_x sensor [12]. It was confirmed by comparison with the chemiluminescence NO_x detector during the steady-state tests that this NO_x sensor is not affected by the water addition.

Figure 13 shows the exhaust NO_x concentration for both tests. This plot shows that using cycle-controlled water injection, it was possible to virtually eliminate the NO_x increase associated with the transient. Figure 14 shows the smoke opacity measured for both cases during the same step-load-transient test. This plot shows that fuel+water coinjection also reduced the smoke opacity level substantially, particularly the second peak in the plot. The effect on opacity is much more evident on the second peak of Fig. 14 because the water injection strategy is slightly delayed (it is not possible to introduce small amounts of water with this prototype system). Hence, there is not much water available early in the transient, when the first smoke peak is emitted.

Cycle-resolved control of the percentage of water injected provides a very fast method for controlling the exhaust emissions of a diesel engine during engine transients, and transient water strategies can be tailored to address specific concerns. An example of this is illustrated on Figs. 15–17, which compare the results of five different water injection schedules during the same step-load-transient test. Figure 15 shows the five transient water injection schedules. Note that all five schedules achieve the same full-load water percentage, but differ in when water injection is first initiated during the up transient. All five water injection schedules and the fuel-only base line experienced similar air-to-fuel ratios during the transient test, and the torque rise rate for all six cases was also nearly identical. Figure 16 shows the exhaust NO_x concentration in the exhaust for all five water injection cases, and the fuel-only base line. It is evident from this plot that, from the standpoint of NO_x emissions, it is desirable to enable the water injection as early as possible during the up transient. Figure 17 shows the smoke opacity for all five water injection schedules and the fuel-only base line. The opacity trace for Schedules "C" and "D" are very low and not visible on this plot. Water injection Schedule "A" produced an additional puff of smoke, not present in the fuel-only case. This was likely caused by excessive water injection into one or more of the cylinders, and the associated effects of excessive cooling. Excessive water addition is commonly observed to increase HC and PM emissions at light engine loads [10]. Water Schedule "E" produced nearly identical smoke opacity as the fuel-only case, indicating that water injection was enabled too late during the up transient to mitigate smoke. Of the possi-

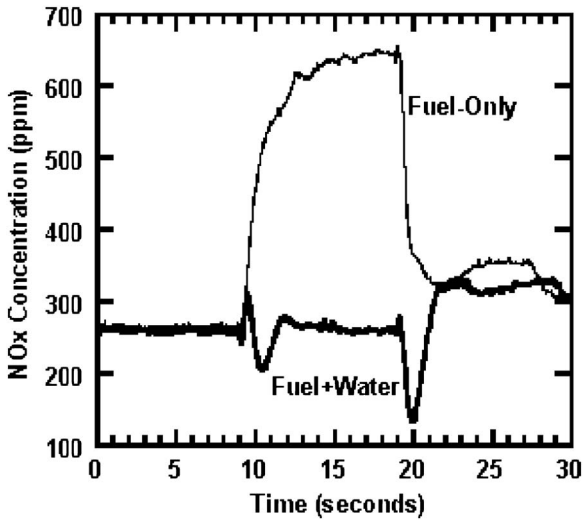

Fig. 13 Exhaust NO_x concentration during the step-load transient

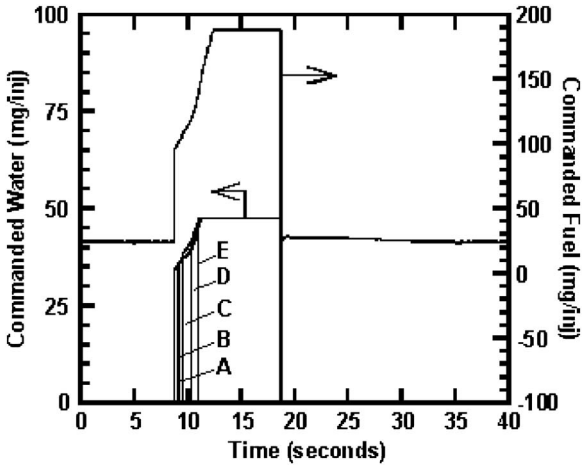

Fig. 15 Five different water injection schedules during a step-load transient.

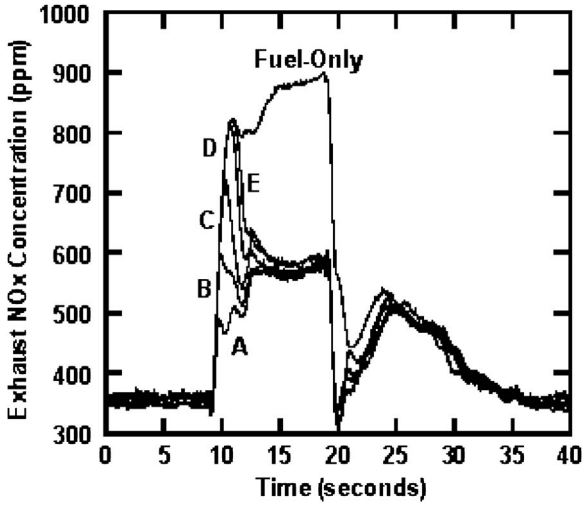

Fig. 16 Exhaust NO_x concentration during step-load transient for five water injection schedules and a fuel-only base line

bilities shown, water Schedule "C" provided the best compromise between NO_x and smoke opacity reductions. It may be noted that the base line (fuel-only) NO_x emission level differs between Figs. 13 and 16. This was caused by differences in the injection timing, as these tests were performed a few days apart with slightly different calibrations (timing more advanced for data in Fig. 16). However, each series of tests compared on a single graph was performed on the same day, and with identical injection timing schedules.

The emission measurement techniques used in this study (prototype NO_x sensor and smoke opacity meter) are not intended to produce accurate quantitative measurements of transient emissions. Rather, they provide a qualitative validation of the water injection system under step-load transients, in a cost effective manner. Similarly, the approximate values of A/F ratio on Fig. 12 are only intended to show that similar enrichment values and durations were achieved for all cases. All measurement devices used had time delays associated with their measurement responses (transport times, sensor response delays, etc.), but these delays are assumed to be constant for each test in a given test sequence. Hence, these time-resolved plots provide good comparative evidence of the benefits of water injection during engine transient conditions, but are not intended to provide accurate absolute values of the emissions benefits.

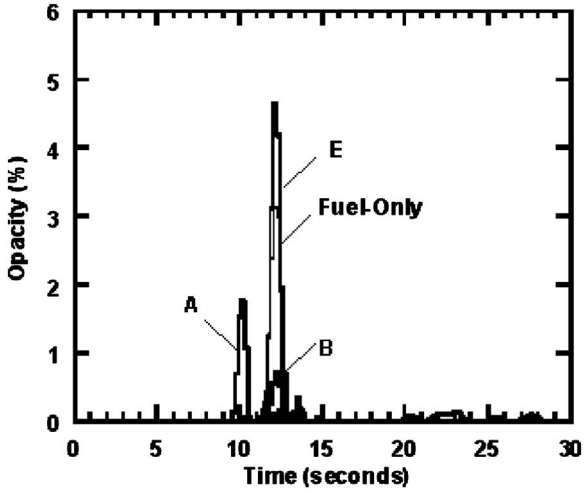

Fig. 17 Smoke opacity during step-load transient for five water injection schedules and a fuel-only base line

By providing cycle-resolved control of the water percentage in the injected mixture, this system has demonstrated the potential for generating optimized strategies for mitigating transient NO_x and smoke emissions. In turn, this may allow for faster engine torque rise rates without exceeding the engine's emission target. This system allows for effective transient emissions control from EGR-equipped engines. Transient control is typically difficult in those engines, because of the inherent transport delay times associated with the EGR plumbing.

Interpretation of Results. The present study concentrated on the design, construction, calibration, and testing of a system for injecting cycle-controlled mixtures of diesel fuel and water into a modern turbocharged heavy-duty diesel engine. Correspondingly, the results presented herein are those of the "end effect" of fuel + water injection on the emissions and performance of the engine. However, some general interpretation of the effects of water of diesel combustion is warranted.

It is well established that water injection reduces NO_x production by lowering the combustion temperatures within the cylinder. Similarly, the effect of EGR on NO_x emissions is known to correlate with the temperature reduction that is achieved in cylinder. The effects of water injection and EGR on smoke and PM emissions are not nearly as well understood. In general, a reduction in oxygen (as through EGR addition) reduces the oxidation rate of carbon particulates and precursors, which in turn increases the engine-out PM emissions. Conversely, it is thought that the presence of water in the combustion zone may increase oxidation rate of carbon particles and precursors under enginelike conditions. This may provide a general explanation as to why fuel + water injection was shown to offset the smoke emission increase due to EGR in this study. Finally, water injection was shown to have a small but positive effect on BSFC in this engine. Although an in-depth investigation of this effect was not pursued in this study, this efficiency improvement may be attributed to an increase in the cylinder contents during the expansion process (due to water addition) and/or a reduction in heat losses to the combustion chamber walls. However, more detailed studies are required to determine the exact contribution of each mechanism.

Conclusions

A number of important conclusions can be drawn from the results presented here.

- Fuel + water coinjection is effective for reducing steady-state NO_x, HC, CO, and smoke emissions from a diesel engine. No increase in ignition delay is incurred with this system.
- A benefit in BSFC may be obtained through the use of fuel + water coinjection, at equivalent NO_x levels than fuel-only base line.
- The combination of fuel + water coinjection and aggressive EGR can be used to produce very low levels of engine-out NO_x and smoke emissions. With the addition of a particulate trap, a heavy duty engine equipped with the fuel + water coinjection system and EGR should be able to meet Euro V emissions levels.
- Fuel + water coinjection with cycle-resoled control of the water percentage is very effective for mitigating step-load-transient NO_x and smoke emissions from a diesel engine. Step-load-transient emissions are generally a good indicator of emission behavior over a full transient test cycle. Because of the fast response of this system, it is fully expected that this method can provide effective transient emissions control for EGR-equipped engines over a transient cycle.
- Further development of this technology is required in order to expand the engine operation range of the fuel + water coinjection system.

Table 2 ESC (OICA) cycle modes and weighing factors

Mode	Speed	% load	Weight factor (%)
1	Low idle	0	15
2	A	100	8
3	B	50	10
4	B	75	10
5	A	50	5
6	A	75	5
7	A	25	5
8	B	100	9
9	B	25	10
10	C	100	8
11	C	25	5
12	C	75	5
13	C	50	5

Table 3 ESC modes for the Volvo D-12 engine

Mode	Speed (rpm)	Torque (N/m)
1	Low Idle (862)	60
2	A (1200)	1866
3	B (1450)	1012
4	B (1450)	1508
5	A (1200)	1012
6	A (1200)	1523
7	A (1200)	514
8	B (1450)	1780
9	B (1450)	509
10	C (1700)	1540
11	C (1700)	398
12	C (1700)	1343
13	C (1700)	896

Acknowledgment

This work was performed at the Southwest Research Institute as part of the Clean Heavy-Duty Engine-II Program between 1996 and 1999. Close collaboration and technical support were provided by Delphi Diesel Systems (formerly Lucas Diesel Systems) and Volvo Truck Corp., for which we are very grateful. We also thank all CHDDE-II participating companies for allowing us to publish the results of this work: Cummins Engine Co., DAF Trucks N.V., Detroit Diesel Corp., Hino Motors, John Deere Corp., Lucas Diesel Systems, Mack Trucks, Renault V. I., Volvo Truck Corp., and Zexel Corp.

Appendix: European Steady-State Cycle Test Cycle

The ESC test cycle (also known as OICA/ACEA cycle) was introduced, together with the European transient cycle (ETC) and the ELR tests, for emission certification of heavy-duty diesel engines in Europe starting in the year 2000. The ESC is a 13-mode, steady-state procedure that replaces the R-49 test. The test definition and procedure can be found, for example, in Ref. [13]. A summary of the ESC test modes and weighing factors is provided in Table 2. The engine speeds (A, B, C) are defined by the following.

The high speed n_{hi} is determined by calculating 70% of the declared maximum net power. The highest engine speed where this power value occurs (i.e., above the rated speed) on the power curve is defined as n_{hi}.

The low speed n_{lo} is determined by calculating 50% of the declared maximum net power. The lowest engine speed where this power value occurs (i.e., below the rated speed) on the power curve is defined as n_{lo}.

The Engine Speeds A, B, and C are then calculated by

$$A = n_{lo} + 0.25(n_{hi} - n_{lo})$$

$$B = n_{lo} + 0.50(n_{hi} - n_{lo})$$

$$C = n_{lo} + 0.75(n_{hi} - n_{lo})$$

For the Volvo D-12 engine used in this study, the ESC mode conditions are shown in Table 3.

References

[1] Valdimanis, E., and Wulfhorst, D. E., 1970, "The Effects of Emulsified Fuels and Water Induction on Diesel Combustion," SAE Paper No. 700736.

[2] Greeves, G., Khan, I. M., and Onion, G., 1979, "Effects of Water Introduction on Diesel Engine Combustion and Emissions," *Proceedings of the 16th International Combustion Symposium*, pp. 321–335.

[3] Andrews, G. E., Bartle, K. D., Pang, S. W., Nurein, A. M., and Williams, P. T., 1988, "The Reduction of Diesel Particulate Emissions Using Emulsified Fuels," SAE Paper No. 880348.

[4] Afify, E. M., Korah, S. S., and Dickey, D. W., 1987, "The Effect of Air Charge Temperature on Performance, Ignition Delay and Exhaust Emissions of Diesel Engines Using W/O Emulsions as Fuel," SAE Paper No. 870555.

[5] Hsu, B. D., 1986, "Combustion of Water-in-Diesel Emulsions in an Experimental Medium Speed Diesel Engine," SAE Paper No. 860300.

[6] Matheaus, C. A., Ryan, T. W., III, Daly, D., Langer, D. A., and Musculus, M. P. B., "Effects of PurinNOx™ Water-Diesel Fuel Emulsions on Emissions and Fuel Economy in a Heavy-Duty Diesel Engine," SAE Paper No. 2002-01-2891.

[7] Hellén, G., 1999, "Paper Carriers to Cut NO_x Emissions by Direct Water Injection," Marine News, Wärtislä NSD, Finland, No. 1, pp. 8–11.

[8] Kohketsu, S., Mori, K., Sakai, K., and Nakagawa, H., 1996, "Reduction of Exhaust Emissions With New Water Injection System in a Diesel Engine," SAE Paper No. 960033.

[9] Wirbeleit, F., Enderle, Ch., Lehner, W., Raab, A., and Binder, K., 1997 "Stratified Diesel Fuel-Water-Diesel Fuel Injection Combined With EGR—The Most Efficient In-Cylinder NO_x and PM Reduction Technology," SAE Paper No. 972962.

[10] Musculus, M. P. B., Dec, J. E., Tree, D. R., Daly, D., Langer, D., Ryan, T. W., III, and Matheaus, A. C., 2002, "Effects of Water-Fuel Emulsions on Spray and Combustion Processes in a Heavy-Duty DI Diesel Engine," SAE Paper No. 2002-01-2892.

[11] Homan, H. S., 1985, "Conversion Factors Among Smoke Measurements," SAE Paper No. 850267.

[12] Kato, N., Kokune, N., Lemire, B., and Walde, T., 1999, "Long-Term Stable NO_x Sensor With Integrated In-Connector Electronics," SAE Paper No. 1999-01-0202.

[13] Anon, DieselNet Emissions Standards, Revision 2000.05 http://www.dieselnet.com/standards/cycles/esc.html

Particle Image Velocimetry Measurements of In-Cylinder Flow in a Four-Stroke Utility Engine and Correlation With Combustion Measurements

Karen E. Bevan
Eaton Corporation,
26201 Northwestern Highway,
Southfield, MI 48037

Jaal B. Ghandhi
125 Engineering Research Building
1500 Engineering Drive
Madison, WI 53706–1687

Large-scale flows in internal combustion engines directly affect combustion duration and emission production. The effect of intake port geometry on combustion performance was studied in a four-stroke spark-ignition utility engine. Three intake port geometries were investigated at three port orientations. In-cylinder flows in orthogonal planes were measured using particle image velocimetry (PIV). The PIV data were processed to calculate the large-scale mean vorticity and mean high-pass filtered velocity. Combustion performance data were separately acquired at two load conditions at a fixed equivalence ratio, and compared with the PIV data. The cumulative distribution functions of the flow parameters did not show significant port-to-port differences in either measurement plane. The mean vorticity and high-pass filtered velocity did exhibit differences due to port orientation in the horizontal plane, but not in the vertical plane. The 0 deg ports (tangential orientation) consistently produced the highest values of large-scale mean vorticity and mean high-pass filtered velocity in the horizontal plane. The kinetic energy present at ignition was also calculated to characterize the flow. The ensemble-averaged values of the mean large-scale vorticity, high-pass filtered velocity, and kinetic energy were compared to the combustion duration. The vertical-plane vorticity and high-pass filtered velocity did not correlate with combustion performance. The horizontal-plane vorticity and high-pass filtered velocity were found to exhibit modest correlation at the fixed torque condition, and somewhat lower correlation at the wide open throttle condition. The correlation between kinetic energy and combustion duration was poor. The best correlation of flow field structure with engine performance was achieved for ports at the 0 deg port orientation. Ports at this orientation generated coherent, large-scale swirl.
[DOI: 10.1115/1.2830547]

Keywords: PIV, in-cylinder flow, intake port, combustion, velocity

Introduction

Early research on spark-ignition engines in passenger cars demonstrated that combustion is slow when the fuel/air mixture is introduced into the engine cylinder in a quiescent manner without large-scale fluid motion and turbulence generation [1]. Thus, modern internal combustion engines are designed to promote turbulent combustion in the engine cylinder through enhanced in-cylinder flow fields. The details of the in-cylinder flow fields have important effects on the progress and efficiency of combustion [2]. Carefully designed in-cylinder flow fields can enhance combustion, yielding shorter burn times, reduced emissions, and improved fuel economy [3]. Therefore, engine manufacturers have focused on the design of especially shaped intake ports to produce large-scale fluid motions, such as swirl and tumble, in the engine cylinder. Furthermore, stringent emission legislation and consumer demands have led to increased efforts in predicting and measuring in-cylinder flow fields and assessing their effects on combustion [2].

The in-cylinder flow field can be significantly affected by minor changes in intake port geometry yielding profound effects on engine performance. Thus, flow improvements can be achieved through inexpensive means. This benefit is especially attractive for small engine manufacturers where engine design is constrained by requirements of low cost, low complexity, and low weight. If the relationship between intake port geometry, in-cylinder flow, and combustion was known a priori, the time and cost of intake port development could be significantly reduced by minimizing prototype testing. Many investigators have developed mathematical expressions to characterize in-cylinder flows and correlate these flows with combustion. Investigations on swirling flows, tumbling flows, and combined swirling/tumbling flows will be discussed.

In several studies, Kent et al. found that increased swirl ratio decreased combustion duration, decreased ignition delay, and increased combustion stability [3–5]. Witze et al. and Inoue et al. also found in related experiments that increased swirl ratio resulted in decreased combustion duration for all spark locations tested [6,7]. Furthermore, Kent et al. showed increased swirl ratio increased burn rate even if the inducted kinetic energy and hence the turbulence production due to the inducted flow were held constant [5].

Hadded and Denbratt examined the tumbling air motion generated by four different intake port/combustion chamber builds in a four-valve, pentroof engine using LDV [8]. Their results showed a correlation between tumble strength, turbulence quantities at ignition, and engine performance. Increased tumble caused high tur-

Contributed by the International Gas Turbine Institute (IGTI) of ASME for publication in the JOURNAL OF ENGINEERING FOR GAS TURBINES AND POWER. Manuscript received August 4, 2005; final manuscript received October 23, 2007; published online March 26, 2008. Review conducted by Jim Cowart.

Table 1 Kohler CH-14 engine specifications

Bore	87 mm
Stroke	67 mm
Displacement	398 cm^3
Compression ratio	8.5:1
Speed	1200 rpm
Power	10.4 kW
Valve configuration	Overhead, single intake/single exhaust
Combustion chamber geometry	Flat-roof, shallow-bowl piston

bulence intensities and smaller integral length scales at ignition. In addition, while the combustion delay angle was gradually reduced with increased tumble, the combustion burn angle did not change significantly.

In 1990, Arcoumanis et al. examined the ability of two cylinder heads to enhance turbulence levels at the time of ignition through the formation of long-lived, large-scale flow vortices [1]. Arcoumanis et al. [1] used a dual-beam LDV system to quantify the three-dimensional in-cylinder flows and study how intake port orientation affected the evolution of the flows during compression. Arcoumanis et al. [1] concluded that stronger tumble results in the release of more turbulent kinetic energy during the breakdown of the flow and this release takes place later in the compression stroke relative to weaker tumble. These factors guarantee higher turbulence levels during the time of ignition but not necessarily a proportional enhancement of the burning rates since during the combustion period; turbulence will be in a state of continuous decay in the absence of any other mechanism of turbulence production.

Trigui et al. characterized an inclined swirling flow in terms of its ability to store intake-generated kinetic energy and release the energy as turbulence at the time of ignition [9]. Trigui et al. studied the intake-generated flow fields in a dynamic water analog rig using three-dimensional PTV and correlated the results with combustion data. The in-cylinder flow was characterized using swirl, tumble, and cross-tumble ratios defined in the conventional manner. Trigui et al. [9] found that total kinetic energy, calculated from a combination of the three ratios, correlated better with burn duration than individual integral flow parameters.

In this investigation, particle image velocimetry (PIV) was employed to quantitatively study intake-generated large-scale flow structures in a motored four-stroke utility engine. PIV is a flow visualization technique capable of producing an instantaneous snapshot of the flow in a two-dimensional plane. In addition to the in-cylinder flow measurements, engine performance measurements were separately acquired. Three simple intake port geometries were investigated at three intake port orientations. The choice of the port geometry was constrained by the need to be easily produced using traditional die casting techniques for use in the utility engine market. Quantitative comparisons showed that limited correlations exist between the in-cylinder flow and combustion data.

Experimental Equipment

In-Cylinder Flow Measurements

Optical Engine. PIV measurements were performed on a single cylinder, Kohler CH-14 utility engine modified for optical access. The engine specifications are shown in Table 1. Optical access to the combustion chamber was provided by a Bowditch-type piston with a sapphire window in the piston crown, and through flat sapphire windows in the cylinder liner [10]. The optical engine retained the original combustion chamber geometry of the production engine. The optical engine was motored at 1200 rpm using a dc dynamometer. Only air and PIV seeding particles were inducted into the engine. The bore extension was lubricant free, which minimized particle adhesion to the optical surfaces. Graphite piston rings were used for sealing.

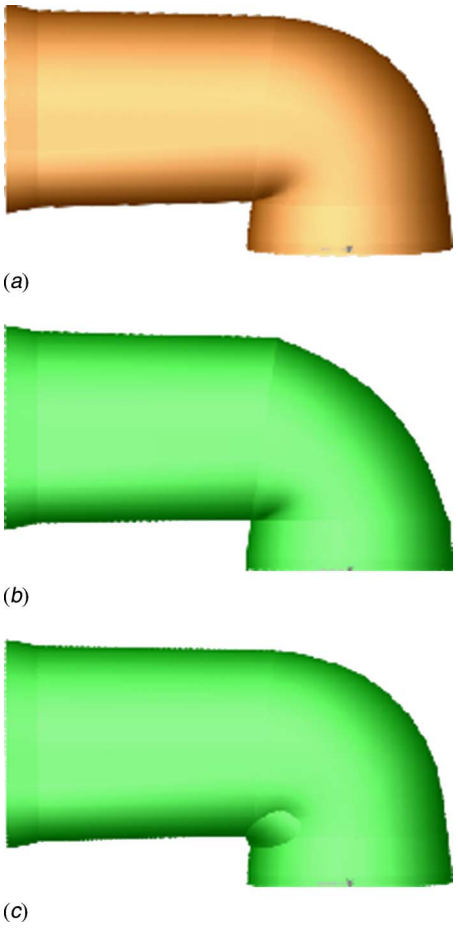

Fig. 1 Solid models of the three intake port geometries used in the experimental measurements. Shown are (*a*) the production port, (*b*) outer port, and (*c*) inner port.

The production Kohler CH-14 cylinder head was modified to accommodate a modular, rotatable intake port. The same cylinder head was used for the in-cylinder flow and combustion measurements. Three intake port geometries were machined as modular blocks that could be press fitted into the modified cylinder head. The intake ports could be rotated counterclockwise 90 deg about the intake valve. A circular tongue in the bottom of the modular port block mated with a circular groove in the cylinder head deck surrounding the intake valve. The tongue and groove ensured that the intake port remained centered around the intake valve as the port was rotated.

Three simple intake port geometries were studied: the production intake port, the production intake port with the outer radius of the port increased slightly, and the production intake port with the inner corner of the port replaced by a rounded fillet. These three intake ports will be referred to as the production port, outer port, and inner port, respectively. Solid models of the three intake port geometries are shown in Fig. 1. In-cylinder flow and combustion measurements were made with the intake ports at three orientations: 0 deg, 45 deg, and 90 deg with respect to the intake port orientation in the production cylinder head. Figure 2 shows the 0 deg and 90 deg intake port orientations with respect to the engine cylinder. The goal of this work was to study port and cylinder geometries typical for small utility engines.

Particle Image Velocimetry System. In PIV, seed particles are added to the air flow and images are acquired of laser light scat-

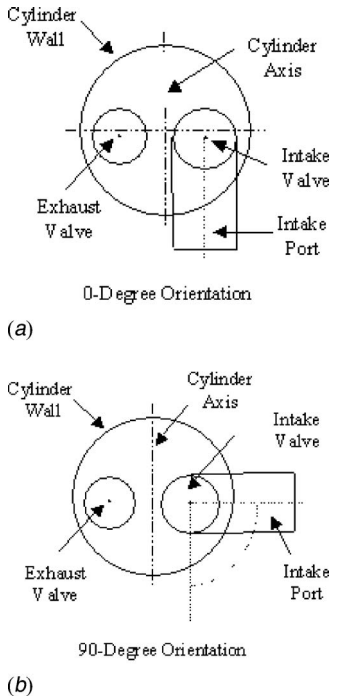

Fig. 2 Top view of engine showing intake port at the (*a*) 0 deg orientation and (*b*) 90 deg orientation with respect to the engine cylinder

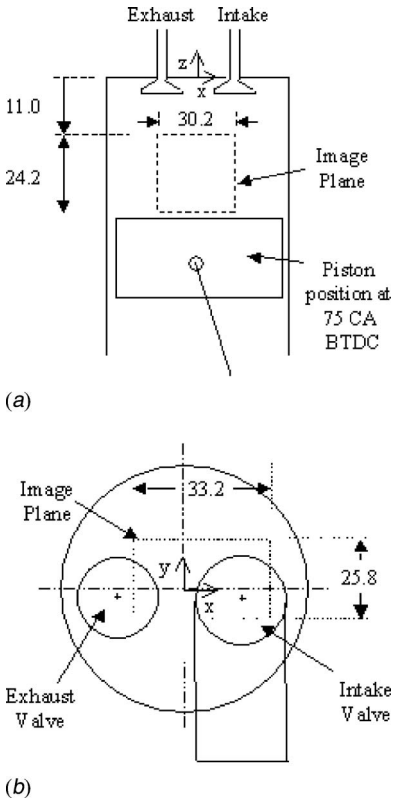

Fig. 3 (*a*) Side view of vertical PIV image plane (dashed) in the engine. The *y* axis (not shown) points into the page. The image plane is located at *y*=0: (*b*) Top view of horizontal PIV image plane (dashed) looking down on engine. The *z*-axis (not shown) points out of the page. The image plane is located at *z* =−14.75 mm. All dimensions are in millimeters.

tered from two coincident sheets separated in time. The images are then interrogated piecewise on a grid to determine the mean particle separation. Details of the full optical setup used in this experiment can be found in Refs. [11,12].

The seed particles chosen for this study were microballoons with a nominal diameter of 35–55 μm and a density of 30 kg/m^3. Using Bassett's equation, the microballoons were found to track 600 Hz motion with 90% amplitude, which corresponds to the cutoff frequency suggested by Bracco [13]. A frequency-doubled diode-pumped Nd:YAG (yttrium aluminum garnet) laser was used to illuminate the seeding particles in the engine for the PIV measurements. The laser was externally triggered to output a burst of five pulses with 100 μs between each pulse. The fourth and fifth pulses in the burst consistently had comparable pulse energies, and were used to illuminate the seeding particles in two consecutive PIV images. One laser pulse illuminated each image. The energy per pulse delivered to the engine cylinder was 1.4 mJ/pulse. The laser beam was formed into a sheet by a Galilean beam expander consisting of confocal cylindrical (−40 mm focal length) and spherical lenses (800 mm focal length). The laser sheet thickness was measured to be 1.2 mm and the sheet width in the transverse direction was measured to be 31 mm using a laser profilometer. A Princeton Instruments MicroMAX interline-transfer thermoelectrically cooled slow-scan camera was used to acquire the PIV images. The camera contained a 1300 $\times$1030 pixel CCD array with 6.7 μm pixels and was operated in a frame-straddled mode. An external trigger initiated two successive image acquisitions of equal exposure time (100 μs) with approximately 200 ns between the images. A 105 mm focal length Nikkor macrolens was used with the camera to achieve the desired magnification (M=0.29). This magnification yielded a particle image diameter of two pixels.

A Laplacian of Gaussian (LoG) edge detection method [14] was employed to improve the signal-to-noise ratio of the in-cylinder flow images prior to PIV analysis. After LoG processing, the PIV images were cross correlated using PIV SLEUTH, an interrogation and validation software program [15]. The PIV images were interrogated on a square grid using 128$\times$128 pixel interrogation zones with 50% overlap of adjacent zones. Smaller interrogation windows had an insufficient number of particle pairs to calculate a meaningful correlation. PIV SLEUTH recorded the three highest cross-correlation peaks for each interrogation zone. The cross-correlation peaks corresponded to the mean displacement of the seeding particles in the interrogation zone. A velocity vector was calculated for each interrogation zone by dividing the mean displacement of the seeding particles by the time between laser pulses (100 μs). The velocity vector represents the velocity of the large-scale flow in the interrogation zone. The flow is described as "large scale" since only scales larger than the PIV interrogation grid size (approximately 3$\times$3 mm^2) could be resolved. Velocity vectors that showed gross discontinuity with their neighbors were replaced by the second- or third-choice candidates. No additional postprocessing was performed on the final vectors chosen. Therefore, the number of absent vectors in the velocity distributions gives an indication of the number of invalid velocity measurements.

The PIV images were acquired in one vertical plane and one horizontal plane of the engine cylinder. The vertical plane passed through the intake and exhaust valves, bisecting the combustion chamber. This plane was imaged at 75 CA BTDC. The horizontal plane was located at 14.75 mm below the top of the combustion chamber and was imaged at 40 CA BTDC. The imaging times were the latest times during the compression stroke that could be imaged due to optical access constraints. In-cylinder flow fields at times closest to TDC were of primary interest given their influence on the combustion process. The vertical and horizontal PIV image planes are shown in Fig. 3. The area of overlap between the two image planes is determined by the thickness of the vertical

laser sheet in the horizontal image plane. Since the planes were imaged at different times, the velocities in the two planes could not be compared.

Engine Performance Measurements. Engine performance tests were conducted on an all-metal single-cylinder engine with the same modified cylinder head. All three intake ports were tested at all three intake port orientations, similar to the in-cylinder flow measurements. The tests were conducted at 1200 rpm.

The goal of the engine performance tests was to study the influence of intake-generated in-cylinder flows on combustion. Therefore, it was desired to limit the effects of local changes in air/fuel ratio on combustion, i.e., mixture inhomogeneities. To achieve this goal, a gaseous propane carburetor was used instead of the production liquid gasoline carburetor to create an essentially homogeneous fuel/air mixture in the engine. The spark timing was fixed at 15.2 CA BTDC to yield approximate MBT conditions at 1200 rpm for all of the intake configurations studied. The fuel-air equivalence ratio Φ was set to 1.20.

Two engine loads were studied for each intake configuration: wide-open throttle (WOT) and fixed torque (11.5 N m). At WOT, the maximum amount of air/fuel mixture is inducted into the engine, and since the load was not held constant, differences in torque output between the engine tests were attributable to both the difference in flow restriction of the intake ports and the quality of the in-cylinder flow field. At the fixed torque condition, the effect of charging efficiency is insignificant, and in-cylinder flow field differences cause differences in the combustion performance. The torque of 11.5 N m corresponds to half of the torque produced by the engine with the 0 deg production port at WOT conditions.

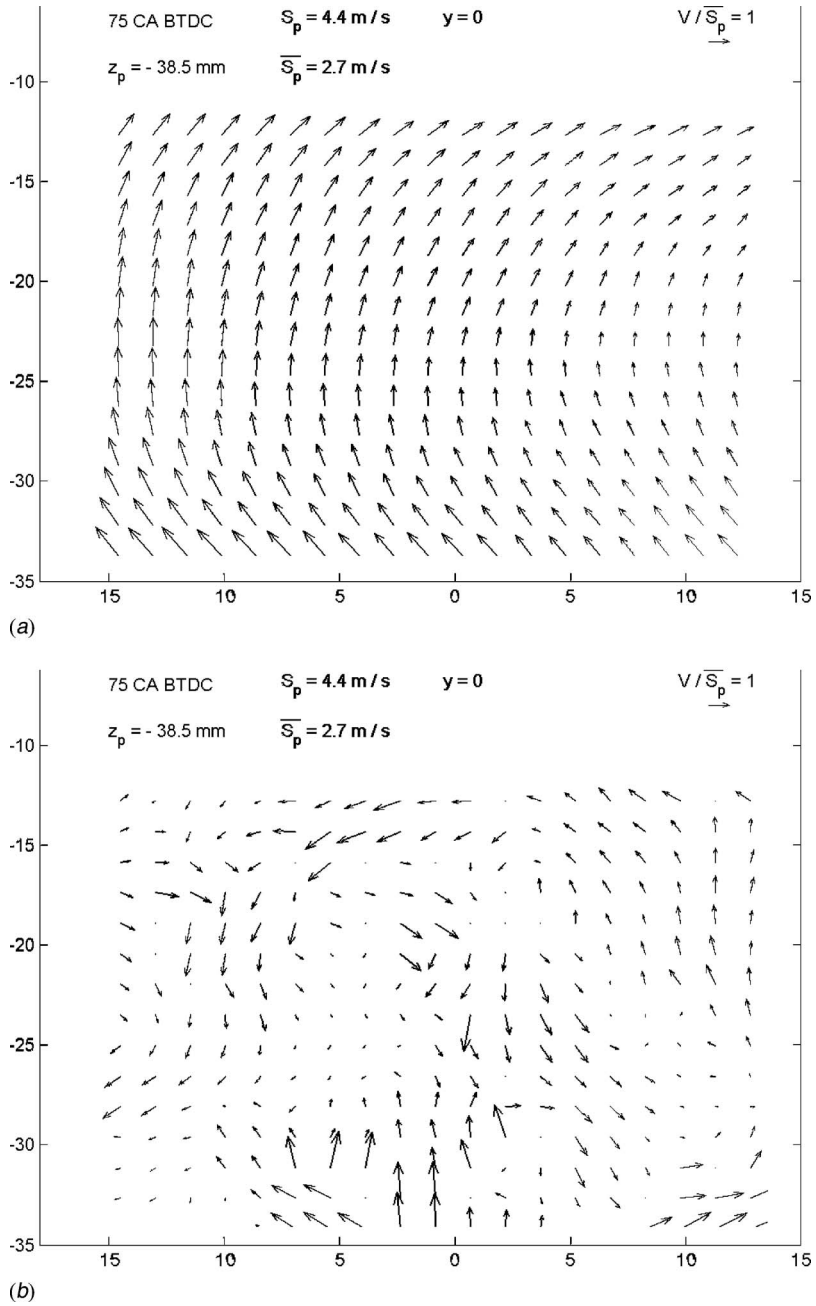

Fig. 4 (*a*) **Ensemble-averaged of 135 PIV velocity distributions and** (*b*) **an instantaneous velocity distribution for the inner port at the 0-degree port orientation. The PIV images were acquired at 75 CA BTDC in the vertical PIV plane.**

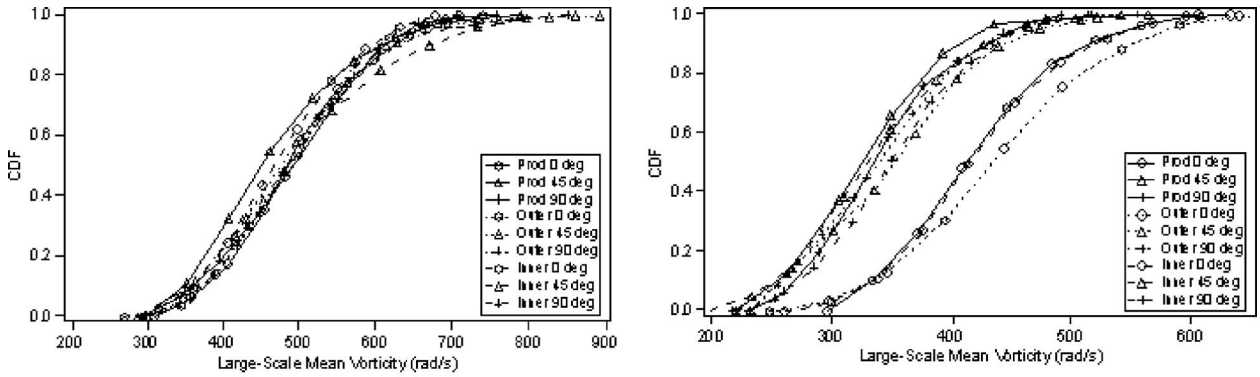

(*a*) (*b*)

Fig. 5 CDFs of large-scale mean vorticity for all intake ports at three intake port orientations: (*a*) vertical plane (*b*) horizontal plane

Cylinder pressure measurements were made using a spark plug-mounted piezoelectric pressure transducer. The pressure data were analyzed to determine the heat release rate based on a simple single-zone model.

Results

In-Cylinder Flow Results. PIV images of the in-cylinder flow were acquired to gain quantitative information about the effect of intake port geometry and intake port orientation on the in-cylinder flow field. PIV provides two components of the velocity at a given time in the cycle θ and a given location. Approximately 150 velocity distributions were acquired for each intake port at each intake port orientation to allow for statistical investigation of the flow field. A more detailed discussion of the flow results, including comparisons with steady flow data, is given in Ref. [12].

In order to investigate the flow field effect on the combustion, a number of calculations were performed with the data as described below. The instantaneous realizations of the flow field were ensemble averaged to examine the average characteristics of the flow field at a particular crank angle. The ensemble averaged velocity distributions are useful for quantifying bulk flow characteristics, such as those measured on a steady flow bench with a swirl or tumble meter. The ensemble average of a quantity Q, $\langle Q(x,y)\rangle$, at each point in the interrogation grid was computed by averaging the instantaneous values at that grid point for N instantaneous realizations of the flow:

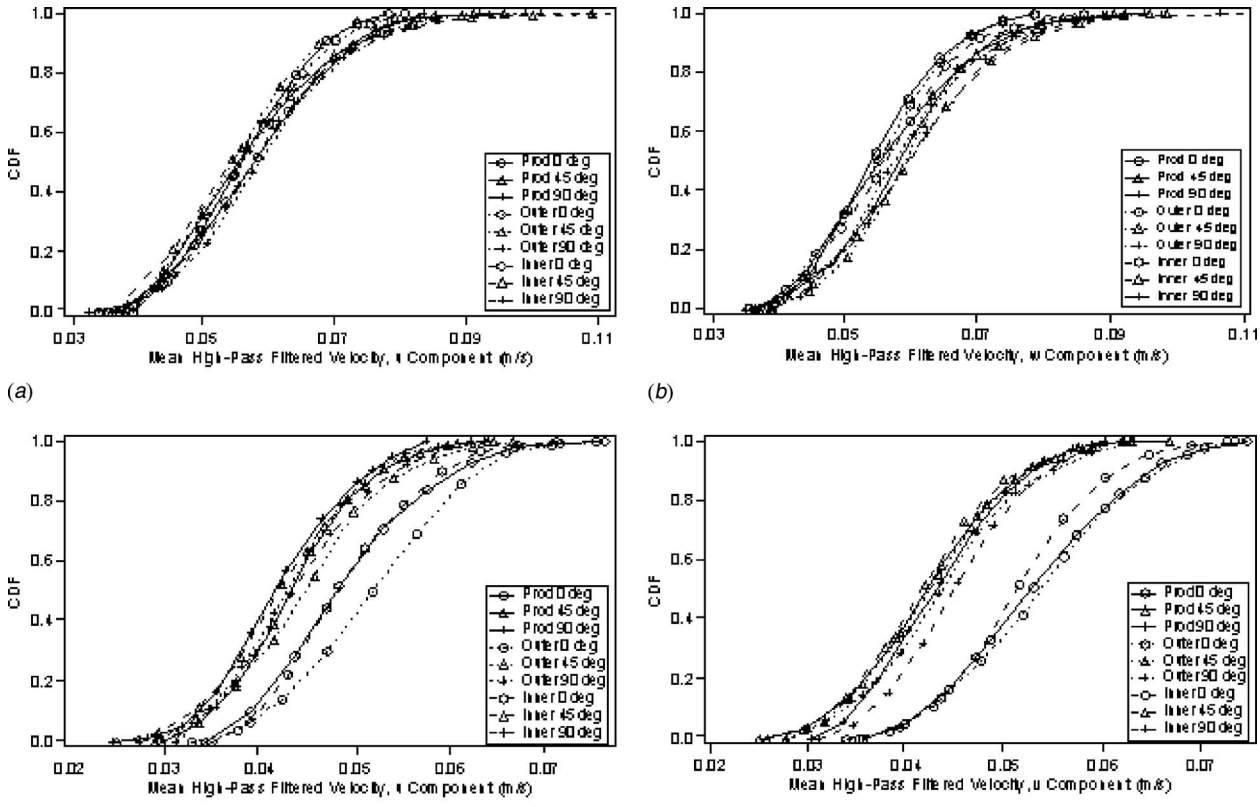

(*a*) (*b*)

(*c*) (*d*)

Fig. 6 CDF of mean high-pass filtered velocity (*a*) vertical-plane *u* component, (*b*) vertical-plane *w* component, (*c*) horizontal-plane *u* component, and (*d*) horizontal-plane *v* component

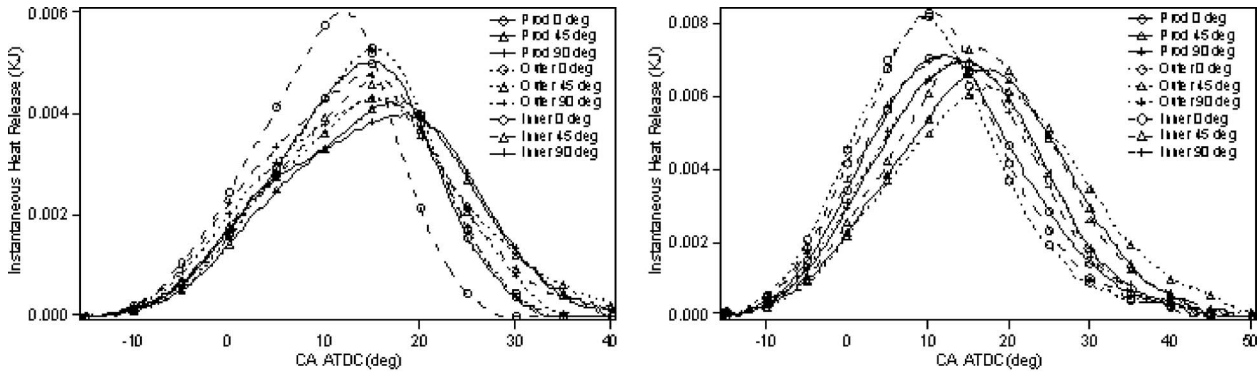

(*a*) (*b*)

Fig. 7 Instantaneous heat release for the (*a*) fixed torque (11.5 N m) and (*b*) WOT conditions with Φ=1.20 for the three intake ports at three intake port orientations (0 deg, 45 deg, and 90 deg)

$$\langle Q(x,y,\theta)\rangle = \frac{1}{N}\sum_{i=1}^{N} Q_i(x,y,\theta) \tag{1}$$

Spatial averaging was also performed on some data, e.g., vorticity, to provide global information about a flow realization. The spatial average of a quantity Q, $\bar{Q}$, is given by

$$\bar{Q}_i = \frac{1}{N_x}\frac{1}{N_y}\sum_{j=1}^{N_x}\sum_{k=1}^{N_y} Q_i(x,y) \tag{2}$$

where N_x and N_y are the number of data points in the x and y directions, respectively.

The flow field can affect the combustion process in two distinct ways. First, higher levels of turbulence at the time of ignition will enhance flame speed. In order to evaluate this effect based on the large-scale image, data provided by PIV, the vorticity ζ and high-pass filtered velocity V_{HP}, were calculated based on the definitions provided in the Appendix. High levels of vertical-plane vorticity or small-scale structure, i.e., high V_{HP}, at the image time were expected to correspond with a breakdown of this structure later in the compression stroke, with the commensurate increase in turbulence. Secondly, coherent large-scale motion of the flow field can enhance combustion. The large-scale motion was characterized in a manner similar to Trigui et al. [9] by calculating the angular momentum per unit mass in the vertical L_V and horizontal L_H planes. See the Appendix for details on the calculations of the angular momentum. Swirl, characterized as horizontal-plane vorticity, also is considered in this category.

Figure 4 shows the ensemble-averaged velocity distribution and an instantaneous velocity distribution for the inner port at the 0 deg port orientation in the vertical PIV plane. The instantaneous velocity distribution shown was randomly chosen from a set of 135 instantaneous velocity distributions. Across the top of the figures, several key parameters are displayed: the time of image acquisition in CA BTDC, the instantaneous and mean piston speeds at the time of image acquisition, S_p and $\bar{S}_p$, respectively, and the piston position at the time of image acquisition, z_p. All of the velocities were normalized by $\bar{S}_p$ and a reference vector of $V/\bar{S}_p=1$ is shown in the upper right corner of the figures.

The ensemble-averaged velocity distribution in Fig. 4 shows that the flow, on average, is moving upward toward the intake valve side of the cylinder. The instantaneous velocity distribution, however, shows that the in-cylinder flow exhibits significant cycle-to-cycle variation on scales smaller than the image field of view. Clearly, the ensemble-averaged results do not fully describe the flow field. The spatially averaged results retain some of this flow field structure.

The large-scale mean vorticity $\bar{\zeta}$ was calculated for each instantaneous velocity distribution in a PIV plane. The cumulative distribution function (CDF), of $\bar{\zeta}$ was calculated for each intake configuration for the two PIV planes, as shown in Fig. 5 [11]. The CDFs show that $\bar{\zeta}$ is similar for all intake configurations in the vertical plane. Thus, the intake configurations produced vertical flow fields that contained large-scale rotational characteristics of similar magnitude and cyclic variability. In the horizontal plane, $\bar{\zeta}$ is highest for the 0 deg ports, which corresponds to a higher level of swirl as was observed in the steady flow tests [12].

The two in-plane components of mean high-pass filtered velocity $(\bar{V}_{HP})_j$ were calculated for each instantaneous velocity distribution in a PIV plane. In the vertical plane, the u and w components of mean high-pass filtered velocity were calculated in the x and z directions, respectively. In the horizontal plane, the u and v components of mean high-pass filtered velocity were calculated in the x and y directions, respectively. See Fig. 3 for the coordinate system definition.

Table 2 10% MFB times (in CA after TDC) and combustion duration (in CA) for nine intake configurations at fixed torque and WOT conditions with Φ=1.20

Port orientation (deg)	Intake Port Geometry		
	Production	Outer	Inner
10% MFB for fixed torque condition			
0	1	1.6	−0.6
45	2.2	2	1.2
90	1.4	0.2	−0.2
10% MFB for WOT condition			
0	−0.2	−1.6	−1
45	2.2	2.6	1.8
90	0.8	0.6	−0.4
Combustion duration for fixed torque condition			
0	21.4	21	18.8
45	24.8	25.8	24.8
90	25.4	24	22.6
Combustion duration for WOT condition			
0	25.6	24	24.2
45	27.4	30	27.2
90	26	25.8	26.4

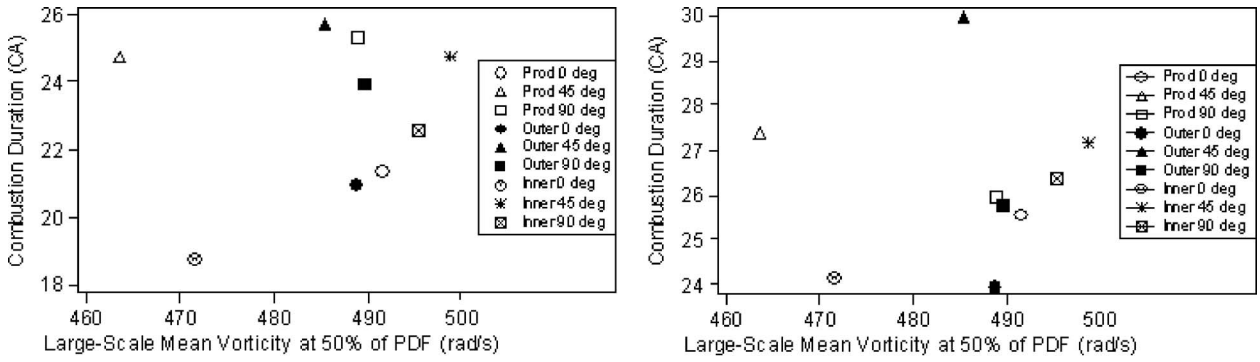

Fig. 8 Combustion duration versus mean value of large-scale mean vorticity for nine intake configurations. Combustion duration calculated for (*a*) fixed torque and (*b*) WOT conditions with $\Phi=1.20$. Mean vorticity calculated from vertical-plane PIV velocity fields.

The CDFs of $(\bar{V}_{\mathrm{HP}})_u$ and $(\bar{V}_{\mathrm{HP}})_w$ in the vertical plane and $(\bar{V}_{\mathrm{HP}})_u$ and $(\bar{V}_{\mathrm{HP}})_v$ in the horizontal plane are shown in Fig. 6. The CDFs show that $(\bar{V}_{\mathrm{HP}})_u$ and $(\bar{V}_{\mathrm{HP}})_w$ were similar for the intake configurations in the vertical plane. The CDFs indicate that the intake configurations produced flow fields containing small-scale flow structures (less than 10 mm) with similar mean velocities. In the horizontal plane, the CDFs show that both velocity components were highest for the 0 deg ports. The CDFs for the horizontal plane indicate that the imaged portion of the flow fields produced by the 0 deg ports contain small-scale flow structures with higher velocity magnitudes than the 45 deg and 90 deg ports. The higher velocities of the small-scale flow structures produced by the 0 deg ports have the potential to enhance in-cylinder turbulent mixing and hence, increase the rate of combustion.

Engine Performance Results

Representative instantaneous heat release plots are shown in Fig. 7 for the fixed torque and WOT cases with $\Phi=1.20$. As expected, the instantaneous heat release curves for the WOT cases are shifted toward earlier crank angles in comparison with the fixed torque cases. The slope of the instantaneous heat release curves for the fixed torque cases are also, in general, not as steep as the curves for the WOT cases, indicating that the instantaneous heat release rate is faster for the WOT cases.

Mass fraction burned (MFB) times were calculated to determine the effect of intake port geometry and orientation on combustion. The time in CA after TDC when 10% of the mass of fuel was burned (10% MFB time) and the time in CA to burn 10%–90% of the mass of fuel (combustion duration) were calculated from the cumulative heat release plots for the fixed torque and WOT cases. Table 2 shows the 10% MFB times and combustion duration for the nine intake configurations at the fixed torque and WOT conditions with $\Phi=1.20$.

Several trends in 10% MFB times and combustion duration were observed for the fixed torque and WOT cases. The load conditions for each trend are given in parentheses. In general, the inner port had the fastest 10% MFB times (fixed torque, WOT) and shortest combustion duration (fixed torque), while the production port had the slowest 10% MFB times (fixed torque) and longest combustion duration (fixed torque). The 0 deg ports produced the fastest 10% MFB times (WOT), and shortest combustion duration (fixed torque, WOT), while the 45 deg ports produced the slowest 10% MFB times (WOT) and longest combustion duration (fixed torque, WOT).

Correlation of In-Cylinder Flow and Engine Performance Results

Large-scale mean vorticity and combustion were compared only as a function of port orientation since there were not significant differences in $\bar{\zeta}$ due to port geometry at a given port orientation. Figures 8 and 9 show combustion duration versus the ensemble-averaged large-scale mean vorticity, $\langle\bar{\zeta}\rangle$, for the vertical and horizontal PIV planes, respectively. The strength of the correlation between combustion duration and $\langle\bar{\zeta}\rangle$ was determined by

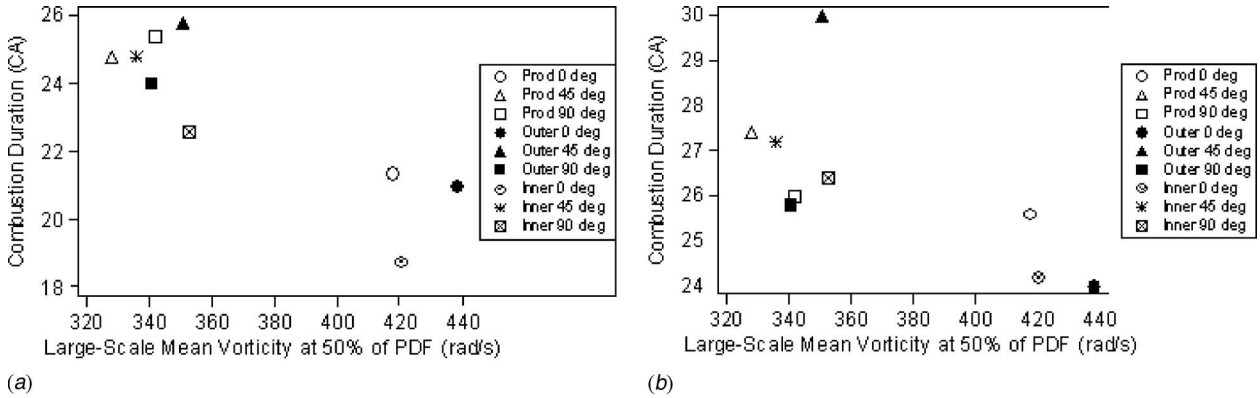

Fig. 9 Combustion duration versus mean value of large-scale mean vorticity for nine intake configurations. Combustion duration calculated for (*a*) fixed torque and (*b*) WOT conditions with $\Phi=1.20$. Mean vorticity calculated from horizontal-plane PIV velocity fields.

Table 3 Strength of the correlation between combustion duration and the mean value of large-scale mean vorticity for two PIV measurement planes and two load conditions

Strength of correlation between combustion duration and mean value of large-scale mean vorticity		
Measurement plane	Load condition	r^2 value
Vertical	Fixed torque	−0.11
Vertical	WOT	−0.14
Horizontal	Fixed torque	0.71
Horizontal	WOT	0.39

the magnitude of the correlation coefficient r, calculated from a linear regression of the data [11]. Table 3 shows the r^2 values corresponding to Figs. 8 and 9. A positive r^2 value indicates that combustion duration decreases with increasing $\langle\bar{\zeta}\rangle$. The strongest correlation was found between combustion duration and $\langle\bar{\zeta}\rangle$ in the horizontal plane for the fixed torque condition, followed by the WOT condition. No correlation was found between combustion duration and $\langle\bar{\zeta}\rangle$ in the vertical plane for either load condition.

The ensemble-averaged mean high-pass filtered velocity and combustion were also compared as a function of port orientation since there were not significant differences in $(\bar{V}_{\mathrm{HP}})_j$ due to port geometry at a given port orientation. Figures 10 and 11 show combustion duration versus $\langle(\bar{V}_{\mathrm{HP}})_u\rangle$ in the vertical and horizontal planes, respectively. Figure 12 shows combustion duration versus the mean value of $\langle(\bar{V}_{\mathrm{HP}})_v\rangle$ for the horizontal plane. Table 4 shows the r^2 values corresponding to Figs. 10–12. The strongest correlations were found between combustion duration and the mean value of both $\langle(\bar{V}_{\mathrm{HP}})_u\rangle$ and $\langle(\bar{V}_{\mathrm{HP}})_v\rangle$ in the horizontal plane for the fixed torque condition, followed by the horizontal plane at the WOT condition. Similar to the vorticity results, no correlation was found between combustion duration and the mean value of $\langle(\bar{V}_{\mathrm{HP}})_u\rangle$ and $\langle(\bar{V}_{\mathrm{HP}})_v\rangle$ in the vertical plane for either load condition.

The correlation between kinetic energy at ignition and 0–90% combustion duration was examined. The kinetic energy E of the in-cylinder flow at the time of ignition was calculated based on the method by Trigui et al. [9]:

$$E = (\mathrm{TR}^2 + \mathrm{CR}^2 + \mathrm{SR}^2) - \alpha(|\mathrm{TR}||\mathrm{CR}| + |\mathrm{TR}||\mathrm{SR}| + |\mathrm{CR}||\mathrm{SR}|) \tag{3}$$

where TR is the tumble ratio defined as normalized angular momentum about the x axis, CR is the cross-tumble ratio defined as normalized angular momentum about the y axis, and SR is the swirl ratio defined as normalized angular momentum about the z axis. Trigui et al. [9] evaluated Eq. (3) using three-dimensional PTV data acquired in a water analog engine at BDC. Equation (3) was modified to accommodate the two-dimensional PIV data acquired in the two PIV planes:

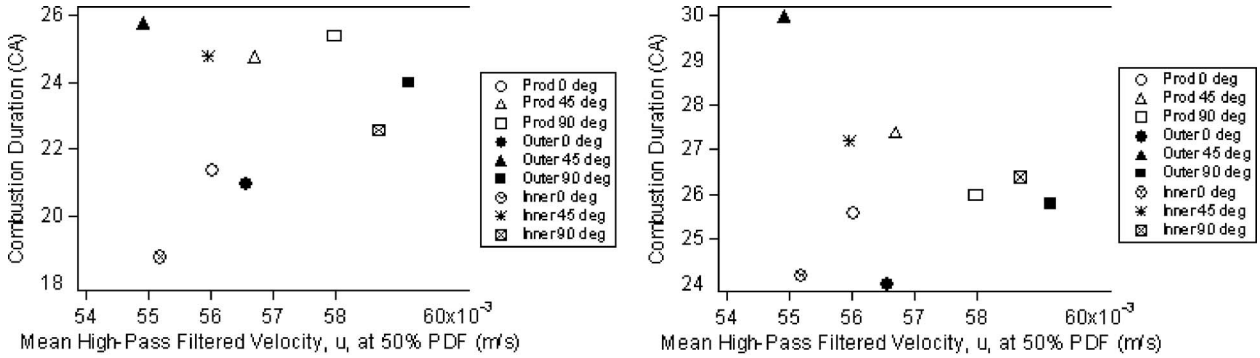

Fig. 10 Combustion duration versus mean value of mean high-pass filtered velocity (*u* component) for nine intake configurations. Combustion duration calculated for (*a*) fixed torque and (*b*) WOT conditions. High-pass filtered velocity calculated for vertical plane.

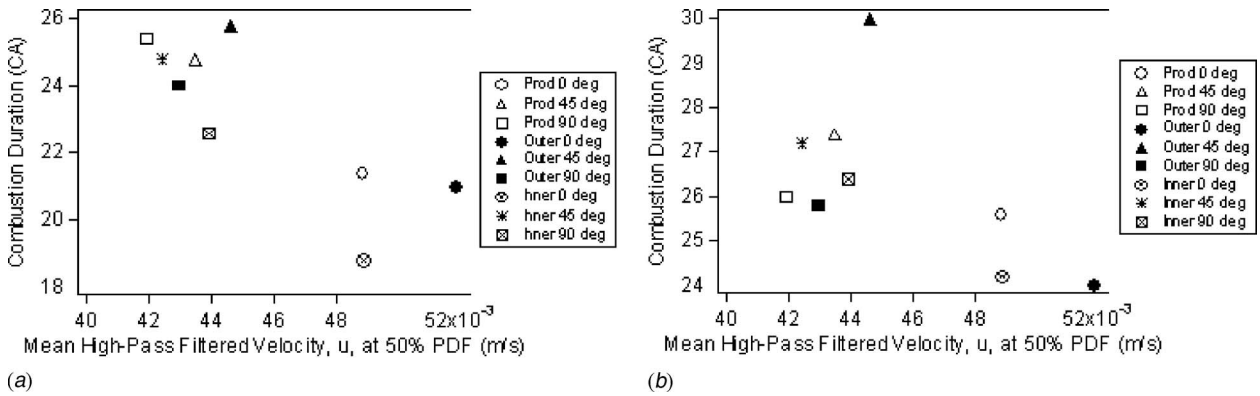

Fig. 11 Combustion duration versus mean value of mean high-pass filtered velocity (*u* component) for nine intake configurations. Combustion duration calculated for (*a*) fixed torque and (*b*) WOT conditions. High-pass filtered velocity calculated for horizontal plane.

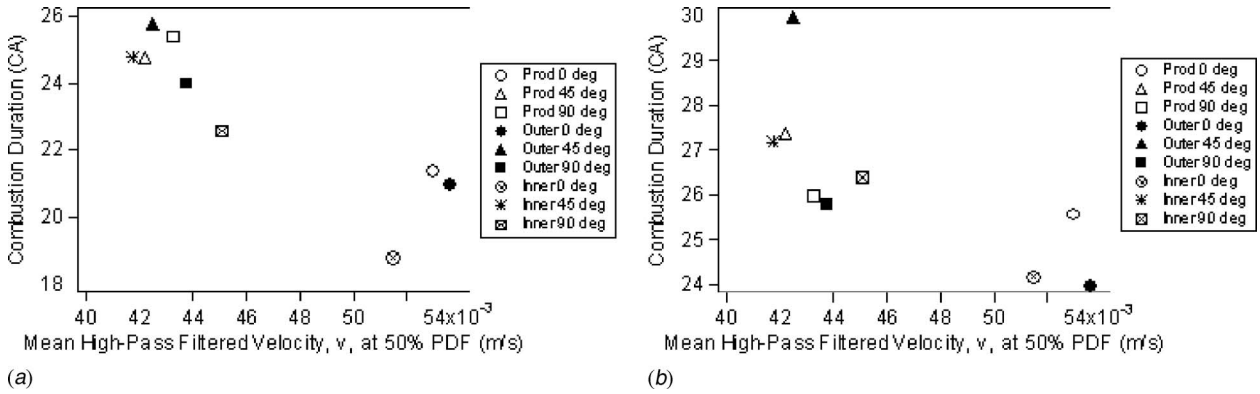

Fig. 12 Combustion duration versus mean value of mean high-pass filtered velocity (*v* component) for nine intake configurations. Combustion duration calculated for (*a*) fixed torque and (*b*) WOT conditions. High-pass filtered velocity calculated for horizontal plane.

$$E = (\langle L_V \rangle^2 + \langle L_H \rangle^2) - \alpha |\langle L_V \rangle| |\langle L_H \rangle| \quad (4)$$

The value of α was optimized using linear regression analysis to give the best linear fit between E and 0–90% combustion duration for the two load conditions. Trigui et al. [9] used a value of 0.55 for α. The value of α was optimized by performing a linear fit of the data for a fixed α value. The quality of the linear fit was then compared for a range of α values. The α value that produced the highest correlation coefficient r provided the best linear fit of the data. A value of r equal to unity indicates a perfectly linear fit of the data.

Figure 13 shows 0–90% combustion duration versus E for the nine intake configurations with the optimized α values. Optimum α values of −95 and −100 were calculated for the fixed torque and WOT conditions, respectively. These α values corresponded to r^2 values of 0.28 and 0.53 for the fixed torque and WOT conditions, respectively. These low r^2 values indicate a poor correlation between 0% and 90% combustion duration and E for the nine intake configurations. While the overall correlation is poor, the 0 deg ports had the highest E values and some of the lowest 0–90% combustion duration times for both load conditions. This finding is similar to the large-scale mean vorticity and mean high-pass filtered velocity results in the horizontal plane for both load conditions.

In contrast to the present results, Trigui et al. [9] found a strong correlation between 0% and 90% combustion duration and E for three different cylinder head configurations with one or two intake valves open [9]. There are several key differences between the in-cylinder flows and measurements in this study and those of Trigui et al. [9] First, the in-cylinder flows in this study were complicated, incoherent flows with no discernable large-scale fluid motion. In contrast, the flows observed by Trigui et al. [9] exhibited large-scale in-cylinder flow structures. Using Eq. (3), coherent large-scale flows will produce significantly different values of E than will incoherent flows. The squared terms in Eq. (3) account for the kinetic energy stored in each of the three angular momentum components, while the mixed terms account for the dissipation of kinetic energy through vortex interaction. The unstructured flows in this study likely emphasized the mixed terms in the Eq. (3) and deemphasized the squared terms.

Another possible explanation for the poor correlation between combustion duration and kinetic energy present at ignition is the use of planar data in lieu of three-dimensional data. Equation (3) was designed to be evaluated with 3D flow data. Trigui et al. [9] used 3 D PTV data with measurements taken at BDC in three orthogonal planes. Based on optical access constraints, similar measurements were not possible with the engine used in this study and Eq. (3) was modified for 2D PIV data. As intake ports are rotated, however, the characteristics of the in-cylinder flow change. For example, the location of the tumble plane in the cylinder changes. Even though defined tumbling and swirling flows were not visualized in this study, the two PIV measurement planes may not have captured the essential characteristics of the flow that control the combustion process. A better correlation between combustion duration and E would be expected if controlling features of the flow (if any), such as a tumbling vortex, were captured in the 2D planes used to calculate E. The use of 3D velocity data would likely improve the correlation as well.

Table 4 Strength of the correlation between combustion duration and the mean value of mean high-pass filtered velocity for two PIV measurement planes and two load conditions

Strength of correlation between combustion duration and mean value of mean high-pass filtered velocity			
Velocity component	Measurement plane	Load condition	r^2 value
u	Vertical	Fixed torque	−0.09
u	Vertical	WOT	−0.09
u	Horizontal	Fixed torque	0.61
u	Horizontal	WOT	0.26
v	Horizontal	Fixed torque	0.75
v	Horizontal	WOT	0.49

Summary and Conclusions

PIV measurements were performed on orthogonal planes in an optical engine to assess the effect of intake port geometry on combustion performance of a utility class engine. The variations to the production port geometry were made within the constraints of the die casting process used to manufacture these engines. Thus, only minor adjustments were made to the production port geometry to the produce the outer and inner ports. The port orientation was varied through a total of 90 deg. The PIV data were processed to calculate the large-scale mean vorticity and mean high-pass filtered velocity, which characterize the in-cylinder flow in a measurement plane in a physically meaningful way that retained cycle-by-cycle differences, and these parameters were correlated with the combustion performance. The CDFs of the flow parameters did not show significant port-to-port differences in either measurement plane. The mean vorticity and high-pass filtered velocity did exhibit differences due to port orientation in the horizontal plane, but not in the vertical plane. The 0 deg ports consistently produced the highest values of large-scale mean vorticity and mean high-pass filtered velocity in the horizontal plane.

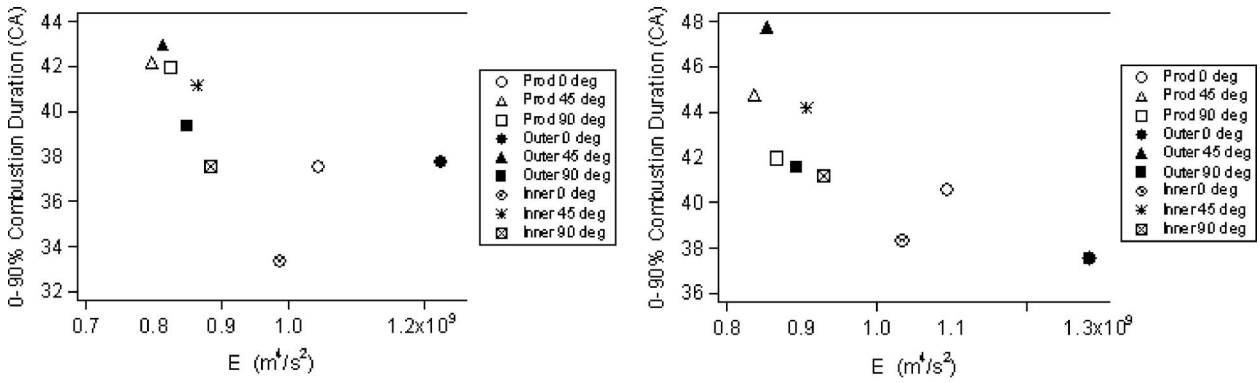

Fig. 13 Combustion duration versus kinetic energy present at ignition, *E*, for nine intake port configurations at the (*a*) fixed torque condition with $\alpha=-95$ and at (*b*) WOT with $\alpha=-100$. The values for α were chosen from linear regression analysis.

The ensemble-averaged values of the mean large-scale vorticity, high-pass filtered velocity, and kinetic energy were compared to the combustion duration. The vertical-plane vorticity and high-pass filtered velocity did not correlate with combustion performance. The horizontal-plane vorticity and high-pass filtered velocity were found to exhibit modest $(0.61<r^2<0.75)$ correlation at the fixed torque condition, and somewhat lower correlation at the WOT condition. The vorticity in the horizontal plane is equivalent to swirl. The kinetic energy present at ignition E was also calculated to characterize the flow. The kinetic energy was correlated to combustion performance using a best-fit method to evaluate the constant α. The values obtained for α were far from the values previously reported in the literature, and the final correlation between E and the combustion duration was poor.

The best correlation of flow field structure with engine performance was achieved for a coherent, large-scale fluid motion—swirl. In the absence of controlling large-scale flow structures, it is likely that small-scale flow structures exerted the greatest influence on the combustion process. Only flow structures greater than 3 mm could be resolved by the PIV system. This is larger than the expected integral length scale at these conditions, and was necessary to observe the large-scale flows, but precludes a full description of all of the energy-containing scales, which may have limited the results. The three port geometries produced similar in-cylinder flows, but different combustion performance. Therefore, it is possible that the subtle port-to-port differences in the flow field that affected combustion performance occurred on a scale that was not resolved by the PIV system or occurred in the cylinder outside of the field-of-view permitted by the cylinder windows.

Acknowledgment

The authors would like to thank the Wisconsin Small Engine Consortium and specifically, Kohler Company, for sponsoring this research. The National Science Foundation and the U.S. Department of Defense are also acknowledged for their support through the NSF and NDSEG fellowships.

Nomenclature

α = parameter calculated from linear regression analysis
BDC = bottom dead center
BTDC = before top dead center
CA = crank angle degree
CCD = charge coupled device
E = kinetic energy of in-cylinder flow
inner = inner intake port geometry
inner 0 deg = inner port at 0 deg port orientation
L_H = angular momentum per unit mass in horizontal plane
LDV = laser Doppler velocimetry
L_V = angular momentum per unit mass in vertical plane
N = number of instantaneous images of flow in an image plane
outer = outer intake port geometry
Φ = fuel/air equivalence ratio
PDF = probability density function
prod = production intake port geometry
PTV = particle tracking velocimetry
r = correlation coefficient
rpm = revolutions per minute of crankshaft
S_p = instantaneous piston speed at time of image acquisition
$\bar{S}_p$ = mean piston speed at time of image acquisition
θ = time in crank angles of image acquisition
TDC = top dead center
V = air flow velocity
V_{HP} = high-pass filtered velocity
$(\bar{V}_{\mathrm{HP}})_u$ = u component of mean high-pass filtered velocity
$\langle(\bar{V}_{\mathrm{HP}})_u\rangle$ = ensemble average of mean high-pass filtered velocity, u component
$\bar{\zeta}$ = large-scale mean vorticity
$\langle\bar{\zeta}\rangle$ = ensemble average of large-scale mean vorticity
z_p = piston position at time of image acquisition

Appendix: Flow Parameter Definitions

Large-Scale Vorticity Calculation

The large-scale vorticity was calculated for each point in the interrogation grid of the instantaneous velocity distribution using the method described by Reuss et al. [16]. The vorticity is described as "large scale" since only scales larger than the PIV interrogation grid size could be resolved. Using Stokes' theorem, the vorticity is related to the circulation Γ of the flow:

$$\int_S \zeta d\vec{S} = \int_S (\nabla \times \mathbf{V}) d\mathbf{S} = \int_C \mathbf{V} \cdot dl = \Gamma \qquad \text{(A1)}$$

where $\mathbf{V}$ is the velocity vector. The circulation was calculated by integrating the tangential component of the velocity around a closed contour C in the flow field. Counterclockwise velocity components were considered positive in sign.

Low-Pass and High-Pass Filtered Velocity Calculations

Low-pass and high-pass spatial filtering were performed on the instantaneous velocity distributions to extract the large-scale and small-scale flow structures, respectively, from the distributions. The low-pass filtering was computed as the convolution of the instantaneous velocity distribution with an axisymmetric Gaussian kernel $w(x,y)$ [17]:

$$w(x,y) = \exp\left[\frac{-(x^2+y^2)}{2A^2}\right] \tag{A2}$$

The low-pass velocity V_{LP} calculated in this manner was then used to determine the high-pass velocity as

$$V_{\mathrm{HP},i}(x,y) = V_i(x,y) - V_{LP,i}(x,y) \tag{A3}$$

Based on the size of the spatial filter, only flow structures greater than 10 mm were retained in the low-pass filtered velocity distribution.

Angular Momentum

The angular momentum per unit mass in the vertical and horizontal PIV planes, L_V and L_H, respectively, was calculated for image i as

$$L_{V/H,i} = \sum_{j=1}^{n} (r_j V_{\perp,j}) \tag{A4}$$

where r_j is the distance from the center of the cylinder to the point of interest, $V_{\perp,j}$ is the velocity vector perpendicular to r_j, and the sum is performed over all of the locations where data were acquired with PIV. The ensemble average over the n images then gives the values $\langle L_V \rangle$ and $\langle L_H \rangle$.

References

[1] Arcoumanis, C., Hu, Z., Vafidis, C., and Whitelaw, J. H., 1990, "Tumbling Motion: A Mechanism for Turbulence Enhancement in Spark-Ignition Engines," SAE Paper No. 900060.

[2] Nino, E., Gajdeczko, B. F., and Felton, P. G., 1993, "Two Color Particle Image Velocimetry in an Engine With Combustion," SAE Paper No. 930872.

[3] Kent, J. C., Mikulec, A., Rimal, L., Adamczyk, A. A., Mueller, S. R., Stein, R. A., and Warren, C. C., 1989, "Observations on the Effects of Intake-Generated Swirl and Tumble on Combustion Duration," SAE Paper No. 892096.

[4] Kent, J. C., Haghgooie, M., Mikulec, A., Davis, G. C., and Tabaczynski, R. J., 1987, "Effects of Intake Port Design and Valve Lift on In-Cylinder Flow and Burnrate," SAE Paper No. 872153.

[5] Mikulec, A., Kent, J. C., and Tabaczynski, R. J., 1988, "The Effect of Swirl on Combustion in a Pancake Chamber Spark Ignition Engine: The Case of Constant Inducted Kinetic Energy," SAE Paper No. 880200.

[6] Witze, P. O., 1982, "The Effect of Spark Location on Combustion in a Variable-Swirl Engine," SAE Paper No. 820044.

[7] Inoue, T., Nakanishi, H., and Iguchi, S., 1980, "The Role of Swirl and Squish in Combustion of the SI Engine," VDI-Berichte, No. 370, p. 181.

[8] Hadded, O., and Denbratt, I., 1991, "Turbulence Characteristics of Tumbling Air Motion in Four-Valve S. I. Engines and Their Correlation With Combustion Parameters," SAE Paper No. 910478.

[9] Trigui, N., Kent, J. C., Guezennec, Y., and Choi, W. C., 1994, "Characterization of Intake Generated Fluid Flow Fields in IC Engines Using 3-D Particle Tracking Velocimetry (3-D PTV)," SAE Paper No. 940279.

[10] Patrie, M. P., 1998, "Particle Image Velocimetry Measurements of In-Cylinder Flows and Correlation With Engine Performance," Ph.D. thesis, Mechanical Engineering Department, University of Wisconsin-Madison.

[11] Bottom, K. E., 2003, "PIV Measurements of In-Cylinder Flow and Correlation With Engine Performance," Ph.D. thesis, Mechanical Engineering Department, University of Wisconsin-Madison.

[12] Bevan, K. E., and Ghandhi, J. B., 2004, "PIV Measurements of In-Cylinder Flow in a Four-Stroke Utility Engine and Correlation With Steady Flow Results," SAE Paper No. 04-SETC-22.

[13] Bracco, F. V., 1988, "Structure of Flames in Premixed-Charge IC Engines," Combust. Sci. Technol., **58**, 209–230.

[14] Schalkoff, R. J., 1989, "Digital Image Processing and Computer Vision," Wiley, New York.

[15] Christenson, K. T., and Soloff, S. M., 1999, PIV SLEUTH, Integrated Particle Image Velocimetry (PIV) Acquisition/Interrogation/Validation Software, Urbana.

[16] Reuss, D. L., Adrian, R. J., Landreth, C. C., French, D. T., and Fansler, T. D., 1989, "Instantaneous Planar Measurements of Velocity and Large-Scale Vorticity and Strain Rate in an Engine Using Particle-Image Velocimetry," SAE Paper No. 890616.

[17] Reuss, D. L., Bardsley, M., Felton, P. G., Landreth, C. C., and Adrian, R. J., 1990, "Velocity, Vorticity, and Strain-Rate Ahead of a Flame Measured in an Engine Using Particle Image Velocimetry," SAE Paper No. 900053.

In-Cylinder Pressure Measurement: Requirements for On-Board Engine Control

Fabrizio Ponti
DIEM,
University of Bologna,
Bologna 40136, Italy

During these last years, passenger vehicles have been equipped with an increasing number of sensors, in an effort to monitor and control their behavior in terms of global performance and emissions. This, together with constantly increasing electronic control unit computing power and data storage capabilities, allowed the development of more efficient engine-vehicle control strategies. In this perspective, new sensors will be employed as soon as their use will be shown to be necessary to design new engine control and diagnostic strategies, and their cost and expected life will be compatible with on-board application. A sensor that has been largely studied in recent years is the in-cylinder pressure one: advanced engine control strategies that make use of the signal coming from such a sensor have been investigated, while reliable and low-cost sensors are being developed to survive for the vehicle life the harsh on-board environment. The signal coming from the in-cylinder pressure is, in fact, very rich in information and could be used, for example, to improve engine torque management (by directly computing the instantaneous indicated torque), to improve air/fuel ratio control, misfire and knock detection capabilities, engine emission estimation (to be used for $DeNO_x$ catalysts purging management as an example), residual gas fraction estimation, etc. Many sensor concepts have been developed, although none seems to actually fully meet both the precision and low-cost requirements necessary for on-board application. This work deals with defining the sensor precision characteristics necessary to effectively implement the aforementioned engine control and diagnostic capabilities improvements. In particular, it will be shown that only the low-frequency signal content has to be precisely measured and is critical for certain application. In addition, the importance of a correct reference of the in-cylinder pressure signal is discussed, and a novel methodology to quickly obtain this information once the engine has been setup with a proper in-cylinder pressure sensor is discussed. [DOI: 10.1115/1.2830549]

Introduction

Increasingly stringent exhaust emission limits and higher fuel economy are the main goals in the development and design of improved engine control systems. The introduction of always more stringent limits is accompanied in the last years by requirements that enforce the vehicle polluting characteristics to be guaranteed over its entire life, and malfunctioning conditions to be detected (OBD II requirements).

In-cylinder pressure based feedback control systems have been demonstrated to be a good method to optimize engine operation over vehicle life [1,2], since cylinder pressure is a fundamental combustion variable that contains information related to the combustion process that takes place in the cylinders.

Using the information from this signal, optimal control for spark timing, air fuel ratio, exhaust gas recirculation, and knock can be designed [3–5]. On the other hand, many papers have been devoted to the correction of possible errors that can affect the in-cylinder pressure signal and to the right management of the information that can be obtained from it [6–21].

Despite the difficulty in managing this signal, many cylinder pressure based engine control systems can be found in the literature [22–33]. Generally, cost, packaging, and durability considerations have limited production applications of these systems. Some of them have also been compromised by poor sensor signal quality or processing algorithm design, both of which may limit system performance and functionality, and reduce system benefits.

The most common type of cylinder pressure sensors are intrusive devices that are installed inside the combustion chamber [34–37]. An effort in the development of this kind of sensors is to reduce their dimension in order to facilitate their packaging within the crowded space of an engine cylinder head. Cost of these sensors is generally high and the harsh mechanical and thermal environment they are exposed to constitutes a big problem in terms of durability.

On the other hand, nonintrusive sensors do not require a direct access to the combustion chamber [38–40], since in-cylinder pressure can be, for example, sensed evaluating the stress conditions in an existing engine component or engine head vibration level. Usually, this kind of sensor is fitted into an existing component and therefore they are generally lower cost than intrusive ones. On the one hand, the signal quality that can be achieved is usually lower and often below the requirements for the development of the engine control strategy.

It is possible to find in the literature many in-cylinder pressure based engine control algorithms with various control functionality, and pressure sensor, sampling, and processing requirements [41–44]. In this work, the attention is focused on those approaches that use the indicated mean effective pressure (IMEP) to design the engine control architecture [45–49]. The objective of the current work is to define the sensor quality, the sampling, and processing requirements that are necessary to correctly evaluate the IMEP and then to implement this kind of approach.

After presenting in the first section of the paper the nature of the relationship between in-cylinder pressure and IMEP, the effects of sampling and crank angle phasing the in-cylinder pressure

Contributed by the International Gas Turbine Institute of ASME for publication in the JOURNAL OF ENGINEERING FOR GAS TURBINES AND POWER. Manuscript received September 20, 2005; final manuscript received September 16, 2007; published online March 26, 2008. Review conducted by Jim Cowart.

Table 1 Amplitude of the angular frequency components of the crank-slider mechanism function $f_m(\theta)$ for typical values of λ

Angular frequency component order	Frequency component amplitude value		
	λ=0.2	λ=0.3	λ=0.4
0	0	0	0
±1	0	0	0
±2	0.50	0.50	0.50
±3	0	0	0
±4	0.05	0.08	0.10
±5	0	0	0
±6	0	0	0
±7	0	0	0
±8	Negligible 0.26×10^{-3}	Negligible 0.90×10^{-3}	Negligible 2.27×10^{-3}
±>8	0	0	0

signal are discussed, defining the minimum requirements needed to correctly evaluate IMEP. Finally, a novel approach to precisely determine the correct angle phasing is introduced.

Relationship Between In-Cylinder Pressure and Indicated Mean Effective Presurre

The nature of the relationship between the in-cylinder pressure signal and the corresponding IMEP value is analyzed in detail in this section. Particular attention is devoted to the analysis of such relationship in the angular frequency domain. It will be demonstrated that only few in-cylinder pressure angular frequency components are necessary to evaluate IMEP values. This will allow designing specific and dedicated sampling strategies particularly useful to implement on-board IMEP based control algorithms.

As it is well known (see the Appendix for further considerations), the IMEP for the mth cylinder of an engine with Z cylinders can be expressed as

$$\mathrm{IMEP}_m = \frac{1}{2}\int_0^{\tau\pi} p_m(\theta)\cdot f_m(\theta)d\theta \tag{1}$$

The function $f_m(\theta)$ is the crank-slider mechanism function for the mth cylinder and can be expressed as

$$f_m(\theta) = \sin(\theta-\theta_{\mathrm{TDC}m}) + \frac{\lambda\sin(2(\theta-\theta_{\mathrm{TDC}m}))}{2\sqrt{1-\lambda^2\sin^2(\theta-\theta_{\mathrm{TDC}m})}} \tag{2}$$

The spectral analysis of the function $f_m(\theta)$ shows that only two angular frequency components (the second and the fourth over an engine cycle) have an amplitude significantly different from zero, while all the other components show zero or very close to zero amplitude values [50], as it can be seen in Table 1.

This observation allows rewriting Eq. (2) in a simplified form.

$$f_m(\theta) = \sin(\theta-\theta_{\mathrm{TDC}m}) + \frac{\lambda}{2}\sin(2(\theta-\theta_{\mathrm{TDC}m})) \tag{3}$$

The maximum difference between the simplified form of the crank-slider mechanism function (3) and the complete one (2) is lower than 5×10^{-3}, being therefore negligible.

For an easier notation from here on, the TDC crankshaft angle position for the mth cylinder will be considered equal to 0. If the in-cylinder pressure signal is sampled, evaluation of IMEP_m is still possible, but particular care has to be put in the choice of the sampling rate, in order to avoid aliasing effects. Particular attention will be devoted in the following sections to the sampling rate best choice, and a specific signal processing is proposed to compensate for eventual aliasing effects.

Assuming that the number of samples per engine cycle, N, is high enough to avoid aliasing problems, and considering that the sampling period is $\Delta\theta=\tau\pi/N$, it is possible to rewrite Eq. (1) into

$$\begin{aligned}\mathrm{IMEP}_m &= \frac{1}{2}\sum_{n=1}^{N} p_m(n\Delta\theta)\cdot f_m(n\Delta\theta)\cdot\Delta\theta \\ &= \frac{\tau\pi}{2N}\sum_{n=1}^{N} p_m(n\Delta\theta)\cdot f_m(n\Delta\theta)\end{aligned} \tag{4}$$

Substituting Eq. (3) into Eq. (4), it is possible to obtain

$$\mathrm{IMEP}_m = \frac{\tau\pi}{2N}\sum_{n=1}^{N} p_m(n\Delta\theta)\cdot\left[\sin(\tau\pi n/N)+\frac{\lambda}{2}\sin(2\tau\pi n/N)\right] \tag{5}$$

Since in the present work, only four stroke engine will be considered, Eq. (5) can be further simplified:

$$\mathrm{IMEP}_m = \frac{2\pi}{N}\sum_{n=1}^{N} p_m(n\Delta\theta)\cdot\left[\sin(4\pi n/N)+\frac{\lambda}{2}\sin(8\pi n/N)\right] \tag{6}$$

Considering the Fourier series representation of the in-cylinder pressure signal, it is possible to state that

$$p_m(n\Delta\theta) = p_{m0} + \sum_{k=1}^{N/2}\left(p_{mk_s}\sin\left(\frac{2k\pi n}{N}\right)\right) + \sum_{k=1}^{N/2}\left(p_{mk_c}\cos\left(\frac{2k\pi n}{N}\right)\right) \tag{7}$$

Substituting Eq. (7) into Eq. (6) and considering that all the products between sinusoidal and/or cosinusoidal wave forms, having different frequencies multiple of the signal fundamental one, give summation equal to 0 over a signal length period (as expressed by the following equations):

$$\begin{aligned}&\sum_{k=1}^{N/2}\left(p_{m0}\sin\left(\frac{2k\pi n}{N}\right)\right)=0 \quad \sum_{k=1}^{N/2}\left(p_{m0}\cos\left(\frac{2k\pi n}{N}\right)\right)=0 \quad \forall\, p_{m0} \\ &\sum_{k=1}^{N/2}\left(p_{mkc}\cos\left(\frac{2k\pi n}{N}\right)\sin\left(\frac{4\pi n}{N}\right)\right)=0 \quad \forall\, k \\ &\sum_{k=1}^{N/2}\left(p_{mkc}\cos\left(\frac{2k\pi n}{N}\right)\sin\left(\frac{8\pi n}{N}\right)\right)=0 \quad \forall\, k \\ &\sum_{k=1}^{N/2}\left(p_{mks}\sin\left(\frac{2k\pi n}{N}\right)\sin\left(\frac{4\pi n}{N}\right)\right)=0 \quad \forall\, k\neq 2 \\ &\sum_{k=1}^{N/2}\left(p_{mks}\sin\left(\frac{2k\pi n}{N}\right)\sin\left(\frac{8\pi n}{N}\right)\right)=0 \quad \forall\, k\neq 4\end{aligned} \tag{8}$$

it is possible to simplify Eq. (6) into

$$\mathrm{IMEP}_m = \frac{2\pi}{N}\left[p_{m2s}\sum_{n=1}^{N/2}\sin^2(4\pi n/N)+\frac{\lambda}{2}p_{m4s}\sum_{n=1}^{N/2}\sin^2(8\pi n/N)\right] \tag{9}$$

If it is further considered that

$$\sum_{n=1}^{N/2}\sin^2(4\pi n/N)=\sum_{n=1}^{N/2}\sin^2(8\pi n/N)=\frac{N}{2} \tag{10}$$

the final expression of IMEP as a function of in-cylinder pressure frequency components can be written as

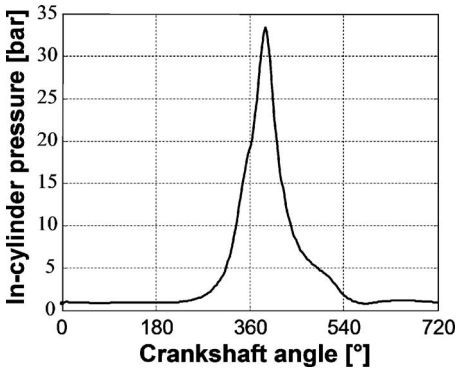

Fig. 1 In-cylinder pressure signal for an L4 MPI engine running at 2200 rpm and full load

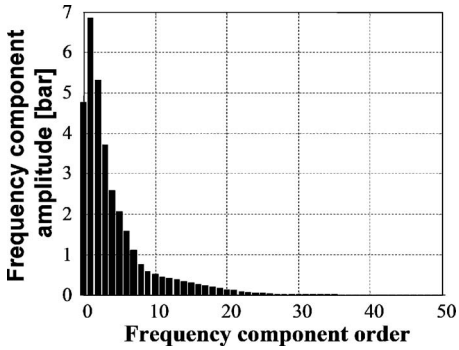

Fig. 2 In-cylinder pressure signal frequency analysis

$$\mathrm{IMEP}_m = \pi\left[p_{m2s} + \frac{\lambda}{2}p_{m4s}\right] \tag{11}$$

From this equation, it is possible to note that the knowledge of the second and fourth in-cylinder pressure signal sinusoidal frequency components over the engine cycle is sufficient to correctly evaluate the IMEP over that cycle for the cylinder taken into account.

This important result will be used in the following to define the minimum sampling rate required for a correct IMEP evaluation and to better understand the effects of a crankshaft angle phasing error.

Another important consideration is that the in-cylinder pressure mean value does not play any role in the evaluation of the IMEP. Therefore, the signal coming from sensors that do not give information on the in-cylinder pressure mean value (for example, the piezoelectric sensors) can be used for IMEP evaluation directly, without any signal preprocessing.

If we consider, for example, the in-cylinder pressure waveform reported in Fig. 1, acquired into a cylinder of an L4 MPI 1.2 l engine (whose characteristics are reported in Table 2) at 2200 rpm and full load, it is possible to determine $p_{m2s}=2.73$ bars and $p_{m4s}=1.88$ bars.

From these values, the IMEP_m can be evaluated to be equal to 9.47 bars. The same value could have been calculated also using the classical approach described by Eq. (1).

Sampling Rate Requirements

Important consequences on the sampling rate arise from the results obtained in the preceding section. It is already known from the literature that in order to evaluate IMEP, it is not necessary to use very high sampling rates for the in-cylinder pressure acquisition system [9–12], but as previously mentioned particular care has to be put in the choice of the sampling rate, in order to avoid aliasing effects. The observation that only the second and fourth in-cylinder pressure frequency components over an engine cycle contribute to the IMEP value helps in defining the minimum sampling rate, as it will be explained in the following.

Table 2 Engine characteristics

Type	Fiat fire L4
Displacement	1.2 l
Cylinder bore	70.8 mm
Stroke	78.9 mm
Connecting rod length	129 mm
$\lambda=r/l$	0.306
Compression ratio	9.8:1
Maximum power	54 kW at 6000 rpm
Maximum torque	106 N m at 4000 rpm

If the second and fourth frequency components were the only present in the in-cylinder pressure signal, it would be sufficient to acquire eight samples per cycle in order to fulfill the sampling theorem requirements. Since the in-cylinder pressure presents a quite wide spectrum, in order to avoid aliasing on the frequency components of interest (second and fourth ones), it is necessary either to prefilter the signal or to use a higher sampling rate. Since prefiltering the signal causes an undesired shifting (that can result in a subsequent phasing error), the second solution is preferable. It is not necessary anyway to use sampling rate as high to completely avoid the aliasing phenomenon over the entire spectrum of the in-cylinder pressure signal, since only the second and fourth frequency components are important and have to be preserved for IMEP evaluation.

As it is known from the sampling theorem, if the sampling rate is such that N samples are acquired per engine cycle, the minimum frequency component that can give rise to an alias overlapping the second frequency component is the $(N\text{-}2)$ one. Similarly, the minimum frequency component that can give rise to an alias overlapping the fourth component is the $(N\text{-}4)$ one. If we want to avoid both alias overlappings, we should choose a sampling frequency such that N-4 is higher than $z_{\max}$, the higher frequency component order significantly different from 0 in the in-cylinder pressure signal.

Therefore, the relationship that has to be satisfied is that the number of samples acquired per engine cycle N has to be higher than $z_{\max}+4$.

$$N = z_{\max} + 4 \tag{12}$$

If we consider, for example, the in-cylinder pressure signal, reported in Fig. 1, acquired in a L4 MPI engine (whose characteristics are reported in Table 2) at 2200 rpm and full load, we can observe from its spectrum, reported in Fig. 2, that no information is contained in the signal at frequency component orders higher than approximately the 25th. This means that the minimum sampling rate that can be usefully employed for the waveform reported in Fig. 1 is approximately 30 samples per engine cycle (i.e., one sample every 24 deg).

In order to apply these considerations to every engine operating condition, only the frequency components with amplitude higher than 1/100 of the second harmonic amplitude have been considered relevant. Therefore, the order of the higher frequency component can be identified and hence the minimum sampling rate can be determined. The chosen sampling rate could still cause aliasing on the interesting frequency components, but they will affect their amplitude less than 1%.

The experimental tests that have been conducted running the engine on a test cell are reported in Fig. 3.

Figure 4 reports the order of the higher frequency component present in the in-cylinder pressure signal (determined as already explained) for the L4 MPI engine under study over the whole

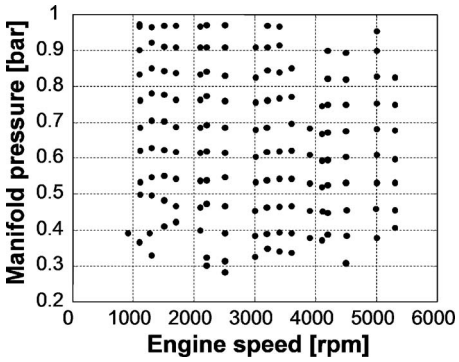

Fig. 3 Steady-state tests conducted

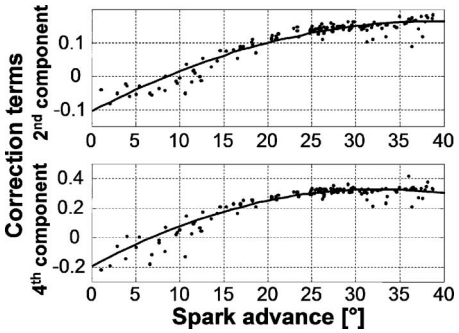

Fig. 5 Correction terms for the second and fourth sinusoidal frequency components

engine operating range. As it can be seen, a possible choice that can be applied to the whole engine operating range is to sample 36 times per engine cycle (once every 20 deg).

If a lower number of samples is used, the second and fourth sinusoidal frequency component will be affected by aliasing. In particular acquiring N samples per cycle will produce a reflection on the second harmonic of the components $N\pm2$, $2N\pm2,\ldots$, and a reflection on the fourth harmonic of the components $N\pm4$, $2N\pm4,\ldots$

If we consider 30 as the higher frequency component present in the in-cylinder pressure signal, and an acquisition with 16 samples per engine cycle, then the frequency components that will affect p_{m2s} and p_{m4s} will be, respectively, the 14th, 18th ones and the 12th, 20th, 28th ones. In particular, from aliasing reflection rules, it is possible to obtain the relationship between the sampled in-cylinder pressure frequency components (16 samples per engine cycle) and the real signal ones:

$$\hat{p}_{m2s} = p_{m2s} - p_{m14s} + p_{m18s}$$
$$\hat{p}_{m4s} = p_{m4s} - p_{m12s} + p_{m20s} - p_{m28s} \tag{13}$$

Using the component $\hat{p}_{m2s}$ and $\hat{p}_{m4s}$ will obviously result in a wrong IMEP_m evaluation, being the mean percent error for the tests of Fig. 3 equal to 13.5%.

In order to compensate for the effect of the aliasing phenomenon, a specific signal processing procedure has been designed. Equation (13) has been rewritten as

$$\hat{p}_{m2s} = p_{m2s}\left(1 - \frac{p_{m14s} - p_{m18s}}{p_{m2s}}\right)$$

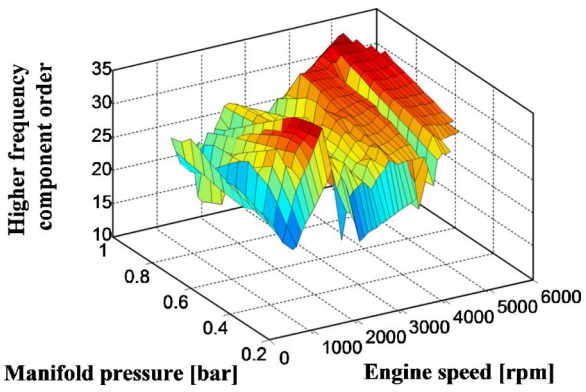

Fig. 4 In-cylinder pressure higher order frequency component over the engine operating range for an L4 MPI engine

$$\hat{p}_{m4s} = p_{m4s}\left(1 - \frac{p_{m12s} - p_{m20s} + p_{m28s}}{p_{m4s}}\right) \tag{14}$$

The terms $(p_{m14s}-p_{m18s})/p_{m2s}$ and $(p_{m12s}+p_{m20s}-p_{m28s})/p_{m4s}$ have been determined from a high sample rate acquisition for the tests reported in Fig. 3, and have been reported in Fig. 5 (where they are referred to as correction terms) as a function of the spark advance (SA).

Figure 5 reports also the best fit of the data that has been obtained with a polynomial function of second degree.

Using the identified polynomial functions, it is possible now to recover the real value of the second and fourth sinusoidal frequency components of the real in-cylinder pressure signal from those obtained sampling the same signal 16 times per engine cycle. This can be done using the polynomial functions identified in Fig. 5 (that has been called $\mathrm{Pol}_2(\mathrm{SA})$ and $\mathrm{Pol}_4(\mathrm{SA})$, respectively) as shown by the following equation:

$$p_{m2s} = \frac{\hat{p}_{m2s}}{1 - \mathrm{Pol}_2(\mathrm{SA})}$$
$$p_{m4s} = \frac{\hat{p}_{m4s}}{1 - \mathrm{Pol}_4(\mathrm{SA})} \tag{15}$$

For the engine taken into account, the identification process yielded

$$\mathrm{Pol}_2(\mathrm{SA}) = -1.76 \times 10^{-4}\mathrm{SA}^2 + 1.38 \times 10^{-2}\mathrm{SA} - 1.04 \times 10^{-1} \tag{16}$$

$$\mathrm{Pol}_4(\mathrm{SA}) = -4.92 \times 10^{-4}\mathrm{SA}^2 + 3.21 \times 10^{-2}\mathrm{SA} - 1.94 \times 10^{-1}$$

Introducing the described signal processing technique, the mean error on IMEP_m evaluation from the 16 samples signal for the same tests of Fig. 3 was reduced to 2.0% with the maximum error on IMEP_m equal approximately to 0.4 bar, as it will be explained in detail in the next section.

Application of this signal processing technique allows obtaining good IMEP_m evaluation with a very low sampling rate (16 samples per engine cycle, i.e., one sample every 45 deg).

LOW Sampling Rate Application

The considerations made in the previous section have been applied to a complete set of steady-state tests, as that presented in Fig. 3. For each test, three different sampling rates have been adopted: 720, 36, and 16 samples per cycle. The higher sample rate signals have been used to obtain reference values for $\mathrm{IMEP}_{m\mathrm{ref}}$, evaluated in a traditional way, using Eq. (4). From the signals acquired for all the sample rates adopted, other evaluations of IMEP_m have been obtained following Eq. (11); results have been named, respectively, $\mathrm{IMEP}_{m\,s720}$, $\mathrm{IMEP}_{m\,s36}$, and $\mathrm{IMEP}_{m\,s16}$. Finally, the application of the proposed correction, to compensate

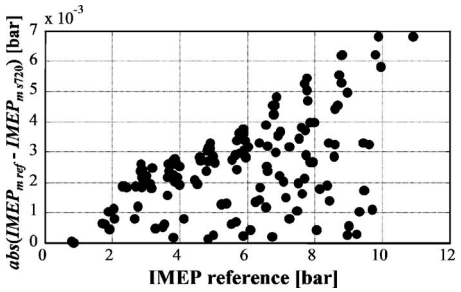

Fig. 6 Comparison between $IMEP_{m\ ref}$ and $IMEP_{m\ s720}$

for the aliasing effect over the second and fourth sinusoidal frequency component with a 16 samples signal, has been considered, obtaining $IMEP_{m\ corr16}$ values.

The following figures present the absolute difference between each $IMEP_m$ evaluation and the reference value toward the $IMEP_m$ reference value itself. Through these figures, it is then possible to determine the accuracy of the different $IMEP_m$ evaluations.

The reference values $IMEP_{mref}$ and $IMEP_{m\ s720}$ have been obtained starting from the very same acquisitions. The difference between them is not equal to 0 due to the approximation of the crank-slider function $f_m(\theta)$ introduced in Eq. (3). That approximation has been introduced under the hypothesis that all the frequency components of the function $f_m(\theta)$ other than the second and the fourth ones show zero or negligible amplitude values. Figure 6 shows that the maximum error introduced adopting this approximation is lower than 0.007 bar and therefore lower than the 0.07% of the full scale value. This result confirms that the approximation employed on $f_m(\theta)$ is acceptable and introduces negligible inaccuracies.

$IMEP_{m\ s36}$ values have been obtained using the same procedure as $IMEP_{m\ s720}$, but starting from the 36 samples per cycle signals. This sampling rate has been chosen in order to maintain as low as possible aliasing effects over the second and fourth in-cylinder pressure frequency components, and then guarantees an acceptable accuracy in $IMEP_m$ evaluation. Following Eq. (12), in fact, it is possible to observe that, if a 36 samples per cycle acquisition is employed, the only frequency components that could cause aliasing effects over the second and fourth in-cylinder pressure frequency components are those at a frequency component order higher than 32. Figure 7 confirms the assumption made that the amplitudes of these high-frequency components are negligible (and consequently their aliasing effects), since they cause errors always lower than 0.05 bar corresponding to a maximum error equal to the 0.5% of the full scale value.

Further lowering the sampling rate, the aliasing effects are not negligible anymore, as expected by previous considerations and as clearly shown in Fig. 8, where $IMEP_{m\ s16}$ values are compared

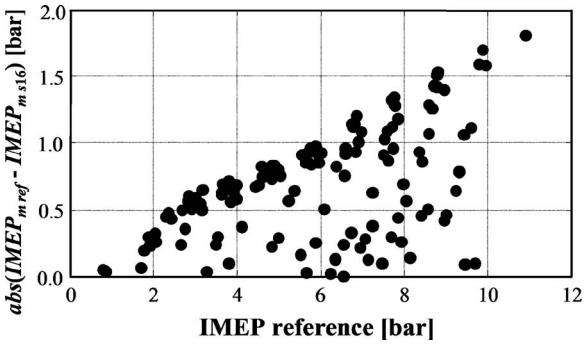

Fig. 8 Comparison between $IMEP_{m\ ref}$ and $IMEP_{m\ s16}$

with the reference values. In this case, errors can be as high as 1.8 bars meaning that accuracy (18% of full scale value) is absolutely unacceptable.

Applying the proposed procedure for aliasing effects compensation allowed obtaining the results reported in Fig. 9. Estimation and compensation of the aliasing effects over the in-cylinder frequency components used for $IMEP_m$ evaluation proved therefore to be effective, reducing the maximum error to approximately 0.34 bar, i.e., 3% of the full scale value; obtained rms is equal to 0.11 bar, i.e., 1.1% of the full scale value. Minimum sampling requirements have been therefore defined and proved to be effective.

Angle Phasing Error Effects on Indicated Mean Effective Pressure Evaluation

As it is well known a crankshaft angle phasing error strongly affects the evaluation of $IMEP_m$ from in-cylinder pressure measurement [51–55]. This error introduces, in fact, an unknown shifting θ_s between the in-cylinder pressure waveform and the corresponding crank-slider mechanism function.

The effects of such a shifting is an alteration of the in-cylinder pressure frequency content and therefore also a modification of the second and fourth sinusoidal frequency component amplitudes that affects $IMEP_m$ evaluation.

The variation of the second and fourth sinusoidal frequency component can be determined observing the modification to the in-cylinder pressure signal frequency representation if a θ_s shifting is applied. Equation (7) suggests that

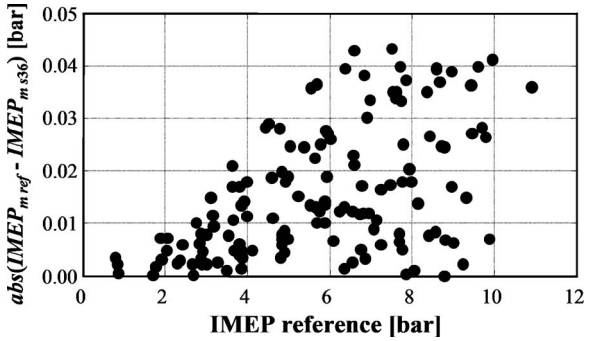

Fig. 7 Comparison between $IMEP_{m\ ref}$ and $IMEP_{m\ s36}$

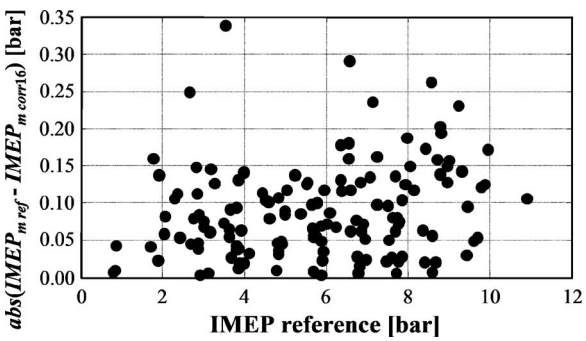

Fig. 9 Comparison between $IMEP_{m\ ref}$ and $IMEP_{m\ corr16}$

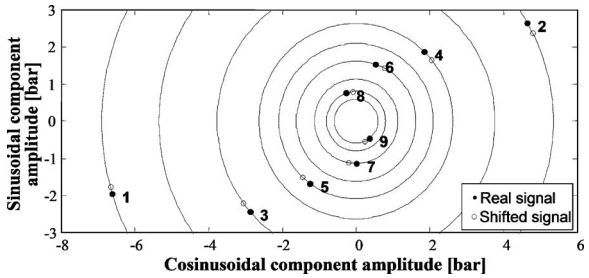

Fig. 10 Frequency component 1–9 representation on the complex plane for the real and shifted in-cylinder pressure wave forms for the same test of Fig. 1 and $\theta_s \cong 3$ deg

$$p_m(n\Delta\theta + \theta_s) = p_{m0} + \sum_{k=1}^{N/2} \left(p_{mk_s} \sin\left(\frac{2k\pi n}{N} + \theta_s \right) \right) + \sum_{k=1}^{N/2} \left(p_{mk_c} \cos\left(\frac{2k\pi n}{N} + \theta_s \right) \right) \quad (17)$$

while a Fourier representation of the signal $p_m(n\Delta\theta + \theta_s)$ will be of the type

$$p_m(n\Delta\theta + \theta_s) = p^1_{m0} + \sum_{k=1}^{N/2} \left(p^1_{mk_s} \sin\left(\frac{2k\pi n}{N} \right) \right) + \sum_{k=1}^{N/2} \left(p^1_{mk_c} \cos\left(\frac{2k\pi n}{N} \right) \right) \quad (18)$$

Therefore, the relationship between the real Fourier coefficients and those obtained if a shifting is applied can be expressed as

$$p^1_{mk_s} = p_{mk_s} \cos(\theta_s) - p_{mk_c} \sin(\theta_s)$$
$$p^1_{mk_c} = p_{mk_s} \sin(\theta_s) + p_{mk_c} \cos(\theta_s) \quad (19)$$

The Fourier coefficients of the shifted signal will differ from the real ones as a consequence of a θ_s rotation of the signal frequency representation in the complex plane, as it is shown in Fig. 10.

The error on the second and fourth sinusoidal frequency component depends therefore on the value of the phasing error and also on the amplitudes of the corresponding co-sinusoidal frequency components. In fact, if the second and fourth cosinusoidal in-cylinder pressure frequency components were 0 or near to 0, the effects of a phasing error on the $IMEP_m$ evaluation would be very small, and vice versa if the cosinusoidal component amplitude is high. Unfortunately, this is the case for the measured in-cylinder pressure, as it is possible to see in Fig. 11.

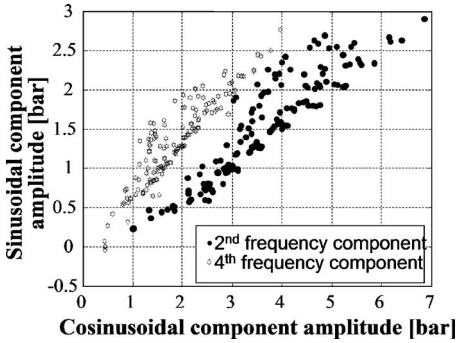

Fig. 11 Second and fourth frequency components representation on a complex plane for the in-cylinder pressure wave forms acquired during the experimental tests reported in Fig. 3

Table 3 $IMEP_m$ percent error

Reference error θ_s	$IMEP_m$ percent error (%)
0.2	0.70
0.4	1.40
0.6	2.10
0.8	2.80
1.0	3.50
1.5	5.27
2.0	7.04

Noting that the ratio between the amplitude of the cosinusoidal and the corresponding sinusoidal frequency components can be roughly considered equal to 2, and that the second and the fourth frequency components are approximately of the same order of magnitude, it is possible to evaluate the effects of a phasing error on $IMEP_m$ evaluation. In fact, from Eqs. (11) and (19), it is possible to obtain under the hypothesis that $p_{mc}/p_{ms} \equiv 2$,

$$\begin{aligned} \mathrm{IMEP}^1_m &= \pi \left[p^1_{m2s} + \frac{\lambda}{2} p^1_{m4s} \right] \\ &\cong \pi \left[p_{m2s} + \frac{\lambda}{2} p_{m4_s} \right] \left(\cos(\theta_s) - \frac{p_{m_c}}{p_{m_s}} \sin(\theta_s) \right) \\ &\cong \mathrm{IMEP}_m(\cos(\theta_s) - 2\sin(\theta_s)) \end{aligned} \quad (20)$$

from which it is possible to obtain the $IMEP_m$ evaluation percent error as a function of the phasing error θ_s (see Table 3).

Values similar to those reported in Table 3 can be found also in the literature, as a confirmation of the great importance of a correct angular referencing for the in-cylinder pressure signal [51–55].

Top Dead Center Position Determination

As we already discussed, the determination of the TDC position is a key problem for the evaluation of $IMEP_m$ from in-cylinder pressure data. Many approaches have been developed and can be found in the literature [51,53–55]. The novel approach here presented is based on the evaluation of the pressure peak position during motored operating conditions.

It is well known that the in-cylinder pressure peak position during motored operating conditions does not correspond to TDC and usually occurs before TDC, due to the irreversibilities caused primarily by heat transfer and blow-by [6,7]. The angular distance between these two positions is usually referred to as "loss angle."

Evaluation of the loss angle is possible only if a different phasing method is available. For example, there exist capacitive sensors that allow dynamic determination of the TDC position by sensing the varying capacitance between piston and sensor probe head.

The method here presented allows evaluating the loss angle and therefore the correct angle phasing without the need of any additional sensor other than the in-cylinder pressure one and a magnetic pickup or an encoder for sensing the actual angular position. The method requires that the engine is motored twice at the same engine speed, but with different sense of rotation. In the case of an engine mounted on a test cell, this can be achieved by simply inverting the voltage supply to the electric motor devoted to cranking the engine.

Running an engine in the opposite direction is obviously only possible during motoring operation and requires particular care since the lubrication could be insufficient due to improper operation of the lubricant pump. This consideration suggests that the engine should be motored in the opposite direction only for a short time interval. This is not a problem since the acquisition of

Table 4 Sensor and measuring chain components characteristics

Pressure sensor Kistler 6053 B60	
Sensitivity K_p	6.84 pC/bar
Charge amplifier Kistler 5007	
Sensitivity K_p	6.84 pC/bar
Range	20 M.U./V
Cutoff frequency	180 kHz
Time constant	Short ($R_f=10^9$ Ω)

the in-cylinder pressure for few engine cycles is already sufficient for the success of the TDC position estimation procedure.

Once the two tests have been performed, the pressure peak position of both the in-cylinder pressure waveforms has to be evaluated. Both the positions differ from the real TDC position for the loss angle presence, but its influence takes different crank angle directions in the two cases. If the loss angle values are identical for the two tests, then the TDC position will be placed exactly in the middle of the two determined peak pressure positions. Since loss angle amplitude depends on heat transfer, blow-by, and sensor characteristics [7], in order to guarantee that the same loss angle values apply to both the tests, engine speed, cylinder filling, and engine thermal status should be identical when running them.

These considerations yield to the following requirements for the tests to be performed:

(a) The regular direction motored test has to be performed at WOT, in order to guarantee approximately the same cylinder filling.
(b) The same engine speed has to be reached and maintained constant for several engine cycles for both the tests.
(c) The tests have to be performed near in time and without firing the engine in between.

The method has been applied to a SI racing engine equipped with a piezoelectric in-cylinder pressure sensor (whose characteristics are reported in Table 4), and an encoder with one degree crank angle resolution.

The engine speed during both motored tests presents a mean value around 1700 rpm, even if the instantaneous fluctuations are very high, as it can be noticed in Fig. 12. Figure 12 has been obtained reporting both the engine speed wave forms as a function of crankshaft angle position. This means that the reverse wave form has been covered from right to left (as suggested by the arrows).

Figure 13 reports in the same way the in-cylinder pressure signals acquired during the same tests.

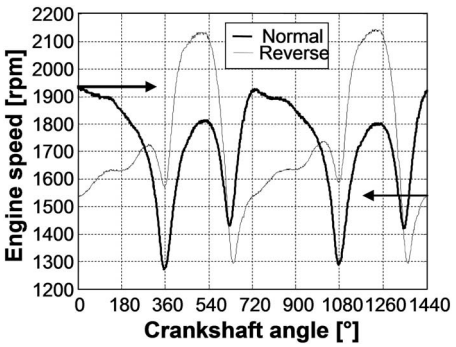

Fig. 12 Instantaneous engine speed during the two motored tests performed for TDC evaluation (one with normal sense of rotation, the other one with reversed rotation)

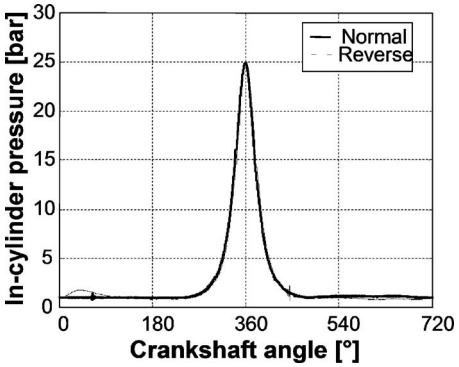

Fig. 13 In-cylinder pressure during the two motored tests performed for TDC evaluation

TDC position has been determined as the position in the middle of the peak pressure positions for the in-cylinder pressure waveforms acquired, as it is possible to see in Fig. 14, where a zoom of Fig. 13 is reported. For each test, in-cylinder pressure and encoder signals have been acquired at 200 kHz sampling rate for 14 consecutive engine cycles. For each engine cycle, the angular position of the pressure peak has been evaluated. As already mentioned, the TDC position (corresponding to 360 deg crankshaft angle in Fig. 15) has been determined as the position in the middle of the peak pressure positions determined for the two tests performed. The loss angle has been evaluated as the mean distance between the peak pressure and the TDC position.

From Fig. 15, it is possible to determine a value for the loss angle of approximately 1.0 deg. The precision of the method can be evaluated in approximately ±0.1 deg. The loss angle has been

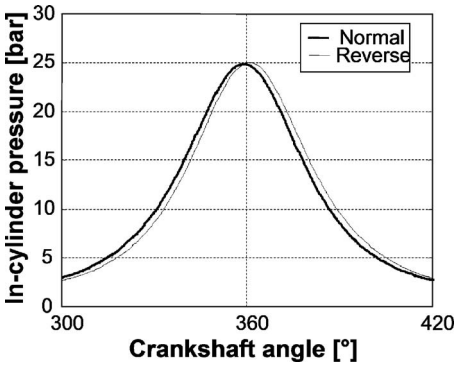

Fig. 14 In-cylinder pressure during the two motored tests performed for TDC evaluation (zoom of Fig. 13)

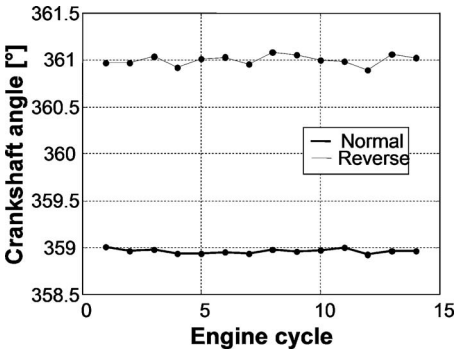

Fig. 15 Peak pressure position and loss angle determination

evaluated for the same engine also using a capacitive sensor, giving as a result the same value obtained with the method here developed.

Conclusions

The relationship between in-cylinder pressure and IMEP has been investigated in order to define the minimum acquisition requirements necessary to implement an IMEP based engine control strategy using in-cylinder pressure measurement. The minimum requirements depend on the spectral content of the in-cylinder pressure signal over the whole engine operating range. In particular it has been demonstrated that only two frequency components (the second and the fourth over an engine cycle) play a role for IMEP evaluation, and the minimum sampling requirements should guarantee the absence of aliasing phenomena over the harmonics of interest.

A particular signal processing technique has been developed in order to reduce this sampling requirements defining a correction factor to be applied when the sampling rate is reduced under the aliasing limit.

The effect over IMEP evaluation due to a phasing error are then discussed and a technique for TDC position is finally presented. This technique has been validated comparing the results with those obtained using a capacitive phase sensor: The two methods gave the same result. This method has been applied successfully to a SI racing engine, but can be applied to any other engine typology and architecture.

Acknowledgment

The author would like to thank Magneti Marelli Spa and, in particular, Mr. Gabriele Serra and Mr. Roberto Flora for their support in the development of the work.

Nomenclature

Z = number of cylinders
θ = crank angle (rad)
$p_m(\theta)$ = relative pressure inside mth cylinder (Pa)
$f_m(\theta)$ = crank-slider mechanism function for the mth cylinder
τ = engine strokes
$\theta_{\mathrm{TDC}m}$ = mth cylinder TDC crank angle position (rad)
r = crank-slider mechanism radius (m)
l = connecting rod length (m)
$\lambda = r/l$ = crank-slider radius/connecting rod ratio
N = samples acquired per engine cycle
n = actual sample
$\Delta\theta$ = crank angle interval between two samples (rad)
k = frequency component order
p_{m0}, p_{mk_s}, p_{mk_c} = in-cylinder pressure Fourier coefficients for the mth cylinder (Pa)
$z_{\max}$ = higher frequency component order over an engine cycle present in the in-cylinder pressure signal
$\hat{p}_{m0}$, $\hat{p}_{mk_s}$, $\hat{p}_{mk_c}$ = sampled in-cylinder pressure Fourier coefficients for the mth cylinder (Pa)
θ_s = crankshaft angle reference error (rad)
θ_l = loss angle (rad)
$W_{\mathrm{cind}m}$ = work per cycle per cylinder (J)
V_d = volume displaced by one cylinder in one engine cycle (m^3)
$T_{\mathrm{ind}m}(\theta)$ = indicated torque for the mth cylinder (N m)
OBD = on-board diagnostics
TDC = top dead center
MPI = multipoint injection
WOT = wide open throttle
SI = spark ignition
rms = root mean square

Appendix: Indicated Mean Effective Pressure Evaluation From In-Cylinder Pressure

IMEP is usually defined as the indicated work per cycle (per cylinder) divided by the cylinder volume displaced per cycle:

$$\mathrm{IMEP}_m = \frac{W_{\mathrm{cind}m}}{V_d} \tag{A1}$$

The indicated work per cycle per cylinder is obtained by integrating around the in-cylinder pressure versus the corresponding cylinder volume throughout the engine cycle on a p-V diagram:

$$W_{\mathrm{cind}m} = \oint p_m dV \tag{A2}$$

Since in-cylinder pressure is usually considered as a function of crank angle, Eq. (A2) can be rewritten as

$$W_{\mathrm{cind}m} = \int_0^{\tau\pi} p_m(\theta)\frac{dV(\theta)}{d\theta}d\theta = A_p r \int_0^{\tau\pi} p_m(\theta) f_m(\theta) d\theta \tag{A3}$$

Therefore, it can be obtained that

$$\mathrm{IMEP}_m = \frac{A_p r}{V_d}\int_0^{\tau\pi} p_m(\theta) f_m(\theta) d\theta = \frac{1}{2}\int_0^{\tau\pi} p_m(\theta) f_m(\theta) d\theta \tag{A4}$$

as it is reported in Eq. (1).

In addition, IMEP_m can be related also to the indicated torque mean value over an engine cycle. Indicated torque can be, in fact, expressed as

$$T_{\mathrm{ind}m}(\theta) = A_p r p_m(\theta) f_m(\theta) \tag{A5}$$

Its mean value over an engine cycle is given by

$$\overline{T_{\mathrm{ind}m}} = \frac{1}{\tau\pi}\int_0^{\tau\pi} T_{\mathrm{ind}m}(\theta) d\theta = \frac{A_p r}{\tau\pi}\int_0^{\tau\pi} p_m(\theta) f_m(\theta) d\theta \tag{A6}$$

Combining Eqs. (A4) and (A6), it is possible to obtain

$$\mathrm{IMEP}_m = \frac{\tau\pi}{V_d}\overline{T_{\mathrm{ind}m}} \tag{A7}$$

References

[1] Amann, C., 1985, "Cylinder-Pressure Measurement and Its Use in Engine Research," SAE Paper No. 852067.
[2] Powell, B. K., Lawson, G. P., and Hogh, G., 1987, "Advanced Real Time Powertrain System Analysis," ASME Paper No. 87-ICE-46.
[3] Hata, Y., Ikeura, K., Morita, T., and Abo, T., 1989, "Engine Control System Using a Cylinder Pressure Sensor," IEE Proc.-D: Control Theory Appl., **136**(2), pp. 84–88.
[4] Muller, R., Hart, M., Truscott, A., Noble, A., Krotz, G., Eickhoff, M., Cavalloni, C., and Gnielka, M., 2000, "Combustion Pressure Based Engine Management System," SAE Paper No. 2000-01-0928.
[5] Watanabe, S., Machida, K., Iijima, K., and Tomisawa, N., 1996, "A Sophisticated Engine Control System Using Combustion Pressure Detection," SAE Paper No. 960042.
[6] Brown, W. L., 1967, "Methods for Evaluating Requirements and Errors in Cylinder Pressure Measurement," SAE Paper No. 670008.
[7] Lancaster, D. R., Krieger, R. B., and Lienesch, J. H., 1975, "Measurement and Analysis of Engine Pressure Data," SAE Paper No. 750026.
[8] Warren, C., Stein, R., and Mencick, D., 1987, "Effect of Thermal Strain on Measurement of Cylinder Pressure," SAE Paper No. 870455.
[9] Randolph, A., 1990, "Methods of Processing Cylinder-Pressure Transducer Signals to Maximize Data Accuracy," SAE Paper No. 900170.
[10] Randolph, A., 1990, "Cylinder Pressure Transducer Mounting Techniques to Maximize Data Accuracy," SAE Paper No. 900171.
[11] Burnt, M., and Lucas, G., 1991, "The Effect of Crankangle Resolution on Cylinder Pressure Analysis," SAE Paper No. 910041.

[12] Kuratle, R., and Marki, B., 1992, "Influencing Parameters and Error Sources During Indication on Internal Combustion Engines," SAE Paper No. 920233.
[13] Connolly, F. T., and Yagle, A. E., 1993, "Modeling and Identification of the Combustion Pressure Process in Internal Combustion Engines," Mech. Syst. Signal Process., **8**(1), pp. 1–19.
[14] Puzinauskas, P., Eves, J., and Tillman, N., 1994, "Measuring Absolute-Cylinder Pressure and Pressure Drop Across Intake Valves of Firing Engines," SAE Paper No. 941881.
[15] Randolph, A., 1994, "Cylinder-Pressure-Based Combustion Analysis in Race Engines," SAE Paper No. 942487.
[16] Burnt, M., and Emtage, A., 1996, "Evaluation of IMEP Routines and Analysis Errors," SAE Paper No. 960609.
[17] Cartwright, A., and Fleck, R., 1996, "Cylinder Pressure Analysis in High Performance Two-Stroke Engines," SAE Paper No. 962535.
[18] Neo, G. H., and Collings, N., 1997, "Pressure Data Analysis of Formula One Racing Engines," SAE Paper No. 970061.
[19] Burnt, M., and Pond, C., 1997, "Evaluation of Techniques for Absolute Cylinder Pressure Correction," SAE Paper No. 970036.
[20] Mergen, H. A., 1998, "Simplified Indicated Engine Performance Data Acquisition and Analysis Using LabVIEW," SAE Paper No. 983044.
[21] Rosseel, E., Sierens, R., and Baert, R. S. G., 1999, "Evaluating Piezo-Electric Transducer Response to Thermal Shock from In-Cylinder Pressure Data," SAE Paper No. 1999-01-0935.
[22] Gassenfeit, E. H., and Powell, J. D., 1989, "Algorithms for Air-Fuel Ratio Estimation using Internal Combustion Engine Cylinder Pressure," SAE Paper No. 890300.
[23] Randolph, A., 1994, "Cylinder-Pressure-Based Combustion Analysis in Race Engines," SAE Paper No. 942487.
[24] Tunestal, P., Wilcutts, M., Lee, A. T., and Hedrick, J. K., 1999, "In-Cylinder Measurement for Engine Cold-Start Control," *International Conference on Control Applications*, Aug. 22–27.
[25] Sellnau, M. C., Matekunas, F., Battiston, P., Chang, C., and Lancaster, D., 2000, "Cylinder Pressure Based Engine Control Using Pressure Ratio Management and Low Cost Non Intrusive Cylinder Pressure Sensor," SAE Paper No. 2000-01-0932.
[26] Tunestal, P., Wilcutts, M., Lee, A. T., and Hedrick, J. K., 2001, "A Method of lean Air-Fuel Ratio Control Using Combustion Pressure Measurement," JSAE Rev., pp. 389–393.
[27] Mladek, M., and Onder, C. H., 2000, "A Model for the Estimation of Inducted Air Mass and the Residual Gas Fraction Using Cylinder Pressure Measurements," SAE Paper No. 2000-01-0958.
[28] Schiefer, D., and Maennel, R., 2003, "Advantages of Diesel Engine Control Using In-Cylinder Pressure Information for Closed-Loop Control," SAE Paper No. 2003-01-0364.
[29] Shimasaki, Y., Suzuki, T., and Ueno, M., 2004, "Study on Engine Management System Using In-Cylinder Pressure Sensor Integrated With Spark Plug," SAE Paper No. 2004-01-0519.
[30] Hasegawa, M., Shimasaki, Y., Yamaguchi, S., Kobayashi, M., Sakamoto, H., Kitayama, N., and Kanda, T., 2006, "Study on Ignition Timing Control for Diesel Engine Using In-Cylinder Pressure Sensor," SAE Paper No. 2006-01-0180.
[31] Kumar, R., Zheng, M., Asad, U., and Reader, G. T., 2007, "Heat Release Based Adaptive Control to Improve Low Temperature Diesel Engine Combustion," SAE Paper No. 2007-01-0772.
[32] Yoon, M., Oh, B., Lee, K., and Sunwoo, M., 2007, "Cylinder Pressure Based Combustion Phasing Control of a CRDI Diesel Engine," SAE Paper No. 2007-01-0772.
[33] Husted, H. L., Kruger, D., Fattic, G., Ripley, G., and Kelly, E., 2007, "Cylinder Pressure-Based Control of Pre-Mixed Diesel Combustion," SAE Paper No. 2007-01-0773.
[34] Anastasia, C. M., and Pestana, G. W., 1987, "A Cylinder Pressure Sensor for Closed Loop Engine Control," SAE Paper No. 870288.
[35] Herden, W., and Kussel, M., 1994, "A New Combustion Pressure Sensor for Advanced Engine Management," SAE Paper No. 940379.
[36] Wolinski, T., Jarmolik, A., and Bock, W., 1999, "Development of Fiber Optic Liquid Crystal Sensor for Pressure Measurement," IEEE Trans. Instrum. Meas., **48**, 2–6.
[37] Wlodarczyk, M., 2006, "High Accuracy Glow Plug-Integrated Cylinder Pressure Sensor for Closed Loop Engine," SAE Paper No. 2006-01-0184.
[38] Brandt, H., and Gibson, F., 1985, "Dynamic Combustion Characteristic Sensor for Internal Combustion Engine," U.S. Patent No. 4,491,010.
[39] Cobb, D., 1992, "Gasket With Encased Load Sensor," U.S. Patent No. 5,121,929.
[40] Mobley, C., 1999, "Non-Intrusive In-Cylinder Pressure Measurement of Internal Combustion Engines," SAE Paper No. 1999-01-0544.
[41] Hubbard, M., Dobson, P., and Powell, D., 1976, "Closed Loop Control of Spark Advance Using a Cylinder Pressure Sensor," ASME J. Dyn. Syst., Meas., Control, pp. 414–420.
[42] Powell, D., and Glaser, I., 1981, "Optimal Closed-Loop Spark Control of an Automotive Engine," SAE Paper No. 810058.
[43] Fuji, I., 1989, "MBT Control Utilizing Crank Angle of Maximum Combustion Pressure," SAE Paper No. 890759.
[44] Liu, J. P., Kleeberg, H., Tomazic, D., Ciaravino, J., and Amer, A., 2006, "A Model for On-Line Monitoring of In-Cylinder Residual Gas Fraction (RGF) and Mass Flowrate in Gasoline Engines," SAE Paper No. 2006-01-0656.
[45] Kobayashi, N., Inoue, T., Nakanishi, K., Kato, K., and Matsuhita, S., 1985, "Development of the Toyota Lean Combustion System," SAE Paper No. 850044.
[46] Watanabe, S., Machida, K., Iijima, K., and Tomisawa, N., 1996, "A Sophisticated Engine Control System Using Combustion Pressure Detection," SAE Paper No. 960042.
[47] Jaine, T., Chamaillard, Y., Charlet, A., and Higelin, P., 2002, "High-Frequency Imep Estimation and Filtering for Torque—Based SI Engine Control," SAE Paper No. 2002-01-1276.
[48] Hamedovic, H., Raichle, F., Breuninger, J., Fischer, W., Dieterle, W., Klenk, M., and Böhme, J. F., 2005, "IMEP-Estimation and In-Cylinder Pressure Reconstruction for Multicylinder SI-Engine by Combined Processing of Engine Speed and One Cylinder Pressure," SAE Paper No. 2005-01-0053.
[49] Grunbacher, E., Kefer, P., and Del Re, L., 2005, "Estimation of the Mean Value Engine Torque Using an Extended Kalman Filter," SAE Paper No. 2005-01-0063.
[50] Ponti, F., and Cavina, N., 2003, "AFR Estimation Using In-Cylinder Pressure Frequency Analysis," to be published on the ASME Journal of Gas Turbines and Power, 2003.
[51] Lecuona, A., and Rodriguez, P. A., 1986, "Evaluation of Pressure and Crank Angle Errors From Reciprocating Engine Indicator Diagrams," SAE Paper No. 860027.
[52] Rocco, V., 1993, "Diesel Engine In-Cylinder Pressure Data Analysis Under T.D.C. Setting Error," SAE Paper No. 930595.
[53] Stas, M., 1996, "Thermodynamic determination of TDC in Piston Combustion Engines," SAE Paper No. 960610.
[54] Morishita, M., and Kushiyama, T., 1998, "An Improved Method for Determining the TDC Position in a PV-Diagram," SAE Paper No. 980625.
[55] Nilsson, Y., and Eriksson, L., 2004, "Determining Tdc Position Using Symmetry and Other Methods," SAE Paper No. 2004-01-1458.

Modeling the Performance of a Turbo-Charged Spark Ignition Natural Gas Engine With Cooled Exhaust Gas Recirculation

Hailin Li
National Research Council Canada,
1200 Montreal Road,
Ottawa, ON, K1A 0R6, Canada
e-mail: hailin.li@nrc-cnrc.gc.ca

Ghazi A. Karim
Department of Mechanical and Manufacturing Engineering,
The University of Calgary,
Calgary, AB, T2N 1N4, Canada
e-mail: karim@enme.ucalgary.ca

A variety of gaseous fuels and a wide range of cooled exhaust gas recirculation (EGR) can be used in turbo-charged spark ignition (S.I.) gas engines. This makes the experimental investigation of the knocking behavior both unwieldy and uneconomical. Accordingly, it would be attractive to develop suitable effective predictive models that can be used to improve the understanding of the roles of various design and operating parameters and achieve a more optimized turbo-charged engine operation, particularly when EGR is employed. This paper presents the simulated performance of a turbo-charged S.I. natural gas engine when employing partially cooled EGR. A two-zone predictive model developed mainly for naturally aspirated S.I. engine applications of natural gas, described and validated earlier, was extended to consider applications employing turbochargers, intake charge after-coolers, and cooled EGR. A suitably detailed kinetic scheme involving 155 reaction steps and 39 species for the oxidation of natural gas is employed to examine the pre-ignition reactions of the unburned mixtures that can lead to knock prior to being fully consumed by the propagating flame. The model predicts the onset of knock and its intensity once end gas auto-ignition occurs. The effects of turbocharging and cooled EGR on the total energy to be released through auto-ignition and its effect on the intensity of the resulting knock are considered. The consequences of changes in the effectiveness of after and EGR-coolers, lean operation and reductions in the compression ratio on engine performance parameters, especially the incidence of knock are examined. The benefits, limitations, and possible penalties of the application of fuel lean operation combined with cooled EGR are also examined and discussed.
[DOI: 10.1115/1.2835058]

Introduction

The ever increasing need for improving air quality, including reducing CO_2 emissions, and the concerns about the cost and long-term availability of fossil fuels is leading attention to alternative fuels usage, especially common gaseous fuels such as natural gas and liquefied petroleum gases. Natural gas is expected to remain widely used. It represents a potential attractive alternative to traditional liquid fuels, due mainly to its relative abundance, low cost, attractive combustion properties, and a superior knock resisting capability [1,2]. However, the operation of common spark ignition (S.I.) engines on natural gas is also associated with certain drawbacks. Notable examples of these are the reduction in brake power and torque at fully open throttle that are due mainly to the displacement of some of the air by the fuel gas and the associated reduction in volumetric efficiency because of the absence of the evaporative cooling encountered with liquid fuels applications [3–5]. The relatively lower heating value and slower flame propagation rates of natural gas-air mixture in comparison also contribute to this power loss.

To enhance the power production capacity of engines, turbochargers are widely applied, especially to heavy duty engines. Their application to natural gas fueled S.I. engines is being increasingly made. However, the onset of knock remains one of the main lingering factors limiting the boost pressure in high compression ratio turbo-charged S.I. gas engines. This is especially significant for large bore stationary gas engines that are more likely to encounter knocking and the relatively high intake mixture temperatures and densities associated with high boost pressures. Accordingly, the avoidance of the onset of knock remains one of the main concerns in turbo-charging S.I. stationary gas engines, particularly as EGR is being increasingly applied.

A variety of approaches has been developed over the years to suppress the onset of knock for both naturally aspirated and turbocharged engines. These commonly include retarding the spark timing, reducing the compression ratio, and leaning or diluting the intake mixture through the application of either excess air or cooled EGR [6,7]. The reduction in the value of the effective compression ratio, which is widely used to reduce the mechanical and thermal load of turbo-charged engines and to suppress the incidence of knock, is closely associated with some reduction in the power production capacity and efficiency. After-coolers are also widely used in turbo-charged heavy duty engine applications to cool the compressed air before entering the engine [8,9].

Turbo-charged S.I. gas engines are operated normally either on stoichiometric mixtures with the application of cooled EGR [6,7,10–12] or fuel-lean mixtures [13–15]. Both approaches can be used without producing knock. Traditional measures, such as those described earlier, offer a wide variety of options to boost knock-free engine performance but tend to make turbo-charged spark ignition engine systems, especially when employing EGR increasingly complex. The simultaneous application of a turbocharger with its own specific characteristics, an after-cooler, and somewhat cooled EGR makes it both highly unwieldy and uneconomical to examine and optimize the combined performance and especially the knocking characteristics of such engines when employing different experimental approaches and fuels. There is a

Contributed by the Internal Combustion Engine Division of ASME for publication in the JOURNAL OF ENGINEERING FOR GAS TURBINES AND POWER. Manuscript received February 2, 2007; final manuscript received December 3, 2007; published online March 28, 2008. Review conducted by Christopher J. Rutland.

need to develop suitable effective predictive models that will reduce the amount of testing and development time needed to produce effective performance. However, research into modeling the onset of knock in turbo-charged S.I. engines especially while taking into consideration varying fuel quality and EGR composition, appears to be still quite limited when compared to that of conventional naturally aspirated S.I. engines [16–18].

A two-zone quasi-dimensional model has been developed and described fully earlier, [e.g., [18–22]]. It was validated with different fuels mainly for naturally aspirated S.I. engine applications. This paper describes the extension of the model to consider its application to turbo-charged S.I. engines that include employment of an intake charge after-cooler and cooled EGR. Various turbochargers with their own specific characteristics can be considered. The relevant values of the intake temperatures and pressures are obtained using a turbo-charger model while the values of efficiencies of the turbine and compressor can be either assumed to be suitably known or may be obtained from the corresponding turbocharger characteristics. The model includes a sufficiently detailed account of the oxidation reactions of the gaseous fuel-air mixture that is essential for effective simulation and the onset of knock prediction. A kinetic reaction scheme of 155 reaction steps and 39 species was incorporated primarily for the prediction of the occurrence of auto-ignition and the knocking intensity for common gaseous fuel mixtures. The associated knock prediction model, developed earlier and described in detail elsewhere [18], was modified so as to consider the effects of turbo-charging and cooled EGR on the incidence of knock, the total energy to be released through auto-ignition and the resulting knock intensity. The effects of changes in the effectiveness of after and EGR-coolers on the intake mixture temperature and accordingly the pre-ignition reactions of the unburned mixture were also examined. Suitable extension and modification to the model are to be described included incorporating experimentally determined correlations of combustion duration values, [20] which are indicative of the mean flame propagation rates, to account for the effects of changes in the extent of EGR employed. The complex interaction of the many possible variables associated with the engine, fuel, turbo-charger, EGR and its cooling, and compressor output for increasingly lean mixture operation were examined in relation to changes in engine performance in general and the onset of knock in particular. Some guidelines, primarily when methane representing natural gas is employed for ensuring enhanced knock-free performance, are then outlined.

Modeling Turbo-Charged S.I. Engines

The common engine turbo-charger consists of a compressor coupled to an exhaust gas powered turbine mounted on a common shaft. Engine exhaust gases are directed by the turbine inlet casing onto the rotor and blades of the turbine and are subsequently discharged through a turbine outlet casing to the atmosphere. The turbine, while using part of the energy of the hot exhaust gases, drives the compressor, which compresses the intake atmospheric air and directs it into the engine induction manifold to supply the engine cylinders with fresh air of higher density than that of the ambient. Figure 1 shows a schematic representation of a typical turbo-charged S.I. engine fitted with intake charge after-cooler and controlled partially cooled EGR. The fuel, which is assumed to be natural gas, is supplied at a sufficiently high pressure to mix satisfactorily with the compressed air. The fraction of exhaust gases recirculated is assumed to be drawn from the exhaust manifold ahead of the turbine cooled and then to flow into the intake manifold without the need for an external pump. The compressed air is cooled by being passed through an "after-cooler." By-pass and pressure-relief valves are assumed to be employed to control the boost pressure level and intake temperature of the air so as to reduce the tendency to knock and control the mechanical and thermal loads [9,22].

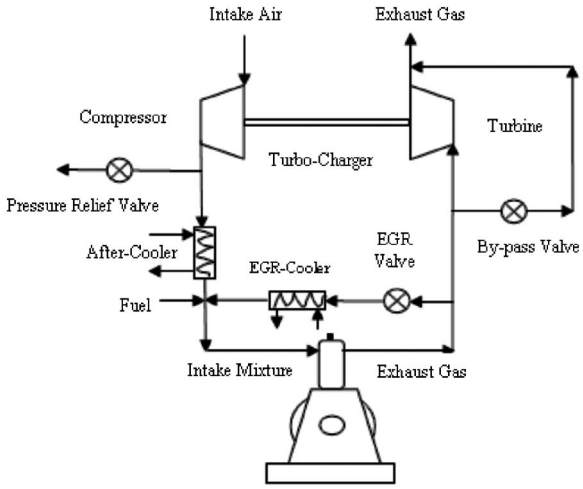

Fig. 1 Schematic diagram of the turbo-charged S.I. engines with cooled EGR being considered

Engine Modeling. A S.I. engine model that was developed earlier validated and described in more detail elsewhere [18–22] is incorporated into the present approach. The model is a two-zone quasi-dimensional simulation that predicts the performance of S.I. gas engines including the onset of knock and estimates its corresponding intensity when it occurs. The intake stroke is simulated while accounting for the presence of residual gases. The simulation of the processes throughout the whole cycle is based on the state of the mixture at the end of the intake stroke. Changes in the state of the cylinder contents are evaluated up to the time of spark ignition while accounting for heat transfer between the surrounding walls and fuel mixture and burned products [23]. Once ignition takes place, an appropriate combustion energy release pattern, based on correlations of relevant experimental data, is employed varying over the entire combustion period [20]. The composition of the burned products during and following flame propagation is calculated while accounting for thermodynamic dissociation. The product composition at the end of expansion is determined and considered to remain unchanged and represents the composition of the recirculated exhaust gas that mixes with the intake charge of fuel and air.

The onset of knock in S.I. engines is accepted to be the outcome of auto-ignition of the unburned end gas before being consumed by the propagating flame. In order to monitor the likelihood of the onset of knock, the pre-ignition reactions within the varying in state end gas region of the charge are evaluated continuously while employing sufficiently detailed description of the reaction kinetics of the corresponding part of the unburned charge. The kinetic scheme employed for the results to be shown in this contribution consisted of 155 elementary reaction steps and involved 39 chemical species, as described by Bade Shretha and Karim [18]. Such an approach has been shown to be employable successfully to predict the onset of knock of S.I. engines when operated on common gaseous fuels such as CH_4, H_2, CO, reformed gases, and some of their mixtures [18,19,24,25].

Knock Model

A knock prediction model developed and described earlier [18,19], is based on establishing whether auto-ignition is to take place or not within the end gas region during the flame propagation period and evaluates the knock intensity once auto-ignition occurs. A dimensionless knock parameter K_n is defined as the calculated, temporally varying preignition total energy released within the varying end gas mass resulting from pre-flame-front oxidation reactions per unit of the instantaneous cylinder volume. This is normalized relative to the corresponding total amount of

energy to be released through normal flame propagation per unit of cylinder swept volume. For a normally aspirated engine, the value of this knock criterion at any crank angle during flame propagation has been shown [18,19] to approximate to the following equation:

$$K_n = \frac{h_{sp} - h_t}{\Delta h_o} \frac{m_{u,t}}{m_o} (CR - 1) \quad (1)$$

where h_{sp} and h_t are the specific enthalpy of the unburned end gas at spark passage and instant time t, respectively, h_o is the effective heating value of the fresh charge, m_u is the corresponding remaining mass of the yet to be consumed end gas at the instant of time t, and m_o is the mass of the initial total fresh charge.

This dimensionless function represents also the incremental increase in the cylinder pressure due to the pre-flame oxidation reaction activity of the current instantaneous mass of the end gas relative to the mean effective combustion pressure [19]. Accordingly, the value of K_n is an integrated function of the normalized energetic consequences of any pre-flame-front oxidation energy release of the corresponding diminishing end gas. The value of K_n will increase very rapidly once auto-ignition is to take place.

For a turbo-charged spark ignition engine with the application of cooled EGR, the energy density of the intake mixture would increase approximately proportionally with the boost pressure ratio and decreases with the increased application of EGR due mainly to the combined effects of the increased charge density and displacement of some of the air-fuel mixture by the recirculated exhaust gases. Accordingly, the effects of turbo-charging and EGR application can be incorporated in a modified form of the knock criterion of Eq. (1) as follows:

$$K_n = \frac{h_{sp} - h_t}{\Delta h_o} \frac{m_u}{m_o} (CR - 1) PR(1 - R_{EGR}) \quad (2)$$

where PR is the absolute boost pressure ratio and R_{EGR} is the EGR ratio, which is defined as the molar fraction of the recirculated exhaust gases in the intake mixture:

$$R_{EGR} = \frac{\dot{N}_{EGR}}{\dot{N}_a + \dot{N}_f + \dot{N}_{EGR}} \quad (3)$$

Where: $\dot{N}_a$, $\dot{N}_f$, and $\dot{N}_{EGR}$ represent the molar flow rate of the air, fuel, and exhaust gas recirculated, respectively.

In an engine cycle calculation, key variables at any instant during the cycle, such as composition, pressure, and temperature values for the assumed two segments of the cylinder charge are calculated together with the corresponding value of K_n. For a naturally aspirated S.I. cooperative fuel research (CFR) engine, the model with experimental verification showed that the onset of borderline knock was encountered when the value of the product of criterion K_n just exceeded a value of (1.0–1.5) [19]. This is merely a reflection of the diminishing fractional mass of the end gas and cumulative pre-ignition energy release at the onset of knock amplified by the value of the compression ratio. In the present investigation, significant S.I. engine knock was considered to occur once the predicted K_n value exceeded 1.5 as defined according to Eq. (2), while for naturally aspirated S.I. engines without EGR, Eq. (2) reduces to the form of Eq. (1).

Turbo-Charger Model

In order to predict the performance of a turbo-charged S.I. engine, the temperatures and pressures of the intake and exhaust gases must be evaluated. Using a relatively simple thermodynamic model, the power generated by the turbine ($\dot{W}_t$) and that needed to drive the compressor ($\dot{W}_c$) are calculated according to Eqs. (4) and (5), respectively:

$$\dot{W}_c = \dot{N}_c \overline{C_{p,a}} T_o [(P_c/P_o)^{K_a - 1/K_a} - 1] / \eta_c \quad (4)$$

$$\dot{W}_t = \dot{N}_t \overline{C_{P,e}} T_e [1 - (P_o/P_e)^{K_e - 1/K_e}] \eta_t \quad (5)$$

where η_c and η_t are the relevant compressor and turbine efficiencies, respectively.

The compressor and turbine are linked through Eq. (6) to achieve their power equilibrium:

$$\dot{W}_c = \dot{W}_t \times \eta_{mech} \quad (6)$$

where η_{mech} is the overall mechanical efficiency of the turbocharger.

From Eqs. (4)–(6), the outlet back pressure of the engine (P_e), which is assumed also to be the inlet pressure to the turbine, and the exit boost pressure of the compressor (P_c) can be linked through Eq. (7):

$$P_e = P_o \left[1 - \frac{\dot{N}_c \overline{C_{pa}} T_o \left[\left(\frac{P_c}{P_o} \right)^{K_a - 1/K_a} - 1 \right]}{\dot{N}_t \overline{C_{Pe}} T_e \eta_c \eta_t \eta_{mech}} \right]^{K_e/1 - K_e} \quad (7)$$

The exit temperature from the compressor (T_c) can be calculated according to Eq. (8):

$$T_c = T_o \left[1 + \left(\left(\frac{P_c}{P_o} \right)^{K_a - 1/K_a} - 1 \right) \Big/ \eta_c \right] \quad (8)$$

For a given operating condition the boost pressure (P_c), the back pressure of the engine (P_e), inlet temperature of the of the turbine (T_e), and the exit temperature of the compressor (T_c) can be calculated. Accounting for any further losses and deviation from this simple approach can be made when necessary.

Mainly to illustrate the utility of this relatively simple modeling approach, the values of η_c and η_t may be assumed to be known constants for the specific operating conditions or alternatively obtained from the characteristic performance maps for the turbocharger turbine and compressor. As an illustrative example, it is assumed for simplicity that both η_c and η_t have a typical constant value of 0.70 [9,26]. However, it is clearly evident that more appropriate varying values of the efficiency need to be obtained for a better simulation of the performance of a specific engine under a set of operating conditions.

EGR Model

The recirculation of cooled exhaust gases slows down both the oxidation reaction of the unburned fuel-air-diluents mixture and the flame propagation rates, due mainly to the diluting effect. Accordingly, the effect of changes in the relative mass of EGR and the effectiveness of its cooling on the combustion rate needs to be examined. Of particular importance is its resulting effect on the temperature and mass of the unburned mixture, which controls the oxidation reaction rate and the tendency to knock. The changes to the mean flame propagation rate can be evaluated through establishing the corresponding changes to the combustion periods, obtained by processing the pressure-time data as described earlier [20]. For the present type of modeling application, changes in the value of the combustion duration with the EGR ratio were established indirectly through examining experimentally the corresponding variation in the combustion duration with the addition of individual diluents to the intake mixture. The relative volumetric amount of diluents added to the intake mixture can be evaluated through a diluents ratio ($R_{diluents}$), defined as:

$$R_{diluents} = \frac{\dot{N}_{diluents}}{\dot{N}_a + \dot{N}_f + \dot{N}_{diluents}} \quad (9)$$

As shown in Fig. 2, the variation in the value of the combustion duration with increasing the amount of diluents added shows similar trends for the three different common diluents considered. The addition of CO_2 to the intake mixture as expected, prolonged the combustion duration more in comparison to that of H_2O or N_2.

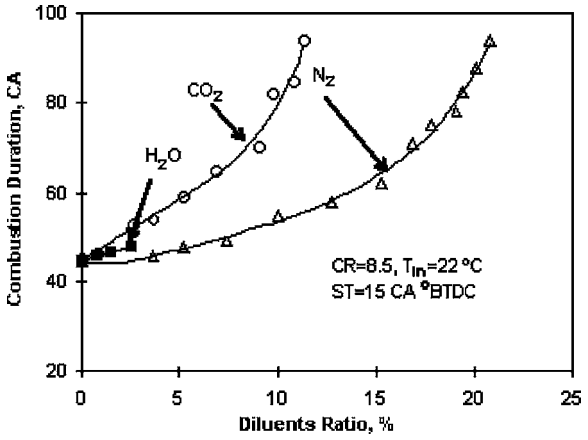

Fig. 2 Experimentally observed variations in the combustion duration in degrees with the amount of CO_2, H_2O and N_2 added to the stoichiometric mixture of CH_4, fully open throttle un-turbo-charged engine

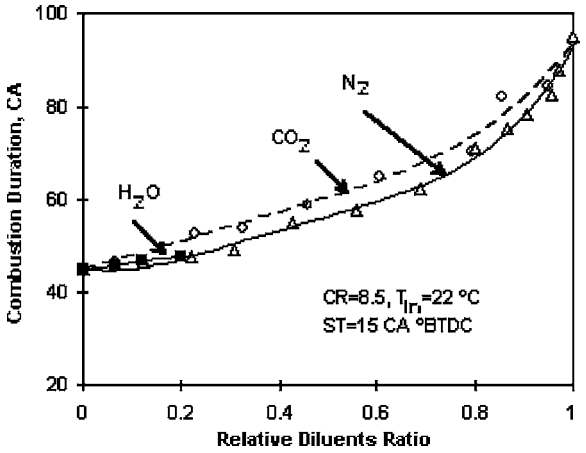

Fig. 3 Experimentally observed variations of combustion duration in degrees with changes in relative diluents ratio of CO_2, H_2O, and N_2 for stoichiometric mixture of CH_4 for fully open throttle un-turbo-charged engine

It is also shown that there exists for any set of operating engine conditions a diluents concentration limit beyond which stable engine operation cannot be maintained with the occurrence of occasional misfire [25]. Such a value may be defined in terms of the maximum diluents ratio that can be tolerated. Our experimentally determined maximum diluents ratios of CO_2 and N_2 were 11.36% and 20.12% by volume, respectively, for stoichiometric operation with CH_4. However, it was inconvenient to determine experimentally the corresponding maximum H_2O vapor ratio due to the limited maximum humidity of the intake mixture. The effect of H_2O addition on the flame propagation rates of CH_4 lies somewhere between those of N_2 and CO_2. Also, the corresponding variation in the values of the combustion duration with relative diluents ratio appears to follow a similar trend. In order to estimate the corresponding value of $R_{H_2O,max}$, it was assumed that its value relative to those of N_2 and CO_2 additives is of similar relationship to the corresponding values found to render a stoichiometric mixture of CH_4 just nonflammable [24]. On this basis, the corresponding estimated value for $R_{H_2O,max}$ becomes 15.4% under the same specific operating conditions considered.

Since the variation in the combustion duration with the addition of the different diluents appears to follow a similar trend, it can be assumed that the variation in the combustion duration with the diluents additions follows approximately a similar trend when considered on the bases of a relative diluents ratio $R_{R_{diluents}}$, which is defined as the diluents ratio relative to its corresponding maximum value [Eq. (10)]. As shown in Fig. 3, the variation of the combustion duration with the relative diluents ratio follows approximately a similar trend for the different diluents examined:

$$R_{R_{diluents}} = \frac{R_{diluents}}{R_{diluents,max}} \tag{10}$$

On this basis, the combustion duration when cooled EGR is applied can be assumed also to correlate approximately with a corresponding relative EGR ratio ($R_{R_{EGR}}$) defined as:

$$R_{R_{EGR}} = \frac{R_{EGR}}{R_{EGR,max}} \tag{11}$$

Since the recirculated exhaust gases are mainly mixtures of the diluents N_2, CO_2, and H_2O, the maximum EGR ratio ($R_{EGR,max}$) when operated at a stoichiometric ratio can be estimated approximately through the corresponding relative contribution of its components, i.e.:

$$R_{EGR,max} = y_{1,e}R_{1,max} + y_{2,e}R_{2,max} + \cdots + y_nR_{n,,max} + \cdots \tag{12}$$

where $y_{i,e}$ is the molar fraction of the diluent component i in the recirculated exhaust gas and $R_{i,max}$ is the maximum diluent ratio tolerated when adding the i, diluent on its own.

The effectiveness of the EGR-cooler and compressor after-cooler when fitted may be defined as:

$$\xi_{cooler} = \frac{T_{c,in} - T_{c,out}}{T_{c,in} - T_{coolant}} \tag{13}$$

where $T_{coolant}$ is the coolant temperature; $T_{c,in}$ and $T_{c,out}$ are the inlet and exit temperatures of the cooled fluid, respectively.

The exit temperature from a cooler can then be estimated as:

$$T_{c,out} = T_{c,in} - \xi_{cooler}(T_{c,in} - T_{coolant}) \tag{14}$$

Simulation Results and Discussion

The model described has been validated against experimental results obtained over a wide range of operating conditions, such as different intake pressures, temperatures, and fuels [18–22,24,25,27,28] for naturally aspirated S.I. engines. In the present contribution, it was extended to indicate the effects of turbo-charging, after-cooling, cooled-EGR, and lean operation on the performance of a typical turbo-charged S.I. natural gas engine. As an example, Fig. 4 shows the effects of increasing the boost pressure ratio through the application of turbo-charging on the limits for knock-free operation for different supply temperatures. As expected, the predicted knock criterion value K_n of Eq. (2) increases rapidly with the boost pressure ratio reflecting the significant effect of turbo-charging on the increased incidence of knock and its intensity, as indicated by the K_n value calculated. This is due mainly to the increased charge temperature and its mass following compression of the fresh fuel-air. The effect of the intake ambient temperature on the knock limit is also demonstrated. A sufficient lowering of the boost pressure ratio is needed to maintain knock-free operation when the supply atmospheric temperature is made relatively higher.

The application of an intake charge after-cooler should lower the temperature of the hot compressed air exiting the compressor and proceeding into the engine cylinder. An example of its effect in reducing the tendency to knock is shown in Fig. 5. An improved cooling effectiveness of the hot compressed air permits a relatively higher boost pressure ratio to be applied without encountering knock. Higher after-cooler effectiveness is needed to permit a greater increase in boost pressure.

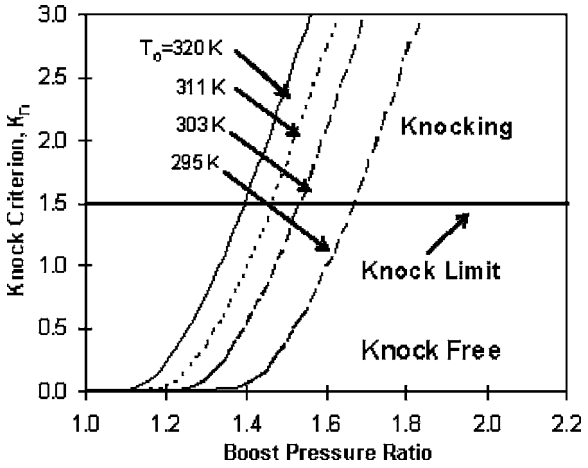

Fig. 4 Variations of the predicted knock criterion with changes in boost pressure ratio for different atmospheric temperature, fuel: CH_4, CR=8.5, ER=1.0, ST=15°CA BTDC, no EGR, fully open throttle

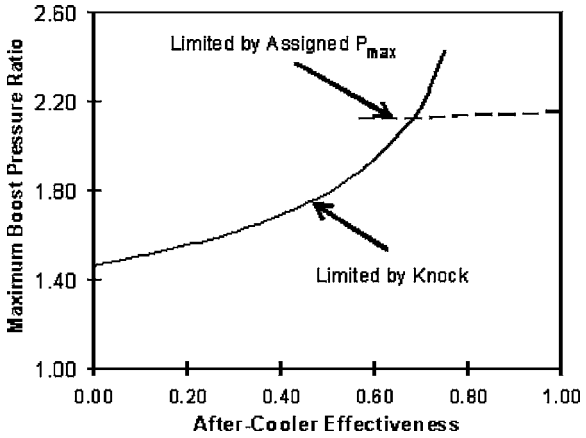

Fig. 6 The maximum boost pressure ratio permissible for stoichiometric operation with changes in after-cooler effectiveness, fuel: CH_4, T_o=311 K, CR=8.5, ST=15°CA BTDC, ER=1.0, K_n=1.50, assigned max. peak cylinder pressure (MPCP) =70 atm, no EGR, fully open throttle

The application of turbo-charging increases the density of the intake mixture and correspondingly the peak cylinder pressure. In practice, the extent of increase in boost pressure applied may become also limited by the value of the maximum peak cylinder pressure permitted even when no knock is encountered. As an illustrative example, the maximum peak cylinder pressure was assumed to have been limited to 70 bar. Fig. 6 shows the maximum boost pressure ratio for knock-free stoichiometric operation when the after-cooler effectiveness is changed. It can be seen that for low values of after-cooler effectiveness, the onset of knock for this case would be the limiting factor, reflecting the significant effect of insufficiently lowering the intake mixture temperature on the tendency to knock. With increasing the after-cooler effectiveness, the tendency to knock is reduced but the assigned maximum boost pressure ratio will be limited through reaching the permitted maximum cylinder pressure. Similarly, Fig. 7 shows the corresponding variation in the value of the maximum usable boost pressure ratio with changes in the value of the after-cooler effectiveness for a range of ambient air temperatures. Consequently, the corresponding knock-free indicated power output, as shown in Fig. 8, displays a significant increase as the compressed air is cooled more effectively.

A lowering of the effective compression ratio of the engine is often employed for turbo-charged engines mainly to reduce the mechanical and thermal loads, especially with high boost pressure, to reduce peak cylinder pressures, and to avoid the onset of knock. Figures 9 and 10 demonstrate the effects of lowering the compression ratio on the predicted knock-free maximum boost pressure ratio and the corresponding indicated power output with changes in the after-cooler effectiveness. A combined lowering of the compression ratio with increasing the effectiveness of cooling the compressed intake charge permits significant increases in the maximum boost pressure ratio and produces higher indicated power output. This is mainly a reflection of the significant influence of changes in the compression ratio and charge mean temperature on the onset of knock and its intensity once it occurs. Also, the effect of changes in the value of the after-cooler effectiveness on the relative maximum boost pressure permissible tends to be relatively weak when higher compression ratios are employed. However, it should be noted that usually high after-cooler effectiveness cannot be achieved readily for small temperature differences between the compressed air and coolant. Hence, a

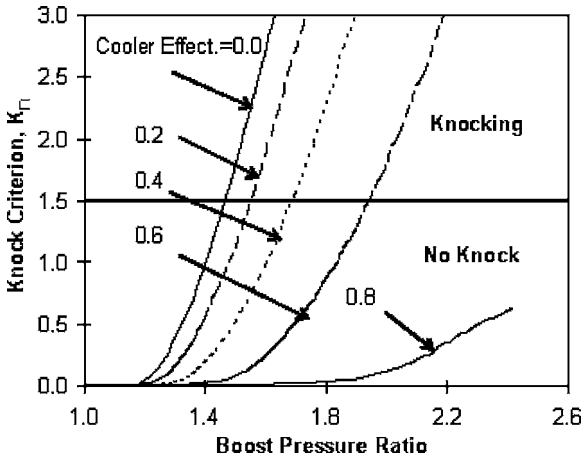

Fig. 5 Variations of the predicted knock criterion with changes in boost pressure ratio for different after-cooler effectiveness, fuel: CH_4, ER=1.0, T_o=311 K, CR=8.5, ST=15°CA BTDC, no EGR, fully open throttle

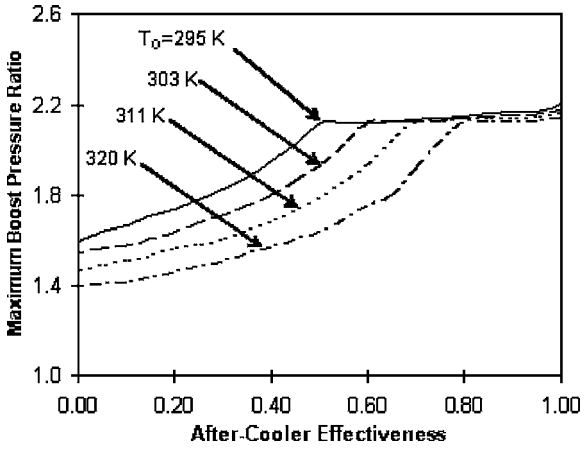

Fig. 7 Variations of the predicted maximum boost pressure ratios with changes in after-cooler effectiveness for different atmospheric temperature, fuel: CH_4, CR=8.5, ER=1.0, ST =15°CA BTDC, K_n=1.5, assigned MPCP=70 atm, no EGR, fully open throttle

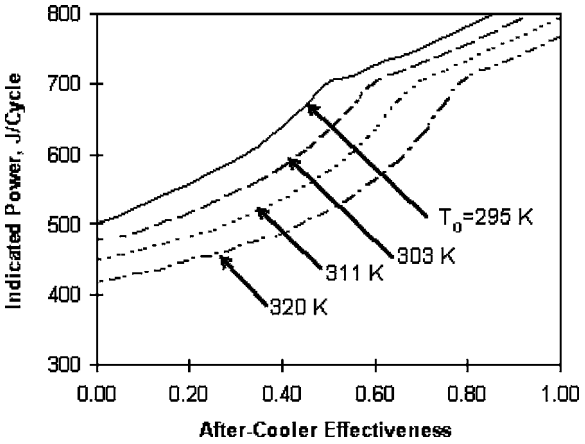

Fig. 8 Variations of the predicted maximum indicated power output with changes in after-cooler effectiveness for different atmospheric temperatures, fuel: CH_4, CR=8.5, ER=1.0, ST =15°CA BTDC, K_n=1.5, assigned MPCP=70 atm, fully open throttle

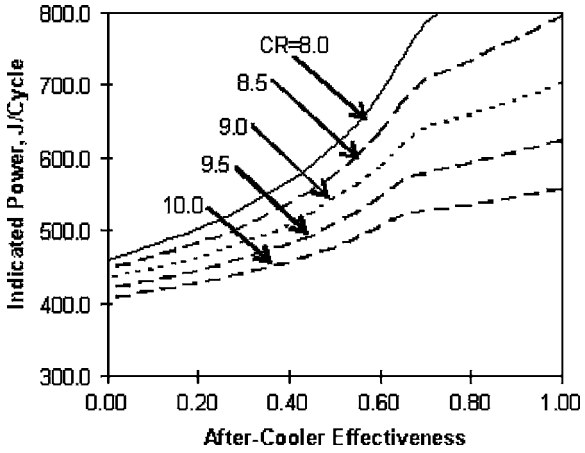

Fig. 10 Variations of the predicted maximum indicated power with changes in after-cooler effectiveness for different compression ratios, fuel: CH_4, T_o=311 K, ER=1.0, ST=15°CA BTDC, K_n=1.5, assigned MPCP=70 atm, fully open throttle

relatively conservative typical value of 0.5 was employed as the effectiveness of the after-cooler in further results displayed, unless otherwise specified.

The employment of cooled EGR has been demonstrated experimentally in addition to reducing NO_x emissions reduces the tendency to knock [6,7,25]. Figure 11 shows the diverse effect on the tendency to knock represented by the corresponding calculated value of the knock criterion of Eq. (2), when the recirculated exhaust gas was cooled to different levels of effectiveness. It is noted that the application of EGR, if it is not well cooled, can increase the tendency to knock. This is a reflection of the significant effect on the onset of knock of the increase in intake mixture temperature resulting from the recirculation of insufficiently cooled exhaust gases (i.e., with a low EGR-cooler effectiveness) despite some increased presence of diluents. It can be observed that for a cooling effectiveness of around 0.4, the value of the knock intensity is approximately constant because of the combined effects of the simultaneous increase in the mass of diluents and the resulting rise in intake mixture temperature. As shown in Fig. 11, a further improvement in the EGR-cooler effectiveness can reduce the value of the predicted knock criterion considerably. Such a desirable effect is further demonstrated in Fig. 12, where the value of the knock criterion is reduced as the EGR-cooler effectiveness is improved permitting higher boost pressure and power output. Operation in the absence of any EGR appears to produce comparable values for the knock criterion as those with a cooling effectiveness of 0.4 when 8% EGR is employed for the specific operating condition shown.

Figures 13 and 14 show an example of the combined effects of increasing EGR ratio and enhancing EGR-cooler effectiveness on the knock-limited boost pressure ratios and associated power output. It can be seen that for the specific conditions shown, EGR is positively effective only for values of cooler effectiveness higher than 0.40 for the knock-limited boost pressure ratio and 0.62 for knock-free power output, respectively. This is due mainly to the reduced energy density resulting from the displacement of the air-fuel mixture by the recirculated exhaust gases. Moreover, as shown in Fig. 15, the indicated power production efficiency deteriorates with increasing the EGR ratio but with a negligible effect due to changes in the EGR-cooler effectiveness. As the EGR ratio is increased, the lowered bulk temperature resulting from the corresponding slowing down of combustion produces prolonged combustion durations combined with a reduction in the energy density. Also, keeping the spark timing constant in these examples rather than employing optimized timing values also contributes to the deterioration in the power production efficiency.

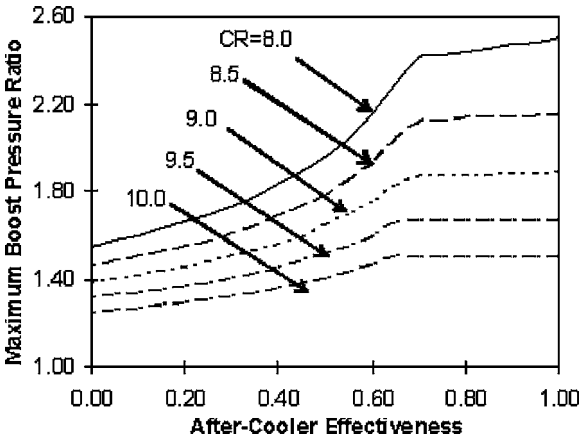

Fig. 9 Variations of the predicted maximum boost pressure ratio with changes in after-cooler effectiveness for different compression ratios, fuel: CH_4, T_o=311 K, ER=1.0, ST=15°CA BTDC, K_n=1.5, assigned MPCP=70 atm, fully open throttle

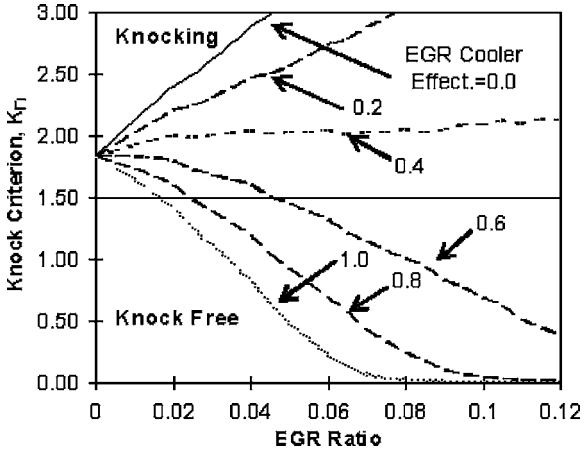

Fig. 11 Variations of the predicted knock criterion with changes in EGR ratios for different EGR-cooler effectiveness, fuel: CH_4, boost pressure ratio=1.85 CR=8.5, ST=15°CA BTDC, T_o=311 K, *ER*=1.0, fully open throttle

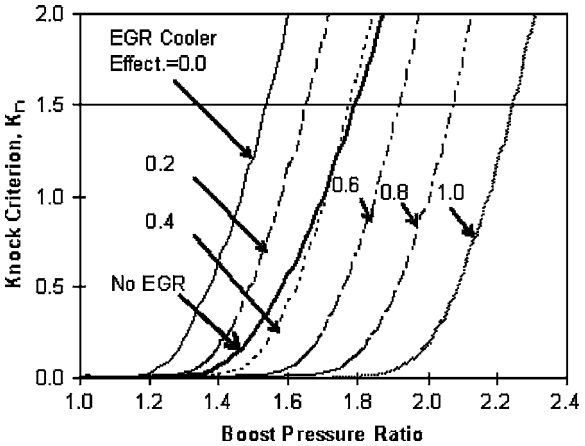

Fig. 12 Variations of the predicted knock criterion with changes in boost pressure ratios for different EGR-cooler effectiveness, EGR rate=8.0%, T_o=311 K, CR=8.5, ST=15°CA BTDC, after-cooler effectiveness=0.5, fuel: CH_4, ER=1.0. The predicted knock criterion without EGR is also plotted for comparison, fully open throttle.

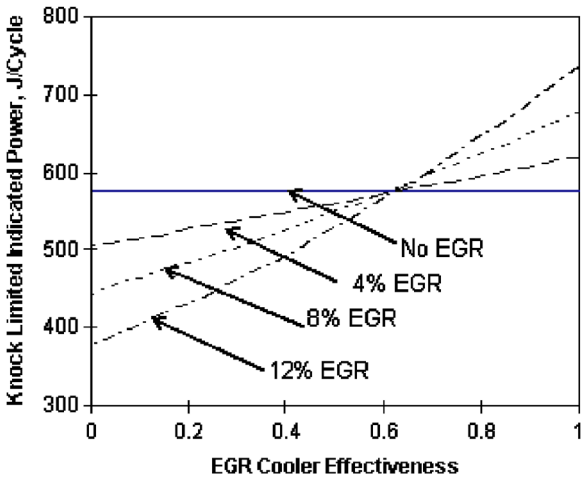

Fig. 14 Variations of the predicted knock-limited maximum indicated power production with increasing EGR cooler effectiveness for different EGR-ratio, fuel: CH_4, ER=1.0, CR=8.5, T_o=311 K, ST=15°CA BTDC, after-cooler effectiveness=0.5, K_n=1.5, assigned MPCP=70 atm, fully open throttle.

The onset of knock could be avoided also through leaning the operating mixture. Figure 16 shows the significant effect of the boost pressure ratio on the knock-limited equivalence ratio for the typical compression ratios of 8.5 and 10.0. As expected, the onset of knock is encountered with a lower boost pressure ratio when using a higher compression ratio. Leaner operation than stoichiometric is required to avoid knock when the boost pressure ratio increases beyond 1.40 and 1.78 for the compression ratios of 10.0 and 8.5, respectively. Figure 17 shows the corresponding indicated power output for these knock-limited equivalence ratios shown in Fig. 16. Relatively higher indicated power output can be achieved with higher compression ratios at stoichiometric mixture conditions, provided knock is not encountered. However, as shown in Fig. 17, for a stoichiometric mixture, operation with a higher compression ratio limits very significantly the boost pressure ratio that can be used due to the onset of knock requiring the mixture to be sufficiently leaned and limiting the maximum indicated power output produced. When lean operation is employed to avoid the onset of knock, increasing the boost pressure ratio further, while not enhancing the indicated power output, the corresponding indicated power production efficiency would increase rapidly, as shown in Fig. 18, which demonstrates the desirable aspects of lean mixture operation.

The benefits and limitations of suppressing the onset of knock through the combined lean mixtures operation and the application of cooled EGR maybe also examined. Figure 19 shows for lean mixture operation, the amount of cooled exhaust gas needed to be recirculated under the specific operating conditions described. As an example, for a boost pressure ratio of 1.75, the onset of knock could be suppressed through leaning the intake mixture down to an equivalence ratio value of 0.71 or recirculating of 9.3% cooled exhaust gases. These approaches produced the predicted engine power output and efficiency shown in Figs. 20 and 21, respectively.

The application of cooled EGR may permit a turbo-charged S.I. engine to run on a stoichiometric mixture to enhance significantly the power production capability but without the benefits of the improvements to the power production efficiency associated with lean mixture operation. Moreover, boosting the intake mixture

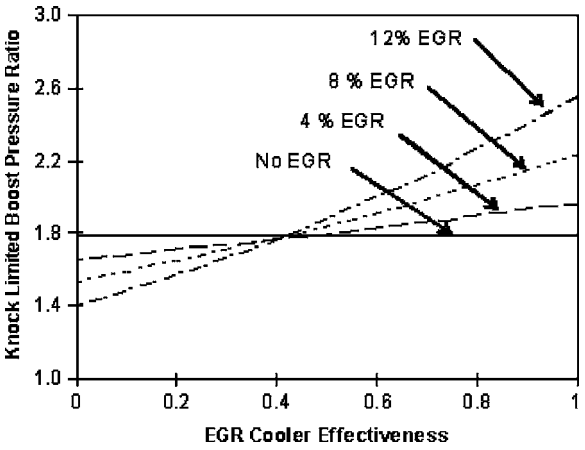

Fig. 13 Comparison in variations of the predicted knock-limited boost pressure ratio with changes in EGR-cooler effectiveness for different EGR ratios, fuel: CH_4, ER=1.0, CR=8.5, T_o=311 K, ST=15°CA BTDC, after-cooler effectiveness=0.5, K_n=1.5, assigned MPCP=70 atm, fully open throttle.

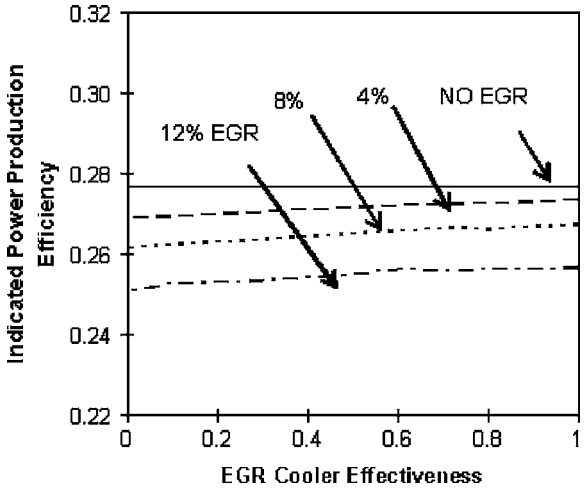

Fig. 15 Variations of the predicted indicated power production efficiency with changes in EGR-cooler effectiveness for different EGR ratios, fuel: CH_4, ER=1.0, CR=8.5, T_o=311 K, ST=15°CA BTDC, after-cooler effectiveness=0.5, K_n=1.5, assigned MPCP=70 atm, fully open throttle.

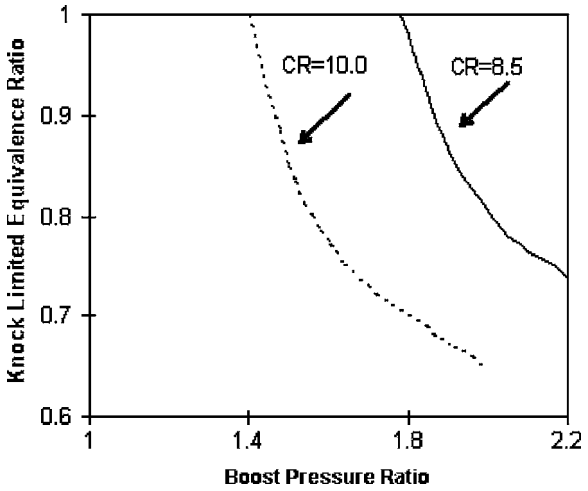

Fig. 16 Variation of the predicted knock-limited equivalence ratios with changes in boost pressure ratio for compression ratios of 8.5 and 10.0, Fuel: CH_4, T_o=311 K, ST=15°CA BTDC, after-cooler effectiveness=0.5, K_n=1.5, no EGR, fully open throttle

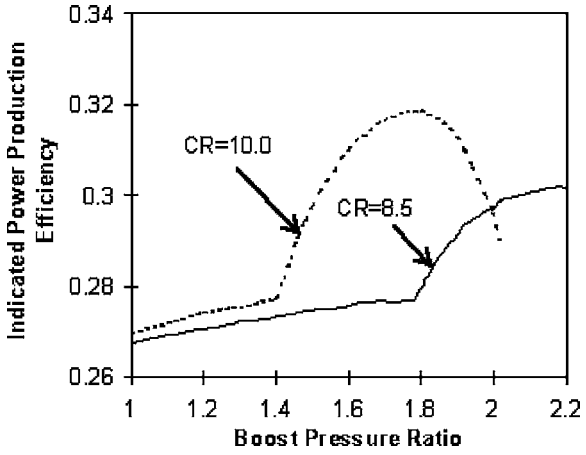

Fig. 18 Variations of the predicted indicated power production efficiency with boost pressure ratio when the equivalence ratios shown in Fig. 16 are applied, fuel: CH_4, T_o=311 K, ST =15°CA BTDC, after-cooler effectiveness=0.5, K_n=1.5, no EGR, fully open throttle

pressure further does not necessarily enhance the power output when lean operation is employed for suppressing the onset of knock. When considering these benefits and limitations of the application of lean operation and cooled EGR, it may be attractive to operate a turbo-charged S.I. engine with lean mixtures combined with effectively cooled EGR so as to optimize performance. Also, the value of the spark timing employed, which was not optimized in the present investigation is expected to affect both power production and its efficiency. This would have required a very considerable further extension and increase in the magnitude of the calculations needed.

Merely to demonstrate the utility of the model described and its application to turbo-charged S.I. gas engines with cooled EGR, the results presented here, though, relate primarily to a specific set of assumed values of the key operating and design parameters, they do show the trends involved. Alternative acceptable values could have been equally obtained for different sizes, speeds and engine designs to provide similarly corresponding performance data.

Conclusions

The two-zone quasi-dimensional model developed and validated earlier mainly for naturally aspirated S.I. engine application to consider engine performance and the incidence of knock, has been extended to consider the incorporation of a turbo-charger and the application of EGR. The requirement for effective intake charge and EGR cooling to obtain improved engine performance could be predicted. Based on the simulation results examined, the following conclusions can be drawn:

- The application of hot EGR could enhance the tendency to knock significantly. The desirable properties of EGR for reducing the tendency to knock and enhancing somewhat the power production could be achieved only when the recirculated exhaust gas is cooled sufficiently.
- For the specific conditions examined, EGR is positively effective for increasing the knock limited boost pressure ratio when the EGR cooler effectiveness values were higher than

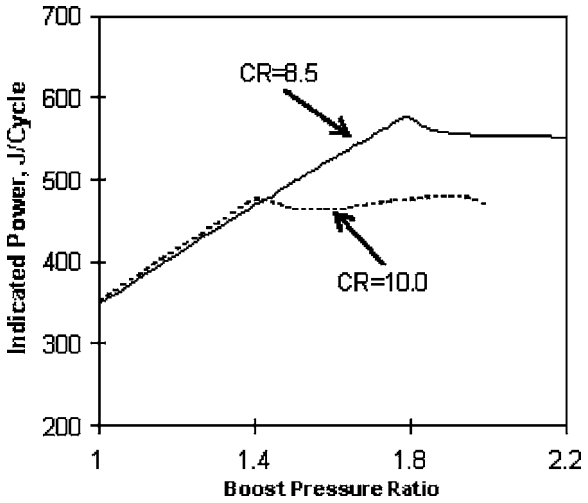

Fig. 17 Variations of the predicted indicated power output with boost pressure ratios when the knock-limited equivalence ratios shown in Fig. 16 are applied, fuel: CH_4, T_o=311 K, ST =15°CA BTDC, after-cooler effectiveness=0.5, K_n=1.5, no EGR, fully open throttle

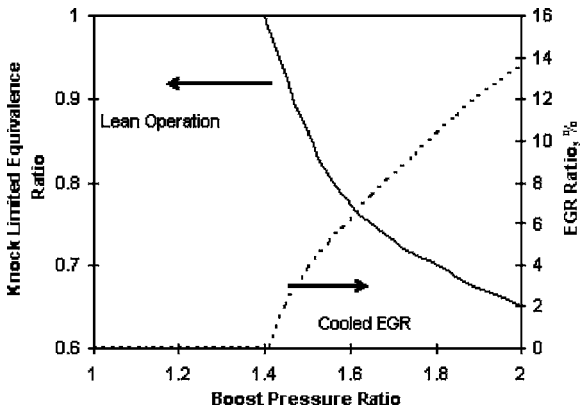

Fig. 19 The suppression of the onset of knock through lean operation or cooled EGR only. There is no EGR for lean operation. Equivalence ratio is kept at 1.0 when cooled EGR is applied. CR=10, ST=15°CA BTDC, T_o=311 K, after-cooler effectiveness=0.5, EGR-cooler effectiveness=0.9, fully open throttle.

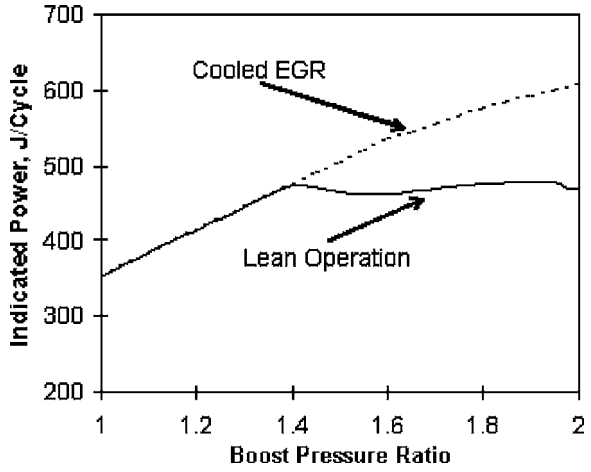

Fig. 20 The comparison of the indicated power production when knock is suppressed through lean operation and the application of cooled EGR, CR=10, ST=15°CA BTDC, T_o=311 K, after-cooler effectiveness=0.5, EGR-cooler effectiveness=0.9, fully open throttle

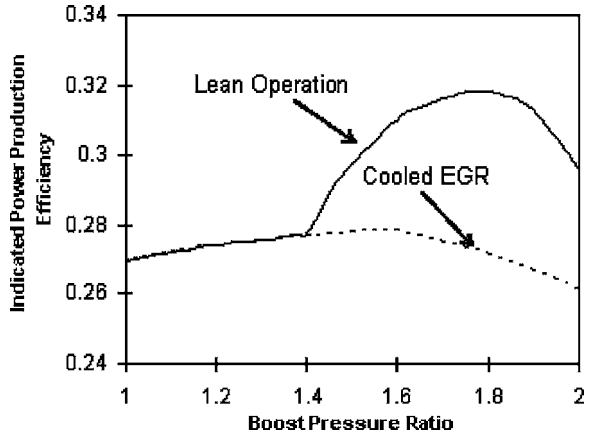

Fig. 21 The comparison of the indicated power production efficiency when knock is suppressed through lean operation and the application of cooled EGR, CR=10, ST=15°CA BTDC, T_o =311 K, after-cooler effectiveness=0.5, EGR-cooler effectiveness=0.9, fully open throttle

0.40. In comparison, for increasing the knock-free power output, an EGR-cooler effectiveness higher than 0.62 is needed.

- To suppress the onset of knock though leaning the mixture, boosting the intake pressure further would not necessarily enhance the indicated power. However, higher power production efficiency may be achieved when this strategy is adopted.
- Suitably lowering the compression ratio, though may lower to some extent the power production efficiency, is effective in enhancing the knock-limited boost pressure ratio, reducing the peak cylinder pressure and correspondingly enhancing the power production capability.

Acknowledgment

The financial support of the Canadian Natural Science and Engineering Research Council (NSERC) is gratefully acknowledged.

Nomenclature

atm = atmosphere, 100 kPa
BTDC = before top-dead center
EGR = Exhaust gas recirculation
ER = equivalence ratio
CR = compression ratio
MPCP = maximum peak cylinder pressure
SI = spark ignition
ST = spark timing
$\bar{C}_{p,a}$ = molar averaged specific heat at constant pressure of the fresh air
$\bar{C}_{p,e}$ = molar averaged specific heat at constant pressure of the exhaust gases
h_{sp} = specific enthalpy of the unburned end gas at spark passage.
h_t = specific enthalpy of the unburned end gas at instant time t
Δh_o = effective heating value of the fresh charge,
K_a = specific heat ratio of the air
K_e = specific heat ratio of the exhaust gases in gas turbine
m_u = remaining mass of the end gas at the instant time t
m_o = mass of the initial fresh charge
$\dot{N}_a$ = molar flow rate of intake air
$\dot{N}_c$ = molar flow rate into the compressor
$\dot{N}_t$ = molar flow rate into the turbine
$\dot{N}_{\mathrm{EGR}}$ = molar flow rate of the recirculated exhaust gases
$\dot{N}_f$ = molar flow rate of intake fuel
P_c = exit pressure of the compressor
P_e = inlet pressure of the turbine
$R_{i,\max}$ = maximum diluents ratio tolerated when adding i diluent to the stoichiometric mixture
$R_{\mathrm{diluents,max}}$ = maximum diluents ratio tolerated in the intake mixture
T_c = exit temperature of the compressor
T_o = inlet temperature of the compressor
T_e = inlet temperature of turbine
T_{coolant} = coolant temperature
$T_{c,\mathrm{in}}$ = inlet temperature of the cooler
$T_{c,\mathrm{out}}$ = exit temperature of the cooler
$\dot{W}_c$ = power needed to drive the compressor
$\dot{W}_t$ = output power of gas turbine
$y_{i,e}$ = molar fraction of diluents component i in the recirculated exhaust gas
η_c = isentropic efficiencies of compressor
η_t = isentropic efficiencies of gas turbine
η_{mech} = The mechanical efficiency of the turbo-charger
ξ_{cooler} = effectiveness of the cooler

References

[1] Weaver, C. S., 1989, "Natural Gas Vehicle-A Review of the State of Art," SAE Paper 892133.
[2] Keith, O., and Coley, T., 1995, *Automotive Fuels Reference Book*, 2nd ed., Society of Automotive Engineers, Inc., Warrendale, PA.
[3] Tennant, C. J., Atkinson, R. J., Traver, M. L., Atkinson, C. M., and Clark, N. N., 1994, "Turbocharging a Bi-Fuel Engine for Performance Equivalent to Gasoline," SAE Paper 942003.
[4] Hyun, C. C., Bok, L. H., Lee, M. C., and Jung, Y. K., 1993, "Development Work on HMC'S Natural Gas-Fueled 1.5 L MPI DOHC Engine," SAE Paper 931869.
[5] Ishii, M., Ishizawa, S., Inada, E., Idoguchi, R., and Sekiba, T., 1994, "Experimental Studies on a Natural Gas Vehicles," SAE Paper 942005.
[6] Grandin, B., Ångströmet, H. E., and Olofsson, E., 1998, "Replacing Fuel Enrichment in a Turbo-Charged S. I. Engine: Lean Burn or Cooled EGR," SAE Paper 982476.
[7] Grandin, B., and Ångströmet, H. E., 1999, "Knock Suppression in Turbo-Charged S. I. Engine by Using Cooled EGR," SAE Paper 1999-01-3505.
[8] Filipi, Z., Petrovic, S., and Popovic, M., 1989, "Development and Experimental Study of a 1.1 L Turbocharged Inter-Cooled Carburetor Engine," SAE Paper 890458.

[9] Watson, N., and Janota, M. S., 1982, *Turbo-Charging the Internal Combustion Engine*, John Wiley and Sons, New York.
[10] Zhang, F., Okamoto, K., Morimoto, S., and Shoji, F., 1999, "Improving Performance and Reliability of Natural Gas Engines for Power Generation-A Concept of Realizing Lower Temperature and High Pressure Combustion," SAE Paper 1999-01-3511.
[11] Zhang, F., Okamoto, K, Shimogata, S., and Shoji, F., 1998, "Methods of Increasing the BMEP (Power Output) for Natural Gas Spark Ignition Engines," SAE Paper 981385.
[12] Nellen, C., and Boulouchos, K., 2000, "Natural Gas Engines for Cogeneration: Highest Efficiency and Near-Zero-Emissions Through Turbocharging, EGR and 3-Way Catalytic Converter," SAE Paper 2000-01-2825.
[13] Clarke, D. P., Such, C. H., Overington, M. T., and Das, P. K., 1992, "A Lean Burn Turbocharged, Natural Gas Engine for the US Medium Duty Automotive Market," SAE Paper 921552.
[14] Glordano, D. D., and Petersen, P. W., 1995, "A Turbo-Charged Lean-Burn 4.3 Litre Natural Gas Engine," SAE Paper 951939.
[15] Umierskin, M., Körfern, T., and Stommeln, P., 1999, "Low Emission and Fuel Consumption Natural Gas Engines With High Power Density for Stationary and Heavy-Duty Application," SAE Paper 1999-01-2896.
[16] Filipi, Z., and Assanis, D. N., 1991, "Quasi-Dimensional Computer Simulation of the Turbo-Charged Spark Ignition Engine and Its Use for 2-Valve and 4-Valve Engine Matching Studies," SAE Paper 910075.
[17] Kusaka, J., Daisho, Y., Ikeda, A., and Saito, H., 1998, "Predicting Engine Performance, NOx Emission and Knock Phenomena in a Spark Ignited Natural Gas Engine," Proceeding of the 22nd CIMAC International Congress on Combustion Engines, Copenhagen, May 18–21, pp. 1283–1298.
[18] Bade Shrestha, S. O., and Karim, G. A., 1999, "A Predictive Model for Gas Fuelled Spark Ignition Engine Applications," SAE Paper 1999-01-3482.
[19] Karim, G. A., 2004, "A Dimensionless Criterion for Predicting the Onset of Knock in Spark Ignition Engine," SAE Paper 2004-01-1992.
[20] Bade Shrestha, S. O., and Karim, G. A., 2001, "An Experimental and Analytical Examination of Combustion Period for Gas Fuelled Spark Ignition Engine Applications," Proc. Inst. Mech. Eng., Part A, **215**(1), pp. 63–74.
[21] Li, H., and Karim, G. A., 2006, "Hydrogen Fueled Spark-Ignition Engines, Predictive and Experimental Performance," ASME J. Eng. Gas Turbines Power, **128**, pp. 230–236.
[22] Bade Shrestha, S. O., and Karim, G. A., 2001, "Considering the Effects of Cyclic Variations When Modeling the Performance of a Spark Ignition Engine," SAE Trans., Journal of Engines, **110**, pp. 2277–2290.
[23] Woschni, G., 1967, "A Universally Applicable Equation for the Instantaneous Heat Transfer Coefficient in the Internal Combustion Engines," SAE Trans., **76**, pp. 3065–3083; SAE Paper 670931.
[24] Li, H., Karim, G. A., and Sohrabi, A., 2004, "S. I. Engine Operation on H_2, CO, CH_4 and Their Mixtures," Proceedings of ICEF2004, ASME Internal Combustion Engine Division 2004 Fall Technical Conference, Long Beach, CA, October 24–27, 2004, Paper No. ICEF2004-931.
[25] Li, H., 2004, "An Experimental and Analytical Examination of Gas Fuelled Spark Ignition Engine—Performance and Combustion," Ph.D thesis, Department of Mechanical and Manufacturing Engineering, The University of Calgary, Alberta, Canada.
[26] Heisler, H., 1995, *Advanced Engine Technology*, Society of Automotive Engineers, Inc., Warrendale, PA.
[27] Lewis, B., and Von Elbe, G., 1987, *Combustion Flames and Explosions of Gases*, Academic Press Inc., New York.
[28] Watanabe, E., and Fukutani, I., 1986, "Knock Reduction of Spark Ignition Engine by EGR," SAE Paper 860034.

Modeling the Effect of Injector Nozzle-Hole Layout on Diesel Engine Fuel Consumption and Emissions

Sung Wook Park

Rolf D. Reitz[1]
Professor
e-mail: reitz@engr.wisc.edu

Engine Research Center,
University of Wisconsin-Madison,
1500 Engineering Drive,
Madison, WI 53706

Numerical simulations were used to study the effect of reduced nozzle-hole size and nozzle tip hole configuration on the combustion characteristics of a high speed direct injection diesel engine. The KIVA code coupled with the CHEMKIN chemistry solver was used for the calculations. The calculations were performed over wide ranges of equivalence ratio and injection timing. Three nozzle-hole layouts were considered: the base line conventional nozzle, and multi- and group-hole configurations. In the multihole case, the number of holes was doubled and the hole size was reduced, while keeping the same hole area as for the base line nozzle. The group-hole configuration used the same hole number and hole size as the multihole case, but pairs of holes were grouped with a close (0.2 mm) *spacing between the holes. The results of the mixture distributions showed that the group-hole configuration provides similar penetration and lower inhomogeneity to those of the base line large hole nozzle with the same nozzle flow area. Consequently, the fuel consumption and pollutant emissions, such as CO and soot, are improved by using the group-hole nozzle instead of the conventional hole nozzle over wide operating ranges. On the other hand, the multihole nozzle has advantages in its fuel consumption and CO emissions over the conventional hole layout at intermediate equivalence ratios (equivalence ratios from 0.56 to 0.84) and conventional injection timings (start of injection:* 15 deg *before top dead center).* [DOI: 10.1115/1.2835352]

Keywords: nozzle-hole layout, group hole, stoichiometric diesel combustion, ISFC, emission reduction

1 Introduction

In diesel engines, the fuel-air mixing process has a strong effect on the combustion and pollutant emissions. The injection technology is also a key issue for the realization of recent diesel combustion technologies, such as homogeneous charge compression ignition (HCCI) [1,2] and stoichiometric diesel combustion [3,4]. In the case of HCCI combustion, the fuel spray needs to be injected with smaller droplet sizes in order to generate a homogeneous charge within a short duration [5]. Much research has been done on fuel injectors for HCCI engines, mainly focused on low-pressure swirl injectors and narrow spray included angles for preventing wall wetting [6,7]. At the same time, the nozzle-hole size has been reduced to produce smaller droplets. By decreasing the nozzle-hole size, the spray tip penetration is reduced due to the low spray momentum. This can reduce wall impingement and decrease CO and soot emissions by promoting premixed combustion at low equivalence ratios. However, as described by Bergstrand and Denbratt [8], at higher load (i.e., rich combustion), CO and soot emissions are increased dramatically because the momentum of the spray is not strong enough to move the fuel vapor to oxygen containing regions. Furthermore, new combustion concepts are exploring rich or stoichiometric combustion for sootless combustion or for the application of a three-way catalyst [3,9].

The concept of stoichiometric combustion is to achieve simultaneous reductions of NO_x, carbon monoxide, and unburned hydrocarbons by using a three-way catalyst [3]. Under stoichiometric combustion, theoretically all of the in-cylinder oxygen should be used to improve the combustion efficiency. Therefore, for stoichiometric combustion, the spray penetration should be long enough to ensure consumption of the available oxygen during the mixing-controlled combustion process.

From this point of view, an injector which can reduce droplet size without sacrificing spray penetration is required for the realization of rich or stoichiometric diesel combustion. In order to maintain the spray tip penetration, Denso has suggested a new concept of nozzle-hole configuration, which is called a group-hole nozzle [10]. The idea is to reduce the nozzle-hole size while maintaining spray penetration by grouping two or three holes with very small interhole spacing (0.16–0.3 mm). They showed that the sprays issuing from group-hole nozzles have smaller Sauter mean diameter (SMD) and similar vapor penetration compared to those from conventional nozzles, resulting in simultaneous reductions of NO_x and particulate matter.

Studies on group-hole nozzles have been performed by several research groups. Nishida et al. [11] investigated the effect of the angle between the two holes in a group on spray behavior and found that the spray from a converging group-hole nozzle (group-hole nozzle with converging angle) showed similar spray tip penetration to that from the parallel group-hole nozzle. However, in cases of a diverging group-hole nozzle, the spray tip penetrations were much shorter because each spray plume behaves like a separate spray. Zhang et al. [12] analyzed impinging spray behavior and vapor concentrations from a group-hole nozzle using an ultraviolet visible laser absorption-scattering imaging technique. Numerical studies on combustion and emissions have been performed by Adomeit et al. [13] and they reported that simultaneous reductions in fuel consumption and emissions were possible at part load by using a group-hole nozzle.

Baik et al. [5] used several kinds of nozzles with the same

[1]Corresponding author.

Manuscript received April 9, 2007; final manuscript received November 22, 2007; published online March 28, 2008. Review conducted by Thomas W. Ryan III.

overall nozzle flow area by changing the number of holes from a single hole to 169 holes. Also, the spacing between the holes was varied from 0.1 mm to 0.2 mm. Although their experiments were not performed with group-hole nozzle injector, their nozzle configurations are quite similar to a group-hole nozzle because the spacing between the holes was very small. They showed that the spray tip penetration and SMD are almost independent of the number of holes, based on experimental results from spray visualization and droplet sizing using a laser diffraction method. However, their experiments were performed only at nonevaporating conditions and did not consider the evaporation characteristics at diesel in-cylinder-like conditions.

As described by previous researchers, the required nozzle configuration is different according to the engine specifications and operating conditions, such as engine load, spray targeting, injection pressure, and fuel amount. In addition, the benefit of the group-hole nozzle is dependent on equivalence ratio. Therefore, comparisons of fuel consumption and emissions of a base line conventional nozzle, against multi- and group-hole nozzles over wide engine operating conditions, are needed to specify optimal nozzle types.

In the present study, fuel consumption and emissions such as NO_x, soot, and CO were predicted with various nozzle-hole configurations: conventional hole and group- and multihole nozzles over wide operating conditions in order to explore optimum nozzle-hole configurations as a function of equivalence ratio and start-of-injection timing.

2 Model Formulation

A modified version of the KIVA-3V RELEASE 2 [14] code was used for the present study. The major model improvements include the KH-RT spray atomization and breakup model [15], the chemical reaction model which is coupled with CHEMKIN-II [16], a reduced Gas Research Institute (GRI) NO_x formation mechanism, and a two-step phenomenological soot model [17]. The renormalized group (RNG) κ-ε model was used for the calculation of in-cylinder flow turbulence.

2.1 Chemical Reaction Mechanism. A reduced *n*-heptane mechanism [16] was used to simulate the diesel combustion process because its ignition characteristics and cetane number are similar to those of diesel fuel. This mechanism was reduced from larger mechanisms such as those of the Lawrence Livermore National Laboratory [18] and Chalmers University mechanisms [19] for improving the efficiency of the calculation time. In order to solve for the chemistry during multidimensional engine simulations, the CHEMKIN-II chemistry solver [20] was coupled with the KIVA code [21]. The KIVA code provides CHEMKIN with the species densities and thermodynamic information in each computational cell, and CHEMKIN returns the results such as the new species concentrations and energy release. The present *n*-heptane mechanism combined with the CHEMKIN solver has been successfully used in many previous studies done at the Engine Research Center, University of Wisconsin-Madison and has shown good agreement with experimental results [17,22–24].

Although the chemical reactions were calculated using the *n*-heptane mechanism, the physical properties of the fuel for calculating droplet breakup, collision/coalescence, and evaporation used those of tetradecane because its physical properties such as boiling point and density are closer to diesel fuel. Conversions between *n*-heptane and tetradecane are done based on mass conservation, as appropriate.

2.2 Emission Models. For simulating NO_x formation, a mechanism was used that is reduced from the GRI NO mechanism containing 22 species and 101 reactions [25]. The present reduced GRI mechanism contains four species and nine reactions and engine-out NO_x was defined as the sum of NO and NO_2 at exhaust valve opening. The remaining reactions of GRI NO mechanism are given in the Appendix.

Table 1 Engine specifications [3]

Engine type	Single-cylinder DI diesel
Bore × stroke	82.9×90.4 mm^2
Compression ratio	16.1:1
Displacement	477 cm^3
Piston type	Open crater
Intake ports	One helical, One directed
Boost pressure	1.3 bars
Swirl ratio (at IVC)	1.83
Intake valve open	10 deg BTDC
Intake valve closure	38 deg ATDC
Exhaust valve open	38 deg BBDC
Exhaust valve closure	8.5 deg ATDC
Injector type	Electrohydraulically controlled
Nozzle type	Minisac
Number of nozzle holes	eight-hole
Hole diameter	0.130 mm
Included spray angle	130 deg

Soot is simulated by a two-step phenomenological model that consists of soot formation and oxidation. In this soot model, soot formation and oxidation rates were calculated by the Hiroyasu soot formation and Nagle–Strickland–Constable oxidation models, respectively [17]. Also, acetylene (C_2H_2) was used as the precursor of soot formation instead of fuel vapor because a soot model that uses fuel vapor predicts unrealistic soot concentrations at low temperatures, which does not coincide with the soot formation region [9]. The present soot model has been validated and has shown good agreement with experiments in many previous studies [17,22,23]. In this paper, the soot formation constant (A_{sf}) was adjusted to 200, based on the validations with experiments, as described below.

3 Calculation Conditions

Parametric studies were conducted sweeping the start-of-injection timing and equivalence ratio with the base line conventional nozzle, and the group- and multihole nozzles. The test engine used for the calculations is a single-cylinder version of a 1.9 l four-cylinder high-speed direct-injection (HSDI) diesel engine. The engine specifications are listed in Table 1, and a 45 deg sector of the combustion chamber was used, considering that the base line configuration had an eight-hole fuel injector nozzle and to improve computational efficiency, as shown in Fig. 1.

3.1 Nozzle-Hole Layouts. Three nozzle layouts were used: the base line conventional nozzle and two nozzle configurations with reduced hole size. The base line conventional nozzle had eight 0.130 mm diameter holes. In the reduced hole size calculations, the number of holes was doubled while keeping the overall nozzle area the same (0.092 mm $\times$ 16 holes) in two ways. The first configuration targets each spray plume uniformly in the radial direction (see Fig. 2(*a*)). Hereafter, this nozzle configuration is referred to as the "multihole nozzle." The other nozzle configuration for reduced hole size used grouped holes. By locating two holes with close spacing as shown in Fig. 3, the spray plume

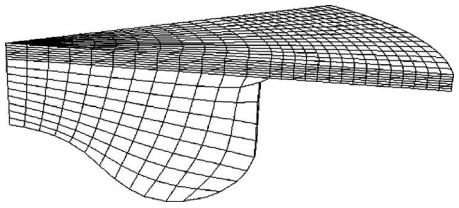

Fig. 1 45 deg sector computational mesh at top dead center

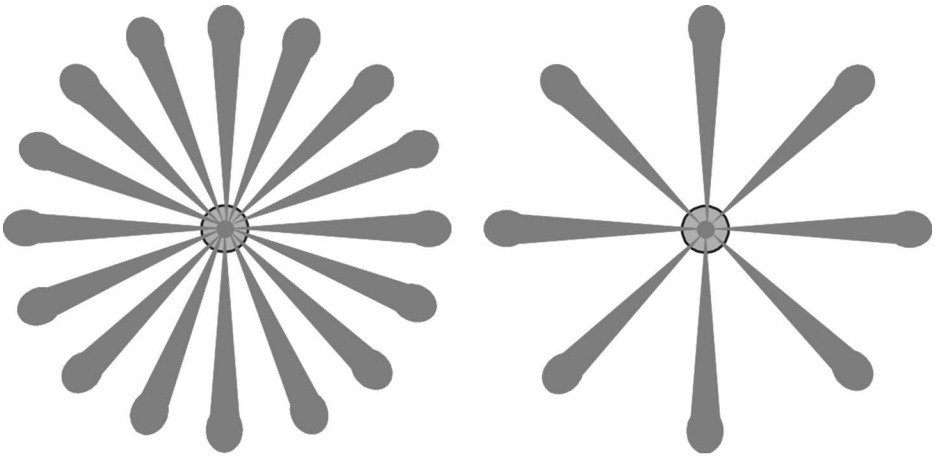

Fig. 2 Bottom-view images of group- and multiholes: (*a*) multi-hole (16 holes) (*b*) group-hole (8 groups of two holes)

issuing from each hole behaves like one spray, as illustrated schematically in Fig. 2(*b*). The goal is to reduce SMD without shortening spray tip penetration [10–12]. Hereafter, the nozzle configuration of Figs. 2(*b*) and 3 is referred to as the "group-hole nozzle."

3.2 Calculation Conditions. In order to investigate the nozzle configuration, parametric studies with varying equivalence ratio and start-of-injection timing are demanded since the requirements for the fuel spray are dependent on the operating conditions. Sweeps of equivalence ratio (from 0.48 to 1.00, corresponding to 0–53% external exhaust gas recirculation (EGR)) and start-of-injection timing (from 40 deg to 5 deg before top dead center (BTDC)) were conducted at 150 MPa injection pressure. The initial in-cylinder pressure corresponded to 1.47 bars and the EGR rate in the calculation is increased from the base line experimental EGR rate to account for internal EGR. The detailed calculation conditions are listed in Table 2.

Because the calculation conditions include equivalence ratios up to stoichiometric, the initial CO at intake valve closure can be an influential parameter. In this study, the initial CO was calculated by the curve-fitting experimental data between CO and CO_2 according to the equivalence ratio. Figure 4 shows the ratio of CO and CO_2 from experiments of Lee [3], which covers wide ranges of injection timing (from 51 deg to 5 deg BTDC) and equivalence ratios (from 0.46 to 1.1). The EGR compositions considered in the present study were O_2, N_2, CO_2, H_2O, and CO.

Work done during the closed valve period (from intake valve closure to exhaust valve opening) was included in calculating indicated specific fuel consumption (ISFC), but pumping loss during the gas exchange process was not considered.

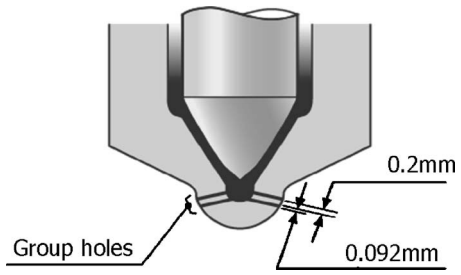

Fig. 3 Configuration of group-hole nozzle [10]

Table 2 Calculation conditions

Nozzle type	Conventional nozzle, group hole, multihole, 130 deg included angle						
Injection pressure	150 MPa						
Start of injection	40–5 deg BTDC						
Initial pressure	1.47 bars						
Equivalence ratio	0.48	0.56	0.67	0.75	0.84	0.92	1.00
Fuel amount (mg/cycle)	15.8	15.8	15.8	15.8	15.8	15.8	17.0
$[O_2]$ (%)	19.1	16.4	14.9	13.3	11.2	10.2	9.5

4 Results and Discussion

4.1 Model Validation. In order to validate the present models, the calculated results were compared with the experimental results presented by Lee [3] for the conditions in Table 2. The experiments only used the conventional nozzle.

Figure 5 shows comparisons of cylinder pressure between experiments and simulations for various equivalence ratios at 150 MPa injection pressure. As can be seen in the figures, the predicted cylinder pressure histories agree well with the experiments both at lean and rich (stoichiometric) conditions. In Fig. 6, the predicted emissions including NO_x (i.e., the sum of NO and NO_2), CO, and soot are also compared with the experiments. It can be seen that the overall calculated trends of emissions as a function of equivalence ratio agree with the experiments reasonably; a decrease in NO_x and an increase in CO and soot occur with increasing equivalence ratio. However, in the results of CO

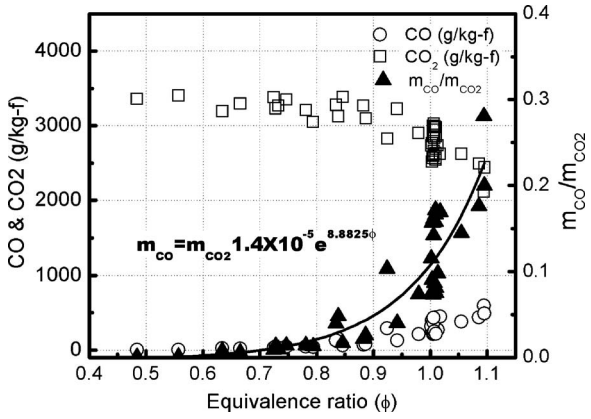

Fig. 4 Measured effect of equivalence ratio on engine-out CO and CO_2 mass fractions [3]

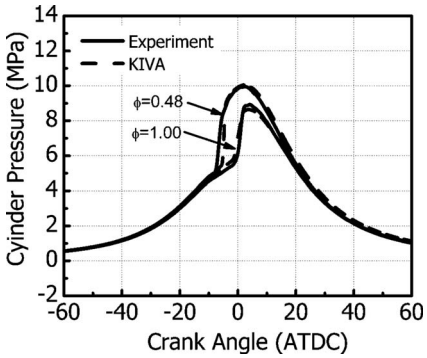

Fig. 5 Comparisons of cylinder pressure between experiments and simulations (equivalence ratio sweep, SOI: 15 deg BTDC)

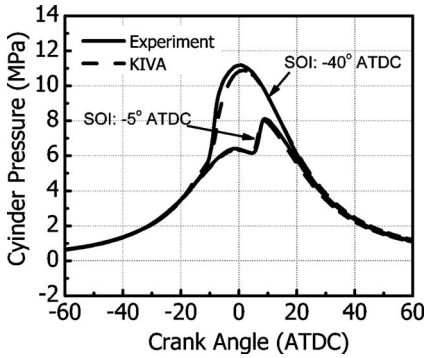

Fig. 7 Comparisons of cylinder pressure between experiments and simulations (SOI sweep, ϕ=0.56)

and soot, it was also found that there are discrepancies in magnitudes with the experiments. It is believed that the discrepancies are partly due to the fact that the injection timing is not considered in calculating the initial composition and also to the poor prediction accuracy of the CO mechanism and soot models. The CO mechanism and soot models need further improvement, along with more accurate specification of the initial composition to reflect the effect of equivalence ratio more accurately [26]. However, the present models are considered to be adequate for trend analysis.

The present model was also validated for various start-of-injection (SOI) timings from 40 deg to 5 deg BTDC. Figure 7 shows the calculated pressure histories for selected injection timings representing premixed charge compression ignition (PCCI) (40 deg BTDC SOI) and late (5 deg BTDC SOI) injection timings. Note that the spray included angle for the calculations was 120 deg in order to compare with the experiments. It can be concluded that the calculated results match with the experiments reasonably in combustion phasing and peak cylinder pressures for all cases.

The calculated exhaust emissions including NO_x, CO, and soot were compared with the experiments in Fig. 8. It can be seen that the calculated emissions are properly captured with respect to SOI timing; however, some discrepancies were found in CO for early injection cases (i.e., SOI before 30 deg BTDC). It is believed that the reason for this discrepancy is that the prediction of intermediate combustion products such as CO is more sensitive to the reaction mechanism and to flow-chemistry interactions, especially for early injection cases, as described by Kong and Reitz [27] and Kim et al. [28]. Also, the peak NO_x emission is seen at 20 deg BTDC injection timing in the calculations, which is not found in the experiments. This indicates that consideration of NO_x in the initial composition at intake valve closure (IVC) might be required.

4.2 Effect of Nozzle-Hole Layout on Fuel-Air Mixing Process. Prior to investigating the effect of nozzle-hole layout on the combustion characteristics, the fuel-air mixing processes were studied because they are highly dependent on the nozzle specifications [29]. In addition, understanding the mixing process can help the analysis of the combustion and emission characteristics.

Figure 9 shows the local equivalence ratio distributions for the different nozzle-hole layouts at top dead center (i.e., near the start of combustion) for cases of 15 deg BTDC SOI and stoichiometric combustion. Note that the equivalence ratio is calculated using the molecular concentrations of carbon, hydrogen, and oxygen atoms of all species except CO_2 and H_2O. As can be seen in the figure, the sprays issuing from the conventional and group-hole nozzles impinge on the wall of the piston bowl and are then guided by the wall geometry. Eventually, the mixture is located over a wide region near the piston wall. On the other hand, the spray from the multihole nozzle does not reach to the wall and forms a stagnated mixture in the piston bowl. It is seen that the spray from the group-hole nozzle has almost the same spray tip penetration as that from the conventional hole nozzle because the momentum

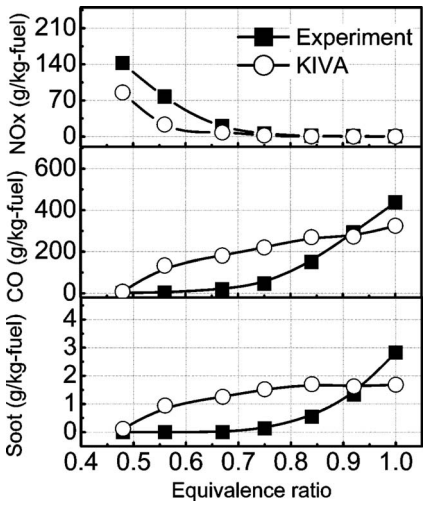

Fig. 6 Model validation for exhaust emissions as a function of equivalence ratio (SOI: 15 deg BTDC)

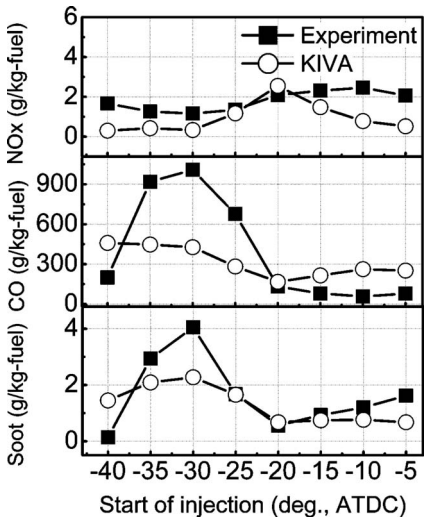

Fig. 8 Model validation for exhaust emissions as a function of SOI timing (ϕ=0.56)

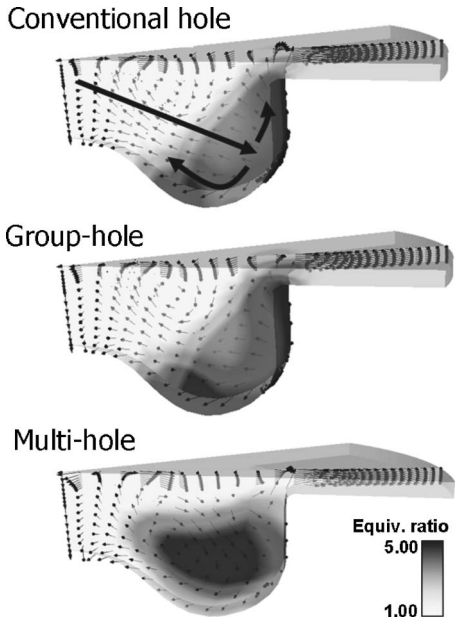

Fig. 9 Local equivalence ratio distributions at top dead center (SOI: 15 deg BTDC, stoichiometric) in the plane of the spray

from each group is the same as that from each hole of the conventional hole nozzle [10,11]. On the other hand, the initial momentum of the spray from the multihole nozzle is half of that from the conventional hole nozzle and this causes shorter spray tip penetration.

Although the images of Fig. 9 illustrate that the spray mixture from the group-hole nozzle shows a wider distribution than that from the multihole nozzle in the indicated cross-sectional plane, it is hard to say that the group-hole nozzle produces more homogeneous charge because the mixture distribution is not rendered. In order to evaluate the uniformity of the fuel-air mixture, the inhomogeneity, an indicator that shows how homogeneous the mixture is, is used as suggested by Sun and Reitz [30]. The inhomogeneity (NSD) is defined as the normalized standard deviation of the local equivalence ratio, considering the local mass distribution as a weighting factor, and is calculated by

$$\mathrm{NSD} = \frac{1}{\bar{\Phi}} \sqrt{\frac{\sum_{i}^{\#\ \mathrm{cells}} (\Phi_i - \bar{\Phi})^2 \delta m_i}{\sum_{i}^{\#\ \mathrm{cells}} \delta m_i}} \tag{1}$$

where

$$\bar{\Phi} = \frac{1}{\bar{\Phi}} \sqrt{\frac{\sum_{i}^{\#\ \mathrm{cells}} \Phi_i \delta m_i}{\sum_{i}^{\#\ \mathrm{cells}} \delta m_i}} \tag{2}$$

As can be seen in the definition of inhomogeneity, a lower inhomogeneity means a more homogeneous fuel-air mixture. Values of inhomogeneity at the start of combustion are shown in Fig. 10 with respect to equivalence ratio. For all tested nozzle-hole configurations, the inhomogeneity is decreased with the increase of equivalence ratio. This is because the ignition delay is increased at higher equivalence ratio (i.e., higher EGR), which allows a longer duration for mixing. The relationship between ignition delay and mixture homogeneity was also shown using fuels

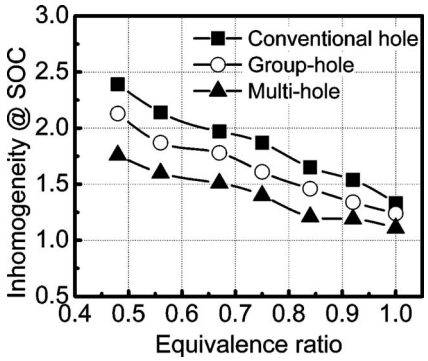

Fig. 10 Effect of nozzle-hole layout on the values of inhomogeneity as a function of equivalence ratio (SOI: 15 deg BTDC)

with different cetane numbers by Kalghatgi et al. [31].

Figure 10 shows that the multihole nozzle produces the most homogeneous charge and the group-hole nozzle also produces more homogeneous charge than a conventional hole. The inhomogeneity of the multihole nozzle is the lowest because it produces the most homogeneous mixture in the azimuthal direction, even though it shows a concentrated distribution of mixture in the bowl, as seen in the cross-section plane shown in Fig. 9. This can be regarded as the advantage of group hole over the conventional hole. Experimental measurements of droplet size measurement of nonevaporating sprays indicate that the small droplets are easily coalesced and that there is little advantage in SMD if the spacing between holes is small (less than 0.5 mm) [5]. However, it is believed that the group-hole nozzle spray can still evaporate more easily compared to the conventional nozzle under conditions in which the effect of droplet coalescence is minimized.

4.3 Effect of Equivalence Ratio. In Fig. 11, indicated specific fuel consumptions for conventional, group-, and multihole nozzles are plotted against equivalence ratio for 15 deg BTDC SOI timing and 150 MPa injection pressure. As can be seen, the group-hole nozzle cases show improved fuel consumption over the conventional hole nozzle for most of the range of equivalence ratios. On the other hand, the fuel consumptions of the multihole nozzle cases are quite different from that of the conventional hole nozzle case; similar fuel consumption for relatively lean combustion cases (0.48 equivalence ratio), improved fuel consumption at intermediate equivalence ratios (equivalence ratios from 0.56 to 0.84), and deteriorated fuel consumption near stoichiometric combustion. The accumulated heat release patterns shown in Fig. 12 provide explanations for these results. In this figure, the combustion phases can be classified as premixed combustion (steep increase in accumulated heat release) and mixing-controlled combustion (slow increase in accumulated heat release). As described

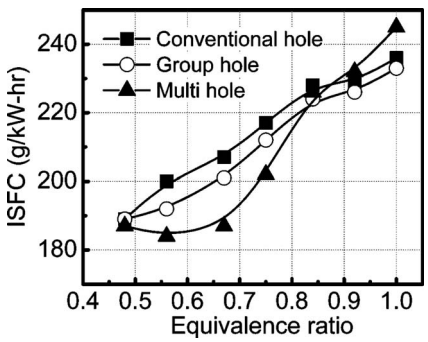

Fig. 11 Fuel consumption according to the nozzle-hole layout (equivalence ratio sweep, SOI: 15 deg BTDC)

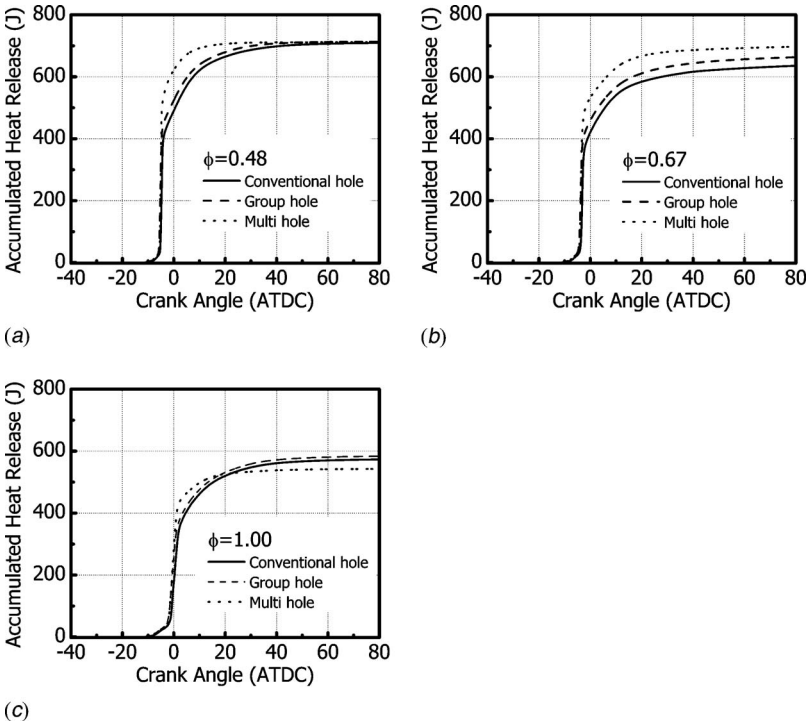

Fig. 12 Accumulated heat release for selected equivalence ratios: (*a*) ϕ =0.48 (*b*) ϕ=0.67 (*c*) stoichiometric

above, the multihole nozzle produces the most homogeneous charge of all the tested nozzle types, which means that the heat release rate during premixed combustion is also the highest. At 0.48 equivalence ratio, the total heat released for each nozzle is almost the same, although more heat is released during the premixed combustion phase of the multihole nozzle case. It is believed that the total heat released for the tested nozzle layouts is similar because more heat is released from the mixing-controlled combustion phases of the conventional and group-hole nozzle cases. However, as the equivalence ratio is increased (see Fig. 12(*b*)), the greater heat release that occurs during the premixed combustion of the multihole case causes a higher total heat release. In the stoichiometric case shown in Fig. 12(*c*), most of the in-cylinder oxygen is used by the mixing-controlled combustion phase because the oxygen concentration is very lean. In other words, in order to minimize CO and HC emissions and to maximize the thermal efficiency, the oxygen located in the squish region should be mixed with fuel vapor transferred by the in-cylinder flow, as illustrated in Fig. 13. From this point of view, the spray from the multihole nozzle has difficulty in accessing the oxygen located in the squish region due to its low momentum, and eventually, the fuel consumption of the multihole nozzle cases is deteriorated.

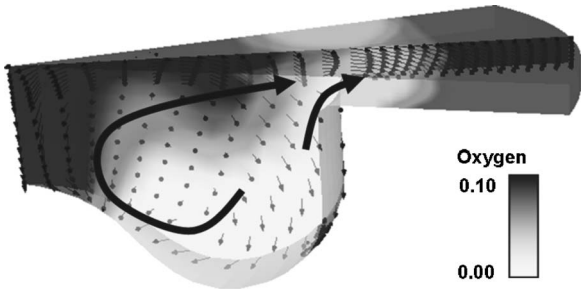

Fig. 13 Access to the oxygen in the squish region at 90% total heat release (group-hole nozzle, SOI: 15 deg BTDC, stoichiometric). Gray scale shows mass fraction of oxygen.

Summarizing the results of Figs. 11 and 12, the optimal nozzle configuration for improved fuel consumption is highly dependent on the oxygen concentration (i.e., equivalence ratio). If the oxygen is sufficient, as in the 0.46 equivalence ratio cases of the present study, the nozzle-hole configuration has little effect on the fuel consumption. At intermediate equivalence ratios, the most dominant factor determining the fuel consumption is the homogeneity of the fuel-air mixture because the total heat release is mostly determined by the premixed combustion phase, as shown in Fig. 12(*b*). That is, the thermodynamic efficiency is closely related to the amount of oxygen entrained with the fuel spray. Near stoichiometric combustion conditions, the mixing-controlled combustion becomes more important on the fuel consumption; therefore, adequate spray tip penetration and fuel-air mixing need to be maintained for improving fuel consumption.

Figure 14 shows the emission characteristics for the different nozzle-hole configurations. In the case of NO_x shown in Fig. 14(*a*), the NO_x emissions of the multihole nozzle cases are the highest and the group-hole nozzle produces slightly higher NO_x compared to the conventional hole nozzle. Considering that the SOI timing is kept at 15 deg BTDC, it can be seen that the heat release during the premixed combustion phase increases the in-cylinder temperature before TDC causing higher NO_x concentrations. In the case of CO, the results of the accumulated heat releases of Fig. 12 provide explanations for the CO emission trends of Fig. 14(*b*) because the main loss in combustion efficiency is caused by unoxidized CO [3]. Also, the lowest soot was predicted in the cases of the multihole nozzle, as seen in Fig. 14(*c*). In Fig. 14(*d*), the HC emission of the group-hole nozzle is lower than that of the conventional nozzle at all tested equivalence ratios. This explains the higher total heat release of the group-hole nozzle

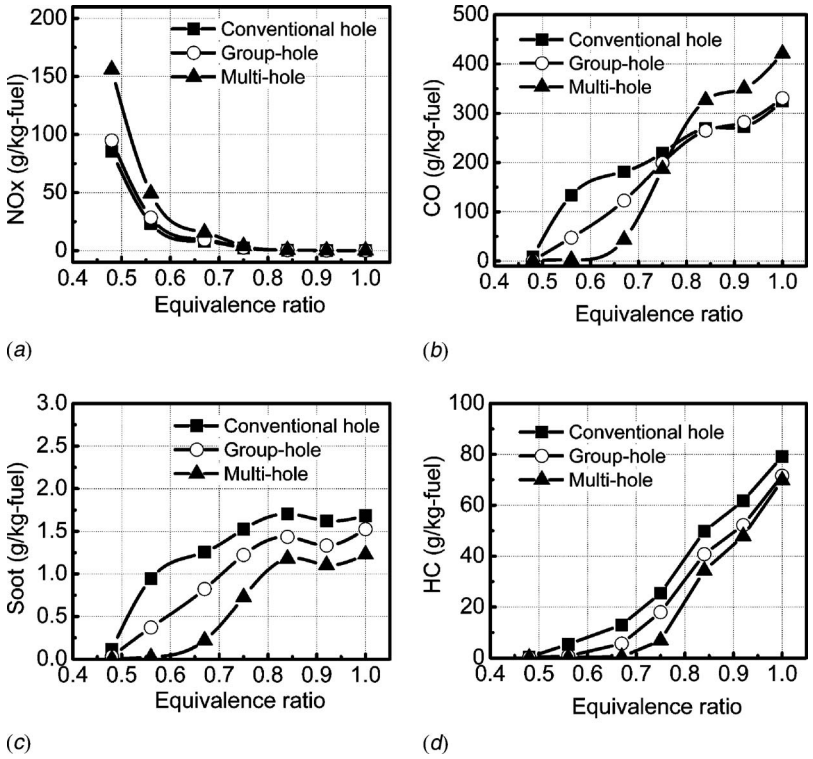

Fig. 14 Effect of nozzle-hole configuration on emissions against equivalence ratio (SOI: 15 deg BTDC) (*a*) NO_x (*b*) CO (*c*) Soot (*d*) HC

compared to that of the conventional nozzle at stoichiometric conditions even though they have similar CO emissions (see Figs. 12(*c*) and 14(*b*)).

4.4 Effect of Start-Of-Injection Timing. Figure 15 shows the indicated specific fuel consumption against SOI timings for selected equivalence ratios corresponding to lean (ϕ=0.48), intermediate (ϕ=0.67), and stoichiometric combustions. For the lean combustion case of Fig. 15(*a*), the fuel consumption is decreased

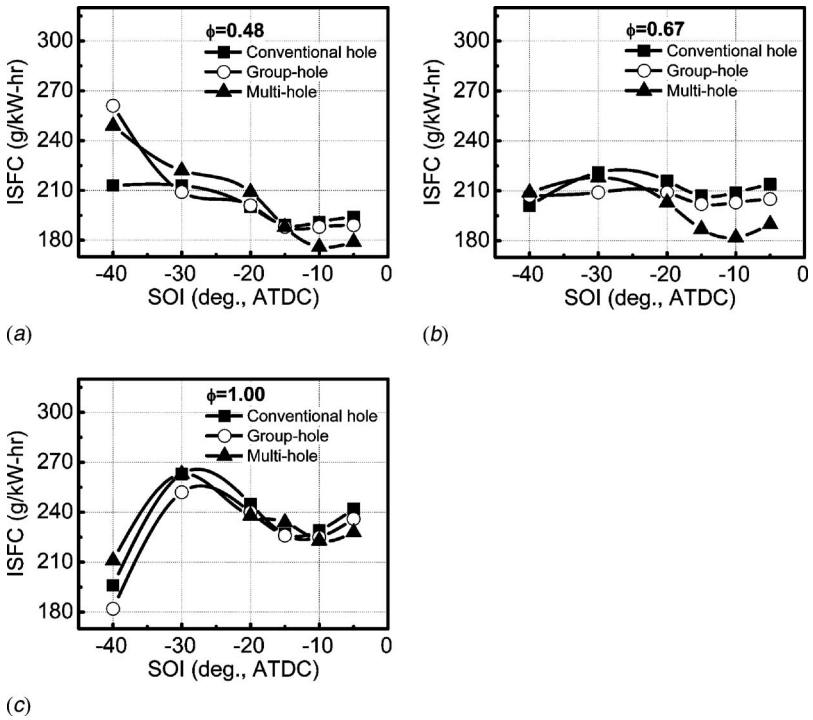

Fig. 15 Effect of SOI on fuel consumption: (*a*) ϕ=0.48 (*b*) ϕ=0.67 (*c*) stoichiometric

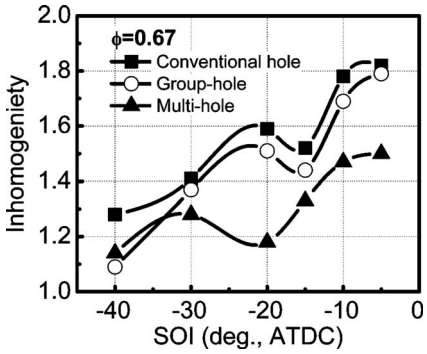

Fig. 16 Inhomogeneity at SOI (ϕ=0.67)

as the injection timing is retarded, showing similar values regardless of the nozzle-hole configuration except at 40 deg BTDC SOI where spray/wall impingement could be important. As described above, in the lean combustion case (see Fig. 11), the nozzle-hole type has little effect on the fuel consumption and the start of combustion timing is a dominant factor. At 40 deg BTDC SOI, the start of combustion of the group-hole nozzle case (18.6 deg BTDC) was very much advanced compared to that of the conventional nozzle-hole case (16.9 deg BTDC). In Fig. 15(*b*), the fuel consumption is seen to be almost independent of the SOI timing except for the late injection cases of the multihole nozzle. The lower inhomogeneity of the multihole nozzle case reduced the fuel consumption, as shown in Fig. 16. For the stoichiometric combustion case, the fuel consumption was lowest at 40 deg BTDC, which is also related to the optimum spray targeting since the injected fuel is optimally split between the bowl and squish regions, which leads to good air utilization. It is believed that at this injection timing, the spray impinges on the top of the piston bowl and some of the fuel flows into the squish region, as shown in Fig. 17. Fuel in the squish region utilizes the oxygen in that region, and this results in the improvement in the fuel consumption.

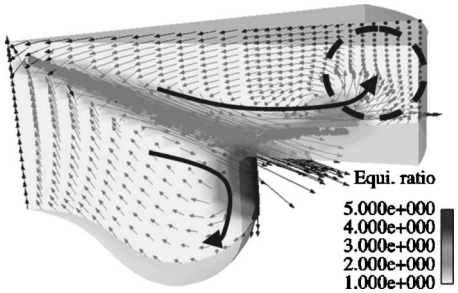

Fig. 17 Spray targeting to improve oxygen utilization (local equivalence ratio distribution at the end of injection, group hole, SOI: 40 deg BTDC)

Predicted CO emissions as a function of SOI timing and equivalence ratios are presented in Fig. 18. As can be seen in this figure, multihole cases have the lowest CO at 0.67 equivalence ratio but the highest CO at stoichiometric conditions over a wide range of SOI timings. It is believed that the low momentum of the multihole nozzle causes difficulties in accessing the oxygen under stoichiometric conditions as described above.

At 0.48 equivalence ratio and 30 deg BTDC SOI injection, the predicted CO emissions of the conventional nozzle are much higher than those of the other nozzle types. In the case of the conventional hole, a higher CO region is located near the piston wall because the higher inhomogeneity decreases combustion efficiency, as shown in Fig. 19.

5 Conclusions

In the present study, numerical calculations of the effects of nozzle-hole configurations on fuel consumption and emission characteristics were performed over wide conditions of equivalence ratio (0.46–1.00) and injection timing (40–5 deg BTDC) at 150 MPa injection pressure using the KIVA CFD code with updated

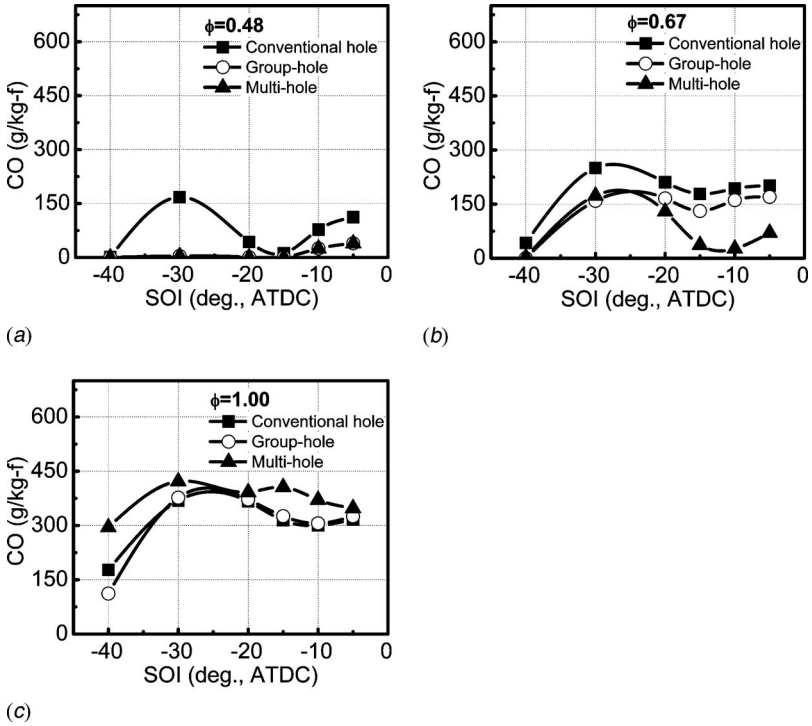

Fig. 18 Effect of SOI timing on CO emissions: (*a*) ϕ=0.48 (*b*) ϕ=0.67 (*c*) stoichiometric

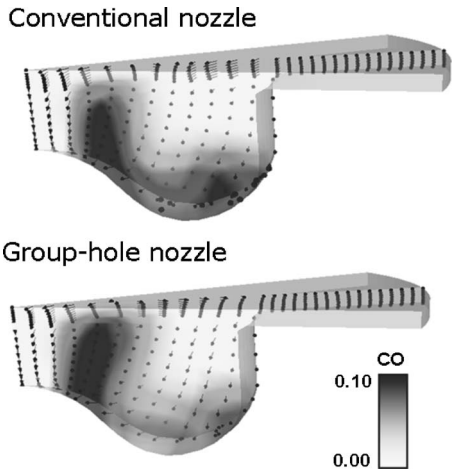

Fig. 19 CO distribution (mass fraction) (ϕ=0.48, SOI: 30 deg BTDC)

models. The following conclusions can be drawn based on the calculation results.

1. At the injection timing of conventional diesel combustion (SOI: 15 deg BTDC), the spray issuing from a group-hole nozzle showed similar spatial fuel-air mixture distribution but lower inhomogeneity compared to that from a conventional hole nozzle. This indicates that the group-hole concept can produce a more homogeneous charge than the conventional hole nozzle without sacrificing spray tip penetration. As a result, the group-hole nozzle improves fuel consumption and reduces CO and soot emissions over wide ranges of equivalence ratio.
2. A multihole nozzle produces the most homogeneous charge among the tested nozzle-hole configurations and showed the best fuel efficiency at intermediate equivalence ratios (0.56–0.84). However, the fuel consumption deteriorated near stoichiometric conditions because of the spray's inability to access the oxygen in the chamber at the injection timings of conventional diesel combustion.
3. As equivalence ratio was varied while keeping SOI at 15 deg BTDC, the multihole nozzle showed the highest NO_x emissions due to the rapid increase of in-cylinder temperature during the premixed combustion process. The NO_x emission of the group-hole nozzle was slightly increased from that of a conventional nozzle hole.
4. At lean combustion conditions, the effect of nozzle configuration is minimal because the access to chamber oxygen is not a factor due to the plentiful oxygen. However, access to the oxygen requires sufficient spray momentum at stoichiometric conditions.
5. At 40 deg BTDC SOI and stoichiometric combustion conditions, the fuel consumption is lowest regardless of the nozzle-hole configuration because of the optimal spray targeting. When the spray is targeted at the top of the piston bowl, the best fuel consumption can be achieved because some fuel vapor flows into the squish region.

Acknowledgment

The authors gratefully acknowledge support for this work from General Motors Research and Development, the ERC Diesel Emissions Reduction Consortium member companies, and DOE LTC Consortium Project No. DE-FC26-06NT42628. They also thank Dr. Youngchul Ra for his help in calculating initial conditions.

Nomenclature

ATDC = after top dead center
BTDC = before top dead center
HCCI = homogeneous charge compression ignition
HRR = heat release rate
ISFC = indicated specific fuel consumption
m_i = total mass in calculation cell i
SOI = start of injection
SMD = Sauter mean diameter
φ = equivalence ratio

Appendix: Reduced GRI Mechanism

Reactions considered			$(k=AT^{**}b\exp(-E/RT))$ A	b	E
1. $N+NO \Leftrightarrow N_2+O$			3.50E+13	0.0	330.0
2. $N+O_2 \Leftrightarrow NO+O$			2.65E+13	0.0	6,400.0
3. $N_2O+O \Leftrightarrow 2NO$			2.90E+13	0.0	23,150.0
4. $N_2O+OH \Leftrightarrow N_2+HO_2$			2.00E+12	0.0	21,060.0
5. $N_2O(+m) \Leftrightarrow N_2+O(+m)$			1.30E+11	0.0	59,620.0
Low-pressure limit: 0.62000E+15 0.00000E+00 0.56100E+05					
H_2	Enhanced by	2.000E+00			
H_2O	Enhanced by	6.000E+00			
CH_4	Enhanced by	2.000E+00			
CO	Enhanced by	1.500E+00			
CO_2	Enhanced by	2.000E+00			
6. $HO_2+NO \Leftrightarrow NO_2+OH$			2.11E+12	0.0	−480.0
7. $NO+O+m \Leftrightarrow NO_2+m$			1.06E+20	−1.4	0.0
8. $NO_2+O \Leftrightarrow NO+O_2$			3.90E+12	0.0	−240.0
9. $NO_2+H \Leftrightarrow NO+OH$			1.32E+14	0.0	360.0

Note that A, units in mole cm s K; E, units in cal/mole.

References

[1] Najt, P. M., and Foster, D. E., 1983, "Compression-Ignited Homogeneous Charge Combustion," SAE Paper No. 830264.

[2] Lee, C. S., Lee, K. H., and Kim, D. S., 2003, "Experimental and Numerical Study on the Combustion Characteristics of Partially Premixed Charge Compression Ignition Engine With Dual Fuel," Fuel, **82**, pp. 553–560.

[3] Lee, S.-S., 2006, "Investigation of Two Low Emissions Strategies for Diesel Engines; Premixed Charge Compression Ignition (PCCI) and Stoichiometric Combustion," Ph.D. thesis, University of Wisconsin-Madison, Madison.
[4] Dronniou, N., Auffret, N., Lejenue, M., and Higelin, P., 2006, "Near-Stoichiometric Diesel Combustion With Reduced Orifices on a Heavy-Duty Diesel Engine," *Proceedings of THIESEL 2006 Conference on Thermo- and Fluid Dynamic Processes in Diesel Engines*.
[5] Baik, S., Blanchard, J. P., and Corradini, M. L., 2003, "Development of Micro-Diesel Injector Nozzles via MEMS Technology and Effect on Spray Characteristics," Atomization Sprays, **13**, pp. 443–474.
[6] Walter, B., and Gatellier, B., 2003, "Near Zero NO_x Emissions and High Fuel Efficiency Diesel Engine: The NADI Concept Using Dual Mode Combustion." Oil Gas Sci. Technol., **58**(1), pp. 101–114.
[7] Lee, K., and Reitz, R. D., 2004, "Investigation of Spray Characteristics from a Low-Pressure Common Rail Injector for Use in a Homogeneous Charge Compression Ignition Engine," Meas. Sci. Technol., **15**, pp. 509–519.
[8] Bergstrand, P., and Denbratt, I., 2001, "Diesel Combustion With Reduced Nozzle Orifice Diameter," SAE Paper No. 2001-01-2010.
[9] Akihara, K., Takatori, Y., Inagaki, K., Sasaki, S., and Dean, A. M., 2001, "Mechanism of the Smokeless Rich Diesel Combustion by Reducing Temperature," SAE Paper No. 2001-01-0655.
[10] Tokudo, H., Itoh, S., and Kinugawa, M., 2005, "Denso Common Rail Technology to Successfully Meet Future Emission Regulation," *Proceedings of the 26th Vienna Motor Symposium*.
[11] Nishida, K., Nomura, S., and Matsumoto, Y., 2006, "Spray and Mixture Properties of Group-Hole Nozzle for D. I. Diesel Engines," *Proceedings of ICLASS 2006*, Paper No. ICLASS06-171.
[12] Zhang, Y., Nishida, K., Nomura, S., and Ito, T., 2003, "Spray Characteristics of Group-Hole Nozzle for D. I. Diesel Engine," SAE Paper No. 2003-01-3115.
[13] Adomeit, P., Rohs, H., Korfer, T., and Busch, H., 2006, "Spray Interaction and Mixture Formation in Diesel Engines With Grouped Hole Nozzle," *Proceedings of THIESEL 2006 Conference on Thermo- and Fluid Dynamic Processes in Diesel Engines*, Valencia, Spain.
[14] Amsden, A. A., 1999, "KIVA-3V Release 2, Improvement to KIVA-3V, Los Alamos National Laboratory," Report No. LA-UR-99-915.
[15] Beale, J. C., and Reitz, R. D., 1999, "Modeling Spray Atomization With the Kelvin-Helmholtz/Rayleigh-Taylor Hybrid Model," Atomization Sprays, **9**, pp. 623–650.
[16] Patel, A., Kong, S.-C., and Reitz, R. D., 2004, "Development and Validation of a Reduced Reaction Mechanism for HCCI Engine Simulations," SAE Paper No. 2004-01-0558.
[17] Kong, S.-C., Sun, Y., and Reitz, R. D., 2007, "Modeling Diesel Spray Flame Lift-Off, Sooting Tendency and NO_x Emissions Using Detailed Chemistry With Phenomenological Soot Model," ASME J. Eng. Gas Turbines Power, **129**, pp. 252–260.
[18] Pitz, W. J., 2000, http://www-cmls.llnl.gov/?url=science_and_technology-chemistry-combustion-nc7h16_reduced_mechanism, Lawrence Livermore National Laboratory.
[19] Golovitchev, V. I., 2000, http://www.tfd.chalmers.se/~valeri/MECH.html, Chalmers University of Technology, Gothenburg, Sweden.
[20] Kee, R. J., Rupley, F. M., and Miller, J. A., 1989, "CHEMKIN-II: A FORTRAN Chemical Kinetics Package for the Analyses of Gas Phase Chemical Kinetics," Sandia Report No. SAND 89–8009.
[21] Kong, S.-C., Marriot, C. D., Reitz, R. D., and Christensen, M., 2001, "Modeling and Experiments of HCCI Engine Combustion Using Detailed Chemical Kinetics With Multidimensional CFD," SAE Paper No. 2001-01-1026.
[22] Kong, S.-C., Kim, H., Reitz, R. D., and Kim, Y., 2007, "Comparison of Combustion Simulations Using Representative Interactive Flamelet Model and Direct Integration of CFD With Detailed Chemistry," ASME J. Eng. Gas Turbines Power, **129**, pp. 245–251.
[23] Kim, M., Reitz, R. D., and Kong, S.-C., 2006, "Modeling Early Injection Processes in HSDI Diesel Engines," SAE Paper No. 2006-01-0056.
[24] Dougan, C. L., Kong, S.-C., and Reitz, R. D., 2005, "Modeling the Effects of Variable Intake Valve Timing on Diesel HCCI Combustion at Varying Load, Speed and Boost Pressures," *Proceedings of ICES05*, Paper No. ICES2005-1020.
[25] Smith, G. P., Golden, D. M., Frenklach, M., Moriarty, N. W., Eiteneer, B., Goldenberg, M., Bowman, C. T., Hanson, R. K., Song, S., Gardiner, W. C., Lissianski, V. V., and Qin, Z., 2000, http://www.me.berkeley.edu/gri_mech/.
[26] Kong, S. C., and Reitz, R. D., 2003, "Numerical Study of Premixed HCCI Engine Combustion and Its Sensitivity to Computational Mesh and Model Uncertainties," Combust. Theory Modell. **7**, pp. 417–433.
[27] Kong, S. C., and Reitz, R. D., 2002, "Application of Detailed Chemistry and CFD to Predict Direct Injection HCCI Engine Combustion and Emissions," Proc. Combust. Inst., **29**, pp. 663–669.
[28] Kim, H., Reitz, R. D., and Kong, S.-C., 2006, "Modeling Combustion and Emissions of HSDI Diesel Engines Using Injectors With Different Included Spray Angles," SAE Paper No. 2006-01-1150.
[29] Park, S. W., 2005, "Internal Structure and Atomization Characteristics of High-Pressure Injection Diesel Sprays," Ph.D. thesis, Hanyang University, Seoul, South Korea.
[30] Sun, Y., and Reitz, R. D., 2006, "Modeling Diesel Engine NO_x and Soot Reduction With Optimized Two-Stage Combustion," SAE Paper No. 2006-01-0027.
[31] Kalghatgi, G. T., Risberg, P., and Angstrom, H.-E., 2006, "Advantages of Fuels With High Resistance to Auto-Ignition in Late-Injection, Low-Temperature, Compression Ignition Combustion," SAE Paper No. 2006-01-3385.

Experimental Investigation of Dynamics Effects on Multiple-Injection Common Rail System Performance

Andrea E. Catania
Alessandro Ferrari
Michele Manno
Ezio Spessa

IC Engines Advanced Laboratory,
Dipartimento di Energetica,
Politecnico di Torino,
C.so Duca degli Abruzzi, 24
10129–Torino, Italy

Fundamental aspects of Common Rail (CR) fuel-injection-system dynamics were investigated, paying specific attention to the wave propagation induced pressure oscillations and to their relationships with the system control parameters and multiple-injection performance. A detailed experimental analysis of the pressure-wave propagation phenomena in a last-generation CR Multijet equipment of the solenoid type was carried out on a high performance new test-bench Moehwald-Bosch MEP2000-CA4000 under real engine simulated conditions. The experimental results include pressure time histories in the rail and at the injector inlet, as well as flow-rate patterns, for both single and multiple injection events. The measured volume of fuel injected at each injection pulse is also reported. The analysis of the system oscillating behavior was carried out with the support of a simple lumped parameter model. Such a model was shown to be capable of predicting the main frequencies of the hydraulic circuit and their dependence on the geometrical parameters. The good agreement between the outcome of this simple model and the experimental data also substantiated the reliable authors' interpretation of the primary cause and effect relations underlying the complex flow phenomena occurring in the system. A refined computational model was developed and validated in a parallel work, providing a hydrodynamic analysis tool that is complementary to experimentation and also a means of hydraulic-system layout design and optimization. Finally, the mutual fluid-dynamic interactions taking place between consecutive injection events by distinct injectors of the same system are investigated in addition to the difference in dynamics of valve covered orifice and Minisac-nozzle injectors. Cycle-to-cycle variations in system performance were also investigated. [DOI: 10.1115/1.2835353]

Introduction

The Common Rail (CR) diesel injection system, which was cast in production approximately ten years ago [1,2], has met an extraordinary success and is responsible of the ever-increasing share of diesel engines in the European automotive market. The main key to this success is the flexibility that can be provided for the most important injection parameters: The pressure level generation is almost independent of the engine speed and of fuel metering; the injection timing and duration can be optimized for every working condition.

The emission regulations have imposed further refinements on CR systems, in order to achieve both optimal fuel consumption and exhaust emissions. The ability of delivering multiple injections, which is one of the most interesting features of such injection systems, allows an improved combustion and heat-release-rate control, resulting in clean and efficient engine performance, especially in conjunction with variable swirl and cooled exhaust gas recirculation (EGR). To achieve this result, CR electroinjectors have thoroughly been investigated by researchers of the automotive field, in order to obtain fast actuations, retaining, at the same time, a good precision of the injected fuel volume.

However, the dynamics of CR hydraulic components can cause sensible perturbations to multiple injections, which hence occur under different conditions from those expected. The wave propagation phenomena arising in the system, subsequent to an injection event, lead to pressure oscillations that influence the injected fuel quantity, particularly when the dwell time between consecutive injections is changed [3]. The dependence of the injected quantity on the system dynamics was also pointed out by other authors [4–7]. The rail pressure is also affected by the system dynamics: Whenever an injection occurs, the pressure in the rail drops because the rail itself does not behave as an infinite volume capacity [3,6]. A sensor for continuously monitoring the pressure at the injector inlet was proposed in Ref. [8] to deliver information to the engine electronic control unit (ECU) and thus adjust the injection parameters, so as to better control the injected fuel quantity. Nevertheless, no one of the above-mentioned works reports a detailed analysis of the pressure-wave propagation phenomena and an investigation of their relationship with the ECU control parameters, system hydraulic layout, and performance.

The present work aims at further investigating the complex dynamic phenomena, which take place in a CR fuel-injection system, with specific attention to the multiple-injection performance, following the work started in Ref. [3], so as to give a contribution to the knowledge of the cause and effect relations underlying the system operation.

The presented experimental results include time histories of the pressure in the rail and at the injector inlet, as well as of flow rate, for both single and multiple injections. The measured volume of fuel injected on each injection pulse is also reported. The influence of the system dynamics on its performance was analyzed. A simple lumped parameter model was developed and applied to better understand the system oscillating behavior. More specifically, it was shown how such a model is capable of predicting the main frequencies of the hydraulic circuit and their dependence on the geometrical parameters. The good agreement between the results of this simple model and the experimental data also sup-

Manuscript received April 13, 2007; final manuscript received November 9, 2007; published online March 28, 2008. Review conducted by Margaret Wooldridge. Paper presented at the ICES 2005.

Fig. 1 Test bench

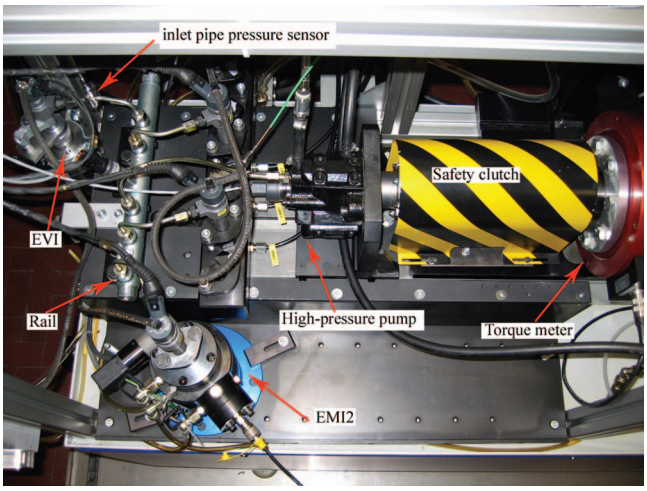

Fig. 3 CR injection-system layout and measuring instruments

ported the reliable authors' interpretation of the cause and effect main relationships governing the complex flow phenomena that occur in the system. A refined computational model was developed and validated in Ref. [9] to provide a hydrodynamic analysis tool complementary to experimentation and a means of hydraulic-system layout design and optimization.

Finally, the mutual fluid-dynamic interactions taking place between consecutive injection events by distinct injectors of the same system were investigated, in addition to the difference in dynamics of valve covered orifice (VCO)- and Minisac-nozzle injectors. Cycle-to-cycle dispersion of system performance was also analyzed.

Experimental Facility

The experiments were carried out on a high performance test-bench Moehwald-Bosch MEP2000-CA4000, recently set up at the IC Engines Advanced Laboratory (ICEAL) of Politecnico di Torino (Figs. 1–3). This facility, having maximum shaft speed and power of 6100 rpm and 35 kW, respectively, is capable of simulating real engine working conditions and also injection-system transient operations. It is equipped with several devices to precisely control shaft speed, oil temperatures, pump feeding pressure, and backpressure at the injectors' pilot valve discharge.

The experimental apparatus includes the following main measuring instruments: The volumetric device EMI2 gauging the injected volume and capable of separately measuring the volume discharged at each shot in multiple injections, the injection-rate indicator EVI of the Bosch type [10], piezoresistive sensors for monitoring the pressures in the rail and at the injector inlet (11 and 12 in Fig. 2), and fluid-temperature sensors. A high precision shaft-torque meter and a needle-lift sensor were also installed.

A National Instruments data acquisition system, provided with homemade acquisition software in LABVIEW programming environment, was used to monitor the system.

Injection System. A second-generation CR injection system of the Multijet solenoid type was considered, made up of a Radialjet CP1 high-pressure pump, 0.550 cm^3/rev in displacement, and of four electroinjectors with either Minisac or VCO nozzles. A 20 cm^3 rail volume and inlet pipes of length 125 mm and diameter 2.4 mm were used. The ISO-4113 oil was used as working fluid, suitable to simulate the diesel fuel. Figures 2 and 3 show the injection-system layout on the test bench and the location of main measuring instruments. Previous tests were made to select the four

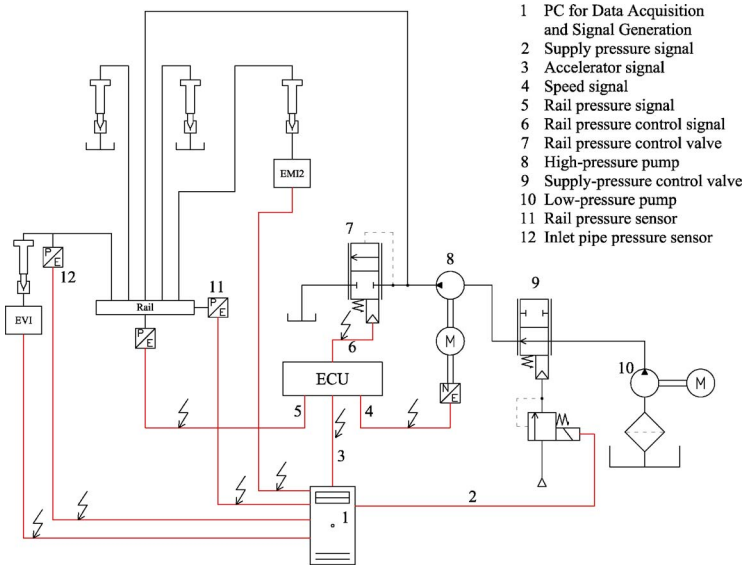

Fig. 2 Test-bench layout and instrumentation

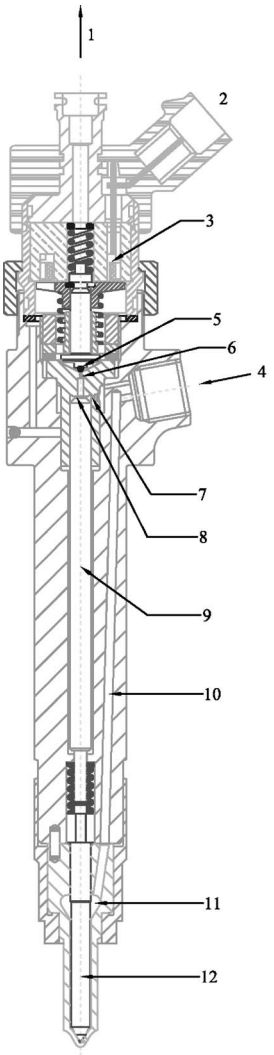

1 Fuel return (low pressure)
2 Electrical connection
3 Triggering element (solenoid valve)
4 Fuel inlet from the rail (high pressure)
5 Valve ball
6 Bleed orifice
7 Feed orifice
8 Valve control chamber
9 Valve control plunger
10 Feed pipe to the nozzle
11 Delivery chamber
12 Nozzle needle

Fig. 4 Electroinjector

injectors with negligible nozzle-to-nozzle variations. Figure 4 gives a detailed electroinjector drawing. An extensive description of the CR system working principles is reported in Ref. [11].

EMI2 Injected Volume Meter. The EMI2 gauges the displacement of a piston that runs in the injection chamber (Fig. 5) by means of a linear variable differential transformer (LVDT). The injected volume is thus determined. A temperature sensor allows

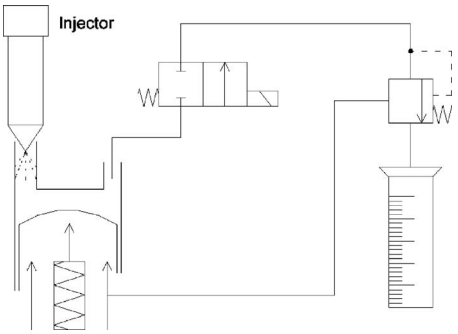

Fig. 5 EMI2 operation scheme

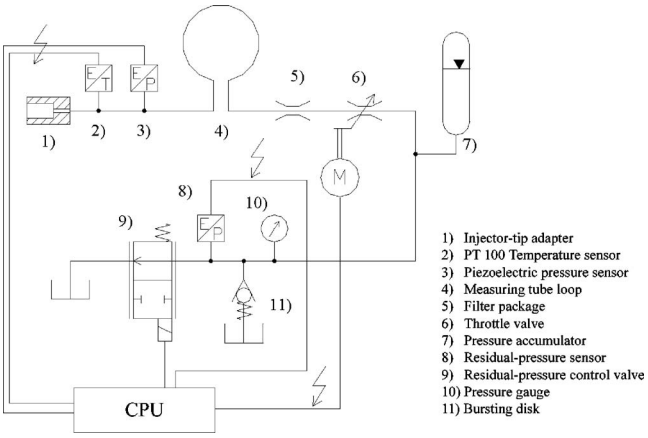

1) Injector-tip adapter
2) PT 100 Temperature sensor
3) Piezoelectric pressure sensor
4) Measuring tube loop
5) Filter package
6) Throttle valve
7) Pressure accumulator
8) Residual-pressure sensor
9) Residual-pressure control valve
10) Pressure gauge
11) Bursting disk

Fig. 6 EVI operation scheme

to evaluate the fluid density and thus to calculate the injected mass. The maximum injected volume is 600 mm^3, with a relative precision of $\pm 0.1\%$.

EVI Injection Discharge-Rate Indicator. The injection takes place into an oil-filled measuring tube (4 in Fig. 6). The fuel discharge gives rise to a pressure wave, whose amplitude is related to the actual discharged flow rate, as will be shown. Oil temperature and pressure were gauged at the initial part of the measuring tube loop (2 and 3 in Fig. 6), downstream from the injector tip adapter (i.e., 1 in Fig. 6). The EVI electronic control unit is able to precisely control the residual pressure in the system (8 and 9 in Fig. 6), so that accurate and repeatable measurements could be carried out.

The actual injected mass flow rate can be evaluated, on the basis of the pressure signal monitored by Sensor 3, as follows. The injection-induced pressure wave travels downstream with a speed $a+u$ [12]. The fluid behind the perturbations has a velocity $u+du$ and a pressure $p+dp$, while the fluid in front of the wave has velocity and pressure u and p (Fig. 7). Considering a moving frame of reference, integral with the compression wave (Fig. 8), the fluid velocity is $a-du$ behind the wave, and a in front of this, so that the mass conservation equations, for an infinitesimal control volume containing the wave front, can be written as follows:

$$\rho a A = (a - du)(\rho + d\rho)A \tag{1}$$

where A represents the pipe cross section. The density rise is

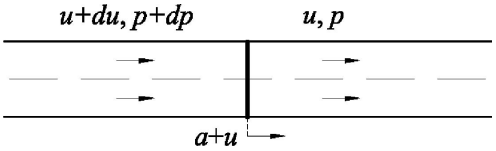

Fig. 7 Pressure wave in the EVI measuring tube

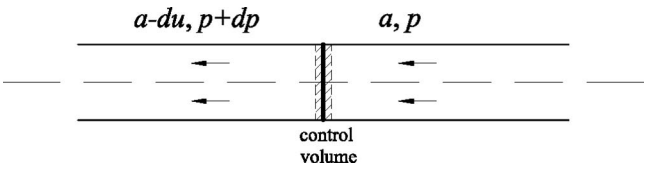

Fig. 8 Reference frame integral with the compression wave in the EVI measuring tube

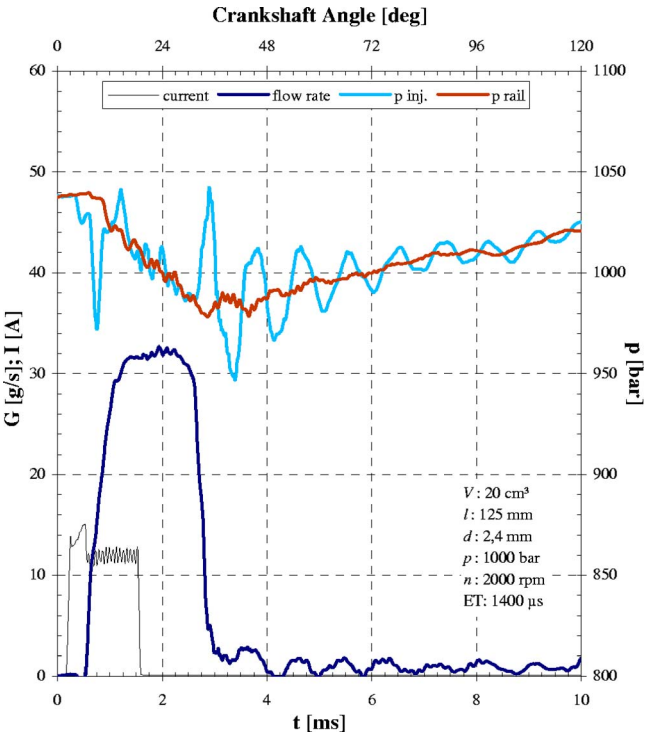

Fig. 9 Pressure, flow rate, and current time histories for ET =1400 μs

$$d\rho = \rho \frac{du}{a} \tag{2}$$

The momentum balance for the control volume yields

$$(\rho + d\rho)(a - du)^2 A - \rho a^2 A = -A dp \tag{3}$$

and thus the pressure rise results:

$$dp = 2\rho a du - a^2 d\rho \tag{4}$$

Combining Eqs. (2) and (4), it is possible to evaluate the velocity change due to the pressure wave:

$$du = \frac{dp}{\rho a} \tag{5}$$

The volume and mass flow rates are then easily calculated by a numerical integration:

$$Q(t) = A \int_0^t du \qquad G(t) = A \int_0^t \rho du \tag{6}$$

Results and Discussion

Single Injection. The system performance was investigated first by a careful analysis of dynamic phenomena occurring for a single injection. Figure 9, which refers to an energizing time (ET) of 1400 μs and to a rail-pressure level of 1000 bars, shows the system behavior during and after the injection event, in terms of rail pressure, injector inlet pressure, injected mass flow rate, and electrical current. The flow-rate fluctuations that appear after the injection event are due to wave reflections at the piezotransducer seat and at the injector tip adapter.

The rail-pressure drop, due to the injector opening, and the pipe-pressure rise induced by its closure are easily recognizable in the figure, which also makes clear that the rail pressure is not constant, as is taken in Ref. [4] instead, but undergoes a reduction of about 50 bars under these conditions. Moreover, examining the current and flow-rate patterns, one can infer that the injection is

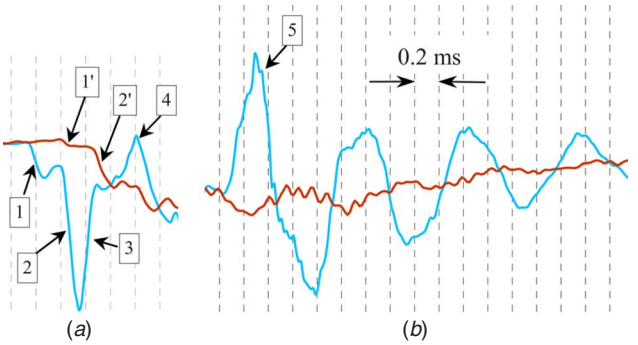

Fig. 10 Pressure waves (*a*) at the start and (*b*) at the end of injection

delayed and is longer than the current signal, whose duration on the contrary is almost coincident with the pilot valve opening time, due to the fast dynamic response of this valve [9].

By a thorough examination of the pressure time histories in Fig. 10, which amplifies pressure signal portions of Fig. 9, it is possible to recognize several interesting phenomena that occur within the injection system soon after the ECU has started the current signal to the electroinjector. The dashed vertical lines visible in this figure are set at intervals of 0.2 ms.

The pressure drop at the injector inlet, marked with 1 in Fig. 10, can be ascribed to the rarefaction wave set off by the sudden opening of the pilot valve. In fact, it is clear from this figure that such pressure drop takes place immediately after the current flows through the solenoid. The rarefaction wave has also effect on the rail pressure, which undergoes a slight drop, marked with 1′ in the figure, occurring about 0.2 ms later than that at the injector inlet. Such a delay is due to the finite propagation speed of the rarefaction wave.

After the opening of the pilot valve, the pressure in the valve control chamber (Fig. 4) rapidly decreases, and thus the nozzle needle starts moving upward, causing a flow rate to be discharged from the injector (Fig. 9). These events trigger another rarefaction wave, which starts at the needle seat and travels upward. Its effects are visible in Fig. 10(*a*) as pressure drops marked with 2 (on the inlet pressure signal) and with 2′ (on the rail-pressure trace).

When this rarefaction wave arrives at the rail, it is reflected as a compression wave, which aims at restoring the original pipe pressure. Such a compression wave reaches the injector inlet and determines a pressure rise, marked as 4 in Fig. 10(*a*). In fact, it is evident that the time delay between 2 and 2′ is the same as between 2′ and 4.

Therefore, the pressure rise marked as 3 must have nothing to do with the rail. In fact, as soon as the needle lift approaches its maximum value, there is no more rarefaction generated, but on the contrary the nozzle orifices determine a flow restriction and thus cause a compression wave to start from the nozzle and move upward. Hence, the pressure rise marked with 3 has to be associated to this latter compression wave [9]. This statement will also be confirmed in the following section, where the effects of two different nozzles (Minisac and VCO) will be compared.

At the end of injection, the needle closure creates a water-hammer effect, so that yet another compression wave arises at the nozzle and travels upward. This event is visible in Fig. 10(*b*) as the pressure peak marked with 5. From now on, the system is completely closed (both the pilot valve and the needle valve are closed) and therefore this compression wave, being reflected in turn by the rail and by the needle, produces the oscillating behavior evident in Figs. 10(*b*) and 9.

It should be pointed out that the presence of all the events shown in Fig. 10(*a*) does not depend on the injection duration (and thus on ET), because these take place whenever the pilot and the needle valves open. On the other hand, the water-hammer

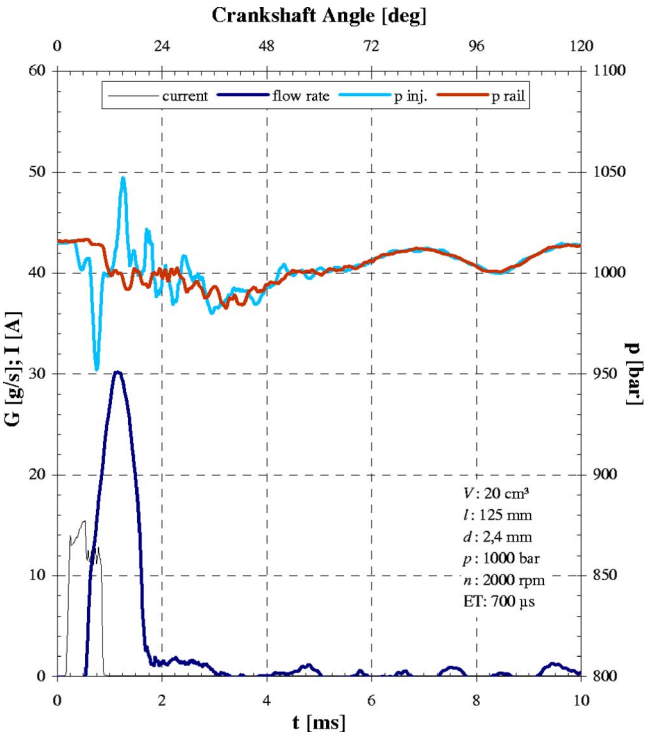

Fig. 11 System response for ET=700 μs

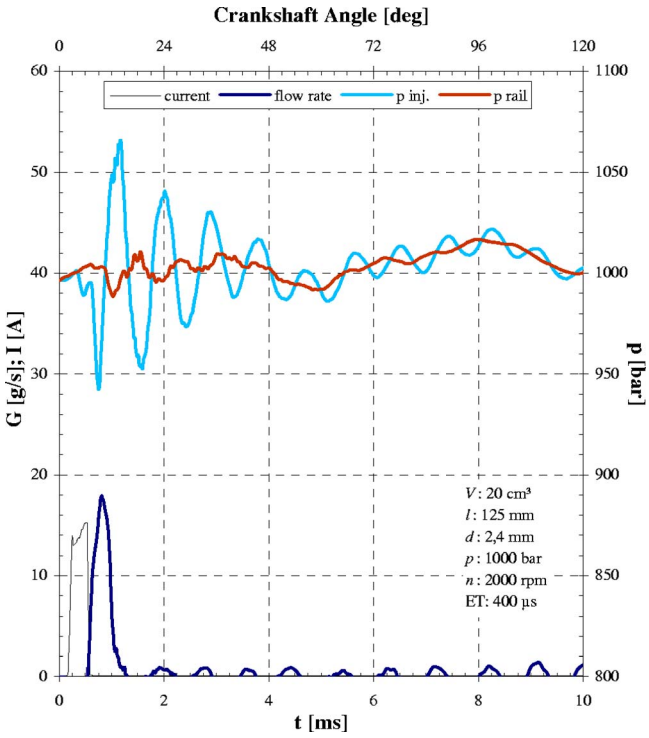

Fig. 12 System response for ET=400 μs

event (5) evidenced in Fig. 10(*b*) is obviously dependent on ET, because it takes place when the needle closes. Therefore, for smaller ET, the time interval between the two pressure peaks marked with 4 and 5 in Fig. 10 becomes smaller as well. As a consequence, both Peak 5 and the resulting oscillations have an amplitude that depends on the ET due to the pressure-wave interactions (which can take place with amplifying or damping effects). The amplitude generally grows with ET (Figs. 9 and 11). Obviously, the hydraulic shear resistances that are present in the system progressively damp the induced oscillations, so that these can disappear before the next injection cycle (Fig. 11).

Figures 11 and 12 show the system response to ETs of 700 and 400 μs, respectively, to highlight how markedly the oscillation amplitude can be influenced by the injection duration. In particular, for small injected quantities (Fig. 12), typical of pilot injections, the oscillations can be remarkable when a resonance occurs, with the merging of Peaks 4 and 5 (Fig. 10). These will affect the subsequent injection, in the case of multiple injections.

Multiple Injections. When, for example, a pilot and a main injection are performed, the pressure oscillations triggered by the pilot injection can have a sensible influence on the subsequent main injection. Figure 13 illustrates the injected volumes for pilot and main injections as functions of the dwell time (DT), that is, the time interval between the end of the pilot-injection current signal and the start of the main-injection current signal:

$$\mathrm{DT} = \left| \frac{\mathrm{SOI}_{\mathrm{main}} - \mathrm{SOI}_{\mathrm{pil}}}{\omega} \right| - \mathrm{ET}_{\mathrm{pil}} \tag{7}$$

This temporal interval is directly related, through the engine speed and the pilot ET, to the starts of the pilot and main injections (i.e., to the instants when the current pulses to the solenoid start), which are expressed as crank angles before top dead center. The test results shown in Fig. 13 were obtained keeping $\mathrm{SOI}_{\mathrm{main}}$ constant at 0 deg and getting the pilot and main injections gradually closer by increasing $|\mathrm{SOI}_{\mathrm{pil}}|$.

It is evident from Fig. 13 that V_{pil} keeps fairly constant with DT, whereas V_{main} shows sensible oscillations as DT varies. Such phenomenon is explained by the pressure oscillations described in the previous paragraph. In particular, it is not surprising that if the main injection takes place when the "opening pressure" (that is, the injection pressure when the needle starts opening) reaches a maximum, the corresponding injected volume will be maximum, and vice versa. The inlet pressure and the injection pressure are closely related, as can be inferred by experimental results, by way of identifying the opening pressure on the inlet pressure time history, taking in mind that there is a slight delay mainly due to the length of the injector drilled passage [9].

In fact, Fig. 14 illustrates the flow processes occurring in the injection system for a DT of 1825 μs, which corresponds to a maximum injected volume (Fig. 13). The arrow in the picture indicates a maximum of pressure at the injector inlet, virtually corresponding to a maximum of pressure in the injector delivery chamber, when the needle valve starts opening. Such a pressure indicates what is intended as nozzle opening pressure, which in this case is very close to a maximum.

On the other hand, Fig. 15 illustrates the system response when the DT is 2300 μs, i.e., a value corresponding to a minimum main injected volume (Fig. 13). In this case, the main injection starts when the opening pressure is around a minimum, as is pointed out by the arrow in Fig. 15.

It is interesting to more closely analyze the relation between the opening pressure and the injected volume. One spontaneous preliminary hypothesis to establish such a relation might be that higher opening pressures imply higher injection pressures along the whole injection event, which would obviously result in higher injected volumes. However, Figs. 14–16, together with other test results, point out that the difference between pressure time histories during the main injection, resulting from the value of the opening pressure, is not much significant, mean pressure being almost the same during injection, and hence such a difference must not be taken as responsible for the different injected volumes. Additional considerations can be drawn from Fig. 16, which compare the mass flow rates for the two main injections shown in Figs. 14 and 15. The nozzle opening delay with respect to the current signal is clearly dependent on the opening pressure: The

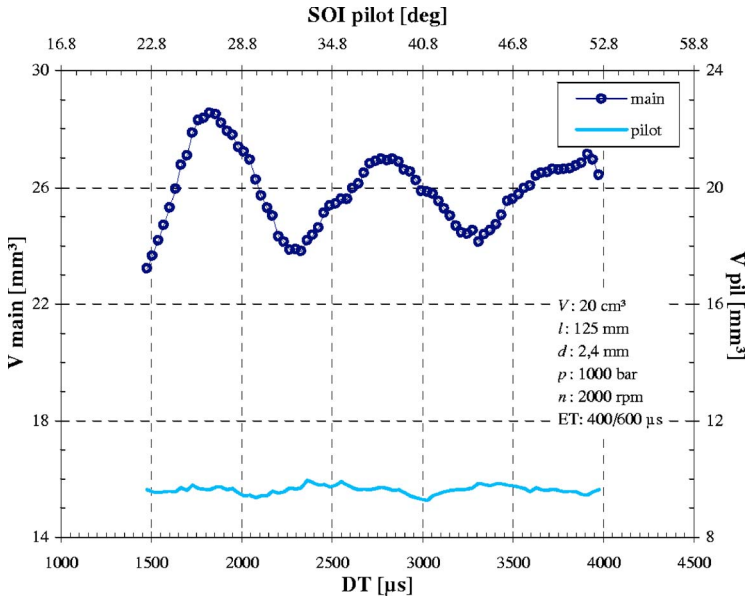

Fig. 13 Injected volumes for pilot and main injections at p_{rail}=1000 bars

higher this pressure is, the lower the delay is. In fact, it results that for DT of 1825 μs (maximum opening pressure), the delay is approximately 350 μs, whereas for DT of 2300 μs (minimum opening pressure), the delay is approximately 380 μs. Such a difference can be explained by considering that if the opening pressure is higher, the force resulting from the pressure actions on the needle valve and control plunger at the nozzle delivery chamber, and within the valve control chamber reaches more quickly the value that determines the nozzle opening. However, this is not the only difference notable in Fig. 16; it is also evident that for the higher opening pressure, the nozzle closes later. A reason for this must be sought in the control chamber dynamics, possibly by means of an accurate numerical model [9], as done in Ref. [13], because experimental data on such a dynamics are very difficult, if not almost impossible, to be acquired.

Therefore, the combined effects of a shorter nozzle opening delay and a retarded nozzle closure result in an injection duration that is much longer in the case of the higher opening pressure, so that the true reason for the different injected volumes has to be found in injection durations rather than in injection pressures. Actually, Fig. 16 also shows that the flow rate can reach higher maximum values for lower opening pressures. This is true when

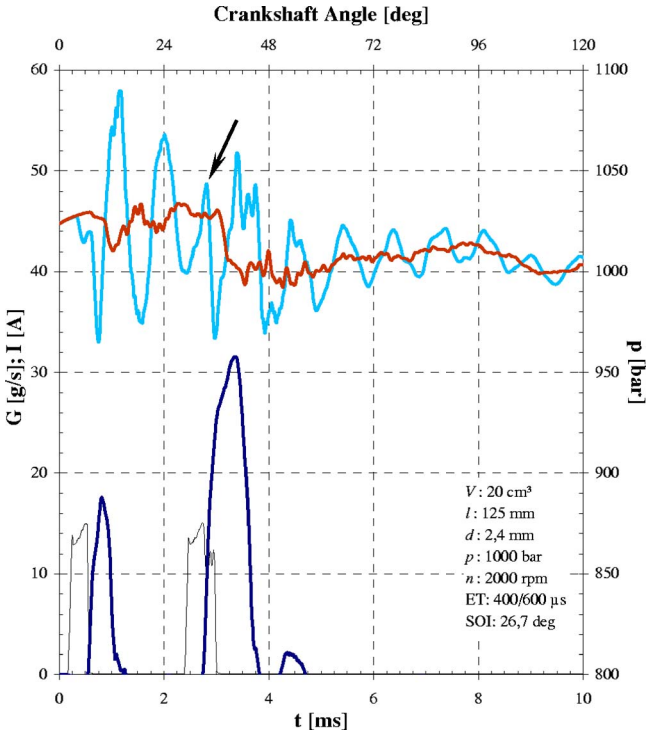

Fig. 14 System response at p_{rail}=1000 bars, ET=400/600 μs, and DT=1825 μs

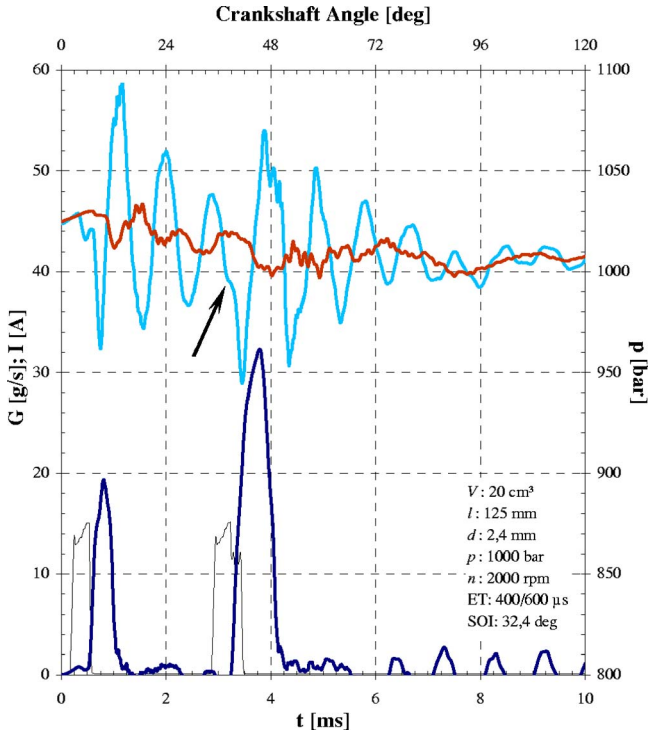

Fig. 15 System response at p_{rail}=1000 bars, ET=400/600 μs, and DT=2300 μs

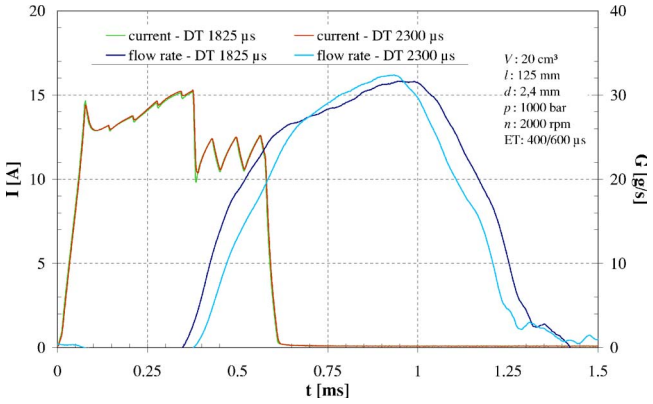

Fig. 16 Comparison between injected flow rates for different DT and same ET

the ET is not too small, i.e., longer than 500 μs, as is usually the case for main injections. Otherwise, if ET is shorter than such a value, then also the maximum injected flow rate depends on the opening injection pressure; however, this is a more common case for pilot or postinjections.

In summary, the main variable affecting the injected volume is the nozzle opening pressure, which exerts its influence through the injection duration. This also explains why the inlet pressure oscillations after injections in Figs. 14 and 15 and the injected volume oscillations in Fig. 13 share the same frequency, i.e., nearly 0.85 ms for the hydraulic-system layout under investigation.

All the above remarks hold for various injection conditions. For example, with p_{rail}=1250 bars and ET of 400 and 900 μs for pilot and main injections, respectively, the injected volume varies as a function of DT according to Fig. 17. Besides, with the same p_{rail}=1250 bars, Fig. 18 shows the system behavior for DT =1755 μs, corresponding to a maximum main injected volume, whereas Fig. 19 presents the results for DT=2230 μs, which corresponds to a minimum main injected volume.

Once again, from a careful examination of the injected flow-rate time history, it can be deduced that high opening pressures give rise to high injected volumes through an increase of the injection duration by both advancing the nozzle opening and delaying its closure (Fig. 20).

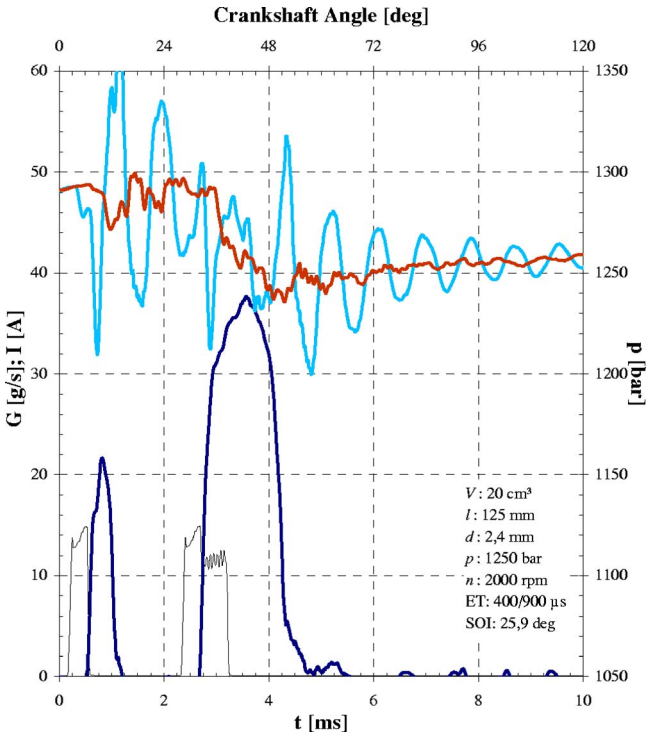

Fig. 18 System response at p_{rail}=1250 bars, ET=400/900 μs, and DT=1755 μs

Moreover, observing the differences between the flow-rate patterns in Fig. 20, it is evident that the injection pressure, which directly shapes the injected flow rate, has an oscillating behavior conforming to that of the inlet pressure.

Lumped Parameter Model. The aforementioned oscillating behavior can be interpreted by a lumped parameter model of the subsystem including rail, inlet pipe, and injector. These components can be thought of as being made up of hydraulic capacitances and inductances. The hydraulic resistances that can be as-

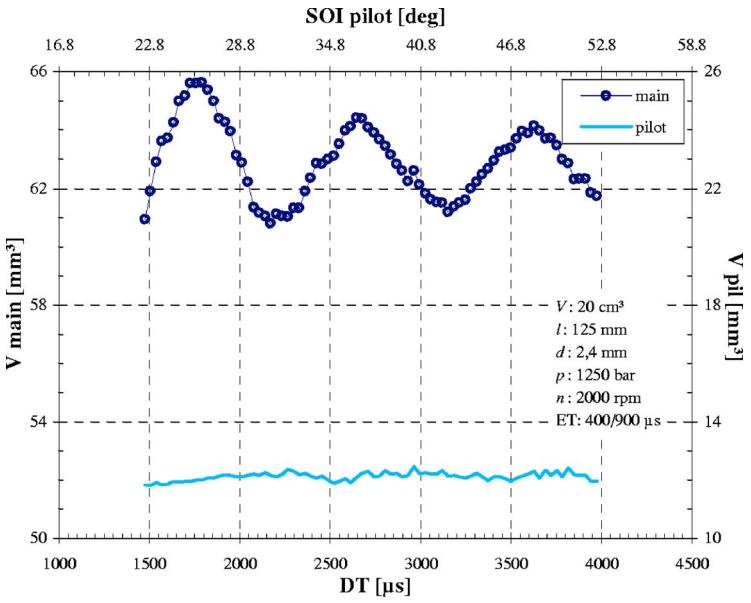

Fig. 17 Injected volumes of pilot and main injections at p_{rail}=1250 bars

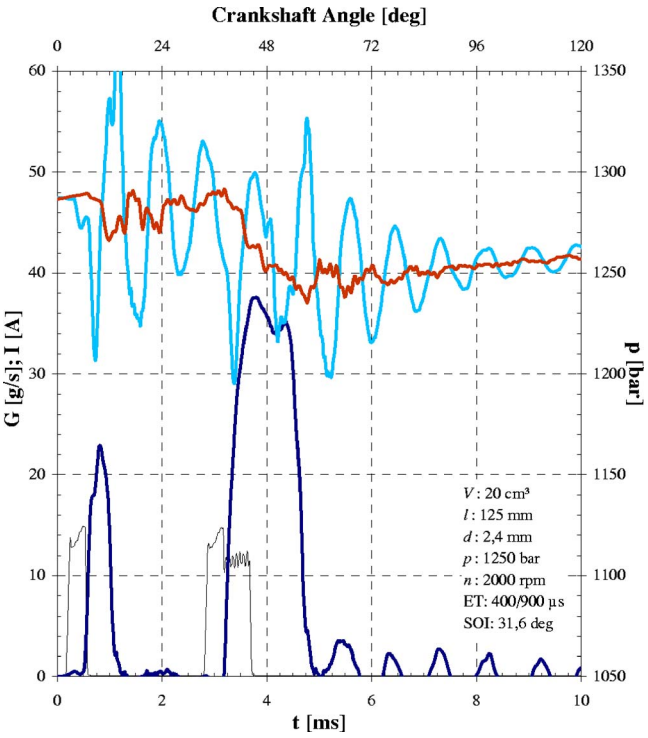

Fig. 19 System response at p_{rail}=1250 bars, ET=400/900 μs, and DT=2230 μs

sociated to the distributed viscous friction losses were neglected because the model has the main purpose of analyzing the system circular frequencies and these are scarcely influenced by the hydraulic resistances.

The system can be schematically described as in Fig. 21, where the rail is connected to the injector through the inlet pipe, which ends at a volume including the valve control chamber and filter volume effects. The feed pipe (marked with 10 in Fig. 4) starts from this volume and terminates at the delivery chamber (11 in Fig. 4). The model does not take any injected mass flow rate into account, because its purpose is to characterize the free oscillations taking place after the needle closure.

The symbols used in Fig. 21 have the following meanings. C_0 is the rail hydraulic capacitance, C_1 is the hydraulic capacitance of the inlet-pipe and upstream-injector volumes, C_2 is the feed pipe and delivery-chamber hydraulic capacitance, G_{01} is the mass flow rate through the inlet pipe, G_{12} is the mass flow rate through the

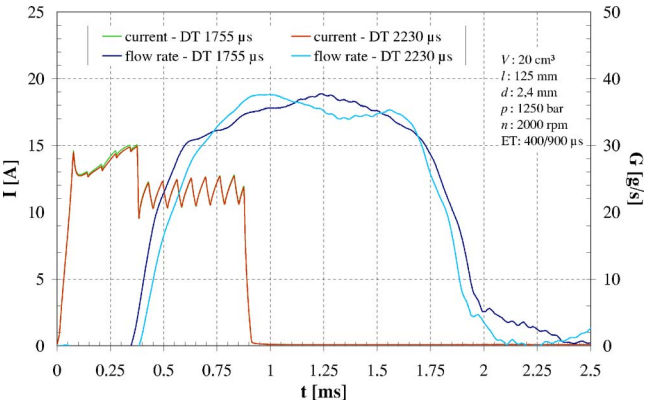

Fig. 20 Comparison between main injected flow rates at p_{rail} =1250 bars

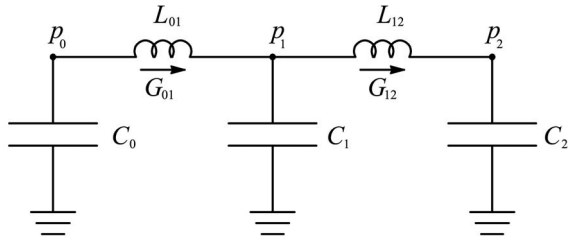

Fig. 21 Rail-pipe-injector *LC* model

feed pipe, L_{01} is the inlet-pipe hydraulic inductance, L_{12} is the feed-pipe hydraulic inductance, p_0 is the rail pressure, p_1 is the pressure upstream of the feed pipe, and p_2 is the delivery-chamber pressure.

The hydraulic capacitance and inductance are defined as

$$C = \frac{V}{a^2} \tag{8}$$

$$L = \frac{l}{A} \tag{9}$$

It should be pointed out that the volumes V, which give rise to hydraulic capacitances, could include both chambers, i.e., zero-dimensional elements, and pipes, that is, one-dimensional elements, which are thus reduced to zero-dimensional elements by spatial integration.

The model equations for the capacitance discharge are

$$\frac{dp_0}{dt} = -\frac{G_{01}}{C_0} \quad \frac{dp_1}{dt} = \frac{G_{01} - G_{12}}{C_1} \quad \frac{dp_2}{dt} = \frac{G_{12}}{C_2} \tag{10}$$

and the inductance equations write

$$L_{01}\frac{dG_{01}}{dt} = p_0 - p_1 \quad L_{12}\frac{dG_{12}}{dt} = p_1 - p_2 \tag{11}$$

By taking the time derivative of Eq. (11), and combining with Eq. (10), one obtains the following two-degree of freedom equation system, whose unknowns are the mass flow rates:

$$L_{01}\frac{d^2G_{01}}{dt} + \left(\frac{1}{C_0} + \frac{1}{C_1}\right)G_{01} - \frac{1}{C_1}G_{12} = 0$$

$$L_{12}\frac{d^2G_{12}}{dt} - \frac{1}{C_1}G_{01} + \left(\frac{1}{C_1} + \frac{1}{C_2}\right)G_{12} = 0 \tag{12}$$

This equation system can be put in matrix form as follows:

$$\mathbf{L}\ddot{\mathbf{G}} + \mathbf{K}\mathbf{G} = \mathbf{0} \tag{13}$$

where

$$\mathbf{L} = \begin{bmatrix} L_{01} & 0 \\ 0 & L_{12} \end{bmatrix} \tag{14}$$

$$\mathbf{K} = \begin{bmatrix} (1/C_0) + (1/C_1) & -1/C_1 \\ -1/C_1 & (1/C_1) + (1/C_2) \end{bmatrix} \tag{15}$$

$$\mathbf{G} = \begin{bmatrix} G_{01} \\ G_{12} \end{bmatrix} \tag{16}$$

The circular frequencies are given by the eigenvalues of the matrix $\mathbf{L}^{-1}\mathbf{K}$:

$$\mathbf{L}^{-1}\mathbf{K} = \begin{bmatrix} 1/L_{01}((1/C_0) + (1/C_1)) & -1/C_1L_{01} \\ -1/C_1L_{12} & 1/L_{12}((1/C_1) + (1/C_2)) \end{bmatrix} \tag{17}$$

which can also be written as

$$\mathbf{L}^{-1}\mathbf{K} = \begin{bmatrix} \omega_{01}^2 & -1/C_1L_{01} \\ -1/C_1L_{12} & \omega_{12}^2 \end{bmatrix} \tag{18}$$

where ω_{01} is the circular frequency associated to the system that includes rail, inlet pipe, and injector upstream volumes, and ω_{12} is the circular frequency of the system containing injector upstream volumes, feed pipe, and delivery chamber.

The resulting circular frequencies for the whole system are

$$\omega^2 = \frac{\omega_{01}^2 + \omega_{12}^2}{2} \mp \sqrt{\left(\frac{\omega_{01}^2 + \omega_{12}^2}{2}\right)^2 - \frac{1}{L_{01}L_{12}}\left(\frac{C_0 + C_1 + C_2}{C_0C_1C_2}\right)} \tag{19}$$

In this case, only the lower frequency has to be considered because it refers to the first system harmonic, which is consistent with the observed free pressure oscillations.

The period of these fluctuations is given by

$$T = \frac{2\pi}{\omega} \tag{20}$$

The physical and geometrical features of the CR system under investigation determine the following model parameters:

$$C_0 = 6.92 \times 10^{-12}\ \text{m s}^2$$

$$C_1 = 4.46 \times 10^{-13}\ \text{m s}^2$$

$$C_2 = 1.29 \times 10^{-13}\ \text{m s}^2$$

$$L_{01} = 27{,}631\ \text{m}^{-1}$$

$$L_{12} = 31{,}812\ \text{m}^{-1}$$

$$T = 0.8\ \text{ms}$$

The theoretical period of 0.8 ms thus obtained has to be compared with the experimentally evaluated period of nearly 0.85 ms (Fig. 10), which is a fairly good agreement, taking the simplicity of the proposed model into account. Therefore, this model can be used as a predictive tool for evaluating the system oscillation frequency if any geometrical quantity is modified. This is useful in order to know, for each given layout, which ET give rise to hydraulic resonance conditions in the nozzle. Hydraulic resonance occurs when the needle closes as soon as the compression wave, due to the rail reflection of the injection-induced depression wave, reaches the nozzle. Thus, the water hammer due to injector closure and the compression wave coming from the rail are in phase, so as to produce very large oscillations in the nozzle. The time required to a pressure wave to travel from the nozzle to the rail and back is equal to half the free oscillation period T for the considered layout. Therefore, for an assigned system configuration, the solenoid ET, which cause resonance, are around the value $T/2$. For each hydraulic circuit configuration, the ET which produce resonance in the nozzle should be better avoided: For the pilot shot, when pilot and main injections occur and for the main shot, when main and postpulses are involved.

Dynamic Interactions Between Injectors. The proposed model allows one to schematize the system consisting of rail, inlet pipe, and injector as a dynamic system with a main frequency that can be estimated by Eq. (19). Such a system can be subjected to resonating conditions if it is excited by other systems with its same frequency.

Figure 22 plots the pressure at the inlet of Injector 1 and in the rail for single (Fig. 22(*a*)) and multiple (Fig. 22(*b*)) injection events in a complete crankshaft cycle. The operation parameters are $p_{\text{rail}}=1000$ bars and $n=2000$ rpm in both cases; for the single injection ET=1000 μs; for the pilot and main injections ET_{pil} =400 μs and $\text{ET}_{\text{main}}=900$ μs, DT=2300 μs. In this latter case, a sensible interaction between injectors can be observed.

Both figures show how the inlet pressure for Injector 1 oscillates very sensibly, as seen before, when it is the same Injector 1 to operate (first injection cycle on the left side in Fig. 22). But also, when other injectors are operating, the pressure at the inlet of Injector 1 undergoes significant fluctuations. This is explained by the fact that each injector gives rise to a dynamic excitation on the rail with a frequency ω, which in turn excites other injectors with the same frequency. If all the inlet-pipe injector subsystems share the same geometrical features, their frequency is the same and therefore the interactions between different injectors are of particular importance.

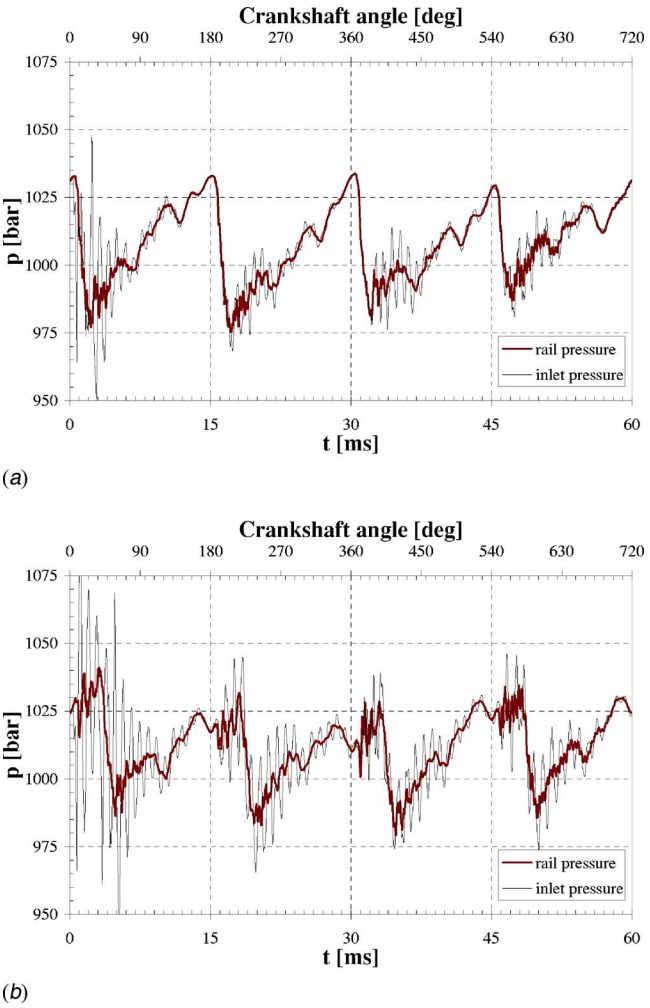

Fig. 22 Pressure distributions at Injector 1 inlet and in the rail: (*a*) main injection only and (*b*) pilot and main injections

Figure 22(*a*) shows that the interaction of other injectors with Injector 1 should not cause disturbances when single injections occur, at least for the present system hydraulic layout, because when Injector 1 is working, the excited pressure fluctuations caused by other injectors are completely damped at injection start. On the other hand, it is evident in Fig. 22(*b*) that adding a pilot injection extends the oscillation duration, which can also be influenced by geometrical modifications, and therefore it is possible to predict that, for some system configurations, injected volume fluctuations could be present also for pilot injections, due to pressure oscillations induced by previous injectors.

Effects of Rail Pressure and Engine Speed on Multiple Injections. The proposed zero-dimensional model gives an insight also into the possible effects of working parameters on the system multiple-injection performance.

The first of these parameters to be taken into account is the rail

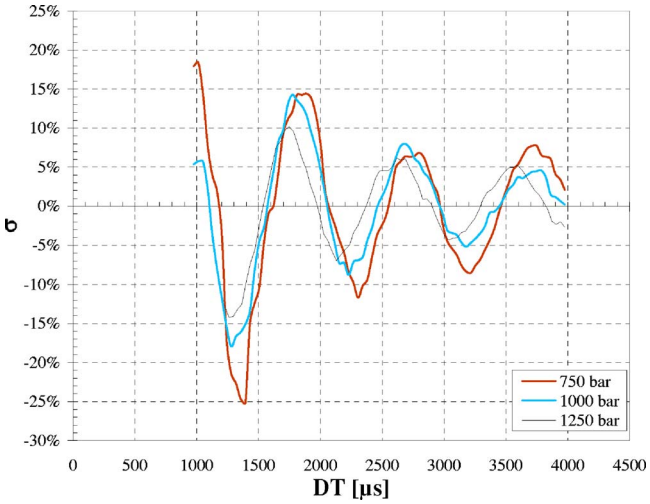

Fig. 23 Main-injection volume deviations for different rail pressures

pressure. The system circular frequencies, from Eq. (19), are slightly modified by pressure values, because these affect the speed of sound a, which is present in hydraulic capacitance definition, Eq. (8). On the other hand, the hydraulic inductance is independent of the pressure level, but depends only on the system geometrical features.

Figure 23 shows the injected volume variations on the main of a double injection, as a function of DT between the pilot and the main injection, for different rail-pressure levels. In this case, operation parameters are $n=2000$ rpm, $ET_{pil}=400$ μs, and $ET_{main}=600$ μs. The main injected volume variations are reported as deviation from its mean value:

$$\sigma = \frac{V_{main} - \bar{V}_{main}}{V_{main}} \times 100 \tag{21}$$

where V_{main} is the main injected volume for each DT and $\bar{V}_{main}$ is its mean value.

It is evident from Fig. 23 that the period T of fluctuations is slightly influenced by the rail pressure, and, in particular, T is smaller for higher pressures. This is consistent with the fact that higher pressures imply higher wave propagation speed.

Figure 24 plots the main injected volume deviation σ versus

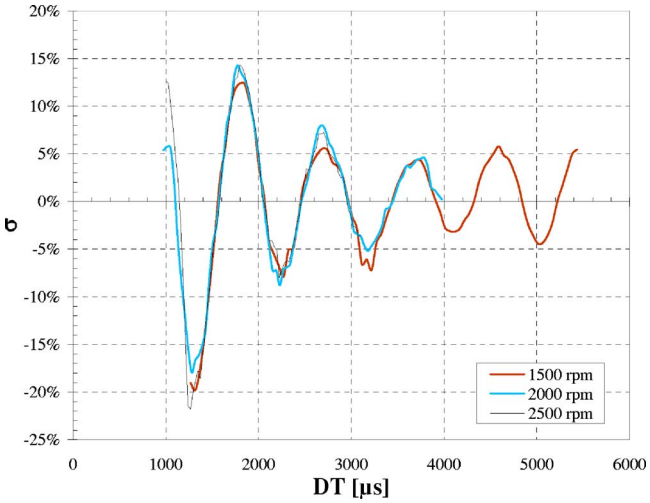

Fig. 24 Main-injection volume deviations for different engine speeds

DT, for pilot and main injections with the same ET as in Fig. 23 and $p_{rail}=1000$ bars, at different engine speeds. It is evident from the figure that the oscillations of the main injected volume are practically independent of the engine speed, because their origin resides in time-dependent phenomena occurring in the system, i.e., wave propagation, and therefore the engine speed is not an influencing factor to be taken into account. However, the same period T turns into different crank-angle intervals if the engine speed varies. Consequently, the main injected volume fluctuations have different periods in the crankshaft-angle domain, whereas they have the same period in the time domain.

Dynamics of Mechanical Mobile Elements. The geometrical features of the hydraulic circuit and the dynamic parameters of the injector mobile elements should be selected so as to avoid also mechanical resonance, that is, high oscillations of both control plunger (9 in Fig. 4) and ball valve (5 in Fig. 4), induced by pressure waves in the injection system. Since the damping effect is low in these mechanical systems (the damping factors are less than 0.3, i.e., subcritical), a pressure forcing term with a frequency close to the mobile-element natural frequencies can produce dynamical instabilities in their movement. Thus, it is important in system design to assure that the hydraulic-system natural frequencies are higher than those of the mechanical elements, as far as possible. Calculations with the homemade numerical model developed in Ref. [9] showed that the control plunger stays integral with the needle during both its raising and lowering. This is due to the fact that the control plunger is assembled inside a chamber containing fuel at tank pressure, so that both the needle and the control piston are forced to each other by the pressure actions working on the control-plunger top in the needle-valve control chamber and on the needle side in the delivery chamber. Therefore, the fundamental natural-frequency value of the needle/control-plunger subsystem can be roughly estimated by the following expression for a one-degree of freedom mass-spring system:

$$\lambda = \frac{1}{2\pi}\sqrt{\frac{k_n}{m_n + m_{cp}}} = 250 \text{ Hz} \tag{22}$$

where m_n and m_{cp} are the masses of needle and control plunger, respectively, and k_n is the stiffness of the spring acting on the needle. As was verified, the mechanical natural frequency λ was lower than the hydraulic-circuit frequency, i.e., $1/T \approx 1175$ Hz and therefore no mechanical resonance phenomena occurred. In particular, the pressure-wave fluctuations turned into reduced fluctuation amplitude of the needle-lift temporal pattern.

The pilot valve is made up of two mobile elements, namely, the pin and the armature (or anchor). When the current excites the solenoid, the armature is attracted by the magnet drawing the pin, which is integral with it during the lifting. However, as soon as the pin element reaches the seat, the armature is allowed to travel with respect to the pin valve, so as to damp the counterblow of this element on the basement.

During virtually all the solenoid excitation time, the pin element is stationary at its maximum lift, that is, 40 μm, for the considered electroinjector setting. Therefore, only the armature can undergo mechanical resonance conditions, due to pressure waves, during its free oscillations with respect to the pin valve. The natural frequency of the armature is provided by

$$\lambda = \frac{1}{2\pi}\sqrt{\frac{k_a}{m_a}} = 310 \text{ Hz} \tag{23}$$

m_a being the mass of the armature and k_a the stiffness of the spring acting on the armature. Such a frequency results to be less than the hydraulic natural frequency. A better solution to further reduce the armature oscillations due to pressure waves, without significantly changing the system performance, could be attained by selecting values of the anchor spring stiffness and mass so as to further reduce the natural frequency in Eq. (23).

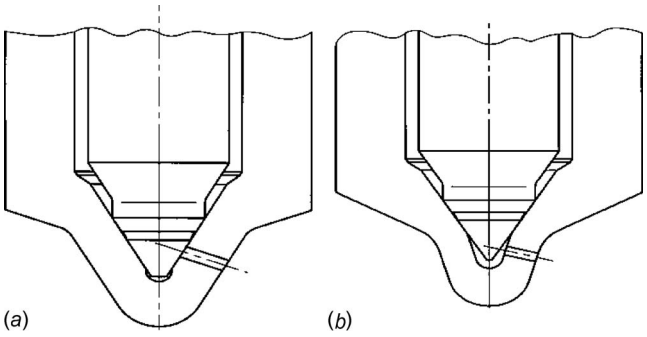

Fig. 25 (*a*) VCO- and (*b*) Minisac-nozzle geometries

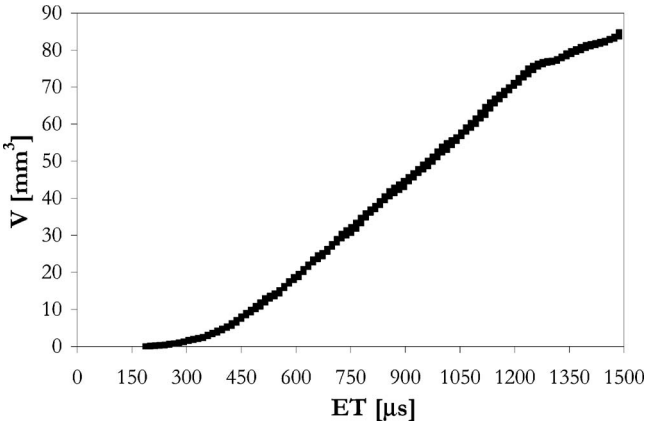

Fig. 27 Cycle-to-cycle variations: Minisac nozzle, p_{rail} =1000 bars, and n=2000 rpm

Nozzle Effects on System Dynamics. The nozzle geometry influence on CR injection system dynamic response was evaluated through a comparison between two different nozzles, namely, VCO (Fig. 25(*a*)) and Minisac (Fig. 25(*b*)); the two nozzles share the same number of holes, the same hole diameter, and the same maximum needle lift.

Figure 26 shows the effects of nozzle configuration on the injected flow rate (a) and the injector inlet pressure (b). The injection parameters are p_{rail}=1000 bars and ET=1500 μs.

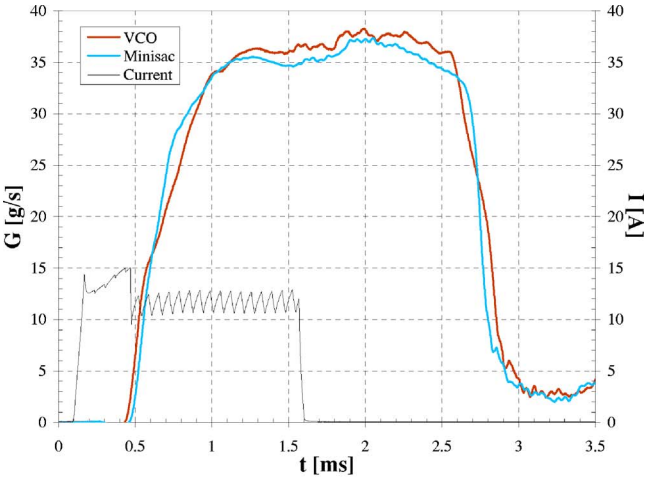

(*a*)

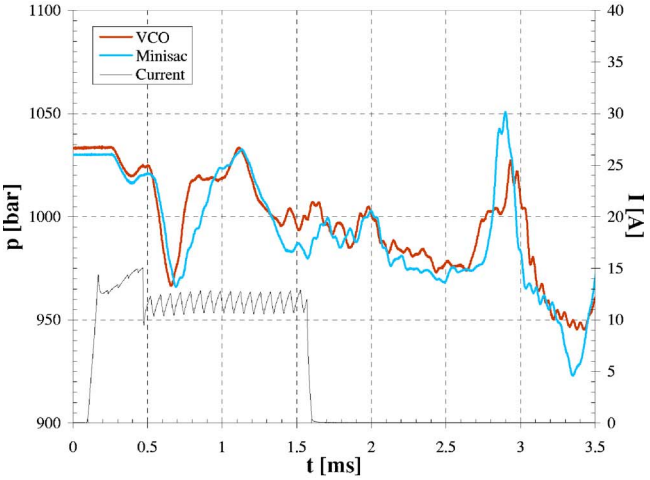

(*b*)

Fig. 26 VCO versus Minisac nozzle: (*a*) injected flow rate and (*b*) inlet pressure

The Minisac nozzle determines a regular flow rate in both the opening and closing phases, whereas the VCO injected flow rate presents a rather uneven pattern in these phases, due to the interference between nozzle tip and injector holes.

Perhaps, more surprising is the sensible influence of nozzle geometry on internal system dynamics. Figure 26(*b*) shows the differences in inlet pressure distributions between VCO and Minisac nozzles. Nevertheless, it should be kept in mind that the nozzle determines the fuel-injection-system boundary condition, so that different behaviors not only in the injected flow rates but also in other system variables are to be expected. In particular, the pressure rise marked as 3 in Fig. 10(*a*) was explained as the result of a compression wave originating from the nozzle. Figure 26(*b*) further substantiates such an explanation, by taking the different time patterns of the pressure rise into account, there. On the other hand, the subsequent pressure rise, marked as 4 in Fig. 10(*a*), does not depend on the nozzle geometry. In fact, as already mentioned, its origin has to be found in the expansion wave due to flow start (marked as 2) and its reflection at the rail.

Another influence of nozzle geometry can be inferred from the pressure peak due to the nozzle closure (Peak 5 in Fig. 10(*b*)). The Minisac nozzle produces a neat and fast closure (as is also shown in Fig. 26(*a*)), and, as a consequence, its pressure peak is rather high with respect to that of VCO geometry. The pressure oscillations arising from the nozzle closing are therefore higher in the case of Minisac-nozzle geometry, and thus in this case, the injected volume fluctuations for multiple injections can be expected to be more pronounced.

Random Cycle-To-Cycle Variations. Experimental tests were made for assessing cycle-to-cycle variations in the injection-system performance. These are due to stochastic dispersions in the whole system mechanics and fluid dynamics that are difficult to separately assess. For a Minisac-nozzle injector, Fig. 27 reports repeated measurement sets of a single injection characteristic. The random fluctuations of V kept less than ± 1.0 mm^3, i.e., relatively low also in consideration of the measurement accuracy (± 0.6 mm^3). A higher dispersion in the injected fuel volume occurred at low nominal rail pressure and engine speed, as shown in Fig. 28. Nevertheless, the cycle-to-cycle variations in this figure are lower than ± 1.3 mm^3.

Figure 29 plots repeated measurement sets of the main fuel volume fluctuations in a pilot-main injection profile (ET_{pil} of 400 μs, ET_{main} of 600 μs, and nominal rail pressure of 1000 bars) when the SOI of the pilot varies. The cycle-to-cycle variation of V with respect to the mean line interpolating the distribution in the figure appears to be low, i.e., comparable to the precision of EMI. This supports the fact that the oscillating behavior of V versus

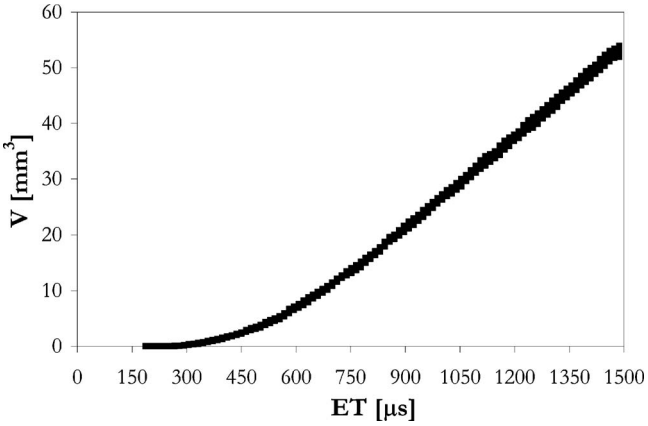

Fig. 28 Cycle-to-cycle variations: Minisac nozzle, p_{rail} =500 bars, and n=1500 rpm

SOI_{pilot} is not of stochastic nature but has a deterministic explanation, based on the system pressure-wave dynamics, as illustrated above. For the same system, but with a VCO nozzle, Fig. 30 plots the injection characteristics taken at p_{rail}=500 bars and n =1500 rpm in 50 measurement sets. This number of tests was the same as in Figs. 27–29, and was shown to be statistically significant. A slightly higher dispersion was observed at the largest ET values, namely, ± 1.8 mm^3, in comparison to Fig. 28.

With reference to the dispersion in performance of injector production, manufacturer tolerances guarantee that discrepancies in fueling between different injectors do not exceed the bounds reported in Table 1, which refer to Multijet electroinjectors of the latest solenoid generation. In general, the production dispersion of VCO-nozzle injectors is higher than that of Minisac-nozzle injectors. In fact, in VCO nozzles, it is the needle to discover the holes during the initial stage of its lift. Therefore, in these injector types, the position of the needle at rest has a significant influence on the injection flow-rate pattern through the overall hole uncovering stage and, in general, during the nozzle opening and closure phases. Since the needle position at rest undergoes stochastic variations from nozzle to nozzle due to production tolerances, significant performance dispersion can occur among distinct VCO-nozzle injectors.

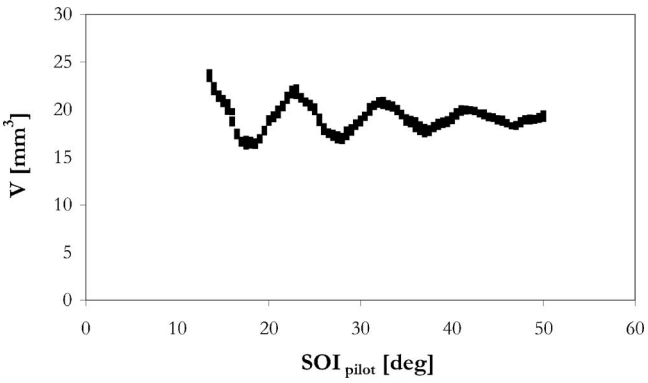

Fig. 29 Cycle-to-cycle variations: Minisac nozzle, p_{rail} =1000 bars, ET=400/600 μs, and n=1500 rpm

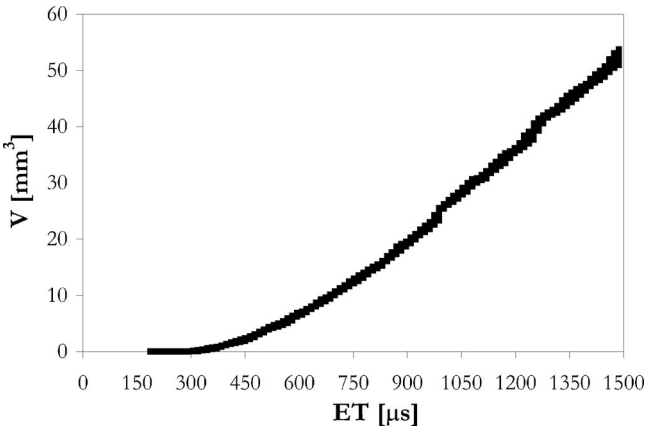

Fig. 30 Cycle-to-cycle variations: VCO nozzle, p_{rail}=500 bars, and n=1500 rpm

Table 1 Injector production tolerances

p_{rail} (bar)	ET (μS)	Acceptable dispersion (mm^3)
1400	840	±4.0
800	640	±2.4
800	250	±1.2
300	710	±2.4

Conclusion

An in-depth experimental investigation of CR injection-system dynamics has been performed, with particular emphasis on multiple-injection events.

The highly unsteady wave propagation phenomena taking place in the system play a major role in a proper understanding of important injection-system characteristics, such as injected volume metering and control. In fact, injection-induced pressure oscillations cause a deterministic dependence of injected volume on DT between consecutive injection shots.

In order to obtain a deeper insight into the cause and effect relationship between the injection-triggered pressure-oscillation frequency and the system hydraulic layout, an effective simple zero-dimensional mathematical model was proposed, allowing the characterization of the rail-pipe-injector subsystem natural frequency. This model was shown to be a reliable tool to better understand the CR dynamic behavior, providing a physical interpretation of injected volume oscillations, their dependence on the operating conditions, in addition to possible dynamic interactions between different injectors. It could also give an insight into the influence of geometrical features, such as pipe diameter to length ratio, on system performance. Experimental-theoretical analysis of system layout effects on multiple-injection performance is currently in progress for their optimization.

An analytical relation between the system free oscillation period under a specified layout and the ET that determines hydraulic resonance in the nozzle was provided. Such ET value should be avoided for the pilot shot when pilot and main injections are performed for reducing disturbances on the injected volumes. Furthermore, the hydraulic frequency was compared to the natural frequencies of the mobile elements in order to identify possible mechanical resonance conditions. For the system under investigation, the natural frequency of mobile elements was shown to be lower than the hydraulic circuit one at all considered working conditions and thus the pressure-wave excited fluctuations gave rise to minor oscillation amplitude of valve lift temporal distributions.

From the analysis of system behavior with different nozzle geometries, such as VCO and Minisac, a clear influence of the nozzle configuration reflects not only on the injection flow rate but also on the whole injector fluid-dynamic response and thus on multiple-injection performance.

Finally, experimental tests were carried out to assess cycle-to-cycle variations in the injection-system performance. The stochastic cyclic dispersion is generally small and increases by lowering rail pressure and engine speed.

Acknowledgment

Financial support to this research was provided by Ministry of University and Research (MUR) under COFIN'04 Project, by Fiat Research Center, and by FA-GM Powertrain. The authors would like to thank S. Canale, G. Bonetto, F. Guglielmo, and E. Rigon of Fiat Research Center for their invaluable technical assistance.

Nomenclature

a = speed of sound
A = pipe cross section
C = hydraulic capacitance
d = pipe diameter
DT = dwell time
ET = energizing time
G = injected mass flow rate
I = current
l = pipe length
L = hydraulic inductance
n = engine speed
p = pressure; rail nominal pressure
Q = injected volume flow rate
SOI = start of injection
t = time
T = free oscillation period
u = velocity
V = injected volume; volume
ρ = density
ω = circular frequency; engine speed

Subscripts

a; cp; n = armature; control plunger; needle
main = main injection
pil = pilot injection
rail = rail nominal pressure

References

[1] Stumpp, G., and Ricco, M., 1996, "Common Rail-An Attractive Fuel Injection System for Passenger Car DI Diesel Engines," SAE Paper No. 960870.
[2] Boehner, W., and Hummel, K., 1997, "Common Rail Injection System of Commercial Diesel Vehicles," SAE Paper No. 970345.
[3] Catania, A. E., Ferrari, A., Manno, M., Pellettieri, R., and Spessa, E., 2004, "Development, Setup and Equipment of a High Performance Diesel Injection-System Test Bench: Preliminary Experimental Results on the Dynamics of a CR System," *Proceedings of LIX ATI Congress*, Vol. 2, pp. 821–834, in Italian.
[4] Catalano, L. A., Tondolo, V. A., and Dadone, A., 2002, "Dynamic Rise of Pressure in the Common-Rail Fuel Injection System," SAE Paper No. 2002-01-0210.
[5] Henein, N. A., Lai, M.-C., Singh, I. P., Zhong, L., and Han, J., 2002, "Characteristics of a Common Rail Diesel Injection System Under Pilot and Post Injection Modes," SAE Paper No. 2002-01-0218.
[6] Bianchi, G. M., Falfari, S., Pelloni, P., Filicori, F., and Milani, M., 2002, "A Numerical and Experimental Study Towards Possible Improvements of Common Rail Injectors," SAE Paper No. 2002-01-0500.
[7] Mulemane, A., Han, J.-S., Lu, P.-H., Yonn, S.-J., and Lai, M.-C., 2004, "Modeling Dynamic Behavior of Diesel Fuel Injection Systems," SAE Paper No. 2004-01-0536.
[8] Torkzadeh, D. D., Kiencke, U., and Keppler, M., 2002, "Introduction of a New Non-Invasive Pressure Sensor for Common-Rail Systems," SAE Paper No. 2002-01-0842.
[9] Catania, A. E., Ferrari, A., and Manno, M., 2005, "Development and Application of a Complete Common-Rail Injection System Mathematical Model for Hydrodynamics Analysis and Diagnostics," ASME ICE Spring Technical Conference, Chicago, IL, Apr. 5–7, Paper No. ICES 2005-1018; Trans. ASME: J. Eng. Gas Turbines Power, in press.
[10] Bosch, W., 1966, "The Fuel Rate Indicator: A New Measuring Instrument for Display of the Characteristics of Individual Injection," SAE Paper No. 660749.
[11] R. Bosch, GmbH, 1999, *Diesel-Engine Management*, Bosch Technical Books, SAE International, Detroit.
[12] LeVeque, R. J., 1992, *Numerical Methods for Conservation Laws*, Birkhäuser, Basel.
[13] Catania, A. E., Ferrari, A., and Spessa, E., 2006, "Numerical-Experimental Study and Solutions to Reduce the Dwell Time Threshold for Fusion-Free Consecutive Injections in a Multijet Solenoid-Type CR Systems," ASME Paper No. ICES2006-1369, ASME Technical Paper Award for Best ICES2006 Paper; Trans. ASME: J. Eng. Gas Turbines Power, in press.

Spray and Combustion Characteristics of Biodiesel/ Diesel Blended Fuel in a Direct Injection Common-Rail Diesel Engine

Hyun Kyu Suh
e-mail: hksuh@hanyang.ac.kr

Hyun Gu Roh
e-mail: rohyungu@hanyang.ac.kr

Chang Sik Lee[1]
Professor
e-mail: cslee@hanyang.ac.kr

Department of Mechanical Engineering,
Hanyang University,
17 Haengdang-dong, Sungdong-gu,
Seoul, 133-791, Korea

The aim of this work is to investigate the effect of the blending ratio and pilot injection on the spray and combustion characteristics of biodiesel fuel and compare these factors with those of diesel fuel in a direct injection common-rail diesel engine. In order to study the factors influencing the spray and combustion characteristics of biodiesel fuel, experiments involving exhaust emissions and engine performance were conducted at various biodiesel blending ratios and injection conditions for engine operating conditions. The macroscopic and microscopic spray characteristics of biodiesel fuel, such as injection rate, split injection effect, spray tip penetration, droplet diameter, and axial velocity distribution, were compared with the results from conventional diesel fuel. For biodiesel blended fuel, it was revealed that a higher injection pressure is needed to achieve the same injection rate at a higher blending ratio. The spray tip penetration of biodiesel fuel was similar to that of diesel. The atomization characteristics of biodiesel show that it has higher Sauter mean diameter and lower spray velocity than conventional diesel fuel due to high viscosity and surface tension. The peak combustion pressures of diesel and blending fuel increased with advanced injection timing and the combustion pressure of biodiesel fuel is higher than that of diesel fuel. As the pilot injection timing is retarded to 15 deg *of BTDC that is closed by the top dead center, the dissimilarities of diesel and blending fuels combustion pressure are reduced. It was found that the pilot injection enhanced the deteriorated spray and combustion characteristics of biodiesel fuel caused by different physical properties of the fuel.* [DOI: 10.1115/1.2835354]

Keywords: biodiesel, injection rate characteristics, spray characteristics, phase Doppler particle analyzer (PDPA), Sauter mean diameter (SMD), combustion characteristics, rate of heat release (ROHR), exhaust emissions

1 Introduction

Biodiesel fuel, an alternative diesel fuel, is an environmentally clean and renewable energy source. It is well known that biodiesel can be mixed with diesel fuel when applied in a diesel engine because of different physical properties, such as higher viscosity, cetane number, and lower heating values compared with conventional diesel fuel [1]. Consequently, biodiesel fuel can be operated in a compression ignition engine with little or no modifications.

Moreover, it can be expected that oxygen, which is implied in the biodiesel at about 11–15%, can enhance the combustion process and the pollutant emissions from the diesel engine. From this point of view, there have been many experimental investigations on the combustion and emission characteristics of biodiesel fuel in the diesel engine [2–7]. In particular, the formation and control of NO_x emissions from biodiesel fueled diesel engines have been of the utmost concern because these *emissions* are closely related to the oxygen concentration in biodiesel fuel [8,9].

The reduction of NO_x emissions can be achieved when applying a pilot fuel injection in a diesel engine. The reduction of NO_x has been reported by many experimental and numerical investigations at various engine operating conditions [10–15].

In spite of these many studies on biodiesel fuel properties and their effect on combustion and emissions, most studies are focused on engine performance rather than on spray and atomization characteristics. The fuel properties and flow characteristics of biodiesel are different from those of conventional diesel fuel as indicated in previous studies [1,16]. These different fuel properties of biodiesel, such as higher viscosity and surface tension, may also influence the fuel atomization characteristics when applied in a diesel engine [17,18]. In the case of a direct injection diesel engine, the injection characteristics in the combustion chamber through the fuel spray nozzle determine the combustion performance and thermal efficiency of the engine. For these reasons, the study of fuel spray characteristics is essential in understanding the compression ignition engine; in particular, investigations into the relationship between spray and engine performance of blended biodiesel fuel should be conducted.

The purpose of this work is to investigate the effect of biodiesel blending fuel on the spray, atomization characteristics, and emissions in a direct injection diesel engine. In order to analyze the influence of the fuel blending ratio and pilot injection of biodiesel fuel on the spray characteristics, the fuel injection rate, spray tip penetration, and droplet size distributions were determined experimentally with various injection parameters. In addition, the combustion and emission characteristics of biodiesel fuels in a four-

[1]Corresponding author.

Contributed by the International Combustion Engine Division of ASME for publication in the JOURNAL OF ENGINEERING FOR GAS TURBINES AND POWER. Manuscript received April 17, 2007; final manuscript received November 17, 2007; published online March 28, 2008. Review conducted by Kalyan Annamalai.

Table 1 Test fuel composition

Compositions of fuel	Ref.	Viscosity (mm^2/s)	Surface tension (N/s)	Density (kg/m^3)
Diesel	D100	2.684	0.026	828
Diesel(95%)+ Soybean oil(5%)	BD5	2.71	0.0261	831
Diesel (80%)+ Soybean oil(20%)	BD20	2.96	0.02637	840

Table 2 Spray analysis system specifications

Spray visualization system	Light source	Ar-ion laser
	Wavelength	514.5 nm
	laser power	1.2 W
ICCD camera	Pixel size	6.7×6.7 μm
	Resolution	1280 (H) $\times$ 1024 (V)
Droplet measuring system	Wavelength	514.5 nm, 488 nm
	Focal length	500 nm for transmitter and receiver
	Collection angle	30 deg

cylinder common-rail direct injection diesel engine were investigated at various injection and engine operating conditions.

2 Experimental Apparatus and Procedure

2.1 Experimental Setup

2.1.1 Test Fuels and Analysis System for Spray Characteristics. The biodiesel test fuel used in this work was derived from soybean oil. The volume based blending ratios of biodiesel with conventional diesel fuel were set at 5% and 20% for analyzing the effect of blending ratio on the spray and combustion characteristics of the biodiesel blending fuel. Properties such as viscosity, surface tension, and density of the mixed fuel were also analyzed to investigate correlations with the spray, combustion, and exhaust emissions characteristics in a diesel engine. The composition and properties of the test fuels are listed in Table 1.

Fuel injection rate characteristics are some of the most important factors because they may be used to design injection systems and combustion chamber shapes. To this end, the injection rates of diesel and biodiesel were measured and the effect of blending ratio and pilot injection were analyzed by using the injection rate measuring system based on Bosch's suggestion [19]. This apparatus calculated the injection rate from the pressure variation obtained by a pressure sensor installed in the injection tube. In this experiment, the pressure in the injection tube was fixed at 4 MPa and 1000 continuous injections were performed and averaged at room temperature conditions (25°C).

Figure 1 shows a schematic diagram of the spray visualization and droplet measuring system. The spray visualization system was composed of an Ar-ion laser (Innova 70C, Coherent), intensified charge coupled device (ICCD) camera (Dicam Pro, Cooke), signal synchronization system, such as injector driver (TDA-3200H, TEMS) and digital delay generator (model 555, Berkeley Nucleonics Corp.), and a personal computer (PC) installed image grabber. The Ar-ion laser emits a laser beam 1.4 mm in diameter with a 514.5 nm wavelength. The cylindrical lenses were equipped to expand the beam and act as a light source by illuminating the fuel spray in the combustion chamber.

The atomization characteristics such as Sauter mean diameter (SMD) and droplet velocity distributions were measured by a phase Doppler particle analyzer (PDPA) system, as shown in Fig. 1. In this system, the Ar-ion laser also used for the light source and the signal analyzer was synchronized with the fuel injection signal to obtain the transient characteristics of the fuel atomization. The laser power was set to 1.2 W in consideration of the data acquisition and rejection rate. Detailed specifications of the spray visualization and droplet measuring systems are shown in Table 2.

Two high pressure pumps can compress the fuel up to 200 MPa, and a digital delay generator controls the fuel injection, ICCD camera, and its exposure time. Nitrogen gas was used to pressurize the combustion chamber to simulate the engine operating conditions.

2.1.2 Experimental Engine and Combustion Characteristics Measuring System. The influence of fuel blending ratio and pilot injection of the biodiesel fuel on the combustion and emission characteristics were studied by using a common-rail diesel engine with four cylinders installed on an eddy current (EC) dynamometer, as shown in Fig. 2.

The experimental engine used in this work is a four-cylinder diesel engine with 75 mm bore and 84.5 mm stroke for a total displacement of 1.493 L. The rated power of the engine is 82.5 kW at 4000 rpm. The engine has a four valve mechanism of the overhead type and a compression ratio of 17.8 to 1.

In order to measure combustion pressure, a piezoelectric combustion pressure sensor (6055B800, Kistler) and data acquisition board were installed. The common-rail injection pressure was controlled by an electric control unit (ECU) equipped with a pro-

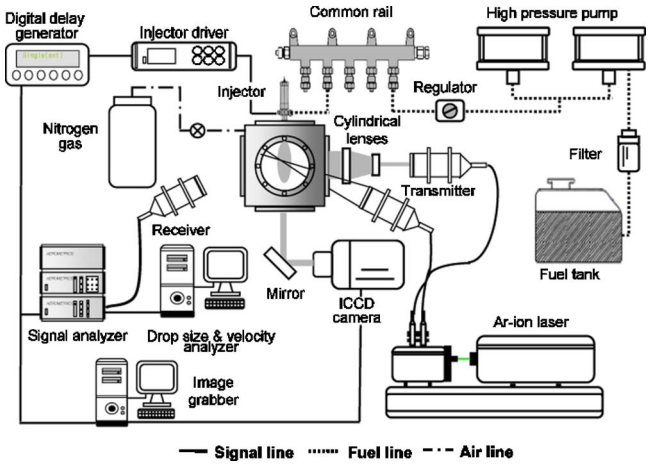

Fig. 1 Spray visualization and droplet measuring system

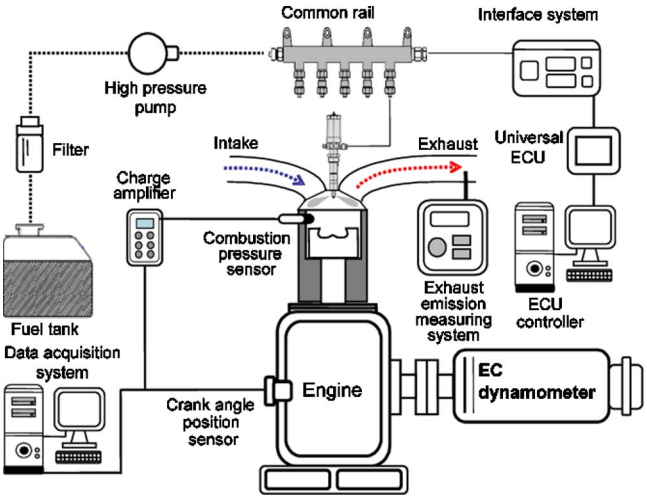

Fig. 2 Four-cylinder test common-rail diesel engine

Table 3 Experimental conditions

Injection system			Common-rail
Ambient temperature (K)			298
Spray analysis	Injection pressure (MPa)		27, 60, 100 (for visualization) 80 (for PDPA)
Ambient pressure (MPa)			0.1, 4
Injected fuel mass	Single injection (mg)		12
	Pilot injection (mg)	Pilot	0.5, 1, 2
		Main	11.5, 11, 10
Combustion analysis	Engine speed (rpm)		800
	Injection pressure (MPa)		27, 100
	Water temperature (°C)		80
	Intake air temperature (°C)		35
	Single injection (ATDC) (deg)		−6 to 3
	Pilot injection (ATDC) (deg)	Pilot	−35 to 15
		Main	0

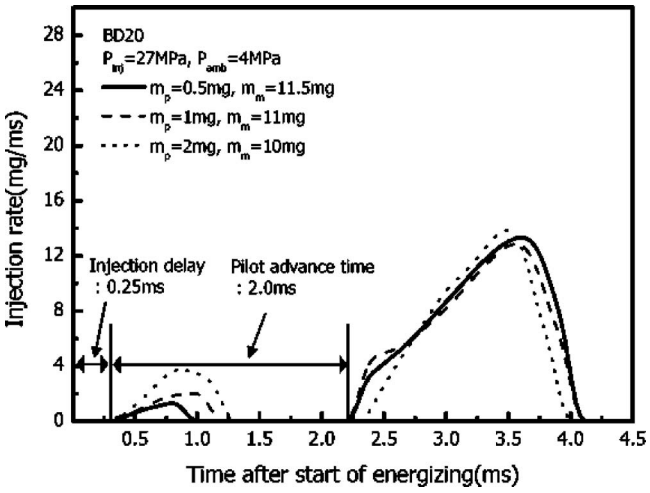

Fig. 3 Effect of injection quantity on the biodiesel fuel injection rate (BD5, P_{inj}=100 MPa, P_{amb}=4 MPa)

grammable controller and a crankshaft position sensor for rpm and crank angle detection was installed. For the control of fuel injection timing and quantities, the universal ECU and interface system were used. The exhaust emissions such as HC, CO, NO_x, and soot were detected and analyzed by an exhaust emissions measuring system (MEXA 554JK, Horiba).

2.2 Experimental Procedures. The fuel injector that was used in this work is a mini-sac type injector with a 0.119 mm hole diameter, seven holes, and a 157 deg injection angle.

For investigations into the effect of the biodiesel blending ratio and pilot injection on fuel spray characteristics, fuel injection quantities were varied, as shown in Table 3. The blending ratio of biodiesel fuel was 5% and 20%, as illustrated in Table 1. The total injected mass for the single and pilot injection cases was fixed at 12 mg. However, the mass of fuel injected in the pilot and main injections was changed for the three pilot injection cases, as shown in Table 3. The fuel injection rate was analyzed at various fuel blending ratios and injection conditions, and spray development was visualized for 60 MPa and 100 MPa of injection pressures to compare the effect of the blending ratio and pilot injection. The fuel atomization profiles were compared at 0.1 MPa of ambient pressure to prevent the floating droplets from interrupting the Doppler signal in the measurement volume. The cutoff range of the droplet diameter measurement by using the droplet measuring system was set from 2 μm to 100 μm, and approximately 30,000 spray droplets were collected and averaged for each measuring point. The mean droplet size and velocity can present as two parameters, which were local and overall values. The local SMD values indicate the mean size at each measuring points in all measuring duration. However, the overall SMD means the accumulations for all droplets captured at all measuring points at a specific time. The atomization characteristics of the droplet were measured in the range from 10 mm to 70 mm in the center line of axial distance. In support of measurement reliability, the data acquisition rate and the valid percentage of droplet measurements were investigated in this study. The droplet valid percentage is over than 95% in the near region of nozzle injector, and it increases with increase of axial distance. The data acquisition rate that provides the droplet atomization information is increased linearly as distance from the nozzle increases. Based on these results, the measuring results in this study can be reliable in all experimental conditions.

In order to study the influence of the blending ratio and pilot injection timing on the combustion characteristics of biodiesel fuel, the common-rail pressures for fuel injection were 27 MPa and 100 MPa, and engine speed was fixed at 800 rpm, to evaluate the engine operating conditions. The reason is to understand the effect of low engine speed on the exhaust emissions such as CO, HC, and NO_x because plenty of these exhaust emissions are generated in low speed and idle condition and also investigates the viscosity effect of biodiesel blending fuel at low engine speed. The temperatures of the intake air and cooling water were fixed because they may influence the power output of the engine. The experimental conditions are summarized in Table 3.

3 Results and Discussion

3.1 Injection Rate Characteristics. In this experiment, the injected fuel mass per cycle was set at a constant 12 mg to study the effect of the blending ratio and pilot injection on biodiesel spray and combustion characteristics.

Figure 3 shows the pilot injection profiles of biodiesel fuel with a 5% blending ratio at 27 MPa of injection pressure and various injection quantities. The m_p and m_m indicate the fuel mass of pilot and main injection, respectively. In all cases, injection delay, which is defined as the time interval from the start of energizing to the start of injection, appeared as 0.25–0.26 ms. The advanced time of the pilot injection was fixed to 2.0 ms in this study, and the main fuel injection started at 2.25 ms; in this case, the effect of pilot injection quantities on the injection delay is negligible. On the other hand, the peak injection rate of the pilot was dissimilar because the injected mass was different; however, the peak injection rate of the main injection was similar because the nozzle equipped in the injector had the same fuel flow rate.

The comparison of single and pilot injection rates of diesel and biodiesel blending fuel is shown in Fig. 4. In the case of single injection, the patterns of the fuel injection profiles were all similar. In the case of pilot injection, the peak injection rate of the main biodiesel injection was a little lower than that of diesel fuel. It can be estimated that as the blending ratio is increased, the peak injection rate of biodiesel fuel cannot reach its maximum value because of the higher fuel viscosity of biodiesel. Generally, the peak fuel injection rate is determined by the nozzle geometry and injection pressure. Based on these results, the increase of the blending ratio induced a decrease of the peak injection rate because the injection velocity reduces. It can be also said that the increase of friction between the nozzle surface and fuel has been shown to reduce the injection velocity and reduce the peak injection rate. Based on the above reasoning, in the case of biodiesel blended with diesel, a higher injection pressure is needed to achieve the same injection characteristics of diesel fuel, for pilot injection.

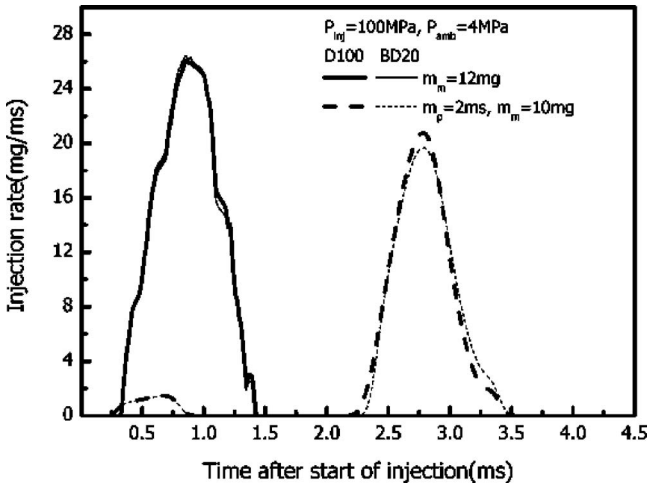

Fig. 4 Comparison of injection rate between single injection and pilot injection conditions (P_{inj}=100 MPa, P_{amb}=4 MPa)

3.2 Spray Evolution Characteristics. The spray characteristics of diesel and biodiesel blended fuel were investigated to study the influence of the viscosity and surface tension of biodiesel on spray development and atomization performance.

Figure 5 shows a comparison of the spray evolution process in the case of single injection and pilot injection of diesel and biodiesel blending fuel at 100 MPa injection pressure as a function of time after start of injection (t_{asoi}). As illustrated in this Fig. 5(*a*), in the case of single injection, it can be observed that the blending ratio of biodiesel fuel has little influence on spray evolution. A reason for this result may be the fuel injection rate, which a large amount of injection quantities influence on the fuel injection performance, as described in Fig. 4. The spray grows during the energizing duration and becomes dilute after 2.7 ms of injection start.

In the case of pilot injection, as shown in Fig. 5(*b*), the main spray is visible in the frozen image 2.0 ms after the start of injection. It was also observed that not only pilot spray but also main

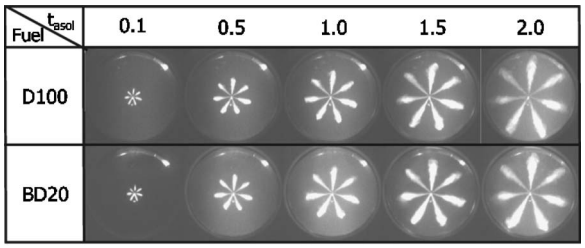

(*a*)

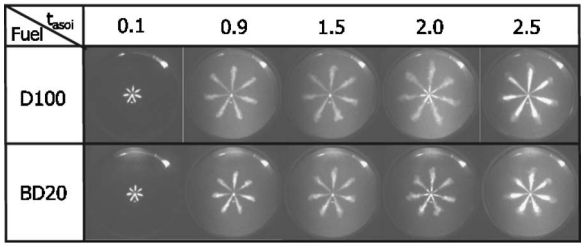

(*b*)

Fig. 5 Comparison of spray evolution between single and pilot injection conditions (P_{inj}=100 MPa, P_{amb}=4 MPa): (*a*) Single injection condition (m_m=12 mg); (*b*) pilot injection condition (m_p=2 mg, m_m=10 mg)

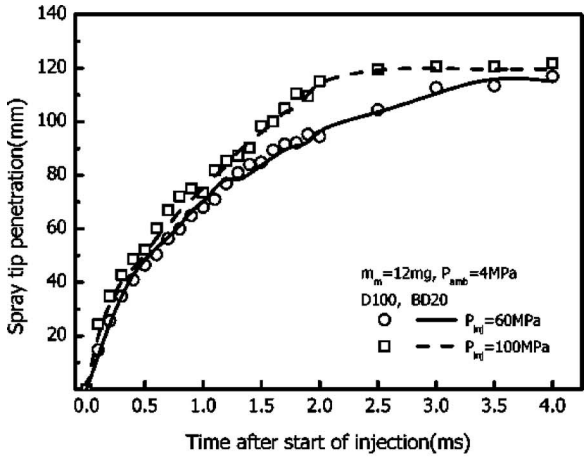

(*a*)

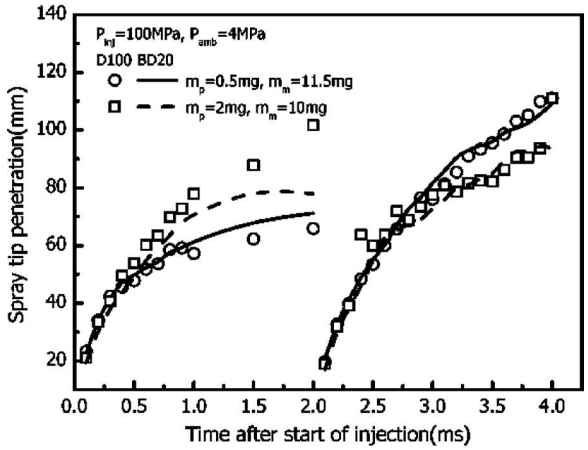

(*b*)

Fig. 6 Comparison of spray tip penetration of diesel and blended biodiesel fuels (P_{inj}=100 MPa, P_{amb}=4 MPa): (*a*) Single injection condition; (*b*) pilot injection condition

spray development is shorter compared to that with diesel fuel. It can be estimated that spray evolution of biodiesel blending fuel becomes lower than that of conventional diesel because the small injected mass and high viscosity of biodiesel cannot overcome the friction between the fuel and nozzle hole surface.

The effect of the biodiesel blending ratio and pilot injection on the spray tip penetrations are analyzed quantitatively in Fig. 6. The spray tip penetration is defined as the maximum distance to which spray can reach from the nozzle tip. As shown in Fig. 6(*a*), the biodiesel fuel spray tip penetration is similar to that of conventional diesel. In addition, the increase of the injection pressure induces longer spray tip penetration of diesel and biodiesel blending fuel. On the basis of these results, the effect of the fuel blending ratio on spray tip penetration is slight in comparison with the injection pressure.

The spray tip penetration of diesel and biodiesel blending fuel on pilot injection conditions is shown in Fig. 6(*b*). In conditions with 0.5 mg pilot injection, both sprays have almost the same spray tip penetration. However, in conditions with 2 mg pilot injection, the diesel spray tip penetration is longer than that of biodiesel. It can be said that the small pilot injection quantities at 0.5 mg of diesel and biodiesel cannot lead to full spray evolution. On the other hand, pilot injection quantities are increased further as 2 mg, diesel fuel injected entirely; however, biodiesel does not because the high viscosity biodiesel develops slowly. As a result,

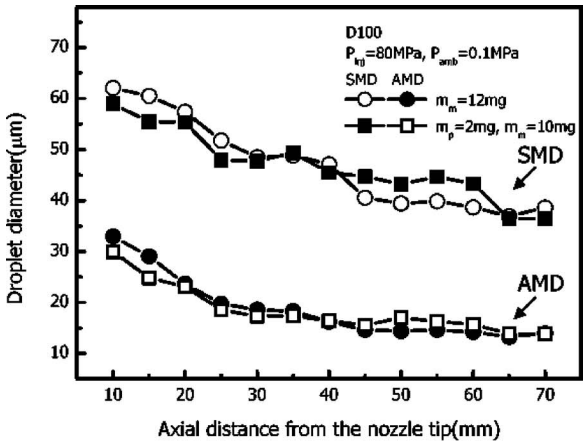

(*a*)

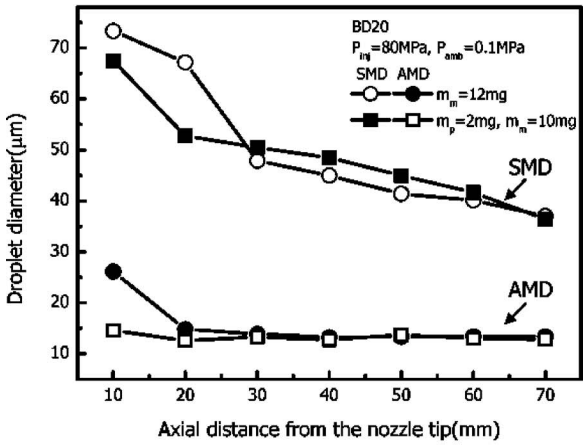

(*b*)

Fig. 7 Droplet diameter distribution of diesel and blended biodiesel fuels (P_{inj}=80 MPa, P_{amb}=0.1 MPa): (*a*) Diesel fuel (D100); (*b*) biodiesel fuel (BD20)

the diesel spray penetration of pilot injection is longer than those of biodiesel. The main spray tip penetration in both cases was similar regardless of blending ratio.

3.3 Fuel Atomization Characteristics. The fuel droplet size is an important parameter in analyzing spray characteristics because it is closely related to the combustion and exhaust emission characteristics in the engine.

In order to compare the effect of the physical properties of biodiesel and diesel fuels on the atomization characteristics, the droplet diameter and axial mean velocity are analyzed at different fuel injection conditions. The influence of single and pilot injections on droplet size distributions according to the axial distance from the nozzle tip is shown in Fig. 7. The SMD and arithmetic mean diameter (AMD) of diesel and biodiesel blending fuel decreased with an increase in the axial distance due to the fuel atomization process. As can be seen in these figures, the pilot injection of diesel and biodiesel had a smaller droplet diameter than the single injection in the near area of nozzle tip. However, the droplet diameter distributions of diesel and blending fuel were reversed at an axial distance of 30 mm. The comparisons of the SMD values show that biodiesel blended fuel is higher than that of conventional diesel fuel, and the AMD values have similar trends. It is generally known that the surface tension is a dominant factor of the droplet breakup mechanism. Therefore, the higher viscosity and surface tension of the biodiesel, due to the increased blending ratio as indicated in Table 1, induced the higher SMD

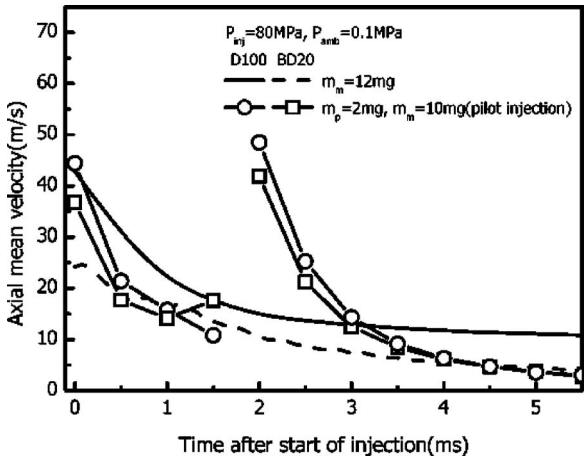

Fig. 8 Axial mean velocity distribution of diesel and blended biodiesel fuels (P_{inj}=80 MPa, P_{amb}=0.1 MPa)

distributions.

The above results may influence the fuel injection velocity. The axial mean velocities of diesel and blending fuel are illustrated in Fig. 8. As previously shown in the injection and spray evolution characteristics, the higher viscosity of biodiesel can become a factor in a lower axial mean velocity because it increases the friction between the nozzle surface and fuel. In the case of the single injection, the spray velocity of biodiesel fuel is slow over the whole injection time. The spray velocity decreased as the time elapsed from the start of injection. However, for pilot injection, the spray velocity increased suddenly at 2.0 ms after the start of injection due to the main spray injection. It may influence the density and size of fuel droplets at the measuring points of the PDPA system. It the can also be observed that pilot injection promotes the spray atomization of biodiesel fuel from the results of the PDPA measurement. In the case of pilot injection, the pilot spray improves the relative velocity between spray and ambient gas, and this influences on the spray velocity of main injection. The higher injection velocity enhances the effect of drag force on the spray droplets; as a result, the fuel atomization of spray is promoted by pilot injection.

Figure 9 shows the droplet distributions of diesel and blending fuel in conditions of single and pilot injections. In the condition of single injection, many diesel fuel droplets were distributed over the whole range of injection time, as illustrated in Fig. 9(*a*). The reason that few biodiesel fuel droplets were detected in the injection duration was thought to be the effect of poor fuel atomization caused by physical fuel properties and a low spray velocity compared with that of conventional diesel fuel. On the other hand, in the case of pilot injection, the number of pilot injection droplets was rapidly decreased, and the main injection droplet distributions of diesel and biodiesel blending fuel became similar because of the effect of fuel atomization influenced by pilot injection, as can be seen in Fig. 9(*b*).

In light of these results for the SMD and axial mean velocity, biodiesel blended with diesel fuel that has higher SMD value and lower axial mean velocity is inferior to diesel fuel in fuel spray performance, and pilot injection can improve the fuel atomization characteristics of biodiesel fuel.

3.4 Combustion Characteristics. The effect of injection timing and blending ratio of biodiesel on combustion pressure, the rate of heat release, and exhaust emission characteristics in a four-cylinder direct injection diesel engine was investigated. The injected fuel masses of single and pilot injections were set constant to 12 mg/cycle by controlling the ECU equipped with a programmable controller. The injection pressure and engine speed were

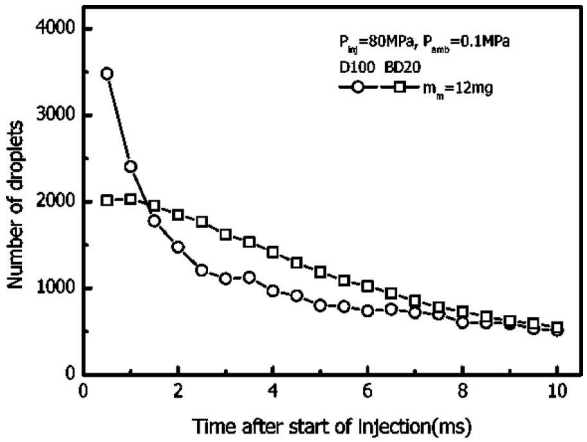

(*a*)

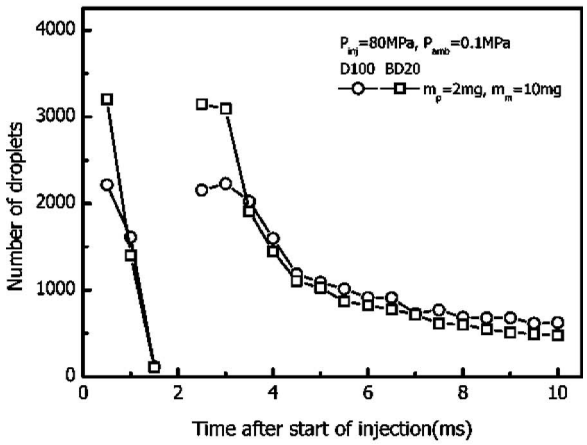

(*b*)

Fig. 9 Number of droplet distributions in single injection and pilot injection conditions (P_{inj}=80 MPa, P_{amb}=0.1 MPa): (*a*) Single injection condition (m_m=12 mg); (*b*) pilot injection condition (m_p=2 mg, m_m=10 mg)

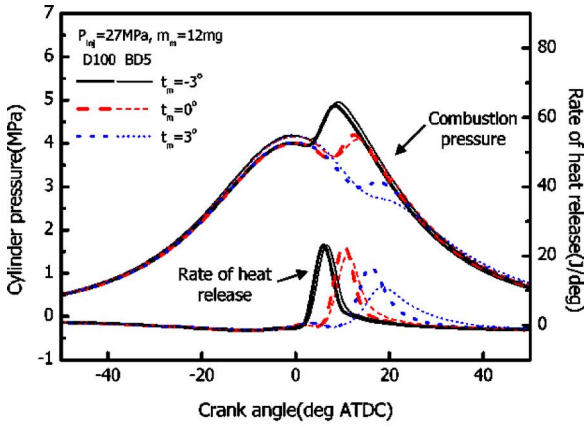

(*a*)

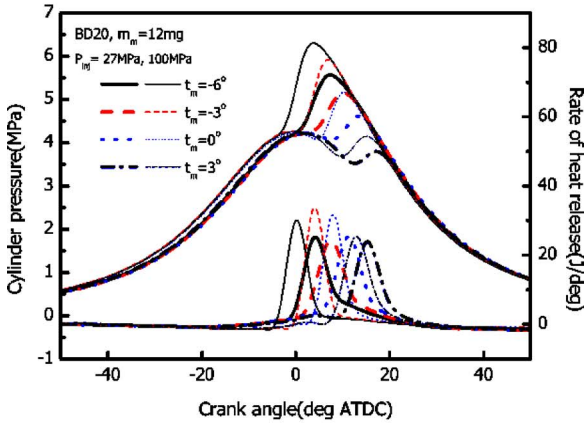

(*b*)

Fig. 10 Combustion characteristics of diesel and biodiesel fuels in main injection conditions: (*a*) Comparison of diesel and biodiesel fuel; (*b*) effect of injection pressure

fixed to 27 MPa and 100 MPa at 800 rpm, respectively, to analyze the combustion characteristics of diesel and biodiesel blending fuel according to the operating conditions.

Figure 10 illustrates the influence of the fuel main injection timing on combustion pressure and heat release rate in a single injection. As illustrated in Fig. 10(*a*), the peak combustion pressures of diesel and blending fuel were increased as the injection timing advanced. The combustion pressure and rate of heat release of BD 5 and diesel were similar. From this result, a 5% volumetric blending ratio of biodiesel likely will not improve combustion performance.

The effect of injection pressure on biodiesel combustion is illustrated in Fig. 10(*b*). As the injection pressure increased to 100 MPa, the combustion pressure and rate of heat release increased. The ignition delay defined as the time interval from the start of injection to the start of combustion also advanced with an increase of injection pressure. From these results, it can be concluded that a higher injection pressure ameliorates the fuel injection and atomization performance of higher viscosity biodiesel fuel. This means that fine atomization also improves biodiesel combustion characteristics. As a result, the combustion pressure and rate of heat release of biodiesel become higher at 100 MPa of injection pressure. Other results obtained from Figs. 10(*a*) and 10(*b*) were that as the blending ratio of biodiesel increased from 5% to 20%, the combustion pressure and heat release rate increased a little.

Figure 11 shows the effect of pilot injection timing on the combustion pressure and rate of heat release characteristics when the main injection timing is top dead center (TDC). Because of the effect of pilot injection, the combustion pressure variations that can be observed for the single injection conditions according to the injection timing are reduced. As the pilot injection timing is retarded to the TDC, the dissimilarity of combustion pressures between diesel and biodiesel disappeared. Moreover, the retarded pilot injection timing in the case of BTDC 35 deg affected the advanced ignition delay and lowered heat release, and consequently, lower NO_x generation can be expected. As shown in Fig. 11(*b*), a high injection pressure enhances the high combustion pressure and rate of heat release. Also, the pilot injection reduces the combustion pressure and heat release in a diesel engine at the constant injected mass from a comparison of the results of Figs. 10 and 11.

The indicated mean effective pressure (IMEP) and coefficient of variation of maximum pressure (COV_{pmax}) of diesel and biodiesel fueled with a diesel engine as a sort of engine performance are shown in Fig. 12. In the case of IMEP, as shown in Fig. 12(*a*), it can be observed that although the IMEP of diesel and blending fuel are similar, the IMEP of BD5 decreased at the main injection timing t_m=3 deg for single injection. On the other hand, in the pilot injection condition, the IMEP of diesel and blending fuel is nearly constant and the value of biodiesel fuel is higher, because the pilot injection has an influence on the fuel combustion. It can be also observed that the cylinder pressure of biodiesel blending fuel decreases slowly and maintains almost constant

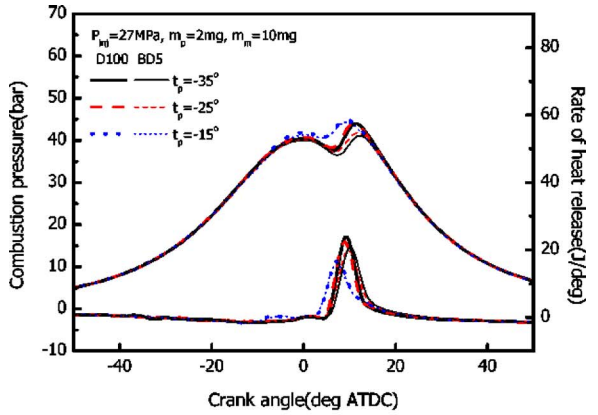

(*a*)

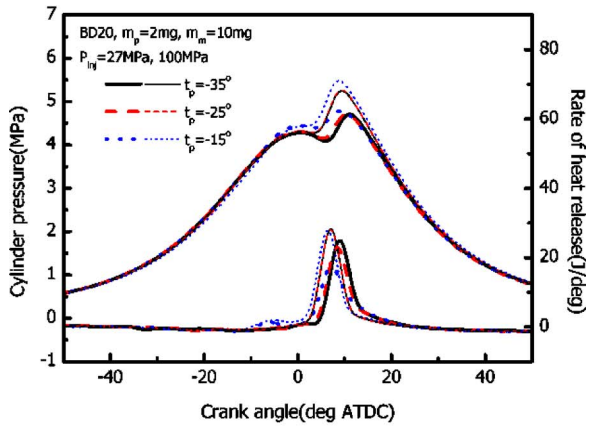

(*b*)

Fig. 11 Combustion characteristics of diesel and biodiesel fuels in pilot injection conditions: (*a*) Comparison of diesel and biodiesel fuel; (*b*) effect of injection pressure

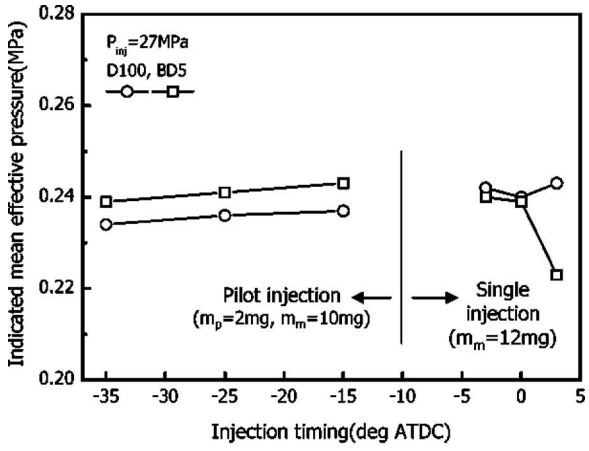

(*a*)

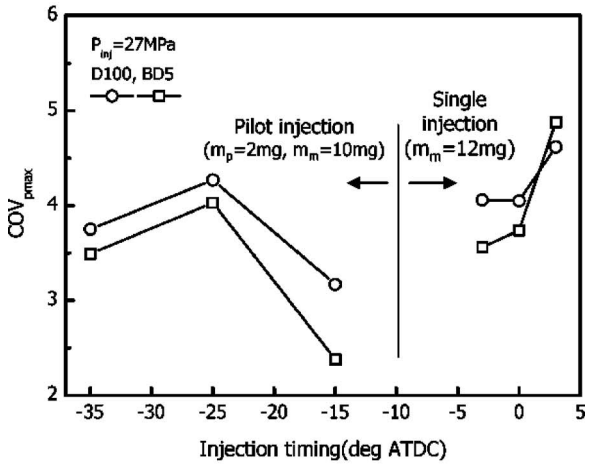

(*b*)

Fig. 12 Effect of injection conditions on the IMEP and COV_{pmax}: (*a*) IMEP; (*b*) COV_{pmax}

value, while diesel fuel cylinder pressure falls quickly after ATDC 50 deg. Therefore, the total cylinder pressure of biodiesel blending fuel during combustion period is higher than that of diesel fuel. As a result, the IMEP of blending fuel is a little higher than diesel fuel. The COV_{pmax}, as an index of combustion stability, was increased as the injection timing was retarded for single injection. Especially, as the time interval between the pilot and main injection was shortened, the COV_{pmax} decreased. From these results, it can be concluded that pilot injection could improve the biodiesel atomization issues from the different properties.

3.5 Exhaust Emission Characteristics. Figure 13 illustrates the effect of injection timing on the exhaust emission characteristics in the cases of single and pilot injections. The CO emission of both fuels in the case of single injection decreased as injection timing advanced. In particular, a rapid increase in CO emission can be observed as the injection timing retarded, because of a longer heat release period. In the case of pilot injection, as the pilot injection timing approached the main injection timing, the CO emissions were decreased as illustrated in Fig. 13(*a*). It can be said that CO was reduced because pilot injection enhanced fuel atomization and improved main injection combustion. However, in the case of 100 MPa of injection pressure, the CO emissions were increased.

In the case of HC, as shown in Fig. 13(*b*), the advance of main injection timing induces low HC generation from the engine. In particular, the excessive retardation of the main injection timing, when t_m=3 deg, can cause a dramatic increase in HC emissions. It can be speculated that as injection timing advances, the ignition delay time becomes shorter, and as a result, the combustion duration time increases. For this reason, the HC emissions of diesel and blending fuel decreased. More HC emissions are generated from diesel fuel than from biodiesel fuel. The effect of pilot injection illustrated that the HC emissions were reduced because the flame core made by pilot injection at the compression stroke may affect the main injection combustion. Higher injection pressure reduced HC emissions from biodiesel fuel in both injection cases.

Generally, NO_x is closely related to the rate of heat release during engine operation. Consequently, the NO_x emissions of biodiesel are higher than that of diesel regardless of injection timing, because the heat release rate of biodiesel is higher. It can be also seen that NO_x is increased as the injection timing is advanced due to the rapid combustion of fuel, and the application of a higher fuel injection pressure might reduce the NO_x emissions, as shown in Fig. 13(*c*). However, in the case of pilot injection, the NO_x emission of biodiesel increased as the injection pressure increased. In the high injection pressure, fine fuel atomization and wider air/fuel mixture distributions can be obtained. Especially, in the case of pilot injection condition, the flame core is generated by small amount of injected fuel, and it induces fast combustion process. As a result, the rate of heat release increases instantly, and the NO_x emissions increase a little in a high pressure injection case. It can be also shown that the NO_x increased dramatically as the pilot injection timing approached the main injection timing because of a high rate of heat release.

Figure 13(*d*) illustrates the soot emission characteristics of die-

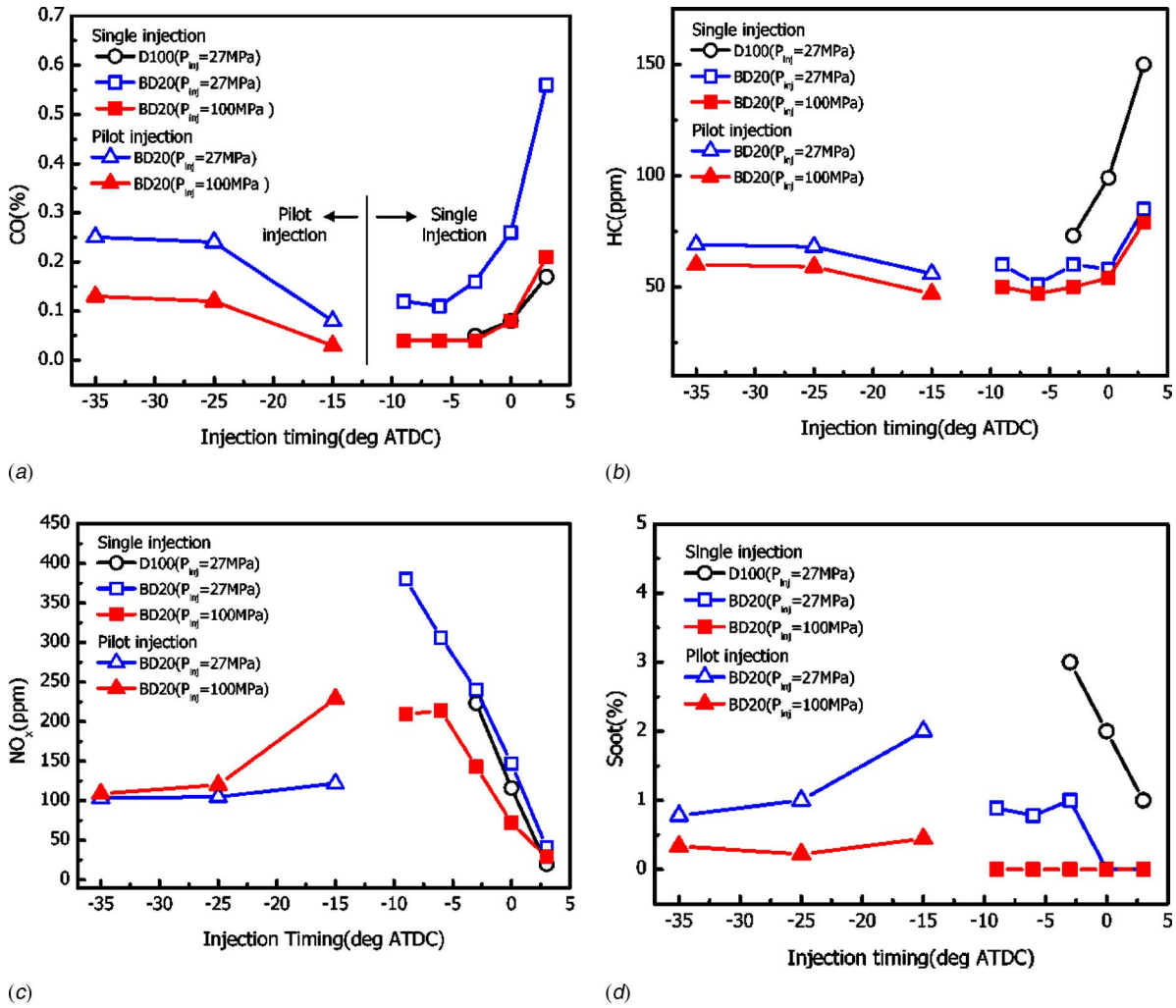

Fig. 13 Exhaust emissions of diesel and biodiesel fuels: (*a*) CO, (*b*) HC, (*c*) NO_x, and (*d*) soot

sel and biodiesel blending fuel. The soot emissions of biodiesel fuel were smaller than those of diesel fuel in all injection conditions. Moreover, there are no soot emissions with 100 MPa for the main injection. These trends can also be observed in the pilot injection conditions. As the time interval between pilot and main injection shortens; more soot emissions are generated. It can be said that soot emissions are increased because of longer ignition delays caused by retarded pilot injection timing and insufficient blending time between air and fuel before the initiation of combustion.

4 Conclusions

In this study, the effect of the blending ratio and pilot injection of biodiesel on fuel atomization performance and combustion characteristics was investigated at various injection and idle engine operating conditions. The conclusions of this study are as follows:

1. In the case of single injection, the patterns of fuel injection profiles for diesel and biodiesel blended fuels are very similar. On the other hand, in the case of pilot injection, an increase of the blending ratio induced a decrease of the peak injection rate. It can be said that the increase in the friction between the nozzle surface and fuel due to biodiesel viscosity has been shown to reduce the injection velocity and reduce the peak injection rate.
2. The effect of fuel blending and injection pressure on single spray tip penetration is slight, and the pilot spray development of biodiesel is shorter compared with the pilot and main injection of diesel fuel. It can be estimated that the injection velocity of biodiesel fuel becomes less than that of conventional diesel because the small injected mass and high viscosity of biodiesel cannot overcome the friction between the fuel and surface of the nozzle hole.
3. A comparison of SMD values shows that the blended biodiesel fuel is higher than that of the conventional diesel fuel because of high surface tension, and the AMD values have similar trends. This implies that the higher viscosity of biodiesel can be a reason for lower axial mean velocity.
4. In the case of single injection, the spray velocity of biodiesel fuel is slow over the whole injection period. However, in the case of pilot injection, the spray velocity increased suddenly 2 ms after the injection starts because of the second main injection.
5. A 5% volumetric blending ratio of biodiesel likely will not improve combustion performance. The higher injection pressure ameliorates the fuel injection and atomization performance of a higher viscosity biodiesel fuel. As a result, the combustion pressure and the rate of heat release of biodiesel become higher at 100 MPa of injection pressure. It also can be seen that pilot injection reduces the combustion pressure and heat release of a diesel engine.
6. The CO emissions of both fuels with single injection decreased with advanced injection timing. The pilot injection

enhanced the fuel atomization and combustion; as a result, the CO emissions were reduced. The advance of main injection timing and pilot injection timing induces low HC generation from the engine. The NO_x emissions of biodiesel were increased as the injection pressure increased due to the higher heat release rate from the higher injection pressure. It can be seen that NO_x increases dramatically as the pilot injection timing approaches the main injection timing because of a high rate of heat release. The soot emissions of biodiesel fuel were less than that of diesel fuel for all injection conditions. Moreover, there were no soot emissions with 100 MPa of main injection.

Acknowledgments

This study was supported by the CEFV (Center for Environmentally Friendly Vehicle) of the Eco-STAR project from MOE (Ministry of Environment, Republic of Korea). Also, this work was financially supported by the Ministry of Education and Human Resources Development (MOE), the Ministry of Commerce, Industry and Energy (MOCIE), and the Ministry of Labor (MOLAB) through the fostering project of the Lab of Excellency. Also, this work was supported by the Second Brain Korea 21 Project in 2006.

Nomenclature

m = fuel mass (mg/cycle)
P = pressure (MPa)
t = time (ms)

Greek

ρ = density (kg/mm^3)
σ = surface tension (N/s)

Subscripts

amb = ambient
asoi = after start of injection
inj = injection
m = main
p = pilot

References

[1] Ramadhas, A. S., Jayaraj, S., and Muraleedharan, C., 2004, "Use of Vegetable as I.C Engine Fuels–A Review," Renewable Energy, **29**, pp. 727–742.
[2] Monyem, A., and Gerpen, J. H. V., 2001, "The Effect of Biodiesel Oxidation on Engine Performance and Emissions," Biomass Bioenergy, **20**, pp. 317–325.
[3] Mustafa, C., Ahmet, E., and Erol, A., 2006, "Performance and Exhaust Emissions of a Biodiesel Engine," Appl. Energy, **83**, pp. 594–605.
[4] Nadi, N., Akhter, S., and Shahadat, Z., 2006, "Improvement of Engine Emissions With Conventional Diesel Fuel and Diesel Biodiesel Blend." Bioresour. Technol., **97**, pp. 372–378.
[5] Laforgia, D., and Ardito, V., 1995, "Biodiesel Fueled IDI Engines Performances, Emissions and Heat Release Investigation," Bioresour. Technol., **51**, pp. 53–59.
[6] Lin, C. Y., and Lin, H. A., 2006, "Diesel Engine Performance and Emission Characteristics of Biodiesel Produced by the Peroxidation Process," Fuel, **85**, pp. 298–305.
[7] Schumacher, L. G., Borgelt, S. C., Fosseen, D., Goetz, W., and Hires, W. G., 1996, "Heavy-Duty Engine Exhaust Emission Tests Using Methyl Ester Soybean Oil/Diesel Fuel Blends," Bioresour. Technol., **57**, pp. 31–36.
[8] Szybist, H. P., Boehman, A. L., Taylor, J. D., and McCormick, R. L., 2005, "Evaluation of Formulation Strategies to Eliminate the Biodiesel NO_x Effect," Fuel Process. Technol., **86**, pp. 1109–1126.
[9] Agarwal, D., Shailendra, S., and Agarwal, A. K., 2006, "Experimental Investigation of Control of NO_X Emissions in Biodiesel-Fueled Compression Ignition Engine," Renewable Energy, **31**, pp. 2356–2369.
[10] Minami, T., Takeuchi, K., and Shimakezi, N., 1995, "Reduction of Diesel Engine NO_x Using Pilot Injection," SAE Paper No. 950611.
[11] Carlucci, P., Ficaralla, A., and Laforgia, D., 2003, "Effect of Pilot Injection Parameters on Combustion for Common Rail Diesel Engines," SAE Paper No. 2003-01-0700.
[12] Zhang, L., 1999, "A Study of Pilot Injection in a DI Diesel Engine," SAE Paper No. 1999-01-3493.
[13] Tennison, P. J., and Reitz, R., 2001, "An Experimental Investigation of the Effects of Common-Rail Injection System Parameters on Emissions and Performance in a High-Speed Direct-Injection Diesel Engine," ASME J. Eng. Gas Turbines Power, **123**, pp. 167–174.
[14] Tanaka, T., Ando, A., and Ishizaka, K., 2002, "Study on Pilot Injection of DI Diesel Engine Using Common-Rail Injection System," JSAE Rev., **23**, pp. 297–302.
[15] Choi, C. Y., and Reitz, R. D., 1999, "An Experimental Study on the Effects of Oxygenated Fuel Blends and Multiple Injection Strategies on DI Diesel Engine Emissions," Fuel, **78**, pp. 1303–1317.
[16] Joshi, R. M., and Pegg, M. J., 2007, "Flow Properties of Biodiesel Fuel Blends at Low Temperatures," Fuel, **86**, pp. 143–151.
[17] Kegl, B., 2006, "Numerical Analysis of Injection Characteristics Using Biodiesel Fuel," Fuel, **85**, pp. 2377–2387.
[18] Wu, Z., Zhu, Z., and Huang, Z., 2006, "An Experimental Study on the Spray Structure of Oxygenated Fuel Using Laser-Based Visualization and Particle Image Velocimetry," Fuel, **85**, pp. 1458–1464.
[19] Bosch, W., 1966, "The Fuel Rate Indicator: A New Measuring Instrument for Display of the Characteristics of Individual Injection," SAE Technical Paper No. 660749.

Optical Diagnostics of Late-Injection Low-Temperature Combustion in a Heavy-Duty Diesel Engine

Thierry Lachaux

Mark P. B. Musculus
e-mail: mpmuscu@sandia.gov

Sandia National Laboratories,
P.O. 969, MS9053,
Livermore, CA 94551

Satbir Singh
Powertrain Systems Research Laboratory,
General Motors Research and Development,
Warren, MI 48090

Rolf D. Reitz
Engine Research Center,
Department of Mechanical Engineering,
The University of Wisconsin, Madison,
1500 Engineering Drive,
Madison, WI 53706

A late-injection, high exhaust-gas recirculation rate, low-temperature combustion strategy is investigated in a heavy-duty diesel engine using a suite of optical diagnostics: chemiluminescence for visualization of ignition and combustion, laser Mie scattering for liquid-fuel imaging, planar laser-induced fluorescence (PLIF) for both OH and vapor-fuel imagings, and laser-induced incandescence for soot imaging. Fuel is injected at top dead center when the in-cylinder gases are hot and dense. Consequently, the maximum liquid-fuel penetration is 27 mm, which is short enough to avoid wall impingement. The cool flame starts 4.5 crank angle degrees (CAD) after the start of injection (ASI), midway between the injector and bowl rim, and likely helps fuel to vaporize. Within a few CAD, the cool-flame combustion reaches the bowl rim. A large premixed combustion occurs near 9 CAD ASI, close to the bowl rim. Soot is visible shortly afterward, along the walls, typically between two adjacent jets. OH PLIF indicates that premixed combustion first occurs within the jet and then spreads along the bowl rim in a thin layer, surrounding soot pockets at the start of the mixing-controlled combustion phase near 17 CAD ASI. During the mixing-controlled phase, soot is not fully oxidized and is still present near the bowl rim late in the cycle. At the end of combustion near 27 CAD ASI, averaged PLIF images indicate two separate zones. OH PLIF appears near the bowl rim, while broadband PLIF persists late in the cycle near the injector. The most likely source of broadband PLIF is unburned fuel, which indicates that the near-injector region is a potential source of unburned hydrocarbons. [DOI: 10.1115/1.2830864]

1 Introduction

Diesel engines are widely used throughout the world and satisfy a large customer demand, partly due to their higher energy efficiency compared to other engines. Pressure from the market for more energy-efficient engines and more stringent emission regulations have motivated improvements in diesel engine technology. Among regulated emissions are nitrogen oxides (NO_x) and particulate matter (PM). NO_x and PM are both affected by the fuel injection timing, pressure, and rate of injection. Recent developments in high-pressure electronically controlled common-rail injection systems give freedom to optimize the fuel injection schedule to reduce NO_x and PM levels as much as possible.

These systems have also enabled new low-temperature combustion (LTC) strategies. LTC strategies can reduce the need for exhaust after treatment by reducing engine out NO_x and PM. To this end, they often use a large amount of exhaust-gas recirculation (EGR) to lower the flame temperature and thereby reduce NO_x production, and allow more time for air and fuel to premix to help decrease PM emissions [1–5]. Many LTC strategies have been demonstrated in diesel-type engines, including double injection such as Toyota's UNIBUS concept [6], early injection [7], or late injection such as modulated kinetics (MK) [1–3]. Unlike other strategies where an early injection yields a more premixed charge, the MK strategy uses a late injection occurring near or somewhat after top dead center (TDC) of the compression stroke. Due to the falling in-cylinder temperature and density after TDC, late fuel injection increases the ignition delay, which is the time between the start of injection (SOI) and the start of combustion. Extending the ignition delay enhances the precombustion air-fuel mixing, but the retarded combustion phasing may also decrease cycle efficiency. However, some have argued that with high swirl, heat transfer losses are reduced so that cycle efficiency can be maintained [1–3].

One significant drawback of MK combustion, and of LTC in general, is the increase of unburned hydrocarbons (UHCs). UHC emissions, as well as soot and NO_x formation, are strongly related to the physical and chemical processes occurring within the combustion chamber. For example, increasing swirl can help to reduce UHC emissions, but they still remain higher than for conventional diesel combustion. Furthermore, many MK studies focused on small size direct injection (DI) diesel engines with large swirl numbers, reentrant piston bowls, and high engine speeds [1–5]. The in-cylinder mixing and combustion process in the quiescent chamber, large bore, and medium speed range of heavy-duty diesel engines may affect MK combustion processes very differently than in small-bore engines.

Using in-cylinder visualization, understanding of the important MK combustion processes can be improved and distilled into a conceptual model, along the lines of Dec's model for conventional diesel combustion [8]. Currently, little in-cylinder visualization data are available for the MK combustion strategy. The few examples include Kimura and co-workers [1–3], who showed that in-cylinder MK combustion is mainly nonsooty. Also, in a previous work [9], we presented combustion luminosity images of MK combustion in a large-bore engine. However, comprehensive visualizations of in-cylinder injection, mixing, and combustion events of the MK strategy are not yet reported in the literature.

In the current study, in-cylinder combustion processes for an EGR-diluted, late-injection condition that is similar to MK combustion, but in a low-swirl heavy-duty diesel engine, are detailed using a set of optical diagnostics. The liquid-fuel jet penetration is investigated using images of Mie scattering from liquid-fuel drop-

Manuscript received October 23, 2007; final manuscript received October 24, 2007; published online April 2, 2008. Review conducted by Dilip R. Ballal.

Table 1 Engine specifications, injector specifications and operating conditions

Engine base type	Single-cylinder four-stroke Cummins N-14, DI Diesel
Number of intake valves	2
Number of exhaust valves	1[a]
Combustion chamber	Quiescent, direct injection
Swirl ratio	0.5
Bore × stroke	139.7×152.4 mm^2
Bowl width, depth	97.8 mm, 15.5 mm
Displacement	2.34 l
Connecting rod length	304.8 cm
Geometric compression ratio	11.2:1
Simulated compression ratio	16:1
Fuel injector type	Common rail, pilot valve actuated
Cup (tip) type	Minisac
Number of holes	8, equally spaced
Spray pattern included angle	152 deg
Rail pressure	1600 bars
Nozzle orifice diameter	0.196 mm
Nozzle orifice L/D	5
SOI	360 CAD (TDC)
Mass injected per cycle	56 mg
DOI	9 CAD
Intake temperature	70°C
Intake pressure	202 kPa
Intake oxygen concentration	12.7% (~60% EGR)
Temperature at TDC	840 K
Density at TDC	22.7 kg/m^3
Engine rotational speed	1200 rpm

[a]In this optically accessible diesel engine, one of the two exhaust valves of the production cylinder head was replaced by a window and periscope.

lets. Two-stage ignition is visualized by chemiluminescence imaging. The liquid-fuel visualization coupled with the chemiluminescence gives information on the temporal dwell between the injection and the ignition processes, which is an indicator of the potential for UHC emission [10]. Planar laser-induced fluorescence (PLIF) of the fuel molecules indicates the leading edge of the penetrating vapor-fuel jet. PLIF of OH marks the high-temperature combustion. Finally, soot is detected using soot luminosity and laser-induced incandescence (LII) techniques. OH and soot visualizations provide a sequence of the main combustion heat release and the soot history.

2 Experimental Setup and Diagnostics

2.1 Engine and Injector. The engine is an optical single-cylinder diesel engine with the same bore and stroke as the production Cummins N-14 heavy-duty engine, 139.7 and 152.4 mm, respectively. This configuration gives a displacement of 2.34 l for the single-cylinder engine. Table 1 provides engine characteristics, injector characteristics, and engine operating conditions. The engine configuration is further described in Refs. [7,8,11].

The quiescent chamber engine has a low-swirl number (0.5). Because of modifications for optical access, the compression ratio is 11.2, compared to 16 for the production engine. To compensate, the intake pressure and temperature are elevated so that the thermodynamic state at TDC is typical of that for the production engine. To reduce the combustion temperature, the intake stream is diluted to 12.7% oxygen concentration (equivalent to approximately 60% EGR) by nitrogen addition. The engine was operated at a single, constant speed of 1200 rpm (rotations per minute) with a gross indicated mean effective pressure of 450 kPa, or roughly 25% of full load.

To provide optical access, the engine is equipped with an extended piston and a flat piston-crown window, as shown in Fig. 1 on the left side. A stationary mirror placed below the piston window provides a view of the combustion chamber to the camera/imaging system. Additional windows located around the top of the cylinder wall provide cross-optical access for laser-based diagnostics. A portion of the piston bowl wall was also fitted with an optical window that matched the contours of the bowl rim, in line with one of the cylinder-wall windows, as shown on the top right Fig. 1. This window allowed laser-sheet access into the combustion bowl of the piston, along the axis of one of the injector fuel jets.

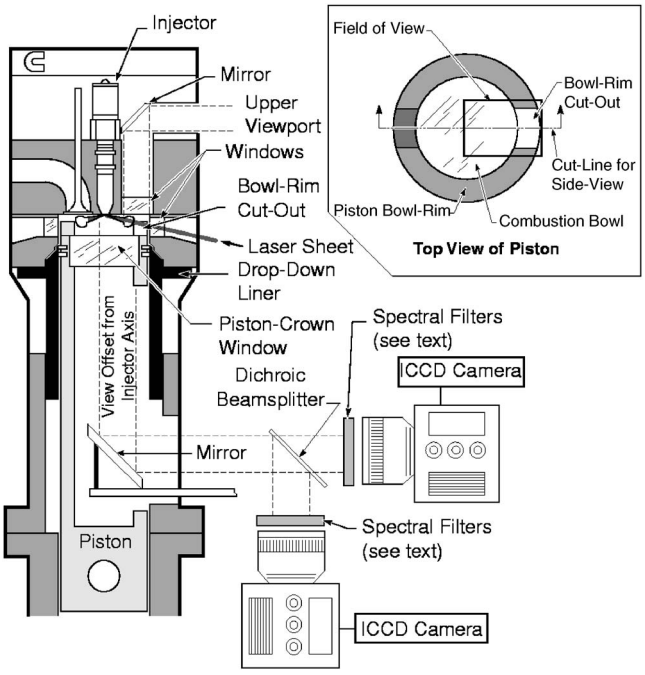

Fig. 1 Engine cross-section schematic and optical diagnostics setup and field of view from the piston window (inset)

The nonproduction common-rail injector is electronically controlled and the rail pressure was 1600 bars. The minisac injector has eight equally spaced 0.196 mm diameter holes and an included angle of 152 deg. To avoid overheating, the optical engine was skip fired once every 10 cycles and an electric dynamometer maintained engine speed between fired cycles. Finally, in the operating conditions, listed in Table 1, the SOI value is the real, physical start of liquid-fuel injection, which is 3 crank angle degrees (CAD) after the electronic firing signal.

2.2 Optical Diagnostics. Two different laser systems were used in this study. First, an optical parametric oscillator, pumped by the third harmonic of a Nd:YAG (yttrium aluminum garnet) laser at 355 nm, generated 10 Hz, 10 ns pulsed laser radiation near 568 nm, which was frequency doubled to near 284 nm with 17 mJ per pulse for the fluorescence diagnostics (described below). Second, a 10 Hz frequency-doubled Nd:YAG laser generated 10 ns pulses at 532 nm with 35 mJ per pulse for the other two laser diagnostics. Both beams were converted into thin (less than 1 mm thick) sheets using a combination of cylindrical and spherical lenses. As shown in Fig. 1, the two sheets were overlapped and directed into the cylinder at a slope of 14 deg from horizontal, which is parallel to the axis of the fuel jet that was in line with the cylinder-wall and piston bowl-rim windows. After being clipped by the window aperture, the sheet was about 35 mm wide inside the combustion chamber.

The combustion chamber was visualized through the piston-crown window using two ultraviolet (UV)-sensitive, gated, intensified charge-coupled device (CCD) video cameras. To achieve simultaneous imaging, the signals were chromatically separated by a 450 nm cut off dichroic beamsplitter, which reflected UV

light and transmitted visible light (see Fig. 1). The camera receiving long-wavelength (visible) light was equipped with a Nikkor 105 mm $f/2.5$, glass lens. The camera receiving short-wavelength (UV) light was equipped with an UV Nikkor 105 mm $f/4.5$ lens. In addition, a filter pack appropriate for the diagnostic of interest was placed in front of the lenses for each camera, as described in the following paragraphs.

The liquid-phase diesel fuel was imaged by collecting the Mie-scattered light from liquid droplets (liquid Mie scattering, or LMS) illuminated by the 532 nm laser sheet and using a 532 nm bandpass filter (BPF). The 532 nm laser beam also induces weak elastic Rayleigh scattering from the vapor phase fuel, but the Mie-scattered light is many orders of magnitude stronger than the Rayleigh scattered light [12]. As a result, only liquid-fuel Mie scattering is discernable within the dynamic range of the camera. A neutral density filter attenuated strong elastic scatter to avoid damaging the intensified CCD camera and to ensure that it operated in its linear regime. The camera electronic gate was set to 120 ns. The technique is described in more details in Ref. [13].

Ignition chemiluminescence and soot luminosity are line-of-sight averaged diagnostics. To avoid excessive smearing due to fluid motion, the camera gate width was set to 70 ms, which is equal to one-half CAD at 1200 rpm. The chemiluminescence emission is due to many species including CH, C_2, and formaldehyde (H_2CO), [14–16], but other radicals are present as well. The emission is relatively weak, so to maximize signal strength, no spectral filters were used and thus no specific species were tracked. The other much stronger source of photonic emission is due to naturally occurring soot incandescence. Soot typically forms after the premixed-combustion phase, and its emission is many orders of magnitude stronger than chemiluminescence [16].

Soot LII was excited by the Nd:YAG laser second harmonic at 532 nm. Three filters, a 480–580 notch filter, a 380-450 BPF and a 330-620 BPF in front of the camera isolated the LII signal from elastic scatter. The camera gate was set to 100 ns. This LII filtering scheme is essentially the same as that described in Refs. [11,17,18].

Finally, a single UV fluorescence technique yielded information about either OH or fuel distributions, depending on the sensitivity of the fluorescence signal to the laser wavelength. First, OH fluorescence was excited at 284.01 nm and fluorescence was observed near 310 nm. A set of three filters (310 nm unblocked narrow BPF, 310 nm blocked BPF with 90 nm full width at half maximum (FWMH), and color glass SWG305) was placed in front of the camera to isolate OH-PLIF from elastically scattered light.

OH, however, displays a unique, well-defined fine-scale rovibrational structure in its fluorescence excitation spectrum. As a result, the OH fluorescence decreases drastically as the laser wavelength is tuned off any of the narrow excitation lines. By contrast, interfering fluorescence from other species, such as polycyclic aromatic hydrocarbon (PAH) soot precursors or fuel aromatics, is insensitive to small changes in the excitation wavelength. Therefore, to identify the extent and spatial location of the interference, the OH-PLIF images were taken at two different wavelengths: on-line, near 284.01 nm, and off-line, near 283.90 nm. A locally stronger on-line signal indicates the presence of OH. More details, including the filter selection criteria, can be found in Ref. [19].

The second fluorescence technique applies when the on-line and off-line fluorescence signal strengths are similar. If no fine-scale absorption structure is apparent, then the fluorescence is from broadband sources (i.e., BB-PLIF). The laser wavelength and filters for the BB-PLIF technique are the same as those for the OH-PLIF technique. Early in the cycle, before significant chemical reactions, the most likely source of BB-PLIF is fluorescing components of the liquid- and vapor-phase fuel. Later in combustion, other species, such as PAH soot precursors and other combustion intermediates, may also contribute to the BB-PLIF. Additional details can be found in Ref. [20].

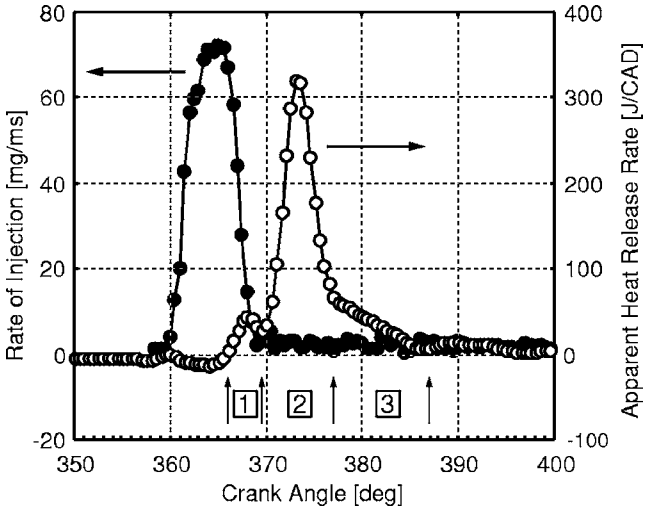

Fig. 2 Mass rate of injection and APHR. The boxed numbers 1, 2, and 3 represent the cool-flame phase, the premixed-combustion phase, and the mixing-controlled phase, respectively

Finally, due to repetition-rate limitations of the lasers (10 Hz), only one image could be acquired for each engine cycle. For each crank angle, images were acquired in sets of 12, from 12 different cycles. Either a representative instantaneous image was then selected from each set, or an ensemble-averaged image was extracted. Depending on the analysis required, these selected images were compiled into temporal sequences.

3 Combustion and Injection Events

3.1 Apparent Heat Release Rate and Combustion Phases. The apparent heat release rate (AHRR) was determined from the cylinder pressure, using an air-standard first-law analysis [21]. Prior to calculating the AHRR, the pressure data were smoothed using a Fourier-series low-pass filter with a Gaussian roll-off function having a transmission of 100% from 0 to 800 Hz and dropping to 1% at 3360 Hz. These cutoff frequencies were selected to remove acoustic ringing caused by combustion pressure oscillations in the cylinder pressure data while retaining the general features of the AHRR. Due to this filtering, the peak of the premixed burn spike in the filtered AHRR was reduced by about 14%, while its width was increased by a factor of 1.2. However, the apparent energy release (area under the AHRR curve) during the premixed burn was virtually unchanged by this filtering technique. The filtering technique does not significantly alter the critical features of AHRR such as the time of transition for different phases of combustion, including the ignition delay.

The injection rate signal and AHRR are plotted on Fig. 2. The injection rate was derived from the spray momentum, measured at atmospheric pressure in a closed vessel, as described in Refs. [7,22]. In the engine, the fuel is injected at TDC where in-cylinder gases reach maximum compression and thereby promote fuel vaporization. The temperature at the start of the injection event (TDC), estimated from a polytropic law, is 840 K. At the SOI (360 CAD), the AHRR starts to decrease, due to cooling by the vaporizing fuel. After vaporization, the AHRR plotted in Fig. 2 exhibits three distinct combustion phases. As discussed in the next section, the precise beginning of the first phase depends on its definition, but using the first zero crossing of the AHRR in Fig. 2, the first "cool-flame" phase starts at 366 CAD. The first phase ends between 369 and 370 CAD, overlapping with the beginning of the second phase, premixed combustion. The premixed-combustion phase lies between 370 and 377 CAD. Finally, the third phase, mixing-controlled combustion, lies between 377 and

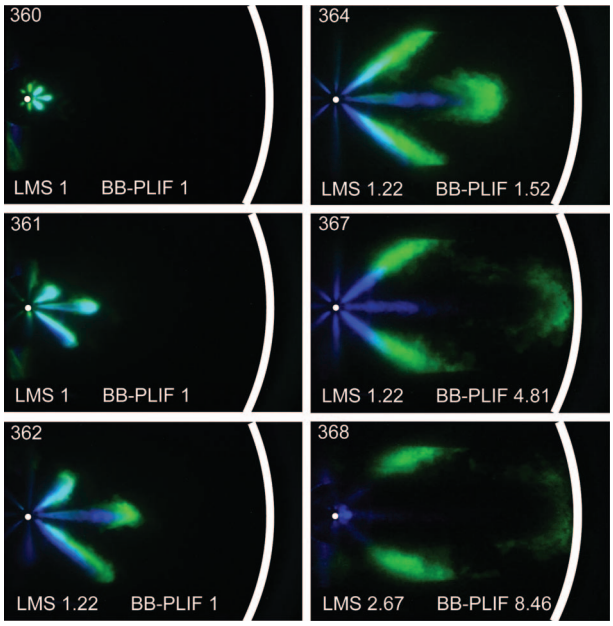

Fig. 3 Liquid-phase (LMS, blue) and vapor-phase (BB-PLIF, green) fuels. The crankshaft angle is displayed on the top left corner and the LMS and BB-PLIF gains are on the bottom of each image. The small white dot marks the injector location and the thick white line indicates the location of bowl rim, 50 mm from the injector.

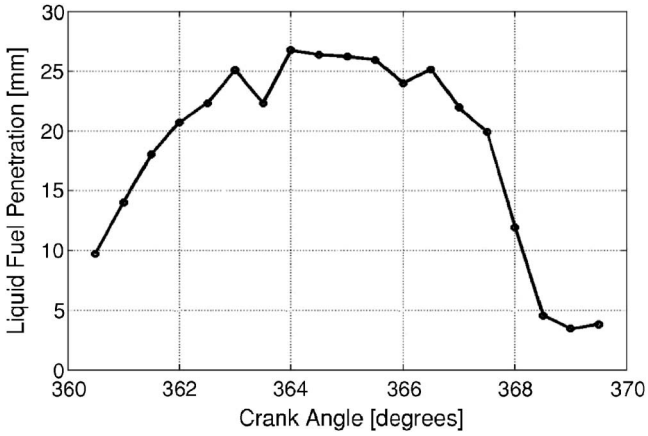

Fig. 4 Liquid length extracted from the LMS instantaneous images

387 CAD.

A previous study [10] related these three combustion phases to typical two-stage chemistry. The low-temperature cool-flame and slow oxidation processes start and end during the first phase. They release a small amount of the total heat and characterize the first-stage chemistry; the maximum AHRR of the cool-flame phase is about 12% of the peak premixed-combustion AHRR. The second-stage chemistry is involved in both the premixed- and mixing-controlled-combustion phases, where the rest of the fuel chemical energy is released.

As for the other LTC strategies, the ignition delay for MK combustion is typically longer than the injection duration so that injection and combustion do not overlap. In these experiments, the cool-flame phase and the injection do overlap slightly, but the premixed-combustion phase does not overlap at all with the injection. Furthermore, the injection rate is rapidly decreasing during the overlap with the cool-flame phase, so significant premixing still occurs before premixed combustion, as will be seen in the next sections.

3.2 Injection and Cool-Flame Phase. Superposition of virtually simultaneous images of LMS and BB-PLIF (fuel) are presented in Fig. 3. A comparison of on-line and off-line signals in the BB-PLIF images (as described in Sec. 2.2 for OH-PLIF), not shown here, indicates that there is no OH-PLIF and nearly all of the BB-PLIF is therefore due to fuel components. The 10 ns laser pulses for LMS and BB-PLIF were separated by 1 ms to avoid any interference in the signals for the two diagnostics. The images are ensemble averaged over 12 cycles. The effective camera gain for each diagnostic is displayed at the bottom of each image, and the relative gain is valid only for a given camera. That is, the gain for the BB-PLIF camera is different from the gain for the LMS camera. The laser sheet propagates from right to left. The field of view is limited by the bowl rim on the right side, and the injector is visible on the left side, indicated by a white dot. The false blue color displays the LMS signal corresponding to the liquid phase of the jet, while the false green color represents the BB-PLIF signal.

The BB-PLIF signal is due to emission from both liquid and vapor fuels, which cannot be distinguished from each other using BB-PLIF images alone. However, comparison with the LMS images, which show only liquid-phase fuel, can provide guidance for interpreting the BB-PLIF images. For example, considering the horizontal jet (3 o'clock position) at 364 CAD and later, the UV beam (BB-PLIF) at 284 nm crosses first the leading edge of the jet and is strongly absorbed by fuel vapor, so that very little laser light reaches the liquid-fuel spray. (Some attenuation is also apparent in the 362 CAD image.) Furthermore, the LMS image at 364 CAD shows that that liquid fuel in the horizontal jet (blue) is entirely upstream of the BB-PLIF signal (green). Consequently, for 364 CAD and later, only the vapor-phase fuel appears in the BB-PLIF images for the horizontal jet. The absorption by the leading edge of the horizontal jet is also responsible for the lack of BB-PLIF signal in the upstream region of the jet at 364 CAD and later.

The initial liquid jet is detected at 360 CAD in Fig. 3. At 361 CAD, some vapor-phase fuel is first visible in the BB-PLIF image outside of the periphery of the liquid-phase fuel in the LMS image. That is, fluorescence in the green BB-PLIF image is from both vapor and liquid fuels, but the liquid-fuel location is clearly identified by the overlapping blue LMS image. Therefore, the purely green color on the periphery of the 361 CAD image (without overlapping of blue color from LMS) indicates vapor fuel only. At 362 CAD, the blue liquid phase penetrates farther, and the green vapor phase expands at the leading edge of the horizontal jet. As aforementioned, the 284 nm light sheet is absorbed by vapor fuel located downstream at the leading edge of the jet, so the fuel closer to the injector tip is not illuminated in the BB-PLIF image. However, the UV laser sheet can reach the sides of the adjacent jets at the 1 o'clock and 5 o'clock positions. These jets show some vapor-fuel fluorescence (green) closer to the injector, in addition to the liquid fluorescence (green and blue overlap). Therefore, the vapor fuel surrounds the entire liquid-phase spray.

At 364 CAD, the vapor-fuel region located at the head of the jet (green) penetrates downstream of the liquid fuel. The shape and geometry of the liquid spray is typical of conventional diesel sprays, which also have short penetration [8,23]. Figure 4 shows the evolution of the liquid length of the horizontal jet, defined as the farthest downstream location where the LMS image intensity is higher than 10% of the difference between the lowest (background) and highest (in the liquid jet) intensities of the image. The signal intensity has been found nearly constant along the background level. The intensity gradient in the LMS images at the tip of the liquid spray is steep, so intensity thresholding works well to measure the liquid penetration. A 10% threshold has been found to provide reliable liquid length measurements [24].

Figure 4 shows that from 363 to 366 CAD, the liquid length

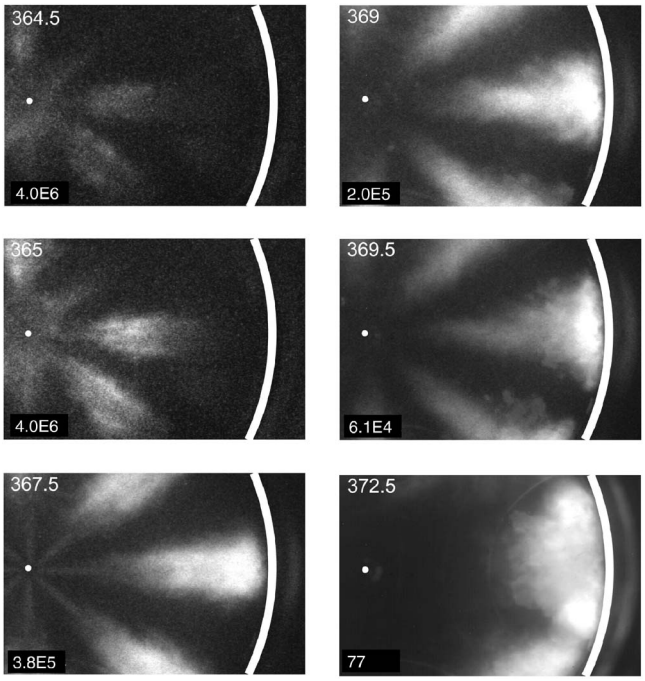

Fig. 5 Chemiluminescence averaged pictures. The crank angle is displayed on the top left corner while the relative gain is displayed at the bottom left corner. The small white dot marks the injector location and the thick white line indicates the location of bowl rim, 50 mm from the injector.

reaches its maximum value of 26–27 mm and remains approximately constant for about 3 CAD. This short-injection liquid length can be compared to predictions of Siebers' scaling law for liquid penetration of steady diesel fuel sprays [25]. In Siebers' spray model for steady jets, the vaporization rate in the downstream part of the jet counterbalances the fuel injection rate. Among many factors, hole diameter, fuel characteristics (volatility, fuel temperature), and thermodynamic factors (ambient density and temperature) affect the liquid length. In our single-cylinder engine with injection near TDC, the ambient density and temperature are approximately 22.7 kg/m^3 and 840 K. For these conditions, the scaling law for steady jets predicts a liquid length of about 35 mm, which is somewhat greater than the 26–27 mm maximum liquid penetration of the jet in the current study (see Fig. 4). Differences in the orifice coefficients or the spray spreading angle may account for some of the difference, as well as the short injection duration of the current study, for which the full, steady liquid length may not be established.

The large distance from the injector to the bowl rim in heavy-duty diesel engines and the high-density, hot in-cylinder environment near TDC help to prevent impingement of liquid fuel on the combustion chamber walls. Impingement sometimes occurs with early-injection LTC strategies [13], and avoiding impingement might prevent additional soot and UHC emissions resulting from wall wetting. Hotta et al. [26] note that in a small indirect injection diesel engine at medium to high-load conditions, wall impingement by the liquid jet creates a locally rich-fuel mixture that causes increased exhaust soot emission. Tsurushima et al. [27] confirm that liquid wall impingement in a small DI diesel engine yields UHC emissions. However, for a large-bore DI diesel engine, Fig. 4 shows that the liquid-fuel penetration is too short to cause wall impingement of the liquid fuel for these near-TDC injection conditions.

Figure 5 displays a sequence of chemiluminescence images. For each CAD, 12 images are ensemble averaged. Chemiluminescence identifies spatial and temporal locations of ignition. The initial signal from chemiluminescence in Fig. 5 is very low relative to the latter in the cycle, as indicated by the high camera gain (displayed at the bottom left corner). The beginning of the first combustion stage is detected at 364.5 CAD, halfway between the injector and the bowl rim. This chemiluminescence occurs 1.5 CAD earlier than the first zero crossing of the AHRR in Fig. 2. The small amount of heat released during the first ignition stage is likely not enough to significantly affect the pressure trace, so it does not increase the AHRR significantly. Moreover, any small increase of pressure, which could occur during the beginning of this first stage ignition, is likely offset by the decrease of pressure from liquid vaporization. Consequently, the actual the start of combustion is somewhat ambiguous, because chemiluminescence emission begins 1.5 CAD earlier than the first zero crossing of the AHRR.

At 367 CAD, referring back to Figs. 3 and 4, the liquid length begins to decrease, while the leading edge of the vapor fuel of the horizontal jet reaches the bowl rim. Again, attenuation by the head of the horizontal jet does not allow the laser to illuminate fuel in the upstream region of the horizontal jet, so no information about upstream vapor fuel is available. However, the adjacent jets, which are illuminated from the side, show that vapor fuel does extend back toward the injector. The region very near the injector for all of the jets is not illuminated due to attenuation by the wide head of the horizontal jet, so no information about vapor fuel very near the injector can be discerned from the later images in Fig. 3.

At 367.5 CAD, the chemiluminescence in Fig. 5 indicates that the combustion zone reaches the bowl rim, and the jets are clearly flattening against the bowl rim. At 367.5 CAD, the top of the piston is close to the fire deck (around 5 mm), thus most of combustion likely occurs within the piston bowl. Combustion is still in the cool-flame phase (Fig. 2), though the camera gain is reduced by an order of magnitude from the 367 CAD image because of increased chemiluminescence intensity.

The physical end of injection occurs near 368 CAD (see Fig. 2). Referring back to the 368 CAD image in Fig. 3, some liquid-fuel spray remains, but with a much shorter length and weaker LMS signal. The heat released by the combustion, including both first-stage and maybe some second-stage reactions, occurs at the same time and likely aids the evaporation process. At 369 CAD in Fig. 5, the reaction zone starts to spread circumferentially along the bowl rim as combustion transitions to the premixed phase.

3.3 Premixed Phase. Near the bowl rim at 369.5 CAD in Fig. 5, the downstream part of the jet becomes much brighter. Eventually, it merges with adjacent jets and forms a large ring along the bowl wall at 372.5 CAD, with much brighter emission as indicated by the decreasing gain. The strong natural luminosity at 372.5 CAD originates from soot, as will be confirmed later in this section by the LII images of Fig. 7. Note that the ring shape appears because of the averaged pictures. Indeed, instantaneous images in Fig. 7 show soot in pockets between two adjacent jets, near the bowl rim.

The peak AHRR also occurs near 372.5 CAD (Fig. 2), where soot luminosity first becomes strong. In a small-bore engine with low EGR, Miles et al. observed soot appearing in the jet similar to conventional diesel injection strategies [4]. For high EGR conditions, with 15% intake O_2 (comparable to the 12.7% level in these experiments), soot formation was delayed and a distinct jet structure was no longer apparent [4]. In our experiment, injection occurring close to TDC leads to a shorter ignition delay, and with very little swirl, the jet structure remains at the onset of soot formation.

Figure 6(*a*) presents the local natural luminosity intensity (both chemiluminescence and soot incandescence) for various CADs, computed with averaged images, along the centerline of the jet from the bowl rim to roughly 8 mm downstream of the injector tip. This intensity is corrected for the varying camera gains. During the combustion sequence, the most intense luminous region moves from upstream to downstream. The intensity from the cool

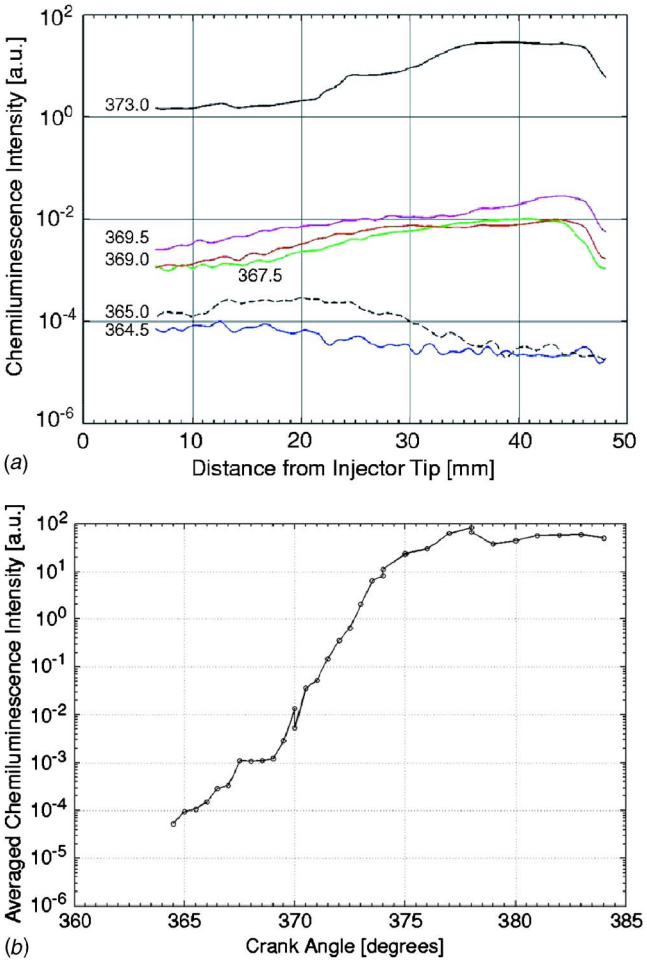

Fig. 6 Natural luminosity intensity, plotted (*a*) along the jet centerline and (*b*) averaged along the centerline

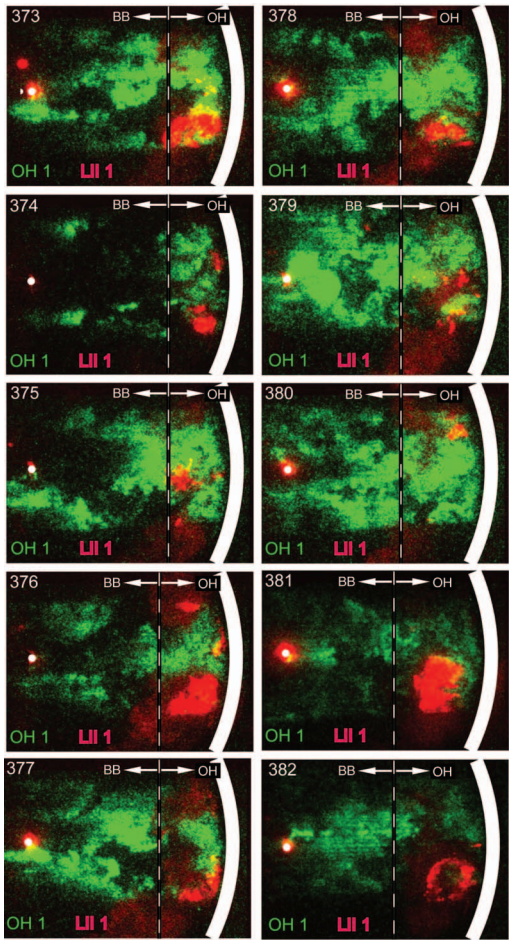

Fig. 7 Instantaneous images from fuel and OH fluorescence (green) and laser-induced incandescence (red). The crank angle is displayed at the top left corner of the picture while the relative gains are displayed at the bottom. The small white dot marks the injector location and the thick white line indicates the location of bowl rim, 50 mm from the injector. The vertical dashed line indicates the approximate separation of fluorescence from OH, on the right, and broadband sources (e.g., fuel), on the left.

flame (364.5–365 CAD) is lower by a factor of 5–6 orders of magnitude than the intensity from soot (373 CAD). In addition, the straight lines on the graph indicate an approximately exponential evolution in time and at least one order of magnitude difference in intensity along the jet centerline.

Figure 6(*b*) presents the combustion natural luminosity intensity described previously but averaged along the jet centerline, versus CAD. The intensity increases by seven orders of magnitude, roughly exponentially with time between 366 CAD where the cool flame occurs and 374 CAD at the AHRR peak. Thereafter, the emission reaches an asymptote corresponding to the strong soot emission. As an alternative method, the combustion intensity was also averaged over a 45 deg sector from the injector tip to the bowl rim. The results are not reported here, but the results are essentially the same as Fig. 6(*b*).

Figure 7 shows instantaneous, simultaneous false-color images of LII (red) and OH PLIF (green). Due to the cycle-to-cycle variation, images are selected as the best representatives at each CAD. First, considering the red LII images, soot is mostly present in large pockets near the bowl rim (downstream in the jet) in both the lower- and the upper-right corners of the laser sheet, as visible at 376 CAD for example. The soot LII in the upper-right corner generally appears weaker because that soot is carried out of the laser sheet by the weak swirl. Recall that the rapidly increasing brightness in the natural luminosity images in Fig. 5 suggested that soot starts to form close to the bowl rim. We reported similar soot locations in earlier experiments at the same operating condition in this engine [20]. Also, in Ref. [28], soot appeared downstream, between adjacent jets in a different DI heavy-duty diesel engine. The interaction at the bowl wall between adjacent jets could form a rich fuel zone, therefore creating soot. It is shown in Ref. [28] that an oxygenated fuel helps to decrease the local equivalence ratio and thereby decreases soot formation at where the jets interact along the bowl wall.

Considering the green OH-PLIF images in Fig. 7, the OH fluorescence, which first appears near 373 CAD, must be discriminated from BB-PLIF, which is also present. Unfortunately, instantaneous on-line and off-line images cannot be acquired at the same time. Rather, the general behavior of on-line OH-PLIF must be compared to the general behavior of off-line OH-PLIF. Figure 8 displays four ensemble-averaged images of OH-PLIF taken on-line (red) superimposed with images taken off-line (green). The pure red color indicates OH fluorescence, because OH fluoresces at the on-line wavelength and not at the off-line wavelength. The pure green color indicates that a compound, which is not OH, fluoresces at the off-line wavelength, and very little OH-PLIF is present. A yellow color indicates that the on-line and off-line signals overlap. In other words, the yellow color indicates that something is fluorescing at both on-line and off-line (not OH) wavelengths, though some OH may be present too. The black color indicates either no fluorescence sources are present, or that the laser light is absorbed and cannot reach the area [29].

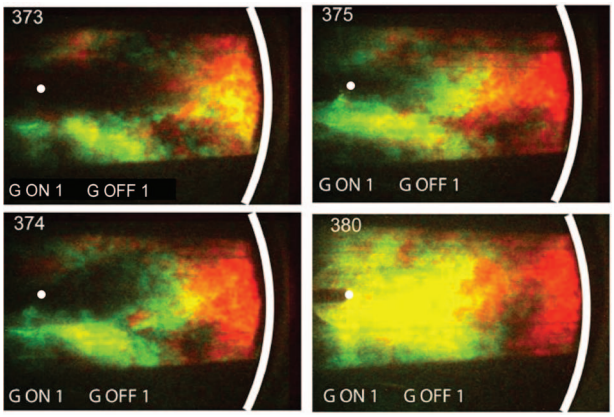

Fig. 8 On-line (red) and off-line (green) ensemble-averaged OH-PLIF images. The crank angle is displayed on the top left corner while the relative gains are displayed on the bottom. The small white dot marks the injector location and the thick white line indicates the location of bowl rim, 50 mm from the injector.

At 373 CAD, OH (red and perhaps yellow) is mainly located between midway from the injector tip to the bowl rim and the bowl rim. The OH becomes more dominant close to the bowl rim at 374 CAD and at 375 CAD, where the red color covers a larger area. Similar to Fig. 7, a dark zone is located between injector tip and midway between the injector tip and the bowl rim at 373 and 374 CAD. As explained earlier, this dark zone is due to the laser-sheet attenuation. From 375 to 380 CAD, most of the OH is located near the bowl rim. Therefore, the fluorescence observed on the right-hand side of the vertical dashed line in Fig. 7, between the two soot pockets from 378 to 380 CAD, is expected to be OH, based on the strong contrast between on-line and off-line averaged images in Fig. 8. The fluorescence signal near the injector, on the left-hand side of the dashed vertical line, is most likely fuel fluorescence. Certainly, it is some product of incomplete combustion, since complete combustion products (H_2O and CO_2) do not fluoresce at these wavelengths. Also, formaldehyde chemiluminescence attributed to cool-flame reactions has been observed upstream of OH chemiluminescence [30], similar to the proximity of cool-flame chemiluminescence (Fig. 5 at 365 CAD) and OH-PLIF (Figs. 7 and 8 near 373 CAD) of the current study.

Figure 9 displays selected representative, instantaneous, superimposed pictures of OH and natural luminosity. Recall that natural luminosity is integrated along the line of sight, while the OH-PLIF originates from the laser sheet only. Comparison with Fig. 7 confirms that the red-colored pockets near the bowl rim are certainly natural luminosity from soot, with strong OH-PLIF generally farther upstream. Similar behavior was reported for an early-injection LTC condition in the same engine, with broad distributions of OH downstream and pockets of soot at the head of the jet [20]. Also, in a constant-volume combustion vessel under similar conditions, with kernels of soot formed downstream of OH chemiluminescence [30].

3.4 Mixing-Controlled Phase. From 378 through 383 CAD in Figs. 7 and 9, fuel and OH fluorescence become more broadly distributed during the mixing-controlled phase. In Fig. 8 (on-line/off-line averaged images), OH typically appears from the bowl rim to half way to the injector tip for 375 to 380 CAD. The complementary region, from the injector through halfway to the bowl rim, has a strong off-line signal. Once again, the most likely source of the off-line signal is unburned fuel. At 383 CAD, the AHRR is very low and the fuel likely remaining near the injector represents a potential source of UHCs.

Large soot pockets remain late in the cycle in Figs. 7 and 9. The AHRR (Fig. 2) indicates that combustion is almost completed by 383 CAD, so much of the soot may survive into the exhaust. In

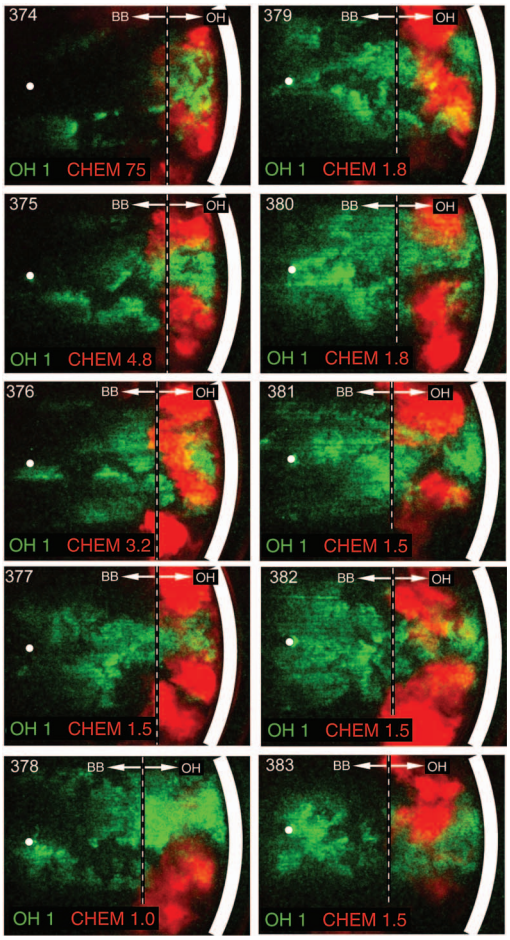

Fig. 9 Instantaneous images of simultaneous OH fluorescence (green) and chemiluminescence and/or soot luminosity (red). Annotation is same as for Fig. 7.

Ref. [18], the authors noted that with a retarded injection and N_2 dilution as a surrogate for EGR, soot increased significantly. They saw more soot LII with less OH-PLIF than in the normal timing. Miles et al. [4] observed that soot was not concentrated near the bowl rim, but rather it was more dispersed throughout the combustion chamber. The more compact soot pockets of the current study could be due to the lower swirl than used in Ref. [4].

3.5 Comparison to Conventional Diesel. Compared to conventional diesel combustion, the LTC strategy implemented here uses a higher rate of EGR, which increases the specific heat capacity, which in turn dramatically decreases combustion temperature. Hasegawa et al. [31] used CHEMKIN/SENKIN [32,33] in shock tube calculations to test separately the heat capacity and oxygen concentration influence on ignition delay. Increasing heat capacity and/or decreasing oxygen concentration both delayed the start of combustion. They also showed that the main heat release is delayed because of a slower reaction rate of H_2CO, as also presented in Ref. [10].

In a conventional diesel combustion strategy, combustion and injection typically overlap temporally. A large fraction of conventional diesel combustion occurs in the mixing-controlled phase with locally rich mixtures and diffusion combustion [21]. The stoichiometric diffusion flame produces locally high-temperature regions favorable to NO_x production. In LTC, due to the longer ignition delay, combustion starts after the end of injection and gives more time for fuel and air to premix. A large fraction of LTC combustion occurs in the premixed combustion phase with a

lower flame temperature because of EGR dilution. Furthermore, the mixing-controlled combustion phase duration is reduced [34]. Both effects may help to decrease the NO_x emissions.

Pickett et al. [35] analyzed soot formation using SENKIN [33] and a two-stage Lagrangian model simulation. Oxygen concentration was shown to affect soot formation processes. LTC strategies with lower intake oxygen concentrations have longer residence times for soot precursor formation in locally fuel-rich mixtures. However, lower temperatures decrease the production rate of soot precursors. As a result of these two contradictory effects, soot precursors first increase with decreasing oxygen concentration (typically down to 15% O_2) then quickly decrease, reaching near-zero levels around 8% O_2 [35]. These results were later verified experimentally by Idicheria and Pickett [36]. In the current study, the reduced oxygen concentration and lower combustion temperatures act to reduce the soot formation relative to conventional diesel combustion.

4 Summary and Conclusions

A LTC strategy with late injection and high EGR was visualized within the combustion chamber in a heavy-duty diesel engine using a set of optical diagnostics: Mie scattering to investigate liquid-fuel droplets, chemiluminescence imaging to visualize ignition and combustion, BB-PLIF and OH-PLIF to indicate the penetrating vapor-fuel jet and the combusting regions, and natural luminosity and LII to detect soot. Three distinct combustion phases can be extracted from the AHRR for this LTC condition: cool flame (first phase), premixed combustion (second phase) and mixing-controlled combustion (third phase). Many features of late-injection LTC combustion are similar to those previously reported for early-injection LTC [20], as summarized in the following paragraphs.

Injection starts at TDC. The liquid jet is relatively short, similar to that in conventional diesel combustion, and with no wall impingement by liquid fuel. From an engineering point of view, the results show that liquid wall impingement is avoided because of the hot, dense in-cylinder conditions at this injection timing. The vapor phase expands quickly after SOI, especially in the leading edge region of the jet.

The cool-flame reactions start before the end of injection, but the main premixed combustion phase occurs after the end of injection. Cool-flame chemiluminescence is first detected halfway between the injector tip and bowl rim. A few CAD later, the chemiluminescence spreads along the bowl rim as the premixed-combustion phase commences and chemiluminescence intensity increases dramatically.

Soot starts to form along the piston bowl wall typically between two adjacent jets. OH radical imaging indicates that premixed combustion first occurs downstream in the jet and then spreads along the bowl rim.

During the mixing-controlled phase, OH is detected in the region halfway between the injector and the bowl rim, while unburned fuel likely remains near the injector. This lingering fuel is a potential source of UHC emissions. Later in the cycle, soot is not completely oxidized in the low-swirl engine of this study, likely contributing to exhaust PM emissions.

Acknowledgment

The experiments were performed at the Combustion Research Facility, Sandia National Laboratories, Livermore, CA. Sandia is a multiprogram laboratory operated by Sandia Corportation, a Lockheed Martin Company, for the United States Department of Energy's (DOE) National Nuclear Security Administration under Contract No. DE-AC04-94AL85000. The United States Government retains and the publisher, by accepting the article for publication, acknowledges that the United States Government retains a nonexclusive, paid-up, irrevocable, worldwide license to publish or reproduce the published form of this manuscript, or allow others to do so, for United States Government purposes. Financial support was provided by DOE's Office of FreedomCAR and Vehicle Technologies, managed by Kevin Stork and Gurpreet Singh. The authors also thank David Cicone of Sandia National Laboratories for his assistance in maintaining the optical-access research engine used in these experiments.

References

[1] Kimura, S., Aoki, O., Ogawa, H., Murakana, S., and Enomoto, Y., 1999, "New Combustion Concept for Ultra-Clean and High-Efficiency Small DI Diesel Engines," SAE Paper No. 1999-01-3681.
[2] Kimura, S., Aoki, O., Kitahara, Y., and Aiyoshizawa, E., 2001, "Ultra-Clean Combustion Technology Combining a Low-Temperature and Premixed Combustion Concept for Meeting Future Emission Standards," SAE Paper No. 2001-01-0200.
[3] Kimura, S., Ogawa, H., Matsui, Y., and Enomoto, Y., 2002, "An Experimental Analysis of Low Temperature and Premixed Combustion for Simultaneous Reduction of NOx and Particulate Emissions in Direct Injection Diesel Engines," Int. J. Engine Res., **3**(4), pp. 249–259.
[4] Miles, P. C., Choi, D., Pickett, L. M., Singh, I. P., Henein, N., Rempel Ewert, B. H., Yun, H., and Reitz, R. D., 2004, "Rate-Limiting Processes in Late-Injection, Low-Temperature Diesel Combustion Regimes," *Thiesel Conference 2004*, Valencia, Spain.
[5] Choi, D., Miles, P. C., Yun, H., and Reitz, R. D., 2004, "A Parametric Study of Low-Temperature, Late-Injection Combustion in a HSDI Diesel Engine," *Sixth International Symposium on Diagnostics and Modeling of Combustion in Internal Combustion Engines (COMODIA)*, Yokohama, Japan, Aug. 2–5.
[6] Yanagihara, H., 2002, "A Study on Combustion Structure of Premixed Compression Ignition Diesel Engines," SAE Paper No. 2002-30-0009.
[7] Musculus, M. P. B., 2004, "On the Correlation between NOx Emissions and the Diesel Premixed Burn," SAE Paper No. 2004-01-1401.
[8] Dec, J. E., 1997, "A Conceptual Model of D. I. Diesel Combustion Based on Lased Sheet Imaging," SAE Paper No. 970873.
[9] Singh, S., Reitz, R. D., and Musculus, M. P. B., 2005, "2-Colors Thermometry Experiments and High-Speed Imaging of Multimode Diesel Engine Combustion," SAE Paper No. 2005-01-3842.
[10] Lachaux, T., and Musculus, M. P. B., 2007, "In-Cylinder Unburned Hydrocarbon Visualization During Low-Temperature Compression-Ignition Engine Combustion Using Formaldehyde PLIF," Proc. Combust. Inst., **31**(2), pp. 2921–2929.
[11] Espey, C., and Dec, J. E., 1993, "Diesel Engine Combustion Studies in a Newly Designed Optical-Access Engine Using High-Speed Visualization and 2-D Laser Imaging," SAE Paper No. 930971.
[12] Zhao, H., and Ladammatos, N., 1999, *Engine Combustion Instrumentation and Diagnostics*, Society of Automotive Engineers, Warrendale, PA.
[13] Dec, J. E., and Espey, C., 1992, "Soot and Fuel Distributions in a D. I. Diesel Engine Via 2-D Imaging," SAE Paper No. 922307.
[14] Hultqvist, A., Christensen, M., Johansson, B., Franke, A., Richter, M., and Alden, M., 1999, "A Study of the Homogeneous Charge Compression Ignition Combustion Process by Chemiluminescence Imaging," SAE Paper No. 1999-01-3680.
[15] Dec, J. E., and Espey, C., 1995, "Ignition and Early Soot Formation in a D. I. Diesel Engine Using Multiple 2-D Imaging Diagnostics," SAE Paper No. 950456.
[16] Dec, J. E., and Espey, C., 1998, "Chemiluminescence Imaging of Autoignition in a DI Diesel Engine," SAE Paper No. 982685.
[17] Dec, J. E., 1992, "Soot Distribution in a D. I. Diesel Engine Using 2-D Imaging of Laser-Induced Incandescence, Elastic Scattering, and Flame Luminosity," SAE Paper No. 920115.
[18] Dec, J. E., and Kelly-Zion, P. L., 2000, "The Effects of Injection Timing and Diluent Addition on Late-Combustion Soot Burnout in a Diesel Engine Based on Simultaneous 2-D Imaging of OH and Soot," SAE Paper No. 2000-01-0238.
[19] Dec, J. E., and Coy, E. B., 1996, "OH Radical Imaging in a DI Diesel Engine and the Structure of the Early Diffusion Flame," SAE Paper No. 960831.
[20] Musculus, M. P. B., 2006, "Multiple Simultaneous Optical Diagnostic Imaging of Early-Injection Low-Temperature Combustion in a Heavy-Duty Diesel Engine," SAE Paper No. 2006-01-0079.
[21] Heywood, J. B., 1988, *Internal Combustion Engine Fundamentals*, McGraw-Hill, New York.
[22] Desantes, J. M., Payri, R., Salvador, F. J., and Gimeno, J., 2006, "Prediction of Spray Penetration by Means of Spray Momentum Flux," SAE Paper No. 2006-01-1387.
[23] Espey, C., and Dec, J. E., 1995, "The Effect of TDC Temperature and Density on the Liquid-Phase Penetration in a D. I. Diesel Engine," SAE Paper No. 952456.
[24] Canaan, R. E., Dec, J. E., and Green, R. M., 1998, "The Influence of Fuel Volatility on the Liquid-Phase Fuel Penetration in a Heavy-Duty D. I. Diesel Engine," SAE Paper No. 980510.
[25] Siebers, D. L., 1999, "Scaling Liquid-Phase Fuel Penetration in Diesel Sprays Based on Mixing-Limited Vaporization," SAE Paper No. 1999-01-0528.
[26] Hotta, Y., Nakakita, K., Inayoshi, M., Ogawa, T., Sato, T., and Yamada, M., 1998, "Combustion Improvement for Reducing Exhaust Emissions in IDI Diesel Engine," SAE Paper No. 980503.
[27] Tsurushima, T., Zhang, L., and Ishii, Y., 1999, "A Study of Unburnt Hydro-

carbon Emission in Small DI Diesel Engines," SAE Paper No. 1999-01-0512.
[28] Mueller, C. J., Pitz, W. J., Pickett, L. M., Martin, G. C., Siebers, D. L., and Westbrook, C. K., 2003, "Effects of Oxygenates on Soot Processes in DI Diesel Engines: Experiments and Numerical Simulations," SAE Paper No. 2003-01-1791.
[29] Pickett, L. M., and Siebers, D. L., 2003, "Fuel Effects on Soot Processes of Fuel Jets at DI Diesel Conditions," SAE Paper No. 2003-01-3080.
[30] Pickett, L. M., Siebers, D. L., and Idicheria, C. A., 2005, "Relationship Between Ignition Processes and the Lift-Off Length of Diesel Fuel Jets," SAE Paper No. 2005-01-3843.
[31] Hasegawa, R., Sakata, I., Koyama, T., and Yanagihara, H., 2003, "Numerical Analysis of Ignition Control in HCCI Engine," SAE Paper No. 2003-01-1817.
[32] Kee, R. J., Rupley, F. M., Meeks, E., and Miller, J. A., 1996, "A FORTRAN Chemical Kinetics Package for the Analysis of Gas Phase Chemical and Plasma Kinetics," Sandia National Laboratories.
[33] Lutz, A. E., Kee, R. J., and Miller, J. A., 1988, "SENKIN: A FORTRAN Program for Predicting Homogeneous Gas Phase Chemical Kinetics With Sensitivity Analysis," Sandia National Laboratories, Report No. SAND87-8248.
[34] Ladommatos, N., Suhair, M. A., Zhao, H., and Hu, Z., 1998, "Effects of EGR on Heat Release in Diesel Combustion," SAE Paper No. 980184.
[35] Pickett, L. M., Caton, J. A., Musculus, M. P. B., and Lutz, A. E., 2006, "Evaluation of the Equivalence Ratio-Temperature Region of Diesel Soot Precursor Formation Using a Two-Stage Lagrangian Model," Int. J. Engine Res., **7**(5), pp. 349–370.
[36] Idicheria, C. A., and Pickett, L. M., 2005, "Soot Formation in Diesel Combustion Under High-EGR Conditions," SAE Paper No. 2005-01-3834.

Reduction of Numerical Parameter Dependencies in Diesel Spray Models

Neerav Abani

Achuth Munnannur

Rolf D. Reitz

Engine Research Center,
University of Wisconsin-Madison,
Madison, WI 53706

Numerical grid and time-step dependencies of discrete droplet Lagrangian spray models are identified. The two main sources of grid dependency are due to errors in predicting the droplet-gas relative velocity and errors in describing droplet-droplet collision and coalescence processes. For reducing grid dependency due to the relative velocity effects, a gas-jet theory is proposed and applied to model diesel sprays. For the time-step dependency, it is identified that the collision submodel results in drop size variation in the standard spray model. A proposed spray model based on the gas-jet theory is found to improve the time-step independency also along with the mesh independency. The use of both Eulerian (collision mesh) and Lagrangian (radius of influence) collision models along with the gas-jet theory is found to provide mesh-independent results.
[DOI: 10.1115/1.2830867]

Introduction

Sprays have been widely modeled by Lagrangian-drop and Eulerian-fluid (LDEF) and Eulerian-liquid–Eulerian-gas (two-fluid) models. Both the models poorly predict spray structure, penetration, and drop sizes for coarse computational fluid dynamics (CFD) meshes. In both models, near-nozzle resolution of the flow is required down to the order of the injector-hole size for better spray predictions. As the near-nozzle resolution is reduced, the prediction becomes poorer. For large bore engines, for example, marine engines, the nozzle diameters are a few hundred microns and the bore size is a few hundred millimeters. Hence, a coarser mesh size for a small engine might be the finest practical mesh size for a large bore engine. Hence, it becomes important to achieve fairly mesh-independent spray models if they are to be universally applicable. The present study adopts the LDEF method, which is already implemented in the KIVA-3V code [1], and a range of uniform mesh sizes from $1D$ to $16D$ is considered, where D is the nozzle diameter. The standard LDEF method overpredicts spray-tip penetration for a fine mesh resolution of the order of the nozzle diameter ($\sim 1D$). This was found to be due to the ineffectiveness of the collision model at this scale. Smaller drop sizes impart higher rates of momentum transfer in the near-nozzle region, resulting in high entrainment rates and hence overpenetration. As the mesh is coarsened to the order of $(4-6)D$, the penetration prediction improves due to an increase in the effectiveness of the collision model with its better prediction of drop sizes. Further coarsening of mesh to the order of $(8-16)D$ again predicts poor spray penetration due to the fact that momentum coupling between the droplets and the gas phase becomes poor. Thus, there is an optimum mesh size that gives a minimum error in spray penetration when the error in both the collision and momentum coupling is exhibited through droplet drag.

Another inherent modeling issue is time-step independency, which has rarely been reported in the literature. It is found that the O'Rourke collision model [2,3] is time step dependent if it follows the assumed Poisson process. This is because the collision model is called at every new time step of the simulation. Hence, for a fine time step, the total number of collisions can exceed that obtained for a coarser time step for the same elapsed time. So, in the case of a fine step, drop sizes can be larger due to the increase in the number of coalescences.

The atomization model employed in LDEF models is popularly based on considerations of Kelvin–Helmholtz and Rayleigh–Taylor (KH-RT breakup) instabilities [4,5]. The grid dependency of spray models has been studied by Abraham [6], who suggested that the nozzle region must be adequately resolved for obtaining an accurate prediction of the spray structure. Abraham [6] found, in the case of jets, that adequate mesh resolution is at least the size of the nozzle radius. A similar work on the near-field study of gas jets and sprays was carried out by Post et al. [7]. They found that none of the Lagrangian-drop models give resolution-independent results when the spatial distribution of the drops is highly nonuniform. This investigation of the near-nozzle region of sprays was thus inconclusive regarding the entrainment characteristics of the gas in the near field. Aneja and Abraham [8] compared the liquid penetration obtained from computations with that of experiments and concluded that the predicted liquid penetration in vaporizing sprays is sensitive to the grid resolution and to the details of O'Rourke's collision model [2,3].

Schmidt and Rutland [9,10] improved the O'Rourke and Bracco collision model by using a separate collision mesh and further sampled potential collision partners so as to speed up collision computations using the "no-time counter" (NTC) approach. They found that due to the nonuniform spatial distribution of the drops, the collision frequency is different on different grids. This affects the Sauter mean diameter (SMD) of the spray drops; hence, different grids result in different vaporization and liquid penetration predictions. In a different approach, Nordin [11] proposed a semideterministic collision model, wherein the droplets do not collide at all if they are traveling in opposite directions. Since a single parcel represents a large number of drops, the assumption that collisions occur only if trajectories intersect is questionable in Monte Carlo simulations and spray calculations.

Another source of grid dependency is the two-way momentum coupling between the two phases. Beard et al. [12] identified that the relative velocity between the two phases can be mesh dependent and results in incorrect penetration predictions. They proposed a method to correct the relative velocity, which is based on an expanding radius of influence (ROI) concept between the droplets and gas. At any instant of time, the droplet relative velocity is interpolated between the droplet's absolute velocity and the CFD cell's velocity at the interface location. Moreover, they considered

Contributed by the Internal Combustion Engine Division of ASME for publication in the JOURNAL OF ENGINEERING FOR GAS TURBINES AND POWER. Manuscript received October 30, 2007; final manuscript received October 31, 2007; published online April 2, 2008. Review conducted by Dilip R. Ballal.

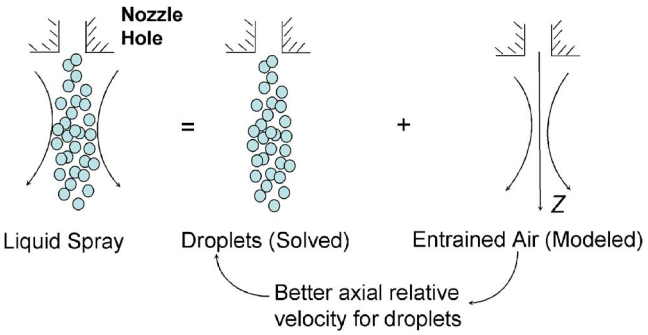

Fig. 1 Schematic of the new diesel spray model

molecular diffusion of the vapor instead of turbulent diffusion in expanding the vapor cloud, which in the case of turbulent jets might be a more reasonable choice.

Lippert et al. [13] proposed resolving the flow field by using an adaptive mesh, which resolves the near-nozzle region finely enough to predict accurate spray structures. They also used a separate collision mesh based on the NTC model. However, use of extra cells near the nozzle means a significant increase in computation times.

In the present model, no extra cells are added as in the adaptive mesh technique. Instead, it is proposed that the air entrainment can be modeled according to the gas-jet theory [14,15]. A subgrid scale model is introduced whereby the axial component of the droplet relative velocity is corrected using the assumption that the relative velocity is that between the liquid droplet in a corresponding gas jet. This corrects the momentum exchange between the droplets and the gas phase, and is independent of mesh resolution. To prove the concept, a fixed collision mesh and the standard O'Rourke and Bracco collision model is used first. That is, for all CFD mesh sizes, a separate collision mesh is considered, as previously suggested [9,10,13]. This separates consideration of collisional processes from mesh resolution issues. The results show that the mesh dependency is greatly reduced in terms of spray penetration, drop size, number of parcels, and spray structure. Next, an improved collision treatment that dynamically computes the collision process without the need for a separate collision mesh is proposed.

Diesel Spray Model

The basic idea of the present model is depicted in Fig. 1. The spray flow has two components: the group of droplets that forms the liquid phase and the air entrained that forms the gas phase. For grid independency, either of the phases could be corrected since they are coupled by their respective transport equations. Previous researchers have focused on minimizing errors in the liquid phase [10,11], but these corrections are mostly based on intuition and have not been tested and proven enough to work at different conditions. Others have increased the accuracy of the gas-phase prediction with increased mesh refinement, but at the cost of increased computational time [13].

The LDEF stochastic spray model considers a group of identical droplets known as a drop parcel, which is tracked in a Lagrangian approach. The gas phase is modeled using an Eulerian approach. The conservation equation for a droplet parcel is represented by the conservation equation of a single droplet in that parcel. As mentioned above, the axial component of the gas-phase velocity in the droplet equations is modeled using the gas-jet theory. Hence, the droplet momentum equation is given as

$$\frac{d\mathbf{U}}{dt} = \frac{3}{8} C_D \frac{\rho_g}{\rho_l} \frac{1}{D} |\mathbf{U} - \mathbf{V}_{\text{gas}}| (\mathbf{U} - \mathbf{V}_{\text{gas}}) \tag{1}$$

where $\mathbf{U}$ is the droplet velocity vector, D is the drop diameter, and $\mathbf{V}$ is the surrounding gas-phase velocity vector. The drag coefficient C_D is assumed to be a function of droplet Reynolds number [1]. $\mathbf{V}$ is given as $\mathbf{V}=(V_x, V_y, V_{\text{gas}})$. V_x and V_y are the perpendicular components of the surrounding gas-phase velocity obtained from the CFD solution, and the axial component (considered as the z direction here) is given by the gas-jet theory as [14,15]

$$V_{\text{gas}} = \min\left[U_{\text{inj}}, \frac{3U_{\text{inj}}^2 d_{\text{eq}}^2}{\left[32\nu_t z \left(1 + \frac{3U_{\text{inj}}^2 d_{\text{eq}}^2 r^2}{256\nu_t^2 z^2} \right)^2 \right]} \right] \tag{2}$$

where U_{inj} is the injection velocity of the liquid jet, which is also assumed to be the injection velocity of the gas jet. z is the axial distance of the droplet parcel from the injector tip and r is the radial distance of the parcel from the spray axis. Thus, the relative velocity between the droplets and the gas phase in the near-nozzle region is assumed to be zero. d_{eq} is the equivalent diameter of the gas jet defined as [14]

$$d_{\text{eq}} = d_{\text{noz}} \sqrt{\frac{\rho_l}{\rho_g}} \tag{3}$$

where d_{noz} is the effective nozzle diameter, and ρ_l and ρ_g are the liquid- and gas-phase densities, respectively. ν_t is the turbulent viscosity for jets given as [14]

$$\nu_t = C_t \pi^{0.5} U_{\text{inj}} d_{\text{eq}}/2 \tag{4}$$

C_t is the entrainment constant, as reported by Abraham [14], who used $C_t=0.0161$. In the present case, $C_t=0.0264$ was selected by trial and error to optimize predictions of spray-tip penetration. These constants determine the turbulent diffusion of a jet and, hence, the turbulent mixing rate. The constant could depend on the type of fluid used as the turbulent mixing process may be different for different injected fluids.

The momentum lost by the droplets due to drag is gained by the surrounding gas phase through the source terms in the conservation equations. The axial component of the source terms is modeled using the modified relative velocity with Eq. (2). The droplet-gas relative velocity is modeled in this way everywhere except in the spray (KH-RT) breakup model. This is because if the relative velocity is very low near the nozzle, the predicted breakup would be slow and the droplet size large. Thus, for the breakup model only, the gas-phase velocity from the CFD prediction is considered. This is also justified by the fact that the gas-jet theory is based on a quasisteady assumption. Hence, the velocity given by Eq. (2) only applies after some time. Since there is no simple way to evaluate what fraction of the quasisteady state velocity causes a breakup, the surrounding gas velocity from the CFD mesh is used to represent the external force in the jet breakup process.

The collision model is based on O'Rourke's model [2,3] that allows the collision of droplets located in a collision cell that is traditionally considered to be the CFD cell itself. However, this gives rise to further mesh dependency. Hence, we first adopt the proposal of Schmidt [9] of using a separate collision mesh (but without the NTC algorithm). To study mesh-dependency effects related to drop drag, we use a single collision mesh for all CFD meshes considered.

If the size of the collision mesh is small, there will be fewer potential collision partners for a parcel, and there may even be no collisions at all if the mesh size is of the order of the drop diameter. A large collision mesh size allows numerous coalescences, but breakup of the resulting large drops is expected due to RT-breakup mechanism. Hence, the collision mesh size was selected based on a sensitivity study, as will be discussed later in the section on results. As a second approach, we also consider the use of a collision cutoff distance for the parcel as a criterion to decide whether two parcels should collide, as is the practice in molecular dynamic simulations [16]. This is a Lagrangian collision model based on each droplet's position, as opposed to the traditional collision model that uses a fixed collision mesh (Eulerian). This is

Table 1 Experimental data by Naber and Siebers [18]: nonevaporative conditions

Experimental conditions		
Fuel		Philips research grade D-2 fuel
Temperature of fuel (T_f)	(K)	451
Density	(kg/m^3)	$844-0.9(T_f-289)$
Injection duration	(m/s)	3
Amount of fuel to be injected	(g m s)	0.056
Diameter of nozzle	(μm)	257
Ambient density	(kg/m^3)	60.6
Ambient temperature	(K)	451
Injection pressure difference	(MPa)	137

an important consideration in nonuniform injection cases. This cutoff distance (henceforth termed ROI) of a parcel is the distance to the most distant parcel that can collide with it in the present time step. There are many ways to estimate ROI. In one approach, the computation of ROI involves checking whether the distance x_{rel} between a parcel and its collision partner is such that

$$x_{\text{rel}} \leqslant u_{\text{rel}} dt \tag{5}$$

where u_{rel} is the relative velocity between the drops and dt is the computational time step. Another approach would be to use a completely deterministic model with contact time estimation [17]. In the present study, the ROI was fixed at 2 mm size consistent with our collision mesh sensitivity analysis, as presented in the section on results and discussion.

Experimental Conditions

A constant volume chamber experiment by Naber and Siebers [18] was considered in the present study. Only nonevaporative conditions were used to compare with the computational results. These conditions are chosen as it is necessary to predict an accurate liquid penetration length in realistic engine cases, as suggested by Aneja and Abraham [8]. In their study, they found that the liquid penetration does not match with different grid sizes. Hence, as a first step in creating a grid-independent spray model under evaporative conditions, it is important to create a grid-independent spray model under nonevaporative conditions so as to predict consistent liquid penetration lengths. The present results are analyzed in a constant volume chamber as a demonstration of approach. It is expected that this approach can be easily extended to model real engine cases and will predict consistent liquid penetrations. Experimental data corresponding to a range of ambient densities were considered. The injection profile is uniform, and more details are given in Table 1.

The discharge and area contraction coefficients based on the exit diameter d_{noz} are 0.62 and 0.81, respectively. The initial drop size and velocity from the injector accounted for these coefficients in the simulations. The jet half angle is an input to the model, which was determined experimentally and is 11 deg for the density ratio of $\rho_{\text{gas}}/\rho_{\text{liq}} \sim 0.9$.

Computational Mesh and Time-Step Details

Six two-dimensional and uniform computational meshes were considered with cell sizes of 4×4 mm, 3×3 mm, 2×2 mm, 1×1 mm, 0.5×0.5 mm, and 0.25×0.25 mm^2, respectively. The separate collision mesh had a uniform cell size of 4×4 mm^2, which was chosen based on a sensitivity study of collision mesh sizes. If the standard CFD (standard KIVA) cell size is considered, then for the fine mesh of 0.25×0.25 mm^2 there would be very few collision partners and, hence, the predicted drop sizes could be very small. KIVA-3V [1] is used for the computations with the modifications of the new model implemented. The 2D mesh is a cylindrical mesh with a 0.5 deg sector. The dimensions of the domain are 10 cm in the axial direction and 4 cm in the radial direction.

For the different CFD mesh sizes, a time step of 1 μs was used. For time-step sensitivity studies, five different time steps were used, namely, 10 μs, 5 μs, 1, 0.5 μs, and 0.1 μs. The time-step study was done on the 4×4 mm^2 mesh after establishing mesh independency.

Results and Discussion

Results for mesh and time-step dependencies are presented separately. First, results from the standard KIVA/LDEF code are presented, and the submodels that cause mesh dependency are identified. The discussion and comparison of mesh dependency is based on a comparison of spray-tip penetration (defined as the location from the nozzle of the leading droplet comprising 95% liquid mass in the domain), overall SMD (i.e., the average drop size of all drops in the spray, regardless of their location), the number of drop parcels in the domain, and the spray structure. In the same section, we discuss the sensitivity of the collision mesh and chose a collision mesh size based on this sensitivity study. Results from the standard KIVA/LDEF model with a consistent separate collision mesh are discussed next. Results of the improved model with a collision mesh and the ROI are presented next. Then, the improved results from the new model are presented and compared with the standard KIVA results.

Mesh Independency

Standard KIVA/LDEF Results. Results from the standard KIVA models for the six different mesh sizes showed significant mesh dependency. Figure 2 shows the spray structure at $t=3$ ms after the beginning of injection, and Fig. 3 shows the spray-tip penetration as a function of time compared with the experimental penetration. The 4×4 mm^2 mesh shows an underpredicted tip penetration, and the fine mesh (0.25×0.25 mm^2) shows overpredicted penetration. Figure 4 shows the predicted overall drop size, and Fig. 5 shows the total number of parcels in the chamber. It can be observed that the drop sizes are reduced as the mesh size is reduced. This is because with the reduction in mesh size, the number of collisions gets reduced. In the limit of 0.25×0.25 mm^2, the collision model becomes ineffective and the predicted drop size becomes of the order of 1 μm. The total number of parcels increases for the smaller sized mesh due to fewer coalescences and effects due to collision with the bottom wall beyond $t=1.5$ ms.

The overpenetration at small mesh sizes can be explained as follows. The small drops produced after a breakup do not collide and coalesce if the collision cell is confined to the small CFD cell. Thus, in the vicinity of the nozzle, large numbers of smaller drops exist having large momentum (equal to the jet momentum). These smaller drops are also subjected to higher drag forces and lose their momentum in a small distance from the nozzle. This results in higher gas-phase momentum near the nozzle, which causes the liquid droplets being injected at later times to overpenetrate. This is a cumulative process from the injector location to positions downstream of the injector. Hence, the gas-phase momentum or the air entrainment rate is overpredicted for the fine mesh case as a consequence of the ineffectiveness of the collision model.

In the case of the coarse mesh (4×4 mm^2), the spray-tip penetration is underpredicted, even though the drop sizes are not unreasonably low. The total momentum lost by many droplets is now transferred to a cell size of 4×4 mm^2, which is larger than an actual volume of influence. This analysis is schematically depicted in Fig. 6, which shows a typical large size CFD mesh and an actual volume of influence of drops. Thus, the drag force transferred from the liquid droplets to the surrounding gas phase is dampened in effect. Thus, the gas-phase momentum is underpredicted and results in underpenetration. This trend in a large cell continues as the gas-phase momentum is always less (due to the

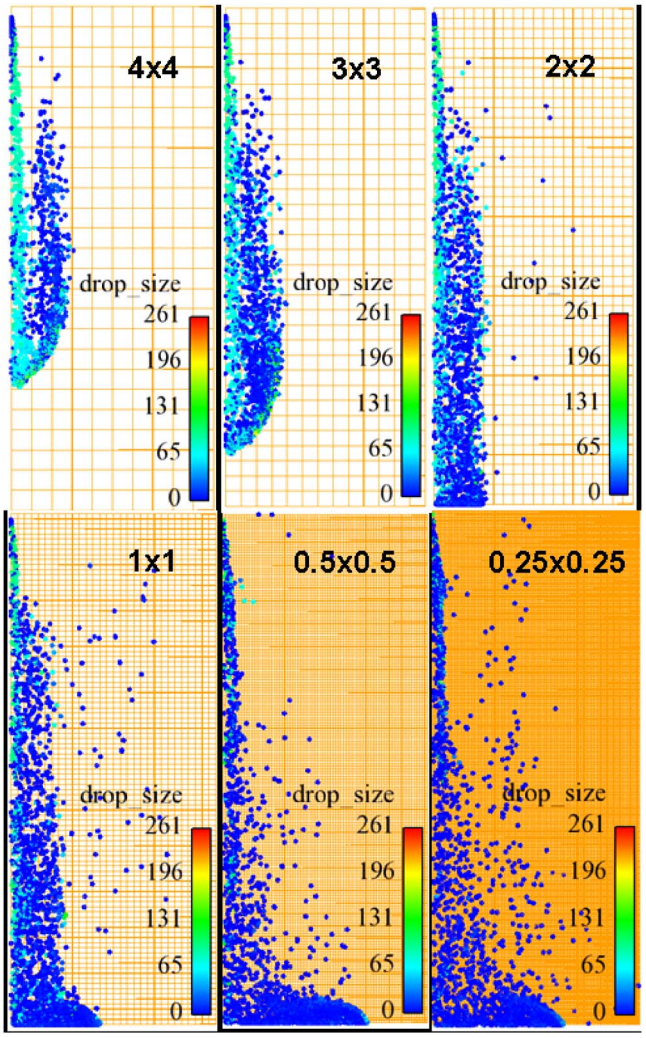

Fig. 2 Standard KIVA: spray structure at t=3.0 ms. ρ_{amb} =60.6 kg/m^3.

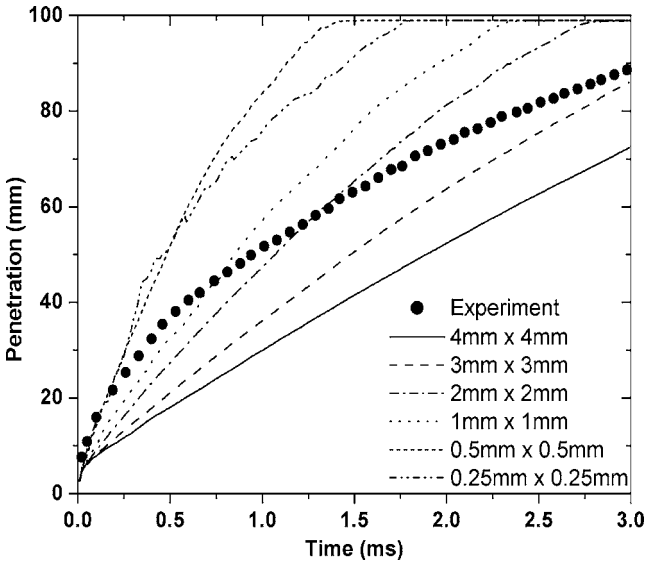

Fig. 3 Standard KIVA: spray-tip penetration. Experimental data from Ref. [18], ρ_{amb}=60.6 kg/m^3.

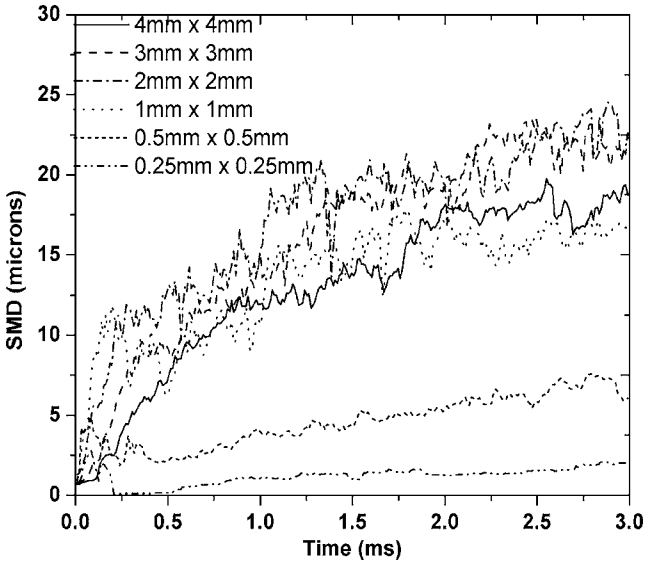

Fig. 4 Standard KIVA: overall SMD. ρ_{amb}=60.6 kg/m^3.

dampening effect of momentum transfer) and the groups of droplets continue to experience more resistance from the gas phase, leading to an overprediction of droplet drag.

Thus, a correct prediction of the gas-phase momentum is crucial in order to get an accurate spray-tip penetration. The collision

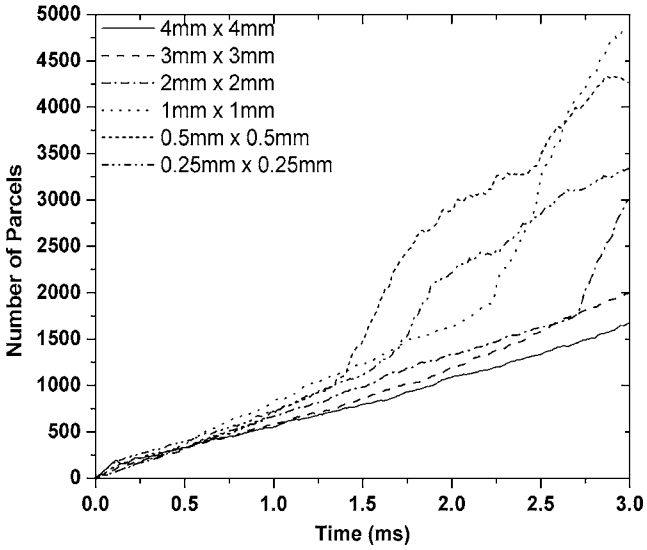

Fig. 5 Standard KIVA: total number of parcels. ρ_{amb} =60.6 kg/m^3.

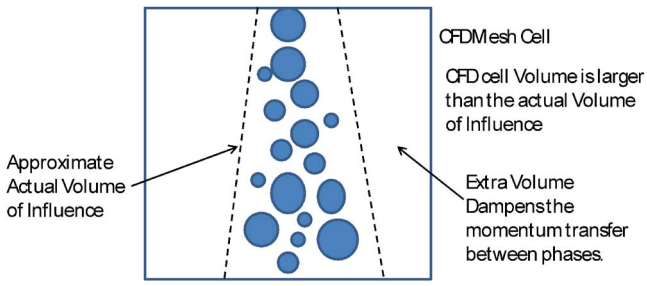

Fig. 6 Coarse mesh illustration

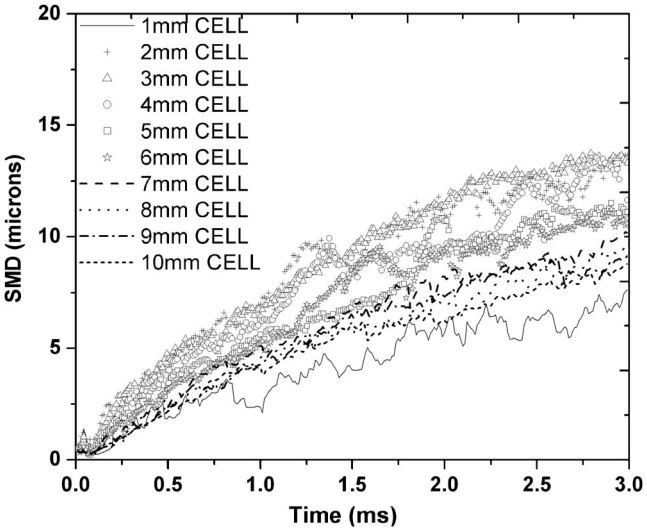

Fig. 7 Collision mesh sensitivity with improved spray model. CFD mesh size of 4×4 mm^2 and $\rho_{amb}=60.6$ kg/m^3.

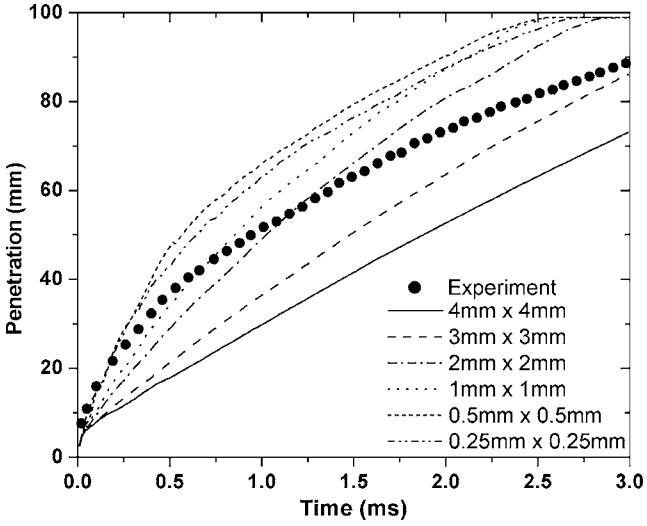

Fig. 9 Standard KIVA with collision mesh: spray-tip penetration. Experimental data from Ref. [18], $\rho_{amb}=60.6$ kg/m^3.

model also affects the drop size, and to separate out this problem the improved model is presented using a separate collision mesh of a uniform cell size of 4×4 mm^2.

Sensitivity Study of Collison Mesh on the Improved Model. The improved spray model was also studied with different collision mesh sizes while keeping the same CFD mesh. This sensitivity was tested separately for all the six different mesh sizes, and the results were very similar quantitatively. These results are the same because the improved model isolates the momentum coupling using the gas-jet velocity prediction and the drop sizes using a separate collision mesh. Since a method to predict a consistent drop-gas relative velocity is available, a consistent drop size remains to be achieved, which depends on the size of the collision mesh. Ten different collision mesh sizes were chosen, with the smallest collision mesh size of 1×1 mm^2 and the largest of 10×10 mm^2. A sample case for a CFD mesh size of 4×4 mm^2 is presented in this section; however, similar results were obtained with other CFD mesh sizes as well. The results show that after about a size of 4×4 mm^2, there is less variation in the predicted drop sizes, as shown in Fig. 7. Figure 8 shows a bar chart of the total number of coalescences with an increase in collision mesh size. As can be observed, after about a 4×4 mm^2 collision mesh size, the slope of the increase in the total number of coalescences is constant. At the same time, Fig. 7 shows that there is no significant increase in the drop size with an increase in collision mesh size. This is due to a balance that is formed between the RT breakup [5] and the coalescences, which produces nearly the same drop size. Thus, a collision mesh of 4×4 mm^2 was chosen.

Standard KIVA/LDEF model results with collision mesh. Based on the results and discussion of the standard KIVA/LDEF in the previous sections, it is evident that the issue of inconsistent spray-tip penetration and drop size remains. In this section we investigate the effect of collision mesh on the standard KIVA/LDEF model. A consistent collision mesh size of 4×4 mm^2 was used with the six different CFD mesh sizes. Figure 9 shows the spray-tip penetration with different meshes, and Figs. 10 and 11 show the corresponding drop size and total number of parcels.

It was found that although the drop size improved in all cases and was consistent, the spray penetration was still inconsistent.

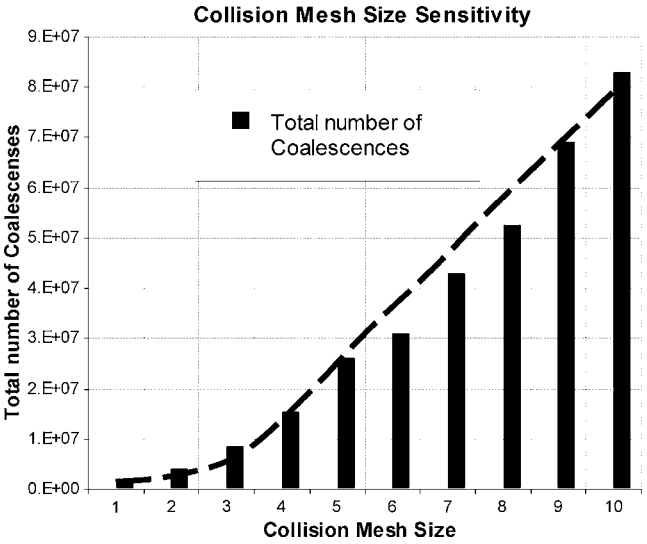

Fig. 8 Total number of coalescences in the domain with increase in collision mesh size

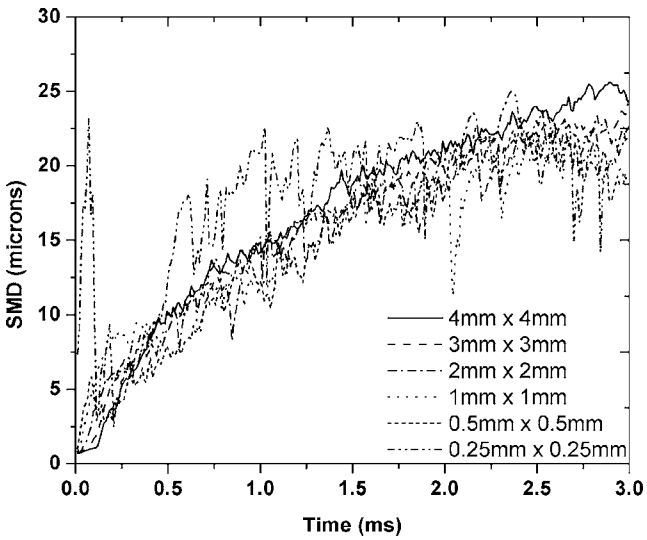

Fig. 10 Standard KIVA with collision mesh: overall SMD. $\rho_{amb}=60.6$ kg/m^3.

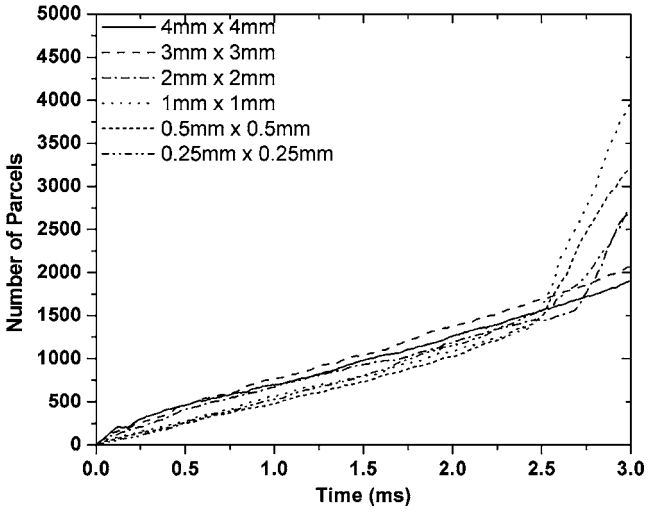

Fig. 11 Standard KIVA+collision mesh: total number of parcels. $\rho_{amb}=60.6$ kg/m^3.

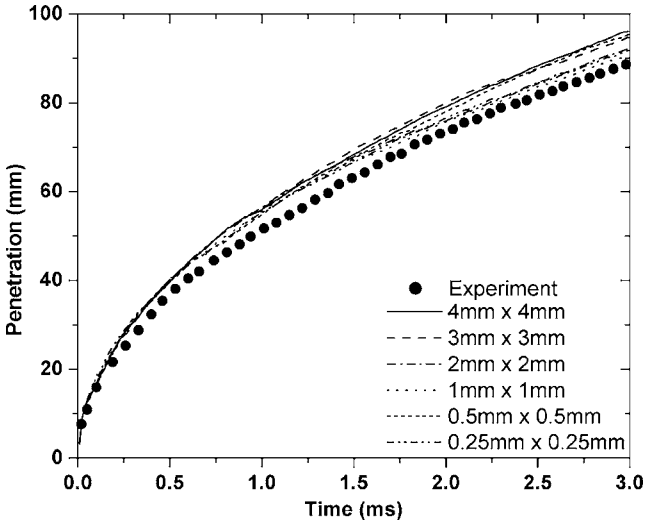

Fig. 13 Improved model with different meshes: spray-tip penetration. Experimental data from Ref. [18], $\rho_{amb}=60.6$ kg/m^3.

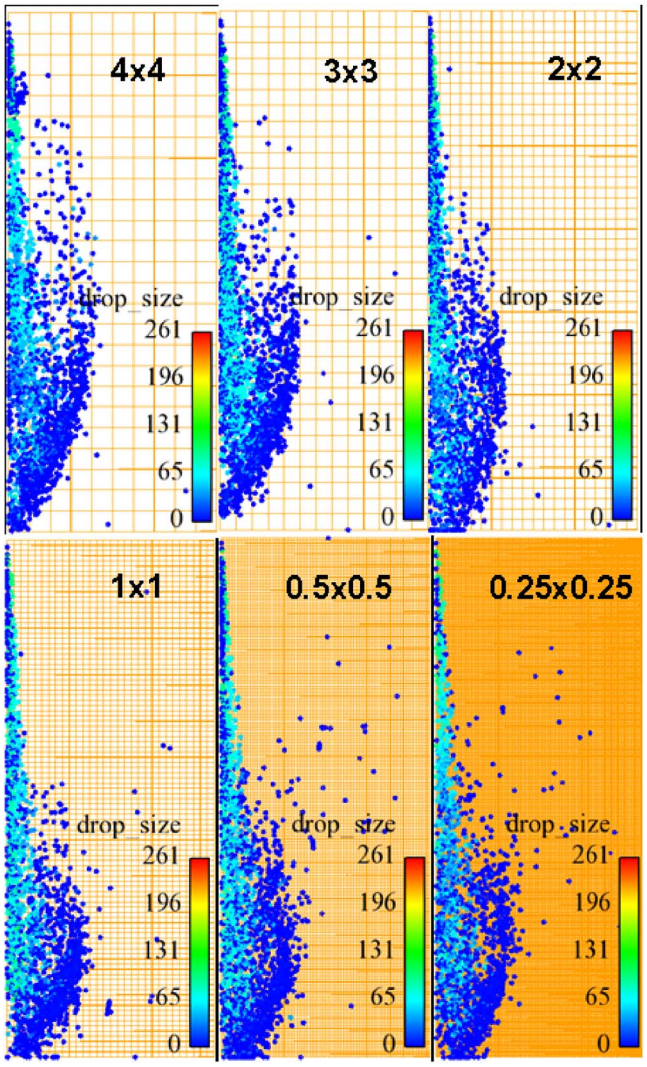

Fig. 12 Improved model: spray structure at $t=3.0$ ms

The fine mesh cases still showed some trends of improvement as compared to the standard KIVA/LDEF models; however, there was still a disagreement with the experimental values. This again confirms that even for the fine mesh, a model to predict an accurate drop-gas relative velocity is needed. In other words, it is important to predict an accurate turbulent diffusivity ν_t (as in Eq. [4]) in the models so as to predict an accurate spray-tip penetration.

Improved diesel spray model results with collision mesh. The improved spray model assumes that the air entrainment can be represented by a gas jet. This at least ensures that a consistent gas-phase momentum is used; hence, a better prediction of the droplet-gas relative velocity results. As discussed earlier, only the axial component of the droplet relative velocity is corrected based on the gas-jet theory.

Figure 12 shows details of the spray structure at $t=3.0$ ms for $\rho_{amb}=60.6$ kg/m^3. Figure 13 shows the predicted spray-tip penetrations as a function of time. Both figures show vastly improved mesh independency in the spray structure and penetration as compared to the standard KIVA/LDEF model. Since the collision

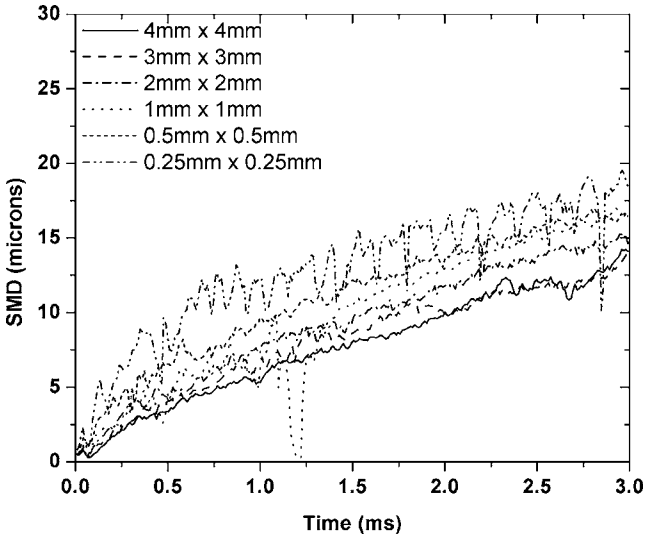

Fig. 14 Improved model with different meshes: overall SMD. $\rho_{amb}=60.6$ kg/m^3.

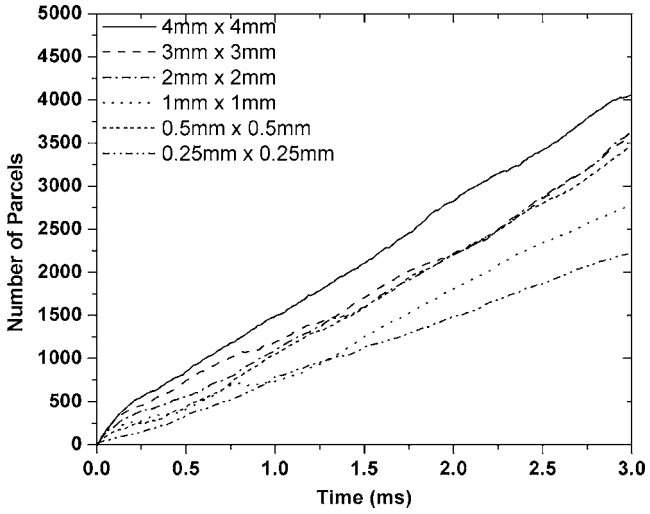

Fig. 15 Improved model with different meshes: total number of parcels. ρ_{amb}=60.6 kg/m^3.

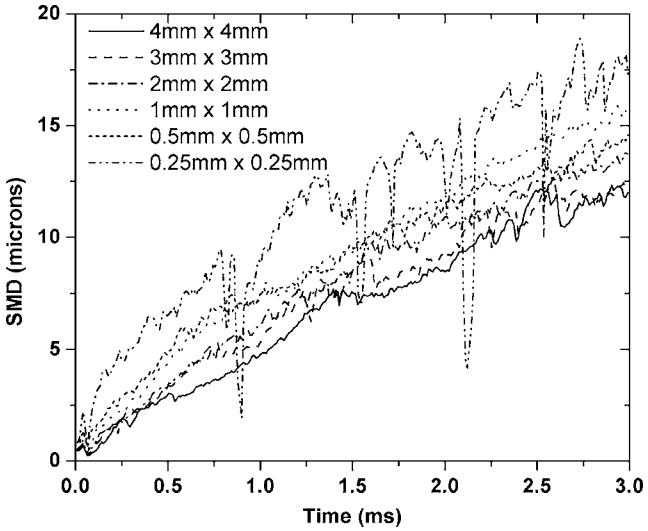

Fig. 17 Improved model with ROI collision model with different meshes: overall SMD. ρ_{amb}=60.6 kg/m^3.

mesh is the same for all six CFD meshes, the effect of the collision model is eliminated from consideration. The drop size and total number of parcels are shown in Figs. 14 and 15 and also show improved grid independency. In particular, the fine mesh case does not predict unreasonably small drop sizes, as observed for standard KIVA/LDEF models. Thus, it can be concluded that using the gas-jet theory in conjunction with a consistent/separate collision mesh, mesh-independent results can be obtained.

Improved diesel spray model results with collision radius of influence. The ROI was selected based on the collision mesh sensitivity results. In the previous section, it was found that the spray drop size is insensitive for a collision mesh of 4×4 mm^2 and above primarily due to the balance achieved in the RT breakup and coalescences. A similar idea of using a separate collisional volume was extended for the Lagrangian approach by considering a ROI of 2 mm, which is half the size of the chosen collisional mesh size, i.e., 4×4 mm^2.

Figure 16 shows the spray-tip penetration with the improved spray model and the collisional ROI. The spray-tip penetration shows adequately mesh-independent results. Figure 17 shows the corresponding drop size variation with different CFD mesh sizes with the ROI collision model. The drop size variation is less compared to the standard LDEF/KIVA case shown in Fig. 4.

Time-Step Independency. After establishing mesh-independent results using the gas-jet theory and the fixed and ROI collision meshes, an assessment of time-step dependency was made. First, results from the standard KIVA are presented for the five different time steps (10–0.1 μs). Only the coarse mesh was used since the new model was proven in the previous sections to be fairly mesh independent.

Standard KIVA/LDEF Results. The results from the standard KIVA help to identify the submodels responsible for the observed time-step dependency seen in Fig. 18. A linear trend is seen where the spray-tip penetration is smaller for Δt=5 μs and 10 μs and the tip penetration improves slightly for finer time steps. Figure 19 shows the drop sizes, and the time step is seen to have a major effect. For smaller time steps, the drop sizes are larger as compared to those at the coarser time steps. This is due to the fact that the collision model is based on an assumed Poisson distribution. For finer time steps, the collision model repeatedly calculates col-

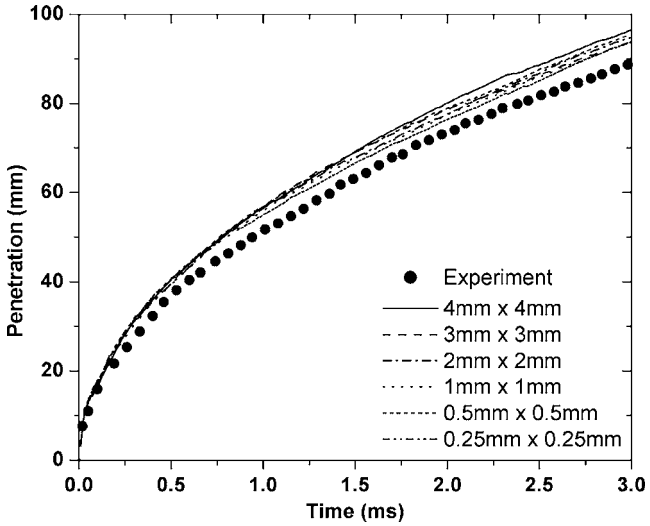

Fig. 16 Improved model (ROI collision model) with different meshes: spray-tip penetration. ρ_{amb}=60.6 kg/m^3.

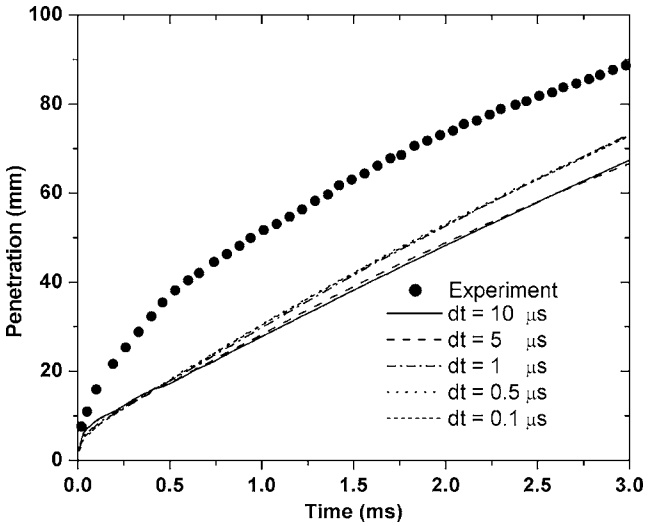

Fig. 18 Standard KIVA: spray-tip penetration with different time steps (4×4 mm^2 mesh)

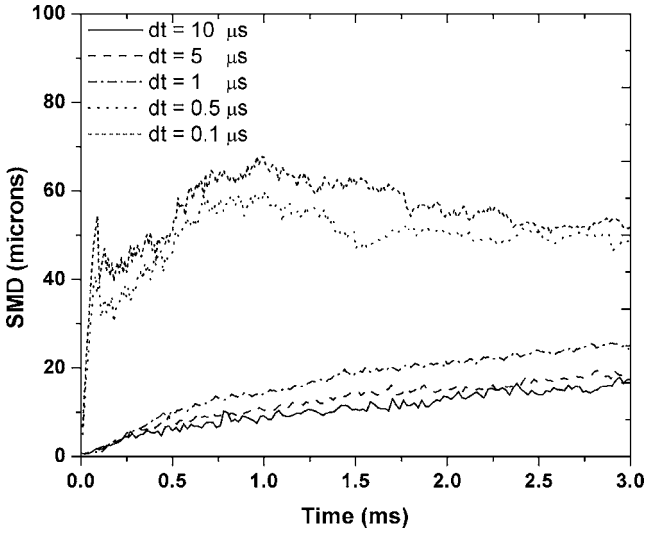

Fig. 19 Standard KIVA: overall SMD with different time steps (4×4 mm² mesh)

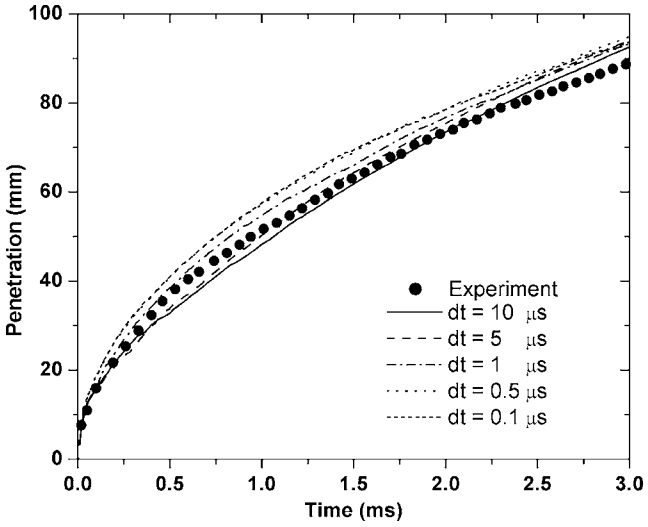

Fig. 21 Improved spray model: spray-tip penetration with different time steps (4×4² mm mesh)

lisions at each time step increment. For the same number of droplets, more collisions and coalescences result. This results in an increase in droplet size for finer time steps. For the range of coarser time steps between 1 μs and 10 μs, this trend is not very severe. Figure 20 shows the number of parcels in the domain. Using a fine time step results in fewer parcels as more coalescence takes place. Thus, it can be concluded that for the standard KIVA/LDEF spray model, using a very fine time step will result in fewer parcels and large drop sizes. This can be critical for evaporating sprays (not considered in the present study).

Improved Diesel Spray Model Results. The improved model predicts a more accurate relative velocity between the droplets and gas and also utilizes a separate collision mesh. Thus, at any given instant of time, irrespective of mesh size, the relative location of droplets will be the same. This results in mesh independency. For the time-step independency, the model is also expected to give an accurate prediction of spray-tip penetration. Figure 21 shows the spray-tip penetration and provides a relatively good prediction at all time steps. Figure 22 shows the corresponding drop size. The variation of overall SMD is reduced considerably as compared to the standard KIVA case (Fig. 19). This is due to the fact that the air entrainment is modeled consistently; thus, for two droplets as potential collision partners, the droplet-droplet relative velocity is the same irrespective of the time step. This ensures a more consistent outcome of the collision model at different time steps as compared to the standard KIVA/LDEF model. Figure 23 shows the total number of parcels in the chamber. The variation in the number of parcels is not as pronounced at different time steps as compared to the standard KIVA results.

Conclusion

A new spray model based on the assumption that the component of the gas velocity in the spray direction can be imposed using the gas-jet theory has been implemented and tested with the standard KIVA/LDEF methodology. The model predicts more accurately the relative velocity of the droplets and gas and also gives improved entrainment rate predictions. For the spray, mesh independency over meshes in the size range of 1–16 times the nozzle diameter has been demonstrated in terms of spray-tip penetration, drop size, number of parcels, and spray structure. The improved spray model was also tested with a separate collision mesh and a

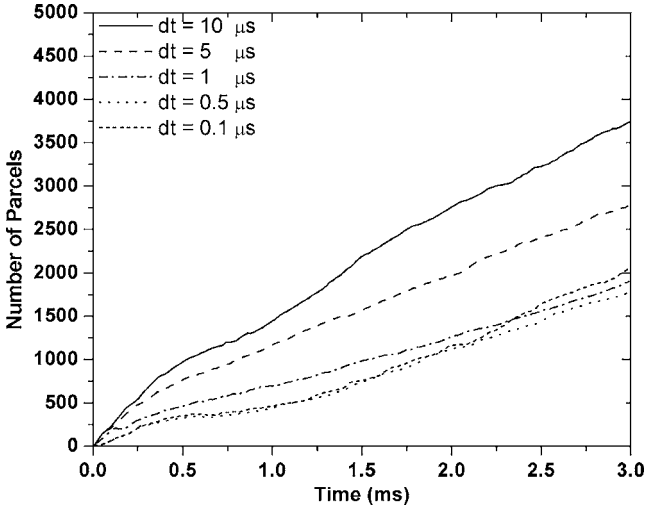

Fig. 20 Standard KIVA: total number of parcels with different time steps (4×4² mm mesh)

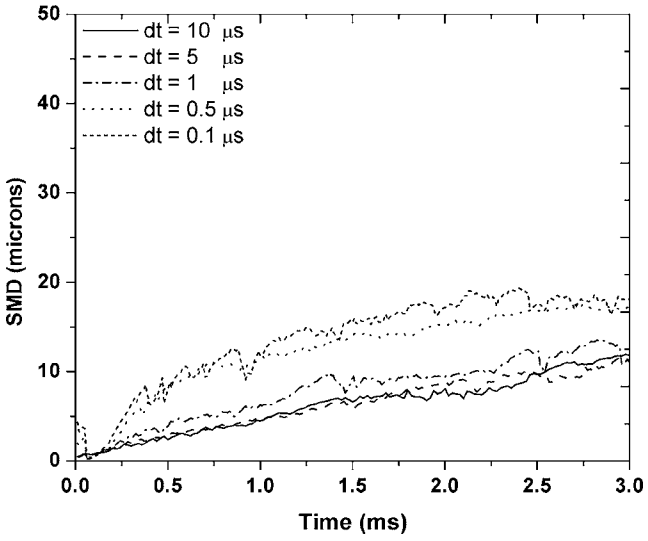

Fig. 22 Improved spray model: overall SMD with different time steps (4×4² mm mesh)

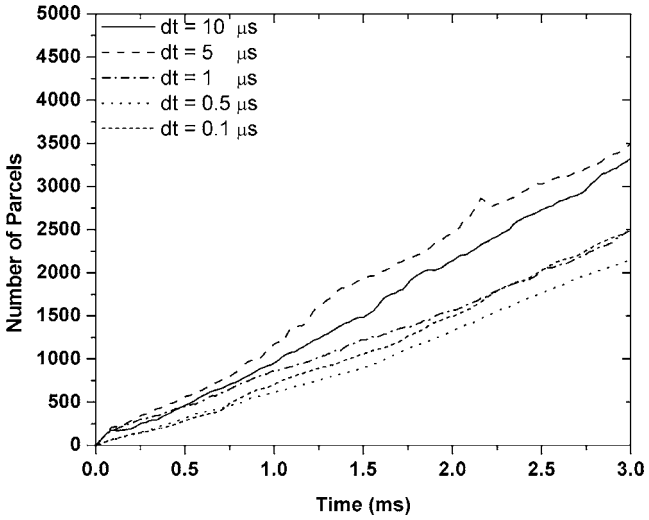

Fig. 23 Improved spray model: total number of parcels with different time steps (4×4 mm² mesh)

ROI approach surrounding the droplets. Both the models reasonably predict mesh-independent spray predictions. It is believed that for a nonuniform spray injection (not studied here), the ROI approach will give better spray predictions and will be the focus of future work.

Time-step dependency of LDEF spray models is rarely investigated. It was observed that the time-step dependency of standard LDEF models results in large variations in the predicted drop sizes, primarily due to the collision model. For small time steps, the collision model predicts increased collision and coalescences; hence, the average drop sizes are larger compared to those with coarser time steps. However, the new spray model also reduces the time-step dependency. This is because the droplet-droplet relative velocity is also more consistently predicted; hence, coalescences are not overpredicted. The time-step dependency of LDEF models is critical for evaporative spray predictions and will be the focus of future research to further improve the time and mesh independencies.

Acknowledgment

Authors acknowledge the support of DOE–Sandia Laboratories and S. C. Johnson for this work.

References

[1] Amsden, A. A., 1997, "KIVA-3V: A Block Structured KIVA Program for Engines With Vertical or Canted Valves," Los Alamos National Laboratory, Technical report No. LA-13313-MS.
[2] O'Rourke, P. J., and Bracco, F. V., 1980, "Modeling Drop Interactions in Thick Sprays and a Comparison With Experiments," *Proceedings of the IMechE Conference on Stratified Charge Automotive Engines*, pp. 101–116.
[3] O'Rourke, P. J., 1981, "Collective Drop Effects on Vaporizing Liquid Sprays," Ph.D. Thesis, Princeton University.
[4] Beale, J. C., and Reitz, R. D., 1999, Atomization Sprays, **9**, pp. 623–650.
[5] Patterson, M. A., and Reitz, R. D., 1998, SAE Technical Paper No. 980131.
[6] Abraham, J., 1997, "What Is Adequate Resolution in the Numerical Computation of Transient Jets," SAE Paper No. 970051.
[7] Post, S., Iyer, V., and Abraham, J., 2000, "A Study of the Near-Field Entrainment in Gas Jets and Sprays Under Diesel Conditions," ASME J. Fluids Eng., **122**, pp. 385–395.
[8] Aneja, R., and Abraham, J., 1998, "How Far Does the Liquid Penetrate in Diesel Engine: Computed Results Vs. Measurements?" Combust. Sci. Technol., **138**(1–6), pp. 233–255.
[9] Schmidt, D. P., and Rutland, C. J., 2000, "A New Droplet Collision Algorithm," J. Comput. Phys., **164**, pp. 62–80.
[10] Schmidt, D. P., and Rutland, C. J., 2004, "Reducing Grid Dependency in Droplet Collision Modeling," ASME J. Eng. Gas Turbines Power, **126**, pp. 227–233.
[11] Nordin, N., 2000, "Complex Chemistry Modeling of Diesel Spray Combustion," Ph.D. thesis, Chalmers University of Technology.
[12] Beard, P., Duclos, J. M., Habchi, C., Bruneaux, G., Mokaddem, K., and Baritaud, T., 2000, "Extension Application to High-Pressure Evaporating Diesel Sprays," SAE Technical Paper No. 2000-01-1893.
[13] Lippert, A. M., Chang, S., Are, S., and Schmidt, D. P., 2005, "Mesh Independence and Adaptive Mech Refinement for Advanced Engine Spray Simulations," SAE Technical Paper No. 2005-01-0207.
[14] Abraham, J., 1996, "Entrainment Characteristics of Transient Jets," Numer. Heat Transfer, Part A, **30**, pp. 347–364.
[15] Schlichting, H., 1976, *Boundary Layer Theory*, McGraw-Hill, New York.
[16] Allen, M. R., and Tildesley, T. J., 1987, *Computer Simulation of Liquids*, Oxford University Press, New York, p. 147.
[17] Sundaram, S., and Collins, L. R., 1996, "Numerical Consideration in Simulating a Turbulent Suspension of Finite Volume Particles," J. Comput. Phys., **124**, pp. 337–350.
[18] Naber, J. D., and Siebers, D. L., 1996, "Effects of Gas Density and Vaporization on Penetration and Dispersion of Diesel Sprays," SAE Technical Paper No. 960034.

Combustion Performance of Liquid Biofuels in a Swirl-Stabilized Burner

Daniel Sequera
Ajay K. Agrawal

Department of Mechanical Engineering,
The University of Alabama,
Tuscaloosa, AL 35487

Scott K. Spear
Daniel T. Daly

Alabama Institute for Manufacturing Excellence,
The University of Alabama,
Tuscaloosa, AL 35487

Fuels produced from renewable sources offer an economically viable pathway to curtail emissions of greenhouse gases. Two such liquid fuels in common usage are biodiesel and ethanol derived from soybean, corn, or other food crops. In recent years, significant effort has been devoted to identify alternate feedstock sources and conversion techniques to diversify the biofuels portfolio. In this study, we have measured emissions from flames of diesel, biodiesel, emulsified bio-oil, and diesel-biodiesel blends. Experiments are conducted in an atmospheric pressure burner with an air-atomized injector and swirling primary air around it to replicate typical features of a gas turbine combustor. Experiments were conducted for fixed air and fuel flow rates, while the airflow split between the injector and the coflow swirler was varied. Results show a significant reduction in emissions as the fraction of total air fed into the atomizer is increased. Blue flames, reminiscent of premixed combustion, and low emissions of nitric oxides and carbon monoxide were observed for all fuel blends. In general, the emissions from biofuel flames were comparable or lower than those from diesel flames. [DOI: 10.1115/1.2836747]

Introduction

Renewable fuels produced from homegrown biomass are expected to constitute a greater portion of the fuel feedstock in the near to midterm. Increased production and use of biofuels will not only benefit the environment but also contribute to the energy security and economic growth. Ideally, the CO_2 emitted from the combustion of biofuels is recycled through the environment to produce biomass or the feedstock for biofuels. A recent study projects that with relatively modest changes in land use and agricultural and forestry practices, an annual supply of 1.36×10^9 dry tons of biomass could be available for large-scale biofuel production in the United States by the mid-21st century, while still meeting demands for forestry products, food, and fiber [1].

Biomass can be converted into solid, gaseous, or liquid fuel depending on the conversion processes and economic factors. Several current biomass technologies are reviewed in Ref. [2]. Co-firing of biomass with coal is among the most cost effective approaches [3]. Since combustion of solid fuels results in higher emissions (e.g., soot and nitric oxides or NO_x), liquid and/or gaseous fuels produced from biomass are likely to become increasingly prevalent in the near term. Biomass can be gasified in air-blown or oxygen-blown gasifiers, followed by the cleanup of the product gas (known as synthetic gas or syngas) containing carbon monoxide (CO) and hydrogen (H_2) as the primary reactants. The biomass syngas can serve as the fuel to generate power in a high-efficiency combined cycle power plant. The combined cycle power plant integrated with the gasification system can operate synergistically with biomass and/or coal as feedstocks, since the syngas produced from gasification of either of these sources (biomass or coal) contains the same reactive ingredients. In recent years, considerable interest has been generated to develop fuel-flexible power systems using advanced gas turbines to achieve high efficiency with ultralow emissions [4]. Lean premixed (LPM) combustion of hydrogen-rich syngas can cause autoignition, flame flashback, and/or dynamic instabilities, which must be eliminated to ensure reliable operation, structural rigidity, and acceptable NO_x and CO emissions [5–7].

In contrast to biomass syngas requiring large scale operation, liquid biofuels offer greater flexibility since the fuel can be transported easily. Liquid biofuels offer the prospects of distributed generation, whereby the power is produced closer to the source without hauling the bulky biomass to a distant central location. At present, ethanol and biodiesel are the two commonly used liquid biofuels. However, the feedstocks for these fuels compete with the food-chain crops. For example, virtually all of the ethanol produced in the US comes from corn and biodiesel is produced by the transesterification of vegetable oils, such as soybean oil. Thus, a long-term strategy will require liquid fuels from biomass feedstocks, such as wood and other energy crops that do not interfere with the food chain.

The biomass must undergo gasification or pyrolysis to produce the liquid fuel. Starting with the biomass syngas, the well-known Fischer–Tropsch (FT) process can be used to produce liquid biofuels of desired composition and physical characteristics. Although the FT process is attractive to produce liquid biofuels for vehicular transportation [8], the fuels produced by pyrolysis of biomass can be economic alternatives for power generation applications. Pyrolysis is the thermal destruction of organic material in the absence of or limited supply of oxygen [3]. In fast pyrolysis, the thermal decomposition occurs at moderate temperatures with a high heat transfer rate to the biomass particles and a short hot-vapor residence time in the reaction zone [9–11]. The main product is the pyrolysis oil, also known as bio-oil, which is usually a dark-brown free-flowing liquid with a distinctive smoky odor. Bio-oils have been successfully tested in diesel engines and gas turbines [12–15], although modifications to the fuel handling system can incur unacceptable financial cost. Thus, a near-term strategy would be to emulsify bio-oil using fuels compatible with the fuel handling equipment. Ikura et al. [16] produced bio-oil emulsified with the diesel fuel. The cost for producing emulsions with zero stratification increased with increasing amounts of bio-oil in the diesel fuel.

The literature review shows few studies on combustion performance of liquid biofuels for gas turbine applications. Thus, the primary objective of this study is to isolate the effects of fuel composition and fluid dynamics on emissions from different liquid fuels in an atmospheric pressure burner replicating typical features of a gas turbine combustor. The burner utilized a commercial twin-fluid injector with primary air swirling around the injector. The fuels include diesel, biodiesel, emulsified bio-oil, and

Manuscript received June 20, 2007; final manuscript received June 22, 2007; published online April 2, 2008. Review conducted by Dilip R. Ballal.

Table 1 NREL bio-oil characteristics

	Bio-oil	Diesel[a]	Biodiesel[b]
Moisture content (wt %)	20.0		
Ash (wt %)	0.018		
Dry elemental composition (wt %)			
Carbon	45.6	86.7	78.61
Hydrogen	7.6	13.5	11.99
Nitrogen	0.05	0.04	2.1[c]
Sulfur	0.02	0.03	<0.004
Oxygen	46.8		9.38

[a]From Ref. 16.
[b]From Ref. 17.
[c]ppm.

diesel-biodiesel blends. Bio-oil emulsions were produced using blends of biodiesel and diesel to increase the amount of biomass derived fuel in the final product. The emulsified bio-oil produced in this manner is expected to require minimal modifications to the fuel handling system. For fixed volume flow rates of fuel and air, experiments were conducted by varying the airflow split between the injector and coflow swirler. Results include visual flame images, and axial and radial profiles of NO_x and CO concentrations at different operating conditions. In the following sections, the fuel preparation steps and experimental setup details are outlined followed by results and discussions.

Fuel Preparation

As mentioned above, the fuels in this study included diesel, biodiesel, emulsified bio-oil, and diesel-biodiesel blends. The diesel fuel used was of a commercial grade (No. 2 diesel fuel) purchased from a local filling station. The biodiesel was supplied by Alabama Biodiesel Corporation (Moundville, AL) and it was a soybean oil methyl ester (SME). Pyrolysis oil, also known as bio-oil (from hardwood), was provided by the National Renewable Energy Laboratory (NREL, Boulder, CO). It was a hot-vapor filtered bio-oil with very low ash content. The bio-oil was approximately one-year old, and was not phase separated or treated with any viscosity reducing agents. The NREL bio-oil composition is summarized in Table 1.

The emulsified bio-oil was formulated by mixing diesel, bio-oil, and "surfactants." The surfactants used in this study was a blend of biodiesel, 2-ethyl-1-hexanol (an alcohol), and *n*-octylamine. The latter two chemicals were purchased from Aldrich (Milwaukee, WI). The emulsified fuel was produced by mixing diesel, biodiesel, bio-oil, alcohol, and amine using a high shear (10,000 rpm) Oster blender (Boca Raton, FL). Mixing was done at room temperature and pressure until an emulsified liquid was obtained in about 2 min. In this study, two types of biodiesel (SME and 90% soybean oil ethyl ester hereafter referred to as SEE) were mixed with diesel by gentle stirring to form diesel-biodiesel fuel blends. These blends are completely miscible over all concentration ranges. Table 2 summarizes the fuels used in this study.

Table 2 Experimental fuel blends (vol %)

Fuel	Diesel	Biodiesel (SME+SEE)	Bio-oil	Alcohol/amine
Diesel	100			
Biodiesel		(100+0)		
Bio-oil	45	(30+0)	15	8/2
SOME	80	(20+0)		
SOEE	80	(0+20)		

Table 3 Water contents in the fuel blends

Fuel	% w/w $\pm 3\sigma$
Diesel	0.021 ± 0.006
Biodiesel	0.10 ± 0.01
Biooil	0.27 ± 0.04
SOME	0.03 ± 0.01
SOEE	0.017 ± 0.004
Bio-oil (as received)[a]	22.9 ± 1.4

[a]Water content most likely increased during storage.

The water content of each fuel was determined by a volumetric Aquastar Karl–Fischer titrator (EM Science, Gibbstown, NJ) with Composite 5 solution as the titrant and anhydrous methanol as the solvent. All measurements were made in triplicate and at 25°C. The water content in the fuel blends is summarized in Table 3.

Experimental Setup

The test apparatus shown schematically in Fig. 1 consists of the combustor assembly and the injector assembly. The primary air enters the system through a plenum filled with marbles to breakdown the large vortical structures. The air passes through a swirler into the mixing section, where the gaseous fuel is supplied during the startup. The reactant(s) enter the combustor through a swirler to improve the fuel-air mixing and to help anchor the flame. Figure 2 shows a schematic diagram and a photograph of the combustor inlet section with the swirler. The swirler had six vanes positioned at 28 deg to the horizontal. The theoretical swirl number was 1.5, assuming that the flow exited tangentially from the swirler vanes. The bulk axial inlet velocity of the primary air was 1.9–2.1 m/s, which resulted in Reynolds number varying from 5960 to 6750. The liquid fuel is supplied from an injector with separate concentric inlets for fuel and atomization air. The injector system runs through the plenum and the mixing chamber. An O-ring within a sleeve is provided at the bottom of plenum to prevent any leakage. The injector is a commercial air-blast atomizer (Delavan Siphon type SNA nozzle) and it creates a swirling flow of atomizing air to breakdown the fuel jet. The injector details are shown in Fig. 3. The combustor itself is a 8.0 cm inside diameter (i.d.) and 46 cm long quartz tube. The combustor is back-side cooled by natural convection.

The liquid fuel is supplied by a peristaltic pump with the range of flows rates from 2 ml/min to 130 ml/min in steps of 2 ml/min. The reported calibration error of the pump is ±0.25% of the flow rate reading. Viton tubes were used to prevent any degradation of the fuel lines. A 25 μm filter was used to prevent dirt and other foreign particles from clogging the injector. The primary and atomizing air is supplied by an air compressor. The air passes through a pressure regulator and a water trap to remove the moisture. Then, the air is split into primary air supply and atomizing air supply lines. The primary air flow rate is measured by a laminar flow element (LFE) calibrated for 0–1000 lpm (liters per minute) of air. The pressure drop across the LFE is measured by a differential pressure transducer. An absolute pressure transducer is used to measure the pressure of air passing through the LFE. The flow rate measured by the LFE is corrected for temperature and pressure as specified by the manufacturer. The atomizing air is measured by a calibrated mass flow meter.

The product gas was sampled continuously by a quartz probe (outside diameter (o.d.)=7.0 mm) attached to a three-way manual traversing system. The upstream tip of the probe was tapered to 1 mm i.d. to quench reactions inside the probe. The sample passed through an ice bath and water traps to remove moisture upstream of the gas analyzers. The dry sample passed through electrochemical analyzers to measure the concentrations of CO and NO_x in ppm. The analyzer also measured oxygen and carbon dioxide concentrations, which were used to cross-check the equivalence ratio

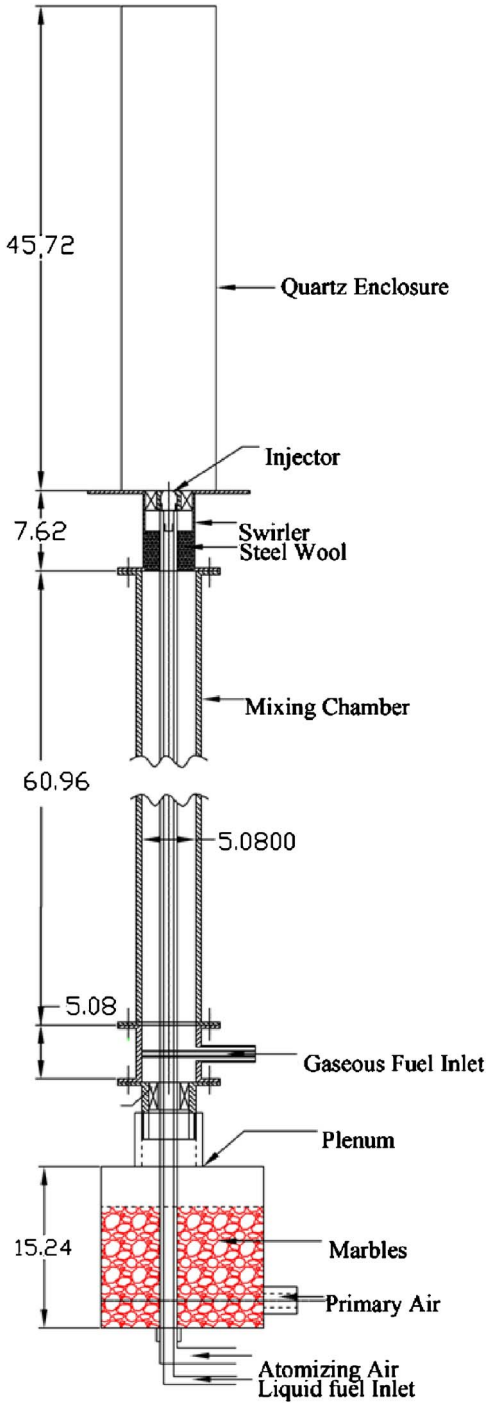

Fig. 1 Schematic diagram of the experimental setup; all dimensions are in cm

obtained from the measured fuel and air flow rates. The uncorrected emission data on dry basis are reported with measurement uncertainty of ± 2 ppm.

The experiment was started by supplying the gaseous methane and then igniting the methane-air reactant mixtures in the combustor. Next, the liquid fuel flow rate was gradually increased to attain the desired value, while the methane flow rate was slowly decreased to zero.

In this study, the volume flow rates of total air (primary +atomizing) and fuel were kept constant, respectively, at 150 standard lpm and 12 ml/min. It would result in small variations in the amount of heat released since the heating value of fuels is

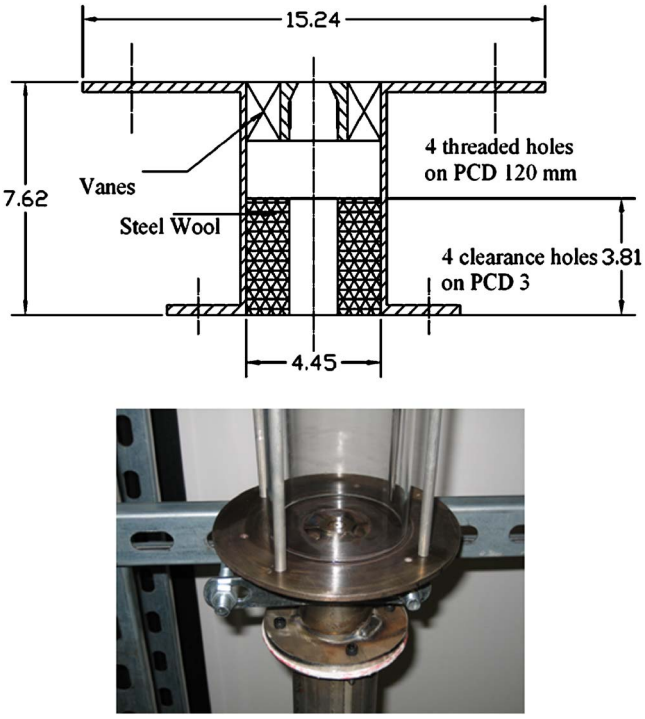

Fig. 2 Schematic diagram (top) and photograph of the swirler (bottom) at the combustor inlet plane; all dimensions are in cm

different. The combustion performance is strongly dependent on the spray characteristics determined by the atomizing air flow rate. Initial experiments indicated yellow, sooty flames dominated by the diffusion mode of combustion for atomizing air flow rates below 10% of the total air. Thus, experiments focused on the premixed combustion mode with strong fuel-air premixing prompted by fine droplets formed with large atomizing air flow rates. Accordingly, the experiments were conducted by varying the percentage of the atomizing air (AA) from 15% to 25% of the total air. Since the overall air-fuel ratio is constant, the effects of AA on combustion emissions can be ascertained from these measurements.

Results and Discussion

Visual Flame Images. Direct photographs of flame were taken by a digital camera to obtain qualitative understanding of the flame characteristics. These photographs are reproduced in Fig. 4

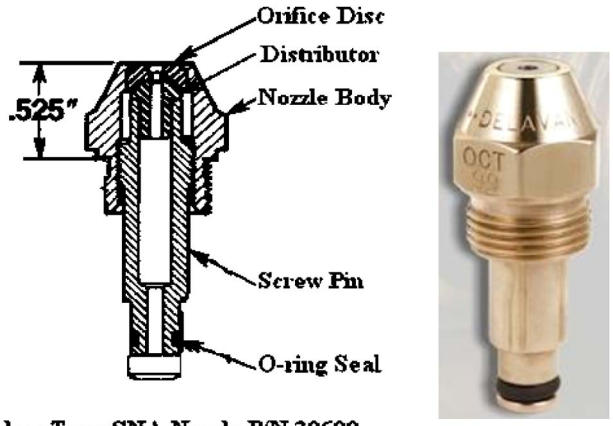

Fig. 3 Injector details

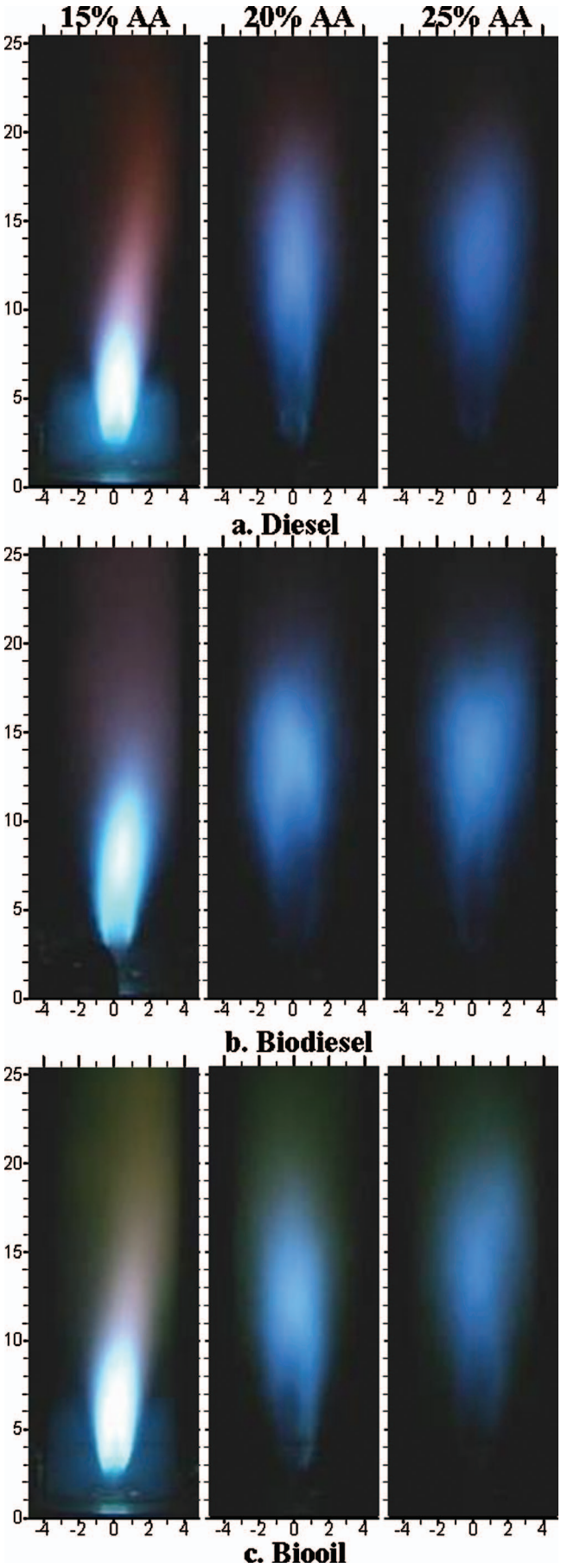

Fig. 4 Effect of AA on visual flame images for different fuels

for diesel, biodiesel, and bio-oil flames. For each case, the flame images are shown for AAs of 15%, 20%, and 25% of the total air. All flames in Fig. 4 show a distinctive blue color typical of the premixed combustion. In contrast, combustion in the diffusion mode produces yellow, sooty flames, because the fuel droplets do not vaporize and premix with air before reactions take place. Results in Fig. 4 suggest that the injector is producing spray with fine droplets that prevaporize and premix with air to form the reactant mixture prior to the combustion. This is also true for the emulsified bio-oil, since it contained a relatively small amount of bio-oil (15% by volume) that is otherwise difficult to prevaporize. Excellent atomization is attributed to the large AA used in this study. Note that the pressure drop associated with AA flow in the injector could increase the operating cost. However, the operating conditions in this study provide a consistent basis to compare different fuels and they also point toward the need to optimize the injector design to cost effectively reduce emissions of soot, NO_x, CO, and unburned hydrocarbons.

Figure 4(*a*) shows that the width and height of the diesel flame increase with increase in the AA. For example, the flame is short and intense for 15% AA compared to that for 25% AA. In the case of 15% AA, the fuel droplets prevaporize to form reactant mixture of higher equivalence ratio, which would burn at an elevated flame temperature. With increase in the AA, the local equivalence ratio of the reactant mixture decreases and hence, the reactions occur at a lower temperature. Note that the temperature of the homogenized products would be the same for both cases since the overall air-fuel ratio is constant. Thus, the observed differences occur because of the local inhomogeneities in the flow field. Clearly, the flow structure has profound impact on flame characteristics, as indicated by Fig. 4(*a*). Figures 4(*b*) and 4(*c*) show that the effects of AA on biodiesel and bio-oil flames is similar to that for diesel flames. The images of bio-oil flames in Fig. 4(*c*) reveal green tint in the postcombustion zone, whose origin is unknown at present.

Effect of Atomizing Air on NO_x and CO Emissions. Figure 5 presents the NO_x and CO emission profiles along the axis of the combustor. The axial distance (z) in these profiles is measured from the combustor inlet plane; thus $z=45$ cm refers to the combustor exit plane. For diesel flames, Fig. 5(*a*) shows that the NO_x concentration is nearly constant in the axial direction. Evidently, all of the NO_x is formed in a short reaction zone within $z=12$ cm. Figure 5(*a*) shows a significant decrease in the NO_x concentrations as the AA is increased from 15% to 20% of the total air. Further increase in AA (to 25%) results in only a modest decrease in the NO_x concentrations. This effect is related to the equivalence ratio (and hence, the reaction zone temperature) of the reactant mixture produced for different AA flow rates, as discussed above. Higher AA produces a leaner reactant mixture that burns at a lower flame temperature to produce lower NO_x concentrations.

For diesel flames, Fig. 5(*b*) shows that the CO concentrations increase and then decrease in the axial direction. Initially, the CO is produced during the fuel breakdown and it is subsequently oxidized in the reaction zone. The increase in the AA tends to decrease the CO emissions since the reactions occur at a lower flame temperature as explained previously. The first data point in Fig. 5(*b*) is likely affected by the large turbulent fluctuations in the fuel-rich regions of the flame. The axial profiles of NO_x and CO concentrations in biodiesel and bio-oil flames in Fig. 5 reveal the same general trends: (i) the NO_x emissions are formed within $z=12$ cm and NO_x concentration is independent of the axial distance for $z>12$ cm; (ii) the NO_x concentration decreases significantly with increase in AA from 15% to 20% of the total air, but marginally for increase in AA from 20% to 25% of the total air; (iii) the CO concentrations initially increase and then decrease in the axial direction; and (iv) the CO concentrations decrease with increase in the AA.

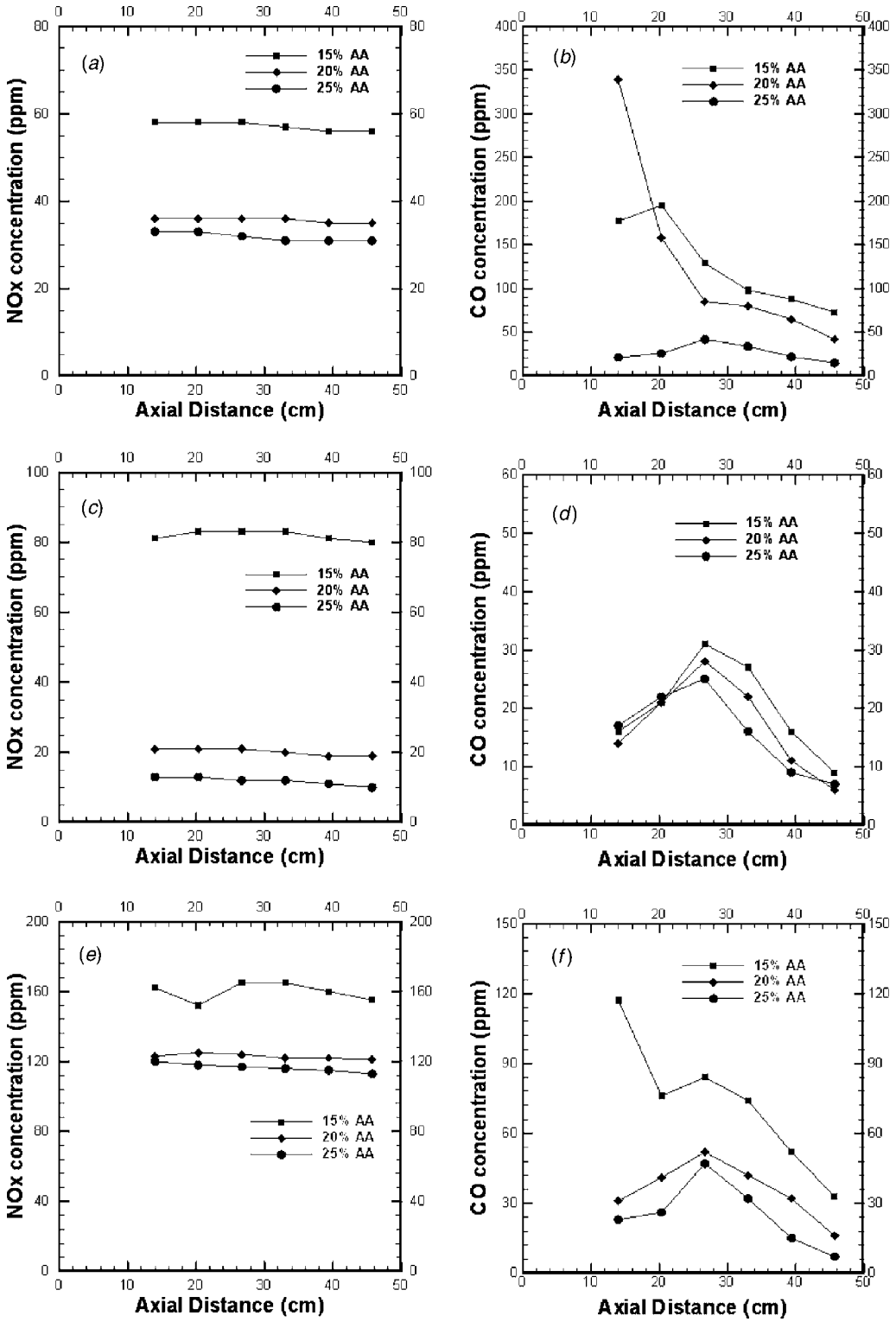

Fig. 5 Axial profiles of NO_x and CO emissions for different fuels; [(*a*) and (*b*)] diesel, [(*c*) and (*d*)] biodiesel and [(*e*) and (*f*)] bio-oil

Emission measurements were also taken at the combustor exit plane to identify unmixedness in the radial direction. For diesel flames, Figs. 6(*a*) and 6(*b*) show that the NO_x and CO concentrations are nearly constant at the combustor exit plane. These results indicate that sufficient flow mixing has taken place within the combustor to form a homogeneous product gas mixture at the exit plane. Figures 6(*a*) and 6(*b*) show that NO_x and CO concentrations at the combustor exit plane decrease with increase in the AA. The radial profiles of NO_x and CO concentrations at combustor exit plane for biodiesel and bio-oil flames in Fig. 6 show the same general trends: (i) the NO_x emissions are constant in the radial direction; (ii) the NO_x concentrations decrease with increase in

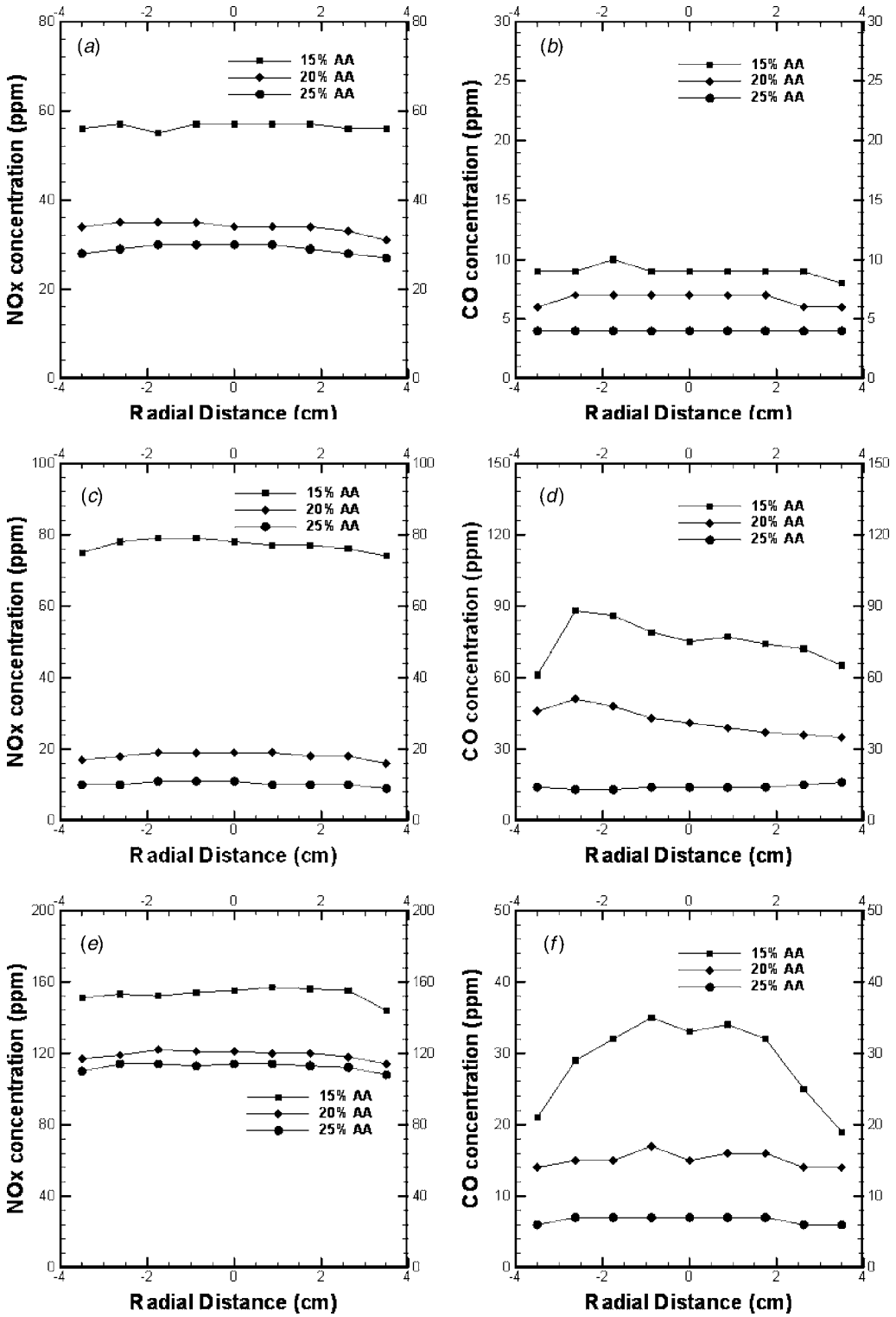

Fig. 6 Radial profiles of NO_x and CO emissions for different Fuels; [(*a*) and (*b*)] diesel, [(*c*) and (*d*)] biodiesel and [(*e*) and (*f*)] bio-oil

the AA; (iii) the CO concentrations are independent of the radial coordinate except for 15% AA in the bio-oil flame, where a parabolic profile is observed; and (iv) the CO emissions decrease with increase in AA.

Overall, the results show that the fluid mechanics associated with the atomization process has significant effect on the flame structure and emissions, and that different fuels respond similarly to the flow-induced effects of the injector. Clearly, emissions are dependent not only on the fuel properties but also on the flame structure determined by the flow processes. Next, the fuel effects are isolated by comparing the NO_x and CO emissions for different fuels using the same volume flow rates of fuel, AA, and total air.

Fuel Effects on NO_x and CO Emissions. Figure 7 shows axial profiles of NO_x and CO emissions for different fuels. Profiles in Figs. 7(*e*) and 7(*f*) show that with 25% AA, the NO_x emissions are

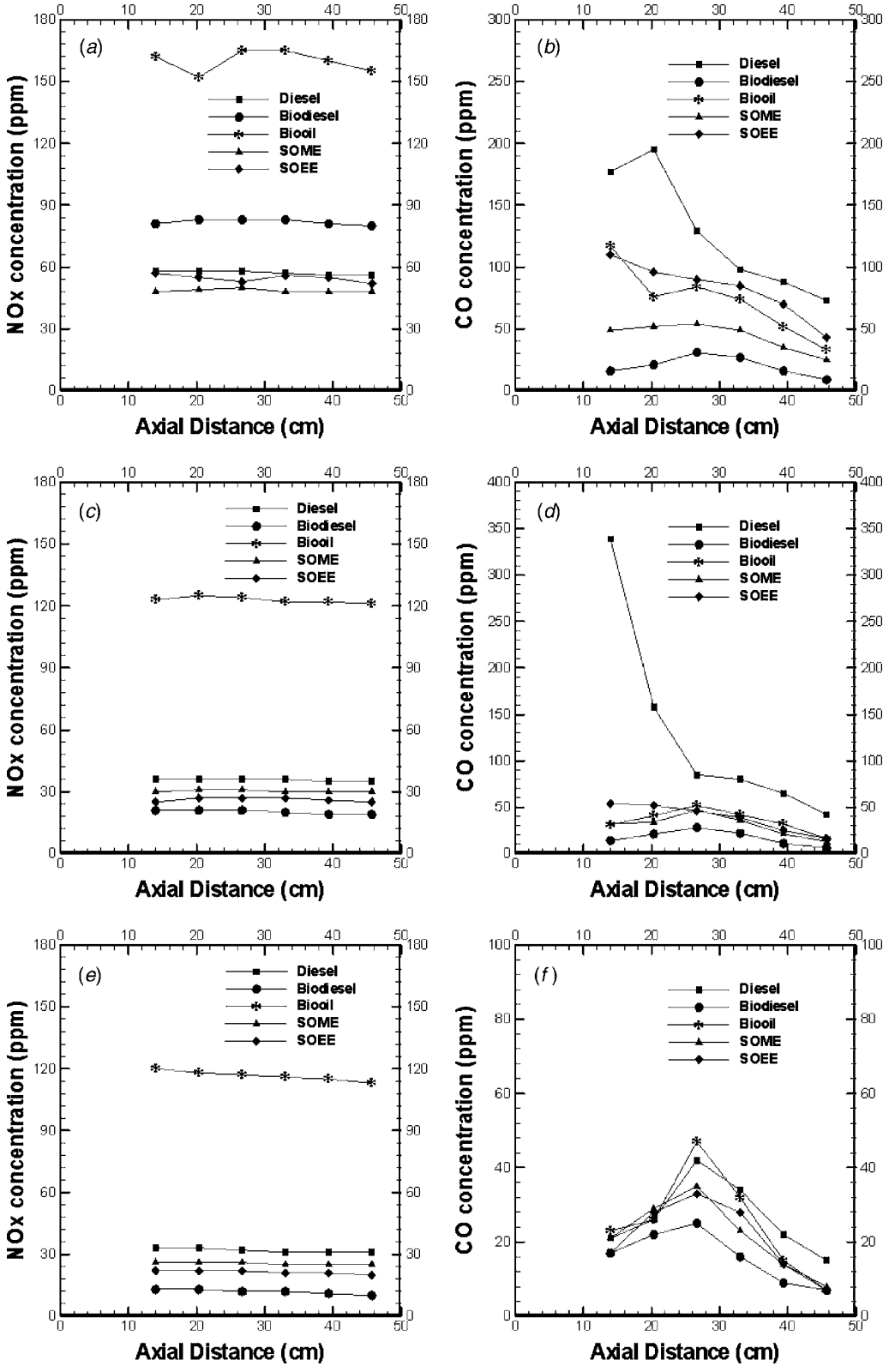

Fig. 7 Axial Profiles of NO_x and CO emissions for different AA flow rates; [(*a*) and (*b*)] 15% AA, [(*c*) and (*d*)] 20% AA, and [(*e*) and (*f*)] 25% AA

highest for the bio-oil and lowest for the biodiesel. Among the three remaining fuels (diesel, SOME, and SOEE), the NO_x emissions are highest for the diesel fuel. The high NO_x emissions with emulsified bio-oil are likely caused by the nitrogen present in the *n*-octylamine used as surfactants. Thus, alternate surfactants must be considered in the future to reduce NO_x emission from the fuel-bound nitrogen. Figure 7(*f*) shows that the CO emissions are generally higher for diesel, lowest for biodiesel, and similar for the remaining fuels (bio-oil, SOME, and SOEE).

Results show that both NO_x and CO emissions are lowest for

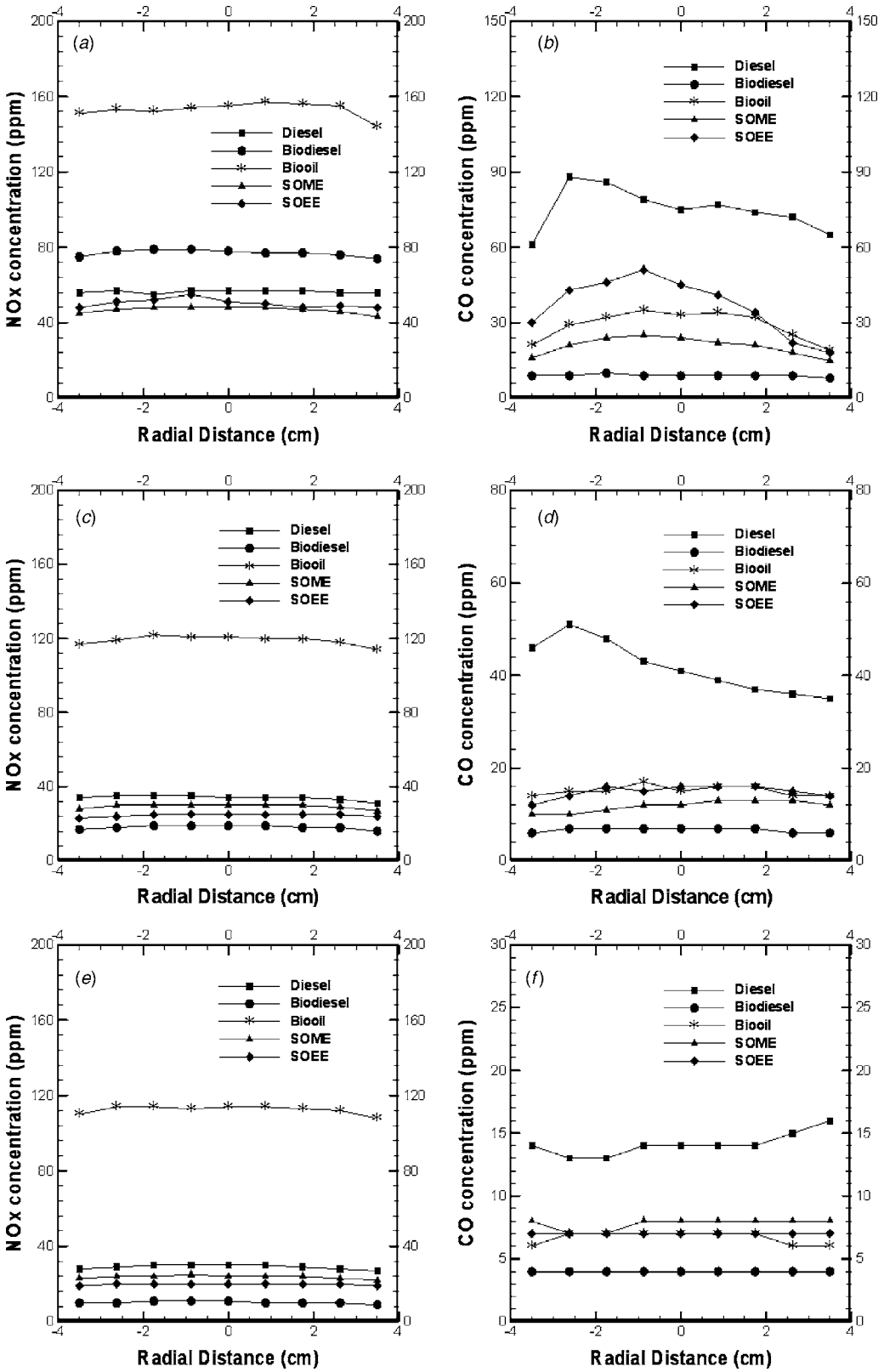

Fig. 8 Radial profiles of NO_x and CO emissions for different AA flow rates; [(*a*) and (*b*)] 15% AA, [(*c*) and (*d*)] 20% AA, and [(*e*) and (f)] 25% AA

biodiesel with 25% AA. The bio-oil CO emissions are low, and by choosing an alternative to the nitrogen-containing surfactant to eliminate the fuel-bound nitrogen, the bio-oil NO_x emissions could be reduced significantly. The CO and NO_x emissions for diesel-biodiesel fuel blends (SOME and SOEE) are generally lower than those for the diesel fuel. Thus, biodiesel, emulsified bio-oil, and biodiesel blends could provide emission performance superior to the diesel fuel. Results for 20% and 15% AA show the

same general trends in Figs. 7(*a*)–7(*d*). The only exception is that the NO_x emissions for biodiesel with 15% AA are higher than those for the diesel fuel. This result suggests that the emission performance must be optimized by tailoring the injector design for a given fuel. The emission measurements at the combustor exit plane are summarized in Fig. 8 for different fuels. Results are consistent with the previous observations, i.e., the biodiesel produced lowest CO and NO_x emissions, bio-oil NO_x emissions are the highest, and the CO emissions are highest for the diesel fuel.

Conclusions

In this study, NO_x and CO emissions from diesel, biodiesel, emulsified bio-oil, and diesel-biodiesel fuel blends were measured in an atmospheric pressure burner simulating typical features of a gas turbine. The emulsified bio-oil was made by blending bio-oil with surfactants containing biodiesel, alcohol, and amine. For a given fuel flow rate, the biodiesel flames produced the least amounts of NO_x and CO concentrations. Diesel flames produced higher CO emissions compared to the other fuels. The high NO_x emissions from bio-oil flames were attributed to the nitrogen-containing surfactants in the fuel. Both NO_x and CO emissions were affected significantly by the fraction of the total air used for atomization; emissions decreased with increase in the AA. Results show that even though the fuel properties are important, the flow effects can dominate the NO_x and CO emissions. For a given fuel, the emissions can be minimized by properly tailoring the injector design and the associated combustion processes.

Acknowledgment

The authors thank Dr. Stefan Czernik of the U.S. Department of Energy, National Renewable Energy Laboratory for supplying the pyrolysis oil. The authors also thank Professor Duane T. Johnson of The University of Alabama Department of Chemical and Biological Engineering and Alabama Biodiesel, Inc. for providing the biodiesel used in this study. Heena Panchasara assisted with post-processing of the data.

Nomenclature

LFE = laminar flow element
SEE = soybean oil ethyl ester
SME = soybean oil methyl ester
SOEE = soybean oil ethyl ester blended with diesel
SOME = soybean oil methyl ester blended with diesel

References

[1] De La Torre Ugarte, D. G., 2003, "The Economic Impact of Bioenergy Crop Production on U.S. Agriculture, US Department of Agriculture and Department of Energy," Agricultural Economic Report No. 816, www.usda.gov/oce/reports/energy/AER816Bi.pdf.

[2] Demirbas, A., 2004, "Combustion Characteristics of Different Biomass Fuels," Prog. Energy Combust. Sci., **30**, pp. 219–230.

[3] Damstedt, B., Pederson, J. M., Hansen, D., Knighton, T., Jones, J., Christensen, C., Baxter, L., and Tree, D., 2007, "Biomass Cofiring Impacts on Flame Structure and Emissions," Proc. Combust. Inst., **31**, pp. 2813–2820.

[4] Richards, G. A., McMillian, M. M., Gemmen, R. S., Rogers, W. A., and Cully, S. R., 2001, "Issues for Low-Emission, Fuel-Flexible Power Systems," Prog. Energy Combust. Sci., **27**, pp. 141–169.

[5] Lieuwen, T., McDonnell, V., Petersen, E., and Santavicca, D., 2006, "Fuel Flexibility Influences on Premixed Combustor Blowout, Flashback, Autoignition, and Stability," ASME Paper No. GT2006-90770.

[6] Jayasuria, J., MAnrique, A., Fakhrai, R., Fredriksson, J., and Fransson, T., 2006, "Gasified Biomass Fuelled Gas Turbine: Combustion Stability and Selective Catalytic Oxidation of Fuel-Bound Nitrogen," ASME Paper No. GT2006-90988.

[7] Moriconi, A., Quirini, C., Moriconi, D., and Moriconi, E., 2005, "Gas Turbine Fed by Gas Produced from Biomass Pyrolysis," ASME Paper No. GT2005-69032.

[8] William, E. Harrison, Clean Fuel Initiative, www.cffs.uky.edu/C1/2002meeting/WPAFBharrison.pdf.

[9] Oasmaa, A., and Czernik, S., 1999, "Fuel Oil Quality of Biomass Pyrolysis Oils—State of the Art for the End Users," Energy Fuels, **13**, pp. 914–921.

[10] Czernik, S., and Bridgewater, A. V., 2004, "Overview of Applications of Biomass Fast Pyrolysis Oil," Energy Fuels, **18**, pp. 590–598.

[11] Mohan, D., Pittman, C. U., and Steele, P. H., 2006, "Pyrolysis of Wood/Biomass for Biooil: A Critical Review," Energy Fuels, **20**, pp. 848–889.

[12] Strenziok, R., Hansen, U., and Knunster, H., 2001, "Combustion of Biooil in a Gas Turbine," *Progress in Thermochemical Biomass Conversion*, A. V. Bridgwater, ed., Blackwell Science, Oxford, pp. 1452–1458.

[13] Bertoli, C., D'Alessio, J., Del Giacomo, N., Lazzaro, M., Massoli, P., and Moccia, V., 2000, "Running Light-Duty DI Diesel Engines With Wood Pyrolysis Oil," SAE Paper No. 200-01-2975.

[14] Lupandin, V., Thamburaj, R., and Nikolayev, A., 2006, "Test Results of the OGT2500 Gas Turbine Engine Running on Alternative Fuels: Biooil, Ethanol, Biodiesel, and Crude Oil," ASME Paper No. GT2005-68488.

[15] Chiaramonti, D., Oasmaa, A., and Solantausta, Y., 2006, "Fast Pyrolysis Oil for Power Generation," ASME Paper No. GT2006-90245.

[16] Ikura, M., Stanciulescu, M., and Hogan, E., 2003, "Emulsification of Pyrolysis Oil Derived Biooil in Diesel Fuel," Biomass Bioenergy, **24**, pp. 221–232.

[17] Gardner, J. M., Biodiesel Fuel Quality Study, http://www.biodiesel.org/resources/reportsdatabase/reports/gen/19951229_gen-227.pdf.

Study of Diesel Jet Variability Using Single-Shot X-Ray Radiography

A. L. Kastengren[1]
e-mail: akastengren@anl.gov

C. F. Powell

Center for Transportation Research,
Argonne National Laboratory,
9700 S. Cass Avenue, Argonne, IL 60439

Y.-J. Wang

J. Wang

Advanced Photon Source,
Argonne National Laboratory,
9700 S. Cass Avenue,
Argonne, IL 60439

*The variability of diesel jet structure, both as a function of time and between individual injection events, has important implications on the breakup and mixing of the jet. It is accepted that diesel jets become unstable due to interactions with the ambient gas, leading to breakup of the jet. This concept is the principle behind the Kelvin–Helmholtz and Rayleigh–Taylor models of diesel atomization. Very little information regarding diesel jet variability is available, however, in the near-nozzle region of the diesel jet, where primary breakup of the jet occurs. This is due to the presence of many small droplets, which strongly scatter visible light and render the spray opaque. X-ray radiography has been successfully used in recent years to probe the structure of diesel sprays with high spatial and temporal resolutions. All of these previous measurements, however, were ensemble averaged, measuring only persistent features of the spray. In the current study, measurements are performed at individual measurement points of single diesel injection events. These measurements are taken at several points near the injector exit for a nonhydroground nozzle with a single axial hole at two injection pressures (*500 bars *and* 1000 bars*). The variability of the start of injection, end of injection, and the time history of the spray density during the injection event are examined, as well as how these quantities change for different transverse positions across the jet.*
[DOI: 10.1115/1.2830861]

Introduction

A key to improving the performance and emissions from diesel engines is an understanding of the spray used to introduce fuel into the engine cylinder. For example, it is well accepted that the timing of the injection event influences the trade-off between soot and NO_x emissions. Moreover, in recent years manufacturers of diesel injection equipment have pursued the use of higher injection pressure and smaller injection holes to achieve better fuel atomization.

For this reason, a great deal of research has been conducted on the behavior of diesel sprays. Unfortunately, while many studies of the penetration speed [1,2] and cone angle [2–4] of sprays have been performed, more detailed information regarding the internal structure of sprays, especially in the near-nozzle region, has been less forthcoming. This dearth of near-nozzle data is due to the dense field of droplets surrounding the spray. These droplets strongly scattering incoming light, making quantitative determinations of spray structure with optical diagnostics problematic.

In contrast, X-ray radiography has been successfully used to examine the internal structure of sprays, even in the dense near-nozzle region. These measurements have been performed on both diesel and gasoline direct injection sprays [5]. Many spray parameters have been analyzed, including penetration speed [6], cone angle, spray density [7], and liquid axial velocity [8]. These studies have yielded important insights regarding the internal structure of these sprays.

Past X-ray radiography measurements, however, have consisted entirely of ensemble-averaged measurements. There are two disadvantages to this property of the measurements. First, shot-to-shot variations in the spray behavior will smear the ensemble-averaged data, especially in regions of highly transient features, such as the leading and trailing edges of the spray. Moreover, ensemble-averaged measurements cannot quantify the extent of the shot-to-shot variations in the spray behavior.

This paper will describe single-shot spray density measurements of two diesel injector sprays using X-ray radiography. The differences between the ensemble-averaged behavior and the behavior of individual shots will be described. The variability of the leading and trailing edges of the spray events will be quantified. Finally, autocorrelations will be performed to determine whether there are preferred time scales in the X-ray absorption in the near-nozzle region.

Experimental Method

The sprays studied in this work were created by a Bosch light-duty diesel common rail injector. The spray was emitted from an axial single-hole minisac nozzle with a diameter of 208 μm and an L/D ratio of 4.7. Two injection events were measured. For the first injection event, the commanded injection duration was 1000 μs, with an injection pressure of 500 bars. For the second injection event, the injection pressure was 1000 bars, with a commanded injection duration of 1000 μs. For both injection events, the spray was emitted into a quiescent vessel filled with N_2 at 5 bar pressure at approximately 25 °C.

The sprays were measured using X-ray radiography. The X-ray radiography technique has been described in detail previously [9]; thus, only a brief description will be given in this work. In the radiography technique, a narrow beam of monochromatic X-rays passes through the spray, which is contained in an especially designed spray chamber with X-ray transparent windows. In general, the X-ray absorption is a strong function of the photon energy of the X-rays. Since simultaneous time- and energy-resolved X-ray intensity measurements are not currently feasible, this dependence would make the determination of spray density problematic. By using a monochromatic beam, the energy dependence becomes irrelevant. The projected density of the fuel M, in mass per unit area of the beam, can be related to the X-ray intensity with and

[1]Corresponding author.

Contributed by the Internal Combustion Engine Division of ASME for publication in the JOURNAL OF ENGINEERING FOR GAS TURBINES AND POWER. Manuscript received October 19, 2007; final manuscript received October 22, 2007; published online April 3, 2008. Review conducted by Dilip R. Ballal.

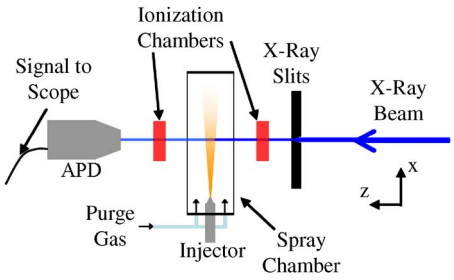

Fig. 1 Experimental setup

without spray present (I and I_0, respectively) and the X-ray absorption coefficient of the fuel (μ) according to the formula:

$$I = I_0 e^{-\mu M} \tag{1}$$

This formula represents a simple application of linear absorption.

The X-ray beam is produced at the 1-BM beamline at the Advanced Photon Source at Argonne National Laboratory. The beam passes through a monochromator and a series of X-ray optics to create a tightly focused, collimated, monochromatic beam. The photon energy of the X-rays is 8 keV. A pair of X-ray slits is used to allow only a small region of the collimated beam to pass through the spray. The beam size used in these experiments was 100 μm full width at half maximum (FWHM) in the axial spray direction and 36 μm FWHM transverse to the spray axis.

The beam then passes through a pressurized spray chamber with especially designed X-ray transparent windows. The steady-state beam intensity is monitored nonintrusively using ionization chambers. The time-varying intensity of the transmitted beam is recorded using an avalanche photodiode (APD) detector. The voltage from the APD detector is sampled at 1 GHz using a Yokogawa DL7480 500 MHz digital oscilloscope with 8 bit resolution. The experimental setup is depicted in Fig. 1.

Once the raw data have been recorded, the data are processed using Eq. (1) and binned, with a time step in the final data of 1.84 μs.

The current radiography technique is by its nature a pointwise measurement technique, providing path-length-integrated data regarding the liquid density in the spray for a single beam path through the spray. To obtain data for various areas of the spray, the spray chamber is moved to several different positions, with measurements taken at each position. In past radiography measurements, several spray events were averaged to provide ensemble-averaged data at each measurement location. In the current measurements, 32 individual spray events are recorded separately at each measurement position. This allows the shot-to-shot variations of the spray to be measured, rather than merely the ensemble-averaged spray behavior.

Three sets of measurements were performed in this study. The base line measurements were taken 0.2 mm downstream of the exit plane of the nozzle, at 500 bar injection pressure. Data were taken at 21 positions from −0.15 mm to 0.15 mm transverse from the nozzle axis, with a spacing between data points of 15 μm. Data were also taken for this injection condition 2.0 mm from the nozzle to examine how the shot-to-shot variations change as the spray breaks up. In this case, data were taken at 21 positions from −0.4 mm to 0.4 mm from the nozzle axis in 40 μm steps. Finally, data were taken 0.2 mm from the nozzle at 1000 bar injection pressure to examine how a higher injection pressure affects the shot-to-shot variations. Data were taken in the transverse direction from −0.15 mm to 0.15 mm from the nozzle in 15 μm steps. The measurement positions are shown in Fig. 2.

Once the raw data have been recorded, the data are processed and binned, providing x-ray intensity data in arbitrary units with a time step of 1.84 μs. To convert this record into transmission, regions at the beginning and end of the data record, when there is no X-ray absorption from the spray, are used to define the base line X-ray intensity. These data of X-ray transmission versus time are then converted to projected mass using Eq. (1).

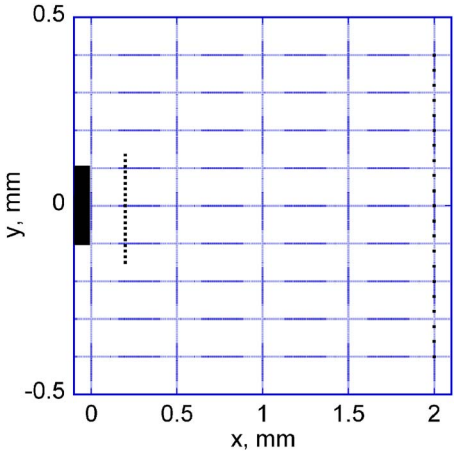

Fig. 2 Measurement positions. The injector orifice diameter and exit plane are shown with the dark box on the left edge of the plot.

Results

Figure 3 shows the averaged projected density versus time data for a position near the center of the nozzle exit ((x,y) $=(0.2\text{ mm}, 0\text{ mm})$) for the 500 bar injection pressure case. It is easily seen that the projected density is zero before the spray event and then suddenly rises to a nearly constant, high value during the spray event. As the injector closes, the projected density drops, though not as suddenly as it increased at the start of injection. There is also a small bump in the data near 1820 μs after commanded SOI. This suggests that perhaps there is a minor bounce in the needle as the injector closes.

The behavior of the projected density for the individual injection events, which make up the ensemble-averaged data shown in Fig. 3, can provide further insights regarding the spray behavior. Figure 4 shows the projected density versus time for four of the 32 individual injection events used to create the data in Fig. 3 near the apparent end of injection. As the projected density begins to decline at the end of the injection event, the behavior for all four injection events is approximately the same, with little jitter. However, many of the injection events show significant pulses of mass after the projected density reaches quite low values. For example, while the top left and bottom right plots do not display this be-

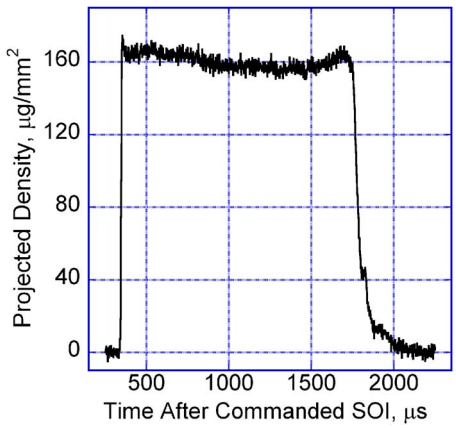

Fig. 3 Ensemble-averaged projected density versus time data for x=0.2 mm, y=0 mm, 500 bar injection pressure

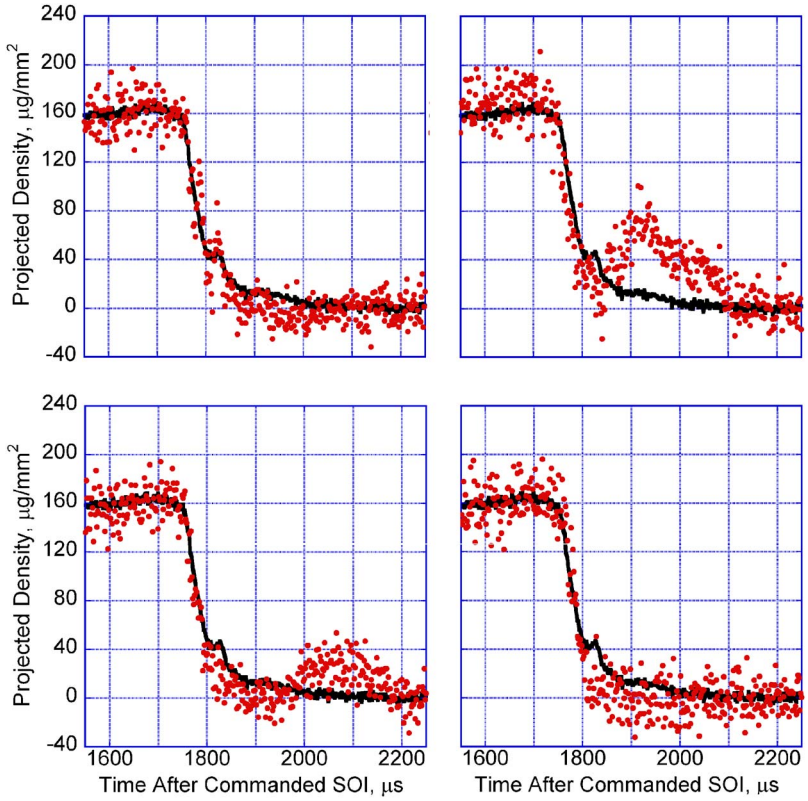

Fig. 4 End-of-injection behavior for four injection events at x=0.2 mm, y=0, 500 bar injection pressure. The ensemble-averaged behavior is shown by the solid line.

havior, the top right plot demonstrates a prominent pulse centered around 1900–2000 μs after SOI. The bottom left plot, on the other hand, displays a less prominent pulse centered around 2100 μs after SOI. Indeed, if one examines the average data alongside the data from individual injection events, the average data seem to decline less steeply as the projected density reaches zero than do the data from the individual injection events; this seems likely to be caused by the pulses of mass seen in some injection events. While the ensemble-averaged data provide a wealth of insight about the spray behavior, their fidelity is limited by shot-to-shot spray variations, especially near the end of the injection event.

Figure 4 also shows the degree of noise in the measurements of individual injection events compared to the ensemble-averaged data. The standard deviation in the projected density at each time step ranges from 10 μg to 20 μg/mm^2. The variability is higher at positions with higher levels of projected density; the authors believe that this additional degree of noise is due to the reduced X-ray intensity for these positions. The noise level is significant, especially in regions of low projected density, such as near the edge of the spray. However, interesting comparisons between different positions and injection conditions can still be made.

Similar data for the same four individual injection events near the start of injection are shown in Fig. 5. The data show that, like the ensemble-averaged data, the projected density rises quite rapidly for the individual injection events from zero to the full steady-state value. There also appears to be very little jitter in the timing of the start of injection, indicating that the ensemble-averaged data indeed give a good representation of the start-of-injection behavior of this spray.

The spray behavior is somewhat different at more downstream locations. Figure 6 shows example individual measurements and the ensemble-averaged result near the start of injection for 500 bar injection pressure at $(x,y)=(2.0\text{ mm},-0.08\text{ mm})$. This point is at the approximate center of the spray plume due to imperfect spray targeting. The average data show an initial maximum, with projected density levels higher than those seen near the nozzle exit. The projected density quickly decreases by over 50%, reaching a minimum approximately 90 μs after fuel first arrives at this position. The projected density then increases to a steady-state value. Even though this behavior is more complex than that shown in Figs. 3 and 5, the individual measurements show a remarkable similarity to the average behavior. This indicates that these features in the averaged data are indeed representative not only of the ensemble-averaged behavior but also of the behavior of individual spray events.

The end-of-injection behavior is also different at more downstream locations than near the nozzle. As shown in Fig. 7, the projected density for the individual measurements tends to closely track the ensemble-averaged behavior. Occasional pulses of mass are observed, such as that seen in the lower left plot approximately 1900 μs after commanded SOI. However, these pulses of mass are less common and have lower peak projected density values than was seen for positions near the nozzle. A potential reason for the lack of mass pulses at this position is that these pulses may move so slowly that they have not reached the measurement position by the end of the data record.

Additional interesting behavior can be seen at higher injection pressure. Figure 8 shows the individual event and ensemble-averaged end-of-injection behavior for 1000 bar injection pressure at $(x,y)=(0.2\text{ mm},0\text{ mm})$. There is a much more prominent bump in the averaged data near 1800 μs after commanded SOI. More importantly, there is much less shot-to-shot variation in the needle bounce behavior. While some events, such as that shown in the lower right plot, showed no significant pulse of mass during the decline at the end of injection, the majority of events did. These pulses were largely centered around 1800 μs after commanded

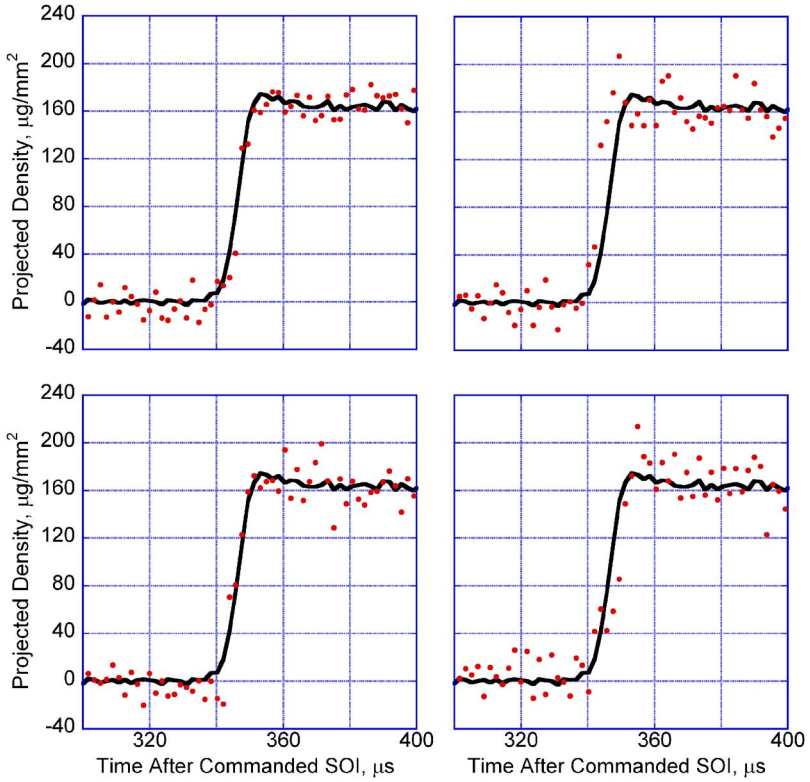

Fig. 5 Start of injection behavior for four injection events at $x=0.2$ mm, $y=0$ mm, 500 bar injection pressure. The ensemble-averaged behavior is shown by the solid line.

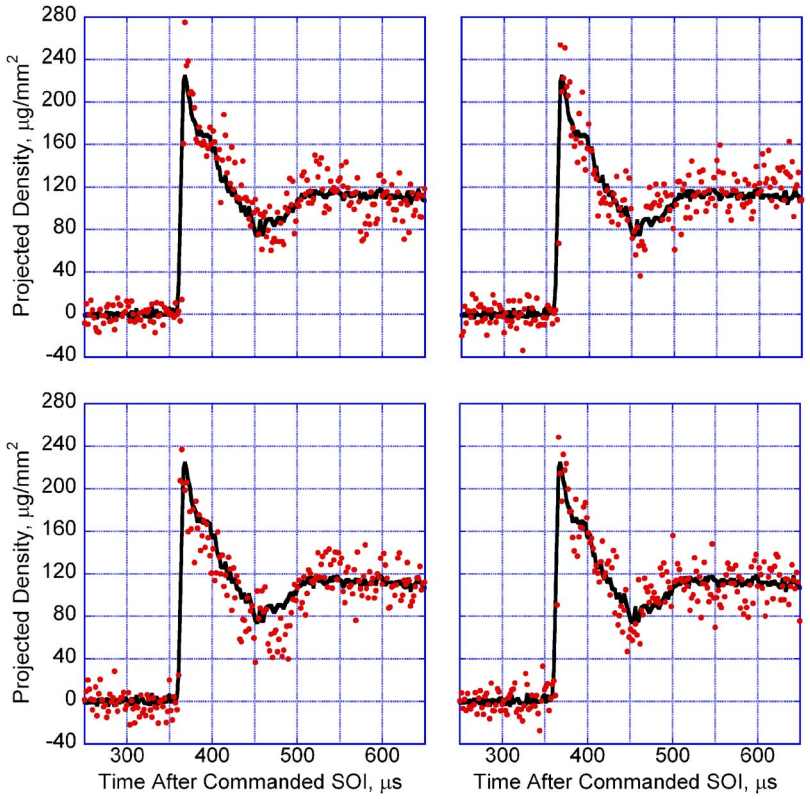

Fig. 6 Start of injection behavior for four injection events at $x=2.0$ mm, $y=-0.08$ mm, 500 bar injection pressure. The ensemble-averaged behavior is shown by the solid line.

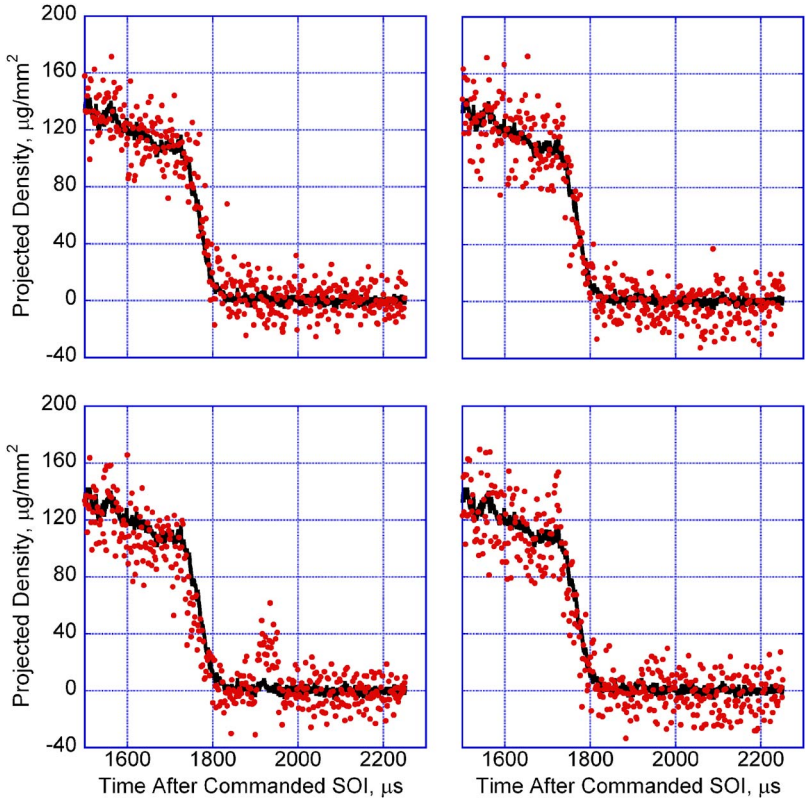

Fig. 7 End-of-injection behavior for four injection events at x=2.0 mm, y=−0.08 mm, 500 bar injection pressure. The ensemble-averaged behavior is shown by the solid line.

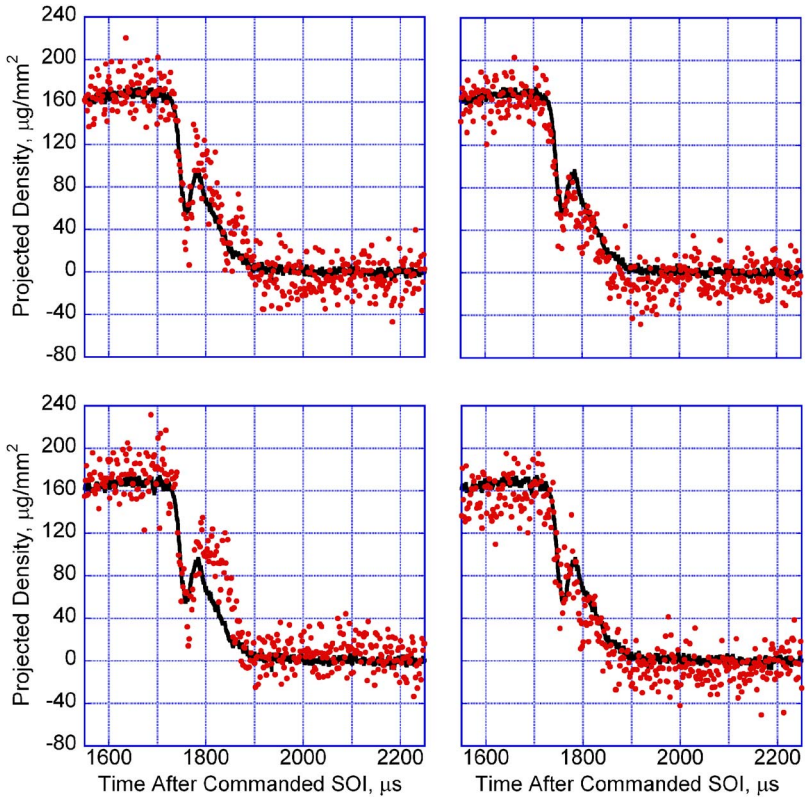

Fig. 8 End-of-injection behavior for four injection events at x=0.2 mm, y=0 mm, 1000 bar injection pressure. The ensemble-averaged behavior is shown by the solid line.

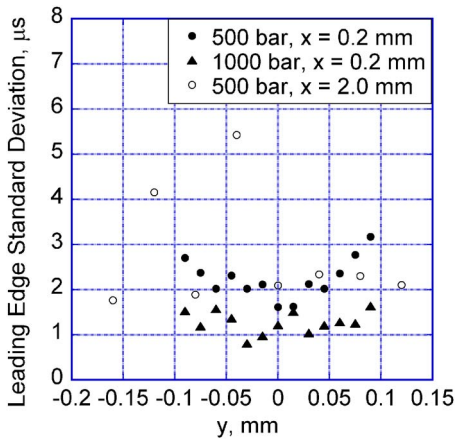

Fig. 9 Variability in the time at which the leading edge passes through radiography measurement locations

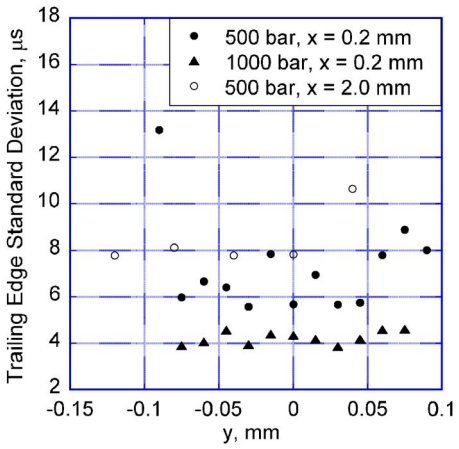

Fig. 10 Variability in the time at which the trailing edge passes through radiography measurement locations

SOI, with few if any mass pulses seen at later times. This seems to indicate that the injector performance at the end of the injection event is more consistent at this higher injection pressure than at 500 bar injection pressure.

Two distinct advantages of the radiography technique are its high temporal resolution and the quantitative nature of its results. These advantages can be used with the current data to find the variability of the time at which the leading edge passes by the radiography measurement locations. To determine the leading edge position, the average projected mass during the steady-state portion of the spray is found. The time at which the projected density increases past 50% of this value is considered the time at which the leading edge passes through a location. To prevent spurious noise spikes from being detected with the thresholding technique, the data are Gaussian filtered before this procedure is performed

The resulting data are shown in Fig. 9. The values plotted are the standard deviation in the timing of the passage of the leading edge at various positions. Several trends can be noted. First, the variability is quite small; the standard deviation is less than 6 μs for all positions measured. The variability in the leading edge timing appears to increase as one nears the edge of the jet for the measurements at $x=0.2$ mm. The variability is also significantly less at higher injection pressure. Finally, the variability is not as consistent at larger axial distances from the nozzle, perhaps due to the higher degree of noise in these data compared to the data nearer the nozzle exit.

This analysis can also be used to find the variability of the trailing edge. This is a capability which optical measurements lack due to the obscuring effect of spray droplets. The results of this analysis are shown in Fig. 10. A few trends are clear. First, the variability in the timing of the passage of the trailing edge is reduced at higher injection pressure. The variability of the trailing edge also appears to be less near the nozzle than further downstream. The uncertainty is also greater at all positions than the uncertainty in the leading edge timing. However, the degree of variability shown in Fig. 10 is still quite small compared to typical engine flow time scales. These data do not reflect the presence of the mass pulses shown in Figs. 4 and 7. It appears, however, that the uncertainty of the main end-of-injection event is quite small.

Another analysis of these single-shot data is to examine the temporal structure of the data. For example, if the cavitation region in the orifice were to pulsate with a preferred frequency, such fluctuations would have important implications regarding the breakup process. To determine the important time scales in the data, an autocorrelation analysis is performed on the central steady-state portion of the data record. The autocorrelation is computed using the procedure given in Bendat and Piersol [10]. The data record is split into a series of short segments, each of which is autocorrelated, and the autocorrelations are averaged together to create an average depiction of the autocorrelation coefficient.

Example results for the autocorrelation are shown in Fig. 11. These data are for $(x,y)=(0.2\text{ mm},0\text{ mm})$ at 1000 bar injection pressure for time steps from 532 μs to 1208 μs after SOI, which appear to be during the steady-state part of the injection event. As the plot shows, the correlation is virtually zero, except at zero time delay, which has a correlation coefficient of 1 by definition. Analyses at other positions and at 500 bar injection pressure show the same results. In short, the time variation in the radiography data during the steady-state portion of the injection event appears to be random.

There are two possible reasons that the autocorrelation is near zero for all time delays other than zero. The first is that there simply may not be large temporal variations in the spray density during the steady-state portion of the injection event. The time variations in the X-ray data would then be dominated by electronic or photon shot noise, which would be expected to give an autocorrelation curve similar to that shown in Fig. 11. The second possible cause for the shape of Fig. 11 is that variations in the spray density could predominantly occur at shorter time scales than can be measured with the current experimental method. For example, the FWHM size of the X-ray beam in the axial direction is 100 μm. If the fluid in the jet moves at the Bernoulli velocity

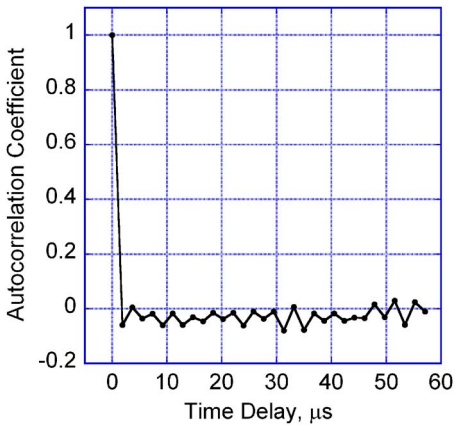

Fig. 11 Average autocorrelation coefficient versus time delay for the central region of the 1000 μs spray at $x=0.2$ mm, $y=0$ mm

for 1000 bar injection pressure (482 m/s), a parcel of fluid will cross the X-ray beam in approximately 200 ns, which is far shorter than the time scales examined in this analysis. Regardless of the cause, these data clearly show that the jet behavior lacks time scales of motion of greater than 2 μs.

Discussion

Noise in the current data seriously limits the conclusions which can be drawn regarding the shot-to-shot variations in spray behavior. While the current degree of noise corresponds to a standard deviation of only 2–4% in the measured X-ray transmission, this corresponds to a degree of noise of 6–12% in projected mass after the application of Eq. (1). A lower degree of noise would allow for more quantitative comparisons to be made between individual injection events. This may be accomplished in the future through the use of improved detectors with less electronic noise and higher X-ray intensity, which would reduce photon shot noise in the measurements.

These data show that, in most respects, the standard ensemble-averaged radiography technique performs well in describing the behavior of individual spray events. For example, the leading edge variability is quite minor, at least in the near-nozzle region studied in this work. The projected density for the steady-state part of the spray event is remarkably similar from shot to shot. The one exception to this good agreement is at the trailing edge, particularly at 500 bar injection pressure. This lends firm support to the applicability of previous X-ray radiography measurements of diesel sprays, which have all been ensemble averaged.

Conclusions

X-ray radiography has been used to quantitatively measure the near-nozzle structure of diesel sprays at 500 bar and 1000 bar injection pressures. X-ray radiography uses the measurement of X-ray absorption through a spray to quantitatively determine the spray mass distribution, in contrast to optical measurement techniques, which often yield qualitative data. Moreover, the X-ray technique is applicable in dense regions of the spray, which are quite difficult to probe with optical techniques due to strong light scattering by spray droplets. Unlike previous radiography measurements, which have all been ensemble averaged, the projected density versus time was recorded for many individual injection events for several positions across the spray. Several conclusions can be drawn from the data.

- Little variability was found in the behavior of the leading edge of the spray for both injection pressures and for two different axial distances at 500 bar injection pressure.
- More variability was found in the timing of the trailing edge of the spray than in the leading edge, though this degree of uncertainty was still smaller than most important engine flow time scales.
- The spray at 500 bar injection pressure showed more variability, both in the leading and trailing edge behaviors, than the spray at 1000 bar injection pressure. This spray also exhibited pulses of mass after the apparent end of injection when examined near the nozzle, suggesting possible needle bounce events. These effects are much less noticeable farther downstream and at higher injection pressure.
- Autocorrelation analysis indicates that there were no dominant time scales of projected density variations of greater than 2 μs, indicating that there were no long time scale variations in the spray that were evident in the radiography data.
- Overall, the data show that ensemble-averaged measurements using X-ray radiography capture most of the same gross flowfield features as measurements of individual spray events.

Acknowledgment

This research was performed at the 1-BM-C beamline of the Advanced Photon Source, Argonne National Laboratory. This work and the use of the APS are supported by the U. S. Department of Energy under Contract No. DE-AC02-06CH11357 and by the Department of Energy FreedomCAR & Vehicle Technologies Program, with Gurpreet Singh as a program manager.

Nomenclature

I = X-ray intensity during the spray event
I_0 = X-ray intensity before the spray event
M = projected density in $\mu g/mm^2$
SOI = start of injection; refers to commanded start of injection unless otherwise indicated
x = axial distance from nozzle exit, mm
y = transverse distance from nozzle exit, mm
μ = X-ray absorption coefficient, $mm^2/\mu g$

References

[1] Desantes, J. M., Payri, R., Salvador, F. J., and Gil, A., 2006, "Development and Validatioan of a Theoretical Model for Diesel Spray Penetration," Fuel, **85**(7–8), pp. 910–917.
[2] Naber, J., and Siebers, D., 1996, "Effects of Gas Density and Vaporization on Penetration and Dispersion of Diesel Sprays," SAE Paper No. 960034.
[3] Lai, M.-C., Wang, T.-C., Xie, X., Han, J.-S., Henein, N., Schwarz, E., and Bryzik, W., 1998, "Microscopic Characterization of Diesel Sprays at VCO Nozzle Exit," SAE Paper No. 982542.
[4] Blessing, M., König, G., Krüger, C., Michels, U., and Schwarz, V., 2003, "Analysis of Flow and Cavitation Phenomena in Diesel Injection Nozzles and Its Effects on Spray and Mixture Formation," SAE Paper No. 2003-01-1358.
[5] Cai, W., Powell, C. F., Yue, Y., Narayanan, S., Wang, J., Tate, M., Renzi, M., Ercan, A., Fontes, E., and Gruner, S., 2003, "Quantitative Analysis of Highly Transient Fuel Sprays by Time-Resolved X-Radiography," Appl. Phys. Lett., **83**(8), pp. 1671–1673.
[6] Cheong, S.-K., Liu, J., Shu, D., Wang, J., and Powell, C. F., 2004, "Effects of Ambient Pressure on Dynamics of Near-Nozzle Diesel Sprays Studied by Ultrafast X-Radiography," SAE Paper No. 2004–01-2026.
[7] Powell, C. F., Ciatti, S., Cheong, S.-K., Liu, J., and Wang, J., 2004, "X-Ray Absorption Measurement of Diesel Sprays and the Effect of Nozzle Geometry," SAE Paper No. 2004-01-2011.
[8] Kastengren, A., Powell, C. F., Riedel, T., Cheong, S.-K., Wang, Y.-J., Im, K.-S., Liu, X., and Wang, J., 2007, "Determination of Diesel Spray Axial Velocity Using X-Ray Radiography," SAE Paper No. 2007-01-0666.
[9] Kastengren, A., and Powell, C. F., 2007, "Spray Density Measurements Using X-Ray Radiography," Proc. Inst. Mech. Eng., Part D (J. Automob. Eng.), **221**(16), pp. 653–662.
[10] Bendat, J., and Piersol, A., 2000, *Random Data Analysis and Measurement Procedures*, Wiley, New York.

Cold Engine Transient Fuel Control Experiments in a Port Fuel Injected CFR Engine

Leonard J. Hamilton
Mechanical Engineering Department,
United States Naval Academy,
590 Holloway Road,
Annapolis, MD 21402
e-mail: ljhamilt@usna.edu

Jim S. Cowart
Mechanical Engineering Department,
United States Naval Academy,
590 Holloway Road,
Annapolis, MD 21402
e-mail: cowart@usna.edu

Air-fuel mixture preparation is particularly challenging during cold engine throttle transients due to poor fuel vaporization and transport delays in port fuel injected (PFI) engines. In this study, a PFI cooperative fuels research engine is used to evaluate torque and to measure in-cylinder and exhaust CO, CO_2, and unburned hydrocarbons during throttle transients at various early stages of engine warmup. Fast flame ionization detectors and nondispersive infrared fast CO and CO_2 detectors are used to provide a detailed cycle-by-cycle analysis. Ttorque after cold throttle transients is found to be comparable to steady-state torque due to allowable spark advance. However, cold transients produce up to four times the unburned hydrocarbons when compared to steady-state operation. Finally, the x-tau fuel control model is evaluated in this challenging operating regime and is found to provide poor transient fuel control due to excessive fueling.
[DOI: 10.1115/1.2830865]

Keywords: mixture preparation, transient fuel control, port fuel injection

Introduction

Intake port fuel injection (PFI) spark ignition (SI) gasoline engines continue to be one of the most cost effective approaches to provide economical yet precise injected fuel control for strict engine emissions and efficiency objectives. Yet, one of the challenges with PFI fuel delivery can be the transport delay of the fuel from the intake port into the engine's cylinders. Fuel "puddling" can occur in the intake port, and these puddle dynamics change as the engine warms up and also as loads and engine speeds change. Thus, overfueling, fueling beyond that expected for a stoichiometric charge of fuel, is frequently necessary in order to account for fuel delays in the intake port as well as for incomplete fuel vaporization with a cold engine and during transient operation. The transient throttle regime is one area in which excess fuel is needed during engine acceleration to overcome intake port fueling delays. Accelerator pumps on carburetors in the past provided this feature. Today, computer controlled fuel injection algorithms do the job. Much excellent work has been done to characterize stabilized engine transient fuel control requirements; however, very little has been done to understand cold engine throttle transients.

Cold engine PFI throttle transients can be very difficult to manage and control due to the combined physical effects of poor fuel vaporization combined with intake port puddle delays. Thus, mixture preparation is a particularly significant challenge during throttle actions while the engine is warming up. Cold engine throttle transients are not uncommon. Many drivers are able to get their engines started and accelerate within seconds after engine startup. From the regulatory perspective, the Federal Test Procedure has a drive away 20 s after engine startup. The engine has had very little opportunity to warm up and thus very little opportunity to heat engine surfaces to aid in the vaporization of intake port injected fuel. Fuel control during throttle opening immediately after start is thus challenging.

Surprisingly, very little published work has been presented on cold engine throttle transients. Some early throttle body injection (TBI)—also called central fuel injection, one or two large fuel injectors that replaced the conventional carburetor—work by Acquino [1] showed significant combustion lean excursions during throttle openings without extra fuel compensation during the throttle transients and, thus, the need for extra fuel enrichment due to manifold wall wetting and poor mixture preparation during engine warmup. Cold engine throttle transients were shown to generate the greatest lean combustion excursions. In addition to performing throttle transients as the engine warmed up, Acquino also looked at the effects of injection timing and various (overall slow) throttle ramp rates. This paper was also one of the earliest presentations of the popular *x*-tau model for controlling transient throttle fueling. The principal diagnostic for this work was a wide range universal exhaust gas oxygen (UEGO) sensor.

A few years later, Fozo and Acquino [2] studied PFI engine throttle transients during engine warmup. Not surprisingly, greater enrichment was required during the throttle transient for colder engine coolant temperature (ECT) values. They also showed the importance of injection timing (closed versus open intake valve injection timing) and injector details on the transient fueling behavior. This work was also UEGO based for determining in-cylinder charge air-fuel ratio (AFR) characteristics.

More recently, Shayler et al. [3] also used UEGO data to characterize cold engine throttle transients as the engine was warming up. Their first throttle transient occurred after the cold engine "stabilized" approximately 30–40 s after startup. Their study showed both *x* (the fraction of injected fuel that goes into the intake port puddle) and tau (time constant related to intake port puddle vaporization) to be very important at the coldest of engine conditions. Additionally, tau was found to have the greatest temperature related effect.

Fast in-cylinder diagnostics have been used by Cowart and Cheng [4] to characterize in-cylinder fueling behavior without the transport and sensor delays inherent with UEGOs. They showed that for a given engine operating condition, fixed *x* and tau values worked well for transient fuel compensation regardless of the throttle rate.

In the above work that looked at throttle transients during warm-up, all of the *x* and tau characterizations were done at various ECTs as the engine warmed up. The time scale after engine startup for these throttle transients is on the order of a few minutes to several minutes since the large thermal mass of the engine and coolant has a warmup period of 10 min or more. While these

Contributed by the Internal Combustion Engine Division of ASME for publication in the JOURNAL OF ENGINEERING FOR GAS TURBINES AND POWER. Manuscript received October 30, 2007; final manuscript received November 5, 2007; published online April 3, 2008. Review conducted by Dilip R. Ballal.

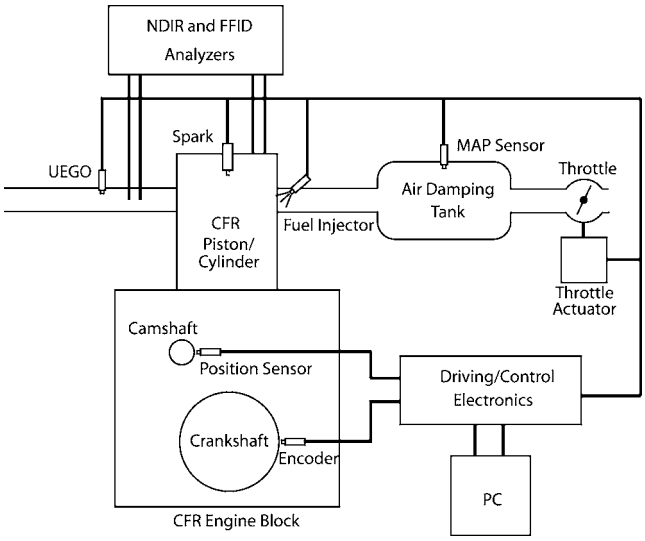

Fig. 1 Experimental apparatus schematic

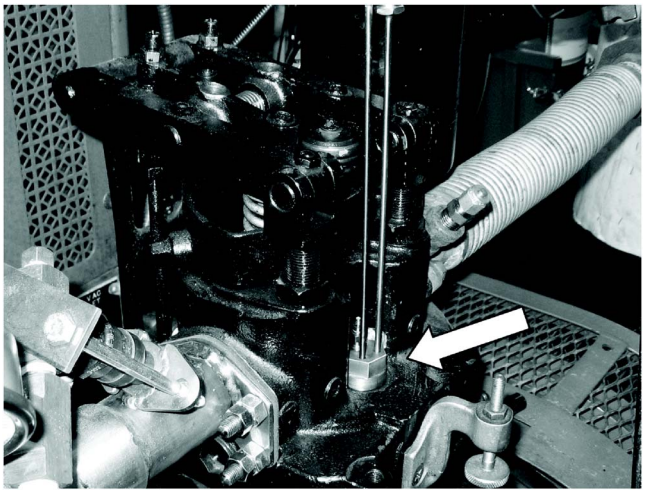

Fig. 2 Probe configuration in the CFR cylinder head

transients are challenging, they are not as difficult to manage as throttle transients immediately after engine startup since the engine is still in the process of stabilizing from the mixture preparation perspective. Thus, to these authors' knowledge, no published research work has examined fast throttle transients during the first minute of engine operation before the ECT has really started to rise. Additionally, in-cylinder diagnostics for such cold transients have not been investigated.

Thus, the objectives of this study are to investigate cold engine throttle transients that occur shortly after engine startup from the performance and emissions perspective. The questions that are to be investigated include the following: How do the emissions and performance of cold engine throttle transients compare to similar stabilized engine steady-state (SS) throttle transients? Also, is the *x*-tau model characterization a valid approach for these cold engine transients?

Experimental Apparatus

The engine used in this study is a cooperative fuels research (CFR) variable compression ratio (CR) gasoline engine. In this study, CR=9 was used. This engine was originally designed for research method octane (RON) testing and motoring method octane (MON) testing. The CFR unit contains a motor-generator for maintaining the engine at a constant of 900 rpm during SS operation. The CFR engine valve train is standard with timings of intake valve opening (IVO) (0.25 mm lift)=10 deg after top center (ATC), intake valve closing (IVC)=34 deg after valve center (ABC), exhaust valve opening (EVO)=40 deg before bottom center (BBC), and exhaust valve closing (EVC)=15 deg ATC. The engine coolant for each engine startup (one start per day) was stable with the laboratory at $20\,^{\circ}\mathrm{C} \pm 1\,^{\circ}\mathrm{C}$.

The original CFR carburetor and ignition system were removed and replaced with a conventional automotive coil and a production Ford™ four-hole fuel injector. This injector was calibrated using pure iso-octane fuel and collecting 1000 injection "shots" into a closed graduated cylinder at various fuel pulse widths. A new intake manifold was constructed using a 30 mm diameter pipe containing a fuel injector port (directed at the intake valve), a 3.7 l transient damping tank, and a throttle. A schematic of the experimental apparatus is shown in Fig. 1.

The fuel injector, ignition coil, and throttle were all controlled by a custom engine controller with associated high power switching electronics external to the PC. The PC was equipped with a Cyber Research™ CYDAS1600 A/D card that interfaces with C code run on the PC. A BEI™ shaft encoder and an optical cam encoder were used by the PC for crank angle degree resolved engine position control. The engine was equipped with an automotive manifold absolute pressure (MAP) sensor on the intake damping tank as well as a UEGO sensor in the exhaust.

Cambustion™ fast flame ionization detectors (FFID) (unit: HFR500) and nondispersive infrared (NDIR) (unit: NDIR500) fast CO and CO_2 detectors were used as the principal diagnostics. Each cambustion™ unit has two sample heads, one for the in-cylinder measurement and one for the exhaust measurement. Each NDIR unit alternates measuring CO_2 and then CO continuously throughout the engine cycle. The Cambustion™ exhaust probes were located in the exhaust manifold just a few centimeters from the CFR cylinder head. The Cambustion™ in-cylinder probes were located in a custom CFR engine plug that replaces the conventional large CFR pressure transducer. This custom plug (located in the "end-gas" region of the engine across from the spark plug) contained both 5 mm (outside diameter) sample probes and a mounting hole for the in-cylinder Kistler™ 6125B noncooled pressure transducer, as shown in Fig. 2.

All of the data were collected on a separate NI™ LABVIEW data acquisition system using crank angle degree pulses from the BEI™ shaft encoder on the engine crankshaft. It is important to note that the exhaust sample is likely to be well mixed as this location is approximately 15 cm downstream of the exhaust valve. The in-cylinder measurements (both FFID and NDIR: CO and CO_2) are local to the end-gas region; however, during the region of the engine cycle at which the data are extracted, the signals are relatively stable, which suggests a relatively homogeneous in-cylinder mixture. The benefit of the in-cylinder signal is that due to the fast response of the Cambustion™ units coupled with the low engine speeds in this study, intracycle information can be obtained, as will be discussed shortly.

Calibration of the Cambustion™ FFID and NDIR units was performed before each engine start up with the Cambustion™ calibration sampling probe attachments. These attachments allow in situ calibration for the exhaust probes by flooding the sample probe inlets with calibration gases. The in-cylinder sampling heads were calibrated outside of the engine cylinder immediately before the engine startup test. Bottled zero and calibration gases were used and specified in the Appendix.

A characteristic engine cycle with all of the key measured signals is shown in Fig. 3. Each of these displayed signals will be discussed next. Not shown are the crank angle degree pulses and bottom center compression (BCC) pulses used for data triggering and cycle reference. It is also important to note that the fuel pulse

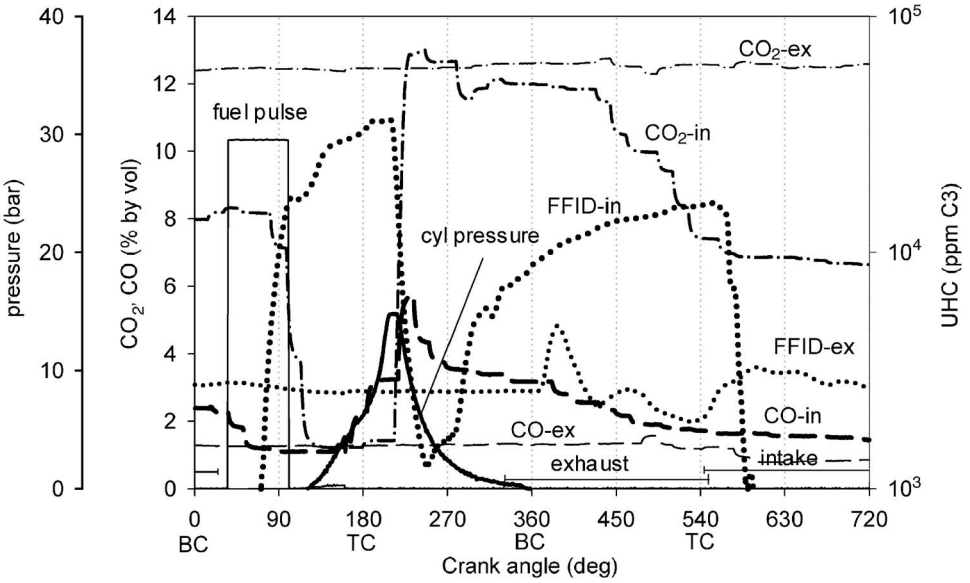

Fig. 3 Representative engine cycle with simultaneous diagnostic signals

is shown during the compression stroke. Since this fuel is injected into the intake port, this fuel will not be inducted until the following IVO period.

Fuel pulse. The fuel pulse was commanded to occur shortly after the Intake Valve Closed (IVC). This early Closed Valve Injection (CVI) timing was chosen to maximize fuel vaporization real time. Injection during IVO was specifically avoided to prevent "bore-washing" and excessive unburned hydrocarbons (UHCs) in the exhaust. The fuel calibration on a cycle-by-cycle basis will be described shortly.

Fast flame ionization detector in-cylinder (FFID-in). Two important pieces of information come from this continuous measurement. The FFID-in fuel vapor concentration plateau peaks ~210 cadeg (=30 deg ATC) just before the main combustion event consumes the fuel-air charge in the end gas. This signal can be used to determine the local AFR just before flame arrival [5]. A second useful measurement from this signal occurs during the expansion and exhaust stroke. Post combustion fuel vapor evolution occurs during the expansion and exhaust strokes of the engine. Evidence of post combustion UHC evolution was seen and quantified recently by the authors in another paper [7]. Data from using the FFID-in during this portion of the cycle can provide some interesting insights into the UHC generation phasing.

CO_2 in-cylinder (CO_2-in). Two important pieces of information also come from the CO_2-in signal. The CO_2-in signal shows a minimum value during the later half of the compression stoke up to just past TC. This signal "valley" will be used for residual fraction determination on the current engine cycle. In order to obtain the current cycle's residual fraction, this minimum CO_2-in is divided by the previous cycle's post combustion CO_2 peak plateau concentration. Thus, a cycle-resolved residual gas determination can be made. Additionally, shortly after this minimum CO_2-in period, the current cycle's post-main-combustion carbon dioxide concentration can be measured from the peak-plateau level ~230–270 cadeg). The shown cycle was collected during throttled operation; thus, the CO_2-in signal during the gas exchange periods is not trustworthy since in-cylinder pressures are near the NDIR sampling chamber pressure and thus a constant stream of sample gases is not realized in the NDIR probe.

CO_2 exhaust and CO exhaust (CO_2-ex and CO-ex). These signals were adjusted for transport and sensor response delays and then averaged over the given cycle's exhaust stroke. Both of these signals were stable in magnitude during the exhaust stroke.

Fast flame ionization detector exhaust (FFID-ex). The FFID exhaust signal was adjusted for transport delay and averaged over the exhaust stroke using a mass flow rate weighted exhaust model [5].

Experimental Procedure

Daily cold start ups without throttle transients were performed to iteratively calibrate the fuel control to its base line level. A commercial grade premium gasoline was used throughout this study. Over a few dozen preparatory engine start ups, the cycle-by-cycle fuel command was established by seeking to maximize the CO_2-in post combustion peak. With CO_2 peaking at stoichiometric mixtures, it is believed that this level produces a stoichiometric in-cylinder charge. Spark was fixed at 20 deg before top center (BTC) for all of the engine start ups and cold engine throttle transients with the exception of the SS transients in which spark was retarded to 10 deg BTC for knock control. This spark timing was observed to produce strong gross indicated mean effective pressure ($IMEP_g$) cycles. It should be noted that this spark timing is somewhat advanced for the very low speed early engine cycles.

Once the base line startup fuel control was calibrated, daily start ups were performed with computer controlled throttle openings. The throttle actuator was very fast; thus, the transients presented in this paper occur in two engine cycles. The transition engine cycle of the transient is denoted by cycle number 0 throughout this paper, and the first wide open throttle (WOT) cycle is denoted as cycle number 1. Cold engine throttle transients were commanded to occur at different times after engine startup, either 5 s, 20 s, 30 s, or 60 s after start up. For comparison, SS throttle transients were performed after the ECT had reached 95°C several minutes after start up. Similar to the startup fuel calibration, all of the transients were calibrated such that the CO_2-in signal was maximized during and immediately after the throttle transient. This fuel calibration will be discussed more shortly. For each cold engine and stabilized engine transient, a number of iterative calibration runs were performed to achieve this fuel calibration, much like the way a production engine fuel calibration is developed. It is important to note that the PC control computer commanded both the throttle transient and the associated transient fueling. This approach is consistent with "drive-by-wire" throttle control in production engines today.

An example of an engine cold start up and throttle transient (5 s after start up) is shown in Fig. 4. The calibrated commanded in-

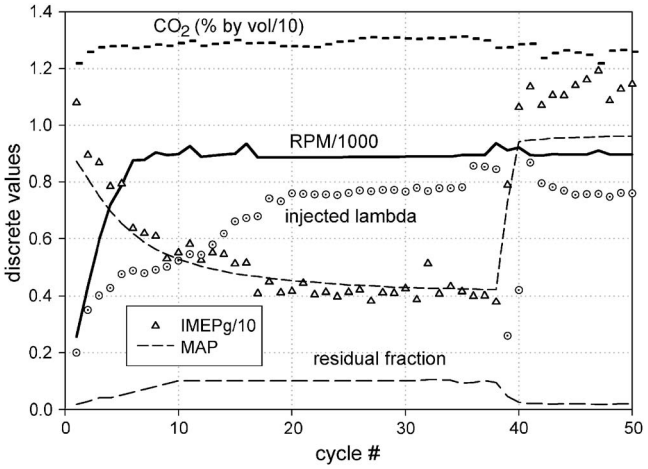

Fig. 4 Base line engine parameters (not including emission measurements)

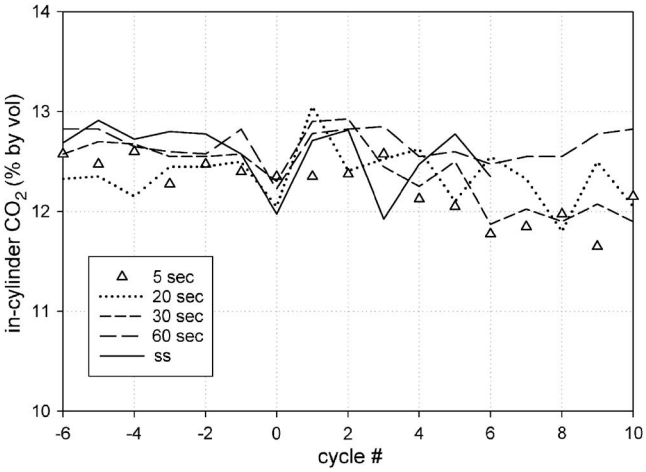

Fig. 5 Post-main-combustion peak in-cylinder CO_2

jected lambda (relative AFR=A/F_{charge} divided by $A/F_{stoichiometric}$) cycle-by-cycle is shown in this figure. It can be observed to increase (enlean) rapidly during the first approximately six engine cycles during startup, then continue to enlean modestly for the next approximately a dozen cycles. After cycle number 20, the injected fuel pulse width is relatively constant. The throttle is commanded to open just prior to cycle 39; thus, this cycle experiences a rise in MAP from approximately 0.4 bar to 0.7 bar. Cycle 40 is the first WOT cycle in this sequence. During the throttle transient, it can be seen that significant fuel enrichment (low commanded lambda levels) is required for nominally stoichiometric in-cylinder air-fuel charge levels. This is consistent with oberserved fuel calibration practices in production engine controllers.

The startup data shown in Fig. 4 also highlights the inverse effects of increasing rpm and decreasing MAP and $IMEP_g$ that is evident for this closed throttle engine start up before the throttle transient. CO_2-in postcombustion plateau levels (in percent) are shown as well as the residual fraction cycle-by-cycle. Since the first engine cycle was not preceded by a combustion event, the residual fraction was zero for this first complete engine cycle (the previous day's engine shutdown was always preceded by at least 15 s of fuel-off motoring). It should be noted that SS stabilized engine WOT residual burned gas percentage for this engine is approximately 3%, while closed throttle residuals are nominally at 10%. The measured in-cylinder burned gas residual fraction is seen to increase after the engine startup, but then to decrease again as the throttle is opened and MAP increases.

As can be seen in Fig. 4, some slight CO_2-in variations result during the throttle transient. These data are rescaled and shown for all of the throttle transient cases in Fig. 5. A variation of approximately 1% (from 12% to 13%) is seen throughout the various throttle transient signals. The SS validation of the in-cylinder and exhaust probes is shown in Fig. 6 as a function of the wide range exhaust gas oxygen sensor. It can be seen that this CO_2-in variation corresponds to a range in lambda from 1.0 to 1.1. As will be shown later, CO levels must be low to be certain that one is on the "lean side" of the CO_2 peak. During the fuel calibration process, CO levels were also used (less than 1%) to ensure that a stoichiometric to a slightly lean fuel calibration was obtained such that engine-out CO and UHC levels were minimized. Thus, the precision of the fuel calibration approach used here results in a variation of 0.1 lambda for in-cylinder AFR.

The resulting commanded fuel calibration is shown in Fig. 7 fuel delivered to the intake port immediately prior to that cycle's intake stroke). It can be seen that as the engine warms up, the transition cycle (0) receives progressively less fuel. Fuel delivered for the first WOT cycle (1) shows an interesting trend. As the engine warms up (e.g., the first throttle transient occurs later after engine startup), less fuel is required. However, it can be seen that many minutes later, after the engine has stabilized in temperature, the fuel delivered for the first WOT cycle is slightly higher that the first WOT cycle for the 5 s after startup throttle transient. This effect will be discussed later in the paper; however, it should be noted that the transition cycle for the SS transient received the

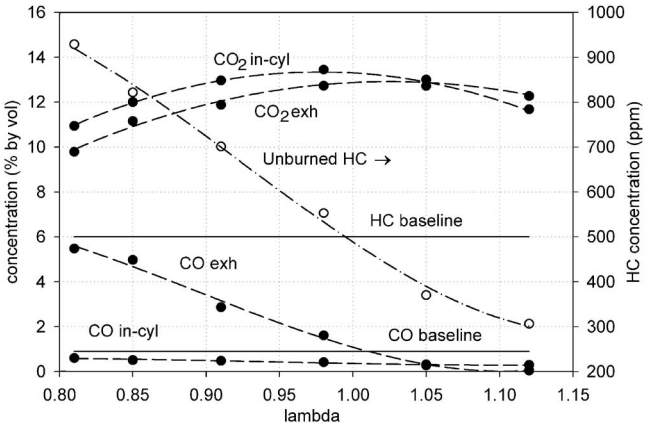

Fig. 6 SS lambda sweep

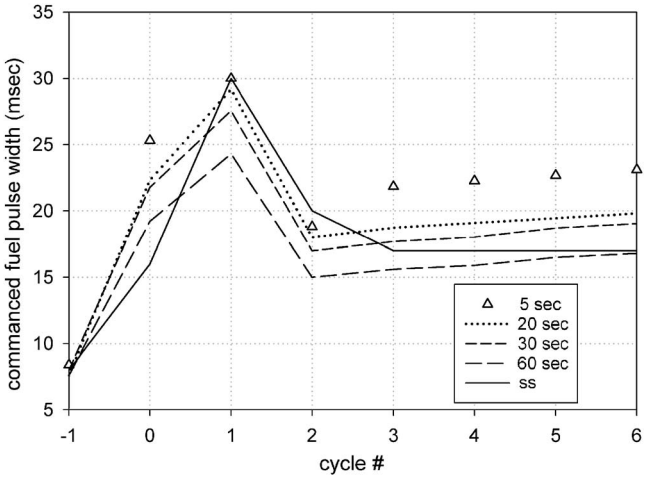

Fig. 7 Commanded fuel pulse width (ms)

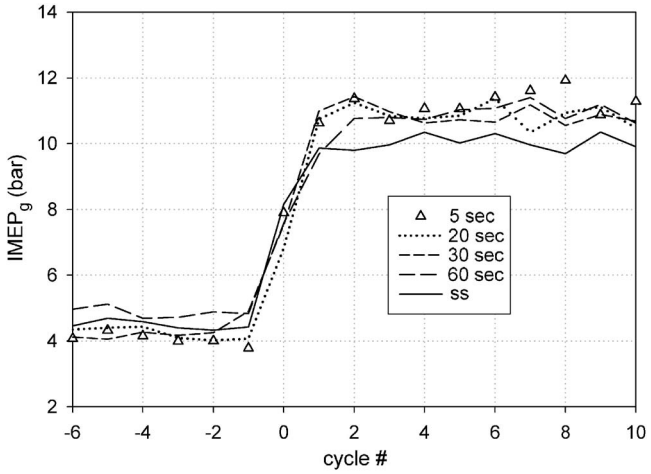

Fig. 8 Cycle-by-cycle IMEP$_g$ (torque)

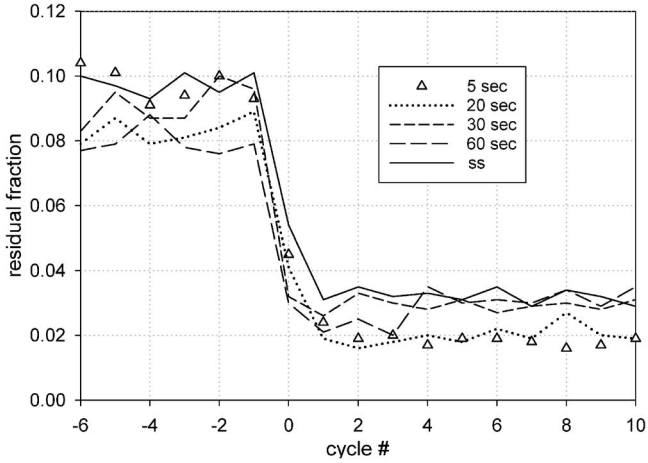

Fig. 10 Cycle-by-cycle residual burned gas fraction

least amount of fueling. For the cold engine transients, the commanded fuel then drops for a few cycles below the post transient stabilized level, while the SS transient ramps down directly toward its posttransient stabilized high load level. These trends will be discussed near the end of the paper when evaluating the *x*-tau model for all of the throttle transients.

Results and Discussion

Indicated engine torque, normalized by the engine's displaced volume is shown in Fig. 8. The closed throttle engine torque levels are nominally at 4–5 bars, and then jump to 10–11 bars after the throttle transient and WOT intake manifold conditions result. It can be seen that the engine acceleration is very fast for all of the throttle transients. The SS WOT levels are the lowest due to the 10 deg of spark retard required to keep the engine from knocking. As a side note, it is very interesting that the cold engine high load condition was quite tolerant of advanced spark, and no audible engine knock resulted despite the very advanced WOT spark timing relative to the SS condition. This is illustrated by the smooth pressure traces shown in Fig. 9.

Next, residual burned gas fraction measured on a cycle-by-cycle basis is shown in Fig. 10. Since closed throttle (low MAP) results in poorer overall engine breathing, the residual fraction for the low load closed throttle cases immediately before the transients is expected to be higher, nominally 8–10%. The residual fraction adjusts very quickly to the high load WOT condition with the transition cycle (0) showing intermediate levels of residual fraction commensurate with its intermediate MAP. A modest secondary effect can be seen in the high load residual fraction. A slight increase in residual fraction with engine temperature (as implied by the time after startup when the transient occurred) is seen. This result is likely due to heating of the engine's intake system (although this was not measured), thus reducing the inlet air charge density (and thus inducted air mass) slightly, while the level of burned in-cylinder residuals is approximately constant.

Cycle-resolved combustion peak cylinder pressures and peak pressure locations, as measured by the in-cylinder Kistler™ pressure transducer, are shown in Figs. 11 and 12 on a cycle-resolved basis around the throttle transients. It can be seen that peak pressures at a closed throttle for the 5 s transient are the lowest. Since the engine started only a few seconds before this transient, the engine walls are very cool, and thus greater charge heat losses occur as compared to the later and SS engine transients. These heat losses lead to overall lower peak in-cylinder pressures and also late peak pressure location (due to slower burn rates), as seen in Fig. 12. The peak pressure for the SS WOT cycles is also low due to retarded spark required for knock control. A burn rate analysis (based on MIT's one zone model [6]) confirms this characterization. Crank angle resolved instantaneous burn rates for the throttled cycle immediately before the throttle transient are shown in Fig. 13. It can be seen that the peak heat release rate advances earlier with longer engine warmup times prior to the throttle open-

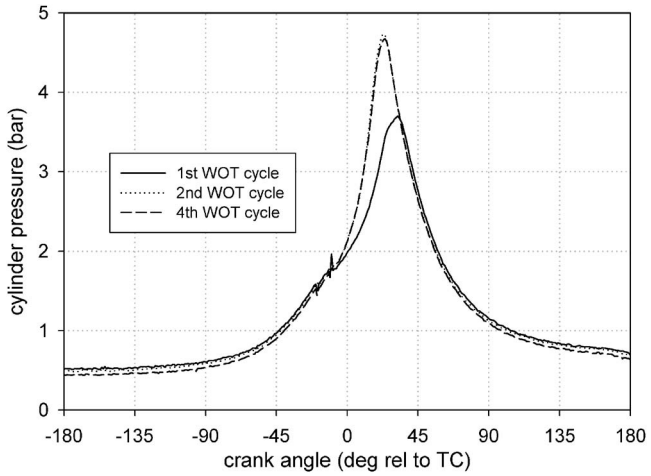

Fig. 9 Cylinder pressure traces for various WOT cycles after 60 s warmup

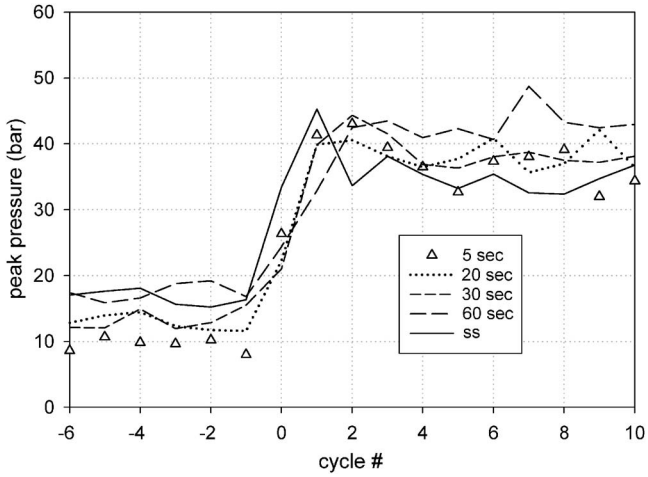

Fig. 11 Cycle-by-cycle peak combustion pressure

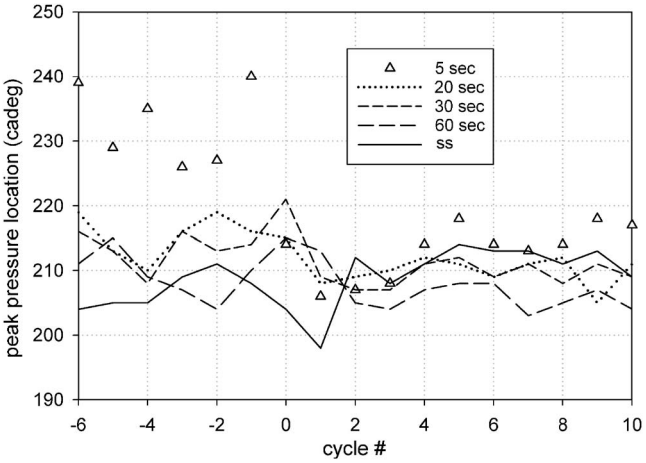

Fig. 12 Peak pressure location (180 deg=top center combustion)

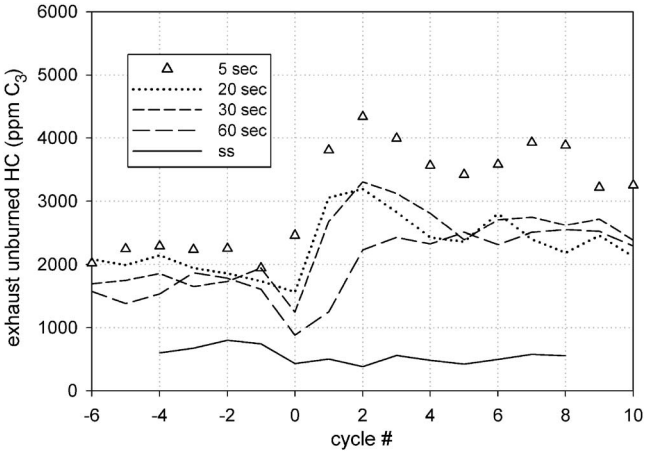

Fig. 15 UHC measured at the exhaust manifold next to the exhaust port

ing. This trend is further confirmed by analyzing WOT cycles 1 s after the various throttle transients. These WOT cycle's heat release results are shown in Fig. 14. Again, as with the throttled cycles prior to the throttle transients, these WOT cycles show earlier peak heat release (for the same spark timing) as the engine has warmed up longer before the throttle transient. The exception is the SS WOT cycle whose spark has been retarded by 10 deg for knock control.

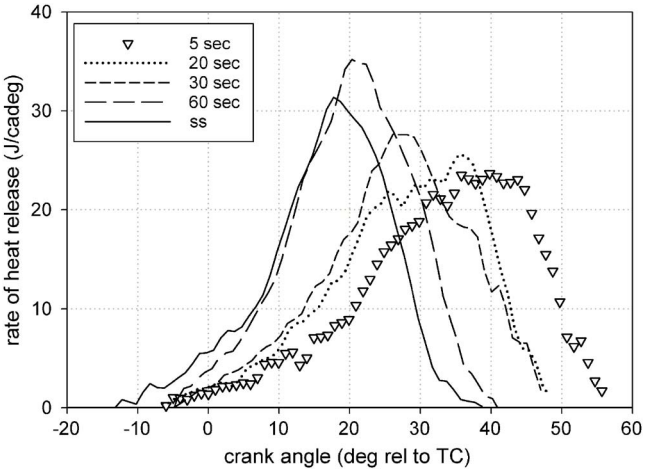

Fig. 13 Heat release rate for throttled operation

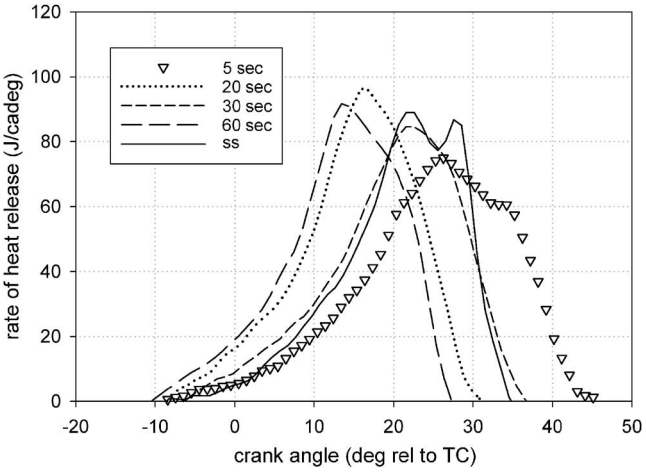

Fig. 14 Heat release rate eight cycles after WOT transition

Overall, the peak pressure phasing is somewhat later than optimal (195–200 cadeg=15–20 deg ATC). At the CR of this study, 20 deg BTC spark timing was shown to give the best torque in the absence of knock for a stabilized engine and was thus chosen as the commanded timing for this study. It is thus believed that the cooler engine temperatures at the time of these throttle transients result in longer burn times, thus later peak pressure locations. From the perspective of general trends, this slightly late spark timing and pressure phasing is not believed to affect the experimental results in any significant way since for the stabilized CFR engine in this configuration, a 10 deg phasing change results in only a 2–3% change in $IMEP_g$.

Exhaust UHCs are shown in Fig. 15 as a function of the different throttle transients. It can be seen that the throttle transient occurring 5 s after startup delivers the highest exhaust UHCs. This is not surprising due to the level of excess enrichment required before, during, and after this engine transient. The UHC level is approximately four times the SS level. As a vehicle's catalytic converter is not yet lit-off at this time, managing this behavior will continue to be a challenge since these emissions just pass through the exhaust system out the tailpipe.

For the transients at 20 s and 30 s after startup, the UHC exhaust emissions are approximately three times the SS levels, with the 60 s transient showing the lowest levels of the cold engine throttle transients. The baseline SS throttle transient levels are seen to be on the order of 300–900 ppm C_3.

In order to glean the source and intracycle timing of these engine-out UHCs, evaluation of the post combustion in-cylinder FFID signal can provide some important insights, as shown by the authors in an earlier work [7]. Peak in-cylinder fuel vapor concentration levels that develop during the expansion and exhaust strokes after the main combustion event has occurred are shown in Fig. 16. Significant levels of post combustion fuel vapor evolution are seen to occur, most likely due to the presence of liquid films in the combustion chamber that survive past the combustion event due to the very cold engine cylinder walls. The greatest high load post combustion fuel vapor levels occur immediately after the throttle transient conducted 5 s after startup and diminish significantly as the throttle transients occur later during the engine warmup. Thus, it is believed that a strong majority of exhaust UHCs evolve during this period. It is also interesting to note that these post combustion in-cylinder fuel vapor levels are fairly high, approaching 1/3 of a pre combustion stoichiometric charge level. Thus, significant oxidation of these in-cylinder fuel vapors must

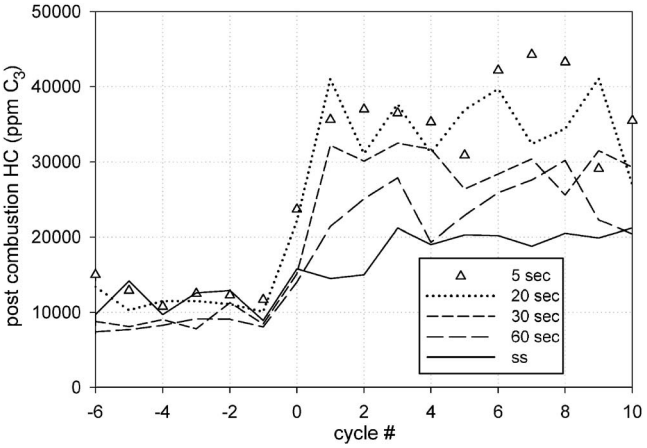

Fig. 16 Postcombustion in-cylinder hydrocarbons

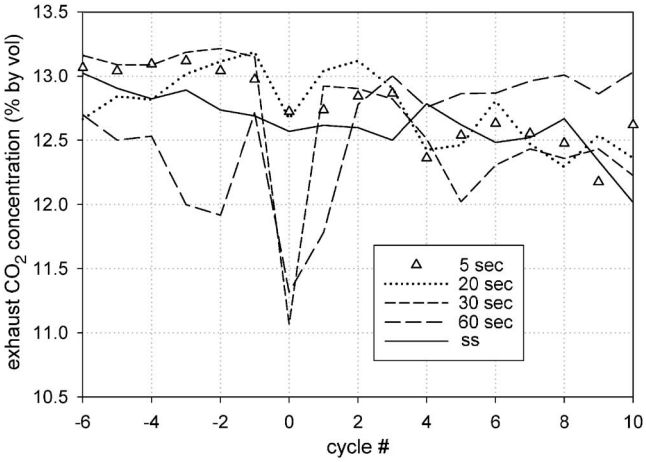

Fig. 18 Exhaust CO_2 concentration

occur during the exhaust stroke in order to obtain these elevated exhaust manifold levels. This measurement could also be locally high since the exhaust stroke produces a rollup vortex [8] that is locally at the cylinder liner-piston ring area, which is also where the in-cylinder FFID probe is located.

Next, exhaust CO levels are shown in Fig. 17. CO-ex levels are highly nonlinear and rise dramatically with increasing enrichment above stoichiometric fuel-air charge levels. For fuel lean fuel-air charges, CO levels are low at just a fraction of a percent. For reference, CO levels at stoichiometric operation are nominally just below 1% and are a strong function of enrichment. It can be seen that the low load CO levels are highly variable before the transients due to subtle differences in low load fuel-air ratio during warmup.

Finally, exhaust CO_2 measurements are shown in Fig. 18. These measurements are very similar to the in-cylinder levels shown in Fig. 5, with the slight exception of the transition cycle (0) for the 30 s and 60 s transients. The two individual cycles are just above the 11% level (with associated low CO-ex levels, as shown in Fig. 18) and are thus approximately 5% leaner than the target AFR range. Despite this modest extra enleanment, the $IMEP_g$ and peak pressure characteristics are still very comparable to the targeted nearly stoichiometric cycles. This shows that there is a reasonable range of fuel control with acceptable engine performance.

The last objective of this work was to evaluate the widely used *x*-tau model with regard to these cold engine transients. The two equations for the *x*-tau model are shown as follows:

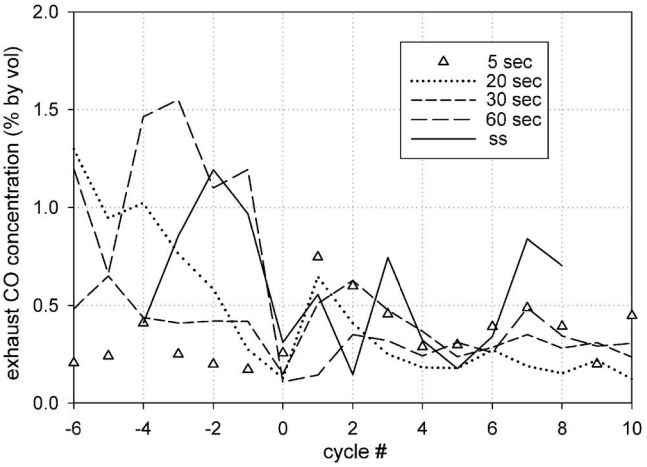

Fig. 17 Exhaust CO concentration

$$m_i = (1 - x)f_i + \frac{M_i}{\text{tau}/\Delta t} \tag{1}$$

$$M_i + 1 = M_i + xf_i - \frac{M_i}{\text{tau}/\Delta t} \tag{2}$$

where m is the mass of fuel delivered to the cylinder, f is the injected fuel mass, and M is the mass of liquid fuel in the intake port puddle. The parameters x and tau are the fraction of the injected fuel that is retained in the port and the time constant for the release of port fuel to the engine's cylinder, respectively. Time per cycle is given by Δt. It has been shown that x and tau are strong functions of numerous engine variables such as MAP, rpm, and ECT.

The results of applying the *x*-tau model to our engine data are shown with three graphs in Fig. 19. The top graph in this figure shows a SS fast throttle transient with the commanded injection sequence to provide a nominal stoichiometric in-cylinder air-fuel charge. This SS transient graph also shows the required in-cylinder fuel mass as a function of the measured engine MAP and residual gas fraction (solid line) and the *x*-tau-model-based in-cylinder fuel mass predictions resulting from using the commanded injection mass with iteratively solved values of x and tau. For this SS case, $x=0.55$ and tau$=0.4$ s. It can be seen that the predicted in-cylinder fueling levels through the transient are very close to the needs of the engine. Thus, as expected, the *x*-tau model is very appropriate for stabilized engine transients.

The middle graph in this figure's sequence shows the 5 s throttle transient injected fuel mass sequence as well as in-cylinder fuel mass requirements with *x*-tau model predicted in-cylinder fuel mass levels with various x values. It can be seen that as x increases (e.g., more fuel to the intake port puddle), which is expected for colder engine operation, less injected fuel goes immediately to the engine and more fuel is retained in the puddle. This trend is directionally correct as significant overfueling is necessary and due to cold engine intake port wall wetting delays. Unfortunately, due to the baseline cold start up fuel enrichment, the stabilized levels of in-cylinder fuel as predicted by the *x*-tau model are highly biased before and after the transient. Thus the model never adequately predicts the required levels of in-cylinder fueling.

The bottom graph in Fig. 19 shows the effect of tau on the predicted in-cylinder fuel delivery for various tau values, with x held at 0.55. Again, an excess fuel bias is in place due to the baseline overfueling required (not including the throttle transient enrichment) just to keep the air-fuel charge close to stoichiometric. Tau can be seen to affect the time at which the predicted in-cylinder fuel charge returns to the nominal high load level.

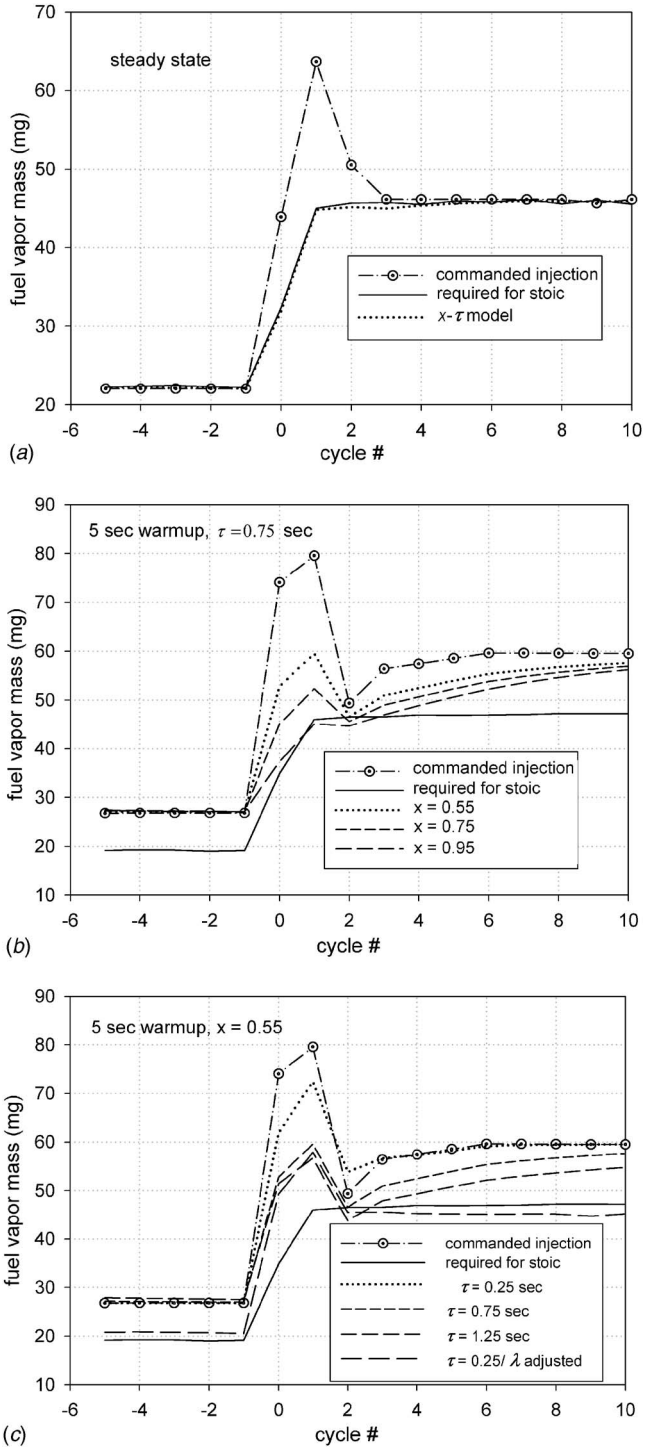

Fig. 19 *x*-tau model fuel compensation

Since this overall bias error exists, an alternative approach to the *x*-tau model was to use a modified commanded fuel injection level that is reduced by multiplying the actual injected amount by the overall lambda injection relative to a true stoichiometric in-cylinder charge. During this 5 s transient, lambda injection is approximately 0.75; thus, all of the commanded fuel masses were reduced by ~25%. Applying the *x*-tau model to this lambda adjusted sequence is shown by the long dash fuel delivery prediction. While post transient operation is improved, this *x*-tau modification still does a poor job of predicting proper injection requirements during the throttle transient itself.

The source of the poor *x*-tau model behavior is evident when looking at the commanded fueling sequence. During the first two cycles (0 and 1) of these fast transients, significant overfueling is required; then, cycle 2 (and, to a lesser extent, cycles, 3–5) requires less than the stabilized high load fueling level. The overfueling from cycles 0 and 1 is delayed on entering the engine for a few engine cycles, thus providing some portion of the in-cylinder fuel vapor for cycles 3–5 and requiring less injected fuel for those specific cycles. Since the *x*-tau model is only a first order puddle model, this dynamic does not fit that trend, and thus it cannot predict the overfueling, then underfueling, that is evident in these cold engine transients.

Conclusions

Cold engine throttle transient experiments were performed shortly after the CFR engine was cold started. The following conclusions can be drawn from this work.

Cold engine fast throttle transient $IMEP_g$ performance is comparable to SS stabilized engine throttle transients. This strong $IMEP_g$ performance is due to the absence of high load engine knock allowing for a significantly more spark advance with the cold engine.

Cold engine throttle transients produce significantly more UHC in the exhaust, up to four times the SS levels for the throttle transient that occurs 5 s after startup. CO levels are comparable to SS engine levels as a result of slightly lean in-cylinder fuel vapor levels.

The *x*-tau model, while providing excellent SS throttle transient in-cylinder fuel mass predictions, does not work well for these cold engine throttle transients that occur shortly after engine startup. It is believed that heavy overfueling for the transients produces a second order puddle emptying effect that is not accounted for by the first order *x*-tau model.

Acknowledgment

The authors would like to gratefully acknowledge the expert assistance of John Hein and Robert Woody in setting up and maintaining the experiments. This work was supported by the Office of Naval Research through the Naval Academy Research Council.

Nomenclature

cadeg = crank angle degrees
$IMEP_g$ = gross indicated mean effective pressure
lambda (λ) = equivalence ratio
ppm C_3 = parts per million (propane based)
tau (τ) = time constant related to intake fuel puddle vaporization
x = mass fraction of injected fuel that goes into the fuel puddle

Suffixes/Subscripts

i = cycle index
in = in cylinder
ex = exhaust

Appendix A: Cambustion™ Settings

FFID (intake and exhaust)
He/H_2 0.8 bar
FID chamber=460 mbar (absolute)
Cp chamber=550 mbar (absolute)
Air (FID flame)=0.25 bar
Sample head=150°C
Probe=200°C
Zero: Pure N_2
Range (0–100k ppm C_3) in-cylinder
Range (0–20k ppm C_3) exhaust
NDIR (intake and exhaust)
Zero: Pure N_2

Span gases:
2% CO–15% CO_2–balN_2
0.5% CO–5% CO_2–balN_2
Filter chamber temperature=45 °C
Head temperature=150 °C
Sample probe temperature=120 °C
Motor/chopper=15,000 rpm
Sample pressure chamber=150 mbar (absolute) (in-cyl); 500 mbar (absolute) (exh)

References

[1] Aquino, C. F., 1981, "Transient A/F Control Characteristics of the 5 Liter Central Fuel Injection Engine," SAE Paper No. 810494.
[2] Fozo, S. R., and Aquino, C. F., 1988, "Transient A/F Characteristics for Cold Operation of a 1.6: Engine With Sequential Fuel Injection," SAE Paper No. 880691.
[3] Shayler, P. J., Teo, Y. C., and Scarisbrick, A., 1995, "Fuel Transport Characteristics of Spark Ignition Engines for Transient Fuel Compensation," SAE Paper No. 950067.
[4] Cowart, J. S., and Cheng, W. K., 2000, "Throttle Movement Rate Effects on Transient Fuel Compensation in a Port Fuel Injected Engine," SAE Paper No. 2000-01-1937.
[5] Cowart, J. S., 2000, "Mixture Preparation Behavior in Port Fuel Injected Ignition Engines During Transient Operations," Ph.D. thesis, MIT.
[6] Chun, K. M., and Heywood, J. B., 1987, "Estimating Heat-Release and Mass-of-Mixture Burned From Spark-Ignition Engine Pressure Data," Combust. Sci. Technol., **54**, pp. 133–143.
[7] Cowart, J. S., 2006, "Post-Combustion Fuel Vaporization During Engine Startup," ASME J. Eng. Gas Turbines Power, **128**(2), pp. 397–402.
[8] Heywood, J. B., 1988, *Internal Combustion Engine Fundamentals*, McGraw-Hill, New York.

The Application of System CFD to the Design and Optimization of High-Temperature Gas-Cooled Nuclear Power Plants

Gideon P. Greyvenstein
Postgraduate School of Nuclear Science and Engineering,
The North-West University,
Private Bag X6001,
Potchefstroom 2520, South Africa
e-mail: gpg@mtechindustrial.com

The objective of this paper is to model the steady-state and dynamic operation of a pebble-bed-type high temperature gas-cooled reactor power plant using a system computational fluid dynamics (CFD) approach. System CFD codes are 1D network codes with embedded 2D or even 3D discretized component models that provide a good balance between accuracy and speed. In the method presented in this paper, valves, orifices, compressors, and turbines are modeled as lumped or 0D components, whereas pipes and heat exchangers are modeled as 1D discretized components. The reactor is modeled as 2D discretized system. A point kinetics neutronic model will predict the heat release in the reactor. Firstly, the layout of the power conversion system is discussed together with the major plant parameters. This is followed by a high level description of the system CFD approach together with a description of the various component models. The code is used to model the steady-state operation of the system. The results are verified by comparing them with detailed cycle analysis calculations performed with another code. The model is then used to predict the net power delivered to the shaft over a wide range of speeds from zero to full speed. This information is used to specify parameters for a proportional-integral-derivative controller that senses the speed of the power turbine and adjusts the generator power during the startup of the plant. The generator initially acts as a motor that drives the shaft and then changes over to a generator load that approaches the design point value as the speed of the shaft approaches the design speed. A full startup simulation is done to demonstrate the behavior of the plant during startup. This example demonstrates the application of a system CFD code to test control strategies. A load rejection example is considered where the generator load is suddenly dropped to zero from a full load condition. A controller senses the speed of the low pressure compressor/low pressure turbine shaft and then adjusts the opening of a bypass valve to keep the speed of the shaft constant at 60 rps. *The example demonstrates how detailed information on critical parameters such as turbine and reactor inlet temperatures, maximum fuel temperature, and compressor surge margin can be obtained during operating transients. System CFD codes is a powerful design tool that is indispensable in the design of complex power systems such as gas-cooled nuclear power plants.* [DOI: 10.1115/1.2835057]

Introduction

When designing a new power plant, one usually starts with a first order cycle analysis to determine the impact of process conditions and cycle layout on the performance of the system. The next level of analysis is to improve the accuracy by taking piping losses, compressor and turbine efficiency, and secondary flows such as leak or bleed flows into account. Such analyses are known as second order cycle analyses.

With the third level of analysis, a simulation model of the system is developed whereby the simple analytical component models employed in the second order analysis are replaced with more advanced implicit or explicit models. System codes usually employ a variety of component models ranging from lookup tables based on component characteristics (as in the case of compressors or turbines) to one-dimensional discretized pipe and heat exchanger models. Third order analyses can either be steady state or transient and are usually used to investigate the impact of component design or operating conditions on system performance. It can also be used to study the dynamic behavior of the system.

Although third order analysis codes (system codes) utilize more advanced component models compared to second order analyses tools, the component models used in these codes are still not as accurate as they can be, and this creates a need for a fourth level analysis where one would analyze subsystems such as the boiler, reactor, or heat exchangers using state-of-the-art specialized tools such as 3D computational fluid dynamics (CFD) codes. CFD codes are, however, slow and not well suited for optimization studies. They are not suited at all for the analysis of complete power plants.

In this paper, an analysis approach is described, which the authors choose to call the system CFD or SCFD approach. This is an extension of third order systems analysis whereby more accurate multidimensional CFD models of selected components are embedded into the system simulation solver. The CFD component models in SCFD codes are usually "tailormade" for the specific component, thereby avoiding the overhead of linking a general CFD code with a systems code. This improves ease of use and also leads to faster execution times.

SCFD codes are used to study both system and component performance under varying or transient operating conditions. It is a versatile design tool that can be used for a wide range of tasks such as uncertainty or sensitivity analysis, sizing of component, system optimization, control studies, and even the construction of training simulators.

Manuscript received January 7, 2007; final manuscript received October 30, 2007; published online March 28, 2008. Review conducted by Dilip R. Ballal.

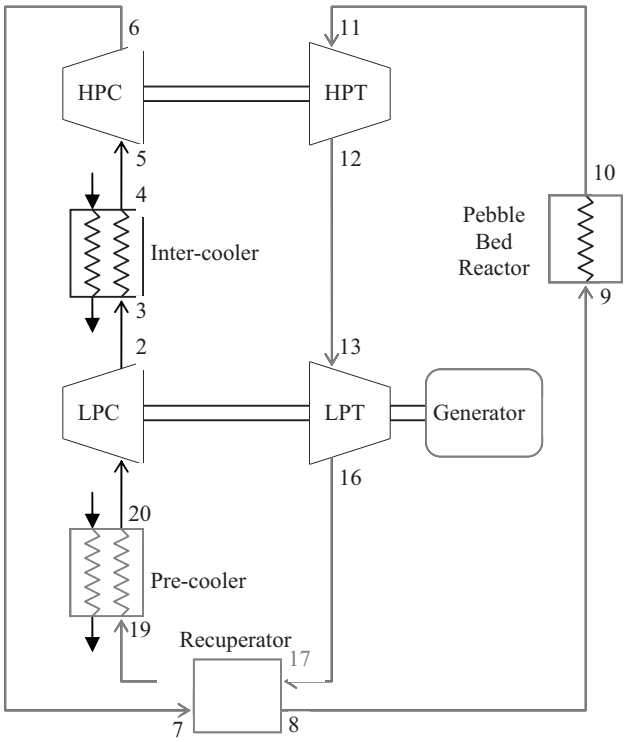

Fig. 1 Schematic layout of a two-shaft power conversion unit (PCU) for a pebble-bed-type HTR

In this paper, the application of the SCFD code FLOWNEX for the design of a pebble-bed-type high temperature reactor (HTR) nuclear power plant will be discussed. In the first part of the paper, a brief description of the HTR power plant will be given. This will be followed by a description of the modeling approach employed in the SCFD code FLOWNEX. In the last part of the paper, a number of case studies will be presented.

Description of Pebble-Bed-Type HTR Power Plant

The power plant that will be considered in this study is a direct two-shaft closed intercooled recuperated Brayton cycle, as shown in Fig. 1. The heat source for the system is a pebble bed reactor. [1,2]

Helium enters the low pressure compressor (LPC) at 1 and is then compressed to state 2. From 3 to 4, helium is cooled in the intercooler where after it is recompressed in the high pressure compressor (HPC) to state 6. The helium is then preheated in the recuperator (7-8) and then further heated to the maximum cycle temperature in the reactor (9-10). The hot high pressure helium is expanded to an intermediate pressure in the high pressure turbine (HPT) (11-12), which drives the HPC. It is then further expanded in the low pressure turbine (LPT) (13-16), which drives both the LPC and the generator. After the LPT, the still hot helium is passed through the recuperator (17-18) where it is cooled to state 18 while at the same time preheating the helium leaving the HPC before it enters the reactor. The helium is then further cooled in the precooler to state 20 before entering the LPC.

Plant Parameters

A second order cycle analysis was performed using a range of pressure ratios (PRs) to determine the optimum overall PR. The input parameters used in this analysis is summarized in Table 1.

The reason why the pressure drop relationship $\Delta p = C_2 Q$ is used for the recuperator as opposed to $\Delta p = C_1 \rho Q^2$ for the precooler and intercooler is that the flow in the recuperator is laminar while the flow in the precooler and intercooler is turbulent.

Table 1 Plant parameters

Parameter	Value
Maximum cycle pressure	7000 kPa
Lowest cycle temperature (T_1, T_4, T_5, T_{20})	24°C
Maximum cycle temperature (T_{10}, T_{11})	900°C
Heat released in the reactor	260 MW
Compressor isentropic efficiency	88%
Turbine isentropic efficiency	91%
Turbomachine mechanical efficiency	99%
Recuperator effectiveness	96%
Compressor and turbine exit velocities	135 m/s
Compressor and turbine exit losses	$\Delta p_0 = 0.3 \times \frac{1}{2}\rho V^2$
Pipe velocities	
Sections 4-5 and 20-1	50 m/s
Sections 8-9, 10-11, and 18-19	80 m/s
Pipe losses	
Primary losses	$0.1 \times \frac{1}{2}\rho V^2$
Secondary losses	$0.4 \times \frac{1}{2}\rho V^2$
Total losses	$0.5 \times \frac{1}{2}\rho V^2$
Pipe inside surface roughness	30 μm
Leak flows	
From 6 to13	1.25%
From 2 to 17	3.75%
Reactor pressure loss	$\Delta p_0 = 21.827 \times \rho Q^2$
Precooler pressure loss	$\Delta p_0 = 0.05684 \times \rho Q^2$
Intercooler pressure loss	$\Delta p_0 = 0.05684 \times \rho Q^2$
Recuperator hot side pressure loss	$\Delta p_0 = 24.047 \times \rho Q^2$
Recuperator cold side pressure loss	$\Delta p_0 = 36.657 \times \rho Q^2$

The second order cycle analysis yielded an optimum overall PR of approximately 3.0. Assuming the PRs of the two compressors to be the same, the PR of each compressor will therefore be $\sqrt{3} = 1.732$.

Normally, FLOWNEX is used to simulate the performance of a given system. In this example, the second order analysis is used to determine near optimum process conditions for the system as a whole, which are then used to determine the component designs. With the component designs fixed, the behavior of the system is investigated under both steady-state and transient operating conditions. In the next section, the FLOWNEX modeling approach will be discussed after which the component models used in the modeling of the sample system shown in Fig. 1 will be discussed.

Systems CFD Approach to the Modeling of Thermal-Fluid Systems

In the SCFD approach, a thermal-fluid system is represented by a network of nodes and elements, as shown in Fig. 2. Elements are components such as pipe increments, valves, compressors, and heat exchangers, while nodes are the end points of elements. Nodes can also be used to represent reservoirs with specified volumes.

Elements can be connected in any arbitrary way at common nodes to form a network. FLOWNEX solves the momentum equation in each element and the continuity and energy equations at

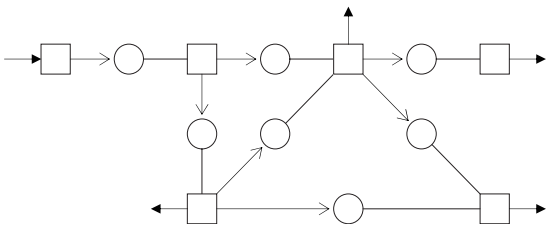

Fig. 2 Discretization of a thermal-fluid system into a network of nodes and elements

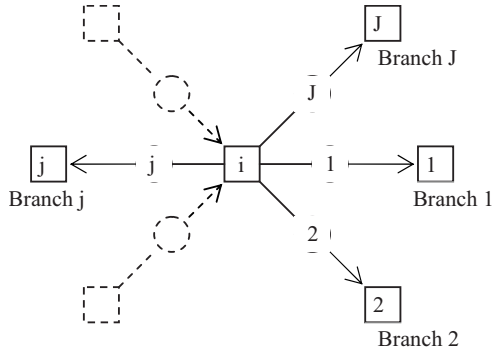

Fig. 3 General node with neighboring nodes connected through branch elements

each node. This gives FLOWNEX a pseudo-CFD capability, which enables it to predict complex phenomena such as pressure and temperature waves in pipes and buoyancy effects in packed beds.

An important feature of the network approach is that elements such as pipes, heat exchangers, and the reactor, although depicted on the system level as single elements or pairs of elements, can be discretized into either subnetworks or multidimensional CFD regions as explained later. FLOWNEX can also handle 2D conductive heat transfer structures connected to flow elements. The discretization of these elements is beyond the scope of this paper.

Numerical Approach for the Solution of the Flow, Pressure, and Temperature Fields. The equations that govern the solution of mass flows, pressures, and temperatures are the continuity, momentum, and energy equations. Consider a general node i with J branches, as shown in Fig. 3.

The continuity equation for node i can be expressed as

$$V_i \frac{\partial \rho_i}{\partial t} = \sum_{j=1}^{J} \rho_j Q_j s_j + d_i \tag{1}$$

where s_j is the "sign" of element j with $s_j=1$ if the positive flow direction of element j is from node j to node i and $s_j=-1$ if the positive flow direction is from node i to node j.

The momentum equation for element j can be written in the following general form:

$$f(\rho_j, Q_j) + \frac{\rho_j \Delta x}{A} \frac{\partial Q_j}{\partial t} + s_j(p_i - p_j) = 0 \tag{2}$$

where Δx is the length of the element and A is the average cross-sectional area.

The energy conservation equation for node i is given by

$$\frac{\partial(m_i h_i)}{\partial t} - V_i \frac{\partial p_i}{\partial t} = \sum_{in,j} [s_j \dot{m}_j (h_j + g z_j) + \dot{E}_j] + d_i^+ (h_{\text{amb}} + g z_i) + (h_i + g z_i)\left(\sum_{\text{out},j} s_j \dot{m}_j - d_i^- \right) + \dot{E}_i \tag{3}$$

Equations (1)–(3) are simultaneously solved with the implicit pressure correction method (IPCM), described elsewhere [3–5].

Calculation of Turbo Machine Shaft Speed. The speed of a turbo machine shaft is governed by the following equation:

$$\frac{d\omega}{dt} = \frac{P}{I\omega} \tag{4}$$

The net shaft power is calculated as

$$P = \eta_{\text{mech}} \sum P_{\text{turbine}} - \sum P_{\text{compressor}} - (P_{\text{grid}}/\eta_{\text{switch}} + P_{\text{house}})/\eta_{\text{gen}} \tag{5}$$

Equation (4) is solved numerically at each time step for all shafts in the system.

PID Controller. A proportional-integral-derivative (PID) controller senses one variable and adjusts the value of another variable according to the following relationship:

$$y = y_0 + P\varepsilon + I \int_0^t \varepsilon d\tau + D \frac{d\varepsilon}{d\tau} \tag{6}$$

The error is defined as follows:

$$\varepsilon = x_0 + b/2 - x \quad \text{if } x > x_0 + b/2$$

$$\varepsilon = x_0 - b/2 - x \quad \text{if } x < x_0 - b/2$$

$$\varepsilon = 0 \quad \text{if } x_0 - b/2 \leqslant x \leqslant x_0 + b/2 \tag{7}$$

In discretized form, as implemented in the solution algorithm, Eq. (6) becomes

$$y = y_0 + P\varepsilon + I \sum_{\tau=1}^{\tau=t} \varepsilon^{\tau} \Delta t + D(\varepsilon - \varepsilon^{o})/\Delta t \tag{8}$$

Component Models

In this section, the different component models used in the FLOWNEX analysis of the system will be briefly discussed.

Restrictors With Loss Coefficient. Compressor and turbine exit losses are modeled with FLOWNEX's RL element. RL elements are used for the following sections in Figs. 2-3, 6-7, 12-13, and 16-17. The pressure drop through a RL element is given by

$$\Delta p_0 = c_L p_{01} \left(1 - \frac{p_s}{p_{01}} \right) \tag{9}$$

while the mass flow rate is given by

$$\dot{m} = c_D \rho V A \tag{10}$$

Using gas dynamics relationships for an ideal gas, the Mach number in the throat can be expressed in terms of p_s/p_{01} as

$$M = \sqrt{\frac{2}{\gamma - 1}\left[\left(1 - \frac{\Delta p_0}{c_L p_{01}} \right)^{1-\gamma/\gamma} - 1 \right]} \tag{11}$$

Using Eqs. (9)–(11) together with values of $\dot{m}$ and ρ obtained from the second order cycle analysis, the throat diameters of the different RL elements were determined as follows.

Section	d (m)
2-3	0.4761
6-7	0.3602
12-13	0.6814
16-17	0.9019

Pipes. The following sections in Fig. 1 represent pipes 4-5, 8-9, 10-11, 18-19, and 20-1. The pressure drop for incompressible flow through pipes is modeled as

$$\Delta p_0 = \left(\frac{fL}{D} + \sum K \right) \tfrac{1}{2} \rho V^2 + \rho g L \cos\theta + \rho L \frac{dV}{dt} \tag{12}$$

For compressible flows the pressure drop is given by

$$\frac{p}{p_0}\Delta p_0 = \left(\frac{fL}{D} + \sum K\right)\tfrac{1}{2}\gamma p M^2 + \rho g L\cos\theta + \rho L\frac{dV}{dt} \quad (13)$$

In Table 1 the primary losses of all pipe sections is specified as $0.1(\frac{1}{2}\rho V^2)$ while the secondary losses is specified as $0.4(\frac{1}{2}\rho V^2)$. The primary loss is defined as

$$\Delta p_{0,P} = \left(f\frac{L}{d}\right)\tfrac{1}{2}\rho V^2$$

while the secondary loss is defined as

$$\Delta p_{0,S} = \sum K\tfrac{1}{2}\rho V^2$$

K is the loss coefficient of components such as bends and valves. This implies that $fL/d=0.1$ and $\Sigma K=0.4$ for all pipes. For turbulent flow, the Darcy friction factor in Eq. (12) is calculated with the Swamee–Jain equation [6], which is given by

$$f_t = 0.25\{\log[(e/3.7D) + 5.74\mathrm{Re}^{-0.9}]\}^{-2} \quad (14)$$

where e is the inside surface roughness and Re is the Reynolds number. For laminar flow ($\mathrm{Re}\leqslant 2300$), the friction factor is given by

$$f_l = \frac{64}{\mathrm{Re}} \quad (15)$$

For transitional flow ($2300\leqslant \mathrm{Re}\leqslant 5000$) FLOWNEX interpolates between f_t and f_l. Using values of $\dot{m}$, ρ, and f obtained from the second order cycle analysis, the lengths and diameters of the different diffusers were determined as follows:

Section	d (m)	L (m)
4-5	0.6929	6.506
8-9	0.6632	6.059
10-11	0.8284	7.539
18-19	0.8657	8.254
20-1	0.9275	8.983

Orifices Used to Model the Leak Flows. Two leak flows, not shown in Fig. 1, are taken into consideration. One is between positions 6 and 13 and one between positions 2 and 17. Theses flows are modeled with FLOWNEX's RD (restrictor with discharge coefficient) element.

The pressure drop for compressible flow through RD elements is given by

$$\Delta p_0 = p_{01}\left(1 - \frac{p_s}{p_{01}}\right) \quad (16)$$

where p_s is the static pressure in the throat of the restrictor.

Using gas dynamics relationships for an ideal gas, the Mach number in the throat can be expressed in terms of p_s/p_{01}:

$$M = \sqrt{\frac{2}{\gamma-1}\left[\left(1 - \frac{\Delta p_0}{p_{01}}\right)^{1-\gamma/\gamma} - 1\right]} \quad (17)$$

where γ=ratio of specific heats.

The mass flow rate through RD elements is given by

$$\dot{m} = c_D\rho V A \quad (18)$$

With the mass flows and pressures known from the second order cycle analysis, FLOWNEX's designer capability was used to determine the orifice diameters. These are as follows:

Section	d (m)
6-13	0.021283
2-17	0.043358

The discharge coefficient c_D of both restrictors is assumed to be 1.0.

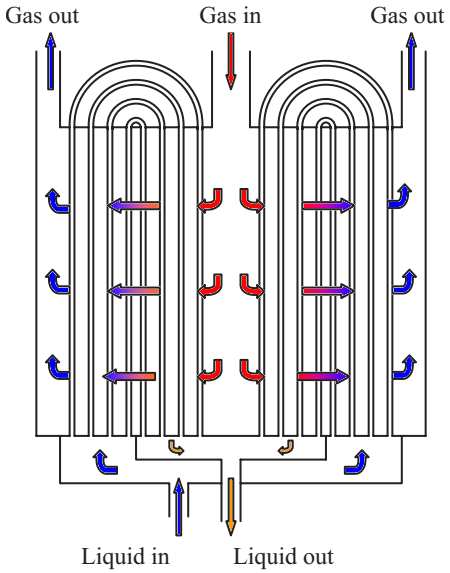

Fig. 4 Flownex's FTX

Precooler and Intercooler. The precooler is modeled with FLOWNEX's (finned tube heat exchanger) (FTX) element. FTX heat exchangers consist of rows of finned tubes spaced along the circumference of a cylindrical pressure vessel. The liquid is normally on the tube side while the gas is on the shell side. The liquid normally flows radially inward while the gas flows radially outward, as shown in Fig. 4.

Pressure Drop. The pressure drop on the tube side is given by

$$\Delta p_0 = \left(\frac{fL}{D} + K_{\mathrm{in}} + K_{\mathrm{out}}\right)\tfrac{1}{2}\rho V^2 + \rho L\frac{dV}{dt} \quad (19)$$

while the pressure drop on the shell side is given by

$$\Delta p_0 = \frac{4fL}{D_h}\tfrac{1}{2}\rho V^2 + \rho L\frac{dV}{dt} \quad (20)$$

where f is the friction factor given as a function of Reynolds number as part of the input data and V is the maximum velocity based on the minimum flow area. The hydraulic diameter is calculated as

$$D_h = \frac{4LA_{\min}}{A_o} \quad (21)$$

where $A_{\min}$ is the minimum flow area on the shell side and A_o is the shell side heat transfer area.

Heat Transfer. Consider a heat exchanger increment as shown in Figs. 5 and 6.

In the above figure, the subscripts denote the following: t, tube side; s, shell side; m, metal; s_i, shell side inlet; s_e, shell side outlet; t_i, tube side inlet; and t_e, tube side outlet.

The shell side heat transfer is calculated as

$$Q_s = A_s U_s\left[\tfrac{1}{2}(T_{s_i} + T_{s_e}) - T_m\right] \quad (22)$$

where A_s is the shell side heat transfer area and U_s is the shell side effective heat transfer coefficient, which is given by

$$U_s = \left(\frac{1}{\eta_{f_s}\lambda_s} + \frac{0.5}{\lambda_m}\right)^{-1} \quad (23)$$

where η_{fs}, fin efficiency on the shell side; λ_t, shell side surface heat transfer coefficient; and λ_m, metal coefficient.

The shell side surface heat transfer coefficient is determined

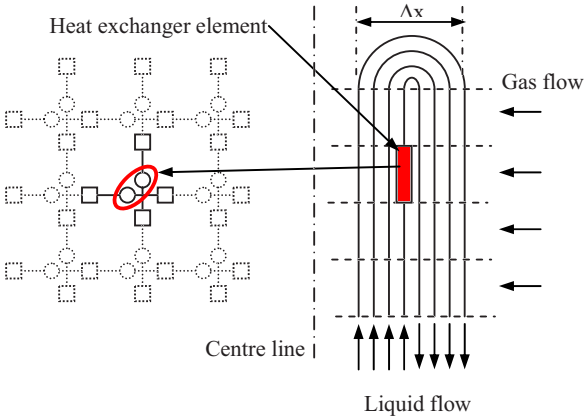

Fig. 5 Discretization of FTX

from a user specified curve, which gives St $Pr^{2/3}$ as a function of the Reynolds number where St is the Standton number and Pr is the Prandtl number.

The metal coefficient is given by

$$\lambda_m = \frac{2\pi kL}{A_s \ln(r_o/r_i)} \tag{24}$$

If there are no extended surfaces (fins) on the tube side, we can write that

$$2\pi L = A_t/r_i \tag{25}$$

where A_t is the tube side heat transfer area. Substitution of Eq. (25) into Eq. (24) leads to

$$\lambda_m = \frac{A_t}{A_s} \frac{k}{r_i \ln(r_o/r_i)} \tag{26}$$

The tube side heat transfer is given by

$$Q_t = A_s U_t \left[T_m - \tfrac{1}{2}(T_{t_i} + T_{t_e}) \right] \tag{27}$$

where U_t is the tube side effective heat transfer coefficient, which is given by

$$U_t = \left(\frac{A_s}{A_t} \frac{1}{\eta_{f_t} \lambda_t} + \frac{0.5}{\lambda_m} \right)^{-1} \tag{28}$$

where η_{ft}, fin efficiency on the tube side surface; and λ_t, tube side surface heat transfer coefficient. The tube side heat transfer coefficient is calculated with the Dittus–Boelter equation, which is given by

$$\frac{\lambda_t D_t}{k} = 0.023\,\mathrm{Re}^{0.8}\,\mathrm{Pr}^n \tag{29}$$

where n is 0.4 for heating and 0.3 for cooling.

Recuperator. The recuperator is modeled with FLOWNEX'S recuperator element. This is a counterflow or parallel heat exchanger (depending on the flow direction of the two streams) divided into a number of increments in the flow direction, as shown in Fig. 7.

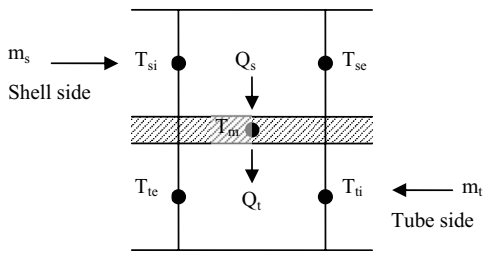

Fig. 6 Notation used to describe heat transfer in a heat exchanger element

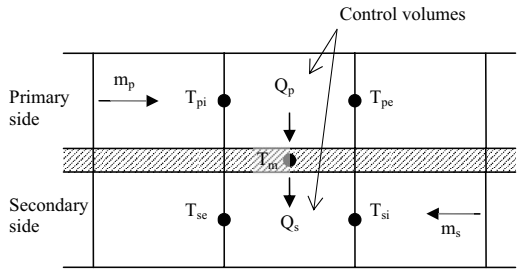

Fig. 7 Discretization of counter/parallel flow heat exchanger

The subscripts in Fig. 7 denote the following: p, primary side; s, secondary side; m, metal; p_i, primary side control volume inlet; p_e, primary side control volume outlet; s_i, secondary control volume side inlet; s_e, secondary control volume side outlet.

Pressure Drop. The pressure drop through a flow conduit increment is given by

$$\Delta p_0 = \frac{fL}{D} \tfrac{1}{2} \rho V^2 + \rho L \frac{dV}{dt} \tag{30}$$

The friction factor is calculated as follows:

$$\mathrm{Re} > 5000: \quad f_t = F_t 0.25 \{ \log[(e/3.7D) + 5.74\,\mathrm{Re}^{-0.9}] \}^{-2} \tag{31}$$

$$\mathrm{Re} < 2300: \quad f_l = \frac{F_l 64}{\mathrm{Re}} \tag{32}$$

where F_t is the turbulent friction multiplier and F_l is the laminar friction multiplier. These multipliers are user specified and are introduced to provide for noncircular cross-sectional channel shapes. For $2300 \leqslant \mathrm{Re} \leqslant 5000$, FLOWNEX interpolates between f_t and f_l.

Heat Transfer. Consider the control volumes shown in Fig. 7. The heat transfer rate to the primary and secondary side fluid control volumes is calculated as follows:

$$Q_p = A_p U_p \left[\tfrac{1}{2}(T_{p_i} + T_{p_e}) - T_m \right] \tag{33}$$

and

$$Q_s = A_p U_s \left[T_m - \tfrac{1}{2}(T_{s_i} + T_{s_e}) \right] \tag{34}$$

The heat transfer coefficients are given by

$$U_p = \left(\frac{1}{\eta_{f_p} \lambda_p} + \frac{A_p}{A_m} \frac{\Delta x}{2k} \right)^{-1} \tag{35}$$

and

$$U_s = \left(\frac{1}{\eta_{f_s} \lambda_s} \frac{A_p}{A_s} + \frac{A_p}{A_m} \frac{\Delta x}{2k} \right)^{-1} \tag{36}$$

where A_p, heat transfer area on the primary side; A_s, heat transfer area on the secondary side; and A_m, heat transfer area in the middle of wall separating the primary side from the secondary side.

For the recuperator model, it is assumed that $A_m = A_s$ and that $\eta_{fp} = \eta_{fs} = 1$. The surface heat transfer coefficients are calculated as follows:

$$\mathrm{Re} > 5000: \quad \lambda_t = \frac{kC_t(0.023)\mathrm{Re}^{0.8}\,\mathrm{Pr}^n}{D_h} \tag{37}$$

$$\mathrm{Re} < 2300: \quad \lambda_l = \frac{k\mathrm{Nu}_l}{D_h} \tag{38}$$

Table 2 Operating points of compressors

Parameter	Units	LP compressor	HP compressor
CMF	(kg/s)sqrt(K)/bar	94.443	52.719
CS	(rev/s)/sqrt(K)	3.481	10.441
PR	Ratio	1.732	1.732
Efficiency	Fraction	0.88	0.88

For $2300 \leqslant \mathrm{Re} \leqslant 5000$, FLOWNEX interpolates between λ_t and λ_l.

Compressors. Compressor performance is usually expressed in terms of the PR and efficiency as functions of nondimensional mass flow and nondimensional speed. The PR of a compressor is defined as the ratio of the total pressure at the outlet (p_{02}) to the total pressure at the inlet (p_{01}). Therefore,

$$\mathrm{PR} = \frac{p_{02}}{p_{01}} \tag{39}$$

The efficiency is defined as

$$\eta = \frac{c_p T_{01}(\mathrm{PR}^{(\gamma-1)/\gamma} - 1)}{w} \tag{40}$$

The nondimensional mass flow is defined as

$$\mathrm{NDM} = \frac{\dot{m}\sqrt{\mathrm{R}T_{01}}}{p_{01}D^2} \tag{41}$$

whereas the nondimensional speed is defined as

$$\mathrm{NDS} = \frac{\mathrm{ND}}{\sqrt{RT_{01}}} \tag{42}$$

For a given machine working with only one type of gas, both R and D will be constant so that it is somewhat more convenient to express the PR and efficiency as functions of corrected mass flow (CMF) and corrected speed (CS), which are defined as

$$\mathrm{CMF} = \frac{\dot{m}\sqrt{T_{01}}}{p_{01}} \tag{43}$$

and

$$\mathrm{CS} = \frac{N}{\sqrt{T_{01}}} \tag{44}$$

The following speed values for the two compressors are assumed: HP compressor, 10,800 rpm; LP compressor, 3600 rpm.

The operating point values of CMF and CS are calculated using the above speed values together with the values of mass flow, pressure, and temperature obtained from the second order cycle analysis. These values together with the PRs and efficiencies are summarized in Table 2.

The PR and efficiency characteristics of the LP compressor are shown in Figs. 8 and 9. These characteristics were obtained by scaling the characteristics of a typical axial flow machine to give the required values of PR and efficiency at the operating point. The characteristics of the HPC have a similar shape but scaled to the right operating conditions.

Turbines. Turbine performance is also expressed in terms of PR and efficiency as functions of CMF and CS. The PR of a turbine is defined as the ratio of the total pressure at the inlet (p_{01}) to the total pressure at the outlet (p_{02}). Therefore,

$$\mathrm{PR} = \frac{p_{01}}{p_{02}} \tag{45}$$

The efficiency is defined as

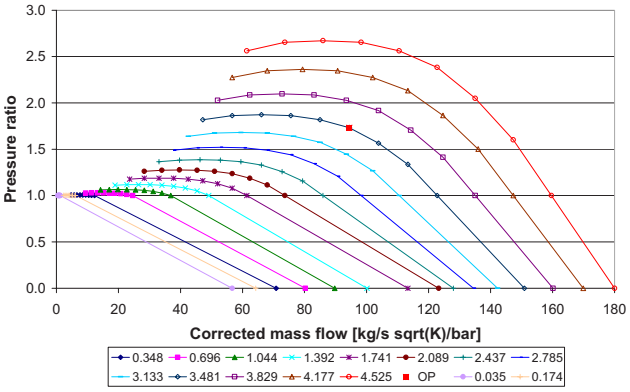

Fig. 8 LPC PR characteristics

$$\eta = \frac{w}{c_p T_{01}(1 - \mathrm{PR}^{(1-\gamma)/\gamma})} \tag{46}$$

where w is the work done by the fluid and γ is the ratio of specific heats.

The CMF and CS are defined as follows:

$$\mathrm{CMF} = \frac{\dot{m}\sqrt{T_{01}}}{p_{01}} \tag{43'}$$

and

$$\mathrm{CS} = \frac{N}{\sqrt{T_{01}}} \tag{44'}$$

The following speed values are assumed for the two turbines: HP turbine, 10,800 RPM; LP turbine, 3600 rpm.

The values of CMF and CS at the operating point are calculated using the above speed values together with the values of mass flow, pressure, and temperature obtained from the second order cycle analysis. These values together with the PR and efficiencies are summarized in Table 3.

The PR and efficiency characteristics of the LP turbine are shown in Figs. 10 and 11. These characteristics were obtained by scaling the characteristics of a typical axial flow machine to give the required values of PR and efficiency at the operating point. The characteristics of the HPT have a similar shape but scaled to the right operating conditions.

Pebble Bed Reactor. FLOWNEX uses a distributed model equivalent to a 2D CFD method to solve the flow, pressure, and temperature distribution inside the pebble bed reactor [7]. Consider a staggered CFD grid in the r-z plane of a cylindrical coordinate system, as shown in Fig. 12.

Figure 13 shows the network representation of the staggered CFD grid with nodes representing the control volume centers and the elements representing the convective fluxes across control volume boundaries.

Equations (1) and (3) are applied to the nodes inside the reactor, whereas an appropriate form of Eq. (2), applicable to flow through a porous medium, is applied to the elements.

The fission heat released inside the pebbles is modeled with a point kinetics neutronics model [8]. The heat transfer inside the pebbles, heat transfer between the pebbles, and heat transfer from the pebble surface to the gas is modeled through an additional network superimposed on the gas flow network, as shown in Fig. 14. A more detailed description of the reactor model can be found elsewhere [9].

Simulations

The FLOWNEX network of the system is shown in Fig. 15. In this section, three cases will be considered, namely, the steady-state

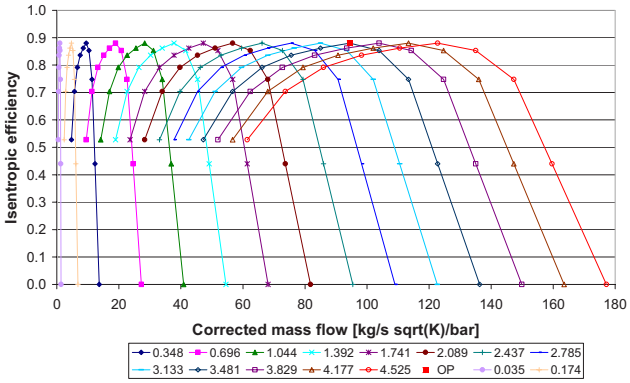

Fig. 9 LPC efficiency characteristics

operation at design condition, startup, and load rejection at full load.

Steady-State Operation at Design Conditions. The only boundary condition of the gas loop is the fixed pressure of 2333.3 kPa at Node 1. The temperature boundary conditions of 22°C are set at Nodes 22 and 25, which are the water side inlets of the precooler and intercooler, respectively. These temperatures affect the helium temperatures through the precooler and intercooler.

The initial speed of the high-pressure turbocharger is intentionally set as 7200 rpm (as opposed to the known value of 10,800 rpm) to demonstrate the code's shaft balancing capability. By specifying an approximate shaft speed and then selecting the appropriate option, FLOWNEX will automatically determine the shaft speed at which the power delivered by the turbine exactly matches the power required by the compressor and any additional loads.

The reactor exit temperature is fixed at 900°C. Alternatively, one can specify a fixed heat transfer. Table 4 compares some Flownex results with the second order cycle analysis results obtained with EES,[1] The agreement between the two sets of results is excellent.

Startup. The initial condition for the startup simulation is the

Table 3 Operating points of turbines

Parameter	Units	LP turbine	HP turbine
CMF	(kg/s)sqrt(K)/bar	72.581	60.644
CS	(rev/s)/sqrt(K)	1.8265	5.2553
PR	Ratio	2.3722	1.230
Efficiency	Fraction	0.91	0.91

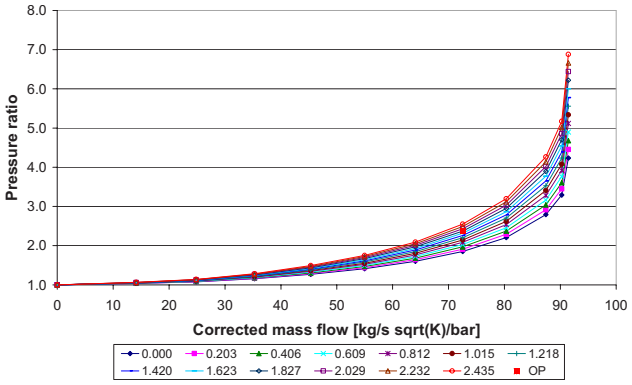

Fig. 10 LPT PR characteristics

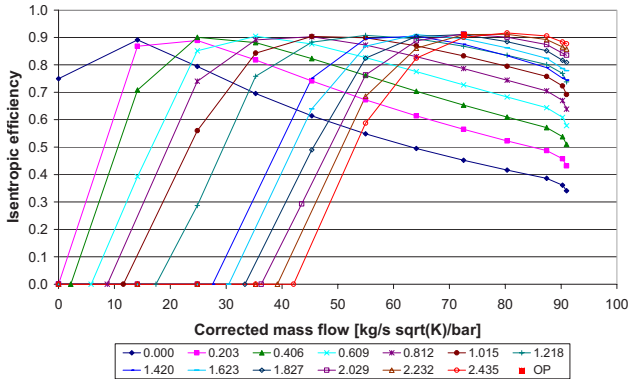

Fig. 11 LPT efficiency characteristics

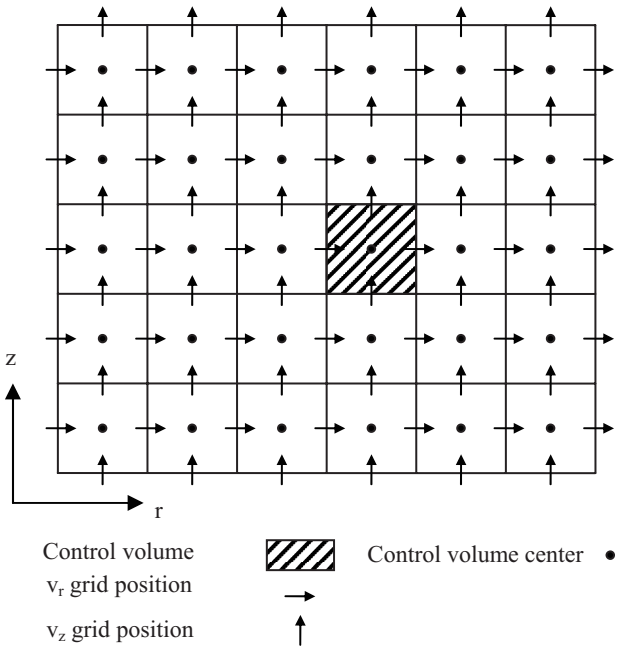

Fig. 12 Staggered CFD grid of the flow domain inside the reactor

[1]Engineering Equation Solver (www.fChart.com).

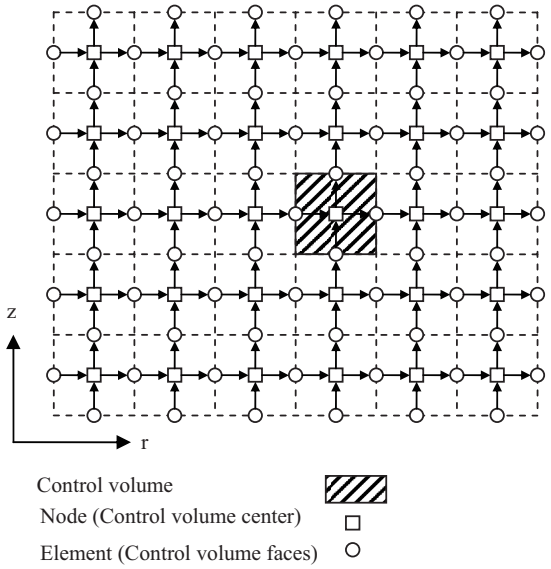

Fig. 13 FLOWNEX network representation of the staggered CFD grid

steady-state solution for a shaft speed of 1 rps for both the HP and LP shafts. The boundary condition for the initial steady-state simulation is a fixed pressure of 3610 kPa at Node 1 and a reactor

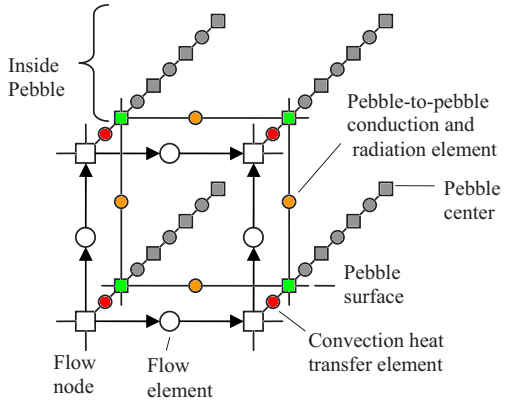

Fig. 14 Network for calculating heat transfer inside the pebbles, between pebbles, and between pebbles and gas

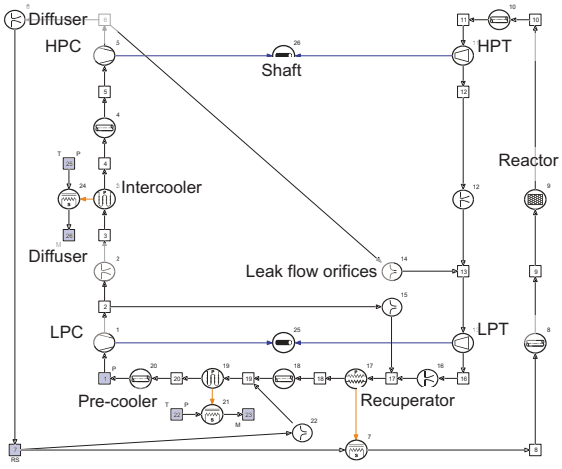

Fig. 15 Flownex network of the direct two-shaft closed intercooled recuperated Brayton cycle PBMR power plant

Table 4 Comparison between FLOWNEX results and second order cycle analysis results obtained with EES

Parameter	Units	Flownex	EES
Mass flow rate	kg/s	127.8	127.8
Network	MW	126.2	126.4
Reactor heat	MW	259.8	260.0
Thermal efficiency	%	48.6	48.6
Maximum cycle pressure	kPa	6967.5	6968.5
HP turbounit shaft speed	rpm	10793	10800
Precooler heat	MW	78.1	78.3
Intercooler heat	MW	53.0	53.0
Recuperator heat	MW	240.2	240.1
LP compressor power	MW	55.1	55.1
HP compressor power	MW	52.9	53.0

outlet temperature of 900°C. The pressure boundary condition at Node 1 was determined through trial and error to give a pressure of 2333.3 kPa after the system has reached full power design point operation. At the start of the transient simulation, the fixed pressure condition at Node 1 is released while the total mass in the system is kept constant.

A controller senses the speed of the LPC/LPT shaft and then adjusts the power of the generator load on the shaft in such a way that the generator initially acts as a motor that drives the shaft and then changes over to a generator load that approaches the design point value as the speed of the shaft approaches the design speed.

Figures 16–20 show the variation of pressures, temperatures, mass flows, shaft speeds and generator power during startup. As can be seen from Fig. 17, the temperature at the inlet of the power

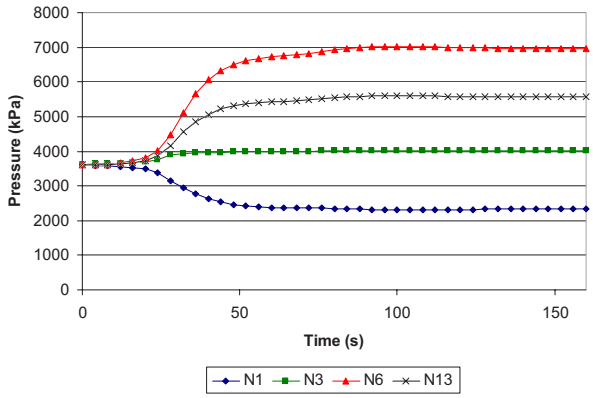

Fig. 16 Variation of pressures during startup (*N*=node)

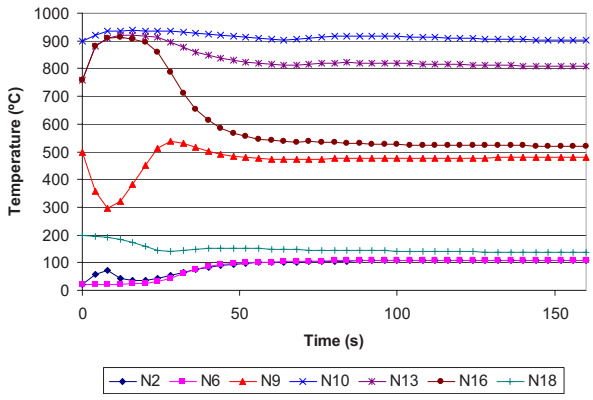

Fig. 17 Variation of temperatures during startup

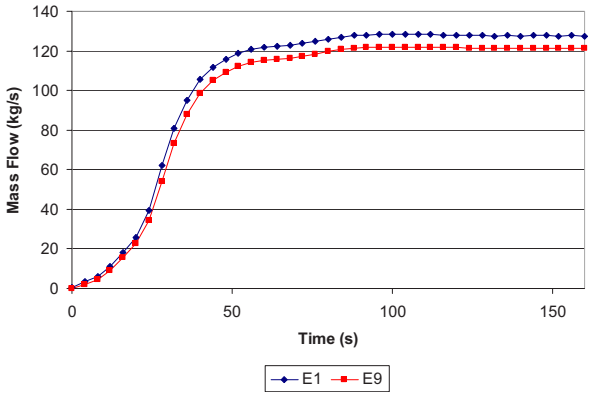

Fig. 18 Variation of mass flows during startup (*E*=element)

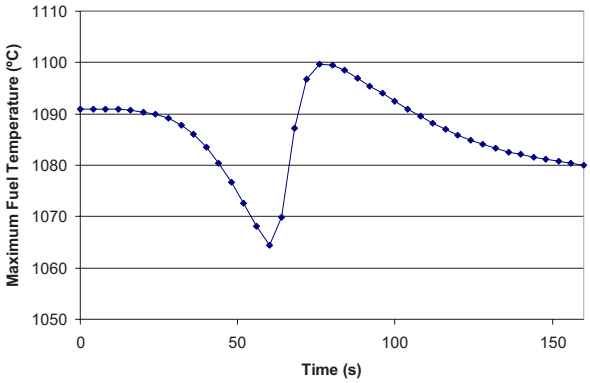

Fig. 21 Maximum fuel temperature during startup

turbine (Node 16) increases above 900°C during startup. Since the power turbine is usually designed for a lower inlet temperature, this may be a problem.

Figure 21 shows the variation of maximum fuel temperature during startup. As can be seen, the maximum fuel temperature does not exceed the maximum allowable value of 1600°C. This is a good example of the information that can be obtained from a system CFD simulation. To obtain the same kind of information without the system CFD approach would require quite more time and effort.

Figures 22 and 23 show the locus plot of the HPC and LPC operating points during startup. While the operating point of the HPC stays well clear of the surge line, the operating point of the LPC at low speeds falls within the surge region. This is undesirable, and it is an issue that warrants further investigation. What this, however, demonstrates is that one cannot select component characteristics with only a steady-state operation in mind. One has to also take into account the impact of component characteristics on system performance during operational transients. This is a task where system CFD analysis is very helpful.

Load Rejection. In this example, the situation is considered where the generator load is suddenly dropped to zero from a full load condition. A controller senses the speed of the LPC/LPT shaft and then adjusts the opening of the bypass valve (Element 22) in an effort to keep the speed of the shaft constant at 60 rps. Figures 24–28 show the variation of pressures, temperatures, mass flows, shaft speeds, and control valve opening during the load rejection transient. As can be seen from Fig. 25 the temperature to the inlet of the reactor increases about 500°C during the load rejection transient. This may be a problem that requires some modifications.

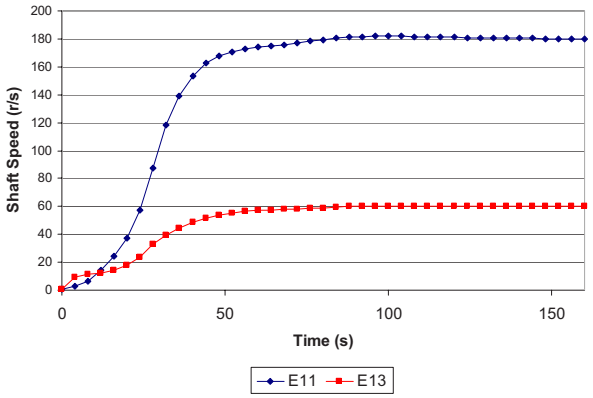

Fig. 19 Variation of shaft speeds during startup (*E*=element)

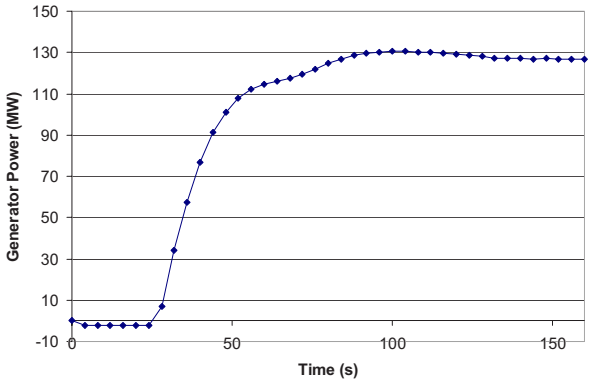

Fig. 20 Variation of generator power during startup

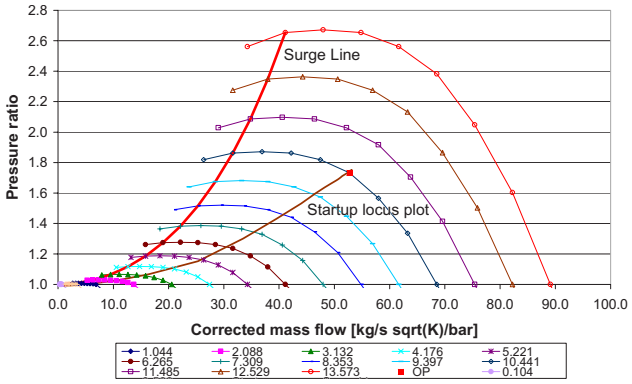

Fig. 22 Locus plot of HPC operating point during startup

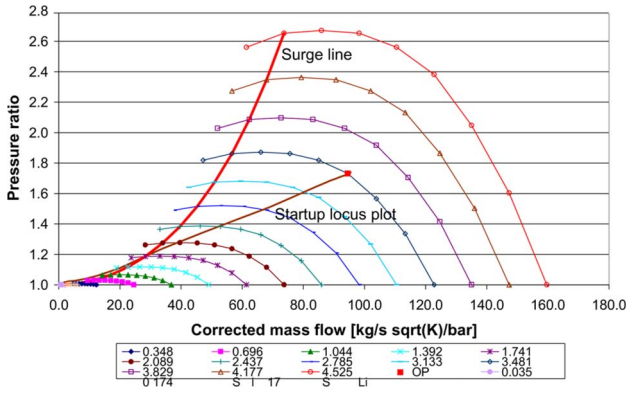

Fig. 23 Locus plot of LPC operating point during startup

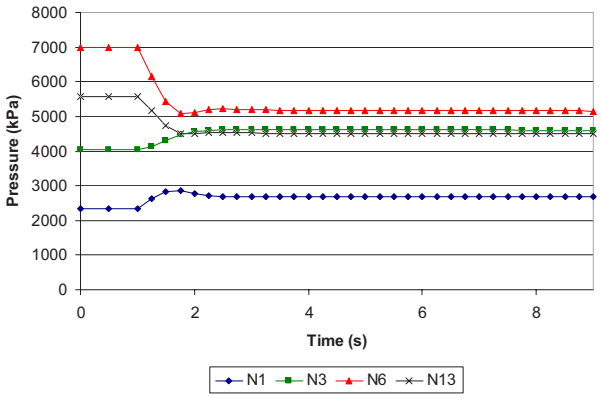

Fig. 24 Variation of pressures during load rejection

From Fig. 27 it can be seen that the speed of the LPT stays nearly constant during the transient, which illustrates the effectiveness of the control mechanism to control the generator speed during sudden variations in the generator load.

This case demonstrates how a SCFD code can be used to test control strategies.

Conclusions

In this paper, the modeling of a pebble-bed-type HTR power plant with the aid of the systems CFD code FLOWNEX is discussed. The different component models are discussed together with a brief description of the overall solution algorithm. The main advantage of the system CFD approach is the excellent balance between accuracy and speed. It allows one to obtain detailed information of component and system performance during both steady-state and transient operation. It is a valuable design tool that finds application in a wide range of design activities such as systems layout, sizing of components, sensitivity analyses, optimization studies, and dynamic characterization. In this paper, it was demonstrated how detailed information on critical parameters such as turbine and reactor inlet temperatures, maximum fuel temperature, and compressor surge margin during operational transients can be obtained. It was also demonstrated how a SCFD code can be used to test control strategies.

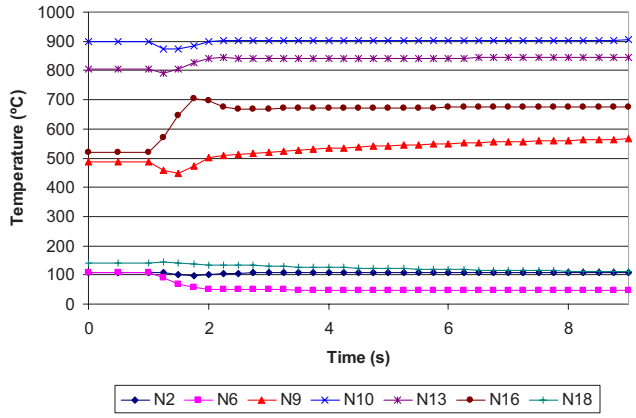

Fig. 25 Variation of temperatures during load rejection

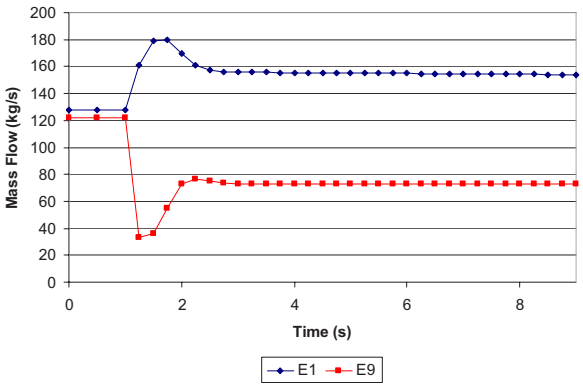

Fig. 26 Variation of mass flows during load rejection

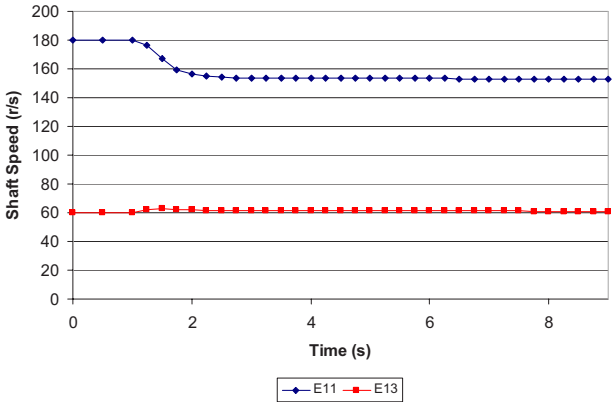

Fig. 27 Variation of shaft speeds during load rejection

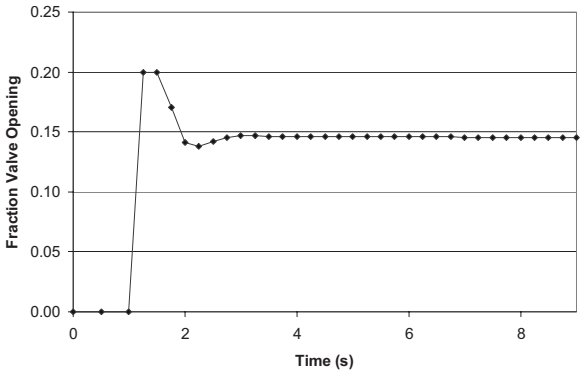

Fig. 28 Variation of valve opening during load rejection

Acknowledgment

The author wishes to thank PBMR (Pty) Ltd. whose financial support made this work possible as well as M-Tech Industrial (Pty) Ltd., developers of the FLOWNEX software.

Nomenclature

b = dead band
C_t = turbulent Nusselt number multiplier
D = diameter or PID controller derivative constant
D_h = hydraulic diameter of the flow conduit
d = mass source
$\dot{E}$ = net energy rate $\dot{Q}-\dot{W}$
f = Darcy friction factor
h = enthalpy
I = controller integral constant or moment of inertia of shaft and all components attached to the shaft
k = thermal conductivity of the tube side fluid
K = loss factor of secondary loss components such as bends or inlets
k = thermal conductivity of the tube wall

L = length of pipe increment
M = Mach number
m = mass of fluid in control volume
$\dot{m}$ = mass flow rate
N = rotational speed
p = static pressure
P = power or controller proportional constant
Pr = Prandtl number
P_{house} = house load (electrical)
P_{grid} = electrical power delivered to grid
$\dot{Q}$ = heat transfer rate
Q = volumetric flow rate
R = gas constant
Re = Reynolds number
RL = restrictor with loss coefficient
r = tube radius
t = time
T = temperature
V = velocity
$\forall$ = volume of control volume
$\dot{W}$ = work done rate
w = specific work
x = controller sensed variable

Greek

x_0 = controller set point
y_0 = controller offset
z = elevation
Δp_0 = $p_{01} - p_{02}$
η = efficiency
ε = error
k = thermal conductivity of the fluid
λ_m = metal heat transfer coefficient
λ = surface heat transfer coefficient
ω = angular speed
θ = angle between flow direction and vertical
ρ = density
τ = time

Subscripts

i = inside or Node i
f = fin
gen = generator
grid = grid
h = hydraulic
in = inlet
j = branch element
mech = mechanical
m = metal
switch = switching efficiency
out = outlet
o = outside
t = tube
turbine = turbine
0 = stagnation conditions
1 = inlet
2 = outlet

Superscripts

o = previous time step
τ = current time step

References

[1] PBMR (Pty) Ltd. Reactor Safety Analysis Report of the South-African Pebble-Bed Modular Reactor (PBMR), Rev. E, Centurion, South Africa.
[2] PBMR Website (www.pbmr.co.za).
[3] Greyvenstein, G. P., and Laurie, D. P., 2002, "A Segregated CFD Approach to Pipe Network Analysis," Int. J. Numer. Methods Eng., **37**, pp. 3685–3705.
[4] Greyvenstein, G. P., 2002, "An Implicit Method for the Analysis of Transient Flows in Pipe Networks," Int. J. Numer. Methods Eng., **53**(5), pp. 1127–1143.
[5] Greyvenstein, G. P., Van Ravenswaay, J. P., and Rousseau, P. G., 2002, "Dynamic Modelling of Heat, Mass and Momentum Transfer in the Pebble Bed Modular Reactor," First International Conference on Heat Transfer, Fluid Mechanics and Thermodynamics (HEFAT 2002), Kruger Park, South Africa.
[6] Swamee, P. K., and Jain, A. K., 1976, "Explicit Equations for Pipe-Flow Problems," J. Hydr. Div., **102**(5), pp. 657–664.
[7] Patankar, S. V., 1980, *Numerical Heat Transfer and Fluid Flow*, McGraw-Hill, New York.
[8] Rousseau, P. G., and Greyvenstein, G. P., 2003, "One-Dimensional Reactor Model for the Integrated Simulation of the PBMR Power Plant," *Proceedings of the First International Conference on Heat Transfer, Fluid Mechanics and Thermodynamics*, Kruger Park, South Africa, Apr. 8–10, 2002.
[9] Du Toit, C. G., Rousseau, P. G., Greyvenstein, G. P., and Landman, W. A., 2005, "A Systems CFD Model of a Packed Bed High Temperature Gas-Cooled Nuclear Reactor," Int. J. Therm. Sci., **45**, pp. 70–85.

Sliding Mode Control of Gas Turbines Using Multirate-Output Feedback

Subrat Panda

Bijnan Bandyopadhyay[1]
e-mail: bijnan@ee.iitb.ac.in

Systems and Control Engineering,
ACRE Building,
IIT Bombay,
Mumbai 400076, India

The advent of electronic controllers in the field of gas turbine control has allowed the implementation of sophisticated control algorithms. The design of a control system requires accurate models of the plant to be controlled. A real-time program for the dynamic simulation of a gas turbine engine has been developed. Most of the control design techniques need the linear representation of a plant at various operating points. In this regard, the linear analysis tool box of MATLAB-SIMULINK (Anon., 2004, SIMULINK: User's Guide, The Math Works, Inc.) has been used to obtain linear models at various operating points. The linear models are discretized at various sampling times. The algorithm for discrete sliding mode control using the output samples has been reviewed and the same has been used to develop a controller for the gas turbine engine. A fast output sampling sliding mode controller is synthesized using a linear model of the engine. The controller developed is implemented in the nonlinear model and simulation with external disturbance is carried out. The responses with and without the controller are compared. It is shown that discrete sliding mode control law can be directly obtained in terms of the output samples and immediate past control function. The control law thus obtained is of practical importance. The algorithm needs the states of the system neither for feedback purpose nor for switching function evaluation. Thus, it is easily implemented in practice. The algorithm is computationally simple and easy to implement on a gas turbine. [DOI: 10.1115/1.2830546]

Keywords: gas turbine engine, mathematical model, nonlinear simulation, linear model generation, discrete time sliding mode, output feedback sliding mode, fast output sampling, multirate output feedback

1 Introduction

Feedback control has been an essential part of gas turbine control from the very beginning. However, it is only recently that computers have been used to implement engine controls. Many engines even today, use hydromechanical controllers, commonly referred to as hydro mechanical units (HMUs), which implement the desired control strategy in terms of cams and mechanical integrators. The changeover to electronic controllers began in the 1970s, which led to higher engine operating efficiencies by allowing tighter engine control, through the use of higher loop gains and improved strategies to reduce transient overshoot or undershoot. It also allows implementation of control algorithms, which would be difficult to implement mechanically. Various control techniques such as state feedback control, linear quadratic control, etc., have been proposed by numerous authors including Watts [1] and De Hoff [2].

A simple and yet robust control technique called sliding mode control is extensively used for numerous practical applications. In the case of sliding mode control, the system states are made to adhere to a selected subset of the state space so as to achieve some desirable dynamics. Traditionally, a relay-based control has been used for this purpose and had its roots in the variable structure system philosophy. Developed in the erstwhile Soviet Union, the concept was pioneered by Vadim Utkin [3]. Researchers have suggested a variety of approaches to obtain sliding mode [4,5].

However, much of the work on sliding mode control had been concentrated on state feedback based control [6–8]. However, it is common knowledge that only the system output is available for the controller design. More often than not, the system output is not coincident with the system state. This leads to the requirement of output feedback based sliding mode control strategies [9,10]. The existing literature on output feedback sliding mode control is very restrictive, by being applicable to only a specific class of systems, even when one looks at the control of linear time invariant (LTI) systems alone. A wider class of systems can be controlled, if one adopts dynamic sliding mode controllers. However, the system complexity is increased in the process. An output feedback sliding mode control philosophy can be applied to almost all controllable and observable systems. We found the answer in the synergy of the multirate-output sampling concept and the concept of discrete-time sliding mode control [11,12]. To the best of the author's knowledge, for the first time sliding mode control is proposed in this paper for gas turbine applications.

A nonlinear gas turbine engine model in MATLAB-SIMULINK [13] environment is created for the control application. The gas turbine is a single spool aeroengine, its data being available in Ref. [14]. Some design point data of the engine are as follows: (a) mass flow at the inlet, 19.9 kg/s; (b) pressure ratio of the compressor, 6.92; (c) fuel flow at maximum power, 0.38 kg/s; (d) rotor speed, 16,540 rpm; (e) thrust of the engine, 14.174 kN.

Several simulations are carried out to test the overall behavior of the engine model. The nonlinear simulation results were validated against the measured data of the engine. Using the linear analysis tool box of MATLAB, linear models at various operating points are obtained. The linear models are later used for controller synthesis using the proposed technique. Nonlinear simulations of the model with the controller are carried out for disturbance rejection. The results of simulation with and without the controller are compared.

2 Engine Model

The first step in developing an engine simulation is the formulation of an analytical model [15]. Here, simulation based on zero-dimensional modeling of the processes in the different gas turbine components with thermodynamic relations and steady-state characteristics (component maps) is attempted. With zero-dimensional modeling, air and gas properties, thermodynamically averaged over the flow cross areas, are used in the calculations.

A gas turbine model, as shown in Fig. 1, is created by arranging (stacking) different predefined components (such as intake, compressors, combustors, turbines, and nozzles) in a configuration similar to the specific gas turbine type to be simulated. The exit gas condition of a component then forms the inlet gas condition of the next component in the configuration.

In order to get a low order dynamic model suitable for control purposes, simplifying modeling assumptions has been made. They are enlisted below.

(a) Constant physiochemical properties are assumed in each main part of the gas turbine, such as specific heat at constant pressure and at constant volume, specific gas constant, and adiabatic exponent.
(b) Heat loss (heat transmission, heat conduction, and heat radiation) is neglected.
(c) In the inlet duct, a constant pressure loss coefficient is

[1]URL: http://www.sc.iitb.ac.in/~bijnan

Manuscript received June 17, 2005; final manuscript received September 13, 2007; published online March 26, 2008. Review conducted by William Rhoden.

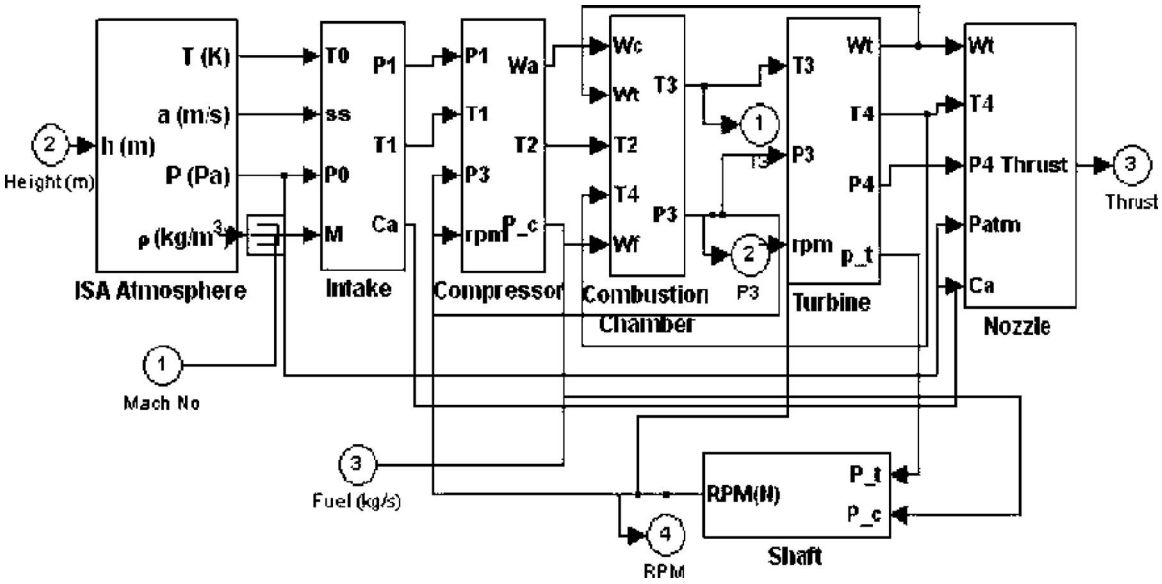

Fig. 1 Engine model created in MATLAB-SIMULINK

assumed. It means that the total pressure loss in the inlet duct is a fixed percentage of its inlet total pressure.

(d) In the compressor, the mass flow rate of air is constant, and there is no energy storage effect: $U2=\text{const}$.

(e) In the combustion chamber, constant efficiency of combustion (η_{comb}) is assumed, constant pressure loss coefficient (σ_{comb}) is assumed, the enthalpy of fuel is neglected, and the combustion chamber is assumed to be a perfectly stirred region (balance volume). It means that a finite dimensional concentrated parameter model is developed and the value of the variables within this balance volume is equal to that at its outlet.

(f) In the turbine, the mass flow rate of gas is constant, and there is no energy storage effect: $U4=\text{const}$.

2.1 Component Creation. The processes in gas turbine components are determined by relations among parameters defined by component maps and thermodynamic equations as given in Ref. [16]. Parameters are air or gas properties and other parameters such as rotor speeds, pressure losses and efficiency of combustion in combustion chamber, energy storage effect in and isentropic efficiency of compressor and turbine, etc.

A predefined design point is calculated first from a set of user specified design point data. The deviation from the design point is calculated by solving a set of nonlinear differential equations. The equations are determined by the mass balance, the heat balance, and the power (energy) balance for all components.

In this model, the mass imbalance that occurs in the combustion chamber is expressed as

$$\frac{dP_3}{dt} = \frac{P_3}{T_3}\left(\frac{dT_3}{dt}\right) + \frac{RT_3}{V_{\text{comb}}}(m_c + m_f - m_t) \tag{1}$$

In the combustion chamber, the conservation balance of the internal energy, where the heat energy flows and the work terms are also taken into account, is expressed as

$$\frac{dT_3}{dt} = \frac{1}{C_v m}[(C_{pa}T_2 m_c + \text{LHV}\,\eta_{cc} m_f - C_{pg}T_4 m_t) - C_v T_3(m_c + m_f - m_t)] \tag{2}$$

The shaft component of the model defines the torque imbalance of the model. The torque or work imbalances between the compressor and turbine are derived from the laws of conservation of momentum and are given as

$$\frac{dN}{dt} = \left(\frac{30}{\pi}\right)^2 \frac{1}{PI}(\text{turbine work} - \text{compressor work}) \tag{3}$$

Similarly, other components of the model are created in the MATLAB-SIMULINK [13] environment.

2.2 State Variables. The first and foremost requirement for simulation of the gas turbine is to identify the variables that will define the plant completely. These variables are known as state variables, which in the presence of externally applied conditions of fuel flow, load, and atmospheric conditions will enable the operating point for each engine component to be found with one step through the engine calculation. The number of state variables required depends on the configuration of the engine.

In the modeling equations above, the set of transformed differential balances includes the dynamic mass balance for the combustion chamber, the pressure form of the state equation derived from the internal energy balance for the combustion chamber, and the intensive form of the overall mechanical energy balance expressed for the number of revolutions N. Therefore, by looking at these equations, we see that the system can be represented completely by three differential equations which are Eqs. (1)–(3). Using this set of state equations, the state vector ($\mathbf{X}$) for the GT model is $\mathbf{X}=(T_3, P_3, N)^T$.

2.3 Input and Output. The engine model is a single input and single output (SISO) system. The fuel flow to the engine is taken as the input to the system. The engine shaft rpm being the only measurable state variable is taken as the output of the system.

3 Review on State and Output Feedback Sliding Mode Control

3.1 Background. Sliding mode control is a robust control scheme based on the concept of changing the structure of the controller in response to the changing state of the system in order to obtain a desired response [17]. A high speed switching control action is used to switch between different structures and the trajectory of the system is forced to move along a chosen switching manifold in the state space. The behavior of the closed loop system is thus determined by the sliding surface.

The biggest advantage of sliding mode control (SMC) is its insensitivity to variation in system parameters, external disturbances, and modeling errors. Sliding mode control enables sepa-

ration of overall system motion into independent partial components of lower dimensions and low sensitivity to plant parameter variations and disturbances. These properties make sliding mode an efficient tool to control high order dynamic plants operating under uncertainty conditions, which is common for control in a wide range of modern technology processes.

The Switching/Sliding Surface: In a sliding mode/variable structure control, the purpose of the switching control law is to drive the plant state trajectory onto a prespecified (user chosen) surface in the state space and to maintain the plant state trajectory for the subsequent time. This surface is called the switching/sliding surface. The switching surfaces are designed such that the system response is restricted to this surface and hence has a desired behavior such as stability or tracking. Although general nonlinear switching surfaces are possible, linear ones are more prevalent in design. The linear switching surface s can be represented as $s=c^T x(t)=0$, where c^T is an $m\times n$ matrix, m the dimension of the input and n the order of the system

3.2 Discrete-Time Sliding Mode Control. The use of digital computers and samplers in the control circuitry in the recent years has made the use of discrete-time system representation more justifiable for controller design than continuous-time representation. In the recent years, considerable efforts have been put in the study of the concepts of discrete-time sliding mode (DSM) controller design [6–8]. In case of the DSM design, the control input is applicable only at sampling instants and the control effort is constant over the entire sampling period. Moreover, when the states reach the switching surface, the subsequent control would be unable to keep the states confined to the surface. As a result, DSM can undergo only quasisliding mode, i.e., the system states would approach the sliding surface but would generally be unable to stay on it.

Gao [7] has introduced a new "reaching law approach" to design the controller for a discrete-time system using state feedback. This reaching law ensures that the system trajectory will hit the switching manifold and thereafter will undergo a zigzag motion about the switching manifold. The magnitude of each successive zigzagging step decreases so that the trajectory stays within a specified band called the quasisliding mode band (QSMB). The reaching law directly dictates the dynamics of the switching function $s(k)$. Then, a SMC control law is synthesized from the reaching law in conjunction with a known model of the plant and the known bounds of perturbations.

For the SMC of a continuous plant, a convenient reaching law is $\dot{s}(t)=-\varepsilon\ \mathrm{sgn}\ (s(t))-qs(t)$, where $\varepsilon>0$, $q>0$ are controlling parameters.

For the SMC of a discrete system, an equivalent form of the reaching law is

$$s(k+1)-s(k)=-q\tau s(k)-\varepsilon\tau\,\mathrm{sgn}(s(k)) \qquad \varepsilon>0 \quad q>0 \quad 1-q\tau>0 \tag{4}$$

where $\tau>0$ is the sampling period. The inequality for τ given in Eq. (4) must hold to guarantee that starting from any initial state, the trajectory will move monotonically toward the switching plane and cross it in a finite time, which implies that the choice of τ is restricted.

Consider the discrete system,

$$x(k+1)=\Phi_\tau x(k)+\Gamma_\tau u(k) \quad y(k)=Cx(k) \tag{5}$$

where x is the n-dimensional state vector, u is a scalar, y is the output vector, and the matrices Φ_τ, Γ_τ, and C are of appropriate dimensions. For all further discussions, we assume that the pair (Φ_τ,Γ_τ) is controllable and the pair (Φ_τ,C) is observable.

Using the reaching law as in Eq. (4) and the definition of the linear switching function as in Sec. 3.1, the state feedback based DSM control is got as

$$u(k)=Fx(k)+\gamma\,\mathrm{sgn}(s(k)) \tag{6}$$

where

$$F=-(c^T\Gamma_\tau)^{-1}[c^T\Phi_\tau-c^TI+q\tau c^T] \tag{7}$$

and

$$\gamma=-(c^T\Gamma_\tau)^{-1}\varepsilon\tau$$

However, this sliding mode control strategy requires full-state feedback. However, in practice, all the states of the system are not always available for measurement, thus posing a problem from the implementation point of view. This prompted the development of output feedback sliding mode control strategies [9,10]. However, sliding mode control strategies based on static output feedback may not exist for all controllable and observable linear systems, whereas dynamic controllers would increase the complexity of the system.

Reference [11] discusses DSMC strategies based on multirate-output feedback. In this technique, the system output is sampled at a rate faster than the control input. Any state feedback based control algorithm can be converted to an output feedback based control algorithm by the use of multirate-output sampling. Consequently, the control algorithm is based on output feedback and at the same time is applicable to all controllable and observable linear systems. Thus, it has the advantage of both state feedback and output feedback control philosophies [11,12].

Let $(\Phi_\tau,\Gamma_\tau,C)$ describe the discrete system sampled at τ s (5) and let (Φ,Γ,C) describe the same system sampled at interval Δ. Let the system input be applied at a sampling interval of τ s and the output be measured after every Δ s, where $\Delta=\tau/N_o$, N_o being an integer greater than or equal to the observability index of the system. Then, a multirate-output feedback representation of the system, with the output sampled at an interval Δ s and the input sampling interval τ s, would be

$$x(k+1)=\Phi_\tau x(k)+\Gamma_\tau u(k)$$

$$y_{k+1}=\mathbf{C}_0x_k+\mathbf{D}_0u_k \tag{8}$$

where

$$y_k=\begin{bmatrix} y(k\tau-\tau) \\ y(k\tau-\tau+\Delta) \\ \vdots \\ y(k\tau-\Delta) \end{bmatrix} \quad C_0=\begin{bmatrix} C \\ C\Phi \\ \vdots \\ C\Phi^{N_o-1} \end{bmatrix} \quad D_0=\begin{bmatrix} 0 \\ C\Gamma \\ \vdots \\ C\sum_{j=0}^{N_o-2}\Phi^j\Gamma \end{bmatrix} \tag{9}$$

From Eqs. (8) and (5), the system state $x(k)$ can be represented as a function of the past multirate output samples and past control as

$$x_k=L_yy_k+L_uu_{k-1} \tag{10}$$

where

$$L_y=\Phi_\tau(C_0^T\mathbf{C}_0)^{-1}C_0^T$$

and

$$L_u=\Gamma_\tau-L_yD_0$$

Thus, by substituting for $x(k)$ in Eq. (6) from Eq. (10), the multirate-output feedback based quasi-SMC law can be derived to be

$$u(k)=F_yy_k+F_uu_{k-1}-(c^T\Gamma_\tau)^{-1}\varepsilon\tau\,\mathrm{sgn}(s(k)) \tag{11}$$

where

$$F_y=-(c^T\Gamma_\tau)^{-1}[c^T\Phi\tau-c^T+q\tau c^T]L_y=FL_y$$

and

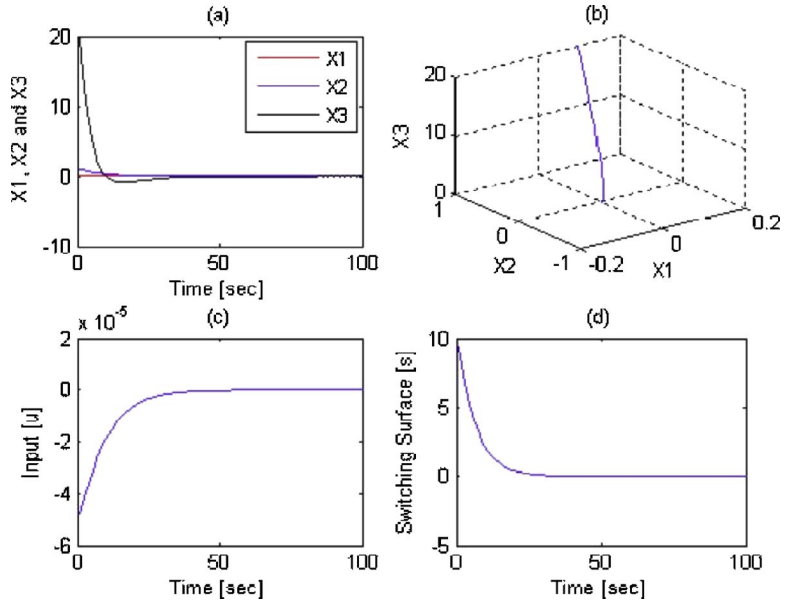

Fig. 2 Linear simulation result

$$F_u = -(c^T\Gamma_\tau)^{-1}[c^T\Phi\tau - c^T + q\tau c^T]L_u = FL_u$$

and the switching surface as

$$s(k) = c^T\Phi_\tau C_0^{-1} y_k + c^T[\Gamma_\tau - \Phi_\tau C_0^{-1} D_0]u(k-1) \qquad (12)$$

Thus, it can be seen from Eqs. (11) and (12) that the states of the system are needed neither for switching function evaluation nor for the feedback purpose.

4 Simulation Results and Discussion

A linear model of the engine at 100% power and static sea level condition is considered for the controller design. The simulation result is shown in Fig. 2. The plot of Fig. 2(*a*) shows the response of the deviation of the state, which converges to zero from given initial condition. The plot of Fig. 2(*b*) shows the phase plot for the system states, which exhibit quasisliding mode motion. Figure 2(*c*) shows the plot of control input from the trim point, which settles to zero because there is no reference. Figure 2(*d*) shows that switching function decreases toward zero from an initial value and stay within a small band in the neighborhood of the switching line. The controller obtained using the linear model is used for the closed loop simulation of the nonlinear engine model. A disturbance in terms of altitude variation is created and controller performance is checked, as shown in the Fig. 3.

5 Conclusion

The controller design for a gas turbine engine using discrete sliding mode has been discussed in this paper, with a brief mention of the modeling and simulation. It is shown that discrete sliding mode control law can be directly obtained in terms of the output samples and immediate past control input. The control law thus obtained is of practical importance. The algorithm needs the states of the system neither for feedback purpose nor for switching function evaluation. Thus, it is easily implementable in practice. The algorithm is computationally simple and easy to implement.

Nomenclature

C_p = specific heat at constant pressure
C_v = specific heat at constant volume
C_{pa} = specific heat of air at constant pressure
C_{pg} = specific heat of gas at constant pressure
LHV = lower heating value of the fuel
m = total mass
m_c = mass flow rate of air in the compressor
m_f = fuel flow rate
m_t = mass flow rate of gas in the turbine
N = speed
N_0 = positive integer greater than observability index of the system
PI = polar moment of inertia of spool
P_3 = combustion chamber pressure
R = gas constant
T_2 = compressor outlet temperature
T_3 = combustion temperature or turbine entry temperature
T_4 = turbine exit temperature
u = input
V_{comb} = combustion volume
η_{cc} = combustor efficiency
π = constant 4 arctan (1.0)

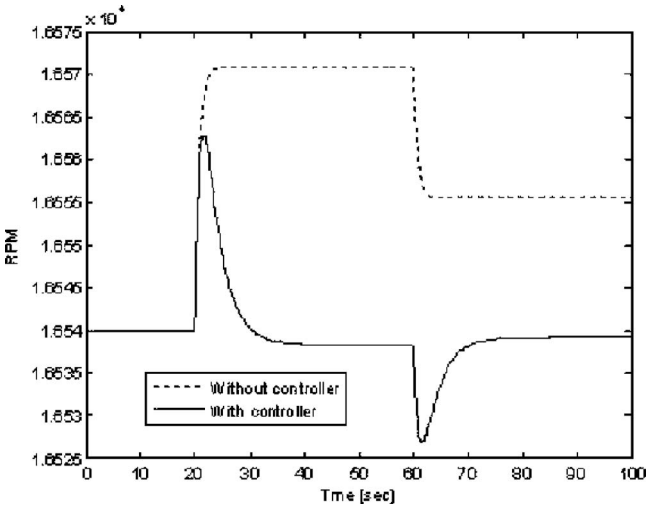

Fig. 3 Nonlinear simulation result

References

[1] Watts, J. W., Dwan, T. E., and Brockus, C. G., 1992, "Optimal State-Space Control of a Gas Turbine Engine," ASME J. Eng. Gas Turbines Power, **114**, pp. 763–767.

[2] De Hoff, R. L., Hall, W. E., Adams, R. J., and Gupta, N. K., 1977, "F 100 Multivariable Control Synthesis," Systems Control Inc., AFAPL-TR-77–35, Vols. I and II.

[3] Utkin, V. I., 1977, "Variable Structure Systems With Sliding Modes," IEEE Trans. Autom. Control, **AC-22**, pp. 212–222.

[4] Furuta, K., and Pan, Y., 2000, "Variable Structure Control With Sliding Sector," Automatica, **36**, pp. 211–228.

[5] Hung, J. Y., Gao, W., and Hung, J. C., 1993, "Variable Structure Control: A Survey," IEEE Trans. Ind. Electron., **IE-40**(1), pp. 2–21.

[6] Katsuhinha, F., 1990, "Sliding Mode Control of a Discrete System," Syst. Control Lett., **14**, pp. 144–152.

[7] Gao, W., Wang, Y., and Homaifa, A., 1995, "Discrete Time Variable Structure Control Systems," IEEE Trans. Ind. Electron., **IE-42**(2), pp. 117–122.

[8] Bartoszewicz, A., 1998, "Discrete—Time Quasi-Sliding Mode Control Strategies," IEEE Trans. Ind. Electron., **IE-45**(1), pp. 633–637.

[9] Diong, B. M., 1993, "On the Invariance of Output Feedback VSCS," *Proceedings of the IEEE Conference on Decision and Control*, pp. 412–413.

[10] Zak, S. H., and Hui, S., 1993, "On Variable Structure Output Feedback Controllers for Uncertain Dynamic Systems," IEEE Trans. Autom. Control, **38**, pp. 1509–1512.

[11] Hagiwara, T., and Araki, M., 1998, "Design of a Stable State Feedback Controller Based on the Multirate Sampling of Plant Output," IEEE Trans. Autom. Control, **33**(9), pp. 812–819.

[12] Bandyopadhyay, B., Thakar, V., Saaj, C. M., and Janardhanan, S., 2004, "Algorithm for Computing Sliding Surface and Sliding Mode Control From Output Samples," *Proceedings of Eighth IEEE Variable Structure Systems Workshop*, Vilanova i la Geltru, Spain, Paper No. 04.

[13] Anon., 2004, *SIMULINK: User's Guide*, The Math Works, Inc.

[14] Gas Turbine Simulation Program, GSP website: http://www.gspteam.com.

[15] Cohen, H., Rogers, G. F. C., and Saravanamuttoo, H. I. H., 1996, "Gas Turbine Theory," Longman Group Limited, England.

[16] Kulikov, G. G., and Thompson, H. A., 2004, *Dynamic Modelling of Gas Turbines*, Springer, London.

[17] Bartoszewicz, A., 1996, "Remarks on Discrete—Time Variable Structure Control Systems," IEEE Trans. Ind. Electron., **IE-43**(1), pp. 235–238.

Low NO_x Advanced Vortex Combustor

Ryan G. Edmonds[1]
e-mail: redmonds@ramgen.com

Joseph T. Williams

Ramgen Power Systems, Inc.,
Bellevue, WA 98005

Robert C. Steele
Electric Power Research Institute,
Palo Alto, CA 94303

Douglas L. Straub

Kent H. Casleton

National Energy Technology Laboratory,
Morgantown, WV 26507

Avtar Bining
California Energy Commission,
Sacramento, CA 95814

A lean-premixed advanced vortex combustor (AVC) has been developed and tested. The natural gas fueled AVC was tested at the U.S. Department of Energy's National Energy Technology Laboratory in Morgantown, WV. All testing was performed at elevated pressures and inlet temperatures and at lean fuel-air ratios representative of industrial gas turbines. The improved AVC design exhibited simultaneous NO_x/CO/*unburned hydrocarbon (UHC) emissions of* 4/4/0 ppmv *(all emissions corrected to 15%* O_2 *dry). The design also achieved less than* 3 ppmv NO_x *with combustion efficiencies in excess of 99.5%. The design demonstrated marked acoustic dynamic stability over a wide range of operating conditions, which potentially makes this approach significantly more attractive than other lean-premixed combustion approaches. In addition, the measured 1.75% pressure drop is significantly lower than conventional gas turbine combustors, which could translate into an overall gas turbine cycle efficiency improvement. The relatively high velocities and low pressure drop achievable with this technology make the AVC approach an attractive alternative for syngas fuel applications.* [DOI: 10.1115/1.2838992]

Introduction

The AVC concept is fundamentally different from conventional swirl-stabilized combustors in the flame stabilization mechanism. The swirling flow of a conventional gas turbine combustor produces a reverse flow along the axis—or core—of the main flow. This back-mixing of hot products ignites the incoming fuel-air mixture and sustains continuous combustion. Achieving less than 3 ppmv NO_x emissions is complicated by the sensitivity to instabilities and sudden flame extinction near the lean blowoff limit [1,2].

In contrast, the AVC flame stabilization is accomplished by a stable vortex adjacent to the main fuel-air flow path. The vortex behavior is virtually independent of the main flow characteristics, which make this method of flame stabilization robust. In order to work properly, the AVC concept must provide flame stabilization by lateral mixing from the vortex region into the main flow. As described in a previous work [3], this is generally accomplished by using wake regions generated by bodies, or struts, immersed in the main flow. This approach ignites the incoming fuel-air mixture by lateral mixing, instead of a back-mixing process. By using geometric features to ignite the incoming fuel-air mixture, instead of pure aerodynamic features, the AVC concept has the potential to be less sensitive to instabilities and process upsets. This is particularly important near the lean flame extinction limit, where small perturbations in the flow can lead to flame extinction.

The results presented are the Phase II development of the AVC concept tested at typical industrial gas turbine operating conditions. The project was a joint effort between Ramgen Power Systems (RPS) and the DOE/NETL with support from the California Energy Commission's Public Interest Energy Research Program. The combustor was nominally 1 MW_t. The emphasis of these tests was to reduce the NO_x emissions within the primary region of the AVC combustor and not to optimize the overall combustor design for the reduction of CO. In Phase I, RPS used the lean-premixed AVC concept to achieve 9 ppmv NO_x and CO [4]. In an independent effort, the U.S. DOE NETL investigated a nonpremixed rich-quench-lean version of the AVC concept to investigate the ability to achieve low emissions and reduce conversion of fuel-bound nitrogen to oxides of nitrogen [5]. The results described below show a dramatic improvement in emission performance for this lean-premixed AVC concept.

Experiment

The AVC hardware tested in this development program was very similar in form to that shown in Bucher et al. [4] (see Fig. 1). The cavity arrangement was not changed significantly, and the main combustor section was also air cooled with some improvements and increased modularity. Downstream of the main combustor, a 14.0 cm (5.5 in.) inner diameter water-cooled section was added for greater CO burnout.

The nominal test conditions are: combustor pressure of 10 atm (147 psi (absolute)), inlet preheat temperature of 603 K (625°F), and total air flow rate of 0.73 kg/s (1.62 lbm/s). Air flow was split into main air, cavity air, and cooling air similar to the combustor described in Bucher et al. [4]. The fuel used in this study was natural gas supplied by the local gas company. Natural gas composition can be found in Edmonds et al. [6].

The existing pressure vessel was fabricated using 24 in. pipe sections and flanges. The combustor components were assembled outside the vessel and lifted into position for testing. The pressure vessel had four 17.8×30.4 cm^2 (7×12 $in.^2$) optical access ports. Optical access was also designed into the AVC for visualization of flow in the cavity region. This was the same test section that was used in the DOE/NETL Simulation and Validation Studies Project [7].

The exhaust gas sample system was updated for measuring 3 ppmv NO_x emissions. The exhaust gas sample was collected through a water-cooled area-weighted sample probe located at the exit of the combustor. The positive pressure gas sample measurements included unburned hydrocarbon (UHC), O_2, NO_x, CO, and CO_2. Sampling details were described in Edmonds et al. [6].

The manufacturer specified instrument accuracy for NO_x was ± 0.2 ppmv. In actual practice, there were several other factors that affected the measurement error, such as process and flow variations. In an attempt to estimate the error in the gas analysis measurements, a three-factor, two-level factorial designed experiment was conducted. This test plan was randomized and the center point was replicated several times to provide an estimate of the

[1]Corresponding author.

Contributed by the International Gas Turbine Institute (IGTI) of ASME for publication in the JOURNAL OF ENGINEERING FOR GAS TURBINES AND POWER. Manuscript received June 26, 2007; final manuscript received July 19, 2007; published online April 3, 2008. Review conducted by Dilip R. Ballal.

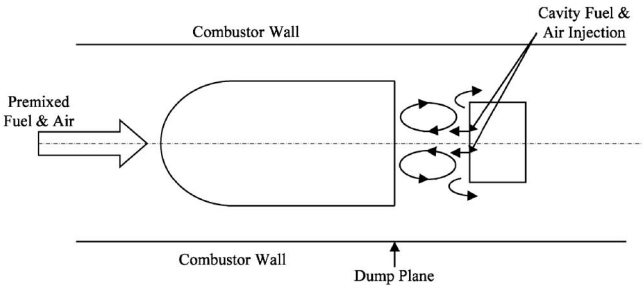

Fig. 1 AVC hardware layout

experimental error. Using this approach and a 95% confidence interval, the NO_x measurements had an uncertainty of ± 1.2 ppmv. An underlying assumption in this error estimate was that the error observed at the center point of the domain was representative of the entire experimental domain.

Results are presented for the following combustor variables:

- cavity equivalence ratio Φ_{cav}
- main equivalence ratio Φ_{main}
- premixer reference velocity

Results and Analysis

Cavity Equivalence Ratio Effect. The cavity equivalence ratio was varied in order to reduce the NO_x emissions and shift the $CO-NO_x$ data to lower combined emissions. These tests were conducted using a 2% liner pressure drop. The cavity equivalence ratio represented the fuel-air ratio of the jets entering the cavity region. These values did not include the local effects of the cooling air; therefore, the actual equivalence ratio in the cavity was lower.

Figure 2 shows the NO_x emissions for the baseline cavity equivalence ratio (i.e., fuel setting 1) and the NO_x levels for lower cavity equivalence ratios. For each fuel setting shown in Fig. 2, the main fuel flow was varied while all other flows and the cooling air pressure drop were kept constant. The different fuel settings represent different levels of fuel flow into the cavity. The NO_x reduction from the baseline fuel setting was approximately 3 ppmv, or in excess of 50%. At a main equivalence ratio of 0.54, the NO_x emissions were below the program goal of 3 ppmv.

Further reductions in the cavity equivalence ratio resulted in flame extinction. It was concluded that these emission levels were optimized for this operating condition and combustor geometry.

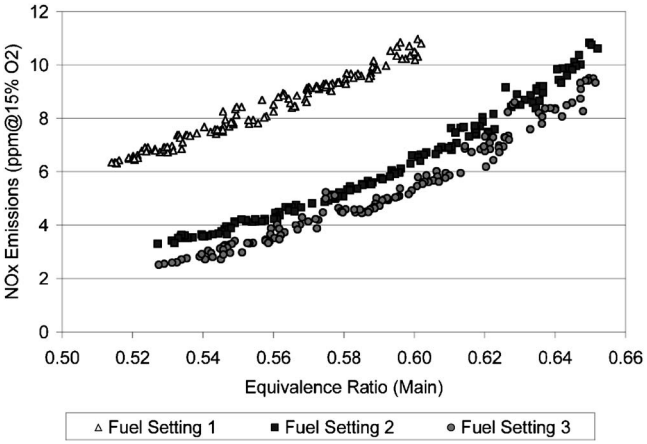

Fig. 2 Effect of cavity equivalence ratio on NO_x emissions. Note: Fuel setting 3 is the leanest cavity operating condition.

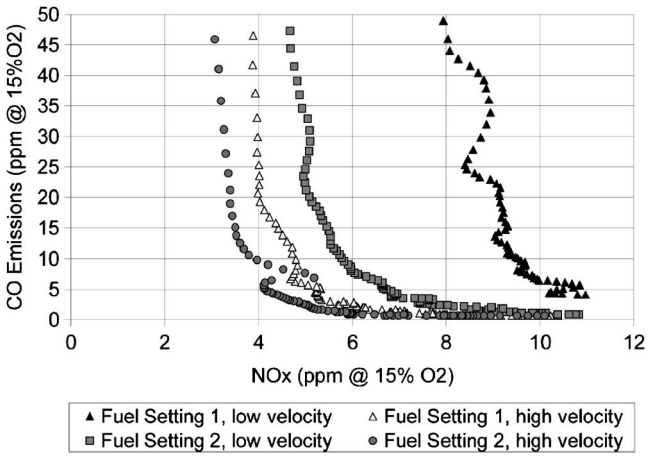

Fig. 3 Effect of cavity equivalence ratio on the $CO-NO_x$ curve. Note: Fuel setting 2 is the leanest cavity operating point for both velocity conditions.

However, with modifications to the combustor configuration, it should be possible to further reduce the cavity equivalence ratio in order to achieve even better performance.

The $CO-NO_x$ data are shown in Fig. 3. This figure shows that the curve shifted to lower NO_x levels for different fuel settings. Furthermore, since each curve shifted to the left but not upward, it was concluded that the CO emissions were insensitive to cavity equivalence ratio. Each curve had the same general form, but moved to decreasing NO_x values with decreasing cavity equivalence ratio.

The emphasis of these tests was to reduce the NO_x emissions within the primary region of the AVC combustor and not to optimize the overall combustor design for reduction of CO to CO_2. The reduction of CO emission was dependent on the postflame zone of the combustion process, which was directly related to the design and shape of the combustor. Optimization of the complete AVC system will be accomplished in the next test program.

The combustor liner cooling air pressure drop was also varied, and results can be found in Edmonds et al. [6]. The cooling air pressure drop varied from 3.5% to 2%. Reducing the pressure drop to 2% increased the operating range for the combustor, allowing for further emission reductions. The primary advantage gained by operating at a lower liner pressure drop was an increase in the cavity equivalence ratio due to decreased cooling air dilution.

Premixer Reference Velocity. Initial results suggested that the reference velocity had no effect on the NO_x and CO emissions. However, experience from exploratory screening tests showed that reduced cavity equivalence ratio could be achieved at a higher bulk reference velocity through the premixer. At high reference velocity, the $CO-NO_x$ curve shifted to the left (see Fig. 3). This test showed that the point at which the CO began to increase suddenly (i.e., the "knee" of the curve) shifted to a lower main equivalence ratio.

The same data showed no variation in the $CO-NO_x$ curve when compared using the total equivalence ratio Φ_{total} based on all air and fuel entering the combustor. This behavior suggests that increasing the reference velocity through the premixer reduced the relative effect of the cooling air. Therefore, the total equivalence ratio was shifted to higher values by increasing the reference velocity, which should produce higher flame temperatures that are favorable for CO oxidation.

Combustion Efficiency. In order to be consistent with the pre-

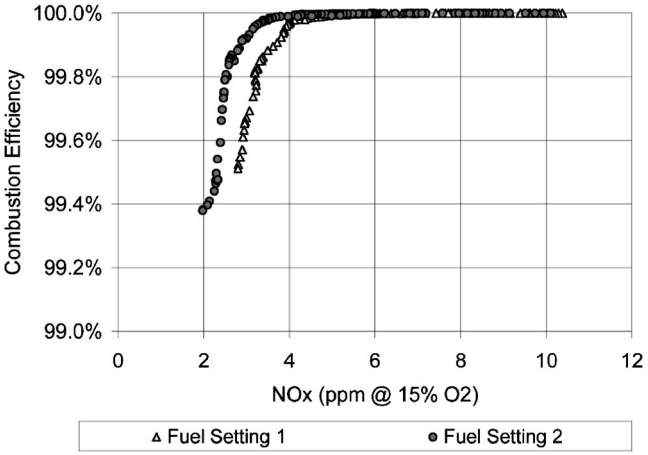

Fig. 4 Combustion efficiency at the highest bulk velocity. Note: Fuel setting 2 is the leanest cavity operating condition.

vious results [4] and to evaluate the completeness of the combustion, the combustion efficiency was calculated based on a heat basis using the following equation [8]:

$$\eta_c = 100\left[1 - 10{,}109\frac{\mathrm{EI_{CO}}}{\mathrm{LHV}} - \frac{\mathrm{EI_{UHC}}}{1000}\right]$$

The terms EI_{CO} and EI_{UHC} represent the CO and UHC emissions expressed in terms of g/kg of fuel. The lower heating value of the fuel is expressed as LHV (J/kg). The second term in brackets represents the energy lost in forming CO instead of CO_2, and the last term in brackets represents the energy lost by unburned fuel.

For the high velocity data shown in Fig. 3, the combustion efficiency was calculated and plotted as a function of the NO_x emissions (see Fig. 4). The combustion efficiency was 99.5% at the NO_x level of 2.5 ppmv. However, for the steep portion of the curve shown in Fig. 4, the uncertainties in combustion efficiency can be significant due to the rapidly changing CO and UHC emissions in this region.

Dynamic Stability. Combustion driven oscillations were evaluated for this AVC configuration. Two high speed pressure transducers (Kistler Model 206) were located in the premixer region of the combustor to detect pressure oscillations. Due to temperature limitations, these sensors were located outside the pressure vessel on semi-infinite coils, a typical approach used in combustor test rigs. Pressure transducer signals were collected on a digital tape recorder (TEAC Model RD-135) at sampling rates of 24,000 samples/s. One transducer was also analyzed using a root mean square (rms) meter, and the output from this rms meter was stored in the data acquisition system. Since the temperature gradient along this semi-infinite coil arrangement was not known, these pressure data were not adjusted for attenuation losses in the system.

The CO emission (primary y axis) and the rms pressure (secondary y axis) as a function of NO_x emissions are shown in Fig. 5 for two main equivalence ratio sweeps. The data shown in Fig. 5 correspond to the high premixer reference velocity data shown in Fig. 3. The rms pressure values remained very low with increasing CO and were about an order of magnitude less than the typically accepted industrial level of 1.5% rms. These rms pressure levels were representative of the levels observed throughout testing. The frequency spectrum of the pressure showed a broad background in which the peak in the background ranged from 250 Hz to 450 Hz. No distinct low frequency peaks were observed in the pressure spectra. Although not an original design goal, the dynamic stability of this design was a significant achievement of this project.

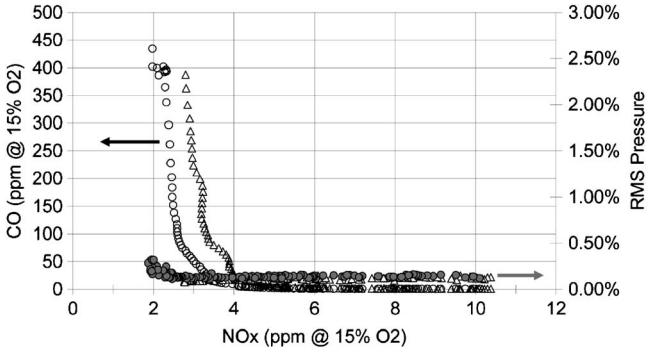

Fig. 5 CO and rms pressure as a function of NO_x

Combustor Pressure Drop. Another advantage of the AVC approach was the elimination of swirl vanes. Generating swirl in the main air flow requires energy that ultimately becomes an efficiency penalty for gas turbines. Gas turbine combustor pressure drops are typically 4–5% at nominal premixer velocities of 150–200 ft/s. The data collected during these tests indicated that the AVC concept was capable of achieving significantly lower pressure drop operation at higher velocities than a conventional swirl-stabilized combustor (see Fig. 6). Preliminary calculations suggest that an increase in overall gas turbine efficiency of up to one full percentage point is attainable with incorporation of the AVC concept. The low pressure drop of the AVC concept is an attractive feature also for applications such as industrial burners.

Emission data taken from Phase 1 and Phase 2 of the AVC development programs are presented in Fig. 7. The lowest combination of CO and NO_x emissions shifted from 10 ppmv and 10 ppmv for Phase 1 to 4 ppmv and 4 ppmv for Phase 2. The scatter in the NO_x data at 4 ppmv was a result of an irregularity in the sample system; however, this variation of 1 ppmv was within the 95% confidence interval for these NO_x measurements. Figure 7 also shows a decrease in NO_x emissions from 6 ppmv to 3 ppmv at a measured CO level of 45 ppmv.

Conclusions

The results show that the AVC approach is capable of achieving less than 3 ppmv NO_x levels at combustion efficiencies in excess of 99.5%. These results have been obtained at realistic industrial gas turbine operating conditions.

The combustor pressure drop was significantly lower than conventional swirl-stabilized combustors translating into efficiency

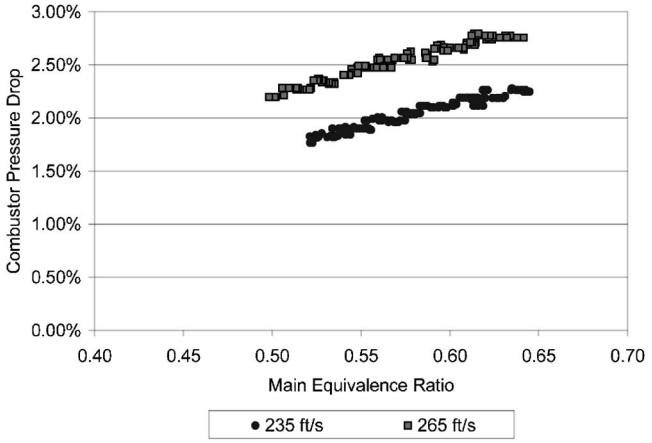

Fig. 6 Combustor pressure drop measurements at two reference velocity conditions

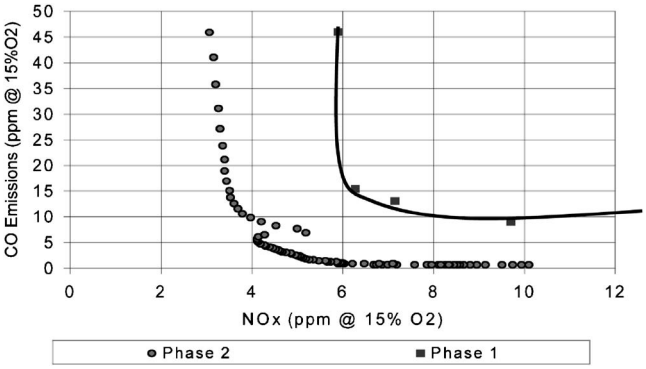

Fig. 7 Comparison of emissions from Phases 1 and 2

improvements in a gas turbine cycle. The AVC combustor pressure drop varied from a minimum of 1.75% at 72 m/s (235 ft/s) bulk premixer velocity to a maximum of 2.8% at 81 m/s (265 ft/s).

The cavity equivalence ratio had a profound effect on the emission performance of this AVC design. A 15% reduction in the cavity equivalence ratio reduced the NO_x emissions by approximately 50% (or about 3 ppmv), without a significant change in the CO emissions. Further reductions in NO_x emissions may be possible by using an approach that reduces the cavity equivalence ratio further without causing flame extinction.

The most noteworthy aspect of the testing was the lack of significant combustion oscillations. A full understanding of this observation will potentially lead to improvements of industrial gas turbine combustor designs.

Acknowledgment

This effort was funded in part by the California Energy Commission under Contract No. 500-02-025. The DOE Fossil Energy Turbines Program provided the remainder of the funding for this effort. We would like to thank Rich Dennis, Tom George, Dan Maloney, and George Richards of the U.S. DOE NETL for their support. Thanks to Mark Tucker and Mike Dera who provided outstanding support during combustion testing at NETL. Thanks also to the scientists at the Air Force Research Laboratory (AFRL), Dale Shouse and Mel Roquemore, for their insights and suggestions.

References

[1] Steele, R. C., Cowell, L. H., Cannon, S. M., and Smith, C. E., 2000, "Passive Control of Combustion Instability in Lean Premixed Combustors," ASME J. Eng. Gas Turbines Power, **122**, pp. 412–419.

[2] Richards, G. A., and Janus, M. C., 1998, "Characterization of Oscillations During Premix Gas Turbine Combustion," ASME J. Eng. Gas Turbines Power, **120**, pp. 294–302.

[3] Hsu, K. Y., Goss, L. P., and Roquemore, W. M., 1998, "Characteristics of a Trapped Vortex Combustor," J. Propul. Power, **14**(1), pp. 57–65.

[4] Bucher, J., Edmonds, R. G., Steele, R. C., Kendrick, D., Chenevert, B., and Malte, P., 2003, "The Development of a Lean Premixed Trapped Vortex Combustor," ASME Paper No. GT2003-38236.

[5] Straub, D. L., Casleton, K. H., Lewis, R. E., Sidwell, T. G., Maloney, D. J., and Richards, G. A., 2005, "Assessment of Rich-Burn Quick-Mix, Lean-Burn Trapped Vortex Combustor for Stationary Gas Turbines," ASME J. Eng. Gas Turbines Power, **127**, pp. 36–41.

[6] Edmonds, R. G., Steele, R. C., Williams, J. T.., Straub, D. L., Casleton, K. H., and Bining, A., 2006, "Ultra-Low NO_x Advanced Vortex Combustor," ASME Paper No. GT2006-90319.

[7] Sidwell, T., Richards, G., Casleton, K., Straub, D., Maloney, D., Strakey, P., Ferguson, D., Beer, S., and Woodruff, S., 2004, "Optically Accessible Pressurized Research Combustor for Computational Fluid Dynamics Model Validation," AIAA J., **44**(3), pp. 434–443.

[8] SAE, 1996–2001, "Procedure for the Calculations of Gaseous Emissions from Aircraft Turbine Engines," Society of Automotive Engineers, Warrendale, PA, SAE Report No. ARP 1533.

Testing of a Small Turbocharger/ Turbojet Sized Simulator Rotor Supported on Foil Bearings

James F. Walton II
Fellow ASME; SAE/ASAIO
e-mail: jwalton@miti.cc

Hooshang Heshmat
Fellow ASME/STLE
e-mail: hheshmat@miti.cc

Michael J. Tomaszewski
e-mail: mtomaszewski@miti.cc

Mohawk Innovative Technology, Inc.
1037 Watervliet-Shaker Road,
Albany, NY 12205

A small rotor designed to simulate a miniature turbojet engine or turbocharger rotor mounted on compliant foil bearings was tested at speeds in excess of 150,000 rpm and temperatures above 260°C (500°F). The simulator rotor-bearing system was operated while positioned in various orientations and was subjected to transient shock impacts exceeding 35g. Subsequent testing was completed to demonstrate the capabilities of miniature thrust foil bearings as well. The tested rotor weighed approximately 400 g and used 15 mm diameter foil journal bearings and a multipad 25 mm diameter double acting thrust foil bearing. Results of the rotor-bearing system dynamics are presented along with experimentally measured natural frequencies, rotor displacements, and thrust load carrying ability. A good correlation between measurement and analysis is observed. Very short rotor acceleration times from rest to maximum speed were also measured. A parallel test simulator has been used to accumulate over 1000 start-stop cycles to demonstrate the life of the bearing and coating. Based on this successful testing, it is expected that the goal of developing oil-free turbochargers and small turbojet engines that operate at high speeds with long life will be achieved. [DOI: 10.1115/1.2830855]

Introduction

Interest in oil-free gas turbine engines for both power and propulsion is rapidly expanding. Engines ranging from mesoscopic sizes intending to operate at speeds approaching 1×10^6 rpm [1–3], to microturbine generators [4–6], to engines producing 1000 shaft hp and those producing more than 22 kN (5000 lb) of thrust are all being pursued. Within this wide range, both the military and commercial markets are pursuing systems that require a small turbojet engine in the 135–300 N (30–65 lb) thrust class. The turbojet engine must be small, lightweight, low cost, durable, fuel efficient, have high performance, and operate reliably, even after being stored for an indefinite period of time. A cross section of a typical small turbojet engine is shown in Fig. 1.

The requirements for high performance, long-life bearings for this new class of machines are severe. Conventional rolling element bearings are severely challenged by the speed and load capacity required. Additionally, unless the process fluid can be used as a lubricant, an external lubrication system will almost certainly be required for the bearings. The alternative of oil-lubricated hydrodynamic bearings is not much more appealing. Again, a lubrication system is required, and at the high speeds envisioned for these machines, there will be significant bearing power loss. The requirement for a lubrication system for either of these alternatives also brings with it the requirements for a sealing system with its inherent losses, leakage, and other environmental concerns associated with the presence of a lubricant.

Eliminating the oil-lubricated bearings and associated supply system will simplify the rotor system, reduce system weight, and enhance performance but will increase internal bearing compartment temperatures, which will ultimately require bearings capable of operating at temperatures approaching 650°C and at high speeds and loads. Besides surviving the extreme temperatures and speeds, the oil-free bearings will also need to accommodate the shock and vibration conditions experienced in mobile applications.

Foil Bearing Background

Although the air lubricated compliant surface foil bearing is less familiar to many designers than rolling element or liquid lubricated hydrodynamic bearings, this is a mature technology as evidenced by the breadth of the completed technology development work [7–16]. The fundamental feasibility and operation of the compliant foil bearing (CFB) for gas turbine engines has also been demonstrated under a wide range of temperature, shock, load, and vibration conditions at speeds in excess of 700,000 rpm, temperatures exceeding 650°C, and loads approaching 4200 N (942 lb) [17,18]. Besides the advances that have increased the load, damping, and temperature capabilities, the application of CFBs to gas turbine engines draws on a long and successful application history. CFBs have been applied to air cycle machines [19], industrial compressors [20], turboexpanders [21], turbochargers [22], cryocoolers, cryogenic pumps, and other extreme environmental systems [23,24]. However, limitations in high-temperature life have limited their application to gas turbine engines until now.

Foil bearings, as shown schematically in Fig. 2, combine a compliant structural support element with a self-generating hydrodynamic component. This twofold mechanism of imparting stiffness and damping to the system makes these bearings unique. The bearing's compliant support structure can consist of one or more corrugated bump foils or cantilevered segments, which offer great flexibility in obtaining dynamic characteristics geared to a specific system. The complaint construction allows the foils to deform under load, be it dynamic rotor motion or the generated hydrodynamic pressures, so that the converging wedge formed between the rotor and bearing surface is maintained even as speed and temperature vary. In essence, the compliance permits the bearing to accommodate rotor centrifugal and thermal growth, as well as thermal and mechanical deformations of the bearing housing, without compromising bearing performance.

Simulator Rig

An existing experimental rotor-bearing test rig was modified for use in demonstrating the operation of a foil bearing supported rotor (two journal bearings and two thrust bearings) at representative speeds and temperatures (see Figs. 3–6). A photograph of all internal rig components, including the shaft and foil bearings, is shown in Fig. 4. The general requirements for small gas turbine engines of up to 290 N thrust typically include operating speeds of between 90,000 rpm and 150,000 rpm, and would experience bearing compartment temperatures of approximately 290°C, assuming that compressor bleed cooling air flow is available for bearing thermal management. Drive power was provided through a simple impulse turbine machined as an integral part of the shafting. A double bucket impulse turbine design was used to minimize thrust loads on the thrust bearing for the initial rotor-bearing dy-

Contributed by the Internal Combustion Engine Division of ASME for publication in the JOURNAL OF ENGINEERING FOR GAS TURBINES AND POWER. Manuscript received October 15, 2004; final manuscript received October 3, 2007; published online March 26, 2008. Review conducted by Dilip R. Ballal.

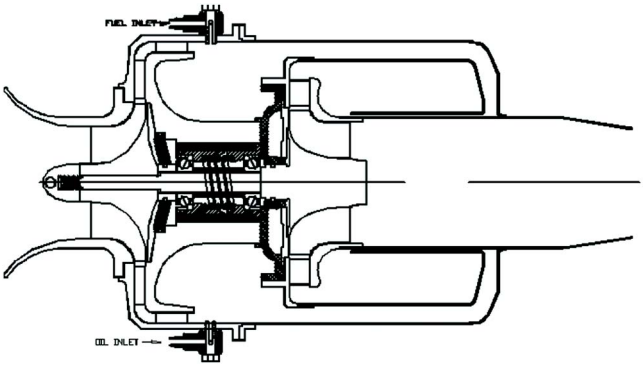

Fig. 1 Typical small turbojet engine cross section with conventional rolling element bearings

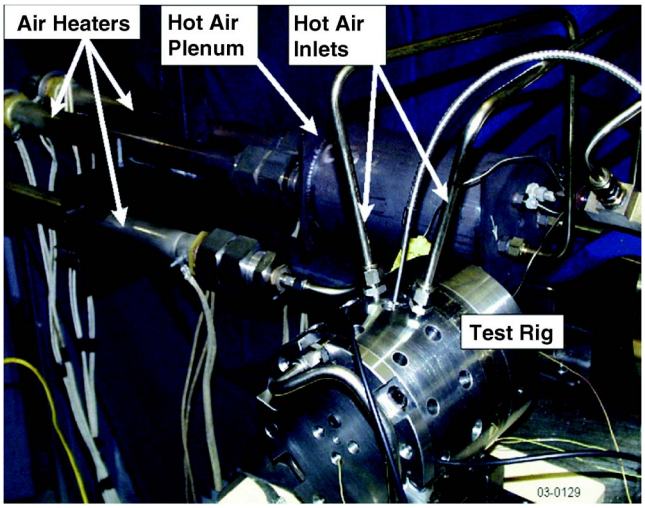

Fig. 3 Rotor-bearing system demonstrator test rig

namic response and stability testing. To accommodate elevated temperatures, the primary rig modifications consisted of adapting an existing heated air system to provide the high bearing compartment temperatures. A series of Hotwatt electrical resistance tubular heaters consisting of four heating units used in two parallel lines provided 20 kW of heating power. The two heated air lines were vented into a single plenum with the plenum outlet directing hot air into the test rig. The test rig cross section shown in Fig. 5 identifies the hot air flow path, bearing locations, and instrumentation. A schematic of the rotor configuration with dimensions is shown in Fig. 6.

Once the rig hardware was fabricated and the shaft balanced to 0.144 g mm/plane, the rig was assembled with workhorse bearings for an ambient test run to 150,000 rpm to verify proper operation and to check instrumentation. The operation of the test rig was very smooth with rotor motions less than 2.15 μm as shown in Fig. 7. Case vibrations were less than 0.15g. The temperature and speed data plot from this check run is shown in Fig. 8. During

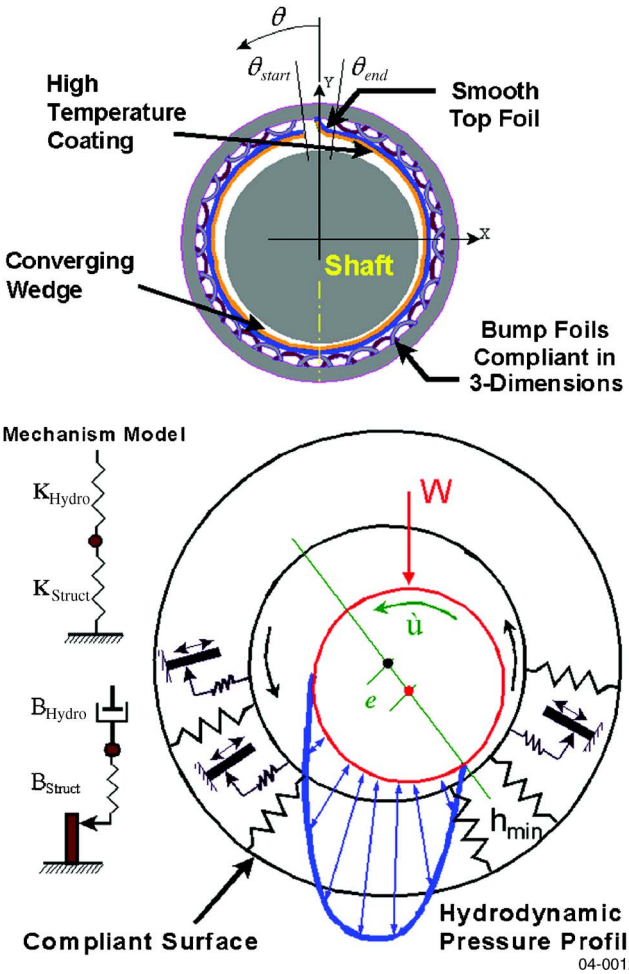

Fig. 2 Compliant foil bearing operating mechanisms

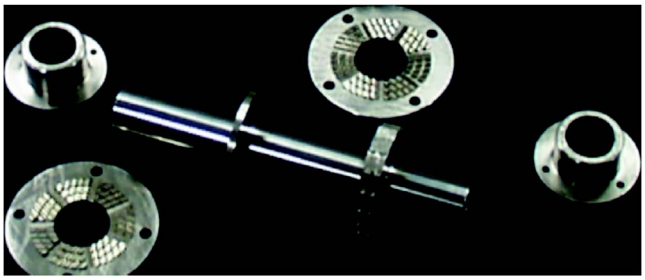

Fig. 4 Test shaft, journal foil bearings, and partially assembled thrust foil bearings

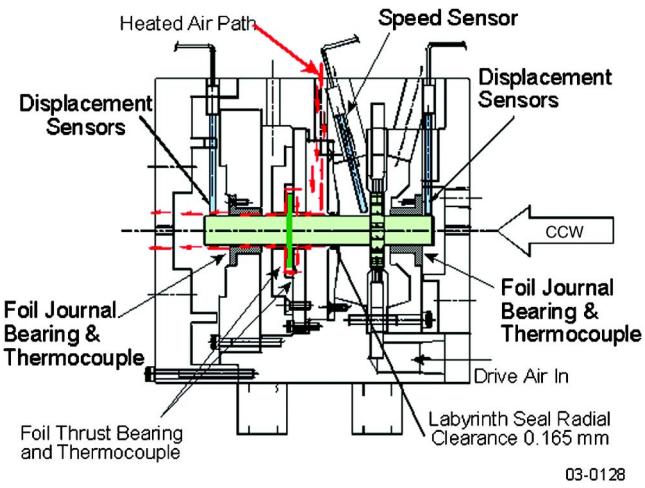

Fig. 5 Test rig cross section and instrumentation

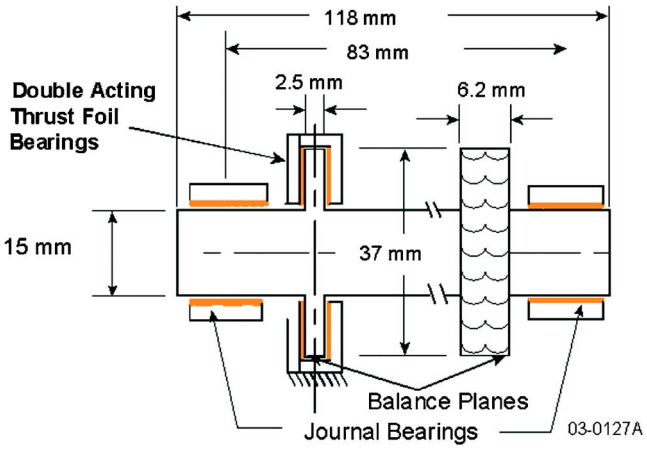

Fig. 6 Test rig dimensions and arrangement

the initial ambient temperature testing, bearing temperature did not exceed 60°C or approximately 21°C above ambient temperatures. These results confirm that thermal runaway is not a factor in rig testing. The rig was then disassembled for inspection and for incorporation of the newly designed journal and thrust foil bearings. All rig internal components were inspected with no discrepancies or abnormalities noted. The rig was reassembled incorporating the newly designed foil journal (two each) and thrust bearings (two each).

The test cell was prepared and the test rig was mounted into place. Instrumentation was connected to the MiTi® high-speed data acquisition system and checked for proper operation. A successful five min prototype bearing ambient check run was made to

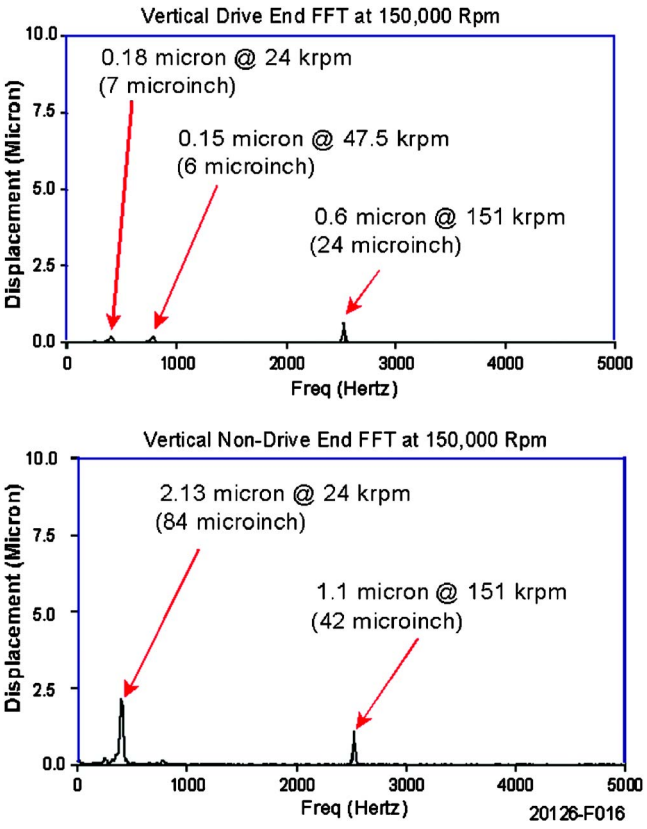

Fig. 7 Instantaneous Fourier fast transform spectrum of rotor motion when operating at 151,500 rpm

150,000 rpm. The operation was smooth throughout the speed range. No thermal spikes were encountered and all instrumentation checked out properly. Based on these results, the decision was made to commence testing. The ambient check run data plot is shown in Fig. 9.

Thermal Testing

The goal of the initial test effort was to run the foil journal bearing to representative speeds, temperatures, and time periods. These parameters were defined for a hot section foil journal bearing at 130,000 rpm and 288°C. Since future system requirements may dictate higher performance operation, the test plan called for testing to 150,000 rpm and at 288°C.

In order to reach these goals, the test plan called for incrementally expanding the operational envelope of the prototype foil journal bearing. The first test was the 5 min ambient temperature check run as described above. The next test conducted was a 15 min run with 205°C air introduced to the inlet of the rig (see Fig. 10). The purpose of this test was to check the operation of the rig inlet heaters and to make an initial determination of the behavior of the journal and thrust bearings in a moderately heated environment. The configuration of the seals within the test rig was such that all internal components were exposed to elevated temperatures. The bearing temperatures were increased to 55–65°C, while the speed was varied between 90,000 rpm and 100,000 rpm. The bearing temperatures were directly related to speed, and none of the bearings showed any sign of thermal runaway, thus indicating proper operation.

With the successful completion of the 15 min initial heated check run with 205°C air to the rig, the next goal was to assure that the bearings would achieve thermal equilibrium when exposed to slightly elevated temperatures for a substantial period of time (see Fig. 11). In this next test, 93°C air was introduced into the rig for 2 h, while the rotor was held at a speed of 85,000 rpm. This test began by incrementally increasing the speed to 150,000 rpm and then stabilizing the speed at 85,000 rpm for 1 h. During the test, the bearing temperatures increased to between 32°C and 43°C and then stabilized. The observed temperature rise was limited since an intermediate shaft seal was not installed and the drive turbine air was delivered at room temperature. This combination of mixed air and a cooler turbine limited the temperature rise. After it was determined that thermal equilibrium was attained with all bearings, the rig was accelerated to 150,000 rpm, decelerated to 70,000 rpm, then accelerated to 100,000 rpm. Bearing temperatures increase and decrease with speed, but, as expected, those bearings at the nondrive end of the rotor are more affected by the speed changes. This 2 h test proved that both the journal and thrust bearings were tolerant of speed variations at slightly elevated shaft temperatures.

Following this test run, the rig was once again disassembled to install an air seal that would allow the heated air to reach both thrust bearings and the nondrive end journal bearing but would prevent elevated temperatures from reaching that portion of the rig, which contained the instrumentation and the drive end journal bearing. This was necessary to assure that the internal instrumentation was not damaged due to continuous exposure to high heat. The rig was then inspected and reassembled with the subject air seal to continue testing.

The next test that was conducted consisted of a series of accelerations/decelerations from 75,000 rpm to 150,000 rpm as 345°C air was supplied by the heaters to the inlet of the rig until the prototype journal bearing reached the target of 290°C (see Fig. 12). The thermal gradients encountered by the bearings during this 1 h 20 min test, coupled with the simultaneous rapid speed excursions, presented some of the most demanding operational conditions that the foil journal and thrust bearings expected to encounter in the candidate application. Once again, the operation of all bearings was flawless. Vibrations were very low, and the bearing thermal response was exactly as expected.

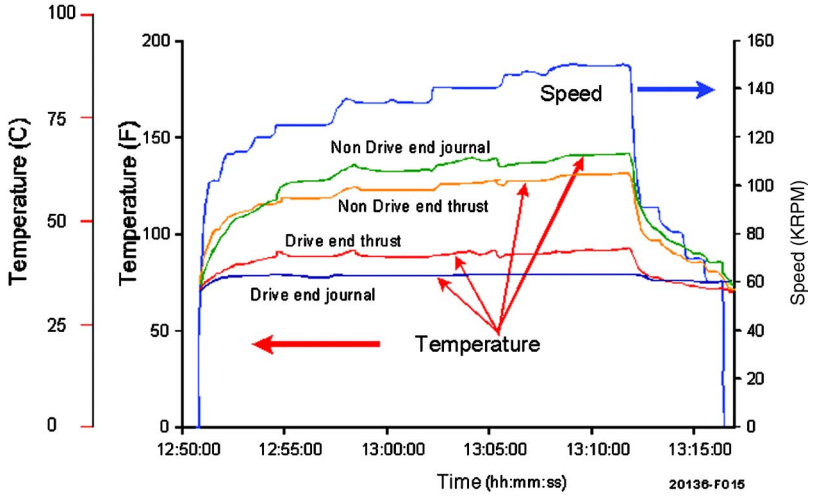

Fig. 8 Rig thermal check out run with slave bearings

Having demonstrated that the prototype foil thrust and journal bearings have met all design intent and have proven that their design is robust with more than adequate margin, the rig was then readied to conduct a 2 h simulated mission test. The 2 h simulated mission test was designed to demonstrate the operational durability of a foil journal bearing operating in the hot section of a small turbojet engine. Since the heated air was directed through the foil thrust bearing, this test would also demonstrate that compliant foil thrust bearings can meet the operational requirements of a completely oil-free engine.

The test began with 345°C air supplied to the inlet of the rig, while a snap (i.e., rapid) acceleration to 150,000 rpm was performed, followed by snap deceleration to 75,000 rpm (see Fig. 13). These snap acceleration and deceleration maneuvers subjected the bearings to high thermal gradients while also imposing transient dynamic loads on the system. The rig was then brought to approximately 260°C, and the speed rapidly increased to 150,000 rpm (115% maximum speed). This subjects the bearing to a full dynamic load while at maximum required temperature. The rig was then kept at a full temperature of 290°C and 115% speed of 150,000 rpm for 1 h and 20 min, after which a snap deceleration to 75,000 rpm was performed to demonstrate dynamic response capability after a full thermal soak.

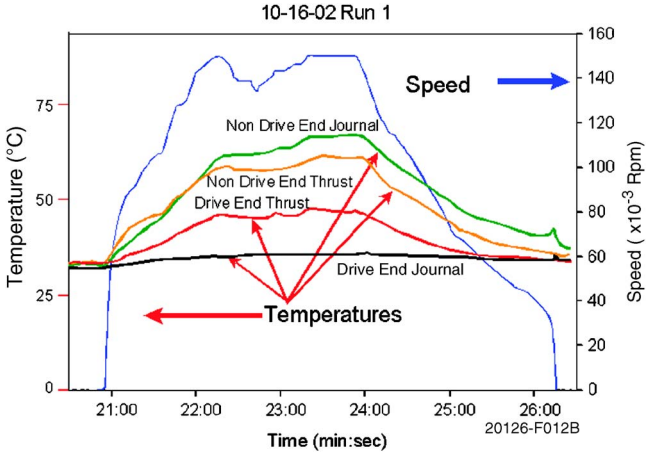

Fig. 9 Prototype bearing ambient check run data plot

Dynamic Testing

Following completion of the thermal testing, tests to demonstrate the robustness of the CFB under severe conditions was conducted. The first in these series of tests was to demonstrate that the CFB continues to operate properly even when subjected to severe shock loads. This series of tests consisted of running the rig at 100,000 rpm, raising one end of the rig to various heights and

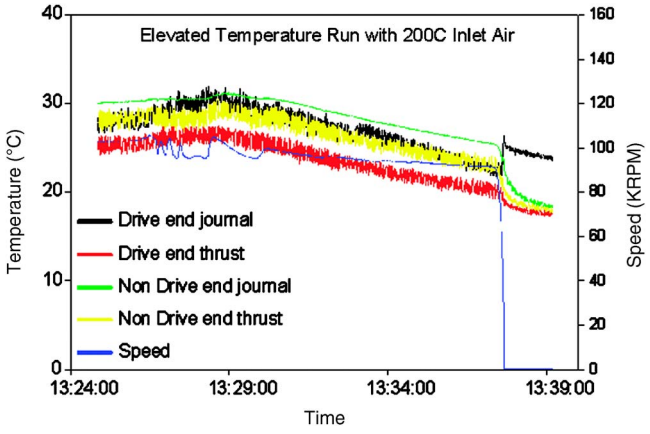

Fig. 10 Initial 15 min heated inlet air check run

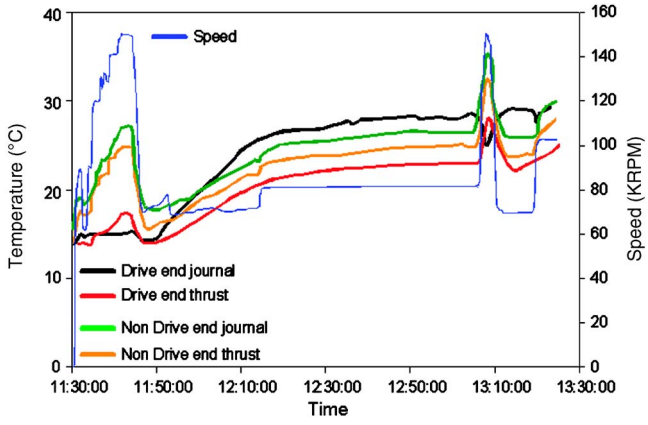

Fig. 11 2 h durability test run with 50°C bearing air

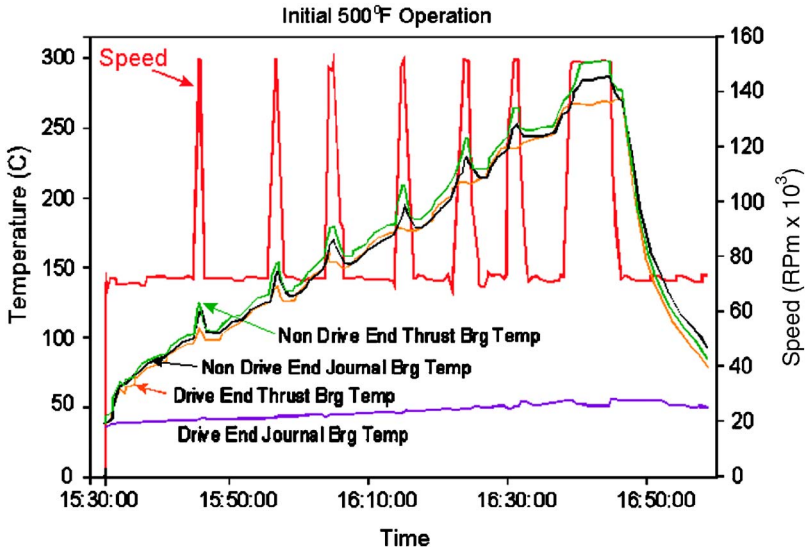

Fig. 12 Cyclic test to 290°C and 150,000 rpm

dropping it. A total of ten different shock tests were conducted at up to 90*g*. As can be seen in Fig. 14, the case mounted accelerometer recorded a shock of 38*g*s. Within approximately 20 ms, rotor motions were nearly normal and were fully recovered in about 75 ms. These *g* forces are well above any that would be experienced during normal flight conditions, demonstrating more than an adequate operating margin. It is understood from this test that the rotor excursion during the transient was a bit high; however, this particular bearing was not designed for the high shock levels tested, yet no evidence of rubs in either the bearing or the shafting was observed. A peak hold synchronous vibration trace of shaft motions was recorded following each shock event. As shown in Fig. 15, the orbit size remains smaller than 2 μm (0.07 mil), and the operation is steady and smooth. At approximately 30,000 rpm, the shaft touches down onto the lubricious coating of the compliant top foil.

The next series of tests were to explore vertical operation of the journal bearing (see Fig. 16). A vertical operation of a compliant foil journal bearing is one of the most challenging operating modes possible. The forces operating on the bearing change drastically compared to a horizontal operation. Without the 1*g* loading on the bearing, the tendency of most hydrodynamic bearing supported rotor systems is to become unstable. In a typical unloaded hydrodynamic bearing, the cross coupling stiffness terms tend to dominate rotor response and cause instability. However, as seen in Fig. 16, very little change in rotor response when compared to a base line horizontal run is observed.

Yet another challenging test of the rotor-bearing system was the +90 deg/−90 deg roll motion (see Fig. 17). As with the other tests, a synchronous tracking plot was recorded during coastdown from 150,000 rpm. The operation appeared normal and did not exhibit any abnormal characteristics. The orbits were small and the system remained stable throughout the test.

A summary of key test results is shown in Fig. 18. It should be noted that, as a result of over ten shock tests at up to 90*g*, over 1 h at temperatures in excess of 260°C, as well as the simulated steady state roll position tests, the rotor operation is only minimally affected. These results clearly show the robustness and durability of the compliant foil bearings for this application.

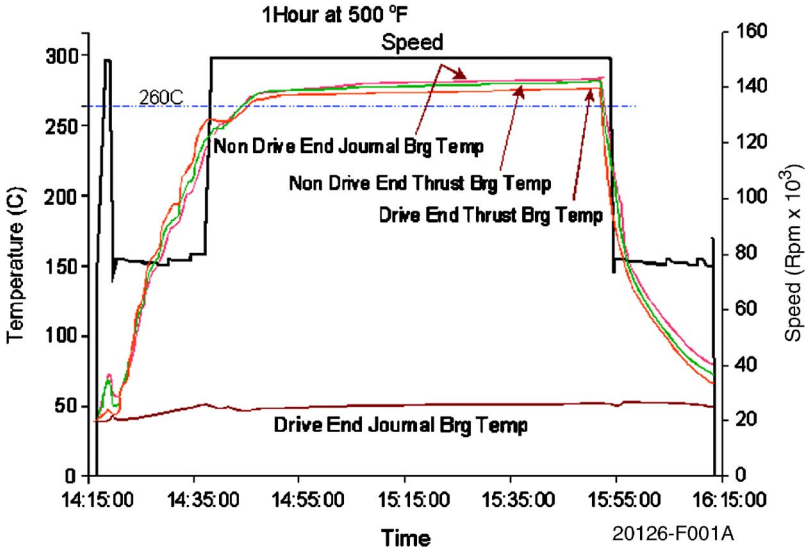

Fig. 13 2 h simulated mission test

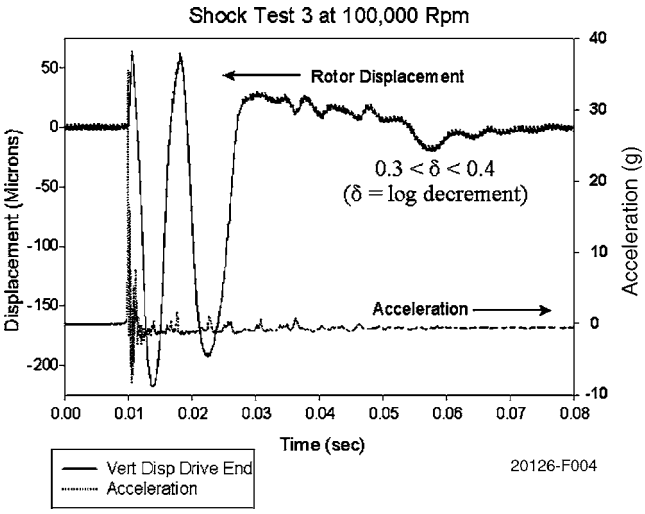

Fig. 14 Rotor shock response while at 100,000 rpm

Conclusions

The feasibility of applying compliant foil bearings to small turbojet engines has been demonstrated under a wide range of temperature, shock, load, and speed conditions. Tests to 150,000 rpm, at bearing temperatures above 260°C, under shock loading to 90*g* and rotor orientations including 90 deg pitch and roll, were all completed successfully. Under all conditions tested, the foil bearing supported rotor remained stable, vibrations were low, and bearing temperatures were stable. Overall, this program has provided the background necessary to develop a completely oil-free turbojet or high efficiency turbofan engine.

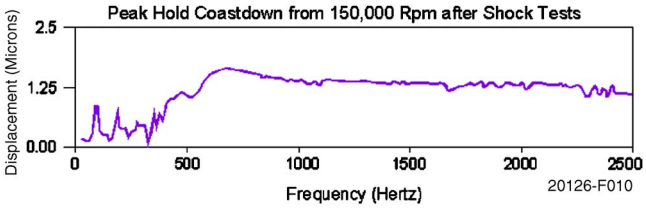

Fig. 15 Postshock test peak vibration during coastdown

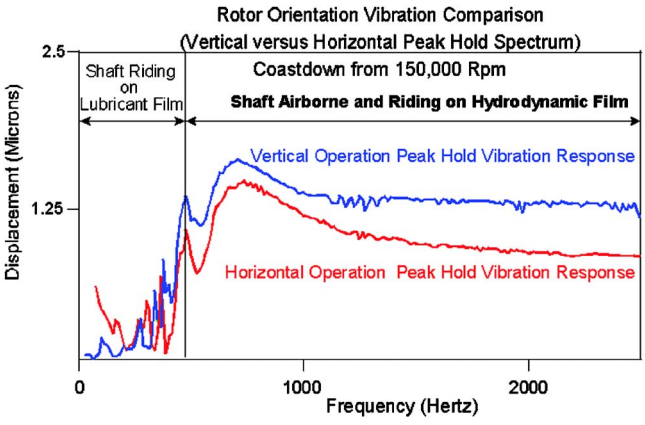

Fig. 16 Comparison of peak rotor vibrations during coastdown for vertical and horizontal shaft orientations

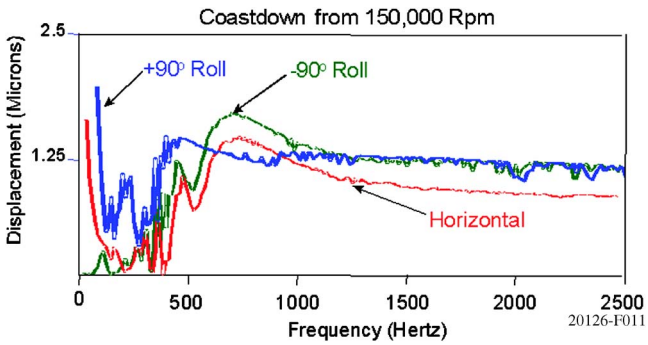

Fig. 17 Peak coastdown vibration after ±90 roll

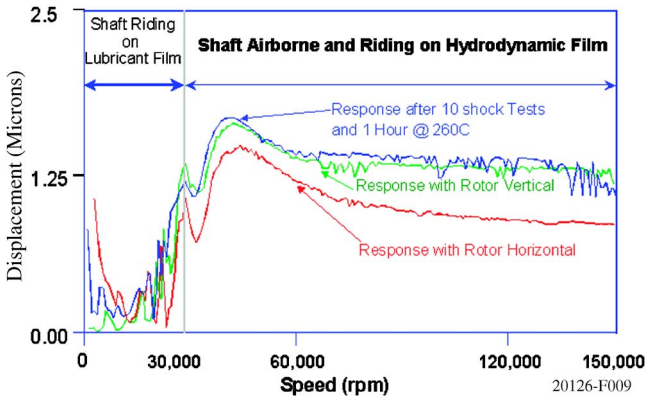

Fig. 18 Summary plot of rotor response after numerous tests

Acknowledgment

The authors would like to thank the Aero Propulsion Directorate of the U.S. Air Force Research Laboratory for supporting this effort under the Small Business Innovative Research program and Mohawk Innovative Technology, Inc. for also supporting the effort. Special thanks are due to David Slezak for his efforts in fabricating the foil bearings used in this test series.

References

[1] Isomura, K., Murayama, M., Yamaguchi, H., Ijichi, N., Asakura, H., Saji, N., Shiga, O., Takahashi, K., Tanaka, S., Genda, T., and Esashi, M., 2002, "Development of Microturbocharger and Microcombustor for a Three-Dimensional Gas Turbine at Microscale," ASME Paper No. GT-2002-3058.

[2] Mohawk Innovative Technology Inc., (MiTi®), 2003, "Mesoscopic Turbojet Simulator Tested at Speeds Above 700,000 rpm on Air Foil Bearings," Mohawk Innovative Technology, Inc. company development newsletter No. 17, pp. 1–4.

[3] Uechi, H., Kimijima, S., and Kasagi, N., 2001, "Cycle Analysis of Gas Turbine-Fuel Cell Hybrid Micro Generation System," *Proceedings of JPGC 01*, New Orleans, LA, June 4–7.

[4] Suriano, F. J., Dayton, R. D., and Woessner, F. G., "Test Experience With Turbine-End Foil Bearing Equipped Gas Turbine Engines," ASME Paper No. 83-GT-73.

[5] O'Brien, P., 1998, "Development of a 50 KW, Low Emmision Turbogenerator for Hybrid Electric Vehicles," International Gas Turbine Congress, Stockholm, Sweden, June 2–5, ASME Paper No. 98-GT-400.

[6] Kim, S. Y., Park. S. R, and Cho, S. Y., 1998, "Performance Analysis of a 50 KW Turbogenerator Gas Turbine Engine," ASME Paper No. 98-GT-209.

[7] Ku, C.-P. R., and Heshmat, H., 1992, "Compliant Foil Bearing Structural Stiffness Analysis: Part I—Theoretical Model Including Strip and Variable Bump Foil Geometry," Trans. ASME, J. Tribol., **114**(2), pp. 394–400.

[8] Ku, C.-P. R., and Heshmat, H., 1993, "Compliant Foil Bearing Structural Stiffness Analysis Part II: Experimental Investigation," Trans. ASME, J. Tribol., **115**(3), pp. 364–369.

[9] Heshmat, H., and Ku, C.-P. R., 1994, "Structural Damping of Self-Acting Compliant Foil Journal Bearings," Trans. ASME, J. Tribol., **116**(1), pp. 76–82.

[10] Ku, C.-P. R., and Heshmat, H., 1994, "Effects of Static Load on Dynamic

Structural Properties in a Flexible Supported Foil Journal Bearings," Trans. ASME, J. Vib. Acoust., **116**(3), pp. 257–262.
[11] Ku, C.-P. R., and Heshmat, H., 1994, "Effects of Frequency on Dynamic Structural Properties in a Self-Acting Foil Journal Bearing," ASME Paper No. 94-GT-100.
[12] Heshmat, H., Gray, S., and Bhushan, B., 1981, "Technology Progress on Compliant Foil Air Bearing Systems for Commercial Applications," Eighth International Gas Bearing Symposium, Leicester Polytechnic, BHRA Fluid Engineering, Cranfield, Bedford, England, Paper No. 6.
[13] Heshmat, H., Shapiro, W., and Gray, S., 1982, "Development of Foil Journal Bearings for High Load Capacity and High-Speed Whirl Stability," ASME J. Lubr. Technol., **104**(2), pp. 149–156.
[14] Heshmat, H., and Shapiro, W., 1984, "Advanced Development of Air-Lubricated Thrust Bearings," Lubr. Eng., **40**(1), pp. 21–26.
[15] Heshmat, H., Walowit, J., and Pinkus, O., 1983, "Analysis of Gas-Lubricated Compliant Thrust Bearings," ASME J. Lubr. Technol., **105**(4), pp. 638–646.
[16] Heshmat, H., Walowit, J., and Pinkus, O., 1983, "Analysis of Gas-Lubricated Compliant Journal Bearings," ASME J. Lubr. Technol., **105**(4), pp. 647–655.
[17] Heshmat, H., Salehi, M., Walton, J. F., and Tomaszewski, M. J., 2004, "Operation of a Mesoscopic Gas Turbine Simulator at Speeds in Excess of 700,000 rpm on Foil Bearings," ASME Turbo Expo 2004, Vienna, Austria.
[18] Swanson, E. E., and Heshmat, H., 2000, "Capabilities of Large Foil Bearings," ASME Paper No. 2000-GT-0387.
[19] Heshmat, H., and Hermel, P., 1993, "Compliant Foil Bearing Technology and Their Application to High Speed Turbomachinery," *The 19th Leeds-Lyon Symposium on Thin Film in Tribology—From Micro Meters to Nano Meters*, Leeds, UK, Sept. 1992, D. Dowson, C. M. Taylor, T. H. C. Childs, and M. Godet, eds., Elsevier Science, New York, pp. 559–575.
[20] Swanson, E. E., Heshmat, H., and Shin, J. S., 2002, "The Role of High Performance Foil Bearings in an Advanced, Oil-Free, Integral Permanent Magnet Motor Driven, High-Speed Turbo-Compressor Operating Above the First Bending Critical Speed," ASME Paper No. GT-2002–30579620.
[21] Walton, J. F., and Heshmat, H., 1999, "Application of Foil Bearings to Turbomachinery Including Vertical Operation," ASME Paper No. 99-GT-391.
[22] Heshmat, H., Walton, J. F., Della Corte, C., and Valco, M., 2000, "Oil-Free Turbocharger Demonstration Paves Way to Gas Turbine Applications," ASME Paper No. 2000-GT-620.
[23] Heshmat, H., 1991, "Analysis of Compliant Foil Bearings With Spatially Variable Stiffness," Paper No. AIAA-91–2102.
[24] Heshmat, H., 1991, "A Feasibility Study on the Use of Foil Bearings in Cryogenic Turbopumps," Paper No. AIAA-91–2103.